FERMILAB-Pub-01/197
hep-ph/0201071
December, 2001

B Physics at the Tevatron: Run II and Beyond

Authors

K. Anikeev[23], *D. Atwood*[18], *F. Azfar*[31], *S. Bailey*[11], *C.W. Bauer*[5], *W. Bell*[10], *G. Bodwin*[1], *E. Braaten*[30], *G. Burdman*[21], *J.N. Butler*[9], *K. Byrum*[1], *N. Cason*[29], *A. Cerri*[33], *H.W.K. Cheung*[9], *A. Dighe*[34], *S. Donati*[33], *R.K. Ellis*[9], *A. Falk*[19], *G. Feild*[45], *S. Fleming*[6], *I. Furic*[23], *S. Gardner*[20], *Y. Grossman*[38], *G. Gutierrez*[9], *W. Hao*[39], *B.W. Harris*[1,26], *J. Hewett*[35], *G. Hiller*[35], *R. Jesik*[14,13], *M. Jones*[32], *P.A. Kasper*[9], *A. El-Khadra*[12], *M. Kirk*[2], *V.V. Kiselev*[17], *J. Kroll*[32], *A.S. Kronfeld*[9], *R. Kutschke*[9], *V.E. Kuznetsov*[4], *E. Laenen*[27], *J. Lee*[8,1], *A.K. Leibovich*[6,9], *J.D. Lewis*[9], *Z. Ligeti*[9,21], *A.K. Likhoded*[17], *H.E. Logan*[9], *M. Luke*[40], *A. Maciel*[28], *G. Majumder*[37], *P. Maksimović*[11,21], *M. Martin*[31], *S. Menary*[46], *P. Nason*[24], *U. Nierste*[9,7], *Y. Nir*[43], *L. Nogach*[17], *E. Norrbin*[22], *C. Oleari*[44], *V. Papadimitriou*[39], *M. Paulini*[6], *C. Paus*[23], *M. Petteni*[13], *R. Poling*[25], *M. Procario*[6], *G. Punzi*[33], *H. Quinn*[35], *A. Rakitine*[23], *G. Ridolfi*[15], *K. Shestermanov*[17], *G. Signorelli*[33], *J.P. Silva*[35], *T. Skwarnicki*[37], *A. Smith*[25], *B. Speakman*[25], *K. Stenson*[42], *F. Stichelbaut*[36], *S. Stone*[37], *K. Sumorok*[23], *M. Tanaka*[41,1], *W. Taylor*[36], *W. Trischuk*[40], *J. Tseng*[23], *R. Van Kooten*[14], *A. Vasiliev*[17], *M. Voloshin*[25,16], *J.C. Wang*[37], *A.B. Wicklund*[1], *F. Würthwein*[23], *N. Xuan*[29], *J. Yarba*[9], *K. Yip*[9,3], *A. Zieminski*[14]

[1] *Argonne National Laboratory, Argonne, Illinois*
[2] *Brandeis Universtiy, Waltham, Massachusetts*
[3] *Brookhaven National Laboratory, Upton, New York*
[4] *University of California, Riverside, California*
[5] *University of California, San Diego, California*
[6] *Carnegie Mellon University, Pittsburgh, Pennsylvania*
[7] *CERN, Geneva, Switzerland*
[8] *Deutsches Elektronen-Synchrotron (DESY), Hamburg, Germany*
[9] *Fermi National Accelerator Laboratory, Batavia, Illinois*
[10] *Glasgow University, Glasgow, United Kingdom*
[11] *Harvard University, Cambridge, Massachusetts*
[12] *University of Illinois, Urbana-Champaign, Illinois*
[13] *Imperial College, London, United Kingdom*
[14] *Indiana University, Bloomington, Indiana*
[15] *INFN, Genoa, Italy*
[16] *Institute for Theoretical and Experimental Physics, Moscow, Russia*
[17] *Institute for High Energy Physics, Protvino, Russia*
[18] *Iowa State University, Ames, Iowa*
[19] *The Johns Hopkins University, Baltimore, Maryland*
[20] *University of Kentucky, Lexington, Kentucky*
[21] *Lawrence Berkeley National Laboratory, Berkeley, California*
[22] *Lund University, Lund, Sweden*
[23] *Massachusetts Institute of Technology, Cambridge, Massachusetts*
[24] *INFN & Università degli Studi di Milano, Milan, Italy*
[25] *University of Minnesota, Minneapolis, Minnesota*
[26] *Robert Morris College, Moon Township, Pennsylvania*
[27] *NIKHEF, Amsterdam, The Netherlands*
[28] *Northern Illinois University, DeKalb, Illinois*
[29] *University of Notre Dame, Notre Dame, Indiana*
[30] *The Ohio State University, Columbus, Ohio*
[31] *Oxford University, Oxford, United Kingdom*
[32] *University of Pennsylvania, Philadelphia, Pennsylvania*
[33] *INFN & Università e Scuola Normale Superiore di Pisa, Pisa, Italy*
[34] *Max-Planck-Institut für Physik, Munich, Germany*
[35] *Stanford Linear Accelerator Center, Stanford, California*
[36] *State University of New York, Stony Brook, New York*
[37] *Syracuse University, Syracuse, New York*
[38] *Technion–Israel Institute of Technology, Haifa, Israel*
[39] *Texas Tech University, Lubbock, Texas*
[40] *University of Toronto, Toronto, Canada*
[41] *University of Tsukuba, Tsukuba, Japan*
[42] *Vanderbilt University, Nashville, Tennessee*
[43] *Weizmann Institute of Science, Rehovot, Israel*
[44] *University of Wisconsin, Madison, Wisconsin*
[45] *Yale University, New Haven, Connecticut*
[46] *York University, Toronto, Canada*

Preface

This report presents the results of the workshop devoted to study *B Physics at the Tevatron: Run II and Beyond*. Like other workshops on the physics potential of Run II of the Tevatron, held at Fermilab from 1998–2000, this workshop brought together theorists from around the world and experimenters from the CDF, DØ, and BTeV collaborations, and elsewhere.

There were two general meetings held at Fermilab: during September 23–25, 1999, and February 24–26, 2000. The working groups also held additional interim meetings to report on their progress and plan further work. The resulting physics studies can be found in Chapters 6–9. The other chapters in this report provide theoretical background on B decays (Chapter 1), common experimental issues (Chapter 2), and brief descriptions of the CDF, DØ, and BTeV detectors (Chapters 3–5).

Flavor physics and CP violation will be a major focus of experimental high-energy physics in the coming decade. The preceding decade verified at a high precision the gauge sector of the Standard Model through a wide range of experimental tests. While many extensions of the Standard Model contain new sources of flavor and CP violation, these sectors of the theory are poorly tested at present. Precise tests of the flavor sector of the Standard Model and the origin of CP violation will come from sometimes competitive and sometimes complementary measurements at the Tevatron and at the e^+e^- B factories. Chapter 10 summarizes the results of the workshops for the most interesting processes.

This report represents the status of the field around the Summer of 2001. Both the state of the theory and the experimental possibilities continue to advance. The results presented here are thus not a final view of what the experiments can achieve. This report concentrates on aspects of B physics accessible mainly to hadron colliders, and it is hoped that it will prove a ready and complete reference and aid new collaboration members and maybe others interested in the field as well.

These workshops could not have been organized without the help of many people. The organizers would like to especially thank the support of Mike Witherell and the Fermilab Directorate; the help of Cynthia Sazama and Patti Poole of the Fermilab Conference Office with the general meetings' organization; and Lois Deringer and Laura Sedlacek in the Fermilab Theory Group for taking care of so many things.

Workshop Structure

The workshop formed four semi-autonomous working groups. Each was led by two theory conveners and a convener from each experiment.

- **CP Violation**
  Yossi Nir, Helen Quinn, Manfred Paulini (CDF), Rick Jesik (DØ), Tomasz Skwarnicki (BTeV)
- **Rare and Semileptonic Decays**
  Aida El-Khadra, Mike Luke, Jonathan Lewis (CDF), Andrzej Zieminski (DØ), Ron Poling (BTeV)
- **Mixing and Lifetimes**
  Ulrich Nierste, Mikhail Voloshin, Christoph Paus (CDF), Neal Cason (DØ), Harry Cheung (BTeV)
- **Production, Fragmentation, Spectroscopy**
  Eric Braaten, Keith Ellis, Eric Laenen, William Trischuk (CDF), Rick Van Kooten (DØ), Scott Menary (BTeV)

Chapters 6 – 9 of this report present the work done in these groups.

The programs of the general meetings, including transparencies of all talks, working group information, and other documentation for this workshop can be found on the World-WideWeb at `http://www-theory.lbl.gov/Brun2/`.

The workshop was organized by Rick Jesik, Andreas Kronfeld, Rob Kutschke, Zoltan Ligeti, Manfred Paulini, and Barry Wicklund.

Contents

List of Figures **xxiv**

List of Tables **xxix**

1 Common Theoretical Issues **1**

1.1 Introduction . . . 1
1.2 CP Violation in the Standard Model . . . 3
1.2.1 Yukawa interactions and the CKM matrix . . . 3
1.2.2 General models . . . 8
1.2.3 CP violation from a unitary CKM matrix . . . 9
1.2.4 Hadronic uncertainties and clean measurements . . . 12
1.3 General Formalism for Mixing and CP Violation . . . 14
1.3.1 Discrete transformations . . . 14
1.3.2 Time evolution and mixing . . . 17
1.3.3 Time evolution of untagged B^0 mesons . . . 23
1.3.4 Time-dependent and time-integrated CP asymmetries . . . 23
1.3.5 Phase conventions . . . 25
1.4 Aspects of CP Violation . . . 26
1.4.1 The three types of CP violation . . . 26
1.4.2 Decays to non-CP eigenstates . . . 29
1.4.3 $\Delta F = 2$ vs. $\Delta F = 1$ CP violation . . . 29
1.5 Theoretical Tools . . . 31
1.5.1 Effective Hamiltonians . . . 31
1.5.2 Heavy quark effective theory . . . 37
1.5.3 Heavy quark expansion . . . 40
1.5.3.1 Inclusive semileptonic B decays . . . 41

1.5.3.2 Inclusive nonleptonic B decays . . . 44
1.5.3.3 B_s width difference, $\Delta\Gamma$ . . . 45
1.5.4 Lattice QCD . . . 45
1.5.4.1 Monte Carlo integration . . . 46
1.5.4.2 Quenched approximation . . . 49
1.5.4.3 Controllable systematic uncertainties . . . 49
1.5.4.4 Strong phases of nonleptonic decays . . . 52
1.6 Constraints from Kaon Physics . . . 52
1.6.1 The neutral kaon system . . . 53
1.6.2 Phenomenology of ϵ_K and ϵ'_K . . . 56
1.6.3 $K \to \pi\nu\bar{\nu}$ . . . 58
1.7 Standard Model Expectations . . . 59
References . . . 62

2 Common Experimental Issues **69**

2.1 Introduction . . . 69
2.2 Separating b and c Hadrons from the Backgrounds . . . 70
2.3 Sources of Backgrounds . . . 73
2.4 Basics of b Production Physics . . . 75
2.5 Production Rates and Interactions Per Crossing . . . 80
2.5.1 The Distribution of Interactions Per Crossing . . . 81
2.6 Flavor Tagging . . . 82
2.6.1 Away Side Tagging . . . 83
2.6.2 Same Side Tagging . . . 84
2.6.3 Overall Tagging Strategy . . . 86
2.7 The Measurement Error on Proper Decay Times . . . 86
2.8 Properties of a Good B Physics Detector . . . 87
2.8.1 Forward vs Central . . . 88
2.8.2 A Precision Vertex Detector . . . 89
2.8.3 Tracking . . . 90
2.8.4 Particle ID . . . 90
2.8.5 Trigger and DAQ . . . 91

2.8.6 EM Calorimetry . . . 92
2.8.7 Muon Detector . . . 92
2.9 Software . . . 93
2.10 Comparison with e^+e^- Machines . . . 94
References . . . 96

3 The CDF Detector 99
3.1 Introduction . . . 99
3.2 CDF Run II Detector . . . 99
3.3 Issues for Central Solenoidal Detectors . . . 105
3.4 Trigger Strategies . . . 106
3.5 Offline Analysis and Simulation . . . 108
3.5.1 Flavor Tagging . . . 108
3.5.2 Monte Carlo Issues . . . 109
References . . . 110

4 The DØ detector 111
4.1 The silicon vertex detector . . . 111
4.2 The central fiber tracker . . . 111
4.3 Electromagnetic pre-shower detectors . . . 113
4.4 Muon Spectrometers . . . 113
4.5 Trigger system . . . 113
4.5.1 Trigger levels . . . 114
4.5.2 Level 1 muon triggers . . . 114
4.5.3 Level 1 muon trigger rates and efficiencies . . . 115
4.5.4 Level 2 and Level 3 muon triggers . . . 116
4.5.5 Low p_T dielectron trigger . . . 118
References . . . 119

5 The BTeV Detector 121
5.1 Introduction . . . 121
5.2 Rationale for a Forward Detector at the Tevatron . . . 121
5.3 Detector Description . . . 122

5.3.1 Dipole Centered on the Interaction Region . . . 123
5.3.2 The Pixel Vertex Detector . . . 123
5.3.3 The Detached Vertex Trigger . . . 125
5.3.4 Charged Particle Identification . . . 126
5.3.5 Electromagnetic Calorimeter . . . 126
5.3.6 Forward Tracking System . . . 127
5.3.7 Muon Detection . . . 128
5.3.8 Data Acquisition System . . . 128
5.4 Simulation and Analysis Tools . . . 128
5.4.1 Tracking and Track Fitting Software . . . 129
5.4.2 Electromagnetic Calorimeter Software . . . 130
5.4.3 Trigger Simulation Software . . . 130
5.4.4 RICH Software . . . 130
5.5 Flavor Tagging . . . 131
5.5.1 Away Side Tagging . . . 131
5.5.1.1 Lepton Tagging . . . 131
5.5.1.2 Kaon Tagging . . . 132
5.5.1.3 Vertex Charge Tagging . . . 132
5.5.1.4 Combining Away Side Tagging Methods . . . 132
5.5.2 Same Side Tagging . . . 133
5.5.3 Summary of Tagging . . . 133
5.6 Schedule . . . 133
5.7 Conclusions . . . 134
References . . . 135

6 CP Violation 137
6.1 Introduction . . . 137
6.1.1 B_s^0–$\bar{B}_s^0$ Mixing . . . 138
6.1.2 B_s^0 Decays . . . 139
6.1.3 CP Violation . . . 140
6.1.4 Tagged Decays . . . 141
6.1.5 Untagged Decays . . . 144

6.1.6 Some Interesting Decay Modes . . . 144
6.1.6.1 $B_s^0 \to J/\psi\phi$ . . . 145
6.1.6.2 $B_s^0 \to J/\psi K_S^0$ . . . 145
6.1.6.3 $B_s^0 \to D_s^{\pm} K^{\mp}$ . . . 147
6.1.7 Penguins in B Decays: General Considerations . . . 148
6.1.8 Penguins in $B^0 \to J/\psi K_S^0$ . . . 150
6.1.9 Penguins in $B^0 \to \pi\pi$ . . . 150
6.1.10 Penguins in $B \to K\pi$ . . . 153
6.1.11 New Physics in B_s^0 Mixing . . . 154
6.1.11.1 Time Dependent CP Asymmetries . . . 155
6.1.11.2 Time Integrated CP Asymmetries . . . 155
6.1.11.3 The Width Difference . . . 155
6.1.11.4 The Semileptonic CP Asymmetry . . . 156
6.2 Study of $B^0 \to J/\psi K_S^0$ . . . 157
6.2.1 $B^0 \to J/\psi K_S^0$: Introduction . . . 157
6.2.2 $B^0 \to J/\psi K_S^0$: CDF Report . . . 158
6.2.3 $B^0 \to J/\psi K_S^0$: DØ Report . . . 160
6.2.4 $B^0 \to J/\psi K_S^0$: BTeV Report . . . 164
6.2.5 $B^0 \to J/\psi K_S^0$: Summary . . . 168
6.3 Study of $B \to \pi\pi/KK$ . . . 168
6.3.1 $B \to \pi\pi/KK$: Introduction . . . 168
6.3.2 $B \to \pi\pi/KK$: CDF Report . . . 170
6.3.2.1 Trigger Issues . . . 170
6.3.2.2 Expected Rates . . . 171
6.3.2.3 Disentangling $\pi\pi$, $K\pi$, KK and πK Final States . . . 172
6.3.2.4 CP Violating Observables . . . 173
6.3.2.5 Measurements on the Tagged Sample . . . 175
6.3.2.6 Extracting CP Violating Phases from $\mathcal{A}_{CP}^{dir}$ and $\mathcal{A}_{CP}^{mix}$ . . . 177
6.3.2.7 Theoretical Error due to $SU(3)$ Breaking . . . 178
6.3.3 $B \to \pi\pi/KK$: DØ Report . . . 179
6.3.4 $B \to \pi\pi/KK$: BTeV Report . . . 181
6.3.5 $B \to \pi\pi/KK$: Summary . . . 187

6.4 Study of $B \to DK$ . . . 189
6.4.1 $B \to DK$: Introduction . . . 189
6.4.1.1 $B_s^0 \to D_s^- K^+$: Introduction . . . 190
6.4.1.2 $B^- \to D^0 K^-$: Introduction . . . 191
6.4.2 $B \to DK$: CDF Report . . . 193
6.4.2.1 $B_s^0 \to D_s^- K^+$: CDF Report . . . 193
6.4.2.2 $B^- \to D^0 K^-$: CDF Report . . . 196
6.4.2.3 Fully Hadronic B Decays Accessible at CDF in RunII . . . 202
6.4.3 $B \to DK$: BTeV Report . . . 203
6.4.3.1 $B_s^0 \to D_s^- K^+$: BTeV Report . . . 203
6.4.3.2 $B^- \to D^0 K^-$: BTeV Report . . . 210
6.4.4 $B \to DK$: Summary . . . 214
6.5 Study of $B \to \rho\pi$ . . . 215
6.5.1 $B \to \rho\pi$: Introduction . . . 215
6.5.2 $B \to \rho\pi$: BTeV Report . . . 217
6.6 Study of $B_s^0 \to J/\psi\,\eta^{(\prime)}$ . . . 221
6.6.1 $B_s^0 \to J/\psi\,\eta^{(\prime)}$: Introduction . . . 221
6.6.2 $B_s^0 \to J/\psi\eta^{(\prime)}$: CDF Report . . . 221
6.6.2.1 Expected Signal . . . 222
6.6.2.2 Reconstruction of Neutrals at CDF . . . 224
6.6.2.3 Expected Background . . . 224
6.6.3 $B_s^0 \to J/\psi\eta^{(\prime)}$: BTeV Report . . . 225
6.6.3.1 Signal Selection . . . 226
6.6.3.2 Background Estimation . . . 229
6.6.3.3 Sensitivity to $\sin 2\beta_s$ . . . 230
6.6.4 $B_s^0 \to J/\psi\eta^{(\prime)}$: Summary . . . 230
6.7 CP Violation: Summary . . . 231
References . . . 235

7 Rare and Semileptonic Decays 241
7.1 Rare Decays: Theory . . . 241
7.1.1 Preliminaries . . . 241

7.1.1.1 The effective Hamiltonian . . . 242
7.1.1.2 Inclusive vs. Exclusive Decays . . . 243
7.1.2 Inclusive Decays . . . 244
7.1.2.1 $B \to X_s\gamma$ . . . 244
7.1.2.2 $B \to X_s\ell^+\ell^-$ . . . 246
7.1.3 Exclusive Decays . . . 251
7.1.3.1 Hadronic Matrix Elements and Form Factors . . . 251
7.1.3.2 Lattice QCD . . . 253
7.1.3.3 $B \to K^*\ell^+\ell^-$ and $B \to K\ell^+\ell^-$ . . . 254
7.1.3.4 $B \to K^*\gamma$ and Related Decays . . . 266
7.1.3.5 $B_{s,d} \to \ell^+\ell^-$ . . . 268
7.1.4 Expectations for Physics Beyond the Standard Model . . . 270
7.2 Rare Decays: Experiment . . . 276
7.2.1 Rare Decays at D0 . . . 276
7.2.1.1 Monte-Carlo Samples . . . 277
7.2.1.2 The Exclusive Channel $B_d^0 \to K^{*0}\mu^+\mu^-$ . . . 279
7.2.1.3 The Inclusive Decay $B \to X_s\ell^+\ell^-$ . . . 282
7.2.1.4 The Exclusive Channel $B_s^0 \to \mu^+\mu^-$ . . . 285
7.2.2 Rare Decays at CDF . . . 285
7.2.2.1 Radiative B Meson Decays . . . 285
7.2.2.2 Radiative b Baryon Decays . . . 287
7.2.2.3 $B_d \to K^{*0}\mu\mu$ Decays . . . 288
7.2.2.4 $B \to \mu^+\mu^-$ . . . 294
7.2.2.5 Summary . . . 294
7.2.3 Rare Decays at BTeV . . . 295
7.2.3.1 The Exclusive Channel $B^0 \to K^{*0}\mu^+\mu^-$ . . . 295
7.2.3.2 The Exclusive Channel $B^+ \to K^+\mu^+\mu^-$ . . . 299
7.2.3.3 The Inclusive Decay $b \to s\ell^+\ell^-$ . . . 300
7.3 Summary of Rare Decays . . . 301
7.4 Semileptonic Decays: Theory . . . 302
7.4.1 Introduction . . . 302
7.4.2 Decays to Charm Flavored Final States . . . 303

7.4.2.1 $B \to D^{(*)}\ell\bar{\nu}$ . . . 303
7.4.2.2 $\Lambda_b \to \Lambda_c\ell\bar{\nu}$ . . . 304
7.4.3 $B \to \pi(\rho)\ell\bar{\nu}$ . . . 306
7.5 Semileptonic Decays: Experiment . . . 306
7.5.1 Semileptonic Decays at CDF . . . 306
7.5.1.1 Introduction . . . 306
7.5.1.2 Physics Goals . . . 307
7.5.1.3 Simulations . . . 308
7.5.1.4 Selection Criteria . . . 308
7.5.1.5 Signal Rate Expectations . . . 310
7.5.1.6 Q^2 Spectrum . . . 312
7.5.1.7 Summary . . . 316
7.5.2 Estimating the BTeV Potential for Semileptonic Decays . . . 316
7.5.2.1 Signal and Background . . . 317
7.5.2.2 Semileptonic Reach . . . 318
7.5.2.3 Summary . . . 321
7.6 Summary of Semileptonic Decays . . . 321
References . . . 322

8 Mixing and Lifetimes **331**
8.1 Overview . . . 331
8.2 Theory of heavy hadron lifetimes . . . 332
8.2.1 OPE for inclusive weak decay rates . . . 333
8.2.2 The parton decay rate . . . 335
8.2.3 Chromomagnetic and time dilation effects in decay rates . . . 336
8.2.4 $L_{eff}^{(3)}$ Coefficients and operators . . . 338
8.2.5 Effects of $L_{eff}^{(3)}$ in mesons . . . 341
8.2.6 Effects of $L_{eff}^{(3)}$ in baryons . . . 343
8.2.7 Relation between spectator effects in baryons and the decays $\Xi_Q \to \Lambda_Q\,\pi$ . . . 348
8.2.8 Summary on predictions for lifetimes . . . 351
8.3 Theory of $B^0 - \overline{B}^0$ mixing . . . 352

8.3.1 Mass difference . . . 352
8.3.2 Width difference . . . 354
8.3.2.1 Calculation . . . 354
8.3.2.2 Phenomenology of $\Delta\Gamma_s$ . . . 358
8.3.2.3 Phenomenology of $\Delta\Gamma_d$ . . . 370
8.3.3 CP Asymmetry in Flavor-specific Decays . . . 371
8.3.4 Angular analysis to separate the CP components . . . 373
8.3.5 CP-odd and CP-even components in $B_s \to J/\psi\phi$ . . . 373
8.3.6 The transversity angle distribution . . . 374
8.3.7 Three-angle distribution in $B_s \to J/\psi(\to l^+l^-)\,\phi(\to K^+K^-)$ . . . 375
8.3.8 Angular moments method . . . 376
8.3.9 $D^0 - \overline{D}^0$ mixing . . . 377
8.3.10 New Physics Effects in Meson Mixing . . . 378
8.3.10.1 B_d Mixing . . . 379
8.3.10.2 B_s Mixing . . . 382
8.3.10.3 Mixing in the Charm Sector . . . 382
8.4 Interesting decay modes . . . 384
8.5 Introduction and Physics Input for CDF . . . 386
8.5.1 Physics Input . . . 386
8.5.2 Detector Simulation . . . 389
8.6 Projections for Δm . . . 393
8.6.1 B_s mixing measurement at CDF . . . 393
8.6.1.1 Projections for Sensitivity to x_s . . . 394
8.6.1.2 Flavor Tagging Efficiency . . . 394
8.6.1.3 B_s Mixing with Semileptonic Decays . . . 396
8.6.1.4 B_s Mixing with Hadronic Decays . . . 399
8.6.2 B_s mixing measurement at DØ . . . 402
8.6.3 Measurement of B_s Mixing in BTeV . . . 406
8.6.3.1 Yields, Resolutions and Signal-to-Background Ratios . . . 406
8.6.3.2 Computation of the x_s Reach . . . 410
8.6.4 Summary of Projections for Mixing . . . 413
8.7 Projections for $\Delta\Gamma$ . . . 414

8.7.1 B_s Lifetime Difference in CDF . . . 414
8.7.1.1 Lifetime Difference Measurements . . . 415
8.7.1.2 Related Branching Fractions . . . 416
8.7.1.3 Combined CDF Projection . . . 418
8.7.2 Estimate of Sensitivity on $\Delta\Gamma$ in BTeV . . . 418
8.7.2.1 Signal yields and backgrounds . . . 418
8.7.2.2 Results for $\Delta\Gamma/\Gamma_{B_s}$ Sensitivity . . . 422
8.7.3 Summary of Projections for $\Delta\Gamma$ . . . 425
8.8 Projections for Lifetimes . . . 426
8.8.1 b Hadron Lifetimes at CDF . . . 426
8.8.1.1 Run I Results at CDF . . . 426
8.8.1.2 Run II Projections for CDF . . . 428
8.8.2 Lifetime measurements at DØ . . . 430
8.8.3 Summary of Projections for Lifetimes . . . 432
8.9 Conclusions . . . 433
References . . . 434

9 Production, Fragmentation and Spectroscopy 441
9.1 Open beauty production . . . 441
9.1.1 The theory of b-quark production . . . 441
9.1.2 Run II reach for b-quark production . . . 445
9.1.3 DØ Study of b Jet Production . . . 445
9.1.3.1 Introduction . . . 446
9.1.3.2 The p_t Spectrum of b Jets . . . 447
9.1.3.3 b Tagging for Run II . . . 448
9.1.3.4 A Measurement Proposal . . . 449
9.1.3.5 Di-b-jets with DØ in Run II. . . . 449
9.1.3.6 b Quark Production . . . 450
9.1.3.7 Conclusion . . . 451
9.1.4 CDF P_T Reach in the B Cross Section . . . 451
9.1.4.1 Run II P_T Reach . . . 452
9.1.4.2 Conclusions . . . 453

9.2 Quarkonium production . . . 454
9.2.1 Spectroscopy . . . 454
9.2.2 Theory of quarkonium production . . . 457
9.2.2.1 Bottomonium . . . 460
9.2.2.2 Charmonium . . . 465
9.2.2.3 Quarkonium polarization . . . 468
9.2.3 Polarization in quarkonium production . . . 470
9.2.3.1 NRQCD predictions for ψ meson polarization . . . 471
9.2.3.2 CDF polarisation measurements from Run I . . . 472
9.2.3.3 Polarization predictions for Run II . . . 472
9.2.3.4 Upsilon production and polarization in CDF Run II . . . 473
9.3 The B_c Meson . . . 476
9.3.1 Spectroscopy . . . 477
9.3.2 Production . . . 478
9.3.3 Theory of B_c Decays . . . 481
9.3.3.1 Lifetime and inclusive decay rates . . . 483
9.3.3.2 Semileptonic and leptonic modes . . . 485
9.3.3.3 Nonleptonic modes . . . 486
9.3.3.4 Discussion and conclusions . . . 487
9.3.4 DØ Study of B_c . . . 488
9.3.4.1 Introduction . . . 488
9.3.4.2 DØ simulations . . . 488
9.3.4.3 Results . . . 489
9.3.5 CDF Projections for B_c^+ yield . . . 491
9.3.5.1 Introduction . . . 491
9.3.5.2 Monte Carlo generation and simulation . . . 492
9.3.5.3 Selection Criteria for the $B_c^+ \to J/\psi\pi^+$ decay channel . . . 492
9.3.5.4 Acceptance Calculation using QFL′ . . . 493
9.3.5.5 Yield estimate for the $B_c^+ \to J/\psi\pi^+$ decay channel . . . 495
9.3.5.6 Yield estimate for the $B_c^+ \to B_s^0\pi^+$ decay channel . . . 497
9.3.5.7 Yield estimate for the $B_c^+ \to J/\psi l^+\nu$ decay channel . . . 498
9.3.5.8 Conclusion . . . 498

9.4 Doubly-heavy Baryons . . . 499
9.4.1 Spectroscopy . . . 499
9.4.2 Production . . . 500
9.4.3 Decays . . . 503
9.4.4 Experimental observability . . . 505
9.5 Fragmentation . . . 508
9.5.1 Perturbative fragmentation . . . 511
9.5.1.1 Heavy-quark fragmentation in e^+e^- collisions . . . 511
9.5.1.2 Impact of SLD data . . . 512
9.5.1.3 Heavy-quark fragmentation in $p\bar{p}$ collisions . . . 514
9.5.2 Fragmentation in the nonperturbative regime . . . 517
9.5.3 Beam drag . . . 520
9.5.4 Heavy-quark fragmentation ambiguities . . . 525
9.5.5 Experimental Impact . . . 528
References . . . 530

10 Summary and Highlights **539**

Index **545**

List of Figures

1.1 The unitarity triangle . . . 10
1.2 Standard Model box diagrams inducing $B_d^0 - \overline{B}_d^0$ mixing. . . . 18
1.3 Standard Model weak decay diagrams . . . 32
1.4 Effective Hamiltonian weak decay diagrams . . . 33
1.5 OPE diagram for semileptonic and radiative B decays. . . . 42
1.6 Analytic structure of $T^{\mu\nu}$ in the $q \cdot v$ plane. . . . 42
1.7 OPE diagrams for nonleptonic B decays. . . . 44
1.8 OPE diagram for the B_s width difference. . . . 45
1.9 The allowed region in the $\bar{\rho} - \bar{\eta}$ plane. . . . 60
1.10 The allowed region in the $\sin 2\alpha - \sin 2\beta$ plane. . . . 61
1.11 The allowed region in the $\sin 2\beta - \gamma$ plane. . . . 61

2.1 A cartoon of a $b\bar{b}$ event . . . 72
2.2 Production cross-section vs η for B mesons (from PYTHIA) . . . 76
2.3 $\sigma(\mu$ from B decay) vs y_μ . . . 77
2.4 $\sigma_{b\bar{b}}$ as a function of $\beta\gamma$ vs η . . . 78
2.5 Production angle correlations for $B\overline{B}$ pairs . . . 79
2.6 Azimuthal angle correlation between $B\overline{B}$ pairs . . . 79
2.7 Quark diagrams for same side tagging . . . 85

3.1 CDF detector elevation view . . . 100
3.2 CDF particle identification . . . 105

4.1 The DØ detector . . . 112
4.2 The DØ silicon vertex detector . . . 112
4.3 Expected impact parameter uncertainty dependence on track momentum and polar angle. . . . 117

4.4 Significance distribution for STT tracks reconstructed in $B_d^0 \to K^{*\circ}\mu^+\mu^-$ events with all four charge particles produced with $p_T \geq 0.5$ GeV/c. . . . 117
4.5 $b\bar{b}$ event tagging efficiency as a function of S_{min} with either one or two tracks in the event satisfying the condition $S > S_{min}$. . . . 118

5.1 A Sketch of the BTeV Detector . . . 122
5.2 The Resolution of the Pixel Devices . . . 124
5.3 The B Momentum Distribution . . . 124
5.4 Separation of $B_s \to D_s^+K^-$ and $B_s \to D_s^+\pi^-$ with the RICH . . . 126
5.5 Radial Distributions of Generated and Detected Photons . . . 127

6.1 Dependence of CMU-CMU $J/\psi K_S^0$ yields on the lower p_T muon threshold at CDF. . . . 159
6.2 Reconstructed $B_s^0 \to J/\psi\phi$ events from CDF RunI data. . . . 161
6.3 Reconstructed $J/\psi \to \mu\mu$ and $K_S^0 \to \pi^+\pi^-$ invariant mass in $B^0 \to J/\psi K_S^0$ events. . . . 162
6.4 Reconstructed B mass in $B \to J/\psi K_S^0$ events. . . . 163
6.5 Distributions of L/σ_L for J/ψ candidates from the decays of b hadrons and prompt J/ψ candidates. . . . 165
6.6 The $J/\psi K_S^0$ invariant mass distribution at BTeV. . . . 166
6.7 Feynman diagrams in charmless hadronic B meson decays contributing to $B^0 \to \pi^+\pi^-$ and $B_s^0 \to K^+K^-$. . . . 169
6.8 Two-track invariant mass for $B \to \pi\pi$, $K\pi$, KK and πK at CDF. . . . 173
6.9 Expected time-dependent CP violation in $B_s^0 \to K^+K^-$ for different values of $\mathcal{A}_{CP}^{dir}$, $\mathcal{A}_{CP}^{mix}$ and $\Delta\Gamma$. . . . 175
6.10 Effect of two-track trigger on $B_s^0 \to K^+K^-$ lifetime distribution. . . . 176
6.11 Impact of $SU(3)$ breaking. . . . 179
6.12 Reconstructed invariant mass for $B^0 \to \pi^+\pi^-$ at DØ. . . . 182
6.13 Distribution of signal and background for the most important vertex and kinematic variables at BTeV. . . . 183
6.14 Two body $\pi^+\pi^-$ mass without and with particle identification at BTeV. . . . 184
6.15 RICH event selection at BTeV. . . . 185
6.16 Two body K^+K^- mass without and with particle identification at BTeV. . . . 187
6.17 Mass plot for the $B_s^0 \to D_s^-K^+$ signal and various physics backgrounds at CDF. . . . 194

6.18 Example signal to background ratio as a function of the dE/dx separation power at CDF. 195
6.19 The error on $\sin(\gamma \pm \delta)$ as a function of the number of $B_s^0 \to D_s^- K^+$ events. 197
6.20 The error on $\sin(\gamma \pm \delta)$ as a function of different parameters at CDF. 197
6.21 Deviation of the value of γ obtained from the fit versus the value used as input in the Monte Carlo study. 199
6.22 Invariant mass distribution of pairs of D daughter particles at CDF. 201
6.23 L/σ_L and mass peaks for B_s^0 and D_s^- at BTeV. 206
6.24 Proper time resolution for B_s^0 : $t_{\rm gen} - t_{\rm rec}$ (ns). 207
6.25 Comparison of $B_s^0 \to D_s^- K^+$ signal and background at BTeV. 209
6.26 Fitted values of γ, δ, and $\Delta\Gamma$. 210
6.27 $B^- \to D^0 K^-$ signal mass and background at BTeV. 212
6.28 Fitted values of γ and b at BTeV. 214
6.29 Invariant $\pi^+\pi^-\pi^0$ mass distributions for background and signal events for $B \to \rho^0\pi^0$ at BTeV. 219
6.30 Distribution of B_s^0 invariant mass minus the nominal PDG mass. 223
6.31 Invariant diphoton mass distribution showing a $\pi^0 \to \gamma\gamma$ and $\eta \to \gamma\gamma$ signal in CDF RunI data. 224
6.32 $B_s^0 \to J/\psi\eta$ background study using CDF RunI J/ψ data. 225
6.33 The invariant mass distributions for $\eta \to \gamma\gamma$, (b) $\eta' \to \pi^+\pi^-\gamma$, and $\eta' \to \pi^+\pi^-\eta$ with $\eta \to \gamma\gamma$ at BTeV. 228
6.34 The dimuon invariant mass and reconstructed B_s^0 mass for all three final states of η and η' summed together. 228
6.35 Distributions of backgrounds in several variables compared with the signal for $\eta' \to \rho\gamma$. 229
6.36 Compilation of measurements of $\sin 2\beta$ as of August 2001. 232

7.1 The differential decay spectrum for the decay $B \to X_s \ell^+\ell^-$. 248
7.2 The normalized forward backward asymmetry. 249
7.3 Constraints on the semileptonic form-factors $V(0)$ and $A_1(0)$ from $B \to K^*\gamma$ data plus HQSS together with the relation from the LEL. 259
7.4 The dilepton invariant mass distribution in $B \to K\mu^+\mu^-$ decays, using the form factors from LCSR. 261
7.5 The dilepton invariant mass distribution in $B \to K^*\mu^+\mu^-$ decays. 261
7.6 The non-resonant forward-backward asymmetry of leptons A_{FB} for $B \to K^* e^+ e^-$ as a function of the dilepton mass s. 264

7.7 Dominant SM diagrams for $B_{s,d} \to \ell^+\ell^-$. 268
7.8 The forward-backward asymmetry in $B_d \to K^{*0}\mu\mu$ decay as a function of $s = M_{\mu\mu}^2$ predicted with the Standard Model, SUGRA and MIA-SUSY. . . 271
7.9 Expected number of dimuon events in $2\,{\rm fb}^{-1}$ data, due to $Q\bar{Q}$ production . 278
7.10 Comparison of the expected dimuon mass distributions for $B_d^0 \to K^{*0}\mu^+\mu^-$ from phase space and predicted by theory. 279
7.11 Trigger rate dependence on the dimuon mass for events preselected with kinematic cuts $|\,\eta^\mu\,| < 1.6$, $p_T^\mu > 1.5$ GeV/c and $p_T^{\mu\mu} > 5$ GeV/c. 280
7.12 Dimuon mass distribution in the decay $B_d^0 \to K^{*0}\mu^+\mu^-$ 282
7.13 Expected dimuon mass distributions due to non-resonant $Q\bar{Q}$ production. . 283
7.14 The calculated differential branching fraction for the decay $B \to X_s\mu^+\mu^-$, as a function of $m_{\mu\mu}$. 284
7.15 A_{FB} with 50 and 400 events of the $B_d \to K^*\mu\mu$ signal and $S/B = 1$. 289
7.16 The forward-backward asymmetry for the background events obtained from the Run 1 data. 291
7.17 The forward-backward asymmetry in Ref [141], and a likelihood function for extracting the asymmetry zero-point M_0. 292
7.18 A_{FB} and M_0 with 1000 $B_d \to K^*\mu\mu$ events and $S/B = 1$. 293
7.19 Distributions of cut variables for signal (points) and $b\bar{b}$ background (hatched) MCFAST events. 296
7.20 Distributions of tagged $B^0 \to K^{*0}\mu^+\mu^-$ signal (left) and 4.4 pb^{-1} of $b\bar{b}$ background (right) MCFAST events. 298
7.21 Expected forward-backward asymmetry and number of events as a function of $m(\mu^+\mu^-)$ for signal events after one year of running. 299
7.22 Distributions of $B^+ \to K^+\mu^+\mu^-$ signal (left) and 10 pb^{-1} of $b\bar{b}$ background (right) events. 301
7.23 Dependence of the trigger rate on the impact parameter cut for the muon-trigger test data and the $b\bar{b} \to \Lambda_b X \to \Lambda_c\mu\nu$ Monte Carlo. 309
7.24 The distributions of $\Delta\phi(\mu, SVT)$, and $M_T(\mu, SVT)$ for the test-run data and the $b\bar{b} \to \Lambda_b \to \Lambda_c\mu\nu$ signal after impact parameter cut. 310
7.25 Distributions of $\Delta\phi(\mu, SVT)$, and $M_T(\mu, SVT)$ for the test-run data (bottom plot) and the $b\bar{b} \to B_s X \to D_s\pi$ signal (top plot). 311
7.26 Monte Carlo simulation of the Q^2 distribution in $\Lambda_b \to \Lambda_c\ell\bar{\nu}$ decay. 313
7.27 The resolution of the reconstructed Q^2 distribution is shown in the top plot. The reconstruction efficiency is shown in the bottom plot. 313
7.28 Q^2 distribution for generator level and reconstructed after correcting for efficiency. 314

7.29 Distribution of the maximum P_T of π's from higher order decays. 315

7.30 Comparison of impact parameter significance of all 3 categories of tracks (protons, kaons and pions). 316

7.31 $D^* - D^0$ mass difference distribution for $B^0 \to D^* \mu\nu$ signal and backgrounds; pKπ invariant mass distribution for $\Lambda_b \to \Lambda_c \mu\nu$ signal and backgrounds. . . 319

7.32 q^2/q^2_{max} resolution for (a) $B^0 \to D^* \mu\nu$ and (b) $\Lambda_b \to \Lambda_c \mu\nu$. 320

7.33 q^2/q^2_{max} resolution for $\Lambda_b \to \Lambda_c \mu\nu$ where the Λ_c comes from Σ_c, and $\Lambda_b \to \Lambda_c \mu\nu$ where half of the Λ_c's come from Σ_c's and half come from Λ_b's. 320

8.1 Graphs for three first terms in OPE for inclusive decay rates: the parton term, the chromomagnetic interaction, and the four-quark term. 334

8.2 The values of the extracted matrix elements x and y in GeV^3 vs. the normalization point parameter $\kappa = \alpha_s(\mu)/\alpha_s(m_c)$. 346

8.3 Leading order diagrams determining Γ^s_{12}. Only the CKM-favored contribution $\xi^{s*2}_c \Gamma^{cc}_{12}$ is shown. 355

8.4 The definitions of angles θ, φ, ψ. Here θ is the "transversity" angle. 374

8.5 The model independent analysis in the $\rho - \eta$ plane 380

8.6 Δm_D in the (a) four generation Standard Model; (b) two-Higgs-doublet model II; and (c) flavor-changing Higgs model with tree-level contributions. 383

8.7 K factor as a function of the $M_{\ell D_s}$ (top), and K factor distribution after the $M_{\ell D_s}$ correction (bottom). 396

8.8 K factor distributions after 3D vertexing correction with vertex detector resolutions of $\sigma_{t_0} = 60$ fs and $\sigma_{L_z} = 50$ μm. 397

8.9 K factor and time resolution for $B_s \to \ell\nu D_s$ decays. 398

8.10 Sensitivity for measuring x_s of the B_s semileptonic decays for the lepton plus displaced track trigger (left) and the two track trigger (right). 399

8.11 Example of a single toy Monte Carlo experiment: the mixed asymmetry distribution, and negative log-likelihood from the fit as a function of x_s . . 401

8.12 Average significance of mixing measurements expected as a function of x_s for various event yields and signal-to-background ratios. 402

8.13 Luminosity required to achieve a 5 standard deviation observation of mixing (left) and the statistical uncertainty as a function of x_s (right). 403

8.14 Effective mass distributions for the reconstructed (a) $\mu^+\mu^-$ system; (b) π^+K^- system; and (c) $\mu^+\mu^-\pi^+K^-$ system. 404

8.15 Reconstructed B_s decay length and proper time distributions. 405

8.16 Mini Monte Carlo proper lifetime plots of a) unmixed and b) mixed decays for a generated value of $x_s = 40$. 411

8.17 The same likelihood function as in part c) of the previous figure but obtained using the integral method described in the text. 412

8.18 The x_s reach of the BTeV detector. The curves indicate the number of years of running required for a measurement with a statistical significance of $5\,\sigma$. 414

8.19 D^+_s, D^-_s invariant mass spectra for the three decay modes $B_s \to D_s D_s$ (solid), $B_s \to D^{(*)}_s D_s$ (large dashes) and $B_s \to D^{(*)}_s D^{(*)}_s$ (small dashes). 417

8.20 The $\mu^+\mu^-$ invariant mass (a) and the K^+K^- invariant mass (b) for a $b\bar{b} \to J/\psi\,\phi X$ background samples. 419

8.21 The $\mu^+\mu^- K^+K^-$ invariant mass for $b\bar{b} \to J/\psi\,\phi X$ background and $B^0_s \to J/\psi\,\phi$ signal samples 420

8.22 (a) Proper time distribution for reconstructed $B^0_s \to J/\psi\,\phi$; (b) Reduced proper time distribution for the same decays, the line is an exponential fit. . 421

8.23 (a) Reduced proper time distribution for reconstructed $B^0_s \to J/\psi\,\phi$ decays that pass the Level 1 vertex trigger; (b) Lifetime correction function. 422

8.24 Summary of lifetime measurements from CDF during Run I. 427

8.25 J/ψ mass distribution. 432

8.26 Λ^0 mass distribution. 432

8.27 Λ^0_b mass distribution. 433

8.28 $\tau(\Lambda^0_b)_{meas} - \tau(\Lambda^0_b)_{gen}$. 433

9.1 Diagrams for heavy quark production at lowest order. 442

9.2 The parton level cross section for the gg process. 443

9.3 The parton level cross section for the $q\bar{q}$ process. 444

9.4 The parton level cross section for the gq process. 445

9.5 Contributions to the total cross section in LO and NLO. 446

9.6 The differential b jet cross section 447

9.7 A summary of all systematic uncertainties expressed as a relative percentage. 448

9.8 A summary of b production (integrated) cross section measurements. 450

9.9 The cross section reach vs. B P_T for electron $E_T > 8$ GeV 453

9.10 The cross section reach vs. B P_T for electron $E_T > 12$ GeV 454

9.11 Spectrum of $c\bar{c}$ mesons. 455

9.12 Spectrum of $b\bar{b}$ mesons 456

9.13 Inclusive cross section for $\Upsilon(1S)$ at Run I. 461

9.14 Inclusive cross section for $\Upsilon(2S)$ at Run I. 462

9.15 Inclusive cross section for $\Upsilon(3S)$ at Run I. 462
9.16 Percentage increase in the inclusive $\Upsilon(1S)$ cross section. 464
9.17 Prompt cross section for J/ψ at Run I. 466
9.18 Prompt cross section for $\psi(2S)$ at Run I. 466
9.19 Percentage increase in prompt J/ψ cross section. 468
9.20 Polarization variable α for prompt J/ψ at Run I. 469
9.21 Polarization variable α for prompt $\psi(2S)$ at Run I. 470
9.22 Polarization variable α for inclusive Υ at Run I. 471
9.23 The fitted polarization of J/ψ mesons from prompt production and B-hadron decay. 473
9.24 The fitted polarization of $\psi(2S)$ mesons from prompt production and B-hadron decay. 474
9.25 The expected precision for a polarization measurement in Run II of promptly produced J/ψ and $\psi(2S)$ mesons. 475
9.26 The differential cross-section for $\Upsilon(1S)$ production measured by CDF in Run I. 476
9.27 The polarisation measured in $\Upsilon(1S)$ decays by CDF in Run I. 477
9.28 Predicted spectrum for the B_c mesons. 478
9.29 Differential cross sections for the B_c meson and doubly-heavy baryons. . . . 480
9.30 Integrated cross sections for the B_c meson and doubly-heavy baryons. . . . 481
9.31 The B_c lifetime calculated in QCD sum rules. 484
9.32 The differential cross section for the B_c meson used in the following studies. 489
9.33 Kinematic distributions of (a) p_T and (b) η for all particles (open histograms) and for B_c semileptonic decay products (dark histograms) 490
9.34 (a) Impact parameter divided by its error for track from $B_c \to J/\psi\ell\nu$; (b) efficiency of future silicon track trigger as a function of cut on b/σ_b. 492
9.35 (a) $\mu^+\mu^-$ invariant mass distribution in $B_c \to J/\psi\ell\nu$ events; (b) tri-lepton invariant mass distribution that can be used to extract the B_c mass. 493
9.36 P_t distribution of B_c^+ mesons 494
9.37 P_t distribution of B^+ mesons 494
9.38 The ratio $\sigma \times BR(B_c^+ \to J/\psi\pi^+)/\ \sigma \times BR(B^+ \to J/\psi K^+$ 496
9.39 Mass distribution of B_c^+ mesons in GeV/c^2 498
9.40 Impact distribution of all charged decay products in the cascade decays of Ξ_{cc}^{++} via Λ_c, D^0, and D^+ compared to the same distribution of the decay products from B_c and B_d^0. 507

9.41 Fit to SLD data of Peterson and Euler nonperturbative fragmentation functions 513
9.42 Functional forms of the nonperturbative fragmentation functions 514
9.43 The effect of a Peterson fragmentation function on the inclusive b cross section. 515
9.44 Effects of beam drag at HERA vs NLO theory and data 520
9.45 Example of a string configuration in a $p\bar{p}$ collision. 522
9.46 (a) Average rapidity shift Δy as a function of y for some different p_T cuts for a $p\bar{p}$ collider at 2 TeV. (b) Average rapidity shift Δy_{sign} as a function of p_T for some different rapidity cuts. 524
9.47 Bottom production at the Tevatron 525
9.48 Bottom production at the Tevatron 526
9.49 Effect of the different four-vector smearing methods on the P_T distribution of the B-meson. 527
9.50 Commutativity of boosting and fragmenting for pseudo-rapidity distribution of the B-meson. 527
9.51 Commutativity of boosting and fragmenting for P_T distribution of the B-meson. 528

List of Tables

1.1 C, P and T transformation properties of quark bilinears . . . 15
1.2 C, P and T transformation properties of bosons . . . 16
1.3 Wilson coefficients in the leading and next-to-leading order . . . 36

2.1 Tevatron parameters for Run II . . . 70
2.2 Approximate values of cross-sections . . . 70
2.3 Summary of the important properties of $b\bar{b}$ production. . . . 80
2.4 Interactions per beam crossing . . . 81

3.1 CDF tracking systems . . . 101
3.2 CDF calorimeter segmentation . . . 102
3.3 CDF central/plug calorimeters . . . 103
3.4 CDF muon detectors . . . 104
3.5 CDF B-physics trigger rates . . . 108
3.6 CDF B-physics event yields . . . 108

4.1 Trigger efficiencies for dimuon events preselected with the kinematic cuts listed 116

5.1 Level 1 Trigger Efficiencies in BTeV . . . 125
5.2 Summary of Tagging Power in BTeV . . . 134

6.1 Summary of flavour tagging methods used in the measurement of $\sin 2\beta$ at CDF. . . . 160
6.2 The expected number of $B^0 \to J/\psi K^0_S$ events at DØ. . . . 163
6.3 Summary of flavour tagging methods at DØ. . . . 164
6.4 Summary of the sensitivity to $\sin 2\,\beta$ using $B \to J/\psi K^0_s$ at BTeV. . . . 167
6.5 Level 1 trigger criteria and event rates for three operating scenarios of the Tevatron. . . . 170

6.6 Parameters used in the Toy Monte Carlo study to determine the errors on the $B \to \pi\pi$, $K\pi$, KK and πK yields. . . . 174
6.7 Inverse of covariance matrix based on analytical calculations. . . . 176
6.8 Expected number of $B^0 \to \pi^+\pi^-$ events at DØ. . . . 181
6.9 Projected yield of $B^0 \to \pi^+\pi^-$ and the uncertainty on $\mathcal{A}_{CP}$ at BTeV. . . . 186
6.10 Projected yield of $B^0_s \to K^+K^-$ and fake rates at BTeV. . . . 188
6.11 Central values of parameter used in the study of $B^0_s \to D^-_s K^+$ at CDF. . . . 196
6.12 Estimated branching ratios of decays involved in the analysis of $B^- \to D^0 K^-$ at CDF. . . . 198
6.13 L2 trigger cuts proposed for multibody B decay selection. . . . 199
6.14 Expected event yields for $B^- \to D^0 K^-$ for different Tevatron operation scenarios. . . . 200
6.15 Branching ratios of potential physics backgrounds at CDF. . . . 200
6.16 Estimated total branching ratio and expected number of events per 1 fb^{-1} for several hadronic B^0 decay modes. . . . 204
6.17 Estimated total branching ratio and expected number of events per 1 fb^{-1} for several hadronic B^+ decay modes. . . . 205
6.18 Estimated total branching ratio and expected number of events per 1 fb^{-1} for several hadronic B^0_s decay modes. . . . 205
6.19 Projected number of reconstructed $B^0_s \to D^-_s K^+$ decays at BTeV. . . . 207
6.20 Comparison of RICH efficiency at BTeV. . . . 209
6.21 Results of fits with variation of input parameters at BTeV. . . . 211
6.22 Selection requirements for $D^0 \to K^-\pi^+$ and $D^0 \to K^+K^-$. . . . 211
6.23 Projected number of reconstructed $B^- \to K^- D^0$ events at BTeV. . . . 212
6.24 Input Values of parameters and results of fit for γ at BTeV. . . . 213
6.25 Selection Criteria for $B \to \rho\pi$ at BTeV. . . . 219
6.26 Summary of BTeV $B \to \rho\pi$ event yields. . . . 220
6.27 Constraints used for the generation of Monte Carlo data for $J/\psi\eta$ at CDF. 222
6.28 Input branching fractions for $B^0_s \to J/\psi\eta^{(\prime)}$ used for BTeV study. . . . 226
6.29 Projected yield of $B^0_s \to J/\psi\eta^{(\prime)}$ and uncertainty on $\sin 2\beta_s$ at BTeV. . . . 230

7.1 SM values of the Wilson coefficients at NLO ($C_7^{\rm eff} \equiv C_7 - C_5/3 - C_6$). . . . 242
7.2 Current status of rare semileptonic B decays. . . . 262
7.3 Form-factor predictions from Ref. [72]. . . . 267

7.4 SM branching ratios for B_d and B_s into $\tau^+\tau^-$, $\mu^+\mu^-$ and e^+e^-. 270
7.5 Expected numbers of events for the $B_d^0 \to K^{*0}\mu^+\mu^-$ process with different analysis cuts. 281
7.6 Expected number of recorded $B \to X_s\mu^+\mu^-$ events in the mass window $3.9 < m_{\mu\mu} < 4.4$ GeV with different analysis cuts. 284
7.7 Expected number of $B_s^0 \to \mu^+\mu^-$ events. 285
7.8 Estimate of sensitivity to $B^0 \to K^{*0}\mu^+\mu^-$ for an integrated luminosity of $2\,\mathrm{fb}^{-1}$. Only backgrounds from $b\overline{b}$ semileptonic decays were included. 298
7.9 Estimate of sensitivity to $B^+ \to K^+\mu^+\mu^-$ for an integrated luminosity of $2\,\mathrm{fb}^{-1}$. 302
7.10 Production cross sections and expected generation rates for signal and background for semileptonic B and Λ_b decay. 318
7.11 Efficiency, expected yields, signal-to-background, and significance for an integrated luminosity of $2\,\mathrm{fb}^{-1}$. 318

8.1 Observables related to $|M_{12}|$, $|\Gamma_{12}|$ and ϕ discussed in Sect. 8.3. 353
8.2 Time evolution of the decay $B_s \to J/\psi(\to l^+l^-)\phi(\to K^+K^-)$ of an initially (i.e. at $t = 0$) pure B_s meson. Here $\bar{\Gamma} \equiv (\Gamma_H + \Gamma_L)/2$. 376
8.3 Time evolution of the decay $\overline{B_s} \to J/\psi(\to l^+l^-)\phi(\to K^+K^-)$ of an initially (i.e. at $t = 0$) pure $\overline{B_s}$ meson. Here $\bar{\Gamma} \equiv (\Gamma_H + \Gamma_L)/2$. 376
8.4 Interesting flavor-specific decays. 384
8.5 Interesting CKM-favored decays into CP-eigenstates. 385
8.6 Interesting CKM-favored decays into CP non-eigenstates accessible to B and $\overline{B}$. 385
8.7 Physics input used for event yield estimates. 387
8.8 Branching fraction estimates for B_s decays. 387
8.9 Branching ratio estimates for Λ_b decays using scale factors described in the text. 389
8.10 Event yields for hadronic B_s decays relevant for CP violation and $\Delta\Gamma_s$ measurements. Only the feasible D_s decays to $\phi\pi$, K^*K and $\pi\pi\pi$ are considered. 390
8.11 Event yields for most sizeable hadronic Λ_b decays. 390
8.12 Event yields corresponding to 2 fb^{-1} for semileptonic B_s decays ($B_s \to \nu\ell D_s X$) for different lepton p_T trigger thresholds. 392
8.13 Level-1 XFT trigger cuts and cross sections for the three Tevatron operating scenarios considered. 392
8.14 Comparison of the various flavor taggers in terms of the ϵD^2 parameter between Run I and expectations for Run II. 395

8.15 Mass Resolutions 405
8.16 Resolutions 405
8.17 Projected yield for $B_s \to D_s^-\pi^+$ in one year of BTeV running. 408
8.18 Projected yield for $B_s \to J/\psi\overline{K}^{*0}$ in one year of BTeV running. 410
8.19 The B_s^0 decay modes studied for $\Delta\Gamma_{B_s}$ sensitivity studies at BTeV. 418
8.20 Projections for yields of B_s^0 decays for $2\,\mathrm{fb}^{-1}$ assuming a total $b\,\bar{b}$ production cross-section of 100 μb. 420
8.21 Projections for yields of B_s^0 decays for $2\,\mathrm{fb}^{-1}$ assuming a total $b\,\bar{b}$ production cross-section of 100 μb. 423
8.22 Projections for statistical errors on lifetimes measured in different modes for 2, 10 and 20 fb^{-1}. 423
8.23 Projections for statistical errors on $\Delta\Gamma_{CP}/\Gamma$ for combining lifetimes from different modes and for using all modes for 2, 10 and 20 fb^{-1}. 424
8.24 Run II projections for the Run I exclusive lifetime measurements at CDF corresponding to 2 fb^{-1}. 429
8.25 Event yield determination after 1 year or 2 fb^{-1}. 431

9.1 Uncertainties in the published $b \to eX$ measurement 452
9.2 Inclusive cross sections for spin-triplet bottomonium states 463
9.3 Direct cross sections for spin-singlet bottomonium states 464
9.4 Prompt cross sections for spin-triplet charmonium states 467
9.5 Direct cross sections for spin-singlet charmonium states 467
9.6 Branching ratios of B_c decay modes 483
9.7 Widths and branching fractions for the semileptonic decay modes of the B_c 486
9.8 Widths and branching fractions of nonleptonic decay modes of the B_c meson. 487
9.9 Widths and branching fractions of charmonium decay modes of the B_c meson.487
9.10 DØ Level 1 muon trigger efficiencies for trilepton final states from semileptonic decay of B_c mesons with $p_T(B_c) > 3$ GeV and $|\eta(B_c)| < 3$. 491
9.11 Theoretical estimations of the branching ratios of two B_c^+ decay modes and of their ratio R. 497
9.12 Theoretical estimates of the width of B_c^+ decay modes involving B_s^0 or B_s^{0*} in the final states. 499
9.13 Mass estimates for baryons with two or more heavy quarks. 501
9.14 Fractional contributions of different modes to the total decay width of doubly-charmed baryons, Ξ_{cc}. 504

9.15 Fractional contributions of different modes to the total decay width of Ξ_{bc} baryons. 504
9.16 Exclusive (spectator) decay modes of doubly-heavy baryon calculated in the framework of QCD sum rules. 505
9.17 Decay rates of cascading semileptonic decays from doubly-heavy baryons. . 506
9.18 Properties and interesting exclusive hadronic decay modes of multiple-charm baryons. 508
9.19 Baryons containing a b and a c quark 509
9.20 Baryons containing two b quarks 509
9.21 Moments of the fragmentation functions at fixed $\langle z \rangle$ for $\epsilon_b = 0.002$ 517
9.22 Moments of the fragmentation functions at fixed $\langle z \rangle$ for $\epsilon_b = 0.006$ 517
9.23 Interplay of boosting ambiguity with acceptance cuts. 528

Chapter 1

Common Theoretical Issues

U. Nierste, Z. Ligeti, A. S. Kronfeld

1.1 Introduction

This chapter provides some of the theoretical background needed to interpret measurements studied by Working Groups 1–3 (and reported in Chapters 6–8, respectively). These three working groups deal with the decay of b-flavored hadrons, and they are independent of the production mechanism. The theory of b decays requires some elementary concepts on symmetries and mixing, some knowledge of the standard electroweak theory, and some information on how the b quark is bound into hadrons. On the other hand, the theory of production, fragmentation, and spectroscopy—the subjects of Working Group 4 (and Chapter 9)—is separate, dealing entirely with aspects of the strong interactions. Hence, the theoretical background needed for Working Group 4 is entirely in Chapter 9, and theoretical issues common to the working groups studying decays are collected together in this chapter.[1] Although the experimental study of CP violation in the B system is just beginning [1–3], there are several theoretical reviews [4–8] that the reader may want to consult for details not covered here.

We start in Sec. 1.2 by reviewing how flavor mixing and CP violation arise in the Standard Model. Experiments of the past decade have verified the $SU(3) \times SU(2) \times U(1)$ gauge structure of elementary particle interactions, in a comprehensive and very precise way. By comparison, tests of the flavor interactions are not yet nearly as broad or detailed. The Standard Model, in which quark masses and mixing arise from Yukawa interactions with the Higgs field, still serves as the current foundation for discussing flavor physics. Sec. 1.2 discusses the standard flavor sector, leading to the Cabibbo-Kobayashi-Maskawa (CKM) matrix, which contains a CP violating parameter for three generations. By construction, the CKM matrix is unitary, which implies several relations among its entries and, hence, between CP conserving and CP violating observables. Furthermore, the same construction shows how, in the Standard Model, neutral currents conserve flavor at the tree level, which is known as the Glashow-Iliopoulos-Maiani (GIM) effect.

We emphasize that in extensions of the Standard Model the CKM mechanisms can exist side-by-side with other sources of CP and flavor violation. Many measurements are

[1] There is, unavoidably, some overlap with theoretical material in Chapters 6–8. We have attempted to use consistent conventions and notation throughout.

therefore needed to test whether the standard patterns prevail. Quark interactions are obscured by confinement, however. Therefore, Sec. 1.2 concludes with a brief summary of the ways of avoiding or reducing uncertainties from nonperturbative QCD, and the much of the rest of the chapter revisits various aspects in greater detail.

Sec. 1.3 covers aspects of B mesons that can be discussed without reference to their underlying dynamics. The strong interactions conserve the quantum numbers P, T, and C of parity, time reversal, and charge conjugation. We therefore start by discussing the transformation properties of currents and hadrons under these discrete symmetry transformations. Once these concepts—and associated phase conventions—are fixed, one can discuss the mixing between neutral mesons. (In the Standard Model, neutral meson mixing is induced through one-loop effects.) Although a flavored neutral meson and its anti-particle form a two-state quantum mechanical system, the particles are not stable, so the two mass eigenstates can have different decay widths in general. Consequently, the physical description of decay during mixing contains formulae that are not always simple and phase conventions that are not always transparent. Sec. 1.3 provides such a general set of formulae, derived with a self-consistent set of conventions.

The general discussion of Sec. 1.3, leads to a useful classification of CP violation. There can be CP violation in mixing, in decay, and in the interference of decays with and without mixing. Sec. 1.4 gives the concrete mathematical definition of these three types of CP violation, illustrated with examples. CP violation in many B decays is principally of one type or another, although in general two or more of these types may be present, as is the case with some kaon decays. We also work through two important examples of CP in the interference of amplitudes: $B \to J/\psi K_S$ and $B_s \to D_s^{\pm} K^{\mp}$, where it is possible to use the CP invariance of QCD to show that the CP asymmetry of these decays is independent of the hadronic transition amplitude.

To gain a comprehensive view of flavor physics, and decide whether the standard model correctly describes flavor-changing interactions, one has to consider QCD. Sec. 1.5 discusses several theoretical tools to separate scales, so that the nonperturbative hadronic physics can be treated separately from physics at higher scales, where perturbation theory is accurate. Indeed, in B decays several length scales are involved: the scale of QCD, $\Lambda_{\rm QCD}$, the mass of the b quark, m_b, the higher masses of the W and Z bosons and the top quark, and, possibly, higher scales of new physics. The first step is to separate out weak (and higher) scales with an operator product expansion, leading to an effective weak Hamiltonian for flavor-changing processes. This formalism applies for all flavor physics. For b quarks, one finds further simplifications, because $m_b \gg \Lambda_{\rm QCD}$. Two tools are used to separate these scales, heavy quark effective theory for hadronic matrix elements, and the heavy quark expansion for inclusive decay rates. Sec. 1.5 also includes a brief overview of lattice QCD, which is a promising numerical method to compute hadronic matrix elements of the electroweak Hamiltonian, when there is at most one hadron in the final state. In particular, we discuss how heavy quark effective theory can be used to control uncertainties in the numerical calculation.

A further predictive aspect of the CKM mechanism, with only one parameter to describe CP violation, is that observables in the B and B_s systems are connected to those in the kaon

system. Sec. 1.6 gives an overview of $K^0-\overline{K}^0$ mixing using the same formalism as in our treatment of $B^0-\overline{B}^0$ mixing in Sec. 1.3. This also gives us the opportunity to introduce the most important constraints from kaon physics: not only those currently available but also those that could be measured in the coming decade. Finally, Sec. 1.7 gives a summary of expectations for measurements of the unitarity triangle, based on global fits of kaon mixing and CP conserving observables in B physics.

1.2 CP Violation in the Standard Model

As mentioned in the introduction, in the Standard Model quark masses, flavor violation, and CP violation all arise from Yukawa interactions among the quark fields and the Higgs field. In this section we review how these phenomena appear, leading to the Cabibbo-Kobayashi-Maskawa (CKM) matrix. From a theoretical point of view, the CKM mechanism could, and probably does, exist along with other sources of CP violation. We therefore also discuss some of the important features of the CKM model, to provide a framework for testing it.

1.2.1 Yukawa interactions and the CKM matrix

Let us begin by recalling some of the most elementary aspects of particle physics. Experiments have demonstrated that there are several species, or flavors, of quarks and leptons. They are the down-type quarks (d, s, b), up-type quarks (u, c, t), charged leptons (e, μ, τ), and neutrinos (ν_e, ν_μ, ν_τ). They interact through the exchange of gauge bosons: the weak bosons $W^\pm$ and Z^0, the photon, and the gluons. These interactions are dictated by local gauge invariance, with gauge group $SU(3)\times SU(2)\times U(1)_Y$. With this gauge symmetry, and the observed quantum numbers of the fermions, at least one scalar field is needed to accommodate quark masses, and, in turns out, the couplings to this field can generate flavor and CP violation.

One of the most striking features of the charged-current weak interactions is that they do not couple solely to a vector current (as in QED and QCD) but to the linear combination of vector and axial vector currents $V-A$. As a consequence, the electroweak theory is a *chiral* gauge theory, which means that left- and right-handed fermions transform differently under the electroweak gauge group $SU(2)\times U(1)_Y$. The right-handed fermions do not couple to $W^\pm$, and they are singlets under $SU(2)$:

$$\begin{aligned} E_R &= (e_R,\mu_R,\tau_R)\,, \qquad & Y_E &= -1\,;\\ U_R &= (u_R,c_R,t_R)\,, \qquad & Y_U &= \frac{2}{3}\,;\\ D_R &= (d_R,s_R,b_R)\,, \qquad & Y_D &= -\frac{1}{3}\,; \end{aligned} \tag{1.1}$$

where the hypercharge Y is given. For convenience below, the three generations are grouped together. The gauge and kinetic interactions for G generations of these fields are

$$\mathcal{L}_R = \sum_{i=1}^{G} \bar{E}^i_R(i\not\partial - g_1 Y_E \not B)E^i_R + \bar{D}^i_R(i\not\partial - g_1 Y_D \not B)D^i_R + \bar{U}^i_R(i\not\partial - g_1 Y_U \not B)U^i_R\,, \tag{1.2}$$

where B is the gauge boson of $U(1)_Y$, with coupling g_1, and D^μ is the covariant derivative of QCD: quarks are triplets under color $SU(3)$. On the other hand, the left-handed fermions do couple to $W^\pm$, so they are doublets under $SU(2)$:

$$\begin{aligned} L_L &= \left(\begin{pmatrix}\nu_e\\ e\end{pmatrix}_L, \begin{pmatrix}\nu_\mu\\ \mu\end{pmatrix}_L, \begin{pmatrix}\nu_\tau\\ \tau\end{pmatrix}_L\right), \qquad & Y_L &= -\frac{1}{2}\,;\\ Q_L &= \left(\begin{pmatrix}u\\ d\end{pmatrix}_L, \begin{pmatrix}c\\ s\end{pmatrix}_L, \begin{pmatrix}t\\ b\end{pmatrix}_L\right), \qquad & Y_Q &= \frac{1}{6}\,. \end{aligned} \tag{1.3}$$

The $SU(2)$ quantum number is called weak isospin, and the third component I_3 distinguishes upper and lower entries. The gauge and kinetic interactions for G generations of these fields are

$$\mathcal{L}_L = \sum_{i=1}^{G} \bar{L}^i_L(i\not\partial - g_1 Y_L \not B - g_2 \not W)L^i_L + \bar{Q}^i_L(i\not\partial - g_1 Y_Q \not B - g_2 \not W)Q^i_L\,, \tag{1.4}$$

where $W = W^a\sigma_a/2$ are the gauge bosons of $SU(2)$, with gauge coupling g_2. Note that as far as gauge interactions are concerned, the generations are simply copies of each other, and $\mathcal{L}_R+\mathcal{L}_L$ possesses a large global flavor symmetry. For G generations, the symmetry group is $U(G)^5$, that is, a $U(G)$ symmetry for each of E_R, U_R, D_R, L_L, and Q_L.

The assignments of $SU(2)$ and $U(1)_Y$ quantum numbers follow from simple, experimentally determined properties of weak decays. For example, by the mid-1980s measurements of decays of b-flavored hadrons had shown the weak isospin of b_L to be $-\frac{1}{2}$ [9]. Consequently, its isopartner t_L had to exist, for symmetry reasons, although several years passed before the top quark was observed at the Tevatron. In contrast, gauge symmetry does not motivate the inclusion of right-handed neutrinos, which would be neutral under all three gauge groups. For this reason, they are usually omitted from the "standard" model.

With only gauge fields and fermions, the model is incomplete. In particular, it does not accommodate the observed non-zero masses of the quarks, charged leptons, and weak gauge bosons $W^\pm$ and Z^0. For example, masses for the charged fermions[2] normally would come from interactions that couple the left- and right-handed components of the field, such as

$$\mathcal{L}_m = -m\left(\bar{\psi}_R\psi_L + \bar{\psi}_L\psi_R\right), \tag{1.5}$$

where, in the case at hand, $\psi\in\{e,\mu,\tau,d,s,b,u,c,t\}$. With the fields introduced above, one would have to combine a component of a doublet with a singlet, which would violate $SU(2)$. Any pairing of left- and right-handed fields with the listed hypercharges would violate $U(1)_Y$ as well.

To construct gauge invariant interactions coupling left- and right-handed fermions, at least one additional field is necessary. For simplicity, let us begin with only the first generation leptons. Consider

$$\mathcal{L}_Y = -ye^{i\delta}\,\bar{l}_L\phi\, e_R - ye^{-i\delta}\,\bar{e}_R\,\phi^\dagger l_L, \tag{1.6}$$

[2] Because it is completely neutral, a right-handed neutrino may have a so-called Majorana mass term, coupling neutrino to neutrino, instead of—or in addition to—a Dirac mass term, coupling neutrino to anti-neutrino. For this reason neutrino masses are even more perplexing than quark and charged lepton masses.

where $\bar{l}_L = (\bar{\nu}_L,\ \bar{e}_L)$, and y is real. If the quantum numbers of ϕ are chosen suitably, then the interaction $\mathcal{L}_I$ would be gauge (and Lorentz) invariant. To preserve Lorentz invariance, ϕ must have spin 0. To preserve invariance under $U(1)_Y$, the hypercharge of ϕ must be $Y_\phi = Y_L - Y_E = +\frac{1}{2}$. To preserve invariance under $SU(2)$ ϕ, must be a doublet,

$$\phi = \begin{pmatrix} \phi^+ \\ \phi^0 \end{pmatrix}. \tag{1.7}$$

The superscripts denote the electric charge $Q = Y + I_3$. An interaction similar to $\mathcal{L}_Y$ was first introduced by Yukawa to describe the decay $\pi^+ \to \mu^+\nu_\mu$, so it is called a Yukawa interaction, and the coupling y is called a Yukawa coupling.

At first glance, the interaction in Eq. (1.6) appears to violate CP, with a strength proportional to $y \sin\delta$. One may, however, remove δ, by exploiting the invariance of $\mathcal{L}_R + \mathcal{L}_L$ under independent changes in the phases of e_R and l_L. Thus, the one-generation Yukawa interaction has only one real parameter, y, and it conserves CP.

Since it is charged under $SU(2) \times U(1)_Y$, the field ϕ has gauge interactions, which are dictated by symmetry. The scalar field may also have self-interactions, which are not dictated by symmetry. If one limits one's attention to renormalizable interactions

$$V(\phi) = -\lambda v^2 \phi^\dagger\phi + \lambda(\phi^\dagger\phi)^2, \tag{1.8}$$

with two new parameters, v and λ. The state with no propagating particles, called the vacuum, is realized when ϕ minimizes $V(\phi)$. The quartic coupling λ must be positive; otherwise the potential energy would be unbounded from below, and the vacuum would be unstable. If $v^2 < 0$, then there is a single minimum of the potential, with vacuum expectation value $\langle\phi\rangle = 0$; this possibility does not interest us here. If $v^2 > 0$, then $V(\phi)$ takes the shape of a sombrero with a three-dimensional family of minima:

$$\langle\phi\rangle = e^{i\langle\xi^a\rangle\sigma_a/2v} \begin{pmatrix} 0 \\ v/\sqrt{2} \end{pmatrix}, \tag{1.9}$$

parametrized by $\langle\xi^a\rangle$. Through an x-independent $SU(2)$ transformation, one can set $\langle\xi^a\rangle = 0$. Although the Lagrangian fully respects local $SU(2)\times U(1)_Y$ gauge symmetry, the vacuum solution of the equations of motion given in Eq. (1.9) does not: this is called spontaneous (as opposed to explicit) symmetry breaking.

Physical particles arise from fluctuations around the solution of the equations of motion, so one writes

$$\phi(x) = e^{i\xi^a(x)\sigma_a/2v} \begin{pmatrix} 0 \\ [v + h(x)]/\sqrt{2} \end{pmatrix}. \tag{1.10}$$

The vacuum expectation values of the fluctuation fields are $\langle\xi^a\rangle = \langle h\rangle = 0$. Masses of the physical particles are found by inserting Eq. (1.10) into the expressions for the interactions in the Lagrangian and examining the quadratic terms. By comparing the $\bar{e}_R e_L$ terms in $\mathcal{L}_Y$ and $\mathcal{L}_m$, one sees that the electron mass in this model is $m_e = yv/\sqrt{2}$. Similarly, from $V(\phi)$ the field h is seen to have a (squared) mass $m_h^2 = 2\lambda v^2$, and from the kinetic energy of the scalar field non-zero masses for three of the gauge bosons arise: $m_{W^\pm}^2 = \frac{1}{4}g_2^2 v^2$ and $m_{Z^0}^2 = \frac{1}{4}(g_1^2 + g_2^2)v^2$, where Z^0 is the massive linear combination of W^3 and B. (The

orthogonal combination is the massless photon γ.) The amplitude for muon decay is, to excellent approximation, proportional to g_2^2/m_W^2. Therefore, one can obtain the vacuum expectation value from the Fermi decay constant, finding $v = 246$ GeV.

Repeating this construction with $(\bar{u}_L,\ \bar{d}_L)$ and d_R requires a doublet with hypercharge $Y_Q - Y_D = +\frac{1}{2}$. The Standard Model uses the same doublet as for leptons. Repeating it with $(\bar{u}_L,\ \bar{d}_L)$ and u_R requires a doublet with hypercharge $Y_Q - Y_U = -\frac{1}{2}$. The Standard Model uses the charge-conjugate

$$\tilde{\phi} \equiv i\sigma_2\phi^* = \begin{pmatrix} \overline{\phi^0} \\ -\phi^- \end{pmatrix} \tag{1.11}$$

of the doublet used for leptons. In the one-generation case, three real Yukawa couplings are introduced, leading to masses for the electron, down quark, and up quark.

With G generations the full set of Yukawa interactions is complicated. It is instructive to leave G arbitrary for now, and to compare the physics for $G = 2$, 3, 4, later on. The generations may interact with each other as in

$$\mathcal{L}_Y = -\sum_{i,j=1}^{G} \left[\hat{y}^e_{ij}\bar{L}^i_L\phi\, E^j_R + \hat{y}^d_{ij}\bar{Q}^i_L\phi\, D^j_R + \hat{y}^u_{ij}\bar{Q}^i_L\tilde{\phi}\, U^j_R + \text{h.c.}\right], \tag{1.12}$$

because no symmetry would enforce a simpler structure. For G generations, the Yukawa matrices are complex $G\times G$ matrices. At first glance, each matrix $\hat{y}^a$ seems to introduce $2G^2$ parameters: G^2 that are real and CP-conserving, and another G^2 that are imaginary and CP violating. But, as in the one-generation case, one must think carefully about physically equivalent matrices before understanding how many physical parameters there really are.

Let us consider the leptons first. As mentioned above, the non-Yukawa part of the Lagrangian is invariant under the following transformation of generations

$$\begin{aligned} E_R &\mapsto RE_R\,, & \bar{E}_R &\mapsto \bar{E}_R R^\dagger, \\ L_L &\mapsto SL_L\,, & \bar{L}_L &\mapsto \bar{L}_L S^\dagger, \end{aligned} \tag{1.13}$$

where $R \in U(G)_{E_R}$ and $S \in U(G)_{L_L}$. That means that the Yukawa matrix $\hat{y}^e$ is equivalent to $y^e = S\hat{y}^e R^\dagger$. By suitable choice, y^e can be made diagonal, real, and non-negative. The leptons' Yukawa interactions now read

$$\mathcal{L}_{Yl} = -\sum_{i=1}^{G} \left[y^e_i \bar{L}^i_L\phi\, E^i_R + \text{h.c.}\right]. \tag{1.14}$$

Note that if S and R achieve this structure, so do $S' = DS$ and $R' = DR$, where $D = \text{diag}\,(e^{i\varphi_1}, \ldots, e^{i\varphi_G})$. Thus, part of the transformation from $\hat{y}^e$ to y^e is redundant and must not be counted twice. (The freedom to choose these phases leads to global conservation of lepton flavor.) Hence, the transformation removes $2G^2 - G$ parameters, leaving G independent entries in y^e. Since all are real, there is no CP violation.

For the quarks the reasoning is the same but the algebra is trickier. There are now three distinct $U(G)$ symmetries, and the non-Yukawa Lagrangian is invariant under

$$\begin{aligned} D_R &\mapsto R_d D_R\,, \qquad \bar{D}_R \mapsto \bar{D}_R R_d^\dagger\,, \\ U_R &\mapsto R_u U_R\,, \qquad \bar{U}_R \mapsto \bar{U}_R R_u^\dagger\,, \\ Q_L &\mapsto S_u Q_L\,, \qquad \bar{Q}_L \mapsto \bar{Q}_L S_u^\dagger\,. \end{aligned} \tag{1.15}$$

One may again exploit S_u and R_u to transform $\hat{y}^u$ into the diagonal, real, non-negative form y^u. Then the transform of $\hat{y}^d$ is, in general, neither real nor diagonal. Instead

$$S_u \hat{y}^d R_d^\dagger = V y^d\,, \tag{1.16}$$

where $y^d = S_d \hat{y}^d R_d^\dagger$ *is* diagonal, real, and non-negative, and

$$V = S_u S_d^\dagger \tag{1.17}$$

is the Cabibbo-Kobayashi-Maskawa (CKM) matrix [10,11]. By construction, V is a $G \times G$ unitary matrix. The quarks' Yukawa interactions now read

$$\mathcal{L}_{Yq} = -\sum_{i,j=1}^{G} \left[y_j^d \bar{Q}_L^i \phi\, V_{ij} D_R^j + \text{h.c.} \right] - \sum_{i=1}^{G} \left[y_i^u \bar{Q}_L^i \tilde{\phi}\, U_R^i + \text{h.c.} \right]. \tag{1.18}$$

If S_u, R_u, and R_d achieve this structure, so do $e^{i\varphi} S_u$, $e^{i\varphi} R_u$, and $e^{i\varphi} R_d$. (The freedom to choose this phase leads to global conservation of total baryon number.) Thus, the manipulations remove $3G^2 - 1$ parameters from the $4G^2$ in two arbitrary $G \times G$ matrices, leaving $G^2 + 1$. Of these, $2G$ are in y^u and y^d, and the other $(G-1)^2$ are in the CKM matrix V. One can also count separately the real and imaginary parameters. Since a $G \times G$ unitary matrix has $\frac{1}{2}G(G-1)$ real and $\frac{1}{2}G(G+1)$ imaginary components, one finds that the CKM matrix has $\frac{1}{2}G(G-1)$ real, CP-conserving parameters, and $\frac{1}{2}(G-1)(G-2)$ imaginary, CP violating parameters. For example, the case $G = 2$ has no CP violation from this mechanism, $G = 3$ has a single CP violating parameter, and $G = 4$ has three.

The CKM matrix V arises from the misalignment of the matrices S_u and S_d. Under circumstances that preserve some of the flavor symmetry, they can be partially aligned, and then V contains even fewer physical parameters. In an example with three generations, if two entries either in y^u or in y^d are equal, partial re-alignment removes one real angle and one phase. Therefore, the CKM mechanism leads to CP violation only if like-charged quarks all have distinct masses.

Substituting Eq. (1.10) into $\mathcal{L}_Y$ and keeping quadratic terms shows that the masses are

$$m_k^a = \frac{v}{\sqrt{2}} y_k^a\,, \tag{1.19}$$

for $k = 1, 2, 3$, and $a = e, d, u$. For quarks this is easiest to see if one sets

$$Q_L = \begin{pmatrix} U_L \\ V D_L \end{pmatrix}, \tag{1.20}$$

which diagonalizes the mass terms for the down-like quarks in Eq. (1.18). In this basis the CKM matrix migrates to the charged-current vertex:

$$\mathcal{L}_{\bar{U}WD} = -\frac{g_2}{\sqrt{2}} \left[\bar{U}_L \not{W}^+ V D_L + \bar{D}_L V^\dagger \not{W}^- U_L \right], \tag{1.21}$$

where $W^\pm = (W^1 \mp iW^2)/\sqrt{2}$. The basis in (1.20), with diagonal mass matrices and the CKM matrix in the charged currents of quarks, is usually adopted in phenomenology.

Note that the neutral current interactions are unaffected by writing V in (1.20). Thus, there are no flavor-changing neutral currents (FCNC) at the tree level in the Standard Model. This is known as the Glashow-Iliopoulus-Maiani (GIM) effect [12]. Even at the loop level, where the FCNCs do arise, the GIM mechanism can suppress processes by a factor m_q^2/m_W^2, which is very small, except in the case of the top quark. GIM suppression and Cabibbo suppression (i.e., factors of λ) both imply near-null predictions for several processes. Observation of any of these would constitute a clear signal of non-standard physics.

Note that quark and lepton masses arise from the same microscopic interactions as CKM flavor violation. In Nature, the quark and lepton masses vary over orders of magnitude. Thus, the large flavor symmetry that would arise in the absence of Yukawa interactions is severely broken. In the Standard Model, the Yukawa couplings are simply chosen to contrive the observed masses. This is unsatisfactory, but we lack the detailed experimental information needed to develop a deeper theory of flavor.

1.2.2 General models

The foregoing discussion makes clear that the unitary CKM matrix arises in an algebraic way. Therefore, the mechanism can survive in models with a more complicated Higgs sector. The Standard Model is a model of economy: a single doublet generates mass for the gauge bosons, charged leptons, down-like quarks, and up-like quarks. In models with two doublets (and three or more generations), the CKM source of CP violations remains, but there can be additional CP violation in the Higgs sector [13].

To emphasize this point, let us consider an extreme example with

$$\mathcal{L}_Y = \bar{L}_L^i \Phi_{ij}^e E_R^j + \bar{Q}_L^i \Phi_{ij}^d D_R^j + \bar{Q}_L^i \tilde{\Phi}_{ij}^u U_R^j + \text{h.c.}, \tag{1.22}$$

where i, j run over generations, and we take the basis in which gauge interactions do not change generations. The tilde on $\tilde{\Phi}_u$ is introduced so that, with $\tilde{\Phi}^u = i\sigma_2 \Phi^{u*}$, all Φ^a are (matrix) fields with hypercharge $+\frac{1}{2}$. Here the Yukawa couplings are absorbed into the fields—Eq. (1.22) is hideous enough as it is. Since all Φ^a are doublets under $SU(2)$, they all would participate in electroweak symmetry breaking.

Suppose the Higgs potential, now a complicated function of all the scalar fields, leads to vacuum expectation values of the form

$$\langle \Phi_{ij}^a \rangle = \begin{pmatrix} 0 \\ \hat{m}_{ij}^a \end{pmatrix}. \tag{1.23}$$

Then the $\hat{m}_{ij}^a$ are mass matrices, and the algebra leading to the real, physical masses m_k^a and the CKM matrix is just as above. The CKM matrix, V, survives and should lead to CP violation, because there is no good reason for the phase in V to be small. There would, however, almost certainly be new sources of CP violation from the Higgs sector.

1.2.3 CP violation from a unitary CKM matrix

In the standard, one-doublet, model, we see that flavor and CP violation arise solely through the CKM matrix. Furthermore, in more general settings, the CKM matrix can still arise, but there may be other sources of CP violation as well. If the CKM matrix is the only source of CP violation, there are many relations between CP-conserving and CP violating observables that arise from the fact that V is a unitary matrix. This section outlines a framework for testing whether these constraints are, in fact, realized.

A useful way [14] of gauging the size of CP violation starts with the commutator of the mass matrices, $C = [\hat{m}^u \hat{m}^{u\dagger}, \hat{m}^d \hat{m}^{d\dagger}]$, which can be re-written

$$C = S_u^\dagger \left[(m^u)^2, V (m^d)^2 V^\dagger \right] S_u \,, \tag{1.24}$$

to show that $\det C$ depends on the physical masses and V. After some algebra one finds

$$\det C = -2i F_u F_d J \,, \tag{1.25}$$

where

$$F_u = (m_u^2 - m_c^2)(m_c^2 - m_t^2)(m_t^2 - m_u^2) \,, \tag{1.26}$$
$$F_d = (m_d^2 - m_s^2)(m_s^2 - m_b^2)(m_b^2 - m_d^2) \,, \tag{1.27}$$
$$J = \mathrm{Im}\left[V_{11} V_{21}^* V_{22} V_{12}^* \right] . \tag{1.28}$$

To arrive at Eq. (1.25) one makes repeated use of the property $VV^\dagger = \mathbb{1}$, especially that

$$J = \mathrm{Im}\left[V_{ij} V_{kj}^* V_{kl} V_{il}^* \right] \sum_m \varepsilon_{ikm} \sum_n \varepsilon_{jln} \,, \tag{1.29}$$

for all combinations of i, j, k, and l. The determinant $\det C$ captures several essential features of CP violation from the CKM mechanism. It is imaginary, reminding us that CP violation stems from a complex coupling. More significantly, there is no CP violation unless F_u, F_d, and J are all different from zero. Non-vanishing F_u and F_d codify the requirements on the quark masses given above. Non-vanishing J codifies requirements on V, which are clearest after choosing a specific parameterization. The key point, however, is that the value taken by J is independent of the parameterization, by construction of $\det C$.

To emphasize the physical transitions associated with the CKM matrix, it is usually written

$$V = \begin{pmatrix} V_{ud} & V_{us} & V_{ub} \\ V_{cd} & V_{cs} & V_{cb} \\ V_{td} & V_{ts} & V_{tb} \end{pmatrix} , \tag{1.30}$$

so that the entries are labeled by the quark flavors. From Eq. (1.21), the vertex at which a b quark decays to a W^- and c quark is proportional to V_{cb}; similarly, the vertex at which a c quark decays to a W^+ and s quark is proportional to V_{cs}^*. Because V is unitary, $|V_{ud}|^2 + |V_{us}|^2 + |V_{ub}|^2 = 1$, and similarly for all other rows and columns. These constraints give information on unmeasured (or poorly measured) elements of V. For example, because

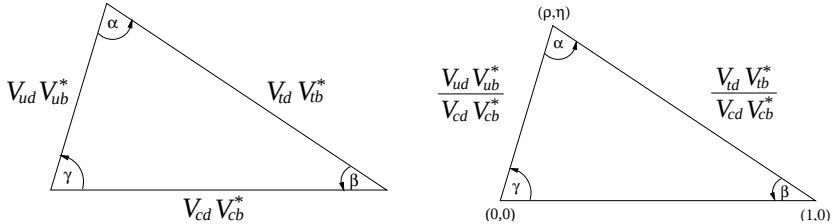

Figure 1.1: The unitarity triangle. The version on the left directly expresses Eq. (1.31). The rescaled version shows the definition of $(\bar{\rho}, \bar{\eta})$.

$|V_{cb}|$ and $|V_{ub}|$ are known to be small, $|V_{tb}|$ should be very close to 1—if, indeed, there are only three generations. Furthermore, $|V_{ts}|$ and $|V_{td}|$ must also be small.

Even more interesting constraints come from the orthogonality of columns (or rows) of a unitary matrix. Taking the first and third columns of V, one has

$$V_{ud} V_{ub}^* + V_{cd} V_{cb}^* + V_{td} V_{tb}^* = 0 \,. \tag{1.31}$$

Equation (1.31) says that the three terms in the sum trace out a triangle on the complex plane. Because it is a consequence of the unitarity property of V, this triangle is called the "unitarity triangle," shown in Fig. 1.1. The lengths of the sides are simply $|V_{ud}V_{ub}^*|$, etc., and the angles are

$$\alpha = \arg\left[-\frac{V_{td}V_{tb}^*}{V_{ud}V_{ub}^*} \right] , \qquad \beta = \arg\left[-\frac{V_{cd}V_{cb}^*}{V_{td}V_{tb}^*} \right] , \qquad \gamma = \arg\left[-\frac{V_{ud}V_{ub}^*}{V_{cd}V_{cb}^*} \right] . \tag{1.32}$$

The notation $\beta \equiv \phi_1$, $\alpha \equiv \phi_2$, $\gamma \equiv \phi_3$ is also used. By construction $\alpha + \beta + \gamma = \pi$. The area of the triangle is $|J|/2$ and the terms trace out the triangle in a counter-clockwise (clockwise) sense if J is positive (negative). In fact, there are five more unitarity triangles, all with area $|J|/2$ and orientation linked to the sign of J.

The unitarity triangle(s) are useful because they provide a simple, vivid summary of the CKM mechanism. Separate measurements of lengths, through decay and mixing rates, and angles, through CP asymmetries, should fit together. Furthermore, when one combines measurements—from the B, B_s, K, and D systems, as well as from hadronic W decays—all triangles should have the same area and orientation. If there are non-CKM contributions to flavor or CP violation, however, the interpretation of rates and asymmetries as measurements of the sides and angles no longer holds. The triangle built from experimentally defined sides and angles will not fit with the CKM picture.

In the parameterization favored by the Particle Data Book [15]

$$V = \begin{pmatrix} c_{12}c_{13} & s_{12}c_{13} & s_{13}e^{-i\delta_{13}} \\ -s_{12}c_{23} - c_{12}s_{23}s_{13}e^{i\delta_{13}} & c_{12}c_{23} - s_{12}s_{23}s_{13}e^{i\delta_{13}} & s_{23}c_{13} \\ s_{12}s_{23} - c_{12}c_{23}s_{13}e^{i\delta_{13}} & -c_{12}s_{23} - s_{12}c_{23}s_{13}e^{i\delta_{13}} & c_{23}c_{13} \end{pmatrix} , \tag{1.33}$$

where $c_{ij} = \cos\theta_{ij}$ and $s_{ij} = \sin\theta_{ij}$. The real angles θ_{ij} may be chosen so that $0 \le \theta_{ij} \le \pi/2$, and the phase δ_{13} so that $0 \le \delta_{13} < 2\pi$. With Eq. (1.33) the Jarlskog invariant becomes

$$J = c_{12}c_{23}c_{13}^2 s_{12}s_{23}s_{13}\sin\delta_{13}\,. \tag{1.34}$$

The parameters must satisfy

$$\delta_{13} \neq 0,\ \pi\,; \qquad \theta_{ij} \neq 0,\ \pi/2\,; \tag{1.35}$$

otherwise J vanishes. Since CP violation is proportional to J, the CKM matrix must not only have complex entries, but also non-trivial mixing; otherwise the KM phase δ_{13} can be removed.

A convenient parameterization of the CKM matrix is due to Wolfenstein [16]. It stems from the observation that the measured matrix obeys a hierarchy, with diagonal elements close to 1, and progressively smaller elements away from the diagonal. This hierarchy can be formalized by defining λ, A, ρ, and η via

$$\lambda \equiv s_{12}\,, \qquad A \equiv s_{23}/\lambda^2\,, \qquad \rho + i\eta \equiv s_{13}e^{i\delta_{13}}/A\lambda^3\,. \tag{1.36}$$

From experiment $\lambda \approx 0.22$, $A \approx 0.8$, and $\sqrt{\rho^2+\eta^2} \approx 0.4$, so it is phenomenologically useful to expand V in powers of λ:

$$V = \begin{pmatrix} 1-\frac{1}{2}\lambda^2 & \lambda & A\lambda^3(\rho - i\eta) \\ -\lambda & 1-\frac{1}{2}\lambda^2 & A\lambda^2 \\ A\lambda^3(1-\rho-i\eta) & -A\lambda^2 & 1 \end{pmatrix} + \mathcal{O}(\lambda^4)\,. \tag{1.37}$$

The most interesting correction at $\mathcal{O}(\lambda^4)$ for our purposes is $\mathrm{Im}\, V_{ts} = -A\lambda^4\eta$. The Jarlskog invariant can now be expressed $J = A^2\lambda^6\eta \approx (7\times10^{-5})\eta$. One sees that CKM CP violation is small not because δ_{13} is small but because flavor violation must also occur, and flavor violation is suppressed, empirically, by powers of λ.

The unitarity triangle in Eq. (1.31) is special, because its three sides are all of order $A\lambda^3$. The triangle formed from the orthogonality of the first and third rows also has this property, but it is not accessible, because the top quark decays before the mesons needed to measure the angles are bound. The other triangles are all long and thin, with sides $(\lambda, \lambda, A\lambda^5)$ (e.g., for the kaon) or $(\lambda^2, \lambda^2, A\lambda^4)$ (e.g., for the B_s meson).

It is customary to rescale Eq. (1.31) by the common factor $A\lambda^3$, to focus on the less well-determined parameters (ρ, η). In the context of the Wolfenstein parameterization, there are many ways to do this. Since we anticipate precision in experimental measurements, and also in theoretical calculations of some important hadronic transition amplitudes, it is useful to choose an exact rescaling. We choose to divide all three terms in Eq. (1.31) by $V_{cd}V_{cb}^*$ and define[3]

$$\bar\rho + i\bar\eta \equiv -\frac{V_{ud}V_{ub}^*}{V_{cd}V_{cb}^*}. \tag{1.38}$$

[3]This definition differs at $\mathcal{O}(\lambda^4)$ from the original one in Ref. [17].

Then the rescaled triangle, also shown in Fig. 1.1, has its apex in the complex plane at $(\bar\rho, \bar\eta)$. The angles of the triangle are easily expressed

$$\alpha = \tan^{-1}\left(\frac{\bar\eta}{\bar\eta^2 + \bar\rho(\bar\rho-1)}\right)\,, \quad \beta = \tan^{-1}\left(\frac{\bar\eta}{1-\bar\rho}\right)\,, \quad \gamma = \tan^{-1}\left(\frac{\bar\eta}{\bar\rho}\right)\,, \tag{1.39}$$

Since $\bar\eta$, $\bar\rho$, and $1-\bar\rho$ could easily be of comparable size, the angles and, thus, the corresponding CP asymmetries could be large.

At the Tevatron there is also copious production of B_s mesons. The corresponding unitarity triangle is

$$V_{us}V_{ub}^* + V_{cs}V_{cb}^* + V_{ts}V_{tb}^* = 0\,, \tag{1.40}$$

replacing the d quark with s. In Eq. (1.40) the first side is much shorter than the other two. Therefore, the opposing angle

$$\beta_s = \arg\left[-\frac{V_{ts}V_{tb}^*}{V_{cs}V_{cb}^*}\right] = \lambda^2\eta + \mathcal{O}(\lambda^4) \tag{1.41}$$

is small, of order one degree. Therefore, the asymmetries in $B_s \to \psi\eta^{(\prime)}$ and $B_s \to \psi\phi$ are much smaller than in the corresponding B decays. On the other hand, this asymmetry is sensitive to new physics in $B_s^0 - \overline{B}_s^0$ mixing. In the standard model, as discussed below, mixing is induced by loop processes. When, as here, there is also Cabibbo suppression, it is easy for the non-standard phenomena to compete. Thus, in the short term a measurement of β_s represents a search for new physics, whereas in the long term it would be a verification of the CKM picture.

The unitarity triangle for the D system comes from the orthogonality of the top two rows of the CKM matrix. It is even longer and thinner than the one for the B_s system. Consequently, a non-zero measurement of the CP asymmetry associated with the small angle is a clear sign of new physics. It seems that experiments to measure the D-system unitarity triangle are not yet feasible.

1.2.4 Hadronic uncertainties and clean measurements

At a superficial level, the way to test the CKM picture is to measure rates and asymmetries that are sensitive to the sides and angles (of all triangles), in as many ways as possible. A serious obstacle, however, is that the quarks are confined in hadrons. Consequently, most relations between experimental observables and Lagrangian-level couplings, like the CKM matrix, involve hadronic matrix elements. In this subsection, we summarize briefly how to treat the matrix elements, with an eye toward identifying processes that are relatively free of hadronic uncertainty.

There are several approaches for treating the hadronic matrix elements, none of which is universally useful. In Sec. 1.5 we introduce some of the essential tools in greater detail. Here we illustrate the possibilities with examples.

- Perfect (or essentially perfect) symmetries of QCD, such as C or CP: When a single CKM factor dominates a process, the QCD part of the amplitude cancels in ratios such as the CP asymmetry in interference between decays with and without mixing. The two best examples are in the asymmetries for[4] $B \to \psi K_S$ and $B_s \to D_s^{\pm} K^{\mp}$. Assuming that CP violation comes only from the CKM matrix, the first class of modes cleanly yields $\sin 2\beta$, and the other pair of modes cleanly yields $\sin(\gamma - 2\beta_s)$.

- Approximate symmetries, such as isospin, flavor $SU(3)$, chiral symmetry, or heavy quark symmetry: The best-known examples are when the symmetry restricts a form factor for semileptonic decays. Isospin and $n \to pe\bar{\nu}_e$ give $|V_{ud}|$; flavor $SU(3)$ and $K \to \pi e\bar{\nu}_e$ give $|V_{us}|$; and heavy quark symmetry and $B \to D^* \ell \bar{\nu}_\ell$ give $|V_{cb}|$. The hadronic uncertainty is now in the deviation from the symmetry limit. An even more intriguing use of isospin is to relate the form factor of $K^0 \to \pi^+ e\bar{\nu}_e$ to that of $K^{0,\pm} \to \pi^{0,\pm}\nu\bar{\nu}$. The rare $\nu\bar{\nu}$ decays are, thus, essentially free of hadronic uncertainties.[5]

- Lattice QCD: This computational method is sound, in principle, for hadronic matrix elements with at most one final-state hadron. Limitations in computer power have led to an approximation, called the quenched approximation, whose error is difficult to quantify. With increases in computer resources, lattice results should, in the future, play a more important role in determining the sides of the unitarity triangles. For more details, see Sec.1.5.4.

- Perturbative QCD for exclusive processes: It may be possible to calculate the strong phases of certain nonleptonic B decays using perturbative QCD. This is in some ways analogous to computing cross sections in hadronic collisions, and the nonperturbative information is captured in light-cone distribution amplitudes [20]. There are, at present, two different approaches [21,22], whose practical relevance remains an open question.

- QCD sum rules: Like lattice and perturbative QCD, sum rules are based on QCD and field theory. Uncertainty estimates are usually semi-quantitative and it is difficult to reduce them in a controlled manner.

- Models of QCD, such as quark models, naive factorization, etc: These techniques can be applied for back-of-the-envelope estimates. There is no prospect for providing a quotable error and, thus, should not be used in quantitative work.

In summary, at the present time the cleanest observables are the CP asymmetries in $\overline{B}{}_d^0$ decays to charmonium+kaon and in $\overline{B}{}_s^0$ decays to $D_s^{\pm} K^{\mp}$. The rare decay $K_L \to \pi^0 \nu\bar{\nu}$ is free of theoretical uncertainties at a similar level, but presents a big experimental challenge. Semileptonic decays restricted by symmetries as well as $K^{\pm} \to \pi^{\pm}\nu\bar{\nu}$ are a step down, but still good. With enough computer power to overcome the quenched approximation, lattice QCD could yield, during the course of Run II, controlled uncertainty estimates for neutral-meson mixing and leptonic and semileptonic decays of a few percent.

[4]Here, and in the rest of this chapter, ψ stands for any charmonium state, J/ψ, ψ', χ_c, etc.

[5]In the charged mode there is an uncertainty stemming from the uncertainty in the charmed quark mass. It has been estimated to be around 5% in $|V_{ts}V_{td}|$ [18]. Power suppressed corrections to $K \to \pi\nu\bar{\nu}$ have also been estimated and found to be small [19].

1.3 General Formalism for Mixing and CP Violation

This section is devoted to the general formalism for meson mixing and CP violation. Much of the material can also be found in other review articles and reports [4,5,8], but some topics require a different viewpoint in the light of the B physics program at a hadron collider: unlike the B factories the Tevatron will be able to study B_s^0 mesons. The two mass eigenstates in the B_s^0 system may involve a sizable width difference $\Delta\Gamma$, which must be included in the formulae for the B_s^0 time evolution. We consequently present these formulae including all effects from a non-vanishing $\Delta\Gamma$.

Many details of the formalism depend on conventions, particularly in the choice of the complex phases that unavoidably appear in any CP violating physical system. We would like to discourage the reader from combining formulae from different sources, so we try to give a comprehensive and self-contained presentation of the subject. We start by introducing the discrete transformation C, P and T in Sec. 1.3.1. Experimentally we know that C, P and T are symmetries of the electromagnetic and strong interactions, so the corresponding quantum numbers can be used to classify the hadron states. The description in Sec. 1.3.2 of the time evolution of the neutral B meson system is applicable to both the B_d^0 and the B_s^0 meson systems. Sec. 1.3.3 deals with untagged B^0 decays and Sec. 1.3.4 presents the formulae for CP asymmetries. Finally, in Sec. 1.3.4 we discuss phase conventions and rephasing invariant quantities.

1.3.1 Discrete transformations

In this section we introduce the parity, P, time reversal, T, and charge conjugation, C, transformations. P and T are defined through their action on coordinate vectors $x = (x^0, x^1, x^2, x^3)$: P flips the sign of the spatial coordinates x^1,x^2,x^3 and T changes the time component $t = x^0$ into $-t$. Adopting the convention $g_{\mu\nu} = \mathrm{diag}(1,-1,-1,-1)$ for the Lorentz metric, one can compactly express the transformations in terms of $x_\mu = g_{\mu\nu}x^\nu$:

$$\begin{aligned} P: &\quad x^\mu \to x_\mu\,, \\ T: &\quad x^\mu \to -x_\mu\,. \end{aligned} \tag{1.42}$$

The definition (1.42) implies that the derivative operator $\partial^\mu = \partial/\partial x_\mu$ and the momentum p^μ transform under P and T in the same way as x^μ. Finally, C interchanges particles and anti-particles. Apart from the weak interactions, these transformations are symmetries of the Standard Model. It is therefore convenient to classify hadronic states by their C, P and T quantum numbers, which are multiplicative and take the values ± 1.

The Lagrangian of the Standard Model and its possible extensions contain bilinear currents of the quark fields, to which gauge bosons and scalar fields couple. For example, as discussed in Sec. 1.2, the W boson field W^μ couples to the chiral vector current $\overline{b}_L \gamma_\mu c_L$. Quark bilinears also appear in composite operators which represent the Standard Model interactions in low energy effective Hamiltonians, cf., Sec. 1.5.1. To understand how these interactions work, it is helpful to list the transformation of the quark bilinears under C, P,

current	$\overline{b}_R\, d_L\,(x^\rho)$	$\overline{b}_L\,\gamma_\mu\, d_L\,(x^\rho)$	$\overline{b}_R\,\sigma_{\mu\nu} d_L\,(x^\rho)$
C	$\overline{d}_R\, b_L\,(x^\rho)\,\eta_C$	$-\overline{d}_R\,\gamma_\mu\, b_R(x^\rho)\,\eta_C$	$-\overline{d}_R\,\sigma_{\mu\nu}\, b_L(x^\rho)$
P	$\overline{b}_L\, d_R\,(x_\rho)\,\eta_P$	$\overline{b}_R\,\gamma^\mu\, d_R\,(x_\rho)\,\eta_P$	$\overline{b}_L\,\sigma^{\mu\nu}\, d_R\,(x_\rho)\,\eta_P$
CP	$\overline{d}_L\, b_R\,(x_\rho)\,\eta_C\eta_P$	$-\overline{d}_L\,\gamma^\mu\, b_L\,(x_\rho)\,\eta_C\eta_P$	$-\overline{d}_L\,\sigma^{\mu\nu}\, b_R\,(x_\rho)\,\eta_C\eta_P$
T	$\overline{b}_R\, d_L\,(-x_\rho)\,\eta_T$	$\overline{b}_L\,\gamma^\mu\, d_L\,(-x_\rho)\,\eta_T$	$\overline{b}_R\,\sigma^{\mu\nu}\, d_L\,(-x_\rho)\,\eta_T$
CPT	$\overline{d}_L\, b_R\,(-x^\rho)\,\eta_C\eta_P\eta_T$	$-\overline{d}_L\,\gamma_\mu\, b_L\,(-x^\rho)\,\eta_C\eta_P\eta_T$	$\overline{d}_L\,\sigma_{\mu\nu}\, b_R\,(-x^\rho)\,\eta_C\eta_P\eta_T$

Table 1.1: C, P and T transformation properties of the chiral scalar, vector and magnetic currents. The coordinate x in parentheses is the argument of both quark fields.

T and the combined transformations CP and CPT. For illustration we specify to currents involving a b and a d field. The generic transformation under some discrete symmetry X is

$$X: \qquad \overline{b}\,\Gamma d \;\;\rightarrow\;\; X\,\overline{b}\,\Gamma d\, X^{-1}, \tag{1.43}$$

and Table 1.1 lists the transformation for the chiral scalar, vector and magnetic currents. Here $\sigma_{\mu\nu} = (i/2)[\gamma_\mu, \gamma_\nu]$. The transformation laws for the currents with opposite chirality are obtained by interchanging $L \leftrightarrow R$ in Table 1.1. The phase factors

$$\eta_X = \eta_X^{bd} = e^{i\left(\phi_X^d - \phi_X^b\right)}, \qquad X = C, P, T\,. \tag{1.44}$$

depend on the quark flavors, but for simplicity the flavor indices of the η_Xs have been omitted in Table 1.1. One can absorb these arbitrary phase factors $\exp(i\phi_X^q)$ into the definitions of the discrete transformations for every quark field in the theory. This feature originates from the freedom to redefine any quark field by a phase transformation

$$q \rightarrow q\, e^{i\phi^q}. \tag{1.45}$$

In the absence of flavor-changing couplings the change in (1.45) is a $U(1)$ symmetry transformation leaving the Lagrangian invariant. The corresponding conserved quantum number is the flavor of the quark q. After including the flavor-changing interactions, the phase transformations in (1.45) change the phases of the flavor-changing couplings. The flavor symmetry is broken and every phase transformation (1.45) leads to a different, but physically equivalent Lagrangian. In the case of the Standard Model these transform the Yukawa couplings and, hence, the CKM matrix from one phase convention into another.

The currents in Table 1.1 create and destroy the meson states with the appropriate quantum numbers. Since the QCD interaction, which binds the quarks into mesons, conserves C, P and T, the meson states transform like the corresponding currents in Table 1.1. For example, the B_d meson is pseudoscalar and transforms under CP as

$$\begin{aligned} CP\,|\overline{B}_d^0\,(P^\rho)\rangle &= -\eta_P^{bd}\,\eta_C^{bd}\,|B_d^0\,(P_\rho)\rangle\,, \\ CP|B_d^0\,(P^\rho)\rangle &= -\eta_P^{bd*}\eta_C^{bd*}\,|\overline{B}_d^0\,(P_\rho)\rangle\,. \end{aligned} \tag{1.46}$$

field	photon, gluon, Z boson $V^\mu\,(x^\rho) = A^\mu(x^\rho)\,, A^{\mu,a}(x^\rho)\,, Z^\mu(x^\rho)$	W boson $W^{\pm,\mu}\,(x^\rho)$	Higgs $H\,(x^\rho)$
C	$-V^\mu\,(x^\rho)$	$-W^{\mp,\mu}\,(x^\rho)$	$H\,(x^\rho)$
P	$V_\mu\,(x_\rho)$	$W_\mu^{\pm}\,(x_\rho)$	$H\,(x_\rho)$
CP	$-V_\mu\,(x_\rho)$	$-W_\mu^{\mp}\,(x_\rho)$	$H\,(x_\rho)$
T	$V_\mu\,(-x_\rho)$	$W_\mu^{\pm}\,(-x_\rho)$	$H(-x_\rho)$
CPT	$-V^\mu\,(-x^\rho)$	$-W^{\mp,\mu}\,(-x^\rho)$	$H\,(-x^\rho)$

Table 1.2: C, $P$and T transformation properties of bosons in the Standard Model.

The vacuum state $|0\rangle$ is invariant under C, P and T. Hence one finds, for example,

$$\langle 0|\,\overline{b}\gamma_\mu\gamma_5 d(x)\,|B_d^0(P)\rangle \stackrel{CP}{=} \langle 0|\,\overline{d}\gamma_\mu\gamma_5 b(x)\,|\overline{B}_d^0(P)\rangle = i f_{B_d} P_\mu e^{-iP\cdot x}\,, \tag{1.47}$$

which is the definition of the B meson decay constant f_{B_d}. The phases $\eta_P^{bd}\eta_C^{bd}$ from the CP transformation of the pseudovector current $\overline{b}\gamma_\mu\gamma_5 d = \overline{b}_R\gamma_\mu d_R - \overline{b}_L\gamma_\mu d_L$ and $\eta_P^{bd*}\eta_C^{bd*}$ from (1.46) cancel in the first relation in (1.47). We can further multiply $|B_d^0(P)\rangle$ and $|\overline{B}_d^0(P)\rangle$ by another common phase factor (unrelated to CP) to choose f_{B_d} positive.

Although C and P are unitary transformations, T is anti-unitary (i.e., $T^\dagger T = 1$ and $\langle T\phi|T\psi\rangle = \langle\psi|\phi\rangle$). Thus, for example,

$$T\,|B_d^0(P^\rho)\rangle = \langle B_d^0(-P_\rho)|\,. \tag{1.48}$$

The anti-unitary property of T means also that c-numbers, such as the CKM matrix, are transformed into their complex conjugates.

Table 1.2 lists the transformation properties of the vector bosons and the scalar Higgs field H appearing in the Standard Model. The transformation properties of the photon and gluon field are deduced from the experimental observation that QED and QCD conserve C, P and Tquantum numbers. For the weak gauge bosons the absence of CP and T violation in the gauge sector fixes the transformation properties of $W^{\pm,\mu}$ and Z^μ under CP and T. The assignment of the C and P transformations to the weak gauge bosons and the Higgs in Table 1.2 is chosen such that the Standard Model conserves C and P in the absence of fermion fields. These assignments do not impose additional selection rules on the Standard Model interactions and therefore have no observable consequences.

From Table 1.1 one can see why the weak interaction in the Standard Model violates C and P. These transformations flip the chirality of the quark fields, but left- and right-handed fields belong to different representations of the $SU(2)$ gauge group. The combined transformation CP, however, maps the quark fields onto fields with the same chirality. Still, the currents and their CP conjugates (i.e., the first and fourth rows of Table 1.1) are not identical: instead they are Hermitian conjugates of each other. Since the Lagrangian of any quantm field theory is Hermitian, it contains for each coupling of a quark current to a vector field its Hermitian conjugate coupling as well. For example, the coupling of the W

to b and u quarks in the Standard Model is

$$\mathcal{L} = -\frac{g_2}{\sqrt{2}} \left[V_{ub}\, \overline{u}_L\, \gamma^\mu b_L\, W_\mu^+ + V_{ub}^*\, \overline{b}_L\, \gamma^\mu u_L\, W_\mu^- \right] . \tag{1.49}$$

From Tables 1.1 and 1.2 one derives the CP transformation

$$CP\, \mathcal{L}\, (CP)^{-1} = -\frac{g_2}{\sqrt{2}} \left[V_{ub}\, \overline{b}_L\, \gamma^\mu u_L\, W_\mu^- + V_{ub}^*\, \overline{u}_L\, \gamma^\mu b_L\, W_\mu^+ \right] , \tag{1.50}$$

which is the same only if $V_{ub} = V_{ub}^*$. This illuminates why CP violation is related to complex phases in couplings. Yet complex couplings alone are not sufficient for a theory to violate CP. A phase rotation (1.45) of the quark fields in the CP transformed Lagrangian changes the phases of the couplings. If we can in this way rotate the phases in $CP\, \mathcal{L}\, (CP)^{-1}$ back into those in $\mathcal{L}$, then CP is conserved. In our example (1.49) the choice $\phi^b - \phi^u = 2 \arg V_{ub}$ would transform $CP\, \mathcal{L}\, (CP)^{-1}$ back into $\mathcal{L}$. As outlined in Sec. 1.2, Kobayashi and Maskawa realized that it is not possible to remove all the phases, once there are more than two quark generations [11].

It is also illustrative to apply the time reversal transformation to (1.49). It does not modify the currents, but, due to its anti-unitary character, it flips the phases of the couplings and thereby leads to the same result as the CP transformation. In our example we have disregarded the changes in the arguments x^ρ of the fields shown in (1.42). Since physical observables depend on the action, $S = \int \mathrm{d}^4x\, \mathcal{L}(x)$, rather than on $\mathcal{L}$, the sign of x^ρ can be absorbed into a change of the integration variables.

From Table 1.1 and Table 1.2 one can verify that the action of the Standard Model is invariant under the combined transformation CPT. The CPT transformation simply turns the currents and the vector fields into their Hermitian conjugates. Due to $\mathcal{L} = \mathcal{L}^\dagger$ one has

$$S = \int \mathrm{d}^4x\, \mathcal{L}(x) = \int \mathrm{d}^4x'\, \mathcal{L}(-x') = \int \mathrm{d}^4x'\, CPT\, \mathcal{L}(x')\, (CPT)^{-1} = CPT\, S\, (CPT)^{-1} . \tag{1.51}$$

This *CPT theorem* holds in any local Poincaré invariant quantum field theory [23]. It implies that particles and antiparticles have the same masses and total decay widths. In certain string theories CPT violation may be possible, and at low energies manifests itself in the violation of Poincaré invariance or of quantum mechanics [24]. In the standard framework of quantum field theory, however, the CPT theorem is built in from the very beginning. For example, the Feynman diagram for any decay or scattering process and its CPT conjugate diagram are simply related by complex conjugation and give the same result for the decay rate or cross section. Unless stated otherwise it is always assumed that CPT invariance holds in all the formulae in this report. In this context it is meaningless to distinguish CP violation and T violation.

1.3.2 Time evolution and mixing

In this section we list the necessary formulae to describe $B_d^0 - \overline{B}_d^0$ mixing and $B_s^0 - \overline{B}_s^0$ mixing. The formulae are general and apply to both B_d^0 and to B_s^0 mesons, although with different values of the parameters. Eqs. (1.52)–(1.62) are even correct for $K^0 - \overline{K}^0$ mixing

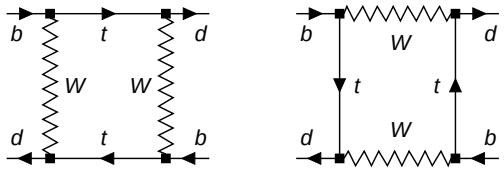

Figure 1.2: Standard Model box diagrams inducing $B_d^0 - \overline{B}_d^0$ mixing.

and $D^0 - \overline{D}^0$ mixing. In the following, the notation B^0 represents either of the two neutral B meson species with the standard convention that B^0 ($\overline{B}^0$) contains a $\overline{b}$ antiquark (a b quark).

$B^0 - \overline{B}^0$ mixing refers to transitions between the two flavor eigenstates $|B^0\rangle$ and $|\overline{B}^0\rangle$. In the Standard Model $B^0 - \overline{B}^0$ mixing is caused by the fourth order flavor-changing weak interaction described by the box diagrams in Fig. 1.2. Such transitions are called $|\Delta B| = 2$ transitions, because they change the bottom quantum number by two units. In the Standard Model $|\Delta B| = 2$ amplitudes are small, so measurements of $B^0 - \overline{B}^0$ mixing could easily be sensitive to new physics.

$B^0 - \overline{B}^0$ mixing induces oscillations between B^0 and $\overline{B}^0$. An initially produced B^0 or $\overline{B}^0$ evolves in time into a superposition of B^0 and $\overline{B}^0$. Let $|B^0(t)\rangle$ denote the state vector of a B meson which is tagged as a B^0 at time $t = 0$, i.e., $|B^0(t=0)\rangle = |B^0\rangle$. Likewise $|\overline{B}^0(t)\rangle$ represents a B meson initially tagged as a $\overline{B}^0$. The time evolution of these states is governed by a Schrödinger equation:

$$i\, \frac{\mathrm{d}}{\mathrm{d}\, t} \left(\begin{array}{c} |B(t)\rangle \\ |\overline{B}(t)\rangle \end{array} \right) = \left(M - i\, \frac{\Gamma}{2} \right) \left(\begin{array}{c} |B(t)\rangle \\ |\overline{B}(t)\rangle \end{array} \right) . \tag{1.52}$$

The *mass matrix* M and the *decay matrix* Γ are t-independent, Hermitian 2×2 matrices. CPT invariance implies that

$$M_{11} = M_{22} , \qquad \Gamma_{11} = \Gamma_{22} . \tag{1.53}$$

$|\Delta B| = 2$ transitions induce non-zero off-diagonal elements in (1.52), so that the mass eigenstates of the neutral B meson are different from the flavor eigenstates $|B^0\rangle$ and $|\overline{B}^0\rangle$. The mass eigenstates are defined as the eigenvectors of $M - i\, \Gamma/2$. We express them in terms of the flavor eigenstates as

$$\begin{aligned} \text{Lighter eigenstate:} \quad & |B_L\rangle = p|B^0\rangle + q|\overline{B}^0\rangle , \\ \text{Heavier eigenstate:} \quad & |B_H\rangle = p|B^0\rangle - q|\overline{B}^0\rangle , \end{aligned} \tag{1.54}$$

with $|p|^2 + |q|^2 = 1$. Note that, in general, $|B_L\rangle$ and $|B_H\rangle$ are not orthogonal to each other.

The time evolution of the mass eigenstates is governed by the two eigenvalues $M_H - i\, \Gamma_H/2$ and $M_L - i\, \Gamma_L/2$:

$$|B_{H,L}(t)\rangle = e^{-(i M_{H,L} + \Gamma_{H,L}/2)t}\, |B_{H,L}\rangle , \tag{1.55}$$

where $|B_{H,L}\rangle$ (without the time argument) denotes the mass eigenstates at time $t = 0$: $|B_{H,L}\rangle = |B_{H,L}(t=0)\rangle$. We adopt the following definitions for the average mass and width and the mass and width differences of the B meson eigenstates:

$$\begin{aligned} m &= \frac{M_H + M_L}{2} = M_{11}\,, & \Gamma &= \frac{\Gamma_L + \Gamma_H}{2} = \Gamma_{11}\,, \\ \Delta m &= M_H - M_L\,, & \Delta\Gamma &= \Gamma_L - \Gamma_H\,. \end{aligned} \tag{1.56}$$

Δm is positive by definition. Note that the sign convention for $\Delta\Gamma$ is opposite to the one used in Refs. [4–6,8]. In our convention the Standard Model prediction for $\Delta\Gamma$ is positive.

We can find the time evolution of $|B(t)\rangle$ and $|\overline{B}(t)\rangle$ as follows. We first invert (1.54) to express $|B^0\rangle$ and $|\overline{B}^0\rangle$ in terms of the mass eigenstates and using their time evolution in (1.55):

$$\begin{aligned} |B^0(t)\rangle &= \frac{1}{2p}\left[e^{-iM_Lt-\Gamma_Lt/2}|B_L\rangle + e^{-iM_Ht-\Gamma_Ht/2}|B_H\rangle\right], \\ |\overline{B}^0(t)\rangle &= \frac{1}{2q}\left[e^{-iM_Lt-\Gamma_Lt/2}|B_L\rangle - e^{-iM_Ht-\Gamma_Ht/2}|B_H\rangle\right]. \end{aligned} \tag{1.57}$$

These expressions will be very useful in the discussion of B_s mixing.[6] With (1.54) we next eliminate the mass eigenstates in (1.57) in favor of the flavor eigenstates:

$$\begin{aligned} |B^0(t)\rangle &= \quad g_+(t)\,|B^0\rangle + \frac{q}{p}\,g_-(t)\,|\overline{B}^0\rangle\,, \\ |\overline{B}^0(t)\rangle &= \frac{p}{q}\,g_-(t)\,|B^0\rangle + \quad g_+(t)\,|\overline{B}^0\rangle\,, \end{aligned} \tag{1.58}$$

where

$$\begin{aligned} g_+(t) &= e^{-imt}\,e^{-\Gamma t/2}\left[\quad \cosh\frac{\Delta\Gamma t}{4}\,\cos\frac{\Delta m\,t}{2} - i\sinh\frac{\Delta\Gamma t}{4}\,\sin\frac{\Delta m\,t}{2}\right], \\ g_-(t) &= e^{-imt}\,e^{-\Gamma t/2}\left[-\sinh\frac{\Delta\Gamma t}{4}\,\cos\frac{\Delta m\,t}{2} + i\cosh\frac{\Delta\Gamma t}{4}\,\sin\frac{\Delta m\,t}{2}\right]. \end{aligned} \tag{1.59}$$

Note that—owing to $\Delta\Gamma \neq 0$—the coefficient $g_+(t)$ has no zeros, and $g_-(t)$ vanishes only at $t = 0$. Hence an initially produced B^0 will never turn into a pure $\overline{B}^0$ or back into a pure B^0. The coefficients in (1.59) will enter the formulae for the decay asymmetries in the combinations

$$\begin{aligned} |g_\pm(t)|^2 &= \frac{e^{-\Gamma t}}{2}\left[\cosh\frac{\Delta\Gamma t}{2} \pm \cos(\Delta m\,t)\right], \\ g_+^*(t)\,g_-(t) &= \frac{e^{-\Gamma t}}{2}\left[-\sinh\frac{\Delta\Gamma t}{2} + i\sin(\Delta m\,t)\right]. \end{aligned} \tag{1.60}$$

[6] The Schrödinger equation, (1.52), is not exactly valid, but the result of the so-called *Wigner-Weisskopf approximation* [25] to the decay problem. In general, there are tiny corrections to the exponential decay laws in (1.57) at very short and very large times [26]. These corrections are irrelevant for the mixing and *CP* studies at Run II, but they must be taken into account in high precision searches for *CPT* violation [27].

In a given theory, such as the Standard Model, one can calculate the off-diagonal elements M_{12} and Γ_{12} entering (1.52) from $|\Delta B|=2$ diagrams. In order to exploit the formulae (1.57)–(1.59) for the time evolution we still need to express Δm, $\Delta\Gamma$ and q/p in terms of M_{12} and Γ_{12}. By solving for the eigenvalues and eigenvectors of $M - i\,\Gamma/2$ one finds

$$(\Delta m)^2 - \frac{1}{4}(\Delta\Gamma)^2 = 4|M_{12}|^2 - |\Gamma_{12}|^2\,, \tag{1.61a}$$

$$\Delta m\,\Delta\Gamma = -4\,\mathrm{Re}\,(M_{12}\Gamma_{12}^*)\,, \tag{1.61b}$$

$$\frac{q}{p} = -\frac{\Delta m + i\,\Delta\Gamma/2}{2M_{12} - i\,\Gamma_{12}} = -\frac{2M_{12}^* - i\,\Gamma_{12}^*}{\Delta m + i\,\Delta\Gamma/2}\,. \tag{1.61c}$$

The relative phase between M_{12} and Γ_{12} appears in many observables related to B mixing. We introduce

$$\phi = \arg\left(-\frac{M_{12}}{\Gamma_{12}}\right). \tag{1.62}$$

Now one can solve (1.61) for Δm and $\Delta\Gamma$ in terms of $|M_{12}|$, $|\Gamma_{12}|$ and ϕ.

The general solution is not illuminating, but a simple, approximate solution may be derived when

$$|\Gamma_{12}| \ll |M_{12}|\,, \qquad \text{and} \qquad \Delta\Gamma \ll \Delta m\,. \tag{1.63}$$

These inequalities hold (empirically) for both B^0 systems. We first note that $|\Gamma_{12}| \leq \Gamma$ always, because Γ_{12} stems from the decays into final states common to B^0 and $\overline{B}^0$. For the B_s^0 meson the lower bound on Δm_{B_s} establishes experimentally that $\Gamma_{B_s} \ll \Delta m_{B_s}$. Hence $\Gamma_{12}^s \ll \Delta m_{B_s}$, and Eqs. (1.61a) and (1.61b) imply $\Delta m_{B_s} \approx 2|M_{12}^s|$ and $|\Delta\Gamma_{B_s}| \leq 2|\Gamma_{12}^s|$, so that (1.63) holds. For the B_d^0 meson the experiments give $\Delta m_{B_d} \approx 0.75\,\Gamma_{B_d}$. The Standard Model predicts $|\Gamma_{12}^d|/\Gamma_{B_d} = \mathcal{O}(1\%)$, but Γ_{12}^d stems solely from CKM-suppressed decay channels (common to B_d^0 and $\overline{B}_d^0$) and could therefore be affected by new physics. New decay channels would, however, also increase Γ_{B_d} and potentially conflict with the precisely measured semileptonic branching ratio. A conservative estimate is $|\Gamma_{12}^d|/\Gamma_{B_d} < 10\%$. Hence for both the B_s^0 and B_d^0 system an expansion in Γ_{12}/M_{12} and $\Delta\Gamma/\Delta m$ is a good approximation, and we easily find

$$\Delta m = 2\,|M_{12}|\left[1 + \mathcal{O}\left(\left|\frac{\Gamma_{12}}{M_{12}}\right|^2\right)\right], \tag{1.64a}$$

$$\Delta\Gamma = 2\,|\Gamma_{12}|\cos\phi\left[1 + \mathcal{O}\left(\left|\frac{\Gamma_{12}}{M_{12}}\right|^2\right)\right]. \tag{1.64b}$$

We also need an approximate expression for q/p in (1.61). It is convenient to define a small parameter

$$a = \mathrm{Im}\,\frac{\Gamma_{12}}{M_{12}} = \left|\frac{\Gamma_{12}}{M_{12}}\right|\sin\phi\,, \tag{1.65}$$

because occasionally we need to keep terms of order a. Then q/p becomes

$$\frac{q}{p} = -e^{-i\phi_M}\left[1 - \frac{a}{2}\right] + \mathcal{O}\left(\left|\frac{\Gamma_{12}}{M_{12}}\right|^2\right), \tag{1.66}$$

where ϕ_M is the phase of M_{12},

$$M_{12} = |M_{12}|\, e^{i\phi_M}\,. \tag{1.67}$$

Note that (1.66) and the normalization condition $|p|^2 + |q|^2 = 1$ imply

$$|p| = \frac{1}{\sqrt{2}}\left(1+\frac{a}{4}\right) + \mathcal{O}\left(\left|\frac{\Gamma_{12}}{M_{12}}\right|^2\right), \qquad |q| = \frac{1}{\sqrt{2}}\left(1-\frac{a}{4}\right) + \mathcal{O}\left(\left|\frac{\Gamma_{12}}{M_{12}}\right|^2\right). \tag{1.68}$$

We are now prepared to exhibit the time-dependent decay rate $\Gamma(B^0(t) \to f)$ of an initially tagged B^0 into some final state f. It is defined as

$$\Gamma(B^0(t) \to f) = \frac{1}{N_B}\,\frac{\mathrm{d}N(B^0(t) \to f)}{\mathrm{d}t}\,, \tag{1.69}$$

where $\mathrm{d}N(B^0(t) \to f)$ denotes the number of decays of a B meson tagged as a B^0 at $t = 0$ into the final state f occurring within the time interval between t and $t + \mathrm{d}t$. N_B is the total number of B^0's produced at time $t = 0$. An analogous definition holds for $\Gamma(\overline{B}^0(t) \to f)$. One has

$$\Gamma(B^0(t) \to f) = \mathcal{N}_f \left|\langle f|B^0(t)\rangle\right|^2, \qquad \Gamma(\overline{B}^0(t) \to f) = \mathcal{N}_f \left|\langle f|\overline{B}^0(t)\rangle\right|^2. \tag{1.70}$$

Here $\mathcal{N}_f$ is a time-independent normalization factor. To calculate $\Gamma(B^0(t) \to f)$ we introduce the two decay amplitudes

$$A_f = \langle f|B^0\rangle\,, \qquad \overline{A}_f = \langle f|\overline{B}^0\rangle\,, \tag{1.71}$$

and the quantity

$$\lambda_f = \frac{q}{p}\,\frac{\overline{A}_f}{A_f} \simeq -e^{-i\phi_M}\,\frac{\overline{A}_f}{A_f}\,\left[1-\frac{a}{2}\right]. \tag{1.72}$$

We will see in the following sections that λ_f plays the pivotal role in CP asymmetries and other observables in B mixing. Finally with (1.58), (1.60) and $|p/q|^2 = (1+a)$ we find the desired formulae for the decay rates:

$$\Gamma(B^0(t) \to f) = \mathcal{N}_f\,|A_f|^2\, e^{-\Gamma t}\left\{\frac{1+|\lambda_f|^2}{2}\,\cosh\frac{\Delta\Gamma\, t}{2} + \frac{1-|\lambda_f|^2}{2}\,\cos(\Delta m\, t)\right.$$
$$\left. -\mathrm{Re}\,\lambda_f\,\sinh\frac{\Delta\Gamma\, t}{2} - \mathrm{Im}\,\lambda_f\,\sin(\Delta m\, t)\right\}, \tag{1.73}$$

$$\Gamma(\overline{B}^0(t) \to f) = \mathcal{N}_f\,|A_f|^2\,(1+a)\,e^{-\Gamma t}\left\{\frac{1+|\lambda_f|^2}{2}\,\cosh\frac{\Delta\Gamma\, t}{2} - \frac{1-|\lambda_f|^2}{2}\,\cos(\Delta m\, t)\right.$$
$$\left. -\mathrm{Re}\,\lambda_f\,\sinh\frac{\Delta\Gamma\, t}{2} + \mathrm{Im}\,\lambda_f\,\sin(\Delta m\, t)\right\}. \tag{1.74}$$

Next we consider the decay into $\overline{f}$, which denotes the CP conjugate state to f,

$$|\overline{f}\rangle = CP|f\rangle\,. \tag{1.75}$$

For example, for $f = D_s^-\pi^+$ the CP conjugate state is $\overline{f} = D_s^+\pi^-$. The decay rate into $\overline{f}$ can be obtained from (1.73) and (1.74) by simply replacing f with $\overline{f}$. Yet $|A_{\overline{f}}|$ and $|A_f|$ are unrelated, unless f is a CP eigenstate, fulfilling $|\overline{f}\rangle = \pm|f\rangle$. On the other hand the CP transformation relates $|\overline{A}_{\overline{f}}|$ to $|A_f|$, so it is more useful to factor out $|\overline{A}_{\overline{f}}|$,

$$\Gamma(B^0(t) \to \overline{f}) = \mathcal{N}_f\left|\overline{A}_{\overline{f}}\right|^2 e^{-\Gamma t}\,(1-a)\left\{\frac{1+|\lambda_{\overline{f}}|^{-2}}{2}\,\cosh\frac{\Delta\Gamma\, t}{2} - \frac{1-|\lambda_{\overline{f}}|^{-2}}{2}\,\cos(\Delta m\, t)\right.$$
$$\left. -\mathrm{Re}\,\frac{1}{\lambda_{\overline{f}}}\,\sinh\frac{\Delta\Gamma\, t}{2} + \mathrm{Im}\,\frac{1}{\lambda_{\overline{f}}}\,\sin(\Delta m\, t)\right\}, \tag{1.76}$$

$$\Gamma(\overline{B}^0(t) \to \overline{f}) = \mathcal{N}_f\left|\overline{A}_{\overline{f}}\right|^2 e^{-\Gamma t}\left\{\frac{1+|\lambda_{\overline{f}}|^{-2}}{2}\,\cosh\frac{\Delta\Gamma\, t}{2} + \frac{1-|\lambda_{\overline{f}}|^{-2}}{2}\,\cos(\Delta m\, t)\right.$$
$$\left. -\mathrm{Re}\,\frac{1}{\lambda_{\overline{f}}}\,\sinh\frac{\Delta\Gamma\, t}{2} - \mathrm{Im}\,\frac{1}{\lambda_{\overline{f}}}\,\sin(\Delta m\, t)\right\}. \tag{1.77}$$

Here we set $\mathcal{N}_{\overline{f}} = \mathcal{N}_f$, because these normalization factors arise from kinematics. In Eqs. (1.73)–(1.77) we consistently keep terms of order a, which appear explicitly in the prefactor in (1.74), (1.76) and are implicit in λ_f through (1.72).[7]

We now apply the derived formalism to the decay rate into a *flavor-specific* final state f meaning that a B^0 can decay into f, while $\overline{B}^0$ cannot. Examples are $f = D_s^-\pi^+$ (from B_s^0) and $f = X\ell^+\nu_\ell$. In such decays $\overline{A}_f = A_{\overline{f}} = 0$ by definition and, hence, $\lambda_f = 1/\lambda_{\overline{f}} = 0$. Therefore,

$$\Gamma(B^0(t) \to f) = \mathcal{N}_f\,|A_f|^2\, e^{-\Gamma t}\,\frac{1}{2}\left[\cosh\frac{\Delta\Gamma\, t}{2} + \cos(\Delta m\, t)\right] \qquad \text{for } \overline{A}_f = 0\,, \tag{1.78}$$

$$\Gamma(B^0(t) \to \overline{f}) = \mathcal{N}_f\left|\overline{A}_{\overline{f}}\right|^2 (1-a)\, e^{-\Gamma t}\,\frac{1}{2}\left[\cosh\frac{\Delta\Gamma\, t}{2} - \cos(\Delta m\, t)\right] \qquad \text{for } A_{\overline{f}} = 0\,. \tag{1.79}$$

Flavor-specific decays can be used to measure Δm via the asymmetry in decays from mixed and unmixed Bs:

$$\mathcal{A}_0(t) = \frac{\Gamma(B^0(t) \to f) - \Gamma(B^0(t) \to \overline{f})}{\Gamma(B^0(t) \to f) + \Gamma(B^0(t) \to \overline{f})}\,. \tag{1.80}$$

The amplitudes A_f and $\overline{A}_{\overline{f}}$ are related to each other by CP conjugation. If there is no CP violation in the decay amplitude (i.e., no *direct CP violation*), $|A_f|$ and $|\overline{A}_{\overline{f}}|$ are equal. This is the case for decays like $B_s \to D_s^-\pi^+$ and $B \to X\ell^+\nu_\ell$ conventionally used to measure Δm. Then the mixing asymmetry in (1.80) reads

$$\mathcal{A}_0(t) = \frac{\cos(\Delta m\, t)}{\cosh(\Delta\Gamma\, t/2)} + \frac{a}{2}\left[1 - \frac{\cos^2(\Delta m\, t)}{\cosh^2(\Delta\Gamma\, t/2)}\right], \tag{1.81}$$

where we have allowed for a non-zero width difference.

[7] We have omitted terms of order $|\Gamma_{12}/M_{12}|^2$ in Eqs. (1.72)–(1.77) and will do this throughout the report. In most applications one can set a to zero and often also $\Delta\Gamma$ can be neglected, so that the expressions in Eqs. (1.73)–(1.77) simplify considerably.

1.3.3 Time evolution of untagged B^0 mesons

Since B^0's and $\overline{B}^0$'s are produced in equal numbers at the Tevatron, the untagged decay rate for the decay $\stackrel{(-)}{B}\!\!\to f$ reads

$$\begin{aligned}\Gamma[f,t] &= \Gamma(B^0(t)\to f)+\Gamma(\overline{B}^0(t)\to f) \\ &= \mathcal{N}_f\,|A_f|^2\left(1+|\lambda_f|^2\right)e^{-\Gamma t}\left[\cosh\frac{\Delta\Gamma t}{2}+\sinh\frac{\Delta\Gamma t}{2}\,A_{\Delta\Gamma}\right]+\mathcal{O}(a)\end{aligned} \tag{1.82}$$

with

$$A_{\Delta\Gamma} = -\frac{2\,\mathrm{Re}\,\lambda_f}{1+|\lambda_f|^2}\,. \tag{1.83}$$

From this equation one realizes that untagged samples are interesting for the determination of $\Delta\Gamma$. The fit of an untagged decay distribution to (1.82) involves the overall normalization factor $\mathcal{N}_f\,|A_f|^2\,(1+|\lambda_f|^2)$. From (1.69) one realizes that by integrating $\Gamma[f,t]$ over all times one obtains the branching ratio for the decay of an untagged B^0 into the final state f:

$$\begin{aligned}\mathcal{B}(\stackrel{(-)}{B}\!\!\to f\,) &= \frac{1}{2}\int_0^\infty \mathrm{d}t\,\Gamma[f,t] \;= \frac{\mathcal{N}_f}{2}\,|A_f|^2\,\frac{\Gamma\,(1+|\lambda_f|^2)-\Delta\Gamma\,\mathrm{Re}\,\lambda_f}{\Gamma^2-(\Delta\Gamma/2)^2}+\mathcal{O}(a) \\ &= \frac{\mathcal{N}_f}{2}\,|A_f|^2\left(1+|\lambda_f|^2\right)\frac{1}{\Gamma}\left[1+\frac{\Delta\Gamma}{2\Gamma}\,A_{\Delta\Gamma}\;+\mathcal{O}\left(\frac{(\Delta\Gamma)^2}{\Gamma^2}\right)\right].\end{aligned} \tag{1.84}$$

Relation (1.84) allows to eliminate $\mathcal{N}_f\,|A_f|^2\,[1+|\lambda_f|^2]$ from (1.82), if the branching ratio is known. If both $\mathcal{B}(\stackrel{(-)}{B}\!\!\to f)$ and $\Delta\Gamma$ are known, a one-parameter fit to the measured untagged time evolution (1.82) allows to determine $A_{\Delta\Gamma}$, which is of key interest for CP studies.

Finally we write down a more intuitive expression for $\Gamma[f,t]$. From (1.70) and (1.57) one immediately finds

$$\Gamma[f,t] = \mathcal{N}_f\left[e^{-\Gamma_L t}\,|\langle f|B_L\rangle|^2+e^{-\Gamma_H t}\,|\langle f|B_H\rangle|^2\right]+\mathcal{O}(a)\,. \tag{1.85}$$

With (1.54) one recovers (1.82) from (1.85). Now (1.85) nicely shows that the decay of the untagged sample into some final state f is governed by two exponentials. If B_s mixing is correctly described by the Standard Model, the mass eigenstates $|B_L\rangle$ and $|B_H\rangle$ are to a high precision also CP eigenstates and (1.85) proves useful for the description of decays into CP eigenstates.

1.3.4 Time-dependent and time-integrated CP asymmetries

The CP asymmetry for the decay of a charged B into the final state f reads

$$a_f = \frac{\Gamma(B^-\to f)-\Gamma(B^+\to\overline{f})}{\Gamma(B^-\to f)+\Gamma(B^+\to\overline{f})} \qquad \text{with } |\overline{f}\rangle = CP\,|f\rangle. \tag{1.86}$$

Defining

$$A_f = \langle f|B^+\rangle \qquad \text{and} \qquad \overline{A}_{\overline{f}} = \langle\overline{f}|B^-\rangle \tag{1.87}$$

in analogy to (1.71) one finds

$$a_f = -\frac{1-\left|\overline{A}_{\overline{f}}/A_f\right|^2}{1+\left|\overline{A}_{\overline{f}}/A_f\right|^2}\,. \tag{1.88}$$

Since charged B mesons cannot mix, a non-zero a_f can only occur through CP violation in the $|\Delta B|=1$ matrix elements A_f and $\overline{A}_{\overline{f}}$. This is called *direct* CP violation and stems from $|A_f|\neq|\overline{A}_{\overline{f}}|$.

Next we consider the decay of a neutral B meson into a CP eigenstate $f=f_{CP}=\eta_f\overline{f}$. Here $\eta_f=\pm1$ is the CP quantum number of f. An example for this situation is the decay $B_s^0\to D_s^+D_s^-$, where $\eta_f=+1$. We define the time-dependent CP asymmetry as

$$a_f(t) = \frac{\Gamma(\overline{B}^0(t)\to f)-\Gamma(B^0(t)\to f)}{\Gamma(\overline{B}^0(t)\to f)+\Gamma(B^0(t)\to f)}\,. \tag{1.89}$$

Using (1.73) and (1.74) one finds

$$a_f(t) = -\frac{A_{CP}^{\mathrm{dir}}\cos(\Delta m\,t)+A_{CP}^{\mathrm{mix}}\sin(\Delta m\,t)}{\cosh(\Delta\Gamma t/2)+A_{\Delta\Gamma}\sinh(\Delta\Gamma t/2)}+\mathcal{O}(a)\,, \tag{1.90}$$

where $A_{\Delta\Gamma}$ is defined in (1.83), and the *direct* and *mixing-induced* (or *interference type*) CP asymmetries are

$$A_{CP}^{\mathrm{dir}} = \frac{1-|\lambda_f|^2}{1+|\lambda_f|^2}\,, \qquad A_{CP}^{\mathrm{mix}} = -\frac{2\,\mathrm{Im}\,\lambda_f}{1+|\lambda_f|^2}\,, \tag{1.91}$$

A_{CP}^{mix} stems from the interference of the decay amplitudes of the unmixed and the mixed B, i.e., of $\overline{B}^0\to f$ and $B^0\to f$. It is discussed in more detail in Sec. 1.4.1. Note that the quantities in (1.91) and (1.83) are not independent, $|A_{CP}^{\mathrm{dir}}|^2+|A_{CP}^{\mathrm{mix}}|^2+|A_{\Delta\Gamma}|^2=1$.

The time integrated asymmetry reads[8]

$$a_f^{\mathrm{int}} = \frac{\int_0^\infty \mathrm{d}t\left[\Gamma(\overline{B}^0(t)\to f)-\Gamma(B^0(t)\to f)\right]}{\int_0^\infty \mathrm{d}t\left[\Gamma(\overline{B}^0(t)\to f)+\Gamma(B^0(t)\to f)\right]} = -\frac{1+y^2}{1+x^2}\,\frac{A_{CP}^{\mathrm{dir}}+A_{CP}^{\mathrm{mix}}\,x}{1+A_{\Delta\Gamma}\,y}\,. \tag{1.92}$$

Here the quantities x and y are defined as

$$x = \frac{\Delta m}{\Gamma}\,, \qquad y = \frac{\Delta\Gamma}{2\,\Gamma}\,. \tag{1.93}$$

Thus, even without following the time evolution, a measurement of a_f^{int} puts constraints on Δm and $\Delta\Gamma$.

[8] Our sign conventions for the CP asymmetries in (1.86) and (1.89) are opposite to those in [8]. Our definitions of A_{CP}^{dir}, A_{CP}^{mix} and $A_{\Delta\Gamma}$ are the same as in [8], taking into account that the quantity $\xi_f^{(q)}$ of [8] equals $-\lambda_f$.

1.3.5 Phase conventions

In Sec. 1.3.1 we learned that there is no unique way to define the CP transformation, because it involves an arbitrary phase factor $\eta_{CP} \equiv \eta_C \eta_P$ (see Table 1.1 and Eq. (1.44)). This arbitrariness stems from the fact that phases of quark fields are unobservable and phase redefinitions as in (1.45) transform the Lagrangian into a physically equivalent one. This feature implies that the phases of the flavor-changing couplings in our Lagrangian are not fixed and the phase rotation (1.45) transforms one phase convention for these couplings into another one. Of course, physical observables are independent of these phase conventions. Hence it is worth noting which of the quantities defined in the previous sections are invariant, when η_{CP} or the phases of the quark fields are changed. It is also important to identify the quantities that do depend on phase conventions to avoid mistakes when combining convention dependent quantities into an invariant observable.

The phases of

$$M_{12}\,,\ \Gamma_{12}\,,\ \frac{q}{p}\,,\ \text{and}\ \frac{\overline{A}_f}{A_f}\,. \tag{1.94}$$

depend on the phase convention of the CP transformation or the phase convention of the CP violating couplings. In particular, the phase ϕ_M of the mixing amplitude M_{12} (defined in (1.67)) is convention dependent. When speaking informally, one often says that a given process, such as $B^0_d \to \psi K_S$, measures the phase of the $|\Delta B|=2$ amplitude, i.e., ϕ_M. Such statements refer to a specific phase convention, in which the decay amplitude of the process has a vanishing (or negligible) phase. The following quantities are independent of phase conventions:

$$\left|\frac{q}{p}\right|\,,\ \left|\frac{\overline{A}_f}{A_f}\right|\,,\ a\,,\ \phi\,,\ \Delta m\,,\ \Delta\Gamma\,,\ \text{and}\ \lambda_f\,. \tag{1.95}$$

The only complex quantity here is λ_f. Its phase is a physical observable.

We have shown that the arbitrary phases accompanying the CP transformation stem from the freedom to rephase the quark fields, see (1.45). The corresponding phase factors η_{CP} in the CP transformed quark bilinears are sufficient to parameterize this arbitrariness and likewise appear in the CP transformations of the mesons and the quantities in (1.94). In some discussions of this issue authors allow for phases different from η_{CP} accompanying the CP transformation (1.46) of the meson states. This is simply equivalent to using our transformation (1.46) followed by a multiplication of $|B^0_d\rangle$ and $|\overline{B}^0_d\rangle$ with extra phase factors (unrelated to CP), which do not affect observables. This would further introduce an extra inconvenient phase into (1.47). The quantities in (1.95) are still invariant under such an extra rephasing and no new information is gained from this generalization. Unless stated otherwise, we will use the phase convention $\eta_{CP} = 1$, i.e.,

$$CP\,|\overline{B}^0(P^\rho)\rangle = -|B^0(P_\rho)\rangle\,, \qquad CP\,|B^0(P^\rho)\rangle = -|\overline{B}^0(P_\rho)\rangle\,. \tag{1.96}$$

For the phases of the CKM elements we use the convention of the Particle Data Group, (1.33).

1.4 Aspects of CP Violation

1.4.1 The three types of CP violation

As discussed in Sec. 1.3.5, there are three phase convention independent physical CP violating observables

$$\left|\frac{q}{p}\right|\,, \qquad \left|\frac{\overline{A}_{\overline{f}}}{A_f}\right|\,, \qquad \lambda_f = \frac{q}{p}\,\frac{\overline{A}_f}{A_f}\,. \tag{1.97}$$

If any one of these quantities is not equal to 1 (or -1 for λ_f), then CP is violated in the particular decay. In fact, there are decays where only one of these types of CP violations occur (to a very good approximation).

CP violation in mixing ($|q/p| \neq 1$)

It follows from Eq. (1.61c) that

$$\left|\frac{q}{p}\right|^2 = \left|\frac{2M^*_{12} - i\,\Gamma^*_{12}}{2M_{12} - i\,\Gamma_{12}}\right|\,. \tag{1.98}$$

If CP were conserved, then the relative phase between M_{12} and Γ_{12} would vanish, and so $|q/p| = 1$. If $|q/p| \neq 1$, then CP is violated. This is called CP violation in mixing, because it results from the mass eigenstates being different from the CP eigenstates. It follows from Eq. (1.54) that $\langle B_H|B_L\rangle = |p|^2 - |q|^2$, and so the two physical states are orthogonal if and only if CP is conserved in $|\Delta B| = 2$ amplitudes.

The simplest example of this type of CP violation is the neutral meson semileptonic decay asymmetry to "wrong sign" leptons

$$\begin{aligned} a_{\rm sl}(t) &= \frac{\Gamma(\overline{B}^0(t) \to \ell^+\nu X) - \Gamma(B^0(t) \to \ell^-\bar\nu X)}{\Gamma(\overline{B}^0(t) \to \ell^+\nu X) + \Gamma(B^0(t) \to \ell^-\bar\nu X)} \\ &= \frac{|p/q|^2 - |q/p|^2}{|p/q|^2 + |q/p|^2} = \frac{1 - |q/p|^4}{1 + |q/p|^4} = a + \mathcal{O}(a^2)\,. \end{aligned} \tag{1.99}$$

The second line follows from Eq. (1.58). In B meson decay such an asymmetry is expected to be $\mathcal{O}(10^{-2})$. The calculation of $|q/p| - 1$ involves $\mathrm{Im}\,(\Gamma_{12}/M_{12})$, which suffers from hadronic uncertainties. Thus, it would be difficult to relate the observation of such an asymmetry to CKM parameters. This type of CP violation can also be observed in any decay for which $A_f \gg A_{\overline{f}}$, such as decays to flavor specific final states (for which $A_{\overline{f}} = 0$), e.g., $B_{(s)} \to D^-_{(s)}\pi^+$. In kaon decays this asymmetry was recently measured by CPLEAR [28] in agreement with the expectation that it should be equal to $4\,\mathrm{Re}\,\epsilon_K$.

CP violation in decay ($|\overline{A}_{\overline{f}}/A_f| \neq 1$)

For any final state f, the quantity $|\overline{A}_{\overline{f}}/A_f|$ is a phase convention independent physical observable. There are two types of complex phases which can appear in $\overline{A}_{\overline{f}}$ and A_f defined

in Eq. (1.71). Complex parameters in the Lagrangian which enter a decay amplitude also enter the CP conjugate amplitude but in complex conjugate form. In the Standard Model such parameters only occur in the CKM matrix. These so-called weak phases enter $\overline{A}_{\overline{f}}$ and A_f with opposite signs. Another type of phase can arise even when the Lagrangian is real, from absorptive parts of decay amplitudes. These correspond to on-shell intermediate states rescattering into the desired final state. Such rescattering is usually dominated by strong interactions, and give rise to CP conserving strong phases, which enter $\overline{A}_{\overline{f}}$ and A_f with the same signs. Thus one can write $\overline{A}_{\overline{f}}$ and A_f as

$$A_f = \sum_k A_k\, e^{i(\,\delta_k+\phi_k)}\,, \qquad \overline{A}_{\overline{f}} = \sum_k A_k\, e^{i(\,\delta_k-\phi_k)}\,, \tag{1.100}$$

where k label the separate contributions to the amplitudes, A_k are the magnitudes of each term, δ_k are the strong phases, and ϕ_k are the weak phases. The individual phases δ_k and ϕ_k are convention dependent, but the phase differences between different terms, $\delta_i - \delta_j$ and $\phi_i - \phi_j$, are physical.

Clearly, if $|\overline{A}_{\overline{f}}/A_f| \neq 1$ then CP is violated. This is called CP violation in decay, or direct CP violation. It occurs due to interference between various terms in the decay amplitude, and requires that at least two terms differ both in their strong and in their weak phases. The simplest example of this is direct CP violation in charged B decays

$$\frac{\Gamma(B^-\to f) - \Gamma(B^+\to \overline{f})}{\Gamma(B^-\to f) + \Gamma(B^+\to \overline{f})} = -\frac{1-|\overline{A}_{\overline{f}}/A_f|^2}{1+|\overline{A}_{\overline{f}}/A_f|^2}\,. \tag{1.101}$$

To extract the interesting weak phases from such CP violating observables, one needs to know the amplitudes A_k and their strong phases δ_k. The problem is that theorists do not know how to compute these from first principles, and most estimates are unreliable. The only experimental observation of direct CP violation so far is $\mathrm{Re}\,\epsilon'_K$ in kaon decays.

This type of CP violation can also occur in neutral B decays in conjunction with the others. In such cases direct CP violation is rarely beneficial, and is typically a source of hadronic uncertainties that are hard to control.

CP violation in the interference between decay and mixing ($\lambda_f \neq \pm 1$)

Another type of CP violation is possible in neutral B decay into a CP eigenstate final state, f_{CP}. If CP is conserved, then not only $|q/p| = 1$ and $|\overline{A}_f/A_f| = 1$, but the relative phase between q/p and $\overline{A}_f/A_f$ also vanishes. In this case it is convenient to rewrite

$$\lambda_{f_{CP}} = \frac{q}{p}\frac{\overline{A}_{f_{CP}}}{A_{f_{CP}}} = \eta_{f_{CP}}\,\frac{q}{p}\frac{\overline{A}_{\overline{f}_{CP}}}{A_{f_{CP}}}\,, \tag{1.102}$$

where $\eta_{f_{CP}} = \pm 1$ is the CP eigenvalue of f_{CP}. This form of $\lambda_{f_{CP}}$ is useful for calculations, because $A_{f_{CP}}$ and $\overline{A}_{\overline{f}_{CP}}$ are related by CP as discussed in the previous subsection. If $\lambda_{f_{CP}} \neq \pm 1$ then CP is violated. This is called CP violation in the interference between

decays with and without mixing, because it results from the CP violating interference between $B^0 \to f_{CP}$ and $B^0 \to \overline{B}^0 \to f_{CP}$.

As derived in Eq. (1.90), the time dependent asymmetry is

$$\begin{aligned} a_f(t) &= \frac{\Gamma(\overline{B}^0(t)\to f) - \Gamma(B^0(t)\to f)}{\Gamma(\overline{B}^0(t)\to f) + \Gamma(B^0(t)\to f)} \\ &= -\frac{(1-|\lambda_f|^2)\cos(\Delta m\, t) - 2\,\mathrm{Im}\,\lambda_f \sin(\Delta m\, t)}{(1+|\lambda_f|^2)\cosh(\Delta\Gamma\, t/2) - 2\,\mathrm{Re}\,\lambda_f \sinh(\Delta\Gamma\, t/2)} + \mathcal{O}(a)\,. \end{aligned} \tag{1.103}$$

This asymmetry is non-zero if any type of CP violation occurs. In particular, it is possible that $\mathrm{Im}\,\lambda_f \neq 0$, but $|\lambda_f| = 1$ to a good approximation, because $|q/p| \simeq 1$ and $|\overline{A}_f/A_f| \simeq 1$. In both the B_d and B_s systems $|q/p| - 1 \lesssim \mathcal{O}(10^{-2})$. Furthermore, if only one amplitude contributes to a decay, then $|\overline{A}_f/A_f| = 1$ automatically. These modes are "clean", because in such cases A_f drops out and

$$a_f(t) = \frac{\mathrm{Im}\,\lambda_f \sin(\Delta m\, t)}{\cosh(\Delta\Gamma\, t/2) - \mathrm{Re}\,\lambda_f \sinh(\Delta\Gamma\, t/2)}\,, \tag{1.104}$$

measures $\mathrm{Im}\,\lambda_f$, which is given by a weak phase. In addition, if $\Delta\Gamma$ can be neglected then $a_f(t)$ further simplifies to $a_f(t) = \mathrm{Im}\,\lambda_f \sin(\Delta m\, t)$.

The best known example of this type of CP violation (and also the one where $|\lambda_f| = 1$ holds to a very good accuracy) is the asymmetry in $B \to \psi K_S$, where ψ denotes any charmonium state. The decay is dominated by the tree level $b \to c\bar{c}s$ transition and its CP conjugate. In the phase convention (1.96) one finds

$$\frac{\overline{A}_{\psi K_S}}{A_{\psi K_S}} = \left(\frac{V_{cb}V_{cs}^*}{V_{cb}^*V_{cs}}\right)\left(\frac{V_{cs}V_{cd}^*}{V_{cs}^*V_{cd}}\right). \tag{1.105}$$

The overall plus sign arises from (1.96) and because ψK_S is CP odd, $\eta_{\psi K_S} = -1$, and the last factor is $(q/p)^*$ in $K^0 - \overline{K}^0$ mixing. This is crucial, because in the absence of $K^0 - \overline{K}^0$ mixing there could be no interference between $\overline{B}^0 \to \psi\overline{K}^0$ and $B^0 \to \psi K^0$. There are also penguin contributions to this decay, which have different weak and strong phases. These are discussed in detail in Chapter 6, where they are shown to give rise to hadronic uncertainties suppressed by λ^2. Then one finds

$$\lambda_{\psi K_S} = -\left(\frac{V_{tb}^*V_{td}}{V_{tb}V_{td}^*}\right)\left(\frac{V_{cb}V_{cs}^*}{V_{cb}^*V_{cs}}\right)\left(\frac{V_{cs}V_{cd}^*}{V_{cs}^*V_{cd}}\right) = -e^{-2i\beta}\,, \tag{1.106}$$

where the first factor is the Standard Model value of q/p in B_d mixing. Thus, $a_{\psi K_S}(t)$ measures $\mathrm{Im}\,\lambda_{\psi K_S} = \sin 2\beta$ cleanly.

Of significant interest are some final states which are not pure CP eigenstates, but have CP self conjugate particle content and can be decomposed in CP even and odd partial waves. In some cases an angular analysis can separate the various components, and may provide theoretically clean information. An example is $B_s \to \psi\,\phi$ discussed in Chapters 6 and 8. There are many cases when CP violation in decay occurs in addition to CP violation

in the interference between mixing and decay. Then the asymmetry in Eq. (1.103) depends on the ratio of different decay amplitudes and their strong phases, which introduce hadronic uncertainties. In some cases it is possible to remove (or reduce) these by measuring several rates related by isospin symmetry. An example is $B_d \to \rho\,\pi$ (or $\pi\,\pi$) discussed in Chapter 6.

1.4.2 Decays to non-CP eigenstates

In certain decays to final states which are not CP eigenstates, it is still possible to extract weak phases model independently from the interference between mixing and decay. This occurs if both B^0 and $\overline{B}^0$ can decay into a particular final state and its CP conjugate, but there is only one contribution to each of these decay amplitudes. In this case no assumptions about hadronic physics are needed, even though $|\overline{A}_f/A_f| \neq 1$ and $|\overline{A}_{\overline{f}}/A_{\overline{f}}| \neq 1$.

The most important example is $B_s \to D_s^{\pm} K^{\mp}$, which allows a model independent determination of γ [29]. Both $\overline{B}_s^0$ and B_s^0 can decay to $D_s^+ K^-$ and $D_s^- K^+$, but the only decay processes are the tree level $b \to c\bar{u}s$ and $b \to u\bar{c}s$ transitions, and their CP conjugates. One can easily see that

$$\frac{\overline{A}_{D_s^+ K^-}}{A_{D_s^+ K^-}} = \frac{A_1}{A_2}\left(\frac{V_{cb}V_{us}^*}{V_{ub}^*V_{cs}}\right), \qquad \frac{\overline{A}_{D_s^- K^+}}{A_{D_s^- K^+}} = \frac{A_2}{A_1}\left(\frac{V_{ub}V_{cs}^*}{V_{cb}^*V_{us}}\right), \tag{1.107}$$

where the ratio of amplitudes, A_1/A_2, includes the strong phases, and is an unknown complex number of order unity. It is important for the utility of this method that $|V_{cb}V_{us}|$ and $|V_{ub}V_{cs}|$ are comparable in magnitude, since both are of order λ^3 in the Wolfenstein parameterization. Eqs. (1.73) and (1.74) show that measuring the four time dependent decay rates determine both $\lambda_{D_s^+ K^-}$ and $\lambda_{D_s^- K^+}$. The unknown A_1/A_2 ratio drops out from their product

$$\lambda_{D_s^+ K^-}\,\lambda_{D_s^- K^+} = \left(\frac{V_{tb}^*V_{ts}}{V_{tb}V_{ts}^*}\right)^2\left(\frac{V_{cb}V_{us}^*}{V_{ub}^*V_{cs}}\right)\left(\frac{V_{ub}V_{cs}^*}{V_{cb}^*V_{us}}\right) = e^{-2i(\gamma - 2\beta_s - \beta_K)}\,. \tag{1.108}$$

The first factor is the Standard Model value of q/p in B_s mixing. The angles β_s and β_K occur in "squashed" unitarity triangles; β_s defined in Eq. (1.41) is of order λ^2 and $\beta_K = \arg(-V_{cs}V_{cd}^*/V_{us}V_{ud}^*)$ is of order λ^4. Thus, this mode can provide a precise determination of γ (or $\gamma - 2\beta_s$); the determination of β_s is discussed in Chapter 6, e.g., from $B_s \to \psi\,\eta^{(\prime)}$.

In exact analogy to the above, the $B_d \to D^{(*)\pm}\pi^{\mp}$ decays can determine $\gamma + 2\beta$, since $\lambda_{D^+\pi^-}\,\lambda_{D^-\pi^+} = \exp\left[-2i(\gamma + 2\beta)\right]$. In this case, however, the two decay amplitudes differ in magnitude by order λ^2, and therefore the CP asymmetries are expected to be much smaller, at the percent level.

1.4.3 $\Delta F = 2$ vs. $\Delta F = 1$ CP violation

At low energies flavor-changing transitions are described by effective Hamiltonians, which are discussed in detail in Sec. 1.5.1. Decays are mediated by the $\Delta F = 1$ Hamiltonian $H^{|\Delta F|=1}$, whereas mixing is induced by the $\Delta F = 2$ Hamiltonian. The changing flavor is

$F = B$ for B decays and $F = S$ for K decays. In kaon physics it is customary to distinguish $\Delta F = 1$ CP violation, which is often called *direct* CP violation, from $\Delta F = 2$ CP violation, called *indirect* CP violation. Here we compare this classification with the three types of CP violation in B decays discussed in Sec. 1.4.1.

If we can find phase transformations of the quark fields in (1.45) which leave the Hamiltonian invariant, $CP\,H^{|\Delta F|=1}(CP)^{-1} = H^{|\Delta F|=1}$, then we conclude that the $|\Delta F| = 1$ interaction conserves CP. Analogously we could define CP violation and CP conservation in $H^{|\Delta F|=2}$, but a B physics experiment probes only one matrix element of $H^{|\Delta F|=2}$, namely M_{12}. One can always find a phase transformation which renders M_{12} real and thereby shifts the CP violation from $H^{|\Delta F|=2}$ completely into $H^{|\Delta F|=1}$. The converse is not true, since one can explore the different couplings in $H^{|\Delta F|=1}$ by studying different decay modes. This leaves three scenarios to be experimentally distinguished:

i) With rephasing of the quark fields one can achieve $CP\,H(CP)^{-1} = H$ for both $H^{|\Delta F|=2}$ and $H^{|\Delta F|=1}$: The theory conserves CP.

ii) One can rephase the quark fields such that $CP\,H^{|\Delta F|=1}(CP)^{-1} = H^{|\Delta F|=1}$, but for this phase transformation $CP\,H^{|\Delta F|=2}(CP)^{-1} \neq H^{|\Delta F|=2}$. This scenario is called *superweak* [30].

iii) $CP\,H^{|\Delta F|=1}(CP)^{-1} \neq H^{|\Delta F|=1}$ for any phase convention of the quark fields. This scenario is realized in the CKM mechanism of the Standard Model.

Historically, after the discovery of CP violation in 1964 [31], it was of prime interest to distinguish the second from the third scenario in kaon physics. The recent establishment of $\epsilon'_K \neq 0$ has shown that possibility iii) is realized in kaon physics.

It is difficult (but possible) to build a viable theory with $\epsilon'_K \neq 0$ in which CP violation in the B system is of the superweak type. Still we can play the rules of the kaon game and ask, what must be measured to rule out the superweak scenario. Clearly, CP violation in decay unambiguously proves $|\Delta F| = 1$ CP violation. CP violation in mixing purely measures CP violation in the $|\Delta F| = 2$ transition. It measures the relative phase between M_{12} and the decay matrix Γ_{12}. Γ_{12} arises at second order in the $|\Delta F| = 1$ interaction, from $\sum_f A_f^* \overline{A}_f$, where A_f and $\overline{A}_f$ are the $|\Delta F| = 1$ decay amplitudes introduced in (1.87). M_{12} receives contributions at first order in $H^{|\Delta F|=2}$ and at second order in $H^{|\Delta F|=1}$. Interference type CP violation measures the difference between the mixing phase $\phi_M = \arg M_{12}$ and twice the weak phase ϕ_f of some decay amplitude $\overline{A}_f$. Both types of CP violations are therefore sensitive to relative phases between $H^{|\Delta F|=2}$ and $H^{|\Delta F|=1}$. Yet the measurement of a single CP violating observable of either type is not sufficient to rule out the superweak scenario, because we can always rephase Γ_{12} or A_f to be real. However, the measurement of interference type CP violation in two different decay modes with different results would prove that two weak phases in $H^{|\Delta F|=1}$ are different. Since $\phi_{f_1} - \phi_{f_2}$ is a rephasing invariant observable, no field transformation in (1.45) can render $H^{|\Delta F|=1}$ real and $|\Delta F| = 1$ CP violation is established. Hence for example the measurement of different CP asymmetries in $B_d \to J/\psi K_S$ and $B_d \to \pi^+\pi^-$ is sufficient to rule out the superweak scenario. Interestingly, ϵ'_K contains both of the discussed types of $\Delta S = 1$ CP violation: CP violation in decay and

the difference of two interference type CP violating phases. Since in both K- and B physics the dominant decay modes have the same weak phases, essentially no new information is gained by comparing CP violation in mixing with interference type CP violation in a dominant decay mode. We will see this in Sec. 1.6 when comparing ϵ_K with the semileptonic CP asymmetry in K_L decays.

1.5 Theoretical Tools

This section provides a brief review of the tools used to derive theoretical predictions for B mixing and decays. The theory of b production and fragmentation is discussed in Chapter 9.

The principal aim of B physics is to learn about the short distance dynamics of nature. Short distance physics couples to b quarks, while experiments detect b-flavored hadrons. One therefore needs to connect the properties of these hadrons in terms of the underlying b quark dynamics. Except for a few special cases, this requires an understanding of the long distance, nonperturbative properties of QCD. It is then useful to separate long distance physics from short distance using an operator product expansion (OPE) or an effective field theory. The basic idea is that interactions at higher scales give rise to local operators at lower scales. This allows us to think about the short distance phenomena responsible for the flavor structure in nature independent of the complications due to hadronic physics, which can then be attacked separately. This strategy can lead to very practical results: the hadronic part of an interesting process may be related by exact or approximate symmetries to the hadronic part of a less interesting or more easily measured process.

In the description of B decays several short distances arise. CP and flavor violation stem from the weak scale and, probably, even shorter distances. These scales are separated from the scale m_B with an OPE, leading to an effective Hamiltonian for flavor changing processes. This is reviewed in Sec. 1.5.1. Furthermore, the b and (to a lesser extent) the c quark masses are much larger than $\Lambda_{\rm QCD}$. In the limit $\Lambda_{\rm QCD}/m_Q \to 0$, the bound state dynamics simplify. Implications for exclusive processes are discussed in Sec. 1.5.2. For inclusive decays one can apply an OPE again, the so-called heavy quark expansion, reviewed in Sec. 1.5.3. Despite the simplifications, these expansions still require hadronic matrix elements, so we briefly review lattice QCD in Sec. 1.5.4.

1.5.1 Effective Hamiltonians

To predict the decay rate of a B meson into some final state f, one must calculate the transition amplitude $\mathcal{M}$ for $B \to f$. In general there are many contributions to $\mathcal{M}$, each of which is, at the quark level, pictorially represented by Feynman diagrams such as those in Fig. 1.3.

Quark diagrams are a poor description for the decay amplitude of a B meson. The quarks feel the strong interaction, whose nature changes drastically over the distances at which it is probed: At short distances much smaller than $1/\Lambda_{\rm QCD}$ the strong interaction can be described perturbatively by dressing the lowest order diagrams in Fig. 1.3 with gluons.

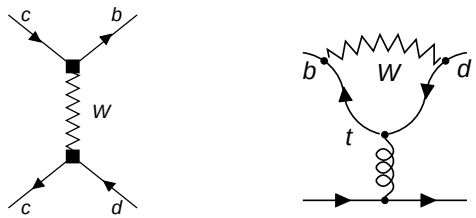

Figure 1.3: Standard Model W exchange diagram and penguin diagram with internal top quark for the decay $b \to c\bar{c}d$.

When traveling over a distance of order $1/\Lambda_{\rm QCD}$, however, quarks and gluons hadronize and QCD becomes nonperturbative. Therefore the physics from different length scales, or, equivalently, from different energy scales must be treated differently. One theoretical tool for this is the *operator product expansion* (OPE) [32]. Schematically the decay amplitude $\mathcal{M}$ is expressed as

$$\mathcal{M} = -\frac{4\,G_F}{\sqrt{2}}\,V_{\rm CKM}\sum_j C_j(\mu)\,\langle f|O_j(\mu)|B\rangle\left[1+\mathcal{O}\Big(\frac{m_b^2}{M_W^2}\Big)\right], \tag{1.109}$$

where μ is a renormalization scale. Physics from distances shorter than μ^{-1} is contained in the Wilson coefficients C_j, and physics from distances longer than μ^{-1} is accounted for by the hadronic matrix elements $\langle f|O_j|B\rangle$ of the local operators O_j. In principle, there are infinitely many terms in the OPE, but higher dimension operators yield contributions suppressed by powers of m_b^2/m_W^2. From a practical point of view, therefore, the sum in (1.109) ranges over operators of dimension five and six.

All dependence on heavy masses $M \gg \mu$ such as m_t, M_W or the masses of new undiscovered heavy particles is contained in C_j. By convention one factors out $4\,G_F/\sqrt{2}$ and the CKM factors, which are denoted by $V_{\rm CKM}$ in (1.109). On the other hand, the matrix element $\langle f|O_j|B\rangle$ of the $B \to f$ transition contains information from scales, such as $\Lambda_{\rm QCD}$, that are below μ. Therefore, they can only be evaluated using nonperturbative methods such as lattice calculations (cf., Sec. 1.5.4), QCD sum rules, or by using related processes to obtain them from experiment.

An important feature of the OPE in (1.109) is the universality of the coefficients C_j; they are independent of the external states, i.e., their numerical value is the same for all final states f in (1.109). Therefore one can view the C_j's as effective coupling constants and the O_j's as the corresponding interaction vertices. Thus one can introduce the *effective Hamiltonian*

$$H^{|\Delta B|=1} = \frac{4\,G_F}{\sqrt{2}}\,V_{\rm CKM}\sum_j C_j\,O_j + \text{h.c.} \tag{1.110}$$

An amplitude calculated from $H^{|\Delta B|=1}$ defined at a scale of order m_b, reproduces the corresponding Standard Model result up to corrections of order m_b^2/M_W^2 as indicated in

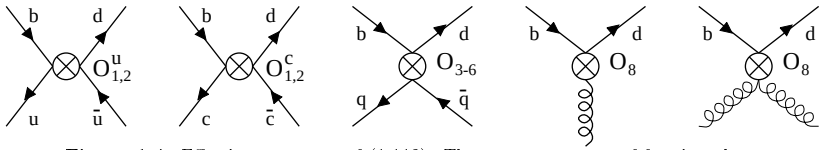

Figure 1.4: Effective operators of (1.112). There are two types of fermion-gluon couplings associated with the chromomagnetic operator O_8.

(1.109). Hard QCD effects can be included perturbatively in the Wilson coefficients, i.e., by calculating Feynman diagrams with quarks and gluons.

The set of operators O_j needed in (1.110) depends on the flavor structure of the physical process under consideration. Pictorially the operators are obtained by contracting the lines corresponding to heavy particles in the Feynman diagrams to a point. The tree level diagram involving the W boson in Fig. 1.3 generates the operator O_2^c shown in Fig. 1.4. In the Standard Model only two operators occur for $b \to c\bar{u}d$ transitions,

$$O_1 = \bar{b}_L^\alpha \gamma_\mu c_L^\beta \, \bar{u}_L^\beta \gamma^\mu d_L^\alpha \,, \qquad O_2 = \bar{b}_L^\alpha \gamma_\mu c_L^\alpha \, \bar{u}_L^\beta \gamma^\mu d_L^\beta \,, \tag{1.111}$$

where α and β are color indices. These arise from W exchange shown in Fig. 1.3, and QCD corrections to it. Operators and Wilson coefficients at different scales μ_1 and μ_2 are related by a renormalization group transformation. $C_{1,2}(\mu_1)$ is not just a function of $C_{1,2}(\mu_2)$, but a linear combination of both $C_1(\mu_2)$ and $C_2(\mu_2)$. This feature is called operator mixing. It is convenient to introduce the linear combinations $O_\pm = (O_2 \pm O_1)/2$, which do not mix with each other. Their coefficients can be more easily calculated and are related to C_1 and C_2 by $C_\pm = C_2 \pm C_1$.

The Hamiltonian for $\Delta B = 1$ and $\Delta C = \Delta S = 0$ transitions consists of more operators, because it must also accommodate for the so-called penguin diagram with an internal top quark, shown in Fig. 1.3. The corresponding operator basis reads

$$\begin{aligned}
O_1^c &= \bar{d}_L^\alpha \gamma_\mu c_L^\beta \, \bar{c}_L^\beta \gamma^\mu b_L^\alpha \,, & O_1^u &= \bar{d}_L^\alpha \gamma_\mu u_L^\beta \, \bar{u}_L^\beta \gamma^\mu b_L^\alpha \,, \\
O_2^c &= \bar{d}_L^\alpha \gamma_\mu c_L^\alpha \, \bar{c}_L^\beta \gamma^\mu b_L^\beta \,, & O_2^u &= \bar{d}_L^\alpha \gamma_\mu u_L^\alpha \, \bar{u}_L^\beta \gamma^\mu b_L^\beta \,, \\
O_3 &= \sum_{q=u,d,s,c,b} \bar{d}_L^\alpha \gamma_\mu b_L^\alpha \, \bar{q}_L^\beta \gamma^\mu q_L^\beta \,, & O_4 &= \sum_{q=u,d,s,c,b} \bar{d}_L^\alpha \gamma_\mu b_L^\beta \, \bar{q}_L^\beta \gamma^\mu q_L^\alpha \,, \\
O_5 &= \sum_{q=u,d,s,c,b} \bar{d}_L^\alpha \gamma_\mu b_L^\alpha \, \bar{q}_R^\beta \gamma^\mu q_R^\beta \,, & O_6 &= \sum_{q=u,d,s,c,b} \bar{d}_L^\alpha \gamma_\mu b_L^\beta \, \bar{q}_R^\beta \gamma^\mu q_R^\alpha \,, \\
O_8 &= -\frac{g}{16\pi^2} \, m_b \, \bar{d}_L \sigma^{\mu\nu} G^a_{\mu\nu} T^a b_R \,.
\end{aligned} \tag{1.112}$$

These operators are also depicted in Fig. 1.4. In O_8, $G^a_{\mu\nu}$ is the chromomagnetic field strength tensor. The operators are grouped into classes, based on their origin: O_1 and O_2 are called *current-current operators*, O_3 through O_6 are called *four-quark penguin operators*, and O_8 is called the *chromomagnetic penguin operator*.[9]

[9] In the literature one also finds O_7 and O_8 with the opposite signs. In QCD and QED the sign of the gauge coupling is convention dependent, and (1.112) is consistent with the values for C_8 in Table 1.3, if the Feynman rule for the quark-gluon coupling is chosen as $+ig$.

The operators in (1.112) arise from the lowest order in the electroweak interaction, i.e., diagrams involving a single W bosons plus QCD corrections to it. In some cases, especially when isospin breaking plays a role, one also needs to consider penguin diagrams which are of higher order in the electroweak fine structure constant α_{ew}. They give rise to the *electroweak penguin operators*:

$$\begin{aligned}
O_7 &= -\frac{e}{16\pi^2} \, m_b \, \bar{d}_L^\alpha \, \sigma^{\mu\nu} F_{\mu\nu} \, b_R^\alpha \,, \\
O_7^{\rm ew} &= \frac{3}{2} \sum_{q=u,d,s,c,b} e_q \, \bar{d}_L^\alpha \gamma_\mu b_L^\alpha \, \bar{q}_R^\beta \gamma^\mu q_R^\beta \,, & O_8^{\rm ew} &= \frac{3}{2} \sum_{q=u,d,s,c,b} e_q \, \bar{d}_L^\alpha \gamma_\mu b_L^\beta \, \bar{q}_R^\beta \gamma^\mu q_R^\alpha \,, \\
O_9^{\rm ew} &= \frac{3}{2} \sum_{q=u,d,s,c,b} e_q \, \bar{d}_L^\alpha \gamma_\mu b_L^\alpha \, \bar{q}_L^\beta \gamma^\mu q_L^\beta \,, & O_{10}^{\rm ew} &= \frac{3}{2} \sum_{q=u,d,s,c,b} e_q \, \bar{d}_L^\alpha \gamma_\mu b_L^\beta \, \bar{q}_L^\beta \gamma^\mu q_L^\alpha \,.
\end{aligned} \tag{1.113}$$

Here $F^{\mu\nu}$ is the electromagnetic field strength tensor, and e_q denotes the charge of quark q. The magnetic (penguin) operator O_7 is also of key importance for the radiative decay $b \to d\gamma$. Eqs. (1.112) and (1.113) reveal that there is no consensus yet on how to number the operators consecutively.

For semileptonic decays the following additional operators occur

$$\begin{aligned}
O_9 &= \frac{e^2}{16\pi^2} \, \bar{d}_L \, \gamma_\mu \, b_L \, \bar{\ell} \, \gamma^\mu \, \ell \,, & O_{10} &= \frac{e^2}{16\pi^2} \, \bar{d}_L \, \gamma_\mu \, b_L \, \bar{\ell} \, \gamma^\mu \gamma_5 \, \ell \,, \\
O_{11} &= \frac{e^2}{32\pi^2 \sin^2\theta_W} \, \bar{d}_L \, \gamma_\mu \, b_L \, \bar{\nu}_L \, \gamma^\mu \, \nu_L \,,
\end{aligned} \tag{1.114}$$

and the counterparts of these with $\bar{d}_L$ replaced by $\bar{s}_L$.

Hence the $\Delta B = 1$ and $\Delta C = \Delta S = 0$ Hamiltonian reads:

$$H^{|\Delta B|=1} = \frac{4\,G_F}{\sqrt{2}} \left\{ \sum_{j=1}^{2} C_j \left(\xi_c O_j^c + \xi_u O_j^u \right) - \xi_t \sum_{j=3}^{11} C_j \, O_j - \xi_t \sum_{j=7}^{10} C_j^{\rm ew} \, O_j \right\} + \text{h.c.} \,, \tag{1.115}$$

where

$$\xi_q = V_{qb}^* V_{qd} \,. \tag{1.116}$$

Note that $\xi_u + \xi_c + \xi_t = 0$ by unitarity of the CKM matrix. The corresponding operator basis for $b \to s$ transitions is obtained by simply exchanging d with s in (1.112), (1.113) and (1.114) and changing ξ_i accordingly.

The operators introduced above are sufficient to describe nonleptonic transitions in the Standard Model to order G_F. In extensions of the Standard Model, on the other hand, the short distance structure can be very different. Additional operators with new Dirac structures, whose standard Wilson coefficients vanish, could enter the effective Hamiltonian. A list of these operators, including their RG evolution, can be found in [33].

In general the QCD corrections to the transition amplitude $\mathcal{M}(B \to f)$ contain large logarithms such as $\ln(m_b/M_W)$ which need to be resummed to all orders in α_s. The OPE

splits these logarithms as $\ln(m_b/M_W) = \ln(\mu/M_W) - \ln(\mu/m_b)$. The former term resides in the Wilson coefficients, the latter logarithm is contained in the matrix element. Such large logarithms can be summed to all orders by solving *renormalization group* (RG) equations for the C_j's. These RG-improved perturbation series are well-behaved. The minimal way to include QCD corrections is the *leading logarithmic approximation*. The corresponding *leading order* (LO) Wilson coefficients comprise $[\alpha_s \ln(m_b/M_W)]^n$ to all orders $n = 0, 1, 2, \ldots$ in perturbation theory. This approximation has certain conceptual deficits and is too crude for the precision of the experiments and the accuracy of present day lattice calculations of the hadronic matrix elements. The *next-to-leading order* (NLO) results for the C_j's comprises in addition terms of order $\alpha_s\,[\alpha_s \ln(m_b/M_W)]^n, n = 0, 1, 2, \ldots$. The Wilson coefficients depend on the unphysical scale μ at which the OPE is performed. Starting from the NLO the C_j's further depend on the *renormalization scheme*, which is related to the way one treats divergent loops in Feynman diagrams. In an exact calculation both the scale and scheme dependence cancels between the coefficients and the matrix elements, but in practice the calculation of matrix elements with the correct scale and scheme dependence can be a non-trivial task. The appearance of the scale and scheme dependence in the coefficients is inevitable. The OPE enforces the short distance physics involving heavy masses like M_W and m_t to belong to the C_j's, while the long distance physics is contained in the matrix elements. But a constant number can be attributed to either of them. Switching from one scheme to another or changing the scale μ just shuffles constant terms between the Wilson coefficients and the matrix elements. There is no unique definition of "scheme independent" Wilson coefficients.

The numerical values for the renormalization group improved Wilson coefficients can be found in Table 1.3. The NLO coefficients are listed for two popular schemes, the *naive dimensional regularization* (NDR) scheme and the *'t Hooft-Veltman* (HV) scheme. These results have been independently obtained by the Rome and Munich groups [34]. The situation with C_8 is special: To obtain the LO values for C_{1-6} in Table 1.3 one must calculate one-loop diagrams. The calculation of C_8, however, already involves two-loop diagrams in the leading order. This implies that even the LO expression for C_8 is scheme dependent. The tabulated value corresponds to the commonly used "effective" coefficient C_8 introduced in [36], which is defined in a scheme independent way. To know the NLO value for C_8 one must calculate three-loop diagrams. The operator basis in (1.112) is badly suited for this calculation and hence a different one has been used [37]. For the basis in (1.112) the NLO value for C_8 is not known, we therefore leave the corresponding rows open. In Table 1.3 small corrections proportional to α_{ew} have been omitted. For the Wilson coefficients of the electroweak penguin operators in (1.113) and the semileptonic operators in (1.114) we refer the reader to [35].

We can derive an effective Hamiltonian for the $|\Delta B| = 2$ transition, which induces B^0_d–$\overline{B}^0_d$ mixing, just in the same way as discussed above for $|\Delta B| = 1$. In the Standard Model only a single operator Q arises:[10]

$$H^{|\Delta B|=2} = \frac{G_F^2}{4\pi^2}\,(V_{tb}V_{td}^*)^2\,C^{|\Delta B|=2}(m_t, M_W, \mu)\,Q(\mu) + h.c. \qquad (1.117)$$

[10] Once again in (1.117), new short distance physics can generate Wilson coefficients for additional operators.

$\alpha_s(M_Z)$	scheme	μ (GeV)	C_1	C_2	C_3	C_4	C_5	C_6	C_8
0.112	LO	4.8	−0.229	1.097	0.010	−0.024	0.007	−0.029	−0.146
		2.4	−0.325	1.149	0.015	−0.033	0.009	−0.043	−0.161
		9.6	−0.155	1.062	0.007	−0.016	0.005	−0.019	−0.133
	NDR	4.8	−0.160	1.066	0.011	−0.031	0.008	−0.035	
		2.4	−0.245	1.110	0.017	−0.043	0.009	−0.052	
		9.6	−0.093	1.036	0.008	−0.021	0.006	−0.023	
	HV	4.8	−0.177	0.993	0.009	−0.024	0.007	−0.026	
		2.4	−0.260	1.020	0.014	−0.033	0.010	−0.038	
		9.6	−0.111	0.975	0.006	−0.015	0.005	−0.017	
0.118	*LO*	4.8	−0.249	1.108	0.011	−0.026	0.008	−0.031	−0.149
		2.4	−0.361	1.169	0.017	−0.036	0.010	−0.048	−0.166
		9.6	−0.167	1.067	0.007	−0.018	0.005	−0.020	−0.135
	NDR	4.8	−0.174	1.073	0.013	−0.034	0.009	−0.038	
		2.4	−0.272	1.124	0.020	−0.047	0.010	−0.060	
		9.6	−0.100	1.039	0.008	−0.024	0.006	−0.025	
	HV	4.8	−0.192	0.993	0.010	−0.026	0.008	−0.028	
		2.4	−0.286	1.022	0.016	−0.036	0.011	−0.042	
		9.6	−0.120	0.972	0.006	−0.017	0.005	−0.018	
0.124	*LO*	4.8	−0.272	1.120	0.012	−0.028	0.008	−0.035	−0.153
		2.4	−0.403	1.194	0.019	−0.040	0.011	−0.055	−0.172
		9.6	−0.180	1.073	0.008	−0.019	0.006	−0.022	−0.138
	NDR	4.8	−0.190	1.082	0.014	−0.037	0.009	−0.043	
		2.4	−0.303	1.142	0.022	−0.054	0.011	−0.069	
		9.6	−0.108	1.042	0.009	−0.025	0.007	−0.028	
	HV	4.8	−0.208	0.993	0.011	−0.028	0.008	−0.031	
		2.4	−0.316	1.025	0.018	−0.040	0.012	−0.048	
		9.6	−0.129	0.970	0.007	−0.018	0.006	−0.019	

Table 1.3: QCD Wilson coefficients in the leading and next-to-leading order. The NLO running of α_s has been used in both the LO and NLO coefficients. $\alpha_s(M_Z) = 0.112,\ 0.118,\ 0.124$ implies $\alpha_s(4.8\,\text{GeV}) = 0.196,\ 0.216,\ 0.238$. The corresponding values of the five-flavor QCD scale parameter $\Lambda_{\overline{\text{MS}}}$ are 159, 226 and 312 MeV. The dependence on $m_t(m_t)$, here taken as 168 GeV, is negligible. The NLO coefficients are listed for the NDR and HV scheme. There are two different conventions for the HV scheme, here we use the one adopted in [34]. The HV coefficients tabulated in [35] are related to our C_j^{HV}'s by $C_j^{HV}([35]) = [1 + 16/3 \cdot \alpha_s(\mu)/(4\pi)]C_j^{HV}$. Small QED corrections have been omitted.

with

$$Q = \overline{d}_L \gamma_\nu b_L \, \overline{d}_L \gamma^\nu b_L . \tag{1.118}$$

The Wilson coefficient is

$$C^{|\Delta B|=2}(m_t, M_W, \mu) = M_W^2 \, S\left(\frac{m_t^2}{M_W^2}\right) \eta_B \, b_B(\mu) \, . \tag{1.119}$$

It contains the *Inami-Lim function* [38]

$$S(x) = x \left[\frac{1}{4} + \frac{9}{4}\frac{1}{1-x} - \frac{3}{2}\frac{1}{(1-x)^2}\right] - \frac{3}{2}\left[\frac{x}{1-x}\right]^3 \ln x \, , \tag{1.120}$$

which is calculated from the box diagram in Fig. 1.2. The coefficients η_B and b_B in (1.119) account for short distance QCD corrections. In the next-to-leading order of QCD one finds $\eta_B = 0.55$ [39]. b_B depends on the renormalization scale $\mu = \mathcal{O}(m_b)$, at which the matrix element $\langle B_d^0 | Q | \overline{B}_d^0 \rangle$ is calculated. $b_B(\mu)$ equals $[\alpha_s(\mu)]^{-6/23}$ in the LO. The μ-dependence of $b_B(\mu)$ cancels the μ-dependence of the matrix element to the calculated order. The same remark applies to the dependence of $b_B(\mu)$ on the renormalization scheme in which the calculation is carried out. One parameterizes the hadronic matrix elements as

$$\langle B^0 | Q(\mu) | \overline{B}^0 \rangle = \frac{2}{3} f_B^2 m_B^2 \frac{\widehat{B}_B}{b_B(\mu)}, \tag{1.121}$$

so that $\widehat{B}_B$ is scale and scheme independent. The effective Hamiltonian for $B_s^0 - \overline{B}_s^0$ mixing is obtained as usual by replacing d with s in (1.117) and (1.118). The Wilson coefficient in (1.119) does not depend on the light quark flavor.

1.5.2 Heavy quark effective theory

In hadrons composed of a heavy quark and light degrees of freedom (light quarks, antiquarks, and gluons), the binding energy, which is of order $\Lambda_{\rm QCD}$, is small compared to the heavy quark mass m_Q. In the limit $m_Q \gg \Lambda_{\rm QCD}$, the heavy quark acts approximately as a static color-triplet source,[11] and its spin and flavor do not affect the light degrees of freedom. This is analogous to atomic physics, where isotopes with different nuclei have nearly the same properties. Thus, the properties of heavy-light hadrons are related by a symmetry, called heavy quark symmetry (HQS) [40–47]. In practice, only the b and c quarks have masses large enough for HQS to be useful.[12] This results in an $SU(2N_h)$ spin-flavor symmetry, where $N_h = 1$ or 2, depending on the problem at hand.

The heavy quark spin-flavor symmetries are helpful for understanding many aspects of the spectroscopy and decays of heavy hadrons from first principles. For example, in the infinite mass limit, mass splittings between b-flavored hadrons can be related to those between charmed hadrons, and many semileptonic and radiative decay form factors can

[11] For the same reason, heavy quark symmetries also apply to hadrons composed of two heavy and a light quark, because the color quantum numbers of the two heavy quarks combine to an antitriplet.

[12] The top quark also satisfies $m_t \gg \Lambda_{\rm QCD}$, but it decays before it hadronizes.

be related to one another. There are corrections to the HQS limit from long distances and from short distances. The former are suppressed by powers of $\Lambda_{\rm QCD}/m_Q$. They must be calculated by nonperturbative methods, but HQS again imposes relations among these terms. The latter arise from the exchange of hard virtual gluons, so they can be calculated accurately in a perturbation series in $\alpha_s(m_Q)$. The heavy quark effective theory (HQET) provides a convenient framework for treating these effects [45–51]. In leading order the effective theory reproduces the model independent predictions of HQS, and both series of symmetry breaking corrections are developed in a systematic, consistent way.

To see how the heavy quark symmetries arise, it is instructive to look at the infinite-mass limit of the Feynman rules. For momentum $p = m_Q v + k$, with $v^2 = 1$ and $k \ll m_Q$, the propagator of a heavy quark becomes

$$\frac{i}{\not{p} - m_Q} = \frac{i(\not{p} + m_Q)}{p^2 - m_Q^2} = \frac{i(m_Q \not{v} + \not{k} + m_Q)}{2 m_Q \, v \cdot k + k^2} = \frac{i}{v \cdot k} \frac{1 + \not{v}}{2} + \ldots \, . \tag{1.122}$$

As $m_Q \to \infty$ it is independent of its mass, and in this way heavy quark *flavor* symmetry emerges. In a Feynman diagram, the quark-gluon vertex appears between two propagators and, hence, for $m_Q \to \infty$, sandwiched between the projection operator

$$P_+(v) = \frac{1 + \not{v}}{2} \, . \tag{1.123}$$

Consequently the gamma matrix at the vertex becomes

$$P_+ \gamma^\mu P_+ = v^\mu \, P_+ \, . \tag{1.124}$$

Thus, both the vertex and the propagator depend on gamma matrices only through P_+. Since $P_+^2 = P_+$, all these factors reduce to a single one, and in this way heavy quark *spin* symmetry emerges.

The construction of HQET [40] starts by removing the mass-dependent piece of the momentum operator by a field redefinition. One introduces a field $h_v(x)$, which annihilates a heavy quark with velocity v [47],

$$h_v(x) = e^{i m_Q v \cdot x} \, P_+(v) \, Q(x) \, , \tag{1.125}$$

where $Q(x)$ denotes the quark field in full QCD. Here the physical interpretation of the projection operator P_+ is that h_v represents just the heavy quark (rather than antiquark) components of Q. If p is the total momentum of the heavy quark, then the field h_v carries the residual momentum $k = p - m_Q v$. Inside a hadron, the residual momentum $k \sim \mathcal{O}(\Lambda_{\rm QCD})$. Since the phase factor in Eq. (1.125) effectively removes the mass of the heavy quark from the states, it is the mass difference

$$\bar{\Lambda} = m_H - m_Q \, , \tag{1.126}$$

where m_H is the hadron mass, that determines the x-dependence of hadronic matrix elements in HQET [51]. It is also this parameter that sets the characteristic scale of the $1/m_Q$ expansion. Because of heavy quark flavor symmetry $\bar{\Lambda} = m_B - m_b = m_D - m_c$, and

because of heavy quark spin symmetry $\bar{\Lambda} = m_{B^*} - m_b$, in both cases up to $\mathcal{O}(\Lambda^2_{\rm QCD}/m_Q)$ corrections. Other heavy hadrons, for example heavy-flavored baryons, have a distinct "$\bar{\Lambda}$", but the flavor symmetry implies $m_{\Lambda_b} - m_b = m_{\Lambda_c} - m_c$, up to $\mathcal{O}(\Lambda^2_{\rm QCD}/m_Q)$.

The HQET Lagrangian is constructed from the field h_v. Including the leading $1/m_Q$ corrections, it is [45,47,48]

$$\mathcal{L}_{\rm HQET} = \bar{h}_v \, iv\cdot D \, h_v + \frac{1}{2m_Q}\Big[O_{\rm kin} + C_{\rm mag}(\mu)\, O_{\rm mag}(\mu)\Big] + \mathcal{O}(1/m_Q^2)\,, \tag{1.127}$$

where $D^\mu = \partial^\mu - ig_s T_a A_a^\mu$ is the color $SU(3)$ covariant derivative. The leading term respects both the spin and flavor symmetries, and reproduces the heavy quark propagator derived above. The symmetry breaking operators appearing at order $1/m_Q$ are

$$O_{\rm kin} = \bar{h}_v \, (iD)^2 \, h_v\,, \qquad O_{\rm mag} = \frac{g_s}{2}\, \bar{h}_v \, \sigma_{\mu\nu}\, G^{\mu\nu}\, h_v\,. \tag{1.128}$$

Here $G^{\mu\nu}$ is the gluon field strength tensor defined by $[iD^\mu, iD^\nu] = ig_s G^{\mu\nu}$. In the rest frame of the hadron, $O_{\rm kin}$ describes the kinetic energy resulting from the residual motion of the heavy quark, whereas $O_{\rm mag}$ corresponds to the chromomagnetic coupling of the heavy quark spin to the gluon field. While $O_{\rm kin}$ violates only the heavy quark flavor symmetry, $O_{\rm mag}$ violates the spin symmetry as well.

In the operators of the electroweak Hamiltonian, the QCD field Q must also be replaced with h_v and a series of higher-dimension operators to describe $1/m_Q$ effects. The short distance behavior can be matched using perturbation theory. The matrix elements of the HQET operators still cannot be calculated in perturbatively, but HQS restricts their form. The best known example is in exclusive semileptonic $b \to c$ corrections. In $B \to D^{(*)}\ell\nu$ and $\Lambda_b \to \Lambda_c \ell\nu$, let v (v') be the velocity of the initial (final) heavy-light hadron. HQS requires that the mesonic decays are described by a set of heavy quark spin- and mass-independent functions of the kinematic variable $w = v\cdot v'$. The baryonic decay is described by another function of w. When $v = v'$ the symmetry becomes larger—from $SU(2)_v \times SU(2)_{v'}$ to $SU(4)$—so there are further restrictions. One is that symmetry limit of the form factor is completely determined by symmetry (at $w = 1$). Furthermore, HQS also requires that the $1/m_Q$ corrections to $B \to D^*\ell\nu$ and $\Lambda_b \to \Lambda_c\ell\nu$ vanish for $w = 1$.

The utility of HQET is not limited to exclusive decays. Matrix elements of the effective Lagrangian play an important role in inclusive semileptonic and radiative decays. One defines

$$\begin{aligned} \lambda_1 &= \frac{1}{2\,m_M}\,\langle M(v)|\, O_{\rm kin}\, |M(v)\rangle\,, \\ d_M\,\lambda_2 &= \frac{1}{2\,m_M}\,\langle M(v)|\, O_{\rm mag}\, |M(v)\rangle\,, \end{aligned} \tag{1.129}$$

where M denotes a B or B^* meson, and $d_M = 3, -1$ for B and B^*, respectively. Strictly speaking, both λ_1 and λ_2 depend on the renormalization scale μ. For λ_1, however, there is no μ dependence if $O_{\rm kin}$ is renormalized in the $\overline{\rm MS}$ scheme. For λ_2, the μ dependence is canceled by the coefficient $C_{\rm mag}(\mu)$ in (1.127).

HQET provides an expansion of the heavy meson masses in terms of the heavy quark masses,

$$m_B = m_b + \bar{\Lambda} - \frac{\lambda_1 + 3\lambda_2}{2m_b} + \ldots\,, \qquad m_{B^*} = m_b + \bar{\Lambda} - \frac{\lambda_1 - \lambda_2}{2m_b} + \ldots\,. \tag{1.130}$$

Consequently, the value of λ_2 is related to the mass splitting between the vector and the pseudoscalar mesons,

$$\lambda_2 = \frac{m_{B^*}^2 - m_B^2}{4} + \mathcal{O}\Big(\Lambda^3_{\rm QCD}/m_b\Big)\,, \tag{1.131}$$

taking $\mu = m_b$ and $C_{\rm mag}(m_b) = 1$. From the measured B and B^* masses one finds $\lambda_2(m_b) \simeq 0.12$ GeV^2. These formulae will play an important role in the description of both inclusive and exclusive heavy meson decays in the following chapters.

It was only recognized recently that HQS also yields important simplifications in the description of heavy-to-light radiative and semileptonic decays in the region of large recoil (small q^2) [52]. In the infinite mass limit, the three form factors which parameterize the vector and tensor current matrix elements in $B \to K\ell^+\ell^-$ are related to a single function of q^2, and the seven form factors which occur in $B \to K^*\ell^+\ell^-$ are related to only two functions of q^2. In contrast to the predictions of HQS in the region of small recoil, in this case it is not known yet how to formulate the subleading corrections suppressed by powers of $\Lambda_{\rm QCD}/m_Q$. Nevertheless, these relations play a very important role in Chapter 7, where they will be discussed in detail.

1.5.3 Heavy quark expansion

In inclusive B decays, when many final states are summed over, certain model independent formulae can be derived. In this section we examine how the large b quark mass, $m_b \gg \Lambda_{\rm QCD}$, allows one to extract reliable information about such decays. In most of the phase space the energy release, which can be as large as $\mathcal{O}(m_b)$, is much larger than the typical scale of hadronic interactions. The large energy release implies a short distance, and we can use the same tools as before—an operator product expansion [53–55] (though not the same OPE as in Sec. 1.5.1) and HQET—to separate short and long distances. In this way, inclusive decay rates can be described with a double series in $\Lambda_{\rm QCD}/m_b$ and $\alpha_s(m_b)$.

Inclusive decay widths are given by the sum over all final states. Schematically, the width is given by

$$\Gamma \sim \sum_X \langle B|O^\dagger|X\rangle\,\langle X|O|B\rangle\,. \tag{1.132}$$

where X is any final state. One can also limit X to X_c or X_u, i.e., to final states with or without a charmed quark, respectively. From Sec. 1.5.1, we see that inclusive semileptonic B decays are mediated by operators of the form

$$O_\ell \sim \bar{q}_L \gamma^\mu b_L\, \bar{\ell}_{L1}\gamma_\mu \ell_{L2}\,, \tag{1.133}$$

and nonleptonic decays are mediated by four-quark operators of the form

$$O_h \sim \bar{q}_L \gamma^\mu b_L\, \bar{q}_{L1}\gamma_\mu q_{L2}\,. \tag{1.134}$$

Although these operators are superficially similar, we shall see that they have to be treated differently, because in O_h hard gluons can be exchanged among all four quark fields. We start by showing in detail how the OPE and HQET are used to describe inclusive semileptonic B decays. We then explain what restrictions arise for nonleptonic decay rates and lifetimes. Finally, we treat the width difference in the B_s system, which is of special interest to Tevatron experiments.

1.5.3.1 Inclusive semileptonic B decays

In semileptonic decays, one may factorize the matrix element of the four-fermion operator

$$\langle X\ell\,\bar\nu_\ell|\,O_\ell\,|B\rangle = \langle X|\,\bar q\,\gamma^\mu P_L\,b\,|B\rangle\,\langle\ell\,\bar\nu_\ell|\,\bar\ell\,\gamma_\mu P_L\,\nu_\ell\,|0\rangle\,, \tag{1.135}$$

neglecting electroweak loop corrections. Then the decay rate can be written in the form

$$\frac{\mathrm{d}^2\Gamma}{\mathrm{d}y\,\mathrm{d}q^2} \sim \int \mathrm{d}(q\cdot v)\,L_{\mu\nu}(p_\ell,p_{\bar\nu})\,W^{\mu\nu}(q\cdot v,q^2)\,, \tag{1.136}$$

where $L_{\mu\nu}$ is the lepton tensor and $W^{\mu\nu}$ is the hadron tensor. The momentum of the decaying b quark is written as $p_b^\mu = m_b v^\mu$, $q^\mu = p_\ell^\mu + p_{\bar\nu}^\mu$, and we have introduced the dimensionless variable $y = 2E_\ell/m_b$. Since the antineutrino is not detected, its energy or, equivalently, $q\cdot v = E_\ell + E_{\bar\nu}$ is integrated over. The lepton tensor $L^{\mu\rho} = 2(p_\ell^\mu p_{\bar\nu}^\rho + p_\ell^\rho p_{\bar\nu}^\mu - g^{\mu\rho}p_\ell\cdot p_{\bar\nu} - i\varepsilon^{\mu\rho\alpha\beta}p_{\ell\alpha}p_{\bar\nu\beta})$. The hadron tensor $W^{\mu\nu}$ contains all strong interaction physics relevant for the semileptonic decay, and it can be expressed as

$$W^{\mu\nu} = \sum_X (2\pi)^3\,\delta^4(p_B - q - p_X)\,\frac{\langle\overline{B}|\,J^{\mu\,\dagger}\,|X\rangle\,\langle X|\,J^\nu\,|\overline{B}\rangle}{2m_B}\,, \tag{1.137}$$

where $J^\mu = \bar q\,\gamma^\mu P_L\,b$.

The optical theorem can be used to relate $W^{\mu\nu}$ to the discontinuity across a cut of the forward scattering matrix element of a time ordered product

$$T^{\mu\nu} = -i\int \mathrm{d}^4x\,e^{-iq\cdot x}\,\frac{\langle\overline{B}|\,T\{J^{\mu\,\dagger}(x)\,J^\nu(0)\}\,|\overline{B}\rangle}{2m_B}\,. \tag{1.138}$$

To show that

$$W^{\mu\nu} = -\frac{1}{\pi}\,\mathrm{Im}\,T^{\mu\nu}\,, \tag{1.139}$$

one inserts a complete set of states between the currents in the two possible time orderings in $T^{\mu\nu}$. Using $\langle A|J(x)|B\rangle = \langle A|J(0)|B\rangle\,e^{i(p_A-p_B)\cdot x}$ and the identity $\theta(x^0) = i/(2\pi)\int_{-\infty}^{+\infty}\mathrm{d}\omega\,[e^{-i\omega x^0}/(\omega+i\varepsilon)]$, the d^4x integration gives (in the B rest frame, so $q\cdot v = q^0$)

$$\begin{aligned} T^{\mu\nu} = &\sum_{X_q}\frac{\langle\overline{B}|\,J^{\mu\,\dagger}\,|X_q\rangle\,\langle X_q|\,J^\nu\,|\overline{B}\rangle}{2m_B\,(m_B - E_X - q^0 + i\varepsilon)}\,(2\pi)^3\,\delta^3(\boldsymbol{q}+\boldsymbol{p}_X) \\ &- \sum_{X_{\bar q bb}}\frac{\langle\overline{B}|\,J^\nu\,|X_{\bar q bb}\rangle\,\langle X_{\bar q bb}|\,J^{\mu\,\dagger}\,|\overline{B}\rangle}{2m_B\,(E_X - m_B - q^0 - i\varepsilon)}\,(2\pi)^3\,\delta^3(\boldsymbol{q}-\boldsymbol{p}_X)\,. \end{aligned} \tag{1.140}$$

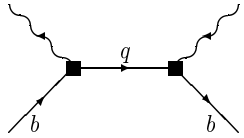

Figure 1.5: OPE diagram for semileptonic and radiative B decays.

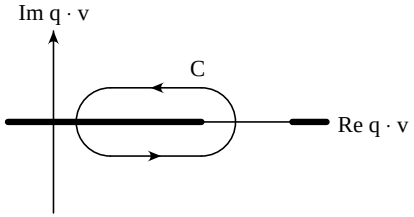

Figure 1.6: The analytic structure of $T^{\mu\nu}$ in the $q\cdot v$ plane, with q^2 fixed. The cuts corresponding to B decay (left) and to an unphysical process (right) are both shown, together with the integration contour for computing the decay rate.

This form shows that, for fixed q^2, $T^{\mu\nu}$ has cuts in the complex q^0 plane corresponding to physical processes. The first sum in Eq. (1.140) corresponds to B decay shown in Fig. 1.5, with intermediate states containing a q quark (and arbitrary number of gluons and light quark-antiquark pairs). It leads to a cut for $q^0 = q\cdot v < (m_B^2 + q^2 - m^2_{X_q^{\min}})/2m_B$, towards the left in Fig. 1.6. For charmed final states $m^2_{X_q^{\min}} = m_D^2$ and for charmless final states $m^2_{X_q^{\min}} = m_\pi^2$. The second sum in Eq. (1.140) corresponds to an unphysical process with a $\bar q$ and two b quarks in the intermediate state. It leads to another cut for $q^0 = q\cdot v > (m^2_{X_{\bar q bb}^{\min}} - m_B^2 - q^2)/2m_B$, towards the right in Fig. 1.6. The imaginary part can be read off using $\mathrm{Im}\,(A+i\varepsilon)^{-1} = -\pi\delta(A)$, and (1.139) follows immediately, because the kinematics of the decay process allow only the first sum to contribute.

Because $W^{\mu\nu}$ is the discontinuity across the left cut in Fig. 1.6, the integral in (1.136) can be replaced with a contour integral of $L_{\mu\nu}T^{\mu\nu}$. The two cuts are well separated (unless $m_q \to 0$ and $q^2 \to m_b^2$), so one may deform the contour away from the cuts [56], as shown in Fig. 1.6. The equivalence of the sum over hadronic states with a contour ranging far from the physical region is called "global duality". This procedure is advantageous, because $T^{\mu\nu}$ can be reliably described by an operator product expansion (OPE) far (compared to $\Lambda_{\rm QCD}$) from its singularities in the complex $q\cdot v$ plane [53–55]. One simply replaces the time ordered product

$$-i\int \mathrm{d}^4x\,e^{-iq\cdot x}\,T\{J^{\mu\,\dagger}(x)\,J^\nu(0)\}\,, \tag{1.141}$$

appearing in Eq. (1.138), with a series of local operators multiplied with Wilson coefficients. The Wilson coefficients of this OPE can again be evaluated in a perturbation series in $\alpha_s(m_b)$. Higher dimension operators in the OPE incorporate higher powers of $\Lambda_{\rm QCD}/m_b$.

Unfortunately, the contour C must still approach the cut near the low $q \cdot v$ endpoint of the integration. Using the OPE directly in the physical region is an assumption called "local duality". It introduces an uncertainty to the calculation, which can be argued to be small. First, in semileptonic and radiative decays the fraction of the contour which has to be within order $\Lambda_{\rm QCD}$ from the cut scales as $\Lambda_{\rm QCD}/m_b$. Second, since the energy release to the hadronic final state is large compared to $\Lambda_{\rm QCD}$, the imaginary part of $T^{\mu\nu}$ is dominated by multiparticle states, so it is expected to be a smooth function. In the end, the violation of local duality is believed to be exponentially suppressed in the $m_Q \to \infty$ limit, but it is not well understood how well it works at the scale of the b quark mass. In semileptonic decay the agreement between the inclusive and exclusive determinations of $|V_{cb}|$ suggests that duality violation is at most a few percent. But there is no known relation between the size of duality violation in semileptonic and nonleptonic B decays [57], or between these processes and others, such as $e^+e^- \to$ hadrons.

At lowest order in $\Lambda_{\rm QCD}/m_b$ the OPE leads to operators of the form $\bar b \Gamma b$ occur, where Γ is any Dirac matrix. For $\Gamma = \gamma^\mu$ or $\gamma^\mu\gamma_5$ their matrix elements are known to all orders in $\Lambda_{\rm QCD}/m_B$

$$\begin{aligned} \langle \overline{B}(p_B)|\, \bar b\, \gamma^\mu b\, |\overline{B}(p_B)\rangle &= 2p_B^\mu = 2m_B\, v^\mu\,, \\ \langle \overline{B}(p_B)|\, \bar b\, \gamma^\mu\gamma_5\, b\, |\overline{B}(p_B)\rangle &= 0\,. \end{aligned} \tag{1.142}$$

by conservation of the b quark number current and parity invariance of strong interactions, respectively. The matrix elements for other gamma matrices can be related by heavy quark symmetry to these plus order $\Lambda^2_{\rm QCD}/m_b^2$ corrections. Consequently, at the leading order in $\Lambda_{\rm QCD}/m_b$ inclusive decay rates are given by the rate for b quark decay, multiplied with a Wilson coefficient that does not depend on the decaying hadron.

To compute subleading corrections in $\Lambda_{\rm QCD}/m_b$, it is convenient to use HQET. There are no order $\Lambda_{\rm QCD}/m_b$ corrections because the matrix element of any gauge invariant dimension-4 two-quark operator vanishes,

$$\langle \overline{B}(v)|\, \bar h_v^{(b)}\, iD_\alpha \Gamma\, h_v^{(b)}\, |\overline{B}(v)\rangle = 0\,, \tag{1.143}$$

because contracting the left-hand side by v^α gives zero due to the equation of motion following from (1.127). Thus, the leading nonperturbative corrections to b quark decay occur at order $\Lambda^2_{\rm QCD}/m_b^2$. The operators that appear are again $O_{\rm kin}$ and $O_{\rm mag}$ so the same hadronic elements λ_1 and λ_2, defined in Eq. (1.129), appear again.

Combining the matrix elements from Eqs. (1.142), (1.143) and (1.129) with the Wilson coefficients leads to expressions of the form

$$\begin{aligned} \frac{{\rm d}^2\Gamma}{{\rm d}y\, {\rm d}q^2} = \begin{pmatrix} b \text{ quark} \\ \text{decay} \end{pmatrix} \times \Bigg\{ 1 + \frac{\alpha_s}{\pi}\, A_1 + \frac{\alpha_s^2}{\pi^2}\, A_2 + \ldots + \frac{f(\lambda_1,\lambda_2)}{m_B^2} \Big[1 + \mathcal{O}(\alpha_s) + \ldots \Big] \\ + \mathcal{O}(\Lambda^3_{\rm QCD}/m_B^3) + \ldots \Bigg\}\,. \end{aligned} \tag{1.144}$$

The differential rate may be integrated to obtain the full rate. The description in (1.144) is model independent, although λ_1 must be determined either from data [58] or from lattice

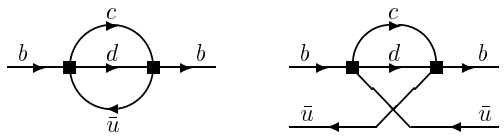

Figure 1.7: OPE diagrams for nonleptonic B decays. The left one is the leading contribution, while the "Pauli interference" diagram on the right corresponds to a dimension-6 contribution of order $16\pi^2\,(\Lambda^3_{\rm QCD}/m_B^3)$.

QCD [59]. For most quantities of interest the functions f, A_1, and the part of A_2 proportional to β_0, the first coefficient of the β-function, are known. Corrections to the $m_b \to \infty$ limit are expected to be under control in parts of the $\overline{B} \to X_q\, \ell\, \bar\nu$ phase space where several hadronic final states are allowed (but not required) to contribute with invariant mass and energy satisfying $m_X^2 \gg m_q^2 + \Lambda_{\rm QCD} E_X$.

1.5.3.2 Inclusive nonleptonic B decays

Inclusive nonleptonic decays can also be studied using the OPE, and much of the discussion in Sec. 1.5.3.1 applies here also. In this case, however, there are no "external" variables, such as q^2 and $q \cdot v$, since all particles in the final state interact strongly. For this reason, only the fully integrated inclusive width can be treated with the OPE, term-by-term in the weak Hamiltonian. For example, the B decay width corresponding to the $b \to c\bar u d$ effective Hamiltonian in (1.110)–(1.111) is given by

$$\begin{aligned} \Gamma &= \frac{1}{2m_B} \sum_X (2\pi)^4\, \delta^4(p_B - p_X)\, \Big| \langle X(p_X)|\, H^{|\Delta B|=1}(0)\, |\overline{B}(p_B)\rangle \Big|^2 \\ &= \frac{1}{2m_B}\, {\rm Im}\, \langle \overline{B}|\, i \int {\rm d}^4x\, T \Big\{ H^{|\Delta B|=1}(x)\, H^{|\Delta B|=1}(0) \Big\}\, |\overline{B}\rangle\,. \end{aligned} \tag{1.145}$$

Because one has to use the OPE directly in the physical region, the results are more sensitive to violations of local duality than in the case of semileptonic and radiative decays. The leading term in the OPE corresponds to the left diagram in Fig. 1.7, whose imaginary part gives the total nonleptonic width.

The result is again of the form shown in Eq. (1.144). An important new ingredient at order $\Lambda^3_{\rm QCD}/m_B^3$ are certain contributions due to four-quark operators involving the spectator quark. They are usually called "weak annihilation", "W exchange", and "Pauli interference" contributions. (The last is sketched on the right in Fig. 1.7). They contain one less loop than the diagram on the left, so they are enhanced by a relative factor of $16\pi^2$. They are expected to be more important than the dimension-5 contributions proportional to λ_1 and λ_2. The matrix elements of the resulting four-quark operators are poorly known. Such contributions are expected to explain the $D^\pm - D^0$ lifetime difference.

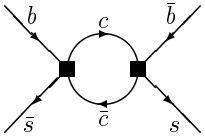

Figure 1.8: OPE diagram for the B_s width difference.

1.5.3.3 B_s width difference, $\Delta\Gamma$

Another important application, especially for the Tevatron, is for the B_s width difference. The off-diagonal element of the width matrix (cf., Sec. 1.3.2) is given by

$$\begin{aligned}\Gamma_{12} &= \frac{1}{2m_{B_s}} \sum_X (2\pi)^4\, \delta^4(p_{B_s} - p_X)\, \langle B_s|\, H^{|\Delta B|=1}\, |X\rangle\, \langle X|\, H^{|\Delta B|=1}\, |\overline{B}_s\rangle \\ &= \frac{1}{2m_{B_s}} \mathrm{Im}\, \langle B_s|\, i \int \mathrm{d}^4x\, T\left\{ H^{|\Delta B|=1}(x)\, H^{|\Delta B|=1}(0)\right\} |\overline{B}_s\rangle\,. \end{aligned} \tag{1.146}$$

The first line defines Γ_{12}, and the second line can be verified by inserting a complete set of intermediate states. The corresponding diagram is shown in Fig. 1.8. Γ_{12} arises from final states X which are common to both B_s and $\overline{B}_s$ decay. Therefore, the spectator quark is involved, and Eq. (1.146) is dominated by the $b \to c\bar{c}s$ part of the weak Hamiltonian, O_1 and O_2 in Eq. (1.112), with the others, O_3 through O_6, making very small contributions.

Thus, the naive estimate of the B_s width difference is $\Delta\Gamma_{B_s}/\Gamma_{B_s} = 2\,|\Gamma_{12}|\cos\phi/\Gamma_{B_s} \sim 16\pi^2(\Lambda^3_{\rm QCD}/m^3_B) \sim 0.1$. In the B_d system the common decay modes of B^0 and $\overline{B}^0$ are suppressed relative to the leading ones by the Cabibbo angle, and therefore the naive estimate is $\Delta\Gamma_{B_d}/\Gamma_{B_d} \lesssim 1\%$. See the discussion following (1.63) and Chapter 8 for more details.

1.5.4 Lattice QCD

If one considers the long term goal of "measuring" the Wilson coefficients of the electroweak Hamiltonian, as outlined elsewhere, then it is clear that it will be important to gain theoretical control over hadronic matrix elements. Since QCD is a completely well-defined quantum field theory, the calculation of hadronic matrix elements should be, in principle, possible. The main difficulty is that hadronic wavefunctions are sensitive mostly to the long distances where QCD becomes nonperturbative.

The difficulties of the bound-state problem in QCD led Wilson [60] to formulate gauge field theory on a discrete spacetime, or lattice. The basic idea starts with the functional integral for correlation functions in QCD

$$\langle O_1 \cdots O_n\rangle = \frac{1}{Z} \int \prod_{x,\mu} dA_\mu(x) \prod_x d\psi(x) d\bar{\psi}(x)\, O_1 \cdots O_n\, e^{-S_{\rm QCD}} \tag{1.147}$$

where Z is defined so that $\langle 1\rangle = 1$. For QCD A_μ is the gluon field, ψ and $\bar{\psi}$ are the quark and antiquark fields, and $S_{\rm QCD}$ is the QCD action. The O_i are operators for creating and

annihilating the hadrons of interest and also terms in the electroweak Hamiltonian. The continuous spacetime is then replaced with a discrete grid of points, or lattice. Then the quark variables live on sites; the gluons on links connecting the sites. With quarks on sites and gluons on links, it is possible to devise lattice actions that respect gauge symmetry. As in discrete approximations to partial differential equations, derivatives in the Lagrangian are replaced with difference operators.

The breakthrough of the lattice formulation is that it turns quantum field theory into a mathematically well-defined problem in statistical mechanics. Condensed matter theorists and mathematical physicists have devised a variety of methods for tackling such problems, only one of which is weak-coupling perturbation theory. In the years immediately following Wilson's work, many of these tools were tried, for example analytical strong coupling expansions. The strong coupling limit is especially appealing, because confinement emerges immediately [61].

Strong coupling is, however, not the whole story. Owing to asymptotic freedom, the continuum limit of lattice QCD is controlled by weak coupling. Unfortunately, strong coupling expansions do not converge quickly enough to reach into the weak-coupling regime, at least with the simple discretizations that have been used till now. Consequently, results from strong coupling expansions for hadron masses and matrix elements are not close enough to continuum QCD to apply to particle phenomenology.

Since such analytical methods have not borne out, the tool of choice now is to compute (the discrete version of) Eq. (1.147) numerically via Monte Carlo integration. This numerical method has, over the years, developed several specialized features, and corresponding jargon, that often make its results impenetrable to non-experts. Moreover, as with any numerical method, there are several sources of systematic uncertainty. Most of the systematic effects can, however, be controlled with effective field theories, i.e., with techniques like those explained in the previous sections. After reviewing the basic elements of the Monte Carlo method, we cover the systematic effects. First is the so-called quenched approximation, which is difficult to control, but also not a fundamental limitation. Other uncertainties, which can be controlled, are reviewed next, emphasizing the role of effective field theories. It is hoped that in this way non-experts can learn to make simple estimates of size systematic uncertainties, without repeating all the steps of the numerical analysis. We end with a comment on the (unsatisfactory) status of computing strong phase shifts for B decays.

1.5.4.1 Monte Carlo integration

This part of the method is well understood and, these days, rarely leads to controversy. For completeness, however, we include a short explanation, focusing on the points that limit the range of applicability of the method. A more thorough treatment aimed at experimenters can be found in Ref. [62].

The first salient observation is that there are very many variables. Continuum field theory has uncountably many degrees of freedom. Field theory on an infinite lattice still has an infinite number of degrees of freedom, but at least countably infinite. (This makes

the products over x in Eq. (1.147) well-defined.) To keep the number finite (for a computer with finite memory), one must also introduce a finite spacetime volume. This may seem alarming, but what one has done is simply to introduce an ultraviolet cutoff (the lattice) and an infrared cutoff (the finite volume). This is usual in quantum field theory, and field theoretic techniques can be used to understand how to extract cutoff-free quantities from numerically calculable cutoff quantities.

Even with a finite lattice, the number of integration variables is large. If one only demands a volume a few times the size of a hadron and also several grid points within a hadron's diameter, one already requires at least, say, 10 points along each direction. In four-dimensional spacetime this leads to $\sim 32 \times 10^4$ gluonic variables. With so many variables, the only feasible methods are based on Monte Carlo integration. The basic idea of Monte Carlo integration is simple: generate an ensemble of random variables and approximate the integrals in Eq. (1.147) by ensemble averages.

Quarks pose special problems, principally because, to implement Fermi statistics, fermionic variables are Grassmann numbers. In all cases of interest, the quark action can be written

$$S_F = \sum_{\alpha\beta} \bar{\psi}_\alpha M_{\alpha\beta} \psi_\beta \,, \tag{1.148}$$

where α and β are multi-indices for (discrete) spacetime, spin and internal quantum numbers. The matrix $M_{\alpha\beta}$ is some discretization of the Dirac operator $\not{D} + m$. Note that it depends on the gauge field, but one may integrate over the gauge fields after integrating over the quark fields. Then, because the quark action is a quadratic form, the integral can be carried out exactly:

$$\int \prod_{\alpha\beta} d\bar{\psi}_\alpha d\psi_\beta \, e^{-\bar{\psi} M \psi} = \det M. \tag{1.149}$$

Similarly, products $\psi_\alpha \bar{\psi}_\beta$ in the integrand are replaced with quark propagators $[M^{-1}]_{\alpha\beta}$. The computation of M^{-1} is demanding, and the computation of $\det M$ (or, more precisely, changes in $\det M$ as the gauge field is changed) is very demanding.

With the quarks integrated analytically, it is the gluons that are subject to the Monte Carlo method. The factor with the action is now $\det M e^{-S}$, where S is now just the gluons' action. Both $\det M$ and e^{-S} are the exponential of a number that scales with the spacetime volume. In Minkowski spacetime the exponent is an imaginary number, so there are wild fluctuations for moderate changes in the gauge field. On the other hand, in Euclidean spacetime, with an imaginary time variable, S is real. In that case (assuming $\det M$ is positive definite) one can devise a Monte Carlo with *importance sampling*, which means that the random number generator creates gauges field weighted according to $\det M e^{-S}$. Because importance sampling is essential, only in Euclidean spacetime is lattice QCD numerically tractable.

Importance sampling works well if $\det M$ is positive. For pairs of equal-mass quarks, this is easy to achieve. As a result, most calculations of $\det M$ are for 2 or 4 flavors. Note that a physically desirable situation with three flavors, with the strange quark's mass different from that of two lighter quarks, must either cope with (occasional) non-positive weights, or find a (new) discretization with $\det M$ positive flavor by flavor.

The choice of imaginary time has an important practical advantage. Consider the two-point correlation function

$$C_2(t) = \langle 0 | \Phi_B(t) \Phi_B^\dagger(0) | 0 \rangle, \tag{1.150}$$

where Φ_B is an operator with the quantum numbers of the B meson at rest. Inserting a complete set of states between B and $B^\dagger$

$$C_2(t) = \sum_n \frac{1}{2m_n} \langle 0 | \Phi_B | B_n \rangle \langle B_n | \Phi_B^\dagger | 0 \rangle e^{i m_n t}, \tag{1.151}$$

where m_n is the mass of $|B_n\rangle$, the nth radial excitation of the B meson. For real t it would be difficult to disentangle all these contributions. If, however, $t = i x_4$, with x_4 real and positive, then one has a sum of damped exponentials. For large x_4 the lowest-lying state dominates and

$$C_2(x_4) = (2m_B)^{-1} |\langle 0 | \Phi_B | B \rangle|^2 e^{-m_B x_4} + \cdots, \tag{1.152}$$

where $|B\rangle$ is the lowest-lying state and m_B its mass. The omitted terms are exponentially suppressed. It is straightforward to test when the first term dominates a numerically computed correlation function, and then fit the exponential form to obtain the mass.

This technique for isolating the lowest-lying state is essential also for obtaining hadronic matrix elements. For $B^0 - \overline{B}^0$ mixing, for example, one must compute the matrix element $\langle B^0 | Q | \overline{B}^0 \rangle$, given in Eq. (1.118). One uses a three-point correlation function

$$C_Q(x_4, y_4) = \langle 0 | \Phi_B(x_4 + y_4) Q(y_4) \Phi_B(0) | 0 \rangle, \tag{1.153}$$

where only the Euclidean times of the operators have been written out. Inserting complete sets of states and taking x_4 and y_4 large enough,

$$C_Q(x_4, y_4) = (2m_B)^{-1} (2m_{\overline{B}})^{-1} \langle 0 | \Phi_B | B \rangle \langle B | Q | \overline{B} \rangle \langle \overline{B} | \Phi_B | 0 \rangle e^{-m_B x_4 - m_{\overline{B}} y_4}. \tag{1.154}$$

The amplitude ($\langle 0 | \Phi_B | B \rangle = \langle \overline{B} | \Phi_B | 0 \rangle$) and mass ($m_B = m_{\overline{B}}$) are obtained from C_2, leaving $\langle B | Q | \overline{B} \rangle$ to be determined from C_Q. Similarly, to obtain amplitudes for B decays to a single hadron (plus leptons or photons), simply replace one of the Φ_B operators with one for the desired hadron and Q with the desired operator. To compute the purely leptonic decay, simply replace Φ_B in C_2 with the charged current.

These methods are conceptually clean and technically feasible for the calculation of masses and hadronic matrix elements with at most one hadron in the final state. The procedure for computing correlation functions is as follows. First generate an ensemble of lattice gluon fields with the appropriate weight. Next form the desired product $O_1 \cdots O_n$, with quark variables exactly integrated out to form propagators M^{-1}. Then take the average over the ensemble. Finally, fit the Euclidean time dependence of Eqs. (1.152) and (1.154). Note that since the same ensemble is used for many similar correlation functions, the statistical fluctuations within the ensemble are correlated. This is not a concern, as long as the correlations are propagated sensibly through the analysis.

1.5.4.2 Quenched approximation

Any perusal of the literature on lattice QCD quickly comes across something called the "quenched approximation." As mentioned above, the factor $\det M$ in Eq. (1.149) is difficult to incorporate. The determinant generates sea quarks inside a hadron. The quenched approximation replaces $\det M$ with 1 *and* compensates the corresponding omission of the sea quarks with shifts in the bare couplings. This is analogous to a dielectric approximation in electromagnetism, and it fails under similar circumstances. In particular, if one is interested in comparing two quantities that are sensitive to somewhat different energy scales, one cannot expect the same dielectric shift to suffice. Another name for the quenched approximation is the "valence" approximation, which makes clearer that the valence quarks (and gluons) in hadrons are treated fully, and the sea quarks merely modeled.

It is not easy to estimate quantitatively the effect of quenching. For α_s [63] and the quark masses [64] one can compute the short distance contribution to the quenching shift, but that is only a start. The quenched approximation can be cast as the first term in a systematic expansion [65], but it is about as difficult to compute the next term as to restore the fermion determinant. In the context of heavy quark physics one should note that the CP-PACS [66] and MILC [67] groups now have unquenched calculations of the heavy-light decay constants f_B, f_{B_s}, f_D, and f_{D_s}. Both have results at several lattice spacings, so they can study the a dependence. Their results are about 10–15% higher than the most mature estimates from the quenched approximation.

1.5.4.3 Controllable systematic uncertainties

By a controllable systematic uncertainty we mean an uncertainty that can be incrementally improved in a well-defined way. In lattice QCD they arise from the ultraviolet and infrared cutoffs, and also from the fact that quark masses are freely adjustable and, for technical reasons, not always adjusted to their physical values. Because these effects are subject to theoretical control, the errors they introduce can largely be reduced to a level that is essentially statistical, given enough computing.

One of the least troublesome systematic effects comes from the finite volume. Finite-volume effects can be understood separately from lattice-spacing effects with an effective massive quantum field theory [68]. In some cases adjusting the volume at will is, at least in principle, a boon, yielding valuable information, such as scattering lengths and resonance widths.

The computer algorithms for computing the quark propagator M^{-1} converge more quickly at masses near that of the strange quark than for lighter masses. Consequently, the Monte Carlo is run at a sequence of light quark masses typically in the range $0.2m_s \lesssim m_q \lesssim m_s$. (The up and down quark masses are far smaller still and not reached.) The dependence on m_q can be understood and controlled via the chiral Lagrangian [69], another effective field theory. A recent development is to show in detail how to extract physical information from results at practical values of the light quark masses [70].

A special difficulty with heavy quarks is the effect of non-zero lattice spacing. The

bottom and charmed quark masses are large in lattice units. For this reason it is frequently (but incorrectly) stated that heavy quarks cannot be directly accommodated by a lattice. From the inception of HQET and NRQCD, these effective field theories have been used to treat heavy quarks, and more recently it has been shown how to use these tools to understand the discretization effects of heavy quarks discretized with the original Wilson formulation [71].

Let us first recall how lattice-spacing effects are controlled for systems of light quarks. Long ago, Symanzik introduced a local effective Lagrangian (LE$\mathcal{L}$) to describe cutoff effects [72]. One writes

$$\mathcal{L}_{\rm lat} \doteq \mathcal{L}_{\rm cont} + \sum_i a^{s_{\mathcal{O}_i}} K_i(a;\mu)\mathcal{O}_i(\mu), \tag{1.155}$$

where $s_{\mathcal{O}_i} = \dim\mathcal{O}_i - 4$. The symbol $\doteq$ means "has the same (on-shell) matrix elements as". For operators such as Q, needed for mixing,

$$Q_{\rm lat} \doteq Z_Q^{-1}(a;\mu)Q_{\rm cont}(\mu) + \sum_i a^{s_{\mathcal{Q}_i}} C_i(a;\mu)\mathcal{Q}_i(\mu), \tag{1.156}$$

where now $s_{\mathcal{Q}_i} = \dim\mathcal{Q}_i - \dim Q$. The continuum operators $\mathcal{O}_i$, $Q_{\rm cont}$, and $\mathcal{Q}_i$ are defined in a mass-independent scheme at scale μ. They do not depend on the lattice spacing a. The coefficients K_i, Z_Q, and C_i account for short distance effects, so they do depend on a.

If a is small enough the higher terms can be treated as perturbations. So, the a dependence of $\langle B|Q_{\rm lat}|\overline{B}\rangle$ is

$$\langle B|Q_{\rm lat}|\overline{B}\rangle = Z_Q^{-1}\langle B|Q_{\rm cont}|\overline{B}\rangle + aK_{\sigma F}\langle B|T\,Q_{\rm cont}\int d^4x\,\bar\psi\sigma\cdot F\psi|\overline{B}\rangle + aC_1\langle B|\mathcal{Q}_1|\overline{B}\rangle, \tag{1.157}$$

keeping only contributions of order a. To reduce the unwanted terms one might try to reduce a greatly, but CPU time goes as $a^{-(5\text{ or }6)}$. It is more effective to use a sequence of lattice spacings and extrapolate, with Eq. (1.157) as a guide. It is even better to adjust things so $K_{\sigma F}$ and K_1 are $\mathcal{O}(\alpha_s^\ell)$ [73] or $\mathcal{O}(a)$ [74], which is called Symanzik improvement. For light hadrons, a combination of improvement and extrapolation is best. Note that one still has to adjust $Q_{\rm lat}$ so that $Z_Q = 1$. In some cases the needed adjustment can be made nonpertubatively, even though it is a short distance quantity. When that is possible, lattice QCD can provide results with no perturbative uncertainty, although perturbative uncertainty may reenter through the electroweak Hamiltonian.

The Symanzik theory, as usually applied, assumes $m_q a \ll 1$. The bottom and charmed quarks' masses in lattice units are at present large: $m_b a \sim$ 1–2 and $m_c a$ about a third of that. It will not be possible to reduce a enough to make $m_b a \ll 1$ for many, many years. So, other methods are needed to control the lattice spacing effects of heavy quarks. There are several alternatives:

1. static approximation [75]
2. lattice NRQCD [76]
3. extrapolation from $m_Q \lesssim m_c$ up to m_b

3′. combine 3 with 1

4. normalize systematically to HQET [77]

5. anisotropic lattices with temporal lattice spacing $a_t \ll a$ [78]

All but the last use the heavy quark expansion in some way. The first two discretize continuum HQET; method 1 stops at the leading term, and method 2 carries the heavy quark expansion out to the desired order. Methods 3 and 3′ keep the heavy quark mass artificially small and appeal to the $1/m_Q$ expansion to extrapolate back up to m_b. Method 4 uses the same lattice action as method 3, but uses the heavy quark expansion to normalize and improve it. Methods 2 and 4 are able to calculate matrix elements directly at the b-quark mass. Method 5 has only recently been applied to heavy-light mesons [79], and, like the other methods, it requires that spatial momenta are much less than m_Q.

The methods can be compared and contrasted by *describing* the lattice theories with HQET [80]. This is, in a sense, the opposite of *discretizing* HQET. One writes down a (continuum) effective Lagrangian

$$\mathcal{L}_{\rm lat} \doteq \sum_n \mathcal{C}^{(n)}_{\rm lat}(m_Q a;\mu) O^{(n)}_{\rm HQET}(\mu), \tag{1.158}$$

with the operators $O^{(n)}_{\rm HQET}$ defined exactly as in Sec. 1.5.2, so they do not depend on m_Q or a. As long as $m_Q \gg \Lambda_{\rm QCD}$ this description makes sense. There are two short distances, $1/m_Q$ and the lattice spacing a, so the short distance coefficients $\mathcal{C}^{(n)}_{\rm lat}$ depend on $m_Q a$. Since all dependence on $m_Q a$ is isolated into the coefficients, this description shows that heavy quark lattice artifacts arise only from the mismatch of the $\mathcal{C}^{(n)}_{\rm lat}$ and their continuum analogs $\mathcal{C}^{(n)}_{\rm cont}$.

For methods 1 and 2, Eq. (1.158) is just a Symanzik LE$\mathcal{L}$. For lattice NRQCD we recover the result that some of the coefficients $\mathcal{C}^{(n)}_{\rm lat}$ have power-law divergences as $a \to 0$ [76]. So, to obtain continuum (NR)QCD, one must add more and more terms to the action. (This is just a generic feature of effective field theories, namely, that accuracy is improved by adding more terms, rather than taking the cutoff too high.) The truncation leaves a systematic error, which, in practice, is usually accounted for conservatively.

Eq. (1.158) is more illuminating for methods 3–5, which use the same actions, but with different normalization conditions. The lattice quarks are Wilson fermions [71], which have the same degrees of freedom and heavy quark symmetries as continuum quarks. Thus, the HQET description is admissible for all $m_Q a$. Method 4 matches the coefficients of Eq. (1.158) term by term to Eq. (1.127), by adjusting the lattice action and operators. In practice, this is possible only to finite order, so there are errors $(\mathcal{C}^{(n)}_{\rm lat} - \mathcal{C}^{(n)}_{\rm cont})\langle O^{(n)}_{\rm HQET}\rangle$. The rough size of matrix element here is $\Lambda_{\rm QCD}^{\dim O-4}$. The coefficients balance the dimensions with a and $1/m_Q$. If $\mathcal{C}^{(n)}_{\rm lat}$ is matched to $\mathcal{C}^{(n)}_{\rm cont}$ in perturbation theory, the difference is of order α_s^ℓ. Method 3 artificially reduces $m_Q a$ until the mismatch is of order $(m_Q a)^2$. This would be fine if $m_Q a$ were small enough, but with currently available lattices, $m_Q a$ is small only if m_Q is reduced until the heavy quark expansion falls apart. In method 5 the temporal

lattice spacing a_t is smaller than the spatial lattice spacing. The behavior of the mismatch $\mathcal{C}^{(n)}_{\rm lat} - \mathcal{C}^{(n)}_{\rm cont}$ for practical values of m_Q and a_t is still an open question [81].

The non-expert can get a feel for which methods are most appropriate by asking himself what order in $\Lambda_{\rm QCD}/m_b$ is needed. For zeroth order, method 1 will do. Perhaps the only quantity where this is sufficiently accurate is the mass of the b quark, where the most advanced calculation [82] neglects the subleading term λ_1/m_b in Eq. (1.130). For matrix elements, the first non-trivial terms are those of Eq. (1.128), so the other methods must be used. With method 3 one should check that $m_Q/\Lambda_{\rm QCD}$ is large enough; so far, all work with this method is worrisome in this respect.

Most of the matrix elements that are of interest to B physics will soon be recalculated, like f_B [66,67] and m_b [82], with two flavors of sea quarks. It seems, therefore, not useful tabulate quenched results. One can consult recent reviews focusing on the status of matrix elements instead [83].

1.5.4.4 Strong phases of nonleptonic decays

In considering CP asymmetries one encounters strong phase shifts. It is therefore interesting to consider computing them in lattice QCD.

A short summary is that this is still an unsolved problem, at least for inelastic decays, such as B decays. This does not mean that it is an unsolvable problem, but at this time numerical lattice calculations are not helpful for computing scattering phases above the inelastic threshold.

Often an even bleaker picture is painted, based on a superficial understanding a theorem of Maiani and Testa [84]. The theorem assumes an infinite volume and is, thus, relevant only to extremely large volumes. In volumes of (2–6 fm)^3 it is possible to disentangle phase information, because the scattering phase shift enters into the finite-volume boundary conditions of the final-state two-body wave function [85]. This works, however, only in the kinematic region with two-body final states. This has been worked out explicitly for kaon decays [86], giving also references to earlier work.

1.6 Constraints from Kaon Physics

There are two strong reasons for the discussion of the neutral kaon system in a report on B physics. First, for more than 30 years the only observation of CP violation was in the neutral kaon system. Over these years the formalism used to describe CP violation has changed, partly because our theoretical understanding of the subject has improved. One example of this development is the present classification of three, rather than two, types of CP violation, as explained in Sec. 1.4.1. Second, the Standard Model expresses all CP violating quantities in terms of the same CKM phase. The consistency of the experiments in B physics with those in the kaon system therefore provides a stringent test of the Standard Model. In practice both B and K data are used to overconstrain the unitarity triangle: the indirect constraints on $\sin 2\beta$, in particular its sign, rely largely on ϵ_K. Any future

inconsistency in the overdetermined unitarity triangle indicates new physics either in the B or K system or in both.

Sec.1.6.1 describes the neutral kaon system with the modern formalism and makes contact with the formalism traditionally used for kaon physics. To show how kaon measurements shape our expectations for B physics, Sec. 1.6.2 discusses the already measured CP violating quantities ϵ_K and ϵ'_K. In a similar vein, Sec. 1.6.3 deals with the rare decays $K^+ \to \pi^+ \nu\bar{\nu}$ and $K_L \to \pi^0 \nu\bar{\nu}$, which are the target of new high-precision kaon experiments.

1.6.1 The neutral kaon system

CP violation in $K^0 - \overline{K}^0$ mixing was discovered in 1964 [31]. The quantity ϵ_K, which is discussed in Sec. 1.6.2, is of key importance to test the CKM mechanism of CP violation, because new physics enters K and B physics in different ways. We introduce the neutral kaon system using the same formalism as for the B-meson system as derived in Sec. 1.3 and translate it to the traditional notation.

The lighter mass eigenstate of the neutral kaon is $|K_S\rangle$ and the heavier one is $|K_L\rangle$, where the subscripts refer to their short and long lifetimes. They are

$$\begin{aligned} |K_S\rangle &= p\,|K^0\rangle + q\,|\overline{K}^0\rangle = \frac{(1+\overline{\epsilon})\,|K^0\rangle - (1-\overline{\epsilon})\,|\overline{K}^0\rangle}{\sqrt{2\,(1+|\overline{\epsilon}|^2)}}\,, \\ |K_L\rangle &= p\,|K^0\rangle - q\,|\overline{K}^0\rangle = \frac{(1+\overline{\epsilon})\,|K^0\rangle + (1-\overline{\epsilon})\,|\overline{K}^0\rangle}{\sqrt{2\,(1+|\overline{\epsilon}|^2)}}\,. \end{aligned} \tag{1.159}$$

The quantity

$$\overline{\epsilon} = \frac{1+q/p}{1-q/p} \tag{1.160}$$

depends on phase conventions. (The parameter $\overline{\epsilon}$ is not to be confused with the well-known parameter ϵ_K, defined in (1.169).)

CP conservation in $|\Delta S| = 2$ transitions corresponds to $\overline{\epsilon} = 0$, in which case $|K_S\rangle$ and $|K_L\rangle$ become the CP even and CP odd eigenstates. CP violation in mixing is well-established from the semileptonic CP asymmetry

$$\begin{aligned} \delta(\ell) &= \frac{\Gamma(K_L \to \ell^+ \nu\,\pi^-) - \Gamma(K_L \to \ell^- \bar{\nu}\,\pi^+)}{\Gamma(K_L \to \ell^+ \nu\,\pi^-) + \Gamma(K_L \to \ell^- \bar{\nu}\,\pi^+)} \\ &= \frac{1-|q/p|^2}{1+|q/p|^2} = \frac{2\,\mathrm{Re}\,\overline{\epsilon}}{1+|\overline{\epsilon}|^2} \;=\; (3.27 \pm 0.12) \times 10^{-3}\,. \end{aligned} \tag{1.161}$$

The quoted numerical value is the average for $\ell = e$ and μ [15]. From (1.161) it is clear that in the kaon system $|q/p|$ is close to one. In the B systems $|q/p|$ is close to one because the width difference is smaller than the mass difference. Here, however, they are comparable [15]

$$\Delta m_K = (0.5301 \pm 0.0014) \times 10^{10}\, s^{-1}, \qquad \Delta\Gamma_K = (1.1174 \pm 0.0010) \times 10^{10}\, s^{-1}\,. \tag{1.162}$$

Hence one concludes that $|q/p| - 1$ is so small, because the relative phase ϕ between M_{12} and $-\Gamma_{12}$ (cf., (1.62)) is close to zero. Expanding in ϕ one easily finds from (1.61) that

$$|M_{12}| = \frac{\Delta m_K}{2} + \mathcal{O}\left(\phi^2\right), \qquad |\Gamma_{12}| = \frac{\Delta\Gamma_K}{2} + \mathcal{O}\left(\phi^2\right), \tag{1.163a}$$

$$\frac{q}{p} = -e^{-i\phi_M}\left[1 - \phi\,\frac{\Delta\Gamma_K/2}{\Delta m_K + i\,\Delta\Gamma_K/2} + \mathcal{O}\left(\phi^2\right)\right]. \tag{1.163b}$$

Hence (1.163b) and (1.161) allow us to solve for the CP violating phase ϕ:

$$\phi = \frac{(\Delta m_K)^2 + (\Delta\Gamma_K/2)^2}{\Delta m_K \Delta\Gamma_K/2}\,\delta(\ell) \;+\; \mathcal{O}\left(\phi^2\right) = (6.6 \pm 0.2) \cdot 10^{-3}\,. \tag{1.164}$$

In the literature on $K \to \pi\pi$ decays the following amplitude ratios are introduced:

$$\eta_{+-} = \frac{\langle \pi^+\pi^-|K_L\rangle}{\langle \pi^+\pi^-|K_S\rangle}\,, \qquad \eta_{00} = \frac{\langle \pi^0\pi^0|K_L\rangle}{\langle \pi^0\pi^0|K_S\rangle}\,. \tag{1.165}$$

If CP were conserved, both would vanish. The moduli and phases of η_{+-} and η_{00} have been measured to be

$$\begin{aligned} |\eta_{+-}| &= (2.285 \pm 0.019) \cdot 10^{-3}\,, \qquad \phi_{+-} = 43.5^\circ \pm 0.6^\circ\,, \\ |\eta_{00}| &= (2.275 \pm 0.019) \cdot 10^{-3}\,, \qquad \phi_{00} = 43.4^\circ \pm 1.0^\circ\,, \end{aligned} \tag{1.166}$$

according to the PDG fit [15]. All three types of CP violation lead to non-zero η_{+-} and η_{00}. To separate $|\Delta S| = 2$ from $|\Delta S| = 1$ CP violation one introduces isospin states

$$\begin{aligned} |\pi^0\pi^0\rangle &= \sqrt{\frac{1}{3}}\,|\,(\pi\pi)_{I=0}\rangle - \sqrt{\frac{2}{3}}\,|\,(\pi\pi)_{I=2}\rangle\,, \\ |\pi^+\pi^-\rangle &= \sqrt{\frac{2}{3}}\,|\,(\pi\pi)_{I=0}\rangle + \sqrt{\frac{1}{3}}\,|\,(\pi\pi)_{I=2}\rangle\,, \end{aligned}$$

and isospin amplitudes

$$A_I = \langle (\pi\pi)_I\,|K^0\rangle\,, \qquad \overline{A}_I = \langle (\pi\pi)_I\,|\overline{K}^0\rangle\,, \qquad I = 0, 2\,. \tag{1.167}$$

The strong final state interaction of the two-pion final states is highly constrained by kinematics and conservation laws: the CP invariance of the strong interaction forbids a two-pion state to scatter into a three-pion state and the rescattering into a state with four or more pions is kinematically forbidden. Furthermore, isospin is an almost exact symmetry of QCD and forbids the rescattering between the two isospin eigenstates. Hence the final state interaction of the $I = 0$ and $I = 2$ states is only elastic and, thus, fully described by two scattering phases. This feature is known as *Watson's theorem* [87]. Hence we can write

$$\begin{aligned} A_I &= |A_I| e^{i\Phi_I} e^{i\delta_I}\,, \qquad \overline{A}_I = -|A_I| e^{-i\Phi_I} e^{i\delta_I}\,, \\ \lambda_I &= \frac{q}{p}\frac{\overline{A}_I}{A_I} = e^{-i(2\Phi_I + \phi_M)}\left[1 - \phi\frac{\Delta\Gamma_K/2}{\Delta m_K + i\,\Delta\Gamma/2}\right] + \mathcal{O}(\phi^2)\,, \end{aligned} \tag{1.168}$$

where the two scattering phases δ_I are empirically determined to be $\delta_0 \approx 37^\circ$ and $\delta_2 \approx -7^\circ$. Several weak amplitudes (with different CP violating phases) contribute to $|A_I|e^{i\Phi_I}$, but the presence of a single strong phase allows to write A_I as in (1.168), ensuring $|\overline{A}_I/A_I| = 1$. Therefore, there is no direct CP violation in $K \to (\pi\pi)_I$. Note that our definition of A_0 and A_2 includes both the weak and strong phases, in accordance with the formalism used in B physics. In the kaon literature the A_I's are commonly defined without the factors $e^{i\delta_I}$.

A simplification arises from the experimental observation that $|A_0| \simeq 22\,|A_2|$, which is called $\Delta I = 1/2$ rule. This enhancement of $|A_0|$ allows to expand in $|A_2/A_0|$. The CP violating quantity ϵ_K reads

$$\epsilon_K = \frac{\eta_{00} + 2\,\eta_{+-}}{3} = \frac{\langle(\pi\pi)_{I=0}|K_L\rangle}{\langle(\pi\pi)_{I=0}|K_S\rangle}\left[1 + \mathcal{O}\left(\frac{A_2^2}{A_0^2}\right)\right] = \frac{1-\lambda_0}{1+\lambda_0}\,. \tag{1.169}$$

Hence ϵ_K is defined in a way that to zeroth and first order in A_2/A_0 only a single strong amplitude contributes and therefore CP violation in decay is absent. The $I = 0$ two-pion state dominates the K_S width Γ_S. Thus $\langle K^0|(\pi\pi)_{I=0}\rangle\langle(\pi\pi)_{I=0}|\overline{K}^0\rangle$ almost saturates Γ_{12}, so that the phase $\phi_M - \phi$ of $-\Gamma_{12}$ equals $-2\Phi_0$ up to tiny corrections of order A_2^2/A_0^2 and Γ_L/Γ_S. This implies that ϵ_K does not provide any additional information compared to the semileptonic asymmetry in (1.161). We find from (1.168)

$$\lambda_0 = 1 - i\,\phi\frac{\Delta m_K}{\Delta m_K + i\,\Delta\Gamma_K} + \mathcal{O}\left(\phi^2, \frac{A_2^2}{A_0^2}, \frac{\Gamma_L}{\Gamma_S}\right), \tag{1.170}$$

and (1.169) evaluates to

$$\epsilon_K = \frac{\phi}{2}\frac{\Delta m_K}{\sqrt{(\Delta m_K)^2 + (\Delta\Gamma_K/2)^2}}\,e^{i\phi_\epsilon} + \mathcal{O}\left(\phi^2, \frac{A_2^2}{A_0^2}, \frac{\Gamma_L}{\Gamma_S}\right) \quad \text{with} \quad \phi_\epsilon = \arctan\frac{\Delta m_K}{\Delta\Gamma_K/2}\,. \tag{1.171}$$

From (1.166) one finds the experimental value:

$$\epsilon_K = e^{i\,(0.97\pm0.02)\,\pi/4}\,(2.28 \pm 0.02) \times 10^{-3}\,. \tag{1.172}$$

Therefore (1.171) yields

$$\phi = (6.63 \pm 0.06) \times 10^{-3}\,, \tag{1.173}$$

in perfect agreement with (1.164). A numerical accident leads to $\Delta m_K \approx \Delta\Gamma_K/2$, which explains why the phase ϕ_ϵ in (1.171) is so close to $\pi/4$.

To first order in ϕ one finds from (1.169)

$$\epsilon_K \simeq \frac{1}{2}\,[1-\lambda_0] \;\simeq\; \frac{1}{2}\left(1 - \left|\frac{q}{p}\right| - i\,\mathrm{Im}\,\lambda_0\right). \tag{1.174}$$

Therefore $\mathrm{Re}\,\epsilon_K$ measures CP violation in mixing and $\mathrm{Im}\,\epsilon_K$ measures interference type CP violation.

CP violation in $|\Delta S| = 1$ transitions is characterized by

$$\begin{aligned}\epsilon'_K = \frac{\eta_{+-} - \eta_{00}}{3} &= \frac{\epsilon_K}{\sqrt{2}}\left[\frac{\langle(\pi\pi)_{I=2}|K_L\rangle}{\langle(\pi\pi)_{I=0}|K_L\rangle} - \frac{\langle(\pi\pi)_{I=2}|K_S\rangle}{\langle(\pi\pi)_{I=0}|K_S\rangle}\right]\left[1 + \mathcal{O}\left(\frac{A_2}{A_0}\right)\right] \\ &= \frac{A_2}{A_0}\,\frac{1}{\sqrt{2}}\left[\frac{1-\lambda_2}{1+\lambda_0} - \frac{(1-\lambda_0)(1+\lambda_2)}{(1+\lambda_0)^2}\right]. \end{aligned} \tag{1.175}$$

Next we use

$$\lambda_2 = \lambda_0\,e^{2\,i\,(\Phi_0 - \Phi_2)}\,, \tag{1.176}$$

and expand to first order in the small phases:

$$\epsilon'_K = \frac{1}{2\sqrt{2}}\,\frac{A_2}{A_0}\,(\lambda_0 - \lambda_2) + \mathcal{O}\left(\frac{A_2^2}{A_0^2}, \phi^2, (\Phi_0 - \Phi_2)^2\right) = \frac{1}{\sqrt{2}}\,\frac{A_2}{A_0}\,i\,(\Phi_2 - \Phi_0)\,. \tag{1.177}$$

A non-vanishing value of ϵ'_K implies different CP violating phases in the two isospin amplitudes and therefore $|\Delta S| = 1$ CP violation. Since experimentally $\mathrm{Re}\,\epsilon'_K > 0$, one finds $\Phi_2 > \Phi_0$. The phase of ϵ'_K is $90^\circ + \delta_2 - \delta_0 \simeq 46^\circ$ and ϵ'_K/ϵ_K is almost real and positive.

Since (1.177) does not depend on q/p, there is no contribution from CP violation in mixing to ϵ'_K. The strong phases drop out in the combination

$$\mathrm{Im}\,\frac{A_0}{A_2}\,\epsilon'_K \simeq \frac{1}{2\sqrt{2}}\,(\mathrm{Im}\,\lambda_0 - \mathrm{Im}\,\lambda_2)\,. \tag{1.178}$$

Since we work to first order in ϕ, we can set $|\lambda_I| = 1$, and therefore (1.178) purely measures interference type CP violation. From the definition in (1.175) one further finds that

$$\mathrm{Re}\,\epsilon'_K \simeq \frac{1}{6}\left(1 - \left|\frac{A_{\pi^0\pi^0}\,\overline{A}_{\pi^+\pi^-}}{\overline{A}_{\pi^0\pi^0}\,A_{\pi^+\pi^-}}\right|\right) \simeq \frac{1}{\sqrt{2}}\,\frac{|A_2|}{|A_0|}\,\sin(\delta_0 - \delta_2)\,(\Phi_2 - \Phi_0) \tag{1.179}$$

originates solely from $|\overline{A}_f/A_f| \neq 1$. Hence $\mathrm{Re}\,\epsilon'_K$ measures CP violation in decay.

Experimentally the quantity $|\eta_{00}/\eta_{+-}|^2 = 1 - 6\,\mathrm{Re}\,\epsilon'_K/\epsilon_K$ has been determined. Recent results are

$$\begin{aligned}\mathrm{Re}\,\frac{\epsilon'_K}{\epsilon_K} &= (20.7 \pm 2.8) \times 10^{-4} \qquad (\text{KTeV}) \quad [88]\,, \\ \mathrm{Re}\,\frac{\epsilon'_K}{\epsilon_K} &= (15.3 \pm 2.6) \times 10^{-4} \qquad (\text{NA48}) \quad [89]. \end{aligned} \tag{1.180}$$

We therefore find from (1.177) that the difference of the CP violating phases is tiny:

$$\Phi_2 - \Phi_0 = (1.5 \pm 0.2) \cdot 10^{-4} \quad (\text{KTeV})\,, \qquad \Phi_2 - \Phi_0 = (1.1 \pm 0.2) \cdot 10^{-4} \quad (\text{NA48})\,. \tag{1.181}$$

1.6.2 Phenomenology of ϵ_K and ϵ'_K

In order to exploit the precise measurement of $\phi = -\arg M_{12}/\Gamma_{12}$ from ϵ_K in (1.173) one must calculate the phases of

$$M_{12} = \frac{1}{2m_K}\,\langle K^0|H^{|\Delta S|=2}|\overline{K}^0\rangle - \mathrm{Disp}\,\frac{i}{4m_K}\int \mathrm{d}^4x\,\langle K^0|H^{|\Delta S|=1}(x)\,H^{|\Delta S|=1}(0)|\overline{K}^0\rangle\,. \tag{1.182}$$

and

$$\Gamma_{12} = \mathrm{Abs}\,\frac{i}{2m_K}\int \mathrm{d}^4x\,\langle K^0|H^{|\Delta S|=1}(x)\,H^{|\Delta S|=1}(0)|\overline{K}^0\rangle \qquad (1.183)$$
$$= \frac{1}{2m_K}\sum_f (2\pi)^4\delta^4(p_K-p_f)\langle K^0|H^{|\Delta S|=1}|f\rangle\,\langle f|H^{|\Delta S|=1}|\overline{K}^0\rangle \simeq \frac{1}{2m_K}\,A_0^*\,\overline{A}_0\,.$$

Here Abs denotes the absorptive part of the amplitude. It is calculated by retaining only the imaginary part of the loop integration while keeping both real and imaginary parts of complex coupling constants. Analogously, the dispersive part Disp is obtained from the real part of the loop integral.

The second term in (1.182) shows that, at second order, also the $|\Delta S| = 1$ Hamiltonian contributes to M_{12}. In the B system the corresponding contribution is negligibly small. The Standard Model $|\Delta S| = 2$ Hamiltonian reads

$$H^{|\Delta S|=2} = \frac{G_F^2}{4\pi^2}\,M_W\left[\lambda_c^{*2}\,\eta_1\,S(x_c)\;+\;\lambda_t^{*2}\,\eta_2\,S(x_t)\right.$$
$$\left.+\,2\,\lambda_c^*\,\lambda_t^*\,\eta_3\,S(x_c,x_t)\right]b_K(\mu)\,Q_K(\mu) + \mathrm{h.c.} \qquad (1.184)$$

It involves the $|\Delta S| = 2$ operator

$$Q_K(\mu) = \overline{d}_L\gamma_\nu s_L\,\overline{d}_L\gamma^\nu s_L\,. \qquad (1.185)$$

In (1.184) $\lambda_q = V_{qd}V_{qs}^*$, $x_q = m_q^2/M_W^2$ and $S(x)$ is the Inami-Lim function introduced in (1.120). The third function $S(x_c,x_t)$ comes from the box diagram with one charmed and one top quark. One finds $S(x_c) \simeq x_c$, $S(x_c,x_t) \simeq x_c(0.6 - \ln x_c)$ and $S(x_t) \simeq 2.4$ for $m_t \simeq 167\,\mathrm{GeV}$ in the $\overline{\mathrm{MS}}$ scheme. Short distance QCD corrections are contained in the η_i's. In the $\overline{\mathrm{MS}}$ scheme the next-to-leading order results are $\eta_1 = 1.4 \pm 0.3$, $\eta_2 = 0.57 \pm 0.01$ and $\eta_3 = 0.47 \pm 0.04$ [90]. η_1 strongly depends on m_c and α_s, the quoted range corresponds to $m_c = 1.3\,\mathrm{GeV}$. A common factor of the QCD coefficients is $b_K(\mu)$, the kaon analogue of $b_B(\mu)$ encountered in (1.119). The matrix element of Q_K is parameterized as

$$\langle K^0|Q_K(\mu)|\overline{K}^0\rangle = \frac{2}{3}\,f_K^2\,m_K^2\,\frac{\widehat{B}_K}{b_K(\mu)}\,, \qquad (1.186)$$

where f_K is the kaon decay constant.

CP violation in the kaon system is related to the squashed unitarity triangle with sides $|\lambda_u|$, $|\lambda_c|$ and $|\lambda_t|$. In the limit $\lambda_t = 0$ all CP violation vanishes, thus CP violation is governed by the small parameter $\mathrm{Im}\,(\lambda_t/\lambda_u)$. This explains the smallness of the measured phases in (1.173) and (1.181). This pattern is a feature of the CKM mechanism of CP violation and need not hold in extensions of the Standard Model. Hence kaon physics provides a fertile testing ground for non-standard CP violation related to the first two quark generations.

The presence of the second term in (1.182) impedes the clean calculation of the mixing phase $\phi_M = \arg M_{12}$ in terms of the CKM phases. It constitutes a long distance contribution, which is not proportional to $\widehat{B}_K$. Since both terms in (1.182) have different weak

phases, ϕ_M involves the ratio of the two hadronic matrix elements. This is different from the case in $B^0-\overline{B}^0$ mixing where only one hadronic matrix element contributes in the Standard Model, which therefore cancels from ϕ_M. The long distance $|\Delta S| = 1$ piece is hard to calculate and is usually eliminated with the help of the experimental value of $\Delta m_K = 2\,|M_{12}|$ in (1.162). Then, however, our expression for the mixing phase ϕ_M still depends on the hadronic parameter $\widehat{B}_K$.

The phases of both ϕ_M and $\arg\Gamma_{12}$ are close to $\arg\lambda_u$, which vanishes in the CKM phase convention. The dominant corrections to ϕ_M stems from the term proportional to λ_t^{*2} in $H^{|\Delta S|=2}$. For $\arg\Gamma_{12}$ we need the $|\Delta S| = 1$ Hamiltonian, which is obtained from the $|\Delta B| = 1$ Hamiltonian in (1.115) by replacing $\xi_{u,c,t}$ with $\lambda_{u,c,t}$ and replacing the b quark field in the operators by an s field. The leading contribution to $\arg(-\Gamma_{12}) \approx -2\,\Phi_0$, is proportional to $\mathrm{Im}\,\lambda_t\,\langle(\pi\pi)_{I=0}|Q_6|\overline{K}^0\rangle/|A_0|$. The $\Delta I = 1/2$ enhancement of $|A_0|$ suppresses Φ_0, which is calculated to $\Phi_0 = \mathcal{O}(2\cdot 10^{-4})$ [91]. Hence in the CKM phase convention $\arg(-\Gamma_{12})$ contributes roughly 6% to the measured phase ϕ in (1.173) and one can approximate $\phi \approx \phi_M$. After expressing the CKM elements in (1.184) in terms of the improved Wolfenstein parameters the constraint from the measured value in (1.173) can be cast in the form [90,92]

$$5.3\times 10^{-4} = \widehat{B}_K A^2\,\overline{\eta}\,\left\{[1-\overline{\rho}+\Delta\,(\overline{\rho},\overline{\eta})]\,A^2\lambda^4\eta_2\,S(x_t) + \eta_3 S(x_c,x_t) - \eta_1 x_c\right\}. \qquad (1.187)$$

In the absence of the small term $\Delta\,(\overline{\rho},\overline{\eta}) = \lambda^2\,(\overline{\rho}-\overline{\rho}^2-\overline{\eta}^2)$ this equation defines a hyperbola in the $(\overline{\rho},\overline{\eta})$ plane. The largest uncertainties in (1.187) stem from $\widehat{B}_K$ and $A = |V_{cb}|/\lambda^2$, which enters the largest term in (1.187) raised to the fourth power. Hence, reducing the error of $|V_{cb}|$ improves the ϵ_K constraint.

It is more difficult to analyze ϵ'_K, because the weak phases Φ_0 and Φ_2 are much harder to compute than ϕ_M. Φ_2 is essentially proportional to $\mathrm{Im}\,\lambda_t\,\langle(\pi\pi)_{I=2}|\,Q_8\,|\overline{K}^0\rangle/|A_2|$. The two matrix elements entering $\Phi_2 - \Phi_0$ are difficult to calculate and numerically tend to cancel each other. Especially there is a controversy about $\langle(\pi\pi)_{I=0}|Q_6|\overline{K}^0\rangle$ and the different theoretical estimates can accommodate for both the KTeV and the NA48 result in (1.181) [91,93]. Even after the experimental discrepancy in (1.180) is resolved, ϵ'_K will not immediately be useful to determine $\mathrm{Im}\,\lambda_t \simeq A^2\lambda^5\overline{\eta}$. Nevertheless, ϵ'_K can be useful to constrain new physics contributions [94]. For recent overviews on ϵ'_K we refer to [95].

1.6.3 $K \to \pi\nu\bar{\nu}$

Rare kaon decays triggered by loop-induced $s \to d$ transitions can provide information on λ_t and thereby on the shape of the unitarity triangle. Final states with charged leptons are poorly suited for a clean extraction of this information, because they involve diagrams with photon-meson couplings. Such diagrams are affected by long distance hadronic effects and are hard to evaluate. The decays $K^+ \to \pi^+\nu\overline{\nu}$ and $K_L \to \pi^0\nu\overline{\nu}$, however, are theoretically very clean, with negligible hadronic uncertainties. The $K \to \pi$ form factors can be extracted from the well-measured $K_{\ell 3}$ decays. So far two $K^+ \to \pi^+\nu\overline{\nu}$ events have been observed [96], corresponding to a branching ratio

$$\mathcal{B}(K^+ \to \pi^+\nu\overline{\nu}) = \left(1.57^{+1.75}_{-0.82}\right)\times 10^{-10}\,. \qquad (1.188)$$

Experimental proposals at BNL and Fermilab aim at a measurement of $K^+ \to \pi^+\nu\overline{\nu}$ and $K_L \to \pi^0\nu\overline{\nu}$ at the 10% level. The constraint on the improved Wolfenstein parameters $(\overline{\rho},\overline{\eta})$ can be cast in the form [35]

$$\frac{\mathcal{B}(K^+ \to \pi^+\nu\overline{\nu})}{4.57 \cdot 10^{-11}} = A^4 X^2(x_t)\left(1-\lambda^2\right)\left[\left(\frac{\overline{\eta}}{1-\lambda^2}\right)^2 + (\rho_0 - \overline{\rho})^2\right]. \quad (1.189)$$

Here $X(x_t) \simeq 1.50$ comprises the dependence on m_t and the NLO short distance QCD corrections [97]. $\rho_0 \approx 1 + 0.27/A^2$ contains the contribution from the internal charm loop [97]. The quoted numerical value corresponds to a $\overline{\rm MS}$ mass of $m_c = 1.3\,{\rm GeV}$. The largest theoretical uncertainty in (1.189), of order 5%, stems from the charm contribution. Further the fourth power of A introduces a sizable parametric uncertainty. The equation in (1.189) describes an ellipse in the $(\overline{\rho},\overline{\eta})$ plane centered at $(\rho_0, 0)$. By inserting typical values for the Wolfenstein parameters (e.g., $\lambda = 0.22$, $A = 0.8$, $\overline{\rho} = 0.2$ and $\overline{\eta} = 0.4$) into (1.189) one finds that (1.188) is compatible with the Standard Model.

In the Standard Model the decay $K_L \to \pi^0\nu\overline{\nu}$ is CP violating. It measures interference type CP violation, the associated phase $\arg\lambda_{\pi^0\nu\overline{\nu}}$ is large, of order $\overline{\eta}/(1-\overline{\rho})$. This is in sharp contrast to the small phases we found in (1.173) and (1.181). A measurement of $\mathcal{B}(K_L \to \pi^0\nu\overline{\nu})$ establishes $\arg\lambda_{\pi^0\nu\overline{\nu}} \neq \phi$ and therefore implies CP violation in the $|\Delta S| = 1$ Hamiltonian. This is the same situation as with $\mathrm{Im}\,(\epsilon'_K A_0/A_2)$ in (1.178), which also proves $|\Delta S| = 1$ CP violation from the difference of two interference type CP violating phases. $K_L \to \pi^0\nu\overline{\nu}$ is even cleaner than $K^+ \to \pi^+\nu\overline{\nu}$, because the charm contribution is negligible. $\mathcal{B}(K_L \to \pi^0\nu\overline{\nu})$ is proportional to $(\mathrm{Im}\,\lambda_t)^2 \propto \overline{\eta}^2$ and therefore determines the height of the unitarity triangle

$$\frac{\mathcal{B}(K_L \to \pi^0\nu\overline{\nu})}{1.91 \cdot 10^{-10}} = A^4 X^2(x_t)\,\overline{\eta}^2\left(1+\lambda^2\right). \quad (1.190)$$

Hence the two discussed branching ratios allow for a precise construction of the unitarity triangle from kaon physics alone. Moreover the ratio of the two branching ratios is almost independent of A and m_t. It allows for a determination of $\sin 2\beta$ with a similar precision as from $a_{CP}(B \to \psi K_S)$ [98]. New physics may enter $s \to d$ transitions in a different way than $b \to s$ and $b \to d$ transitions. Hence comparing of the unitarity triangles from K physics and from B physics provides an excellent test of the Standard Model.

1.7 Standard Model Expectations

This section outlines what is known about the CKM matrix at the present time, and what the pattern of expectations is for some of the most interesting processes in the Standard Model.

Since most of the existing data apart from $\sin 2\beta$ come from CP conserving measurements, it is convenient to present the constraints on the CKM matrix using the Wolfenstein parameterization. Magnitudes of CKM matrix elements are simply related to λ, A, $\bar{\rho}$, and $\bar{\eta}$. The best known of these is λ, the Cabibbo angle, which is known at the 1% level. The parameter A is determined by $|V_{cb}|$, which is known with a 5% error. The uncertainty in $\bar{\rho}$ and $\bar{\eta}$ is significantly larger. The most important constraints come from

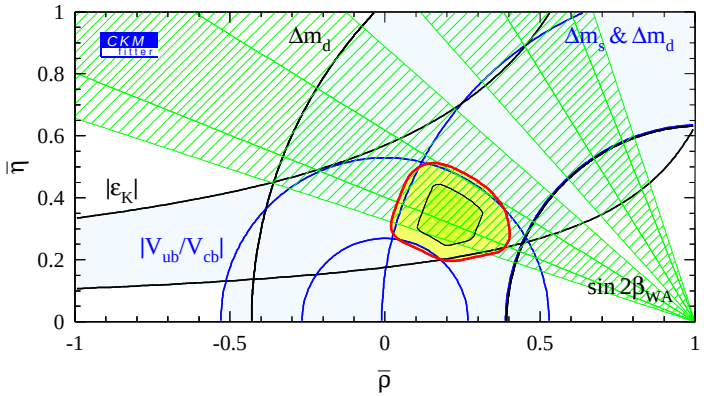

Figure 1.9: The allowed region in the $\bar{\rho} - \bar{\eta}$ plane. Also shown are the individual constraints, and the world average $\sin 2\beta$. (From Ref. [99].)

- CP violation in $K^0 - \overline{K}^0$ mixing described by the ϵ_K parameter;
- $|V_{ub}/V_{cb}|$ measured from semileptonic B decays;
- $B^0 - \overline{B}^0$ mixing;
- The lower limit on $B_s - \overline{B}_s$ mixing.

A problem in translating these to constraints on the CKM matrix is related to theoretical uncertainties. We follow the point of view adopted in the BaBar book [4] that no confidence level can be attached to model dependent theory errors. Fig. 1.9 shows the result of such an analysis from Ref. [99]. Fig. 1.10 shows the same fit on the $\sin 2\alpha - \sin 2\beta$ plane. Note that any value for $\sin 2\alpha$ would still be allowed if $|V_{ub}|$ were slightly larger, or if Δm_{B_s} were slightly smaller than their allowed ranges. Fig. 1.11 shows the allowed range in the $\sin 2\beta - \gamma$ plane, and that γ is already constrained.

Some of the uncertainties entering these constraints will be significantly reduced during Run II. The hadronic matrix elements B_K, $f^2_{B_d} B_{B_d}$, and $f^2_{B_s} B_{B_s}$ need to be determined by unquenched lattice QCD calculations. The theoretical uncertainties in $|V_{ub}|$ and $|V_{cb}|$ will also be reduced to the few percent level by unquenched lattice calculations of the exclusive $\overline{B}^0_d \to \pi\,\ell\,\bar{\nu}$ and $\overline{B}^0_d \to D^{(*)}\ell\,\bar{\nu}$ form factors in the region of phase space where the momentum of the final hadron is small. As discussed in Sec. 1.5.4, these lattice calculations are straightforward in principle, but a variety of uncertainties must be brought under control. The uncertainties in these two CKM matrix elements may be reduced in the next few years, even without recourse to lattice QCD, using inclusive semileptonic decays. The error in $|V_{cb}|$ may be reduced to 2–3% with precise determinations of a short distance b quark mass and by gaining more confidence about the smallness of quark-hadron duality violation. On a similar timescale the error in $|V_{ub}|$ may be reduced to the 5–10% level [100] by pursuing several model independent determinations.

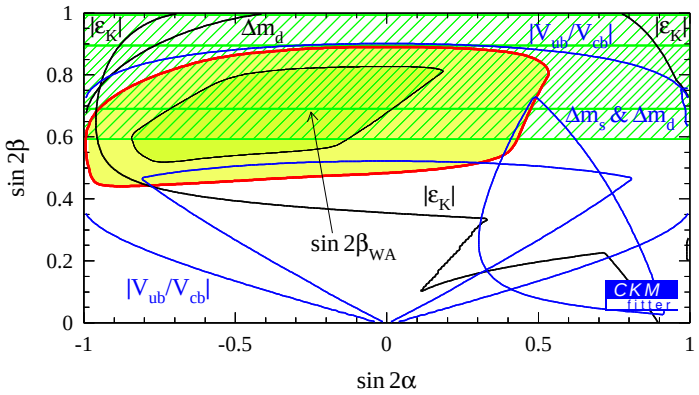

Figure 1.10: The allowed region in the $\sin 2\alpha - \sin 2\beta$ plane [99].

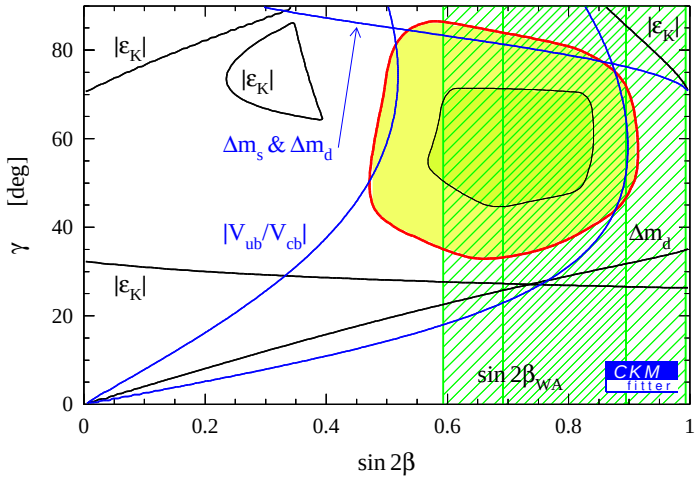

Figure 1.11: The allowed region in the $\sin 2\beta - \gamma$ plane [99].

References

[1] T. Affolder *et al.*, CDF Collaboration, Phys. Rev. D **61** (2000) 072005.

[2] B. Aubert *et al.*, BABAR Collaboration, Phys. Rev. Lett. **86** (2001) 2515.

[3] A. Abashian *et al.*, BELLE Collaboration, Phys. Rev. Lett. **86** (2001) 2509.

[4] *The BaBar Physics Book: Physics at an Asymmetric B Factory*, ed. P. F. Harrison and H. R. Quinn, SLAC-R-0504.

[5] G. C. Branco, L. Lavoura and J. P. Silva, *CP Violation* (Clarendon Press, Oxford, 1999).

[6] A. V. Manohar and M. B. Wise, *Heavy Quark Physics* (Cambridge University Press, 2000).

[7] I. I. Bigi and A. I. Sanda, *CP Violation* (Cambridge University Press, New York, 2000).

[8] *B decays at the LHC*, ed. P. Ball *et al.*, hep-ph/0003238 [CERN-TH/2000-101].

[9] See, for example, P. Langacker, in *Proceedings of the 24th International Conference on High Energy Physics*, ed. R. Kotthaus and J. H. Kühn (Springer-Verlag, Berlin, 1989).

[10] N. Cabibbo, Phys. Rev. Lett. **10** (1963) 531.

[11] M. Kobayashi and T. Maskawa, Prog. Theor. Phys. **49** (1973) 652.

[12] S. L. Glashow, J. Iliopoulos and L. Maiani, Phys. Rev. D **2** (1970) 1285.

[13] J. F. Gunion, H. E. Haber, G. L. Kane and S. Dawson, *The Higgs Hunter's Guide* (Addison-Wesley, Redwood City, Calif., 1989).

[14] C. Jarlskog, Phys. Rev. Lett. **55** (1985) 1039.

[15] D. E. Groom *et al.* [Particle Data Group], Eur. Phys. J. C **15** (2000) 1.

[16] L. Wolfenstein, preprint No. NSF-ITP-90-29 (unpublished); Phys. Rev. D **43** (1991) 151.

[17] A. J. Buras, M. E. Lautenbacher, G. Ostermaier, Phys. Rev. D **50** (1994) 3433.

[18] G. Buchalla and A. J. Buras, Phys. Rev. D **54** (1996) 6782.

[19] A. F. Falk, A. Lewandowski and A. A. Petrov, Phys. Lett. B **505** (2001) 107; G. Buchalla and G. Isidori, Phys. Lett. B **440** (1998) 170.

[20] G. P. Lepage and S. J. Brodsky, Phys. Rev. D **22** (1980) 2157.

[21] C.-H. V. Chang and H-n. Li, Phys. Rev. D **55** (1997) 5577; T.-W. Yeh and H-n. Li, Phys. Rev. D **56** (1997) 1615; Y.-Y. Keum, H-n. Li and A. I. Sanda, Phys. Lett. B **504** (2001) 6; Phys. Rev. D **63** (2001) 054008; Y.-Y. Keum and H-n. Li, Phys. Rev. D **63** (2001) 074006.

[22] M. Beneke, G. Buchalla, M. Neubert and C. T. Sachrajda, Phys. Rev. Lett. **83** (1999) 1914; Nucl. Phys. B **591** (2000) 313; hep-ph/0007256.

[23] G. Lüders, Dan. Mat. Phys. Medd. **28** (1954) 5; W. Pauli in *Niels Bohr and the Development of Physics*, ed. W. Pauli, L. Rosenfeld and V. Weisskopf (McGraw-Hill, New York, 1955); G. Lüders, Ann. Phys. **2** (1957).

[24] V. A. Kostelecky and S. Samuel, Phys. Rev. Lett. **63** (1989) 224; **66** (1991) 1811; Phys. Rev. D **39** (1989) 683; **40** (1989) 1886. V. A. Kostelecky and R. Potting, Nucl. Phys. B **359** (1991) 545; Phys. Lett. B **381** (1996) 89; J. Ellis, J. L. Lopez, N. E. Mavromatos and D. V. Nanopoulos, Phys. Rev. D **53** (1996) 3846.

[25] V.F. Weisskopf and E.P. Wigner, Z. Phys. **63** (1930) 54; **65** (1930) 18; T. D. Lee, R. Oehme and C. N. Yang, Phys. Rev. **106** (1957) 340.

[26] L.A. Khalfin, Zh. Eksp. Teor. Fiz. **33** (1957) 1371.

[27] Y. I. Azimov, Phys. Atom. Nucl. **59** (1996) 856, and references therein.

[28] A. Angelopoulos *et al.*, CPLEAR Collaboration, Phys. Lett. B **444** (1998) 43.

[29] R. Aleksan, I. Dunietz and B. Kayser, Z. Phys. C **54** (1992) 653.

[30] L. Wolfenstein, Phys. Rev. Lett. **13** (1964) 562.

[31] J. H. Christenson, J. W. Cronin, V. L. Fitch and R. Turlay, Phys. Rev. Lett. **13** (1964) 138. Phys. Rev. **140** (1965) B74.

[32] K. G. Wilson, Phys. Rev. **179** (1969) 1499.

[33] A. J. Buras, M. Misiak and J. Urban, Nucl. Phys. B **586** (2000) 397.

[34] G. Altarelli, G. Curci, G. Martinelli and S. Petrarca, Nucl. Phys. B **187** (1981) 461; A. J. Buras and P. H. Weisz, Nucl. Phys. B **333** (1990) 66; A. J. Buras, M. Jamin, M. E. Lautenbacher and P. H. Weisz, Nucl. Phys. B **370** (1992) 69, Addendum **375** (1992) 501; Nucl. Phys. B **400** (1993) 37.

[35] G. Buchalla, A. J. Buras and M. E. Lautenbacher, Rev. Mod. Phys. **68** (1996) 1125.

[36] M. Ciuchini, E. Franco, G. Martinelli, L. Reina and L. Silvestrini, Phys. Lett. B **316** (1993) 127; M. Ciuchini, E. Franco, G. Martinelli, L. Reina and L. Silvestrini, Phys. Lett. B **334** (1994) 137; M. Ciuchini, E. Franco, L. Reina and L. Silvestrini, Nucl. Phys. B **421** (1994) 41.

[37] K. Chetyrkin, M. Misiak and M. Münz, Phys. Lett. B **400** (1997) 206.

[38] T. Inami and C. S. Lim, Progr. Theor. Phys. **65** (1981) 297, **65** (1981) 1772(E).

[39] A. J. Buras, M. Jamin and P. H. Weisz, Nucl. Phys. B **347** (1990) 491.

[40] N. Isgur and M. B. Wise, Phys. Lett. B **232**, 113 (1989); **237**, 527 (1990).

[41] E. V. Shuryak, Phys. Lett. **93B** (1980) 134; Nucl. Phys. B **198** (1982) 83.

[42] S. Nussinov and W. Wetzel, Phys. Rev. D **36** (1987) 130.

[43] M. B. Voloshin and M. A. Shifman, Sov. J. Nucl. Phys. **45** (1987) 292 [Yad. Fiz. **45** (1987) 463]; **47** (1988) 511 [**47** (1988) 801].

[44] H. D. Politzer and M. B. Wise, Phys. Lett. B **206** (1988) 681; **208** (1988) 504.

[45] E. Eichten and B. Hill, Phys. Lett. B **234** (1990) 511; **243** (1990) 427.

[46] B. Grinstein, Nucl. Phys. B **339** (1990) 253.

[47] H. Georgi, Phys. Lett. B **240** (1990) 447.

[48] A. F. Falk, B. Grinstein and M. E. Luke, Nucl. Phys. B **357** (1991) 185.

[49] A. F. Falk, H. Georgi, B. Grinstein and M. B. Wise, Nucl. Phys. B **343** (1990) 1.

[50] J.D. Bjorken, *Proceedings of the 18th SLAC Summer Institute on Particle Physics*, Stanford, California, July 1990, edited by J.F. Hawthorne (SLAC, Stanford, 1991).

[51] M. E. Luke, Phys. Lett. B **252** (1990) 447.

[52] J. Charles, A. Le Yaouanc, L. Oliver, O. Pene and J. C. Raynal, Phys. Rev. D **60** (1999) 014001.

[53] M. B. Voloshin and M. A. Shifman, Sov. J. Nucl. Phys. **41** (1985) 120; J. Chay, H. Georgi and B. Grinstein, Phys. Lett. B **247** (1990) 399.

[54] I. I. Bigi, N. G. Uraltsev and A. I. Vainshtein, Phys. Lett. B **293** (1992) 430, **297** (1993) 477(E); I. I. Bigi, M. Shifman, N. G. Uraltsev and A. Vainshtein, Phys. Rev. Lett. **71** (1993) 496.

[55] A. V. Manohar and M. B. Wise, Phys. Rev. D **49** (1994) 1310; B. Blok, L. Koyrakh, M. Shifman and A. I. Vainshtein, *ibid.* **49** (1994) 3356, **50** (1994) 3572(E); T. Mannel, Nucl. Phys. B **413** (1994) 396.

[56] E. C. Poggio, H. R. Quinn and S. Weinberg, Phys. Rev. D **13** (1976) 1958.

[57] A. F. Falk, M. B. Wise and I. Dunietz, Phys. Rev. D **51** (1995) 1183.

[58] M. Gremm, A. Kapustin, Z. Ligeti and M. B. Wise, Phys. Rev. Lett. **77** (1996) 20; A. F. Falk, M. E. Luke and M. J. Savage, Phys. Rev. D **53** (1996) 6316; Z. Ligeti, M. E. Luke, A. V. Manohar and M. B. Wise, Phys. Rev. D **60** (1999) 034019.

[59] M. Crisafulli, V. Giménez, G. Martinelli and C. T. Sachrajda, Nucl. Phys. B **457** (1995) 594; V. Giménez, G. Martinelli and C. T. Sachrajda, *ibid.* **486** (1997) 227; Phys. Lett. B **393** (1997) 124; A. S. Kronfeld and J. N. Simone, Phys. Lett. B **490** (2000) 228, **495** (2000) 441(E).

[60] K. G. Wilson, Phys. Rev. D **10** (1974) 2445.

[61] J. B. Kogut, Rev. Mod. Phys. **55** (1983) 775.

[62] M. Di Pierro, "From Monte Carlo integration to lattice quantum chromodynamics: An introduction," hep-lat/0009001 [FERMILAB-FN-699].

[63] A. X. El-Khadra, G. Hockney, A. S. Kronfeld and P. B. Mackenzie, Phys. Rev. Lett. **69** (1992) 729.

[64] P. B. Mackenzie, Nucl. Phys. B Proc. Suppl. **34** (1994) 400; C. T. H. Davies *et al.*, Phys. Rev. Lett. **73** (1994) 2654 [hep-lat/9404012]; B. J. Gough *et al.*, *ibid.* **79** (1997) 1622 [hep-ph/9610223].

[65] J. Sexton and D. Weingarten, Phys. Rev. D **55** (1997) 4025.

[66] A. Ali Khan *et al.*, CP-PACS Collaboration, Nucl. Phys. B Proc. Suppl. **83** (2000) 265, 331 [hep-lat/9911039, hep-lat/9909052]; Phys. Rev. D **64** (2001) 034505 [hep-lat/0010009].

[67] C. Bernard *et al.*, MILC Collaboration, Nucl. Phys. B Proc. Suppl. **83** (2000) 289 [hep-lat/9909121]; **94** (2001) 346 [hep-lat/0011029].

[68] M. Lüscher, Commun. Math. Phys. **104** (1986) 177; **105** (1986) 153.

[69] J. Gasser and H. Leutwyler, Ann. Phys. **158** (1984) 142.

[70] S. Sharpe and N. Shoresh, Phys. Rev. D **62** (2000) 094503 [hep-lat/0006017].

[71] K. G. Wilson, in *New Phenomena in Subnuclear Physics*, edited by A. Zichichi (Plenum, New York, 1977).

[72] K. Symanzik, in *Recent Developments in Gauge Theories*, ed. G. 't Hooft *et al.* (Plenum, New York, 1980); in *Mathematical Problems in Theoretical Physics*, edited by R. Schrader *et al.* (Springer, New York, 1982); Nucl. Phys. B **226**, 187, 205 (1983).

[73] B. Sheikholeslami and R. Wohlert, Nucl. Phys. B **259** (1985) 572.

[74] K. Jansen *et al.*, Phys. Lett. B **372** (1996) 275 [hep-lat/9512009]; M. Lüscher, S. Sint, R. Sommer, P. Weisz and U. Wolff, Nucl. Phys. B **491** (1997) 323 [hep-lat/9609035].

[75] E. Eichten, Nucl. Phys. B Proc. Suppl. **4** (1987) 170; E. Eichten and B. Hill, Phys. Lett. B **234** (1990) 511.

[76] G. P. Lepage and B. A. Thacker, Nucl. Phys. B Proc. Suppl. **4** (1987) 199; B. A. Thacker and G. P. Lepage, Phys. Rev. D **43** (1991) 196.

[77] A. X. El-Khadra, A. S. Kronfeld, and P. B. Mackenzie, Phys. Rev. D **55** (1997) 3933 [hep-lat/9604004].

[78] T. R. Klassen, Nucl. Phys. B **509** (1998) 391; Nucl. Phys. B Proc. Suppl. **73** (1999) 918.

[79] S. Collins, *et al.*, Phys. Rev. D **64** (2001) 055002 [hep-lat/0101019].

[80] A. S. Kronfeld, Phys. Rev. D **62** (2000) 014505 [hep-lat/0002008].

[81] J. Harada, A. S. Kronfeld, H. Matsufuru, N. Nakajima and T. Onogi, Phys. Rev. D **64** (2001) 074501 [hep-lat/0103026].

[82] G. Martinelli and C. T. Sachrajda, Nucl. Phys. B **559** (1999) 429 [hep-lat/9812001]; V. Giménez, L. Giusti, G. Martinelli and F. Rapuano, JHEP **0003** (2000) 018 [hep-lat/0002007].

[83] S. Hashimoto, Nucl. Phys. B Proc. Suppl. **83** (2000) 3 [hep-lat/9909136]; C. Bernard, *ibid.* **94** (2001) 159 [hep-lat/0011064].

[84] L. Maiani and M. Testa, Phys. Lett. B **245** (1990) 585.

[85] M. Lüscher, Nucl. Phys. B **354** (1991) 531.

[86] L. Lellouch and M. Lüscher, Commun. Math. Phys. **219** (2001) 31. See also Sec. 7 of L. Lellouch, Nucl. Phys. B Proc. Suppl. **94** (2001) 142 [hep-lat/0011088], for a simple summary.

[87] K. M. Watson, Phys. Rev. **88** (1952) 1163.

[88] A. Alavi-Harati *et al.*, KTeV Collaboration, Phys. Rev. Lett. 83 (1999) 22; J. Graham, KTeV Collaboration, Fermilab Seminar, `http://kpasa.fnal.gov:8080/public/epsprime/ktev2001.ps.gz`, 8 June 2001.

[89] I. Augustin *et al.*, NA48 Collaboration, Phys. Lett. B **465** (1999) 335; G. Unal, NA48 Collaboration, CERN seminar, 10 May 2001. `http://na48.web.cern.ch/NA48/Welcome/images/talks/cern_seminar01/talk.ps.gz`

[90] A. J. Buras, M. Jamin and P. H. Weisz, Nucl. Phys. B **347** (1990) 491; S. Herrlich and U. Nierste, Nucl. Phys. B **419** (1994) 292; Phys. Rev. D **52** (1995) 6505; Nucl. Phys. B **476** (1996) 27.

[91] M. Ciuchini, E. Franco, G. Martinelli and L. Reina, Phys. Lett. B **301** (1993) 263; A. Buras, M. Jamin and M. E. Lautenbacher, Nucl. Phys. B **408** (1993) 209; S. Bertolini, J. O. Eeg, M. Fabbrichesi and E. I. Lashin, Nucl. Phys. B **514** (1998) 93.

[92] U. Nierste, in *Proceedings of the Workshop on K Physics*, ed. L. Iconomidou-Fayard (Editions Frontières, Gif-Sur-Yvette, 1997), [hep-ph/9609310]; hep-ph/9510383.

[93] Y. Keum, U. Nierste and A. I. Sanda, Phys. Lett. B **457** (1999) 157; E. Pallante and A. Pich, Phys. Rev. Lett. **84** (2000) 2568; A. J. Buras, M. Ciuchini, E. Franco, G. Isidori, G. Martinelli and L. Silvestrini, Phys. Lett. B **480** (2000) 80;

[94] A. J. Buras and L. Silvestrini, Nucl. Phys. B **546** (1999) 299; A. Masiero and H. Murayama, Phys. Rev. Lett. **83** (1999) 907; A. J. Buras, G. Colangelo, G. Isidori, A. Romanino and L. Silvestrini, Nucl. Phys. B **566** (2000) 3;

[95] A. J. Buras, hep-ph/9908395; U. Nierste, Nucl. Phys. Proc. Suppl. **86** (2000) 329; M. Jamin, hep-ph/9911390; S. Bertolini, hep-ph/0002114; M. Ciuchini and G. Martinelli, hep-ph/0006056.

[96] S. Adler *et al.*, E787 Collaboration, hep-ex/0111091; Phys. Rev. Lett. **84** (2000) 3768.

[97] G. Buchalla and A. J. Buras, Nucl. Phys. B **400** (1993) 225; Nucl. Phys. B **412** (1994) 106.

[98] G. Buchalla and A. J. Buras, Phys. Lett. B **333** (1994) 221, Ref. [18]; Y. Grossman and Y. Nir, Phys. Lett. B **398** (1997) 163; Y. Nir and M. P. Worah, Phys. Lett. B **423** (1998) 319; A. J. Buras, A. Romanino and L. Silvestrini, Nucl. Phys. B **520** (1998) 3.

[99] A. Höcker, H. Lacker, S. Laplace and F. Le Diberder, Eur. Phys. J. C21 (2001) 225; and updates at `http://www.slac.stanford.edu/~laplace/ckmfitter.html`.

[100] C.W. Bauer, Z. Ligeti and M. Luke, Phys. Rev. D **64** (2001) 113004; Phys. Lett. B **479** (2000) 395. A.K. Leibovich, I. Low and I.Z. Rothstein, Phys. Lett. B **486** (2000) 86.

Chapter 2

Common Experimental Issues

R. Kutschke, M. Paulini

2.1 Introduction

This chapter will discuss the experimental issues which underlie B physics at CDF, DØ and BTeV. Many of these issues also apply to charm physics, which will also be discussed. The chapter will be painted in fairly broad strokes and the reader is referred to the subsequent chapters and to the experiments' own Technical Design Reports (TDR) [1] [2] [3] [4] for more details on specific experiments.

During Run II, the Fermilab Tevatron will collide counter-rotating proton p and anti-proton $\bar{p}$ beams at a center-of-mass energy of 2 TeV. Some other design parameters of the Tevatron for Run II are summarized in Table 2.1. In rough terms there are three processes which take place at this energy and which are important to the design of a B physics experiment. These are the production of $b\bar{b}$ pairs, the production of $c\bar{c}$ pairs and all of the light quark and gluon processes which contribute to the background; the cross-sections for these processes are summarized in Table 2.2. There are no known processes which produce a single b or a single $\bar{b}$ at a significant rate, only processes which produce pairs. Despite this, one usually talks about b production, not $b\bar{b}$ production. Similarly, there are important sources of $c\bar{c}$ production but not of single c or $\bar{c}$ production. The theory behind the production of heavy quark pairs in $p\bar{p}$ collisions is discussed in chapter 9. There are, of course, many other interesting processes which occur, including top quark production, Higgs boson production and perhaps even the production of supersymmetric particles. The cross-sections for these processes, however, are small enough that they do not have any impact on how one designs a B physics experiment for the Tevatron.

After a $b\bar{b}$ pair is produced, it hadronizes to form pairs of b hadrons including B mesons, such as B_d, B_u, B_s, B_c, and b baryons such as Λ_b, Ξ_b, Ω_b, Ξ_{bc}, Ω_{cc} etc. All of these states decay weakly, with a significant lifetime and, therefore, with a significant decay length. Excited states of these b hadrons are also produced, all of which decay strongly or electromagnetically to one of the weakly decaying b hadrons. A similar picture exists for the hadronization of $c\bar{c}$ pairs into hadrons. Therefore the route to all of b and c physics goes through the weakly decaying states.

One shorthand which will be used in the following is,

$$\sigma_{BG} = \sigma_{tot} - \sigma_{c\bar{c}} - \sigma_{b\bar{b}}. \tag{2.1}$$

Quantity	Value
Center of Mass Energy	2 TeV
Peak Instantaneous Luminosity	2×10^{32} cm^{-2} s^{-1}
Yearly Integrated Luminosity	2 fb^{-1}/year
Time between bunch crossings	396 ns for $\simeq$ 2 years
	132 ns afterwards
Luminous region	$(\sigma_x, \sigma_y, \sigma_z) = (0.003, 0.003, 30.)$ cm

Table 2.1: Tevatron parameters for Run II. The conversion from peak instantaneous luminosity to yearly integrated luminosity assumes that a year consists of 10^7 useful seconds, as discussed in Section 2.5.

Quantity	Value (mb)	Comment
σ_{tot}	≈ 75	Total hadronic cross-section including elastic, diffractive and inelastic processes.
$\sigma_{c\bar{c}}$	≈ 1	Charm pair production cross-section.
$\sigma_{b\bar{b}}$	≈ 0.1	Beauty pair production cross-section.
σ_{BG}	≈ 75	The chapter's short-hand for $\sigma_{tot} - \sigma_{c\bar{c}} - \sigma_{b\bar{b}}$.

Table 2.2: Approximate values of the cross-sections which are of interest to a B physics experiment using $p\bar{p}$ collisions at a center-of-mass energy of 2 TeV. The estimate for the total cross-section is from Ref. [5]. The estimate of $\sigma_{b\bar{b}}$ is discussed in Section 2.4.

This stands for the "background" cross-section; that is for the total hadronic cross-section with the $c\bar{c}$ and $b\bar{b}$ pieces excluded. The $c\bar{c}$ piece is treated separately because it is interesting to study in its own right and because it has a few critical properties which are more like b's than background. At our current level of precision, $\sigma_{BG} \simeq \sigma_{tot} \simeq 75$ mb [5]. This includes elastic $p\bar{p}$ scattering, diffractive scattering and inelastic scattering. Because $\sigma_{BG} \simeq \sigma_{tot}$ many authors are are careless about distinguishing between the two.

Throughout this chapter, the z axis is defined to lie along the beam direction and quantities such as p_T are measured with respect to this axis. The variable φ is the azimuth around the z axis and θ is the polar angle relative to the z axis.

2.2 Separating b and c Hadrons from the Backgrounds

Inspection of Table 2.2 shows that the cross-section for b production is about 1.5 parts in 1000 of the total cross-section. Moreover, many of the B physics processes of interest have

product branching fractions of 10^{-6} or smaller.[1] Therefore one is often looking for signals of a few parts per billion of the total cross-section!

The signature which allows one to see this needle in a haystack is the lifetime of the b quark. The B_d, B_u and B_s mesons each have a lifetime τ of approximately 1.5 ps, or $c\tau = 450$ μm. When the momentum spectrum of the B mesons is folded in, the mean decay length of all produced B mesons is on the order of a few mm. Therefore almost all B mesons decay inside the beam pipe. The resolution on the decay length varies from one decay mode to another and from one experiment to another but typical values fall in the range of 50 μm to 100 μm; therefore the B decay vertices will be well resolved and will be readily separated from the $p\bar{p}$ interaction vertex. The B_c, the weakly decaying b baryons and the weakly decaying charmed hadrons have somewhat shorter lifetimes [6], but most of them have a long enough lifetime that their decay vertices too will also be well separated from $p\bar{p}$ interaction vertex.

The myriad background processes, with their much larger cross-sections, do not produce particles which have this type of decay length signature. This brings us to the magic bullet: it is the presence of distinct secondary vertices which allows the experiments to extract the b and c signals from the background.

About 85% of all weakly decaying b hadrons decay into one charmed hadron plus long lived particles. Long lived particles include pions, kaons, protons, photons, charged leptons and neutrinos, all of which are stable enough to escape the interaction region and leave tracks in the detector. Some of these particles, such as the K^0_S and Λ do decay but their lifetimes are very long compared to the those of the b and c hadrons.[2] About 15% of weakly decaying b hadrons decay into 2 charmed hadrons, plus long lived particles; the decay $B^0 \to D^{*+}D^{*-}$ is an example. And about 1% of all weakly decaying b hadrons decay into only long lived particles; the decay $B^0 \to \pi^+\pi^-$ is an example. Therefore a typical $b\bar{b}$ event has 5 distinct vertices, all inside the beam pipe: the primary $p\bar{p}$ interaction vertex, the two secondary B decay vertices and the two tertiary c decay vertices. On the other hand, many of the most interesting decays involve charmless decays of the b and a typical event containing one of these these decays has 4 vertices inside the beam pipe: the primary $p\bar{p}$ vertex, the vertex from the signal charmless b, and the b and c vertices from the other b (or $\bar{b}$) produced in the $p\bar{p}$ interaction.

To be complete, one more detail must be added to the description of typical $b\bar{b}$ events. For the running conditions anticipated for Run II, each beam crossing which contains a $b\bar{b}$ interaction will also contain several background interactions which contain no $b\bar{b}$ or $c\bar{c}$ pairs. This is discussed in more detail in Section 2.5.1. Fig. 2.1 shows a cartoon of a $b\bar{b}$ event with one charmless b decay. Throughout this chapter the word "event" should be understood to include all of the interactions within one beam crossing, both the signal and background interactions.

[1] The product branching fraction is defined as the product of all of the branching fractions in a decay chain. An example of such a decay chain is $B_d \to J/\psi K^0$, $J/\psi \to \mu^+\mu^-$, $K^0 \to K^0_S$, $K^0_S \to \pi^+\pi^-$. The branching fraction for the first decay is about 1×10^{-3}, but the product of all branching fractions in the chain is much smaller, about 2×10^{-5}.

[2] The one exception is the τ lepton but the branching ratio of $b \to c\tau\nu$ is small, $(2.6 \pm 0.4)\%$ [6].

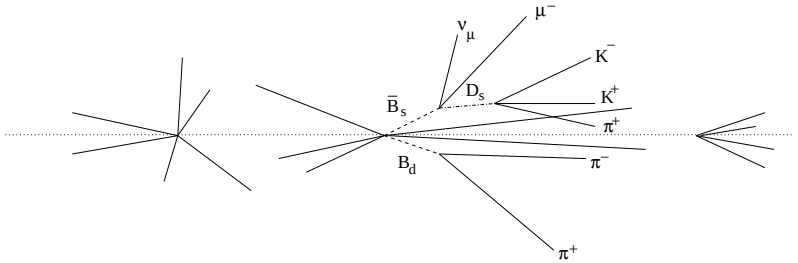

Figure 2.1: A cartoon of an interesting $b\bar{b}$ event at the Tevatron. In this beam-crossing the bunches undergo three independent primary interactions. The one in the middle produces a $b\bar{b}$ pair plus some other hadrons while the ones to either side are background interactions. In this event, one b undergoes a charmless decay while the other decays semileptonically to charm, which decays hadronically to light hadrons. The cartoon is meant to emphasize the topological properties of an event: it is not to scale and does not correctly represent the number of tracks in a vertex or the distribution of track directions.

Similarly, a typical $c\bar{c}$ interaction has three distinct vertices inside the beam pipe: the primary vertex plus two secondary vertices, which come from the decay of the two charmed hadrons. A typical beam crossing which contains a $c\bar{c}$ interaction will also contain a few background interactions.

In an event containing a $b\bar{b}$ or a $c\bar{c}$ pair, the stable daughters of the b and c hadrons usually have a large impact parameter with respect to the primary vertex. Because the beam spot is very narrow, roughly 30 μm in diameter, these tracks will also have a large $r\varphi$ impact parameter with respect to the beam line. A track is said to be detached if the impact parameter, divided by its error, is large; this definition is used both for 2D and 3D impact parameters.

While the reconstruction of the full vertex topology of an event is a very powerful tool to reduce backgrounds, it is often too inefficient or too slow to be useful. In particular present computing technologies are too slow to allow full exploitation of the topology at trigger time. However a powerful trigger can be made by looking for the presence of a few detached tracks. All of CDF, DØ and BTeV have design triggers which make some sort of detachment requirement, with the sophistication of that requirement changing from one experiment to the next. BTeV exploits detachment at all trigger levels, including level 1, while the other experiments introduce detachment cuts only at higher levels. The reader is referred to chapters 3 to 5 for further details about the triggers of each experiment.

In addition to detachment, there are other properties which can be used to identify events which contain b quarks. For example, selecting events with one or two leptons of moderate to high p_T is an excellent way to select events containing $b\bar{b}$ pairs while rejecting background events. CDF and DØ have successfully used single lepton and di-lepton triggers, without any detachment requirement, to select events for their Run I B physics program. All of the Run II detectors plan some sort of lepton triggers, including single high p_T leptons, di-leptons and $\psi \to \mu^+\mu^-$ triggers. The experiments envisage some, but not all, of these

triggers also to include detachment information. For example, when evidence of detachment is present, one can lower p_T thresholds and still have an acceptable background suppression. But when detachment information is ignored, or unavailable, the triggers require higher p_T thresholds. Those triggers which do not include detachment information will provide a useful sample for calibrating the detachment based triggers.

One of the limitations of Run I was that the experiments could only trigger on b events with leptons in the final state. For Run II and beyond, both CDF and BTeV have triggers which rely only on detachment and which are capable of triggering all hadronic final states. The development of triggers which rely only on detachment is one of the major advances since Run I.

Because of their topological similarities to $b\bar{b}$ events, some $c\bar{c}$ events will also pass these triggers. Charm events, however, have properties which are intermediate to the b events and the background events: their decay lengths are shorter, their impact parameters smaller and their stable daughters have both a softer momentum spectrum and a softer p_T spectrum. Therefore the cuts which reduce the background to an acceptable level are much less efficient for $c\bar{c}$ events than they are for $b\bar{b}$ events. The CDF and DØ experiments do not expect that significant $c\bar{c}$ samples will pass their trigger and have not discussed a charm physics program. They can, of course, do some charm physics with the charm which is produced via B decay. BTeV, on the other hand, expects that a significant fraction of the events which pass their trigger, will contain $c\bar{c}$ events and they plan a charm physics program to exploit that data.

In summary, the long lifetimes of the weakly decaying b and c hadrons are the magic bullet which allow the b and c physics to be extracted from the background. At trigger time minimal cuts will be made on detachment and the offline analyses will make more complete use of the topological information. Various lepton based triggers, some with detachment requirements and some without, will form a second set of triggers.

2.3 Sources of Backgrounds

The most pernicious backgrounds are those which peak in the signal region and which can fake signals. One example of this is a true $B^0 \to K^+\pi^-$ being misreconstructed as a $B^0 \to \pi^+\pi^-$ decay; this results in a peak which is almost at the correct mass, with almost the correct width. This sort of problem is very mode specific and will be discussed, as needed, in the working group chapters.

A second class of backgrounds is combinatoric background within true $b\bar{b}$ and $c\bar{c}$ events, events which have the correct topological properties to pass the trigger. Suppose that one is looking for the decay, $B^0 \to D^-\pi^+$ followed by $D^- \to K^+\pi^-\pi^-$. All $b\bar{b}$ and $c\bar{c}$ events which produce a reconstructed $D^- \to K^+\pi^-\pi^-$ candidate have potential to produce background. If another track, perhaps from the main vertex, forms a good vertex with the D^- candidate this will be considered, incorrectly, as a B candidate. This sort of background will not peak near the B mass but it will produce background entries throughout the $D^-\pi^+$ mass plot, thereby diluting the signal. This sort of background can be reduced by

demanding that tracks which participate in a B candidate be inconsistent with the primary vertex. In addition, improved vertexing precision will reduce the number of random $D^-\pi^+$ combinations which form a vertex with an acceptable χ^2.

There are many other background sources of secondary vertices and detached tracks: strange particles, interactions of particles with the detector material, misreconstructed tracks, multiple interactions per beam crossing, and mis-reconstructed vertices. While none of these backgrounds can create fake mass peaks at the B mass, they can dilute signals and they can overwhelm a poorly designed trigger.

At first thought one might summarily dismiss the strange hadrons as a source of background. After all, they typically have lifetimes 100 to 1000 times longer than those of the b hadrons; so only a small fraction will decay inside the beam pipe with a decay length typical of that for B decay. However they are produced about a few thousand times more frequently, a few per background interaction. Moreover the most probable decay time of an exponential distribution is zero, so some of the strange hadrons will have decay lengths of a few mm. There is a powerful countermeasure against most of the strange particle background: the trigger must ignore tracks with an impact parameter which is too large. One might worry that the contradictory requirements of a large detachment but a small impact parameter might leave no window to accept the physics. The answer is clear if one recalls the definition of detachment, an impact parameter divided by its error: make the error small. In practice the detectors have sufficiently good resolution that this background is reduced to acceptable level.

The strange hadrons have masses much less than the those of the b hadrons; therefore, an isolated decay of a strange particle is unlikely to be confused for a b decay. If however, another track, or tracks, pass close enough to the strange particle decay vertex that the reconstruction code incorrectly assigns that track to that strange particle's decay vertex, the combination can contribute combinatorial background beneath a B signal. This sort of background can be reduced by building a vertex detector with sufficiently high precision.

Another source of background comes from the interaction of the tracks with the detector and support materials. Photons can pair convert and hadrons can undergo inelastic collisions. There may be several of these secondary interactions for each primary $p\bar{p}$ interaction. Again, this sort of background can be suppressed, at the trigger level, by excluding tracks with too much detachment. And, in the offline analysis, one can exclude vertices which occur in the detector material. Having excellent resolution on vertex position is again the secret to background reduction.

Other sorts of interaction with the detector material includes Rutherford scattering and the tails of multiple Coulomb scattering. At the trigger level, the way to deal with these tracks is to make sure that the detachment cuts are large enough. At the offline reconstruction level, these tracks can often be rejected by cutting on the confidence level of the track fit.

Mis-reconstructed tracks are tracks which have incorrect hit assignments. The most direct way to deal with this problem is to ensure a sufficiently small occupancy in the detectors. For example, the upper limit for the long dimension of the BTeV pixels is set by such a study — if the pixels are too long then the two track separation degrades and

errors in pattern recognition result. This, in turn, creates false detached tracks. In the offline analysis, one can also reject mis-reconstructed tracks on the basis of a bad track fit confidence level.

Multiple interactions in one beam crossing are another source of background. Consider the case that two background interactions occur in the same beam crossing. In this case there are two chances that a background interaction might trigger the detector. But there is the additional complication that the trigger might fire based on some information from one vertex and some information from the other vertex. This last problem can be reduced by doing 3D vertexing in the trigger.

At the Tevatron the luminous region has a length of $\sigma_z \approx 30$ cm so it is reasonable to expect the triggers to behave acceptably with a few background interactions per beam crossing; most of the time the interactions will be well separated. When testing trigger algorithms it is important to measure how the trigger degrades with an increasing number of interactions per crossing. The trigger performance should degrade smoothly, without sudden drops.

The last background class is misreconstructed vertices, which includes both errors made when all of the tracks are well measured but also errors made when one of the tracks suffers from one of the diseases mentioned above. The solution is to ensure sufficient tracking precision that fake track rates are small and sufficient vertex precision that the rates for accidental vertices are small.

The above discussion has presented a number of factors which bound the detachment required at the trigger level from below and which bound impact parameter cuts from above. Using detailed simulations of their detector response, the experiments have shown that their proposed triggers will reduce these backgrounds to an acceptable level and that their detectors have enough rejection power to obtain an acceptable signal-to-background ratio during offline analysis. The common thread running through the discussion is that improved vertex resolution reduces every one of these backgrounds.

2.4 Basics of b Production Physics

At a $p\bar{p}$ collider, it is usually most convenient to describe particle production in terms of three variables, p_T, y and φ, where p_T is the transverse momentum of the particle with respect to the beam line, φ is the azimuth around the beam line and where the rapidity, y, is a measure of the polar angle, θ, relative to the beam line,

$$y = \frac{1}{2} \ln \left(\frac{E + P_\parallel}{E - P_\parallel} \right) . \tag{2.2}$$

For historical reasons people sometimes work in units of pseudo-rapidity, η, instead of y,

$$\eta = -\ln (\tan \theta/2) . \tag{2.3}$$

For massless particles $\eta = y$ and for highly relativistic particles η approaches y. The utility of the variable η can be seen in Fig. 2.2, which shows the prediction of the PYTHIA Monte

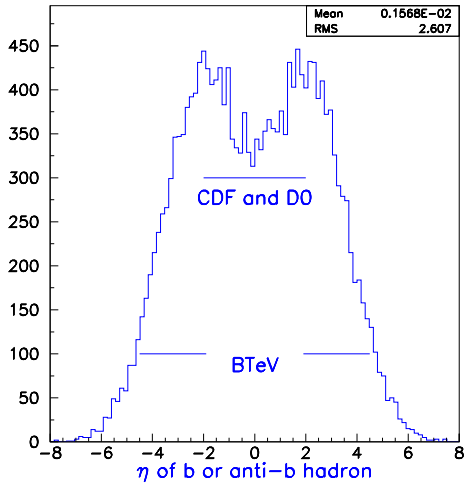

Figure 2.2: The production cross-section of B mesons vs η. The plot is from the PYTHIA event generator and does not contain detector effects. The horizontal lines show the regions of η which are covered by the three detectors. CDF and DØ do not cover all regions of η with equally quality; the barrel region, in which they make their best measurements covers approximately $|\eta| < 1.0$.

Carlo event generator for the production of b flavored hadrons as a function of η. The production is approximately flat in the central η region, falling off at large $|\eta|$, a general feature of particle production in hadronic collisions. The figure also shows the regions of η which are covered by the three detectors.

During Run I, both CDF and DØ studied the production of b quarks in $p\bar{p}$ collisions at a center-of-mass energy of 1.8 TeV. Both CDF and DØ have studied the central rapidity region $|\eta| < 1$ and DØ has also studied the forward region, $2.4 < y < 3.2$. The data of DØ are shown in Fig. 2.3. Both CDF and DØ find that the $b\bar{b}$ production cross-section in the central region is underestimated by the Mangano, Nason and Ridolfi (MNR) next-to-leading order QCD calculation [7] by a factor of more than two. The DØ data in the higher y^μ region is 3.6 ± 0.8 times higher than the QCD calculation.

When predicting their sensitivities for physics at Run II, CDF and DØ normalize their predictions to the cross-sections which they measured in Run I. Not only does BTeV not have previous data, there are no experimental data at all over much of the range of the BTeV acceptance, $1.9 \leq |\eta| \leq 4.5$. Instead BTeV uses the following procedure. When integrated over η and p_T, the QCD predictions shown in Fig. 2.3 predict a total $b\bar{b}$ production cross-section of 50 μb. Since all of the experimental data is more than a factor of two above the theoretical calculations, BTeV estimates the total cross-section to be 100μb. BTeV then uses the predictions of PYTHIA to describe how the cross-section is distributed over p_T, η, φ.

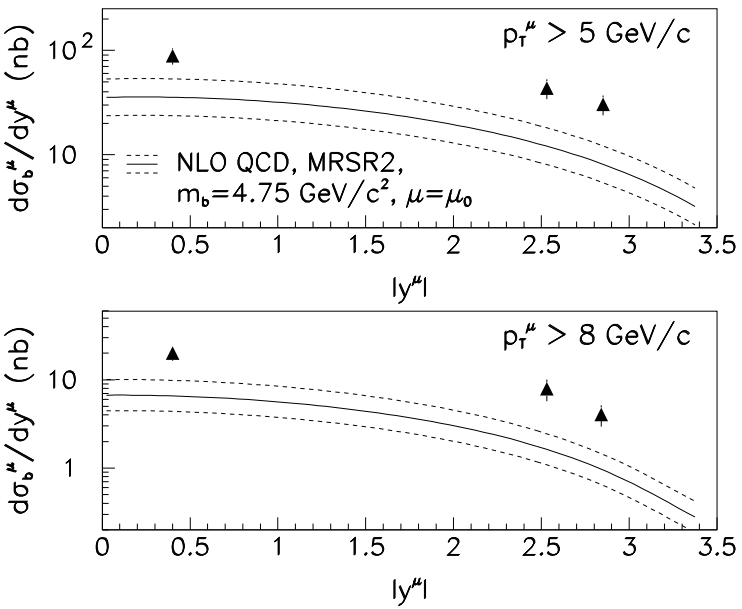

Figure 2.3: The cross-section for muons from b-decay as a function of the rapidity the of muon, y^μ, measured by DØ . The solid curve is the prediction of the next-to-leading order QCD calculation for a b-quark mass of 4.75 GeV. The dashed curves represent the estimated theoretical 1σ error band.

Within regions of phase space covered by CDF and DØ `PYTHIA` has done a good job of describing the most important experimental correlations.

Other properties of $b\bar{b}$ production are illustrated in Fig. 2.4 through 2.6. Fig. 2.4 shows, for B mesons, the prediction of the `PYTHIA` event generator for the cross-section as a function of $\beta\gamma$ vs η. The figure shows that the bulk of the cross-section is concentrated in the central region and that forward going B mesons have a much higher momentum than do B mesons produced in the central region. This implies that in the forward region a greater fraction of the cross-section has long decay lengths, while in the central region there are more events to start with. The implications of this tradeoff will be discussed further in Section 2.8.1.

Fig. 2.5 illustrates another of the the properties of $b\bar{b}$ production, that b hadron and the $\bar{b}$ hadron have an RMS separation of about one unit of η. The figure was made using generator level tracks from the `PYTHIA` event generator and shows the cross-section as a function of the polar angle of one B vs the polar angle of the other B. In a two-arm forward detector, such as BTeV, if one B is produced in a particular arm, then the other B is highly likely to be produced in the same arm. This is important for measurements

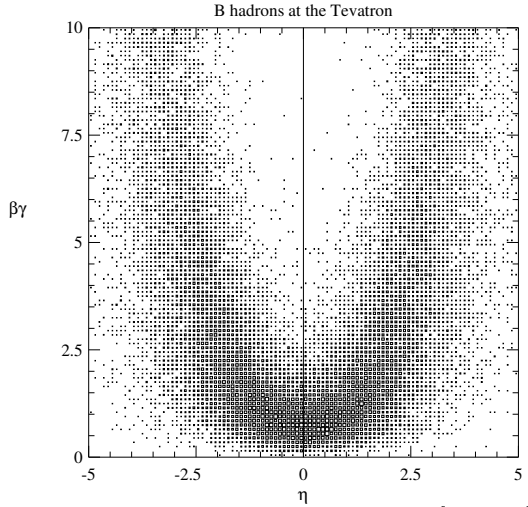

Figure 2.4: The production cross-section for B mesons as a function of $\beta\gamma$ and η plane. The plot is from the `PYTHIA` event generator and does not contain detector effects.

which make use of opposite side tagging (see Section 2.6). The choice of axes for this figure, θ rather than η, exaggerates this effect. Some other consequences of this distribution are discussed in Section 2.8.1.

Fig. 2.6 shows the azimuthal correlation between a b and its $\bar{b}$ partner. The data are for DØ events in which two muons are reconstructed, both consistent with coming from the decay of a b hadron. The horizontal axis is $\delta\varphi$, the difference in azimuth between the two muons. Since the selection criteria imply that the two B's have a significant momentum, the muons tend to follow the B direction. Therefore $\delta\varphi$ is a measure of the difference in azimuth between the two b hadrons in the event. The band shows the prediction of MNR [7]. The b hadrons are preferentially produced back to back in azimuth and the gross shape is reproduced well by the model. It has already been noted that the MNR prediction underestimates the cross-section.

While the production of $b\bar{b}$ pairs is well described by perturbative QCD and knowledge of the structure functions of the proton, the hadronization, or fragmentation, of these quarks into the final state hadrons is described by models. These models are usually realized as computer codes for event generators, the most commonly used being `PYTHIA` [8], `ISAJET` [9] and `HERWIG` [10]. One of the properties which must be input to the event generators is the fraction of time that the b quark fragments into each of the allowed hadrons, B^-, $\bar{B}^0$, $\bar{B}_s$, B_c^- or one of the b baryons. A recent measurement from CDF [11] gives, $f_u : f_d : f_s : f_{\rm baryon}$ = $0.375 \pm 0.023 : 0.375 \pm 0.023 : 0.160 \pm 0.044 : 0.090 \pm 0.029$, with the assumption that $f_u = f_d$. If they release this assumption they obtain, $f_d/f_u = 0.84 \pm 0.16$. It is generally

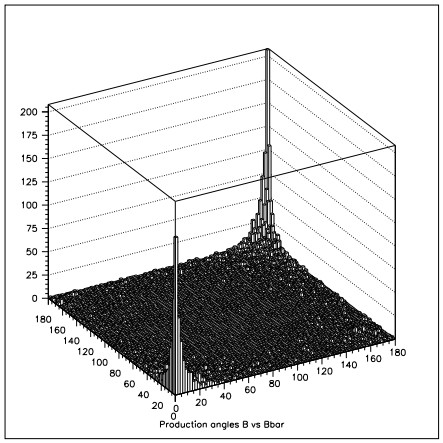

Figure 2.5: The production angle (in degrees) for the hadron containing a b quark plotted versus the production angle for a hadron containing $\bar{b}$ quark. The plot is from the PYTHIA event generator and does not contain detector effects. One must be careful interpreting this plot since the natural axes are η, not θ.

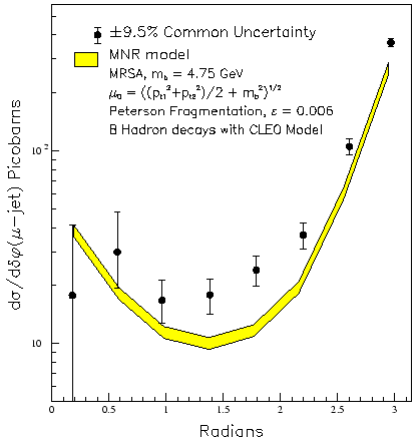

Figure 2.6: The differential $\delta\varphi$ cross-sections for $p_T^{\mu} > 9$ GeV/c, $|\eta^{\mu}| < 0.6$, $E_T^{\bar{b}} > 10$ GeV, $|\eta^{\bar{b}}| < 1.5$ compared with theoretical predictions. The data points have a common systematic uncertainty of ±9.5%. The uncertainty in the theory curve arises from the error on the muonic branching fraction and the uncertainty in the fragmentation model.

1. The mechanisms which produce heavy flavors produce $b\bar{b}$ pairs but not single b or $\bar{b}$ quarks. Similarly for charm production.
2. The cross-section for $b\bar{b}$ production, integrated over all η and p_T, is about 100 μb and that for $c\bar{c}$ production is about 1 mb.
3. The $b\bar{b}$ cross-section is approximately flat in η over the central region, and falls off at large $|\eta|$. See figure 2.2.
4. b hadrons produced in the forward region have a higher momentum than those produced in the central region. See figure 2.4.
5. The pair of b hadrons from one $b\bar{b}$ pair are approximately approximately back to back in φ and have an RMS separation in η of about one unit of η.
6. The production ratio of $B_u : B_d : B_s$:baryons is, $f_u : f_d : f_s : f_{\rm baryon} = 0.375 \pm 0.023 : 0.375 \pm 0.023 : 0.160 \pm 0.044 : 0.090 \pm 0.029$ [11].

Table 2.3: Summary of the important properties of $b\bar{b}$ production.

presumed that, except for threshold effects, the fragmentation process is independent of the production process and is roughly independent of energy. For comparison the same production fractions measured at LEP and SLD are [12], $f_u : f_d : f_s : f_{\rm baryon} = 0.401 \pm 0.010 : 0.401 \pm 0.010 : 0.100 \pm 0.012 : 0.099 \pm 0.017$. In both of these measurements, the production of B_c mesons is too small to be significant. In the standard event generators the choice of hadron species for the b quark is independent of the choice of hadron species for the $\bar{b}$ quark. This cannot be exactly true since there is presumably some production via the $\Upsilon(4S)$ resonance, which decays only to $B^0\overline{B}^0$ or B^+B^-. Moreover the $B^0\overline{B}^0$ production from the $\Upsilon(4S)$ is coherent. While it is likely that these effects do occur, they can be safely ignored for purposes of this workshop. If there is enough resonant production to affect the physics results, the amount of such production can be easily measured with the Run II data.

The major points of this section are summarized in Table 2.3.

2.5 Production Rates and Interactions Per Crossing

The design value for the peak instantaneous luminosity during Run II is 2×10^{32} cm^{-2} s^{-1}. This specifies the luminosity at the start of a fill, when the beam intensities are greatest. As a fill progresses the instantaneous luminosity will drop. Also there will be shutdowns, both planned and unplanned, throughout the running period. The rule of thumb for converting the peak instantaneous luminosity to the yearly integrated luminosity is to assume that a year contains 10^7 seconds of running at the peak instantaneous luminosity. This is about one third of the actual number of seconds in a year, which accounts both for the drop in luminosity as a fill progresses and for a normal amount of down-time. Therefore a peak instantaneous luminosity of 2×10^{32} cm^{-2} s^{-1} corresponds to 2 fb^{-1}/year.

Rate	$b\bar{b}$	$c\bar{c}$	Total
Interactions/s	2×10^4	2×10^5	1.5×10^7
Interactions/year	2×10^{11}	2×10^{12}	1.5×10^{14}
Interactions/crossing @ 396 ns	0.008	0.08	6
Interactions/crossing @ 132 ns	0.003	0.03	2

Table 2.4: Summary of production rates for $b\bar{b}$ pairs, $c\bar{c}$ pairs and total interactions for the design peak luminosity of the Tevatron during Run II, 2×10^{32} cm^{-2} s^{-1} (2 fb$-$1/year). The interactions per bunch crossing are given twice, once for the bunch structure planned for early in Run II, 396 ns between bunch crossings, and once for the bunch structure planned for later in Run II, 132 ns between bunch crossings.

Given $\sigma_{b\bar{b}} = 100$ μb from Table 2.2, the above luminosities imply $b\bar{b}$ yield of 20,000/s or 2×10^{11}/year, about 3 to 4 orders of magnitude larger than the projected yields at the e^+e^- B factories.

Given $\sigma_{tot} = 75$ mb, from Table 2.2, a luminosity of 2×10^{32} cm^{-2} s^{-1} implies a total interaction rate of 1.5×10^7/s. During the first few years of Run II the bunch structure of the Tevatron will be 396 ns between bunch crossings. At the design luminosity this would correspond to about 6 interactions per crossing but it is not expected that the design luminosity will be achieved this early in the run. After the first few years of Run II the bunch structure of the Tevatron will be changed to have 132 ns between bunch crossings. The purpose of this change is to allow an increase in luminosity while reducing the number interactions per beam crossing. At 132 ns between bunches, the design luminosity corresponds to about 2 interactions per bunch crossing.

The above discussion, along with the corresponding numbers for $c\bar{c}$ production, is summarized in Table 2.4.

The presence of multiple background interactions has many consequences for the design of the detector. It was already mentioned that the trigger must be robust against multiple background interactions in one beam crossing. The presence of multiple interactions must also be considered when designing the granularity of detectors to ensure that the occupancy is acceptably low.

2.5.1 The Distribution of Interactions Per Crossing

To a good approximation, if there are multiple interactions in one beam crossing, they are statistically independent of each other. This is not strictly true because, once the first interaction takes place, there are fewer beam particles left to participate in future interactions. However, in the limit that the number of particles per bunch is much larger than the number of interactions per crossing, each interaction can be treated as independent of all others.

Each of these independent interactions has some probability to produce a signal interaction and some probability to produce a background interaction. There are two, equivalent ways of looking at the distribution of signal and background interactions among the multiple interactions in one event. These equivalent ways are related to each other by the following identity. Given two independent Poisson processes, signal and background for example, the probability to observe n_1 interactions from the first process and n_2 interactions from the second process is,

$$\begin{aligned} P(n_1, n_2) &= \frac{(\mu_1)^{n_1}}{n_1!}\, e^{-\mu_1}\, \frac{(\mu_2)^{n_2}}{n_2!}\, e^{-\mu_2} \\ &= \left[\frac{\mu^n}{n!}\, e^{-\mu}\right] \left[f^{n_1}(1-f)^{n-n_1} \frac{n!}{n_1!(n-n_1)!}\right], \end{aligned} \tag{2.4}$$

where $f = \mu_1/\mu$ and $\mu = \mu_1 + \mu_2$. The first factor in [] is the Poisson probability to observe $n = n_1 + n_2$ interactions in total, while the second factor in [] is the binomial probability that the n interactions are split into n_1 from the first process and $n - n_1$ from the second process.

One can also show the general case, that the sum of M independent Poisson processes is itself a Poisson process with a mean $\mu = \mu_1 + \mu_2 + \ldots + \mu_M$. In the general case, the factor multiplying the overall Poisson distribution will be a multinomial distribution, with the $M - 1$ independent parameters, μ_1/μ, μ_2/μ, $\ldots \mu_{M-1}/\mu$.

The two equivalent descriptions are: first, one can say that the total number of interactions within a beam crossing is Poisson distributed with a mean of μ and that within each beam crossing the interactions are distributed among the possible types according to a multinomial distribution. Second, one can say that there are M independent pieces to the cross-section and that each piece contributes to each beam crossing a Poisson distributed number of interactions with mean μ_M.

This second description is less well known but it allows one to more easily answer the following question: describe a typical beam crossing which produces a $b\bar{b}$ pair. For definiteness, consider the numbers summarized in Table 2.4 for the case of 132 ns bunch spacing; $\mu_{b\bar{b}} = 0.003$, $\mu_{c\bar{c}} = 0.03$, and $\mu_{BG} = 2.0$. Clearly most beam crossings will contain no $b\bar{b}$ pairs. An event which contains a typical $b\bar{b}$ pair will contain exactly one such pair and it will be accompanied by a Poisson distributed number of $c\bar{c}$ interactions with a mean of 0.03 interactions per crossing and by a Poisson distributed number of background interactions with a mean of 2.0 interactions per crossing.

2.6 Flavor Tagging

One of the main B physics goals of all three experimental programs is to make precision measurements of mixing mediated CP violating effects, some of which are discussed in chapter 6 of this report. Also, x_s has yet to be measured and that is interesting to measure in its own right. In order to perform any mixing related study it is necessary to know

whether a particular meson was produced as a $B^0(B_s)$ or as a $\bar{B}^0(\bar{B}_s)$. Making such a determination is called flavor tagging the B meson.[3]

Every tagging method sometimes produces the wrong answer and the effectiveness of flavor tagging is characterized by an effective tagging efficiency $\epsilon\, D^2$, where $\epsilon = (N_R + N_W)/N$, $D = (N_R - N_W)/(N_R + N_W)$, N is the number of reconstructed signal events before tagging, N_R the number of right flavor tags, and where N_W is the number of wrong flavor tags. Another useful expression is $D = (1 - 2w)$ where $w = N_W/(N_R + N_W)$ is the fraction of wrong sign tags; from this expression it is clear that the tagging power goes to zero when the wrong sign tag fraction reaches 50%. Maximizing ϵD^2 is critical to the design of every experiment.

The quantity D is known as the dilution. This choice of nomenclature has the anti-intuitive result that a large dilution is good while a small dilution is bad. Never-the-less it is the standard nomenclature.

Tagging algorithms can be broken down into two classes, away side tagging and same side tagging. In away side tagging, or opposite side tagging, one looks at some property of the other b hadron in the event to determine its b quantum number. Since b quarks are produced as $b\bar{b}$ pairs, one can infer the flavor of the signal B meson. In same side tagging one uses the correlations which exist between the signal B meson and the charge of nearby tracks produced either in the fragmentation chain or in the decay of B^{**} resonances. For tagging B^0 mesons the correlation is with a charged pion, while for B_s mesons the correlation is with a charged kaon.

2.6.1 Away Side Tagging

The perfect away side tag would be to fully reconstruct the other b hadron in the event and to discover that it is a B^- or a Λ_b, neither of which undergoes flavor mixing. In this case one knows that the other b hadron contains a b quark and that the signal B meson must have been born with a $\bar{b}$ quark. So the signal B is tagged as being born as a B^0 or as a B_s. In practice the efficiency for reconstructing a complete b hadron on the away side is much too small to be useful. Instead one looks for inclusive properties of b hadrons which are different from those of $\bar{b}$ hadrons. Four such properties have been explored: lepton tagging, kaon tagging, jet charge tagging and vertex charge tagging.

Lepton tagging exploits the sign of the lepton in the decays $b \to X\ell^-$ compared to $\bar{b} \to X\ell^+$, where ℓ is either an electron or a muon. The branching fractions for these decays is roughly 10% into each of the e and μ channels. There is some dilution in this tag from the decay chain $b \to c \to X\ell^+$ compared to $\bar{b} \to \bar{c} \to X\ell^-$. However the two different sources of leptons have different kinematic properties and different vertex topology properties. So good separation between these two sources of leptons can be achieved. Another factor causes

[3] There is another, and very different concept called b tagging. If a lepton is part of a jet, and if the p_T of the lepton with respect to the jet axis is sufficiently large, then that lepton is most probably from the decay of a b quark within the jet. A sample of jets containing such a lepton will be heavily enriched in b jets. This technique was used extensively in Run I to tag samples of b jets which were used in the W boson and top quark physics programs. This technique is mostly of interest for top physics, not for B physics itself.

further dilution. In an ensemble of tags, the away side b hadron will be some mixture of B^+, B^0, B_s and several b baryons. The B^+ and the b baryons do not mix and so the observation of the sign of the lepton is a clear tag. However, 17.4% of the B^0 mesons will oscillate to $\bar{B}^0$ mesons before decaying [6] and will, therefore, give an incorrect tag. The B_s system, which is fully mixed, provides no tagging power at all.

Kaon tagging exploits the charge of the kaon in the away side decay chain, $b \to c \to XK^-$ compared with $\bar{b} \to \bar{c} \to XK^+$. Because of the large product branching fraction this tag has a much higher efficiency than lepton tags but historically has had worse dilution. With the improved vertexing power and particle identification capabilities of the of the Run II detectors one expects significantly improved dilutions. As with lepton tagging, there is tagging dilution from the mixing of the away side B^0 and B_s. It is often noted that a typical B_s decay contains two kaons of opposite strangeness and so contributes no power to kaon tagging. While this is true, one must remember that the B_s system is fully mixed and had no tagging power to start with.

A method called "jet charge tagging" exploits the fact that the sign of the momentum weighted sum of the particle charges of the opposite side b jet is the same as the sign of the charge of the b quark producing this jet. In a simple version, the jet charge $Q_{\rm jet}$ can be calculated as

$$Q_{\rm jet} = \frac{\sum_i q_i \, (\vec{p_i} \cdot \hat{a})}{\sum_i \vec{p_i} \cdot \hat{a}}, \tag{2.5}$$

where q_i and $\vec{p_i}$ are the charge and momentum of track i in the jet and $\hat{a}$ is a unit vector along the jet axis. On average, the sign of the jet charge is the same as the sign of the b quark that produced the jet.

Vertex charge tagging involves reconstructing the full vertex topology of the away side. This does not necessarily constitute full reconstruction of the away side since the away side decay will usually contain π^0's, photons, K^0_S and K^0_L. However these missing particles do not modify the charges of the remnant vertices. If the vertices have been correctly reconstructed, and if the away side secondary vertex has a charge of ± 1, then the flavor of the away side b is known. If the charge of the away side secondary vertex is zero, then there is no tagging power. Also, if the away side tertiary vertex has charge ± 1, one can infer the flavor of the away side b.

2.6.2 Same Side Tagging

Same side tagging exploits charge correlations between the a B^0, or $\bar{B}^0$, and the nearest pion in the fragmentation chain. Fig. 2.7 illustrates the idea behind the method.

One can think of the hadronization, or fragmentation, processes as pulling light quark pairs from the vacuum and forming hadrons from nearby quarks. In order to form a B^0 or a $\bar{B}^0$ meson the light quark pair which is nearest in the fragmentation chain to the initial heavy quark must have been a $d\bar{d}$ pair. This leaves a d or $\bar{d}$ quark at the dangling end of the fragmentation chain. If the second nearest light quark pair is $u\bar{u}$ pair then the nearest meson in the fragmentation chain will be a π^- or π^+, which can be used to tag the flavor of the initial b or $\bar{b}$. If the second nearest light quark pair is a $d\bar{d}$ pair then the nearest meson

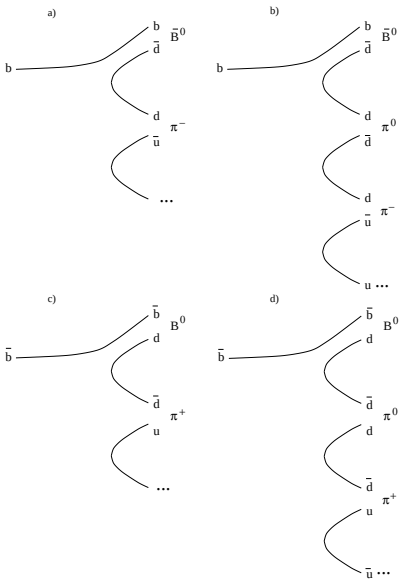

Figure 2.7: Four quark diagrams for the fragmentation of b and $\bar{b}$ quarks to B^0 and $\bar{B}^0$ mesons. The charged pion which is nearest in the fragmentation chain to the B meson tags the birth flavor of the B meson. The notation ...indicates that the fragmentation chain continues out of the picture.

is a π^0, which itself has no tagging power. However the dangling end of the fragmentation chain remains a d or $\bar{d}$ and, if the third nearest light quark pair is a $u\bar{u}$ pair, then the second nearest meson will be a π^- or π^+ which can be used as a flavor tag. The bottom line is that the charge of the nearest charged pion tags the birth flavor of the B^0 or $\bar{B}^0$ meson.

The question now is to discover an algorithm that will identify the charged pion that is the nearest charged pion in the fragmentation chain. CDF successfully developed such an algorithm in Run I. To select the same side tag pion, all tracks within a cone of radius 0.7 in $\eta\,\varphi$ space, centered around the direction of the B meson, were considered. Same side tag candidate tracks were required to originate from the B production point (the primary event vertex), and were therefore required to satisfy $d_0/\sigma_{d_0} < 3$, where σ_{d_0} is the uncertainty on the track $r\,\varphi$ impact parameter d_0. This selection produced, on average, 2.2 same side tag candidate tracks per B candidate. String fragmentation models indicate that particles produced in the b quark hadronization chain have a small momenta transverse to the direction of the b quark momentum. CDF thus selected as the tag the track that had the minimum component of momentum, $p_T^{\rm rel}$, orthogonal to the momentum sum of the track and the B meson.

The same fragmentation chain argument can be used to show that the nearest charged

kaon in the fragmentation chain can be used to tag the flavor of B_s and $\bar{B}_s$ mesons. If the nearest kaon is a K^+, then the meson is a B_s but if the nearest kaon is a K^-, then the meson is a $\bar{B}_s$. If, however, the nearest kaon is neutral, then there is no kaon tagging power because the nearest charged neighbor will be a pion. While there does remain a charge correlation with the nearest charged pion, the author is not aware of any work done to exploit this.

Compared with away side tagging methods, the same side tagging methods have a higher efficiency but a worse dilution. That is, they almost always find a candidate charged track but it is not always the correct one. Because of its high efficiency, same side tagging makes an important contribution to the total tagging power of an experiment.

2.6.3 Overall Tagging Strategy

The various methods described above have quite different properties. For example lepton tagging has a relatively low efficiency but a very good dilution. Same side tagging and jet charge tagging, on the other hand, are more efficient but have poorer dilutions. At CDF in RunI Kaon tagging was intermediate in both efficiency and dilution; better particle identification capability in the CDF Run II detector and in BTeV will significantly improve the dilution for this tag. The optimal tagging strategy is some method which involves all of the the tagging techniques. Any such strategy must account for the correlations among the away side tagging methods; same side tagging is statistically independent of all away side methods. One very simple strategy is to poll each method in order of decreasing dilution and to accept the first method that gives an answer. A more powerful idea is to combine all of the methods into an overall likelihood ratio, a linear discriminant or a neural net. The strategy employed by CDF in their RunI analysis of $\sin 2\beta$ is described in reference [13].

For further details one should consult the chapters for the specific experiments and the references therein.

2.7 The Measurement Error on Proper Decay Times

It is instructive to describe how one measures the proper decay time of a b hadron and to see that, for the decays of interest, the error on the proper decay time is, to a good approximation, independent of momentum.

To measure the proper decay time one reconstructs the primary interaction vertex at which the b hadron was produced and the secondary vertex at which the b hadron decayed. The proper decay time, t, is then given by $t = Lm/pc = L/\beta\gamma c$, where L is the decay length measured by the separation of the vertices, p is the measured momentum of the b hadron, m is the mass of the b hadron, c is the speed of light, and where β and γ are the usual Lorentz parameters for the b hadron. The uncertainty on the decay length contains contributions from the error on the primary vertex position, the error on the secondary vertex position and the error on the momentum of the b. In all three experiments the contributions from the position errors are much larger than those from the error on the momentum. And the

multiplicity of the primary vertex is usually much higher than that of the secondary vertex, making the error on the primary vertex position smaller than that of the secondary vertex; therefore the error on the proper decay time is dominated by the error on the position of the secondary vertex. The relevant part of the error on the secondary vertex is the projection of its error ellipse onto the flight direction of the b hadron. That is the dominant contribution to the error is just,

$$\sigma_t(\text{dominant contribution}) = \sigma_L^{(2ndry)}/(\beta\gamma c), \tag{2.6}$$

where $\sigma_L^{(2ndry)}$ is the contribution of the secondary vertex to the decay length.

There is one familiar exception to this rule. When using semi-leptonic decays to reconstruct the b, the momentum carried by the missing neutrals is poorly known and the error in the proper decay time has important contributions from the error in the momentum.

To understand how σ_t depends on momentum, consider two different instances of the decay $B^0 \to \pi^+\pi^-$. In the the first case the B^0 has some definite momentum and the decay takes place at a particular point in some detector. Suppose that the momentum is large enough that both pions are boosted forward along the B flight direction in the lab. In the second case, the B^0 decays at exactly the same space point and with the same center-of-mass decay angles as in case 1, but it has a larger momentum. The decay products of this decay are then measured in the same detector. Further suppose that the detector is sufficiently uniform that each track from these two decays is equally well measured. The main difference between these two cases is that the lab frame opening angle between the two pions will be smaller in case 2 than in case 1. Because the opening angle is smaller, the point at which the tracks intersect is more poorly known. In particular the component of the vertex position along the b flight direction in the lab is more poorly known. This is purely a geometric effect. One result of this geometric effect is that the error on the secondary vertex position grows like γ; that is $\sigma_L^{(2ndry)} \propto \gamma$. Plugging this into Eq. 2.6 gives $\sigma_t \propto 1/(\beta c)$. Therefore, for $\beta \simeq 1.0$, the error on the proper decay time is independent of momentum. This property has been exploited by experiments such as E687, E791, SELEX and FOCUS to make precision measurements of the charmed hadron lifetimes.

The above analysis holds approximately for multi-body decays of b hadrons. It will fail for very small boosts, in which case the decay products travel both forwards and backwards along the b flight direction. It will also fail if the decay products of the b hadron are slow enough that their errors are dominated by multiple scattering and not by the measurement errors in the apparatus.

The above analysis is only valid if the two decays are measured by the same detector. It is not useful for comparing two very different detectors; in that case there are no short cuts and one must compute the resolution of each detector.

2.8 Properties of a Good B Physics Detector

A detector for doing b and c physics at a hadron collider must have the following components, a high precision vertex detector, a tracking system giving excellent momentum resolution,

excellent particle identification (ID) capability, and a robust trigger integrated into a high bandwidth DAQ. And it is very desirable to have electromagnetic calorimetry so that modes containing photons and π^0's can be measured.

It would also be useful to have hadronic calorimetry which is precise enough to reconstruct a K_L^0. Because the K_L^0 has opposite CP quantum numbers to the K_S^0, many tests of the weak interactions can be made by comparing exclusive final states which differ by substituting a K_L^0 for a K_S^0. None of the three experiments, however, anticipate a significant ability to reconstruct K_L^0 mesons.

There are many other constraints on the detector design. For example, all of the detector elements must have sufficiently fine granularity to deal with the high multiplicities which occur in $p\bar{p}$ collisions. The detector must be able to deal with several such interactions in one beam crossing. And it is important to design the detector with as little mass as possible in the fiducial volume.

The three experiments have approached these challenges from different directions and with different constraints.

2.8.1 Forward vs Central

At first glance the most striking difference among the three detectors is that CDF and DØ are central detectors while BTeV is a forward detector. But there is a much more important distinction — BTeV is a dedicated B physics detector while CDF and DØ are multipurpose detectors whose primary mission is high p_T physics, including precision top quark physics, the search for the Higgs boson and the search for supersymmetric particles. Some of the constraints imposed on CDF and DØ are not intrinsic limitations of the central geometry; rather they are consequences of their optimization for a different spectrum of physics.

But there do remain some issues for which either the forward or central geometry has an advantage. First, BTeV has a harder particle ID job than either CDF or DØ because BTeV must identify tracks over a much wider range of momentum. However the forward geometry allows for a RICH detector which gives BTeV better overall hadronic particle ID. Second, BTeV has a somewhat higher efficiency for reconstructing the decay products of the second B in the event, given that the first B has already been reconstructed. The reasons behind this involve the interplay of production dynamics with the myriad constraints of detector design. Third, the forward geometry is more open than the central geometry, thereby simplifying the mechanical design and maintenance. In a central geometry, on the other hand, one unit of η is much more opened up in space than in the forward region. Since multiplicities are approximately uniform in η, this allows a device with coarse granularity to have the same multi-track separation power as does a fine granularity device in the forward region; this has advantages in channel count. Many of the advantages discussed in this paragraph are tied to available technologies and the situation might well change with new developments in detector technologies.

The B mesons produced in the forward region have higher momenta, and consequently longer decay lengths, than do those produced in the central region. Before drawing any

conclusions about the merits of forward produced B's, one must take many other things into account. Not all B's produced in the central region have low momentum and the ones which pass all analysis cuts have much higher momentum than the average B meson. There are more B mesons produced in the central region than in the forward region so central detectors can tolerate a smaller efficiency for their topological cuts and still have a comparable event yield. Higher momentum B mesons have poorer resolution on their decay vertex positions (see Section 2.7); this cuts the advantage of the highest momentum B mesons in forward detectors. The decay products of higher momentum B mesons undergo less multiple scattering than do those of lower momentum B mesons; this helps to improve resolutions. And the details of the detector design turn out to be the critical. The net result is that, after all analysis cuts, the early designs for the Run II CDF detector had a significantly poorer resolution on proper decay time than does BTeV. But with the addition of Layer-00, CDF now has a resolution on proper decay time, after all analysis cuts, which is comparable to that of BTeV.

At trigger time a different set of priorities is present. For example, in the lowest level of the BTeV trigger, the track fitting algorithms are crude and it is important that most B meson daughters are of high enough momentum that multiple scattering is a small enough effect to treat in a crude fashion.

The most important difference which arises from of BTeV being a dedicated experiment, while CDF and D0 are not, is in the trigger and DAQ systems. The BTeV trigger and DAQ system reconstructs tracks and makes a detachment based trigger decision at the lowest trigger level. Every beam crossing is inspected in this way. CDF and DØ, on the other hand, must live within bandwidth budgets that were established before this sort of trigger was feasible. Therefore they have detachment information available only at level 2 and higher. For similar reasons their triggers have a higher p_T cut than does the BTeV trigger.

2.8.2 A Precision Vertex Detector

First and foremost it is necessary to have a high precision vertex detector. The importance of the vertex detector to the trigger has already been emphasized. Also, excellent resolution on proper decay time, which results from excellent vertex resolution, is necessary to study the time dependence of mixing mediated CP violating effects in the B_s system.

In a typical offline analysis chain, the vertex resolution appears to a high power. A typical candidate-driven $B^0 \to \pi^+\pi^-$ analysis might proceed as follows. First one finds a B^0 candidate and demands that the candidate B have a well defined vertex with a good χ^2. Next, one must find the primary vertex of the $b\bar{b}$ interaction and care must be taken to ensure that this vertex is not contaminated by tracks from the other b hadron. One demands that the secondary vertex be well separated from the primary vertex. For some analyses it will be necessary to exclude B candidates if other tracks from the event are consistent with coming from the B decay vertex. Finally, one applies the available tagging methods. Each of these steps exploits the vertexing power of the experiment in a slightly different way. With so many steps, poor resolution has many chances to strike.

The vertex detector must have as low a mass as possible. Less mass implies less multiple

scattering and better vertex resolution. But a more important effect is that less mass reduces the number of interactions of signal tracks in the detector materials. When a signal track interacts in the detector, it is often unusable for physics and the event is lost. Examples include tracks which undergo inelastic hadronic interactions before reaching the particle ID device and photons which pair convert in the detector material.

A final consideration is the occupancy of the vertex detector. The occupancy is defined as the fraction of channels which are hit during a typical beam crossing. As the occupancy rises, the number of hit combinations which must be considered grows exponentially and pattern recognition becomes more difficult. If the occupancy is less than a few percent, offline pattern recognition is straight forward and standard algorithms compute sufficiently quickly. The driving factor in behind BTeV's choice of a pixel detector, rather than a strip detector, was to reduce the occupancy to approximately 10^{-4}. With this very low occupancy, even very simple, pattern recognition algorithms are efficient and produce low background levels; this allows their use at the lowest level of the trigger.

2.8.3 Tracking

The vertex detector must be supplemented by a tracking system with excellent momentum resolution. For most decay modes of interest, the mass resolution on the b hadron is dominated by the momentum resolution of the apparatus. If the mass resolution can be decreased by, say, 10%, one will get a 10% improvement in signal-to-background ratio without loss of signal efficiency. In a decay chain with several intermediate mass constraints this can add up.

Again it is important to minimize the mass in the tracking system and pay careful attention to the expected occupancy.

2.8.4 Particle ID

It is important to have a excellent particle identification with the ability to separate, with high efficiency, all of e, μ, π, K, p over a broad momentum range. All of the detectors have triggering modes which require lepton identification (lepton ID). Particle ID is also critical for reducing backgrounds which arise when one B decay mode is mistaken for another, such as $B_s \to D_s\pi$ being mistaken for $B_s \to D_sK$. Finally, excellent particle ID is crucial for a large ϵD^2 for kaon tagging.

All of the experiments have excellent lepton ID. Muon ID is done by finding tracks which penetrate a hadron shield. Electron ID is done by matching tracks in the tracking system with clusters of energy in the electromagnetic calorimeter.

BTeV is a dedicated B physics experiment and one of the factors driving the decision to build a forward spectrometer, not a central one, was that the forward geometry has room for a Ring Imaging Cherenkov counter (RICH). This provides the power to separate π, K, p from one another. On the other hand, the CDF and DØ detectors were originally optimized for high p_T physics, which did not require powerful π, K, p separation. Therefore the early

designs for the CDF and DØ Run II detectors did not include any device to do hadronic particle ID. Since then CDF has added a time of flight (TOF) system to perform π, K, p separation.

The reader is referred to the chapters 3 to 5 for further details.

2.8.5 Trigger and DAQ

In order to have a broad based B physics program, it is important to have an open trigger which is able to trigger on many B decay modes. This must be accompanied by a high bandwidth DAQ system which can move the data off the detector, move it between trigger levels and store it until a trigger decision is made.

The job of the trigger is to sort through the much more copious background interactions and extract a high purity b sample to write to tape. Ideally the trigger should be sensitive to some general property of b events, and have a high efficiency for a wide variety of B decay modes; it is not enough that the trigger performs well on some list of benchmark decay modes. This allows the greatest flexibility to explore ideas which are first thought of long after the trigger design was frozen. Of course one must verify that the trigger works well on the modes which we know now to be important.

A detachment based trigger meets all of these requirements; in particular it can trigger on all hadronic decay modes, a capability which was missing from the previous generation of experiments. A lepton based trigger, while missing the all hadronic modes, does meet many of the requirements and it will provide a redundant triggering method to calibrate the detachment based triggers.

The background rejection needed by the trigger is set by several things. Each level of the trigger must reduce the background to a low enough level that the bandwidth to the next level is not saturated. One must also consider the total amount of data which is written to tape; if too much data is written to tape, the main data reconstruction pass will take too long and the production of physics papers will be delayed. The cost of archival media is also an issue.

A final consideration is projecting results to higher instantaneous luminosities. As the luminosity increases, several limiting effects arise: one might reach the bandwidth limit of the DAQ system; one might exceed the amount of buffering at some level of the DAQ; the dead time might become too large. Once one of these limits is reached, the normal response is to raise some trigger threshold or to prescale some trigger. Typically one tries to sacrifice either the triggers which carry the least interesting physics or the triggers with poor signal to background ratios.

During an extended Run II but it is very likely that some of the B physics triggers will need to be modified to deal with the increased luminosity but it is difficult to project in detail what might need to be done. These decisions will depend, in part, on an understanding of backgrounds which is not yet available. Depending on the characteristics of the backgrounds, the trigger efficiency for some B physics channels may be unaffected while the trigger efficiency for other B physics channels may drop significantly.

The collaborations have concentrated their B physics trigger simulations on the conditions which will be present early in Run II, up to a luminosity of around $2 \times 10^{32}\,\mathrm{cm}^2\mathrm{s}^{-1}$. So they have decided not to present projections for integrated luminosities of 10 and 30 fb^{-1}.

2.8.6 EM Calorimetry

A good electromagnetic calorimeter (EMcal) is necessary for the reconstruction of decay modes which contain final state photons and π^0's. It is also necessary for electron ID, which can be used in triggering, in flavor tagging, in many searches for physics beyond the standard model.

There is one high profile decay mode for which the EMCal is critical, the analysis of the Dalitz plot for the decay $B^0 \to \pi^+\pi^-\pi^0$, a mode which measures the CKM angle α. The $\Upsilon(4S)$ machines are rate limited and are likely not to have sufficient statistics to make a definitive measurement of this quantity. The Tevatron detectors have the rate and, provided the EMCal technology is good enough, the measurement can be done.

A final use for an EMCal is to help sort out strong interaction effects which are entangled with the weak interaction physics that it the main goal. It is most straightforward to disentangle the strong interaction effects when all isospin permutations of the final state can be measured. The classic example of this are the decays $B^0 \to \pi^+\pi^-$, $B^0 \to \pi^0\pi^0$, and $B^+ \to \pi^+\pi^0$. While this complete set of decay modes is probably not measurable at the Tevatron, it illustrates the point.

All of the detectors have electromagnetic calorimetry. Both BTeV and CDF have discussed a B physics program which exploits it.

The EMCal system has a unique sensitivity to the issue of track density. As the number of tracks in the detector goes up, the occupancy of the calorimeter goes up. In the case of the tracking detectors one can compensate for high occupancy by making a more granular detector. This works because each track usually makes a small, localized signal in a tracking detector. In the case of a calorimeter, showers are extended objects which, by design, deposit energy in neighboring crystals or cells. Increasing the granularity of the detector will not make the showers any smaller. One can compensate for high occupancy by choosing calorimeter materials in which showers are contained in a smaller volume; if such materials are available, have sufficient energy resolution and radiation tolerance, and are affordable, then they can be used to make a calorimeter which can tolerate higher multiplicities.

2.8.7 Muon Detector

The final major hardware component in a B physics experiment is a muon detector system. This provides muon identification (ID) for such purposes as flavor tagging, reconstruction of J/ψ candidates, reconstruction of semileptonic decays, and searches for rare or forbidden decays. These last two classes include modes such as $B^0 \to \mu^+\mu^-$ and $B^0 \to e^+\mu^-$. A second job of these system is to provide an element of the trigger system; in some cases this is a stand alone trigger element and in other cases it is used in conjunction with other detector components to make a trigger decision.

The basic design of a muon detector is an iron or steel shield, many hadronic interaction lengths thick, which absorbs hadrons. Muons which penetrate this shield are detected by some sort of wire chamber tracking detector, or perhaps a scintillator, placed behind the shield. When possible other detector components, such as calorimeters and flux returns are used as part of the shielding. In another variation, iron shielding can be magnetized to allow measurement of the muon momentum in the muon system alone. This gives several benefits: it allows one to design a muon based trigger with a well defined p_T cut and it allows better matching between tracks in the muon system and tracks in the main tracking system.

2.9 Software

The software used by CDF, DØ and BTeV can be thought of in four classes, event generators, the B decay code, detector simulation tools and reconstruction code. The three experiments use common tools for the first two classes of software but generally use their own, detector specific software for the last two classes. The one exception is the MCFast fast simulation package which was used by both BTeV and CDF. MCFast is described extensively in the BTeV TDR [4]. BTeV is a new experiment which has tools which are quite advanced for such a young experiment but which are still primitive on an absolute scale. After Run I, CDF and DØ embarked on a major retooling of their software infrastructure, which was incomplete at the time of the workshop. So all of the results presented here use preliminary versions of code. At the level of precision required for the studies performed at this workshop, all of these tools are good enough.

The event generators are programs which generate the physics of a $p\bar{p}$ interaction; its output is usually just a list of vertices and particles which come out of those vertices. These programs are typically the intellectual property of the theoretical physicists who developed the model which is implemented in the program. The generators used by CDF, DØ and BTeV are `PYTHIA` [8], `ISAJET` [9] and `HERWIG` [10]. Generally these programs are used only to predict the shapes of the differential cross-sections, not for the absolute cross-sections. CDF and DØ have tuned the parameters of their event generators to match their Run I data. BTeV, on the other hand, has no such data against which to tune the codes. Therefore BTeV is using the programs as is.

The event generators have been carefully developed to simulate the properties of $p\bar{p}$ collisions but much less care was taken in their model of how b hadrons decay. To circumvent this, the b and c hadrons produced by the event generators are handed to a separate code to simulate their decay. Until recently this code was the QQ code, which was developed and maintained by CLEO, and which contains their integrated knowledge about the decays of B's and D's. The BaBar collaboration also has such a program, `EVTGEN` which will soon replace QQ. The results of the workshop were obtained using QQ.

The next step in a typical simulation is to compute the detector response to the simulated events. All of the experiments have both a fast simulation program and a detailed simulation program. A typical fast simulation program uses a simplified and/or parameterized description of the detector response and directly produces smeared 4-vectors for the

tracks which were input to it. It may also declare that a track is outside of the fiducial volume and is not reconstructible. The output of the fast simulation can usually be used as is to perform the simulated analysis.

A typical full simulation is based on the `GEANT` 3 program from CERN. This is a program which knows how to describe a detector by building it up from a library of known shapes. It also has extensive knowledge of the interactions of particles with materials. It takes tracks from the event generator and propagates them through the detailed description of the detector, at each step checking to see how the track interacted with the material. If a particle interacts in the detector material to produce new particles, those new particles are also propagate through the detector. If a shower starts in material, `GEANT` 3 will follow the daughters through each stage of the shower, and deposit the energy of the shower in the appropriate detector cells. The output of this simulation is typically a list of pulse heights or arrival times for hits in individual detector cells. This information is then passed to the reconstruction program and the trigger simulation codes.

At the time of the workshop, the experiments were still evaluating at the `GEANT` 4 program, the C++ based successor to `GEANT` 3.

CDF and DØ have data samples from Run I which can be used. Signal yields can be projected from the Run I signal yields by computing the ratio of efficiencies in the old and new detectors. This avoids the need to make assumptions about the total cross-section, as BTeV must do. CDF and DØ use background samples from Run I to estimate background levels in Run II. BTeV must rely entirely on simulations for this purpose.

The reconstruction code starts with raw hits, either from the detector or from a simulation of the detector, calibrates them, find tracks, fits them, finds showers, applies the particle ID algorithms and so on. The output of this step is the measured properties of tracks and showers, which can be used directly for physics analysis.

The trigger simulation codes start with the same raw hits as the reconstruction code. In some cases the codes emulate the trigger hardware and produce trigger decisions which should very closely represent the real trigger behavior. In other cases the simulation codes

For more details on the software of each experiment, consult their TDRs [1] [2] [3] [4] and chapters 3 to 5 in this report.

2.10 Comparison with e^+e^- Machines

For most of their lifetime the Tevatron experiments will be in competition with the detectors from the $\Upsilon(4S)$ e^+e^- factories, BaBar and Belle. The charm physics program of BTeV will also face competition from CLEO-c. While these programs are competition, they also complement the Tevatron program. Some precision measurements will be best done in the cleaner environment of e^+e^-: they have a well determined initial state, either pure $B^0\bar{B}^0$ or B^+B^-, with no additional tracks in the event. And the production of B mesons represents about 20% of their total cross-section, which greatly simplifies triggering and removes many trigger biases. Similar advantages hold for the open charm program at CLEO-c.

On the other hand, the Tevatron experiments have a significant rate advantage which give it the advantage for many rare decay modes and in those measurements which are statistically limited. Only the Tevatron experiments have access to the decays of the B_s and b baryons, which are necessary to complete the program of over constraining the CKM matrix. See, for example, the discussion of B_s mixing in chapter 8.

References

[1] The CDF II Collaboration, R. Blair *et al.*, *The CDF II Detector Technical Design Report*, Fermilab-Pub-96/390-E. This Report may be found at the url: `http://www-cdf.fnal.gov/upgrades/tdr/tdr.html`.

[2] The CDF II Collaboration, *"Update to Proposal P-909: Physics Performance of the CDF II Detector with an Inner Silicon Layer and a Time-of-Flight Detector"*, submitted to the Fermilab Director and PAC, 5 Jan 1999.

[3] The DØ Collaboration, "The DØ Upgrade", submitted to the Fermilab PAC August 1996, Fermilab Pub-96/357-E, `http://higgs.physics.lsa.umich.edu/dzero/d0doc96/d0doc.html`.

[4] The BTeV Collaboration, "Proposal for an Experiment to Measure Mixing, CP Violation and Rare Decays in Charm and Beauty Particle Decays at the Fermilab Collider — BTeV", Submitted to the Fermilab Director and PAC, May 2000. This report may be found at the URL: `http://www-btev.fnal.gov/public_documents/btev_proposal/index.html`

[5] The CDF Collaboration, F. Abe *et al.*, Phys. Rev. D **50**, 5550 (1994).
The E-811 Collaboration, C. Avila *et al.*, Phys. Lett. **B445** 419 (1999).

[6] The Particle Data Group, D. E. Groom *et al.*, The European Physical Journal **C15**, 1 (2000).

[7] M. Mangano, P. Nason and G. Ridolfi, Nucl. Phys. **B373**, 295 (1992).

[8] H. U. Bengtsson and T. Sjostrand, Comp. Phys. Comm. **46**, 43 (1987).

[9] F. Paige and S. Protopopescu, Brookhaven National Laboratory Report BNL-37066 (1985) (unpublished).

[10] G. Marchesini and B.R Webber, Nucl. Phys. **B310**, 461 (1988); Nucl. Phys. **B330**, 261 (1988);
I. G. Knowles, Nucl. Phys. **B310**, 571 (1988);
G. Abbiendi, *et al.*, Comp. Phys. Comm. **67**, 465 (1992).

[11] The CDF Collaboration, T. Affolder *et al.*, Phys. Rev. Lett. **84**, 1663 (2000).

[12] D. Abbaneo *et al.*, "Combined results on b hadron production rates, lifetimes, oscillations and semileptonic decays," hep-ex/0009052.

[13] The CDF Collaboration, T. Affolder *et al.* Phys. Rev. D **61**, 072005 (2000) [hep-ex/9909003].

[14] The CDF Collaboration, F. Abe *et al.*, Phys. Rev. Lett. **75** 1451 (1995).

[15] The DØ Collaboration, R. Abbott *et al.*, Phys. Rev. Lett. **74** 3548 (1995).

[16] D. Fein, "Tevatron Results on b-Quark Cross Sections and Correlations", presented at Hadron Collider Physics (HCP99), Bombay, January 1999.

[17] The DØ Collaboration, B. Abbott *et al.*, Phys. Rev. Lett. **84** 5478 (2000) [hep-ex/9907029].

[18] The DØ Collaboration, B. Abbott *et al.*, "The $b\bar{b}$ Production Cross Section and Angular Correlations in $p\bar{p}$ Collisions at $\sqrt{s} = 1.8$ TeV", Phys. Lett. **B487** 264 (2000) [hep-ex/9905024].

Chapter 3

The CDF Detector

M. Paulini, A.B. Wicklund

3.1 Introduction

The CDF detector has evolved over a twenty year period. CDF was the first experiment at the Tevatron to perform quantitative measurements of b-quark production, using single-lepton and J/ψ samples in Run 0 (1988-1989). CDF was the first hadron collider experiment to successfully employ a silicon vertex detector (SVX). The four layer, axial readout SVX (Run Ia) and SVX' (Run Ib) detectors were used to discover the top quark through detection of the b-quark decay chain. They were also used for a systematic program of b-physics studies, including B-lifetimes, $B\overline{B}$ mixing, discovery of the B_c, and measurement of CP violation in the $B^0 \to J/\psi K^0_S$ mode. In the course of this program, CDF has developed the techniques to identify B hadron final states in J/ψ and $\ell\nu D$ semileptonic modes, and to flavor tag these states using away-side lepton and jet-charge tags and toward side fragmentation correlations. As a byproduct, CDF has developed control sample strategies to calibrate particle identification using relativistic rise $\mathrm{d}E/\mathrm{d}x$, to optimize flavor tagging efficiency, and to measure material effects (energy loss and radiation length corrections) needed for precision mass measurements. CDF has published over fifty papers on B physics with the Run 0 and Run I data. In addition to Run I physics data, CDF recorded data on a variety of specialized triggers in order to estimate rates and backgrounds for the Run II program. Although the Run II B-physics program at CDF will be technically more challenging than Run I, CDF starts with the advantage of extensive experience and benchmark data.

The upgraded CDF detector and physics program for Run II is described in detail in the CDF Technical Design Report [1]. The additional upgrades for time-of-flight and innermost silicon detector are described in the PAC proposal P909 [2]. Below we summarize the Run II detector configuration, with expected performance including particle identification, issues for central solenoidal detectors, CDF B-physics trigger plans, and offline analysis issues.

3.2 CDF Run II Detector

The main upgrades to the CDF detector for Run II can be summarized as follows:

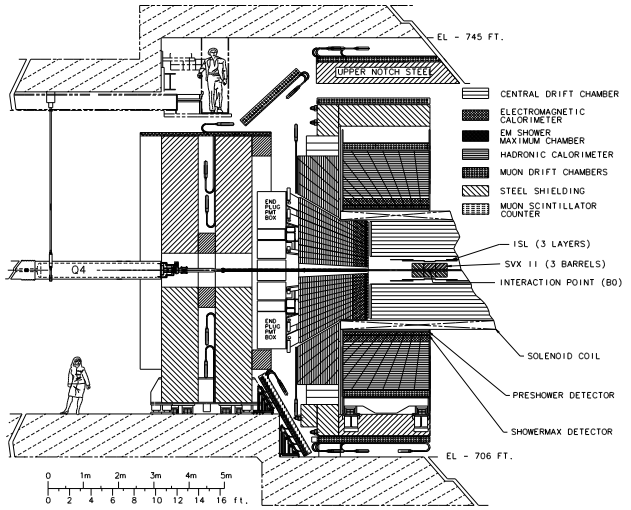

Figure 3.1: Elevation view of the Run II CDF detector

- Fully digital DAQ system designed for 132 ns bunch crossing times
- Vastly upgraded silicon detector
  - 707,000 channels compared with 46,000 in Run I
  - Axial, stereo, and 90° strip readout
  - Full coverage over the luminous region along the beam axis
  - Radial coverage from 1.35 to 28 cm over $|\eta| < 2$
  - Innermost silicon layer("L00") on beampipe with 6 μm axial hit resolution
- Outer drift chamber capable of 132 ns maximum drift
  - 30,240 sense wires, 44-132 cm radius, 96 $\mathrm{d}E/\mathrm{d}x$ samples possible per track
- Fast scintillator-based calorimetry out to $|\eta| \simeq 3$
- Expanded muon coverage out to $\eta \simeq 1.5$
- Improved trigger capabilities
  - Drift chamber tracks with high precision at Level-1
  - Silicon tracks for detached vertex triggers at Level-2
- Expanded particle identification via time-of-flight and $\mathrm{d}E/\mathrm{d}x$

COT	
Radial coverage	44 to 132 cm
Number of superlayers	8
Measurements per superlayer	12
Readout coordinates of SLs	+2° 0° -2° 0° +2° 0° -2° 0°
Maximum drift distance	0.88 cm
Resolution per measurement	180 μm
Rapidity coverage	$\|\eta\| \leq 1.0$
Number of channels	30,240
Layer 00	
Radial coverage	1.35 to 1.65 cm
Resolution per measurement	6 μm (axial)
Number of channels	13,824
SVX II	
Radial coverage	2.4 to 10.7 cm, staggered quadrants
Number of layers	5
Readout coordinates	r-ϕ on one side of all layers
Stereo side	r-z, r-z, r-sas, r-z, r-sas (sas $\equiv \pm 1.2°$ stereo)
Readout pitch	60-65 μm r-ϕ; 60-150 μm stereo
Resolution per measurement	12 μm (axial)
Total length	96.0 cm
Rapidity coverage	$\|\eta\| \leq 2.0$
Number of channels	423,900
ISL	
Radial coverage	20 to 28 cm
Number of layers	one for $\|\eta\| < 1$; two for $1 < \|\eta\| < 2$
Readout coordinates	r-ϕ and r-sas (sas$\equiv \pm 1.2°$ stereo) (all layers)
Readout pitch	110 μm (axial); 146 μm (stereo)
Resolution per measurement	16 μm (axial)
Total length	174 cm
Rapidity coverage	$\|\eta\| \leq 1.9$
Number of channels	268,800

Table 3.1: Design parameters of the CDF tracking systems

$\|\eta\|$ Range	$\Delta\phi$	$\Delta\eta$
0. - 1.1 (1.2 h)	15°	~ 0.1
1.1 (1.2 h) - 1.8	7.5°	~ 0.1
1.8 - 2.1	7.5°	~ 0.16
2.1 - 3.64	15°	$0.2 - 0.6$

Table 3.2: CDF II Calorimeter Segmentation

The CDF detector features excellent charged particle tracking and good electron and muon identification in the central region. The detector is built around a 3 m diameter 5 m long superconducting solenoid operated at 1.4 T. The overall CDF Run II detector schematic is shown in elevation view in Fig. 3.1. The CDF tracking system includes a central outer drift chamber (COT), a double-sided five layer inner silicon detector (SVX II), a double-sided two layer intermediate silicon tracker (ISL), and a single layer rad-hard detector mounted on the beampipe (L00). COT tracks above 1.5 GeV/c are available for triggering at Level-1 (XFT); SVX layers 0-3 are combined with XFT tracks at Level-2 (SVT). The main parameters of the CDF tracking system are summarized in Table 3.1.

Outside the solenoid, Pb-scintillator electromagnetic (EM) and Fe-scintillator hadronic (HAD) calorimeters cover the range $|\eta| < 3.6$. Both the central ($|\eta| < 1.1$) and plug ($1.1 < |\eta| < 3.6$) electromagnetic calorimeters have fine grained shower profile detectors at electron shower maximum, and preshower pulse height detectors at approximately $1X_o$ depth. Electron identification is accomplished using E/p from the EM calorimeter and also in the shower maximum and preshower detectors; using $HAD/EM \sim 0$; and using shower shape and position matching in the shower max detectors. Together with COT dE/dx, CDF gets $\sim 10^{-3}$ π/e rejection in the central region. The calorimeter cell segmentation is summarized in Table 3.2. A comparison of the central and plug calorimeters is given in Table 3.3.

The calorimeter steel serves as a filter for muon detection in the central (CMU) and extension (CMX) muon proportional chambers, over the range $|\eta| < 1$, $p_T > 1.4$ GeV/c. Additional iron shielding, including the magnet yoke, provides a muon filter for the upgrade muon chambers (CMP) in the range $|\eta| < 0.6$, $p_T > 2.2$ GeV/c. The (non-energized) forward toroids from Run I provide muon filters for intermediate $1.0 < |\eta| < 1.5$ muon chambers (IMU) for $p_T > 2$ GeV/c. Scintillators for triggering are included in CMP, CMX, and IMU. Muon identification is accomplished by matching track segments in the muon chambers with COT/SVX tracks; matching is available in $R\Phi$ for all detectors and in the Z views in CMU and CMX. The muon systems are summarized in Table 3.4.

The Run II CDF detector configuration allows electron and muon identification with drift chamber tracking over the range $|\eta| < 1.0$, with additional coverage out to $|\eta| \sim 1.5$ using stand-alone silicon tracking. Typical thresholds are $p_T > 1$ GeV/c (electrons), $p_T > 1.5$ GeV/c (muons). Calibration of electron and muon identification is accomplished *in situ* with large samples of J/ψ's and photon conversions.

	Central	Plug
EM:		
Thickness	$19X_0, 1\lambda$	$21X_0, 1\lambda$
Sample (Pb)	$0.6X_0$	$0.8X_0$
Sample (scint.)	5 mm	4.5 mm
WLS	sheet	fiber
Light yield	160 pe/GeV	300 pe/GeV
Sampling res.	$11.6\%/\sqrt{E_T}$	$14\%/\sqrt{E}$
Stoch. res.	$14\%/\sqrt{E_T}$	$16\%/\sqrt{E}$
Shower Max. seg. (cm)	$1.4\phi\times$(1.6-2.0) Z	0.5×0.5 UV
Pre-shower seg. (cm)	$1.4\phi \times 65$ Z	by tower
Hadron:		
Thickness	4.5λ	7λ
Sample (Fe)	1 to 2 in.	2 in.
Sample (scint.)	10 mm	6 mm
WLS	finger	fiber
Light yield	~ 40 pe/GeV	39 pe/GeV

Table 3.3: Central and Plug Upgraded Calorimeter Comparison

	CMU	CMP	CMX	IMU
Pseudo-rapidity coverage	$\lvert\eta\rvert \leq 0.6$	$\lvert\eta\rvert \leq 0.6$	$0.6 \leq \lvert\eta\rvert \leq 1.0$	$1.0 \leq \lvert\eta\rvert \leq 1.5$
Drift tube cross-section	2.68 x 6.35 cm	2.5 x 15 cm	2.5 x 15 cm	2.5 x 8.4 cm
Drift tube length	226 cm	640 cm	180 cm	363 cm
Max drift time	800 ns	1.4 μs	1.4 μs	800 ns
Total drift tubes (present)	2304	864	1536	none
Total drift tubes (Run II)	2304	1076	2208	1728
Scintillation counter thickness		2.5 cm	1.5 cm	2.5 cm
Scintillation counter width		30 cm	30-40 cm	17 cm
Scintillation counter length		320 cm	180 cm	180 cm
Total counters (present)		128	256	none
Total counters (Run II)		269	324	864
Pion interaction lengths	5.5	7.8	6.2	6.2-20
Minimum muon p_T	1.4 GeV/c	2.2 GeV/c	1.4 GeV/c	1.4-2.0 GeV/c
Multiple scattering resolution	12 cm/p	15 cm/p	13 cm/p	13-25 cm/p

Table 3.4: Design Parameters of the CDF II Muon Detectors. Pion interaction lengths and multiple scattering are computed at a reference angle of $\theta = 90°$ in CMU and CMP, at an angle of $\theta = 55°$ in CMX, and for a range of angles for the IMU.

Photon identification is done using the EM calorimetry, using the preshower and shower maximum detectors to separate π^0/γ. Channels like $B \to J/\psi\eta$ can be reconstructed with the calorimeter. Rare decays such as $B \to K^*\gamma$ use photon conversions to obtain precision γ reconstruction.

Asymptotic tracking resolutions are $\sigma(p_T) \simeq 0.0007\ p_T^2$ ($|\eta| < 1.1$), and $\sigma(p_T) \simeq 0.004\ p_T^2$ ($|\eta| < 2$ -stand-alone SVX tracking). The SVX detectors provide typical impact parameter resolution of 15 ($R-\phi$- view) and 30 (Z- view) μm. For example, this results in mass resolution of around 20 MeV for $B^0 \to \pi^+\pi^-$ and proper time resolution of 45 fs for $B_s^0 \to D_s^-\pi^+$.

Particle identification to separate pions, kaons, protons, and electrons is provided by $\mathrm{d}E/\mathrm{d}x$ and time-of-flight (TOF) detectors ($|\eta| < 1$):

- $1/\beta^2\ \mathrm{d}E/\mathrm{d}x$ in both COT and SVX
- Relativistic rise $\mathrm{d}E/\mathrm{d}x$ in COT

  $\simeq 1\ \sigma\ \pi - K$ separation, $p > 2$ GeV/c
- TOF bars outside the COT (1.4 m radius)

  $\simeq 100$ ps resolution

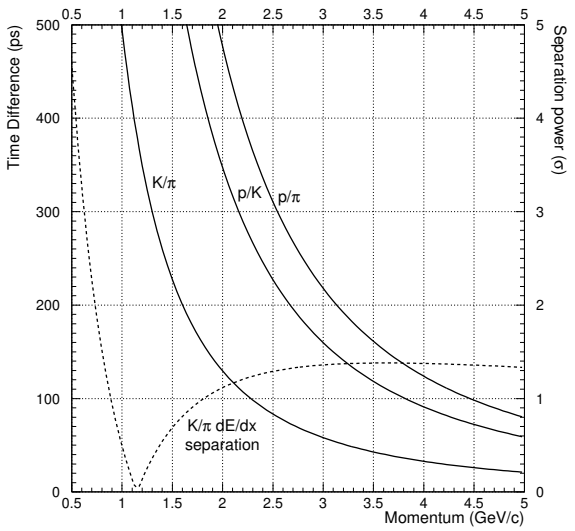

Figure 3.2: Time difference as a function of momentum for π, K, p at a radius of 140 cm, expressed in ps and separation power, assuming 100 ps resolution. The dashed line shows the K/π separation using dE/dx in the COT.

2σ $K-\pi$ separation at 1.5 GeV/c

Figure 3.2 shows the expected separation as a function of momentum. The low momentum particle identification provides flavor tagging with kaons, both on the away side $\overline{b}$-jet, and on the same side as the trigger B (e.g., B_s^0 correlated with K^+, $\overline{B_s^0}$ with K^-); it should also provide useful kaon separation for charm reconstruction, e.g. $B_s^0 \to D_s^- \pi^+$. Above 2 GeV/c, the COT dE/dx provides a statistical separation of pions and kaons. This will be crucial for determination of CP asymmetries in $B^0 \to \pi^+\pi^-$ and $B_s^0 \to K^+K^-$. The dE/dx and TOF calibrations can be determined *in situ* using pions and protons from K_S and Λ decays, kaons from $\phi \to K^+K^-$, electrons from conversion photons, and muons from J/ψ decay.

3.3 Issues for Central Solenoidal Detectors at the Tevatron

In the Run II detector full charged particle tracking using the SVX and the COT is confined to $\eta < 1.1$. Since all B-physics triggers are track based, and rely on COT tracks in the Level-1 trigger, the B triggers are basically limited to this η range. Furthermore, in order

to achieve a reasonable Lorentz boost for the triggered B hadrons, it is necessary to select events with $p_T(B)$ above some minimum cutoff, typically of order 4-6 GeV/c. In terms of production rates, this is not really a severe limitation. At 10^{32} luminosity, the total $b\overline{b}$ production rate is around 10 kHz at the Tevatron (eg. 10^{11} events per fb^{-1}), much more than the CDF data acquisition rate of $\simeq$75 Hz to tape. Since B production at high p_T peaks at small $|y|$, the kinematic restriction is such that about 6% of B-hadrons are produced in the region $|y| < 1$ and $p_T > 6$ GeV/c (e.g., 1.2 kHz of $B+\overline{B}$ at 10^{32}.

Thus, the basic trigger strategy is to select B decays to specific final states in the central region, for example $B^0 \to J/\psi K_S$ or $B_s^0 \to D_s^- \pi^+$, with charged particle tracks confined to $|\eta| < 1$. For mixing and CP studies, flavor tagging is accomplished using either the away-side $\overline{B}$ or same-side fragmentation correlations. The fragmentation correlations give a highly efficient flavor tag ($\simeq$ 70% in Run I), since the tagging tracks are guaranteed to be in the central region. The away side tagging would be limited if tracking were confined to $|\eta| < 1$, but the stand-alone SVX tracking extends the coverage in η, and so is expected to greatly improve efficiency for jet-charge and lepton tagging of away-side b-jets.

There are some advantages to the central detector configuration:

- The Tevatron beamspot is small ($\sim$ 25μm) in the transverse plane. This feature is exploited at the trigger level in CDF Run II, using the SVX detector to identify large-impact parameter tracks from B decays in the level-2 trigger. This requires the Tevatron beam to be aligned parallel to the detector axis, due to the long ($\sim$ 60cm) luminous region in Z. The SVT- trigger will yield a highly pure sample of inclusive B decays, approximately 10^8 $b\overline{b}$ events per fb^{-1}.
- With the $p_T(B)$ cut, the proper time resolution is adequate for demanding analyses such as B_s mixing (e.g., 45 fs on $B_s \to D_s^- \pi^+$)
- The $p_T(B)$ requirement also improves the ratio of B production to QCD background. While the total $b\overline{b}$ cross section is of order 0.2% of the minimum bias rate, the high-p_T b-jet cross section is measured to be 2% of the QCD jet rate, in the p_T range of interest for CDF.
- In the central region, tracks are well spread out in Z, and CDF has demonstrated highly efficient track reconstruction for $b\overline{b}$ events.

3.4 Trigger Strategies

The main B-physics goals for CDF Run II make use of the following final states. Of course in each case, other final states, both inclusive and exclusive, are used as calibration samples, and so the triggers must be designed to be inclusive.

- $B^0 \to J/\psi K_S$ for $\sin 2\beta$
- $B_s^0 \to J/\psi\phi$ for CP and $\Delta\Gamma$

- $B \to \mu^+\mu^- K^{(*)}$ rare decays
- $B_s^0 \to D_s^- \pi^+$ for B_s mixing
- $B_s \to D_s^- \ell^+ \nu$ for B_s mixing
- $B_{(s)}^0 \to K^{*0}\gamma, \phi\gamma$ using photon conversion $\gamma \to e^+e^-$
- $B^0 \to \pi^+\pi^-$, $B_s^0 \to K^+K^-$ for CKM angle γ

This is of course only a partial list. CDF has a three-level trigger design. Level-1 is pipelined so as to be deadtimeless. Digitized data are stored in 42×132 ns buffers to create and count trigger primitives (electrons, muons, COT tracks, and combinations of these). Level-2 is a global trigger that allows finer grained electron and muon track matching, and more sophisticated combinations of trigger primitives (for example, opposite charged lepton pairs with invariant mass requirements). Level-2 finds SVT-tracks using four SVX II layers; these are matched to the XFT/COT tracks found in level-1 to define high resolution, large impact parameter b-decay candidates. Level-2 also matches electrons to the central shower-maximum detector. Finally, Level-3 provides offline quality tracking and calorimeter reconstruction.

Using Run I data, CDF has carefully optimized the use of bandwidth for Run II triggers. The basic trigger requirements can be summarized as follows:

- Dimuons and dielectrons

  Level-1: Two leptons with COT matched to muon chambers or central calorimeter

  Level-2,3: Additional mass, charge, and $\Delta\Phi$ cuts

- Single Leptons

  Level-1: Single leptons matched to muon chambers or central calorimeter

  Level-2,3: Additional requirement of accompanying SVT track

- B hadronic triggers

  Level-1: two tracks, opposite charge, $\Delta\Phi$ cuts

  Level-2,3: two SVX tracks, impact parameter and ct cuts

Thresholds for dilepton and two-track triggers are typically 1.5-2.0 GeV/c, and for single leptons 3-4 GeV/c. Level-3 can make additional cuts in order to divide the data into manageable data sets; for example, a high mass cut will be used to define a $B \to \pi\pi$ stream based on the two-track triggers, while other SVX track requirements will be used to make a $b \to c$ generic hadronic sample.

The total trigger bandwidth, including B physics, is designed to be 40 kHz (level-1), 300 Hz (Level-2) and 75 Hz Level-3). Thus, the maximum rate level-3 would be 750 nb at 10^{32} luminosity. B triggers are expected to require about half of that bandwidth. Table 3.5 gives the expected bandwidth requirements for the trigger streams.

Trigger	L1 σ [nb]	L2 σ [nb]	L3 σ [nb]
$B \to h^+h^-$	252,000	560	100
$B \to \mu\mu(X)$	1100	90	40
$J/\psi \to ee$	18000	100	6
Lepton plus displaced track	9000	130	40

Table 3.5: Trigger rates for the main CDF II B-physics triggers

Physics Channel	Event yield (2 fb^{-1})
$b \to J/\psi X$	28,000,000
$B^0 \to J/\psi K_S^0$	28,000
$B_s \to D_s\pi$	10,000
$B_s \to D_s\ell\nu$	30,000
$B \to \mu^+\mu^- K^{(*)}$	50
$B \to K^*\gamma$	200
$B \to \pi\pi, K\pi, KK$	30,000

Table 3.6: Event yields expected from CDF Run II B-physics triggers

3.5 Offline Analysis and Simulation

CDF has estimated rates for literally hundreds of reconstructable decay modes that come in on the lepton or SVT two-track triggers. Table 3.6 lists some examples.

Detailed studies of the physics reach expected for CDF may be found elsewhere in this document. We discuss briefly two issues that enter into calculations of sensitivity, namely flavor tagging and generic simulation.

3.5.1 Flavor Tagging

CDF measured the flavor tagging efficiencies and dilutions for three methods in the Run I mixing and $\sin 2\beta$ analyses: "same side" (fragmentation correlation) tagging, jet-charge tagging, and soft electron and muon tagging. To understand the "same side" tagging at least qualitatively, CDF analyzed B^{**} production using large samples of semileptonic $B \to D^{(*)}\ell\nu$ decays and applied these to tune the PYTHIA event generator. This gave qualitative agreement with observed same-side tagging efficiencies, including the observed differences between B^0 and B^+ tagging caused by kaons and protons. For jet-charge algorithms, the tagging was optimized initially using PYTHIA and HERWIG event generators, but actual efficiencies and dilutions were measured with data, for example, by fitting the $B^0\overline{B^0}$ mixing amplitude or by direct comparison of tagging in $B^\pm \to J/\psi K^\pm$. Soft lepton tags

were calibrated similarly. For the $\sin 2\beta$ analysis the combined tagging efficiency, including correlations between tags, was $\epsilon D^2 = 6.3 \pm 1.7\%$.

CDF extrapolates the Run I efficiencies and dilutions to Run II conditions, taking into account the standalone silicon tracking to $|\eta| \sim 2$, and including kaon tagging based on TOF. This gives estimates of $\epsilon D^2 \sim 9.1\%$ for $B^0 \to J/\psi K_S$ and $\epsilon D^2 \sim 11.3\%$ for $B_s \to D_s^- \pi^+$. The basic strategies for calibrating and optimizing the tagging efficiencies for each method would be similar to Run I. For example, the same side tags can be optimized using semileptonic decays $B^{0,+} \to D^{(*)} \ell \nu$ and $B_s^0 \to D_s^{(*)} \ell \nu$, including the effects of fragmentation kaons. Opposite side tags can be optimized on the same semileptonic channels, or on inclusive samples such as $b \to J/\psi X$ (e.g., by comparing tagging rates for prompt and long lived J/ψ's). Same-side tags for $\sin 2\beta$ can be calibrated using $B^\pm \to J/\psi K^\pm$ and $B^0 \to J/\psi K^{*0}$. Opposite side tags would be calibrated using $B^\pm \to J/\psi K^\pm$. Thus, there are a variety of data channels and cross checks that are available to understand each tagging method. Event generator Monte Carlo's play a role in helping to model same-side tags, including the effects of kaons, and in understanding correlations and variations of dilution with kinematics.

3.5.2 Monte Carlo Issues

CDF has adopted a GEANT based detector simulation for Run II, which is used for optimization of track reconstruction, muon matching, jet energy analysis, SVT response, etc. The calorimeter response has to be tuned to match data from testbeam, Run I, and eventually Run II. It is obviously straightforward to understand the efficiency for signals such as $B^0 \to \pi^+\pi^-$, where the generation is trivial, and the detector response depends only on tracking and SVT efficiency. The main concern for B triggers is backgrounds. For lepton-based triggers, these can be estimated from Run I data. For hadronic triggers such as $B^0 \to \pi^+\pi^-$, CDF can set limits on backgrounds using Run I data, and can use the PYTHIA generator (plus SVT simulation) to estimate the backgrounds from real $b\bar{b}$ events. The backgrounds that dominate $B^0 \to \pi^+\pi^-$ at the trigger level do not appear to come from real $b\bar{b}$ events but from QCD backgrounds that fake the impact parameter trigger; this conclusion comes from comparison of trigger rates with $b\bar{b}$ Monte Carlo, and also by examining Run I data, comparing high mass two-track rates rates from QCD and real $b\bar{b}$ events. Thus, while CDF can certainly estimate backgrounds from real $b\bar{b}$ events in the SVT two-track trigger sample (these come in due to real b-hadron lifetimes), it cannot reliably simulate "QCD" backgrounds in this sample (these depend critically on offline SVX reconstruction).

References

[1] The CDFII Collaboration, "The CDF Detector Technical Design Report", FERMILAB-Pub-96/390-E

[2] The CDFII Collaboration "Proposal for Enhancement of the CDF II Detector: an Inner Silicon Layer and a Time of Flight Detector", submitted to the PAC, October 1998

Chapter 4

The DØ detector

R. Jesik, F. Stichelbaut, K. Yip, A. Zieminski

The DØ Run II detector [1] shown in Fig. 4.1 builds on the detector's previous strengths of excellent calorimetry and muon detection in an extended rapidity range. The major addition to the apparatus is a precision tracking system, consisting of a silicon vertex detector surrounded by an eight layer central fiber tracker. These detectors are located inside a 2 T solenoid magnet.

4.1 The silicon vertex detector

The silicon vertex detector(SMT), shown in Fig. 4.2, is a hybrid barrel and disk design. The central detector, covering $|z| < 32$ cm, consists of six barrels with disks interspersed between them. Each barrel module consists of four radial layers of detector ladders located at a radius of 2.7, 4.5, 6.6, and 9.5 cm, respectively. Layers one and three have 50 μm pitch double sided silicon microstrip detectors (with axial and 90° strips) in the four inner barrels, and have single sided (axial strip) detectors in the two end barrels. Layers two and four have double sided detectors with axial and 2° stereo strips. Each disk module has twelve wedge-shaped double sided detectors (extending radially from 2.7 to 10 cm) with 30° stereo angle. The forward detector consists of six disks of similar design (three located near each end of the central detector) plus four larger 24-wedge disks made of single sided detectors, located at z = ± 110 cm and ± 120 cm. The detector is read out using SVX-II chips and has 800,000 total channels. The silicon vertex detector provides tracking information out to $|\eta| = 3$ and gives a reconstructed vertex position resolution of 15-40 μm in $r - \phi$ and 75-100 μm in z, depending on the track multiplicity of the vertex.

4.2 The central fiber tracker

The central fiber tracker consists of 74,000 scintillating fibers mounted on eight concentric carbon fiber cylinders at radii from 19.5 to 51.5 cm. Each cylinder supports four layers of fibers, one doublet in the axial direction and one doublet oriented at a 3° helical stereo angle for odd numbered cylinders and at −3° for even ones. The fibers are multi-clad and have a diameter of 830 μm. Clear fiber waveguides carry the light for about ten meters

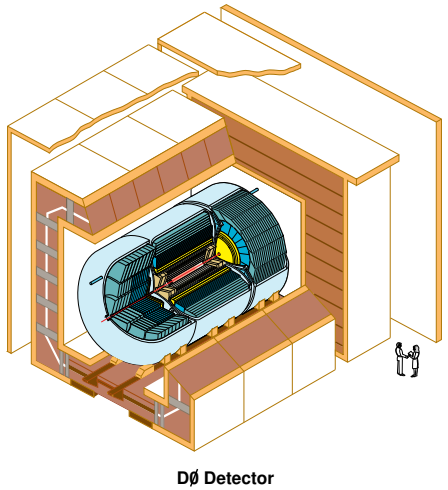

Figure 4.1: The DØ detector

from the scintillating fibers to the visible light photon counters situated in cryostats under the calorimeter. These are silicon devices that have a quantum efficiency of over 80% and a gain of about 50,000. They operate at a temperature of about 10 K. Digitization is also performed with SVX-II chips and the axial fibers are used to form fast level 1 trigger track objects.

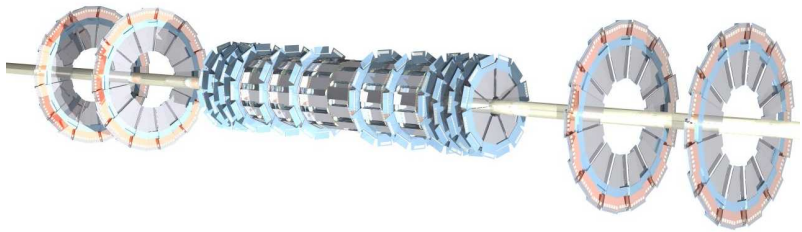

Figure 4.2: The DØ silicon vertex detector

The combined silicon vertex detector and central fiber tracker have excellent tracking performance. The full coverage of the entire combined detector extends out to $|\eta| = 1.6$. Tracks will be reconstructed with high efficiency ($\sim$ 95% in the central region) with a resolution of $\sigma_{p_T}/p_T^2 \sim 0.002$. The silicon detector disks allow efficient tracking out to an $|\eta|$ of 3.

4.3 Electromagnetic pre-shower detectors

Another important piece of the upgrade is the new pre-shower detectors attached to the inner surfaces of the calorimeter cryostats. These scintillating strip detectors greatly improve electron identification by providing a finer grain spatial match to the inner tracker than is obtained by the calorimeter alone. This reduces electron trigger backgrounds by a factor of 5-10. We will be able to trigger on electrons with p_T down to 1.5 GeV/c, and out to an $|\eta|$ of 2.5.

The calorimeter itself remains unchanged from its Run I configuration. It is a uranium-liquid argon sampling calorimeter with fine longitudinal and transverse segmentation, $\Delta\eta \times \Delta\phi = 0.1 \times 0.1$, that allows electromagnetic showers to be distinguished from hadronic jets. It has full coverage out to $|\eta| = 4$ with energy resolutions of $15\%/\sqrt{E}$ for electromagnetic showers and $80\%/\sqrt{E}$ for hadronic jets.

4.4 Muon Spectrometers

The central part of the muon system (covering the $|\eta| < 1$ range) includes 94 proportional drift tubes (PDT), barrel scintillator counters (A-PHI) and cosmic ray veto scintillator counters. There are three PDT layers (A, B, and C) with three or four 5-cm-thick, ±5-cm-wide drift cells per layer. A $r-\phi$ magnetic field, with an average magnitude of 16.7 kGauss, is contained in an iron toroid sandwiched between layers A and B of the PDT system. The A-PHI counters have nine segments in the z direction and 80 segments in the ϕ direction. There are 630 A-PHI counters in total.

The forward muon system (located at both endcaps) covers the η $[\pm 1, \pm 2]$ region of the DØ detector. It includes mini-drift tubes (MDT's with A, B, and C layers) with three or four decks of 1-cm square cells per layer. Iron toroids are located between the A and B layers of the MDT systems. The average magnitude of the field is 16.0 kGauss. Three layers of PIXEL scintillating counters, located next to corresponding MDT stations, have a 4.5° ϕ-segmentation and a 0.1 η-segmentation.

The upgraded muon system offers excellent efficiency, purity, and coverage. We are able to trigger on muons with p_T down to 1.5 GeV/c, and out to an $|\eta|$ of 2.

4.5 Trigger system

Significant upgrades to the trigger and data acquisition systems are also required to operate in the high luminosity ($L = 2 \times 10^{32}\text{cm}^{-2}\ \text{S}^{-1}$), high rate (7 MHz) environment of the upgraded TeVatron. The DØ Run II trigger consists of three levels.

4.5.1 Trigger levels

The first level (L1) trigger consists of signals from the axial layers of the CFT, the pre-shower detectors, the calorimeter, and the muon scintillators and tracking chambers. The level 1 trigger hardware for each of these systems examine the event and report information to an array of front-end digitizing crates which have sufficient memory to retain data from 32 crossings. Trigger decisions are made in less than 4.2 μs at this level, providing deadtimeless operation with a maximum accept rate of 10 kHz. Upon a level 1 trigger accept, the entire event is digitized and moved into a series of 16 event buffers to await a level 2 decision.

The level 2 (L2) trigger will reduce the L1 accept rate of 10 kHz by roughly a factor of 10 within 100 μs by correlating multi-detector objects in an event. In the first stage, or preprocessor stage, each detector system builds a list of trigger information. This information is then transformed into physics objects such as energy clusters or tracks. The time required for the formation of these objects is about 50 μs. These objects are then sent to the level 2 global processor where they are combined and trigger decisions are made. For example, spacial coorelations between tracking segments, pre-shower depositions, and calorimeter energy depostions may all be used to select electron candidates. The deadtime of the level 2 trigger is expected to be less than 5%.

The third and final stage (L3) of the trigger will reconstruct events in a farm of PC processors with a final accept rate of 50 Hz.

4.5.2 Level 1 muon triggers

DØ Level 1 muon trigger (L1MU) [3] identifies muon candidates by using combinatorial logic that makes use of tracks from L1 Central Fiber Tracker (L1CFT) trigger and hits from all muon detector elements: drift chambers and scintillation counters. The central, north and south regions of the detector are divided into octants. The L1MU triggers are formed locally in each octant. For the purpose of this report the L1MU trigger terms are labelled by two digits and two letters : L1MU(i, j, A, B).

- The first number refers to the number of muons requested:
- The second number corresponds to an approximate value of the muon p_T threshold in GeV/c. The nominal values are 2,4,7 and 11 GeV/c.
- The first letter refers to the covered η^μ region:
  - C = Central, with $|\eta^\mu| \leq 1$;
  - A = All, with $|\eta^\mu| \leq 1.6$;
  - X = eXtended, with $|\eta^\mu| \leq 2$.
- Finally, the second letter describes the muon tag criterium:
  - M stands for Medium tag, requiring a L1CFT track matched with the PDT or MDT centroids, and with at least one layer-scintillator confirmation.

– T stands for Tight tag, requiring a L1CFT track combined with the PDT or MDT centroids, and with a two layer-scintillator confirmation.

4.5.3 Level 1 muon trigger rates and efficiencies

Performance of various muon triggers was evaluated in Ref. [2]. For this analysis we concentrated on:

- the single muon trigger L1MU(1,4,A,T)
- and the dimuon trigger L1MU(2,2,A,M).

The η^μ coverage of both triggers extends to $\mid \eta^\mu \mid \leq 1.6$ and effective muon p_T thresholds are 2 GeV/c for the dimuon trigger and 4 GeV/c for the single muon trigger. Muons with $p_T > 1.5$ GeV/c have a chance to penetrate the calorimeter, muons with $p_T > 3.5$ GeV/c have a chance to be detected in the entire muon detector, including B and C layers outside of the toroid magnet.

To estimate the QCD trigger rates, we used the dijet ISAJET events generated in 6 p_T intervals (2–5, 5–10, 10–20, 40–80 and 80–500) with 1, 3, 5 or 7 additional minimum bias interactions (p_T between 1 and 100 GeV/c) per event. The background trigger rates were computed with the assumptions of an instantaneous luminosity of 2×10^{32} cm^{-2}s^{-1}, a beam crossing time interval of 132 ns and a dijet total cross section of 57 mb. Studies of Ref. [2] indicate that the expected Level 1 trigger rates at this instantaneous luminosity are approximately 400 Hz and 80 Hz for the L1MU(2,2,A,T) and L1MU(1,4,A,T) triggers, respectively. The event samples used in these studies contained about 1000 events each. Therefore some rate calculation could suffer from large fluctuation due to the small number of selected events. The absolute rates obtained from these samples could be underestimated by a factor up to two.

For the trigger efficiency studies we have used a sample of $B_d^0 \to K_s + J/\psi$ events processed through the latest version of D0GEANT and the trigger simulator. Trigger efficiencies are normalized to the numbers of events with $\mid \eta^\mu \mid < 1.6$ and kinematic cuts imposed on p_T^μ, and $p_T^{\mu\mu}$ as specified in the Table 4.1. A large difference between efficiencies for the L1MU(1,4,A,M) and L1MU(1,4,A,T) triggers reflects the fact that the "tight" tag condition requires two scintillator signals for each muon. This requirement reduces the geometrical acceptance of the trigger due to a limited coverage of the scintillating counters at the bottom of the detector.

The trigger rates at the instantenous luminosity of 2 $10^{32} cm^{-2} s^{-1}$ due to dimuons from the genuine $Q\bar{Q}$ signal are $\approx$ 13 Hz ($\approx$ 4 Hz for $p_T^{\mu\mu} > 5$ GeV/c). The 13 Hz combines contributions from: $c\bar{c}$ pair production (2.5 Hz), $b\bar{b}$ pair production (9.5 Hz) and $b \to J/\psi + X$ decays (1.0 Hz). A requirement of dimuon $p_T^{\mu\mu} > 2$ GeV/c reduces the rate to 9 Hz.

To estimate the contribution from J/ψ production to the single muon trigger rate, we normalized the relevant Monte Carlo samples ($b \to J/\psi + X$ and prompt J/ψ's) to the

$p_T^{\mu\mu}$	> 2.0 GeV/c	> 5.0 GeV/c	> 5.0 GeV/c
p_T^{μ}	> 1.5 GeV/c	> 1.5 GeV/c	> 3.0 GeV/c
L1MU(2,2,A,M)	27%	46%	57%
L1MU(1,4,A,M)	33%	69%	78%
L1MU(1,4,A,T)	15%	32%	49%
dimuon or single (M)	41%	71%	80%
dimuon or single (T)	32%	55%	67%

Table 4.1: Trigger efficiencies for dimuon events preselected with the kinematic cuts listed

CDF measurement of the J/ψ cross sections in the kinematic range $p_T^{J/\psi} > 5$ GeV/c and $\mid \eta(J/\psi) \mid < 0.6$ [5]. With this normalization we find that the irreducible L1 trigger rate for signal events is at least 4.0 Hz for prompt J/ψ's and 0.8 Hz for J/ψ's from b-quark decays (J/ψ with $p_T^{J/\psi} > 2$ GeV/c and $\mid \eta^{J/\psi} \mid < 1.5$).

4.5.4 Level 2 and Level 3 muon triggers

The second level of the muon trigger (L2MU) uses calibration and more precision timing information to improve the quality of muon candidates. Fast processors and a highly parallelized data pathway are the basis of the L3 muon trigger (L3MU). L3MU improves the resolution and the rejection efficiency of L2MU candidates. This is accomplished by performing local muon tracking, by adding inputs form the calorimeter and the sillicon micro-strip tracker (SMT) and by performing more analytical calculations on CFT tracks and PDT and A-PHI hits with the calibrated data. The performance of the L2MU and L3MU triggers has not been fully evaluated at the time of this writing.

In addition, we expect to have the STT (Silicon Tracker Trigger) preprocessor installed in the middle of 2002. The STT will be part of the Level 2 trigger and will provide an option of triggering on displaced vertices (impact parameter significance). It will also further improve momentum resolution of muon tracks.

The STT will allow to tag B decays using displaced secondary vertices or tracks with large impact parameters. The expected impact parameter resolution in the transverse plane can be parametrized as [2]:

$$\sigma^2(d_0) = (12.6\ \mu\mathrm{m})^2 + \left(\frac{36.6\ \mu\mathrm{m}\, GeV}{p \times \sin^{3/2}\theta} \right)^2 \qquad (4.1)$$

This dependence on particle momentum and polar angle is illustrated in Fig. 4.3.

In Fig. 4.4 we show the impact parameter significance, $S = d_0/\sigma(d_0)$, for the $B_d^0 \to K^{*\circ}\mu^+\mu^-$ decay products, under the condition that all four charged particles are produced with $p_T \geq 0.5$ GeV/c (muons with $p_T \geq 1.5$ GeV/c). On the average 1.8 particles from the $B_d^0 \to K^{*\circ}\mu^+\mu^-$ decay will have an impact parameter significance greater than 2.

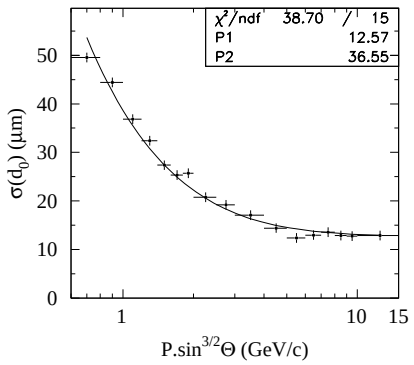

Figure 4.3: Expected impact parameter uncertainty dependence on track momentum and polar angle.

This number increases to 3.2 for events preselected by a request of a 400 μm transversal separation between primary and secondary vertices.

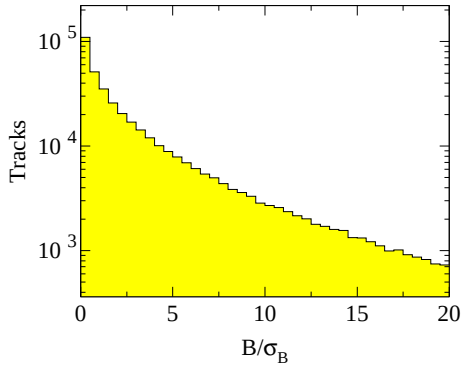

Figure 4.4: Significance distribution for STT tracks reconstructed in $B_d^0 \rightarrow K^{*\circ}\mu^+\mu^-$ events with all four charge particles produced with $p_T \geq 0.5$ GeV/c.

Therefore, once STT becomes operational, we intend to use a simple B tagging algorithm based on the number of tracks in the event with a significance greater than S_{min} to improve our Level 2 trigger rates for selecting $b\bar{b}$ events. The algorithm was tested on charged tracks with $p_T > 0.5$ GeV/c; $\mid \eta \mid < 1.6$; and with hits in at least 3 layers of the SVX [2]. As shown in Fig. 4.5 an efficiency of 50% can be achieved by requesting at least two tracks per event with an impact parameter significance greater than 2. Similarily, requiring at least one track with an impact parameter significance greater than 5 permits the reduction of

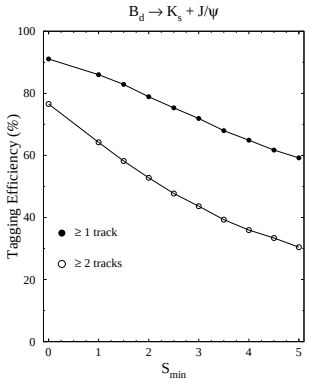

Figure 4.5: $b\bar{b}$ event tagging efficiency as a function of S_{min} with either one or two tracks in the event satisfying the condition $S > S_{min}$.

the background rate by a factor 10 while keeping 50% of the signal (assuming a primary vertex smearing of 30 μm).

Finally, we have studied the effect of the STT trigger on the separation of the J/ψ signal due to b-quark decays from the prompt J/ψ production. In case we need to suppress the prompt J/ψ signal, requiring at least one track with $\mid S_B \mid > 2.5$ provides a factor 7 reduction at the 30% cost to the non-prompt J/ψ signal.

4.5.5 Low p_T dielectron trigger

DØ has also introduced a dielectron trigger [4] aimed at detection of soft electron pairs, primarily from J/ψ dielectron decays. Level 1 electron candidates are selected with a transverse energy deposit $E_T > 2.0\ GeV$ in the EM calorimeter trigger towers, and with a low $p_T > 1.5$ GeV/c track coincident with a pre-shower cluster. The two "electrons" are required to have opposite signs and to match within a quadrant in ϕ with the EM deposits. In the forward rapidity region ($1.5 < |\eta| < 2.5$) the trigger is based on EM deposits and preshower clusters only, since no tracking coverage is available.

The dielectron Level 2 trigger is based on a refined spatial matching between tracks and 0.2×0.2 EM trigger towers as well as on the information on the EM fraction of the clusters and their isolation. Finally, invariant mass and angular criteria are applied to select J/ψ dielectron decays.

Efficiencies and rates for this trigger have been estimated using *ISAJET* generated events overlaid with 2 extra interactions. Trigger rates at the nominal Run II luminosity are expected to be below 1 kHz at Level 1 and about 150 Hz at Level 2. The expected yield of triggered $B_d^0 \rightarrow J/\psi\ K_s^0$ events is 15×10^3 for an integrated luminosity of $2\,\mathrm{fb}^{-1}$.

References

[1] S. Abachi *et al.* *"The DØ upgrade"*, DØNote 2542, http://www-d0.fnal.gov/hardware/upgrade/upgrade.html.

[2] F. Stichelbaut, M. Narain and A. Zieminski, *Triggers for B Physics Studies in Run II*, DØ note 3354 (December 1997).

[3] K. Jones *et al.*, http://hound.physics.arizona.edu/l1mu/l1mu.htm; C. Leonidopoulos (for the DØ Collab.) CHEP 2001 talk - in press.

[4] P. Grannis and A. Lucotte, *"Extending the sensitivity to sin(2β) in the $B^0/\bar{B}^0$ system using a low pt electron $J/\psi \to e^+e^-$ trigger at the upgrade DØ detector"*, DØ Note 3596 (1999).

[5] F. Abe *et al.*, CDF Collaboration, Phys. Rev. Lett. **76**, 4675 (1996).

[6] DØ RunII GEANT, http://www-d0.fnal.gov/newd0/d0atwork/computing/MonteCarlo/.

Chapter 5

The BTeV Detector

R. Kutschke, for the BTeV Collaboration [1]

5.1 Introduction

On May 15, 2000 the BTeV Collaboration submitted their proposal [2] to the Fermilab management and on June 27, 2000 the Fermilab director announced that BTeV experiment had been given Stage I approval. The information given in this chapter is abstracted from that proposal. Much additional information is available in the proposal, including the physics case for the experiment, a detailed description of the proposed detector, a description of the simulation tools used to evaluate the detector design, a summary of the physics reach, a cost estimate and extensive appendices.

This chapter will discuss the reasons for choosing a forward detector, followed by overviews of the detector, the simulation tools and the analysis software. Some illustrative results will also be included. As discussed in section 2.4 of this report, all BTeV event yields were computed under the presumption that the cross-section for $b\bar{b}$ production at the Tevatron is 100 μb. All effieciencies and background levels were computed for an average 2 interactions per beam crossing, which corresponds to a luminosity of $2{\times}10^{32}$ cm^{-2}s^{-1} and an interval of 132 ns between beam crossings.

5.2 Rationale for a Forward Detector at the Tevatron

The BTeV detector is a double arm forward spectrometer which covers from 10 to 300 mrad, with respect to the colliding beam axis.[1] It resembles a pair of fixed target detectors arranged back-to-back. In Section 2.1 of the BTeV proposal [2] the reasons for this choice are explained in detail; a summary is presented here.

According to QCD calculations of b quark production, there is a strong correlation between the B momentum and pseudorapidity, η. Near η of zero, $\beta\gamma \approx 1$, while at larger values of $|\eta|$, $\beta\gamma$ can easily reach values well beyond 6. This is important because the mean decay length increases with $\beta\gamma$ and, furthermore, the momenta of the decay products are larger, suppressing multiple scattering errors. As discussed in section 2.8.1 this is most important in the trigger.

[1] BTeV refers to both the proton direction and the antiproton directions as forward.

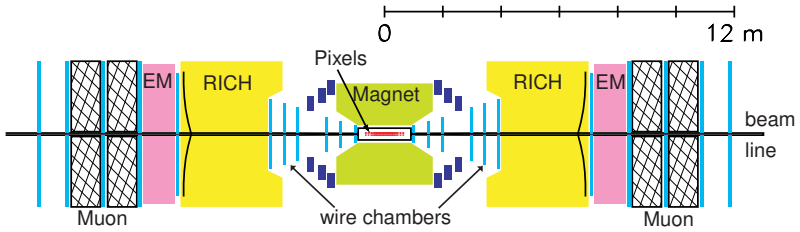

Figure 5.1: A sketch of the BTeV detector. The two arms are identical.

A crucially important attribute of $b\bar{b}$ production at hadron colliders is that the η of the b hadron and that of its companion $\bar{b}$ hadron are strongly correlated: when the decay products of a b-flavored hadron are within the acceptance of one arm of the spectrometer, the decay products of the accompanying $\bar{b}$ are usually within the acceptance of the *same* arm of the detector. This allows for reasonable levels of flavor tagging.

The long B decay length, the correlated acceptance for both b hadrons and the suppression of multiple scattering errors make the forward direction an ideal choice.

5.3 Detector Description

A sketch of the BTeV detector is shown in Fig. 5.1. The geometry is complementary to that used in current collider experiments. The detector looks similar to a fixed target experiment, but has two arms, one along the proton direction and the other along the antiproton direction.

The key design features of BTeV include:

- A dipole located on the IR, which gives BTeV an effective "two arm" acceptance;
- A precision vertex detector based on planar pixel arrays;
- A detached vertex trigger at Level 1 that makes BTeV efficient for most final states, including purely hadronic modes;
- Excellent particle identification using a Ring Imaging Cherenkov Detector (RICH);
- A high quality $PbWO_4$ electromagnetic calorimeter capable of reconstructing final states with single photons, π^o's, η's or η''s; it can also identify electrons;
- Precision downstream tracking using straw tubes and silicon microstrip detectors, which provide excellent momentum and mass resolution;
- Excellent identification of muons using a dedicated detector with the ability to supply a dimuon trigger; and

- A very high speed and high throughput data acquisition system which eliminates the need to tune the experiment to specific final states.

Each of these key elements of the detector is discussed in detail in Part II of the proposal [2] and is discussed briefly below.

5.3.1 Dipole Centered on the Interaction Region

A large dipole magnet, bending vertically and with a 1.6 T central field, is centered on the interaction region. This is the most compact way to provide momentum measurements in both arms of the spectrometer. Moreover the pixel detector is inside the magnetic field, which gives the Detached Vertex Trigger the capability of rejecting low momentum tracks. Such tracks undergo large multiple Coulomb scattering and might sometimes be misinterpreted as detached tracks.

5.3.2 The Pixel Vertex Detector

In the center of the magnet there is a silicon pixel vertex detector. This detector serves two functions: it is an integral part of the charged particle tracking system, providing accurate vertex information for the offline analysis; and it delivers very clean, precision space points to the BTeV vertex trigger.

BTeV has tested prototype pixel devices in a test beam at Fermilab. These devices consist of 50 μm $\times$ 400 μm pixel sensors bump-bonded to custom made electronics chips, developed at Fermilab. The position resolution achieved in the test beam is shown in Fig. 5.2; overlayed on that figure is resolution function used in the Monte Carlo simulation. The measured resolution is excellent and exceeds the requirement of 9 μm.

The critical quantity for a b experiment is L/σ_L, where L is the distance between the primary (interaction) vertex and the secondary (decay) vertex, and σ_L is its error. The efficacy of this geometry is illustrated by considering the distribution of the resolution on the B decay length, L, for the decay $B^o \to \pi^+\pi^-$. Fig. 5.3 shows the r.m.s. error in the decay length as a function of momentum; it also shows the momentum distribution of the B's accepted by BTeV. The following features are noteworthy:

- The B's used by BTeV peak at $p = 30$ GeV/c and average about 40 GeV/c.
- The mean decay length is equal to 450 μm $\times p/M_B$.
- The error on the decay length is smallest near the peak of the accepted momentum distribution. It increases at lower values of p, due to multiple scattering, and increases at larger values of p due to the smaller angles of the Lorentz-boosted decay products.

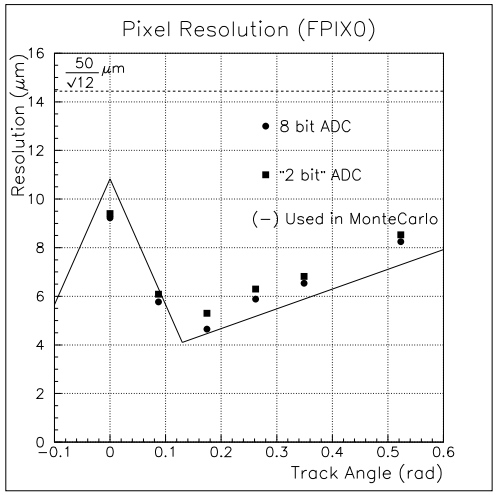

Figure 5.2: The resolution achieved in the test beam run using 50 μm wide pixels and an 8-bit ADC (circles) or a 2-bit ADC (squares), compared with the simulation (line).

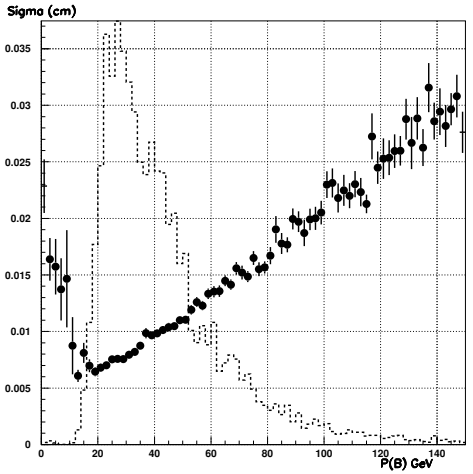

Figure 5.3: The B momentum distribution for $B^o \to \pi^+\pi^-$ events (dashed) and the error in decay length σ_L as a function of momentum.

Process	Eff. (%)
Minimum bias	1
$B_s \to D_s^+ K^-$	74
$B^0 \to D^{*+}\rho^-$	64
$B^0 \to \rho^0\pi^0$	56
$B^0 \to J/\psi K_s$	50
$B_s \to J/\psi K^{*o}$	68
$B^- \to D^0 K^-$	70
$B^- \to K_s\pi^-$	27
$B^0 \to$ 2-body modes	63
$(\pi^+\pi^-, K^+\pi^-, K^+K^-)$	

Table 5.1: Level 1 trigger efficiencies for minimum-bias events and for various processes of interest. For the minimum bias events the efficiency is quoted as a percentage of all events but for the signal channels the efficiencies are quoted as a percentage of those events which pass the offline analysis cuts. All trigger efficiencies are determined for an average of two interactions per crossing.

5.3.3 The Detached Vertex Trigger

It is impossible to record data from each of the 7.5 million beam crossings per second. A prompt decision, colloquially called a "trigger," must be made to record or discard the data from each crossing. The main BTeV trigger is provided by the silicon pixel detector. The Level 1 Vertex Trigger inspects every beam crossing and, using only data from the pixel detector, reconstructs the primary vertices and determines whether there are detached tracks which could signify a B decay. Since the b's are at high momentum, the multiple scattering of the decay products is minimized, allowing for triggering on detached heavy quark decay vertices.

With outstanding pixel resolution, it is possible to trigger efficiently at Level 1 on a variety of b decays. The trigger has been fully simulated, including the pattern recognition code. Table 5.1 summarizes the results of the trigger simulations. The trigger efficiencies are generally above 50% for the b decay states of interest and at the 1% level for minimum bias background. The efficiencies for signal channels are quoted as a percentage of events which pass the offline analysis cuts. This is an appropriate statistic because most of the b decays are not useful for doing physics: their decay products lie outside of the fiducial volume of the detector, their decay lengths are not long enough, their decay products can be ambiguously assigned to several candidate vertices and so on. Separate Monte Carlo runs were performed to measure overall event rates and bandwidth requirements and to ensure that the trigger is efficient for generic b and c decays.

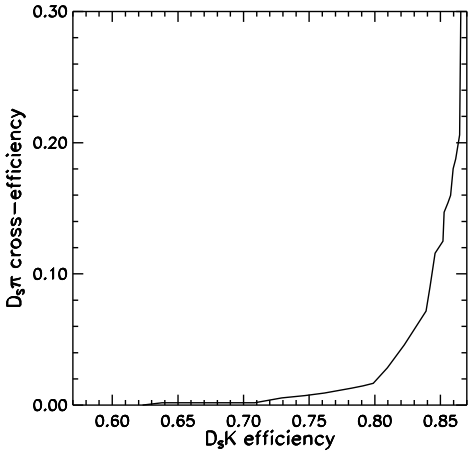

Figure 5.4: The efficiency to detect the fast K^- in the reaction $B_s \to D_s^+ K^-$ versus the rate to misidentify the π^- from $B_s \to D_s^+\pi^-$ as a K^-.

5.3.4 Charged Particle Identification

Charged particle identification is an absolute requirement for an experiment designed to study the decays of b and c quarks. The relatively open forward geometry has sufficient space to install a Ring Imaging Cherenkov detector (RICH), which provides powerful particle ID capabilities over a broad range of momentum. The BTeV RICH detector must separate pions from kaons and protons in a momentum range from 3 to 70 GeV/c. The lower momentum limit is determined by soft kaons useful for flavor tagging, while the higher momentum limit is given by two-body B decays. Separation is accomplished using a gaseous freon radiator to generate Cherenkov light in the optical frequency range. The light is then focused by mirrors onto Hybrid Photo-Diode (HPD) tubes. To separate kaons from protons below 10 GeV/c an aerogel radiator will be used.

As an example of the usefulness of this device, Fig. 5.4 shows the efficiency for detecting the K^- in the decay $B_s \to D_s^+ K^-$ versus the rejection for the π^- in the decay $B_s \to D_s^+\pi^-$. One sees that high efficiencies can be obtained with excellent rejections.

5.3.5 Electromagnetic Calorimeter

In BTeV, photons and electrons are detected when they create an electromagnetic shower in crystals of $PbWO_4$, a dense and transparent medium that produces scintillation light. The amount of light is proportional to the incident energy. The light is sensed by photomultiplier tubes (or possibly hybrid photodiodes). The crystals are 22 cm long and have a small transverse cross-section, 26 mm × 26 mm, providing excellent segmentation. The energy and position resolutions are exquisite,

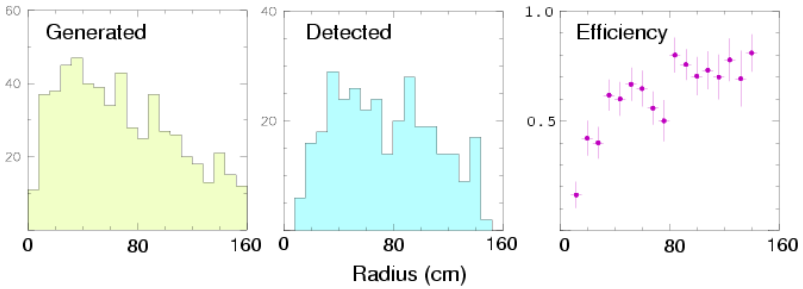

Figure 5.5: The radial distribution of generated and detected photons from $B^o \to K^*\gamma$ and the resulting efficiency. The detector response was simulated by GEANT and clusters of hit crystals were formed by the BTeV clustering software. This software is derived from software used for the Crystal Ball and CLEO experiments. The charged tracks from the K^* were required to hit the RICH. The simulation was run at 2 interactions/crossing.

$$\frac{\sigma_E}{E} = \sqrt{\frac{(1.6\%)^2}{E} + (0.55\%)^2}\ , \tag{5.1}$$

$$\sigma_x = \sqrt{\frac{(3500\ \mu m)^2}{E} + (200\ \mu m)^2}\ , \tag{5.2}$$

where E is in units of GeV. This leads to an r.m.s. π^o mass resolution between 2 and 5 MeV/c^2 over the π^o momentum range 1 to 40 GeV/c.

The crystals are designed to point at the center of the interaction region. They start at a radial distance of 10 cm with respect to the beam-line and extend out to 160 cm. They cover ∼210 mrad. This is smaller than the 300 mrad acceptance of the tracking detector; the choice was made to reduce costs. For most final states of interest, this leads to a loss of approximately 20% in signal.

At 2 interactions per crossing the calorimeter has a high rate close to the beam pipe, where the reconstruction efficiency and resolution is degraded by overlaps with other tracks and photons. As one goes out to larger radius, the acceptance becomes quite good. This can be seen by examining the efficiency to reconstruct the γ in the decay $B^o \to K^*\gamma$, $K^* \to K^-\pi^+$. For this study the decay products of the K^* are required to reach the RICH detector. Fig. 5.5 shows the radial distributions of the generated γ's, the reconstructed γ's and the γ efficiency. The shower reconstruction code, described in Chapter 12 of the proposal, was developed from that used for the CLEO CsI calorimeter; for reference, the efficiency of the CLEO barrel electromagnetic calorimeter is 89%.

5.3.6 Forward Tracking System

The other components of the charged-particle tracking system are straw-tube wire proportional chambers and, near the beam where occupancies are high, silicon microstrip detectors.

These devices are used primarily for track momentum measurement, K_s detection and the Level 2 trigger. These detectors measure the deflection of charged particles by the BTeV analyzing magnet and give BTeV excellent mass and momentum resolution for charged particle decay modes.

5.3.7 Muon Detection

Muon detection is accomplished by insisting that the candidate charged track penetrate several interaction lengths of magnetized iron and insuring that the momentum determined from the bend in the toroid matches that given by the main spectrometer tracking system. The muon system is also used to trigger on the dimuon decays of the J/ψ. This is important not only to gather more signal but as a cross check on the efficiency of the main trigger, the Detached Vertex Trigger.

5.3.8 Data Acquisition System

BTeV has a data acquisition system (DAQ) which is capable of recording a very large number of events. The full rate of B's whose decay products are in the detector is very high, over 1 kHz. The rate from direct charm is similar. Some other experiments are forced by the limitations of their data acquisition system to make very harsh decisions on which B events to accept. BTeV can record nearly all the potentially interesting B and charm candidates in its acceptance. Therefore it can address many topics that might be discarded by an experiment whose DAQ is more restrictive. Since nature has a way of surprising us, the openness of the BTeV trigger and the capability of the DAQ are genuine strengths which permit the opportunity to learn something new and unanticipated.

5.4 Simulation and Analysis Tools

The physics reach of BTeV has been established by an extensive and sophisticated program of simulations, which is described in detail in Part III of the BTeV proposal [2]. For this study $p\bar{p} \to b\bar{b}X$ events were generated using `PYTHIA` [3] and the b hadrons were decayed using `QQ`. These packages are discussed in chapter 2 of this report. To model the detector response to these events, two detector simulation packages have been used, BTeVGeant and MCFast. BTeVGeant is a GEANT [4] based simulation of the BTeV detector which contains a complete description of the BTeV geometry including the materials needed for cooling, support and readout. GEANT models all physical interactions of particles with material and allows us to see the effects of hard to calculate backgrounds. Most of the results presented in this report were obtained using BTeVGeant. Some of the results presented here, and all earlier BTeV results, were obtained using MCFast [5], a fast parameterized simulation environment which allows the user to quickly change the detector design without the need to do any coding. BTeVGeant writes an MCFast geometry file which describes the same detector in simplified fashion; in this way the number, size and resolution of detector elements is synchronized between the two simulation tools. MCFast models the most of the

processes that GEANT does, energy loss, multiple scattering, pair creation, bremstrahlung, and hadronic interactions, but in a simplified fashion; for example some of the detector components are described by simpler shapes, the model of multiple scattering is purely gaussian and the model of energy deposition in the calorimeter is parametric.

Chapter 13 of the proposal shows quantitative comparisons between MCFast and BTeVGeant. From these studies one sees that MCFast is a reliable tool for computing resolutions, efficiencies and the level of backgrounds which arise from real tracks; the slower, more complete, BTeVGeant is necessary when occupancies and event confusion are the critical issues.

In most circumstances the simulations are done at the hit level, not at the digitization level. That is, the simulation packages produce smeared measurements, not a stream of device addresses and digitized pulse heights thta simulate the raw, experimental data stream. Digitization level simulations have been done to address the issue of required bandwidth at various levels of the trigger and DAQ systems.

For some of the physics studies presented in this report very high statistics Monte Carlo runs were required to reliably estimate the background level. These studies were performed on a farm of 500 MHz dual Pentium III Linux machines; over a period of 3 months an average of about 30 machines (60 CPUs) per day were available. To give one example, over a period of about 1 month, 4.5 million generic $b\bar{b}$ events were produced to investigate backgrounds in the channel $B^0 \to \rho\pi$.

Brief descriptions of simulation and analysis software for some specific subsystems were given in section 5.3 of this report. References to the relevant TDR sections were also given. In order to make this report a little more stand alone, a few more details are given below.

5.4.1 Tracking and Track Fitting Software

In both packages the simulation code keeps track of which tracking hits were created by which particles. This information is not used by the trigger code, which does full pattern recognition, but it is used to check the results of the trigger package and to debug it. Both simulation packages smear pixel hits using resolution functions with non-gaussian tails that were measured in the test beam. Hits in the other tracking detectors are modeled with gaussian resolution functions.

In the offline analysis package no pattern recognition is done; instead the Monte Carlo truth table is used to collect all of the hits which belong on a track. Each hit list is then Kalman filtered to give the track parameters and their covariance matrix in the neighborhood of the interaction region. Extrapolating from the excellent performance of the pattern recognition in the trigger, the final pattern recognition codes are expected to be be highly efficient and to find few false tracks; therefore the approximation of perfect pattern recognition gives a reliable estimate of what BTeV will achieve.

5.4.2 Electromagnetic Calorimeter Software

BTeVGeant does a complete development of electromagnetic and hadronic showers in all materials and follows the products of these showers into neighbouring detector volumes. When a track or photon within a shower traverses one of the $PbWO_4$ crystals, BTeVGeant deposits energy from that track or photon in the crystal. The total energy deposited in crystal is summed over each beam crossing and a parametric function is then used to convert the total deposited energy into a measured energy plus the error on the measured energy. For each crystal, a record is kept of how much energy was deposited for which track. This information is only used to characterize and debug the reconstruction code — it is not used by the reconstruction code.

When modelling shower development, it is necessary to stop tracing new particles when their energy drops below some cut-off. If these cut-off values are set too high, then the showers are too narrow, resulting in artificially clean events and artificially good energy resolution. If, on the other hand, these cut-off values are set too low, then simulations are prohibitively slow. The studies done to resolve of these tradeoffs are discussed in detail in Section 12.1.5 of the BTeV proposal. The final result is that, because adequate CPU power was available, no significant compromises in the quality of the simulation were necessary.

MCFast does the same calorimeter bookkeeping as BTeVGeant but the model of shower development is parametric, rather than a detailed following of each generation of particles. Both packages create identical data structures so that the same shower reconstruction and user analysis codes will work on events from both simulation packages.

5.4.3 Trigger Simulation Software

Chapter 9 of the proposal describes the overall plan for the trigger and it describes in detail the algorithm for the Level 1 Detached Vertex Trigger. This algorithm has been coded in C and is callable from by user code within either BTeVGeant or MCFast. A few pieces of the code have been ported to the target DSP's and carefully timed. The rest is written in a high level language for ease of algorithm development.

Similarly a prototype for the Level 2 trigger has also been coded. Since Level 2 will run on standard processes, the code represents a true prototype, and is not just a clone of the algorithm.

The physics analyses presented in the BTeV Proposal [2] and in this report have been used as models for possible Level 3 algorithms.

The trigger results presented in Table 5.1, and the results presented in chapters 6 through 8 were obtained using this trigger simulation software.

5.4.4 RICH Software

For most of the results presented in this workshop, nominal RICH efficiencies and misidentification probabilities were used. It was assumed that if a reconstructed track contained a

hit in the chambers between the RICH and the EMCal, then that track could be identified by the RICH.

In a few selected analyses, notably, $B_s \to D_s K$, a more detailed simulation was used. For this analysis tracks passing through the RICH generated photons which were propagated through the aerogel and chamber gas and reflected from the mirror. They were then propagated to the detector plan where a model of the HPD efficiency was applied. A pattern recognition algorithm was then run to find Cherenkov rings from the list of HPD hits. Particle ID decisions were made using these reconstructed rings. The physics reach predicted by these simulations is presented in chapter 6.

5.5 Flavor Tagging

Section 2.6 of this report describes the flavor tagging strategies which are available to B physics experiments at the Tevatron. In Chapter 15 of the BTeV proposal presents a preliminary study of the tagging power which can be achieved with the BTeV detector. This section will summarize the results of that study. Mixing of the opposite side B meson has not yet been included in the results shown here. The upcoming sections describe the algorithms used for tagging, and tagging powers which they achieve are summarized in Table 5.2.

5.5.1 Away Side Tagging

Three different away side tagging methods have been studied, lepton tagging, kaon tagging and vertex charge tagging. The first step in all three methods is to select tracks which are detached from all primary vertices in the event. In events with multiple primary vertices, detached tracks are only considered if they are associated with the same primary vertex as is the signal candidate.

5.5.1.1 Lepton Tagging

The lepton tagging algorithm must deal with possible wrong-sign tags which result from the cascade $b \to c \to \ell^+$. Because leptons from $b \to \ell^-$ and $b \to c \to \ell^+$ have quite different transverse momentum (p_T) distributions, good separation can be achieved. If there was more than one lepton tag candidate in an event, the highest p_T lepton was chosen to be the tag.

Candidates for muon tags were selected from the detached track list if they had a momentum greater than 4.0 GeV/c. A tagging muon with $p_T > 1.0$ GeV/c was considered to be from the process $b \to \ell^-$, while one with $p_T < 0.5$ GeV/c was considered to be from the process $b \to c \to \ell^+$, thereby flipping the sign of the tag.

Candidates for electron tags were selected using a parametrized electron efficiency and hadron misidentification probability. The tagging lepton was required to have $p_T > 1.0$ GeV/c and was always assumed to come from the process $b \to \ell^-$. There were not enough MC events to study electrons from $b \to c \to \ell^+$.

5.5.1.2 Kaon Tagging

Because of the large branching ratio for $b \to c \to K^- X$, kaon tagging is the most potent tagging method at e^+e^- B factories. At BTeV, in which the multiplicity of the underlying event is much greater, excellence in both particle identification and vertex resolution is required to exploit kaon tagging. Both are strong points of the forward detector geometry.

Candidates for kaon tags were selected from the secondary track list if they were identified as kaons in the RICH detector. If there was more than one kaon tag candidate in an event, the kaon with the largest normalized impact parameter with respect to the primary vertex was selected.

5.5.1.3 Vertex Charge Tagging

In this method a search was made for a detached vertex which is consistent with being from the charged decay products of the other b. The charge of that vertex determines the charge of the b. When the opposite side b hadronizes into a $\bar{B}^0$ or a $\bar{B}^0_s$, the tagging vertex has a neutral charge and there is no useful vertex tagging information in the event. However this method has the advantage that it is not affected by mixing of the away side b.

Tracks from the secondary list were accepted provided they had $p_T > 100$ MeV/c and provided they had $\Delta\eta < 4$ with respect to the direction of the signal B^0 candidate. The tracks from the secondary list were sorted into candidate vertices and only vertices with a detachment of at least $1.0\,\sigma$ from the primary vertex were accepted. If more than one vertex was found in an event, the one with the highest transverse momentum was selected; if no secondary vertices passed the selection cuts and if there was at least one track with $p_T > 1.0$ GeV/c, then the highest p_T track was selected. If the charge of the selected vertex is non-zero, then it determines the flavor of the away side b.

This tagging method is similar to jet charge tagging used by other experiments but BTeV has not yet investigated the possibility of weighting the tracks by their momenta.

5.5.1.4 Combining Away Side Tagging Methods

In many events, several of the same side tagging methods may give results; moreover it can happen that two methods will give contradictory answers. BTeV has not yet optimized the method of combining all tagging information but have used the following simple algorithm. The methods were polled in decreasing order of dilution and the first method to give an answer was accepted. That is, if lepton tagging gave a result, the result was accepted; if not, and if kaon tagging gave a result, the kaon tag was accepted; if not, and if the vertex charge tagging gave a result, the vertex charge tag was accepted.

5.5.2 Same Side Tagging

BTeV has studied the power of same side kaon tagging for B_s mesons. For this study tracks were selected provided they had a momentum greater than 3.0 GeV/c, were identified as kaons in the RICH and had an impact parameter with respect to the primary vertex less than 2 σ. It was further required that the system comprising the B_s candidate plus the candidate tagging track have an invariant mass less than 7.0 GeV/c^2. If more than one track passed these cuts, then the track closest in ϕ to the B_s direction was selected.

For same side tagging of B_d events BTeV expects to use B^{**} decays. This study is at an early, conceptual stage. The flag in Pythia to turn on B^{**} production has not been used. Instead BTeV has used a sample of simulated $B \to \psi K_s$ decays and has selected events in which the B and the next pion in the generator track list have an invariant mass in the range 5.6 - 5.8 GeV/c^2. It was assumed that 30% of these events will come from B^{**} decays and therefore be right sign tags. The remainder 70% of the events were assumed to have an equal number of right sign and wrong sign tags.

5.5.3 Summary of Tagging

The results from the tagging study are summarized in Table 5.2. These results are preliminary and one should be aware that all algorithms have yet to exploit the full power available to them. In particular, the vertexing information has yet to be fully exploited. For example, the $b \to \ell^-$ and $b \to c \to \ell^+$ samples differ not only in their p_T spectra; they have distinctly different topological properties. Similarly, kaon tagging can be improved if there is evidence that the kaon comes from a tertiary vertex, indicative of the $b \to c \to K^-$ cascade. Finally, the vertex charge algorithm should expect to find two vertices on the away side, the b decay vertex and the c decay vertex; the charge of both vertices provides tagging power. Other tagging methods have yet to be studied such as using a D^* from the decay of the opposite side B. Finally, we have not yet explored the optimal use of the correlations among all of the methods. Therefore, the results quoted in Table 5.2 probably underestimate the tagging power of BTeV, even though they do not yet incorporate mixing on the away side. Therefore the BTeV results quoted in this report are presented using nominal values of $\epsilon = 0.7$ and $D = 0.37$, giving $\epsilon D^2 = 0.1$. The studies presented in the present chapter should be regarded as evidence that these nominal values lie well within the ultimate reach of the experiment.

5.6 Schedule

The BTeV program is an ambitious one. Its goal is to begin data taking in 2005/6. This timing is well-matched to the world B physics program. The e^+e^- B factories and the Fermilab collider experiments will have had several years of running, the first results in, and their significance thoroughly digested. It should be clear what the next set of goals is and BTeV will be guaranteed to be well-positioned to attack them. This schedule also gives BTeV a good opportunity to have a head start in its inevitable competition with LHC-b,

Tag Type	ϵ	D	ϵD^2
Muon	4.5%	0.66	2.0%
Electron	2.3%	0.68	1.0%
Kaon	18%	0.52	4.9%
Vertex Charge	32%	0.36	4.1%
Same Side Kaon	40%	0.26	2.6%
Same Side Pion	88%	0.16	2.2%
Total for B_s			14.6 %
Total for B_d			14.2 %
Total for B_s with overlaps	65%	0.37	8.9%

Table 5.2: Results of first generation studies of tagging power in BTeV. In the text it is discussed that these studies are incomplete and that they likely underestimate the tagging power which can be realized.

especially since BTeV can be installing and operating components of its detector in the collision hall well in advance of 2005. Finally, this schedule is sensibly related to BTeV's plan to conduct a rigorous R&D program which includes a sequence of engineering runs to test the technically challenging systems in the BTeV design. We believe that the scale of the BTeV construction effort is comparable to the scale of one of the current detector upgrades. The time scale is comparable as well.

5.7 Conclusions

BTeV is a powerful and precise scientific instrument capable of exquisite tests of the Standard Model. It has great potential to discover new physics via rare or CP violating decays of heavy quarks. Details of the physics reach of BTeV and can be found in chapters 6 through 9 of this report and a summary table can be found in the executive summary [6] of the BTeV Proposal.

References

[1] A list of the BTeV Collaboration can be found in Ref. [2].

[2] "Proposal for an Experiment to Measure Mixing, CP Violation and Rare Decays in Charm and Beauty Particle Decays at the Fermilab Collider — BTeV", Fermilab, May 2000. This is available at the URL, `http://www-btev.fnal.gov/public\_documents/btev\_proposal`.

[3] H. U. Bengtsson and T. Sjostrand, Comp. Phys. Comm. **46**, 43 (1987).

[4] GEANT: CERN Program Library Long Writeup W5013, `http://wwwinfo.cern.ch/asdoc/geant\_html3/geantall.html`.

[5] P. Avery *et al.*, "MCFast: A Fast Simulation Package for Detector Design Studies", in the Proceedings of the International Conference on Computing in High Energy Physics, Berlin, (1997). Documentation can be found at `http://www-cpd.fnal.gov/mcfast.html`.

[6] The executive summary is part of the BTeV Proposal, Ref. [2] and can be found separately on the BTeV Proposal web page.

Chapter 6

CP Violation

D. Atwood, S. Bailey, W. Bell, J. Butler, A. Cerri, S. Donati, A. Falk, S. Gardner, Y. Grossman, R. Jesik, P.A. Kasper, R. Kutschke, G. Majumder, P. Maksimović, Y. Nir, L. Nogach, M. Paulini, M. Petteni, M. Procario, G. Punzi, H. Quinn, K. Shestermanov, G. Signorelli, J. Silva, T. Skwarnicki, S. Stone, A. Vasiliev, B. Wicklund, F. Würthwein, J. Yarba, K. Yip

6.1 Introduction [†]

CP violation is still one of the least tested aspects of the Standard Model. Many extensions of the Standard Model predict that there are new sources of CP violation, beyond the single Kobayashi-Maskawa phase in the CKM mixing matrix for quarks. Considerations related to the observed baryon asymmetry of the Universe imply that such new sources must exist. The experimental study of CP violation is then highly motivated.

For 37 years, CP violation has only been observed in the neutral K-meson system. Very recently, the first observations of CP violation in the B-meson system have been reported by the e^+e^- B factories [1] providing the first tests of the Standard Model picture of CP violation. In the near future, more experimental tests will be performed including the Tevatron experiments. The greater the variety of CP violating observables measured, the more stringently will the Standard Model be tested. If deviations from the Standard Model predictions are observed, the information from different meson decays will provide crucial clues for the type of new physics that can account for such deviations.

This situation makes the search for CP violation in the B_s^0 decays highly interesting. B_s^0 mesons cannot be studied at the B-factories operating at the $\Upsilon(4S)$ resonance. Hadron colliders, on the other hand, with their high statistics, provide an opportunity to measure CP violation in the B_s^0 system with high accuracy in addition to allowing studies of certain B^0 modes.

In the context of the Standard Model, the main goal is to measure the phases of CKM elements accurately. These are conveniently described as angles of unitarity triangles. In particular, all relevant phases can be expressed in terms of two large angles,

$$\beta \equiv \arg\left(-\frac{V_{cd}V_{cb}^*}{V_{td}V_{tb}^*}\right), \qquad \gamma \equiv \arg\left(-\frac{V_{ud}V_{ub}^*}{V_{cd}V_{cb}^*}\right), \tag{6.1}$$

[†] Authors: A. Falk, Y. Grossman, Y. Nir, H. Quinn.

and two small angles,

$$\beta_s \equiv \arg\left(-\frac{V_{ts}V_{tb}^*}{V_{cs}V_{cb}^*}\right) = \mathcal{O}(\lambda^2), \qquad \beta_K \equiv \arg\left(-\frac{V_{cs}V_{cd}^*}{V_{us}V_{ud}^*}\right) = \mathcal{O}(\lambda^4), \tag{6.2}$$

where $\lambda = 0.22$ is the Wolfenstein parameter. CP violation in B_s^0 decays allows, in particular, a determination of γ and β_s.

Much of the following discussion is based on Refs. [2–4] where more details can be found.

6.1.1 B_s^0–$\bar{B}_s^0$ Mixing

Here we introduce only what is needed to define notations that are important for CP violation. B_s^0 mixing and measurements to determine it are discussed in Chapter 8. A B_s^0 meson is made from a b-type antiquark and an s-type quark, while the $\bar{B}_s^0$ meson is made of a b-type quark and an s-type antiquark. The heavy, B_s^H, and light, B_s^L, mass eigenstates can be written as linear combinations of B_s^0 and $\bar{B}_s^0$:

$$\begin{aligned} |B_s^L\rangle &= p|B_s^0\rangle + q|\bar{B}_s^0\rangle, \\ |B_s^H\rangle &= p|B_s^0\rangle - q|\bar{B}_s^0\rangle, \end{aligned} \tag{6.3}$$

with

$$|q|^2 + |p|^2 = 1. \tag{6.4}$$

In writing (6.3), we assume CPT conservation and use of part of the freedom to re-phase the meson states:

$$\begin{aligned} |B_s\rangle &\to e^{i\zeta}|B_s\rangle, \\ |\bar{B}_s\rangle &\to e^{i\bar{\zeta}}|\bar{B}_s\rangle. \end{aligned} \tag{6.5}$$

The mass difference Δm_s and width difference $\Delta\Gamma_s$ are defined as follows:

$$\Delta m_s \equiv M_H - M_L, \qquad \Delta\Gamma_s \equiv \Gamma_L - \Gamma_H, \tag{6.6}$$

so that $\Delta m_s > 0$ by definition and the Standard Model prediction is that $\Delta\Gamma_s > 0$. The average mass and width are given by

$$M_{B_s^0} \equiv \frac{M_H + M_L}{2}, \qquad \Gamma_s \equiv \frac{\Gamma_H + \Gamma_L}{2}. \tag{6.7}$$

It is useful to define dimensionless ratios x_s and y_s:

$$x_s \equiv \frac{\Delta m_s}{\Gamma_s}, \qquad y_s \equiv \frac{\Delta\Gamma_s}{2\Gamma_s}. \tag{6.8}$$

The time evolution of the mass eigenstates is simple, following from the fact that they have well defined masses and decay widths:

$$|B_s^H(t)\rangle = e^{-iM_Ht}\, e^{-\Gamma_H t/2}|B_s^H\rangle,$$
$$|B_s^L(t)\rangle = e^{-iM_Lt}\, e^{-\Gamma_L t/2}|B_s^L\rangle. \quad (6.9)$$

The time evolution of the strong interaction eigenstates is complicated and obeys a Schrödinger-like equation:

$$i\frac{d}{dt}\begin{pmatrix} B_s \\ \bar{B}_s \end{pmatrix} = \left(M - \frac{i}{2}\Gamma\right)\begin{pmatrix} B_s \\ \bar{B}_s \end{pmatrix}, \quad (6.10)$$

where M and Γ are Hermitian 2×2 matrices. The off-diagonal elements in these matrices are not invariant under the re-phasing (6.5),

$$M_{12} \to e^{i(\bar{\zeta}-\zeta)}M_{12}, \qquad \Gamma_{12} \to e^{i(\bar{\zeta}-\zeta)}\Gamma_{12}. \quad (6.11)$$

Therefore, physical parameters can only depend on $|M_{12}|$, $|\Gamma_{12}|$ and $\arg(M_{12}\Gamma_{12}^*)$. Indeed, the relations between the parameters in the mass eigenbasis and in the interaction eigenbasis can be written as follows:

$$(\Delta m_s)^2 - \frac{1}{4}(\Delta\Gamma_s)^2 = 4|M_{12}|^2 - |\Gamma_{12}|^2,$$
$$\Delta m_s \Delta\Gamma_s = -4\mathrm{Re}\,(M_{12}\Gamma_{12}^*), \quad (6.12)$$

and

$$\frac{q}{p} = -\frac{\Delta m_s + \frac{i}{2}\Delta\Gamma_s}{2M_{12} - i\Gamma_{12}}. \quad (6.13)$$

6.1.2 B_s^0 Decays

We define the decay amplitudes for B_s^0 and $\bar{B}_s^0$ into a final state f:

$$A_f \equiv \langle f|B_s^0\rangle, \qquad \bar{A}_f \equiv \langle f|\bar{B}_s^0\rangle. \quad (6.14)$$

In addition to their dependence on the re-phasing (6.5), these amplitudes are affected by re-phasing of $|f\rangle$,

$$|f\rangle \to e^{i\zeta_f}|f\rangle. \quad (6.15)$$

Under (6.5) and (6.15), we have

$$A_f \to e^{i(\zeta-\zeta_f)}A_f, \qquad \bar{A}_f \to e^{i(\bar{\zeta}-\zeta_f)}\bar{A}_f, \qquad q/p \to e^{i(\zeta-\bar{\zeta})}q/p. \quad (6.16)$$

We learn that of the three complex parameters, A_f, $\bar{A}_f$ and q/p, one can construct three real quantities,

$$|A_f|, \quad |\bar{A}_f|, \quad |q/p|, \quad (6.17)$$

and one phase, that is the phase of

$$\lambda_f \equiv \frac{q}{p}\frac{\bar{A}_f}{A_f}, \quad (6.18)$$

that are phase-convention independent and, consequently, could be observable. Note that $|\lambda_f| = |q/p| \times |\bar{A}_f/A_f|$ is not independent of the parameters of (6.17), but $\arg(\lambda_f)$ is.

6.1.3 CP Violation

The CP transformation interchanges B_s^0 and $\bar{B}_s^0$:[1]

$$CP|B_s^0\rangle = e^{i\xi}|\bar{B}_s^0\rangle, \qquad CP|\bar{B}_s^0\rangle = e^{-i\xi}|B_s^0\rangle. \quad (6.19)$$

The phase ξ is not invariant under the re-phasing (6.5),

$$\xi \to \xi + \zeta - \bar{\zeta}. \quad (6.20)$$

We also define $\bar{f}$ to be the CP conjugate state of f:

$$CP|f\rangle = e^{i\xi_f}|\bar{f}\rangle, \qquad CP|\bar{f}\rangle = e^{-i\xi_f}|f\rangle. \quad (6.21)$$

CP is a good symmetry if there exist some phases ξ and ξ_f such that the Lagrangian is left invariant under (6.19) and (6.21). For CP to be a good symmetry of the mixing process, it is required then that

$$M_{12}^* = e^{2i\xi}M_{12}, \qquad \Gamma_{12}^* = e^{2i\xi}\Gamma_{12}. \quad (6.22)$$

In terms of the observable parameters in Eq. (6.17), this gives the condition

$$|q/p| = 1. \quad (6.23)$$

For CP to be a good symmetry of the decay processes, it is required that

$$\bar{A}_{\bar{f}} = e^{i(\xi_f-\xi)}A_f, \qquad A_{\bar{f}} = e^{i(\xi_f+\xi)}\bar{A}_f. \quad (6.24)$$

In terms of the observable parameters in Eq. (6.17), this results in the condition

$$|\bar{A}_{\bar{f}}/A_f| = |\bar{A}_f/A_{\bar{f}}| = 1. \quad (6.25)$$

Finally, for CP to be a good symmetry of processes that involve both mixing and decay, it is required that

$$\lambda_f\lambda_{\bar{f}} = 1. \quad (6.26)$$

For final CP eigenstates f_{CP}, such that $|\bar{f}_{CP}\rangle = \pm|f_{CP}\rangle$, the condition (6.26) translates into $|\lambda_{f_{CP}}| = 1$, which just combines (6.23) and (6.25), and

$$\mathrm{Im}\,\lambda_{f_{CP}} = 0. \quad (6.27)$$

Violation of each of the three conditions for CP symmetry, (6.23), (6.25) and (6.27), corresponds to a different type of CP violation:

1. CP violation in mixing, which occurs when the B_s^H and B_s^L mass eigenstates cannot be chosen to be CP eigenstates:

$$|q/p| \neq 1. \quad (6.28)$$

[1] Unless specified otherwise we use the phase convention $\xi = \pi$ throughout this report, see Sect. 1.3.1.

2. CP violation in decay, when the $B_s^0 \to f$ and $\bar{B}_s^0 \to \bar{f}$ decay amplitudes have different magnitudes:

$$|\bar{A}_{\bar{f}}/A_f| \neq 1. \tag{6.29}$$

3. CP violation in interference between decays with and without mixing, which occurs in decays into final states that are common to B_s^0 and $\bar{B}_s^0$:

$$\mathrm{Im}\,(\lambda_f \lambda_{\bar{f}}) \neq 0. \tag{6.30}$$

In particular, for final CP eigenstates,

$$\mathrm{Im}\,\lambda_{f_{CP}} \neq 0. \tag{6.31}$$

The effects of CP violation in mixing in the B_s^0 system are small. The lower bound on Δm_s [5] as of August 2001,

$$\Delta m_s \geq 14.6\ \mathrm{ps}^{-1}, \tag{6.32}$$

and the measured B_s^0 lifetime [6],

$$\tau(B_s^0) = (1.46 \pm 0.06)\ \mathrm{ps}, \tag{6.33}$$

imply that $|\Gamma_{12}/M_{12}| \leq \mathcal{O}(0.05)$. For $|\Gamma_{12}/M_{12}| \ll 1$, we have (see (6.13))

$$\left|\frac{q}{p}\right| - 1 = -\frac{1}{2}\mathrm{Im}\left(\frac{\Gamma_{12}}{M_{12}}\right). \tag{6.34}$$

Therefore, experimental data give $|q/p| - 1 \leq \mathcal{O}(0.1)$. Moreover, Γ_{12} comes from long distance contributions, where effects of new physics are expected to be negligible. Consequently, the Standard Model calculation of Γ_{12} [7], which yields values of $\Delta\Gamma_s/\Gamma_s$ between $\mathcal{O}(0.15)$ [8] and $\mathcal{O}(0.05)$ [9], is expected to hold model independently. Within the Standard Model, $\mathrm{Im}\,(\Gamma_{12}/M_{12})$ is further suppressed by the smallness of β_s, the relative phase between Γ_{12} and M_{12} defined in Eq. (6.2). We conclude that the deviation of $|q/p|$ from unity is very small:

$$\mathrm{Im}\,(\Gamma_{12}/M_{12}) \begin{cases} \leq \mathcal{O}(10^{-2}) & \text{model independent,} \\ = \mathcal{O}(10^{-4}) & \text{standard model.} \end{cases} \tag{6.35}$$

We can therefore safely neglect CP violation in mixing, and we do so from here on.

6.1.4 Tagged Decays

We consider the time evolution of a state $|B_s(t)\rangle$ ($|\bar{B}_s(t)\rangle$) which was tagged as $|B_s\rangle$ ($|\bar{B}_s\rangle$) at time $t = 0$. The time evolution can be read from Eqs. (6.3) and (6.9):

$$\begin{aligned} |B_s(t)\rangle &= g_+(t)|B_s\rangle + (q/p)g_-(t)|\bar{B}_s\rangle, \\ |\bar{B}_s(t)\rangle &= (p/q)g_-(t)|B_s\rangle + g_+(t)|\bar{B}_s\rangle, \end{aligned} \tag{6.36}$$

where

$$g_\pm(t) \equiv \frac{1}{2}\left(e^{-iM_L t}e^{-\Gamma_L t/2} \pm e^{-iM_H t}e^{-\Gamma_H t/2}\right). \tag{6.37}$$

Then, we get the following decay rates:

$$\begin{aligned} \Gamma[B_s(t) \to f] &= |A_f|^2\left\{|g_+(t)|^2 + |\lambda_f|^2|g_-(t)|^2 + 2\mathrm{Re}\left[\lambda_f g_+^*(t)g_-(t)\right]\right\}, \\ \Gamma[B_s(t) \to \bar{f}] &= |\bar{A}_{\bar{f}}|^2\left|\frac{q}{p}\right|^2\left\{|g_-(t)|^2 + |\lambda_{\bar{f}}^{-1}|^2|g_+(t)|^2 + 2\mathrm{Re}\left[\lambda_{\bar{f}}^{-1}g_+(t)g_-^*(t)\right]\right\}, \\ \Gamma[\bar{B}_s(t) \to f] &= |A_f|^2\left|\frac{p}{q}\right|^2\left\{|g_-(t)|^2 + |\lambda_f|^2|g_+(t)|^2 + 2\mathrm{Re}\left[\lambda_f g_+(t)g_-^*(t)\right]\right\}, \\ \Gamma[\bar{B}_s(t) \to \bar{f}] &= |\bar{A}_{\bar{f}}|^2\left\{|g_+(t)|^2 + |\lambda_{\bar{f}}^{-1}|^2|g_-(t)|^2 + 2\mathrm{Re}\left[\lambda_{\bar{f}}^{-1}g_+^*(t)g_-(t)\right]\right\}. \end{aligned} \tag{6.38}$$

Assuming $|q/p| = 1$, we find

$$\begin{aligned} \mathcal{A}_f(t) &= \frac{\Gamma[\bar{B}_s(t) \to f] - \Gamma[B_s(t) \to f]}{\Gamma[\bar{B}_s(t) \to f] + \Gamma[B_s(t) \to f]} \\ &= -\frac{(1 - |\lambda_f|^2)\cos(\Delta m_s t) - 2\,\mathrm{Im}\,\lambda_f \sin(\Delta m_s t)}{(1 + |\lambda_f|^2)\cosh(\Delta\Gamma_s t/2) - 2\,\mathrm{Re}\,\lambda_f \sinh(\Delta\Gamma_s t/2)}. \end{aligned} \tag{6.39}$$

Consider cases where the decay amplitudes are each dominated by a single weak phase. Then

$$|A_f| = |\bar{A}_{\bar{f}}|, \qquad |A_{\bar{f}}| = |\bar{A}_f|, \tag{6.40}$$

and

$$\lambda_f = |\lambda_f|e^{i(\phi_f + \delta_f)}, \qquad \lambda_{\bar{f}}^{-1} = |\lambda_f|e^{i(-\phi_f + \delta_f)}, \tag{6.41}$$

where ϕ_f (δ_f) is the relevant weak (strong) phase. Eqs. (6.38) can be rewritten for this case as follows:

$$\begin{aligned} \Gamma[B_s(t) \to f] &= \frac{|A_f|^2 e^{-\Gamma_s t}}{2}\Big\{(1 + |\lambda_f|^2)\cosh(\Delta\Gamma_s t/2) + (1 - |\lambda_f|^2)\cos(\Delta m_s t) \\ &\quad -2|\lambda_f|\cos(\delta_f + \phi_f)\sinh(\Delta\Gamma_s t/2) - 2|\lambda_f|\sin(\delta_f + \phi_f)\sin(\Delta m_s t)\Big\}, \\ \Gamma[B_s(t) \to \bar{f}] &= \frac{|A_f|^2 e^{-\Gamma_s t}}{2}\Big\{(1 + |\lambda_f|^2)\cosh(\Delta\Gamma_s t/2) - (1 - |\lambda_f|^2)\cos(\Delta m_s t) \\ &\quad -2|\lambda_f|\cos(\delta_f - \phi_f)\sinh(\Delta\Gamma_s t/2) + 2|\lambda_f|\sin(\delta_f - \phi_f)\sin(\Delta m_s t)\Big\}, \\ \Gamma[\bar{B}_s(t) \to f] &= \frac{|A_f|^2 e^{-\Gamma_s t}}{2}\Big\{(1 + |\lambda_f|^2)\cosh(\Delta\Gamma_s t/2) - (1 - |\lambda_f|^2)\cos(\Delta m_s t) \\ &\quad -2|\lambda_f|\cos(\delta_f + \phi_f)\sinh(\Delta\Gamma_s t/2) + 2|\lambda_f|\sin(\delta_f + \phi_f)\sin(\Delta m_s t)\Big\}, \\ \Gamma[\bar{B}_s(t) \to \bar{f}] &= \frac{|A_f|^2 e^{-\Gamma_s t}}{2}\Big\{(1 + |\lambda_f|^2)\cosh(\Delta\Gamma_s t/2) + (1 - |\lambda_f|^2)\cos(\Delta m_s t) \\ &\quad -2|\lambda_f|\cos(\delta_f - \phi_f)\sinh(\Delta\Gamma_s t/2) - 2|\lambda_f|\sin(\delta_f - \phi_f)\sin(\Delta m_s t)\Big\}. \end{aligned} \tag{6.42}$$

When the final state is a CP eigenstate, CP symmetry requires $\lambda_{f_{CP}} = \eta_f = \pm 1$, where η_f is the CP parity of the final state. Since the ratio (6.39) vanishes for $\lambda_f = \pm 1$, we conclude that $\mathcal{A}_{f_{CP}}$ is an appropriate definition of the CP asymmetry in the $B_s^0 \to f_{CP}$ decay.

When the decay process into a final CP eigenstate is dominated by a single CP violating phase or by a single strong phase, we have no CP violation in decay, $|\bar{A}_{f_{CP}}/A_{f_{CP}}| = 1$. Consequently, for such modes, CP violation is purely a result of interference between decays with and without mixing and the expression for the CP asymmetry simplifies considerably:

$$\begin{aligned}\mathcal{A}_{f_{CP}}(t) &= \frac{\Gamma[\bar{B}_s(t)\to f_{CP}]-\Gamma[B_s(t)\to f_{CP}]}{\Gamma[\bar{B}_s(t)\to f_{CP}]+\Gamma[B_s(t)\to f_{CP}]} \\ &= \frac{\mathrm{Im}\,\lambda_{f_{CP}}\sin(\Delta m_s t)}{\cosh(\Delta\Gamma_s t/2)-\mathrm{Re}\,\lambda_{f_{CP}}\sinh(\Delta\Gamma_s t/2)}. \end{aligned} \tag{6.43}$$

Experimentally, the value of $y_s \equiv \Delta\Gamma_s/(2\Gamma_s)$ is not yet known. As long as experimental errors are large compared to $\Delta\Gamma_s/\Gamma_s$, it is valid to use the simpler formulae that apply for the case $y_s = 0$. In this approximation using, for consistency, $|q/p| = 1$, Eqs. (6.38) simplify as follows:

$$\begin{aligned}
\Gamma[B_s(t)\to f] &= |A_f|^2 e^{-\Gamma_s t}\left\{\cos^2\!\left(\frac{\Delta m_s}{2}t\right)+|\lambda_f|^2\sin^2\!\left(\frac{\Delta m_s}{2}t\right)-\mathrm{Im}\,(\lambda_f)\sin(\Delta m_s t)\right\},\\
\Gamma[B_s(t)\to \bar{f}] &= |\bar{A}_{\bar{f}}|^2 e^{-\Gamma_s t}\left\{\sin^2\!\left(\frac{\Delta m_s}{2}t\right)+|\lambda_{\bar{f}}^{-1}|^2\cos^2\!\left(\frac{\Delta m_s}{2}t\right)+\mathrm{Im}\,(\lambda_{\bar{f}}^{-1})\sin(\Delta m_s t)\right\},\\
\Gamma[\bar{B}_s(t)\to f] &= |A_f|^2 e^{-\Gamma_s t}\left\{\sin^2\!\left(\frac{\Delta m_s}{2}t\right)+|\lambda_f|^2\cos^2\!\left(\frac{\Delta m_s}{2}t\right)+\mathrm{Im}\,(\lambda_f)\sin(\Delta m_s t)\right\},\\
\Gamma[\bar{B}_s(t)\to \bar{f}] &= |\bar{A}_{\bar{f}}|^2 e^{-\Gamma_s t}\left\{\cos^2\!\left(\frac{\Delta m_s}{2}t\right)+|\lambda_{\bar{f}}^{-1}|^2\sin^2\!\left(\frac{\Delta m_s}{2}t\right)-\mathrm{Im}\,(\lambda_{\bar{f}}^{-1})\sin(\Delta m_s t)\right\}.
\end{aligned} \tag{6.44}$$

If, in addition, Eqs. (6.40) and (6.41) hold, that is for decay channels that are dominated by a single weak phase, the expressions (6.44) for the decay rates are further simplified:

$$\begin{aligned}
\Gamma[B_s(t)\to f] &= |B_f|^2 e^{-\Gamma_s t}\left\{1+a_{\rm dir}\cos(\Delta m_s t)-\sqrt{1-a_{\rm dir}^2}\,\sin(\phi_f+\delta_f)\sin(\Delta m_s t)\right\},\\
\Gamma[B_s(t)\to \bar{f}] &= |B_f|^2 e^{-\Gamma_s t}\left\{1-a_{\rm dir}\cos(\Delta m_s t)-\sqrt{1-a_{\rm dir}^2}\,\sin(\phi_f-\delta_f)\sin(\Delta m_s t)\right\},\\
\Gamma[\bar{B}_s(t)\to f] &= |B_f|^2 e^{-\Gamma_s t}\left\{1-a_{\rm dir}\cos(\Delta m_s t)+\sqrt{1-a_{\rm dir}^2}\,\sin(\phi_f+\delta_f)\sin(\Delta m_s t)\right\},\\
\Gamma[\bar{B}_s(t)\to \bar{f}] &= |B_f|^2 e^{-\Gamma_s t}\left\{1+a_{\rm dir}\cos(\Delta m_s t)+\sqrt{1-a_{\rm dir}^2}\,\sin(\phi_f-\delta_f)\sin(\Delta m_s t)\right\},
\end{aligned} \tag{6.45}$$

where

$$B_f = \frac{1}{2}(1+|\lambda_f|^2)A_f, \qquad a_{\rm dir} = \frac{1-|\lambda_f|^2}{1+|\lambda_f|^2}. \tag{6.46}$$

Finally, if f in (6.45) is a CP eigenstate, then

$$|A_{f_{CP}}| = |\bar{A}_{f_{CP}}|, \qquad |\lambda_{f_{CP}}| = 1, \qquad \delta_{f_{CP}} = 0. \tag{6.47}$$

Consequently, we get:

$$\begin{aligned}
\Gamma[B_s(t)\to f_{CP}] &= |A_{f_{CP}}|^2 e^{-\Gamma t}\left\{1-\sin(\phi_{f_{CP}})\sin(\Delta m_s t)\right\},\\
\Gamma[\bar{B}_s(t)\to f_{CP}] &= |A_{f_{CP}}|^2 e^{-\Gamma t}\left\{1+\sin(\phi_{f_{CP}})\sin(\Delta m_s t)\right\}.
\end{aligned} \tag{6.48}$$

The CP asymmetry defined in Eq. (6.43) is then given by

$$\begin{aligned}
\mathcal{A}_{f_{CP}}(t) &= -\mathrm{Im}\,\lambda_{f_{CP}}\sin(\Delta m_s t),\\
\mathrm{Im}\,\lambda_{f_{CP}} &= \sin\phi_{f_{CP}}.
\end{aligned} \tag{6.49}$$

6.1.5 Untagged Decays

The expectation that $y_s \equiv \Delta\Gamma_s/(2\Gamma_s)$ is not negligible, opens up the interesting possibility to learn about CP violation from untagged B_s^0 decays [10]. The untagged decay rates are given by

$$\begin{aligned}
\Gamma_f(t) &\equiv \Gamma[B_s(t)\to f]+\Gamma[\bar{B}_s(t)\to f]\\
&= \frac{1}{2}|A_f|^2 e^{-\Gamma_s t}\left\{\left(1+\left|\frac{p}{q}\right|^2\right)\left[\left(1+|\lambda_f|^2\right)\cosh\frac{\Delta\Gamma_s t}{2}-2\mathrm{Re}\,\lambda_f\sinh\frac{\Delta\Gamma_s t}{2}\right]\right.\\
&\quad\left.+\left(1-\left|\frac{p}{q}\right|^2\right)\left[\left(1-|\lambda_f|^2\right)\cos(\Delta m_s t)-2\mathrm{Im}\,\lambda_f\sin(\Delta m_s t)\right]\right\}\\
&= |A_f|^2 e^{-\Gamma_s t}\left[\left(1+|\lambda_f|^2\right)\cosh\frac{\Delta\Gamma_s t}{2}-2\mathrm{Re}\,\lambda_f\sinh\frac{\Delta\Gamma_s t}{2}\right],
\end{aligned} \tag{6.50}$$

where for the last equality we used $|q/p| = 1$.

Consider now the case of an untagged decay into a final CP eigenstate. For channels that are dominated by a single weak phase, we have $|\lambda_{f_{CP}}| = 1$. For time $t \lesssim 1/\Gamma_s$, we can rewrite (6.50) to first order in y_s:

$$\Gamma_f(t) = 2|A_f|^2 e^{-\Gamma_s t}\left[1-y_s\mathrm{Re}\,\lambda_f(\Gamma_s t)\right]. \tag{6.51}$$

The sensitivity to CP violation is through the dependence on $\mathrm{Re}\,\lambda_{f_{CP}}$, and therefore requires that y_s is not very small.

6.1.6 Some Interesting Decay Modes

In this section we describe several B_s^0 decay channels that will provide useful information on CP violation. We give examples of CP violation in the interference of decays with and without mixing for both final CP eigenstates and final non CP eigenstates, and CP violation in decay for final CP eigenstates. We do not discuss CP violation in mixing in semileptonic decays, because the effect is expected to be very small. A recent review of many interesting aspects of CP violation in B_s^0 decays can be found in [11].

6.1.6.1 $B_s^0 \to J/\psi\phi$

The CP asymmetry in the $B_s^0 \to J/\psi\phi$ decay is subject to a clean theoretical interpretation because it is dominated by CP violation in interference between decays with and without mixing. The branching ratio has been measured [12]:

$$\mathcal{B}(B_s^0 \to J/\psi\phi) = (9.3 \pm 3.3) \times 10^{-4}. \tag{6.52}$$

The quark sub-process $\bar{b} \to \bar{c}c\bar{s}$ is dominated by the W-mediated tree diagram:

$$\frac{\bar{A}_{J/\psi\phi}}{A_{J/\psi\phi}} = -\eta_{J/\psi\phi}\left(\frac{V_{cb}V_{cs}^*}{V_{cb}^*V_{cs}}\right). \tag{6.53}$$

The penguin contribution carries a phase that is similar to (6.53) up to effects of $\mathcal{O}(\lambda^2) \sim 0.04$. Hadronic uncertainties enter the calculation then only at the level of a few percent.

Note that since J/ψ and ϕ are vector-mesons, the CP parity of the final state, $\eta_{J/\psi\phi}$, depends on the relative angular momentum, and the asymmetry may be diluted by the cancellation between even- and odd-CP contributions. It is possible to use the angular distribution of the final state to separate the CP parities. The decay may be dominated by the CP even final state. If this is established, the CP asymmetry is more readily interpreted.

As concerns the mixing parameters, the Standard Model gives

$$\frac{q}{p} = -\left(\frac{V_{ts}V_{tb}^*}{V_{ts}^*V_{tb}}\right). \tag{6.54}$$

Deviations from a pure phase are of $\mathcal{O}(10^{-4})$ and were neglected in (6.54).

Combining (6.53) and (6.54) into (6.18), we find

$$\mathrm{Im}\,\lambda_{J/\psi\phi} = (1 - 2f_{\rm odd})\sin 2\beta_s\,, \tag{6.55}$$

where β_s is defined in Eq. (6.2) and $f_{\rm odd}$ is the fraction of CP odd final states. We learn the following:

(i) A measurement of the CP asymmetry in $B_s^0 \to J/\psi\phi$ will determine the value of the very important CKM phase β_s (see (6.43) or (6.49)) [13].

(ii) The asymmetry is small, of order of a few percent, and may be even further diluted by cancellation between CP odd and CP even contributions.

(iii) An observation of an asymmetry that is significantly larger than $\mathcal{O}(\lambda^2)$ will provide an unambiguous signal for new physics. Specifically, it is likely to be related to new, CP violating contributions to B_s^0-$\bar{B}_s^0$ mixing [14].

6.1.6.2 $B_s^0 \to J/\psi K_S^0$

Interference between tree and penguin contributions to B_s^0 decays is often sensitive to the CKM phase γ of Eq. (6.1). Since the angle γ is much more difficult to determine than β

($\sin 2\beta$ will be determined cleanly from the CP asymmetry in $B^0 \to J/\psi K_S^0$), the sensitivity of B_s^0 decays to this angle is highly interesting. On the other hand, since this interference effect is a manifestation of CP violation in decay, its calculation involves hadronic parameters that are poorly known. It is possible, however, to use various B^0 decays that are related by flavour $SU(3)$ symmetry to the corresponding B_s^0 decays to determine both γ and the hadronic parameters. More precisely, the relevant symmetry is U-spin, that is an $SU(2)$ subgroup that interchanges d and s quarks. U-spin breaking effects, like all $SU(3)$ breaking effects, are not particularly small ($\sim m_K/\Lambda_{\chi SB}$) or well known, and will limit the accuracy of this determination. Note, however, that since the s and d quarks have both charge $-1/3$, electroweak penguins do not break this symmetry.

Proposals for such a determination of CKM phases and hadronic parameters have been made for $\bar{b} \to \bar{c}c\bar{d}(\bar{s})$ decays, such as $B_s^0 \to J/\psi K_S^0$ ($B^0 \to J/\psi K_S^0$) [15], for $\bar{b} \to \bar{c}c\bar{s}(\bar{d})$ decays, such as $B_s^0 \to D_s^+ D_s^-$ ($B^0 \to D^+D^-$) [15], and for $\bar{b} \to \bar{u}u\bar{s}(\bar{d})$ decays, such as $B_s^0 \to K^+K^-$ ($B^0 \to \pi^+\pi^-$) [16]. To demonstrate the sensitivity of B_s^0 decays to γ and the need to use additional information to overcome the hadronic uncertainties, we will discuss the $B_s^0 \to J/\psi K_S^0$ mode and mention only very briefly the other two channels.

Measuring CP violation in the $B_s^0 \to J/\psi K_S^0$ decay will be useful for the extraction of the CKM phase γ and will provide an estimate of the size of penguin uncertainties in the extraction of β from $B^0 \to J/\psi K_S^0$ [15]. There is no experimental information on this mode yet. Theoretical estimates give

$$\mathcal{B}(B_s^0 \to J/\psi K_S^0) = \mathcal{O}(2 \times 10^{-5}). \tag{6.56}$$

The quark sub-process, $\bar{b} \to \bar{c}c\bar{d}$ has contributions from a tree diagram with a CP violating phase $\arg(V_{cb}^*V_{cd})$, and three types of penguin diagrams with CP violating phases $\arg(V_{qb}^*V_{qd})$, for $q = u, c, t$. Using CKM unitarity, one can write

$$\frac{\bar{A}_{J/\psi K_S^0}}{A_{J/\psi K_S^0}} = -\eta_{J/\psi K_S^0}\left(\frac{A_1V_{cb}V_{cd}^* + A_2e^{i\theta}V_{ub}V_{ud}^*}{A_1V_{cb}^*V_{cd} + A_2e^{i\theta}V_{ub}^*V_{ud}}\right)\left(\frac{V_{ud}V_{us}^*}{V_{ud}^*V_{us}}\right). \tag{6.57}$$

Here, A_1 and A_2 are real and θ is the relative strong phase shift. The last factor on the right hand side of Eq. (6.57) comes from K-$\bar{K}$ mixing, since that is essential in producing a K_S^0 meson from the outgoing K^0 and $\bar{K}^0$ mesons. The small measured value of ϵ_K guarantees that this factor is essentially model independent [14].

Since A_2/A_1 is not particularly small, and there is no reason to assume that θ is small, $|\lambda_{J/\psi K_S^0}| = |\bar{A}_{J/\psi K_S^0}/A_{J/\psi K_S^0}|$ (we use $|q/p| = 1$) could significantly differ from unity:

$$|\lambda_{J/\psi K_S^0}|^2 - 1 \approx 4\,\frac{A_2}{A_1}\left|\frac{V_{ub}V_{ud}}{V_{cb}V_{cd}}\right|\sin\theta\sin\gamma. \tag{6.58}$$

The deviation of $|\lambda_{J/\psi K_S^0}|$ from unity can be measured (see Eq. (6.39)). We learn from Eq. (6.58) that any non-zero value of $|\lambda_{J/\psi K_S^0}|^2 - 1$ requires non-zero $\sin\gamma$, but that to extract the value of this fundamental parameter, we need to know the hadronic parameters, A_2/A_1 and $\sin\theta$. U-spin symmetry relates these hadronic parameters to corresponding ones

in the $B^0 \to J/\psi K^0_S$ decay. Consequently, measurements of various observables in both the $B^0_s \to J/\psi K^0_S$ and $B^0 \to J/\psi K^0_S$ decays will allow us to extract the phase γ as well as the hadronic parameters [15]. This extraction is model independent, with accuracy that depends on the size of U-spin breaking.

A similar analysis applies to the $B^0_s \to D^+_s D^-_s$ and $B^0 \to D^+ D^-$ decays [15], and to the $B^0_s \to K^+K^-$ and $B^0 \to \pi^+\pi^-$ decays [16]. For the $B^0_s \to D^+_s D^-_s$ decay, the experimental upper bound is [17]

$$\mathcal{B}(B^0_s \to D^+_s D^-_s) \leq 0.218, \tag{6.59}$$

while theoretical estimates give [15]

$$\mathcal{B}(B^0_s \to D^+_s D^-_s) = \mathcal{O}(8 \times 10^{-3}). \tag{6.60}$$

For the $B^0_s \to K^+K^-$ decay, the experimental upper bound is [18]

$$\mathcal{B}(B^0_s \to K^+K^-) \leq 5.9 \times 10^{-5}, \tag{6.61}$$

while theoretical estimates give [16]

$$\mathcal{B}(B^0_s \to K^+K^-) = \mathcal{O}(1.4 \times 10^{-5}). \tag{6.62}$$

6.1.6.3 $B^0_s \to D^\pm_s K^\mp$

Final $D^\pm_s K^\mp$ states are different from the states that we discussed so far in this section because they are not CP eigenstates. Yet, both B^0_s and $\bar{B}^0_s$ can decay into either of these states, and therefore CP violation in the interference of decays with and without mixing affects the time dependent decay rates. Consequently, it is possible to use the four time dependent decay rates to extract the angle γ [19].

The quark sub-processes are $\bar{b} \to \bar{c}u\bar{s}$, $\bar{b} \to \bar{u}c\bar{s}$, and the two CP-conjugate processes. These are all purely tree-level processes. It is important that the ratio between the magnitudes of the CKM combinations is of order one:

$$R_u \equiv \left|\frac{V_{ub}V_{cs}}{V_{cb}V_{us}}\right| = 0.41 \pm 0.05. \tag{6.63}$$

The interference effects, which are crucial for this measurement, are large.

For the CP violating parameters, we have:

$$\begin{aligned} \lambda_{D^+_s K^-} &= \rho \left(\frac{V_{ts}V^*_{tb}}{V^*_{ts}V_{tb}}\right)\left(\frac{V_{cb}V^*_{us}}{V^*_{ub}V_{cs}}\right), \\ \lambda_{D^-_s K^+} &= \frac{1}{\rho}\left(\frac{V_{ts}V^*_{tb}}{V^*_{ts}V_{tb}}\right)\left(\frac{V_{ub}V^*_{cs}}{V^*_{cb}V_{us}}\right), \end{aligned} \tag{6.64}$$

where ρ is related to strong interaction physics. From Eq. (6.39) (or from (6.38)) it is clear that measurements of the four time dependent decay rates would allow a determination of both $\lambda_{D^+_s K^-}$ and $\lambda_{D^-_s K^+}$. Then we can find

$$\lambda_{D^+_s K^-}\lambda_{D^-_s K^+} = \left(\frac{V_{ts}V^*_{tb}}{V^*_{ts}V_{tb}}\right)^2 \left(\frac{V_{cb}V^*_{cs}}{V^*_{cb}V_{cs}}\right)\left(\frac{V_{ub}V^*_{us}}{V^*_{ub}V_{us}}\right) = \exp[-2i(\gamma - 2\beta_s - \beta_K)]. \tag{6.65}$$

We learn that a measurement of the four decay rates will determine $\gamma - 2\beta_s$, up to very small corrections of $\mathcal{O}(\beta_K)$.

There is no experimental information on this mode at present. The theoretical estimates give [19]:

$$\begin{aligned} \mathcal{B}(B^0_s \to D^-_s K^+) &= \mathcal{O}(2.4 \times 10^{-4}), \\ \mathcal{B}(B^0_s \to D^+_s K^-) &= \mathcal{O}(1.4 \times 10^{-4}). \end{aligned} \tag{6.66}$$

6.1.7 Penguins in B Decays: General Considerations

As discussed above, CP violating asymmetries are often of particular experimental interest because of their simple dependence on the weak phase of the quantum mechanical amplitude of a decay. This is most useful for probing fundamental physics if this weak phase can be related reliably to the phase of an element of the CKM matrix. This is difficult to do if there are two or more distinct quark-level transitions with different CKM structure which can mediate the decay. For reasons which will be clear momentarily, this problem is commonly known as "penguin pollution."

To illustrate the problem, let us take a simplified version of a concrete example. Consider the decay $B^0 \to \pi^+\pi^-$, which requires the quark-level transition $\bar{b} \to u\bar{u}\bar{d}$. The leading contributions to this transition are from a product of two weak currents, $\bar{b}_L\gamma^\mu u_L\,\bar{u}_L\gamma_\mu d_L$, and from a one-loop operator induced by a virtual t quark, $\bar{b}\gamma^\mu T^a d\,\bar{u}\gamma_\mu T^a u$. These two pieces carry distinct weak phases, and the overall amplitude is of the form (notation in this section is adapted from Ref. [20])

$$A(B^0 \to \pi^+\pi^-) = V_{ud}V^*_{ub}M^{(u)} + V_{td}V^*_{tb}M^{(t)} = e^{i\gamma}T + e^{-i\beta}P\,. \tag{6.67}$$

Here the notations T and P are inspired by the fact that the leading contributions to the two terms have tree and penguin topologies, but it is important to understand that (6.67) is in fact a *general* decomposition of the amplitude in terms of the weak phases $e^{i\gamma}$ and $e^{-i\beta}$. Note that $M^{(u)}$ and $M^{(t)}$ depend on both short-distance and long-distance physics. The long-distance parts, for which the leading contributions are

$$\begin{aligned} M^{(u)} &\propto \langle \pi^+\pi^- | \bar{b}_L\gamma^\mu u_L\,\bar{u}_L\gamma_\mu d_L\,|B^0\rangle\,, \\ M^{(t)} &\propto \langle \pi^+\pi^- | \bar{b}\gamma^\mu T^a d\,\bar{u}\gamma_\mu T^a u\,|B^0\rangle\,, \end{aligned} \tag{6.68}$$

depend on nonperturbative strong interactions and are not yet amenable to calculation from first principles. Since the two contributions to the amplitude have different weak phases and, in general, different strong phases, there is the possibility not only of CP violation in the interference between decays with and without mixing, but also of CP violation in the decay itself. The time-dependent CP violating asymmetry takes the general form

$$\mathcal{A}_{CP}(t) = a_{\rm dir}\cos\Delta m t - \sqrt{1-a^2_{\rm dir}}\,\sin 2\alpha_{\rm eff}\,\sin\Delta m t\,, \tag{6.69}$$

where $a_{\rm dir}$ was defined in Eq. (6.46). In the limit $P = 0$, we have $a_{\rm dir} = 0$ and $\alpha_{\rm eff} = \alpha = \pi - \beta - \gamma$. As can be seen from Eq. (6.69), the quantities $a_{\rm dir}$ and $\alpha_{\rm eff}$ may be

extracted directly from the time-dependent experimental analysis. To determine α from these measurements one needs to know also the ratio $|P/T|$ [20]:

$$\cos(2\alpha - 2\alpha_{\rm eff}) = \frac{1}{\sqrt{1-a_{\rm dir}^2}}\left[1 - \left(1 - \sqrt{1-a_{\rm dir}^2}\,\cos 2\alpha_{\rm eff}\right)\left|\frac{P}{T}\right|^2\right]. \qquad (6.70)$$

In the absence of either an experimental bound on or a theoretical calculation of $|P/T|$, it is not possible to extract α cleanly from a measurement of $\mathcal{A}_{CP}(t)$.

Whether or not it is possible to constrain $|P/T|$ in some way depends entirely on the process under consideration. The literature on proposals for doing so is extensive. At this point, we make a number of general comments:

(i) The essential problem is that the CP violating phase of the decay amplitude is not known, because it depends on $|P/T|$, which depends in turn on hadronic physics. (Statements about overall weak phases should be understood in the context of some definite phase convention.)

(ii) The ratio $|P/T|$ itself depends on CKM matrix elements, but this only complicates the form of the constraints on the Unitarity Triangle without introducing further uncertainties.

(iii) The two contributions with different weak phases, denoted T and P above, are commonly called "tree" and "penguin" contributions. This is something of a misnomer. There are three penguin diagrams, each with a different weak phase, but one of these weak phases can be rewritten in terms of the other two phases using unitarity of the CKM matrix. Thus the charm quark "penguin" contribution to $B^0 \to \pi^+\pi^-$, proportional to $V_{cd}V_{cb}^* = -V_{ud}V_{ub}^* - V_{td}V_{tb}^*$, is absorbed into both T and P in (6.67), while the up "penguin" provides a contribution solely to T.

(iv) Similarly, it is irrelevant whether a penguin with a light quark in the loop is thought of as a "penguin" or a "rescattering" contribution. This terminology is often used in the context of modeling hadronic matrix elements, but in fact there is no physically meaningful distinction between the two processes.

(v) There are, in fact, two sorts of penguin diagrams which contribute to B decays: "gluonic" penguins and "electroweak" penguins. Although the electroweak penguins are typically much smaller, in general they may not be neglected. The two types of penguins typically induce transitions with distinct flavour (*e.g.* isospin) structures, which can complicate or even invalidate proposals to bound penguin contributions through flavour symmetries. The relative importance of electroweak penguins depends on the decay under consideration.

(vi) In the case above, the contributions to P are suppressed by

$$r_{PT} \approx \frac{\alpha_s}{12\pi}\ln\frac{m_t^2}{m_b^2} = \mathcal{O}(0.1). \qquad (6.71)$$

Note that $\alpha_s \ln(m_t^2/m_b^2)$ is not a small factor and appears at leading logarithmic order in RG-improved perturbation theory. In other cases, penguin contributions might also be

suppressed by powers of the CKM suppression factor λ. If $|P/T|$ can be shown to be very small, then it is not necessary to know it precisely. However, typically even $|P/T|$ of the order of 10-20% is significant enough to require a constraint or calculation with high confidence.

(vii) Any new physics terms, whatever their weak phases, can always be written as a sum of two terms with weak phases γ and $-\beta$. The impact of new physics is thus only to change the ratio of $|P/T|$ from that expected in the SM. We learn from this that we are only sensitive to new physics in cases where we have some knowledge of the ratio $|P/T|$. For example, in cases where relationships between channels, such as those from isospin or $SU(3)$, can be used to determine or constrain the ratio P/T in a given channel from that in another, one is sensitive to any new physics that does not respect this flavour symmetry [21].

6.1.8 Penguins in $B^0 \to J/\psi K_S^0$

The process $B^0 \to J/\psi K_S^0$ is one in which the penguin contribution turns out to be relatively harmless, and it is instructive to begin by seeing why this is so.

The decay is mediated by the quark transition $\bar{b} \to c\bar{c}\bar{s}$. The dominant contribution is from tree level W exchange, proportional to $V_{cs}V_{cb}^*$. In the Wolfenstein parameterization, $V_{cs}V_{cb}^*$ is real and of order λ^2. In analogy to (6.67) it is convenient to choose the decomposition

$$A(B^0 \to J/\psi K_S^0) = T_{J/\psi K} + e^{i\gamma}P_{J/\psi K}\,. \qquad (6.72)$$

The leading penguin diagram has a virtual t quark in the loop and is proportional to $r_{PT}V_{ts}V_{tb}^*$ (see Eq. (6.71)), which up to the r_{PT}-factor is the same size as $V_{cs}V_{cb}^*$. However, if we use unitarity to write $V_{ts}V_{tb}^* = -V_{cs}V_{cb}^* - V_{us}V_{ub}^*$, we see that $\beta_s = \arg(-V_{ts}V_{tb}^*/V_{cs}V_{cb}^*)$ is small, of order $|V_{us}V_{ub}^*/V_{cs}V_{cb}^*| = \mathcal{O}(\lambda^2)$. Therefore this penguin diagram actually contributes mostly to $T_{J/\psi K}$ in the decomposition (6.72); the contribution to $|P_{J/\psi K}/T_{J/\psi K}|$ is of order $r_{PT}\lambda^2$, below the level of 1%. The other potentially dangerous contribution is from the u penguin, proportional to $V_{us}V_{ub}^*$. The weak phase of this term is $e^{i\gamma}$, but its magnitude is $\mathcal{O}(\lambda^4)$. Hence its contribution to $|P_{J/\psi K}/T_{J/\psi K}|$ is also of order $r_{PT}\lambda^2$. Finally, the c penguin diagram is proportional to $V_{cs}V_{cb}^*$ and contributes only to $T_{J/\psi K}$.

The "penguin pollution" in $B^0 \to J/\psi K_S^0$ is thus below the level of 1%, even though penguin diagrams themselves contribute at a higher level. Since the weak phase of $A(B^0 \to J/\psi K_S^0)$ is known to high accuracy, the time-dependent CP asymmetry in this mode provides a clean extraction of a parameter in the CKM matrix (in this case, $\sin 2\beta$). Only new physics effects could lead to a significant difference between the asymmetry measured in this decay and $\sin 2\beta$. This example illustrates nicely the fact that the real issue is how well we know the weak phase of the decay amplitude. The inclusion of electroweak penguins, which have the same phase structure, does not change the argument.

6.1.9 Penguins in $B^0 \to \pi\pi$

The penguin contributions in $B^0 \to \pi^+\pi^-$ are a much more difficult problem, one which has received intense attention in recent years. Much of what has been learned is collected

in Ref. [20]. We parameterize

$$A(B^0 \to \pi^+\pi^-) = e^{i\gamma} T_{\pi\pi} + e^{-i\beta} P_{\pi\pi} \,. \tag{6.73}$$

The leading contribution to $T_{\pi\pi}$ comes from W exchange and is proportional to $V_{ud}V_{ub}^*$; in addition, $T_{\pi\pi}$ gets a contribution from penguin diagrams with a virtual u quark. The leading contribution to $P_{\pi\pi}$ is from a t penguin diagram, proportional to $V_{td}V_{tb}^*$. Since both $|V_{ud}V_{ub}^*|$ and $|V_{td}V_{tb}^*|$ are of order λ^3, $|P_{\pi\pi}/T_{\pi\pi}|$ is suppressed only by the the factor r_{PT}. If nonperturbative QCD enhances the hadronic matrix element in $P_{\pi\pi}$ as compared to that in $T_{\pi\pi}$, then the penguin contribution might be significant enough to pollute the extraction of α.

One may make a rough estimate of $|P_{\pi\pi}/T_{\pi\pi}|$ from the decay $B^0 \to K^+\pi^-$, which is convenient to parameterize by

$$A(B^0 \to K^+\pi^-) = e^{i\gamma} T_{K\pi} + P_{K\pi} \,. \tag{6.74}$$

In this case, the leading contribution to $T_{K\pi}$ is of order $|V_{us}V_{ub}^*| = \mathcal{O}(\lambda^4)$, while the t penguin piece of $P_{K\pi}$ is of order $|V_{ts}V_{tb}^*| = \mathcal{O}(\lambda^2)$, times a loop factor. Hence one might expect that if QCD enhances the penguin contribution to $B \to \pi\pi$, then $B \to K\pi$ would be dominated by penguin processes. Let us make the following assumptions for the moment: (i) flavour $SU(3)$ symmetry in the QCD matrix elements; (ii) electroweak penguins and "color suppressed" processes are negligible; (iii) penguins dominate $B \to K\pi$, so $T_{K\pi}$ may be ignored in $\mathcal{B}(B^0 \to K^+\pi^-)$; (iv) penguins make a small enough contribution to $B \to \pi\pi$ that $P_{\pi\pi}$ may be ignored in $\mathcal{B}(B^0 \to \pi^+\pi^-)$. Then it is straightforward to derive the relation

$$\left|\frac{P_{\pi\pi}}{T_{\pi\pi}}\right| = \left|\frac{P_{\pi\pi}}{P_{K\pi}}\right| \left|\frac{P_{K\pi}}{T_{\pi\pi}}\right| \simeq \left|\frac{V_{td}}{V_{ts}}\right| \sqrt{\frac{\mathcal{B}(B^0 \to K^+\pi^-)}{\mathcal{B}(B^0 \to \pi^+\pi^-)}} \,. \tag{6.75}$$

The current constraints on the Unitarity Triangle yield roughly [22]

$$0.1 \lesssim |V_{td}/V_{ts}| \lesssim 0.25 \,. \tag{6.76}$$

A recent CLEO measurement of the B branching ratios gives [23]

$$\begin{aligned} \mathcal{B}(B^0 \to \pi^+\pi^-) &= (4.3^{+1.6}_{-1.4} \pm 0.5) \times 10^{-6}, \\ \mathcal{B}(B^0 \to K^\pm\pi^\mp) &= (17.2^{+2.5}_{-2.4} \pm 1.2) \times 10^{-6} \,. \end{aligned} \tag{6.77}$$

Thus we obtain the rough estimate

$$0.2 \lesssim |P_{\pi\pi}/T_{\pi\pi}| \lesssim 0.5 \,. \tag{6.78}$$

More elaborate analyses can somewhat lower the upper bound, but it is clear that penguin effects are unlikely to be negligible in $B \to \pi\pi$. In view of the shift (6.70) of the measured α to $\alpha_{\rm eff}$, the problem of "penguin pollution" in the extraction of α is a serious one.

A variety of solutions to this problem have been proposed, falling roughly into two classes. Each class requires assumptions, and each has implications for the B physics goals at Tevatron RunII and beyond.

The first type of approach is to convert the estimate given above into an actual measurement of $|P_{K\pi}|$ from the process $B \to K\pi$. (The list of papers on this subject is long. Early works include [24–26]. For a much more complete list of references, see Ref. [20].) Once $|P_{K\pi}|$ is known, flavour $SU(3)$ is used to relate $|P_{K\pi}|$ to $|P_{\pi\pi}|$. One must then include a number of additional effects:

(i) Electroweak penguins. The effects of these are calculable [27].

(ii) Color suppressed and rescattering processes. These must be bounded or estimated using data and some further assumptions.

(iii) $SU(3)$ corrections. Some, such as f_K/f_π, can be included, but $SU(3)$ corrections generally remain a source of irreducible uncertainty.

(iv) Better knowledge of $|V_{td}/V_{ts}|$. This will be forthcoming from $\Delta m_s/\Delta m_d$, a crucial measurement which should be made during RunII.

The $SU(3)$ relations typically take as inputs a variety of modes related to $B \to \pi\pi$ by $SU(3)$ symmetries, such as $B^0 \to (K^\pm\pi^\mp, K^0\pi^0)$, $B^\pm \to (K^\pm\pi^0, K^0\pi^\pm)$, and $B_s^0 \to (K^\pm\pi^\mp, K^+K^-, K^0K^0)$. Both CP-averaged rates and CP asymmetries can play a role. The implication for RunII is that it is very important to measure accurately as many of these branching fractions, both tagged and untagged, as is possible. Upper bounds on branching ratios are also important. The choice of the most useful analysis will depend ultimately on which modes can be measured most accurately.

The second type of approach is to exploit the fact that the penguin contribution $P_{\pi\pi}$ to $B \to \pi\pi$ is pure $\Delta I = \frac{1}{2}$, while the tree contribution $T_{\pi\pi}$ contains a piece which is $\Delta I = \frac{3}{2}$. This is not true of the electroweak penguins [28], but these and other isospin violating corrections such as π^0-η mixing are expected to be small and only become the dominant corrections in the case that the penguin effects are also small [29]. Isospin symmetry allows one to form a relation among the amplitudes for $B^0 \to \pi^+\pi^-$, $B^0 \to \pi^0\pi^0$ and $B^+ \to \pi^+\pi^0$,

$$\frac{1}{\sqrt{2}} A(B^0 \to \pi^+\pi^-) + A(B^0 \to \pi^0\pi^0) = A(B^+ \to \pi^+\pi^0). \tag{6.79}$$

There is also a relation for the charge conjugate processes. A simple geometric construction then allows one to disentangle the unpolluted $\Delta I = \frac{3}{2}$ amplitudes, from which $\sin 2\alpha$ may be extracted cleanly [30].

The key experimental difficulty is that one must measure accurately the flavour-tagged rate for $B^0 \to \pi^0\pi^0$. Since the final state consists only of four photons, and the branching fraction is expected to be approximately at the level of 10^{-6}, this is very hard. There is as yet no proposal to accomplish this measurement with any current or future detector. It has been noted that an upper bound on this rate, if sufficiently strong, would also allow one to bound $P_{\pi\pi}$ usefully [31].

An alternative is to perform an isospin analysis of the process $B^0 \to \rho\pi \to \pi^+\pi^-\pi^0$ [32, 33]. Here one must study the time-dependent asymmetry over the entire Dalitz plot, probing variously the intermediate states $\rho^\pm\pi^\mp$ and $\rho^0\pi^0$. The advantage here is that final states with two π^0's need not be considered. On the other hand, thousands of cleanly reconstructed

events would be needed. A very important question for any future B experiment is whether it will be capable of performing this measurement.

Finally, one might attempt to calculate the penguin matrix elements, at which point only more precise information on V_{td} is needed in order to know the level of contamination. Model-dependent analyses are not really adequate for this purpose, since the goal is the extraction of fundamental parameters. Precise calculations of such matrix elements from lattice QCD are far in the future, given the large energies of the π's and the need for an unquenched treatment. Lattice calculations performed in the Euclidean regime also have difficulty including final state interactions. Recently, a new QCD-based analysis of the $B \to \pi\pi$ matrix elements has been proposed [34]. The idea originates in the suggestion that these matrix elements factorize, in a novel sense, for asymptotically large values of m_B, an idea with its roots in the "color transparency" picture of Bjorken. This method is based on classifying the diagrams in terms of a limited number of unknown functions with calculable short distance corrections. At present, the phenomenological relevance of this technique for realistic $m_B = 5.28$ GeV/c^2 is not yet well understood. In particular, it is not yet clear whether m_B is really in the regime where both soft final state interactions and Sudakov logarithms may be neglected. Furthermore, another recent analysis [35] based on similar ideas seems to be in substantial disagreement about the details of this factorization. One may hope that additional progress on this front will be forthcoming.

6.1.10 Penguins in $B \to K\pi$

Analyses analogous to those which constrain $|P_{\pi\pi}|$ through the measurement of $|P_{K\pi}|$ may allow one to extract the CKM matrix element γ through studies of direct CP violation (see the reviews in [36–38] and references therein). For example, the ratio [27,39]

$$R_* = \frac{\mathcal{B}(B^+ \to K^0\pi^+) + \mathcal{B}(B^- \to K^0\pi^-)}{2\left[\mathcal{B}(B^+ \to K^+\pi^0) + \mathcal{B}(B^- \to K^-\pi^0)\right]} \tag{6.80}$$

is directly sensitive to $\cos\gamma$, and [40]

$$R = \frac{\mathcal{B}(B^0 \to K^+\pi^-) + \mathcal{B}(\bar{B}^0 \to K^-\pi^+)}{\mathcal{B}(B^+ \to K^0\pi^+) + \mathcal{B}(B^- \to K^0\pi^-)} \tag{6.81}$$

can be sensitive to $\sin\gamma$ if $R < 1$. The spirit of these analyses is to disentangle tree and penguin contributions through the use of $SU(3)$ symmetry and additional dynamical assumptions. The theoretical issues are much the same as before: one must find a way to control electroweak penguins, avoid making too many dynamical assumptions such as the neglect of rescattering or color suppressed processes, and include $SU(3)$ corrections. The number of such proposals is extensive and growing. What they typically have in common is that, as before, they profit from the accurate measurement of a wide variety of charmless hadronic two-body B^0, B^+ and B_s^0 decays. In addition to those mentioned above, the modes $B \to \eta^{(\prime)}K$ have been proposed for the extraction of γ [41]. The experimental challenge is to measure or bound as many of these decays as possible, with as much precision as can be obtained.

6.1.11 New Physics in B_s^0 Mixing

The SM predicts that the CP asymmetries in the leading B_s^0 decays are all very small. Consequently, these asymmetries will constitute good probes of new physics. Since the reason for the SM prediction is the smallness of the relative phase between the mixing amplitude and the leading decay amplitudes (β_s), there are two possible sources for deviations from this predictions: new contributions to the decays or new contributions to the mixing. The leading B_s^0 decay amplitudes are tree level, CKM favored, and therefore relatively large. In most new physics scenarios there are no competing new contributions to these amplitudes. In contrast, the mixing amplitude is an electroweak loop and thus relatively small. Indeed, many new physics models accommodate, or even predict, large new CP violating contributions to B_s^0 mixing [4,42–50].

Since in the SM the B_s^0 mixing amplitude is much larger than the B^0 mixing amplitude, roughly by a factor of order $|V_{ts}/V_{td}|^2$, it may seem that a significant new physics contribution to B_s^0 mixing is always associated with a relatively much larger new contribution to B^0 mixing. This, however, is not always the case. The new contributions to the mixing are often flavour dependent and might have a hierarchy that is similar to (or even stronger than) the SM Yukawa structure.

The question that we would like to answer in this section is the following: If there is a contribution from new physics to B_s^0 mixing that is of magnitude similar to the SM and relative phase of order one, how can we find it? There are, in principle, many ways to demonstrate the presence of new physics in B_s^0 mixing. Which ones will be useful with realistic experimental analyses and theoretical uncertainties depends on some (as yet) unknown parameters, both of Nature (*e.g.* Δm_s) and of the experiments. In the following we discuss several observables that are sensitive to new physics in B_s^0 mixing. For each of them we explain what are the requirements for the method to be interesting in practice.

New physics effects in B_s^0 mixing can also be found indirectly. A measurement of $\Delta m_d/\Delta m_s$ determines one side of the unitarity triangle in the SM. With new physics, it may be inconsistent with other constraints on the unitarity triangle. In such a case one does not know which of the observables are modified by new physics. In the discussion below we do not elaborate on indirect effects and focus our attention on direct indications of new physics in B_s^0 mixing.

The relevant effects of new physics can be described by two new parameters, r_s and θ_s [51–54], defined by

$$r_s^2 e^{2i\theta_s} \equiv \frac{\langle B^0|H_{\rm eff}^{\rm full}|\bar{B}^0\rangle}{\langle B^0|H_{\rm eff}^{\rm SM}|\bar{B}^0\rangle}\,, \tag{6.82}$$

where $H_{\rm eff}^{\rm full}$ is the effective Hamiltonian including both SM and new physics contributions, and $H_{\rm eff}^{\rm SM}$ includes only the SM box diagrams. We work in the Wolfenstein parametrization where, to a good approximation, both $V_{cb}V_{cs}^*$ and $V_{tb}V_{ts}^*$ are real. In other words, we take $\beta_s = 0$. With these convention and approximation, θ_s is the relative phase between the B_s^0 mixing amplitude and any real amplitude. In particular, the CP asymmetry for decays into final CP eigenstates that are mediated by $b \to c\bar{c}s$ is given by

$$a_{CP} = \pm\sin 2\theta_s, \tag{6.83}$$

and also

$$\arg(-\Gamma_{12}^* M_{12}) = 2\theta_s = \phi_s, \tag{6.84}$$

where ϕ_s is defined in (1.62).

6.1.11.1 Time Dependent CP Asymmetries

The most promising way to discover new physics contributions to M_{12} is through measurements of the mass difference Δm_s and various time dependent CP asymmetries. Note that while in the SM $\Delta m_s \lesssim 30$ ps^{-1}, this may not be the case in the presence of new physics. A larger value of Δm_s makes its measurement more difficult. For example, a measurement of the time dependent CP asymmetry in the $B_s^0 \to J/\psi\phi$ channel will directly determine $\sin 2\theta_s$. If a value that is above the few percent level is found, it would provide a clean signal of new physics. Note that $J/\psi\phi$ is not a pure CP eigenstate, and therefore an angular analysis is required to project out the CP even and CP odd parts and to measure $\sin 2\theta_s$. However, it may be the case that the presence of new physics can be demonstrated even without such an analysis. Other time dependent CP asymmetries for transitions mediated by real quark level decay amplitudes, *e.g.* $B_s^0 \to D_s^{+(*)} D_s^{-(*)}$, can provide similar tests. Again, we emphasize that a non vanishing CP asymmetry in the $D_s^{(*)} D_s^{(*)}$ channel, which is not a CP eigenstate, is a clean signal for new physics in the B_s^0 mixing amplitude.

If B_s^0 oscillations turn out to be too fast to be traced, the above methods cannot be applied. Below we describe various other methods that are sensitive to θ_s and do not require that the fast oscillations are traced.

6.1.11.2 Time Integrated CP Asymmetries

For the B^0 system, one can use time integrated asymmetries. The dilution factor due to the time integration, $D \sim x_q/(1+x_q^2)$ is not very small for $x_d \sim 0.7$. For the B_s^0 system, however, $x_s \gg 1$, leading to a strong dilution of the time integrated asymmetries, $D \sim 1/x_s$. In principle, however, the time integrated asymmetry can be measured. Since expected SM effects are small, any non vanishing asymmetry would be an indication for new physics. The goal here is not necessarily to make a precise measurement of the asymmetry, but rather to demonstrate that it is not zero. Assuming, for example, $x_s \sim 40$, and $\sin\theta_s \sim 0.8$, the time integrated asymmetry in $B_s^0 \to J/\psi\phi$ is of $\mathcal{O}(0.02)$. If the combined statistical and systematic experimental error on such asymmetry measurements is below 1%, the presence of a non vanishing asymmetry can be established.

6.1.11.3 The Width Difference

If the B_s^0 width difference (y_s) can be measured, there are more ways to see the effects of θ_s [10,55]. Note that new physics in the mixing amplitude always reduces y_s compared to its SM value. This fact can be readily seen from the following equation:

$$\Delta\Gamma_s = 2|\Gamma_{12}|\cos 2\theta_s. \tag{6.85}$$

Since we assume that new physics affects M_{12} but not Γ_{12}, the only modification of the right hand side can be a reduction of $\cos 2\theta_s$ compared to its SM value of one. The reduction of y_s can be understood intuitively as follows. In the absence of CP violation, the two mass eigenstates are also CP eigenstates. The large $\Delta\Gamma_s$ in the SM is an indication that most of the $b \to c\bar{c}s$ decays are into CP even final states. With CP violation, the mass eigenstates are no longer approximate CP eigenstates. Then, both mass eigenstates decay into CP even final states. Consequently, $\Delta\Gamma_s$ is reduced.

A large enough y_s, say $\mathcal{O}(0.1)$, would allow various ways of finding a non vanishing θ_s [55]. We now discuss one such method which makes use of both flavour specific decays (semileptonic decays are flavour specific; $b \to c\bar{u}d$ decays are also flavour specific to a very good approximation) and decays into final CP eigenstates.

The time dependent decay rate of a flavour specific mode, f, is given by:

$$\Gamma\left[f\left(t\right)\right] = \Gamma\left[\bar{f}\left(t\right)\right] = \frac{\Gamma\left(B_s \to f\right)}{2}\left\{e^{-\Gamma_L t} + e^{-\Gamma_H t}\right\}. \tag{6.86}$$

Both Γ_H and Γ_L and, therefore, also $\Delta\Gamma_s$, can be extracted from such a measurement. The time dependent decay rate into a CP even final state from a $b \to c\bar{c}s$ transition is given by:

$$\Gamma(B \to CP_{\rm even}, t) \propto \cos^2\theta_s\, e^{-\Gamma_L t} + \sin^2\theta_s\, e^{-\Gamma_H t}. \tag{6.87}$$

For a decay into a CP odd state, Γ_L and Γ_H are interchanged. In principle, a three parameter fit of a decay into a CP even state can be used to measure Γ, $\Delta\Gamma$ and θ_s using Eq. (6.87). Even if this cannot be done in practice, θ_s can be measured by comparing the measurements of $\Delta\Gamma$ from flavour specific decays and CP eigenstate decays. Experimentally, most of the data are expected to be taken for small Γt. Then, using $\Delta\Gamma t \ll 1$, Eq. (6.87) becomes

$$\Gamma(B \to CP_{\rm even}, t) \propto e^{-\Gamma_+ t}, \qquad \Gamma_+ \equiv \left(\Gamma + \frac{\Delta\Gamma\left|\cos 2\theta_s\right|}{2}\right). \tag{6.88}$$

Using Γ and $\Delta\Gamma$ as measured from the flavour specific data, a one parameter fit to the decay rate gives θ_s. Actually, such a fit determines

$$2(\Gamma_+ - \Gamma) = \Delta\Gamma\left|\cos(2\theta_s)\right|. \tag{6.89}$$

By comparing it to the real width difference, $\Delta\Gamma$, we get

$$\left|\cos 2\theta_s\right| = \frac{2(\Gamma_+ - \Gamma)}{\Delta\Gamma}. \tag{6.90}$$

This method would be particularly useful if θ_s is neither very small nor very large. For $\theta_s \sim \pi/4$ the width difference becomes too small to be measured. For $\theta_s \sim 0$ the required precision of the measurement is very high.

6.1.11.4 The Semileptonic CP Asymmetry

The semileptonic asymmetry, $a_{\rm sl}$, which is sensitive to θ_s [56–60], does not require a measurement of either x_s or y_s. In the SM, $a_{\rm sl}$ is very small:

$$a_{\rm sl} \approx {\rm Im}\left(\Gamma_{12}/M_{12}\right) = |\Gamma_{12}/M_{12}| \times \sin 2\theta_s = \mathcal{O}(10^{-4}). \tag{6.91}$$

With new physics, the first factor, $|\Gamma_{12}/M_{12}| = \mathcal{O}(10^{-2})$, cannot be significantly enhanced, but the second, $\sin 2\theta_s$, could. Actually, if $\sin 2\theta_s \sim 1$ the semileptonic asymmetry is expected to be of $\mathcal{O}(10^{-2})$. Since in the SM $a_{\rm sl}$ is negligibly small, any observation of a non vanishing asymmetry is a clear signal for new physics. Whether such a measurement is possible depends, among other things, on the actual value of the asymmetry: a factor of a few in one or the other direction can make a significant difference as the purely experimental systematic uncertainties are expected to be at the percent level.

6.2 Study of $B^0 \to J/\psi K^0_S$

In the following sections, we report the results of studying the prospects of the CDF, DØ and BTeV experiments for measuring CP violation in different B decay modes. The outline of the following sections consists of a brief theoretical introduction to the particular decay modes of interest, the prospects of the three Tevatron experiments (not all detectors are capable of measuring all modes and we do not necessarily have always reports from all three experiments) followed by a brief summary. We start with the study of $B^0 \to J/\psi K^0_S$.

6.2.1 $B^0 \to J/\psi K^0_S$: Introduction †

As discussed in the introduction in Sec. 6.1 (see Sec. 6.1.6.2 and 6.1.8), a single weak phase dominates the decay $B^0 \to J/\psi K^0_S$, so that the CP asymmetry in this channel is dominated by the interference between decays with and without B-$\bar{B}$ mixing. Identical considerations apply to the study of $B^0_s \to J/\psi\phi$. Assuming the CKM matrix to be unitary, there are two distinct decay topologies, characterized by the CKM matrix elements $V_{cs}V^*_{cb}$ and $V_{us}V^*_{ub}$, indicating CP violation in direct decay to be suppressed by $\mathcal{O}(\lambda^2)$. Nevertheless, the two decays are sensitive to different CKM information. We find for $B^0_s \to J/\psi\phi$

$$\lambda_{J/\psi\phi} = \eta_{J/\psi\phi}\left(\frac{V^*_{tb}V_{ts}}{V_{tb}V^*_{ts}}\right)\left(\frac{V_{cb}V^*_{cs}}{V^*_{cb}V_{cs}}\right) \Rightarrow \mathrm{Im}\,\lambda_{J/\psi\phi} = \sin 2\beta_s \ . \tag{6.92}$$

The first set of CKM factors reflects B^0_s-$\bar{B}^0_s$ mixing in the Standard Model, whereas the second set reflects those of the assumed dominant decay topology in $\bar{b} \to \bar{c}c\bar{s}$. As discussed in Section 6.1.6.2, we obtain for $B^0 \to J/\psi K^0_S$

$$\lambda_{J/\psi K^0_S} = \eta_{J/\psi K^0_S}\left(\frac{V^*_{tb}V_{td}}{V_{tb}V^*_{td}}\right)\left(\frac{V_{cb}V^*_{cs}}{V^*_{cb}V_{cs}}\right)\left(\frac{V^*_{cd}V_{cs}}{V_{cd}V^*_{cs}}\right) \Rightarrow \mathrm{Im}\,\lambda_{J/\psi K^0_S} = \sin 2\beta \ , \tag{6.93}$$

where the first set of CKM factors now reflects B^0-$\bar{B}^0$ mixing and the second set reflects those of the dominant decay topology in $\bar{b} \to \bar{c}c\bar{s}$. Finally, the third set reflects K-$\bar{K}$ mixing necessary to realize the K^0_S final state. Indeed, K-$\bar{K}$ mixing must occur in order to generate interference between the $B^0 \to J/\psi K^0$ and $\bar{B}^0 \to J/\psi \bar{K}^0$ decay channels. We have assumed, as in the B^0_s case, that B^0-$\bar{B}^0$ mixing is controlled by a pure phase. The

† Authors: S. Gardner and R. Jesik.

quality of this assumption is likely to be less impressive than in the B^0_s case. Nevertheless, it still ought to be good with $(|q/p| - 1) < \mathcal{O}(10^{-2})$ [61]. In the case of K-$\bar{K}$ mixing, the deviation of $|q/p|$ from unity is empirically known; the non-zero semileptonic asymmetry $[\Gamma(K_L \to \pi^-\ell^+\nu_\ell) - \Gamma(K_L \to \pi^+\ell^-\bar{\nu}_\ell)]/[\Gamma(K_L \to \pi^-\ell^+\nu_\ell) + \Gamma(K_L \to \pi^+\ell^-\bar{\nu}_\ell)]$ implies that $|q/p| - 1 \sim -3 \cdot 10^{-3}$ [62]. Thus K-$\bar{K}$ mixing can also be typified by a pure phase. The top quark contribution to K-$\bar{K}$ mixing is strongly suppressed by CKM factors, so that the charm quark determines $(q/p)_K$. Note that β_s is itself $\mathcal{O}(\lambda^2)$, whereas β is $\mathcal{O}(1)$. Thus, an asymmetry $\mathcal{A}_{CP}$ in $B^0_s \to \phi K^0_S$ considerably larger than $\mathcal{O}(\lambda^2)$ would signal the presence of new physics in B^0_s-$\bar{B}^0_s$ mixing.

In the case of $B^0_s \to J/\psi\phi$, the CP of the final state depends on the partial wave in which the vector mesons sit, so that an analysis of the angular distribution is required in order to extract weak phase information [13]. The information encoded in the time-dependent angular distributions of $B \to VV$ decays can be quite rich, and an angular analysis of $B^{0/+}(t) \to J/\psi(\to \ell^+\ell^-)K^*(\to \pi^0 K^0_S)$ [13,63–65] is sensitive to $\cos 2\beta$ as well [13,66]. The expected determination of $\sin 2\beta$ from $\mathcal{A}_{CP}$ in $B^0 \to J/\psi K^0_S$ leaves a four-fold discrete ambiguity in the angle β, so that the determination of $\cos 2\beta$ [54,67,68] plays an important role in resolving the value of β itself. Unfortunately, $\cos 2\beta$ appears in conjunction with a signed hadronic parameter. However, under the assumption of U-spin symmetry, the latter can be extracted from the CP asymmetry in $B^0_s \to J/\psi\phi$, so that $\cos 2\beta$ can be determined as well [66].

Since both decay modes $B^0 \to J/\psi K^0_S$ and $B^0_s \to J/\psi\phi$ are very similar from an experimental point of view (trigger and reconstruction efficiencies), we will focus in the following experimental sections on describing the strategies to reconstruct $B^0 \to J/\psi K^0_S$ and give estimates for $\sin 2\beta$. We will add the estimates for $B^0_s \to J/\psi\phi$ event yields as appropriate.

6.2.2 $B^0 \to J/\psi K^0_S$: CDF Report †

For the measurement of $\sin 2\beta$ in the $B^0 \to J/\psi K^0_S$ channel [69], CDF expects to reconstruct in 2 fb^{-1} of data in RunII about 20,000 $J/\psi K^0_S$ events with $J/\psi \to \mu^+\mu^-$ and $K^0_S \to \pi^+\pi^-$. Starting with $\sim$400 $J/\psi K^0_S$ events [70] reconstructed in 110 pb^{-1} in RunI, this number is obtained in the following way. To estimate the increase in J/ψ and $J/\psi K^0_S$ signals, we first measure the inclusive J/ψ signal yields in each of the Level 2 trigger paths used in RunIb. We scale these to RunII conditions with the following modifications:

- 2 fb^{-1}/110 pb^{-1} for the total RunII integrated luminosity $\Rightarrow \times$ 20 gain in event yield
- Assume increase of $\times$1.1 from $\sqrt{s} = 1.8$ TeV $\to$ 2.0 TeV
- Wider muon stub gates $\Rightarrow \times$ 1.36 gain in efficiency
- Increased muon coverage with CMX miniskirt $\Rightarrow \times$1.396 increase
- Remove RunI wedge cuts $\Rightarrow \times$ 1.1 gain in efficiency

† Authors: M. Paulini and B. Wicklund.

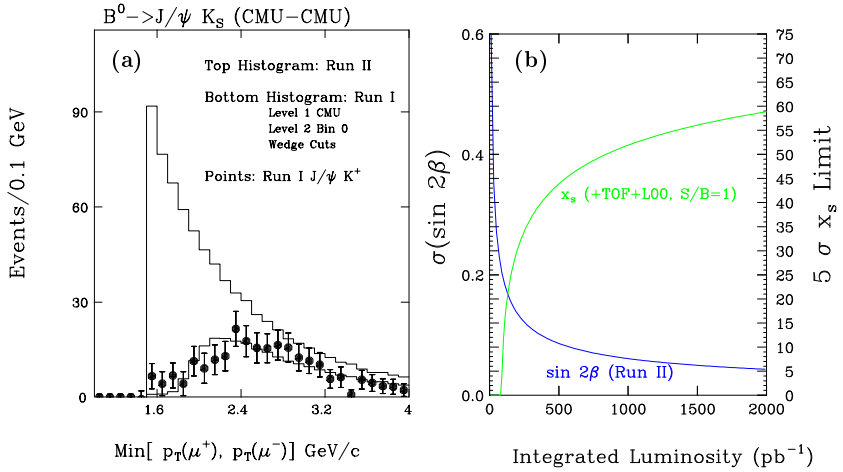

Figure 6.1: Dependence of CMU-CMU $J/\psi K^0_S$ yields on the lower p_T muon threshold at CDF: Run II trigger (top histogram), Run I trigger (bottom histogram). The points are the $B^+ \to J/\psi K^+$ CMU-CMU signal in Run I. (b) Uncertainty on $\sin 2\beta$ (left scale) and 5σ reach for x_s (right scale) as functions of integrated luminosity.

- Add RunII trigger cuts on $m_T^{\mu\mu}$ and $\Delta\phi^{\mu\mu} \Rightarrow \times$ 0.85 loss in efficiency
- Add lower $p_T^{\mu\mu}$ threshold of 2.0 $\to$ 1.5 GeV/c for central muons (CMU) $\Rightarrow \times$ 2 for CMU-CMU dimuons

The effects of these cuts were modeled for $J/\psi K^0_S$ Monte Carlo events, to get the relative change in yield for each modification. Figure 6.1(a) shows the dependence of lowering the muon p_T threshold for the $J/\psi K^0_S$ yields in CMU-CMU from a generator-level Monte Carlo study. The upper histogram is for the proposed RunII trigger with a p_T threshold of 1.5 GeV/c, while the lower histogram is the convolution of the RunI CMU-CMU trigger with the Level 1 stub gate. The solid points are the sideband subtracted yields for the $B^+ \to J/\psi K^+$ CMU-CMU signal in RunI.

For 2 fb^{-1} luminosity, this gives a net increase of a factor of $\times$50 in the $J/\psi K^0_S$ yield over the 400 events found in RunI. Assuming the same K^0_S finding efficiency as in RunI, this yields 20,000 fully reconstructed $B^0 \to J/\psi K^0_S$ events. CDF also plans to trigger on $J/\psi \to e^+e^-$, which would increase the number of $J/\psi K^0_S$ events by $\sim$50% [69]. The yield of 20,000 $J/\psi K^0_S$ events thus represents a conservative estimate.

In RunII, CDF expects to improve the effective tagging efficiencies $\varepsilon\mathcal{D}^2$ of the B flavour tagging methods, as summarized in Table 6.1. The extended lepton coverage with the completed muon extension systems and the plug calorimeter results in a total $\varepsilon\mathcal{D}^2$ of 1.7% for lepton tagging. A significant improvement in $\varepsilon\mathcal{D}^2 \sim 3\%$ is possible for jet charge

Flavour tag	$\varepsilon\mathcal{D}^2$ RunI	$\varepsilon\mathcal{D}^2$ RunII	Calib. sample	Sample size
Same side tag	$(1.8 \pm 0.4 \pm 0.3)\%$ [70]	2.0% [69]	$J/\psi K^{*0}$	$\sim 30,000$
Jet charge tag	$(0.78 \pm 0.12 \pm 0.08)\%$ [71]	3.0% [69]	$J/\psi K^+$	$\sim 50,000$
Lepton tag	$(0.91 \pm 0.10 \pm 0.11)\%$ [71]	1.7% [69]	$J/\psi K^+$	$\sim 50,000$
Kaon tag	–	2.4% [72]	$J/\psi K^+$	$\sim 50,000$

Table 6.1: Summary of flavour tagging methods used in the measurement of $\sin 2\beta$, the measured $\varepsilon\mathcal{D}^2$ values from RunI and the data samples used to calibrate the tagging algorithms in RunII.

tagging. The extended coverage of the SVX II detector together with ISL as well as their improved pattern recognition capabilities will substantially enhance the purity of the jet charge algorithm. Together with a value of $\varepsilon\mathcal{D}^2 \sim 2\%$ assumed for same side tagging, this yields a total $\varepsilon\mathcal{D}^2 \sim 9.1\%$ in RunII including opposite side kaon tagging made possible with a Time-of-Flight detector [72]. This results in an error of $\sigma(\sin 2\beta) \sim 0.05$ on a measurement of the CP violation parameter $\sin 2\beta$.

Starting with nominal assumptions on flavour tagging efficiencies and signal-to-background ratios (S/B), the reach on $\sin 2\beta$ can be calculated as a function of integrated luminosity. This is shown in Figure 6.1(b) together with the 5σ reach for the $B^0_s \bar{B}^0_s$ oscillation parameter x_s (right scale).

With respect to estimating the yield of $B^0_s \to J/\psi\phi$ events in 2 fb^{-1} in RunII, we compare the number of observed events in $B^0_s \to J/\psi\phi$ to the number of $B^0 \to J/\psi K^0_S$ events with comparable signal-to-noise in RunI data. Here, we restrict our estimate to J/ψ events fully reconstructed in the RunI silicon vertex detector. We observe a signal of about 80 $B^0_s \to J/\psi\phi$ events in RunI as shown in Figure 6.2. With about 200 $B^0 \to J/\psi K^0_S$ events [70] reconstructed in CDF's RunI silicon detector, we find the number of $B^0_s \to J/\psi\phi$ is approximately 40% the number of $B^0 \to J/\psi K^0_S$. With 20,000 $J/\psi K^0_S$ events estimated above, we expect about 8000 $B^0_s \to J/\psi\phi$ events in 2 fb^{-1} in RunII.

6.2.3 $B^0 \to J/\psi K^0_S$: DØ Report †

One of DØ's primary physics goals is a measurement of CP violation in the golden mode $B^0 \to J/\psi K^0_S$, with $J/\psi \to \mu^+\mu^-$ and $K^0_S \to \pi^+\pi^-$. The measured asymmetry is defined by

$$\mathcal{A}_{CP} = \frac{\Gamma(\overline{B}^0 \to J/\psi K^0_S) - \Gamma(B^0 \to J/\psi K^0_S)}{\Gamma(\overline{B}^0 \to J/\psi K^0_S) + \Gamma(B^0 \to J/\psi K^0_S)}. \tag{6.94}$$

Measured as a function of time, the asymmetry is directly related to the CKM angle β:

$$\mathcal{A}_{CP}(t) = \sin 2\beta \cdot \sin \Delta m_d t. \tag{6.95}$$

†Authors: R. Jesik and K. Yip.

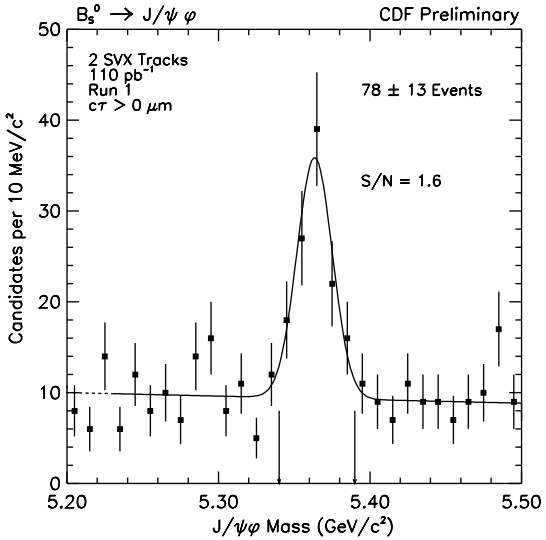

Figure 6.2: Reconstructed $B^0_s \to J/\psi\phi$ events from CDF Run I data with positive B^0_s lifetime.

This measurement involves the full reconstruction of the final state, the reconstruction of the primary and B decay vertices, and a determination of the B flavour at production. The J/ψ decay into dimuons provides a relatively clean trigger signature. With DØ's upgraded muon scintillation counter arrays, these events can be triggered on at the 30% level (see Chapter 4).

This study is based on a sample of 10,000 Monte Carlo events generated by Pythia plus QQ. The DØ detector response was obtained with a full GEANT simulation. An average of 1.1 additional minimum bias interactions were added to the generated events. This sample was also analyzed using MCFAST for comparison.

All of the four tracks comprising the candidate B meson are required to have a hit in each of the 16 layers of the Central Fiber Tracker (CFT). This effectively forces the tracks to be confined in the central rapidity range $|\eta| < 1.6$. The tracks are also required to have at least 8 hits in the silicon detector out of a maximum number of 10 hits possible on average. The CFT hit requirement is dropped for the other tracks in the events. These tracks, which are used for primary vertex finding and flavour tagging, are reconstructed out to $|\eta| < 3.0$.

The trigger for these events requires at least two oppositely charged tracks in the muon system with matching tracks in the CFT with $p_T > 1.5$ GeV/c. The muon tracks must pass the track quality cuts mentioned above during offline reconstruction, and the pair must form a common vertex. The J/ψ vertex defines the B decay vertex in these events. The

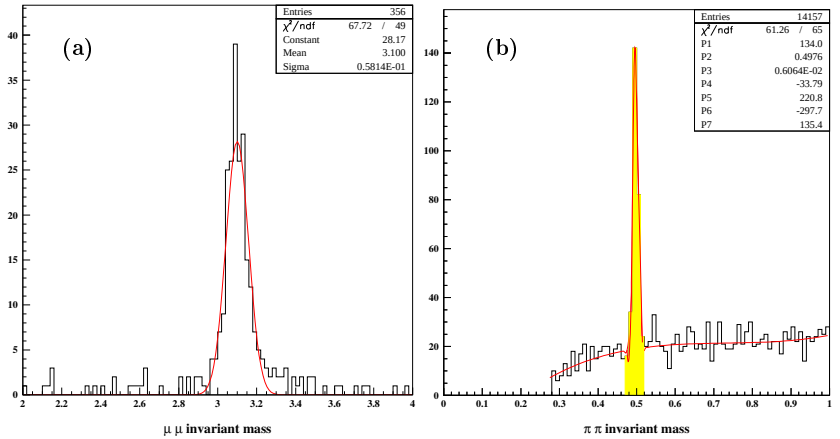

Figure 6.3: Reconstructed (a) $J/\psi \to \mu\mu$ and (b) $K^0_S \to \pi^+\pi^-$ invariant mass in $B^0 \to J/\psi K^0_S$ events.

reconstructed invariant mass of the muon pairs is shown in Fig. 6.3(a). The momentum of combinations with a reconstructed invariant mass within $3\,\sigma$ of the nominal J/ψ mass is re-determined in a kinematic fit with the J/ψ mass constraint imposed.

The most difficult part of the analysis is the reconstruction of the two soft pions from the K^0_S decay in the hadronic $p\bar{p}$ environment with a detector designed to do high p_T physics. At present, DØ's track finding software only reconstructs tracks with p_T greater than 0.5 GeV/c. This is a stringent cutoff for K^0_S detection. Lowering this threshold has been shown to be viable for B physics events. It remains to be seen if it will be possible to lower the momentum threshold for more complicated events, such as $t\bar{t}$. Thus, we will use the default cutoff of 0.5 GeV/c for this study. K^0_S candidates are formed by combining pairs of oppositely charged tracks which do not point back to the primary vertex – an impact parameter significance of at least three is required for each track. The track pairs are also required to form a common vertex downstream of that of the J/ψ. The invariant mass of these pairs (assuming they are pions) is shown in Fig. 6.3(b). A clear K^0_S peak is observed, and track pairs with a reconstructed mass within $3\,\sigma$ of the actual K^0_S mass undergo a kinematic fit determining new momentum vectors after imposing the K^0_S mass constraint. The K^0_S candidate's momentum vector is then required to point back to the J/ψ vertex to within $3\,\sigma$, and is combined with that of the mass constraint J/ψ to form the candidate B momentum, which is then required to point back to the primary vertex.

The invariant mass spectrum of B candidates which pass these criteria is shown in Fig. 6.4. A clear signal is obtained with a width of about 10 MeV/c^2. The corresponding proper decay time resolution is 90 fs. We obtain a reconstruction efficiency for the entire decay chain of 8.5%, resulting in 34,000 fully reconstructed $B^0 \to J/\psi K^0_S$ ($J/\psi \to \mu^+\mu^-$, $K^0_S \to \pi^+\pi^-$) decays in 2 fb^{-1} (see Table 6.2). For comparison, the MCFAST study gives

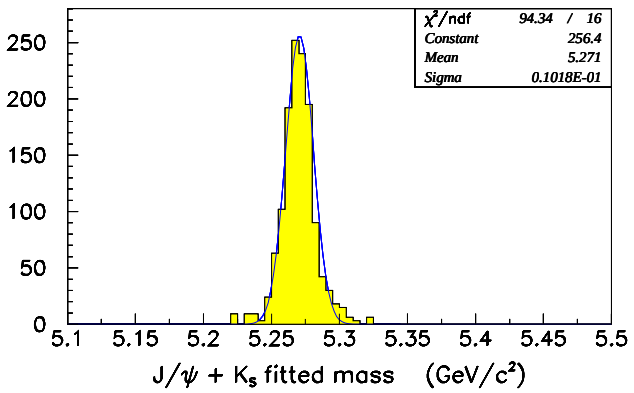

Figure 6.4: Reconstructed B mass in $B \to J/\psi K^0_S$ events after mass and vertex constraints.

an efficiency of 10%.

The other crucial element in this analysis is tagging the initial flavour of the decaying B^0 meson. One method for doing this makes use of the correlation between the charge of a nearby pion and the B flavour due to fragmentation or B^{**} production. This requires the reconstruction of soft pions from the primary vertex. Two other methods use information from the other B hadron in the event. If the B decays semileptonically, its flavour is determined by the charge of the lepton. If not, its flavour can be determined by the p_T weighted net charge of its jet. The effectiveness of a tagging method is quantified by the effective tagging efficiency $\varepsilon\mathcal{D}^2$, where ε is the tagging efficiency and $\mathcal{D}$ is the dilution factor. $\mathcal{D}$ is equal to $2P-1$, where P is the probability that the method tags the B flavour correctly. Extrapolating from the effective tagging efficiencies measured by CDF in RunI

Integrated luminosity	2 fb^{-1}
$\sigma_{b\bar{b}}$	158 μb
$f(b\bar{b} \to B^0, \bar{B}^0)$	0.8
Kinematic acceptance	0.31
$\mathcal{B}(B^0 \to \mu^+\mu^-\pi^+\pi^-)$	2.0×10^{-5}
Trigger efficiency	0.30
Reconstruction efficiency	0.085
Number of reconstructed $B^0 \to J/\psi K^0_S$	34,000
Effective tagging efficiency ($\varepsilon\mathcal{D}^2$)	0.10

Table 6.2: The expected number of $B^0 \to J/\psi K^0_S$ events at DØ.

Flavour tag	$\varepsilon\mathcal{D}^2$ CDF RunI	$\varepsilon\mathcal{D}^2$ DØ RunII
Same side tag	$(1.8 \pm 0.4 \pm 0.3)\%$	2.0%
Jet charge tag	$(0.78 \pm 0.12 \pm 0.08)\%$	3.1%
Lepton tag	$(0.91 \pm 0.10 \pm 0.11)\%$	4.7%

Table 6.3: Summary of flavour tagging methods at DØ.

(see Section 6.2.2), DØ expects to achieve an effective tagging efficiency of $\varepsilon\mathcal{D}^2 \sim 10\%$. The breakdown of the effective tagging efficiency for each of the flavour tagging methods is shown in Table 6.3. The increase over CDF RunI efficiencies is primarily due to DØ's extended rapidity range for tracking and lepton identification.

The accuracy of a time dependent $\sin 2\beta$ measurement is given by:

$$\sigma(\sin 2\beta) \approx e^{x_d^2\Gamma^2\sigma_t^2} \sqrt{\frac{1+4x_d^2}{2x_d^2}} \frac{1}{\sqrt{\varepsilon\mathcal{D}^2 N}} \sqrt{1+\frac{B}{S}}, \qquad (6.96)$$

where x_d and Γ are the mixing parameter and decay width of the B^0, σ_t is the proper time resolution (which is about 90 fs), N is the number of reconstructed signal events, and S/B is the signal to background ratio (extracted from RunI data to be about 0.75). With these considerations, DØ will be able to measure $\sin 2\beta$ in the dimuon mode with an uncertainty of 0.04 in 2 fb^{-1} of data. Similar accuracy will be achieved in the dielectron mode. This precision is quite competitive with CDF's projections and both experiments will reach B factory sensitivities with further data taking.

Similarly, DØ will look for CP violation in $B^0_s \to J/\psi\phi$ decays. DØ expects a sample of 1400 fully reconstructed events in 2 fb^{-1} in RunII. Although the expected Standard Model asymmetry in this channel is not within our experimental reach, an observation would be a clear signal of new physics.

6.2.4 $B^0 \to J/\psi K^0_S$: BTeV Report †

As discussed in Section 6.1, the decay $B^0 \to J/\psi K^0_S$ is the golden mode for measuring the angle β of the unitarity triangle. While $\sin 2\beta$ has been measured before the BTeV experiment begins operation, the collaboration aims to significantly improve that measurement. This section will present the reconstruction efficiency, trigger efficiency and signal to background ratio for the decay chain $B^0 \to J/\psi K^0_S$, $J/\psi \to \mu^+\mu^-$ and $K^0_S \to \pi^+\pi^-$.

For this study, Monte Carlo events were generated using Pythia and QQ and the detector response was simulated using BTeVGeant. The output of BTeVGeant was analyzed as would be real data. When designing analysis cuts, it is important to understand both the efficiency of the cuts on signal events and the power of the cuts to reject background. Because of the narrow widths of the J/ψ and the K^0_S, the dominant source of background

†Authors: P.A. Kasper and R. Kutschke.

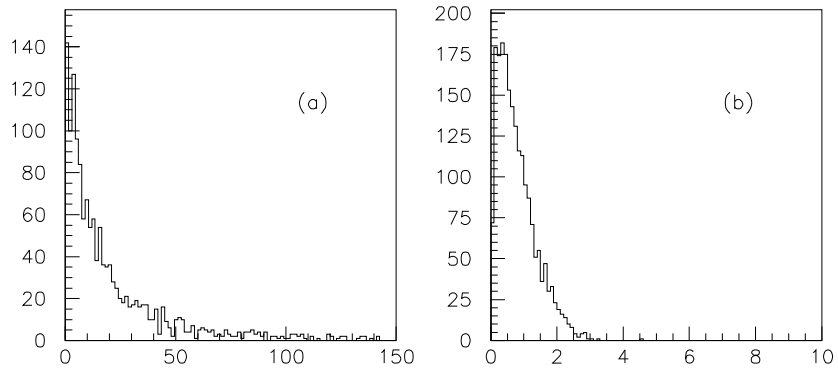

Figure 6.5: Distributions of L/σ_L for (a) J/ψ candidates from the decays of b hadrons and (b) prompt J/ψ candidates. The prompt candidates are suppressed by requiring $L/\sigma_L > 4$.

entries is combinations of real $J/\psi \to \mu^+\mu^-$ decays with real $K^0_S \to \pi^+\pi^-$ decays. CDF found that prompt J/ψ's constitute a large fraction of the total J/ψ production [73] and, extrapolating from their results, one expects that J/ψ's from B decays comprise only about 5% of the total J/ψ production including the regions of high pseudorapidity. However, the background from prompt J/ψ production is strongly suppressed by the topological cuts, leaving decays of the type $b \to J/\psi X$ as the dominant source of background.

The analysis was performed as follows. Each event was required to have an identified primary vertex that was successfully fitted. A track was identified as a muon candidate provided the Monte Carlo truth table indicated that it was a muon, it had a momentum of more than 5.0 GeV/c and it had a hit in the most downstream muon detector. J/ψ candidates were formed by combining pairs of oppositely charged muon candidates and requiring that the invariant mass of the $\mu^+\mu^-$ pair be within $3\,\sigma$ of the known mass of the J/ψ. It was also required that the $\mu^+\mu^-$ pair pass a fit to a common vertex and the vertex be detached from the primary vertex by at least $L/\sigma_L > 4$, where L is the distance between the two vertices and σ_L is the error on L. As illustrated in Figure 6.5, this cut rejects 99.95% of the background from prompt J/ψ's while keeping 80% of the signal. A fit was performed to constrain the $\mu\mu$ mass to that of the J/ψ.

All other tracks with a momentum of at least 0.5 GeV/c were accepted as pion candidates, provided they missed the primary vertex by $d > 3\,\sigma_d$, where d is the impact parameter between the track and the primary vertex, while σ_d is the error on d. K^0_S candidates were selected by combining oppositely charged pairs of pion candidates and requiring that the $\pi^+\pi^-$ invariant mass be within $3\,\sigma$ of the known K^0_S mass. It was also required that K^0_S candidates pass a fit to a common vertex. Finally, the mass of the K^0_S candidate was constrained to that of the known K^0_S table mass.

A B^0 candidate was defined as the combination of a J/ψ candidate and a K^0_S candidate

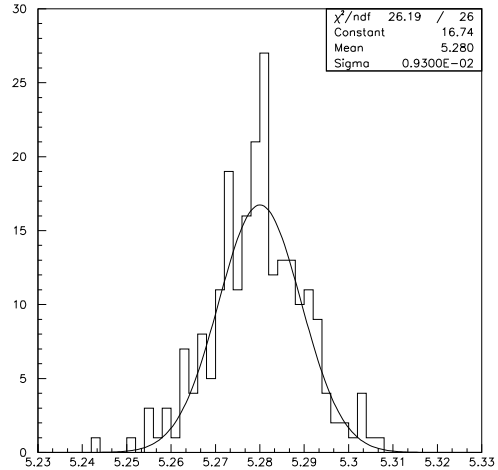

Figure 6.6: The $J/\psi K^0_S$ invariant mass distribution for candidates which survive the selection criteria described in the text.

which pointed back to the primary vertex. To reduce combinatorial background, it was required that the K^0_S candidate points back to the J/ψ vertex within $3\,\sigma$ and that the K^0_S impact parameter with respect to the J/ψ vertex divided by its impact parameter with respect to the primary vertex be less than 2.0.

The invariant mass spectrum of B candidates which pass the above criteria is shown in Figure 6.6. A clear signal with a width of $\sigma = 9.3$ MeV/c^2 is seen at the mass of the B^0. The efficiency for a $B^0 \to J/\psi K^0_S$ decay to fall into the mass peak is 0.040 ± 0.002 and the mean resolution on the proper decay time is 40-50 fs.

As mentioned above, the dominant source of background arises from decays of the type $b \to J/\psi X$. This background was studied by generating large samples of such decays, using Pythia and QQ. These samples were passed through the MCFast based detector simulation and analyzed as real data. This study predicted that the signal to background ratio in this channel is approximately $S/B = 10$.

The BTeV trigger simulation (see Sec. 5.4.3) was run on events which passed the analysis cuts, and the Level 1 trigger was found to have an efficiency of $(52 \pm 3)\%$. This decay mode can also be triggered by muon and dimuon triggers with an estimated trigger efficiency of 50%. Furthermore, it is estimated that the combined Level 2 trigger efficiency is 90%.

In Section 5.5, it is estimated that the effective tagging efficiency $\varepsilon\mathcal{D}^2$ for B^0 decays is 0.10. There are two methods which can be used to extract $\sin 2\beta$ from the reconstructed, tagged $J/\psi K^0_S$ candidates, a time integrated method and a time dependent method. The

Luminosity	$2 \times 10^{32}\,\mathrm{cm}^{-2}\,s^{-1}$
Running time	10^7 s
$\sigma_{b\bar{b}}$	$100\,\mu$b
Number of $B\bar{B}$ events	2×10^{11}
$\mathcal{B}(\bar{b} \to B^0)$	0.4
Number of B^0 or $\bar{B}^0$	1.6×10^{11}
$\mathcal{B}(B^0 \to J/\psi K^0_S)$	4.45×10^{-4}
$\mathcal{B}(J/\psi \to \mu^+\mu^-)$	0.061
$\mathcal{B}(K^0_S \to \pi^+\pi^-)$	0.6861
ϵ(Geometric + Cuts)	0.04
Level 1 Trigger efficiency	0.75
Level 2 Trigger efficiency	0.90
Number of reconstructed $B^0 \to J/\psi K^0_S$	80,500
Tagging efficiency $\varepsilon\mathcal{D}^2$	10%
S/B	10
Resolution on proper decay time	0.043 ps
$\sigma(\sin 2\beta)$, time integrated	0.030
$\sigma(\sin 2\beta)$, time dependent	0.025

Table 6.4: Summary of the sensitivity to $\sin 2\beta$ using $B \to J/\psi K^0_s$ at BTeV.

sensitivity of the time integrated method is given by,

$$\sigma(\sin 2\beta) = \frac{1 + x_d^2}{x_d}\sqrt{\frac{1}{\varepsilon\mathcal{D}^2 N}}\sqrt{\frac{S+B}{S}}\,, \tag{6.97}$$

while the sensitivity of the time dependent method is given by,

$$\sigma(\sin 2\beta) \approx \mathrm{e}^{x_d^2\Gamma_d{}^2\sigma_t^2}\sqrt{\frac{1+4x_d^2}{2x_d^2}}\sqrt{\frac{1}{\varepsilon\mathcal{D}^2 N}}\sqrt{\frac{S+B}{S}}\,, \tag{6.98}$$

where N is the number of tagged decays, $x_d = 0.723 \pm 0.032$ [62] is the B^0 mixing parameter, σ_t is the resolution on the proper decay time and where $\Gamma_d = (0.641 \pm 0.016) \times 10^{12}\ \mathrm{s}^{-1}$ [62] is the natural width of the B^0. For the B^0, the time dependent method yields a sensitivity which is about 20% better than that given by the time integrated method. In previous documents the BTeV collaboration has reported the sensitivity on $\sin 2\beta$ using the time integrated method but in this document the time dependent method will be quoted. The above discussion is summarized in Table 6.4 which reports a sensitivity of $\sigma(\sin 2\beta) = 0.025$.

6.2.5 $B^0 \to J/\psi K^0_S$: Summary †

The main goal of measuring the CP violating asymmetry in the so-called golden-plated decay mode $B^0 \to J/\psi K^0_S$ is to determine the phase β within the Standard Model. It is given in terms of CKM matrix elements as $\beta \equiv \arg(-V_{cd}V^*_{cb}/V_{td}V^*_{tb})$. Evaluating the sensitivity of the Tevatron experiments towards measuring $\sin 2\beta$ was motivated by using $B^0 \to J/\psi K^0_S$ as a benchmark process for all three experiments and as a comparison with the expectations of the B factories.

With 2 fb^{-1} of integrated luminosity, CDF expects to reconstruct 20,000 $B^0 \to J/\psi K^0_S$ events with $J/\psi \to \mu^+\mu^-$ and $K^0_S \to \pi^+\pi^-$, a net increase of a factor of ~ 50 compared to the $J/\psi K^0_S$ yield in RunI. Assuming a total effective tagging efficiency of $\varepsilon\mathcal{D}^2 \sim 9.1\%$, as discussed in Sec. 6.2.2, this results in an error on a measurement of $\sin 2\beta$ of $\sigma(\sin 2\beta) \sim 0.05$ at CDF. The DØ experiment expects to measure $\sin 2\beta$ with similar precision. DØ will reconstruct about 34,000 $B^0 \to J/\psi K^0_S$ events with $J/\psi \to \mu^+\mu^-$ and $K^0_S \to \pi^+\pi^-$ in 2 fb^{-1}. DØ uses a total effective tagging efficiency of $\varepsilon\mathcal{D}^2 \sim 10\%$ derived from CDF's Run I experience of B flavour tagging (see Sec. 6.2.2). This gives DØ an uncertainty of $\sigma(\sin 2\beta) \sim 0.04$.

While $\sin 2\beta$ will have been measured before the BTeV experiment will turn on, the goal of the BTeV collaboration is to significantly improve the precision of that measurement. Within one year of running at design luminosity, BTeV expects to reconstruct about 80,000 $B^0 \to J/\psi K^0_S$ events with $J/\psi \to \mu^+\mu^-$ and $K^0_S \to \pi^+\pi^-$. Together with an effective tagging efficiency of $\varepsilon\mathcal{D}^2 \sim 10\%$, as discussed in Sec. 6.2.4, this will allow BTeV to measure $\sin 2\beta$ with an error of $\sigma(\sin 2\beta) \sim 0.025$. At that point in time, the B physics community will clearly have entered the area of precision CKM measurements.

6.3 Study of $B \to \pi\pi/KK$

6.3.1 $B \to \pi\pi/KK$: Introduction †

One of the key physics goals of RunII is the study of CP violation in B meson decays. At the time the CDF Technical Design Report [69] was written, the most important decay modes were believed to be $B^0 \to J/\psi K^0_S$ and $B^0 \to \pi^+\pi^-$. Time dependent CP violation in the former mode measures $\sin 2\beta$ [74], while the decay $B^0 \to \pi^+\pi^-$ usually appears in the literature as a tool to determine $\alpha = 180^\circ - \beta - \gamma$. Using standard phase conventions, β and γ are the phases of the CKM matrix elements V_{td} and V^*_{ub}, respectively.

As discussed in Section 6.1.7 from a theoretical aspect, penguin contributions are expected to affect the determination of α severely [75]. Experimentally, the CLEO collaboration [23] has shown that "penguin pollution" in $B^0 \to \pi^+\pi^-$ is sufficiently large to make the extraction of fundamental physics parameters from the measured CP asymmetry rather difficult. Any evaluation of the physics reach in measuring CP violation in $B^0 \to \pi^+\pi^-$ does

†Author: M. Paulini.
†Author: F. Würthwein.

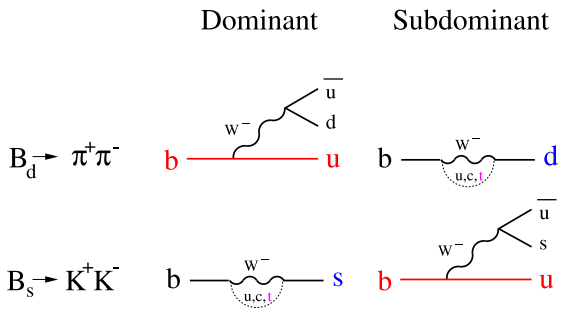

Figure 6.7: Feynman diagrams in charmless hadronic B meson decays contributing to $B^0 \to \pi^+\pi^-$ and $B_s^0 \to K^+K^-$.

therefore require a strategy to dis-entangle "penguin" contributions from "tree" diagrams in order to lead to a meaningful measurement of short distance physics.

Figure 6.7 shows the two dominant Feynman diagrams in charmless hadronic B decays contributing to $B^0 \to \pi^+\pi^-$ and $B_s^0 \to K^+K^-$. Simple counting of vertex factors indicates that $b \to s\bar{u}u$ "penguin" and $b \to u\bar{u}d$ "tree" transitions are roughly of the same magnitude, while $b \to d\bar{u}u$ "penguin" and $b \to u\bar{u}s$ "tree" transitions are suppressed by $\mathcal{O}(\lambda)$ with respect to these dominant amplitudes. Defining ΔS as the change in strangeness quantum number, it is thus expected that transitions with $\Delta S = 0$ are dominated by external W-emission ("tree") decays. In contrast, $\Delta S = 1$ transitions generally receive their dominant contributions from gluonic penguin decays.

A large number of strategies to disentangle penguin and tree contributions can be found in the literature [75,76]. However, they generally require either very large data sets or involve hard to quantify theoretical uncertainties. In the following, we evaluate a strategy of measuring the CKM angle γ [16] which is particularly well matched to the capabilities of the Tevatron as it relates CP violating observables in $B_s^0 \to K^+K^-$ and $B^0 \to \pi^+\pi^-$. Combining the CP violating observables in these two decays with the CP violation measured in $B^0 \to J/\psi K_s^0$ allows for a measurement of γ up to a fourfold ambiguity. The utility of $B_s^0 \to K^+K^-$ to probe γ was already pointed out in several previous publications [77], and the use of CP violating asymmetries in B to $K^\pm\pi^\mp$ decays is discussed in Ref. [78].

The decays $B^0 \to \pi^+\pi^-$ and $B_s^0 \to K^+K^-$ are related to each other by interchanging all down and strange quarks, i.e. through the so-called "U-spin" subgroup of the SU(3) flavour symmetry of strong interactions. The strategy proposed in Ref. [16] uses this symmetry to relate the ratio of hadronic matrix elements for the penguin and tree contributions, and thus uses $B_s^0 \to K^+K^-$ to correct for the penguin pollution in $B^0 \to \pi^+\pi^-$.

This strategy does not rely on certain "plausible" dynamical or model-dependent assumptions, nor are final-state interaction effects [79] of any concern. These led to considerable attention in the recent literature on measuring γ from $B \to \pi K$ decays [80]. The theoretical accuracy is only limited by U-spin-breaking effects. We evaluate the likely size

Scenario	$T_{\rm bunch}$ [ns]	$\mathcal{L}$ [cm^{-2}s^{-1}]	$\langle N_{p\bar{p}} \rangle$	L1 cross section [μb]	L1 rate [kHz]	L2 cross section [nb]	L2 rate [Hz]
A	396	0.7×10^{32}	2	252 ± 18	18	360 ± 100	25
B	132	2.0×10^{32}	2	152 ± 14	30	196 ± 74	39
C	396	1.7×10^{32}	5	163 ± 16	28	84 ± 48	14

Table 6.5: Level 1 trigger criteria and event rates as well as Level 2 trigger cross sections and event rates for three operating scenarios of the Tevatron during Run II [81].

of these effects and find them to be small compared to the expected experimental error on γ in RunII.

6.3.2 $B \to \pi\pi/KK$: CDF Report [†]

6.3.2.1 Trigger Issues

The key to measuring the CP asymmetry in $B^0 \to \pi^+\pi^-$ is to trigger on this decay mode in hadronic collisions. CDF will do this with its three level trigger system where the throughput of each level will be increased by more than an order of magnitude from the RunI trigger scheme to accommodate the shorter $p\bar{p}$ crossing interval (initially 396 ns and later in Run II 132 ns), and the increase in instantaneous luminosity by one order of magnitude. The maximum output of Level 1 and Level 2 will be 50 kHz and 300 Hz, respectively. The trigger rates presented in the following have been studied using minimum bias data for Level 1 and data sets collected with specialized test triggers taken during RunIb for Level 2.

At Level 1, two oppositely charged tracks found by the XFT track processor [69] are used. The XFT can find tracks of $p_T > 1.5$ GeV/c that traverse the full radius of the COT with a momentum resolution $\Delta p_T/p_T^2 < 0.015$ (GeV/c)$^{-1}$ and an azimuthal resolution at superlayer 6 ($r = 106$ cm) of $\Delta\phi_6 < 0.0015$ rad. The two-track module compares the values of p_T and ϕ_6 from all pairs of tracks to valid trigger patterns in a lookup table. Three sets of two-track trigger criteria [81] are listed in Table 6.5 corresponding to three possible operating conditions of the Tevatron. Scenarios A, B and C cover the possible bunch separations ($T_{\rm bunch}$), instantaneous luminosity ($\mathcal{L}$) and mean number of interactions per crossing ($\langle N_{p\bar{p}} \rangle$). The Level 1 trigger cross sections are listed in Table 6.5. CDF expects to allocate a maximum of 30 kHz to the two-track trigger at Level 1.

At Level 2, CDF uses the SVT [69], which associates clusters formed from axial strips in the SVX II with tracks of $p_T > 2$ GeV/c found by the XFT. This provides a measurement of the impact parameter of the track in the plane transverse to the beam axis. This measurement is sufficiently precise to resolve the true large impact parameters of tracks coming from the decays of heavy flavour from the impact parameters of tracks originating from QCD jets, which have non-zero impact parameter only due to measurement resolution. The

[†]Author: F. Würthwein.

assumed impact parameter resolutions for the SVT [81] are $\sigma_d = (19 + 40\ \mathrm{GeV}/c/p_T)\ \mu$m for tracks that miss the hybrid in Layer 0 of SVX II and $\sigma_d = (19 + 80\ \mathrm{GeV}/c/p_T)\ \mu$m for tracks that pass through the hybrid in Layer 0. The expected Level 2 trigger rates are given in Table 6.5 and are well below the total Level 2 bandwidth of 300 Hz. At Level 3, the full event information is available further reducing the trigger rate.

The data collection of B_s^0 decay modes for the measurement of B_s^0 flavour oscillations at CDF in Run II is also based on the two-track hadronic trigger. The Level 1 two-track trigger scheme is the same as for $B^0 \to \pi\pi$ as summarized in Table 6.5. The Level 2 trigger selection requirements have been slightly adjusted [81] to achieve a better efficiency for triggering on any two tracks from the hadronic B_s^0 decay (see also Section 8.6 and in particular Sec. 8.6.2).

6.3.2.2 Expected Rates

As discussed in Section 6.3.1, the decays $B^0 \to K^+\pi^-$ and $B_s^0 \to K^+K^-$ are $\Delta S = 1$ transitions, and are expected to be dominated by gluonic penguin decays. In contrast, $B^0 \to \pi^+\pi^-$ and $B_s^0 \to \pi^+K^-$ are expected to receive their dominant contributions from external W-emission ("tree"). For the decays $B^0 \to K^+K^-$ and $B_s^0 \to \pi^+\pi^-$ neither of the initial quarks is present in the final state. These transitions are thus expected to be highly suppressed as they require either W-exchange or in-elastic final state re-scattering.

Experimental information on these decays comes from the CLEO experiment [23]. They measured $\mathcal{B}(B^0 \to K^+\pi^-) = (17.2^{+2.5}_{-2.4} \pm 1.2) \times 10^{-6}$, $\mathcal{B}(B^0 \to \pi^+\pi^-) = (4.3^{+1.6}_{-1.4} \pm 0.5) \times 10^{-6}$, and $\mathcal{B}(B^0 \to K^+K^-) < 1.9 \times 10^{-6}$ at 90% Confidence Level. Average over charge conjugate decays is implied in all three of these measurements. In addition, CLEO measured $[\mathcal{B}(B^0 \to K^+\pi^-) - \mathcal{B}\bar{B}^0 \to K^-\pi^+)]/[\mathcal{B}(B^0 \to K^+\pi^-) + \mathcal{B}(\bar{B}^0 \to K^-\pi^+)] = -0.04 \pm 0.16$ [82]. More recent results from BaBar and Belle [83] might point towards a more favorable ratio of $B^0 \to \pi^+\pi^-/B^0 \to K^+\pi^-$. To be conservative, we base our projections on the published CLEO numbers [23].

The corresponding B_s^0 decays have not been observed. However, we can make an educated guess regarding their branching fractions by assuming $SU(3)$ flavour symmetry as follows:

$$\begin{aligned} \mathcal{B}(B_s^0 \to K^+K^-) &= (F_K/F_\pi)^2 \times \mathcal{B}(B^0 \to K^+\pi^-)\,, \\ \mathcal{B}(B_s^0 \to \pi^+K^-) &= (F_K/F_\pi)^2 \times \mathcal{B}(B^0 \to \pi^+\pi^-)\,. \end{aligned} \tag{6.99}$$

The factor $(F_K/F_\pi)^2$ accounts for $SU(3)$ breaking. Assuming factorization $F_K(F_\pi)$ is given by the $B \to K(B \to \pi)$ form factor, and thus $(F_K/F_\pi)^2 \sim 1.3$. Taking into account the production ratio of $f_s/f_d \sim 0.4$ [84], we expect the following relative yields:

$$(B^0 \to K\pi) : (B^0 \to \pi\pi) : (B_s^0 \to KK) : (B_s^0 \to \pi K) \ \sim\ 4 \ :\ 1 \ :\ 2 \ :\ 0.5. \tag{6.100}$$

The $B^0 \to \pi^+\pi^-$ signal yield is obtained from Monte Carlo simulation taken from Ref. [81]. We rescale the yield cited there by the CLEO branching fractions quoted above and the updated measurement of the B cross section $\sigma_B = (3.35 \pm 0.46 \pm 0.50)\ \mu$b [85] using fully reconstructed $B^+ \to J\psi K^+$ decays. From this estimate, CDF expects 5060 to 9160 fully

reconstructed $B^0 \to \pi^+\pi^-$ events in 2 fb^{-1}. To be conservative, we choose 5000 $B^0 \to \pi^+\pi^-$ and 20,000 $B^0 \to K^+\pi^-$ events for this study. With the event ratio given in Eq. (6.100), we arrive at an expected $B_s^0 \to K^+K^-$ and π^+K^- yield of 10,000 and 2500 events, respectively. Yields in the two $K\pi$ final states refer to the sum of $K^+\pi^-$ and $K^-\pi^+$.

To answer the question whether CDF will be able to extract these large signals from potentially enormous backgrounds, we discuss physics backgrounds such as $B \to K\pi$ and combinatorial background separately. A study using specialized test trigger data, described in Ref. [86], addresses the issue of combinatorial background. This study finds two events in a region of ± 500 MeV/c^2 around the nominal B mass. Based on trigger simulations and the branching fractions listed above, CDF expects 0.08 signal events in the sum of all two track decays of the B^0 and B_s^0 within a signal window of ± 50 MeV/c^2 around the nominal B mass. From this we conclude a signal-to-background ratio (S/B) not worse than 0.4.

Based on the measured cross sections and Monte Carlo simulation of the trigger efficiency for generic B decays, CDF expects that roughly 1/4 of the two-track hadronic trigger rate is from $b\bar{b}$ and $c\bar{c}$ each. Backgrounds from these two sources result in a two-track invariant mass spectrum far away from the B signal region. We thus expect the dominant backgrounds to come from mis-measured tracks without true lifetime. Detailed studies of this type of background can only be done once data with the new Run II silicon detector is available. However, it is not unreasonable to expect the 3-dimensional vertexing capabilities of SVX II to improve upon the S/B of 0.4 obtained from the Run I estimates.

6.3.2.3 Disentangling $\pi\pi$, $K\pi$, KK and πK Final States

Figure 6.8(a) shows the expected invariant mass peaks for 20,000 $B^0 \to K^\pm\pi^\mp$, 5000 $B^0 \to \pi^+\pi^-$, 10,000 $B_s^0 \to K^+K^-$ and 2500 $B_s^0 \to K^\mp\pi^\pm$, on top of 56250 events of combinatorial background. In each case the pion mass is used to calculate the track energy. The four mass peaks are not particularly distinct and are shown separately in Figure 6.8(b). This initial simulation indicates a $\pi\pi$ invariant mass resolution of about 25 MeV/c^2. The flat background generated is equivalent to a signal/background ratio of 3/1 over the region $5.2 < m_{\pi\pi} < 5.3$ GeV/c^2, rather than the $S/B \sim 0.4$ from the previous section.

A $B^0 \to \pi^+\pi^-$ signal can be extracted from the physics backgrounds from $B \to K\pi$ and $B_s^0 \to KK$ decays by making use of the invariant $\pi\pi$ mass distribution as well as the $\mathrm{d}E/\mathrm{d}x$ information provided by the COT. Using the specific energy loss $\mathrm{d}E/\mathrm{d}x$, we expect a K-π separation of 1.3 σ for track momentum $p_T > 2$ GeV/c. Note, the $B_s^0 \to K^+K^-$ peak lies directly under the $B^0 \to \pi^+\pi^-$ signal requiring particle identification through $\mathrm{d}E/\mathrm{d}x$.

Given the limited particle identification capabilities provided by invariant mass resolution and $\mathrm{d}E/\mathrm{d}x$, it is important to demonstrate how well CDF can separate the four final states using mass and $\mathrm{d}E/\mathrm{d}x$ alone. To assess this issue, we generate a sample of 93,750 events drawn from the four signal hypotheses as shown in Table 6.6. We also include combinatoric background, where the ratio of $K\pi : \pi\pi : KK = 1 : 2 : 1$ in the background sample is a completely arbitrary choice. We then perform a Maximum Likelihood fit to determine the yields for the four signal and three background hypotheses. Comparing the errors on the yields as returned from the fit with $1/\sqrt{N}$ of the number of generated events,

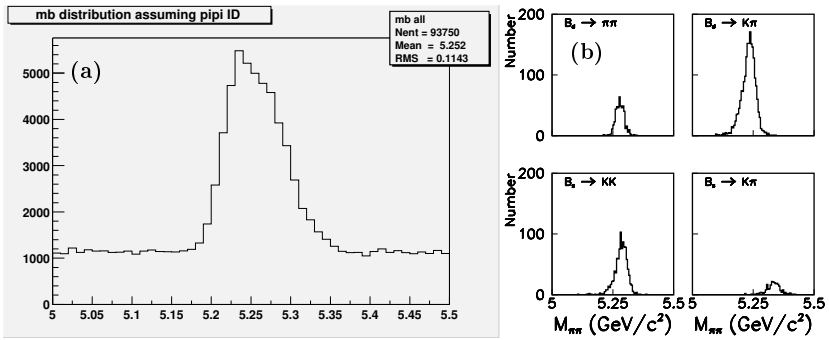

Figure 6.8: Two-track invariant mass assuming pion hypothesis for $B \to \pi\pi$, $K\pi$, KK and πK final states (a) added together and (b) shown separately.

we can calculate an "effective" signal/background ratio =: S/B for the four signal samples as follows:

$$\sigma_{\rm yield}/{\rm yield} = \sqrt{\frac{1+B/S}{\rm yield}} \tag{6.101}$$

The relative errors on the yields and the effective signal/background are listed in Table 6.6.

In summary, we expect the $B \to \pi\pi$, $K\pi$, KK and πK yields in the untagged sample to be measured with an uncertainty of only a few percent. In the absence of exact knowledge of relative production cross sections for B^0 and B_s^0, as well as branching fractions this fit to the untagged sample is crucial in determining the denominator for the measured CP asymmetry. Separating $\pi\pi$, $K\pi$ and KK is less of a problem for the numerator as we are helped here by the vast difference in oscillation frequency.

From the Monte Carlo exercise described above, we conclude that separating the various B decays into two track hadronic final states is not a limiting factor in the measurement of the time dependent CP asymmetries.

6.3.2.4 CP Violating Observables

Two of the four signal modes of interest ($B^0 \to K^\pm\pi^\mp$ and $B_s^0 \to K^\mp\pi^\pm$) are self-tagging, two ($B^0 \to \pi^+\pi^-$ and $B_s^0 \to K^+K^-$) are CP eigenstates for which we expect sizable yields, and two ($B_s^0 \to \pi^+\pi^-$ and $B^0 \to K^+K^-$) are unlikely to be observed at CDF during RunII, unless final state re-scattering and/or new physics effects in these decays are sizable. For the self-tagging decay modes, one can distinguish in principle two CP violating observables, depending on whether or not the B has mixed before it decayed:

	$K\pi$	$\pi\pi$	KK
B^0	20,000	5000	0
σ	0.95%	2.8%	-
B_s^0	2500	0	10,000
σ	4.8%	-	1.6%
bkg	14,000	28,000	14,000
	"Effective" S/B		
B_s^0:	0.21	-	0.64
B^0:	1.24	0.34	-

Table 6.6: Parameters used and results obtained in the Toy Monte Carlo study to determine the errors on the $B \to \pi\pi$, $K\pi$, KK and πK yields in the untagged sample.

$$\begin{aligned}
\text{unmixed:}\quad & \frac{(B^0 \to K^+\pi^-) - (\bar{B}^0 \to \pi^+K^-)}{(B^0 \to K^+\pi^-) + (\bar{B}^0 \to \pi^+K^-)} = \frac{|A|^2 - |\bar{A}|^2}{|A|^2 + |\bar{A}|^2} \\
\text{mixed:}\quad & \frac{(B^0 \to K^-\pi^+) - (\bar{B}^0 \to \pi^-K^+)}{(B^0 \to K^-\pi^+) + (\bar{B}^0 \to \pi^-K^+)} = -\frac{|A|^2 - |q/p|^4|\bar{A}|^2}{|A|^2 + |q/p|^4|\bar{A}|^2}
\end{aligned} \tag{6.102}$$

In practice, i.e. within the Standard Model where $|q/p| - 1 \ll 1$, and even for many reasonable extensions of the Standard Model, we expect at most $|q/p| - 1 \sim \mathcal{O}(10^{-2})$. Furthermore, $|p/q| \neq 1$ is probably better searched for with doubly tagged inclusive $b\bar{b}$ samples. The classic example analysis is to search for a charge asymmetry $(\ell^+\ell^+ - \ell^-\ell^-)/(\ell^+\ell^+ + \ell^-\ell^-)$ in events where both b and $\bar{b}$ decay semileptonically. In the following, we therefore will not consider a time dependent analysis nor tagging for the two self-tagging decay modes.

For the decays into CP eigenstates there are three CP violating observables $\mathcal{A}_{CP}^{dir}$, $\mathcal{A}_{CP}^{mix}$, and $\mathcal{A}_{\Delta\Gamma}$. Either $\mathcal{A}_{CP}^{dir} \neq 0$, or $\mathcal{A}_{CP}^{mix} \neq 0$, or $|\mathcal{A}_{\Delta\Gamma}| \neq 1$ would indicate CP violation. In fact, the three observables are related for each decay mode separately by:

$$(\mathcal{A}_{CP}^{dir})^2 + (\mathcal{A}_{CP}^{mix})^2 + (\mathcal{A}_{CP}^{\Delta\Gamma})^2 = 1. \tag{6.103}$$

The time dependent rate asymmetry is given by:

$$\begin{aligned}
\frac{(B_s^0 \to K^+K^-) - (\bar{B}_s^0 \to K^+K^-)}{(B_s^0 \to K^+K^-) + (\bar{B}_s^0 \to K^+K^-)} &= \frac{2e^{-\langle\Gamma\rangle t}}{e^{-\Gamma_H t} + e^{-\Gamma_L t} + \mathcal{A}_{CP}^{\Delta\Gamma}(e^{-\Gamma_H t} - e^{-\Gamma_L t})} \\
&\quad \times (\mathcal{A}_{CP}^{mix} \sin\Delta m t + \mathcal{A}_{CP}^{dir} \cos\Delta m t)
\end{aligned} \tag{6.104}$$

In other words, the oscillation amplitude $\mathcal{A}_{CP} = \sqrt{(\mathcal{A}_{CP}^{dir})^2 + (\mathcal{A}_{CP}^{mix})^2}$ is modulated by an exponentially rising (or falling) "pre-factor" as shown in Figure 6.9. The size of this effect depends on the size of the lifetime difference, $\Delta\Gamma = \Gamma_H - \Gamma_L \neq 0$ and on

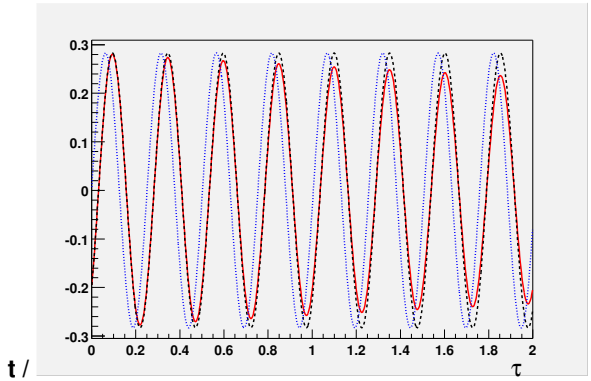

Figure 6.9: Red (solid), black (dashed), and blue (dotted) curves show the expected time-dependent CP violation in $B_s^0 \to K^+K^-$ for different values of $\mathcal{A}_{CP}^{dir}$, $\mathcal{A}_{CP}^{mix}$ and $\Delta\Gamma$. The red (black) curve assumes 0.2 (0.2) and -0.2 (0.0) for $\mathcal{A}_{CP}^{dir}$ ($\mathcal{A}_{CP}^{mix}$), whereas the blue curve assumes that both $\mathcal{A}_{CP}^{dir}$ and $\Delta\Gamma$ are zero.

$|\mathcal{A}_{CP}^{\Delta\Gamma}| \neq 1$. For B^0 we can safely assume $\Delta\Gamma/\Gamma = 0$, and ignore this modulation. For B_s^0 we expect $\Delta\Gamma/\Gamma \sim 20\%$. Figure 6.9 shows that this may lead to an $\sim 7\%$ change of the oscillation amplitude per unit of lifetime. Given the experimental sensitivity discussed in Section 6.3.2.5, we do not expect to observe this effect in the first 2 fb^{-1} of data in RunII. We therefore ignore it in the present discussion. The analysis in the two decay modes into CP eigenstates thus reduces to a fit of the time dependence of the CP violating rate asymmetries to the sum of a sine and a cosine term.

6.3.2.5 Measurements on the Tagged Sample

As discussed in Section 6.3.2.4 above, the time dependent CP asymmetry in $B^0 \to \pi^+\pi^-$ and $B_s^0 \to K^+K^-$ is given by:

$$\mathcal{A}_{CP} = \mathcal{A}_{CP}^{dir} \cos\Delta mt + \mathcal{A}_{CP}^{mix} \sin\Delta mt \qquad (6.105)$$

It is straightforward to derive the expected errors on the coefficients $\mathcal{A}_{CP}^{mix}$ and $\mathcal{A}_{CP}^{dir}$ analytically [87]. For simplification, we use the abbreviations $A = \mathcal{A}_{CP}^{dir}$ and $B = \mathcal{A}_{CP}^{mix}$ in the following:

$$\begin{aligned}
G_{AA} &= N \times e^{-t_0}(1 + f(t_0)) \\
G_{BB} &= N \times e^{-t_0}(1 - f(t_0)) \\
G_{AB} &= N \times e^{-t_0}(2x\cos(2xt_0) + \sin(2xt_0))/(1+4x^2) \\
N &= 0.5 \times N_{t_0=0} \times \varepsilon\mathcal{D}^2 \times \frac{S/B}{S/B+1}\, e^{-(x\sigma_t/\tau)^2} \\
f(t_0) &= (\cos 2x\, t_0 - 2x \sin 2x\, t_0)/(1+4x^2). \qquad (6.106)
\end{aligned}$$

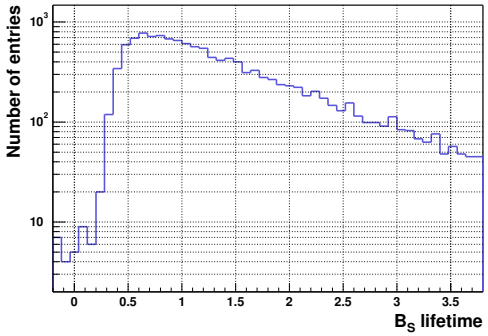

Figure 6.10: Effect of two-track trigger on $B_s^0 \to K^+K^-$ lifetime distribution.

$N_{\pi\pi}^{t_0=0.5}$	=	5000	$N_{KK}^{t_0=0.5}$	=	10,000	Resulting values for G_{AA}, G_{BB}, G_{AB}
t_0	=	0.5	σ_t/τ	=	0.03	
x_d	=	0.7	x_s	=	25	
$(\varepsilon\mathcal{D}^2)_{\pi\pi}$	=	0.091	$(\varepsilon\mathcal{D}^2)_{KK}$	=	0.113	
$(S/B)_{\pi\pi}$	=	1/2	$(S/B)_{KK}$	=	1	

	$B^0 \to \pi^+\pi^-$	$B_s^0 \to K^+K^-$
G_{AA}	72	161
G_{BB}	79	161
G_{AB}	44	3.2

Table 6.7: Inverse of covariance matrix based on analytical calculations.

Here G_{AA}, G_{BB}, and G_{AB} are the three elements of the inverse of the covariance matrix, t_0 is the minimum lifetime cut implied by the trigger, "S/B" is the signal/background ratio, and $x = \Delta m/\Gamma$, while σ_t is the expected proper time resolution. While deriving Equation (6.106), we made the approximation $\mathcal{A}_{CP} \times \mathcal{D} \ll 1$.

Figure 6.10 shows the proper time in units of B_s^0 lifetime for a Geant based Monte Carlo simulation of $B_s^0 \to K^+K^-$, followed by track reconstruction. The depletion for small lifetimes is due to the impact parameter requirements in the trigger (scenario A, see Table 6.1) [81]. This shows that $t_0 = 0.5$ is a reasonable value to pick for our estimates.

Table 6.7 shows the values that we consider for the various parameters entering the equations above. It is probably worthwhile mentioning that the effective signal/background from the untagged study is not relevant here. The oscillation frequencies are sufficiently different between B_s^0 and B^0 that $KK \leftrightarrow \pi\pi$ misidentification does not enter the numerator of $\mathcal{A}_{CP}$ in any significant way. We verified this with a fit to a Toy Monte Carlo that uses only $m_{\pi\pi}$ and proper time as input, and assumes the relative yields to be known, e.g. from a fit to the untagged sample. The correlation coefficient between CP violating asymmetries in $B^0 \to \pi^+\pi^-$ and $B_s^0 \to K^+K^-$ is negligible, despite the fact that the two signal peaks overlap almost exactly in the invariant two-track mass $m_{\pi\pi}$.

6.3.2.6 Extracting CP Violating Phases from $\mathcal{A}_{CP}^{dir}$ and $\mathcal{A}_{CP}^{mix}$

Let us define $\vartheta = arg(\bar{A}/A)/2$, the CP violating phase in the decay, and $\phi = arg(q/p)/2$, the CP violating phase in mixing for some phase convention. CP violation in the interference of mixing and decay is then given by:

$$\mathcal{A}_{CP}^{mix}(t) = \frac{\Gamma(\bar{B}^0 \to f_{CP}) - \Gamma(B^0 \to f_{CP})}{\Gamma(\bar{B}^0 \to f_{CP}) + \Gamma(B^0 \to f_{CP})} = -\sin 2(\phi + \vartheta) \times \sin \Delta m t \,. \tag{6.107}$$

In the limit where we ignore anything but the dominant contribution to the decay amplitude $\mathcal{A}_{CP}^{mix}(J/\psi K^0)$ and $\mathcal{A}_{CP}^{mix}(\pi^+\pi^-)$ measure $\sin 2\beta$ and $\sin 2(\beta+\gamma)$, respectively, while $\mathcal{A}_{CP}^{dir} = 0$ in both cases. If nature was that simple then a non-zero $\mathcal{A}_{CP}^{mix}(K^+K^-)$ or $\mathcal{A}_{CP}^{mix}(J/\psi\phi)$ would be a clear sign of new physics, and any difference between e.g. $\mathcal{A}_{CP}^{mix}(K^+K^-)$ and $\mathcal{A}_{CP}^{mix}(J/\psi\phi)$ would signal new physics in penguin loops. Allowing for gluonic penguins in $B^0 \to \pi^+\pi^-$ and $b \to u\bar{u}d$ contributions to $B_s^0 \to K^+K^-$ leads to non-zero $\mathcal{A}_{CP}^{dir}$ if and only if there is also a CP conserving phase difference between dominant and sub-dominant decay processes, i.e. "penguins" and "trees".

In the following, we discuss one particular suggestion by Fleischer [16] that relates $B_s^0 \to K^+K^-$ to $B^0 \to \pi^+\pi^-$ using U-spin symmetry, a subgroup of flavour $SU(3)$. This is neither the only nor necessarily the most promising use of experimental information but is meant to give a flavour of what can be achieved with RunII data at CDF. The basic idea is as follows. We decompose the two decay amplitudes into the sum of a part that has the CP violating phase of $\bar{b} \to \bar{c}c\bar{d}$, and a part that has the same CP violating phase as $\bar{b} \to \bar{u}u\bar{d}$. For the standard phase conventions these are 0 and γ, respectively. We then rewrite the four CP violating asymmetries in terms of the modulus d, the CP conserving phase θ describing the ratio of hadronic matrix elements for these two parts, the CP violating phase γ and the two CP violating phases for B^0 and B_s^0, ϕ_d and ϕ_s, respectively.

In the limit of U-spin symmetry the two sets of d and θ in $B^0 \to \pi^+\pi^-$ and $B_s^0 \to K^+K^-$ (denoted by $'$) are related via:

$$\begin{aligned} \theta' &= \theta \,, \\ d' &= d \times \left(\frac{1-\lambda^2}{\lambda^2}\right). \end{aligned} \tag{6.108}$$

To be specific:

$$\begin{aligned} \mathcal{A}_{CP}^{dir} &= \pm \frac{2d \sin\theta \sin\gamma}{1 - 2d\cos\theta\cos\gamma + d^2} \,, \\ \mathcal{A}_{CP}^{mix} &= \frac{\sin 2(\phi+\gamma) - 2d\cos\theta\sin(2\phi+\gamma) + d^2 \sin 2\phi}{1 - 2d\cos\theta\cos\gamma + d^2} \,. \end{aligned} \tag{6.109}$$

Here, $2\phi = arg(q/p)$ is the CP violating phase of mixing. The equations for B^0 and B_s^0 are thus identical except for the replacement of $d, \theta, \phi_d \;\leftrightarrow\; d', \theta', \phi_s$, and $\mathcal{A}_{CP}^{dir}(\pi^+\pi^-) = -\mathcal{A}_{CP}^{dir}(K^+K^-)$. The latter sign change being due to $V_{us}/V_{cd} = -1$.

In principle, this leads to a system of four equations with the five unknowns $d, \theta, \phi_s, \phi_d$, and γ. Furthermore, if $\theta \sim 0$ then two of the four equations are degenerate within our experimental sensitivity ($\mathcal{A}_{CP}^{dir}(\pi^+\pi^-) \sim \mathcal{A}_{CP}^{dir}(K^+K^-) \sim 0$), leading to only three independent equations and five unknowns. To arrive at a system of equations that is solvable, we add $\mathcal{A}_{CP}^{mix}(J/\psi K^0) = \sin 2\phi_d$ as an additional constraint, and fix $\phi_s = 0$, which is correct for the Standard Model to within $O(\lambda^2)$.

We then perform a χ^2 fit of hypothetical measurements of the two asymmetries $\mathcal{A}_{CP}^{dir}$ and the three asymmetries $\mathcal{A}_{CP}^{mix}$ and their errors to the corresponding theoretical expressions that relate them to the fit parameters β, γ, θ and d. We choose the following nominal values:

$$\begin{aligned} \beta &= 22.2^\circ \pm 2.0^\circ \,, \\ \gamma &= 60^\circ \,, \\ \theta &= 0 \,, \\ d &= 0.3 \,. \end{aligned} \tag{6.110}$$

This results in the expected "measurements" $\mathcal{A}_{CP}^{dir}(\pi^+\pi^-) = 0$, $\mathcal{A}_{CP}^{mix}(\pi^+\pi^-) = -0.316$, $\mathcal{A}_{CP}^{dir}(K^+K^-) = 0$ and $\mathcal{A}_{CP}^{mix}(K^+K^-) = 0.266$. The error on β is slightly larger than the CDF projections as discussed in Section 6.2.2. For the errors on $\mathcal{A}_{CP}^{dir}$ and $\mathcal{A}_{CP}^{mix}$ in $\pi^+\pi^-$ and K^+K^-, we choose the inverse error matrices as quoted in Table 6.7. This nominal fit returns:

$$\begin{aligned} \gamma &= (60.0^{+5.4}_{-6.8})^\circ \,, \\ \beta &= (22.2 \pm 2.0)^\circ \,, \\ \theta &= (0.0^{+10.8}_{-10.5})^\circ \,, \\ d &= 0.3^{+0.11}_{-0.07} \,. \end{aligned} \tag{6.111}$$

An exhaustive scan of the parameter space showed that the error on γ changes by a factor of ~ 3 over the range $d = 0.1$ to 0.5. Variations in the other parameters are less important. Further details may be found in reference [88].

6.3.2.7 Theoretical Error due to $SU(3)$ Breaking

In this section, we study the dependence of the fit for γ on the assumption of $SU(3)$ symmetry. This is done by calculating the "measured" values for the four CP violating asymmetries in $B^0 \to \pi^+\pi^-$ and $B_s^0 \to K^+K^-$ with $de^{i\theta} \neq d'e^{i\theta'}$, while strict $SU(3)$ symmetry is used in the fit.

$SU(3)$ breaking for form factors or decay constants is known to be a 10-15% effect. Both of these are "long distance" effects in the sense that they describe meson formation, rather than physics at the weak scale. This type of $SU(3)$ breaking affects amplitudes but tends to cancel in appropriately chosen ratios of amplitudes. For the rate asymmetries that we care about here such "long distance" $SU(3)$ breaking corrections do indeed cancel, e.g. within factorization models Eq. (6.108) is exact. An $SU(3)$ breaking effect that matters would

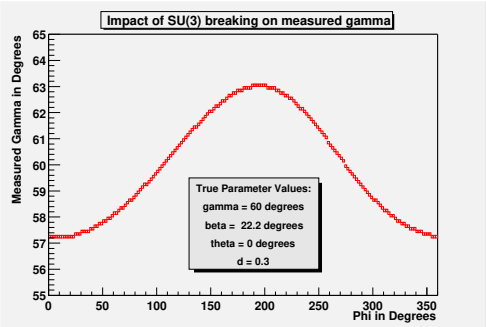

Figure 6.11: Impact of $SU(3)$ breaking.

have to alter the ratio of hadronic matrix elements for penguin and tree diagrams. This means, it would have to invalidate Equation (6.108). To what extend such effects should be expected, remains an open question. Future data for these and other processes will tell us the range of such effects.

We can model a potential effect of this type by using different sets of d, θ for B_s^0 and B^0 when calculating the four hypothetical CP violating asymmetries, but using the same d, θ for B_s^0, B^0 when minimizing the χ^2. In principle, one might expect an increase in χ^2 at the minimum, i.e. a poorer fit, as well as a systematic shift in γ returned by the fit. To be conservative, we chose 20% $SU(3)$ breaking and implement it as follows:

$$\overrightarrow{\Delta d} = (d \times e^{i\theta})_{B_s^0} - (d \times e^{i\theta})_{B^0} = |\overrightarrow{\Delta d}| \times e^{i\phi} = 0.2 \times d \times e^{i\phi}\,. \qquad (6.112)$$

In other words, the set of possible $SU(3)$ breaking effects that we consider is given by a circle with radius $0.2 \times d$. We can then plot $\gamma_{\rm measured}$ as a function of ϕ for fixed $\gamma_{\rm true}$. This is shown in Figure 6.11 for our nominal fit parameters. We conclude that 20% $SU(3)$ breaking leads to a systematic error on γ of at most ± 3 degrees for our nominal set of parameters.

6.3.3 $B \to \pi\pi/KK$: DØ Report [†]

As discussed in Section 6.1.7 and 6.3.1, a measurement of the CP asymmetry in the decay $B^0 \to \pi^+\pi^-$ was once thought to be the "golden" mode to determine the CKM angle α. But an unexpectedly small branching ratio and large penguin contributions have made this analysis, however, much more difficult than expected. The situation is more complicated without significant π/K separation, as the decay $B_s^0 \to K^+K^-$ lies in the same reconstructed mass range as the $\pi^+\pi^-$ signal. In addition, the fully hadronic final state poses another problem for DØ as it is not possible to trigger on the $\pi\pi$ final state directly. The

[†] Authors: R. Jesik and M. Petteni.

background rate for two tracks with p_T thresholds set low enough to collect these events is well above the maximum Level 1 trigger rate of 10 kHz. However, it will be possible to trigger on these decays for the case of the other B hadron in the event decaying semileptonically. Due to the semileptonic branching ratio, this requirement has an efficiency of 10% at best. But since the initial flavour of the $B \to \pi\pi$ decay has to be tagged in order to measure the CP asymmetry, an opposite side lepton tag is one of the most effective ways to do this.

The trigger requires one lepton with p_T greater then 3.0 GeV/c plus two other tracks with p_T greater than 1.5 GeV/c. In order to minimize the number of fake tracks, all three tracks must have a hit in each of the Central Fiber Tracker's (CFT) eight axial layers. To limit background rates, an isolation cut is made in which two of the tracks are required to have no other tracks with p_T above 1.5 GeV/c within the same, or adjacent, CFT sectors (the CFT is divided into 80 equal sectors at the trigger level). To further lower background rates, multiple interactions are removed by rejecting events which have more than 68 sectors exceeding a threshold of 12% occupancy.

This study is based on a Monte Carlo sample of B^0 and B_s^0 decays generated by Pythia plus QQ. The B^0 mesons were forced to decay into $\pi^+\pi^-$ and $K^+\pi^-$ final states with proportion according to branching ratios as measured by CLEO [23]. The B_s^0 mesons were forced into K^+K^- and $K^-\pi^+$ final states. The branching ratios for the B_s^0 decays were extrapolated from the measured values for B^0 using spectator quark flavour invariance. The relative fraction of B^0 to B_s^0 meson events in this sample was as generated by Pythia, which agrees with RunI measurements from CDF [84]. Kinematic cuts of $p_T > 4$ GeV/c and $|\eta| < 3$ were made on the B mesons at generator level, leaving a final sample of about 300,000 events.

The DØ detector acceptance was simulated using MCFAST. Imposing the trigger p_T, isolation, and hit requirements on this sample leaves a trigger acceptance of 0.76% for these events. Since the DØ muon system is not represented in MCFAST, the trigger acceptance is corrected by a factor of 78% to account for the holes in the bottom of the detector. This efficiency is determined using a full GEANT simulation. An additional efficiency of 98% per track is imposed in order to take into account hit in-efficiencies not present in the MCFAST analysis. The efficiency of the high occupancy rejection of this trigger was found to be 80% using a full GEANT simulation. These factors bring the trigger efficiency to a 0.45% level.

The offline reconstruction of these events is simply a refinement of the trigger requirements using information from the full detector. All tracks are required to have a hit in each of the 8 stereo layers of the CFT, in addition to the 8 axial hits required by the trigger. The tracks are also required to have at least 8 hits in the silicon detector (the maximum number of hits is 10 on average). The efficiency of these requirements is 90%. With these considerations, summarized in Table 6.8, we expect to reconstruct 1400 $B^0 \to \pi^+\pi^-$ events in 2 fb^{-1} of data. Similarly, DØ expect 5600 $B^0 \to K^+\pi^-$, 2500 $B_s^0 \to K^+K^-$, and 600 $B_s^0 \to K^+\pi^-$ events in this sample.

The mass resolution of the B^0 meson in this channel is 44 MeV/c^2 as can be seen in Fig.6.12(a). Figure 6.12(b) shows the mass distributions for all four channels assuming that the final state particles are pions. From this plot it can be seen that it is not possible to

Integrated luminosity	2 fb^{-1}
$\sigma_{b\bar{b}}$	158 μb
$f(b\bar{b} \to B^0, \bar{B}^0)$	0.8
Kinematic acceptance	0.31
$\mathcal{B}(B^0 \to \pi^+\pi^-)$	4.3×10^{-6}
Trigger efficiency	4.5×10^{-3}
Reconstruction efficiency	0.9
Number of reconstructed $B^0 \to \pi^+\pi^-$	1400
Effective tagging efficiency ($\varepsilon\mathcal{D}^2$)	0.40

Table 6.8: Expected number of $B^0 \to \pi^+\pi^-$ events at DØ.

separate the $B^0 \to \pi^+\pi^-$ decays from $B_s^0 \to K^+K^-$ based on the reconstructed mass. The situation is further complicated by the fact that the $B^0 \to K^+\pi^-$ decay lies directly over the two channels of interest. Fortunately, B_s^0 mesons oscillate at a much faster frequency than B^0 mesons. With the use of a multi-variant fit it could be possible to separate all the contributions. It should be noted that the reconstructed samples are already flavour tagged by the requirement of the lepton in the trigger. The soft lepton tag has a dilution of 63% and ε will be very near unity, leading to an effective tagging efficiency of $\varepsilon\mathcal{D}^2 = 0.40$. Work is progressing on how well the CP asymmetries can be measured and on how well they can be translated into extracting CKM parameters.

6.3.4 $B \to \pi\pi/KK$: BTeV Report †

The decay of $B^0 \to \pi^+\pi^-$ is the traditional choice for measuring $\sin 2\alpha$, but the evidence of large penguin amplitudes in the observation of $B^0 \to K^+\pi^-$ by the CLEO collaboration [23] implies that a simple extraction of $\sin 2\alpha$ from this mode is no longer likely. However, since this mode has been used to benchmark so many experiments, it is still worthwhile to understand. In addition, it may be useful for the extraction of γ when combined with a measurement of $B_s^0 \to K^+K^-$ as explained in Sections 6.1 and 6.3.1.

The data for this study are generated using Pythia while QQ is used to decay the heavy particles. The detector simulation is performed using the BTeVGeant simulation package. We also compare our result with the result obtained using MCFast. Each signal event which is simulated by BTeVGeant (or MCFast) contains one signal interaction ($b\bar{b}$) and n background interactions (minimum bias), where n has a Poisson distribution of mean 2. This corresponds to the BTeV design luminosity of 2×10^{32} cm^{-2} s^{-1}.

To find this decay, BTeV selects two oppositely charged tracks with a displaced vertex and an invariant mass close to the B^0 mass. Most of the background rejection against random combinations comes from the displaced B vertex and the momentum balance of

† Authors: G. Majumder, M. Procario, S. Stone.

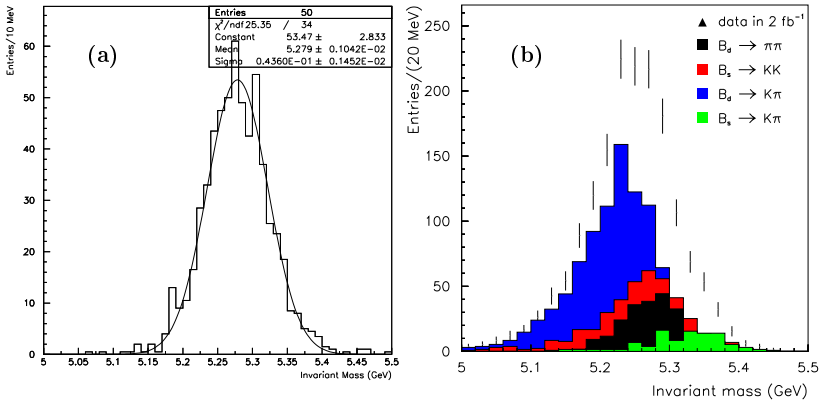

Figure 6.12: (a) Reconstructed invariant mass for $B^0 \to \pi^+\pi^-$ at DØ. (b) Expected two track invariant mass signal assuming both tracks are pions.

the $\pi^+\pi^-$ combination with respect to the direction of the B. While particle identification is vital to reject backgrounds from decays like $B^0 \to K^+\pi^-$, $B_s^0 \to \pi^+K^-$ and $B_s^0 \to K^+K^-$, it has a small effect on random combinations since most particles are pions.

To start this analysis, BTeV first fits the primary vertices using all tracks which have at least 4 silicon pixel hits. For the two tracks to be considered as B daughter candidates, they must satisfy the following criteria. Each track must have $p_T > 0.5$ GeV/c and at least one track must have $p_T > 1.5$ GeV/c. Each track must project into the RICH detector acceptance, because particle identification is required later. The distance of closest approach (DCA) of the track with respect to the primary vertex must be less than 1 cm, which reduces backgrounds from long lived particles, e.g. K_S^0, Λ, ... It is also required that the DCA divided by its error of each track be > 3 which removes tracks from the primary vertex.

BTeV attempts to fit a secondary vertex with pairs of tracks that satisfy the above criteria. For each secondary vertex found, the following selection criteria are applied: The absolute distance between the primary and secondary vertices (L) must be greater than 0.5 mm and $L/\sigma_L > 4$. Considering all other tracks that do not come from this primary vertex and forming a χ^2 with each of these tracks and the selected two tracks for a secondary vertex, combinations with $\chi^2 < 10$ are rejected, since this might indicate a many-body B decay. The B^0 direction is calculated from the primary and secondary B vertex positions and the invariant mass of the two tracks (assumed to be $\pi^\pm$) must be within 2 σ of m_{B^0}. Using the selection criteria defined above, gives an acceptance and reconstruction efficiency of 8% for $B^0 \to \pi^+\pi^-$, not including trigger efficiency or particle identification.

Figure 6.13 shows a comparison of signal and background for several of the variables used above. The background distributions are generated considering all oppositely charged two-track combinations except for the signal $\pi^+\pi^-$.

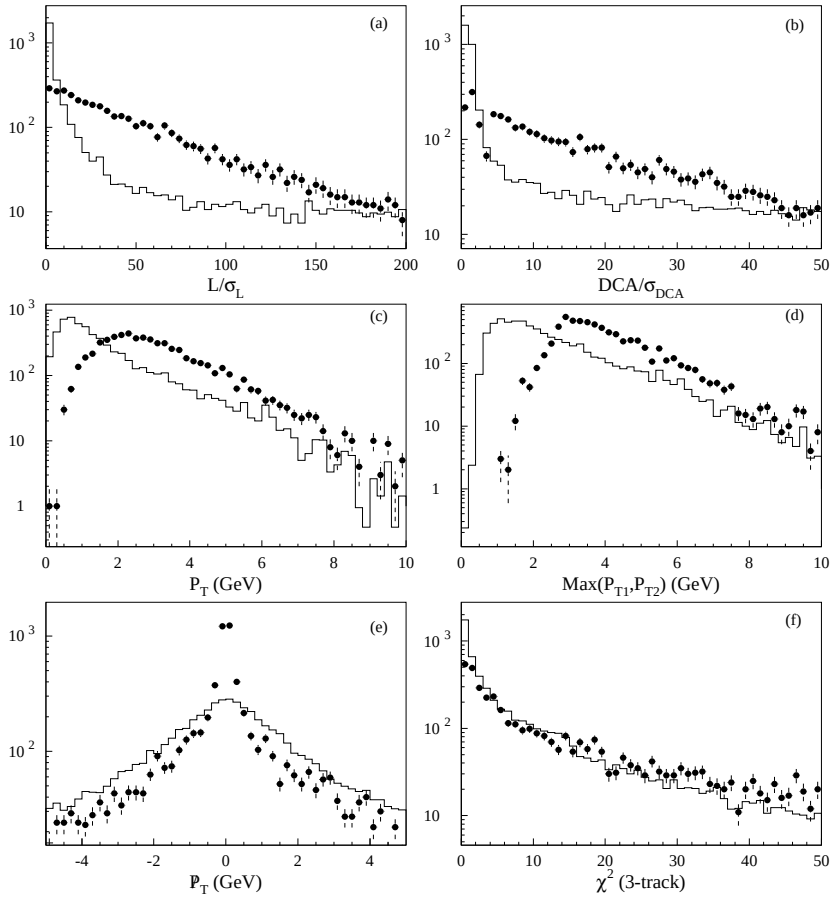

Figure 6.13: Distribution of signal (circles) and background (line) for the most important vertex and kinematic variables. (a) Normalized distance between primary and secondary vertex, L/σ_L, (b) normalized DCA of track with respect to the primary vertex, DCA/σ_{DCA}, (c) transverse momentum of a track, (d) maximum value of transverse momentum of two tracks, (e) p_T imbalance of $\pi^+\pi^-$ with respect to the B^0 direction and (f) χ^2 of secondary vertex using the $\pi^+\pi^-$ with an additional track candidate.

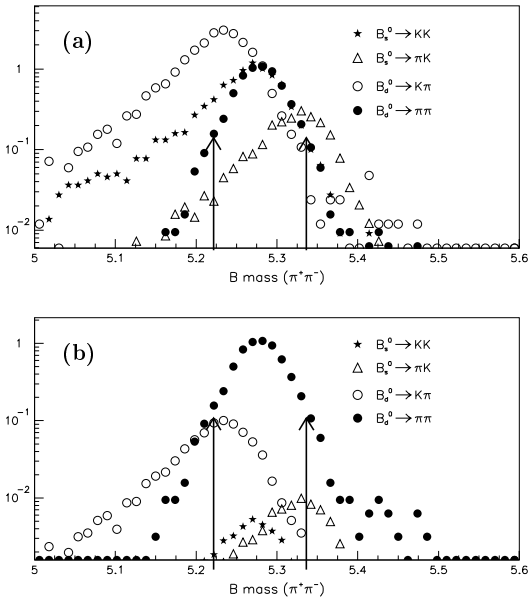

Figure 6.14: Two body ($\pi^+\pi^-$) mass plot (a) without and (b) with particle identification. Different decay channels are normalized by their production cross sections. The arrows indicate the range of the signal mass window. (Note the log scale.)

It has been shown by the BCD group [89] that the dominant background to $B^0 \to \pi^+\pi^-$ comes from random combinations of tracks in events coming from B's. Tracks from real B's are already displaced from the primary vertex and have a higher probability of faking a secondary vertex compared to $c\bar{c}$ and minimum bias events.

In addition to background from generic $b\bar{b}$ events, there are several exclusive decay modes of B mesons that can mimic a $B^0 \to \pi^+\pi^-$ decay. The decay $B_s^0 \to K^+K^-$, which is due to a hadronic penguin decay mechanism, is the most important, along with other contributions from $B^0 \to K^+\pi^-$ and $B_s^0 \to \pi^+K^-$. Recent CLEO measurements of some of the B^0 decay modes give $\mathcal{B}(B^0 \to \pi^+\pi^-) = 0.43 \times 10^{-5}$ and $\mathcal{B}(B^0 \to K^+\pi^-) = 1.7 \times 10^{-5}$ [23]. In order to normalize the B_s^0 contribution, we use a B_s^0 production rate which is 35% of the B^0 rate [12] and assume that the penguin and $b \to u$ decays of the B_s^0 have the same branching ratios as the B^0. Using these results as input, and without π/K discrimination, the two-pion mass plots for the four different two-body decay modes are shown in Fig. 6.14(a). These plots indicate that kinematic separation is inadequate to discriminate among these decays.

The BTeV detector will have an excellent RICH detector for particle identification. BTeV can virtually eliminate two-body backgrounds using the RICH. The simulated back-

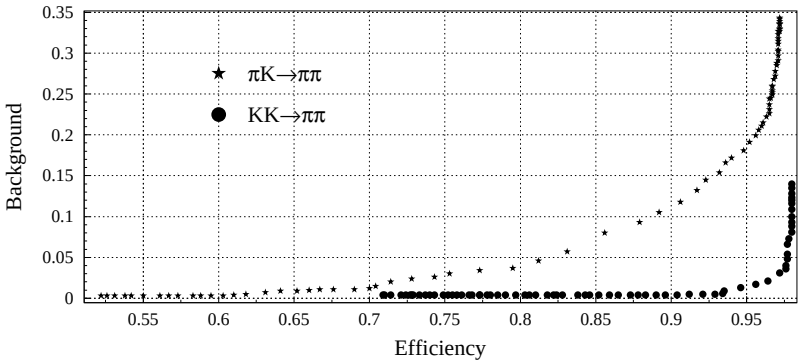

Figure 6.15: RICH event selection: $\pi^+\pi^-$ signal efficiency versus contamination from other two-body decay modes.

ground tracks (all tracks including all other interactions in that event) were passed through the RICH simulation code. The efficiency versus background contamination is shown in Fig. 6.15. For an 80% $\pi^+\pi^-$ signal efficiency, the contamination from $\pi^\pm K^\mp$ (K^+K^-) is 4.0% (0.5)%.

Since the primary purpose of the Level 1 trigger is to reject light quark backgrounds, there is a strong correlation between triggered events and reconstructed events. The BTeVGeant simulation shows that 64% of the selected events pass the Level 1 trigger condition. Given a Level 2 efficiency of 90%, this leaves 23,700 events per year of running after applying the acceptance, reconstruction efficiency, particle ID efficiency, and trigger efficiency but before flavour tagging.

Besides the two-body B decay background samples, a full BTeVGeant simulation of $b\bar{b}$ backgrounds was performed. In order to reduce the CPU time required to simulate a sufficiently large data sample of $b\bar{b}$ decays, a method to preselect events at the generator level which are likely to cause difficulties, was investigated. BTeV found that the difference between the reconstructed and generated p_T of the tracks is fairly small and Gaussian. On the basis of the small observed differences, BTeV preselected the generator events before the BTeVGeant simulation. The preselection criteria are based on the p_T (>0.4 GeV/c) of each track, the sum of the p_T (>1.8 GeV/c) of two tracks, the opening angle of the tracks, the extrapolation of tracks to the RICH chamber, etc. In order to reject background at the generator level, a small fraction of event selection efficiency had to be sacrificed.

These preselection requirements reduce the generic $b\bar{b}$ event sample by a factor of 100. From this sample, only 4 events (two $\pi^+\pi^-$, one $K^+\pi^-$ and one π^+K^-) have a $\pi^+\pi^-$ mass that lies within 200 MeV/c^2 of m_{B^0}. Applying the RICH identification leads to an 80% efficiency for the two $\pi^+\pi^-$ events and a 4% efficiency for each of the $K^+\pi^-$ and π^+K^- events. Thus, there are 1.68 background events. If we scale to the B signal region which

Luminosity	$2 \times 10^{32}\,\mathrm{cm}^{-2}\,\mathrm{s}^{-1}$
Running time	10^7 sec
Integrated Luminosity	2000 pb^{-1}
$\sigma_{b\bar{b}}$	100 μb
Number of $B\bar{B}$ events	2×10^{11}
Number of B^0 events	1.5×10^{11}
$\mathcal{B}(B^0 \to \pi^+\pi^-)$	0.43×10^{-5}
Reconstruction efficiency	8.0%
Trigger efficiency (Level 1)	64%
Trigger efficiency (Level 2)	90%
RICH I. D. efficiency	80%
Number of reconstructed $B^0 \to \pi^+\pi^-$	2.37×10^4
Background after RICH rejection	
$B^0 \to K^+\pi^-$	0.27×10^4
$B_s^0 \to \pi^+K^-$	0.03×10^4
$B_s^0 \to K^+K^-$	0.02×10^4
B-generic	0.46×10^4
S/B	3
Tagging efficiency $\varepsilon\mathcal{D}^2$	10.0%
$\sigma(\mathcal{A}_{CP})$	2.36×10^{-2}

Table 6.9: Projected yield of $B^0 \to \pi^+\pi^-$ and the uncertainty on $\mathcal{A}_{CP}$ from a BTeVGeant simulation.

is 115 MeV/c^2 and multiply by the combined Level 1 and Level 2 trigger efficiency (64% × 90%), we expect ≈ 4,600 $b\bar{b}$ background events from one year of running BTeV at the design luminosity of 2×10^{32} cm^{-2}s^{-1}. The remaining contributions (from the two-body decay channels) are listed in Table 6.9 and add up to 3,200 events per year. Therefore, the total background is 7,600 events per year leading to a signal-to-background ratio of 3:1 with a 25% error.

The effective tagging efficiency ($\varepsilon\mathcal{D}^2$), discussed in Section 5.5, is estimated to be 10%. Using the tagging efficiency and the $B^0 \to \pi^+\pi^-$ yield, we can obtain an uncertainty on the CP asymmetry. Based on one year of running at design luminosity, BTeV expects an uncertainty on $\mathcal{A}_{CP}$ of 0.024, as summarized in Table 6.9.

As mentioned in Section 6.3.1, measuring both $B^0 \to \pi^+\pi^-$ and $B_s^0 \to K^+K^-$ may allow an extraction of γ. To this end, BTeV has also looked for $B_s^0 \to K^+K^-$ signal events. This analysis is nearly identical to the $B^0 \to \pi^+\pi^-$ analysis after interchanging $B^0 \to \pi^+\pi^-$ and $B_s^0 \to K^+K^-$ samples from signal to background (and vice versa). As in the $B^0 \to \pi^+\pi^-$

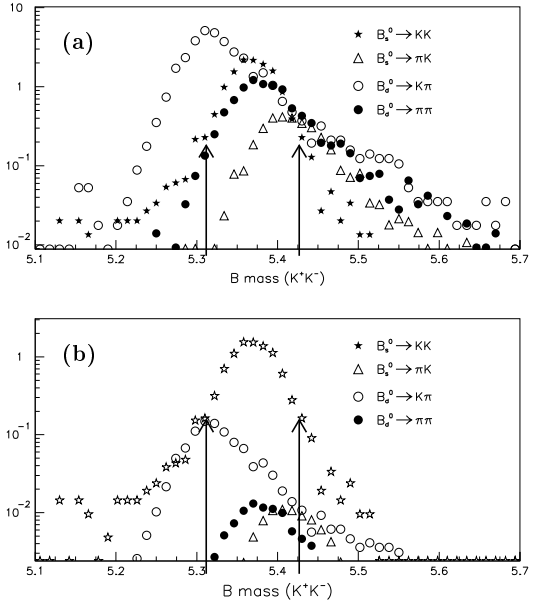

Figure 6.16: Two body (K^+K^-) mass plot (a) without and (b) with particle identification. Different decay channels are normalized by their production cross sections. The arrows indicate the range of the signal mass window. (Note the log scale.)

analysis, other two-body decay modes can mimic the signal as shown in Fig. 6.16(a).

From the RICH simulation, BTeV finds that at an 80% signal efficiency for $B_s^0 \to K^+K^-$, they accept 5% (1.5)% $\pi^+\pi^-(K^+\pi^-, \pi^+K^-)$ background events as K^+K^-. It is clear from Fig. 6.16(b) that by using the RICH information, BTeV can reject most of the backgrounds which are coming from other two-body decay modes.

The expected $B_s^0 \to K^+K^-$ yield, including the acceptance, reconstruction efficiency, trigger efficiency, and particle ID efficiency is 33,000 events per year at the design luminosity. This is summarized in Table 6.10.

6.3.5 $B \to \pi\pi/KK$: Summary †

Several years ago, the most important decay modes for the study of CP violation in the B system were believed to be $B^0 \to J/\psi K_S^0$ and $B^0 \to \pi^+\pi^-$. As discussed in Sec. 6.2,

† Author: M. Paulini.

Luminosity	$2 \times 10^{32}\,\mathrm{cm}^{-2}\,\mathrm{s}^{-1}$
Running time	10^7 sec
Integrated Luminosity	2000 pb^{-1}
$\sigma_{b\bar{b}}$	100 μb
Number of $B\bar{B}$ events	2×10^{11}
Number of B_s^0 events	0.52×10^{11}
$\mathcal{B}(B_s^0 \to K^+K^-)^\dagger$	1.7×10^{-5}
Reconstruction efficiency	8.1%
Trigger efficiency (Level 1)	64%
Trigger efficiency (Level 2)	90%
RICH I. D. efficiency	80.0%
Number of reconstructed $B_s^0 \to K^+K^-$	3.29×10^4
Background after RICH rejection	
$B^0 \to K^+\pi^-$	0.39×10^4
$B_s^0 \to \pi^+K^-$	0.04×10^4
$B^0 \to \pi^+\pi^-$	0.04×10^4
B-generic	0.04×10^4
S/B	6.6

Table 6.10: Projected yield of $B_s^0 \to K^+K^-$ and fake rates († indicates estimated branching fractions.)

time dependent CP violation in the former mode measures $\sin 2\beta$ [74], while the decay $B^0 \to \pi^+\pi^-$ usually appears in the literature as a tool to determine $\alpha = 180° - \beta - \gamma$. However, the CLEO collaboration [23] has shown that the so-called penguin pollution in $B^0 \to \pi^+\pi^-$ is sufficiently large to make the extraction of fundamental physics parameters from the measured CP asymmetry rather difficult. An evaluation of measuring CP violation in $B^0 \to \pi^+\pi^-$ does therefore require a strategy to distinguish penguin contributions from tree diagrams. A large number of strategies to disentangle both contributions is discussed in the literature [75,76]. However, they generally require either very large data sets or involve hard to quantify theoretical uncertainties.

For this workshop, CDF evaluated a strategy of measuring the CKM angle γ as suggested by Fleischer in Ref. [16]. This method is particularly well matched to the capabilities of the Tevatron as it relates CP violating observables in $B_s^0 \to K^+K^-$ and $B^0 \to \pi^+\pi^-$. Both decays are related to each other by interchanging all down and strange quarks, i.e. through the so-called "U-spin" subgroup of the SU(3) flavour symmetry of strong interactions. The strategy proposed in Ref. [16] uses this symmetry to relate the ratio of hadronic matrix elements for penguins and trees, and thus uses $B_s^0 \to K^+K^-$ to correct for the penguin pollution in $B^0 \to \pi^+\pi^-$.

With the two-track hadronic trigger, CDF expects to reconstruct at least 5000 $B^0 \to \pi^+\pi^-$ and 20,000 $B^0 \to K^\pm\pi^\mp$ events in 2 fb^{-1} of data assuming the branching ratios measured by CLEO [23], in particular $\mathcal{B}(B^0 \to \pi^+\pi^-) = (4.3^{+1.6}_{-1.4} \pm 0.5) \times 10^{-6}$. The question whether CDF will be able to extract these signals from potentially enormous backgrounds, has been studied throughout this workshop. With respect to combinatorial background, a signal-to-background ratio not worse than $S/B \sim 0.4$ can be expected. Regarding physics backgrounds from $B \to K\pi$ and $B_s^0 \to KK$ decays, a $B^0 \to \pi^+\pi^-$ signal can be extracted by exploiting the invariant $\pi\pi$ mass distribution as well as the $\mathrm{d}E/\mathrm{d}x$ information provided by CDF's Central Outer Tracker. From this, CDF expects the $B \to \pi\pi$, $K\pi$, KK and πK yields in the untagged sample to be measured with an uncertainty of only a few percent.

Measurements on the tagged sample determines the time dependent CP asymmetry for $B^0 \to \pi^+\pi^-$ and $B_s^0 \to K^+K^-$ which is given by: $\mathcal{A}_{CP} = \mathcal{A}_{CP}^{dir} \cos\Delta mt + \mathcal{A}_{CP}^{mix} \sin\Delta mt$. With the strategy suggested in Ref. [16], the studies performed during this workshop indicate that a measurement of the CKM angle γ to better than 10° could be feasible at CDF with 2 fb^{-1} of data. The utility of these modes depends on how well the uncertainty from flavour $SU(3)$ breaking can be controlled. Data for these and other processes should tell us the range of such effects. The resulting Standard Model constraints could be quite stringent. CDF estimates of possible SU(3) breaking effects show that 20% SU(3) breaking leads to a systematic error of less than half the statistical precision given above. This encouraging result might allow CDF to make a significant contribution to our understanding of the CKM unitarity triangle within the first 2 fb^{-1} of Tevatron data in RunII.

Since the BTeV experiment will operate a RICH detector for particle identification, excellent π-K separation can be achieved and two-body physics backgrounds can virtually be eliminated at BTeV. Based on one year of running at design luminosity, BTeV expects to reconstruct about 20,000 $B^0 \to \pi^+\pi^-$ events with small background contamination at the 10^{-4} level from $B^0 \to K^+\pi^-$, $B_s^0 \to \pi^+K^-$ and $B_s^0 \to K^+K^-$. With this event yield, BTeV expects an uncertainty on the CP asymmetry $\mathcal{A}_{CP}$ of 0.024, as summarized in Table 6.9. BTeV did not study a possible extraction of γ using the method proposed in Ref. [16] as discussed above, but has estimated the yield for a $B_s^0 \to K^+K^-$ signal to be 33,000 events per year at design luminosity (see Sec. 6.3.4).

6.4 Study of $B \to DK$

6.4.1 $B \to DK$: Introduction †

The CKM angle γ can be extracted via two related sets of four decay processes, $B^- \to K^- D^0(\bar{D}^0)$ and the CP conjugate decays, or $B_s^0(\bar{B}_s^0) \to K^\pm D_s^\mp$. In both of these cases, the sensitivity to CP violation is achieved through the interference of the two quark level processes $b \to c\bar{u}s$ and $b \to u\bar{c}s$.

The final state particles for the most interesting decay channels in this category contain combinations of K's and π's. Hence, an important feature of any detector is its ability to

† Author: D. Atwood.

identify these particles, resolve their momenta and perform K-π separation. In addition, backgrounds, often from decay modes with branching fractions that are orders of magnitude larger, must be well controlled. Otherwise, the CP asymmetry will be diluted and the precision of measuring γ will suffer.

We briefly review first the extraction of γ from B_s^0 decays and then summarize how the angle γ can be obtained from $B \to D^0K$.

6.4.1.1 $B_s^0 \to D_s^- K^+$: Introduction

The necessary interference effect is achieved through mixing of the initial state via $B_s^0\bar{B}_s^0$ oscillation. For example, we could have either a direct decay amplitude for $B_s^0 \to D_s^- K^+$ ($\bar{b} \to c\bar{u}s$ channel) or first a $B_s^0 \to \bar{B}_s^0$ transition and then the $\bar{B}_s^0 \to D_s^- K^+$ ($b \to c\bar{u}s$ channel) decay. Note that the two decay amplitudes are not CP conjugates (in contrast to the case of final CP eigenstates) and therefore carry different strong phases. These phases cannot be reliably calculated with currently available theoretical methods. Therefore enough data must be gathered to fit simultaneously for γ and the strong phase difference δ.

The time dependent decay rates for the four relevant processes are given in Eq. (6.42) and reproduced here using $\phi_{D_s^+K^-} = -\gamma$.

$$
\begin{aligned}
\Gamma(B_s^0 \to D_s^- K^+) &= \frac{|A_f|^2 e^{-\Gamma_s t}}{2}\Big\{(1+|\lambda_f|^2)\cosh(\Delta\Gamma_s t/2) + (1-|\lambda_f|^2)\cos(\Delta m_s t) \\
&\quad -2|\lambda_f|\cos(\delta+\gamma)\sinh(\Delta\Gamma_s t/2) - 2|\lambda_f|\sin(\delta+\gamma)\sin(\Delta m_s t)\Big\}, \\
\Gamma(B_s^0 \to D_s^+ K^-) &= \frac{|A_f|^2 e^{-\Gamma_s t}}{2}\Big\{(1+|\lambda_f|^2)\cosh(\Delta\Gamma_s t/2) - (1-|\lambda_f|^2)\cos(\Delta m_s t) \\
&\quad -2|\lambda_f|\cos(\delta-\gamma)\sinh(\Delta\Gamma_s t/2) + 2|\lambda_f|\sin(\delta-\gamma)\sin(\Delta m_s t)\Big\}, \\
\Gamma(\bar{B}_s^0 \to D_s^- K^+) &= \frac{|A_f|^2 e^{-\Gamma_s t}}{2}\Big\{(1+|\lambda_f|^2)\cosh(\Delta\Gamma_s t/2) - (1-|\lambda_f|^2)\cos(\Delta m_s t) \\
&\quad -2|\lambda_f|\cos(\delta+\gamma)\sinh(\Delta\Gamma_s t/2) + 2|\lambda_f|\sin(\delta+\gamma)\sin(\Delta m_s t)\Big\}, \\
\Gamma(\bar{B}_s^0 \to D_s^+ K^-) &= \frac{|A_f|^2 e^{-\Gamma_s t}}{2}\Big\{(1+|\lambda_f|^2)\cosh(\Delta\Gamma_s t/2) + (1-|\lambda_f|^2)\cos(\Delta m_s t) \\
&\quad -2|\lambda_f|\cos(\delta-\gamma)\sinh(\Delta\Gamma_s t/2) - 2|\lambda_f|\sin(\delta-\gamma)\sin(\Delta m_s t)\Big\}.
\end{aligned}
\tag{6.113}
$$

Here, we abbreviated A_f for $A_{D_s^-K^+}$ and λ_f for $\lambda_{D_s^-K^+}$. The primary concern is to extract γ from these rates. In the following, we will assume that Δm_s and $\Delta\Gamma_s$ are already known since they can be determined more accurately with other modes. All four parameters, $|A_{D_s^-K^+}|$, $|\lambda_{D_s^-K^+}|$ and $\delta \pm \gamma$, can, in principle, be extracted from the time dependent data for the four decay processes. For example, the overall normalization $|A_{D_s^-K^+}|^2$ can be extracted from $\Gamma[B_s^0(t=0) \to D_s^- K^+]$ and $\Gamma[\bar{B}_s^0(t=0) \to D_s^- K^+]$, and the value of $|\lambda_{D_s^-K^+}|$ can then be obtained from $\Gamma[B_s^0(t=0) \to D_s^- K^+]$ and $\Gamma[\bar{B}_s^0(t=0) \to D_s^- K^+]$. In actuality, one performs a simultaneous fit for $|\lambda|$, $|A|$, δ and γ from the experimental data on

the four channels. Note, the measurements determine only $\sin(\delta \pm \gamma)$ and $\cos(\delta \pm \gamma)$. This determines both δ and γ (which we are most interested in) up to the two fold ambiguity,

$$(\delta, \gamma); \quad (\delta + \pi, \gamma + \pi). \tag{6.114}$$

Aside from the issue of gathering enough statistics to obtain accurate time dependent rates, there are two situations for which data may not be able to unambiguously fit all the coefficients as suggested above:

(1) Δm_s is so large that the time resolution is insufficient to extract the "sin" and "cos" terms.

(2) $\Delta\Gamma_s/\Gamma_s$ is so small that the "sinh" term does not become large enough to be distinguished.

In case (1) the crucial problem is the finite time resolution of the detector. To get a feeling for how this affects the data, let us assume the time resolution of the detector has a Gaussian spread with a width σ/Γ_s. If $x_s\sigma \gg 1$, the oscillating terms will be damped due to the smearing by $\sim \exp(-x_s^2\sigma^2/2)$ and only the "cosh" and "sinh" terms survive. In this regime we are, in effect, seeing B_s^0 states as incoherent mixtures of B_s^L and B_s^H, without the knowledge of the coherence between the states encoded in the oscillatory terms. If the data allows us to isolate the "sinh" and "cosh" terms, we will be able to extract $\cos(\delta + \gamma)$ and $\cos(\delta - \gamma)$. This then allows us to determine (δ, γ) up to the following ambiguity:

$$(\pm\delta, \pm\gamma); \quad (\pm\gamma, \pm\delta); \quad (\pi \pm \delta, \pi \pm \gamma); \quad (\pi \pm \gamma, \pi \pm \delta). \tag{6.115}$$

In particular, γ has an 8-fold ambiguity between $\{\pm\gamma, \pi \pm \gamma, \pm\delta, \pi \pm \delta\}$. This could be reduced to a 4-fold ambiguity if a second final state, such as $D_s^- K^*$, is also analyzed in a similar fashion, provided the two values of δ are significantly different.

In case (2), that is, if $\Delta\Gamma_s/\Gamma_s$ is so small that the "sinh" and "cosh" terms cannot be measured, we are in a similar situation except that we now can only determine $\sin(\delta + \gamma)$ and $\sin(\delta - \gamma)$. In this case, a given solution (δ, γ) produces the same results as:

$$\begin{aligned}(\delta, \gamma); \quad (\pi + \delta, \pi + \gamma); \quad (\pi - \delta, -\gamma); \quad (-\delta, \pi - \gamma); \quad (\frac{\pi}{2} - \gamma, \frac{\pi}{2} - \delta); \\ (-\frac{\pi}{2} - \gamma, -\frac{\pi}{2} - \delta); \quad (\frac{\pi}{2} + \gamma, -\frac{\pi}{2} + \delta); \quad (-\frac{\pi}{2} + \gamma, \frac{\pi}{2} + \delta).\end{aligned} \tag{6.116}$$

Consequently, γ has an 8-fold ambiguity between $\{\pm\gamma, \pi \pm \gamma, \frac{\pi}{2} \pm \delta, -\frac{\pi}{2} \pm \delta\}$ and again an additional mode such as $D_s^- K^*$ will reduce this to a 4-fold ambiguity if the two modes have significantly different values of δ.

6.4.1.2 $B^- \to D^0 K^-$: Introduction

In the Standard Model $b \to c\bar{u}s$ and $b \to \bar{c}us$ transitions have a relative CKM phase γ. In the case of the $B^- \to K^- D^0(\bar{D}^0)$ decay mode, the sensitivity to γ is achieved through the

interference of common decay modes of the D^0 and $\bar{D}^0$ channels. The Gronau-London-Wyler (GLW) method [90] extracts γ by measuring the $B^\pm$ decay rates to $D^0/\bar{D}^0$ mesons. If the D^0 and $\bar{D}^0$ decay to a CP eigenstate, then the two decays $B^- \to K^- D^0$ and $B^- \to K^- \bar{D}^0$ lead to a common final state and can give rise to CP violating effects. However, the two interfering amplitudes are very different in magnitude and thus the interference effects are limited to $\mathcal{O}(10\%)$. Another problem is that it is necessary to measure separately the branching ratios $\mathcal{B}(B^- \to K^- D^0)$ and $\mathcal{B}(B^- \to K^- \bar{D}^0)$. While the former can be measured in a straightforward way, the latter is very difficult to measure.

Recently Atwood, Dunietz and Soni [91] have pointed out that CP violation can be greatly enhanced for decays to final states that are common to both D^0 and $\bar{D}^0$ but are not CP eigenstates. In particular, large asymmetries are possible for final states f such that $D^0 \to f$ is doubly Cabibbo suppressed and $\bar{D}^0 \to f$ is Cabibbo allowed.

The Atwood, Dunietz and Soni method requires the determination of branching ratios for at least two distinct final states f_1 and f_2.

We define the following quantities :

$$a = \mathcal{B}(B^- \to K^- D^0) \tag{6.117}$$

$$b = \mathcal{B}(B^- \to K^- \bar{D}^0) \tag{6.118}$$

$$c(f_1) = \mathcal{B}(D^0 \to f_1), \qquad c(f_2) = \mathcal{B}(D^0 \to f_2) \tag{6.119}$$

$$c(\bar{f}_1) = \mathcal{B}(D^0 \to \bar{f}_1), \qquad c(\bar{f}_2) = \mathcal{B}(D^0 \to \bar{f}_2) \tag{6.120}$$

$$d(f_1) = \mathcal{B}(B^- \to K^- f_1), \qquad d(f_2) = \mathcal{B}(B^- \to K^- f_2) \tag{6.121}$$

$$\bar{d}(f_1) = \mathcal{B}(B^+ \to K^+ f_1), \qquad \bar{d}(f_2) = \mathcal{B}(B^+ \to K^+ f_2) \tag{6.122}$$

Assume that we can measure the quantities a, $c(f_1)$, $c(f_2)$, $c(\bar{f}_1)$, $c(\bar{f}_2)$, $d(f_1)$, $d(f_2)$, $\bar{d}(f_1)$ and $\bar{d}(f_2)$ but not b.

We can express $d(f_1)$ in terms of a, b, $c(f_1)$, $c(\bar{f}_1)$, the strong phase ξ_1 and the weak phase γ.

$$d(f_1) = a \times c(f_1) + b \times c(\bar{f}_1) + 2\sqrt{a \times b \times c(f_1) \times c(\bar{f}_1)}\cos(\xi_1 + \gamma) \tag{6.123}$$

$$\bar{d}(f_1) = a \times c(f_1) + b \times c(\bar{f}_1) + 2\sqrt{a \times b \times c(f_1) \times c(\bar{f}_1)}\cos(\xi_1 - \gamma) \tag{6.124}$$

$$d(f_2) = a \times c(f_2) + b \times c(\bar{f}_2) + 2\sqrt{a \times b \times c(f_2) \times c(\bar{f}_2)}\cos(\xi_2 + \gamma) \tag{6.125}$$

$$\bar{d}(f_2) = a \times c(f_2) + b \times c(\bar{f}_2) + 2\sqrt{a \times b \times c(f_2) \times c(\bar{f}_2)}\cos(\xi_2 - \gamma) \tag{6.126}$$

These four equations contain the four unknowns ξ_1, ξ_2, b and γ which can be determined up to discrete ambiguities. Adding additional decay modes will reduce the ambiguities. The strong phases ξ_i are related to the D decay phase shifts δ_i by the relation :

$$\xi_1 - \xi_2 = \delta_1 - \delta_2. \tag{6.127}$$

If the D decay phase shifts can be determined elsewhere then we have an extra constraint on the equations. This method measures direct CP violation and does not require tagging nor time-dependent measurements. If we add a third decay mode we have six equations with five unknowns which will help to resolve ambiguities.

6.4.2 $B \to DK$: CDF Report

We summarize the study of measuring the unitarity triangle angle γ at CDF in RunII, first using the decay mode $B_s^0 \to D_s^- K^+$ and second exploiting the decay $B^- \to D^0 K^-$.

6.4.2.1 $B_s^0 \to D_s^- K^+$: CDF Report †

As outlined in Sec. 6.4.1.1 above, the decay mode $B_s^0 \to D_s^- K^+$ probes the unitarity triangle angle γ by CP violation due to interference of decays with and without mixing [19,92] (see also Sec. 6.1.3). The weak amplitude of $B_s^0 \leftrightarrow \bar{B}_s^0$ mixing is approximately real, as is the weak amplitude of the decay $B_s^0 \to D_s^- K^+$. But the decay $\bar{B}_s^0 \to D_s^- K^+$ has a non-zero phase which is approximately the angle γ of the unitarity triangle. Thus, the overall CP violating weak phase of this decay is γ to the accuracy of the Wolfenstein parameterization of the CKM matrix ($\mathcal{O}(10^{-4})$).

The decay rates given in Eq. (6.113) allow the extraction of $\sin(\gamma \pm \delta)$. If $\Delta\Gamma_s/\Gamma_s$ is large enough, $\cos(\gamma \pm \delta)$ may additionally be extracted [10]. Since the $\cos(\gamma \pm \delta)$ terms are identical for the same final states, tagging is unnecessary to measure $\cos(\gamma \pm \delta)$ and a much larger untagged sample may be used. Extracting $\cos(\gamma \pm \delta)$ with the untagged sample has the additional benefit of not needing to resolve the rapid $B_s^0 \leftrightarrow \bar{B}_s^0$ oscillations. Unfortunately, the two measurements cannot extract γ separately, but they can be used to constrain the tagged fit and resolve discrete ambiguities in extracting γ from $\sin(\gamma \pm \delta)$.

If $\Delta\Gamma_s/\Gamma_s$ is too small to allow an extraction of $\cos(\gamma \pm \delta)$, theoretical input on δ will likely be necessary. Although a measurement of $\sin(\gamma \pm \delta)$ may exclude much of the (γ, δ) plane, the discrete ambiguities are such that projecting onto the γ axis usually does not exclude much of γ, even with fairly small errors on $\sin(\gamma \pm \delta)$. The current theoretical prediction of $|\delta| < 5^\circ$ [93], however, is sufficient to exclude most discrete ambiguities.

An additional subtlety which must be considered is the possibility of measuring an unphysical value of $\sin(\gamma \pm \delta) > 1$. If either $\sin(\gamma \pm \delta)$ is very near or at 1, even measurements with small errors would frequently produce unphysical results of $\sin(\gamma \pm \delta) > 1$. Thus a technique such as the unified approach of Feldman and Cousins [94] must be used to convert the measured amplitude of $\sin(\gamma \pm \delta)$ to the quantities of interest, γ and δ, rather than relying upon a straightforward trigonometric transformation.

† Authors: S. Bailey and P. Maksimović.

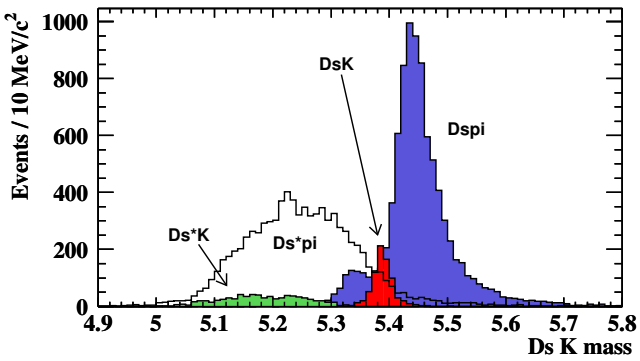

Figure 6.17: Mass plot for the $B_s^0 \to D_s^- K^+$ signal (marked DsK) and various physics backgrounds. The S/B in the signal region is 1/3 before any particle identification.

Background Studies

The reduction of backgrounds will be one of the primary challenges for using the $B_s^0 \to D_s^- K^+$ mode at CDF. The physics backgrounds which closely mimic the signal are given below where the branching ratios used in this study are estimated branching fractions.

Background Mode	$\mathcal{B} \times 10^{-3}$	Signal Mode	$\mathcal{B} \times 10^{-3}$
$B_s^0 \to D_s^- \pi^+$	3.0	$B_s^0 \to D_s^- K^+$	0.2
$B_s^0 \to D_s^{*-} \pi^+$	3.0	$B_s^0 \to D_s^+ K^-$	0.1
$B_s^0 \to D_s^{*-} K^+$	0.2		
$B_s^0 \to D_s^{*+} K^-$	0.1		
$B^0 \to D_s^- \pi^+$	0.1		
$B^0 \to D_s^{*-} \pi^+$	0.1		

As shown in Figure 6.17, reconstructing the physics backgrounds as $B_s^0 \to D_s^- K^+$ produces a mass shift away from the B_s^0 mass such that the S/B in the B_s^0 mass region is 1/3 even though the ratio of branching fractions is much worse.

Combinatoric backgrounds are expected to be the primary concern. A S/B study for $B_s^0 \to D_s^- \pi^+$ using CDF Run I data concluded that a S/B in the range 1/2 to 2/1 was reasonable for that mode. That study was statistics limited and did not consider the S/B improvements that will be achieved using the 3-dimensional vertexing capabilities of the SVX II detector and $\mathrm{d}E/\mathrm{d}x$ cuts. Without including those improvements, scaling for branching fractions produces a nominal combinatoric S/B for $B_s^0 \to D_s^- K^+$ of 1/15.

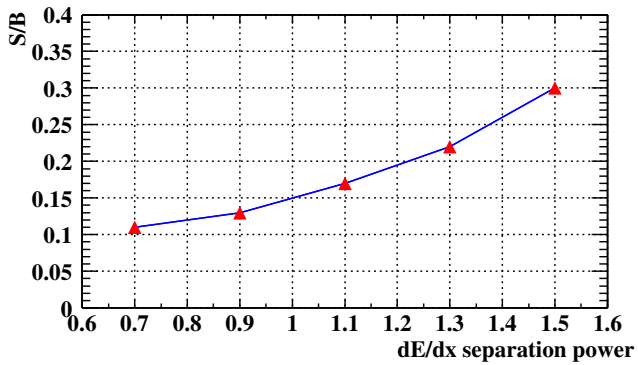

Figure 6.18: Example signal to background ratio S/B as a function of the $\mathrm{d}E/\mathrm{d}x$ separation power between kaons and pions.

Figure 6.18 shows the resulting S/B (physics and combinatoric) after applying $\mathrm{d}E/\mathrm{d}x$ cuts as a function of the $\mathrm{d}E/\mathrm{d}x$ separation power. The cuts used here have a constant signal efficiency corresponding to 850 signal events. For this study we use a nominal S/B of 1/6 which corresponds to a $\mathrm{d}E/\mathrm{d}x$ separation power of $1.1\,\sigma$.

Results of Toy Monte Carlo Study

To study CDF's sensitivity to measuring γ using this mode, we wrote a Toy Monte Carlo plus fitter. We generated signal events according to the decay rate Equations (6.113) and added background events with appropriate proper time dependencies. The events were smeared by a Gaussian resolution function and (mis)assigned an observed flavour according to a mistag probability. We fit these data using an unbinned likelihood method and compared the results and their errors with the input values.

The central values used as input parameters for this study are given in Table 6.11. The left table lists physical parameters to be measured over which we have no control. The chosen values are based upon Standard Model predictions [95]. The right table lists parameters which are CDF dependent and may be improved with effort. Their values are chosen based upon other CDF II studies. N is the number of reconstructed events before flavour tagging is applied. Our study shows that CDF expects to reconstruct about 850 $B_s^0 \to D_s^- K^+$ signal events in 2 fb^{-1} of Run II data. While studying the dependence of the error upon a given parameter, we kept the rest of the parameters fixed at these values.

Figure 6.19 shows the dependence of the error on the number of pre-tagged signal events for both $S/B = 1/6$ (upper points) and $S/B = 1/1$ (lower points). The points correspond to approximately 2, 5, 10, and 20 fb^{-1} of data.

Figure 6.20 shows how the errors scale with the proper time resolution σ_t, the effective

Parameter	Standard Model Estimate	Parameter	CDF II Estimate
γ	90°	σ_t	0.03
δ	10°	$\varepsilon\mathcal{D}^2$	0.113
$\lvert A_f\rvert/\lvert\bar{A}_f\rvert$	$\sqrt{1.4/2.4}$	$N(B_s^0 \to D_s^- K^+)$	850
x_s	20	S/B	1/6
x_d	0.723		
$\Delta\Gamma_s/\Gamma_s$	0.16		

Table 6.11: Central values of parameter used in the study of $B_s^0 \to D_s^- K^+$ at CDF.

tagging efficiency $\varepsilon\mathcal{D}^2$, the B_s^0 mixing parameter x_s and the ratio of decay amplitudes ρ. The triangles represent the error using the central values of the input parameters, while the squares are the errors from varying one parameter while leaving the others fixed. The curves are the theoretical errors discussed below. The lower points and curves are for $S/B = 1/1$ for comparison.

The expected error on $\sin(\gamma \pm \delta)$ is closely modeled by the following expression:

$$\sigma(\sin(\gamma \pm \delta)) = \frac{1}{\mathcal{D}_{res}} \frac{1}{\mathcal{D}_{bkg}} \frac{1}{\mathcal{D}_{fit}} \frac{1}{\sqrt{\varepsilon\mathcal{D}^2 N}} \tag{6.128}$$

where $\mathcal{D}_{res} = e^{-\sigma_t^2 x_s^2/2}$, $\mathcal{D}_{bkg} = \sqrt{\frac{S}{S+B}}$, $\varepsilon\mathcal{D}^2$ is the effective flavour tagging efficiency and $\mathcal{D}_{fit}$ is normalized to the error obtained using the central values of the input parameters. A discussion of the terms of this equation may be found in Ref. [96]. There was very little dependence of the errors upon the values of γ, δ and $\Delta\Gamma_s/\Gamma_s$.

In conclusion, an initial measurement of γ using $B_s^0 \to D_s^- K^+$ should be possible with CDF in Run II. Within the first 2 fb^{-1}, the expected error on $\sin(\gamma \pm \delta)$ is around 0.4 to 0.7 depending upon what the background levels turn out to be. By the end of Run II an uncertainty near 0.1 may be achievable. The most limiting factors for CDF II are the background levels and the overall signal size. There are significant uncertainties on these parameters, but our Toy Monte Carlo studies indicate that Eq. (6.128) is an accurate predictor of the error over a wide range of input parameters.

6.4.2.2 $B^- \to D^0 K^-$: CDF Report †

In this section, we evaluate the prospects of measuring the CKM angle γ using the decay channel $B^- \to D^0 K^- \to [K\pi]K^-$ at CDF in Run II. This requires the knowledge of all branching fractions involved, where we list the estimated branching ratios used as input for this study in Table 6.12.

†Authors: A. Cerri, G. Punzi and G. Signorelli.

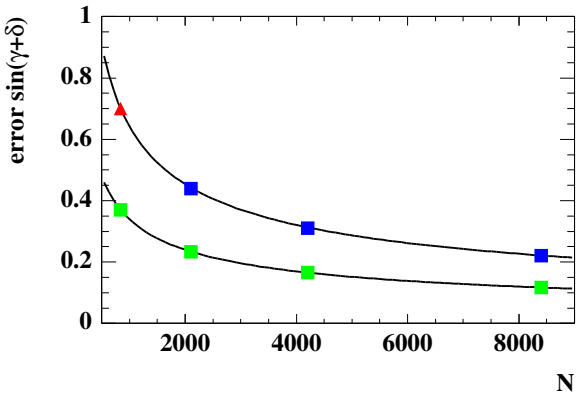

Figure 6.19: The error on $\sin(\gamma \pm \delta)$ from Toy Monte Carlo experiments as a function of the number of observed $B_s^0 \to D_s^- K^+$ events N. The points correspond to approximately 2, 5, 10, and 20 fb^{-1} of data.

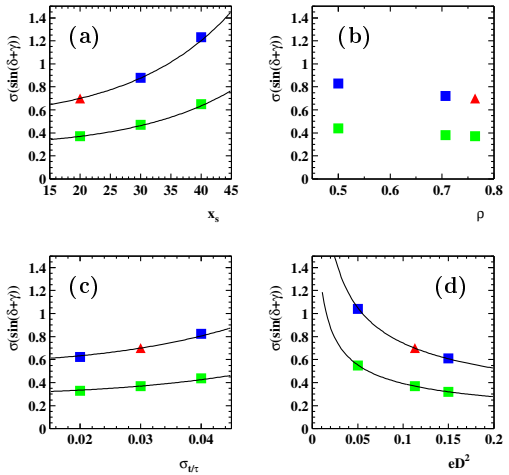

Figure 6.20: The error on $\sin(\gamma \pm \delta)$ from Toy Monte Carlo experiments as a function of (a) x_s, (b) the ratio of decay amplitudes ρ, (c) the proper time resolution σ_t and (d) the effective flavour tagging efficiency $\varepsilon \mathcal{D}^2$. The triangle is the error using the central values of all parameters with a $S/B = 1/6$. The curve is the theoretically expected error. The lower points and curves are for $S/B = 1/1$.

$\mathcal{B}(B^+ \to K^+ \bar{D}^0) = 2.6 \pm 0.08 \times 10^{-4}$	CLEO
$\mathcal{B}(B^+ \to K^+ D^0) \approx 2 \times 10^{-6}$	Estim. [91]
$\mathcal{B}(\bar{D}^0 \to K^- \pi^+) = 1.3 \pm 0.3 \times 10^{-4}$	CLEO
$\mathcal{B}(\bar{D}^0 \to K^+ \pi^-) = 3.8 \pm 0.1 \times 10^{-2}$	PDG

Table 6.12: Estimated branching ratios of decays involved in the analysis of $B^- \to D^0 K^- \to [K\pi]K^-$ at CDF.

Beginning with Equations (6.123) - (6.126) as shown in Sec. 6.4.1.2, the number of events in each channel, which we will shortly refer to as $X_{1/2}$ and $Y_{1/2}$, is given by

$$X_{1/2} = d_{1/2} \cdot [\sigma_B \, \eta_{1/2} \, \epsilon_{1/2} \, \mathcal{L}] \quad \text{and} \quad Y_{1/2} = \bar{d}_{1/2} \cdot [\sigma_B \, \eta_{1/2} \, \epsilon_{1/2} \, \mathcal{L}] \tag{6.129}$$

where σ_B is the B^+ production cross section, $\epsilon_{1/2}$ is the detector acceptance times the trigger efficiency for the corresponding channel, $\eta_{1/2}$ is the efficiency on the signal from offline requirements and $\mathcal{L}$ is the integrated luminosity. From the measurement of X_1, X_2, Y_1 and Y_2, as well as knowing $[\sigma_B \eta_{1/2} \epsilon_{1/2} \mathcal{L}]$, it is formally possible to invert the relations given in Eqs. (6.123) - (6.126) to obtain a value for $\cos(\xi_{1/2} + \gamma)$ and $\cos(\xi_{1/2} - \gamma)$.

As a first step, we evaluate the resolution on the angle γ when γ lies in the range $60^\circ < \gamma < 100^\circ$ and ξ in the range $-10^\circ < \xi < 30^\circ$, as suggested by Standard Model fits [97]. We use a Toy Monte Carlo to estimate the resolution on the studied parameters in the following way. We extract γ and ξ within their range and the values of all branching fractions from Gaussian distributions around their nominal values. With these parameters, and a given signal to noise ratio, we calculate the expectation values of the number of events in each channel, $\bar{x}$ and $\bar{y}$. X and Y are then obtained from a Poisson distribution around those values. From such "pseudo-measurements" we obtain the values of $\widehat{\gamma}$ and $\widehat{\xi}$ that maximize the likelihood. We then plot the distribution of the experimental error $\widehat{\gamma} - \gamma$, averaged over the whole range of γ and ξ considered, and extract its sigma by a Gaussian fit. In Figure 6.21 we show an example distribution using 140 observed events, zero background, and a 10% uncertainty on all branching ratios involved. The sigma of this distribution is about 9°.

Given the good behavior of the resolution function even with this small sample, we decided it was more convenient to replace the Monte Carlo method by a semi-analytical calculation of the resolution using the standard approximation based on the Hessian matrix of the Likelihood function. This makes it easier to plot the dependence on various parameters. We explicitly checked that this method gives the same results as the Toy Monte Carlo.

Collection of Data Sample

The data sample considered here, $B^- \to D^0 K^- \to [K\pi]K^-$, will be accumulated with the two-track hadronic trigger used for the collection of $B \to \pi\pi/KK$ events (see Sec. 6.3.2.1).

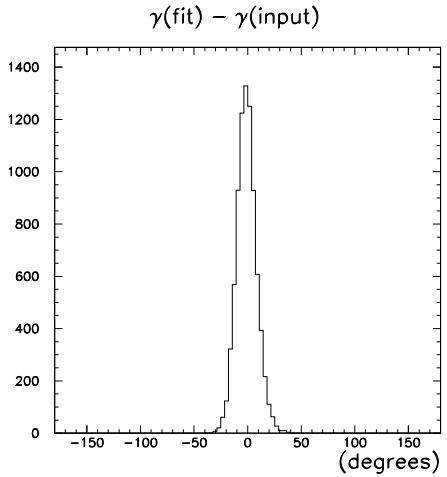

Figure 6.21: Deviation of the value of γ obtained from the fit and the value of γ used as input in the Monte Carlo study. We neglected backgrounds and assumed a 10% uncertainty on the four branching ratios. Note, one of the four branching fractions, namely $D^0 \to K^-\pi^+$, is at present known to better than 3%.

2 SVT tracks with $p_T > 2$ GeV/c
100 μm $< d <$ 1 mm for the two tracks
$\vec{p_T} \cdot \vec{X}_V > 0.2$ GeV/$c \cdot$ cm

Table 6.13: L2 trigger cuts proposed for multibody B decay selection.

To optimize the event selection efficiency, we performed a study of varying Level2 trigger requirements and ended up with a slightly modified version of the hadronic two-track trigger. In Table 6.13 we show the L2 selection requirements as proposed for the multi-body B decay selection. For the determination of the corresponding number of expected signal events, we use a B^+ production cross section of (3.35 ± 0.68) μb and integrated luminosities of 2, 10 and 30 fb^{-1} (see Table 6.14). The Level2 trigger efficiencies for the $[K\pi]K^-$ final state are 0.59%, 0.52% and 0.40% for the three different Tevatron operating scenarios A, B and C, respectively.

Background

The reduction of backgrounds is the most important issue to address at CDF. Note, the signal we are considering here is two orders of magnitude smaller than the number of $B^0 \to \pi^+\pi^-$ events. A detailed study of the contribution of the combinatoric background

Int. Luminosity	Scenario A	Scenario B	Scenario C
2 fb$^-$1	135	120	90
	(1:14)	(1:12)	(1:9)
10 fb$^-$1	675	585	450
	(1:70)	(1:60)	(1:45)
30 fb$^-$1	2025	1755	1350
	(1:200)	(1:175)	(1:135)

Table 6.14: Expected event yields for $B^- \to [K\pi]K^-$ for different Tevatron operation scenarios. The worst S : B ratio that can be tolerated when requiring a resolution on γ better than $\approx 30^\circ$ is given in parenthesis.

Channel	$\mathcal{B}$
$B^+ \to \bar{D}^0 K^+$	2.6×10^{-4}
$B^+ \to D^0 K^+$	2×10^{-6}
$B^+ \to \bar{D}^0 \pi^+$	5×10^{-3}
$B^0 \to \bar{D}^0 \pi^+(\pi^-)$	2.1×10^{-3}
$\bar{D}^0 \to K^-\pi^+$	1.3×10^{-4}
$\bar{D}^0 \to \pi^- K^+$	3.8×10^{-2}
$\bar{D}^0 \to \pi^-\pi^+$	1.5×10^{-3}

Channel	yield/S
$B^+ \to [K^-\pi^+]K^+$	1
$B^+ \to [\pi^- K^+]K^+$	47
$B^+ \to [\pi^-\pi^+]K^+$	2
$B^+ \to [K^-\pi^+]\pi^+$	3
$B^+ \to [\pi^- K^+]\pi^+$	910
$B^+ \to [\pi^-\pi^+]\pi^+$	36

Table 6.15: Branching ratios of potential physics backgrounds. The right table lists the relative abundance of each final state configuration with respect to the signal. Note, the channel $B^+ \to [\pi^- K^+]\pi^+$ is about 1000 times larger than the signal.

has not been performed. To obtain a reliable background estimate, we will need real RunII data. We therefore concentrate on the "physics background" consisting of B decay channels which are difficult to separate from the signal. Most of them differ from the signal only in the identity of the final sate particles. Some of them are given in Table 6.15. The channel $B^\pm \to D^0\pi^\pm$ is kinematically almost identical to the signal $B^\pm \to D^0 K^\pm$ and its branching ratio is an order of magnitude larger. The decay $B^0 \to D^{*-}\pi^+ \to \bar{D}^0(\pi^-)\pi^+$ is similar to the previous one, with the difference that the reconstructed fake B^+ meson has a reduced mass. $\bar{D}^0 \to \pi^+\pi^-$ decay modes are potential backgrounds. The decay $B^+ \to [K^+\pi^-]K^+$ results from combining the two Cabibbo-allowed decays, and is potentially the most dangerous channel, being two orders of magnitude larger than our signal.

A detailed description of CDF's capability to separate signal from background is beyond the scope of this report, but we want to give the reader an idea of possible methods for signal to background reduction. Figure 6.22 shows the invariant mass distribution of pairs of D daughter particles, obtained by assigning the pion mass to the particle with the same

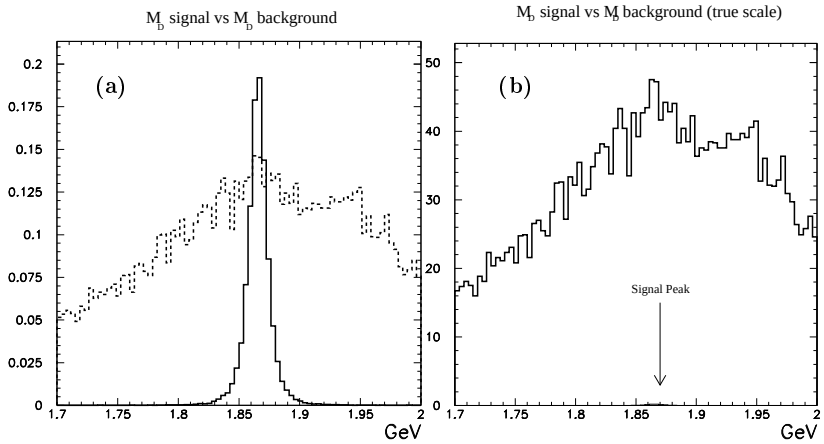

Figure 6.22: Invariant mass distribution of pairs of D daughter particles, obtained by assigning the pion mass to the particle with the same charge as the B^- meson and the kaon mass to the other particles. In (a) the scale is arbitrary, while in (b) the correct normalization between physics backgrounds and signal is used.

charge as the B^- meson and the kaon mass to the other particles. In Figure 6.22(a) the scale is arbitrary, while in (b) the correct normalization between physics backgrounds and signal is used.

We plan to perform the signal to physics background separation both with particle identification and kinematics. If we assign incorrect rest masses to the final state particles, both the D and B mass distributions will appear wider and/or shifted. A special case is the contribution of B^0 mesons, where a charged pion is lost and the reconstructed "B^-" has a significantly lower mass. We see from Table 6.15 that the size of this background is 40% of the corresponding contribution from real B^-. However, in a window of ± 50 MeV/c^2 around the nominal B^- mass, only a fraction of 3.9% of B^0 decays remain. We therefore neglect the contribution of B^0 with respect to real B^-.

A more refined analysis is needed to reject real B^- background by exploiting the mass differences due to missassigned particle identities. Many different methods of various degree of refinement can be used. Here we only want to give an example illustrating that a powerful background rejection is achievable. Let's assume we consider final states with three particles, $[a^+b^-]c^+$, and want to identify a, b and c. We can formulate several hypotheses, e.g. $I = \{a = K;\ b = \pi;\ c = K\}$. Given a set of hypotheses $\mathcal{I} = \{I_1, \ldots, I_N\}$, we can compute the distances d from the true PDG masses [62]

$$d_D(I_k) = \left| M(D|I_k) - M(D)_{\text{true}} \right| \quad \text{and} \quad d_B(I_k) = \left| M(B|I_k) - M(B)_{\text{true}} \right|. \tag{6.130}$$

We call

$$d_T(I_k) = \sqrt{d_D(I_k)^2 + d_B(I_k)^2} \tag{6.131}$$

and consider the right hypothesis I_k for which $d_T(I_k)$ is smallest.

With this algorithm we obtain signal efficiencies of $(90 \pm 1)\%$ and $(0.8 \pm 0.2)\%$ for background events. This method provides more than a factor of 100 in background rejection, reducing the physics background to a level of $B/S = 9:1$.

The B/S ratio can be further improved by using CDF's particle identification capabilities from the energy loss measurement $\mathrm{d}E/\mathrm{d}x$ in the COT. From this study we expect the combined application of kinematical selections and particle identification to have a sufficient rejection power against physics backgrounds. However, we expect the combinatoric background to be an important issue. From the numbers in Tab. 6.14 we see that if the combinatoric background were negligible, a resolution of 15° on γ can be achieved assuming $\mathcal{B}(B^+ \to K^+D^0)$ is determined with sufficient precision ($\approx 20\%$).

In conclusion, we discussed a method for measuring γ in Run II using charged B decays. We expect to collect a small but significant sample of both candidate channels for this analysis by using the two-track hadronic trigger at CDF. The physics background can be brought down to the same level as the signal, but there could be considerable combinatoric background. If we are able to reduce the combinatoric background to a level comparable to the signal, we expect a significant measurement of γ with this method in RunII.

6.4.2.3 Fully Hadronic B Decays Accessible at CDF in Run II [†]

The selection of the decay modes $B_s^0 \to D_s^- K^+$ and $B^- \to D^0 K^-$ is based on collecting these events with the two-track hadronic trigger which was originally designed to select a large sample of $B^0 \to \pi^+\pi^-$ decays but is also used to obtain $B_s^0 \to D_s^-\pi^+$ events for the measurement of B_s^0 flavour oscillations (see Sec. 6.3.2.1). In the context of evaluating the yield of fully reconstructed $B^- \to D^0 K^-$ events, a more systematic study has been performed to explore the event yields of other potential CP modes that could be collected with the two-track hadronic trigger at CDF. The list of decay modes compiled was assembled under the aspect of some interest being expressed in the literature for a particular decay mode. Because of CDF's poor efficiency to reconstruct decays involving photons, decay modes with neutral particles in the final state were not considered in this study. The list of decays has been completely specified up to the final state daughters and a rough estimate of the involved branching fractions was determined. We briefly want to summarize the results of this study to give the reader an idea about event yields for potential CP modes that could be collected at CDF with the two-track hadronic trigger.

The study of the different decay modes used a Monte Carlo generator that simulates only a single B hadron and its decay products which was completely appropriate for this study. The final event yield is the result of an event selection based on a parametric simulation of the two-track trigger path and a rough geometric acceptance calculation for the whole event, including parametrized detector and trigger efficiencies. The estimate of the total number of expected events assumes a B^+ production cross section of $(3.35 \pm 0.68)\ \mu b$ for $|y| \leq 1$ and $p_T(B) \geq 6$ GeV/c.

[†]Author: A. Cerri.

In Table 6.16 we list the estimated total branching ratio and the expected number of events per 1 fb^{-1} for several neutral B decay modes. The corresponding numbers of events for B^+ and B_s^0 decay modes are listed in Table 6.17 and Table 6.18, respectively. It is clear from that study that the two-track hadronic trigger will allow CDF to collect significant datasets of fully hadronic B decays. This will be the source of a rich B physics program at CDF involving many different B decay modes.

6.4.3 $B \to DK$: BTeV Report [†]

Several suggestions on how to measure the CKM angle γ have been discussed in Section 6.1. While discrete ambiguities are inherent in each of these methods, using several methods will help remove some of these ambiguities as well as help control systematic errors. We report first the BTeV studies for CP Violation in $B_s^0 \to D_s^- K^+$ followed by $B^- \to D^0 K^-$ in Section 6.4.3.2.

6.4.3.1 $B_s^0 \to D_s^- K^+$: BTeV Report

A study of the reconstruction efficiency has been performed for the decay modes

$$\begin{aligned} &B_s^0 \to D_s^- K^+,\ D_s^- \to \phi\pi^-,\ \phi \to K^+K^- \text{ and} \\ &B_s^0 \to D_s^- K^+,\ D_s^- \to K^{*0}K^-,\ K^{*0} \to K^+\pi^-. \end{aligned} \tag{6.132}$$

The events were generated with Pythia and the detector modeled using BTeVGeant. Each event consists of a $b\bar{b}$ interaction and a mean of two minimum bias interactions, to simulate a luminosity of 2×10^{32} cm^{-2}s^{-1}. Loose cuts were applied initially and the tighter cuts were chosen after the background was studied.

For the $D_s^- \to \phi\pi^-$ decay mode the following requirements were used. At least one of the kaons from the ϕ decay and also the K^+ from the B_s^0 decay were required to be identified in the RICH. The impact parameter with respect to the primary vertex had to be $> 3\,\sigma$ for all four charged tracks. To reduce the background due to "detached" tracks that come from other interactions, we require that the impact parameter with respect to the primary vertex be less than 0.2 cm for all tracks. The ϕ and D_s^- were required to be within $\pm 2.5\,\sigma$ of their nominal mass. The distance between the primary vertex and D_s^- decay vertex has to be $L < 8.0$ cm and $L/\sigma_L(D_s^-) > 10.0$. We also require $L/\sigma_L(B_s^0) > 4.0$. The transverse momentum of the B_s^0 with respect to its line of flight from the primary vertex was required to be less than 1.0 GeV/c. The impact parameter with respect to the primary vertex was required to be less than $3\,\sigma$ for the reconstructed B.

The distributions of L/σ_L and the mass peaks for the D_s^- and B_s^0 are shown in Fig 6.23. The combined geometric acceptance and reconstruction efficiency was found to be 4.5%. If we require both kaons from the ϕ decay to be identified in the RICH, the efficiency drops to 2.5%. Of the events that passed these analysis cuts, 74% passed the secondary vertex trigger. For the $D_s^- \to K^{*0}K^-$ mode, we used the same cuts except that both kaons from

[†] Author: P.A. Kasper.

Decay	Subsequent Decay	Total $\mathcal{B}$	N per 1 fb^{-1}
$B^0 \to \pi^+\pi^-$		$4.3 \cdot 10^{-6}$	4900 ± 2100
$B^0 \to D^\pm\pi^\mp$	$D^\pm \to K^\mp\pi^\pm\pi^\pm$	$2.7 \cdot 10^{-4}$	81000 ± 18000
$B^0 \to D^{*\pm}\pi^\mp$	$D^{*-} \to \bar{D}^0\pi^-, D^0 \to K^-\pi^+$	$7.9 \cdot 10^{-5}$	20000 ± 4600
$B^0 \to D^{*\pm}\pi^\mp$	$D^{*-} \to \bar{D}^0\pi^-, D^0 \to K_S^0\pi^+\pi^-$	$4 \cdot 10^{-5}$	7100 ± 1600
$B^0 \to D^{*\pm}\pi^\mp$	$D^{*-} \to \bar{D}^0\pi^-, D^0 \to K^-\pi^+\pi^+\pi^-$	$1.5 \cdot 10^{-4}$	17000 ± 4200
$B^0 \to D^0 K_S^0$	$D^0 \to K^-\pi^+, K_S^0 \to \pi^+\pi^-$	$5 \cdot 10^{-7}$	92 ± 21
$B^0 \to D^0 K_S^0$	$D^0 \to K_S^0\pi^+\pi^-, K_S^0 \to \pi^+\pi^-$	$2.5 \cdot 10^{-7}$	21 ± 5.3
$B^0 \to D^0 K_S^0$	$D^0 \to K^-\pi^+\pi^+\pi^-, K_S^0 \to \pi^+\pi^-$	$9.7 \cdot 10^{-7}$	74 ± 19
$B^0 \to D^0 K^{*0}$	$D^0 \to K^-\pi^+, K^{*0} \to K^+\pi^-$	$2.5 \cdot 10^{-7}$	71 ± 16
$B^0 \to D^0 K^{*0}$	$D^0 \to K_S^0\pi^+\pi^-, K^{*0} \to K^+\pi^-$	$1.3 \cdot 10^{-7}$	17 ± 4.1
$B^0 \to D^0 K^{*0}$	$D^0 \to K^-\pi^+\pi^+\pi^-, K^{*0} \to K^+\pi^-$	$4.9 \cdot 10^{-7}$	60 ± 14
$B^0 \to D_{1,2} K^{*0}$	$D_{1,2} \to (\pi^+\pi^-, K^+K^-)\, K^{*0} \to K^+\pi^-$	$1 \cdot 10^{-8}$	$2.3 \pm .5$
$B^0 \to D^{*0} K^{*0}$	$D^{0*} \to D^0\pi^0, D^0 \to K^-\pi^+$	$1 \cdot 10^{-7}$	22 ± 5
$B^0 \to D^{*0} K^{*0}$	$D^{0*} \to D^0\pi^0, D^0 \to K_S^0\pi^+\pi^-$	$5 \cdot 10^{-8}$	7.4 ± 1.8
$B^0 \to D^{*0} K^{*0}$	$D^{0*} \to D^0\pi^0, D^0 \to K^-\pi^+\pi^+\pi^-$	$2 \cdot 10^{-7}$	21 ± 5.2
$B^0 \to D_1 K_S^0$	$D_1 \to (\pi^+\pi^-, K^+K^-)\,, K_S^0 \to \pi^+\pi^-$	$4 \cdot 10^{-8}$	6 ± 1.4
$B^0 \to \phi K_S^0$	$\phi \to K^+K^-, K_S^0 \to \pi^+\pi^-$	$3 \cdot 10^{-6}$	350 ± 85
$B^0 \to D^+D^-$	$D^\pm \to K^\mp\pi^\pm\pi^\pm$	$3 \cdot 10^{-6}$	560 ± 130
$B^0 \to D^{*+}D^{*-}$	$D^{*-} \to \bar{D}^0\pi^-, D^0 \to K^-\pi^+$	$4 \cdot 10^{-7}$	69 ± 16
$B^0 \to D^{*+}D^{*-}$	$D^{*-} \to \bar{D}^0\pi^-, D^0 \to K_S^0\pi^+\pi^-$	$2 \cdot 10^{-7}$	13 ± 3.4
$B^0 \to D^{*+}D^{*-}$	$D^{*-} \to \bar{D}^0\pi^-, D^0 \to K^-\pi^+\pi^+\pi^-$	$7.8 \cdot 10^{-7}$	49 ± 13
$B^0 \to D^{*+}D^{*-}K_S^0$	$D^{*-} \to \bar{D}^0\pi^-, D^0 \to K^-\pi^+$	$4.5 \cdot 10^{-6}$	450 ± 110
$B^0 \to D^{*+}D^{*-}K_S^0$	$D^{*-} \to \bar{D}^0\pi^-, D^0 \to K_S^0\pi^+\pi^-$	$2.3 \cdot 10^{-6}$	86 ± 27
$B^0 \to D^{*+}D^{*-}K_S^0$	$D^{*-} \to \bar{D}^0\pi^-, D^0 \to K^-\pi^+\pi^+\pi^-$	$8.8 \cdot 10^{-6}$	260 ± 86
$B^0 \to \rho^0\rho^0$	$\rho^0 \to \pi^+\pi^-$	$1 \cdot 10^{-6}$	330 ± 72
$B^0 \to D^+D^-K_S^0$	$D^\pm \to K^\mp\pi^\pm\pi^\pm$, $K_S^0 \to \pi^+\pi^-$	$7 \cdot 10^{-6}$	630 ± 160
$B^0 \to D^\pm\pi^\mp K_S^0$	$D^\pm \to K^\mp\pi^\pm\pi^\pm$, $K_S^0 \to \pi^+\pi^-$	$1 \cdot 10^{-5}$	1000 ± 260
$B^0 \to D_{CP}^0\pi^+\pi^-$	$D_{CP}^0 \to \pi^+\pi^-, K^+K^-$	$1 \cdot 10^{-5}$	2900 ± 640
$B^0 \to K^{*+}\pi^-$	$K^{*+} \to K_S^0\pi^+ \to \pi^+\pi^-\pi^+$	$2 \cdot 10^{-6}$	400 ± 91
$B^0 \to D_s^\pm K^\mp$	$D_s^\pm \to \phi\pi^\pm$, $\phi \to K^+K^-$	$4.1 \cdot 10^{-6}$	1000 ± 220
$B^0 \to D^0\rho^0$	$D^0 \to K^-\pi^+$	$1.5 \cdot 10^{-5}$	3900 ± 870
$B^0 \to D^0\rho^0$	$D^0 \to K_S^0\pi^+\pi^-$	$7 \cdot 10^{-6}$	1100 ± 250
$B^0 \to D^0\rho^0$	$D^0 \to K^-\pi^+\pi^+\pi^-$	$3 \cdot 10^{-5}$	4300 ± 1000
$B^0 \to \rho^0 K_S^0$	$\rho^0 \to \pi^+\pi^-$, $K_S^0 \to \pi^+\pi^-$	$2.6 \cdot 10^{-5}$	2400 ± 620
$B^0 \to D_s^- K^+$	$D_s^\pm \to \phi\pi^\pm$, $\phi \to K^+K^-$	$7 \cdot 10^{-6}$	1700 ± 380

Table 6.16: Estimated total branching ratio and expected number of events per 1 fb^{-1} for several hadronic B^0 decay modes.

Decay	Subsequent Decay	Total $\mathcal{B}$	N per 1 fb^{-1}
$B^\pm \to D^0 K^\pm$	$D^0 \to K^-\pi^+$	$7.5 \cdot 10^{-8}$	28 ± 6.1
$B^\pm \to D^0 K^\pm$	$D^0 \to K^0_S\pi^+\pi^-$	$3.8 \cdot 10^{-8}$	5.4 ± 1.3
$B^\pm \to D^0 K^\pm$	$D^0 \to K^-\pi^+\pi^+\pi^-$	$5.2 \cdot 10^{-8}$	8.2 ± 1.9
$B^\pm \to K^{*\pm}\rho^0$	$\rho^0 \to \pi^+\pi^-$, $K^{*+} \to K^0_S\pi^+$, $K^0_S \to \pi^+\pi^-$	$1.7 \cdot 10^{-6}$	180 ± 45
$B^\pm \to \pi^\pm\rho^0$	$\rho^0 \to \pi^+\pi^-$	$9 \cdot 10^{-6}$	3400 ± 730
$B^\pm \to \pi^+\pi^-\pi^\pm$		$3.5 \cdot 10^{-5}$	16000 ± 3500
$B^\pm \to K^+K^-\pi^\pm$		$1.5 \cdot 10^{-5}$	5300 ± 1200
$B^\pm \to K^\pm K^0_S$	$K^0_S \to \pi^+\pi^-$	$6.8 \cdot 10^{-6}$	200 ± 67
$B^\pm \to \pi^\pm K^0_S$	$K^0_S \to \pi^+\pi^-$	$1.6 \cdot 10^{-5}$	340 ± 130
$B^\pm \to \phi K^\pm$	$\phi \to K^+K^-$	$1.2 \cdot 10^{-5}$	3800 ± 830

Table 6.17: Estimated total branching ratio and expected number of events per 1 fb^{-1} for several hadronic B^+ decay modes.

Decay	Subsequent Decay	Total $\mathcal{B}$	N per 1 fb^{-1}
$B^0_s \to K^*\bar{K}^*$	$K^{*0} \to K^\pm\pi^\mp$	$1 \cdot 10^{-6}$	110 ± 24
$B^0_s \to K^{*+}K^{*-}$	$K^{*\mp} \to K^0\pi$, $K^0 \to \pi\pi$	$1 \cdot 10^{-6}$	78 ± 18
$B^0_s \to \bar{D}^0\phi$	$D^0 \to K^-\pi^+$, $\phi \to K^+K^-$	$1.1 \cdot 10^{-7}$	12 ± 2.7
$B^0_s \to \bar{D}^0\phi$	$D^0 \to K^0_S\pi^+\pi^-$, $K_S \to \pi^+\pi^-$	$5.3 \cdot 10^{-8}$	$2.2 \pm .5$
$B^0_s \to \bar{D}^0\phi$	$D^0 \to K^-\pi^+\pi^-\pi^+$, $\phi \to K^+K^-$	$2.2 \cdot 10^{-7}$	14 ± 3.3
$B^0_s \to \bar{D}^0\bar{K}^{*0}$	$D^0 \to K^-\pi^+$, $K^{*0} \to K^\pm\pi^\mp$	$4.6 \cdot 10^{-6}$	430 ± 96
$B^0_s \to \bar{D}^0\bar{K}^{*0}$	$K^{*0} \to K^\pm\pi^\mp$	$2.2 \cdot 10^{-6}$	140 ± 33
$B^0_s \to \bar{D}^0\bar{K}^{*0}$	$K^{*0} \to K^\pm\pi^\mp$	$9 \cdot 10^{-6}$	600 ± 140
$B^0_s \to D^\pm_s\pi^\mp$	$D^\pm_s \to \phi\pi^\pm$, $\phi \to K^+K^-$	$5.3 \cdot 10^{-5}$	6200 ± 1400
$B^0_s \to D^\pm_s\pi^\mp\pi^+\pi^-$	$D^\pm_s \to \phi\pi^\pm$, $\phi \to K^+K^-$	$1.4 \cdot 10^{-4}$	7700 ± 1800

Table 6.18: Estimated total branching ratio and expected number of events per 1 fb^{-1} for several hadronic B^0_s decay modes.

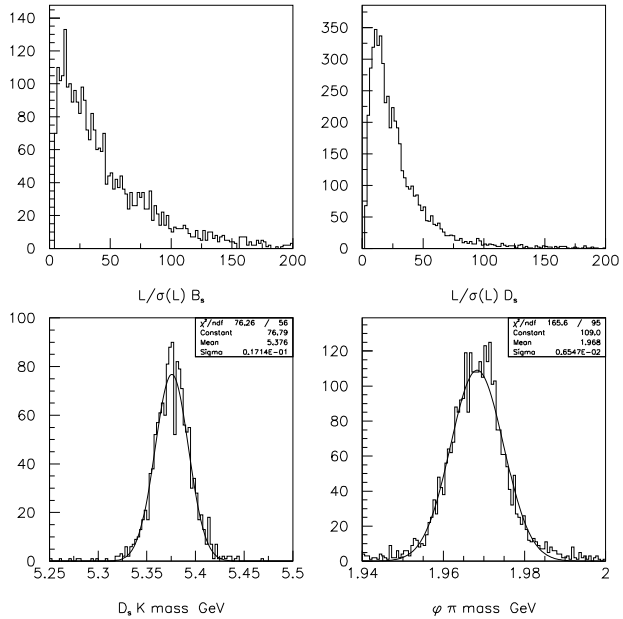

Figure 6.23: L/σ_L and mass peaks for B^0_s and D^-_s at BTeV.

the D^-_s decay were required to be identified in the RICH. The combined reconstruction efficiency and geometric acceptance for the $D^-_s \to K^{*0}K^-$ mode was found to be 2.3%, and the trigger efficiency for the events passing the analysis cuts was 74%.

The results of the tagging study described in Sec. 5.5 indicate that we can expect a tagging efficiency $\varepsilon = 0.70$ and a dilution $\mathcal{D} = 0.37$ giving an effective tagging efficiency $\varepsilon\mathcal{D}^2 = 0.10$. The expected number of events in 10^7 seconds is shown in Table 6.19.

As the CP asymmetry is diluted by a factor of $e^{-\sigma_t^2 x_s^2/2}$, good time resolution is important. Fig 6.24 is a plot of the generated proper time ($t_{\rm gen}$) minus the reconstructed proper time ($t_{\rm rec}$) for events passing the selection criteria described above. A Gaussian fit to the residual $t_{\rm gen} - t_{\rm rec}$ distribution gives a proper time resolution $\sigma_t = 0.043$ ps. Given $\tau_{B^0_s} = 1.54$ ps, we obtain $\sigma_t/\tau = 0.03$.

Background Studies

Background can arise from real physics channels such as $B^0_s \to D^-_s\pi^+$ and $B^0_s \to D^{*-}_s\pi^+$ where the pion is misidentified as a kaon or comes from random combinations of a real D^-_s with a K from the other B hadron in the event or the primary interaction vertex.

Luminosity	$2 \times 10^{32}\,\mathrm{cm}^{-2}\mathrm{s}^{-1}$	
Running time	10^7 s	
Integrated Luminosity	2 fb^{-1}	
$\sigma_{b\bar{b}}$	100 μb	
Number of $b\bar{b}$ events	2×10^{11}	
Number of $B_s^0 + \bar{B}_s^0$	5×10^{10}	
$\mathcal{B}(B_s^0 \to D_s^- K^+)^\dagger$	2×10^{-4}	
$\mathcal{B}(B_s^0 \to D_s^+ K^-)^\dagger$	1×10^{-4}	
$\mathcal{B}(D_s^- \to \phi\pi^-) \times \mathcal{B}(\phi \to K^+K^-)$	1.8×10^{-2}	
$\mathcal{B}(D_s^- \to \bar{K}^{*0}K^-) \times \mathcal{B}(\bar{K}^{*0} \to K^-\pi^+)$		2.2×10^{-2}
Reconstruction efficiency	0.045	0.023
Trigger efficiency L1	0.74	0.74
Trigger efficiency L2	0.90	0.90
Number of reconstructed $B_s^0(\bar{B}_s^0) \to D_s^- K^+$	8000	5100
Tagging efficiency ε	0.70	
Number of tagged events	5600	3570

Table 6.19: Projected number of reconstructed $B_s^0 \to D_s^- K^+$ decays († indicates estimated branching fractions).

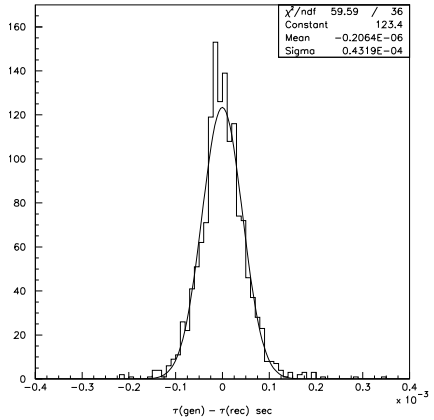

Figure 6.24: Proper time resolution for B_s^0 : $t_{\rm gen} - t_{\rm rec}$ (ns).

The combinatoric background was studied in two steps. First, generic $b\bar{b}$ events were generated in order to study the signal to background of $D_s^- \to \phi\pi^-$. Preliminary results indicate we can achieve $S/B \sim 1$ and estimate that most of the combinatoric background will come from real D_s^-.

Second, "B" $\to D_s^- X, D_s^- \to \phi\pi^-$ events were generated to determine the background from real D_s^- combinations with other tracks in the event. The D_s^- can be from directly produced charm or from B decays. Although the charm production cross-section is expected to be about a factor of 10 higher than the $b\bar{b}$ production cross-section, the trigger efficiency for charm events is much lower.

The background events were reconstructed as described above for the signal except that all pion tracks were used as kaon candidates to simulate misidentification in the RICH. A pion misidentification rate was imposed later.

For 900,000 "$\bar{B}$" $\to D_s^- X, D_s^- \to \phi\pi^-$ events, 10 events remained in the mass window 5.0 - 6.0 GeV/c^2 after all the cuts above were applied. In all these events the kaon candidate was really a pion. We then use a pion misidentification rate of 2% and estimate that the combinatoric background is about 1% of the signal.

Background can also come from decays such as $B_s^0 \to D_s^- \pi^+$, $B_s^0 \to D_s^{*-}\pi^+$ where the pion is misidentified as a kaon. Most of the background comes from $B_s^0 \to D_s^- \pi^+$. For decays where there is a missing particle there is very little overlap of the reconstructed mass with the signal region. The signal and scaled background are shown in Fig. 6.25. We expect that this will be the largest source of background and estimate $S/B \sim 7$. These results assume that pions are misidentified as kaons at a rate of 2%. We have used the stand-alone simulation of the RICH detector described in Sec. 5.4 to study the efficiency of the signal versus efficiency of the background from misidentified pions. The results are shown in Table 6.20.

Extracting ρ and $\sin\gamma$ from a Toy Monte Carlo Study

A Toy Monte Carlo study was performed to determine the expected error on γ. For the first study, the input values of the parameters were chosen to be $x_s = 30.0$, $\rho = |A_f|/|\bar{A}_f| = 0.7$, $\sin\gamma = 0.75$, $\delta = 10^\circ$ and $\Delta\Gamma/\Gamma = 0.16$. With the Toy Monte Carlo, a set of "events" (i.e. proper times) was generated and split into the four decay modes with correct time distributions. The proper times were then smeared with a Gaussian of width $\sigma_t = 0.03\,\tau$, and a cutoff at low t which simulated a L/σ_L cut: $t_{\rm min} = 0.25\,\tau$. A fraction of the events were assigned to come from the "wrong flavour" parent. A mistag fraction of 32% is used. Background events with a pure exponential time distribution are added to the "signal" events. The background is assumed to have the same lifetime as the signal.

A maximum likelihood fit was used to find the values of ρ, γ, δ and $\Delta\Gamma$. One thousand trials were done, each of 6,800 events. The fitted values of the parameters are shown in Figure 6.26 . The values of the input parameters were varied to study the impact on the error. The results of the fits are shown in Table 6.21.

In conclusion, the ability of BTeV to measure the angle γ of the unitarity triangle

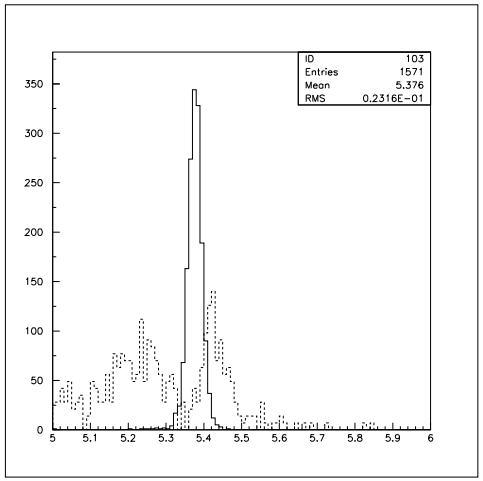

Figure 6.25: Comparison of $B_s^0 \to D_s^- K^+$ signal and background from $B_s^0 \to D_s^- X$, where X contains at least one pion misidentified as a K.

$B_s^0 \to D_s^- K^+$	$B_s^0 \to D_s^- \pi^+$
0.62	0.00000
0.66	0.00184
0.73	0.00551
0.75	0.00735
0.76	0.00919
0.78	0.01287
0.79	0.01471
0.80	0.01654
0.81	0.01838
0.82	0.04596
0.84	0.07700
0.85	0.12132
0.86	0.17647

Table 6.20: Comparison of RICH efficiency for $B_s^0 \to D_s^- K^+$ versus $D_s^- \pi^+$ at BTeV.

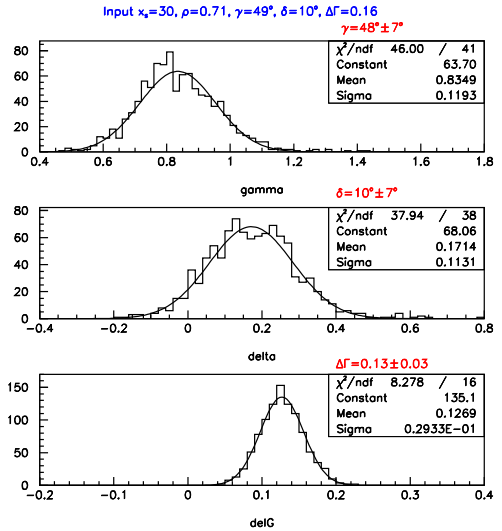

Figure 6.26: Fitted values of γ, δ, and $\Delta\Gamma$.

depends on several factors which are not well known at the moment, in particular the branching fractions for $B_s^0 \to D_s^- K^+$ and the B_s^0 mixing parameter x_s.

Using the estimates of branching fractions given in Ref. [19], we expect to have about 9200 reconstructed and tagged events per year at a luminosity of 2×10^{32} cm^{-2}s^{-1}. The study of the sensitivity to γ presented above was done assuming 6800 tagged events and gave error on γ of about 7°. We expect that this will improve with the increased number of events.

6.4.3.2 $B^- \to D^0 K^-$: BTeV Report

The reconstruction efficiency of the proposed BTeV detector for $B^- \to K^- D^0$ has been studied for two D^0 decay modes: $D^0 \to K^+\pi^-$ and $D^0 \to K^- K^+$. Note that the $K^- K^+$ decay mode represents a CP eigenstate. In this case, even though the branching fraction for $B^- \to K^- \bar{D}^0, \bar{D}^0 \to K^+ K^-$ is expected to be only 1% of $B^- \to K^- D^0$, $D^0 \to K^+ K^-$, we could still obtain a CP asymmetry up to 20%. The events are generated with PYTHIA and the detector is modeled with MCFAST.

The reconstruction efficiency is determined requiring that all tracks be reconstructed and can be identified in the RICH with momentum between 3 and 70 GeV/c hitting the forward tracking plane downstream of the RICH. We assume that 98% of tracks in this momentum range are correctly identified. The final analysis cuts are selected to give a clean D^0 signal

x_s	ρ	δ	γ	$\Delta\Gamma$	$\sigma(\gamma)$	$\sigma(\Delta\Gamma)$
20	0.71	10°	49°	0.16	6°	0.03
30	0.71	10°	49°	0.16	7°	0.03
40	0.71	10°	49°	0.16	8°	0.03
30	0.50	10°	49°	0.16	8°	0.03
30	0.71	10°	30°	0.16	6°	0.03
30	0.71	10°	90°	0.16	15°	0.04
30	0.71	0°	49°	0.16	6°	0.03
30	0.71	20°	49°	0.16	6°	0.03
30	0.71	10°	49°	0.06	8°	0.04
30	0.71	10°	49°	0.26	6°	0.03

Table 6.21: Results of fits with variation of input parameters at BTeV.

$L/\sigma(B^-)$	> 10.0
$L/\sigma(D^0)$	> 4.0
χ^2 (B vertex)	< 5.0
χ^2 (D vertex)	< 10
B point back to prim. vertex	
D^0 mass window	1.85 - 1.88 GeV/c^2

Table 6.22: Selection requirements for $D^0 \to K^-\pi^+$ and $D^0 \to K^+K^-$.

and reduce background from random combinations with kaons. The selection requirements are shown in Table 6.22. The reconstructed signal is shown in Fig 6.27. The fitted Gaussian has a width of 17 MeV/c^2.

The combined geometric acceptance and reconstruction efficiency is 2.6% for the $D^0 \to K^+\pi^-$ mode and 2.3% for the $D^0 \to K^+K^-$ mode. The trigger efficiency for events that pass the final analysis cuts is about 60% for both modes. The expected number of events is shown in Table 6.23.

Background Studies

Generic $b\bar{b}$ and $c\bar{c}$ events were studied and it was found that for both types of events the $D^0 \to K^-\pi^+$ and $D^0 \to K^-K^+$ signals had $S/B > 5$ using the same cuts as for the D^0 in the $B^- \to K^-D^0$ decays. Therefore only background arising from real D^0 mesons need to be considered.

Charm events with a $D^0 \to K^-\pi^+$ have a probability of 3.3% of passing the D^0 analysis cuts. The events which pass the cuts have a trigger efficiency of 10% and 0.6% of these events have another detached K. Generic $b\bar{b}$ events with a D^0 have a 7.0% probability of

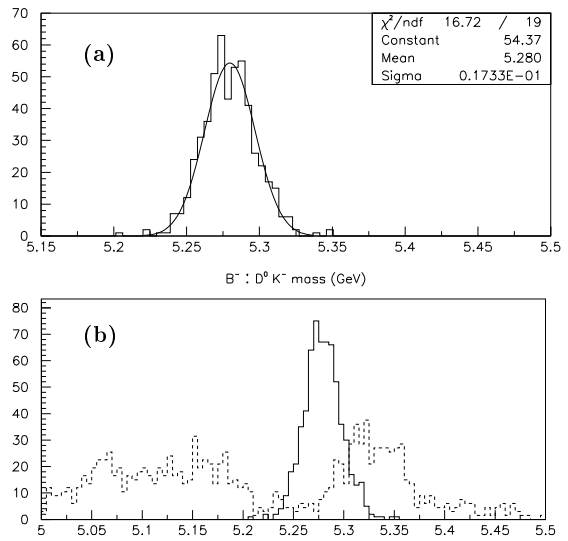

Figure 6.27: (a) $B^- \to D^0K^-$ mass [GeV/c^2]. (b) Signal (solid line) and background (dashed line) from $B^- \to \pi^-D^0$ and $B^- \to \pi^-D^0X$ where the π^- is misidentified as a K^-.

Decay Mode	$K^-(K^+\pi^-)$	$K^-(K^+K^-)$
Luminosity	2×10^{32} cm^{-2}s^{-1}	
Running time	10^7 sec	
Integrated Luminosity	2 2 fb^{-1}	
$\sigma_{b\bar{b}}$	100 μb	
Number of $B^\pm$	1.5×10^{11}	
Branching ratio	1.7×10^{-7}	1.1×10^{-6}
Reconstruction efficiency	0.026	0.022
Trigger efficiency	0.6	0.6
Number of reconstructed $B^\pm$	410	2500

Table 6.23: Projected number of reconstructed $B^- \to K^-D^0$ events at BTeV.

	test 1	test 2	test 3	test 4
b ($\times 10^{-5}$)	2.2	2.2	2.2	2.2
ξ_1	45°	0°	90°	70°
ξ_2	30°	45°	10°	30°
γ	65°	75°	85°	50°
γ fit	$(67 \pm 10)°$	$(75 \pm 7)°$	$(85.0 \pm 2.4)°$	$(50.0 \pm 3.2)°$

Table 6.24: Input Values of parameters and results of fit for γ at BTeV.

passing the D^0 analysis cuts. These events have a trigger efficiency of 35% and 4.0% of these have another detached K. Therefore we estimate that a generic $b\bar{b}$ event is 50 times more likely to contribute to background than a $c\bar{c}$ event. Thus even though the charm production cross-section is much larger than the $b\bar{b}$ cross-section, more background will come from $b\bar{b}$ events.

Background in both modes $B^- \to K^-[K^+\pi^-]$ and $B^- \to K^-[K^+K^-]$ could arise from:

- $B^- \to \pi^- D^0$ where the π^- is misidentified as a K^-, and similar decays such as $B^- \to \pi^- D^{*0}$ and $B^- \to \rho^- D^0$ where there is a missing π^0 and the π^- is misidentified. These decays all have a significantly higher branching fraction than the signal. If we assume that the probability of misidentifying a π^- as a K^- is 2%, the relative signal and background from these modes is shown in Fig 6.27(b). This is the most significant source of background for the $D^0 \to K^+K^-$ mode.

- "B" $\to \bar{D}^0 X$ events where the $\bar{D}^0$ forms a good vertex with a K^- from the other B hadron or from the underlying event. This was studied by generating "B" $\to \bar{D}^0 X$ with $\bar{D}^0 \to K^+\pi^-$ events using the same reconstruction as for the signal. We generated 1.6 million "B" $\to \bar{D}^0 X, \bar{D}^0 \to K^+\pi^-$ events. After applying the selection requirements, no events remained in the mass window 5.0 - 5.5 GeV/c^2, while one event was found in the 5.5 - 6.0 GeV/c^2 mass window.

  We assume this type of background has the same trigger efficiency as the signal. We estimate, we can achieve $S/B \sim 1$ in the $D^0 \to K^+\pi^-$ mode, and we expect this to be the dominant source of background for this mode. This type of background will be insignificant in the $D^0 \to K^+K^-$ mode because both the signal and background come from singly Cabibbo suppressed decays.

Extracting γ from Toy Monte Carlo Studies

To estimate our ability to measure γ, several sets of input parameters (b, γ, ξ_1, ξ_2) were chosen (see Equations (6.123) to (6.126)) and for each set the expected number of events in each channel was calculated. Then 1000 trials were done for each set, smearing the number of events by $\sqrt{N+B}$. For each trial values for b and γ are calculated. The fitted values of b and γ are shown in Table 6.24 and Fig.6.28.

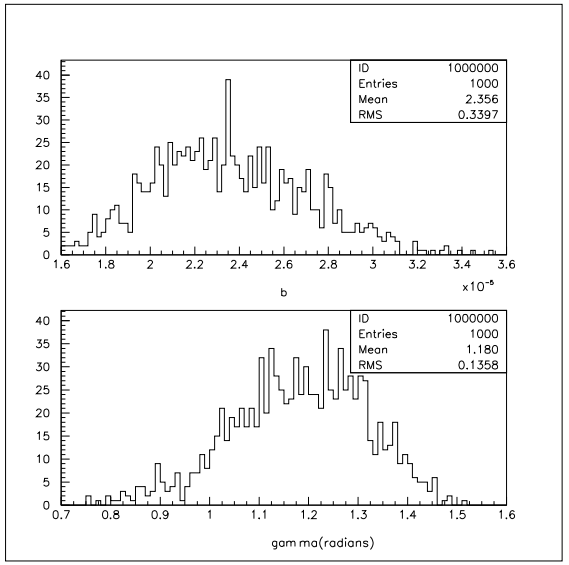

Figure 6.28: Fitted values of γ and b for input values $\gamma = 65°$ (1.13 rad) and $b = 2.2 \times 10^{-5}$.

In conclusion, we expect to reconstruct about 400 $B^\pm \to (K\pi)K^\pm$ and 2500 $B^\pm \to (KK)K^\pm$ events per year at design luminosity. With this number of events, γ can be measured to $\pm 10°$ for most values of γ, ξ_1 and ξ_2. The error on γ depends on the value of γ and the strong phases, in particular the error decreases with increasing difference in the strong phases. If we assume that the ratio of Cabibbo favored to doubly Cabibbo suppressed branching fractions is the same for the two decay modes, then the equations have no solution for $|\xi_1| = |\xi_2|$.

6.4.4 $B \to DK$: Summary †

The CKM angle γ can be extracted via related sets of $B \to DK$ decay processes. The two decay modes $B_s^0 \to D_s^- K^+$ and $B^- \to D^0 K^-$ have been studied in this section as an alternative method of measuring γ. The ability to measure the angle γ in the decay mode $B_s^0 \to D_s^- K^+$ depends on several factors which are not well known at the moment, in particular the branching fractions for $B_s^0 \to D_s^- K^+$ and the B_s^0 mixing parameter Δm_s. The lack of knowledge of certain branching fractions creates similar uncertainties to evaluate the prospects of determining the angle γ from $B^- \to D^0 K^-$ decays.

The reduction of backgrounds, in particular physics backgrounds from the Cabibbo

†Author: M. Paulini.

allowed process $B_s^0 \to D_s^- \pi^+$, is the primary challenge for CDF in extracting the $B_s^0 \to D_s^- K^+$ signal. Exploiting the $D_s^- K^+$ invariant mass as well as $\mathrm{d}E/\mathrm{d}x$ information of the final state particles, the performed studies show that a signal-to-background ratio of 1/6 can be achieved. Assuming branching fractions as outlined in Sec. 6.4.2.1, a nominal signal of 850 $B_s^0 \to D_s^- K^+$ events can be expected at CDF in 2 fb^{-1}. Thus, an initial measurement of γ should be possible at CDF in the beginning of RunII. Within the first 2 fb^{-1} of data, the expected error on $\sin(\gamma \pm \delta)$ is 0.4 to 0.7 depending on the assumed background levels. By the end of RunII an uncertainty near 0.1 for γ may be achievable. The most limiting factors for CDF II are the background levels and the overall signal size.

Since the BTeV detector will have a RICH detector providing excellent π-K separation, physics backgrounds and a clean extraction of the $B_s^0 \to D_s^- K^+$ signal will play a minor role for BTeV. With the caveats mentioned in Sec. 6.4.3.1, BTeV expects to collect about 9200 reconstructed events per year at design luminosity of 2×10^{32} cm^{-2}s^{-1}. The study of the sensitivity to γ presented above was done assuming 6800 tagged events and gave error on γ of about 7°.

A similar conclusion can be drawn for the CDF and BTeV prospects of measuring the angle γ with charged B decays using $B^- \to D^0 K^-$. CDF expects to collect a small sample of about 100 signal candidates with the two-track hadronic trigger in 2 fb^{-1} in RunII. There is optimism that the physics background can be brought down to the same level as the signal, but there could be considerable combinatoric background. If the combinatoric background can also be reduced to a level comparable to the signal, CDF would be in the position to measure γ with an uncertainty in the order of 10-20° in RunII. A study to explore the event yields of other potential CP modes that can be collected with the two-track hadronic trigger showed that this device will allow CDF to accumulate significant datasets of fully hadronic B decays. The two-track hadronic trigger will be the source of a rich B physics program involving many different B decay modes at CDF in RunII.

BTeV expects to reconstruct about 400 $B^- \to [K\pi]K^-$ events per year at design luminosity. With this number of events, γ can be measured to $\pm 10°$ for most values of γ, ξ_1 and ξ_2. In summary, comparing both decay channels $B_s^0 \to D_s^- K^+$ and $B^- \to D^0 K^-$ considered for extracting the angle γ, it appears that the B_s^0 decay mode offers better prospects of determining γ from the four time-dependent asymmetries.

6.5 Study of $B \to \rho\pi$

6.5.1 $B \to \rho\pi$: Introduction [†]

Snyder and Quinn [33] have proposed a method to measure the CKM phase $\alpha = \pi - \beta - \gamma$ using the decays $B^0 \to \{\rho^+\pi^-, \rho^0\pi^0, \rho^-\pi^+\} \to \pi^+\pi^-\pi^0$ and CP conjugate. The method consists in constructing the Dalitz plot for the three pions in the final state [98,99]. This is then fitted for the expression of the rate as a function of all amplitudes, relative weak phases and relative strong phases for this system. The ρ-resonances are described by a

[†] Authors: H.R. Quinn and J.P. Silva.

Breit-Wigner function. The presence of non-zero decay widths is a source of CP-even phases which interfere with the CP-odd and CP-even phases already present in the $B \to \rho\pi$ decay amplitudes and B^0-$\bar{B}^0$ mixing. The rich interference patterns that arise are the hallmark of this method.

The decay amplitudes may be written as

$$a(B^0 \to \pi^+\pi^-\pi^0) = f_+ a_{+-} + f_- a_{-+} + f_0 a_{00}, \tag{6.133}$$

where $a_{ij} = a(B^0 \to \rho^i \pi^j)$, with $(i,j) = (+,-),(-,+)$ or $(0,0)$, and similarly for the CP-conjugate mode. From the Dalitz plot, the coefficient of $|f_i|^2$ fixes $|a_i|^2$, the coefficient of $f_+ f_0^*$ fixes $\arg(a_+ a_0^*)$, the coefficient of $f_- f_0^*$ fixes $\arg(a_- a_0^*)$, and the coefficient of $f_+ f_-^*$ fixes $\arg(a_+ a_-^*)$. Each individual $B \to \rho\pi$ ($|a_i|^2$) band lies close to the edges of the Dalitz plot, because the mass of the ρ meson is much smaller than the mass of the B meson. Moreover, since the B and π are spinless, the ρ must have helicity zero. As a result, the functions f_k contain the Breit-Wigner resonance multiplied by the cosine of the helicity angle θ_k:

$$f_k(s) = \frac{1}{s - m_\rho^2 + i\,\Pi(s)} \cos\theta_k. \tag{6.134}$$

This throws the events into the corners of the Dalitz plot, which contain the overlap $(a_i a_j^*)$ regions between the different channels. In the Breit-Wigner form in Eq.(6.134), s is the square of the invariant mass of the ρ, θ_k is the angle between the line of flight of the ρ and the direction of a daughter pion (in the ρ rest frame), and the choice of the exact form for the function $\Pi(s)$ is the source of systematic uncertainties. The form advocated by the BaBar Physics Book [3] is

$$\Pi(s) = \frac{m_\rho^2}{\sqrt{s}} \left(\frac{p(s)}{p(m_\rho^2)} \right)^3 \Gamma_\rho(m_\rho^2), \tag{6.135}$$

where $p(s) = \sqrt{s/4 - m_\pi^2}$ is the momentum of the daughter pion in the ρ rest frame.

Using the unitarity of the CKM matrix, we may write all decay amplitudes as a sum of two terms. The first term is proportional to $|V_{ub}^* V_{ud}|$ and receives contributions from tree level and penguin diagrams. The second term is proportional to $|V_{tb}^* V_{td}|$ and receives contributions from penguin diagrams alone. Combining this with the isospin decomposition of the decay amplitudes [32], one may write [32,33]

$$\begin{aligned} a_{+-} &= e^{i\gamma}\, T_{+-} + e^{-i\beta}(P_1 + P_0), \\ a_{-+} &= e^{i\gamma}\, T_{-+} + e^{-i\beta}(-P_1 + P_0), \\ a_{00} &= e^{i\gamma}\, T_{00} + e^{-i\beta}(-P_0). \end{aligned} \tag{6.136}$$

There are also electroweak penguin diagrams, but these are expected to be very small in these channels [3,100]. P_0 and P_1 describe the penguin contributions to the final state with isospin 0 and 1, respectively. The T and P amplitude parameters contain magnitudes and CP-even phases, and the relative weak phase between their terms is $\alpha = \pi - \beta - \gamma$. The amplitudes for the CP conjugate decays are obtained simply by changing the signs of the weak phase.

There are ten observables in these decay amplitudes: nine parameters are the magnitudes and CP-even phases in the T and P terms, except for an irrelevant overall phase; the last parameter is α. Eight of the amplitude parameters may be fixed using untagged data alone, with the ninth one fixed by the tagged time-integrated data [101]. Nevertheless, time-dependent data are needed to fix the CP violating phase α. For example, one may construct [33,67]

$$a_{\rm sum} = a_{+-} + a_{-+} + 2a_{00} = e^{i\gamma}(T_{+-} + T_{-+} + 2T_{00}). \tag{6.137}$$

Therefore, using $q/p = e^{-2i\beta}$, one obtains for the interference CP violating quantity present in the time-dependent decay rate,

$$\mathcal{I}m\frac{q}{p}\frac{\bar{a}_{\rm sum}}{a_{\rm sum}} = \sin 2\alpha. \tag{6.138}$$

Since q/p was used, any new phase due to new physics contributions to B^0-$\bar{B}^0$ mixing will affect this determination of α. In contrast, the relative weak phase between the T and P terms (α) appears in direct CP violating observables, which are not affected by any new physics contributions to B^0-$\bar{B}^0$ mixing. Unfortunately, these direct CP violating observables are always affected by the unknown hadronic matrix elements in the T and P terms.

6.5.2 $B \to \rho\pi$: BTeV Report [†]

There are three final states in $B^0 \to \pi^+\pi^-\pi^0$ decays: $B^0 \to \rho^0\pi^0$, $B^0 \to \rho^+\pi^-$ and $B^0 \to \rho^-\pi^+$. CLEO has measured the average branching ratio of the latter two modes to be $(2.8^{+0.8}_{-0.7} \pm 0.4) \times 10^{-5}$ and limits the $\rho^0\pi^0$ branching fraction to $< 5.1 \times 10^{-6}$ at 90% confidence level [102]. The energy and angular resolution of the CDF and DØ electromagnetic calorimeters is not good enough to detect π^0's produced in these decays with good efficiency and low background. Even though detection of converted photons may provide sufficient resolution, the reconstruction efficiency of this method is too low to accumulate large statistics samples in this rare decay mode. Large statistics is necessary for the analysis of the interfering amplitudes. Furthermore, one of the charged pions is soft in the kinematic regions where the $\rho^0\pi^0$ interferes with the $\rho^\pm\pi^\mp$, which makes it more difficult to trigger on these events. BTeV, with its crystal calorimeter and generic vertex trigger, should be able to collect and reconstruct a substantial sample of $B \to \rho\pi$ events.

The reconstruction efficiencies for $B \to \rho\pi$ and backgrounds were studied by BTeV using a full GEANT simulation for $\rho^\pm\pi^\mp$ and $\rho^0\pi^0$ separately. All signal and background samples were generated with a mean of two interactions per crossing. While signal events are relatively easy to generate, backgrounds are more difficult to estimate. For channels with branching ratios on the order of 10^{-5} and efficiencies on the order of 1%, it is necessary to generate at least 10^7 $b\bar{b}$ background events. This is a difficult task that requires large amounts of CPU time and data storage. Since almost 90% of the time spent in generating the events is in the electromagnetic calorimeter, BTeV passes all the generated events through the tracking system and performs a preliminary analysis on the charged tracks

[†] Authors: J. Butler, G. Majumder, L. Nogach, K. Shestermanov, S. Stone, A. Vasiliev and J. Yarba.

before generating the calorimeter information. The output of this procedure is as realistic as running all the events through the entire GEANT process but saves a factor of three in computing time.

BTeV looks for events containing a secondary vertex formed by two oppositely charged tracks. One of the most important selection requirements for discriminating the signal from the background is that the events have well measured, and separated primary and secondary vertices. Both the primary and the secondary vertex fits are required to have a small chisquare ($\chi^2/{\rm dof} < 2$). The distance between the primary and the secondary vertices, divided by the error, must be large ($L/\sigma_L > 4$). The two vertices must also be separated from each other in the plane transverse to the beam. BTeV defines r_T in terms of the primary interaction vertex position (x_P, y_P, z_P) and the secondary decay vertex position (x_S, y_S, z_S) as $r_T = \sqrt{(x_P - x_S)^2 + (y_P - y_S)^2}$ and removes events where the secondary vertex is close to the reconstructed primary vertex. Furthermore, to insure that the charged tracks do not originate from the primary vertex, both the π^+ and the π^- candidates are required to have a large impact parameter with respect to the primary vertex (DCA > 100 μm).

Events passing these selection criteria are passed through the electromagnetic calorimeter simulation which uses GEANT. To find photons from the π^0 decay energies detected in the calorimeter are clustered. Local energy maxima are taken for photon candidates. The photon candidates are required to have a minimum energy of 1 GeV and pass the shower shape cut which requires $E9/E25 > 0.85$. The shower shape cut is used to select electromagnetic showers. We reduce the background rate by ensuring that the photon candidates are not too close to the projection of any charged tracks on the calorimeter. For $\rho^\pm\pi^\mp$, the minimum distance requirement is > 2 cm, while for $\rho^0\pi^0$, we require the minimum distance > 5.4 cm. Candidate π^0's are two-photon combinations with invariant mass between 125 and 145 MeV/c^2.

Kinematic cuts can greatly reduce the background to $B \to \rho\pi$ while maintaining the signal efficiency. Minimum energy and transverse momentum (p_T) requirements are placed on each of the three pions. Here p_T is defined with respect to the B direction which is defined by the position of the primary and secondary vertices. We demand that the momentum vector of the reconstructed B candidate points back to the primary vertex. The cut is implemented by requiring p_T balance among the π^+, π^- and π^0 candidates relative to the B meson direction and then divided by the sum of the p_T values for all three particles ($\Delta p_T/\Sigma p_T$). BTeV also applies a cut on the B decay time requiring the B candidate to live less than 5.5 proper lifetimes ($t/\tau_B < 5.5$). The selection criteria for the two modes are summarized in Table 6.25.

For this study, we generated three large samples of events using BTeVGeant: 125,000 $B^0 \to \rho^0\pi^0$ events, 125,000 $B^0 \to \rho^+\pi^-$ events, and 4,450,000 generic $b\bar{b}$ background events. The results of the analysis after applying the cuts in Table 6.25 are presented in Figure 6.29(a) and (b) for $\rho^0\pi^0$ and Fig 6.29(c) and (d) for $\rho^+\pi^-$. The background mass spectra are Fig. 6.29(a) and (c), while the signal events are Fig. 6.29(b) and (d).

The mass resolution for the B meson is approximately 28 MeV/c^2. The mean π^0 mass value in the $B \to \rho\pi$ events is 135 MeV/c^2 with a resolution of about 3 MeV/c^2. The relevant yields for $\rho\pi$ are shown in Table 6.26. The reconstruction efficiency is (0.36 ± 0.02)% for

Criteria	$\rho^{\pm}\pi^{\mp}$	$\rho^0\pi^0$
Primary vertex criteria	$\chi^2 < 2$	$\chi^2 < 2$
Secondary vertex criteria	$\chi^2 < 2$	$\chi^2 < 2$
r_T [cm]	0.0146	0.0132
Normalized distance L/σ	> 4	> 4
Distance L [cm]	< 5	< 5
DCA of track [μm]	> 100	> 100
t/τ_B	< 5.5	< 5.5
E_{π^+} [GeV]	> 4	> 4
E_{π^-} [GeV]	> 4	> 4
$p_T(\pi^+)$ [GeV/c]	> 0.4	> 0.4
$p_T(\pi^-)$ [GeV/c]	> 0.4	> 0.4
Isolation for γ [cm]	> 2.0	> 5.4
E_{π^0} [GeV]	> 5	> 9
$p_T(\pi^0)$ [GeV/c]	> 0.75	> 0.9
$\Delta p_T/\Sigma p_T$	< 0.06	< 0.066
m_{π^0} [MeV/c^2]	$125 - 145$	$125 - 145$
m_ρ [GeV/c^2]	$0.55 - 1.1$	$0.55 - 1.1$

Table 6.25: Selection Criteria for $B \to \rho\pi$ at BTeV.

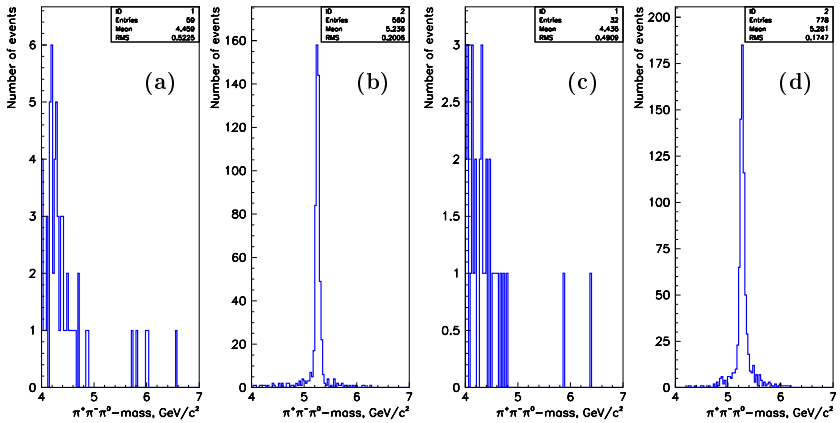

Figure 6.29: Invariant $\pi^+\pi^-\pi^0$ mass distributions for (a) background and (b) signal events for $B \to \rho^0\pi^0$. Invariant $\pi^+\pi^-\pi^0$ mass for (c) background and (d) signal events for $B \to \rho^+\pi^-$.

Quantity	$\rho^{\pm}\pi^{\mp}$	$\rho^0\pi^0$
Branching ratio	2.8×10^{-5}	0.5×10^{-5} (†)
Efficiency	0.0044	0.0036
Trigger efficiency (Level 1)	0.6	0.6
Trigger efficiency (Level 2)	0.9	0.9
S/B	4.1	0.3
Signal/10^7 s	9,400	1,350
$\varepsilon\mathcal{D}^2$	0.10	0.10
Flavour tagged yield	940	135

Table 6.26: Summary of BTeV $B \to \rho\pi$ event yields († indicates estimated branching fractions).

$\rho^0\pi^0$ and $(0.44 \pm 0.02)\%$ for $\rho^+\pi^-$. The background was obtained by considering the mass interval between 5 and 7 GeV/c^2. The signal interval is taken as $\pm 2\sigma$ around the B mass or ± 56 MeV/c^2.

The final numbers of both signal and background events are reduced by including the Level 1 and Level 2 trigger efficiency, but the S/B ratio is not significantly changed. From this study BTeV expects to reconstruct about 9,400 $\rho^{\pm}\pi^{\mp}$ events and 1,350 $\rho^0\pi^0$ events per year (940 and 135 fully tagged events), with signal-to-background levels of approximately 4:1 and 1:3, respectively.

BTeV has not yet done a full simulation of the sensitivity to α. Final results will depend on several unknown quantities including the branching ratio for $\rho^0\pi^0$ and the ratio of tree to penguin amplitudes. The analysis by Snyder and Quinn [33] showed that with 2,000 background free events they could always find a solution for α and the accuracy was in the range of 5-6°. BTeV can collect these 2,000 events in 2×10^7 seconds, but some backgrounds will be present. The effect of backgrounds, including contributions from other B decays into three pions, and the influence of experimental cuts need to be addressed. One example of the former could arise from the decay chains $B \to B^*\pi \to \pi\pi\pi$ [103]. One example of the latter is the experimental inability to access the corner of the Dalitz plot containing the $f_+f_-^*$ interference term. This corner is lost because soft π^0 mesons have large backgrounds which must be eliminated. Fortunately, this region probes $\arg(a_+\, a_-^*) = \arg(a_+\, a_0^*) - \arg(a_-\, a_0^*)$, and the right-hand side can be obtained from the $f_+f_0^*$ and $f_-f_0^*$ interference regions [104] in which the π^0 is energetic. Assuming that the background presence will dilute experimental sensitivity by a factor 2, BTeV should be able to measure α with an accuracy of about 10°. As described in the previous section, Quinn and Silva [101] have proposed using non-flavour tagged rates as additional input, which should improve the accuracy of the α determination.

6.6 Study of $B_s^0 \to J/\psi\,\eta^{(\prime)}$

6.6.1 $B_s^0 \to J/\psi\,\eta^{(\prime)}$: Introduction

The CP asymmetry in the decay $B_s^0 \to J/\psi\eta^{(\prime)}$ is subject to a clean theoretical interpretation because it is dominated by CP violation from interference between decays with and without mixing. The branching ratio has not yet been measured:

$$\mathcal{B}(B_s^0 \to J/\psi\eta) < 3.8 \times 10^{-3}. \tag{6.139}$$

The calculation of the CP asymmetry is very similar to that of the $B_s^0 \to J/\psi\phi$ mode which is discussed in Section 6.1.6.1. The quark subprocess $\bar{b} \to \bar{c}c\bar{s}$ is dominated by the W-mediated tree diagram:

$$\frac{\bar{A}_{J/\psi\eta^{(\prime)}}}{A_{J/\psi\eta^{(\prime)}}} = \eta_{J/\psi\eta^{(\prime)}} \left(\frac{V_{cb}V_{cs}^*}{V_{cb}^*V_{cs}}\right). \tag{6.140}$$

The penguin contribution carries a phase that is similar to Eq. (6.140) up to effects of $\mathcal{O}(\lambda^2) \sim 0.04$. Hadronic uncertainties enter the calculation then only at the level of a few percent.

Unlike the $J/\psi\phi$ mode, here the final state consists of a vector meson and a pseudoscalar. Consequently, the final state is a CP eigenstate, $\eta_{J/\psi\eta} = -1$, and there is no dilution from cancellation between CP-even and odd contributions.

The CP asymmetry is then given by

$$\mathrm{Im}\,\lambda_{J/\psi\eta^{(\prime)}} = -\sin 2\beta_s. \tag{6.141}$$

From a study of $B_s^0 \to J/\psi\eta^{(\prime)}$ we will learn the following:

(i) A measurement of the CP asymmetry in $B_s^0 \to J/\psi\eta^{(\prime)}$ will determine the value of the very important CKM phase β_s.

(ii) The asymmetry is small, of the order of a few percent.

(iii) An observation of an asymmetry that is significantly larger than $\mathcal{O}(\lambda^2)$ will provide an unambiguous signal for new physics. Specifically, it is likely to be related to new, CP violating contributions to $B_s^0\bar{B}_s^0$ mixing.

6.6.2 $B_s^0 \to J/\psi\eta^{(\prime)}$: CDF Report †

Although the CDF detector is equipped with a well-segmented calorimeter for the detection of electrons, it is less suited for the detection of low energy photons. However, at CDF it is not impossible to reconstruct neutral mesons such as π^0 or η decaying into two photons

† Authors: W. Bell, M. Paulini, B. Wicklund.

from energy depositions in CDF's electromagnetic calorimeter. Although a measurement of the CP violating angle β_s will probably be best approached using the B_s^0 decay mode into $J/\psi\phi$, where CDF will accumulate a large statistics sample in RunII, we present here a preliminary study for the event yield of $B_s^0 \to J/\psi\eta^{(\prime)}$. We will concentrate only on the decay mode $B_s^0 \to J/\psi\eta$ followed by $\eta \to \gamma\gamma$. In this section, we will estimate the event yield in 2 fb^{-1} of data using RunI data as well as Monte Carlo extrapolations, show the feasibility of reconstructing $\eta \to \gamma\gamma$ with the CDF calorimeter using RunI data and estimate the expected background for reconstructing a B_s^0 signal.

6.6.2.1 Expected Signal

To estimate the expected signal of $B_s^0 \to J/\psi\eta$ in 2 fb^{-1} in RunII, we normalize this B_s^0 decay mode to the $B^+ \to J/\psi K^+$ channel as many uncertainties such as production cross sections or trigger efficiencies cancel in the ratio and relative acceptances are more reliably calculated using Monte Carlo studies. We can then use the ratio of the two expected data signals to obtain the number of $B_s^0 \to J/\psi\eta$ events from the expected number of $B^+ \to J/\psi K^+$ in RunII.

The starting point for this analysis is the generation of $B_s^0 \to J/\psi\eta$ where $\eta \to \gamma\gamma$ is chosen as the most favourable η decay mode accounting for $(39.3 \pm 0.3)\%$ [62] of the decay width. In addition, the decay channel $B^+ \to J/\psi K^+$ was also produced. Table 6.27 gives a summary of the kinematic constraints applied to the generated Monte Carlo data. The photon resolution in the CDF calorimeter was assumed to be $\sigma(E_T) = 0.136\sqrt{E_T}$ [105] for this study. The four-momenta of the daughter particles were then combined to obtain the invariant mass of the B_s^0 candidates. In order to improve the mass resolution effected by the energy resolution, the B_s^0 four momentum can be corrected using the following relation:

$$\vec{B_s^0} = \vec{J/\psi} + \frac{m_\eta^{\mathrm{PDG}}}{m_\eta^{\mathrm{rec}}} \times (\vec{\gamma_1} + \vec{\gamma_2}) \tag{6.142}$$

Here, $\vec{B_s^0}$, $\vec{J/\psi}$ and $\vec{\gamma}$ refer to the four vector quantities of the respective particles while

p_T of both muons	≥ 2.0 GeV/c
η of both muons	≤ 0.6
η of both photons	≤ 1.0
E_T of both photons	≥ 1.0 GeV
p_T of both muons	≥ 2.0 GeV/c
p_T of K^+	≥ 1.25 GeV/c
η of both muons	≤ 0.6
η of K^+	≤ 1.0

Table 6.27: Constraints used for the generation of Monte Carlo data. At the top the constraints for $J/\psi\eta$ are described, while $J/\psi K^+$ is listed at the bottom.

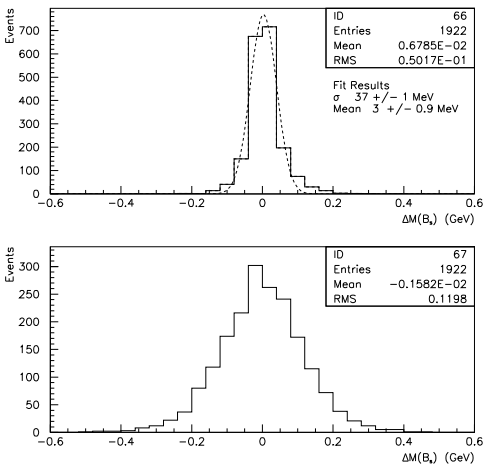

Figure 6.30: Distribution of B_s^0 invariant mass minus the nominal PDG mass value after (top) and before (bottom) the correction described in the text.

$m_\eta^{\rm PDG}$ and $m_\eta^{\rm rec}$ are the η table mass from the PDG [62] and the reconstructed diphoton mass, respectively. After mass constraining the $J/\psi \to \mu^+\mu^-$ dimuon combination to the nominal J/ψ mass and applying the correction given in Eq. (6.142), a B_s^0 mass resolution of better than 40 MeV/c^2 can be achieved at CDF. The improvement from the uncorrected to the corrected B_s^0 invariant mass minus the nominal B_s^0 PDG mass value is illustrated in Figure 6.30.

To determine the expected signal for $B_s^0 \to J/\psi\eta$ in RunII, we used the ratio

$$\frac{f_s}{f_u}\frac{\mathcal{B}(B_s^0 \to J/\psi\eta)\mathcal{B}(\eta \to \gamma\gamma)}{\mathcal{B}(B^+ \to J/\psi K^+)}\frac{N(J/\psi\eta)}{N(J/\psi K^+)} \qquad (6.143)$$

relating the $J/\psi\eta$ signal rate to the number of $B^+ \to J/\psi K^+$ events. The ratio of the fragmentation fractions $f_s/f_u = 0.427$ is taken from Ref. [84] and the $B_s^0 \to J/\psi\eta$ branching fraction is estimated to $\mathcal{B}(B_s^0 \to J/\psi\eta) = 4.8 \times 10^{-4}$ from corresponding B^0 decays. The number of reconstructed $J/\psi\eta$ and $J/\psi K^+$ events starting with 1×10^6 B^+/B_s^0 mesons were approximately 1800 versus 6700. The ratio in Eq. (6.143) finally yields approximately 0.022.

The expected number of fully reconstructed $B^+ \to J/\psi K^+$ events in 2 fb^{-1} of data has been estimated in Section 6.2.2 to be approximately 50,000 (see also Table 6.1). With this number and the ratio from Eq. (6.143) we estimate to observe about 1100 $B_s^0 \to J/\psi\eta$ decays in 2 fb^{-1} in RunII. The $B^+ \to J/\psi K^+$ Monte Carlo generation was also checked against the observed number of RunIb signal events including acceptance factors.

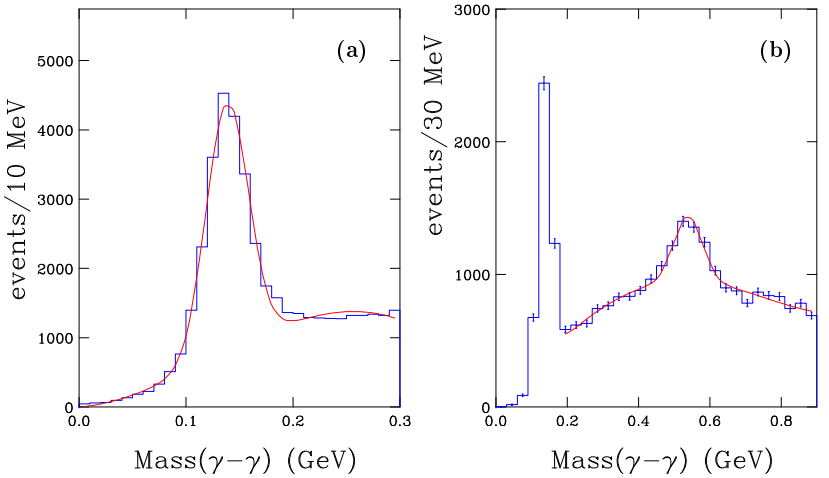

Figure 6.31: Invariant diphoton mass distribution showing a (a) $\pi^0 \to \gamma\gamma$ and (b) $\eta \to \gamma\gamma$ signal in CDF RunI data.

6.6.2.2 Reconstruction of Neutrals at CDF

To demonstrate the feasibility of observing neutral particles such as $\pi^0 \to \gamma\gamma$ or $\eta \to \gamma\gamma$ with the CDF calorimeter, we investigated the reconstruction of low energy photons using RunI data. Using the RunI exclusive electron trigger data, which represent a data sample enhanced in $b\bar{b}$ events, we combined photon candidates in separate calorimeter towers with $E_T^\gamma > 1$ GeV. Using requirements on $E_{\rm had}/E_{\rm em}$, isolation and the pulse height in the strip chambers, we find almost 18,000 $\pi^0 \to \gamma\gamma$ candidates on a low background as shown in Figure 6.31(a). A similar search for $\eta \to \gamma\gamma$ candidates yields a signal of about 1600 events as can be seen in Figure 6.31(b).

6.6.2.3 Expected Background

To estimate the expected background rate for $B_s^0 \to J/\psi\eta$ in RunII, $J/\psi \to \mu\mu$ data from RunI were used. These data were also exploited to improve the $\eta \to \gamma\gamma$ selection as suggested by the Monte Carlo. We again use $B^+ \to J/\psi K^+$ as the reference mode and estimate from the observed $J/\psi K^+$ signal together with Eq. (6.143) to detect six $B_s^0 \to J/\psi\eta$ events in the RunI J/ψ data. To obtain an idea about the shape of the background underneath a potential $B_s^0 \to J/\psi\eta$ signal, the two-dimensional distribution of $m(\gamma\gamma)$ versus $m(B_s^0)$ is plotted in Figure 6.32(a). It appears from that figure that a large proportion of the background can be excluded by a cut around the η invariant mass. Using a ± 120 MeV/c^2 window around the nominal η mass, we observe the distribution of $J/\psi\eta$ background events from RunI J/ψ data shown in Figure 6.32(b). Overlaid onto the data

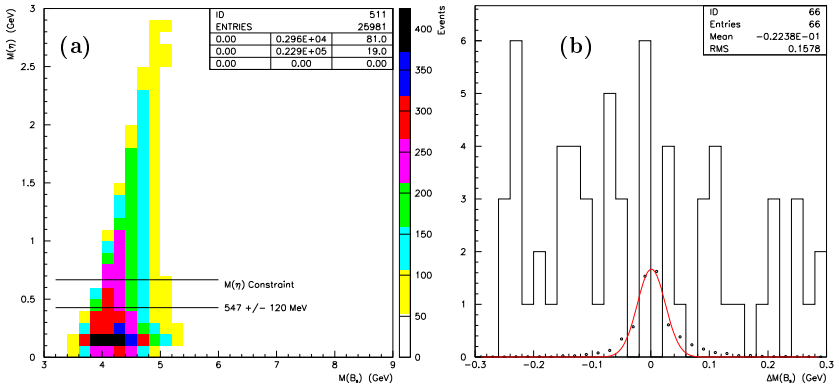

Figure 6.32: $B_s^0 \to J/\psi\eta$ background study using CDF Run I J/ψ data. (a) Two-dimensional distribution of $m(\gamma\gamma)$ versus $m(B_s^0)$ before a cut around the η invariant mass. (b) Background events from Run I J/ψ data passing the $J\psi\eta$ selection. Overlaid is the Monte Carlo expectation scaled to the six events expected.

is the Monte Carlo expectation scaled to the six signal events estimated. The Monte Carlo expectation is plotted as points and as a Gaussian fit to the MC data.

To summarize this preliminary study, CDF expects to reconstruct a signal of approximately 1000 $B_s^0 \to J/\psi\eta$ events in 2 fb^{-1} under RunII running conditions. A resolution of the B_s^0 signal of better than 40 MeV/c^2 can be expected. Using RunI J/ψ data to study the background, we observed a combinatoric background at the level of six events per 40 MeV/c^2 bin. Further background reduction using CES and CPR should be possible.

6.6.3 $B_s^0 \to J/\psi\eta^{(\prime)}$: BTeV Report †

The CP violating angle, β_s, defined in Section 6.1, can be measured by using B_s^0 decay modes. The all-charged mode $B_s^0 \to J/\psi\phi$ is one way to measure this, but due to the fact that this is a vector-vector final state of mixed-CP, a complicated angular analysis is required and therefore a very large data sample must be obtained. The channels $B_s^0 \to J/\psi\,\eta'$ and $B_s^0 \to J/\psi\,\eta$, can be used to determine the angle β_s from a simple asymmetry measurement.

We estimate the relevant branching ratios using the quark model. The η and η' wave functions are given in terms of the quark wave functions as:

$$\Psi(\eta) = (u\bar{u} + d\bar{d} - s\bar{s})/\sqrt{3}, \tag{6.144}$$
$$\Psi(\eta') = (u\bar{u} + d\bar{d} + 2s\bar{s})/\sqrt{6}. \tag{6.145}$$

† Authors: G. Majumder, S. Stone.

Decay	Branching Fraction
$\mathcal{B}(B_s^0 \to J/\psi\eta)^\dagger$	3.3×10^{-4}
$\mathcal{B}(B_s^0 \to J/\psi\eta')^\dagger$	6.7×10^{-4}
$J/\psi \to \mu^+\mu^-$	0.059
$\eta \to \gamma\gamma$	0.392
$\eta' \to \rho\gamma$	0.308
$\eta' \to \pi^+\pi^-\eta$	0.438

Table 6.28: Input branching fractions for $B_s^0 \to J/\psi\eta^{(\prime)}$ used for the BTeV study. Note, † indicates estimated branching fractions.

Thus the branching ratios are related to the measured decay $B^0 \to J/\psi K^0$, taking equal B lifetimes as

$$\mathcal{B}(B_s^0 \to J/\psi\eta) = \frac{1}{3}\mathcal{B}(B^0 \to J/\psi K^0), \tag{6.146}$$
$$\mathcal{B}(B_s^0 \to J/\psi\eta') = \frac{2}{3}\mathcal{B}(B^0 \to J/\psi K^0). \tag{6.147}$$

It should be noted that a large enhancement in one of these rates is possible, as implied by the large branching fraction for $B \to \eta' K$.

We consider only the decays $\eta \to \gamma\gamma$, $\eta' \to \rho^0\gamma$ and $\eta' \to \pi^+\pi^-\eta$. The J/ψ will be reconstructed in the $\mu^+\mu^-$ decay mode. All input branching ratios used for this study are listed in Table 6.28.

6.6.3.1 Signal Selection

We now discuss selection requirements for $B_s^0 \to J/\psi\eta^{(\prime)}$ signal events. First of all, the signal channels contain photons. They are selected as isolated energy depositions in the $PbWO_4$ calorimeter that are at least 7 cm away from any track intersection and satisfy the following criteria: $E_\gamma > 0.5$ GeV, E9/E25 > 0.95, and the second moment mass is required to be less than 100 MeV/c^2.

We now list the criteria for the individual particles.

$J/\psi \to \mu^+\mu^-$

- Both muons should have hits in the rear end of the RICH and at least one must be identified in the muon system.
- p_T of each muon > 0.2 GeV/c and at least one with $p_T > 1.0$ GeV/c.
- χ^2 of common vertex of both muons < 4.
- Invariant mass within 100 MeV/c^2 of the J/ψ mass.

$\eta \to \gamma\gamma$

- Each photon has $E_\gamma > 4$ GeV and $p_T > 0.4$ GeV/c.
- Invariant mass of two-photon combinations must be within 15 MeV/c^2 of the η mass.

$\eta' \to \rho^0\gamma$

- Two oppositely charged tracks, each with momenta greater than 1 GeV/c are taken as $\pi^+\pi^-$ candidates.
- The $\pi^+\pi^-$ invariant mass must be within 0.55 GeV/c^2 of the ρ mass.
- The $\pi^+\pi^-$ must form a common secondary vertex with the $\mu^+\,\mu^-$ from the J/ψ with a fit χ^2 <10.
- Addition of a single photon ($p_T > 0.3$ GeV/c) to these tracks produces an invariant mass within 15 MeV/c^2 of the η' mass.

$\eta' \to \pi^+\pi^-\eta$

- The same selection criteria as for η defined above, except that for each photon $p_T > 0.2$ GeV/c is required.
- Two oppositely charged tracks, each with momenta greater than 1 GeV/c are taken as $\pi^+\pi^-$ candidates.
- The $\pi^+\pi^-$ must form a common secondary vertex with the $\mu^+\,\mu^-$ from the J/ψ with a fit χ^2 <10.
- The η and the $\pi^+\pi^-$ have an invariant mass within 15 MeV/c^2 of the η' mass.

Signal events are also required to satisfy the following general criteria. A good primary vertex must exist. The distance between the primary and secondary vertices must be $L >$ 50 μm for η' and $>$ 100 μm for η. We require L/σ_L >3. The normalized distance of closest approach with respect to the primary vertex (DCA/σ_{DCA}) of each charged track must be greater than 3. No additional track is consistent with the B_s^0 vertex. The opening angle between the 'B'-direction and the particle direction is required to be $<$ 10 mrad and $<$ 15 mrad for $J/\psi\eta'$ and $J/\psi\eta$, respectively. Here the 'B'-direction is defined by the vector joining the primary and secondary vertices and the particle direction is defined as the vector sum of the momenta of all measured particles. The invariant mass of $J/\psi\,\eta$ or $J/\psi\,\eta'$ have to be within $\pm$40 MeV/c^2 of the B_s^0 mass ($\sigma_{M_B} = 19$ MeV/c^2).

We show in Fig. 6.33 the invariant mass distributions of signal candidates for $\gamma\gamma$, $\rho^0\gamma$ and $\pi^+\pi^-\eta$. The $\mu^+\mu^-$ mass distribution from J/ψ decays is shown in Fig. 6.34(a). We can improve the B mass distributions by constraining the dimuons to be at the nominal J/ψ mass. This greatly improves the four-vector of the reconstructed J/ψ. After applying this constrained fit we find the B_s^0 mass distributions shown in Fig. 6.34(b). Note, that we could also constrain the η and η' masses to their nominal values using the same fitting technique. This will be done for future analyses.

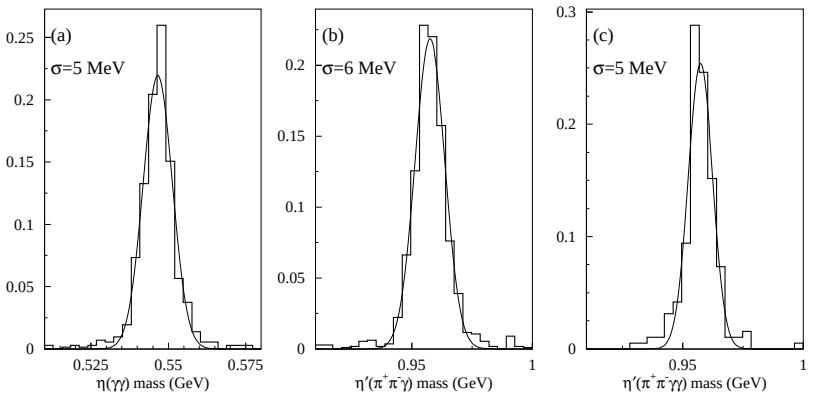

Figure 6.33: The invariant mass distributions for (a) $\eta \to \gamma\gamma$, (b) $\eta' \to \pi^+\pi^-\gamma$, and $\eta' \to \pi^+\pi^-\eta$ with $\eta \to \gamma\gamma$ at BTeV. The Gaussian mass resolutions are indicated.

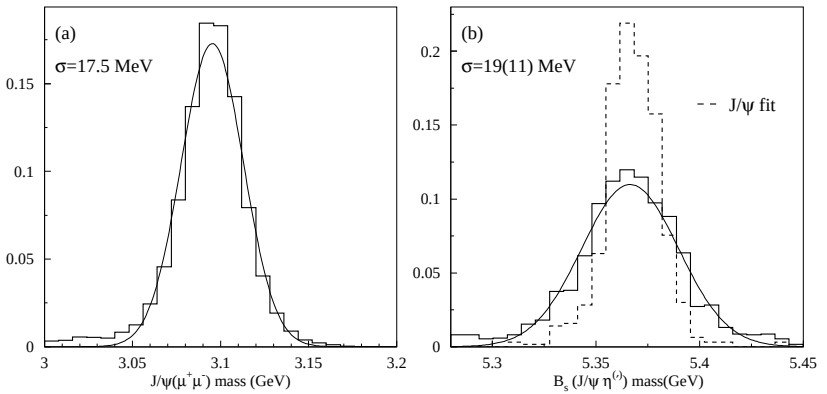

Figure 6.34: (a) The dimuon invariant mass. (b) The reconstructed B_s^0 mass for all three final states of η and η' summed together. The solid curve is without constraining the $\mu^+\mu^-$ to the J/ψ mass, while the dashed curve is with this constraint. The B_s^0 mass resolution improves from 19 to 11 MeV/c^2.

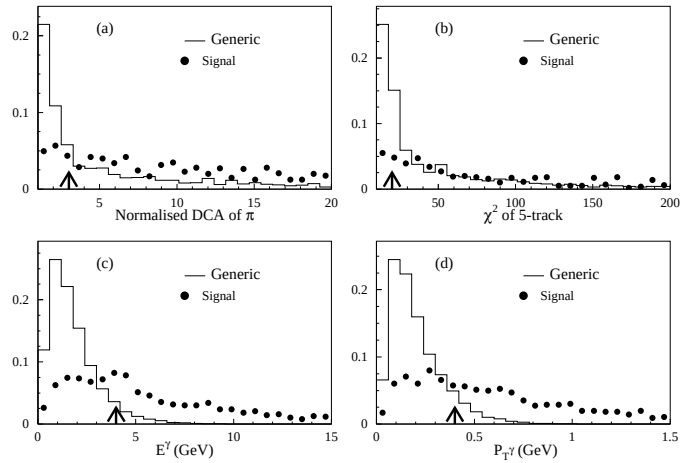

Figure 6.35: Distributions of backgrounds in several variables compared with the signal. For $\eta' \to \rho\gamma$ (a) DCA/σ_{DCA}, (b) χ^2 of adding an additional track to the $J/\psi\pi^+\pi^-$ vertex. For $\eta \to \gamma\gamma$ (c) energy of the photons and (d) the transverse momentum of the photons with respect to the beam direction. The arrows show the position of the selection requirements.

6.6.3.2 Background Estimation

The dominant background to these decay modes is from $b(\bar{b}) \to J/\psi\,X$. To calculate reconstruction efficiencies of signals and of background, Monte Carlo events were generated using Pythia and QQ to decay the heavy particles. Only events with real $J/\psi \to \mu^+\mu^-$ decays were kept for further analysis. The events were traced through the BTeV detector simulation using the GEANT simulation package. We add to the $b\bar{b}$ background events another set of light quark background distributed with a mean Poisson multiplicity of two. Distributions of several variables for both signal and background are compared in Fig. 6.35.

The results discussed below are based on $\sim$ 4,500 detector simulated signal events (each channel), which were preselected in generator level using the criteria that all particles of these signals are within the geometrical acceptance region of the detector. Similarly, 40,000 background events are also preselected from 5.8 million generic $b\bar{b}$ events. To determine backgrounds we only looked at the dimuon channels, and the $\gamma\gamma$ decay of the η and the $\rho^0\gamma$ decay of the η'.

After all selection criteria, one event survived in each of the $J/\psi\,\eta$ and $J/\psi\,\eta'$ channels within a wide B_s^0 mass window of 400 MeV/c^2 (signal mass window is 44 MeV/c^2). This leads to a signal-to-background expectation for $J/\psi\,\eta$ and $J/\psi\,\eta'$, of 15:1 and 30:1. It is not surprising that the backgrounds are so low. We therefore feel confident that we can add the $\eta' \to \pi^+\pi^-\eta$ modes in without adding significant background.

Luminosity	$2 \times 10^{32}\,\mathrm{cm}^{-2}\,\mathrm{s}^{-1}$		
Running time	10^7 sec		
Integrated Luminosity	2000 pb^{-1}		
$\sigma_{b\bar{b}}$	100 μb		
Number of $b\bar{b}$ events	2×10^{11}		
Number of B_s^0 events	0.5×10^{11}		
	$B_s^0 \to J/\psi\,\eta'$		$B_s^0 \to J/\psi\,\eta$
	$\eta' \to \rho^0\gamma$	$\eta' \to \pi^+\pi^-\eta$	$\eta \to \gamma\gamma$
Reconstruction efficiency [%]	1.2	0.60	0.71
S/B	30:1	-	15:1
Level1 Trigger efficiency [%]	85	85	75
Level2 Trigger efficiency [%]	90	90	90
Number of reconstructed signal events	5670	1610	1920
Tagging efficiency $\varepsilon\mathcal{D}^2$	0.1		
Total Number tagged	994		
$\sigma(\sin 2\beta_s)$	0.033		

Table 6.29: Projected yield of $B_s^0 \to J/\psi\eta^{(\prime)}$ and uncertainty on $\sin 2\beta_s$ at BTeV.

6.6.3.3 Sensitivity to $\sin 2\beta_s$

The expected yield of signal events and the resulting asymmetry measurement are given in Table 6.29. The trigger efficiency consists of Level1 efficiencies from the detached vertex trigger, the dimuon trigger and the Level2 trigger.

The accuracy on $\sin 2\beta_s$ is not precise enough to measure the Standard Model predicted value, which is comparable to the error, in 10^7 seconds of running. The low background level makes it possible to loosen the cuts and gain acceptance. We could also add in the $J/\psi \to e^+e^-$ decay mode. This will not be as efficient as $\mu^+\mu^-$ due to radiation of the electrons, but will be useful. We also believe that ways can be found to improve flavour tagging efficiency, especially for B_s^0. Furthermore, we will have many years of running, and we can expect some improvement from the use of $B_s^0 \to J/\psi\phi$.

6.6.4 $B_s^0 \to J/\psi\eta^{(\prime)}$: Summary †

A measurement of the CP asymmetry in $B_s^0 \to J/\psi\eta^{(\prime)}$ will determine the value of the CKM phase β_s. The asymmetry is expected to be small within the Standard Model, of the order of a few percent. This means that an observation of an asymmetry that is significantly

†Author: M. Paulini.

larger than $\mathcal{O}(\lambda^2)$, will provide an unambiguous signal for new physics which is likely to be related to new CP violating contributions to B_s^0-$\bar{B}_s^0$ mixing.

Although the CDF detector is not ideally suited for the detection of low energy photons, it is not impossible to reconstruct neutral mesons such as π^0 or η decaying into two photons from energy depositions in CDF's electromagnetic calorimeter. Although a measurement of the CP violating angle β_s will probably be best approached using the B_s^0 decay mode into $J/\psi\phi$, a preliminary study for the event yield of $B_s^0 \to J/\psi\eta^{(\prime)}$ has been performed. To estimate the expected signal of $B_s^0 \to J/\psi\eta$, CDF normalized this decay mode to the $B^+ \to J/\psi K^+$ channel. As discussed in Sec. 6.6.2, CDF estimates to observe about 1000 $B_s^0 \to J/\psi\eta$ decays in 2 fb^{-1} in RunII. To demonstrate the feasibility of observing neutral particles such as $\pi^0 \to \gamma\gamma$ or $\eta \to \gamma\gamma$ with the CDF calorimeter, the reconstruction of low energy photons using RunI data has been investigated (see Sec. 6.6.2). From this preliminary study, a resolution on the B_s^0 signal of better than 40 MeV/c^2 can be expected. To estimate the expected background rate for $B_s^0 \to J/\psi\eta$ in RunII, $J/\psi \to \mu\mu$ data from RunI were used. A combinatoric background at the level of 6 events per 40 MeV/c^2 bin were observed, while further background reduction using CES and CPR should be possible.

Photons are reconstructed as isolated energy depositions in BTeV's fine segmented $PbWO_4$ calorimeter. For the signal selection of $B_s^0 \to \psi\eta^{(\prime)}$, BTeV considered the decays $\eta \to \gamma\gamma$, $\eta' \to \rho^0\gamma$ and $\eta' \to \pi^+\pi^-\eta$. From these decays modes, BTeV expects to reconstruct almost 10,000 B_s^0 signal events with a mass resolution of about 20 MeV/c^2. For the resulting asymmetry measurement an uncertainty $\sigma(\sin 2\beta_s)$ of about 0.03 is expected from this signal yield. Although this accuracy is not precise enough to measure the value of $\sin 2\beta_s$ predicted by the Standard Model, which is comparable to the error, this is an encouraging result. It gives optimism to probe physics beyond the Standard Model with $B_s^0 \to J/\psi\eta^{(\prime)}$ within a few years of running at design luminosity at BTeV.

6.7 CP Violation: Summary †

Since the time the Workshop on B Physics at the Tevatron was held in September 1999 and February 2000 and the time this write-up is coming to a completion, a significant amount of time has elapsed. It therefore constitutes a non-trivial task to report the findings of the workshop but to also include actual updates that the heavy flavour physics community has witnessed. An incredibly successful turn-on of both B factories together with an exceptional performance of both their detectors, BaBar and Belle, has already produced a wealth of new measurements including the first observation of CP violation in the B^0 meson system [1]. A compilation of our current knowledge on the value of $\sin 2\beta$ is shown in Figure 6.36. The individual measurements are listed in Refs. [1,106] while the quoted average is taken from Ref. [107]. Clearly, the recent measurements of $\sin 2\beta$ from BaBar and Belle establish CP violation in B^0 decays while the results from OPAL, CDF and ALEPH [106] were still compatible with $\sin 2\beta$ being zero.

With the official start of RunII in March 2001, the Tevatron aims to turn the findings

† Author: M. Paulini.

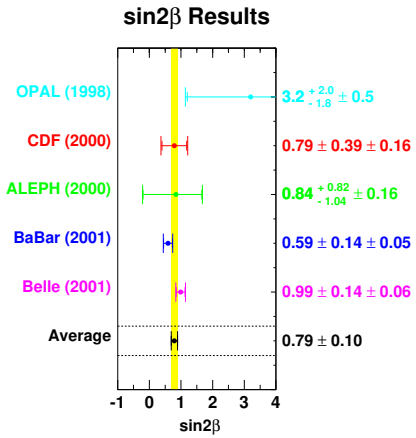

Figure 6.36: Compilation of measurements of $\sin 2\beta$ as of August 2001 [1,106]. The displayed average on $\sin 2\beta$ is taken from Ref. [107].

of the B Physics at the Tevatron Workshop into real measurements of CP violation in the B meson system confirming the exciting results on $\sin 2\beta$ from the B factories.

Evaluating the sensitivity of measuring $\sin 2\beta$ was motivated by using $B^0 \to J/\psi K_S^0$ as a benchmark process and as a comparison to the expectations (and presented measurements) of the B factories. With 2 fb^{-1} of integrated luminosity, CDF expects to measure $\sin 2\beta$ with a precision of $\sigma(\sin 2\beta) \sim 0.05$. The DØ experiment estimates to obtain a similar precision on $\sin 2\beta$ quoting $\sigma(\sin 2\beta) \sim 0.04$. While $\sin 2\beta$ will have been measured to a fair accuracy before the BTeV experiment will turn on, the goal of the BTeV collaboration is to significantly improve the precision of that measurement. Within one year of running at design luminosity, BTeV expects to measure $\sin 2\beta$ with an error of $\sigma(\sin 2\beta) \sim 0.025$.

Considering the status of the CKM unitarity triangle in a couple of years from now, the angle β is measured from $B^0 \to J/\psi K_S^0$ decays by the B factories now, assisted by complimentary measurements at CDF and DØ in the near future. In addition, we will have more information about the leg of the unitarity triangle opposite the angle β: V_{ub}/V_{cb} will be measured more precisely by the observation of higher statistics $b \to u$ transitions at CLEO and the B factories. However, the ultimate precision on determining V_{ub} from data will probably be limited by theoretical uncertainties. The information that will finally allow to over-constrain the CKM triangle, is the observation of $B_s^0\bar{B}_s^0$ oscillations anticipated at CDF if the oscillation parameter Δm_s is less than 40 ps^{-1}. The question might then be, what will be the next "precision CKM measurement" after $\sin 2\beta$ and Δm_s?

Several years ago, the decay $B^0 \to \pi^+\pi^-$ appeared in the literature as a tool to determine $\alpha = 180° - \beta - \gamma$ as the second CKM angle to be measured after β had been determined. As we now know, the so-called "penguin pollution" in $B^0 \to \pi^+\pi^-$ is sufficiently large and intro-

duces a significant theoretical uncertainty in the extraction of fundamental physics parameters from the measured CP asymmetry in this channel. BTeV studied a method to measure the CKM phase $\alpha = \pi - \beta - \gamma$ using the decays $B^0 \to \{\rho^+\pi^-, \rho^0\pi^0, \rho^-\pi^+\} \to \pi^+\pi^-\pi^0$ as proposed by Snyder and Quinn [33]. From this study BTeV expects to reconstruct about 9,400 $\rho^\pm\pi^\mp$ events and 1,350 $\rho^0\pi^0$ events per year with reasonable signal-to-background levels. CDF evaluated for this workshop a strategy of measuring the CKM angle γ using $B^0 \to \pi^+\pi^-$ and $B_s^0 \to K^+K^-$ as suggested by Fleischer in Ref. [16]. This method is particularly well matched to the capabilities of the Tevatron as it relates CP violating observables in B^0 and B_s^0 decays. The studies performed during this workshop indicate that a measurement of the CKM angle γ to better than 10° could be feasible at CDF with 2 fb^{-1} of data. The utility of these modes depends on how well the uncertainty from flavour $SU(3)$ breaking can be controlled. Data for these and other processes should be able to tell us the range of such effects. A study by CDF shows that 20% effects from $SU(3)$ breaking lead to an uncertainty of only $\sim 3^\circ$ on γ. Of course, BTeV will also be able to exploit this method. Based on one year of running, BTeV expects to reconstruct about 20,000 $B^0 \to \pi^+\pi^-$ events with small background contamination from $B^0 \to K^+\pi^-$, $B_s^0 \to \pi^+K^-$ and $B_s^0 \to K^+K^-$ and estimates an uncertainty on the CP asymmetry $\mathcal{A}_{CP}^{\pi\pi}$ of 0.024.

Another well suited method of determining the unitarity triangle angle γ has been studied by measuring CP violation in the decay mode $B_s^0 \to D_s^- K^+$. This will allow a clean measurement of $\gamma + 2\beta_s$ in a tree-level process. Four time-dependent asymmetries need to be measured in the presence of large physics backgrounds, in particular from the Cabibbo allowed process $B_s^0 \to D_s^-\pi^+$. An initial measurement of γ should be possible at CDF in RunII. Within the first 2 fb^{-1} of data, the expected error on $\sin(\gamma \pm \delta)$ is 0.4 to 0.7 depending on the assumed background levels. By the end of RunII an uncertainty on γ near 0.1 may be achievable. Since the BTeV detector will have excellent π-K separation provided by a RICH detector, physics backgrounds will play a minor role and a $B_s^0 \to D_s^- K^+$ signal of about 9200 reconstructed events can be collected per year. This will allow a determination of the angle γ to better than 10°.

A similar conclusion can be drawn for the CDF and BTeV prospects of measuring the angle γ with charged B decays using $B^- \to D^0K^-$. CDF expects to collect a small sample of D^0K^- candidates with the two-track hadronic trigger in 2 fb^{-1} in RunII while BTeV will reconstruct about 400 $B^- \to [K\pi]K^-$ events per year at design luminosity. With this number of events, BTeV can measure γ with an uncertainty of about $\pm 10^\circ$ for most of the assumed parameter space. There is optimism at CDF that the physics background can be brought down to the same level as the signal, but there could be considerable combinatoric background which is difficult to evaluate without RunII collision data. Comparing both decay channels, $B_s^0 \to D_s^- K^+$ and $B^- \to D^0K^-$, considered for extracting the angle γ, the B_s^0 decay mode offers better prospects of determining γ from the four time-dependent asymmetries.

Looking for physics beyond the Standard Model, measuring the CP asymmetry in $B_s^0 \to J/\psi\eta^{(\prime)}$ has been evaluated. This decay mode will determine the value of the CKM phase β_s but the asymmetry is expected to be small within the Standard Model. Although the CDF detector is not ideally suited for the detection of low energy photons, CDF estimates to observe about 1000 $B_s^0 \to J/\psi\eta$ decays with a resolution on the B_s^0 signal of better than

40 MeV/c^2 in 2 fb^{-1} in RunII. However, BTeV will probably be the experiment to probe the CP asymmetry in $B_s^0 \to J/\psi\eta^{(\prime)}$, achieving an uncertainty $\sigma(\sin 2\beta_s)$ of about 0.03 in one year of data taking. This precision approaches the level of the value of $\sin 2\beta_s$ predicted by the Standard Model.

Even after the discovery of CP violation in the B system by BaBar and Belle [1], CP violation is still one of the least tested aspects of the Standard Model. It is clear that RunII at the Tevatron will offer many important CP violation measurements which will be complementary to the results that we expect from the e^+e^- B factories. After CP violation had been observed only in the neutral K meson system for 37 years, the discovery of CP violation in the neutral B meson system has been made at the B factories awaiting confirmation at the Tevatron. The next few years will provide further tests of the Standard Model picture of CP violation and will hopefully unveil the holy grail of heavy flavour physics in its entire beauty.

References

[1] B. Aubert *et al.* [BABAR Collaboration], Phys. Rev. Lett. **87**, 091801 (2001) [hep-ex/0107013];
K. Abe *et al.* [Belle Collaboration], Phys. Rev. Lett. **87**, 091802 (2001) [hep-ex/0107061].

[2] G. C. Branco, L. Lavoura and J. P. Silva, "CP Violation," *Oxford, UK: Clarendon (1999) 511 p.*

[3] P. F. Harrison and H. R. Quinn [BABAR Collaboration], "The BaBar Physics Book: Physics at an Asymmetric B factory," SLAC Report SLAC-R-504 (1998).

[4] Y. Nir, Proceedings of the XXVII SLAC Summer Institute on Particle Physics "CP Violation in and beyond the Standard Model," hep-ph/9911321.

[5] LEP working group on B oscillations, see information on the following world-wide web URL: `http://lepbosc.web.cern.ch/LEPBOSC/`.

[6] G. Blaylock, in *Proc. of the 19th Intl. Symp. on Photon and Lepton Interactions at High Energy LP99* ed. J.A. Jaros and M.E. Peskin, Int. J. Mod. Phys. A **15S1**, 80 (2000) [eConfC **990809**, 80 (2000)] [hep-ex/9912038].

[7] M. Beneke, G. Buchalla, C. Greub, A. Lenz and U. Nierste, Phys. Lett. B **459**, 631 (1999) [hep-ph/9808385].

[8] S. Hashimoto, K. I. Ishikawa, T. Onogi and N. Yamada, Phys. Rev. D **62**, 034504 (2000) [hep-ph/9912318].

[9] D. Becirevic, D. Meloni, A. Retico, V. Gimenez, V. Lubicz and G. Martinelli, Eur. Phys. J. C **18**, 157 (2000) [hep-ph/0006135].

[10] I. Dunietz, Phys. Rev. D **52**, 3048 (1995) [hep-ph/9501287].

[11] R. Fleischer, Nucl. Instrum. Meth. A **446**, 1 (2000) [hep-ph/9908340].

[12] F. Abe *et al.* [CDF Collaboration], Phys. Rev. D **54**, 6596 (1996) [hep-ex/9607003].

[13] A. S. Dighe, I. Dunietz, R. Fleischer, Eur. Phys. J. C **6**, 647 (1999) [hep-ph/9804253].

[14] Y. Nir and D. J. Silverman, Nucl. Phys. B **345**, 301 (1990).

[15] R. Fleischer, Eur. Phys. J. C **10**, 299 (1999) [hep-ph/9903455].

[16] R. Fleischer, Phys. Lett. B **459**, 306 (1999) [hep-ph/9903456].

[17] R. Barate *et al.* [ALEPH Collaboration], Eur. Phys. J. C **4**, 387 (1998).

[18] D. Buskulic *et al.* [ALEPH Collaboration], Phys. Lett. B **384**, 471 (1996).

[19] R. Aleksan, I. Dunietz and B. Kayser, Z. Phys. C **54**, 653 (1992).

[20] J. Charles, Phys. Rev. D **59**, 054007 (1999) [hep-ph/9806468].

[21] Y. Grossman, M. Neubert and A. L. Kagan, JHEP **9910**, 029 (1999) [hep-ph/9909297].

[22] S. Plaszczynski and M. Schune, hep-ph/9911280.

[23] D. Cronin-Hennessy *et al.* [CLEO Collaboration], Phys. Rev. Lett. **85**, 515 (2000) [hep-ex/0001010].

[24] Y. Nir and H. R. Quinn, Phys. Rev. Lett. **67**, 541 (1991).

[25] J. P. Silva and L. Wolfenstein, Phys. Rev. D **49**, 1151 (1994) [hep-ph/9309283].

[26] O. F. Hernandez, D. London, M. Gronau and J. L. Rosner, Phys. Lett. B **333**, 500 (1994) [hep-ph/9404281].

[27] M. Neubert and J. L. Rosner, Phys. Lett. B **441**, 403 (1998) [hep-ph/9808493].

[28] R. Fleischer, Int. J. Mod. Phys. A **12**, 2459 (1997) [hep-ph/9612446].

[29] S. Gardner, Phys. Rev. D **59**, 077502 (1999) [hep-ph/9806423] and [hep-ph/9906269].

[30] M. Gronau and D. London, Phys. Rev. Lett. **65**, 3381 (1990).

[31] Y. Grossman and H. R. Quinn, Phys. Rev. D **58**, 017504 (1998) [hep-ph/9712306].

[32] H. J. Lipkin, Y. Nir, H. R. Quinn and A. Snyder, Phys. Rev. D **44**, 1454 (1991).

[33] A. E. Snyder and H. R. Quinn, Phys. Rev. D **48**, 2139 (1993).

[34] M. Beneke, G. Buchalla, M. Neubert and C. T. Sachrajda, Phys. Rev. Lett. **83**, 1914 (1999) [hep-ph/9905312]; Nucl. Phys. B **591**, 313 (2000) [hep-ph/0006124].

[35] Y. Keum, H. Li and A. I. Sanda, Phys. Lett. B **504**, 6 (2001) [hep-ph/0004004].

[36] A. J. Buras and R. Fleischer, Eur. Phys. J. C **11**, 93 (1999) [hep-ph/9810260].

[37] M. Neubert, JHEP **9902**, 014 (1999) [hep-ph/9812396].

[38] M. Gronau, hep-ph/9904329.

[39] M. Neubert and J. L. Rosner, Phys. Rev. Lett. **81**, 5076 (1998) [hep-ph/9809311].

[40] R. Fleischer and T. Mannel, Phys. Rev. D **57**, 2752 (1998) [hep-ph/9704423].

[41] M. Gronau and J. L. Rosner, Phys. Rev. D **53**, 2516 (1996) [hep-ph/9509325].

[42] I.I. Bigi *et al.*, in "CP Violation," edited by C. Jarlskog *Singapore: World Scientific (1989) 723 p.*

[43] Y. Nir, "CP violation," *Lectures given at 20th Annual SLAC Summer Institute on Particle Physics: The Third Family and the Physics of Flavor*, SLAC-PUB-5874; Phys. Lett. B **327**, 85 (1994) [hep-ph/9402348].

[44] Y. Grossman, Nucl. Phys. B **426**, 355 (1994) [hep-ph/9401311].

[45] M. Gronau and D. London, Phys. Rev. D **55**, 2845 (1997) [hep-ph/9608430].

[46] A. G. Cohen, D. B. Kaplan, F. Lepeintre and A. E. Nelson, Phys. Rev. Lett. **78**, 2300 (1997) [hep-ph/9610252].

[47] Y. Grossman, Y. Nir and R. Rattazzi, in "Heavy Flavours II", eds. A.J. Buras and M. Lindner, (World Scientific, Singapore, 1998) p. 755 [hep-ph/9701231].

[48] L. Randall and S. Su, Nucl. Phys. B **540**, 37 (1999) [hep-ph/9807377].

[49] G. Barenboim, J. Bernabeu, J. Matias and M. Raidal, Phys. Rev. D **60**, 016003 (1999) [hep-ph/9901265].

[50] G. Barenboim and M. Raidal, Phys. Lett. B **457**, 109 (1999) [hep-ph/9903270].

[51] J. M. Soares and L. Wolfenstein, Phys. Rev. D **47**, 1021 (1993).

[52] N. G. Deshpande, B. Dutta and S. Oh, Phys. Rev. Lett. **77**, 4499 (1996) [hep-ph/9608231].

[53] J. P. Silva and L. Wolfenstein, Phys. Rev. D **55**, 5331 (1997) [hep-ph/9610208].

[54] Y. Grossman, Y. Nir and M. P. Worah, Phys. Lett. B **407**, 307 (1997) [hep-ph/9704287].

[55] Y. Grossman, Phys. Lett. B **380**, 99 (1996) [hep-ph/9603244].

[56] Z. Xing, Eur. Phys. J. C **4**, 283 (1998) [hep-ph/9705358].

[57] A. I. Sanda and Z. Xing, Phys. Rev. D **56**, 6866 (1997) [hep-ph/9708220].

[58] R. N. Cahn and M. P. Worah, Phys. Rev. D **60**, 076006 (1999) [hep-ph/9904480].

[59] G. Barenboim, G. Eyal and Y. Nir, Phys. Rev. Lett. **83**, 4486 (1999) [hep-ph/9905397].

[60] M. P. Worah, hep-ph/9905267.

[61] H. Quinn, "B^0-$\bar{B}^0$ Mixing" in C. Caso *et al.* "Review of Particle Physics," Eur. Phys. J. C **3**, 1 (1998).

[62] C. Caso *et al.* [Particle Data Group Collaboration], Eur. Phys. J. C **3**, 1 (1998); D. E. Groom *et al.* [Particle Data Group Collaboration], Eur. Phys. J. C **15**, 1 (2000).

[63] B. Kayser, M. Kuroda, R. D. Peccei and A. I. Sanda, Phys. Lett. B **237**, 508 (1990).

[64] I. Dunietz, H. R. Quinn, A. Snyder, W. Toki and H. J. Lipkin, Phys. Rev. D **43**, 2193 (1991).

[65] A. S. Dighe, I. Dunietz, H. J. Lipkin and J. L. Rosner, Phys. Lett. B **369**, 144 (1996) [hep-ph/9511363].

[66] A. S. Dighe, I. Dunietz and R. Fleischer, Phys. Lett. B **433**, 147 (1998) [hep-ph/9804254].

[67] Y. Grossman and H. R. Quinn, Phys. Rev. D **56**, 7259 (1997) [hep-ph/9705356].

[68] Y. Grossman, B. Kayser and Y. Nir, Phys. Lett. B **415**, 90 (1997) [hep-ph/9708398]; J. Charles, A. Le Yaouanc, L. Oliver, O. Pene and J. C. Raynal, Phys. Lett. B **425**, 375 (1998) [Erratum-ibid. B **433**, 441 (1998)] [hep-ph/9801363]; L. Wolfenstein, Phys. Rev. D **57**, 6857 (1998) [hep-ph/9801386]; B. Kayser, in "Proceedings of the Moriond Workshop on Electroweak Interactions and Unified Theories", Les Arcs, France (1997) [hep-ph/9709382].

[69] The CDF II Collaboration, R. Blair *et al.*, *The CDF II Detector Technical Design Report*, Fermilab-Pub-96/390-E. This Report may be found at the following world-wide web URL: `http://www-cdf.fnal.gov/upgrades/tdr/tdr.html`.

[70] F. Abe *et al.* [CDF Collaboration], Phys. Rev. Lett. **81**, 5513 (1998) [hep-ex/9806025].

[71] F. Abe *et al.* [CDF Collaboration], Phys. Rev. D **60**, 072003 (1999) [hep-ex/9903011].

[72] The CDF II Collaboration, *"Proposal for Enhancement of the CDF II Detector: An Inner Silicon Layer and a Time-of-Flight Detector"*, Proposal P-909 submitted to the Fermilab Director and PAC, 23 Oct 1998.

[73] F. Abe *et al.* [CDF Collaboration], Phys. Rev. Lett. **79**, 572 (1997).

[74] A. B. Carter and A. I. Sanda, Phys. Rev. Lett. **45**, 952 (1980); Phys. Rev. D **23**, 1567 (1981); I. I. Bigi and A. I. Sanda, Nucl. Phys. B **193**, 85 (1981).

[75] See, for instance, M. Gronau, Phys. Lett. B **300**, 163 (1993) [hep-ph/9209279]; Ref. [25]; R. Aleksan, F. Buccella, A. Le Yaouanc, L. Oliver, O. Pene and J. C. Raynal, Phys. Lett. B **356**, 95 (1995) [hep-ph/9506260]; F. DeJongh and P. Sphicas, Phys. Rev. D **53**, 4930 (1996) [hep-ph/9507439]; R. Fleischer and T. Mannel, Phys. Lett. B **397**, 269 (1997) [hep-ph/9610357]; M. Ciuchini, E. Franco, G. Martinelli and L. Silvestrini, Nucl. Phys. B **501**, 271 (1997) [hep-ph/9703353]; P. S. Marrocchesi and N. Paver, Int. J. Mod. Phys. A **13**, 251 (1998) [hep-ph/9702353].

[76] For reviews, see, for instance, Y. Nir, in Proceedings of the 18th International Symposium on Lepton-Photon Interactions (LP '97), Hamburg, Germany, 28 July-1 August 1997, eds. A. De Roeck and A. Wagner (World Scientific, Singapore, 1998), p. 295 [hep-ph/9709301]; R. Fleischer, Int. J. Mod. Phys. A **12**, 2459 (1997) [hep-ph/9612446]; M. Gronau, Nucl. Phys. Proc. Suppl. **65**, 245 (1998) [hep-ph/9705440] and also Ref. [3].

[77] R. Fleischer and I. Dunietz, Phys. Rev. D **55**, 259 (1997) [hep-ph/9605220];
C. S. Kim, D. London and T. Yoshikawa, Phys. Rev. D **57**, 4010 (1998) [hep-ph/9708356];
R. Fleischer, Phys. Rev. D **58**, 093001 (1998) [hep-ph/9710331].

[78] M. Gronau and J. L. Rosner, Phys. Lett. B **482**, 71 (2000) [hep-ph/0003119];
C. Chiang and L. Wolfenstein, Phys. Lett. B **493**, 73 (2000) [hep-ph/0004255].

[79] See, for instance, L. Wolfenstein, Phys. Rev. D **52**, 537 (1995);
M. Neubert, Phys. Lett. B **424**, 152 (1998) [hep-ph/9712224];
A. F. Falk, A. L. Kagan, Y. Nir and A. A. Petrov, Phys. Rev. D **57**, 4290 (1998) [hep-ph/9712225];
D. Atwood and A. Soni, Phys. Rev. D **58**, 036005 (1998) [hep-ph/9712287];
J. M. Gerard and J. Weyers, Eur. Phys. J. C **7**, 1 (1999) [hep-ph/9711469];
A. N. Kamal, Phys. Rev. D **60**, 094018 (1999) [hep-ph/9901342].

[80] See, for instance, Ref. [36]; Ref. [39]; Ref. [40];
M. Gronau and J. L. Rosner, Phys. Rev. D **57**, 6843 (1998) [hep-ph/9711246];
R. Fleischer, Eur. Phys. J. C **6**, 451 (1999) [hep-ph/9802433].

[81] The CDF II Collaboration, *"Update to Proposal P-909: Physics Performance of the CDF II Detector with an Inner Silicon Layer and a Time-of-Flight Detector"*, submitted to the Fermilab Director and PAC, 5 Jan 1999.

[82] S. Chen *et al.* [CLEO Collaboration], Phys. Rev. Lett. **85**, 525 (2000) [hep-ex/0001009].

[83] B. Aubert *et al.* [BABAR Collaboration], hep-ex/0008057;
H. Aihara [BELLE Collaboration], hep-ex/0010008.

[84] F. Abe *et al.* [CDF Collaboration], Phys. Rev. D **60**, 092005 (1999);
T. Affolder *et al.* [CDF Collaboration], Phys. Rev. Lett. **84**, 1663 (2000) [hep-ex/9909011].

[85] F. Bedeschi, FERMILAB-CONF-01-006-E, *Contributed to 20th Physics in Collision Conference, Lisbon, Portugal, 29 Jun - 1 Jul 2000.*

[86] S. Donati and G. Punzi, internal CDF Note 4212 (unpublished).

[87] C. Blocker, F. Würthwein, internal CDF note 5274 (unpublished).

[88] F. Würthwein, internal CDF note 5271 (unpublished).

[89] O. R. Long, N. S. Lockyer, P. T. Keener, F. Azfar, K. T. McDonald, J. G. Heinrich and L. A. Roberts, "Monte Carlo Simulation of $B^0 \to \pi^+\pi^-$ from pp Interactions at $\sqrt{s}$=40 TeV", UPR/216E, PRINCETON/HEP/92-07,SSCL/PP/139(1992).

[90] M. Gronau and D. Wyler, Phys. Lett. B **265**, 172 (1991).

[91] D. Atwood, I. Dunietz and A. Soni, Phys. Rev. Lett. **78**, 3257 (1997) [hep-ph/9612433].

[92] R. Aleksan, B. Kayser and D. London, hep-ph/9312338.

[93] A. F. Falk and A. A. Petrov, Phys. Rev. Lett. **85**, 252 (2000) [hep-ph/0003321].

[94] G. J. Feldman and R. D. Cousins, Phys. Rev. D **57**, 3873 (1998) [physics/9711021].

[95] A. Ali and B. Kayser, hep-ph/9806230.

[96] K. T. McDonald, "Maximum likelihood analysis of CP violating asymmetries," PRINCETON-HEP-92-04.

[97] F. Parodi, P. Roudeau and A. Stocchi, hep-ph/9802289.

[98] R. H. Dalitz, Phil. Mag. **44**, 1068 (1953)

[99] E. Fabri, Nuovo Cimento **11**, 479 (1954).

[100] R. N. Cahn, J. Charles, F. Le Diberder, and S. Versillé, internal BaBar Note No. 430 (unpublished).

[101] H. R. Quinn and J. P. Silva, Phys. Rev. D **62**, 054002 (2000) [hep-ph/0001290].

[102] C. P. Jessop *et al.* [CLEO Collaboration], Phys. Rev. Lett. **85**, 2881 (2000) [hep-ex/0006008].

[103] A. Deandrea, R. Gatto, M. Ladisa, G. Nardulli and P. Santorelli, Phys. Rev. D **62**, 036001 (2000) [hep-ph/0002038].

[104] H. R. Quinn, talk for Working Group 1 presented at the "Workshop on B Physics at the Tevatron - RunII and Beyond", Fermilab, February 2000.

[105] L. Balka *et al.*, Nucl. Instrum. Meth. A **267**, 272 (1988).

[106] K. Ackerstaff *et al.* [OPAL collaboration], Eur. Phys. J. C **5**, 379 (1998) [hep-ex/9801022];
T. Affolder *et al.* [CDF Collaboration], Phys. Rev. D **61**, 072005 (2000) [hep-ex/9909003];
R. Barate *et al.* [ALEPH Collaboration], Phys. Lett. B **492**, 259 (2000) [hep-ex/0009058].

[107] S. Olsen, plenary talk presented at *XX International Symposium on Lepton and Photon Interactions at High Energies LP01*, 23rd-28th July 2001, Rome, Italy.

Chapter 7

Rare and Semileptonic Decays

Christian W. Bauer, Gustavo Burdman, Aida X. El-Khadra, JoAnne Hewett, Gudrun Hiller, Michael Kirk, Jonathan Lewis, Heather E. Logan, Michael Luke, Ron Poling, Alex Smith, Ben Speakman, Kevin Stenson, Masa Tanaka, Andrzej Zieminski

7.1 Rare Decays: Theory

7.1.1 Preliminaries

The Flavor-changing-neutral-current (FCNC) transitions, such as $b \to s$ and $b \to d$, arise only at the loop level in the Standard Model (SM). These decays provide tests of the detailed structure of the theory at the level of radiative corrections where Glashow-Iliopoulos-Maiani (GIM) cancellations are important, and are sensitive to CKM matrix elements: the flavor structure of a generic $b \to s$ amplitude T is $T = \sum_i \lambda_i T_i$, where $\lambda_i = V_{ib}V_{is}^*$ and the sum runs over all up-quark flavors $i = u, c, t$. Using CKM unitarity $\sum_i \lambda_i = 0$ and $\lambda_u \ll \lambda_t$ we obtain $T = \lambda_t(T_t - T_c)$.

Furthermore, in many extensions of the Standard Model, loop graphs with new particles (such as charged Higgses or supersymmetric partners) contribute at the same order as the SM contribution. Precision measurements of these rare processes therefore provides a complementary probe of new physics to that of direct collider searches. Finally, these rare decays are subject to both perturbative and non-perturbative QCD effects, which can be studied here.

The most interesting FCNC B decays at the Tevatron are $B \to X_s\gamma$, $B \to X_s\ell^+\ell^-$, $B_{s,d} \to \ell^+\ell^-$, and the corresponding exclusive modes for the first two. (A fourth decay, $B \to X_{s,d}\nu\bar{\nu}$, is theoretically cleaner, but because of the neutrinos in the final state is not likely to be accessible at a hadron collider.) Of these decays, the exclusive modes $B \to K^{(*)}\ell^+\ell^-$ are likely to be the most important at the Tevatron in the near future: inclusive $B \to X_s\gamma$ is difficult to measure at a hadron collider, while the SM branching fraction for $B_s \to \mu^+\mu^-$ is at the 10^{-9} level. Furthermore, as we shall discuss, the theoretical prediction for inclusive $B \to X_s\ell^+\ell^-$ is poorly behaved in the large q^2 region, where it is easiest to measure. In this section, we focus on tests of the SM via these decays.

C_1	C_2	C_3	C_4	C_5	C_6	$C_7^{\rm eff}$	C_9	C_{10}
-0.25	$+1.11$	$+0.01$	-0.03	$+0.01$	-0.03	-0.31	$+4.34$	-4.67

Table 7.1: SM values of the Wilson coefficients at NLO ($C_7^{\rm eff} \equiv C_7 - C_5/3 - C_6$).

7.1.1.1 The effective Hamiltonian

Radiative corrections to the FCNC decay amplitudes contain terms of order $\alpha_s \ln m_W^2/m_b^2$, which are enhanced by the large logarithm of m_W/m_b and make perturbation theory poorly behaved. To make precision calculations, these terms must be summed to all orders. This is most conveniently performed using an effective field theory and the renormalization group, as discussed in Chapter 1.

The effective field theory for $b \to s$ transitions is thoroughly summarized in a review article by Buchalla *et al.*, [1]. Here we briefly outline the general features which are universal for the channels discussed in this chapter. The effective Hamiltonian is obtained by integrating out heavy degrees of freedom (the top quark and $W^\pm$ bosons in the SM) from the full theory [2]:

$$\mathcal{H}_{\rm eff} = -4\frac{G_F}{\sqrt{2}}V_{ts}^*V_{tb}\sum_{i=1}^{10} C_i(\mu)O_i(\mu) \tag{7.1}$$

where μ is the renormalization scale, and the operators O_i are

$$\begin{aligned}
O_1 &= (\bar{s}_{L\alpha}\gamma_\mu b_{L\alpha})(\bar{c}_{L\beta}\gamma^\mu c_{L\beta}), & O_6 &= (\bar{s}_{L\alpha}\gamma_\mu b_{L\beta})\textstyle\sum_{q=u,d,s,c,b}(\bar{q}_{R\beta}\gamma^\mu q_{R\alpha}),\\
O_2 &= (\bar{s}_{L\alpha}\gamma_\mu b_{L\beta})(\bar{c}_{L\beta}\gamma^\mu c_{L\alpha}), & O_7 &= \tfrac{e}{16\pi^2}m_b\bar{s}_{L\alpha}\sigma_{\mu\nu}b_{R\alpha}F^{\mu\nu},\\
O_3 &= (\bar{s}_{L\alpha}\gamma_\mu b_{L\alpha})\textstyle\sum_{q=u,d,s,c,b}(\bar{q}_{L\beta}\gamma^\mu q_{L\beta}), & O_8 &= \tfrac{g}{16\pi^2}m_b\bar{s}_{L\alpha}T^a_{\alpha\beta}\sigma_{\mu\nu}b_{R\beta}G^{a\mu\nu},\\
O_4 &= (\bar{s}_{L\alpha}\gamma_\mu b_{L\beta})\textstyle\sum_{q=u,d,s,c,b}(\bar{q}_{L\beta}\gamma^\mu q_{L\alpha}), & O_9 &= \tfrac{e^2}{16\pi^2}\bar{s}_{L\alpha}\gamma^\mu b_{L\alpha}\bar{\ell}\gamma_\mu\ell,\\
O_5 &= (\bar{s}_{L\alpha}\gamma_\mu b_{L\alpha})\textstyle\sum_{q=u,d,s,c,b}(\bar{q}_{R\beta}\gamma^\mu q_{R\beta}), & O_{10} &= \tfrac{e^2}{16\pi^2}\bar{s}_{L\alpha}\gamma^\mu b_{L\alpha}\bar{\ell}\gamma_\mu\gamma_5\ell
\end{aligned} \tag{7.2}$$

(note that these operators are not the same as the O_i's for the $|\Delta B| = 1$ Hamiltonian discussed in Chapter 1). The subscripts L and R denote left and right-handed components, and we have neglected the strange quark mass $m_s \ll m_b$. The coefficient $C_i(m_W)$ are systematically calculable in perturbation theory, and the renormalization group equations are used to lower to renormalization scale to $\mu = m_b$. The renormalization group scaling is a significant effect, enhancing (for example) the $B \to X_s\gamma$ rate by a factor of ~ 2. Details on the renormalization scale dependence, the renormalization group equations and analytical formulae can be found in [2]. The SM values at $\mu = 4.8$ GeV of the C_i at NLO are given in Table 7.1.

While $C_7^{\rm eff}$ measures the $bs\gamma$ coupling strength, an analogous correspondence can be made for C_{10}: comparing the charge assignments of lepton-Z-couplings $|(\bar{\ell}\ell Z|_V)/(\bar{\ell}\ell Z|_A)| = |1 - 4\sin^2\Theta_W| \simeq 0.08$ shows that the Z-penguin contribution to C_9 (V) is suppressed with respect to C_{10} (A) and can be neglected as a first approximation: C_{10} probes the effective $\bar{s}_L Z b_L$ vertex modulo the box contribution [3].

Different FCNC decays are sensitive to different linear combinations of the C_i's, and so each of the decays of interest provides independent information. The quark-level transition $b \to s\gamma$ is largely governed by O_7, while $b \to s\ell^+\ell^-$ receives dominant contributions from O_7, O_9 and O_{10}, and $B_s \to \ell^+\ell^-$ is primarily due to O_{10}. As discussed in the next section, the current measurement of $B \to X_s\gamma$ is in excellent agreement with theory, but this is only sensitive to the magnitude of the photon penguin $C_7^{\rm eff}$. In contrast, $b \to s\ell^+\ell^-$ is sensitive to the sign of this coefficient, as well as to O_9 and O_{10}.

7.1.1.2 Inclusive vs. Exclusive Decays

The Wilson coefficients in Eq. (7.1) can be measured in either exclusive or inclusive decays of b flavored hadrons. The theoretical tools used to study exclusive and inclusive decays are very different. Experimental measurements of exclusive and inclusive decays are also faced with different challenges. Hence, it is convenient to consider them separately.

In inclusive decays one can avoid the theoretical difficulties associated with the physics of hadronization by using quark-hadron duality together with the operator product expansion (OPE) [4]. Quark-hadron duality allows us to relate inclusive decays of B hadrons into hadronic final states to decays into partons (see Section 5.3 of Chapter 1). Using an OPE it can be shown that the B decay is given by the corresponding parton-level decay. There are perturbative and nonperturbative corrections which must be taken into account. The leading nonperturbative corrections to this expression scale like $(\Lambda_{\rm QCD}/m_b)^2$, which is of order a few percent. There are some caveats, both in the application of the OPE and in the assumption of quark-hadron duality.

The size of the corrections in the OPE typically grow as the final state phase space is restricted. If the phase space is restricted to too small a region the OPE breaks down entirely. This is an important consideration when experimental cuts are taken into account. A familiar example is the endpoint region above the $b \to c$ kinematic limit of the charged lepton spectrum in semileptonic $b \to u$ decay, which is important for measuring $|V_{ub}|$. In this region the standard OPE breaks down, and a class of leading twist operators in the OPE must be resummed to all orders. As we will discuss in Section (7.1.2.2), the OPE also breaks down in the high lepton q^2 region of $B \to X_s\ell^+\ell^-$, but in this region the twist expansion also break down.

The range of validity of quark-hadron duality and the size of the corrections which violate it are unknown, at present. There are theoretical reasons to believe that these corrections are small (and it has been suggested that duality violation is reflected in the asymptotic nature of the OPE) [5]. However, it has also been argued [6] that duality violations are much larger than commonly expected. As the data improve and more inclusive quantities are measured, the comparison between theory and experiment will provide an indication of the size of duality violations.

While theoretically appealing, inclusive rare decays are very difficult to measure, particularly in a hadronic environment. It is likely that they will be constructed by measuring a series of exclusive decays. Hence, it will be much easier to measure exclusive rare decays at the Tevatron.

In theoretical studies of exclusive decays, we must deal with nonperturbative QCD corrections to the quark-level process, as manifest in hadronization effects, for example. Lattice QCD is the only first principles tool for calculations of nonperturbative QCD effects. Unfortunately, results from lattice QCD calculations are incomplete, at present. Furthermore, numerical simulations based on lattice QCD are time consuming and expensive. The prospects for lattice QCD calculations of rare exclusive decays with small and controlled errors are excellent, as discussed in detail in Section 7.1.3.2. At present, however, we have to deal with hadronic uncertainties which result in a loss of sensitivity to the interesting short distance physics. It is therefore important to use a variety of theoretical strategies for calculations of these decays. We include model-independent approaches based on approximate symmetries as well as calculations which use a variety of different models in our discussion of exclusive decays in Section 7.1.3.

7.1.2 Inclusive Decays

7.1.2.1 $B \to X_s\gamma$

As discussed in Chapter 1, the theoretical description of the inclusive decay $B \to X_s\gamma$ is particularly clean as it is essentially given by the partonic weak decay $b \to s\gamma$ with small corrections of order $1/m_b^2$ [4] in the HQET expansion (although as the photon energy cut is raised above ~ 2 GeV the nonperturbative Fermi motion of the b quark becomes a significant effect [8]). Although it is a difficult task for hadron colliders to measure the photon energy spectrum governing the inclusive channel, it is discussed here for completeness.

The radiative decay is a magnetic dipole transition and is thus mediated by the operator O_7. The corresponding Wilson coefficient $C_7(\mu)$ is evolved to the b-quark scale via the effective Hamiltonian of Eq. (7.1), with the basis for this decay consisting of the first eight operators in the expansion. The perturbative QCD corrections to the coefficients introduce large logarithms of the form $\alpha_s^n(\mu)\log^m(\mu/M_W)$, which are resummed order by order via the RGE. The next-to-leading order logarithmic QCD corrections have been computed and result in a much reduced dependence on the renormalization scale in the branching fraction compared to the leading-order result. The inclusion of the QCD corrections enhance the rate by a factor of ~ 2, yielding agreement with the present experimental observation.

The higher-order QCD calculation to NLO precision involves several steps, requiring corrections to both the Wilson coefficients and the matrix element of O_7 in order to ensure a scheme independent result. For C_7, the NLO computation entails the calculation of the $\mathcal{O}(\alpha_s)$ terms in the matching conditions [10], and the renormalization group evolution of $C_7(\mu)$ must be computed using the $\mathcal{O}(\alpha_s^2)$ anomalous dimension matrix [9]. For the matrix element, this includes the QCD bremsstrahlung corrections [11] $b \to s\gamma + g$, and the NLO virtual corrections [12]. Summing these contributions to the matrix element and expanding them around $\mu = m_b$, one arrives at the decay amplitude

$$\mathcal{M}(b \to s\gamma) = -\frac{4G_F V_{tb}V_{ts}^*}{\sqrt{2}} D\langle s\gamma|O_7(m_b)|b\rangle_{tree}\,, \tag{7.3}$$

with

$$D = C_7(\mu) + \frac{\alpha_s(m_b)}{4\pi}\left(C_i^{(0)eff}(\mu)\gamma_{i7}^{(0)}\log\frac{m_b}{\mu} + C_i^{(0)eff}r_i\right) . \qquad (7.4)$$

Here, the quantities $\gamma_{i7}^{(0)}$ are the entries of the effective leading order anomalous dimension matrix, the r_i are computed in [12], and the index i sums over the operator basis. The first term in Eq. (7.4), $C_7(\mu)$, must be computed at NLO precision, whereas it is consistent to use the leading order values of the other coefficients. The NLO expression for $C_7(\mu)$ is too complicated to present here, however, for completeness, we give the leading order result,

$$C_7^{(0)eff} = \eta^{16/23}C_7(M_W) + \frac{8}{3}\left(\eta^{14/23} - \eta^{16/23}\right)C_8(M_W) + C_2(M_W)\sum_{i=1}^{8} h_i\eta^{a_i} , \qquad (7.5)$$

where $\eta \equiv \alpha_s(M_W)/\alpha_s(\mu)$ and $h_i\,, a_i$ are known numerical coefficients [1]. The form of this result will be relevant for our discussion of new physics contributions to $B \to X_s\gamma$, and clearly demonstrates the mixing between O_7 and the chromomagnetic dipole operator as well as the four quark operator.

There are also long-distance effects arising from emission of a gluon from a charm loop which are only suppressed by powers $\Lambda_{\rm QCD}m_b/m_c^2$. The effects of these operators has been estimated to be small, contributing to the rate at the few percent level [13].

After employing an explicit lower cut on the photon energy in the gluon bremsstrahlung correction, the partial width is given by

$$\Gamma(B \to X_s\gamma) = \Gamma(b \to s\gamma) + \Gamma(b \to s\gamma + g)^{E_\gamma > (1-\delta)E_\gamma^{max}} , \qquad (7.6)$$

where $E_\gamma^{max} = m_b/2$, and δ is a parameter defined by the condition that E_γ be above the experimental threshold. In addition, the 2-loop electroweak corrections have been computed [14] and are found to reduce the rate by $\sim 3.6\%$. The resulting branching fraction is then obtained by scaling the partial width for $B \to X_s\gamma$ to that for B semileptonic decay as the uncertainties due to the values of the CKM matrix elements and the m_b^5 dependence of the widths cancel in the ratio. The Standard Model prediction for the branching faction is then found to be [1]

$$B(B \to X_s\gamma) = (3.28 \pm 0.30) \times 10^{-4} . \qquad (7.7)$$

This is in good agreement with the observations by CLEO and ALEPH [16] which yield $B = (3.15 \pm 0.35 \pm 0.41) \times 10^{-4}$ and $B = (3.38 \pm 0.74 \pm 0.85) \times 10^{-4}$, respectively, with the 95% C.L. bound of $2 \times 10^{-4} < B(B \to X_s\gamma) < 4.5 \times 10^{-4}$. The inclusive decays are measured by analyzing the high energy region of the photon energy spectrum. A good theoretical description of the spectral shape is thus essential in order to perform a fit to the spectrum and extrapolate to the total decay rate. Higher order analyses of the spectrum within HQET have been performed in Ref. [17,18], where it is found that the shape of the spectrum is dominated by QCD dynamics and is insensitive to the presence of new physics. Measurement of the spectral moments of the photon energy distribution can also be used to determine the HQET parameters $\bar{\Lambda}$ and λ_1 with small theoretical uncertainty [19].

[1] Ref. [15] argues that the running charm quark mass rather than the pole mass should be used in the two loop matrix element; this results in a slightly higher central value $(3.73 \pm 0.30) \times 10^{-4}$.

The CKM suppressed mode, $B \to X_d\gamma$, is computed in similar fashion with the substitution $s \to d$ in the above formulae and in the complete set of operators. There is also a slight modification of the 4-quark operators O_1 and O_2 to include the contributions from $b \to u$ [20] transitions. The NLO predicted branching fraction spans the range $6.0 \times 10^{-6} \le B(B \to X_d\gamma) \le 2.6 \times 10^{-5}$ with the main uncertainty arising from the imprecisely determined values of the CKM elements. This CKM suppressed channel populates the high energy region of the photon energy spectrum and hence $B \to X_s\gamma$ constitutes the main background source. Observation thus requires a veto of strange hadrons in the hadronic X_d system.

7.1.2.2 $B \to X_s\ell^+\ell^-$

The decay $B \to X_s\ell^+\ell^-$ is suppressed relative to $B \to X_s\gamma$ by an additional factor of the electromagnetic coupling constant $\alpha \simeq 1/137$, and has not yet been observed. The SM prediction for the branching fraction is

$$B(B \to X_s e^+e^-) = (8.4 \pm 2.3) \cdot 10^{-6}, \qquad B(B \to X_s\mu^+\mu^-) = (5.7 \pm 1.2) \cdot 10^{-6} \qquad (7.8)$$

which may be compared with the current experimental 90% C.L. upper bounds of $5.7 \cdot 10^{-5}$ and $5.8 \cdot 10^{-5}$ [64] respectively. Unlike $B \to X_s\gamma$, which is only sensitive to the magnitude of $C_7^{\rm eff}$, this decay has the appeal of being sensitive to the signs and magnitudes of the Wilson coefficients $C_7^{\rm eff}$, C_9 and C_{10}, which can all be affected by physics beyond the standard model. To extract the magnitudes and phases of all three Wilson coefficients, several different measurements must be performed. It has been shown in [21,22] that information from the dilepton invariant mass spectrum and the differential forward-backward asymmetry is sufficient to extract these parameters.

The decay amplitude

Since over most of phase space the differential rate is well approximated by the parton model, we first consider the parton level results. From the effective Hamiltonian (7.1) one easily obtains the parton level decay amplitude

$$\begin{aligned}\mathcal{A}(b \to s\ell^+\ell^-) = \frac{G_F\alpha}{\sqrt{2}\pi}V_{ts}^*V_{tb}\Big[&\left(C_9^{\rm eff} - C_{10}\right)(\bar{s}\gamma_\mu Lb)(\bar{\ell}\gamma^\mu L\ell) \\ &+ \left(C_9^{\rm eff} + C_{10}\right)(\bar{s}\gamma_\mu Lb)(\bar{\ell}\gamma^\mu R\ell) \\ &- 2C_7^{\rm eff}\left(\bar{s}i\sigma_{\mu\nu}\frac{q^\nu}{q^2}(m_sL + m_bR)b\right)(\bar{\ell}\gamma^\mu\ell)\Big] . \end{aligned} \qquad (7.9)$$

where $C_7^{\rm eff}$ is defined in Eq. (7.5). The additional operators O_9 and O_{10} receive contributions only from penguin and box diagrams in the matching and are therefore of order α. The coefficient C_9 contains a term proportional to $\alpha\log(\mu/m_W)$ at one loop, and so logarithms of the form $\alpha_s^{n+1}\log^n(m_b/m_W)$ must be summed to obtain leading logarithmic accuracy. Thus, the one loop matrix element of O_9 is required as well as the two loop running of C_9. This amount to the identification $C_9^{\rm eff} \equiv C_9^{\rm eff}(\hat{s})$, where

$$C_9^{\rm eff}(\hat{s}) = C_9\eta(\hat{s}) + Y(\hat{s})\,. \tag{7.10}$$

The one-loop matrix elements of the four-Fermi operators are represented by the function $Y(\hat{s})$, which in the NDR scheme is given by [2,23]

$$\begin{aligned} Y(\hat{s}) &= g(\hat{m}_c,\hat{s})\,(3\,C_1 + C_2 + 3\,C_3 + C_4 + 3\,C_5 + C_6) \\ &\quad -\frac{1}{2}g(1,\hat{s})\,(4\,C_3 + 4\,C_4 + 3\,C_5 + C_6) - \frac{1}{2}g(0,\hat{s})\,(C_3 + 3\,C_4) \\ &\quad +\frac{2}{9}\,(3\,C_3 + C_4 + 3\,C_5 + C_6)\ , \end{aligned} \tag{7.11}$$

where

$$\begin{aligned} g(z,\hat{s}) &= -\frac{8}{9}\ln(\frac{m_b}{\mu}) - \frac{8}{9}\ln z + \frac{8}{27} + \frac{4}{9}y - \frac{2}{9}(2+y)\sqrt{|1-y|} \\ &\quad \times\left[\Theta(1-y)\left(\ln\frac{1+\sqrt{1-y}}{1-\sqrt{1-y}} - i\pi\right) + \Theta(y-1)\,2\arctan\frac{1}{\sqrt{y-1}}\right], \end{aligned} \tag{7.12}$$

$$g(0,\hat{s}) = \frac{8}{27} - \frac{8}{9}\ln\left(\frac{m_b}{\mu}\right) - \frac{4}{9}\ln\hat{s} + \frac{4}{9}i\pi\,, \tag{7.13}$$

with $y = 4z^2/\hat{s}$. The one loop matrix element of O_9 as a function of the dilepton invariant mass is written as

$$\eta(\hat{s}) = 1 + \frac{\alpha_s(\mu)}{\pi}\omega(\hat{s})\ , \tag{7.14}$$

where

$$\begin{aligned} \omega(\hat{s}) &= -\frac{2}{9}\pi^2 - \frac{4}{3}{\rm Li}_2(\hat{s}) - \frac{2}{3}\ln\hat{s}\ln(1-\hat{s}) - \frac{5+4\hat{s}}{3(1+2\hat{s})}\ln(1-\hat{s}) \\ &\quad -\frac{2\hat{s}(1+\hat{s})(1-2\hat{s})}{3(1-\hat{s})^2(1+2\hat{s})}\ln\hat{s} + \frac{5+9\hat{s}-6\hat{s}^2}{6(1-\hat{s})(1+2\hat{s})} \end{aligned} \tag{7.15}$$

and we have neglected the strange quark mass.

It is convenient to normalize the rate of $b\to s\ell^+\ell^-$ to that for semileptonic $b\to c\ell\bar{\nu}$ decay

$$d\mathcal{B}(B\to X_s\ell^+\ell^-) = \mathcal{B}_{sl}\frac{d\Gamma(B\to X_s\ell^+\ell^-)}{\Gamma(B\to X_c\ell\nu_\ell)}\,. \tag{7.16}$$

This introduces the normalization constant

$$\mathcal{B}_0 = \mathcal{B}_{sl}\frac{3\alpha^2}{16\pi^2}\frac{|V_{ts}^*V_{tb}|^2}{|V_{cb}|^2}\frac{1}{f(\hat{m}_c) + [\alpha_s(m_b)/\pi]A_0(\hat{m}_c)}\,. \tag{7.17}$$

In this expression $f(\hat{m}_c)$ is the well known phase space factor for the parton decay rate $b\to c\ell\bar{\nu}$

$$f(\hat{m}_c) = 1 - 8\hat{m}_c^2 + 8\hat{m}_c^6 - \hat{m}_c^8 - 24\hat{m}_c^4\log\hat{m}_c, \tag{7.18}$$

and $A_0(\hat{m}_c)$ is the $\mathcal{O}(\alpha_s)$ QCD correction to the semileptonic $b\to c$ decay rate [24].

Parton model differential decay rate and forward-backward asymmetry

The forward-backward asymmetry in inclusive $b\to s\ell^+\ell^-$ has been studied in detail [21]. From the amplitude of the decay $b\to s\ell^+\ell^-$ (7.9) the dilepton invariant mass distribution in the parton model can easily be calculated

$$\begin{aligned} \frac{d\mathcal{B}}{d\hat{s}} &= \frac{4}{3}\mathcal{B}_0\Big[(1-\hat{s})^2(1+\hat{s})\left(|C_9^{\rm eff}|^2 + C_{10}^2\right) \\ &\quad + 2(1-\hat{s})^2(2+\hat{s})\frac{|C_7^{\rm eff}|^2}{\hat{s}} + 6(1-\hat{s})^2\,{\rm Re}\left(C_9^{\rm eff}\right)C_7^{\rm eff}\Big]\,. \end{aligned} \tag{7.19}$$

A plot of this distribution is shown by the solid line in Figure 7.1. The divergence at $\hat{s}=0$ is due to the intermediate photon going on shell an is a well known feature of this decay. In this limit the differential decay rate reduces to the $B\to s\gamma$ rate with an on-shell photon in the final state, convoluted with the fragmentation function which describes the probability for the photon to fragment into a lepton pair.

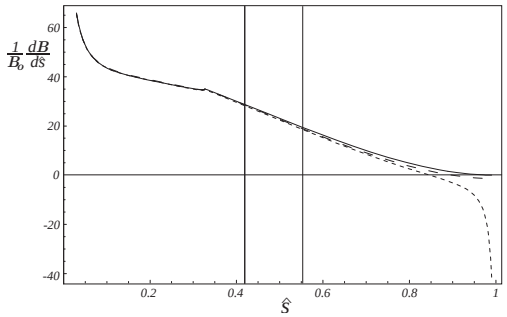

Figure 7.1: The differential decay spectrum $\frac{1}{\mathcal{B}_0}\frac{d\mathcal{B}}{d\hat{s}}$ for the decay $B\to X_s\ell^+\ell^-$. The solid line shows the free quark prediction, the long-dashed line includes the $\mathcal{O}(\Lambda/m_b^2)$ corrections and the short-dashed line contains all corrections up to $\mathcal{O}(\Lambda/m_b^3)$.

The differential forward-backward asymmetry is defined by

$$\frac{d\mathcal{A}}{d\hat{s}} = \int_0^1 dz\ \frac{d\mathcal{B}}{dx\,d\hat{s}} - \int_{-1}^0 dx\ \frac{d\mathcal{B}}{dx\,d\hat{s}} \tag{7.20}$$

where

$$x = cos\theta = \frac{\hat{u}}{\hat{u}(\hat{s},\hat{m}_s)} \tag{7.21}$$

parameterizes the angle between the b quark and the ℓ^+ in the dilepton CM frame. An experimentally more useful quantity is the normalized FB asymmetry defined by

$$\frac{d\bar{\mathcal{A}}}{d\hat{s}} = \frac{d\mathcal{A}}{d\hat{s}}\Big/\frac{d\mathcal{B}}{d\hat{s}}\,. \tag{7.22}$$

In the parton model the differential forward-backward asymmetry is given by

$$\frac{d\mathcal{A}}{d\hat{s}} = -4\,\mathcal{B}_0(1-\hat{s})^2\left[\hat{s}\,\mathrm{Re}\left(C_9^{\mathrm{eff}}(\hat{s})\right)C_{10} + 2C_{10}C_7^{\mathrm{eff}}\right], \tag{7.23}$$

which is shown by the solid line in Figure 7.2.

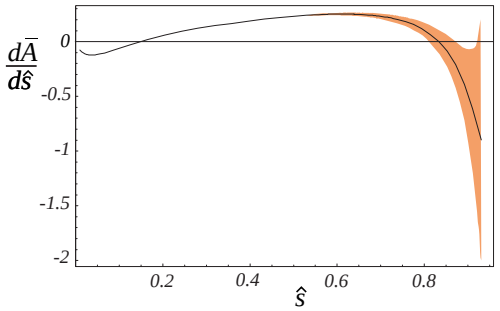

Figure 7.2: The normalized forward backward asymmetry. The three curves show the mean value and the 1σ uncertainty of the forward backward asymmetry.

Charmonium resonances

Both the dilepton invariant mass spectrum and the differential forward-backward asymmetry contain a cusp at the threshold of $c\bar{c}$ pair production. For such values of $\hat{s}$ long distance contributions from tree level processes $B \to B^{(*)}\psi^{(\prime)}$, followed by $\psi^{(\prime)} \to \ell^+\ell^-$, are important, which can not be calculated perturbatively. The location of the first two $c\bar{c}$ resonances are indicated in Figs. 7.1 and 7.2 by the two vertical lines.

Since the $c\bar{c}$ resonance contributions cannot be calculated model independently, suitable cuts on the dilepton invariant mass are conventionally applied to eliminate these resonance contributions. Such cuts naturally divide the available phase space into two separate regions: a low $\hat{s}$ region for $s \le M_\psi^2 - \delta$ and a high $\hat{s}$ region for $s \ge M_{\psi'}^2 + \delta'$, where $\delta^{(\prime)}$ depends on the exact values of the experimental cuts. The region of phase space below the ψ resonance is contaminated by background from sequential B decays. This background can only be suppressed if the inclusive process is measured by summing over a large number of individually reconstructed final states. In the region above the ψ' resonance, there is almost no background from other B decays, making the measurement much easier. It is the latter region of phase space that is accessible to experiments at the Tevatron.

Power corrections to the dilepton invariant mass spectrum and the forward-backward asymmetry

Nonperturbative physics can be parameterized by matrix elements of higher dimensional operators. This is done by performing an OPE as described in Chapter 1. The leading

corrections arise at order $\mathcal{O}(\Lambda_{QCD}/m_b)^2$ and can be parameterized by the matrix elements of two dimension five operators. Both matrix elements, λ_1 and λ_2 have been measured, albeit with large uncertainties for λ_1. At order $\mathcal{O}(\Lambda_{QCD}/m_b)^3$ there are seven operators contributing, with none of the matrix elements known. Calculating the contributions from these dimension six operators therefore do not improve the theoretical accuracy, but can be used to investigate the convergence of the OPE and estimate theoretical uncertainties. The contributions of the dimension five operators to the differential decay rate and the forward backward asymmetry were calculated in Ref. [25] and the calculation including all power corrections up to order $\Lambda_{\mathrm{QCD}}^3/m_b^3$ is presented in Ref. [26].

The effects of these corrections on the differential decay rate are shown in Figure 7.1 by the long and short dashed lines, respectively. It is obvious from Figure 7.1 that the effect of higher dimensional operators is negligible below the ψ resonance, whereas it is large in the large $\hat{s}$ region. This can also be seen by calculating the branching ratio with an upper cut on the dilepton invariant mass 100 MeV below m_ψ, $\hat{s} = 0.35$. Including a cut $\hat{s} > 0.01$ to eliminate the fragmentation divergence at low q^2 the expansion in $1/m_b$ yields

$$\int_{0.01}^{0.35} d\hat{s}\frac{d\mathcal{B}}{d\hat{s}} = 22.0\left[1 + 0.5\frac{\lambda_1}{m_b^2} + 1.2\left(\frac{\lambda_2}{m_b^2} - \frac{\rho_2}{m_b^3}\right) - 3.7\frac{\rho_1}{m_b^3}\right] \tag{7.24}$$

where the ρ_i's and f_1 are unknown matrix elements of order Λ_{QCD}^3, and we have neglected contributions of a comparable size coming from T-products, which may be absorbed into a redefinition of λ_1 and λ_2. All numerical coefficients are of order unity and the OPE is therefore converging well. In the region above the resonances the situation looks quite different. Imposing a lower cut 100 MeV above the ψ' resonance, $\hat{s} = 0.59$, the partially integrated branching ratio is

$$\int_{0.59}^{1} d\hat{s}\frac{d\mathcal{B}}{d\hat{s}} = 3.8\left[1 + 0.5\frac{\lambda_1}{m_b^2} - 35.4\left(\frac{\lambda_2}{m_b^2} - \frac{\rho_2}{m_b^3}\right) + 161.8\frac{\rho_1}{m_b^3} + 147.4\frac{f_1}{m_b^3}\right]. \tag{7.25}$$

From this expression it is clear that the convergence of the OPE is very poor and the branching ratio above the ψ' resonance can not be calculated well.

Higher dimensional operators can also be included for the forward-backward asymmetry. This leads to

$$\begin{aligned}\frac{d\mathcal{A}}{d\hat{s}} = {} & C_7^{\mathrm{eff}}C_{10}\Big[-8(1-\hat{s})^2 - \frac{4\left(3+2\hat{s}+3\hat{s}^2\right)\lambda_1}{3m_b^2} + \frac{4\left(7+10\hat{s}-9\hat{s}^2\right)\lambda_2}{m_b^2} \\ & + \frac{4\left(5+2\hat{s}+\hat{s}^2\right)\rho_1}{3m_b^3} - \frac{4\left(7+10\hat{s}-9\hat{s}^2\right)\rho_2}{m_b^3}\Big] \\ & + C_9^{\mathrm{eff}}(\hat{s})C_{10}\Big[-4\hat{s}(1-\hat{s})^2 - \frac{2\hat{s}\left(3+2\hat{s}+3\hat{s}^2\right)\lambda_1}{3m_b^2} + \frac{2\hat{s}\left(9+14\hat{s}-15\hat{s}^2\right)\lambda_2}{m_b^2} \\ & - \frac{2\hat{s}\left(1+2\hat{s}+5\hat{s}^2\right)\rho_1}{3m_b^3} - \frac{2\hat{s}\left(1+6\hat{s}-15\hat{s}^2\right)\rho_2}{m_b^3}\Big]\end{aligned} \tag{7.26}$$

It is clear from this expression that the third order terms do not have abnormally large coefficients, and therefore introduce only small variations relative to the second order expressions. The normalized forward-backward asymmetry, however, inherits the poor behavior

of the differential branching ratio in the endpoint region $\hat{s} \to 1$. The normalized asymmetry is shown in Figure 7.2, with the shaded region representing the uncertainties due to $(\Lambda_{QCD}/m_b)^3$ terms. From this Figure it is clear that the nonperturbative uncertainties on the differential asymmetry are small below the ψ resonance, whereas they are large above the ψ'.

7.1.3 Exclusive Decays

The Wilson coefficients defined in Section 7.1.1.1 contain the short distance information that allows us to test the one loop structure of the standard model. The exclusive decays we will consider in this section can be used to determine these coefficients. However, these decays also depend on the hadronic matrix elements of the operators in Eqs. (7.2), which describe the transition from the initial state b flavored hadron to the final state hadron. These hadronic matrix elements are dominated by nonperturbative QCD effects. They are calculable in principle from lattice QCD, the only *ab initio* framework available for quantitative calculations of nonperturbative QCD.

At present, lattice QCD calculations of these processes are incomplete. This results in important uncertainties in theoretical predictions of exclusive rare decays, with a corresponding loss of sensitivity to the interesting short distance physics. We therefore need a variety of other theoretical tools at our disposal. These include model independent approaches based on approximate symmetries, such as heavy quark and chiral symmetry, and model-dependent approaches based on phenomenologically motivated models. While not rigorous, model calculations can serve to guide lattice calculations and provide a simple framework for studying these processes.

The rest of this section is organized as follows. After introducing the matrix elements and form factor parameterizations in Section 7.1.3.1, we discuss results and prospects from lattice QCD in Section 7.1.3.2. Rare semileptonic decays are discussed in Section 7.1.3.3 which describes results and constraints from model independent approaches first, followed by a summary of model-dependent results. Section 7.1.3.4 gives a discussion of the status of theoretical predictions for exclusive radiative decays. Finally, Section 7.1.3.5 discusses results for $B_{s,d} \to l^+ l^-$ decays.

7.1.3.1 Hadronic Matrix Elements and Form Factors

The hadronic matrix elements can be parametrized in terms of form factors which are functions of the momentum transfer between the initial and final state hadrons.

For the $B \to K\ell^+\ell^-$ decay the hadronic matrix elements of the operators O_7, O_9 and O_{10} (which were defined in Eqs. (7.2)) are parametrized as

$$\langle K(k)|\bar{s}\sigma_{\mu\nu}q^\nu b|B(p)\rangle = i\,\frac{f_T}{m_B+m_K}\Big\{(p+k)_\mu q^2 - q_\mu(m_B^2-m_K^2)\Big\}\,, \tag{7.27}$$

$$\langle K(k)|\bar{s}\gamma_\mu b|B(p)\rangle = f_+(p+k)_\mu + f_-\,q_\mu\,, \tag{7.28}$$

with $f_T(q^2)$ and $f_\pm(q^2)$ unknown functions of $q^2=(p-k)^2=m^2_{\ell^+\ell^-}$. In the SU(3) limit $f_\pm$ in (7.28) are the same as the form factors entering in the semileptonic decay $B\to\pi\ell\nu$.

For the vector meson mode, $B\to K^*\ell^+\ell^-$, we have the "semileptonic" matrix element

$$\begin{aligned}\langle K^*(k,\epsilon)|\bar{s}_L\gamma_\mu b_L|B(p)\rangle = \frac{1}{2}\Big\{& ig\,\epsilon_{\mu\nu\alpha\beta}\epsilon^{*\nu}(p+k)^\alpha(p-k)^\beta - f\,\epsilon^*_\mu \\ & - a_+\,(\epsilon^*\cdot p)\,(p+k)_\mu - a_-\,(\epsilon^*\cdot p)\,(p-k)_\mu\Big\}\,,\end{aligned} \tag{7.29}$$

where ϵ_μ is the K^* polarization four-vector. The form factors defined in (7.29) can be identified, in the $SU(3)$ limit, with those appearing in the semileptonic transition $B\to\rho\ell\nu$. The matrix element of the penguin operator takes the form

$$\begin{aligned}\langle K^*(k,\epsilon)|\bar{s}_L\sigma_{\mu\nu}q^\nu b_R|B(p)\rangle = & \,i\epsilon_{\mu\nu\alpha\beta}\epsilon^{*\nu}p^\alpha k^\beta\,2T_1 \\ & + T_2\left\{\epsilon^*_\mu(m_B^2-m_{K^*}^2) - (\epsilon\cdot p)\,(p+k)_\mu\right\} \\ & + T_3(\epsilon\cdot p)\left\{q_\mu - \frac{q^2}{m_B^2-m_{K^*}^2}\,(p+k)_\mu\right\},\end{aligned} \tag{7.30}$$

Radiative decays receive a contribution from the local operator O_7 – also called the magnetic dipole operator – and its associated Wilson coefficient. This is also sometimes called the short distance contribution, since another contribution comes from non-local operators. These non-local operators are due to (i) the process $B\to VV^*$ with the subsequent conversion of the neutral vector meson V^* to a real photon, and (ii) weak annihilation and W exchange diagrams with subsequent γ radiation. Contributions from non-local operators are sometimes also called long distance contributions.

The hadronic matrix element of the magnetic dipole operator for the $B\to V\gamma$ decay, were V represents a vector meson, is generally written in terms of three form factors, with

$$\begin{aligned}\langle V(p,\epsilon)|\bar{s}\sigma_{\mu\nu}q^\nu(1+\gamma_5)b|B(p_B)\rangle = & \,2i\epsilon_{\mu\nu\rho\sigma}\epsilon^{*\nu}p_B^\rho p^\sigma T_1(q^2) \\ & + \Big[\epsilon^*_\mu(m_B^2-m_V^2) - (\epsilon^*\cdot q)(p_B+p)_\mu\Big]\,T_2(q^2) \\ & + (\epsilon^*\cdot q)\Big[q_\mu - \frac{q^2}{m_B^2-m_V^2}\,(p_B+p)_\mu\Big]T_3(q^2)\,,\end{aligned} \tag{7.31}$$

where ϵ^* represents the polarization vector of the vector meson, and q corresponds to the momentum of the outgoing photon. This simplifies for the case of an on-shell photon, where the coefficient of T_3 vanishes and $T_2(0)=-iT_1(0)$. Hence in the physical cases of interest here, the decay width can be expressed in terms of a single form factor,

$$\Gamma(B\to V+\gamma) = \frac{\alpha G_F^2}{32\pi^4}|V_{tb}V_{ts}^*|^2(m_b^2+m_s^2)m_B^3\left(1-\frac{m_V^2}{m_B^2}\right)^3|C_7^{(0)eff}(m_b)|^2\,|T_1^{B\to V}(q^2=0)|^2\,, \tag{7.32}$$

and the branching fraction is computed by scaling to the semileptonic rate as usual.

7.1.3.2 Lattice QCD

Lattice QCD methods are well suited for theoretical calculations of the hadronic matrix elements (and form factors) which describe rare decays. However, because of the lack of experimental information on rare semileptonic decays (such as $B \to K\ell^+\ell^-$), they have not been studied on the lattice to date. Results from lattice calculations of rare radiative decays do exist, and are discussed in more detail in Section 7.1.3.4.

The hadronic matrix elements which describe rare semileptonic decays (as shown in Eqs. (7.28–7.30)) are similar to the matrix elements for semileptonic decays, such as $B \to \pi\ell\bar{\nu}$. These have been studied extensively using lattice methods. We can use the existing results from lattice calculations of $B \to \pi\ell\bar{\nu}$ to discuss the prospects for lattice calculations of rare decays, like $B \to K^{(*)}\ell^+\ell^-$.

Current lattice calculations of the $B \to \pi\ell\bar{\nu}$ form factors are accurate to about $15-20\%$ [27]. It would be relatively straightforward to perform a lattice QCD calculation of the form factors for $B \to K\ell^+\ell^-$ with a similar accuracy using current technology. The quoted uncertainty includes all systematic errors except for the quenched approximation – unquenched results do not yet exist for these decays. From unquenched calculations of other quantities, we can estimate the expected size of the effect to be in the range of $10-15\%$. Apart from the quenched approximation, the most important errors in lattice QCD calculations are due to statistics (from the Monte-Carlo integration), the chiral extrapolation, the lattice spacing, and perturbation theory (see Section 5.3 of Chapter 1 for a detailed discussion of how these errors arise).

Lattice QCD calculations are in principle improvable to arbitrary precision. In practice, the accuracy of lattice calculations depends on the computational effort and available technology. Numerical simulations based on lattice QCD are time consuming and computationally expensive. In the following, we shall discuss the prospects for reducing the total uncertainty in lattice QCD calculations to a few percent. We assume that there will be reasonable growth in the computational resources available for these lattice QCD calculations.

Improving the statistical and chiral extrapolation errors is straightforward; it just requires more computer time. This is within reach of the computational resources which should become available to lattice QCD calculations within the next few years.

Lattice spacing errors can be reduced by explicitly reducing the lattice spacing ($a \to 0$) used in the calculations. However, the computational cost of a lattice calculation scales like $1/a^{6-10}$. In general, lattice spacing errors are proportional to terms which grow like $(a\Lambda)^n$ where Λ is the typical momentum scale of the process in question. Typical lattice spacings used in numerical simulations are in the range $0.05\,\mathrm{fm} \lesssim a \lesssim 0.2\,\mathrm{fm}$, so that $a\Lambda \ll 1$ for momenta of order $\Lambda_{\rm QCD}$. The power n (and hence the size of lattice spacing errors) depends on the discretization used in the calculation. With the (improved) lattice actions currently in use, $n = 2$. With highly improved lattice actions we can increase the power to $n = 4$. The situation is a bit more complicated in the presence of heavy quarks. However, as discussed in detail in Section 1.5.3, the lattice spacing errors associated with heavy quarks can be as easily controlled as the errors associated with the light degrees of freedom. In summary, we can keep lattice spacing errors under control at the few percent

(or less) level, by using highly improved actions in simulations at relatively coarse lattice spacings. The big advantage of this strategy is its low computational cost. It is therefore also the best strategy for realistic unquenched calculations.

There is a further restriction for semileptonic decays which arises from the need to control lattice spacing errors. The hadronic matrix elements (and form factors) for semileptonic decays are functions of the daughter recoil momentum. Since lattice spacing errors increase with increasing recoil momentum, the momentum range accessible to lattice QCD calculations is limited. At present, in order to keep lattice errors under control, most calculations impose an upper momentum cut of

$$\boldsymbol{p}_{\rm recoil} < 1\,\mathrm{GeV}\,. \tag{7.33}$$

For decays like $B \to D\ell\bar{\nu}$ this is not a problem, as the allowed recoil range is also small. However, for decays of B mesons into light hadrons we can obtain the matrix elements and form factors only over part of the allowed range. In particular, the high recoil region, $\boldsymbol{p}_{\rm recoil} \propto m_B/2$, which corresponds to q^2 small or near zero, is not directly accessible to lattice QCD calculations.

A remedy used in early calculations is to extrapolate the form factors from the high q^2 region to low q^2 assuming a functional form for the shape of the form factors. This procedure introduces a model dependent systematic error into the calculation which can't be quantified. This was an acceptable compromise for early lattice calculations intended to establish the method. However, it is certainly undesirable for first principles calculations designed to test the standard model.

If there is significant overlap between the recoil momentum ranges accessible in lattice QCD calculations and experimental measurements, then we can avoid model dependent extrapolations and limit the comparison between theory and experiment to the common recoil momentum range. Indeed, this appears to be the case for $B \to \pi\ell\bar{\nu}$, and will most likely also be true for rare semileptonic decays such as $B \to K\ell^+\ell^-$. However, as discussed in the following section, the high recoil region is of particular phenomenological interest in $B \to K^{(*)}\ell^+\ell^-$ decays.

It is possible to increase the recoil momentum range accessible to lattice calculations by using highly improved actions, especially in combination with asymmetric lattices [28]. However, lattice calculations of radiative decays such as $B \to K^*\gamma$ remain problematic. With a real photon, the two body decay takes place at maximum recoil or $q^2 = 0$. If we want to avoid model-dependent extrapolations, we will need to develop better techniques for dealing with this high recoil physics.

7.1.3.3 $B \to K^*\ell^+\ell^-$ and $B \to K\ell^+\ell^-$

In the following, we review results for calculations of the form factors in Eqs. (7.28–7.30) from different theoretical approaches. The prospects for lattice QCD results were already discussed in the previous section. We first present the constraints derived from heavy quark symmetry (HQS), followed by results from SU(3) symmetry and finally from the large energy limit (LEL).

We then review results obtained from calculations using phenomenological models. A vast variety of models are available for these calculations. Here, we present the relevant features of current models. Although predictions from different models still disagree with each other, the situation has greatly improved since the experimental observation of exclusive B decays to light hadrons.

Predictions from HQET

As discussed in Chapter 1, the Dirac structure of b quarks simplifies in the Heavy Quark Limit, $m_b \gg \Lambda_{\rm QCD}$, allowing relations between different form factors to be derived. For example, in the rest frame of the heavy quark, $v^\mu = (1,\vec{0})$, the heavy quark field obeys $\gamma_0 h_0 = h_0$, and so

$$\bar{h}_b i\sigma_{0i} h_b = \bar{h}_b \gamma_i h_b, \qquad \bar{h}_b i\sigma_{0i}\gamma_5 h_b = -\bar{h}_b \gamma_i \gamma_5 h_b. \tag{7.34}$$

By making use of (7.34) we can now obtain relations among the form factors in (7.27) and (7.28). They are [29]

$$f_T(q^2) = -\frac{m_B + m_K}{2m_B}\left(f_+(q^2) - f_-(q^2)\right), \tag{7.35}$$

$$T_1(q^2) = \frac{f(q^2) - 2(q\cdot p)\, g(q^2)}{2m_B}, \tag{7.36}$$

$$T_2(q^2) = T_1(q^2) - \frac{f(q^2) - 2(m_B^2 + k\cdot p)\, g(q^2)}{2m_B}\left(\frac{q^2}{m_B^2 - m_{K^*}^2}\right), \tag{7.37}$$

$$T_3(q^2) = \frac{m_B^2 - m_{K^*}^2}{2m_B}\left\{a_+(q^2) - a_-(q^2) + 2g(q^2)\right\}. \tag{7.38}$$

In terms of the symmetries of the HQET, Eqs. (7.35–7.38) are a result of the Heavy Quark *Spin* Symmetry (HQSS) that arises in the heavy quark limit due to the decoupling of the spin of the heavy quark [30]. This is a very good symmetry when considering B decays, a measure of which is for instance the quantity

$$\frac{m_{B^*} - m_B}{m_B} \simeq 0.009 \sim \left(\frac{0.45}{4.8}\right)^2 \tag{7.39}$$

which is in agreement with the HQET prediction of $O(\Lambda_{\rm QCD}^2/m_b^2)$. Thus the relations (7.35-7.38), which are valid over the entire physical region [31], will receive only small corrections. They allow us to express all the hadronic matrix elements entering in $B \to K^{(*)}\ell^+\ell^-$ processes, in terms of the "semileptonic" form factors f, g and $a_\pm$.

Furthermore, there is an additional $SU(2)_F$ flavor symmetry in the heavy quark limit, leading to relations among form factors occurring in the decays of charm and bottom hadrons [29,30]. For instance in $H \to \pi\ell\nu$ one obtains

$$(f_+ - f_-)^{B\to\pi} = C_{BD}\sqrt{\frac{m_B}{m_D}}\,(f_+ - f_-)^{D\to\pi}, \tag{7.40}$$

$$(f_+ + f_-)^{B\to\pi} = C_{BD}\sqrt{\frac{m_D}{m_B}}\,(f_+ + f_-)^{D\to\pi}, \tag{7.41}$$

where $C_{BD} = (\alpha_s(m_B)/\alpha_s(m_D))^{-6/25}$ is a leading logarithmic QCD correction to the heavy quark currents [32]. Similar scaling relations are obtained for $H \to \rho\ell\nu$,

$$f^{B\to\rho} = C_{BD}\sqrt{\frac{m_B}{m_D}}\, f^{D\to\rho}, \tag{7.42}$$

$$g^{B\to\rho} = C_{BD}\sqrt{\frac{m_D}{m_B}}\, g^{D\to\rho}, \tag{7.43}$$

$$(a_+ - a_-)^{B\to\rho} = C_{BD}\sqrt{\frac{m_D}{m_B}}\,(a_+ - a_-)^{D\to\rho}. \tag{7.44}$$

In the above relations the form factors must be evaluated at the same value of the hadronic energy recoil $v\cdot k$, not the same value of q^2. The semileptonic D decays have a maximum recoil energy of about 1 GeV, whereas B decays go up to $\simeq m_B/2$. Thus the use of data from D decays requires an extrapolation from the low to the high recoil regions of phase space, for which the $v\cdot k$ dependence of the form factors must be assumed. In addition, the relations (7.40-7.44) are valid in the leading order in the HQET and will receive corrections of the order of $\bar{\Lambda}/2m_c \simeq 0.15$, with $\bar{\Lambda}$ the effective mass of the light degrees of freedom. Then, the corrections to the flavor symmetry are likely to be larger than those to the spin symmetry. For instance, in the $H \to \pi\ell\nu$, corrections as large as $20\% - 30\%$ are possible [33]. On the other hand, it was shown in Ref. [34] that the $B \to K^*\gamma$ rate can be well reproduced by using both the spin and the flavor symmetries in HQET to relate the $D \to K^*\ell\nu$ form factors to $T_1(0)$ determining the radiative branching fraction, with the additional assumption of a monopole q^2 dependence for the form factors f and g all the way from $q^2 = 16.5$ GeV^2 to $q^2 = 0$.

Other Theoretical Approaches

SU(3):

A necessary ingredient in the application of the HQSS relations (7.35-7.38) to predictions for $B \to K^{(*)}\ell^+\ell^-$ making use of the semileptonic form factors in $B \to (\pi\rho)\ell\nu$ is the assumption of well-behaved $SU(3)$ symmetry relations. Intuitively, and since the form factors are determined by the strong interactions, we expect that at very high recoil energies $SU(3)$ is a very good approximation. For rare B decays, where most of the events occur in this region of phase space, we should be confident that $SU(3)$ corrections are small. However, it is difficult to make a quantitative statement about the size of the $SU(3)$ breaking in a completely model independent way. For instance, in the constituent quark model picture, a relevant quantity parameterizing $SU(3)$ breaking could be

$$\delta_3 \equiv \frac{\tilde{m}_s - \tilde{m}_d}{E_h}, \tag{7.45}$$

where $\tilde{m}_q$ are constituent quark masses and E_h is the recoil energy of the hadron. Thus, for standard values of the strange and down constituents masses this suggests and $SU(3)$ breaking below 10% in most of phase space. On the other hand, the deviations from 1 of the double ratio $F^{(B\to\rho)}/F^{(B\to K^*)}/F^{(D\to\rho)}/F^{(D\to K^*)}$, with F some arbitrary form factor,

were estimated in Ref. [35] by calculating the effects of chiral loops. The effect was found to be smaller than 3% and, although there could be contributions from higher orders, adds credibility to the use of $SU(3)$ relations.

The short distance structure of the B_s meson decays $B_s \to (\eta^{(\prime)}, \phi)\ell^+\ell^-$ is the same as that of $B \to K^{(*)}\ell^+\ell^-$. In the SU(3) limit the branching ratios should be the same. Thus, although departures from the SU(3) predictions could be as large as $20 - 30\%$, our understanding of the B modes gives us a very good starting point for the B_s decays.

Large Energy Limit (LEL):

In addition the symmetries of the heavy quark limit, additional simplifications occur for exclusive decays in which the recoil energy of the light meson is large, the so-called Large Energy Limit (LEL) [18,36–45]. In this limit, interactions of the light quark with soft or hard collinear gluons do not change its helicity, giving rise to additional symmetries, and corresponding additional relations between form factors. These were first noted in [37], based on symmetries of the "large energy effective theory" (LEET) [36]. (Although LEET is not a well-defined effective theory, these relations remain true in the LEL [18,39, 41].) In addition to the heavy quark symmetry relations in Eqs. (7.35–7.38), the additional symmetries of the LEL gives new relations among the form factors defined in Eqs. (7.27–7.29).

The main result of the LEL which is important for our discussion here, is the fact that all of the form factors in $H \to (P,V)\ell^+\ell^-$ can be expressed by a total of *three* functions of the heavy mass M and the recoil energy E. For example, the $H \to P\ell^+\ell^-$ form factors can be written as [37]

$$\begin{aligned} f_+(q^2) &= \xi(M,E)\,, \\ f_-(q^2) &= -\xi(M,E)\,, \\ f_T(q^2) &= \left(1 + \frac{m_P}{M}\right)\xi(M,E)\,, \end{aligned} \tag{7.46}$$

where $\xi(M,E)$ is an unknown function of M and E. Simple inspection shows that the previously derived HQSS relation Eq.(7.35) is satisfied. For the vector meson final state, the form factors obey

$$\begin{aligned} g(q^2) &= \frac{1}{M}\,\xi_\perp\,, \\ f(q^2) &= -2E\,\xi_\perp\,, \\ a_+(q^2) &= \frac{1}{M}\left\{\xi_\perp - \frac{m_V}{E}\xi_\parallel\right\}\,, \\ a_-(q^2) &= \frac{1}{M}\left\{-\xi_\perp + \frac{m_V}{E}\xi_\parallel\right\}\,, \end{aligned} \tag{7.47}$$

where $\xi_\perp(M,E)$ and $\xi_\parallel(M,E)$ refer to the transverse and longitudinal polarizations, respectively.

Additionally, there will be expressions for the "penguin" form factors $T_i(q^2)$, $i = 1,2,3$, in terms of $\xi_\perp$ and $\xi_\parallel$, which satisfy the HQSS relations in Eqs. (7.36–7.38). The power of

the predictions in Eqs. (7.46–7.47) will become apparent later when computing observables in $B \to K^{(*)}\ell^+\ell^-$ decays. Let us now only note in passing one example: the ratio of the vector form factor $g(q^2)$ to the axial-vector form factor $f(q^2)$

$$R_V \equiv \frac{g(q^2)}{f(q^2)} \simeq -\frac{1}{2\,E_{K^*}\,m_B}\,, \tag{7.48}$$

only depends on kinematical variables and is unaffected by hadronic uncertainties. This ratio determines, for instance the ratio of the two transverse polarizations in $B \to (K^*, \rho)$ decays.

Corrections to the LEL relations arise from (i) radiative corrections to the heavy light vertex, (ii) hard gluon exchange with the spectator quark and (iii) nonperturbative corrections which scale like $\Lambda_{\rm QCD}/E_h$. $E_h \sim O(m_b)$ is the recoil energy of the light hadronic state. The leading contribution to (i) was calculated in Refs. [40,41], while (ii) was calculated in Ref. [40]. An effective field theory formulation of the LEL appears to be much more complicated than HQET, but there has been much recent work in this direction [18,39,41]. Such a formulation should allow the nonperturbative corrections (iii) to be parametrized, but thus far this has not been done. The theory of exclusive decays in the LEL is currently a very active field, and much additional theoretical work on this subject is to be expected in the future, in particular clarifying the size of the corrections to the limit.

The various LEL relations may be experimentally tested: for example, an experimental measurement of the ratio of the transverse polarizations Γ_+/Γ_- in the semileptonic decay $B \to \rho\ell\nu$ will provide a test of the relation (7.48). In addition, the relation (7.48), together with the experimental data on $b \to s\gamma$ decays, has been used to put constraints on the form-factors entering the $B \to K^*$ matrix element at $q^2 = 0$. This can be seen in Figure 7.3, from which we can fit the vector and axial-vector form-factors giving $V(0) = 0.39 \pm 0.06$ and $A_1(0) = 0.29 \pm 0.02$. Here,

$$V \equiv -(m_B + m_{K^*})g\,, \qquad A_1 \equiv \frac{f}{m_B + m_{K^*}}\,, \tag{7.49}$$

Model Calculations

The model independent statements described above are not enough to specify all the hadronic matrix elements needed in the decays of interest. Furthermore, lattice QCD calculations of the rare decay form factors are incomplete, at present.

Model calculations are much easier. On the one hand, they tend to be based on uncontrolled approximations. This leads to uncertainties which are difficult (if not impossible) to estimate. On the other hand, models can provide very useful parameterizations of the physics and may help us understand the region of validity of some of those assumptions.

In heavy-to-light transitions, such as $B \to K^{(*)}\ell^+\ell^-$ and $B \to (\pi\rho)\,\ell\nu$, the rate receives most of its contributions from the large recoil region where $E_h > 1$ GeV. We therefore expect those models that incorporate – in one way or another – our understanding of the

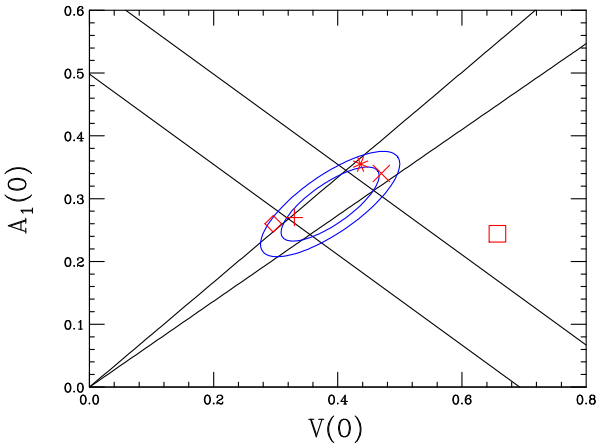

Figure 7.3: Constraints on the semileptonic form-factors $V(0)$ and $A_1(0)$ from $B \to K^*\gamma$ data plus HQSS (thicker band) together with the relation from the LEL (cone). The ellipses correspond to 68% and 90% confidence level intervals. Central values of model predictions are also shown and correspond to BSW [46] (vertical cross), ISGW2 [50] (diamond), MS [51] (star), LCSR [42] (diagonal cross) and LW [34] (square), respectively.

hadronization of a light quark with relatively large energies to be best suited for these processes. For example, calculations in the light-cone, performed at $q^2 < 0$, and matched at $q^2 = 0$ with the physical region [46,47], as well as light-cone sum rule (LCSR) calculations [48] will give the correct asymptotic behavior of the form factors in QCD as one takes $q^2 \to -\infty$. Relativistic quark models such as Refs. [49,52,53], include all relativistic effects from the start, instead of treating them as corrections. An important aspect of the transition form factors in these decays, is that their q^2-dependence may not be trivial. The widely used assumption of monopole behavior

$$F(q^2) = \frac{F(0)}{1 - q^2/M_*^2}\,, \tag{7.50}$$

where $F(q^2)$ is a given form factor and M_* is the mass of a nearby resonance, may receive large corrections in heavy-to-light transitions. This is not the case in D and $B \to D^{(*)}\ell\nu$ decays, where the energy release is small compared to the mass gap to heavier resonances, and the nearest (or single) pole approximation is good. In $B \to$ light transitions the form factors are sensitive to the influence of additional resonances at high recoil. In fact, a sum rule for the resonance contributions can be derived [54] once the asymptotic behavior in the $q^2 \to -\infty$ limit, which is known in QCD, is imposed. This leads to a suppression of the monopole behavior in favor of a mixed q^2 dependence in agreement with QCD predictions in the appropriate limit. This also agrees with results from LCSR calculations.

In summary, the phenomenological models we consider, capture at least some of the

important physics (especially at high recoil). Until reliable lattice QCD results come on line, we can combine the model results with model independent results from HQET and LEL, as well as bounds on form factors from dispersion relations [55]. All of this taken together results in rather constrained form factors. Another strategy for reducing theoretical uncertainties, is the identification of observables which are insensitive to differences in the model predictions.

The issue with $c\bar{c}$ resonances, cuts

Rare decays receive a contribution from diagrams which contain $q\bar{q}$ loops. The $q\bar{q}$ loops can hadronize into vector mesons before decaying electromagnetically. The contribution of $c\bar{c}$ loops at q^2 values near the resonance masses, $q^2 \sim m_V^2$, where $V = J/\psi, \psi', \psi'' \ldots$ is an important background to rare decays. It contributes via $B \to K, K^*V \to K, K^*\ell^+\ell^-$. Of the six charmonium resonances [56], the dominant ones, $J/\psi(3097)$ and $\psi'(3686)$, divide the spectra naturally into three regions: a low q^2-region below the J/ψ, a mid q^2-region between the J/ψ and the ψ', and a high q^2-region above the ψ'., This is shown in Figure 7.4. The resonance regions can be included into the calculation by the parameterization given in [57] which is based on dispersion relations and experimental data on $e^+e^- \to$ hadrons. For a discussion of other approaches [35,58] see Refs. [3,59]. All methods result in a modification of the function Y in $C_9^{\rm eff}$ and rely on factorization.

Kinematic cuts in q^2 are required to allow a reliable extraction of the short distance coefficients from experimental measurements. Figures 7.4 and 7.5 show the difference between the differential decay rate for $B \to K, K^*\mu^+\mu^-$ with and without inclusion of the resonant $c\bar{c}$ states. The lower curves only include non-resonant (or pure short distance) contributions, while the upper curves also include the contribution from resonant $c\bar{c}$ states (according to Ref. [57]). It is clear from these figures that the low q^2-region is the preferred region for comparing theory and experiment, because this region i) receives the largest contribution to the rate and ii) is not affected by higher $c\bar{c}$ resonances.

Branching ratios and invariant dilepton mass distributions

Table 7.2 lists the non-resonant branching ratios for the various $B \to K, K^*\ell^+\ell^-$ channels in the standard model[2]. The kinematic range of the dilepton mass is $4m_\ell^2 \le q^2 < (m_B - m_{(K,K^*)})^2$. The $B \to K^*\ell^+\ell^-$ decays receive a contribution from the photon pole, $|C_7^{\rm eff}|^2/q^2$. The rate for $B \to K^*e^+e^-$ is enhanced compared to the rate for the corresponding decay into muons, because of the greater sensitivity to the photon pole in the decay into electrons. (The photon pole is absent for decays into pseudoscalar K mesons, see Figure 7.4).

The dilepton invariant mass distributions for the $B \to K, K^*\mu^+\mu^-$ decays are shown in Figures 7.4 and 7.5, respectively. Imposing the cuts $0.25\,{\rm GeV}^2 \le q^2 < 8.0\,{\rm GeV}^2$ (low q^2 region), and including the charmonium resonances according to Ref. [57] we obtain the following partially integrated standard model branching ratios: $\Delta\mathcal{B}_H$ for $B \to H\mu^+\mu^-$:

[2] More stringent experimental bounds have recently been published by CLEO [63].

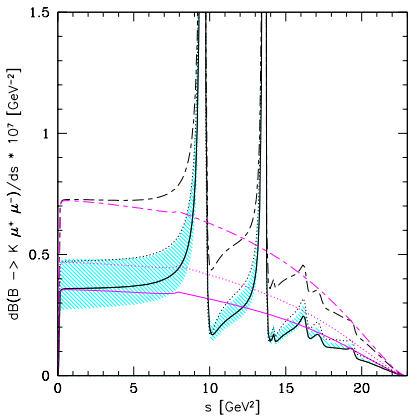

Figure 7.4: The dilepton invariant mass distribution in $B \to K\mu^+\mu^-$ decays, using the form factors from LCSR. Resonant $c\bar{c}$ states are parametrized as in Ref. [57]. The solid line represents the SM and the shaded area depicts the form-factor related uncertainties. The dotted line corresponds to the SUGRA model with $R_7 = -1.2$, $R_9 = 1.03$ and $R_{10} = 1$. The long-short dashed lines correspond to an allowed point in the parameter space of the MIA-SUSY model, given by $R_7 = -0.83$, $R_9 = 0.92$ and $R_{10} = 1.61$. The corresponding pure short-distance spectra are shown in the lower part of the plot. Figure taken from Ref. [42].

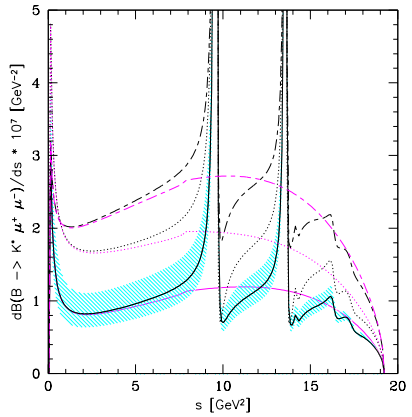

Figure 7.5: The dilepton invariant mass distribution in $B \to K^*\mu^+\mu^-$ decays. Legends are the same as in Figure 7.4. Figure taken from Ref. [42].

mode	SM branching ratio	data	Exp. reference
$b \to se^+e^-$	$8.4 \pm 2.3 \times 10^{-6}$	$< 10.1 \times 10^{-6}$	BELLE [60]
$b \to s\mu^+\mu^-$	$5.7 \pm 1.2 \times 10^{-6}$	$< 19.1 \times 10^{-6}$	BELLE [60]
$B \to Ke^+e^-$	$5.7 \pm 2.0 \times 10^{-7}$	$(0.48^{+0.32+0.09}_{-0.24-0.11}) \times 10^{-6}$	BELLE [61]
$B \to K\mu^+\mu^-$	$5.7 \pm 2.0 \times 10^{-7}$	$(0.99^{+0.40+0.13}_{-0.32-0.14}) \times 10^{-6}$	BELLE [61]
$B \to K\ell^+\ell^-$	$5.7 \pm 2.0 \times 10^{-7}$	$(0.75^{+0.25}_{-0.21} \pm 0.09) \times 10^{-6}$	BELLE [61]
$B \to K\ell^+\ell^-$	$5.7 \pm 2.0 \times 10^{-7}$	$< 0.6 \times 10^{-6}$	BABAR [62]
$B \to K^*e^+e^-$	$2.3 \pm 0.8 \times 10^{-6}$	$< 5.1 \times 10^{-6}$	BELLE [60]
$B \to K^*\mu^+\mu^-$	$1.9 \pm 0.7 \times 10^{-6}$	$< 3.0 \times 10^{-6}$	BELLE [60]

Table 7.2: Current status of rare semileptonic B decays. SM branching ratios are taken from [25,42], and upper bounds are given at 90% C.L.

$\Delta\mathcal{B}_K = 2.90 \times 10^{-7}$ and $\Delta\mathcal{B}_{K^*} = 7.67 \times 10^{-7}$. The theoretical uncertainty in these branching fractions has been estimated to be $\pm 30\%$ [42].

For comparison, in a generic non-standard model scenario, choosing $C_7^{\rm eff} = -C_7^{\rm eff}|_{SM}$ and C_9, C_{10} equal to their standard model values, we obtain $\Delta\mathcal{B}_K = 3.63 \times 10^{-7}$ and $\Delta\mathcal{B}_{K^*} = 13.09 \times 10^{-7}$. The enhancement results from constructive interference of $C_7^{\rm eff}$ with C_9.

The Forward-Backward Asymmetry $A_{FB}(q^2)$

As discussed in Sec. 7.1.2.2, the forward-backward asymmetry of the leptons in inclusive $b \to s\ell^+\ell^-$ provides a means of measuring the Wilson coefficients C_7, C_9 and C_{10}. The latter two may be sensitive to different aspects of the physics at short distances and disentangling their contributions, as well as the sign of C_7, will result in additional constraints on New Physics.

In this section we discuss the forward-backward asymmetry for exclusive decays. In addition to the branching ratios and the decay distributions, exclusive decays to vector mesons carry angular information sensitive to the short distance physics. Here we are concerned with the potential for cleanly extracting short distance physics from the asymmetry in exclusive modes, such as $B \to K^*\ell^+\ell^-$, $B_s \to \phi\ell^+\ell^-$, etc. In principle, one might expect that theoretical predictions for exclusive modes are much more uncertain than predictions for inclusive decays due to the presence of hadronic form factors. However, as we will discuss, the LEL relations (7.46-7.47) allow for a clean determination of the Wilson coefficient $C_9^{\rm eff}$ in terms of $C_7^{\rm eff}$, through a measurement of the position of the zero of $A_{FB}(q^2)$.

The angular distribution in $B \to K^*\ell^+\ell^-$ is given by

$$\frac{d^2\Gamma}{dq^2 d\cos\theta} = \frac{G_F^2\alpha^2 |V_{tb}^* V_{ts}|^2}{768\pi^5 m_B^2} \boldsymbol{k} q^2 \Big\{ (1+\cos\theta)^2 \left[|H_+^L|^2 + |H_-^R|^2 \right] + (1-\cos\theta)^2 \left[|H_-^L|^2 + |H_+^R|^2 \right] + 2\sin^2\theta |H_0|^2 \Big\}, \quad (7.51)$$

where $\boldsymbol{k}$ is the K^* spatial momentum, and θ is the angle between the ℓ^+ and the B meson in the dilepton center-of-mass frame. The transverse helicity amplitudes in terms of the form factors take the form [65]

$$H_\alpha^L = \left[C_7 \frac{m_b\,(m_B - E_{K^*} + \eta_\alpha \boldsymbol{k})}{q^2} + \frac{C_9 - C_{10}}{2}\right](f + \eta_\alpha 2 m_B \boldsymbol{k} g)\ , \tag{7.52a}$$

$$H_\alpha^R = \left[C_7 \frac{m_b\,(m_B - E_{K^*} + \eta_\alpha \boldsymbol{k})}{q^2} + \frac{C_9 + C_{10}}{2}\right](f + \eta_\alpha 2 m_B \boldsymbol{k} g)\ , \tag{7.52b}$$

where $\alpha = +, -$, $\eta_\alpha = (1, -1)$, and E_{K^*} is the K^* energy in the B rest frame. The index α in Eqs. (7.52) refers to the $+, -$ polarizations of the K^*, and the L, R subscripts refer to left and right-handed leptons. The longitudinal helicity amplitude is described by

$$H_0^L = \frac{m_B^2}{m_{K^*}\sqrt{q^2}}\Bigg\{C_7 \frac{m_b}{q^2 m_B}\left\{f[E_{K^*}(m_B - E_{K^*}) - \boldsymbol{k}^2] + 2g\, m_B \mathbf{k}^2 (m_B - 2E_{K^*})\right\} + \frac{(C_9 - C_{10})}{2}\left[2\boldsymbol{k}^2 a_+ - \frac{E_{K^*}}{m_B} f\right]\Bigg\}\ , \tag{7.53}$$

and H_0^R is given by replacing $(C_9 - C_{10})/2$ with $(C_9 + C_{10})/2$ in Eq. (7.53).

The forward-backward asymmetry for leptons as a function of the dilepton mass squared $m_{\ell\ell}^2 = q^2$ is now defined as

$$A_{FB}(q^2) = \frac{\displaystyle\int_0^1 \frac{d^2\Gamma}{dx\,dq^2}\,dx - \int_{-1}^0 \frac{d^2\Gamma}{dx\,dq^2}\,dx}{\dfrac{d\Gamma}{dq^2}}\ , \tag{7.54}$$

where $x \equiv \cos\theta$. We can write A_{FB} in terms of the helicity amplitudes defined in Eqs. (7.52) and (7.53):[3]

$$A_{FB}(q^2) = \frac{3}{4}\,\frac{|H_-^L|^2 + |H_+^R|^2 - |H_+^L|^2 - |H_-^R|^2}{|H_-^L|^2 + |H_+^R|^2 + |H_+^L|^2 + |H_+^R|^2 + |H_0^L|^2 + |H_0^R|^2}\ . \tag{7.55}$$

As it can be seen from Eqs. (7.52) and (7.55), the asymmetry is proportional to the Wilson coefficient C_{10} and vanishes with it. Furthermore, it is proportional to a combination of $C_9^{\rm eff}$ and $C_7^{\rm eff}$ such that it has a zero in the physical region if the following condition is satisfied [38]

$$\mathrm{Re}\,[C_9^{\rm eff}] = -\frac{m_b}{q_0^2} C_7^{\rm eff}\left\{\frac{T_1}{g} + (m_B^2 - m_{K^*}^2)\,\frac{T_2}{f}\right\}\ , \tag{7.56}$$

where q_0^2 is the position of the zero of A_{FB} and all q^2-dependent quantities are evaluated at q_0^2. This relation depends on the form factors T_1 and T_2; however, it was noted in Ref. [38] that the location of the zero of the asymmetry was approximately constant in a variety of form-factor models, as shown in Figure 7.6. This is a consequence of helicity conservation of the K^* in the large energy limit in these models, arising from the relativistic treatment of quark spin.

[3] The sign of $A_{FB}(q^2)$ defined in this way will change when considering $\bar{B}^0$ or B^- decays.

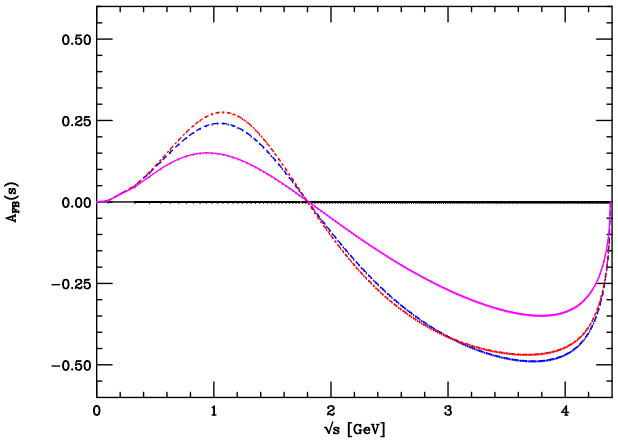

Figure 7.6: The non-resonant forward-backward asymmetry of leptons A_{FB} defined in (7.54), for $B \to K^* e^+ e^-$ as a function of the dilepton mass s, from Ref. [38]. The asymmetry is computed by making use of the semileptonic form factors from the BSW* model of Ref. [46] (solid line), the light-cone QCD sum rule calculation of Ref. [48] (dashed line) and the relativistic quark model of Ref. [49] (dot-dashed line).

The model independence of the location of the zero in the asymmetry was shown to be a consequence of the large energy limit of QCD in Ref. [42]. After we apply the HQSS and LEL relations (7.47) to (7.56) we find

$$Re[C_9^{\rm eff}] = -\frac{2 m_B m_b}{q_0^2} C_7^{\rm eff} + \ldots \tag{7.57}$$

where we have neglected the mass of the K^*, which is formally subleading.

Radiative corrections to the location of the asymmetry zero (7.57) were calculated in [40,41,44] and are at the few percent level. Ref. [44] finds the location of the zero in the SM to be

$$q_0^2 = 4.2 \pm 0.6\ \mathrm{GeV}^2 \tag{7.58}$$

where the largest uncertainty comes from the scale dependence of the Wilson coefficients and the estimate of formally subleading $O(m_{K^*}^2/m_B^2)$ terms.

We conclude that the measurement of the zero of the forward-backward asymmetry for leptons in $B \to K^* \ell^+ \ell^-$ constitutes a test of the short distance structure of the Wilson coefficients C_9 and C_7 through Eq. (7.57). It should be stressed that there are unknown nonperturbative corrections to the relation (7.57) which formally scale as $\Lambda_{\rm QCD}/E_H$, but whose size is unknown. Thus, experimental tests of LEL relations will be important in establishing the reliability and accuracy of this approach.

The Forward-Backward CP Asymmetry

The forward-backward CP asymmetry (A_{FB}^{CP}) has been proposed in Ref. [3] as an observable to probe non-standard CP violation in FCNC Z-penguins. It is defined from the forward-backward asymmetry of the previous subsection as

$$A_{FB}^{CP}(s) = \frac{A_{FB}^{(\bar{B})}(s) + A_{FB}^{(B)}(s)}{A_{FB}^{(\bar{B})}(s) - A_{FB}^{(B)}(s)} \,. \tag{7.59}$$

This definition isolates the phase of C_{10} and the effect scales in units of the phase of $C_9^{\rm eff}$, which has a CP conserving phase encoded in the function Y from the 4-Fermi operators $A_{FB}^{CP}(s) \sim (\mathrm{Im}\, C_{10}/\mathrm{Re}\, C_{10})(\mathrm{Im}\, C_9^{\rm eff}/\mathrm{Re}\, C_9^{\rm eff})$, see Ref. [3] for details. Using the high q^2 integration region above the ψ' (only here $\mathrm{Im}\, C_9^{\rm eff}$ is sizeable) $14.5\mathrm{GeV}^2 \le q^2 < (m_B - m_{K^*})^2$ yields $\Delta A_{FB}^{CP} = (0.03 \pm 0.01) \times \mathrm{Im}\, C_{10}/\mathrm{Re}\, C_{10}$. Despite the substantial uncertainties related with higher ψ''s resonances, the forward-backward CP asymmetry is a unique probe of the flavor sector, since the SM background due to CKM phases is very small $< 10^{-3}$ and ΔA_{FB}^{CP} can be sizeable in case of large CP violating phases of C_{10}.

CP asymmetries in the rate

We define a direct CP violating asymmetry distribution between the dilepton mass spectra in $\bar{B} \to \bar{H}\ell^+\ell^-$ decays and the CP conjugate process $B \to H\ell^+\ell^-$ as [69][4]

$$A_H^{CP}(s) = \frac{\dfrac{d\Gamma_{\bar{H}}^{\bar{B}}}{ds} - \dfrac{d\Gamma_H^B}{ds}}{\dfrac{d\Gamma_{\bar{H}}^{\bar{B}}}{ds} + \dfrac{d\Gamma_H^B}{ds}} \tag{7.60}$$

Here H can be a pseudoscalar or vector final state meson, for example, K or K^*. For a non-zero A_H^{CP} in the SM we have to reintroduce the CKM suppressed piece $\lambda_u(T_u - T_c)$ (see Section 7.1.1) into the amplitude, e.g. [66]. In addition to the charmonium background discussed in Section 7.1.3.3 now intermediate $u\bar{u}$ resonances ρ, ω have to be taken into account [67]. To reduce the related uncertainties one uses kinematical cuts $q^2 \gtrsim m_\rho^2, m_\omega^2$ analogous to the $c\bar{c}$ sector.

Unlike the radiative modes induced by $b \to s\gamma$ where $A_\gamma^{CP} \sim \alpha_s$ [68], the CP asymmetry in $b \to s\ell^+\ell^-$ transitions starts at the lowest order: the SM contribution to A_H^{CP} stems from interference between the weak phase and the CP conserving imaginary part of $C_9^{\rm eff}$. Both lead to very small values of A_H^{CP} in the SM: as in any $b \to s$ transition CKM structure dictates $A^{CP} \sim \mathrm{Im}\,(\lambda_u/\lambda_t) = \lambda^2\eta < 2\%$, where λ, η are Wolfenstein parameters. The second suppression comes from the strong phase $\mathrm{Im}\, Y(q^2) \ll C_9$, which holds everywhere except at $q^2 \sim m_V^2$. Integrating $A_H^{CP}(s)$ over the low q^2-region $1.4\mathrm{GeV}^2 \le q^2 < 8.4\mathrm{GeV}^2$ yields $A_{K,K^*}^{CP} \simeq 0.1\%$ in the SM [69], comparable with the findings for the inclusive $B \to X_s\ell^+\ell^-$ decays $(a_{CP})_s = -0.19^{+0.17}_{-0.19}\%$ [66], which uses different cuts ($1\mathrm{GeV}^2 \le q^2 < 6\mathrm{GeV}^2$) and a slightly different CP asymmetry (sign and normalization), see footnote 4 and Ref. [66] for details.

[4] An alternative definition is $A_H^{CP\prime}(s) = \left(\frac{d\Gamma_{\bar{H}}^{\bar{B}}}{ds} - \frac{d\Gamma_H^B}{ds}\right)/(\Gamma_{\bar{H}}^{\bar{B}} + \Gamma_H^B)$ [66,70].

Supersymmetric effects in the CP asymmetry in exclusive $B \to K, K^*\ell^+\ell^-$ decays have been studied in Refs. [69,70]. The presence of non-SM CP phases can change the sign and magnitude of A_H^{CP}: In the low q^2-region, $1.4\mathrm{GeV}^2 \le q^2 < 8.4\mathrm{GeV}^2$, the integrated asymmetry is still not large $|A_{K,K^*}^{CP}| \lesssim 1\%$ [69], but can exceed the SM asymmetry.

7.1.3.4 $B \to K^*\gamma$ and Related Decays

Exclusive radiative decays are experimentally relatively easily accessible, since their final states can be completely reconstructed. The study of these decays is well motivated as they can provide information on the ratio of CKM elements V_{td}/V_{ts}, and assist in the reduction of the theoretical error on the determination of V_{ub} from $B \to \rho\ell\nu$. In addition they are sensitive to loop effects of new interactions which may result in CP violating effects in the charge asymmetry of $B \to K^*\gamma$. Unfortunately, these transitions are also sensitive to theoretical uncertainties of two different origins. First, there is the uncertainty due to the poorly known hadronic matrix elements of the short distance operators which contribute to the rate. The second uncertainty is due to long distance contributions (see the discussion in Section 7.1.3.1). More theoretical effort is needed in this area. At present, CLEO has observed two channels [71], with the branching fractions, $B(B^0 \to K^{*0}\gamma) = (4.55\ ^{+0.72}_{-0.68} \pm 0.34) \times 10^{-5}$, $B(B^+ \to K^{*+}\gamma) = (3.76\ ^{+0.89}_{-0.83} \pm 0.28) \times 10^{-5}$, and $B(B \to K_2^*(1430)\gamma) = (1.66\ ^{+0.59}_{-0.53} \pm 0.13) \times 10^{-5}$.

As shown in Section 7.1.3.1, the short distance contribution to radiative decays depends on only one form factor, $T_1(q^2 = 0)$. This form factor has been calculated from a wide variety of theoretical approaches. A sampling of some more recent results [72] is given in Table 7.3 for the case of $B \to K^*\gamma$. The LCSR results listed there are in good agreement with the CLEO data. However, Table 7.3 also shows that there are significant differences among the theoretical predictions of the form factor $T_1^{B\to K^*}(q^2 = 0)$, and the related ratio of rates for exclusive to inclusive decays, R_{K^*}.

We note that the lattice results shown in Table 7.3 do not contain a complete analysis of all systematic errors. The calculations date back to 1994 and 1995, a time when improved actions and heavy quark methods were just being established. The results were obtained in the quenched approximation. Both calculations use pole dominance to extrapolate the form factors from the high q^2 region (where it was calculated) to the physical $q^2 = 0$ point. Both calculations are performed at heavy quark masses below the b quark mass, and they both rely on heavy quark extrapolations to obtain results for the B meson decay.

Estimates for the rates of decays into higher K^* resonances are cataloged in Ref. [73]. In the case of the $K_2^*(1430)$ mode, the CLEO data appears to favor the model of Veseli and Olsson, which predicts $B(B \to K_2^*(1430)\gamma) = (1.73 \pm 0.80) \times 10^{-5}$. We note that theoretical predictions do not yet exist for the decay $B_s \to \phi\gamma$, which is not accessible to the B factories.

Ref.	$T_1^{B\to K^*}(0)$	$\frac{T_1^{B\to K^*}(0)}{T_1^{B\to\rho}(0)}$	$B(B\to K^*\gamma)(\times 10^{-5})$	R_{K^*}
LCSR	0.32 ± 0.05	1.32 ± 0.1	4.8 ± 1.5	0.16 ± 0.05
LCSR	0.31 ± 0.04	1.14 ± 0.02	4.45 ± 1.13	0.16 ± 0.05
LCSR	0.38 ± 0.06	1.33 ± 0.13	$--$	0.20 ± 0.06
LQCD	$0.10 \pm 0.01 \pm 0.3$	$--$	$--$	$0.060 \pm 0.012 \pm 0.034$
LQCD	$0.16^{+0.02}_{-0.01}$	$--$	$--$	$0.16^{+0.04}_{-0.03}$

Table 7.3: Form-factor predictions from Ref. [72]. LCSR denotes calculations based on light-cone sum rules, and LQCD denotes calculations based on lattice QCD.

We can determine the ratio of CKM elements, V_{td}/V_{ts} from the ratio of exclusive decay rates,

$$\frac{\Gamma(B\to\rho\gamma)}{\Gamma(B\to K^*\gamma)} = \Phi\frac{|T_1^{B\to\rho}(0)|^2}{|T_1^{B\to K^*}(0)|^2}\frac{|V_{td}|^2}{|V_{ts}|^2}\,. \tag{7.61}$$

Φ is a phase space factor. The ratio of form factors in Eq. (7.61), $T_1^{B\to\rho}(0)/T_1^{B\to K^*}(0)$, is mostly sensitive to SU(3) breaking effects. Since other theoretical uncertainties are likely to cancel, the ratio may be more accurately calculated than the form factors themselves.

Eq. (7.61) assumes that the decay rates are dominated by contributions from the short distance operator. This is the case for $B\to K^*\gamma$, where long distance effects have been estimated to be no more than $\simeq 5\%$ [74,75], and where the theoretical estimates of R_{K^*} are tend to be consistent with experiment. However, the long distance contributions to $B\to\rho\gamma$ can be large [75,76] and can potentially destroy the validity of Eq. (7.61), since they have a different CKM dependence. These contributions arise from (i) the decay $B\to\rho V^*$ (which is due to the contributions of internal c- and u-quark loops) with the subsequent conversion of the neutral vector meson V^* to a photon, (ii) weak annihilation and W exchange diagrams with subsequent γ radiation, and (iii) final state interactions. If these these effects are included, the resulting theoretical error in determinations of V_{td} from Eq. (7.61) has been estimated to be $\sim 35\%$ [75].

Finally, we consider the radiative baryon decay, $\Lambda_b\to\Lambda\gamma$. This decay is well suited for the hadron collider environment, and has an estimated Standard Model branching ratio of $B(\Lambda_b\to\Lambda\gamma)\sim 5\times 10^{-5}$ [77,78]. Like the corresponding decays of B mesons, the underlying quark transition is $b\to s\gamma$ and described by the short distance effective Hamiltonian in Eq. (7.1). However, the spin 1/2 baryons makes more degrees of freedom accessible to experiments. In particular, one can probe the $V-A$ structure of the Standard Model and search for contributions of non-standard helicity in the FCNC dipole operator.

Measurement of final state polarization in $\Lambda_b\to(\Lambda\to\pi p)\gamma$ decays has been recently discussed in [78] along with asymmetries related to initial Λ_b polarization. This work corrected the expression for the Λ polarization asymmetry of the original work [77]. (The older calculation was not in agreement with existing calculations of general spin correlations for baryon $\to$ baryon-vector decays). Note that the Λ asymmetry observable is theoretically simple, since the amplitude into an on-shell photon involves only one form factor, which

drops out in the asymmetry [78]. The relevant single form factor can be extracted from $\Lambda_c\to\Lambda\ell\bar{\nu}_\ell$ decays using heavy quark spin and flavor symmetry [77] and can be used for an estimate of the new physics reach [78]. In addition, the long distance effects due to vector-meson dominance and weak annihilation diagrams are estimated to be small [77]. Hence, $\Lambda_b\to\Lambda\gamma$ decays is dominated by short distance physics and is particularly clean, theoretically. It offers unique opportunities to test the helicity structure of the underlying theory, but also to study CP violation [78] by comparing decays of the Λ_b and its conjugate $\bar{\Lambda}_b$.

7.1.3.5 $B_{s,d}\to\ell^+\ell^-$

The decay $B_q\to\ell^+\ell^-$, where $q=d$ or s and $\ell=e$, μ or τ, proceeds through loop diagrams and is of fourth order in the weak coupling. In the SM, the dominant contributions to this decay come from the W box and Z penguin diagrams shown in Figure 7.7. Because the

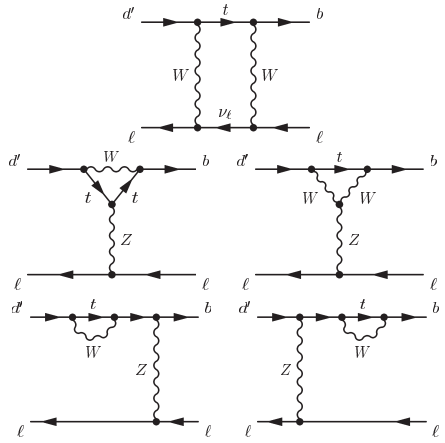

Figure 7.7: Dominant SM diagrams for $B_{s,d}\to\ell^+\ell^-$.

contributions with a top quark in the loop are dominant, at low energies of order m_b the decay can be described by a local $\bar{b}q\bar{\ell}\ell$ coupling via the effective Hamiltonian,

$$\mathcal{H}_{\rm eff} = -4\frac{G_F}{\sqrt{2}}V_{tq}^*V_{tb}\left[C_{10}O_{10}+C_SO_S+C_PO_P\right], \tag{7.62}$$

where O_{10} is given in Eq. 7.2 and the other two operators are

$$O_S = -\frac{e^2}{16\pi^2}\bar{q}_{L\alpha}b_{R\alpha}\bar{\ell}\ell, \qquad O_P = -\frac{e^2}{16\pi^2}\bar{q}_{L\alpha}b_{R\alpha}\bar{\ell}\gamma_5\ell, \tag{7.63}$$

where we have neglected contributions proportional to the q mass. The vector leptonic operator $\bar{\ell}\gamma^\mu\ell$ does not contribute for on–shell leptons because it gives zero when contracted with the B_q momentum.

The diagrams in Figure 7.7 were calculated in [79] and contribute only to the Wilson coefficient C_{10}. There is no contribution from a photonic penguin because of the photon's purely vector coupling to leptons. There are also contributions to the Wilson coefficient C_S from a SM Higgs penguin [80] and to the Wilson coefficient C_P from the would–be neutral Goldstone boson penguin [81], but these contributions to the amplitude are suppressed by a factor of m_b^2/M_W^2 relative to the dominant contributions and can be ignored. We keep C_S and C_P here for completeness because they can be significant in some extensions of the SM. A recent review may be found in [82].

The Wilson coefficients are evaluated at the high scale $\sim \mathcal{O}(M_W)$ and then run down to the low scale $\sim \mathcal{O}(m_B)$, where the hadronic matrix elements of the operators are evaluated. This running in general leads to QCD corrections enhanced by large logarithms of the ratio of scales, which must be resummed. The operator O_{10} has zero anomalous dimension because it is a $(V-A)$ quark current, which is conserved in the limit of vanishing quark masses. Thus the renormalization group evolution of C_{10} is trivial. The operators O_S and O_P have the same form as a quark mass term and thus have the anomalous dimension of a quark mass. In the SM and many extensions, C_S and C_P are proportional to m_b. Thus the running of these Wilson coefficients is properly taken into account by replacing $m_b(M_W)$ with $m_b(m_B)$ in C_S and C_P.

Evaluating the hadronic matrix elements, the resulting branching ratio is

$$\mathcal{B}(B_q \to \ell^+\ell^-) = \frac{G_F^2\alpha^2 m_{B_q}^3 \tau_{B_q} f_{B_q}^2}{64\pi^3}|V_{tb}^* V_{tq}|^2 \sqrt{1-\frac{4m_\ell^2}{m_{B_q}^2}} \times \left[\left(1-\frac{4m_\ell^2}{m_{B_q}^2}\right)\left|\frac{m_{B_q}}{m_b+m_q}C_S\right|^2 + \left|\frac{2m_\ell}{m_{B_q}}C_{10} - \frac{m_{B_q}}{m_b+m_q}C_P\right|^2\right], \quad (7.64)$$

where τ_{B_q} is the B_q lifetime, f_{B_q} is the B_q decay constant normalized according to $f_\pi = 132$ MeV, and we retain the Wilson coefficients C_S and C_P for completeness.

The SM decay amplitude is given by the Wilson coefficient [79]

$$C_{10} = -Y(x_t)/\sin^2\theta_W, \quad (7.65)$$

where $x_t = m_t^2(m_t)/M_W^2 = 4.27 \pm 0.26$ with m_t evaluated in the $\overline{\rm MS}$ scheme at $\mu = m_t$ (giving $m_t(m_t) = 166$ GeV). The function $Y(x_t)$ is given by $Y(x_t) = Y_0(x_t) + \frac{\alpha_s}{4\pi}Y_1(x_t)$ at NLO. At LO [79],

$$Y_0(x_t) = \frac{x_t}{8}\left[\frac{x_t-4}{x_t-1} + \frac{3x_t}{(x_t-1)^2}\log x_t\right] = 0.972\left[\frac{m_t(m_t)}{166\,\text{GeV}}\right]^{1.55}, \quad (7.66)$$

where we have taken the central value of x_t and parameterized the remaining m_t dependence.

As explained above, the operator O_A has zero anomalous dimension and so the QCD running of the Wilson coefficient from the electroweak scale to the B_q mass scale is trivial. Nontrivial QCD corrections first arise at NLO and require the calculation of two-loop diagrams [83,84]. The result of the two-loop calculation in the $\overline{\rm MS}$ scheme is [84]

	B_d	B_s
$\tau^+\tau^-$	$3.4^{+2.7}_{-2.0}\times 10^{-8}$	$9.2^{+1.9}_{-1.8}\times 10^{-7}$
$\mu^+\mu^-$	$1.6^{+1.3}_{-0.9}\times 10^{-10}$	$4.3^{+0.9}_{-0.8}\times 10^{-9}$
e^+e^-	$3.8^{+3.0}_{-2.2}\times 10^{-15}$	$1.0\pm 0.2\times 10^{-13}$

Table 7.4: SM branching ratios for B_d and B_s into $\tau^+\tau^-$, $\mu^+\mu^-$ and e^+e^-. The difference in the relative size of the errors in the B_d and B_s branching ratios is due primarily to the difference in the relative size of the errors in V_{td} and V_{ts}.

$$Y_1(x) = \frac{x^3+2x}{(x-1)^2}\text{Li}_2(1-x) + \frac{x^4-x^3+14x^2-2x}{2(x-1)^3}\log^2 x + \frac{-x^4-x^3-10x^2+4x}{(x-1)^3}\log x + \frac{4x^3+16x^2+4x}{3(x-1)^2} + \left[\frac{2x^2-4x}{(x-1)} + \frac{-x^3+7x^2}{(x-1)^2} + \frac{-6x^2}{(x-1)^3}\log x\right]\log\left(\frac{\mu^2}{M_W^2}\right). \quad (7.67)$$

Here μ is the renormalization scale at which the top quark mass is renormalized. Numerically, $Y_1(x_t) = 2.65$, and the NLO contributions give (taking the central value of x_t) $Y(x_t) = 1.026 \times Y_0(x_t) = 0.997$.

The SM predictions for the branching fractions are given in Table 7.4, where parameter and hadronic uncertainties have been taken into account.[5]

The uncertainties in the branching ratios are due primarily to the uncertainties in $|V_{td}|$, $|V_{ts}|$, and f_{B_q}. An additional uncertainty in the branching ratios due to scheme dependence in the definition of $\sin^2\theta_W$ is not taken into account; we estimate it to be about 8%.

7.1.4 Expectations for Physics Beyond the Standard Model

Supersymmetry

It is customary to define ratios of Wilson coefficients renormalized at a scale $\mu = m_b$

$$R_i \equiv \frac{C_i}{C_{i\,SM}} \quad (7.68)$$

parameterizing possible enhancement/decrease w.r.t. the SM Wilson coefficients. Analytical expressions of the MSSM C_i are given in [89], [90].

[5] We use the following parameters: $\alpha = 1/128$ (at M_Z), $s_W^2 = 1 - M_W^2/M_Z^2 = 0.2222$, $\bar{m}_t(m_t) = 166 \pm 5$ GeV, $m_{B_d} = 5279.4$ MeV, $m_{B_s} = 5369.6$ MeV, $\tau_{B_d} = 1.548 \pm 0.032$ ps, $\tau_{B_s} = 1.493 \pm 0.062$ ps, $|V_{tb}| = 0.999$, $|V_{td}| = 0.009 \pm 0.003$, $|V_{ts}| = 0.039 \pm 0.002$, $f_{B_d} = 208 \pm 10 \pm 11$ MeV, and $f_{B_s} = 250 \pm 10 \pm 13^{+8}_{-0}$ MeV. All numbers are taken from the PDG [86] except for f_{B_d} and f_{B_s} which are taken from Ref. [87]. For f_{B_d} and f_{B_s} the statistical and systematic errors are listed separately, and the third error for f_{B_s} comes from the uncertainty in the strange quark mass.

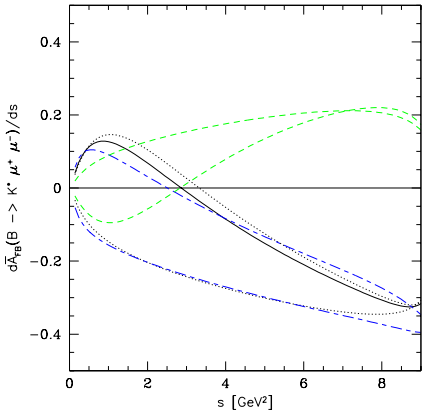

Figure 7.8: The forward-backward asymmetry in $B_d \to K^{*0}\mu\mu$ decay as a function of $s = M^2_{\mu\mu}$ predicted with the Standard Model (solid line), the SUGRA (dotted), and MIA-SUSY (long-short dashed line) [42].

Supersymmetric effects on R_7, R_9, R_{10} are studied in three scenarios [42], respecting bounds on $b \to s\gamma$ and direct searches: an effective SUSY model based on minimal flavor violation (MFV) [91], [93], where there are no extra sources of flavor violation besides the ones present already in the Yukawa couplings of the SM, a (minimal and/or relaxed) supergravity (SUGRA) scenario with universal initial conditions at the GUT scale [92] which is effectively MFV like, and a model with generic squark off-diagonal entries parametrized by the mass insertion approximation (MIA) [94].

To summarize: In MFV and SUGRA only very small deviations from the SM in $C_{9,10}$ are possible: $R_9, R_{10} \sim 1$, while $C_7^{\rm eff}$ can vary a lot. However, imposing the $b \to s\gamma$ constraint on the modulus we get $0.8 < |R_7| < 1.2$ allowing roughly for two solutions: $R_7 \sim 1$ (SM like sign) and $R_7 \sim -1$. Note that the opposite-of-the-SM-sign for $C_7^{\rm eff}$ is only possible for large $\tan\beta$ [42], [92]. Effects of non SM valued R_i in SUGRA and MIA-SUSY on the invariant mass spectra in $B \to K, K^*\mu^+\mu^-$ decays are shown in Figure 7.4 and Figure 7.5, respectively. Figure 7.8 shows a comparison of the forward-backward asymmetry in the standard model with SUGRA and MIA-SUSY models.

The MIA-SUSY scenario is one example of a model with non-standard FCNC Z-couplings [3]. Here drastic effects are possible in C_{10} [94], which at present is best constraint by $|C_{10}| < 10$ [3,42] or equivalently $|R_{10}| <$ 2-3, namely

- An enhanced $|C_{10}|$, which results in enhanced branching ratios $\mathcal{B}(b \to s\ell^+\ell^-)$
- $sign(C_{10}) = -sign(C_{10}^{\rm SM})$ causing a sign flip in the forward-backward asymmetry (see Section 7.1.3.3). This is not measurable in the rate, which is proportional to $\supset |C_{10}|^2$.

- A non zero forward-backward-CP asymmetry [3], if C_{10} has a $\mathcal{O}(1)$ phase (see Section 7.1.3.3).

All of these effects are currently not excluded, but none of them can be saturated in a MFV scenario with family universal initial conditions.

Let us put this quite strong statement into a broader context. SUSY as a realistic extension of the SM has to be broken, which is supposed to happen at energies much higher than the weak scale. Experiments in b-physics now have the power to probe the flavor structure of SUSY breaking, i.e. to discriminate between scenarios which are MFV like, and those who are not. The popular models of SUGRA, gauge mediation GMSB, anomaly mediation AMSB and the non-supersymmetric 2HDM are all MFV, but in a general MSSM this does not have to be the case. One example which is non-MFV is given in e.g. [96]. We compile some powerful observables and experimental signatures, which could decide this. MFV is ruled out, if

- $\sin 2\beta$ is small [97]
- $a_{CP}^{Dir}(B \to X_s\ell^+\ell^-) > \mathcal{O}(1)\%$ for low dilepton mass
- $A_{FB}(B \to K^*\ell^+\ell^-)$ flips sign
- $A_{FB}^{CP}(B \to K^*\ell^+\ell^-)$ is significant
- there a large 'wrong' (opposite to the SM ones) helicity contributions found e.g. in $b \to s\gamma$

Finally, at large $\tan\beta$ there can be large supersymmetric contributions to the scalar operators C_S and C_P (see Sec. 7.1.3.5) leading to large enhancements of $\mathcal{B}(B_{s,d} \to \ell^+\ell^-)$ by orders of magnitude [98].

Anomalous Triple Gauge Boson Couplings

The Triple Gauge Boson Couplings (TGC) are an important feature of the gauge sector of the SM. In principle, they may be affected by new physics coming from a scale Λ where this may be, for instance, the scale at which the dynamics responsible for electroweak symmetry breaking becomes apparent. Imposing CP conservation, the most general form of the WWN ($N = \gamma, Z$) couplings can be written as [99]

$$\mathcal{L}_{WWN} = g_{WWN}\Big\{ i\kappa_N W_\mu^\dagger W_\nu N^{\mu\nu} + ig_1^N \left(W_{\mu\nu}^\dagger W^\mu N^\nu - W_{\mu\nu} W^{\dagger\mu} N^\nu\right) + g_5^V \epsilon^{\mu\nu\rho\sigma}(W_\mu^\dagger \partial_\rho W_\nu - W_\mu \partial_\rho W_\nu^\dagger) N_\sigma + i\frac{\lambda_N}{M_W^2} W_{\mu\nu}^\dagger W_\lambda^\nu N^{\nu\lambda} \Big\}, \quad (7.69)$$

with the conventional choices being $g_{WW\gamma} = -e$ and $g_{WWZ} = -g\cos\theta$. Deviations from the SM values for the TGC are constrained directly from LEPII [100] and Tevatron [101] measurements of gauge boson production. On the other hand, FCNC decay processes at

low energies, such as loop-induced B and K decays, probe these vertices indirectly. The effects of anomalous TGC in rare B decays have been extensively studied in the literature. For instance, the effects of the dimension four anomalous $WW\gamma$ coupling $\Delta\kappa_\gamma$ in $b \to s\gamma$ transitions were first considered in [102], whereas this plus the dimension six coupling λ_γ where studied in [103,104]. These plus the corresponding CP violating couplings and their effects in the $b \to s\gamma$ branching fractions were also considered in [105]. Finally, the anomalous WWZ couplings and their effects in $b \to s\mu^+\mu^-$ were studied in Ref. [107]. In Ref. [108] the effects in $b \to s\ell^+\ell^-$ are correlated with those in $K \to \pi\nu\bar{\nu}$ decays. There it is shown that 50% deviations in these branching fractions are possible. This remains the case even after we consider the latest results from LEPII [100]. For instance, from the two-parameter fits in Ref. [100] with $\Delta\kappa_\gamma$ and Δg_1^Z, the 95% C.L. bound for Δg_1^Z is $[-0.08, 0.025]$. The largest contributions come from Δg_1^Z. This sensitivity stems from the fact that the effects induced by Δg_1^Z in rare B and K decays are logarithmically sensitive to the high energy scale Λ [108]. In addition, this kind of values for Δg_1^Z would induce an enhancement of ϵ'/ϵ [109].

Since Δg_1^Z affects almost exclusively the Wilson coefficient C_{10}, it will not change the position of the zero of the forward-backward asymmetry in $B \to K^*\ell^+\ell^-$. However, the overall value of A_{FB} will be affected.

Finally, we comment on the CP violating anomalous TGC. The main effect there comes from the dimension-four γW^+W^- coefficient $\tilde{\kappa}$. This is bound from $b \to s\gamma$ to be in the interval $(-0.60, 0.60)$. For instance, this bound translates into [108] $A_{CP}(B^\pm \to K^\pm\ell^+\ell^-) < 1\%$.

Anomalous Couplings of Fermions to SM Gauge Bosons

The new physics above the energy scale Λ may also modify the effective interactions of the SM fermions to the electroweak gauge bosons. In principle, this also has a parallel in low energy QCD, as it is pointed out in Ref. [110], where symmetry alone is not enough to determine the axial coupling of nucleons to pions. In fact, the departure of this coupling from unity is a non-universal effect, only determined by the full theory of QCD. Thus, in Ref. [110] it is suggested that in addition to the effects in the EWSB sector of the theory, it is possible that the interactions of fermions with the NGBs are affected by the new dynamics above Λ, resulting in anomalous interactions with the electroweak gauge bosons. This is particularly interesting if fermion masses are dynamically generated, as is the case with the nucleon mass. Interestingly, the proximity of the top quark mass to the electroweak scale $v = 246$ GeV, hints the possibility the top mass might be a dynamically generated "constituent" mass. Thus, it is of particular interest to study the couplings of third generation quarks to electroweak gauge bosons.

The anomalous couplings of third generation quarks to the W and the Z can come from dimension-four and dimension-five operators. The indirect effects of the dimension-four operators have been considered in relation to electroweak observables in Ref. [110,111], as well as the $b \to s\gamma$ transitions [112]. The constraints on dimension-five operators from electroweak physics have been studied in Ref. [113]. In Ref. [114] the effects of all dimension-four and dimension-five operators in B FCNC transitions such as $b \to s\gamma$ and $b \to s\ell^+\ell^-$ were considered.

Dimension-four Operators:
In a very general parameterization, the dimension-four anomalous couplings of third generation quarks can be written in terms of the usual physical fields as,

$$\mathcal{L}_4 = -\frac{g}{\sqrt{2}}\left[C_L\,(\bar{t}_L\gamma_\mu b_L) + C_R\,(\bar{t}_R\gamma_\mu b_R)\right] W^{+\mu} - \frac{g}{2\,c_W}\left[N_L^t\,(\bar{t}_L\gamma_\mu t_L) + N_R^t\,(\bar{t}_R\gamma_\mu t_R)\right] Z^\mu + \text{h.c.}\,, \tag{7.70}$$

where s_W (c_W) is the sine (cosine) of the weak mixing angle, θ_W. The dimension-four operators defined in Eq. (7.70) induce new contributions to the $b \to s\gamma$ and $b \to sZ$ loops as well as the box diagram. They appear in the effective Hamiltonian formulation as shifts of the Wilson coefficients $C_7(M_W)$, $C_9(M_W)$ and $C_{10}(M_W)$.

The measured $b \to s\gamma$ branching ratio imposes a stringent bound on C_R as its contribution to C_7 is enhanced by the factor m_t/m_b. This has been discussed in the literature [112], where the obtained bounds on C_R : $-0.05 < C_R < 0.01$. In principle, this appears to make C_R unnaturally small if it were to be generated by some strong dynamics at the scale Λ. However, it is possible to generate such value for C_R in a large variety of generic strongly coupled theories. For instance, the pseudo-Nambu-Goldstone Bosons (pNGBs) of Extended Technicolor (ETC) that result from the breaking of the various fermion chiral symmetries, generate at one loop a small C_R proportional to m_b [114]:

$$C_R \simeq \frac{1}{4\pi}\frac{m_b m_t}{f_\pi^2}\log\left(\frac{m_\pi^2}{m_t^2}\right). \tag{7.71}$$

This is well within experimental bounds in all ETC incarnations, and it is even smaller in modern ETC theories such as Topcolor-assisted Technicolor [115], where the top quark mass entering in (7.71) is only a few GeV. Thus, here the fact that C_R is small reflects its origin in the explicit ETC-breaking of chiral symmetry responsible for m_b. Another hint of this, is the fact that in general C_R contributes to the renormalization of the b-quark line with a term which does not vanish with m_b:

$$\Sigma(m_b) = \frac{g^2}{32\pi^2}\,C_R\,m_t\,(x-4)\,\log\left(\frac{\Lambda^2}{M_W^2}\right). \tag{7.72}$$

Thus if we take into account the potential role of chiral symmetry in suppressing C_R and we rescale this coefficient by defining $\hat{C}_R$ as

$$C_R = \frac{m_b}{\sqrt{2}v}\hat{C}_R, \tag{7.73}$$

(where $v = 246$ GeV), the rescaled bounds on $\hat{C}_R$ are $\mathcal{O}(1)$, leaving the possibility that natural values of this coefficient may still lead to deviations in these decay modes.

On the other hand, the effect in $b \to s\ell^+\ell^-$ is dominated by the coefficients C_L, N_L^t and N_R^t. In principle, these coefficients are constrained by electroweak precision measurements,

most notably $\epsilon_1 = \Delta\rho = \alpha T$ and R_b [111]. Once these constraints are taken into account, the effects in FCNC B decays [114] are below 15%.

Dimension-five Operators:
Although in principle dimension-five operators -which involve two gauge bosons or one gauge boson and one derivative- are suppressed by the new physics scale Λ, it is possible that they may have important effects in $b \to s\ell^+\ell^-$ decays. In Ref. [114] all 17 independent operators are considered. Even after the constraints from electroweak precision measurements and $b \to s\gamma$ are included 50% to 75% deviations in the branching ratios are possible.

New Physics in the Higgs Sector

The sector responsible for Electroweak Symmetry Breaking (EWSB) is the least understood aspect of the SM. The simplest picture, where one Higgs doublet gives rise to M_W and M_Z, and its Yukawa couplings to fermions give them their masses, is likely to be an effective picture only valid at low energies. Besides the extension of the Higgs sector necessary in supersymmetric theories, it is possible to imagine various more exotic scalar sectors. The simplest extension to a two-Higgs doublet sector results in three possible realizations. In the first one only one doublet gives masses to the fermions (Model I). Another possibility is that each doublet is responsible for giving masses for either the up or the down type fermions (Model II). Both these models avoid tree-level FCNCs in the scalar sector [116]. Model II is also the Higgs sector of the MSSM. Finally, the more general possibility (Model III) allows for such FCNC interactions to take place [117]. The presence of the additional scalar states will in general contribute to FCNC processes. In the case of Models I and II, this happens through the one-loop contributions of charged scalars. These have been studied extensively in the literature [118]. For instance, $b \to s\gamma$ constraints the mass of the charged Higgs in Model II to be roughly $m_{H^\pm} > 300$ GeV, almost independently of the values $\tan\beta$ [91]. For $m_{H^\pm} > 300$ GeV and large $\tan\beta$, $\mathcal{B}(B_{s,d} \to \ell^+\ell^-)$ can vary by a factor of two from its SM value in Model II [120]. The phenomenology of Model III has been studied in Ref. [119]. Experimental measurements in $b \to s\ell^+\ell^-$ modes such as $B \to K^{(*)}\ell^+\ell^-$ and $B_s \to \ell^+\ell^-$ are going to have an important impact on the parameter space of these models.

Strong Dynamics

If strong dynamics were responsible for the breaking of the electroweak symmetry at the TeV scale, there could be remnant effects at the weak scale. These could manifest as small deviations in the SM model couplings. In this case, the EWSB sector of the SM can be described by an effective Lagrangian [121] where the leading order corresponds to the SM and higher order corrections come in through higher dimensional operators, and are therefore suppressed by the scale $\Lambda \simeq \mathcal{O}(\infty)$ TeV. Among the possible effects relevant for FCNC B decays are the anomalous triple gauge boson couplings discussed in Section 7.1.4 and the anomalous couplings of fermions to SM gauge bosons of Section 7.1.4. Additionally, corrections to the Nambu-Goldstone boson (NGB) propagators lead, at next to leading order in $\mathcal{L}_{\text{eff.}}$, to non-standard four fermion operators [122]. These are constrained by measurements of $Z \to b\bar{b}$ and $B^0 - \bar{B}^0$ mixing. They also contribute at one-loop to

$b \to s$ as well as $s \to d$ transitions which were studied in Ref. [123]. Their contribution to $b \to s\gamma$ is negligible since it only starts at two loops. However, the $b \to s\ell^+\ell^-$ processes receive potentially large deviations, which are correlated with similar deviations in $K^{(+,0)} \to \pi^{(+,0)}\nu\bar{\nu}$.

Finally, many specific scenarios of strong dynamics in the EWSB sector have relatively light scalar states some of which may contribute to FCNC through loops, or even in some cases at tree level. To a large extent, the phenomenology relevant to $b \to s\ell^+\ell^-$ decay modes is similar to that of multi-Higgs models. Model-dependent specifics can be see in Ref. [124] for extended technicolor and in Ref. [125] the topcolor flavor signals were extensively studied. In most cases the power of $b \to s\gamma$ to constrain the masses and couplings of these scalar states is limited due to the possibility of cancellations. Modes such as $B \to K^*\ell^+\ell^-$ will be much more constraining.

7.2 Rare Decays: Experiment

7.2.1 Rare Decays at D0

We have investigated D0 options to study several rare B-decay processes in Run II:

- $B_d^0 \to K^{*0}\mu^+\mu^-$ decay followed by $K^{*o} \to K^\pm\pi^\mp$, with the expected combined branching ratio of 0.67 $\times 1.5\times 10^{-6}$.
- inclusive $b \to s\mu^+\mu^-$ decay with the expected SM branching ratio of 6×10^{-6}.
- exclusive $B_s^0 \to \mu^+\mu^-$ decay, with the expected SM branching ratio of 4×10^{-9}.

With its extended muon coverage and excellent muon identification, D0 can easily trigger on the semileptonic decay of B mesons into muons. In particular, we expect that the dimuon trigger, with an effective transverse momentum (p_T) threshold for individual muons of 1.5-2 GeV/c in the pseudorapidity range $|\eta^\mu| < 1.6$, will run unprescaled even at the highest luminosities. Thanks to the installation of the central and forward preshowers in Run II, D0 will also be able to trigger on low p_T dielectrons. However, because of the limited bandwidth available at the level one (10 kHz) and level two (1 kHz) of the current trigger system, the rate of low threshold lepton triggers could become unacceptable. We are protecting ourselves against this possibility by adding a level 2 trigger preprocessor using the data from the Silicon Vertex Detector (SMT). The processor will allow to trigger on events containing tracks with large impact parameters in the transversal plane, coming from the decay of B/D mesons.

Various trigger combinations and kinematic cuts have been considered to optimize selection of the rare decay processes. The expected numbers of events are quoted for an integrated luminosity of 2 fb^{-1} and the B meson production cross section normalized to $\sigma(B_d^0) = 3.2\mu b$ for $p_T^B > 6$ GeV, $|\text{y(B)}| < 1$. The combined trigger efficiency for the proposed dimuon and the single muon trigger is 55% for events with two muons with $p_T^\mu > 1.5$

GeV/c, $|\eta^\mu)| < 1.6$, and $p_T^{\mu\mu} > 5$ GeV/c. We have verified that, with these kinematic cuts, trigger efficiency is independent of the dimuon mass.

We found in our Run I analysis [129] that for the inclusive $B \to X_s\mu^+\mu^-$ decay it would be necessary to restrict the search to a limited dimuon mass range of (3.9-4.4) GeV, representing $\approx 7\%$ of the decays [130], in order to avoid the sequential decays $B \to D + \mu + X_1; D \to \mu + X_2$ and J/ψ and $\psi(2s)$ resonances. However, even in this limited dimuon mass window, we expect only 1000 signal events compared to 100,000 $Q\bar{Q} \to \mu^-\mu^+ + X$ physics background events, with muons originating from two different b quarks. Some additional kinematic cuts on the event topology and multivertex searches could improve the signal to background ratio, however, it does not seem worth the effort. There is only a limited interest in measuring the small and least theoretically known part of the dimuon mass spectrum.

The process $B_s^0 \to \mu^+\mu^-$ is also rather hopeless to measure, unless the branching ratio is boosted by some additional, non SM contributions, like Higgs doublet exchanges. We expected fewer than 5 recorded $B_s^0 \to \mu^+\mu^-$events in 2 fb^{-1} of data.

On the other hand, D0 has a fair chance to make a competitive measurement of the $B_d^0 \to K^{*0}\mu^+\mu^-$ decay, including the rate, and the decay asymmetry dependence on the dimuon mass. We have generated relevant Monte Carlo events combining the ISAJET production information with the predicted decay distributions, taken from Ref. [141]. A simple analysis of the Monte Carlo events was based on the CDF experiences from their attempt to isolate this channel in the Run I data [132,140]. Details of the investigations are described in the next sections.

7.2.1.1 Monte-Carlo Samples

This study is based on various Monte-Carlo samples generated with the ISAJET program at $\sqrt{s} = 2$ TeV, with events selected by the presence of two muons in the final state. Only a small sample of events has been processed through the current D0 event simulator, D0RECO and the current Level 1 trigger simulator. For the remaining events, the detector response was simulated using an older version of the muon trigger simulator.

The physics background is primarily due to $Q\bar{Q} \to \mu\mu X$ events, where Q stands for a c or b quark. A large sample of such events was generated with the NLO-QCD ISAJET version 7.22 in FOUR bins of p_T^b: (2–3) GeV/c, (3–5) GeV/c, (5–10) GeV/c, and (5–80) GeV/c. Only 80K events with 2 muons satisfying the acceptance cuts $p_T^\mu > 1.5$ GeV/c and $|\eta^\mu| < 2$ were kept for Geanting. We compared the p_T^b differential spectrum for all events, $d\sigma^b/dp_T^b$, to the MNR [131] prediction and renormalized the ISAJET weigths to match the MNR p_T^b and p_T^c spectra In addition, the absolute normalization of this sample was done using the CDF measurement of $b \to J/\psi$ production cross section at 1.8 TeV [133], extrapolated to the c.m. energy of 2 TeV (cross section increased by 25%). A smaller sample of $Q\bar{Q} \to \mu\mu X$, again in the p_T^b ranges from 2 GeV/c to 80 GeV/c, was generated with ISAJET 7.37 to confirm previous results.

The expected dimuon mass distribution due to $Q\bar{Q}$ production is shown in Fig. 7.9 for events with both muons satisfying the conditions $p_T^\mu > 1.5$ GeV/c and and $|\eta^\mu| < 1.6$. The dimuon mass spectrum for muons originating from different b quarks is relatively flat

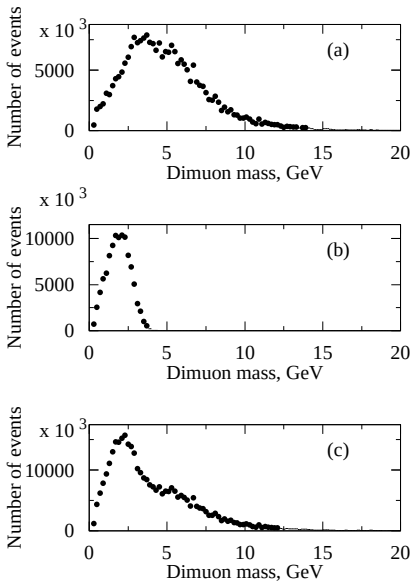

Figure 7.9: Expected number of dimuon events in 2 fb^{-1} of data, due to $Q\bar{Q}$ production, as a function of the dimuon mass for muons with $p_T^{\mu\mu} > 2.0$ GeV/c, $p_T^\mu > 1.5$ GeV/c and $|\eta^\mu| < 1.6$: (a) muons from different b quarks, (b)sequential b quark decays, and (c) total. Trigger and reconstruction efficiencies are not included. Events were generated with ISAJET V7.22 and normalized to the MNR differential p_T^Q distributions with the absolute normalization based on the measured $b \to J/\psi + X$ cross section.

between 2 GeV and 7 GeV, where the dominant process is the gluon splitting into $b\bar{b}$ pairs (Fig. 7.9 (a)). The mass spectrum resulting from sequential $b \to c \to s$ quark decays has a maximum around $m_{\mu\mu} = 2$ GeV and does not extend beyond the $m_{\mu\mu} = 4$ GeV (Fig. 7.9 (b)).

The signal samples of events were generated with ISAJET 7.37, using the leading order only and a single p_T^b bin between 2 and 80 GeV/c. ISAJET decays B_d^0 mesons into $K^*\mu^+\mu^-$ system according to the three-body phase space. Therefore ISAJET events had to be weighted to match expected decay spectra, as calculated in Ref. [141]. The event weight depends on two observables: the dimuon mass and the energy of the negative muon in the B_d^0 rest frame. We have verified that the distributions of weighted Monte Carlo events are consistent with predictions of Ref. [141]. The expected non-resonant dimuon mass distributions for the $B_d^0 \to K^{*0}\mu^+\mu^-$ process from phase space and those predicted by the theory are shown in Fig. 7.10 (a). The predicted asymmetry plot is shown in Fig. 7.10 (b).

The primary vertex position was generated at $(0,0,z_0)$, with z_0 following a Gaussian

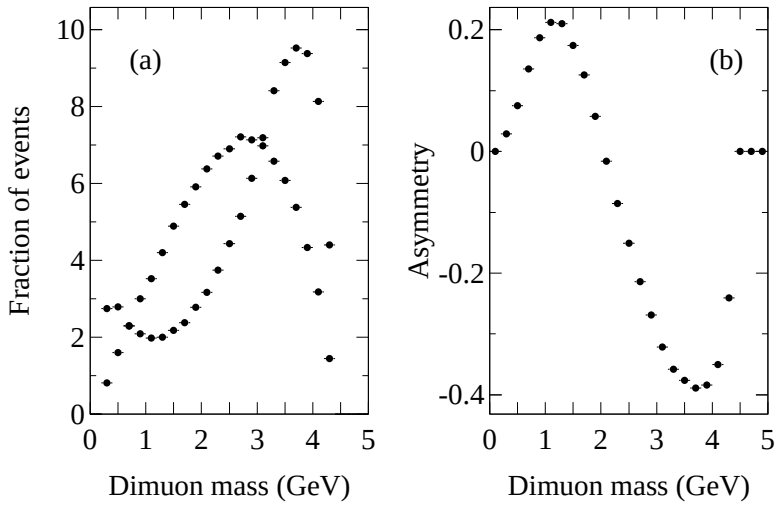

Figure 7.10: Comparison of the expected non-resonant dimuon mass distributions for the $B_d^0 \to K^{*0}\mu^+\mu^-$ process from phase space and predicted by theory (a). Predicted asymmetry as a function of dimuon mass (b).

distribution with a width of 25 cm.

The combined single muon/dimuon trigger rates at the instantaneous luminosity of 2 $10^{32} cm^{-2} s^{-1}$ due to dimuons from the genuine $Q\bar{Q}$ signal are $\approx$ 13 Hz ($\approx$ 4 Hz for $p_T^{\mu\mu} >$ 5 GeV/c). The 13 Hz combines contributions from: $c\bar{c}$ pair production (2.5 Hz), $b\bar{b}$ pair production (9.5 Hz) and $b \to J/\psi + X$ decays (1.0 Hz). A requirement of $p_T^{\mu\mu} > 2$ GeV/c reduces the rate to 9 Hz (see Chapter 4.5.2).

It turns out that there is little trigger efficiency dependence on the dimuon mass for events selected with kinematic cuts used in this analysis. This is illustrated in Fig. 7.11, where we plot results of our investigations from early 1998. Therefore, muon/dimuon trigger efficiencies for the inclusive $b \to J/\psi$ production, discussed in Chapter 4.5.3 apply to the entire $B_d^0 \to K^{*0}\mu^+\mu^-$ sample and the trigger does not significantly distort the dimuon spectrum once the kinematic cuts are introduced.

7.2.1.2 The Exclusive Channel $B_d^0 \to K^{*0}\mu^+\mu^-$

In this section we summarize results for the process $B_d^0 \to K^{*0}\mu^+\mu^-$with $K^{*o} \to \pi^\pm K^\mp$. Expected numbers of events were obtained under the following assumptions:

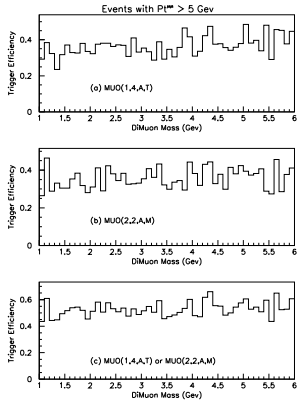

Figure 7.11: Trigger rate dependence on the dimuon mass for events preselected with kinematic cuts $|\eta^\mu| < 1.6$, $p_T^\mu > 1.5$ GeV/c and $p_T^{\mu\mu} > 5$ GeV/c. These results were obtained with the Sep. 97 version of the muon trigger simulator.

- integrated luminosity of 2 fb^{-1}
- production cross section normalized to $\sigma(B_d^0) = 3.2\mu b$ for $p_T^B > 6$ GeV, $|y(B)| < 1$. This assumption results in the predicted number of produced B_d^0 or $\bar{B}_d^0$ equal to 1.4×10^{11}, the same number as obtained assuming $\sigma_{b\bar{b}} = 100\mu$b and $B(\bar{b} \to B^0) = 0.35$ (see also Tables 6.4 and 7.8).
- B_d decay branching ratio $B(B_d^0 \to K^{*0}\mu^+\mu^-) = 1.5 \times 10^{-6}$ and $B(K^{*o} \to \pi^\pm K^\mp) = 0.67$.
- two muons with $p_T^\mu > 1.5$ GeV/c and $|\eta^\mu| < 1.6$
- dimuon pair transverse momentum $p_T^{\mu\mu} > 5.0$ GeV/c.
- Level 1 trigger efficiencies for a combined trigger L1MU(2,2,A,M) and L1MU(1,4,A,T) as discussed in Chapter 4.5.3 (Table 4.1). Level 2 and Level 3 trigger efficiencies are unknown at the time of this writing and are set to 1.0.
- track reconstruction efficiency of 95% per track (81% per event).

Analysis cuts included:

- primary - secondary vertex separation in the transverse plane of 400 μm
- charged particles from the $K^{*o} \to \pi^\pm K^\mp$ decay with transverse momenta: $p_T^{\pi(K)} > 0.5$ GeV/c and $|\eta^{\pi(K)}| < 1.6$

$p_T^{\mu\mu}$ >	5.0 GeV/c	5.0 GeV/c
p_T^{μ} >	1.5 GeV/c	3.0 GeV/c
Muon (dimuon) kinematic acceptance,ϵ_μ	0.052	0.014
Level 1 trigger efficiency, ϵ_{Lev1}	0.55	0.67
Level 2 & 3 trigger efficiency,ϵ_{Lev23}	1.00	1.00
Number of recorded events	4000	1350
$\epsilon_{analysis}$	0.17	0.22
ϵ_{reco}	0.81	0.81
Number of reco. events prior to the IP cuts	550	250
IP signif. > 2 for at least 3 tracks	490	220
IP signif. > 2 for all 4 tracks	310	130

Table 7.5: Expected numbers of events for the $B_d^0 \to K^{*0}\mu^+\mu^-$ process with different analysis cuts.

- K^{*o} transverse momentum > 2 GeV/c
- dimuon invariant mass outside the J/ψ ((3.05 − 3.15) GeV) or $\psi(2s)$ ((3.62 − 3.76) GeV) mass windows.
- isolation $I > 0.6$, where I is the transverse momentum of the B candidate divided by the scalar sum of transverse momenta of the B and all other tracks. CDF has established efficiency for this cut as 0.92 ± 0.06 [140].
- the transverse plane impact parameter significance > 2 requirement for either three out of four tracks or all four tracks from the $B_d^0 \to K^{*0}\mu^+\mu^-$ decay.

Table 7.5 lists expected event rates for various kinematic cuts. The inclusion of the $B_d^0 \to e^+e^-K^*$ decay mode could result in a 50% increase in the number of observed events.

As an illustration, the dimuon mass distribution for the reconstructed sample of 630 events is shown in Fig. 7.12(a). The minima in the distribution are due to the removal of the J/ψ and $\psi(2s)$ mass bands. A corresponding plot, assuming a 1:1 signal to background ratio, is shown in Fig. 7.12 (c). The background was distributed according to the three body phase space and its rate estimate is based on the CDF extrapolations from their run I experience. An independent MCFAST Monte Carlo background evaluation has not yet been completed.

We conclude that the number of expected events, combined with relatively modest background level, will enable D0 to establish the signal and to measure its $q^2 = m^2_{\mu\mu}$ dependence. However, the numbers quoted in Table 7.5 represent an optimistic scenario, based on the D0 nominal trigger and track reconstruction efficiencies. A reduction in the per track reconstruction efficiency from 95% to 88% (a value used by CDF) and an inclusion of a Level 2&3 trigger efficiency of 50% (the STT preprocessor - see Chapter 4.5.4) would drop the number of expected events listed in Table 7.5 by a factor of three. The clue to a

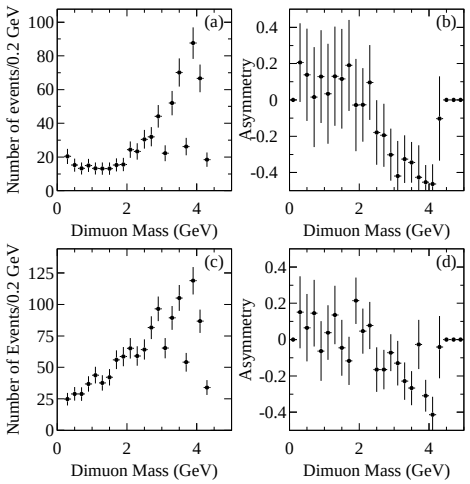

Figure 7.12: (a) Dimuon mass distribution in decay $B_d^0 \to K^{*0}\mu^+\mu^-$, and (c) assuming 1:1 signal to background ratio. (b) Predicted asymmetry signal as function of dimuon mass, and (d) assuming the background level as in (c).

successful measurement of the $B_d^0 \to K^{*0}\mu^+\mu^-$ process with the D0 detector is our claimed ability to trigger on low mass dimuons over large rapidity range.

The $B_d^0 \to K^{*0}\mu^+\mu^-$ process is expected to exhibit an asymmetry in the $cos\theta$ distribution, where θ is the μ^+ decay angle between the direction of the B_d and the direction of μ^+ in the rest frame of the $\mu^+\mu^-$ rest frame. This asymmetry manifests itself as a difference in the energy distributions of μ^+ and μ^- in the B_d rest frame, at a given dimuon mass. The asymmetry is expected to vary with the dimuon mass from approximately 0.2 at small masses to -0.4 around 3.5 GeV. The sign reversal of the asymmetry occurs at the dimuon mass of ≈ 2 GeV and turns out to be relatively model independent.

The predicted asymmetry signal as a function of the dimuon mass for the same sample of events is shown in Fig. 7.12(b). A related plot, assuming a 1:1 signal to background ratio, is shown in Fig. 7.12 (d). The observed asymmetries, corrected for the assumed background contribution are 0.13±0.13 and -0.31±0.06 for $m_{\mu\mu} < 2$ GeV and $m_{\mu\mu} > 2$ GeV, respectively.

7.2.1.3 The Inclusive Decay $B \to X_s\ell^+\ell^-$

This process, although theoretically the most interesting to measure, is very difficult to separate experimentally in hadronic collisions. The expected $\mu^+\mu^-$ spectrum due to the heavy quark production is shown in Fig. 7.13 (onia states are removed). The muons are

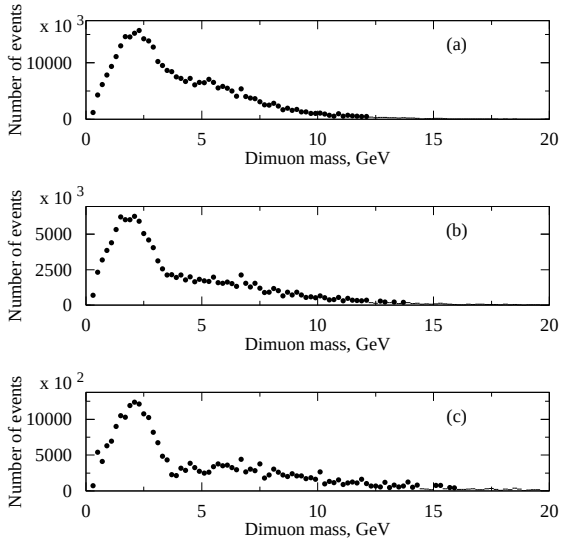

Figure 7.13: Expected dimuon mass distributions due to the non-resonant $Q\bar{Q}$ production. Both muons are required to have $p_T^\mu > 1.5$ GeV/c (3.0 GeV/c in (c)) and $\mid \eta^\mu \mid < 1.6$ and the dimuon p_T must be greater than: (a) 2 GeV/c, (b,c) 5 GeV/c. Trigger and reconstruction efficiencies are not included. Events were generated with ISAJET V7.22 and normalized to the MNR differential p_T^Q distributions with an absolute normalization based on the measured $b \to J/\psi + X$ cross section.

selected with transverse momenta greater than 1.5 GeV/c and $\mid \eta^\mu \mid < 1.6$. The mass region below 3.9 GeV is dominated by the sequential b-quark decays, for which one of the muon tracks originates from the B hadron vertex, whereas the other from the charm decay vertex. At larger masses muon pairs are produced predominantly by semi leptonic decays of b and $\bar{b}$ quarks with the $b\bar{b}$ pair resulting from a gluon splitting. Therefore the muon tracks are expected to point to two different vertices.

The expected dimuon mass spectrum for the $B \to X_s\mu^+\mu^-$ process smeared by the expected experimental resolution is shown in Fig. 7.14. The dimuon mass range (3.9 - 4.4) GeV represents only 7% of the spectrum (expected number of events is 30 % larger for (3.8 $< m_(\mu\mu) <$ 4.4) GeV). The dominant $Q\bar{Q}$ physics background could be slightly reduced by increasing the required transverse momentum of the muon pair, as shown in Fig. 7.13. Imposing kinematic cuts similar to those described for the $B_d^0 \to K^{*0}\mu^+\mu^-$ analysis leads to the expected number of events listed in the Table 7.6. The numbers are quoted for the assumed branching ratio for the $B \to X_s\mu^+\mu^-$ decay of $6{\times}10^{-6}$.

The signal is overwhelmed by the physics background, with a 1:1000 ratio. The back-

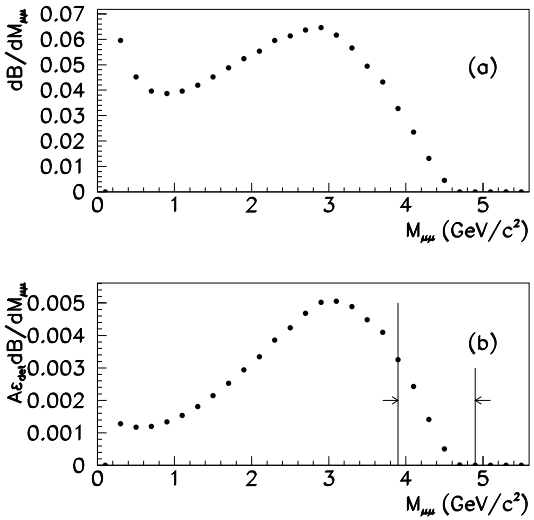

Figure 7.14: The calculated differential branching fraction for the decay $B \to X_s\mu^+\mu^-$, as a function of $m_{\mu\mu}$. (b) the same differential branching fraction modified by the response of the D0 detector. The arrows indicate the search window used in this analysis.

$p_T^{\mu\mu}$ p_T^μ	> 2.0 GeV/c > 1.5 GeV/c	> 5.0 GeV/c > 1.5 GeV/c	> 5.0 GeV/c > 3.0 GeV/c
Trigg. effic. (%)	32	55	67
Recorded	2300	1750	1000
Vtx separation cut of 400 μm	1200	1050	650
$b\bar{b}$ Bkgd (no analysis cuts)	1,900,000	400,000	100,000

Table 7.6: Expected number of recorded $B \to X_s\mu^+\mu^-$ events in the mass window $3.9 < m_{\mu\mu} < 4.4$ GeV with different analysis cuts.

$p_T^{\mu\mu}$	> 2.0 GeV/c	> 5.0 GeV/c	> 5.0 GeV/c
p_T^{μ}	> 1.5 GeV/c	> 1.5 GeV/c	> 3.0 GeV/c
Signal events after cuts	6	3	1.5

Table 7.7: Expected number of $B_s^0 \to \mu^+\mu^-$ events.

ground estimates are based on the ISAJET 7.37 version. The earlier ISAJET versions, like V7.22, predict the background level twice as large. Additional cuts on the event topology and a requirement of a common muon vertex will reduce the background by factors 3-10, not sufficient to establish the $B \to X_s\mu^+\mu^-$ signal.

7.2.1.4 The Exclusive Channel $B_s^0 \to \mu^+\mu^-$

The expected number of events for the $B_s^0 \to \mu^+\mu^-$ mode is summarized in Table 7.7. We assume that B_s mesons are produced with a rate equal to 40% of that for B_d mesons [138]. The quoted numbers are for the $B_s^0 \to \mu^+\mu^-$ branching ratio of 4×10^{-9}. The analysis cuts include: (i) the B_s isolation cut, I$>$ 0.6, (ii) the requirement that the transverse decay length in the B_s rest frame exceeds 100 μm, and an impact parameter significance for each muon track greater than 2. A 95% reconstruction efficiency per track is also assumed.

With the expected number of events there are limited chances to measure this branching ratio, unless its actual value is significantly boosted up by some non-SM processes. The background rates have not yet been estimated.

7.2.2 Rare Decays at CDF

In Run 1I CDF expects to collect a large enough b sample to observe rare b decays with branching ratios of order 10^{-6}, including $b \to s\gamma$ (radiative) decays and $b \to s\mu\mu$ decays. In this section, we describe the prospects for CDF in Run 1I for measurements in several channels: $B_{d,s} \to K^{*0}\gamma$, $\Lambda_b \to \Lambda\gamma$, $B_d \to K^{*0}\mu\mu$, and $B_{d,s} \to \mu\mu$. We will discuss trigger selections for these channels and estimates signal yields. We also study the potential to measure the forward-backward asymmetry A_{FB} in the $B_d \to K^{*0}\mu\mu$ decays and show some ideas to extract the zero position of A_{FB} as a function of $M_{\mu\mu}$.

7.2.2.1 Radiative B Meson Decays

BaBar and Belle are expected to observe approximately 20 $B \to K^*\gamma$ decays per 1 fb^{-1} of $\Upsilon(4S)$ data. Each experiment plans to obtain or order 100 fb^{-1} within 3 years (1000 $B \to K^*\gamma$). However, these projections are recently getting much better, and each experiment may obtain several 100 fb^{-1} of data by 2004. Our goal is to implement a trigger to collect of order 1000 $B \to K^*\gamma$ events during Run 1I. Our studies of radiative decays of B_s and Λ_b are unique to the Tevatron.

In Run 1, CDF included a dedicated trigger for radiative b decays, searching for a photon associated with a nearby pair of tracks [135]. In this trigger, we required two energetic oppositely-charged tracks, each with $p_T > 2$ GeV/c, in the vicinity of the photon. We collected 22.3 pb^{-1} of data in Run 1B with $E_T(\gamma) > 10$ GeV, and 6.6 pb^{-1} in Run 1C with $E_T(\gamma) > 6$ GeV and obtained upper limits on the branching fractions for B_d and B_s radiative decays to be 1.6×10^{-4} and 2.5×10^{-4}, respectively. Another search for radiative b decays used photon conversions. One of the conversion electrons was triggered with an 8 GeV threshold [136,137]. The two methods had similar acceptance after all cuts, but because it relied on tracking information to reconstruct the photon, the conversion method had superior B-mass resolution and a more straightforward analysis procedure. Also, the conversion method has a ready normalization in the kinematically similar $B^0 \to J/\psi\, K^{*0}, J/\psi \to e^+e^-$ mode.

In order to trigger on radiative B meson decays, we can take advantage of the long lifetime of b hadrons and use the SVT track processor to find charged-particle tracks significantly displaced from the beamline. We will use the same trigger selection as for semileptonic decays discussed in Section 7.5.1, requiring a 4 GeV electron associated with a track of $p_T > 2$ GeV/c found by the SVT to have an impact parameter d_0 greater than 120 μm. Furthermore, we require the angle between the electron and track to be less than 90° and the transverse mass to be less than 5 GeV/c^2. Because of the lower electron threshold, after kinematic cuts made in the Run I analysis to purify the sample, this trigger selection has about a factor of 3 greater acceptance for radiative decays than the inclusive 8 GeV electron requirement that was used in Run I but with a substantially lower trigger rate. The rate for the same-side electron plus displaced track selection is expected to be 9 Hz at a luminosity of 10^{32} cm^{-2} s^{-1}.

An estimate of the signal yield for $B_d \to K^{*0}\gamma$ is obtained by scaling the Run 1 analysis results with the ratio of the acceptances between Run 1 and Run 1I. The Run 1 analysis yield can be described as [137],

$$N(\text{Run I}) = \frac{Br(B_d \to K^{*0}\gamma)}{(4.36 \pm 1.13) \times 10^{-5}}. \tag{7.74}$$

The expected signal yield of the Run 1 analysis was 1.03 ± 0.17 events with $Br(B_d \to K^{*0}\gamma) = 4.5\times10^{-5}$. To calculate the acceptance ratio between Run 1 and Run 1I, we require all the tracks (e^+, e^-, K^+, and π^-) to have $p_T > 400$ MeV/c and to pass through the full tracking volume to ensure high resolution and reconstruction efficiency. We also require the same offline selection cuts as the Run 1 analysis ($c\tau(B) > 100$ μm and $|d_0(K,\pi)| > 4.5\sigma = 100$ μm). We correct for the improved SVX acceptance in Run II and the relative efficiencies of the Run I and Run II track processors, and we assume the SVT tracking efficiency to be 0.88 per track. We also assume the photon conversion probability before the central drift-chamber tracking volume to be 6% in Run 1 and 8% in Run 1I. Other efficiencies are assumed to cancel in the ratio. For the $B_s \to K^{*0}\gamma$ channel, we expect the branching fraction to be scaled by $|V_{td}|^2/|V_{ts}|^2 \sim 0.16$ relative to $Br(B_d \to K^{*0}\gamma)$, and the ratio of the production rates for B_s and B_d mesons is $f_s/f_s = 0.426 \pm 0.07$ [138]. Thus the expected yield is

$$N(B_s \to K^{*0}\gamma) \sim \frac{f_s}{f_d}\frac{|V_{td}|^2}{|V_{ts}|^2} N(B_d \to K^{*0}\gamma) \sim 0.07 \times N(B_d \to K^{*0}\gamma). \quad (7.75)$$

For the same-side 4 GeV electron plus displaced track selection, we expect the following signal yields after all cuts:

$$N(B_d \to K^{*0}\gamma) = (170 \pm 40) \times \frac{\int \mathcal{L}\ (\mathrm{fb}^{-1})}{2\ \mathrm{fb}^{-1}} \times \frac{Br(B_d \to K^{*0}\gamma)}{4.5 \times 10^{-5}} \quad (7.76)$$

$$N(B_s \to K^{*0}\gamma) = (12 \pm 4) \times \frac{\int \mathcal{L}\ (\mathrm{fb}^{-1})}{2\ \mathrm{fb}^{-1}} \times \frac{Br(B_d \to K^{*0}\gamma)}{4.5 \times 10^{-5}}. \quad (7.77)$$

Note that lowering the electron threshold to 3 GeV would increase the acceptance by about 50% but would lead to significantly higher trigger rates.

7.2.2.2 Radiative b Baryon Decays

Since the Λ baryon has a long lifetime ($c\tau = 8$ cm), most of the Λ decays from $\Lambda_b \to \Lambda\gamma \to p\pi ee$ events are expected to be outside of the SVX fiducial volume, so there would be a low probability for the proton from the Λ to be reconstructed by the SVT. A way to trigger on this channel is to find an electron from the conversion and find a displaced track that originates from the opposite b quark. This electron plus opposite-side displaced track selection is also described in detail in Section 7.5.1. We would require an electron with a 4 GeV threshold and a displaced track found by the SVT with $p_T > 2$ GeV/c and $d_0 > 120\,\mu$m with a large opening angle between the two ($\Delta\phi > 90°$) and transverse mass $M_T > 5\,\mathrm{GeV}/c^2$ such that the electron and track not come from the decay of a single b hadron.

The expected yield for the Run 1 $\Lambda_b \to \Lambda\gamma$ search can be summarized in terms of the acceptance as [139],

$$N(\text{Run I}) = \frac{Br(\Lambda_b \to \Lambda\gamma)}{(2.80 \pm 0.95) \times 10^{-4}}. \quad (7.78)$$

Thus the expected signal events of the Run 1 analysis is 0.16 ± 0.06 events with $Br(\Lambda_b \to \Lambda\gamma) = 4.5 \times 10^{-5}$. To calculate the acceptance ratio between Run 1 and Run 1I, we require all the tracks (e^+, e^-, p, and π^-) to have $p_T > 400$ MeV/c and pass through the full tracking volume.

In the Run 1 analysis, we required $p_T(\Lambda) > 4$ GeV/c for the Λ decays reconstructed without SVX tracks and $p_T(\Lambda) > 2$ GeV/c with $|d_0(\Lambda)| > 70$ μm for those reconstructed with SVX tracks. For the Run 1I estimate, the Λ is required to decay before the ISL (Radius < 20 cm) to improve signal purity. This allows us to lower the $p_T(\Lambda)$ threshold to 2 GeV/c. The opposite-side SVT track required to be in the tracking fiducial with $p_T > 2$ GeV/c and 120 μm $< |d_0| < 2$ mm. The signal yield with the opposite-side 4 GeV electron plus displaced-track trigger is found to be

$$N(\text{Run II}) = (5.0 \pm 2.1) \times \frac{\int \mathcal{L}\ (\mathrm{fb}^{-1})}{2\ \mathrm{fb}^{-1}} \times \frac{Br(\Lambda_b \to \Lambda\gamma)}{4.5 \times 10^{-5}}. \quad (7.79)$$

7.2.2.3 $B_d \to K^{*0}\mu\mu$ Decays

Because the trigger rate for dimuon events peaks at low $\mu\mu$ mass, to trigger on $J/\psi \to \mu^+\mu^-$ decays at high luminosity, CDF expects to impose a cut on transverse mass $2 < M_T < 4\,\mathrm{GeV}/c^2$ for J/ψ selections. However, the low-mass region is needed in the study of $B_d \to K^{*0}\mu\mu$ decays. Since the looser dimuon transverse mass window cut ($M_T < 5$ GeV/c^2) for rare decays increases the Level 2 trigger rate by about factor of 4, we need further background reductions. We plan two complementary trigger options:

- Improving muon purity by requiring one of the trigger muons to be found in the outer (CMP) muon chambers
- Requiring there to be a track of 2.0 GeV/c found to be displaced by the SVT with $|d_0| > 120\,\mu$m.

In the second case, the SVT-selected track can be one of the two muons or a hadron track. We expect the combined trigger rate for the two selections to be about 10 Hz at a luminosity of $10^{32}\,\mathrm{cm}^{-2}\,\mathrm{s}^{-1}$.

The signal yield is obtained by using the same procedure as the radiative decays. The expected yield of the Run 1 analysis can be described as [140]

$$N(\text{Run I}) = \frac{Br(B_d \to K^{*0}\mu\mu)}{(1.65 \pm 0.33) \times 10^{-6}}, \quad (7.80)$$

and the expected signal events of the Run 1 analysis is 0.91 ± 0.18 events with $Br(B_d \to K^{*0}\mu\mu) = 1.5 \times 10^{-6}$. To calculate the acceptance ratio between Run 1 and Run 1I, we make the kinematic and geometric fiducial cuts as with the radiative decays. We also require the same offline selection cut as Run 1 analysis ($L_{XY}(B) > 400$ μm and $|d_0(\mu, K, \pi)| > 2\sigma \simeq 50\,\mu$m). We correct for the increased acceptance of the muon triggers in Run II. For the dimuon + SVT trigger, we assume the SVT tracking efficiency to be 0.88 per track. Any other efficiencies are assumed to be canceled in the ratio. Thus for an assumed branching ratio of 1.5×10^{-6}, in $2\,\mathrm{fb}^{-1}$ CDF expects to observe 44 ± 9 events with the tight muon selection and 36 ± 7 events with the dimuon plus SVT selection for a combined yield of 61 ± 12 events.

Forward-Backward Asymmetry

The Forward-Backward asymmetry in the $B_d \to \mu\mu K^{*0}$ decay is defined as

$$A_{FB} = \frac{N(\cos\Theta > 0) - N(\cos\Theta < 0)}{N(\cos\Theta > 0) + N(\cos\Theta < 0)} = \frac{N_F - N_B}{N_F + N_B} \quad (7.81)$$

where Θ is the angle between the direction of the B_d and the direction of the μ^+ in the rest frame of the $\mu^+\mu^-$ system. Note that the definition for the B_d meson is the same as that for the $\overline{B}_d$ meson so flavor tagging is not necessary to measure A_{FB}. In general A_{FB} depends on the decay kinematics. Standard Model calculations predict the distribution of

A_{FB} as a function of the dimuon mass to cross the zero around $\sqrt{s} = M_{\mu\mu} = 2$ GeV/c. As discussed in Section 7.1.3.3, the A_{FB} distribution strongly depends on the $B \to K^*$ form factor; however, the zero position (M_0) is stable under various form-factor parameterizations. Figure 7.8 compares the A_{FB} distributions predicted by the Standard Model with several SUSY models. Some new physics models predict there to be no zero in the A_{FB} distribution.

Figure 7.15 shows the expected A_{FB} distributions with 50 and 400 $B_d \to K^{*0}\mu\mu$ events after all the trigger and offline requirements. The solid line in the figure corresponds to the Monte Carlo generated distribution.

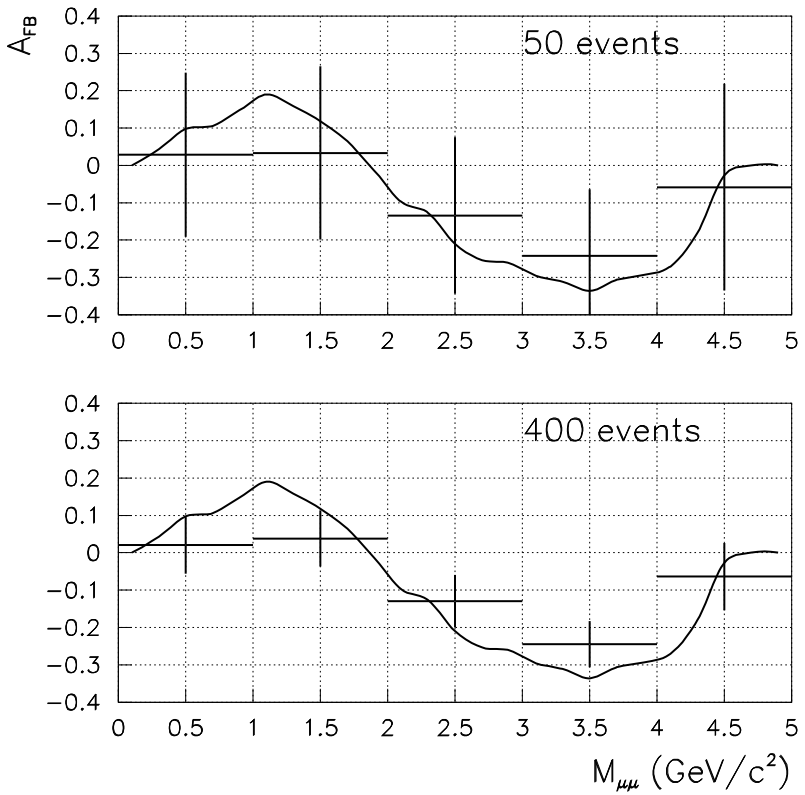

Figure 7.15: A_{FB} with 50 and 400 events of the $B_d \to K^*\mu\mu$ signal and $S/B = 1$.

Asymmetry in Background Events

Figure 7.16 shows the A_{FB} distribution as a function of $M_{\mu\mu}$ for the background, estimated from the same dataset as the Run 1 $B_d \to K^*\mu\mu$ search [140]. We define four background regions,

- non-b SR : (non-b-like B mass signal region event),
- non-b SB : (non-b-like B mass side-band event),
- B mass b SR : (b-like B mass signal region event),
- B mass b SB : (b-like B mass side-band event),

where the cuts are defined as,

- non-b-like : prompt; specifically L_{XY}, $d_0(\mu)$, $d_0(K)$, and $d_0(\pi) < 1\sigma$,
- b-like : displaced; specifically $L_{XY} > 2\sigma$, and $d_0(\mu)$, $d_0(K)$, and $d_0(\pi) > 1\sigma$,
- signal region : $|M_{B_d} - M_{\mu\mu K\pi}| < 100$ MeV/c^2,
- side-band : 100 MeV/c^2 $< |M_{B_d} - M_{\mu\mu K\pi}| < 600$ MeV/c^2.

In the above σ indicates the r.m.s. uncertainty of each quantity. There is no significant forward-backward asymmetry in any of the background samples.
.

Extraction of A_{FB} Zero Point

To extract the zero-point of the asymmetry with respect to $M_{\mu\mu}$, we define the significance of A_{FB} as

$$\mathcal{S} = \frac{N_F - N_B}{\sqrt{N_F + N_B + N_{BG}}}. \tag{7.82}$$

We define a likelihood function to extract the zero position:

$$\mathcal{L} = \mathcal{S}(M_{\mu\mu} < M) - \mathcal{S}(M_{\mu\mu} > M) = \mathcal{S}^- - \mathcal{S}^+. \tag{7.83}$$

The likelihood is expected to be maximal at a mass M_0 where $A_{FB}(M_0) = 0$. Figure 7.17 shows the A_{FB} and likelihood distributions in a Monte Carlo sample of 10000 signal events and no background events. We repeated the same analysis for the case of 50 (400) signal events and a 1:1 signal-to-background ratio under the assumption there is no background asymmetry. The results are shown in Figure 7.18. The histograms show the distribution of M_0 values for 1000 trials with signal sizes of 50 and 400 events. The points are results for a generated samples with no forward-backward asymmetry. Therefore, it appears that it will be difficult to extract the asymmetry zero point after only 2 fb^{-1} in Run IIa, but the prospects are much more promising for 15 fb^{-1} in Run IIb. However, more work needs to be done on defining an asymmetry significance.

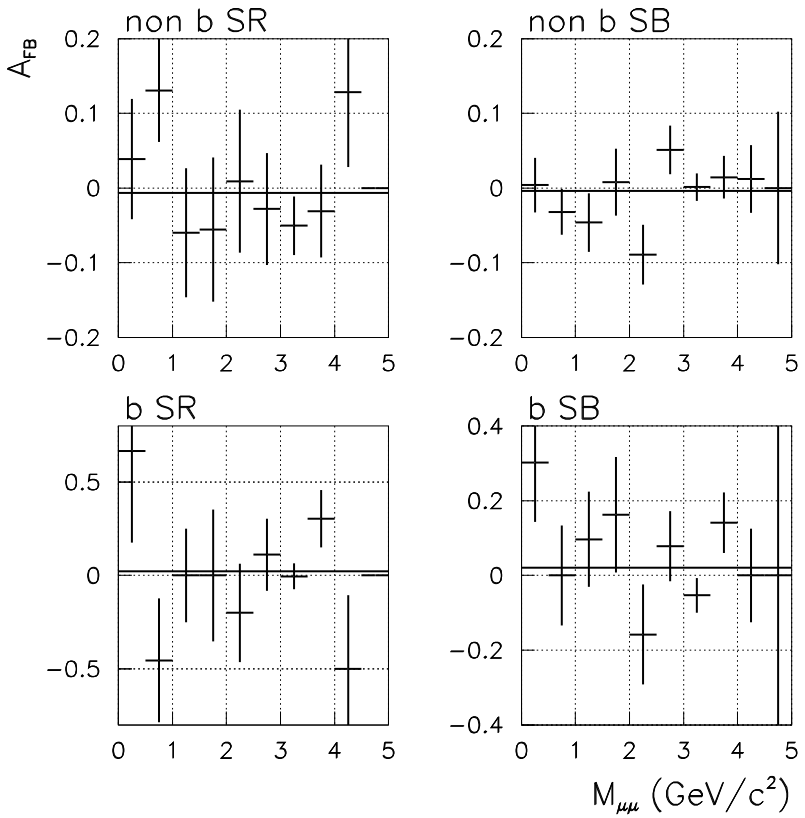

Figure 7.16: The forward-backward asymmetry for the background events obtained from the Run 1 data.

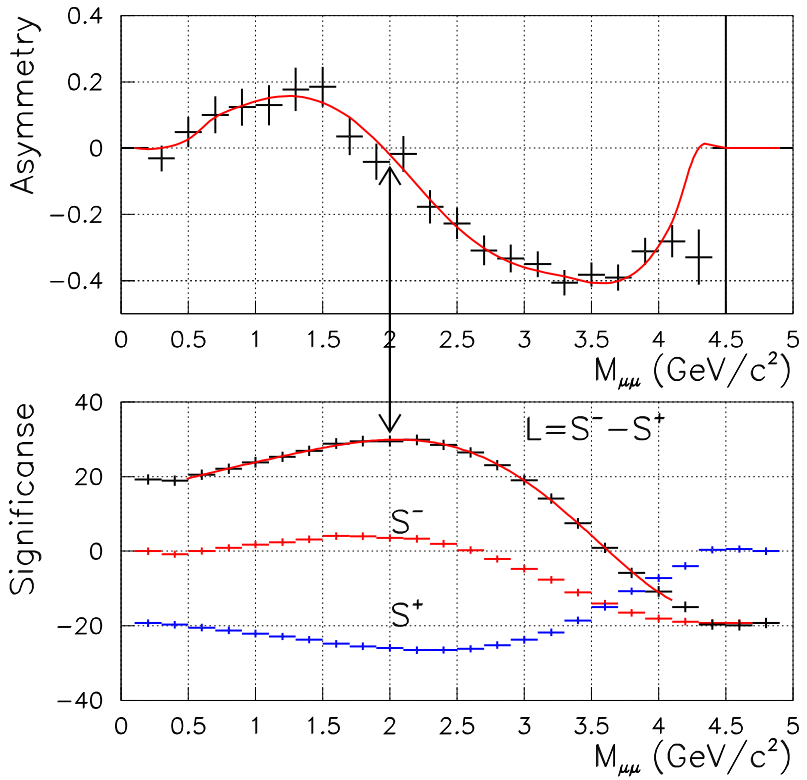

Figure 7.17: The forward-backward asymmetry in Ref [141], and a likelihood function for extracting the asymmetry zero-point M_0.

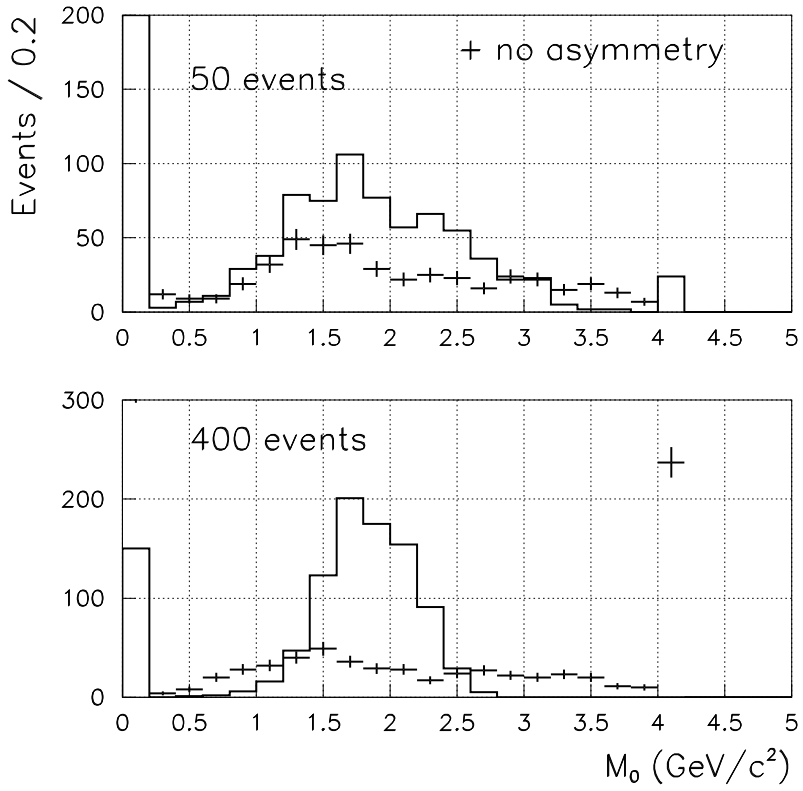

Figure 7.18: A_{FB} and M_0 with 1000 $B_d \to K^* \mu\mu$ events and $S/B = 1$.

7.2.2.4 $B \to \mu^+\mu^-$

The dimuon triggers are also useful to study the two-body decay $B_{d(s)} \to \mu^+\mu^-$. Since the Standard Model predicts the branching fraction of $B_d \to \mu^+\mu^-$ to be much lower than the reach of CDF in Run II, we give an expected "single-event sensitivity" instead of the signal yield. Single-event sensitivity is defined as branching ratio for which we would expect to observe one event in $2\,\text{fb}^{-1}$.

The sensitivity is obtained by using the same procedure as the $B_d \to \mu\mu K^{*0}$ decays. The result of the Run 1 analysis is [140], b

$$\mathcal{S}(B_d \to \mu\mu) = (2.0 \pm 0.5) \times 10^{-7} \tag{7.84}$$
$$\mathcal{S}(B_s \to \mu\mu) = (6.0 \pm 1.6) \times 10^{-7}. \tag{7.85}$$

The Run 1I expectation is obtained by scaling the Run 1 sensitivity for the same trigger selections as CDF plans to use for $B^0 \to \mu^+\mu^- K^{*0}$. Combining the results for the two trigger paths, we find the sensitivities to be

$$\mathcal{S}(B_d \to \mu\mu) = 3.5 \times 10^{-9} \times \frac{2\ \text{fb}^{-1}}{\int \mathcal{L}\ (\text{fb}^{-1})} \tag{7.86}$$
$$\mathcal{S}(B_s \to \mu\mu) = 1.0 \times 10^{-8} \times \frac{2\ \text{fb}^{-1}}{\int \mathcal{L}\ (\text{fb}^{-1})}. \tag{7.87}$$

Given the Standard module prediction B_d and B_s branching fractions of 1.5×10^{-10} and 3.5×10^{-9} respectively, we would expect a few $B_s \to \mu\mu$ signal in $15\ \text{fb}^{-1}$ of Run IIb.

7.2.2.5 Summary

We have examined the sensitivity of Run 1I CDF for the four rare-decay modes $B_d(s) \to K^{*0}\gamma$, $\Lambda_b \to \Lambda\gamma$, $B_d \to K^{*0}\mu\mu$, and $B_d(s) \to \mu\mu$. The expected signal yields are obtained by scaling the results of the Run 1 analyses:

$$N(B_d \to K^{*0}\gamma) = (170 \pm 50) \times \frac{\int \mathcal{L}}{2\ \text{fb}^{-1}} \times \frac{Br(B_d \to K^{*0}\gamma)}{4.5 \times 10^{-5}}, \tag{7.88}$$
$$N(B_s \to K^{*0}\gamma) = (12 \pm 4) \times \frac{\int \mathcal{L}}{2\ \text{fb}^{-1}} \times \frac{Br(B_d \to K^{*0}\gamma)}{4.5 \times 10^{-5}}, \tag{7.89}$$
$$N(\Lambda_b \to \Lambda\gamma) = (4.0 \pm 1.7) \times \frac{\int \mathcal{L}}{2\ \text{fb}^{-1}} \times \frac{Br(\Lambda_b \to \Lambda\gamma)}{4.5 \times 10^{-5}}, \tag{7.90}$$
$$N(B_d \to K^{*0}\mu\mu) = (59 \pm 12) \times \frac{\int \mathcal{L}}{2\ \text{fb}^{-1}} \times \frac{Br(B_d \to K^{*0}\mu\mu)}{1.5 \times 10^{-6}}, \tag{7.91}$$
$$\mathcal{S}(B_d \to \mu\mu) = 3.5 \times 10^{-9} \times \frac{2\ \text{fb}^{-1}}{\int \mathcal{L}}, \tag{7.92}$$
$$\mathcal{S}(B_s \to \mu\mu) = 1.0 \times 10^{-8} \times \frac{2\ \text{fb}^{-1}}{\int \mathcal{L}}. \tag{7.93}$$

We also studied the forward-backward asymmetry in the $B_d \to K^{*0}\mu\mu$ decay and showed some ideas to extract the zero position of the A_{FB} distribution.

7.2.3 Rare Decays at BTeV

Because the Tevatron produces more than 10^{11} b hadrons per year, we should be able to observe some of these decays and to set stringent limits on others. The precise vertexing of the BTeV silicon pixel detector will allow us to easily differentiate b decays from non-b backgrounds in the Tevatron environment. We present the expected sensitivities from studies of some of these decay channels.

7.2.3.1 The Exclusive Channel $B^0 \to K^{*0}\mu^+\mu^-$

Since we expect large backgrounds under the signal, an understanding of these backgrounds is critical to understanding our sensitivity. The various sources of background are:

- b-events where portions of the two b hadrons in the event appear to form a vertex downstream of the production point. In approximately 1% of all $b\bar{b}$ events both B hadrons decay semileptonically producing two real muons. In addition, there is a charged kaon in at least one of the b's over 90% of the time.
- Minimum bias events where three particles conspire to fake a secondary vertex and two of the particles either decay downstream of the magnet or make hadronic showers which leave a signal in the muon detector (hadron punch-through).
- Charm events with one or more real muons and kaons.
- More generally, any admixture of b, charm, minimum bias events, primary interactions and secondary decays, combined with hadronic punch-through.
- Decays from single B mesons where two charged pions fake muons.

The basic weapons to combat these backgrounds are:

- Excellent discrimination between the primary and secondary vertex, which eliminates backgrounds from minimum bias events and from the underlying event within a true b event. Tracks which are not part of the b vertex are easily rejected by requiring a non-zero vertex fit probability, as shown in Fig. 7.19(a). Also, the normalized decay length (L/σ_L), shown in Fig. 7.19(c), provides additional discrimination against background.
- Excellent mass resolution (of order 17 MeV) on the final state, as shown in Fig. 7.20.
- Excellent "point-back" resolution of the reconstructed b candidate with respect to the primary vertex. This will help to reject vertices that have been artificially pieced together from particles from the two separate b's in the event. The normalized B impact parameter (b_B/σ_{b_B}) with respect to the primary vertex is quite different for signal and background events, as shown in Fig. 7.19(b).

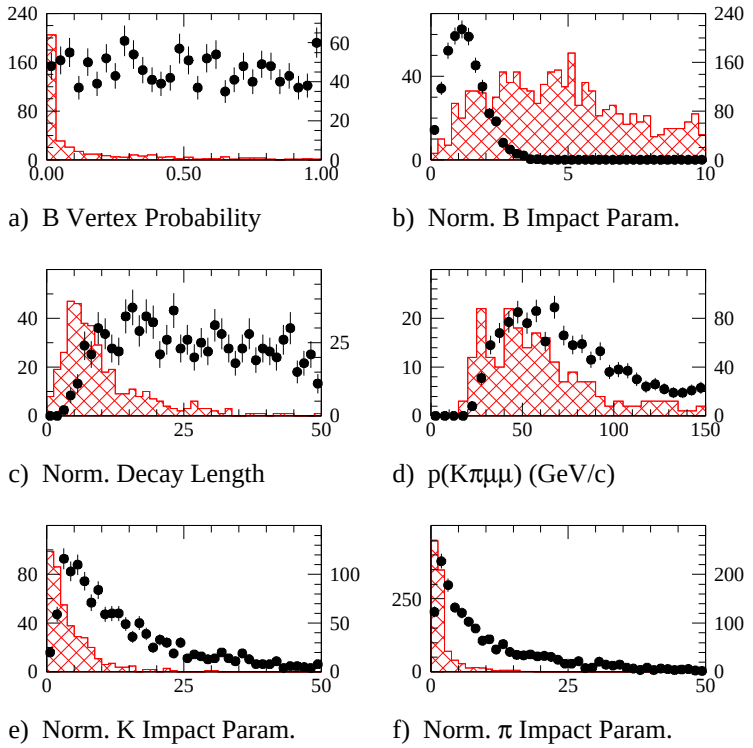

Figure 7.19: Distributions of cut variables for signal (points) and $b\bar{b}$ background (hatched) MCFAST events.

- The ability to reject combinations which include tracks that are from the primary vertex or other vertices in the event, by cutting on the impact parameter of the track with respect to that vertex. Figures 7.19(e) and (f) show the normalized impact parameter of the kaon and pion with respect to the primary vertex $(b_K/\sigma_{b_K}$ and $b_\pi/\sigma_{b_\pi})$.

In addition, the signal-to-background depends on the quality of both the muon detector and the particle identification.

$B^0 \to K^{*0}\mu^+\mu^-$ events were selected using the following criteria:

- Two muons of opposite charge, each with momentum greater than 5 GeV/c. Both muon tracks were required to have at least one hit in the muon chambers.

- K track momentum greater than 3 GeV/c. The kaon track was also required to have at least one hit in the forward drift chamber between the RICH and calorimeter. Perfect π/K separation and 100% efficiency for reconstructing the Cherenkov photons of tracks which traverse the RICH is assumed.
- Good primary vertex with probability greater than 0.01.
- Good b vertex with probability greater than 0.01.
- Decay length greater than 7σ.
- B impact parameter with respect to the primary vertex less than 2.5σ.
- K impact parameter with respect to the primary vertex greater than 2.5σ.
- π impact parameter with respect to the primary vertex greater than 2.5σ.
- B momentum greater than 20 GeV/c.
- $|m(K\pi) - m_{K^{*0}}| < 50$ MeV/c^2.
- Cut 100 MeV/c^2 about the J/ψ and ψ' nominal masses to remove regions dominated by $B \to \psi K^*$ and $B \to \psi' K^*$, which interfere with the signal.

Of 4.4 pb^{-1} of MCFAST $b\bar{b}$ background events generated (about one million events), nine pass the selection criteria. For 2 fb^{-1} of data (one year of running at a luminosity of 2×10^{32} cm^{-2} s^{-1}), this would correspond to 4090 events in the range 4.7 GeV/c^2 < $m(K\pi\mu\mu) < 5.7$ GeV/c^2, shown in Fig. 7.20. The width of the B^0 mass peak obtained from the MCFAST signal Monte Carlo sample is 17 MeV/c^2. Thus, we can expect about 280 background events from semileptonic $b\bar{b}$ decays under the B^0 mass peak, as shown in Table 7.8. Considering that we expect about 2240 signal events, this corresponds to a signal to background ratio of about 8.

We did not include the decay $B^- \to \psi K^-$ as a background. That decay is large compared to the rare decay being considered here and will interfere with the rare decay and distort the dimuon mass distribution in the vicinity of 3 GeV/c^2. This, however, is a physics contribution and will certainly be observed and studied based on a mass cut on the dimuon. In fact, this state can be used to calibrate the efficiency of the analysis and can be used as a normalization for a measurement of the relative branching fraction.

A sample of 2 fb^{-1} of signal MCFAST Monte Carlo events were generated according to the Standard Model prediction for A_{fb} and Q^2 [141]. Figure 7.21 shows the distributions of A_{fb} and number of events as a function of $m(\mu^+\mu^-)$ for this sample, after all cuts have been applied. With our estimated signal to background, we should be able to easily observe and measure the position of a zero in the asymmetry if it exists, or make a strong case for non-Standard Model physics, if it does not.

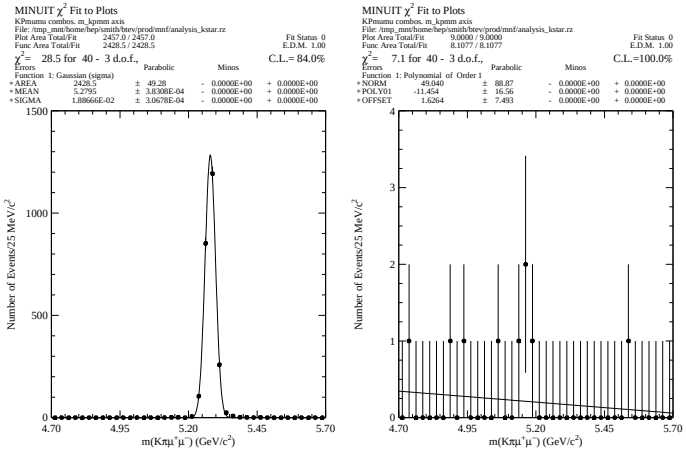

Figure 7.20: Distributions of tagged $B^0 \to K^{*0}\mu^+\mu^-$ signal (left) and 4.4 pb^{-1} of $b\bar{b}$ background (right) MCFAST events.

Integrated Luminosity	2 fb^{-1}
$b\bar{b}$ Cross Section	100μb
Number of $b\bar{b}$ Pairs Produced	2×10^{11}
$N_{B^0} + N_{\overline{B}^0}$ Produced	1.4×10^{11}
Est. $\mathcal{B}(B^0 \to K^{*0}\mu^+\mu^-)$	$(1.5 \pm 0.6) \times 10^{-6}$
$\mathcal{B}(K^{0*} \to K^+\pi^-)$	0.67
Number of Signal Events Produced	1.4×10^5
$\epsilon_{\rm trig}$	80%
$\epsilon_{\rm cuts}$	2.0%
Number of Signal Events	2240
Number of Background in Signal Box	280
Signal/Background	8

Table 7.8: Estimate of sensitivity to $B^0 \to K^{*0}\mu^+\mu^-$ for an integrated luminosity of 2 fb^{-1}. Only backgrounds from $b\bar{b}$ semileptonic decays were included in this study.

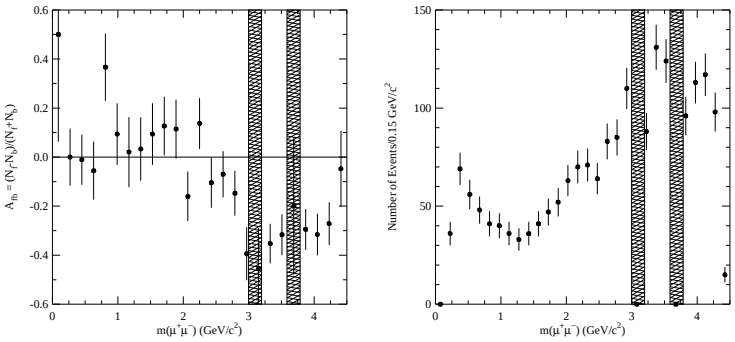

Figure 7.21: Expected forward-backward asymmetry (left) and number of events (right) as a function of $m(\mu^+\mu^-)$ for signal events after one year of running. No background is included in these plots.

7.2.3.2 The Exclusive Channel $B^+ \to K^+\mu^+\mu^-$

While the channel $B^+ \to K^+\mu^+\mu^-$ is not as rich as $B^0 \to K^{*0}\mu^+\mu^-$, in that the asymmetry A_{fb} is expected to be small within the Standard Model and beyond the Standard Model, a measurement of the decay rate is still a sensitive probe of new physics. In particular, measurement of the differential decay rate will provide input to determine the magnitude and sign of the Wilson coefficients C_7, C_9, C_{10}.

Most of the backgrounds to this channel are the same as those listed for the $B^0 \to K^{*0}\mu^+\mu^-$ analysis in Section 7.2.3.1. Events for this study were selected using nearly the same criteria as the $B^0 \to K^{*0}\mu^+\mu^-$ analysis:

- K track momentum greater than 4 GeV/c. The kaon track was also required to have at least one hit in the forward drift chamber between the RICH and calorimeter. Perfect π/K separation and 100% efficiency for reconstructing the Cherenkov photons is assumed.
- Two muons with momentum greater than 5 GeV/c. Both muon tracks were required to have at least one hit in the muon chambers.
- Good primary vertex with probability greater than 0.01.
- Good b vertex with probability greater than 0.01.
- Decay length greater than 7σ.
- B impact parameter with respect to the primary vertex less than 2.5σ.
- K impact parameter with respect to the primary vertex greater than 2.5σ.

- B momentum greater than 20 GeV/c.
- Cut 100 MeV/c^2 about the J/ψ and ψ' nominal masses to remove regions dominated by $B \to \psi K^*$ and $B \to \psi' K^*$, which interfere with the signal.

We have not simulated all sources of background. Our estimates indicate that the most serious background is from events with pairs of b's, each of which undergoes semileptonic decay. The background contribution was estimated by applying the selection criteria to a sample of 2.5 million MCFAST semileptonic $b\bar{b}$ events, corresponding to a luminosity of 10 pb^{-1}. Of these events, 41 passed the selection cuts and fall within a 1 GeV/c^2 window centered on the B^+ nominal mass. Extrapolating to an integrated luminosity of 2 fb^{-1}, we expect about 8200 events in this window. Assuming a uniform distribution across the B mass window (this is conservative, since it is actually falling, as shown in Fig. 7.22), one can expect about 560 events within the 2σ of the B^+ mass.

The overall efficiency for this state, with cuts designed to achieve good background rejection, is about 3.0%. Table 7.9 gives a calculation of the yield obtained for an integrated luminosity of 2 fb^{-1}. We include in this calculation a triggering efficiency of 80% for those events which satisfy all the analysis cuts. This is consistent with what we expect to get from the dimuon trigger (70%) 'or-ed' with the vertex trigger which recovers almost half of what the muon trigger failed to accept. The number of signal events passing the trigger and all selection criteria is approximately 1680. This gives an impressive signal-to-background ratio of 3.

The reason that BTeV can achieve excellent signal-to-background is due in a large part to a powerful particle identification system. For example, the version of the CDF detector described in the CDF II Technical Design Report [126], lacks particle identification for tracks above 1 GeV/c. So although CDF expects a signal of 100-300 $B^+ \to K^+\mu^+\mu^-$ events in Run II for that version of the detector, they would be exposed to background from all pions in the event conspiring with the muons to create background. It is unlikely that CDF's signal-to-background in Run II (0.1 in Run I) will approach that expected at BTeV. In BTeV, because of the RICH, only the kaons can contribute to the background and there are fewer of them.

7.2.3.3 The Inclusive Decay $b \to s\ell^+\ell^-$

Studies are underway to determine if the BTeV detector will provide enough background rejection to make a competitive measurement of inclusive $b \to s\ell^+\ell^-$. The method under study is similar to that used by CLEO [127] [128], in which a kaon and 0-4 pions are combined with the dilepton pair. For the purposes of this study, no neutral pion candidates are allowed in the combination.

The ability to precisely reconstruct b vertices in BTeV will be instrumental in removing combinations involving non-b daughters.

Unlike the exclusive modes, an inclusive measurement would provide a *model independent* determination of the Wilson coefficients. It is important to avoid restricting this

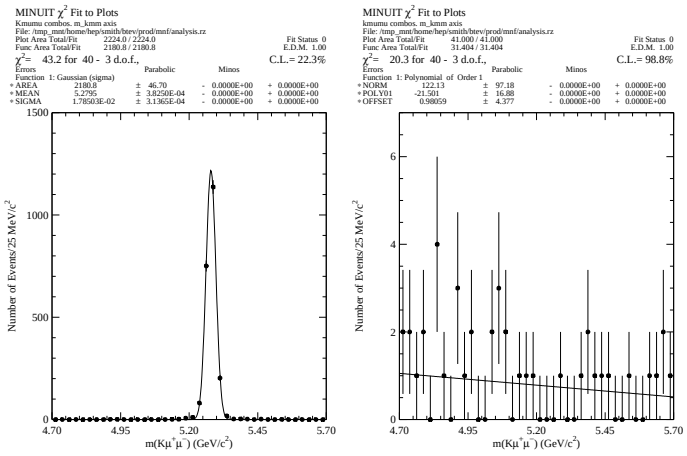

Figure 7.22: Distributions of $B^+ \to K^+\mu^+\mu^-$ signal (left) and 10 pb^{-1} of $b\bar{b}$ background (right) events.

measurement to only the high $m(\ell^+\ell^-)$ region above the ψ', as this introduces model dependence.

7.3 Summary of Rare Decays

Rare b decays provide detailed tests of the flavor structure of the SM at the loop level, and as such provide a complementary probe of new physics to that of direct collider searches. While radiative $b \to s\gamma$ decays are sensitive only to the magnitude of the Wilson coefficient C_7, the semileptonic rare decays $b \to s\ell^+\ell^-$ and the purely leptonic decays $B_{d,s} \to \ell^+\ell^-$ are sensitive to additional operators, and so further constrain new physics.

Inclusive decays are in general cleaner theoretically than exclusive, while experimentally the difficulty is in the opposite order. Because of the difficulty of inclusive measurements, theoretical techniques to handle exclusive modes in a model-independent fashion are extremely important. There has been much recent theoretical interest in the large energy limit (LEL) of QCD, which simplifies exclusive heavy-light decays in the limit that the decay products are produced at large recoil. This has particular application to $B \to K^*\ell^+\ell^-$ decays. In particular, the position of the zero in the forward-backward asymmetry in this decay has been shown to be model-independent. We look forward to additional advances in the theoretical understanding of the LEL.

In Run IIa, the radiative b decays $B_d \to K^{*0}\gamma$, $B_s \to K^{*0}\gamma$ and $\Lambda_b \to \Lambda\gamma$ are expected to be measured, while the purely leptonic decays $B_d \to \mu^+\mu^-$ and $B_s \to \mu^+\mu^-$ are not expected to be visible at the SM level. Probably the most important decay studied in this

Integrated Luminosity	2 fb^{-1}
$b\bar{b}$ Cross Section	100μb
Number of $b\bar{b}$ Pairs Produced	2×10^{11}
Number of B^+/B^- Produced	1.4×10^{11}
Est. $\mathcal{B}(B^+ \to K^+\mu^+\mu^-)$	$(4.0 \pm 1.5) \times 10^{-7}$
Number of Signal Events Produced	5.6×10^4
Trigger Efficiency	80%
Selection Cut Efficiency	3.0%
Number of Background Events in Signal Box	560
Number of Signal Events	1680
Signal/Background	3

Table 7.9: Estimate of sensitivity to $B^+ \to K^+\mu^+\mu^-$ for an integrated luminosity of 2fb^{-1}.

section for Run II is $B \to K^*\ell^+\ell^-$. While this decay should be seen at 2fb^{-1}, precision study (particularly of the zero in the forward-backward asymmetry) will require larger integrated luminosity. The inclusive measurement $b \to X_s\ell^+\ell^-$ is most easily seen for large dimuon mass (above the $\psi(2S)$), but in this region the theory breaks down, and so the measurement is of limited interest. BTeV is currently studying the feasibility of building up an inclusive measurement for lower dimuon invariant mass from exclusive measurements involving a kaon and 0-4 pions.

7.4 Semileptonic Decays: Theory

7.4.1 Introduction

Semileptonic decays have long been used to determine elements of the CKM matrix. Examples are the determination of $|V_{ud}|$ from nuclear $\beta-$decay, $|V_{us}|$ from K_{l3} decays, and $|V_{cb}|$ from $B \to D^{(*)}\ell\bar{\nu}$ [86]. In every one of these three cases a flavor symmetry (isospin, SU(3) flavor, and HQS, respectively) greatly simplifies the theoretical understanding of the hadronic matrix element in question. In the symmetry limit, and at zero recoil, current conservation ensures that the matrix element is exactly normalized. While the deviations from the symmetry limit may be difficult to calculate, they tend to be small. Hence, the overall theoretical uncertainty on the decay process is under control. Given good experimental measurements, the associated CKM element can be reliably determined.

For semileptonic decays of b flavored hadrons to light mesons flavor symmetries are not sufficient to constrain the hadronic matrix elements. Ultimately, theoretical predictions based on lattice QCD will allow for an accurate determination of $|V_{ub}|$ from measurements of exclusive decays. Currently, the best determination of $|V_{ub}|$ comes from measurements of the inclusive decay spectrum of $b \to u\ell\bar{\nu}$ [86]. However, the kinematic cuts which are necessary to eliminate the huge charm background introduce additional theoretical difficulties, similar

to those discussed in Section 7.1.2.2. As a result, theoretical uncertainties, which are not well known, currently dominate the determination of $|V_{ub}|$ [86].

It is important that the Tevatron experiments fully explore their accessible range of exclusive semileptonic B (and B_s) decays to light hadrons. While semileptonic B decays will also be measured at the B factories, the hadronic environment has the advantage that not only B meson decays but also B_s and Λ_b decays may be studied. In particular, measurements of semileptonic B_s and Λ_b decays can provide additional information on the parameters of the heavy quark and chiral expansions. For example, a measurement of the decay $\Lambda_b \to \Lambda_c \ell \bar{\nu}$, can test HQET predictions at $\mathcal{O}(1/m_{b,c})$. Measurements of B_s decays provide tests of SU(3) symmetry violations.

Since inclusive semileptonic decays are notoriously difficult to study at hadron colliders, we focus our discussion in this section on exclusive decays. In Section 7.4.2 we first review the determination of $|V_{cb}|$ from $B \to D^{(*)} \ell \bar{\nu}$ decays, and then discuss the decay $\Lambda_b \to \Lambda_c \ell \bar{\nu}$. Section 7.4.3 contains our discussion of semileptonic B decays to light hadrons.

7.4.2 Decays to Charm Flavored Final States

7.4.2.1 $B \to D^{(*)} \ell \bar{\nu}$

As discussed in Chapter 1, heavy quark symmetry allows all the form factors, which appear in semileptonic $B \to D^{(*)}$ decay, to be related, at leading order in $1/m_{b,c}$, to a single universal function, the Isgur-Wise function $\xi_(w)$. Corrections to these relations have been calculated to $\mathcal{O}(1/m_{b,c}^2)$ and $O(\alpha_s^2)$. See, for example, Ref. [142].

We can write the differential decay rate as

$$\frac{d\Gamma(B \to D^* \ell \bar{\nu})}{dw} = \frac{G_F^2 |V_{cb}|^2}{48\pi^3} (m_B - m_{D^*})^2 \, m_{D^*}^3 \sqrt{w^2-1} (w+1)^2 \times \left(1 + \frac{4w}{w+1} \frac{m_B^2 - 2w m_B m_{D^*} + m_{D^*}^2}{(m_B - m_{D^*})^2} \right) \mathcal{F}(w)^2 \tag{7.94}$$

where the corrections to the symmetry limit are included in the form factor $\mathcal{F}(w)$. At zero recoil $\mathcal{F}(1)$ coincides with the Isgur-Wise function up to perturbative and $O(1/m_{b,c}^2)$ corrections, which can be parametrized as follows [144]:

$$\mathcal{F}(1) = \eta_A \left(1 + \delta_{1/m^2} \right) . \tag{7.95}$$

η_A contains the perturbative QCD (and QED) corrections which have been calculated to $\mathcal{O}(\alpha_s^2)$ [143]. δ_{1/m^2} contains the power corrections, which start at $\mathcal{O}(1/m_{b,c}^2)$ for this case. The power corrections must be calculated from nonperturbative methods. They have have been estimated from a number of different approaches, which include non-relativistic quark models and QCD sum rules. Once the perturbative and nonperturbative corrections are included, Ref. [144] gives the value

$$\mathcal{F}(1) = 0.91 \pm 0.04 , \tag{7.96}$$

where the error is dominated by the uncertainty in the nonperturbative corrections. The uncertainty in Eq. (7.96) leads to a theoretical error on V_{cb} which is similar in size to the current experimental error. Hence, a significant reduction of the uncertainty on V_{cb} will require a more accurate theoretical calculation of $\mathcal{F}(1)$.

The $B \to D^{(*)} \ell \bar{\nu}$ transition has also been studied in lattice QCD calculations. The first calculations concentrated on the slope of the Isgur Wise function [145]. At that point, the errors on the form factors were too large to be competitive with the results shown above. Since the experimental results have to be extrapolated to zero recoil, theoretical predictions of the slope can help reduce the error associated with the extrapolation.

Ref. [146] introduces a new method based on ratios of matrix elements, which exploits heavy quark flavor symmetry to calculate the form factors at zero recoil with high precision. The ratios from which the form factors are obtained become exactly equal to unity in the flavor symmetry limit, where all errors cancel. Away from the symmetry limit, the errors are proportional to $\mathcal{F}(1) - 1$ (instead of $\mathcal{F}(1)$). As a result, as shown in Ref. [146], the statistical and systematic errors on $\mathcal{F}(1)$ are small, $2 - 3\%$. The results are obtained in the quenched approximation. Given a sufficient computational effort, the prospects for improved theoretical predictions of $\mathcal{F}(1)$ are excellent.

The form factors in semileptonic B_s decay are related to those in B decay via SU(3). The leading SU(3)-breaking chiral corrections to the Isgur-Wise function were calculated in Ref. [85].

7.4.2.2 $\Lambda_b \to \Lambda_c \ell \bar{\nu}$

Semileptonic $\Lambda_b \to \Lambda_c$ decays, which cannot be studied at the Υ(4S), not only provide an alternate means to obtain $|V_{cb}|$, but more importantly provide a test of the heavy quark expansion at subleading order.

The most general expressions for the matrix element of the vector and axial vector currents between Λ_b and Λ_c states are

$$\begin{aligned} \langle \Lambda_c(v',s') | \bar{c} \gamma^\mu b | \Lambda_b(v,s) \rangle &= \bar{u}(v',s') \left[g_1 \gamma^\mu + g_2 v^\mu + g_3 v'^\mu \right] u(v,s) \\ \langle \Lambda_c(v',s') | \bar{c} \gamma^\mu \gamma_5 b | \Lambda_b(v,s) \rangle &= \bar{u}(v',s') \left[g_1 \gamma^\mu + g_2 v^\mu + g_3 v'^\mu \right] u(v,s) \end{aligned} \tag{7.97}$$

where the states have been labelled with their four-velocities instead of their momenta, and the form factors F_i and G_i are functions of $w \equiv v \cdot v'$. At leading order in $1/m_c$ and α_s all six form factors are related to a universal form factor,

$$\begin{aligned} f_1(w) = g_1(w) = -f_2(w) = -g_2(w) = \xi_\Lambda(w) \\ f_3(w) = g_3(w) = 0 \end{aligned} \tag{7.98}$$

where $\xi_\Lambda(1) = 1 + O(\alpha_s(m_c))$.

Because the light degrees of freedom in a Λ_Q baryon are in a spin 0 state, the subleading corrections to the heavy quark limit take a simpler form than for mesons [148]. In contrast

with $B \to D^{(*)}$ decay, in which three new form functions and one constant (in addition to the Isgur-Wise function) are required to specify the form factors at $O(1/m_{b,c})$, the form factors for $\Lambda_b \to \Lambda_c$ transitions are determined at $O(1/m_{b,c})$ in terms of the Isgur-Wise function and one additional parameter,

$$\bar{\Lambda}_\Lambda = m_{\Lambda_b} - m_b + O(1/m_b^2) = m_{\Lambda_c} - m_c + O(1/m_c^2) \simeq 700\,\mathrm{MeV}. \tag{7.99}$$

Since m_b may be determined in a number of ways (such as Upsilon sum rules [150], moments of spectra in inclusive B decays [151] and lattice calculations of the $\bar{b}b$ spectrum [152]), precision measurements of the $\Lambda_b \to \Lambda_c \ell \bar{\nu}$ form factors provide a stringent test of HQET at subleading order.

Including corrections up to $O(1/m_{b,c})$ in the heavy quark expansion, the form factors (7.97) satisfy the relations [148]

$$\begin{aligned}
f_1(w) &= \left[1 + \left(\frac{\bar{\Lambda}_\Lambda}{2m_c} + \frac{\bar{\Lambda}_\Lambda}{2m_b}\right)\right] \xi_\Lambda(w), \\
f_2(w) &= g_2(w) = -\frac{\bar{\Lambda}_\Lambda}{m_c}\left(\frac{1}{1+w}\right) \xi_\Lambda(w), \\
f_3(w) &= -g_3(w) = -\frac{\bar{\Lambda}_\Lambda}{m_b}\left(\frac{1}{1+w}\right) \xi_\Lambda(w), \\
g_1(w) &= \left[1 - \left(\frac{\bar{\Lambda}_\Lambda}{2m_c} + \frac{\bar{\Lambda}_\Lambda}{2m_b}\right)\left(\frac{1-w}{1+w}\right)\right] \xi_\Lambda(w).
\end{aligned} \tag{7.100}$$

Thus, measuring the form factors in $\Lambda_b \to \Lambda_c$ decay provides a stringent test of the subleading corrections to HQET. Complete differential distributions for these decays are given in Ref. [149], including the effects of Λ_b polarization.

An important background to $\Lambda_b \to \Lambda_c$ semileptonic decay comes from Λ_b decays to excited charmed hadrons, which then decay via emission of a soft photon or pion to a Λ_c. At leading order in the heavy quark expansion this branching fraction would be predicted to be small, since the light degrees of freedom in an excited baryon are orthogonal to those in a Λ_b in the heavy quark limit, but, as discussed in Ref. [153], there are large $O(\Lambda_{\rm QCD}/m_c)$ corrections to this statement (note that because $\bar{\Lambda}$ for baryons is roughly twice that in mesons, $1/m_c$ effects are expected to be correspondingly larger in baryons). These authors considered the HQET expansion for semileptonic Λ_b decays to the spin 1/2 $\Lambda_c(2593)$ and its spin symmetry partner the spin 3/2 $\Lambda_c(2625)$. Using large N_c arguments to determine the corresponding matrix elements, they estimated the branching fraction to these two states to be

$$\frac{\Gamma(\Lambda_b \to (\Lambda_c^*(2593) + \Lambda_c^*(2625))\ell\bar{\nu}_\ell)}{\Gamma(\Lambda_b \to X\ell\bar{\nu}_\ell)} \sim 25 - 33\%. \tag{7.101}$$

Decays from excited baryons are therefore expected to provide a significant background to semileptonic $\Lambda_b \to \Lambda_c$ decay.

To date, most of the lattice QCD calculations of beauty systems have concentrated on the meson sector. Lattice QCD calculations of $\Lambda_b \to \Lambda_c l\nu$ do not yet exist. However, it should be straightforward to extend the lattice analysis of $B \to D^{(*)} l\nu$ decays described in the previous section to the baryon decay $\Lambda_b \to \Lambda_c l\nu$.

7.4.3 $B \to \pi(\rho)\ell\bar{\nu}$

The best determination of $|V_{ub}|$ comes at present from the measurements of the inclusive decay spectrum of $b \to u\ell\bar{\nu}$ [86]. However, in order to reduce the huge charm background, one has to impose kinematic cuts on the charged lepton energy, for example. Because such cuts restrict the available final state phase space, they can introduce large nonperturbative corrections in the OPE, or cause the OPE to break down entirely. Kinematic cuts in different variables, such as the hadronic invariant mass [154] or the q^2 spectrum [155], have been proposed in order to reduce the theoretical uncertainties, which currently dominate the errors on $|V_{ub}|$. This work together with improved experimental measurements of the inclusive $b \to u\ell\bar{\nu}$ decay at the B factories will lead to a better determination of $|V_{ub}|$.

Here, we explore the potential of accurate determinations of $|V_{ub}|$ via exclusive decays. In contrast to the cases discussed in the previous section, in the case of exclusive heavy hadron decays to light hadrons flavor symmetries alone do not provide sufficient constraints on the hadronic matrix elements (and form factors). Heavy quark spin and flavor symmetries and SU(3) symmetry yield relations among the form factors for $B \to \pi(\rho)\ell\bar{\nu}$, $D \to \pi(\rho)\ell\bar{\nu}$, $D \to K^{(*)}\ell\bar{\nu}$, $B \to K^{(*)}\ell^+\ell^-$, $B \to K^{(*)}\gamma$, and related B_s and D_s decays. The expected corrections to these relations vary from a few to 20 %. This is discussed in more detail in Section 7.1.3.3. If we want to get absolute predictions for the form factors, we must rely on nonperturbative methods such as lattice QCD.

A number of improved lattice QCD calculations of the exclusive semileptonic decay $B \to \pi\ell\bar{\nu}$ have recently become available [27]. At present, the uncertainties in the lattice QCD calculations are still large; the errors on the form factors are roughly $15 - 20\%$ (see Section 7.1.3.2). Reducing these theoretical errors will require a significant effort and the commitment of sufficient computational resources to such calculations. Ultimately, lattice QCD calculations will provide accurate predictions of the hadronic form factors in the high recoil momentum region. In order to use these predictions for determinations of $|V_{ub}|$, we need experimental measurements of partial differential decay rates, with matching precision.

7.5 Semileptonic Decays: Experiment

7.5.1 Semileptonic Decays at CDF

7.5.1.1 Introduction

In this report, we describe CDF's prospects for study of semileptonic decays. Specifically, we focus on the decay of the Λ_b baryon which is not produced at the e^+e^- B factories. The primary interest is total and differential decay rates. These measurements are limited by statistical uncertainties. Therefore, our studies have largely focussed on trigger strategies to optimize event yields versus trigger bandwidth. We have considered the possibility of measuring the differential decay rate $(1/\Gamma)d\Gamma/dQ^2$. Semileptonic B decay events are also useful as a control sample for study of tagging methods or as a backup sample for measuring B_s-$\overline{B}_s$ flavor oscillations. However, except for a discussion of possible trigger selections, we

leave discussion of these topics to other sections of the Workshop report.

The strategy for extracting semileptonic decay events is to take advantage of the high purity of lepton triggers as well as the significant impact parameters of B decay daughters. CDF's three-level trigger system in Run II will provide the tools necessary to maintain the trigger rate at a manageable level while maintaining a high efficiency for B-decay events. Specifically, the eXtremely Fast Tracker (XFT) will offer a significant improvement for the Run II trigger over the Run I trigger by providing tracking information in Level 1. This capability enables a track to be matched to an electromagnetic calorimeter cluster for improved electron identification or to be matched to a track segment in the muon system for better muon identification as well as a track-only trigger. In Level 2 the Silicon Vertex Tracker (SVT) will add SVX information to the XFT tracks and provide impact parameter information and thus provide the possibility of a displaced-track trigger.

7.5.1.2 Physics Goals

The semileptonic decay of heavy baryons can be described by five form factors. However, in Heavy Quark Effective Theory (HQET) these reduce to a single universal form factor in next-to-leading order. This is to be contrasted to meson decays in which the form factors reduce to a single form factor only at leading order. Measuring the differential decay rate as a function of the momentum transfer Q^2 in Λ_b decays can provide stringent tests of HQET. Because Q^2 is the mass of the lepton-neutrino pair, we must know the neutrino momentum. With the possibility of using 3D vertex reconstruction in Run 2, we can find the Λ_b direction and derive the neutrino momentum up to a quadratic ambiguity. This is described in more detail in Section 7.5.1.6 where we describe the potential for measuring the differential decay rate $(1/\Gamma)d\Gamma/dQ^2$ in $\Lambda_b \to \Lambda_c \ell\nu$ decays. In the Run I Λ_b lifetime analysis, 197 ± 25 semileptonic $\Lambda_b \to \Lambda_c l\nu$, $\Lambda_c \to pK\pi$, were partially reconstructed [156]. We use the cuts and yield from that analysis to provide a basis for Run II yields.

Semileptonic decays may also provide a good sample for measuring B_s mixing for lower values of x_s. Using semileptonic decays provides a fall-back position if the yield is high and the all-hadronic trigger can not collect enough data. Two possibilities exist for studying B_s mixing through semileptonic decay channels. The lepton may be used to tag the event and then one must fully reconstruct the away-side B_s, or Same-Side-Tagging, Jet-Charge or Soft-Lepton tagging may be used to measure x_s from the "first wiggle" in $B_s \to D_s \ell\nu X$ decays. 360 events were reconstructed in Run I in the 8 GeV inclusive lepton trigger data through the decay $B_s \to D_s \ell\nu X$ where $D_s \to \phi\pi$ or KK^{*0}. Details of the expected time resolution and x_s reach are discussed in the report of Working Group 3. Because the neutrino momentum is unknown, mixing measurement using semileptonic decays suffer from poor resolution of the decay time. The all-hadronic decay $B_s \to D_s\pi$, where $D_s \to \phi\pi$ or KK^{*0} and the B_s is fully reconstructed, offers the prospect for the greatest reach in Δm_s. Therefore, we have studied the prospect of a trigger on a tagging lepton and an opposite-side displaced track which could come from a hadronic B_s decay.

7.5.1.3 Simulations

To study the efficiency of the possible trigger selections for the signals of interest, we use a simple parametric Monte Carlo simulation to compare the Run II geometric and kinematic acceptance to that of published Run I physics analyses. We use the measured yields for normalization. In our Monte Carlo studies, we generate single b quarks according to next-to-leading-order QCD. The B hadrons that result after Peterson ($\epsilon = 0.006$) [157] fragmentation smearing are forced to decay to modes of interest using the CLEO Monte Carlo QQ [158]. To model detector performance, we apply Gaussian smearing to the generated quantities in these Monte Carlo events.

We assume that the offline track-reconstruction and analysis-cut efficiencies will be the same as in Run I. Since we determine our yields relative to Run I, we do not correct for these effects. The part of the detector and the trigger that is substantially different from Run I is the silicon detector (SVXII). We model the SVXII as 5 concentric cylinders at the mean radii of the 5 layers. We account for the gaps between silicon sensors and assume that there is an additional 2% hit inefficiency per layer.

In this study we want to compare the acceptance for decays in the reconstruction fiducial. Therefore, we require all charged particles in a final state to have transverse momentum P_T exceeding $0.5\,\mathrm{GeV}/c$ and to leave the COT drift chamber at its outside radius. Furthermore, after accounting for geometry and expected hit efficiency, we require all tracks to have hits in 4 of 5 SVX layers, and if a track is to be considered fiducial for the SVT, it must be of $P_T > 2\,\mathrm{GeV}/c$ and have hits in the 4 inner layers. We also require electrons and muons to project to the fiducial regions of the central calorimeter and muon detectors, respectively. We also model the trigger efficiencies with parameterizations.

Since the output of the trigger is dominated by backgrounds, it is not possible to determine trigger rates from pure Monte Carlo samples. Instead, we simulate the performance of the Run II trigger system using data taking Run I using trigger thresholds significantly lower than were used in normal operation and below the cuts we intend to apply in Run II. We model the performance of the Run II trigger electronics using a version of the Run II simulations modified for the Run I detector configurations. The instantaneous luminosities of the test runs correspond to 0.4 to 1.4 $\times 10^{32}\,\mathrm{cm}^{-2}\,\mathrm{s}^{-1}$ with 36-bunch operation, allowing us to model the change in trigger performance as a function of instantaneous luminosity. We correct the results for the increased muon and silicon detector acceptances.

7.5.1.4 Selection Criteria

There are various event properties that can be examined in the Level 1 and Level 2 trigger systems. Because the Level 1 bandwidth is large and there is substantial overlap with other proposed trigger selections, we propose using only a single-lepton selection in Level 1 which limits systematic effects. For Level 2, we want to take advantage of the decay properties of b hadrons, especially the long lifetime. The SVT allows us to select displaced tracks. We can also take advantage of b production and decay kinematics to select tracks associated with the lepton in the Level 2 trigger. Our proposed trigger signature is a lepton with a

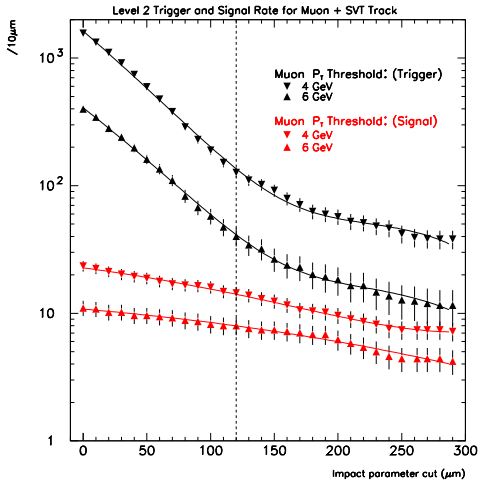

Figure 7.23: Dependence of the trigger rate on the impact parameter cut on tracks found by the SVT for the muon-trigger test data (top two curves) and the $b\bar{b} \to \Lambda_b X \to \Lambda_c \mu\nu$ Monte Carlo (bottom two curves). The vertical scale is arbitrary. The dashed line shows an impact parameter cut of 120 μm.

displaced track. Additional handles include the angle between the lepton and the displaced track found by SVT $\Delta\phi(\ell, SVT)$ and the transverse mass M_T of the lepton track pair. ($M_T^2 \simeq p_{T,1}p_{T,2}(1-\cos\Delta\phi)/c^2$) For tracks coming from the decay of a single B, we expect the angle to be small and the two-particle mass to be less than the B mass.

Figure 7.23 shows the dependence of Level 2 trigger rate on the impact parameter cut applied to tracks found by SVT in events with trigger muons for the test-run data and for the Monte Carlo simulations of the benchmark channel the $b\bar{b} \to \Lambda_b X \to \Lambda_c \mu\nu, \Lambda_c \to pK\pi$ mode. The trigger rate falls sharply with impact parameter up to about 120 μm. Above 150 μm, the decrease in trigger rate is approximately equal to that for the signal, indicating a background of real semileptonic B-decay events. Therefore cutting on impact parameter beyond 150 μm will not increase purity. For consistency with other CDF selections, we expect to cut at 120 μm. Figure 7.24 shows the distributions of $\Delta\phi$ versus transverse mass for events in test run data in which a track has been found by the SVT simulation with $|d_0| > 120\,\mu$m. Requiring $\Delta\phi < 90^\circ$ and $M_T < 5\,\mathrm{GeV}/c^2$ gives substantial background reduction without loss of the semileptonic-decay signal. For the proposed trigger selection with a $4\,\mathrm{GeV}/c$ cut on lepton momentum, we expect a trigger cross section of 53 ± 8 nb for muons and 90 ± 36 nb for electrons. At a luminosity of $10^{32}\,\mathrm{cm}^{-2}\,\mathrm{s}^{-1}$ (*i.e.* $100\,\mu\mathrm{b}^{-1}\mathrm{s}^{-1}$) this corresponds to a rate of 14 ± 4 Hz out of a total Level 2 trigger budget of 300 Hz. Note that this trigger rate is about a factor of 3 lower than would be achieved with an inclusive 8 GeV lepton sample as was used in Run I.

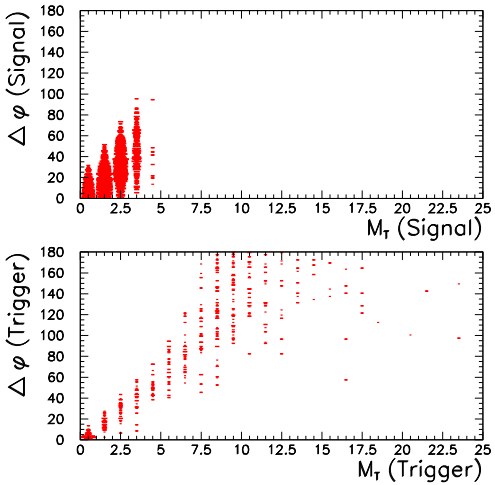

Figure 7.24: The distributions of $\Delta\phi(\mu, SVT)$, and $M_T(\mu, SVT)$ for the test-run data (bottom plot) and the $b\bar{b} \to \Lambda_b \to \Lambda_c \mu\nu$ signal (top plot) after impact parameter cut.

We have also considered the effectiveness of a trigger using a lepton and a displaced track in order to extract a sample of B decays that can be fully reconstructed and have an away-side lepton tag. Our benchmark process for this type of event is $B_s \to D_s\pi, D_s \to \phi\pi$ or KK^{*0}. As with the lepton and displaced track from the decay of a single B, the effectiveness of a cut on the impact parameter does not improve beyond $|d_0| \simeq 150\,\mu$m and is independent of the muon P_T. The $\Delta\phi(\mu, SVT)$ and M_T distributions for simulation of the benchmark process are compared to the trigger background from the simulation on the test data in Figure 7.25 after requiring $|d_0| > 120\mu$m. The requirements $\Delta\phi(\mu, SVT) > 90^\circ$ and $M_T > 5\,\mathrm{GeV}/c^2$ reduce backgrounds with only a small reduction in the singal. For the proposed trigger selection with a $4\,\mathrm{GeV}/c$ cut on lepton momentum, we expect a trigger cross section of 48 ± 8 nb for muons and 120 ± 40 nb for electrons. At a luminosity of $10^{32}\,\mathrm{cm}^{-2}\,\mathrm{s}^{-1}$ this corresponds to a rate of 16 ± 4 Hz.

7.5.1.5 Signal Rate Expectations

To complete the study, we evaluate the various trigger criteria in terms of the expected Run II event yield. Monte Carlo samples are generated for the semileptonic decays of interest and passed through the trigger scenarios. The number of Run II events expected is based on the ratio of the acceptance for the proposed Run II semileptonic triggers and the Run I semileptonic trigger scaled by acceptance and efficiency ratios.

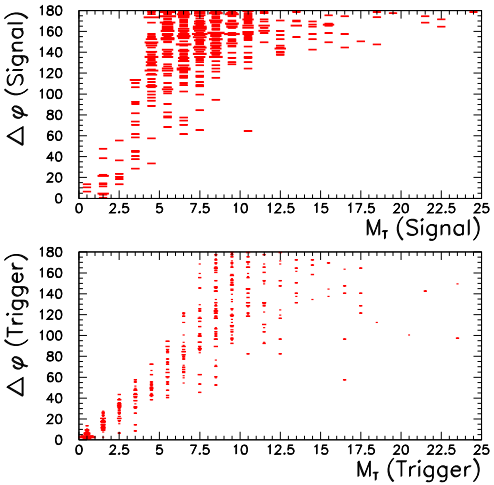

Figure 7.25: Distributions of $\Delta\phi(\mu, SVT)$, and $M_T(\mu, SVT)$ for the test-run data (bottom plot) and the $b\bar{b} \to B_s X \to D_s\pi$ signal (top plot).

The Run I acceptance A_I is the acceptance for the Run I 8 GeV inclusive lepton trigger. The Run II acceptance A_{II} corresponds to the Run II trigger of interest. To account for the Run I trigger efficiency, the Monte Carlo events were required to pass a trigger model based on the Run I Level-2 inclusive lepton trigger efficiency [159] [160]. There are additional factors which affect the number of events expected in Run II. The SVX acceptance will be greater in Run II: $A_{(SVXII)} = 1.4 \times A_{(SVXI)}$. In addition, we assume the total acceptance gained by the central muon-system upgrade to be a factor of 1.4. The increase in the instantaneous luminosity in Run II also increases the number of expected events, we assume the ratio between Run I and Run II to be:

$$\mathcal{L}_{II}/\mathcal{L}_I = 2\ \text{fb}^{-1}/100\ \text{pb}^{-1} = 20\,. \tag{7.102}$$

To normalize our sample with the Run I events sample, the same offline selection cuts are applied. For $\Lambda_b \to \Lambda_c\ell\nu$ decay the cuts are:

- $P_T(K, \pi, p) \geq (0.7, 0.6, 1.5)$ GeV/c;
- $3.5 \leq \text{M}(\ell\Lambda_c) \leq 5.6$ GeV/c^2;
- $P_T(\Lambda_c) \geq 5.0$ GeV/c.

We also require the kaon, pion and proton to be within a cone of 0.8 in η-ϕ space. The decay channel $B_s \to D_s\pi$ has not been reconstructed so we only estimate the efficiency of

the lepton + track trigger selection relative to the all-hadronic trigger [161]. This estimate does not include the reduction in yield from "analysis" cuts.

The number of events expected in Run II N_{II} with respect to the number of events reconstructed in Run I N_I for each decay channel is calculated using the following relation:

$$\frac{N_{II}}{N_I} = \frac{A_{II}}{A_I} \cdot \frac{\mathcal{L}_{II}}{\mathcal{L}_I} \cdot A_{(SVXII)}\,. \tag{7.103}$$

The expected yield for $\Lambda_b \to \Lambda_c\ell\nu$ decays with the same-side 4 GeV/c lepton plus displaced-track selection described above is 25000 in 2 fb^{-1} of Run II. For $B_s \to D_s\ell\nu$ decays, we expect 33000 events.

The yield of $B_s \to D_s\pi$ decay events from the opposite-side 4 GeV lepton trigger selection described above is 106 events in 2 fb^{-1} without correction for reconstruction and analysis cut efficiencies. This number can be directly compared to the yield of 10600 expected under the same assumptions from required two displaced tracks with $P_T > 2$ GeV/c as described in Proposal P-909 [161]. Although tagging dilutions and efficiencies are outside the scope of this section, it is clear that including the tagging lepton as the primary trigger element is an inferior procedure to a trigger on particles of the signal decay.

7.5.1.6 Q^2 Spectrum

As discussed in Section 2, semileptonic decays of B baryons present the possibility of measuring the momentum transfer Q^2 in Λ_b decays. To study the feasibility of such a measurement, we generate $\Lambda_b \to \Lambda_c\ell\nu$ decays. For $\Lambda_b \to \Lambda_c\ell X$, where X is not observed, we can describe the kinematics using the following energy and momentum conservation rules:

$$\begin{aligned} E_{\Lambda_b} &= E_{\ell\Lambda_c} + E_X\,; \\ p_X = |p_X|^2 &= |p_{\Lambda_b} - p_{\ell\Lambda_c}|^2 = p^2_{\Lambda_b} + p^2_{\ell\Lambda_c} - 2p_{\Lambda_b}p_{\ell\Lambda_c}\cos\theta\,. \end{aligned} \tag{7.104}$$

This method is described in more detail in [162]. In our toy Monte Carlo sample, we use P_{Λ_b}, P_{Λ_c}, and P_ℓ and 3D-vertex and kinematic constraints to reconstruct P_ν. The Q^2 distributions from the Monte Carlo event generator, after kinematic cuts, and after detector smearing as well as the reconstructed Q^2 distribution are shown in Figure 7.26. The resolution of the Q^2 reconstruction is shown in Figure 7.27 (top plot). The ratio of the generated Q^2 distribution to the physical solution gives the reconstruction efficiency and is shown in Figure 7.27.

As a check of our the ability to measure the Q^2 distribution in Run II, we perform a simple Monte Carlo experiment. We generate two independent samples of $\Lambda_b \to \Lambda_c\ell\nu$. One sample is used to make a generator level Q^2 distribution. The other sample is normalized to the expected Run II yield. Kinematic and resolution smearing were applied to the normalized sample. The Q^2 distribution is calculated after correcting for the reconstruction efficiency. The generated and reconstructed distribution is shown in Figure 7.28. This shows that given the number of expected events in Run II we can reasonably expect to reconstruct the Q^2 distribution. However, there are higher-order Λ_b decays which complicate the reconstruction.

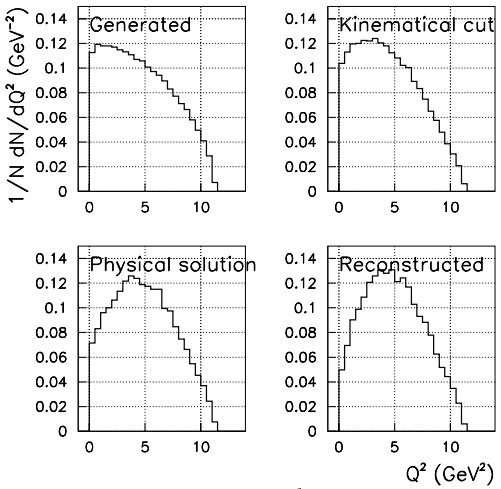

Figure 7.26: Monte Carlo simulation of the Q^2 distribution. The generated distribution is shown in the top left. The distribution after the kinematic cuts is in the top right. The distribution after the detector resolution has been applied is shown in the lower right. The distribution using the kinematic constraints and 3D-vertexing is shown in the lower right.

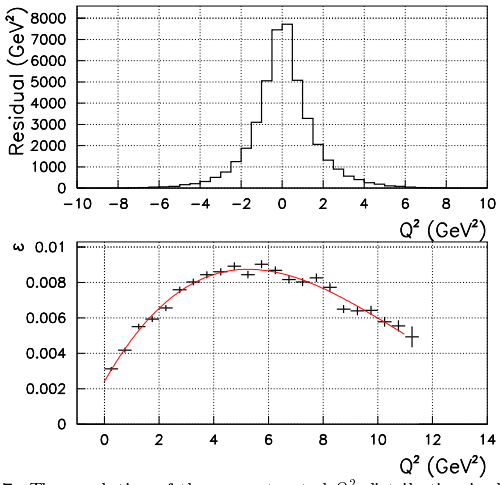

Figure 7.27: The resolution of the reconstructed Q^2 distribution is shown in the top plot. The reconstruction efficiency is shown in the bottom plot.

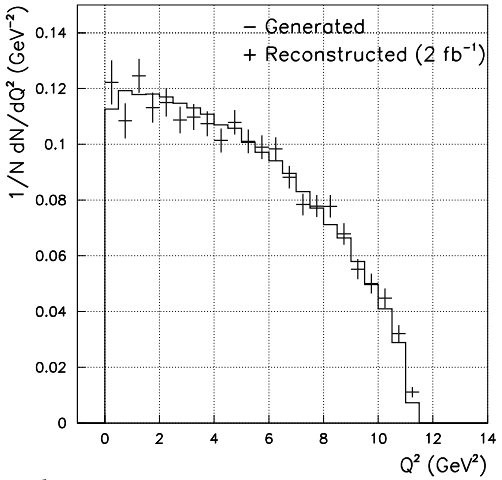

Figure 7.28: Q^2 distribution for generator level and reconstructed after correcting for efficiency.

Higher-order Contamination

The branching ratio for semileptonic Λ_b decays to higher-order baryons may not be not negligible and can contaminate the decay channel of interest. We investigate the kinematic properties of these higher-order decays to determine a method to reject these events efficiently. Presumably the dominant source of contamination is decays with a Λ_c and two pions. The possible states are:

$$\begin{array}{l}\Lambda_b \to [\Sigma_c \pi^+]_{I=0} \ell \bar{\nu}_\ell \\ \quad \hookrightarrow \Lambda_c^+ \pi^- \\ \quad\quad \hookrightarrow pK^-\pi^+\end{array} \tag{7.105}$$

$$\begin{array}{l}\Lambda_b \to [\Sigma_c^{++} \pi^-]_{I=0} \ell \bar{\nu}_\ell \\ \quad \hookrightarrow \Lambda_c^+ \pi^+ \\ \quad\quad \hookrightarrow pK^-\pi^+\end{array} \tag{7.106}$$

$$\begin{array}{l}\Lambda_b \to \Lambda_c^+ \pi^+ \pi^- \ell \bar{\nu}_\ell \\ \quad \hookrightarrow pK^-\pi^+\end{array} \tag{7.107}$$

$$\begin{array}{l}\Lambda_b \to [\Sigma_c^{+} \pi^0]_{I=0} \ell \bar{\nu}_\ell \\ \quad \hookrightarrow \Lambda_c^+ \pi^0 \\ \quad\quad \hookrightarrow pK^-\pi^+\end{array} \tag{7.108}$$

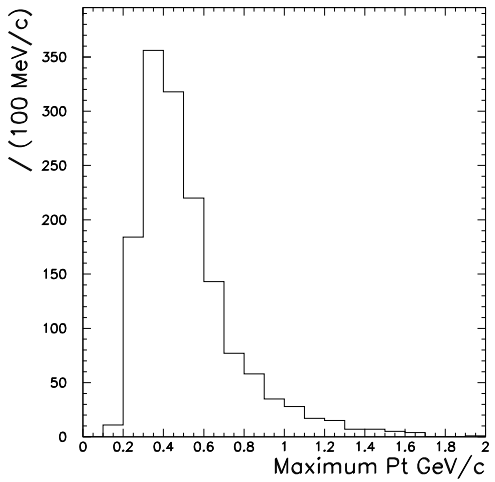

Figure 7.29: Distribution of the maximum P_T of π's from higher order decays.

The Λ_b channels (7.105)–(7.107) contain charged pions and can potentially be identified while channel (7.108) will be impossible to see. However, if we can identify events from mode (7.107) we can use them with proper normalization subtract the effect of mode (7.108).

To study rejection methods, we generate a sample of the decays which have additional charged pions and apply trigger requirements and the offline cuts detailed in Section 7.5.1.5. In addition, we require that the pions from higher order decays be within a cone in η-ϕ of 0.8 centered on the Λ_c direction. The P_T distribution of these charged pions from higher-order decays is shown in Figure 7.29. Estimating that the minimum P_T which will be reconstructed is 0.3 GeV/c, then approximately 75% of the charged higher order pions will be reconstructed.

In addition to the extra decay pions, we also study tracks coming from primary interaction which might be confused with Λ_b-daughter tracks and cause too many events to be rejected. To model these tracks we generate a Monte Carlo sample using PYTHIA tuned to reflect prompt particle distributions in CDF B events [163]. For events that pass the same trigger and offline requirements as in the trigger study, we compare the impact parameter of the three categories of tracks: Λ_c-daughter tracks, charged pions from higher-order decays and tracks from the primary vertex. The impact-parameter significance (d/σ_d) with respect to the primary vertex and to the Λ_b-decay vertex for the three categories of tracks is shown in Figure 7.30. If we reject events with an additional track associated with the Λ_c-lepton vertex The requirement that the impact parameter significance $(d_0^{\Lambda_b}/\sigma_{d_0}^{\Lambda_b} < 2)$, random associations with primary tracks would cause about 10% of the good $(\Lambda_b \to \Lambda_c, \ell, \nu)$ events to be eliminated, but would tag almost 100% of the higher order decays. Thus a small fraction

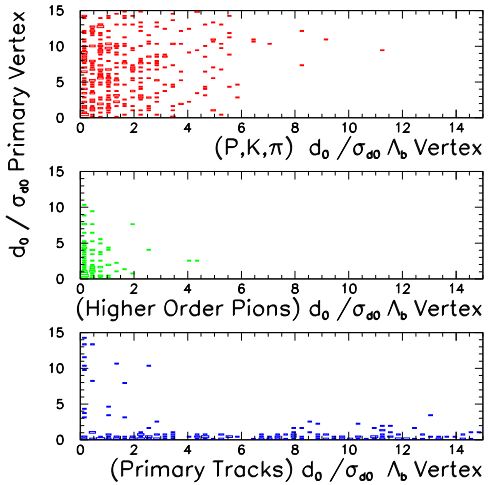

Figure 7.30: Comparison of impact parameter significance of all 3 categories of tracks (protons, kaons and pions) from Λ_c (top plot), higher order pions (middle plot), and tracks from primary vertex (bottom plot)) with respect to Λ_b vertex and the Primary Vertex. All tracks must be within a cone of $\Delta R < 0.8$ with $P_T > 0.3$ GeV/c.

of the time real $\Lambda_b \to \Lambda_c, \ell, \nu$ events will be thrown out but the remaining events will be a relatively pure sample free of higher order Λ_b decays. This coupled with demonstrated ability to calculate the missing neutrino momentum leaves us optimistic about measuring Q^2 in Run II.

7.5.1.7 Summary

We have shown that a lepton + displaced track trigger can produce substantial samples of semileptonic b hadron decays for study and fits well within CDF's overall trigger budget for Run II. We expect $\sim$ 25000 Λ_b decays in 2 fb^{-1}. We have shown that a measurement Q^2 decay in Λ_b decay using the impact parameter information to reject tracks from higher order decays and the primary vertex is feasible. We recognize that fact that further studies are needed to solidify this claim.

7.5.2 Estimating the BTeV Potential for Semileptonic Decays

Using techniques developed for fixed-target charm experiments (including E691 [164], E687 [165], and E791 [166,167]) we demonstrate that BTeV has the necessary capability to extract

information from semileptonic decays. Given the large number of b-hadrons reconstructed by BTeV, the semileptonic reach will be extraordinary.

7.5.2.1 Signal and Background

The signal and background were generated using the MCFast Monte Carlo program. A full description of this program can be found elsewhere [168,169]. MCFast is designed to be a fast and accurate detector simulation with speed and flexibility achieved through parameterization. The MCFast tracing includes the effect of magnetic fields, multiple Coulomb scattering, bremsstrahlung, dE/dx, decays in flight, pair conversions and secondary hadronic interactions. The simulation assumed a luminosity of $2{\times}10^{32}\,\mathrm{cm}^{-2}\mathrm{s}^{-1}$ and included multiple interactions per event. The muon identification code used in this analysis starts by making an acceptance cut. Potential muon tracks must have momentum greater than 5 GeV/c. All tracks are projected through the three muon stations using the track parameters determined from the Kalman filter. If the projection misses any of the stations the track is thrown out. If the track is associated with a muon particle it is identified as a muon. If the track is not a muon then a misidentification probability is determined and a random number is generated to determine if the particle is misidentified as a muon.

The misidentification probability decreases as the momentum increases and decreases as the radius increases. The misidentification rate varies from 7% for 5 GeV/c tracks near the beam to 0.2% for 50 GeV/c tracks at the outer edge of the muon system. The misidentification rate (away from the central region) is loosely based on the measured misidentification rate from the FOCUS experiment. FOCUS is a fixed-target charm experiment which used a ∼180 GeV photon beam at a rate of approximately 10 MHz. BTeV and FOCUS have similar muon rates and momenta. The BTeV detector has two advantages over the FOCUS muon system. The BTeV detector has much finer granularity and the shielding is magnetized which, by allowing a momentum measurement, provides another handle to distinguish real muons from fakes.

The signal modes analyzed were $B^0 \to D^{*-}(\overline{D}^0(K^+\pi^-, K^+\pi^-\pi^-\pi^+)\pi^-)\mu^+\nu$ and $\Lambda_b^0 \to \Lambda_c^-(pK^-\pi^+)\mu^+\nu$. In each case, ∼120,000 events were simulated. Three sources of background were simulated: minimum bias events, charm events, and generic b events (without the signal mode). The cross sections for minimum bias, charm, and b events obtained from Pythia [170] are shown in Table 7.10 along with the predicted numbers of events from one year (10^7 s) of running at a luminosity of $2{\times}10^{32}\,\mathrm{cm}^{-2}\mathrm{s}^{-1}$.

Clearly it is impossible to simulate 10^{14} events given the current state of computing; simulating more than 10^8 events is prohibitive. Therefore we try to estimate the background based on a simulation of 4.2 million minimum bias events, 4.8 million $c\bar{c}$ events, and 1.5 million $b\bar{b}$ events. Given the large number of produced b-hadrons we can certainly make stringent cuts and still retain a large sample of events. Unfortunately, using these stringent cuts eliminates nearly all of our (limited) background which makes it difficult to determine the significance or signal-to-noise ratio of the signal. Since the signals analyzed require detached vertices, reconstructed charm particles, and muons, we assume that the background will be dominated by c and b events, not minimum bias events. Therefore, we

Species	Quark cross section (mb)	Hadron fraction	Branching Ratio	Total produced for 2 fb^{-1}
Min bias	75	100%	100%	1.5×10^{14}
Charm	0.75	100%	100%	1.5×10^{12}
generic b	0.10	100%	100%	2.0×10^{11}
$B^0 \to D^*\mu\nu$	0.10	75%	0.35%	5.3×10^{8}
$\Lambda_b \to \Lambda_c\mu\nu$	0.10	10%	0.20%	4.0×10^{7}

Table 7.10: Production cross sections and expected generation rates for signal and background. Cross sections for $b\bar{b}$ production are estimated from D0 data. The minimum bias cross section is taken to be the $p\bar{p}$ total cross section at 2 TeV. The charm cross section is assumed to be 1% of the minimum bias cross section. Branching ratios are from Ref. [171] except $\Lambda_b \to \Lambda_c\mu\nu$ which is estimated at 4%.

can safely tighten our cuts enough to eliminate all of the minimum bias events which were simulated.

Using these cuts keeps 4 (1) $c\bar{c}$ and 26 (13) $b\bar{b}$ events for the $B^0 \to D^*(D^0(K\pi, K3\pi)\pi)\mu\nu$ ($\Lambda_b \to \Lambda_c(pK\pi)\mu\nu$) decay mode. Figure 7.31 shows the result of scaling the signal and background events to an integrated luminosity of 2 fb^{-1} and distributing the background events evenly through the mass plot. The yield, significance, signal-to-background, and efficiency is tabulated in Table 7.11. These results include a conservative trigger efficiency (50%) which is what is expected from the detached vertex trigger. A detached muon trigger is also planned which will increase the trigger efficiency.

Decay mode	Efficiency	Yield	$S/\sqrt{S+B}$	S/B
$B^0 \to D^*(D^0(K\pi, K3\pi)\pi)\mu\nu$	0.44%	2,300,000	1,430	21
$\Lambda_b \to \Lambda_c(pK\pi)\mu\nu$	0.31%	120,000	210	1.0

Table 7.11: Efficiency, expected yields, signal-to-background, and significance for an integrated luminosity of 2 fb^{-1}. Efficiency includes acceptance, trigger efficiency, reconstruction efficiency and cut efficiency. Significance and signal-to-background are calculated by integrating over a $\pm 2\sigma$ region around the mass peak.

7.5.2.2 Semileptonic Reach

To determine the form factors associated with a particular semileptonic decay we would like to have all the kinematic information associated with the decay chain. The most important quantity is q^2 which is the square of the virtual W mass; i.e. the invariant mass of the lepton and neutrino. Reconstructing the momentum vector is not a trivial exercise, however. The technique used to reconstruct the neutrino momentum, pioneered by E691 and used by E687 and E791 among others [164–167], is particularly suited to BTeV as it requires good vertex resolution compared to the vertex separation. The production and decay vertex of the b-hadron gives the b-hadron momentum vector direction. The neutrino momentum perpendicular to the b-hadron momentum vector is easily measured

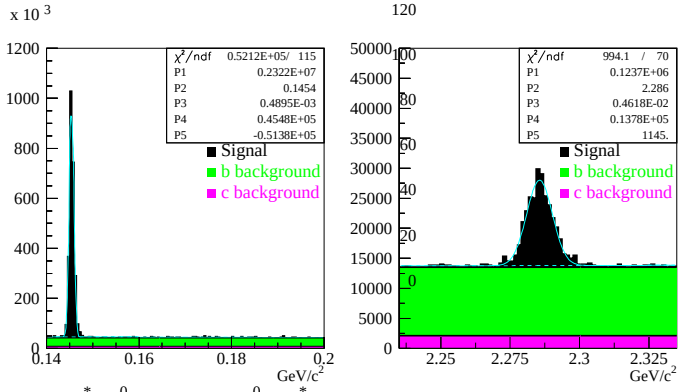

(a) D^*–D^0 Mass diff ($B^0 \to D^* \mu\nu$) (b) pKπ Inv mass ($\Lambda_b \to \Lambda_c \mu\nu$)

Figure 7.31: (a) $D^* - D^0$ Mass difference distribution for $B^0 \to D^*(D^0(K\pi, K3\pi)\pi)\mu\nu$ signal events and $b\bar{b}$ and $c\bar{c}$ background events. (b) pKπ invariant mass distribution for $\Lambda_b \to \Lambda_c(pK\pi)\mu\nu$ signal events and $b\bar{b}$ and $c\bar{c}$ background events. In both plots, the background events have been spread evenly through the mass range.

because it must balance all of the other decay products. The neutrino momentum parallel to the b-hadron momentum can be determined (up to a quadratic ambiguity) by assuming the invariant mass of the b-hadron. We pick the low momentum solution for the parallel component of the neutrino momentum as Monte Carlo studies indicate this is correct more often.

The most recent published results using this method come from E791 [167]. Using a 500 GeV/c π^- beam, they reconstruct over 6,000 $D^+ \to \overline{K}^{*0}\ell\nu$ decays. From this sample they obtain form factor measurements of $r_V = V(0)/A_1(0) = 1.87 \pm 0.08 \pm 0.07$ and $r_2 = A_2(0)/A_1(0) = 0.73 \pm 0.06 \pm 0.08$. From the 3,000 muon decays, they also measure $r_3 = A_3(0)/A_1(0) = 0.04 \pm 0.33 \pm 0.29$. Defining the q^2 resolution as the RMS of the generated q^2 minus the reconstructed q^2 divided by q^2_{max}, E791 had a q^2 resolution of 0.17. From the MCFast simulation with the standard selection criteria and reconstructing the neutrino momentum as described above, BTeV has a q^2 resolution of approximately 0.14 as shown in Fig. 7.32. With 6,000 events, the E791 results give smaller errors than most lattice QCD calculations. With a similar q^2 resolution and 100 times more data, BTeV will also be able to challenge theoretical predictions or provide values which can be input into other calculations.

One additional difficulty in extracting information from these semileptonic decays comes from b semileptonic decays into charm excited states which decay into the state being investigated. For example, in the decay $\Lambda_b^0 \to \Sigma_c^+ \mu\nu$, the Σ_c^+ can decay to $\Lambda_c^+ \pi^0$. Assuming the π^0 is lost, this event will be reconstructed as a signal $\Lambda_b^0 \to \Lambda_c^+ \mu\nu$ event and the neutrino reconstruction (which assumes the invariant mass of the $\Lambda_c^+ \mu\nu$ is equal to the Λ_b^0) will be

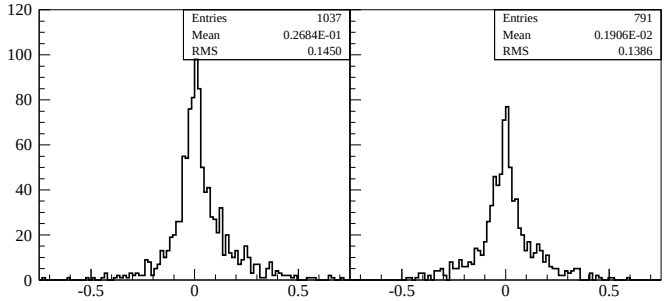

(a) q^2/q^2_{max} resolution, $B^0 \to D^* \mu\nu$ (b) q^2/q^2_{max} resolution, $\Lambda_b \to \Lambda_c \mu\nu$

Figure 7.32: q^2/q^2_{max} resolution for (a) $B^0 \to D^*(D^0(Kn\pi)\pi)\mu\nu$ and (b) $\Lambda_b \to \Lambda_c(pK\pi)\mu\nu$.

inaccurate. The q^2 resolution for these events is shown in Fig. 7.33a. Assuming an equal mixture of $\Lambda_b \to \Lambda_c$ and $\Lambda_b \to \Sigma_c$ decays gives the q^2 resolution shown in Fig. 7.33b. This shows a resolution only slightly degraded (0.14 to 0.15) but with a bias equal to 1/3 of the RMS. BTeV has excellent π^0 reconstruction capabilities [169] which should make it possible to measure the relative branching ratios and correct for this bias.

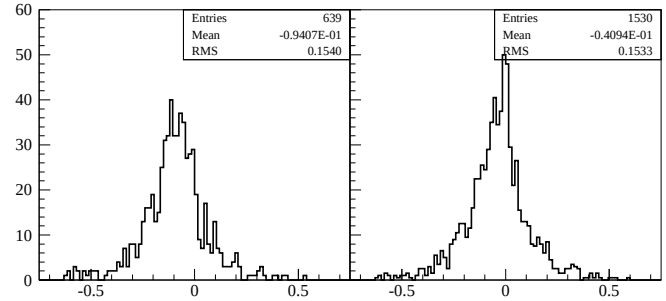

(a) q^2/q^2_{max} resolution, $\Lambda_b \to \Sigma_c \mu\nu$ (b) q^2/q^2_{max} resolution, $\Lambda_b \to (\Sigma_c, \Lambda_c)\mu\nu$

Figure 7.33: q^2/q^2_{max} resolution for (a) $\Lambda_b \to \Lambda_c(pK\pi)\mu\nu$ where the Λ_c comes from a Σ_c and (b) $\Lambda_b \to \Lambda_c(pK\pi)\mu\nu$ where half of the Λ_c's come from Σ_c's and half come directly from Λ_b's.

Since BTeV has a very efficient vertex trigger at Level 1, the semielectronic decays can also be studied. Even though the acceptance of the ECAL is much smaller than that of the muon detectors we expect significant numbers of reconstructed decays in the electronic modes which can be used for systematic studies as well as just increasing the statistics.

7.5.2.3 Summary

This study only provides a cursory look at some of the semileptonic physics available with BTeV. There are many other semileptonic decay modes of b-hadrons which are well within the grasp of BTeV. These decay modes include $B \to \rho \ell \nu$ to determine V_{ub} and B_s semileptonic decay modes to check SU(3). In addition, BTeV will have many semileptonic charm decays available for study.

7.6 Summary of Semileptonic Decays

The study of exclusive semileptonic decays complements the studies on CP violation and mixing discussed in Chapters 6 and 8, since semileptonic decays can, in principle, provide determinations of CKM elements such as $|V_{ub}|$ and $|V_{cb}|$.

For any useful comparison between theory and experiment, we need experimental measurements of q^2 (and other) distributions. This is a challenging task especially in a hadron collider environment, because it requires the reconstruction of the neutrino momentum. Studies at both, CDF and BTeV, have established the feasibility of neutrino momentum reconstruction and subsequent measurement of q^2 distributions with good resolution.

The decay $\Lambda_b \to \Lambda_c \ell \overline{\nu}$ is of particular interest. It can only be be studied at hadron colliders and provides information on the parameters of the heavy quark expansion at subleading order.

Tevatron experiments should explore the full range of semileptonic decays, including B and B_s meson decays to light hadrons. It is important to have measurements of many different semileptonic heavy-to-light decays, with as high an accuracy as possible, for two reasons. First, these measurements can provide tests of heavy flavor and SU(3) symmetry relations. Second, we should expect significant improvements in theoretical predictions of exclusive heavy-to-light form factors, based for example, on lattice QCD, in the time frame for Run II, and certainly by the time BTeV comes on line. These measurements will help to establish the reliability of lattice QCD calculations, and of the corresponding determinations of CKM elements, such as $|V_{ub}|$, from them.

References

[1] G. Buchalla, A.J. Buras, and M.E. Lautenbacher, *Rev. Mod. Phys.* **68**, 1125 (1996).

[2] A.J. Buras *et.al.*, *Nucl. Phys.* **B424**, 374 (1994); A.J. Buras and M. Münz, *Phys. Rev.* **D52**, 186 (1995); M. Misiak, *Nucl. Phys.* **B393**, 3 (1993); **Erratum**, *Nucl. Phys.* **B439**, 461 (1995).

[3] G. Buchalla, G. Hiller and G. Isidori, *Phys. Rev.* **D63**, 014015 (2001).

[4] M. Voloshin and M. Shifman, *Sov. J. Nucl. Phys.* **41**, 120 (1985); J. Chay, H. Georgi and B. Grinstein, *Phys. Lett.* **B247**, 399 (1990); A.V. Manohar and M.B. Wise, *Phys. Rev.* **D49**, 1310 (1994); T. Mannel, *Nucl. Phys.* **B413**, 396 (1994); I.I. Bigi, N.G. Uraltsev and A.I. Vainshtein, *Phys. Lett.* **B293**, 430 (1992); I.I. Bigi, M. Shifman, N.G. Uraltsev and A.I. Vainshtein, *Phys. Rev. Lett.* **71**, 496 (1993); B. Blok, L. Koyrakh, M. Shifman and A.I. Vainshtein, *Phys. Rev.* **D49**, 3356 (1994); Erratum, *Phys. Rev.* **D50**, 3572 (1994); A. Falk, M. Luke, and M.J. Savage, *Phys. Rev.* **D49**, 337 (1994).

[5] M. A. Shifman, proceedings of the workshop on Continuous Advances in QCD, Minneapolis 1994 (held in Minneapolis, MN, 18-20 Feb 1994), p. 249, `hep-ph/9405246`.

[6] N. Isgur, `hep-ph/9809279`.

[7] T. Inami and C.S. Lim, *Prog. Theor. Phys.* **65**, 29 (1981).

[8] R. D. Dikeman, M. Shifman and N. G. Uraltsev, *Int. J. Mod. Phys.* **A11**, 571 (1996). C. Bauer, *Phys. Rev.* **57**, 5611 (1998) [Erratum-ibid. D **60**, 099907 (1998)]; A. L. Kagan and M. Neubert, *Eur. Phys. J. C* **7**, 5 (1999).

[9] M. Misiak and M. Münz, *Phys. Lett.* **B344**, 308 (1995); K. Chetyrkin, M. Misiak and M. Münz, *Phys. Lett.* **B400**, 206 (1997) [Erratum-ibid. B **425** (1997) 414].

[10] K. Adel and Y.-P. Yao, *Phys. Rev.* **D49**, 4945 (1994); C.Greub and T. Hurth, *Phys. Rev.* **D56**, 2934 (1997).

[11] A. Ali and C. Greub, *Z. Phys.* **C49**, 431 (1991); *Phys. Lett.* **B259**, 182 (1991); *Phys. Lett.* **B361**, 46 (1995); N. Pott, *Phys. Rev.* **D54**, 938 (1996).

[12] C. Greub, T. Hurth, and D. Wyler, *Phys. Lett.* **B380**, 385 (1996); *Phys. Rev.* **D54**, 3350 (1996).

[13] M. B. Voloshin, *Phys. Lett.* **B397**, 275 (1997); A. K. Grant, A. G. Morgan, S. Nussinov and R. D. Peccei, *Phys. Rev.* **D56**, 3151 (1997); Z. Ligeti, L. Randall and M. B. Wise, *Phys. Lett.* **B402**, 178 (1997;)

[14] A. Czarnecki and W. Marciano, *Phys. Rev. Lett.* **81**, 277 (1998); P. Gambino and U. Haisch, *JHEP* 0009 (2000) 001; P. Gambino and U. Haisch, *JHEP* 0110 (2000) 020.

[15] P. Gambino and M. Misiak, *Nucl. Phys.* **B611**, 338 (2001).

[16] CLEO Collaboration, T.E. Coan *et al.*,, *Phys. Rev. Lett.* **84**, 5283 (2000); CLEO Collaboration, S. Ahmed *et al.*,, `hep-ex/9908022`; ALEPH Collaboration, R. Barate *et al.*,, *Phys. Lett.* **B429**, 169 (1998); CLEO Collaboration, M.S. Alam *et al.*,, *Phys. Rev. Lett.* **74**, 2885 (1995); CLEO Collaboration, R. Amar *et al.*,, *Phys. Rev. Lett.* **71**, 674 (1993).

[17] A Kagan and M. Neubert, Eur. Phys. J. **C7**, 5 (1999); A.K. Leibovich, I.Z. Rothstein, *Phys. Rev.* **D61**, 074006 (2000).

[18] C.W. Bauer, S. Fleming, and M. Luke, *Phys. Rev.* **D63**, 014006 (2001);

[19] A. Kapustin and Z. Ligeti, *Phys. Lett.* **B55**, 318 (1995); C. Bauer, *Phys. Rev.* **D57**, 5611 (1998), E: **D60**, 099907 (1999).

[20] A. Ali and C. Greub, *Phys. Lett.* **B287**, 191 (1992); G. Ricciardi, *Phys. Lett.* **B355**, 313 (1995).

[21] A. Ali, G. Giudice and T. Mannel, *Z. Phys.* **C67**, 417 (1995); P. Cho, M. Misiak and D. Wyler, *Phys. Rev.* **D54**, 3329 (1996); T. Goto *et al.*, *Phys. Rev.* **D55**, 4273 (1997); G. Buchalla and G. Isidori, *Nucl. Phys.* **B525**, 333 (1998).

[22] C. Huang, W. Liao, and Q. Yan, *Phys. Rev.* **D59**, 011701 (1999); J. Hewett and J. D. Wells, *Phys. Rev.* **D55**, 5549 (1997); E. Lunghi, A. Masiero, I. Scimemi, and L. Silvestrini, *Nucl. Phys.* **B568**, 120 (2000).

[23] A.J. Buras and M.Münz, *Phys. Rev.* **D52**, 186 (1985).

[24] Y. Nir, *Phys. Lett.* **221**, 184 (1989).

[25] A. Ali, G. Hiller, L. T. Handoko and T. Morozumi, *Phys. Rev.* **D55**, 4105 (1997); A. Ali and G. Hiller, *Phys. Rev.* **D58**, 074001 (1998).

[26] C. W. Bauer and C. N. Burrell, *Phys. Lett.* **B469**, 248 (1999), *Phys. Rev.* **D62**, 114028 (2000).

[27] A. El-Khadra, A. Kronfeld, P. Mackenzie, S. Ryan, J. Simone, *Phys. Rev.* **D64**, 014502 (2001); S. Aoki *et al.*,, *Nucl. Phys. B* (Proc. Suppl.)**94**, 329 (2001.)

[28] S. Collins *et al.*,, *Phys. Rev.* **D64**, 055002 (2001).

[29] N. Isgur and M. B. Wise, *Phys. Rev.* **D42**, 2388 (1990).

[30] N. Isgur and M. B. Wise, *Phys. Lett.* **B232**, 113 (1989); *Phys. Lett.* **B237**, 527 (1990).

[31] G. Burdman and J. F. Donoghue, *Phys. Lett.* **B270**, 55 (1991).

[32] H. Politzer and M. B. Wise, *Phys. Lett.* **B206**, 681 (1988).

[33] G. Burdman, Z. Ligeti, M. Neubert and Y. Nir, *Phys. Rev.* **D49**, 2331 (1994).

[34] Z. Ligeti and M. B. Wise, *Phys. Rev.* **60**, 117506 (1999).

[35] Z. Ligeti, I.W. Stewart and M.B. Wise, *Phys. Lett.* **B420**, 1998 (359).

[36] M. Dugan and B. Grinstein, *Phys. Lett.* **B255**, 583 (1991).

[37] J. Charles *et al.*, *Phys. Rev.* **D60**, 014001 (1999).

[38] G. Burdman, *Phys. Rev.* **D57**, 4254 (1998).

[39] U. Aglietti and G. Corbo, *Int. J. Mod. Phys.* **A15**, 363 (2000).

[40] M. Beneke and T. Feldmann, *Nucl. Phys.* **B592**, 3 (2001).

[41] C. W. Bauer, S. Fleming, D. Pirjol and I. W. Stewart, *Phys. Rev.* **D63**, 114020 (2001).

[42] A. Ali, P. Ball, L. Handoko, and G. Hiller, *Phys. Rev.* **D61**, 074024 (2000).

[43] G. Burdman and G. Hiller, *Phys. Rev.* **D63**, 113008 (2001).

[44] M. Beneke, T. Feldmann and D. Seidel, `hep-ph/0106067`.

[45] S. W. Bosch and G. Buchalla, `hep-ph/0106081`.

[46] M. Bauer, B. Stech and M. Wirbel, *Z. Phys.* **C29**, 637 (1985).

[47] J. G. Körner and G. A. Schuler, Z. Phys. **C38**, 511 (1987).

[48] P. Ball and V. M. Braun, *Phys. Rev.* **D55**, 5561 (1997).

[49] D. Melikhov, N. Nikitin and S. Simula, *Phys. Lett.* **B410**, 210 (1997).

[50] N. Isgur and N. Scora, *Phys. Rev.* **52**, 2783 (1995).

[51] D. Melikhov and B. Stech, *Phys. Rev.* **62**, 014006 (2000).

[52] B. Stech, *Phys. Lett.* **B354**, 447 (1995).

[53] J. M. Soares, *Phys. Rev.* **D54**, 6837 (1996).

[54] G. Burdman and J. Kambor, *Phys. Rev.* **D55**, 2817 (1997); G. Burdman, proceedings of the International Conference on B Physics and CP Violation (Honolulu, Hawaii, 24-28 Mar 1997), p.402, `hep-ph/9707410`.

[55] C. G. Boyd, B. Grinstein and R. Lebed, *Phys. Rev. Lett.* **74**, 4603 (1995); *Nucl. Phys.* **B461**, 493 (1996); *Phys. Rev.* **D56**, 6895 (1997); C. G. Boyd and R. Lebed, *Nucl. Phys.* **B485**, 275 (1997); L. Lellouch, *Nucl. Phys.* **B479**, 353 (1996).

[56] C. Caso *et.al.* (PDG Collaboration), *Eur. Phys. J.* **C3**(1998)1.

[57] F. Krüger and L.M. Sehgal, *Phys. Lett.* **B380**, 199 (1996).

[58] A. Ali, T. Mannel and T. Morozumi, *Phys. Lett.* **B273**, 505 (1991).

[59] A. Ali and G. Hiller, *Phys. Rev.* **D60**, 034017 (1999).

[60] K. Abe *et al.* [Belle Collaboration], hep-ex/0107072.

[61] K. Abe *et al.* [BELLE Collaboration], hep-ex/0109026.

[62] B. Aubert *et al.* [BABAR Collaboration], hep-ex/0107026.

[63] S. Anderson *et al.* (CLEO Collaboration), CLNS 01/1739, hep-ex/0106060.

[64] S. Glenn *et al.* (CLEO Collaboration), *Phys. Rev. Lett.* **80**, 2289 (1998).

[65] G. Burdman, *Phys. Rev.* **52**, 6400 (1995).

[66] A. Ali and G. Hiller, *Eur. Phys. J.* **C8**, 619 (1999).

[67] F. Krüger and L.M. Sehgal, *Phys. Rev.* **D55**, 2799 (1997).

[68] C. Greub, H. Simma and D. Wyler, *Nucl. Phys.* **B434**, 39 (1995); A. L. Kagan and M. Neubert, *Phys. Rev.* **D58**, 094012 (1998).

[69] F. Krüger and J.C. Romão, *Phys. Rev.* **D62**, 034020 (2000).

[70] E. Lunghi and I. Scimemi, *Nucl. Phys.* **B574**, 43 (2000).

[71] M.S. Alam *et.al.* (CLEO Collaboration), Phys. Rev. Lett.74(1995)2885;
S. Ahmed *et.al.* (CLEO Collaboration), CLEO CONF 99–10 (hep–ex/9908022).

[72] A. Ali, V.M. Braun, and H. Simma, *Z. Phys.* **C63**, 437 (1994); L. Del Debbio *et al.*,, *Phys. Lett.* **B416**, 392 (1998); S. Narison, *Phys. Lett.* **B327**, 354 (1994); P. Ball and V.M. Braun, *Phys. Rev.* **D58**, 094016 (1998); C. Bernard, P. Hsieh, and A. Soni, *Phys. Rev. Lett.* **72**, 1402 (1994); K. C. Bowler *et.al.*, *Phys. Rev.* **D51**, 4955 (1995).

[73] S. Veseli, M.G. Olsson, *Phys. Lett.* **B367**, 309 (1996); A. Ali, T. Ohl, and T. Mannel, *Phys. Lett.* **B298**, 195 (1993); T. Altomari, *Phys. Rev.* **D37**, 677 (1988).

[74] E. Golowich and S. Pakvasa, *Phys. Rev.* **D51**, 1215 (1995); N.G. Deshpande, X.-G. He, and J. Trampetic, *Phys. Lett.* **B367**, 362 (1996).

[75] B. Grinstein and D. Pirjol, *Phys. Rev.* **D62**, 093002 (2000).

[76] D. Atwood, B. Blok, and A. Soni, *Int. J. Mod. Phys.* **A11**, 3743 (1996); J.F. Donoghue, E. Golowich, and A.A. Petrov, *Phys. Rev.* **D55**, 2657 (1997).

[77] T. Mannel and S. Recksiegel, *J. Phys.* **G24**, 979 (1998).

[78] G. Hiller and A. Kagan, hep-ph/0108074.

[79] T. Inami and C. S. Lim, *Prog. Theor. Phys.* **65**, 297 (1981) [Erratum **65**, 1772 (1981)].

[80] B. Grządkowski and P. Krawczyk, *Z. Phys.* **C18**, 43 (1983).

[81] P. Krawczyk, *Z. Phys.* **C44**, 509 (1989).

[82] G. Buchalla, A. J. Buras and M. Lautenbacher, *Rev. Mod. Phys.* **68**, 1125 (1996).

[83] G. Buchalla and A. J. Buras, Nucl. Phys. **B398**, 285 (1993); *Nucl. Phys.* **B400**, 225 (1993);

[84] M. Misiak and J. Urban, *Phys. Lett.* **B451**, 161 (1999).

[85] E. Jenkins and M. J. Savage, *Phys. Lett.* **B281**, 331 (1992).

[86] D. Groom *et al.*,, *Eur. Phys. J.* **C15**, 1 (2000.)

[87] A. Ali Khan *et al.* [CP-PACS Collaboration], *Phys. Rev.* **D64**, 034505 (2001).

[88] S. Glenn *et al.* (CLEO Collaboration), Phys. Rev. Lett. **80**, 2289 (1998); B.Abbott *etal.* (DØ Collaboration), Phys. Lett. **B223**, 419 (1998); C.Albajar *et al.* (UA1 Collaboration), Phys. Lett. **B262**, 163 (1991). Also, a recent search in exclusive channels: T. Affolder *et al.* (CDF Collaboration), *Phys. Rev. Lett.* **83**, 3378 (1999).

[89] S. Bertolini *et.al.*, *Nucl. Phys.* **B353**, 591 (1991).

[90] P. Cho, M. Misiak and D. Wyler, *Phys. Rev.* **D54**, 3329 (1996).

[91] J.L. Hewett and J.D. Wells, *Phys. Rev.* **D55**, 5549 (1997).

[92] T. Goto *et.al.*, *Phys. Rev.* **D55**, 4272 (1997); T. Goto, Y. Okada and Y. Shimizu, *Phys. Rev.* **D58**, 094006 (1998).

[93] M. Ciuchini *et.al.*, *Nucl. Phys.* **B534**, 3 (1998).

[94] E. Lunghi, A. Masiero, I. Scimemi and L. Silvestrini, *Nucl. Phys.* **B568**, 120 (2000).

[95] Oscar Vives and Antonio Masiero, Lectures given by A. Masiero at the International School on Subnuclear Physics (Erice, Italy, 29 August–7 September 1999) hep-ph/0003133.

[96] A. Masiero and H. Murayama, *Phys. Rev.* **83**, 907 (1999).

[97] A. J. Buras and R. Buras, *Phys. Lett.* **B501**, 223 (2001); M. Dine, E. Kramer, Y. Nir and Y. Shadmi, *Phys. Rev.* **D64**, 116005 (2001).

[98] C.-S. Huang, W. Liao, Q.-S. Yan and S.-H. Zhu, *Phys. Rev.* **D63**, 114021 (2001)[Erratum-ibid. D **64**, 059902 (2001)]; C.-S. Huang and Q.-S. Yan, *Phys. Lett.* **B442**, 209 (1998); C.-S. Huang, W. Liao and Q.-S. Yan, *Phys. Rev.* **D59**, 011701 (1999); C. Hamzaoui, M. Pospelov and M. Toharia, *Phys. Rev.* **D59**, 095005 (1999); K. S. Babu and C. Kolda, *Phys. Rev. Lett.* **84**, 228 (2000); P. H. Chankowski and L. Slawianowska, *Phys. Rev.* **D63**, 054012 (2001); A. Dedes, H.K. Dreiner, U. Nierste, *Phys. Rev. Lett.* **87**, 251804 (2001).

[99] K. Hagiwara, K. Hikasa, R. D. Peccei and D. Zeppenfeld, *Nucl. Phys.* **B282**, 253 (1997).

[100] *A Combination of Preliminary Measurements of Triple Gauge Boson Coupling Parameters measured by the LEP Experiments*, the LEP electroweak working group, LEPEWWG/TGC/2000-01.

[101] F. Abe *et al.*, the CDF collaboration, *Phys. Rev. Lett.* **78**, 4536 (1997); S. Abachi *et al.*, the D0 collaboration, *Phys. Rev. Lett.* **78**, 3634 (1997); B. Abott *et al.*, the *D*0 collaboration, contributed to the XVIII International Symposium on Lepton-Photon Interactions, Hamburg, Germany, July 28 - August 1, 1997.

[102] S. Chia, *Phys. Lett.* **B240**, 465 (1990).

[103] K. Numata, *Z. Phys.* **C**52, 691 (1991).

[104] T. Rizzo, *Phys. Lett.* **B315**, 571 (1993).

[105] X.-G. He and B. McKellar, *Phys. Lett.* **B320**, 168 (1994).

[106] X.-G. He, *Phys. Lett.* **B319**, 327 (1993).

[107] G. Baillie, *Z. Phys.* **C**61, 667 (1994).

[108] G. Burdman, *Phys. Rev.* **D59**, 035001 (1998).

[109] X.-G. He, *Phys. Lett.* **B460**, 405 (1999).

[110] R. D. Peccei and X. Zhang, *Nucl. Phys.* **B337**, 269 (1990); R. D. Peccei, S. Peris, and X. Zhang, *Nucl. Phys.* **B349**, 305 (1991).

[111] E. Malkawi and C.–P. Yuan, *Phys. Rev.* **D50**, 4462 (1994).

[112] K. Fujikawa and A. Yamada, *Phys. Rev.* **D49**, 5890 (1994); F. Larios, M. A. Pérez, and C.-P. Yuan, *Phys. Lett.* **B457**, 334 (1999).

[113] O. J. P. Éboli, M. C. Gonzalez–García, and S. F. Novaes, *Phys. Lett.* **B415**, 75 (1997).

[114] G. Burdman, M. C. Gonzalez–García, and S. F. Novaes, *Phys. Rev.* **D61**, 114016 (2000).

[115] C. T. Hill, Phys. Lett. **B345**, 483 (1995); K. Lane and E. Eichten, *Phys. Lett.* **B352**, 382 (1995); K. Lane, *Phys. Rev.* **D54**, 2204 (1996).

[116] S. Glashow and S. Weinberg, *Phys. Rev.* **D15**, 1958 (1977).

[117] W. S. Hou, *Phys. Lett.* **B296**, 179 (1992); D. Chang, W. S. Hou and W. Y. Keung, *Phys. Rev.* **D48**, 217 (1993).

[118] W. S. Hou and R. S. Willey, *Phys. Lett.* **B202**, 591 (1988); B. Grinstein, M. J. Savage and M. B. Wise, *Nucl. Phys.* **B319**, 271 (1989); T. M. Aliev, M. Savci and A. Ozpineci, *Phys. Lett.* **B410**, 216 (1997). .

[119] D. Atwood, L. Reina and A. Soni, *Phys. Rev.* **D55**, 3156 (1997); T. M. Aliev and I. O. Iltan, *Phys. Lett.* **B451**, 175 (1999).

[120] M. J. Savage, *Phys. Lett.* **B266**, 135 (1991); W. Skiba and J. Kalinowski, *Nucl. Phys.* **B404**, 3 (1993); Y.-B. Dai, C.-S. Huang and H.-W. Huang, *Phys. Lett.* **B390**, 257 (1997); H. E. Logan and U. Nierste, *Nucl. Phys.* **B586**, 39 (2000); C.-S. Huang, W. Liao, Q.-S. Yan and S.-H. Zhu, *Phys. Rev.* **D63**, 114021 (2001), [Erratum-ibid **D64** 059902 (2001)] ; C. Bobeth *et.al.*, *Phys. Rev.* **D64**, 074014 (2001).

[121] A. Longhitano, *Phys. Rev.* **D22**, 1166 (1980); A. Longhitano, *Nucl. Phys.* **B188**, 118 (1981). For a more recent presentation see T. Applequist and G. Wu, *Phys. Rev.* **D48**, 3235 (1993).

[122] J. Bernabéu, D. Comelli, A. Pich and A. Santamaria, *Phys. Rev. Lett.* **78**, 2902 (1997).

[123] G. Burdman, *Phys. Lett.* **B409**, 442 (1997).

[124] B. Balaji, *Phys. Rev.* **D52**, 1699 (1996).

[125] D. Kominis, *Phys. Lett.* **B358**, 312 (1995); G. Buchalla, G. Burdman, C. T. Hill and D. Kominis, *Phys. Rev.* **D53**, 5185 (1996).

[126] "The CDF II Detector Technical Design Report", CDF collaboration, FERMILAB-Pub-96/390-E (1996).

[127] CLEO Collaboration, M.S. Alam *et al*, *Phys. Rev. Lett.* 74, 2885, (1995).

[128] CLEO Collaboration, S. Glenn *et al*, *Phys. Rev. Lett.* **80**, 2289 (1998).

[129] B. Abbott *et al.*, D0 Collaboration, Phys. Lett. B**423**, 419 (1998).

[130] O. Baer and N. Pott, Phys. Rev. **D 55**, 1684 (1997).

[131] M. Mangano, P. Nason and G. Ridolfi, Nucl. Phys. **B373**, 295 (1992).

[132] F. Abe *et al.*, CDF Collaboration, Phys. Rev. Lett., **76**, 4675 (1996).

[133] F. Abe *et al.*, CDF Collaboration, Phys. Rev. Lett., **79**, 572 and 578 (1997).

[134] *Triggers for B Physics Studies in Run II*, F. Stichelbaut, M. Narain and A. Zieminski, D0 note 3354 (December 1997).

[135] K. Kordas, *et al.* CDF Note 3771.

[136] A. B. Wicklund, CDF Note 4354.

[137] M. Tanaka, *et al.* CDF Note 4804.

[138] T. Affolder *et al.* [CDF Collaboration], Phys. Rev. Lett. **84**, 1663 (2000).

[139] M. Tanaka, *et al.* CDF Note 5125.

[140] T. Affolder *et al.* [CDF Collaboration], Phys. Rev. Lett. **83**, 3378 (1999); W. Erdmann, *et al.* CDF Note 4517.

[141] C. Greub, A. Ioannisian and D. Wyler, Phys. Lett. **B346**, 149 (1995).

[142] A. V. Manohar and M. B. Wise, "Heavy quark physics," *Cambridge Monographs on Particle Physics, Nuclear Physics, and Cosmology, Vol. 10.*

[143] A. Czarnecki, *Phys. Rev. Lett.* **76**, 4124 (1996); A. Czarnecki and K. Melnikov, *Nucl. Phys.* **B505**, 65 (1997).

[144] P. F. Harrison and H. R. Quinn [BABAR Collaboration], "The BaBar physics book: Physics at an asymmetric B factory," SLAC-R-0504 *Papers from Workshop on Physics at an Asymmetric B Factory (BaBar Collaboration Meeting), Rome, Italy, 11-14 Nov 1996, Princeton, NJ, 17-20 Mar 1997, Orsay, France, 16-19 Jun 1997 and Pasadena, CA, 22-24 Sep 1997.*

[145] C. Bernard, Y. Shen and A. Soni, *Phys. Lett.* **B317**, 164 (1993); UKQCD Collaboration (K.C. Bowler *et al.*,), *Phys. Rev.* **D52**, 5067 (1995); T. Bhattacharya and R. Gupta, *Nucl. Phys. B* (Proc. Suppl.)**42**, 935 (1995); *Nucl. Phys. B* (Proc. Suppl.)**47**, 481 (1996); J. Mandula and M.C. Ogilvie, *Nucl. Phys. B* (Proc. Suppl.)**34**, 480 (1994); T. Draper and C. McNeile, *Nucl. Phys. B* (Proc. Suppl.)**47**, 429 (1996); C. Bernard *et al.*,, *Nucl. Phys. B* (Proc. Suppl.)**63**, 374 (1998); J. Christensen, T. Draper and C. McNeile, *Nucl. Phys. B* (Proc. Suppl.)**63**, 377 (1998); S. Hashimoto and H. Matsufuru, *Phys. Rev.* **D54**, 4578 (1996.)

[146] S. Hashimoto, *et al.*,, *Phys. Rev.* **D61**, 014502 (2000); J. Simone, *et al.*,, *Nucl. Phys. B* (Proc. Suppl.)**83**, 334 (2000), `hep-lat/9910026`; S. Hashimoto, *et al.*,, Fermilab-PUB-01-317-T, `hep-ph/0110253`.

[147] A. Kronfeld, *Phys. Rev.* **D62**, 014505 (2000).

[148] H. Georgi, B. Grinstein and M. B. Wise, *Phys. Lett.* **B252**, 456 (1990).

[149] J. G. Korner and M. Kramer, *Phys. Lett.* **B275**, 495 (1992).

[150] M. B. Voloshin, Int. J. Mod. Phys. A10 (1995) 2865; A. A. Penin and A. A. Pivovarov, *Phys. Lett.* **B435**, 413 (1998); K. Melnikov and A. Yelkhovsky, *Phys. Rev.* **D59**, 114009 (1999); A. H. Hoang, *Phys. Rev.* **D61**, 034005 (2000); M. Beneke and A. Signer, *Phys. Lett.* **B471**, 233 (1999); A. H. Hoang, hep-ph/0008102.

[151] Z. Ligeti, M. Luke, A.V. Manohar and M.B. Wise, *Phys. Rev.* **D60**, 034019 (1999); A. Kapustin and Z. Ligeti, *Phys. Lett.* **B355**, 318 (1995); M.B. Voloshin, Phys. Rev. D51 (1995) 4934; A. F. Falk, M. Luke and M. J. Savage, *Phys. Rev.* **D53**, 6316 (1996); *Phys. Rev.* **D53**, 2491 (1996).

[152] V. Gimenez, et al., *JHEP* 0003 (2000) 018; S. Collins, hep-lat/0009040.

[153] A. K. Leibovich and I. W. Stewart, *Phys. Rev.* **D57**, 5620 (1998).

[154] A. Falk, Z. Ligeti, M. Wise, *Phys. Lett.* **B406**, 225 (1997).

[155] C. Bauer, Z. Ligeti, M. Luke, *Phys. Lett.* **B479**, 395 (2000).

[156] T. Miao, "Measurement of Λ_b Lifetime From $\Lambda_b \to \Lambda_c \ell \nu$", CDF Note 3395 (1995).

[157] C. Peterson *et al.*, Phys. Rev. **D 27**, 105 (1983); J. Chrin, A. Phys **C 36**, 163 (1987).

[158] P. Avery, K. Read and G. Trahern, "QQ: A Monte Carlo Generator", CLEO Internal Software Note CSN-212, Cornell University, 1985.

[159] W. Taylor *et al.*, "Run 1B Level 2 CEM_8_CFT_7_5 and XCES Electron Trigger Efficiencies", CDF Note 4691 (1998).

[160] J. Done *et al.*, "Study of Level 2 Inclusive Muon Trigger Efficiency in Run 1B", CDF Note 4017 (1999).

[161] The CDF Collaboration "Update to Proposal P-909: Physics Performance of the CDF II Detector with An Inner Silicon Layer and A Time of Flight Detector", (1999).

[162] M. Tanaka "B_s Mixing with Semileptonic Decays in Run II", CDF Note 5290 (2000).

[163] D. Vučinić, P. Sphicas, P. Maksimović, "Observation of B(2P) States in Semileptonic B Decays", CDF Note 3852 (1998).

[164] E691 Collaboration, J.C. Anjos *et al.*, Phys. Rev. Lett. **440**, 435 (1990).

[165] E687 Collaboration, P.L. Frabetti *et al.*, Phys. Lett. **B307**, 262 (1993).

[166] E791 Collaboration, E.M. Aitala *et al.*, Phys. Rev. Lett. **80**, 1393 (1998).

[167] E791 Collaboration, E.M. Aitala *et al.*, Phys. Lett. **B440**, 435 (1998).

[168] MCFast description: http://www-pat.fnal.gov/mcfast.html.

[169] BTeV proposal: http://www-btev.fnal.gov/public_documents/btev_proposal/index.html.

[170] T. Sjöstrand, Computer Physics Commun. **82** (1994) 74.

[171] Particle Data Group, D.E. Groom *et al.*, Eur. Phys. J. **C15**, 1 (2000).

Chapter 8

Mixing and Lifetimes

K. Anikeev, F. Azfar, N. Cason, H.W.K. Cheung, A. Dighe, I. Furic, G. Gutierrez, J. Hewett, R. Jesik, M. Jones, P. Kasper, J. Kroll, V.E. Kuznetsov, R. Kutschke, G. Majumder, M. Martin, U. Nierste, Ch. Paus, S. Rakitin, S. Stone, M. Tanaka, W. Taylor, J. Tseng, M. Voloshin, J. Wang, N. Xuan

8.1 Overview

In hadron colliders b-flavored hadrons are produced with a large boost. Therefore they are a fertile ground for measurements of decay time distributions. The neutral B_d^0 and B_s^0 mesons mix with their antiparticles, which leads to oscillations between the flavor eigenstates. A measurement of the oscillation frequency allows to determine the mass difference Δm_q, $q = d, s$, between the two physical mass eigenstates. The rapid oscillations in $B_s^0 - \overline{B}_s^0$ mixing have not been resolved yet and their discovery has a high priority for the B physics program at Run II. Once this has been achieved, the mass difference Δm_s will be known very precisely. By combining this information with the already measured Δm_d one will precisely determine the length of one side of the unitarity triangle.$\Delta m_d/\Delta m_s$ will have a larger impact on our knowledge of the unitarity triangle than any previously measured quantity and even than a precisely measured $\sin(2\beta)$. Accurately measured decay distributions will further reveal the pattern of b-hadron lifetimes. The large mass of the b quark compared to the QCD scale parameter Λ_{QCD} allows to expand the widths in terms of Λ_{QCD}/m_b. Differences among the total widths are dominated by terms of order $16\pi^2(\Lambda_{QCD}/m_b)^3$, the measurements of lifetime differences therefore probe the heavy quark expansion at the third order in the expansion parameter. From Run II we expect valuable new information on the lifetimes of the B^+, B_d^0 and B_s^0 mesons, the width difference $\Delta\Gamma_s$ between the two physical B_s meson eigenstates the lifetimes of the Λ_b and eventually also of other b-flavored baryons. From the current experimental situation it is not clear whether the heavy quark expansion can be applied to baryon lifetimes, and Run II data will help to settle this question.

This chapter first discusses the theory predictions for the various quantities in great detail. Where possible, we derive simple 'pocket-calculator' formulae to facilitate the analysis of the measurements. It is described which fundamental information can be gained from the various measurements. Some quantities are sensitive to physics beyond the Standard Model and we show how they are affected by new physics. Then we summarize the experimental techniques and present the results of the Monte Carlo simulations.

8.2 Theory of heavy hadron lifetimes †

The dominant weak decays of hadrons containing a heavy quark, c or b, are caused by the decay of the heavy quark. In the limit of a very large mass m_Q of a heavy quark Q the parton picture of the hadron decay should set in, where the inclusive decay rates of hadrons, containing Q, mesons $(Q\bar{q})$ and baryons (Qqq), are all the same and equal to the inclusive decay rate $\Gamma_{parton}(Q)$ of the heavy quark. Yet, the known inclusive decay rates [1] are conspicuously different for different hadrons, especially for charmed hadrons, whose lifetimes span a range of more than one order of magnitude from the shortest $\tau(\Omega_c) = 0.064 \pm 0.020$ ps to the longest $\tau(D^+) = 1.057 \pm 0.015$ ps, while the differences of lifetime among b hadrons are substantially smaller. The relation between the relative lifetime differences for charmed and b hadrons reflects the fact that the dependence of the inclusive decay rates on the light quark-gluon 'environment' in a particular hadron is a pre-asymptotic effect in the parameter m_Q, which effect vanishes as an inverse power of m_Q at large mass.

A theoretical framework for systematic description of the leading at $m_Q \to \infty$ term in the inclusive decay rate $\Gamma_{parton}(Q) \propto m_Q^5$ as well as of the terms relatively suppressed by inverse powers of m_Q is provided [2–4] by the operator product expansion (OPE) in m_Q^{-1}. Existing theoretical predictions for inclusive weak decay rates are in a reasonable agreement, within the expected range of uncertainty, with the data on lifetimes of charmed particles and with the so far available data on decays of B mesons. The only outstanding piece of present experimental data is on the lifetime of the Λ_b baryon: $\tau(\Lambda_b)/\tau(B_d) \approx 0.8$, for which ratio a theoretical prediction, given all the uncertainty involved, is unlikely to produce a number lower than 0.9. The number of available predictions for inclusive decay rates of charmed and b hadrons is sufficiently large for future experimental studies to firmly establish the validity status of the OPE based theory of heavy hadron decays, and, in particular, to find out whether the present contradiction between the theory and the data on $\tau(\Lambda_b)/\tau(B_d)$ is a temporary difficulty, or an evidence of fundamental flaws in theoretical understanding.

It is a matter of common knowledge that application of OPE to decays of charmed and b hadrons has potentially two caveats. One is that the OPE is used in the Minkowski kinematical domain, and therefore relies on the assumption of quark-hadron duality at the energies involved in the corresponding decays. In other words, it is assumed that sufficiently many exclusive hadronic channels contribute to the inclusive rate, so that the accidentals of the low-energy resonance structure do not affect the total rates of the inclusive processes. Theoretical attempts at understanding the onset of the quark-hadron duality are so far limited to model estimates [5,6], not yet suitable for direct quantitative evaluation of possible deviation from duality in charm and b decays. This point presents the most fundamental uncertainty of the OPE based approach, and presently can only be clarified by confronting theoretical predictions with experimental data. The second possible caveat in applying the OPE technique to inclusive charm decays is that the mass of the charm quark, m_c, may be insufficiently large for significant suppression of higher terms of the expansion in m_c^{-1}. The relative lightness of the charm quark, however, accounts for a qualitative, and even semi-quantitative, agreement of the OPE based predictions with the observed large

† Author: Mikhail Voloshin

spread of the lifetimes of charmed hadrons: the nonperturbative effects, formally suppressed by m_c^{-2} and m_c^{-3} are comparable with the 'leading' parton term and describe the hierarchy of the lifetimes.

Another uncertainty of a technical nature arises from poor knowledge of matrix elements of certain quark operators over hadron, arising as terms in OPE. These can be estimated within theoretical models, with inevitable ensuing model dependence, or, where possible, extracted from the experimental data. With these reservations spelled out, we discuss here the OPE based description of inclusive weak decays of charm and b hadrons, with emphasis on specific experimentally testable predictions, and on the measurements, which would less rely on model dependence of the estimates of the matrix elements, thus allowing to probe the OPE predictions at a fundamental level.

8.2.1 OPE for inclusive weak decay rates

The optical theorem of the scattering theory relates the total decay rate Γ_H of a hadron H_Q containing a heavy quark Q to the imaginary part of the 'forward scattering amplitude'. For the case of weak decays the latter amplitude is described by the following effective operator

$$L_{eff} = 2\,\mathrm{Im}\left[i\int d^4x\, e^{iqx}\, T\left\{L_W(x), L_W(0)\right\}\right], \tag{8.1}$$

in terms of which the total decay rate is given by[1]

$$\Gamma_H = \langle H_Q|\, L_{eff}\,|H_Q\rangle\,. \tag{8.2}$$

The correlator in equation (8.1) in general is a non-local operator. However at $q^2 = m_Q^2$ the dominating space-time intervals in the integral are of order m_Q^{-1} and one can expand the correlator in x, thus producing an expansion in inverse powers of m_Q. The leading term in this expansion describes the parton decay rate of the quark. For instance, the term in the nonleptonic weak Lagrangian $\sqrt{2}\,G_F\,V(\overline{q}_{1\,L}\gamma_\mu\,Q_L)(\overline{q}_{2L}\gamma_\mu\,q_{3L})$ with V being the appropriate combination of the CKM mixing factors, generates through Eq. (8.1) the leading term in the effective Lagrangian

$$L^{(0)}_{eff,\,nl} = |V|^2\,\frac{G_F^2\,m_Q^5}{64\,\pi^3}\,\eta_{nl}\,\left(\overline{Q}Q\right), \tag{8.3}$$

where η_{nl} is the perturbative QCD radiative correction factor. This expression reproduces the well known formula for the inclusive nonleptonic decay rate of a heavy quark, associated with the underlying process $Q \to q_1\,q_2\,\overline{q}_3$, due to the relation $\langle H_Q|\overline{Q}Q|H_Q\rangle \approx \langle H_Q|Q^\dagger Q|H_Q\rangle = 1$, which is valid up to corrections of order m_Q^{-2}. One also sees form this example, that in order to separate individual semi-inclusive decay channels, e.g., nonleptonic with specific flavor quantum numbers, or semileptonic, one should simply pick up the corresponding relevant part of the weak Lagrangian L_W, describing the underlying process, to include in the correlator (8.1).

[1] We use here the non-relativistic normalization for the *heavy* quark states: $\langle Q|Q^\dagger Q|Q\rangle = 1$.

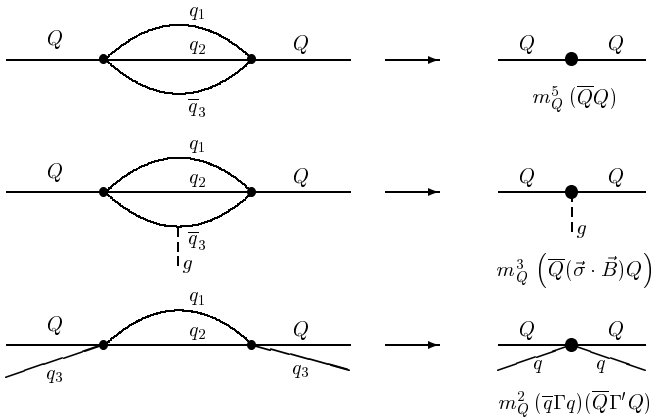

Figure 8.1: Graphs for three first terms in OPE for inclusive decay rates: the parton term, the chromomagnetic interaction, and the four-quark term.

The general expression for first three terms in the OPE for L_{eff} has the form

$$\begin{aligned} L_{eff} &= L^{(0)}_{eff} + L^{(2)}_{eff} + L^{(3)}_{eff} \\ &= c^{(0)}\,\frac{G_F^2\,m_Q^5}{64\,\pi^3}\left(\overline{Q}Q\right) + c^{(2)}\,\frac{G_F^2\,m_Q^3}{64\,\pi^3}\left(\overline{Q}\,\sigma^{\mu\nu}G_{\mu\nu}\,Q\right) + \frac{G_F^2\,m_Q^2}{4\,\pi}\sum_i c_i^{(3)}\,(\overline{q}_i\Gamma_i q_i)(\overline{Q}\Gamma_i' Q)\,, \end{aligned} \tag{8.4}$$

where the superscripts denote the power of m_Q^{-1} in the relative suppression of the corresponding term in the expansion with respect to the leading one, $G_{\mu\nu}$ is the gluon field tensor, q_i stand for light quarks, u, d, s, and, finally, Γ_i, Γ_i' denote spin and color structures of the four-quark operators. The coefficients $c^{(a)}$ depend on the specific part of the weak interaction Lagrangian L_W, describing the relevant underlying quark process.

One can notice the absence in the expansion (8.5) of a term suppressed by just one power of m_Q^{-1}, due to non-existence of operators of suitable dimension. Thus the decay rates receive no correction of relative order m_Q^{-1} in the limit of large m_Q, and the first pre-asymptotic corrections appear only in the order m_Q^{-2}.

The mechanisms giving rise to the three discussed terms in OPE are shown in Figure 8.1. The first, leading term corresponds to the parton decay, and does not depend on the light quark and gluon 'environment' of the heavy quark in a hadron. The second term describes the effect on the decay rate of the gluon field that a heavy quark 'sees' in a hadron. This term in fact is sensitive only to the chromomagnetic part of the gluon field, and contains the operator of the interaction of heavy quark chromomagnetic moment with the chromomagnetic field. Thus this term depends on the spin of the heavy quark, but does not depend on the flavors of the light quarks or antiquarks. Therefore this effect does not

split the inclusive decay rates within flavor $SU(3)$ multiplets of heavy hadrons, but generally gives difference of the rates, say, between mesons and baryons. The dependence on the light quark flavor arises from the third term in the expansion (8.5) which explicitly contains light quark fields. Historically, this part is interpreted in terms of two mechanisms [2,8,9]: the weak scattering (WS) and the Pauli interference (PI). The WS corresponds to a cross-channel of the underlying decay, generically $Q \to q_1\, q_2\, \overline{q}_3$, where either the quark q_3 is a spectator in a baryon and can undergo a weak scattering off the heavy quark: $q_3\, Q \to q_1\, q_2$, or an antiquark in meson, say $\overline{q}_1$, weak-scatters (annihilates) in the process $\overline{q}_1\, Q \to q_2\, \overline{q}_3$. The Pauli interference effect arises when one of the final (anti)quarks in the decay of Q is identical to the spectator (anti)quark in the hadron, so that an interference of identical particles should be taken into account. The latter interference can be either constructive or destructive, depending on the relative spin-color arrangement of the (anti)quark produced in the decay and of the spectator one, thus the sign of the PI effect is found only as a result of specific dynamical calculation. In specific calculations, however, WS and PI arise from the same terms in OPE, depending on the hadron discussed, and technically there is no need to resort to the traditional terminology of WS and PI.

In what follows we discuss separately the effects of the three terms in the expansion (8.5) and their interpretation within the existing and future data.

8.2.2 The parton decay rate

The leading term in the OPE amounts to the perturbative expression for the decay rate of a heavy quark. In b hadrons the contribution of the subsequent terms in OPE is at the level of few percent, so that the perturbative part can be confronted with the data in its own right. In particular, for the B_d meson the higher terms in OPE contribute only about 1% of the total nonleptonic as well as of the semileptonic decay rate. Thus the data on these rates can be directly compared with the leading perturbative term in OPE.

The principal theoretical topic, associated with this term is the calculation of QCD radiative corrections, i.e. of the factor η_{nl} in Eq. (8.3) and of a similar factor, η_{nl}, for semileptonic decays. It should be noted, that even at this, perturbative, level there is a known long-standing problem between the existing data and the theory in that the current world average for the semileptonic branching ratio for the B mesons, $B_{sl}(B) = 10.45 \pm 0.21\%$, is somewhat lower than the value $B_{sl}(B) \geq 11.5$ preferred from the present knowledge of theoretical QCD radiative corrections to the ratio of nonleptonic to semileptonic decay rates (see, e.g., [10]). However, this apparent discrepancy may in fact be due to insufficient 'depth' of perturbative QCD calculation of the ratio η_{nl}/η_{sl}. In order to briefly elaborate on this point, we notice that the standard way of analyzing the perturbative radiative corrections in the nonleptonic decays is through the renormalization group (RG) summation of the leading log terms and the first next-to-leading terms [11,12] in the parameter $L \equiv \ln(m_W/m_b)$. For the semileptonic decays the logarithmic dependence on m_W/m_b is absent in all orders due to the weak current conservation at momenta larger than m_b, thus the correction is calculated by the standard perturbative technique, and a complete expression in the first order in α_s is available both for the total rate [13,14] and for the lepton spectrum [15]. In reality however the parameter $L \approx 2.8$ is not large, and non-logarithmic terms may well compete

with the logarithmic ones. This behavior is already seen from the known expression for the logarithmic terms: when expanded up to the order α_s^2 the result of Ref. [16] for the rate of decays with single final charmed quark takes the form

$$\frac{\Gamma(b \to c\bar{u}d) + \Gamma(b \to c\bar{u}s)}{3\,\Gamma(b \to ce\bar{\nu})} = 1 + \frac{\alpha_s}{\pi} + \frac{\alpha_s^2}{\pi^2}\left[4\,L^2 + \left(\frac{7}{6} + \frac{2}{3}\,c(m_c^2/m_b^2)\right) L\right], \qquad (8.5)$$

where, in terms of notation of Ref. [16], $c(a) = c_{22}(a) - c_{12}(a)$. The behavior of the function $c(a)$ is known explicitly [16] and is quite weak: $c(0) = 19/2$, $c(1) = 6$, and $c(m_c^2/m_b^2) \approx 9.0$ for the realistic mass ratio $m_c/m_b \approx 0.3$. One can see that the term with the single logarithm L contributes about two thirds of that with L^2 in the term quadratic in α_s. Under such circumstances the RG summation of the terms with powers of L does not look satisfactory for numerical estimates of the QCD effects, at least at the so far considered level of the first next-to-leading order terms, and the next-to-next-to-leading terms can be equally important as the two known ones, which would eliminate the existing impasse between the theory and the data on $B_{sl}(B)$. One can present some arguments [17] that this is indeed the case for the b quark decay, although a complete calculation of these corrections is still unavailable.

8.2.3 Chromomagnetic and time dilation effects in decay rates

The corrections suppressed by two powers of m_Q^{-1} to inclusive decay rates arise from two sources [7]: the $O(m_Q^{-2})$ corrections to the matrix element of the leading operator, $(\overline{Q}Q$, and the second term in OPE (8.5) containing the chromomagnetic interaction. The expression for the matrix element of the leading operator with the correction included is written in the form

$$\langle H_Q|\overline{Q}Q|H_Q\rangle = 1 - \frac{\mu_\pi^2(H_Q) - \mu_g^2(H_Q)}{2\,m_Q^2} + \ldots, \qquad (8.6)$$

where μ_π^2 and μ_g^2 are defined as

$$\begin{aligned} \mu_\pi^2 &= \langle H_Q|\overline{Q}\,(i\vec{D})^2\,Q|H_Q\rangle\,, \\ \mu_g^2 &= \langle H_Q|\overline{Q}\,\frac{1}{2}\sigma^{\mu\nu}G_{\mu\nu}Q|H_Q\rangle\,, \end{aligned} \qquad (8.7)$$

with D being the QCD covariant derivative. The correction in equation (8.6) in fact corresponds to the time dilation factor m_Q/E_Q, for the heavy quark decaying inside a hadron, where it has energy E_Q, which energy is contributed by the kinetic part ($\propto \mu_\pi^2$) and the chromomagnetic part ($\propto \mu_g^2$). The second term in OPE describes the effect of the chromomagnetic interaction in the decay process, and is also expressed through μ_g^2.

The explicit formulas for the decay rates, including the effects up to the order m_Q^{-2} are found in [7] and for decays of the b hadrons read as follows. For the semileptonic decay rate

$$\Gamma_{sl}(H_b) = \frac{|V_{cb}|^2\,G_F^2\,m_b^5}{192\,\pi^3}\,\langle H_b|\bar{b}b|H_b\rangle\,\left[1 + \frac{\mu_g^2}{m_b^2}\left(\frac{x}{2}\,\frac{d}{dx} - 2\right)\right]\,\eta_{sl}\,I_0(x,\,0,\,0)\,, \qquad (8.8)$$

and for the nonleptonic decay rate

$$\Gamma_{nl}(H_b) = \frac{|V_{cb}|^2\, G_F^2\, m_b^5}{64\,\pi^3}\, \langle H_b|\bar{b}b|H_b\rangle \left\{ \left[1 + \frac{\mu_g^2}{m_b^2}\left(\frac{x}{2}\frac{d}{dx} - 2\right)\right] \eta_{nl}\, I(x) - 8\eta_2\, \frac{\mu_g^2}{m_b^2}\, I_2(x) \right\} . \tag{8.9}$$

These formulas take into account only the dominant CKM mixing V_{cb} and neglect the small one, V_{ub}. The following notation is also used: $x = m_c/m_b$, $I_0(x,y,z)$ stands for the kinematical suppression factor in a three-body weak decay due to masses of the final fermions. In particular,

$$I_0(x,0,0) = (1-x^4)(1-8\,x^2+x^4) - 24\,x^4\,\ln x\,, \tag{8.10}$$
$$I_0(x,x,0) = (1-14\,x^2-2\,x^4-12x^6)\sqrt{1-4\,x^2} + 24\,(1-x^4)\,\ln\frac{1+\sqrt{1-4\,x^2}}{1-\sqrt{1-4\,x^2}}\,.$$

Furthermore, $I(x) = I_0(x,0,0) + I_0(x,x,0)$, and

$$I_2(x) = (1-x^2)^3 + \left(1+\frac{1}{2}x^2+3x^4\right)\sqrt{1-4\,x^2} - 3x^2\,(1-2x^4)\ln\frac{1+\sqrt{1-4\,x^2}}{1-\sqrt{1-4\,x^2}}\,.$$

Finally, the QCD radiative correction factor η_2 in Eq. (8.9) is known in the leading logarithmic approximation and is expressed in terms of the well known coefficients C_+ and C_- in the renormalization of the nonleptonic weak interaction: $\eta_2 = (C_+^2(m_b) - C_-^2(m_b))/6$ with

$$C_-(\mu) = C_+^{-2}(\mu) = \left[\frac{\alpha_s(\mu)}{\alpha_s(m_W)}\right]^{4/b}\,, \tag{8.11}$$

and b is the coefficient in the QCD beta function. The value of b relevant to b decays is $b = 23/3$.

Numerically, for $x \approx 0.3$, the expressions for the decay rates can be written as

$$\Gamma_{sl}(H_b) = \Gamma_{sl}^{parton}\left(1 - \frac{\mu_\pi^2(H_b)-\mu_g^2(H_b)}{2\,m_b^2} - 2.6\frac{\mu_g^2(H_b)}{m_b^2}\right)\,,$$
$$\Gamma_{nl}(H_b) = \Gamma_{nl}^{parton}\left(1 - \frac{\mu_\pi^2(H_b)-\mu_g^2(H_b)}{2\,m_b^2} - 1.0\frac{\mu_g^2(H_b)}{m_b^2}\right)\,, \tag{8.12}$$

where Γ^{parton} is the perturbation theory value of the corresponding decay rate of b quark.

The matrix elements μ_π^2 and μ_g^2 are related to the spectroscopic formula for a heavy hadron mass M,

$$M(H_Q) = m_Q + \overline{\Lambda}(H_Q) + \frac{\mu_\pi^2(H_Q)-\mu_g^2(H_Q)}{2\,m_Q} + \ldots \tag{8.13}$$

Being combined with the spin counting for pseudoscalar and vector mesons, this formula allows to find the value of μ_g^2 in pseudoscalar mesons from the mass splitting:

$$\mu_g^2(B) = \frac{3}{4}\left(M_{B^*}^2 - M_B^2\right) \approx 0.36\,GeV^2\,. \tag{8.14}$$

The value of μ_π^2 for B mesons is less certain. It is constrained by the inequality [18], $\mu_\pi^2(H_Q) \geq \mu_g^2(H_Q)$, and there are theoretical estimates from the QCD sum rules [19]: $\mu_\pi^2(B) = 0.54 \pm 0.12\,GeV^2$ and from an analysis of spectroscopy of heavy hadrons [20]: $\mu_\pi^2(B) = 0.3 \pm 0.2\,GeV^2$. In any event, the discussed corrections are rather small for b hadrons, given that $\mu_g^2/m_b^2 \approx 0.015$. The largest, in relative terms, effect of these corrections in B meson decays is on the semileptonic decay rate, where it amounts to $4-5$ % suppression of the rate, which rate however is only a moderate fraction of the total width. In the dominant nonleptonic decay rate the effect is smaller, and, according to the formula (8.12) amounts to about $1.5-2$ %.

The effect of the m_Q^{-2} corrections can be evaluated with a somewhat better certainty for the ratio of the decay rates of Λ_b and B mesons. This is due to the fact that $\mu_g^2(\Lambda_b) = 0$, since there is no correlation of the spin of the heavy quark in Λ_b with the light component, having overall quantum numbers $J^P = 0^+$. Then, applying the formula (8.12) to B and Λ_b, we find for the ratio of the (dominant) nonleptonic decay rates:

$$\frac{\Gamma_{nl}(\Lambda_b)}{\Gamma_{nl}(B)} = 1 - \frac{\mu_\pi^2(\Lambda_b)-\mu_\pi^2(B)}{2\,m_b^2} + 0.5\frac{\mu_g^2(B)}{m_b^2}\,. \tag{8.15}$$

The difference of the kinetic terms, $\mu_\pi^2(\Lambda_b)-\mu_\pi^2(B)$, can be estimated from the mass formula:

$$\mu_\pi^2(\Lambda_b) - \mu_\pi^2(B) = \frac{2\,m_b\,m_c}{m_b-m_c}\left[\overline{M}(B) - \overline{M}(D) - M(\Lambda_b) + M(\Lambda_c)\right] = 0 \pm 0.04\,GeV^2\,, \tag{8.16}$$

where $\overline{M}$ is the spin-averaged mass of the mesons, e.g., $\overline{M}(B) = (M(B) + 3M(B^*))/4$. The estimated difference of the kinetic terms is remarkably small. Thus the effect in the ratio of the decay rates essentially reduces to the chromomagnetic term, which is also rather small and accounts for less than 1% difference of the rates. For the ratio of the semileptonic decay rates the chromomagnetic term is approximately four times larger, but then the contribution of the semileptonic rates to the total width is rather small. Thus one concludes that the terms of order m_b^{-2} in the OPE expansion for the decay rates can account only for about 1% difference of the lifetimes of Λ_b and the B mesons.

The significance of the m_Q^{-2} terms is substantially different for the decay rates of charmed hadrons, where these effects suppress the inclusive decays of the D mesons by about 40% with respect to those of the charmed hyperons in a reasonable agreement with the observed pattern of the lifetimes.

It should be emphasized once again that the m_Q^{-2} effects do not depend on the flavors of the spectator quarks or antiquarks. Thus the explanation of the variety of the inclusive decay rates within the flavor $SU(3)$ multiplets, observed for charmed hadrons and expected for the b ones, has to be sought among the m_Q^{-3} terms.

8.2.4 $L_{eff}^{(3)}$ Coefficients and operators

Although the third term in the expansion (8.5) is formally suppressed by an extra power of m_Q^{-1}, its effects are comparable to, or even larger than the effects of the second term. This

is due to the fact that the diagrams determining the third term (see Fig. 8.1) contain a two-body phase space, while the first two terms involve a three-body phase space. This brings in a numerical enhancement factor, typically $4\pi^2$. The enhanced numerical significance of the third term in OPE, generally, does not signal a poor convergence of the expansion in inverse heavy quark mass for decays of b, and even charmed, hadrons the numerical enhancement factor is a one time occurrence in the series, and there is no reason for similar 'anomalous' enhancement among the higher terms in the expansion.

Here we first present the expressions for the relevant parts of $L^{(3)}_{eff}$ for decays of b and c hadrons in the form of four-quark operators and then proceed to a discussion of hadronic matrix elements and the effects in specific inclusive decay rates. The consideration of the effects in decays of charmed hadrons is interesting in its own right, and leads to new predictions to be tested experimentally, and is also important for understanding the magnitude of the involved matrix elements using the existing data on charm decays.

We start with considering the term $L^{(3)}_{eff}$ in b hadron nonleptonic decays, $L^{(3,b)}_{eff,nl}$, induced by the underlying processes $b \to c\overline{u}\,d$, $b \to c\,\overline{c}\,s$, $b \to c\,\overline{u}\,s$, and $b \to c\,\overline{c}\,d$. Unlike the case of three-body decay, the kinematical difference between the two-body states $c\overline{c}$ and $c\overline{u}$, involved in calculation of $L^{(3,b)}_{eff,nl}$ is of the order of $m_c^2/m_b^2 \approx 0.1$ and is rather small. At present level of accuracy in discussing this term in OPE, one can safely neglect the effect of finite charmed quark mass[2]. In this approximation the expression for $L^{(3,b)}_{eff,nl}$ reads as [4]

$$
\begin{aligned}
L^{(3,b)}_{eff,nl} = |V_{cb}|^2\,\frac{G_F^2\,m_b^2}{4\pi}\Big\{&\tilde{C}_1\,(\overline{b}\Gamma_\mu b)(\overline{u}\Gamma_\mu u) + \tilde{C}_2\,(\overline{b}\Gamma_\mu u)(\overline{u}\Gamma_\mu b)\\
&+ \tilde{C}_5\,(\overline{b}\Gamma_\mu b + \frac{2}{3}\overline{b}\gamma_\mu\gamma_5 b)(\overline{q}\Gamma_\mu q) + \tilde{C}_6\,(\overline{b}_i\Gamma_\mu b_k + \frac{2}{3}\overline{b}_i\gamma_\mu\gamma_5 b_k)(\overline{q}_k\Gamma_\mu q_i)\\
&+ \frac{1}{3}\,\tilde{\kappa}^{1/2}\,(\tilde{\kappa}^{-2/9}-1)\,\Big[2\,(\tilde{C}_+^2-\tilde{C}_-^2)\,(\overline{b}\Gamma_\mu t^a b)\,j_\mu^a\\
&- (5\tilde{C}_+^2+\tilde{C}_-^2-6\,\tilde{C}_+\,\tilde{C}_-)(\overline{b}\Gamma_\mu t^a b + \frac{2}{3}\overline{b}\gamma_\mu\gamma_5 t^a b)j_\mu^a\Big]\Big\}\,,
\end{aligned}
\tag{8.17}
$$

where the notation $(\overline{q}\,\Gamma\,q) = (\overline{d}\,\Gamma\,d) + (\overline{s}\,\Gamma\,s)$ is used, the indices i, k are the color triplet ones, $\Gamma_\mu = \gamma_\mu\,(1-\gamma_5)$, and $j_\mu^a = \overline{u}\gamma_\mu t^a u + \overline{d}\gamma_\mu t^a d + \overline{s}\gamma_\mu t^a s$ is the color current of the light quarks with $t^a = \lambda^a/2$ being the generators of the color $SU(3)$. The notation $\tilde{C}_\pm$, is used as shorthand for the short-distance renormalization coefficients $C_\pm(\mu)$ at $\mu = m_b$: $\tilde{C}_\pm \equiv C_\pm(m_b)$. The expression (8.17) is written in the leading logarithmic approximation for the QCD radiative effects in a low normalization point μ such that $\mu \ll m_b$ (but still, at least formally, $\mu \gg \Lambda_{QCD}$). For such μ there arises so called 'hybrid' renormalization [22], depending on the factor $\tilde{\kappa} = \alpha_s(\mu)/\alpha_s(m_b)$. The coefficients $\tilde{C}_A$ with $A = 1,\ldots,6$ in Eq. (8.17) have the following explicit expressions in terms of $\tilde{C}_\pm$ and $\tilde{\kappa}$:

$$
\begin{aligned}
\tilde{C}_1 &= \tilde{C}_+^2 + \tilde{C}_-^2 + \frac{1}{3}(1-\kappa^{1/2})(\tilde{C}_+^2 - \tilde{C}_-^2)\,,\\
\tilde{C}_2 &= \kappa^{1/2}\,(\tilde{C}_+^2 - \tilde{C}_-^2)\,,
\end{aligned}
$$

[2]The full expression for a finite charmed quark mass can be found in [21]

$$
\begin{aligned}
\tilde{C}_3 &= -\frac{1}{4}\,\Big[(\tilde{C}_+ - \tilde{C}_-)^2 + \frac{1}{3}(1-\kappa^{1/2})(5\tilde{C}_+^2 + \tilde{C}_-^2 + 6\tilde{C}_+\tilde{C}_-)\Big]\,,\\
\tilde{C}_4 &= -\frac{1}{4}\,\kappa^{1/2}\,(5\tilde{C}_+^2 + \tilde{C}_-^2 + 6\tilde{C}_+\tilde{C}_-)\,,\\
\tilde{C}_5 &= -\frac{1}{4}\,\Big[(\tilde{C}_+ + \tilde{C}_-)^2 + \frac{1}{3}(1-\kappa^{1/2})(5\tilde{C}_+^2 + \tilde{C}_-^2 - 6\tilde{C}_+\tilde{C}_-)\Big]\,,\\
\tilde{C}_6 &= -\frac{1}{4}\,\kappa^{1/2}\,(5\tilde{C}_+^2 + \tilde{C}_-^2 - 6\tilde{C}_+\tilde{C}_-)\,.
\end{aligned}
\tag{8.18}
$$

The expression for the CKM dominant semileptonic decays of b hadrons, associated with the elementary process $b \to c\,\ell\,\nu$ does not look to be of an immediate interest. The reason is that this process is intrinsically symmetric under the flavor $SU(3)$, and one expects no significant splitting of the semileptonic decay rates within $SU(3)$ multiplets of the b hadrons. The only possible effect of this term, arising through a penguin-like mechanism can be in a small overall shift of semileptonic decay rates between B mesons and baryons. However, these effects are quite suppressed and are believed to be even smaller than the ones arising form the discussed m_b^{-2} terms.

For charm decays there is a larger, than for b hadrons, variety of effects associated with $L^{(3)}_{eff}$ that can be studied experimentally, and we present here the relevant parts of the effective Lagrangian. For the CKM dominant nonleptonic decays of charm, originating from the quark process $c \to s\,u\,\overline{d}$, the discussed term in OPE has the form

$$
\begin{aligned}
L^{(3,\,\Delta C=\Delta S)}_{eff,nl} = \cos^4\theta_c\,\frac{G_F^2\,m_c^2}{4\pi}\Big\{&C_1\,(\overline{c}\Gamma_\mu c)(\overline{d}\Gamma_\mu d) + C_2\,(\overline{c}\Gamma_\mu d)(\overline{d}\Gamma_\mu c)\\
&+ C_3\,(\overline{c}\Gamma_\mu c + \frac{2}{3}\overline{c}\gamma_\mu\gamma_5 c)(\overline{s}\Gamma_\mu s) + C_4\,(\overline{c}_i\Gamma_\mu c_k + \frac{2}{3}\overline{c}_i\gamma_\mu\gamma_5 c_k)(\overline{s}_k\Gamma_\mu s_i)\\
&+ C_5\,(\overline{c}\Gamma_\mu c + \frac{2}{3}\overline{c}\gamma_\mu\gamma_5 c)(\overline{u}\Gamma_\mu u) + C_6\,(\overline{c}_i\Gamma_\mu c_k + \frac{2}{3}\overline{c}_i\gamma_\mu\gamma_5 c_k)(\overline{u}_k\Gamma_\mu u_i)\\
&+ \frac{1}{3}\,\kappa^{1/2}\,(\kappa^{-2/9}-1)\,\Big[2\,(C_+^2 - C_-^2)\,(\overline{c}\Gamma_\mu t^a c)\,j_\mu^a - (5C_+^2 + C_-^2)(\overline{c}\Gamma_\mu t^a c + \frac{2}{3}\overline{c}\gamma_\mu\gamma_5 t^a c)j_\mu^a\Big]\Big\}\,,
\end{aligned}
\tag{8.19}
$$

where, θ_c is the Cabibbo angle, and the coefficients without the tilde are given by the same expressions as above for the b decays (i.e., those with tilde) with the replacement $m_b \to m_c$. The part of the notation in the superscript $\Delta C = \Delta S$ points to the selection rule for the dominant CKM unsuppressed nonleptonic decays. One can rather realistically envisage however a future study of inclusive rates for the once CKM suppressed decays of charmed hadrons[3], satisfying the selection rule $\Delta S = 0$ and associated with the quark processes $c \to d\,u\,\overline{s}$ and $c \to d\,u\,\overline{d}$. The corresponding part of the effective Lagrangian for these processes reads as

[3]Even if the inclusive rate of these decays is not to be separated experimentally, they contribute about 10% of the total decay rate, and it is worthwhile to include their contribution in the balance of the total width.

$$L^{(3,\Delta S=0)}_{eff,nl} = \cos^2\theta_c \sin^2\theta_c \frac{G_F^2 m_c^2}{4\pi}\left\{ C_1\,(\overline{c}\Gamma_\mu c)(\overline{q}\Gamma_\mu q) + C_2\,(\overline{c}_i\Gamma_\mu c_k)(\overline{q}_k\Gamma_\mu q_i) \right.$$
$$+ C_3\,(\overline{c}\Gamma_\mu c + \frac{2}{3}\overline{c}\gamma_\mu\gamma_5 c)(\overline{q}\Gamma_\mu q) + C_4\,(\overline{c}_i\Gamma_\mu c_k + \frac{2}{3}\overline{c}_i\gamma_\mu\gamma_5 c_k)(\overline{q}_k\Gamma_\mu q_i) \qquad (8.20)$$
$$+ 2\,C_5\,(\overline{c}\Gamma_\mu c + \frac{2}{3}\overline{c}\gamma_\mu\gamma_5 c)(\overline{u}\Gamma_\mu u) + 2\,C_6\,(\overline{c}_i\Gamma_\mu c_k + \frac{2}{3}\overline{c}_i\gamma_\mu\gamma_5 c_k)(\overline{u}_k\Gamma_\mu u_i)$$
$$\left. + \frac{2}{3}\kappa^{1/2}(\kappa^{-2/9}-1)\left[2\,(C_+^2 - C_-^2)\,(\overline{c}\Gamma_\mu t^a c)\,j_\mu^a - (5C_+^2 + C_-^2)(\overline{c}\Gamma_\mu t^a c + \frac{2}{3}\overline{c}\gamma_\mu\gamma_5 t^a c)\,j_\mu^a\right]\right\},$$

where again the notation $(\overline{q}\,\Gamma\,q) = (\overline{d}\,\Gamma\,d) + (\overline{s}\,\Gamma\,s)$ is used.

The semileptonic decays of charm, the CKM dominant, associated with $c \to s\,\ell\,\nu$, and the CKM suppressed, originating from $c \to s\,\ell\,\nu$, contribute to the semileptonic decay rate, which certainly can be measured experimentally. The expression for the part of the effective Lagrangian, describing the m_Q^{-3} terms in these decays is [17,24,25]

$$L^{(3)}_{eff,\,sl} = \frac{G_F^2 m_c^2}{12\pi}\left\{ \cos^2\theta_c\left[L_1\,(\overline{c}\Gamma_\mu c + \frac{2}{3}\overline{c}\gamma_\mu\gamma_5 c)(\overline{s}\Gamma_\mu s) + L_2\,(\overline{c}_i\Gamma_\mu c_k + \frac{2}{3}\overline{c}_i\gamma_\mu\gamma_5 c_k)(\overline{s}_k\Gamma_\mu s_i)\right]\right.$$
$$+ \sin^2\theta_c\left[L_1\,(\overline{c}\Gamma_\mu c + \frac{2}{3}\overline{c}\gamma_\mu\gamma_5 c)(\overline{d}\Gamma_\mu d) + L_2\,(\overline{c}_i\Gamma_\mu c_k + \frac{2}{3}\overline{c}_i\gamma_\mu\gamma_5 c_k)(\overline{d}_k\Gamma_\mu d_i)\right]$$
$$\left. - 2\,\kappa^{1/2}(\kappa^{-2/9}-1)\,(\overline{c}\Gamma_\mu t^a c + \frac{2}{3}\overline{c}\gamma_\mu\gamma_5 t^a c)\,j_\mu^a\right\}, \qquad (8.21)$$

with the coefficients L_1 and L_2 found as

$$L_1 = (\kappa^{1/2} - 1), \qquad L_2 = -3\,\kappa^{1/2}\,. \qquad (8.22)$$

8.2.5 Effects of $L^{(3)}_{eff}$ in mesons

The expressions for the terms in $L^{(3)}_{eff}$ still leave us with the problem of evaluating the matrix elements of the four-quark operators over heavy hadrons in order to calculate the effects in the decay rates according to the formula (8.2). In doing so only few conclusions can be drawn in a reasonably model independent way, i.e., without resorting to evaluation of the matrix elements using specific ideas about the dynamics of quarks inside hadrons. The most straightforward prediction can in fact be found for b hadrons. Namely, one can notice that the operator (8.17) is symmetric under the flavor U spin (an SU(2) subgroup of the flavor $SU(3)$, which mixes s and d quarks). This is a direct consequence of neglecting the small kinematical effect of the charmed quark mass. However the usual (in)accuracy of the flavor $SU(3)$ symmetry is likely to be a more limiting factor for the accuracy of this symmetry, than the corrections of order m_c^2/m_b^2. Modulo this reservation the immediate prediction from this symmetry is the degeneracy of inclusive decay rates within U spin doublets:

$$\Gamma(B_d) = \Gamma(B_s)\,, \qquad \Gamma(\Lambda_b) = \Gamma(\Xi_b^0)\,, \qquad (8.23)$$

where $\Gamma(B_s)$ stands for the average rate over the two eigenstates of the $B_s - \overline{B}_s$ oscillations. The data on decay rates of the cascade hyperon Ξ_b^0 are not yet available, while the currently

measured lifetimes of B_d and B_s are within less than 2% from one another. Theoretically, the difference of the lifetimes, associated with possible violation of the $SU(3)$ symmetry and with breaking of the U symmetry of the effective Lagrangian (8.17), is expected to not exceed about 1%.

For the non-vanishing matrix elements of four-quark operators over pseudoscalar mesons one traditionally starts with the factorization formula and parameterizes possible deviation from factorization in terms of 'bag constants'. Within the normalization convention adopted here the relations used in this parameterization read as

$$\langle P_{Q\overline{q}}|(\overline{Q}\Gamma_\mu q)\,(\overline{q}\Gamma_\mu Q)|P_{Q\overline{q}}\rangle = \frac{1}{2}\,f_P^2\,M_P\,B\,,$$
$$\langle P_{Q\overline{q}}|(\overline{Q}\Gamma_\mu Q)\,(\overline{q}\Gamma_\mu q)|P_{Q\overline{q}}\rangle = \frac{1}{6}\,f_P^2\,M_P\,\tilde{B}\,, \qquad (8.24)$$

where $P_{Q\overline{q}}$ stands for pseudoscalar meson made of Q and $\overline{q}$, f_P is the annihilation constant for the meson, and B and $\tilde{B}$ are bag constants. The parameters B and $\tilde{B}$ generally depend on the normalization point μ for the operators, and this dependence is compensated by the μ dependence of the coefficients in $L^{(3)}_{eff}$, so that the results for the physical decay rate difference do not depend on μ. If the normalization point μ is chosen at the heavy quark mass (i.e. $\mu = m_b$ for B mesons, and $\mu = m_c$ for D mesons) the predictions for the difference of total decay rates take a simple form in terms of the corresponding bag constants (generally different between B and D):

$$\Gamma(B^\pm) - \Gamma(B^0) = |V_{cb}|^2\,\frac{G_F^2 m_b^3 f_B^2}{8\pi}\left[(\tilde{C}_+^2 - \tilde{C}_-^2)\,B(m_b) + \frac{1}{3}\,(\tilde{C}_+^2 + \tilde{C}_-^2)\,\tilde{B}(m_b)\right]$$
$$\approx -0.025\,\left(\frac{f_B}{200\,MeV}\right)^2\,ps^{-1}\,, \qquad (8.25)$$

$$\Gamma(D^\pm) - \Gamma(D^0) = \cos^4\theta_c\,\frac{G_F^2 m_c^3 f_D^2}{8\pi}\left[(C_+^2 - C_-^2)\,B(m_c) + \frac{1}{3}\,(C_+^2 + C_-^2)\,\tilde{B}(m_c)\right]$$
$$\sim -0.8\,\left(\frac{f_D}{200\,MeV}\right)^2\,ps^{-1}\,, \qquad (8.26)$$

where the numerical values are written in the approximation of exact factorization: $B = 1$, and $\tilde{B} = 1$. It is seen from the numerical estimates that, even given all the theoretical uncertainties, the presented approach is in reasonable agreement with the data on the lifetimes of D and B mesons. In particular, this approach describes, at least qualitatively, the strong suppression of the decay rate of $D^\pm$ mesons relative to D^0, the experimental observation of which has in fact triggered in early 80-s the theoretical study of preasymptotic in heavy quark mass effects in inclusive decay rates. For the B mesons the estimate (8.25) is also in a reasonable agreement with the current data for the discussed difference $(-0.043 \pm 0.017\,ps^{-1})$.

8.2.6 Effects of $L^{(3)}_{eff}$ in baryons

The weakly decaying heavy hyperons, containing either c or b quark are: $\Lambda_Q \sim Qud$, $\Xi^{(u)}_Q \sim Qus$, $\Xi^{(d)}_Q \sim Qds$, and $\Omega_Q \sim Qss$. The first three baryons form an $SU(3)$ (anti)triplet. The light diquark in all three is in the state with quantum numbers $J^P = 0^+$, so that there is no correlation of the spin of the heavy quark with the light component of the baryon. On the contrary, in Ω_Q the two strange quarks form a $J^P = 1^+$ state, and a correlation between the spins of heavy and light quarks is present. The absence of spin correlation for the heavy quark in the triplet of hyperons somewhat reduces the number of independent four-quark operators, having nonvanishing diagonal matrix elements over these baryons. Indeed, the operators entering $L^{(3)}_{eff}$ contain both vector and axial bilinear forms for the heavy quarks. However the axial part requires a correlation of the heavy quark spin with that of a light quark, and is thus vanishing for the hyperons in the triplet. Therefore only the structures with vector currents are relevant for these hyperons. These structures are of the type $(\overline{c}\gamma_\mu\, c)(\overline{q}\,\gamma_\mu\, q)$ and $(\overline{c}_i\,\gamma_\mu\, c_k)(\overline{q}_k\,\gamma_\mu\, q_i)$ with q being d, s or u. The flavor $SU(3)$ symmetry then allows to express, for each of the two color combinations, the matrix elements of three different operators, corresponding to three flavors of q, over the baryons in the triplet in terms of only two combinations: flavor octet and flavor singlet. Thus all effects of $L^{(3)}_{eff}$ in the triplet of the baryons can be expressed in terms of four independent combinations of matrix elements. These can be chosen in the following way:

$$\begin{aligned}
x &= \left\langle \frac{1}{2}\,(\overline{Q}\,\gamma_\mu\, Q)\,[(\overline{u}\,\gamma_\mu u) - (\overline{s}\,\gamma_\mu s)]\right\rangle_{\Xi^{(d)}_Q - \Lambda_Q} \\
&= \left\langle \frac{1}{2}\,(\overline{Q}\,\gamma_\mu\, Q)\,\Big[(\overline{s}\,\gamma_\mu s) - (\overline{d}\,\gamma_\mu d)\Big]\right\rangle_{\Lambda_Q - \Xi^{(u)}_Q}\,, \\
y &= \left\langle \frac{1}{2}\,(\overline{Q}_i\,\gamma_\mu\, Q_k)\,[(\overline{u}_k\,\gamma_\mu u_i) - (\overline{s}_k\,\gamma_\mu s_i)]\right\rangle_{\Xi^{(d)}_Q - \Lambda_Q} \\
&= \left\langle \frac{1}{2}\,(\overline{Q}_i\,\gamma_\mu\, Q_k)\,\Big[(\overline{s}_k\,\gamma_\mu s_i) - (\overline{d}_k\,\gamma_\mu d_i)\Big]\right\rangle_{\Lambda_Q - \Xi^{(u)}_Q}\,,
\end{aligned} \tag{8.27}$$

with the notation for the differences of the matrix elements: $\langle\mathcal{O}\rangle_{A-B} = \langle A|\mathcal{O}|A\rangle - \langle B|\mathcal{O}|B\rangle$, for the flavor octet part and the matrix elements:

$$\begin{aligned}
x_s &= \frac{1}{3}\,\langle H_Q|(\overline{Q}\,\gamma_\mu\, Q)\,\Big((\overline{u}\,\gamma_\mu\, u) + (\overline{d}\,\gamma_\mu\, d) + (\overline{s}\,\gamma_\mu\, s)\Big)\,|H_Q\rangle \\
y_s &= \frac{1}{3}\,\langle H_Q|(\overline{Q}_i\,\gamma_\mu\, Q_k)\,\Big((\overline{u}_k\,\gamma_\mu\, u_i) + (\overline{d}_k\,\gamma_\mu\, d_i) + (\overline{s}_k\,\gamma_\mu\, s_i)\Big)\,|H_Q\rangle
\end{aligned} \tag{8.28}$$

for the flavor singlet part, where H_Q stands for any heavy hyperon in the (anti)triplet.

The initial, very approximate, theoretical estimates of the matrix elements [4] were essentially based on a non-relativistic constituent quark model, where these matrix elements are proportional to the density of a light quark at the location of the heavy one, i.e., in terms of the wave function, proportional to $|\psi(0)|^2$. Using then the same picture for the

matrix elements over pseudoscalar mesons, relating the quantity $|\psi(0)|^2$ to the annihilation constant f_P, and assuming that $|\psi(0)|^2$ is approximately the same in baryons as in mesons, one arrived at the estimate

$$y = -x = x_s = -y_s \approx \frac{f_D^2\, M_D}{12} \approx 0.006\, GeV^2\,, \tag{8.29}$$

where the sign relation between x and y is inferred from the color antisymmetry of the constituent quark wave function for baryons. Since the constituent picture was believed to be valid at distances of the order of the hadron size, the estimate (8.29) was applied to the matrix elements in a low normalization point where $\alpha_s(\mu) \approx 1$. For the matrix elements of the operators, containing s quarks over the Ω_Q hyperon, this picture predicts an enhancement factor due to the spin correlation:

$$\langle\Omega_Q|(\overline{Q}\,\Gamma_\mu\, Q)(\overline{s}\,\Gamma_\mu\, s)|\Omega_Q\rangle = -\langle\Omega_Q|(\overline{Q}_i\,\Gamma_\mu\, Q_k)(\overline{s}_k\,\Gamma_\mu\, s_i)|\Omega_Q\rangle = \frac{10}{3}\,y \tag{8.30}$$

Although these simple estimates allowed to correctly predict [4] the hierarchy of lifetimes of charmed hadrons prior to establishing this hierarchy experimentally, they fail to quantitatively predict the differences of lifetimes of charmed baryons. We shall see that the available data indicate that the color antisymmetry relation is badly broken, and the absolute value of the matrix elements is larger, than the naive estimate (8.29), especially for the quantity x.

It should be emphasized that in the heavy quark limit the matrix elements (8.27) and (8.28) do not depend on the flavor of the heavy quark, provided that the same normalization point μ is used. Therefore, applying the OPE formulas to both charmed and b baryons, one can extract the values for the matrix elements from available data on charmed hadrons, and then make predictions for b baryons, as well as for other inclusive decay rates, e.g., semileptonic, for charmed hyperons.

The only data available so far, which would allow to extract the matrix elements, are on the lifetimes of charmed hyperons. Therefore, one has to take into account several essential types of inclusive decay, at least those that contribute to the total decay rate at the level of about 10%. Here we first concentrate on the differences of the decay rates within the $SU(3)$ triplet of the hyperons, which will allow us to extract the non-singlet quantities x and y, and then discuss the $SU(3)$ singlet shifts of the rates.

The differences of the dominant Cabibbo unsuppressed nonleptonic decay rates are given by

$$\begin{aligned}
\delta_1^{nl,\,0} &\equiv \Gamma^{nl}_{\Delta S=\Delta C}(\Xi_c^0) - \Gamma^{nl}_{\Delta S=\Delta C}(\Lambda_c) = \cos^4\theta_c\,\frac{G_F^2\, m_c^2}{4\pi}\,[(C_5 - C_3)\,x + (C_6 - C_4)\,y]\,, \\
\delta_2^{nl,\,0} &\equiv \Gamma^{nl}_{\Delta S=\Delta C}(\Lambda_c) - \Gamma^{nl}_{\Delta S=\Delta C}(\Xi_c^+) = \cos^4\theta_c\,\frac{G_F^2\, m_c^2}{4\pi}\,[(C_3 - C_1)\,x + (C_4 - C_2)\,y]\,.
\end{aligned} \tag{8.31}$$

The once Cabibbo suppressed decay rates of Λ_c and Ξ_c^+ are equal, due to the $\Delta U = 0$ property of the corresponding effective Lagrangian $L^{(3,1)}_{eff,nl}$ (Eq. (8.21)). Thus the only difference for these decays in the baryon triplet is

$$\delta^{nl,1} \equiv \Gamma^{nl}_{\Delta S=0}(\Xi_c^0) - \Gamma^{nl}_{\Delta S=0}(\Lambda_c)$$
$$= \cos^2\theta_c \sin^2\theta_c \frac{G_F^2 m_c^2}{4\pi}\left[(2C_5 - C_1 - C_3)\,x + (2C_6 - C_2 - C_4)\,y\right] . \quad (8.32)$$

The dominant semileptonic decay rates are equal among the two Ξ_c baryons due to the isotopic spin property $\Delta I = 0$ of the corresponding interaction Lagrangian, thus there is only one non-trivial splitting for these decays:

$$\delta^{sl,0} \equiv \Gamma^{sl}_{\Delta S=-1}(\Xi_c) - \Gamma^{sl}_{\Delta S=-1}(\Lambda_c) = -\cos^2\theta_c \frac{G_F^2 m_c^2}{12\pi}\left[L_1\,x + L_2\,y\right] . \quad (8.33)$$

Finally, the Cabibbo suppressed semileptonic decay rates are equal for Λ_c and Ξ_c^0, due to the $\Delta V = 0$ property of the corresponding interaction. Thus the only difference for these is

$$\delta^{sl,1} \equiv \Gamma^{sl}_{\Delta S=0}(\Lambda_c) - \Gamma^{sl}_{\Delta S=0}(\Xi_c^+) = -\sin^2\theta_c \frac{G_F^2 m_c^2}{12\pi}\left[L_1\,x + L_2\,y\right] . \quad (8.34)$$

Using the relations (8.31)–(8.34) on can find expressions for two differences of the measured total decay rates, $\Delta_1 = \Gamma(\Xi_c^0) - \Gamma(\Lambda_c)$ and $\Delta_2 = \Gamma(\Lambda_c) - \Gamma(\Xi_c^+)$, in terms of the quantities x and y:

$$\Delta_1 = \delta_1^{nl,\,0} + \delta^{nl,1} + 2\,\delta^{sl,0}$$
$$= \frac{G_F^2 m_c^2}{4\pi}\cos^2\theta\left\{x\left[\cos^2\theta\,(C_5 - C_3) + \sin^2\theta\,(2C_5 - C_1 - C_3) - \frac{2}{3}L_1\right]\right.$$
$$\left. + y\left[\cos^2\theta\,(C_6 - C_4) + \sin^2\theta\,(2C_6 - C_2 - C_4) - \frac{2}{3}L_2\right]\right\}, \quad (8.35)$$

and

$$\Delta_2 = \delta_2^{nl,\,0} - 2\,\delta^{sl,0} + 2\,\delta^{sl,1}$$
$$= \frac{G_F^2 m_c^2}{4\pi}\left\{x\left[\cos^4\theta\,(C_3 - C_1) + \frac{2}{3}\left(\cos^2\theta - \sin^2\theta\right)L_1\right]\right.$$
$$\left. + y\left[\cos^4\theta\,(C_4 - C_2) + \frac{2}{3}\left(\cos^2\theta - \sin^2\theta\right)L_2\right]\right\}. \quad (8.36)$$

By comparing these relations with the data, one can extract the values of x and y. Using the current data for the total decay rates: $\Gamma(\Lambda_c) = 4.85 \pm 0.28\,ps^{-1}$, $\Gamma(\Xi_c^0) = 10.2 \pm 2\,ps^{-1}$, and the updated value [26] $\Gamma(\Xi_c^+) = 3.0 \pm 0.45\,ps^{-1}$, we find for the μ independent matrix element x

$$x = -(0.04 \pm 0.01)\,GeV^3\left(\frac{1.4\,GeV}{m_c}\right)^2 , \quad (8.37)$$

while the dependence of the thus extracted matrix element y on the normalization point μ is shown in Fig. 8.2.[4]

[4]It should be noted that the curves at large values of κ, $\kappa > \sim 3$, are shown only for illustrative purpose. The coefficients in the OPE, leading to the equations (8.35,8.36), are purely perturbative. Thus, formally, they correspond to $\alpha_s(\mu) \ll 1$, i.e., to $\kappa \ll 1/\alpha_s(m_c) \sim (3-4)$.

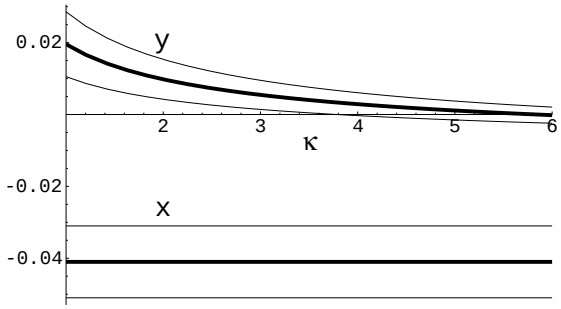

Figure 8.2: The values of the extracted matrix elements x and y in GeV^3 vs. the normalization point parameter $\kappa = \alpha_s(\mu)/\alpha_s(m_c)$. The thick lines correspond to the central value of the data on lifetimes of charmed baryons, and the thin lines show the error corridors. The extracted values of x and y scale as m_c^{-2} with the assumed mass of the charmed quark, and the plots are shown for $m_c = 1.4\,GeV$.

Notably, the extracted values of x and y are in a drastic variance with the simplistic constituent model: the color antisymmetry relation, $x = -y$, does not hold at any reasonable μ, and the absolute value of x is substantially enhanced[5]

Once the non-singlet matrix elements are determined, they can be used for predicting differences of other inclusive decay rates within the triplet of charmed hyperons as well as for the b baryons. Due to correlation of errors in x and y it makes more sense to express the predictions directly in terms of the total decay rates of the charmed hyperons. The thus arising relations between the rates do not depend on the normalization parameter μ. In this way one finds [28] for the difference of the Cabibbo dominant semileptonic decay rates between either of the Ξ_c hyperons and Λ_c:

$$\Gamma_{sl}(\Xi_c) - \Gamma_{sl}(\Lambda_c) \approx \delta^{sl,0} = 0.13\,\Delta_1 - 0.065\,\Delta_2 \approx 0.59 \pm 0.32\,ps^{-1} . \quad (8.38)$$

When compared with the data on the total semileptonic decay rate of Λ_c, $\Gamma_{sl}(\Lambda_c) = 0.22 \pm 0.08\,ps^{-1}$, this prediction implies that the semileptonic decay rate of the charmed cascade hyperons can be 2–3 times larger than that of Λ_c.

The predictions found in a similar way for the inclusive Cabibbo suppressed decay rates are [28]: for nonleptonic decays

$$\delta^{nl,1} = 0.082\,\Delta_1 + 0.054\,\Delta_2 \approx 0.55 \pm 0.22\,ps^{-1} \quad (8.39)$$

and for the semileptonic ones

$$\delta^{sl,1} = \tan^2\theta_c\,\delta^{sl,0} \approx 0.030 \pm 0.016\,ps^{-1} . \quad (8.40)$$

[5]A similar, although with a smaller enhancement, behavior of the matrix elements was observed in a recent preliminary lattice study [27].

For the only difference of the inclusive rates in the triplet of b baryons, $\Gamma(\Lambda_b) - \Gamma(\Xi_b^-)$, one finds an expression in terms of x and y, or alternatively, in terms of the differences Δ_1 and Δ_2 between the charmed hyperons,

$$\Gamma(\Lambda_b) - \Gamma(\Xi_b^-) = \cos^2\theta_c |V_{cb}|^2 \frac{G_F^2 m_b^2}{4\pi} \left[(\tilde{C}_5 - \tilde{C}_1)\, x + (\tilde{C}_6 - \tilde{C}_2)\, y \right] \tag{8.41}$$
$$\approx |V_{cb}|^2 \frac{m_b^2}{m_c^2} (0.85\,\Delta_1 + 0.91\,\Delta_2) \approx 0.015\,\Delta_1 + 0.016\,\Delta_2 \approx 0.11 \pm 0.03\, ps^{-1}\,.$$

When compared with the data on the total decay rate of Λ_b this result predicts about 14% longer lifetime of Ξ_b^- than that of Λ_b.

The singlet matrix elements x_s and y_s (cf. Eq. (8.28)) are related to the shift of the average decay rate of the hyperons in the triplet:

$$\overline{\Gamma}_Q = \frac{1}{3} \left(\Gamma(\Lambda_Q) + \Gamma(\Xi_Q^1) + \Gamma(\Xi_Q^2) \right)\,. \tag{8.42}$$

For the charmed baryons the shift of the dominant nonleptonic decay rate is given by [29]

$$\delta_{nl}^{(3,0)} \overline{\Gamma}_c = \cos^4\theta \frac{G_F^2 m_c^2}{8\pi} (C_+^2 + C_-^2)\, \kappa^{5/18}\, (x_s - 3\, y_s)\,, \tag{8.43}$$

while for the b baryons the corresponding expression reads as

$$\delta^{(3)} \overline{\Gamma}_b = |V_{cb}|^2 \frac{G_F^2 m_b^2}{8\pi} (\tilde{C}_+ - \tilde{C}_-)^2\, \tilde{\kappa}^{5/18}\, (x_s - 3\, y_s)\,. \tag{8.44}$$

The combination $x_s - 3\, y_s$ of the $SU(3)$ singlet matrix elements cancels in the ratio of the shifts for b hyperons and the charmed ones:

$$\delta^{(3)} \overline{\Gamma}_b = \frac{|V_{cb}|^2}{\cos^4\theta} \frac{m_b^2}{m_c^2} \frac{(\tilde{C}_+ - \tilde{C}_-)^2}{C_+^2 + C_-^2} \left[\frac{\alpha_s(m_c)}{\alpha_s(m_b)} \right]^{5/18} \delta_{nl}^{(3,0)} \overline{\Gamma}_c \approx 0.0025\, \delta_{nl}^{(3,0)} \overline{\Gamma}_c\,. \tag{8.45}$$

(One can observe, with satisfaction, that the dependence on the unphysical parameter μ cancels out, as it should.) This equation shows that relatively to the charmed baryons the shift of the decay rates in the b baryon triplet is greatly suppressed by the ratio $(\tilde{C}_+ - \tilde{C}_-)^2/(C_+^2 + C_-^2)$, which parametrically is of the second order in α_s, and numerically is only about 0.12.

An estimate of $\delta^{(3)}\overline{\Gamma}_b$ from Eq. (8.45) in absolute terms depends on evaluating the average shift $\delta_{nl}^{(3,0)}\overline{\Gamma}_c$ for charmed baryons. The latter shift can be conservatively bounded from above by the average total decay rate of those baryons: $\delta_{nl}^{(3,0)}\overline{\Gamma}_c < \overline{\Gamma}_c = 6.0 \pm 0.7\, ps^{-1}$, which then yields, using Eq. (8.45), an upper bound $\delta^{(3)}\overline{\Gamma}_b < 0.015 \pm 0.002\, ps^{-1}$. More realistically, one should subtract from the total average width $\overline{\Gamma}_c$ the contribution of the 'parton' term, which can be estimated from the decay rate of D_0 with account of the $O(m_c^{-2})$ effects, as amounting to about $3\, ps^{-1}$. (One should also take into account the semileptonic contribution to the total decay rates, which however is quite small at this level of accuracy). Thus a realistic evaluation of $\delta^{(3)}\overline{\Gamma}_b$ does not exceed $0.01\, ps^{-1}$, which constitutes only about

1% of the total decay rate of Λ_b. Thus the shift of the total decay rate of Λ_b due to the effects of $L_{eff}^{(3)}$ is dominantly associated with the $SU(3)$ non-singlet difference (8.42). The shift of the Λ_b decay rate with respect to the average width $\overline{\Gamma}_b$ due to the non-singlet operators is one third of the splitting (8.42), i.e., about 5%. Adding to this the 1% shift of the average width and another 1% difference from the meson decays due to the suppression of the latter by the m_b^{-2} chromomagnetic effects, one concludes that at the present level of theoretical understanding it looks impossible to explain a more than 10% enhancement of the total decay rate of Λ_b relative to B_d, where an ample 3% margin is added for the uncertainties of higher order terms in OPE as well as for higher order QCD radiative effects in the discussed corrections. In other words, the expected pattern of the lifetimes of the b hyperons in the triplet, relative to B_d, is

$$\tau(\Xi_b^0) \approx \tau(\Lambda_b) < \tau(B_d) < \tau(\Xi_b^-)\,, \tag{8.46}$$

with the "best" theoretical estimate of the differences to be about 7% for each step of the inequality.

For the double strange hyperons Ω_c and Ω_b there is presently no better approach to evaluating the four-quark matrix elements, than the use of simplistic relations, like (8.30) based on constituent quark model. Such relations imply that the effects of the strange quark, WS and PI, in the Ω_Q baryons are significantly enhanced over the same effects in the cascade hyperons. In charmed baryons a presence of strange spectator quark enhances the decay through positive interference with the quark emerging from the $c \to s$ transition in the decay. For Ω_c this implies a significant enhancement of the total decay rate [4], which is in perfect agreement with the data on the Ω_c lifetime. Also a similar enhancement is expected for the semileptonic decay rate of Ω_c. In b baryons, on the contrary, the interference effect for a spectator strange quark is negative. Thus the nonleptonic decay rate of Ω_b is expected to be suppressed, leaving Ω_b most probably the longest-living particle among the b baryons.

8.2.7 Relation between spectator effects in baryons and the decays $\Xi_Q \to \Lambda_Q\, \pi$

Rather unexpectedly, the problem of four-quark matrix elements over heavy hyperons is related to decays of the type $\Xi_Q \to \Lambda_Q\, \pi$. The mass difference between the charmed cascade hyperons Ξ_c and Λ_c is about 180 MeV. The expected analogous mass splitting for the b hyperons should be very close to this number, since in the heavy quark limit

$$M(\Xi_b) - M(\Lambda_b) = M(\Xi_c) - M(\Lambda_c) + O(m_c^{-2} - m_b^{-2}). \tag{8.47}$$

Therefore in both cases are kinematically possible decays of the type $\Xi_Q \to \Lambda_Q\, \pi$, in which the heavy quark is not destroyed, and which are quite similar to decays of ordinary 'light' hyperons. Surprisingly, the rate of these decays for both Ξ_c and Ξ_b is not insignificantly small, but rather their branching fraction can reach a level of few per mill for Ξ_c and of one percent or more for Ξ_b [30].

The transitions $\Xi_Q \to \Lambda_Q\,\pi$ are induced by two underlying weak processes: the 'spectator' decay of a strange quark, $s \to u\,\overline{u}\,d$, which does not involve the heavy quark, and the 'non-spectator' weak scattering (WS)

$$s\,c \to c\,d \tag{8.48}$$

trough the weak interaction of the $c \to d$ and $s \to c$ currents. One can also readily see that the WS mechanism contributes only to the decays $\Xi_c \to \Lambda_c\,\pi$ and is not present in the decays of the b cascade hyperons. An important starting point in considering these transitions is that in the heavy quark limit the spin of the heavy quark completely decouples from the spin of the light component of the baryon, and that the latter light component in both the initial an the final baryons forms a $J^P = 0^+$ state with quantum numbers of a diquark. Since the momentum transfer in the considered decays is small in comparison with the mass of the heavy quark the spin of the amplitudes with spin flip of the heavy quark, and thus of the baryon, are suppressed by m_Q^{-1}. In terms of the two possible partial waves in the decay $\Xi_Q \to \Lambda_Q\,\pi$, the S and P, this implies that the P wave is strongly suppressed and the decays are dominated by the S wave.

According to the well known current algebra technique, the S wave amplitudes of pion emission can be considered in the chiral limit at zero four-momentum of the pion, where they are described by the PCAC reduction formula (pole terms are absent in these processes):

$$\langle \Lambda_Q\,\pi_i(p=0)\,|H_W|\,\Xi_Q\rangle = \frac{\sqrt{2}}{f_\pi}\,\langle \Lambda_Q\,|\left[Q_i^5,\,H_W\right]|\,\Xi_Q\rangle\,, \tag{8.49}$$

where π_i is the pion triplet in the Cartesian notation, and Q_i^5 is the corresponding isotopic triplet of axial charges. The constant $f_\pi \approx 130\,MeV$, normalized by the charged pion decay, is used here, hence the coefficient $\sqrt{2}$ in Eq. (8.49). The Hamiltonian H_W in Eq. (8.49) is the nonleptonic strangeness-changing Hamiltonian:

$$\begin{aligned} H_W = \sqrt{2}\,G_F\cos\theta_c\sin\theta_c\Big\{&(C_+ + C_-)\left[(\overline{u}_L\,\gamma_\mu\,s_L)\,(\overline{d}_L\,\gamma_\mu\,u_L) - (\overline{c}_L\,\gamma_\mu\,s_L)\,(\overline{d}_L\,\gamma_\mu\,c_L)\right] \\ &+\,(C_+ - C_-)\left[(\overline{d}_L\,\gamma_\mu\,s_L)\,(\overline{u}_L\,\gamma_\mu\,u_L) - (\overline{d}_L\,\gamma_\mu\,s_L)\,(\overline{c}_L\,\gamma_\mu\,c_L)\right]\Big\}\,. \end{aligned} \tag{8.50}$$

In this formula the weak Hamiltonian is assumed to be normalized (in LLO) at $\mu = m_c$. The terms in the Hamiltonian (8.50) without the charmed quark fields describe the 'spectator' nonleptonic decay of the strange quark, while those with the c quark correspond to the WS process (8.48).

It is straightforward to see from Eq. (8.49) that in the PCAC limit the discussed decays should obey the $\Delta I = 1/2$ rule. Indeed, the commutator of the weak Hamiltonian with the axial charges transforms under the isotopic SU(2) in the same way as the Hamiltonian itself. In other words, the $\Delta I = 1/2$ part of H_W after the commutation gives an $\Delta I = 1/2$ operator, while the $\Delta I = 3/2$ part after the commutation gives an $\Delta I = 3/2$ operator. The latter operator however cannot have a non vanishing matrix element between an isotopic singlet, Λ_Q, and an isotopic doublet, Ξ_Q. Thus the $\Delta I = 3/2$ part of H_W gives no contribution to the S wave amplitudes in the PCAC limit.

Once the isotopic properties of the decay amplitudes are fixed, one can concentrate on specific charge decay channels, e.g., $\Xi_b^- \to \Lambda_b\,\pi^-$ and $\Xi_c^0 \to \Lambda_c\,\pi^-$. An application of the PCAC relation (8.49) with the Hamiltonian from Eq. (8.50) to these decays, gives the expressions for the amplitudes at $p = 0$ in terms of baryonic matrix elements of four-quark operators:

$$\begin{aligned} &\langle \Lambda_b\,\pi^-(p=0)\,|H_W|\,\Xi_b^-\rangle \\ &= \frac{\sqrt{2}}{f_\pi}\,G_F\cos\theta_c\sin\theta_c\,\langle\Lambda_b\,|\,(C_+ + C_-)\left[(\overline{u}_L\,\gamma_\mu\,s_L)\,(\overline{d}_L\,\gamma_\mu\,d_L) - (\overline{u}_L\,\gamma_\mu\,s_L)\,(\overline{u}_L\,\gamma_\mu\,u_L)\right] \\ &\quad + (C_+ - C_-)\left[(\overline{d}_L\,\gamma_\mu\,s_L)\,(\overline{u}_L\,\gamma_\mu\,d_L) - (\overline{u}_L\,\gamma_\mu\,s_L)\,(\overline{u}_L\,\gamma_\mu\,u_L)\right]|\,\Xi_b^-\rangle \\ &= \frac{\sqrt{2}}{f_\pi}\,G_F\cos\theta_c\sin\theta_c\,\langle\Lambda_b\,|\,C_-\left[(\overline{u}_L\,\gamma_\mu\,s_L)\,(\overline{d}_L\,\gamma_\mu\,d_L) - (\overline{d}_L\,\gamma_\mu\,s_L)\,(\overline{u}_L\,\gamma_\mu\,d_L)\right] \\ &\quad - \frac{C_+}{3}\left[(\overline{u}_L\,\gamma_\mu\,s_L)\,(\overline{d}_L\,\gamma_\mu\,d_L) + (\overline{d}_L\,\gamma_\mu\,s_L)\,(\overline{u}_L\,\gamma_\mu\,d_L) + 2\,(\overline{u}_L\,\gamma_\mu\,s_L)\,(\overline{u}_L\,\gamma_\mu\,u_L)\right]|\,\Xi_b^-\rangle\,, \end{aligned} \tag{8.51}$$

where in the last transition the operator structure with $\Delta I = 3/2$ giving a vanishing contribution is removed and only the structures with explicitly $\Delta I = 1/2$ are retained, and

$$\begin{aligned} \langle \Lambda_c\,\pi^-(p=0)\,|H_W|\,\Xi_c^0\rangle = \langle \Lambda_b\,\pi^-(p=0)\,|H_W|\,\Xi_b^-\rangle + \frac{\sqrt{2}}{f_\pi}\,G_F\cos\theta_c\sin\theta_c \\ \times\,\langle \Lambda_c|\,(C_+ + C_-)\,(\overline{c}_L\,\gamma_\mu\,s_L)\,(\overline{u}_L\,\gamma_\mu\,c_L) + (C_+ - C_-)\,(\overline{u}_L\,\gamma_\mu\,s_L)\,(\overline{c}_L\,\gamma_\mu\,c_L)|\,\Xi_c^0\rangle\,. \end{aligned} \tag{8.52}$$

In the latter formula the first term on the r.h.s. expresses the fact that in the heavy quark limit the 'spectator' amplitudes do not depend on the flavor or the mass of the heavy quark. The rest of the expression (8.53) describes the 'non-spectator' contribution to the amplitude of the charmed hyperon decay. Using the flavor $SU(3)$ symmetry the latter contribution can be related to the non-singlet matrix elements (8.27) (normalized at $\mu = m_c$) as

$$\begin{aligned} \Delta A &\equiv \langle \Lambda_c\,\pi^-(p=0)\,|H_W|\,\Xi_c^0\rangle - \langle \Lambda_b\,\pi^-(p=0)\,|H_W|\,\Xi_b^-\rangle \\ &= \frac{G_F\cos\theta_c\sin\theta_c}{2\sqrt{2}\,f_\pi}\,\left[(C_- - C_+)\,x - (C_+ + C_-)\,y\right]\,. \end{aligned} \tag{8.53}$$

Furthermore, with the help of the equations (8.35) and (8.36) relating the matrix elements x and y to the differences of the total decay widths within the triplet of charmed hyperons, one can eliminate x and y in favor of the measured width differences. The resulting expression has the form

$$\begin{aligned} \Delta A &\approx -\frac{\sqrt{2}\,\pi\cos\theta_c\sin\theta_c}{G_F\,m_c^2\,f_\pi}\left[0.45\left(\Gamma(\Xi_c^0) - \Gamma(\Lambda_c)\right) + 0.04\left(\Gamma(\Lambda_c) - \Gamma(\Xi_c^+)\right)\right] \\ &= -10^{-7}\left[0.97\left(\Gamma(\Xi_c^0) - \Gamma(\Lambda_c)\right) + 0.09\left(\Gamma(\Lambda_c) - \Gamma(\Xi_c^+)\right)\right]\left(\frac{1.4\,GeV}{m_c}\right)^2\,ps\,, \end{aligned} \tag{8.54}$$

where, clearly, in the latter form the widths are assumed to be expressed in ps^{-1}, and $m_c = 1.4\,GeV$ is used as a 'reference' value for the charmed quark mass. It is seen from

Eq. (8.54) that the evaluation of the difference of the amplitudes within the discussed approach is mostly sensitive to the difference of the decay rates of Ξ_c^0 and Λ_c, with only very little sensitivity to the total decay width of Ξ_c^+. Using the current data the difference ΔA is estimated as

$$\Delta A = -(5.4 \pm 2) \times 10^{-7} , \tag{8.55}$$

with the uncertainty being dominated by the experimental error in the lifetime of Ξ_c^0. An amplitude A of the magnitude, given by the central value in Eq. (8.55) would produce a decay rate $\Gamma(\Xi_Q \to \Lambda_Q \, \pi) = |A|^2 \, p_\pi/(2\pi) \approx 0.9 \times 10^{10} \, s^{-1}$, which result can also be written in a form of triangle inequality

$$\sqrt{\Gamma(\Xi_b^- \to \Lambda_b \, \pi^-)} + \sqrt{\Gamma(\Xi_c^0 \to \Lambda_c \, \pi^-)} \geq \sqrt{0.9 \times 10^{10} \, s^{-1}} . \tag{8.56}$$

Although at present it is not possible to evaluate in a reasonably model independent way the matrix element in Eq. (8.52) for the 'spectator' decay amplitude, the inequality (8.56) shows that at least some of the discussed pion transitions should go at the level of $0.01 \, ps^{-1}$, similar to the rates of analogous decays of 'light' hyperons.

8.2.8 Summary on predictions for lifetimes

We summarize here specific predictions for the inclusive decay rates, which can be argued with a certain degree of theoretical reliability, and which can be possibly experimentally tested in the nearest future.

B mesons:

$$\tau(B_d)/\tau(B_s) = 1 \pm 0.01 . \tag{8.57}$$

Charmed hyperons:

$$\begin{aligned} \Gamma_{sl}(\Xi_c) = (2-3) \, \Gamma_{sl}(\Lambda_c) \qquad \Gamma_{sl}(\Omega_c) > \Gamma_{sl}(\Xi_c) , \\ \Gamma^{nl}_{\Delta S=-1}(\Xi_c^+) \approx \Gamma^{nl}_{\Delta S=-1}(\Lambda_c) , \\ \Gamma^{nl}_{\Delta S=-1}(\Xi_c^0) - \Gamma^{nl}_{\Delta S=-1}(\Lambda_c) \approx 0.55 \pm 0.22 \, ps^{-1} . \end{aligned} \tag{8.58}$$

b hyperons:

$$\begin{aligned} \tau(\Xi_b^0) \approx \tau(\Lambda_b) < \tau(B_d) < \tau(\Xi_b^-) < \tau(\Omega_b) , \\ \Gamma(\Lambda_b) - \Gamma(\Xi_b^-) \approx 0.11 \pm 0.03 \, ps^{-1} , \\ 0.9 < \frac{\tau(\Lambda_b)}{\tau(B_d)} < 1 . \end{aligned} \tag{8.59}$$

Strangeness decays $\Xi_Q \to \Lambda_Q \, \pi$: The $\Delta I = 1/2$ rule should hold in these decays, so that $\Gamma(\Xi_Q^{(d)} \to \Lambda_Q \pi^-) = 2 \, \Gamma(\Xi_Q^{(u)} \to \Lambda_Q \pi^0)$. The rates are constrained by the triangle inequality (8.56).

8.3 Theory of $B^0 - \overline{B}^0$ mixing †

In Sect. 1.3.2 the time evolution of the $B^0 - \overline{B}^0$ system has been discussed. $B^0 - \overline{B}^0$ mixing involves three physical, rephasing-invariant quantities: $|M_{12}|$, $|\Gamma_{12}|$ and the phase ϕ defined in (1.62). In the following we will discuss how they are related to physical observables. The discussed quantities are summarized in Table 8.1.

8.3.1 Mass difference

The mass difference Δm can be measured from the tagged time evolutions in (1.73-1.77) from any decay $B^0 \to f$, unless $\lambda_f = \pm 1$, in which case the oscillatory terms vanish. The time evolution is especially simple for flavor-specific decays, which are characterized by $\lambda_f = 0$. The corresponding formulae can be found in (1.79) and (1.80). Interesting flavor-specific modes are tabulated in Table 8.4. Time integrated measurements determine $x_q = \Delta m_q/\Gamma_q = \Delta m_q \tau_{B_q}$, $q = d, s$, defined in (1.93). While unfortunately it is common practice to quote measurements of Δm_q in terms of x_q, it should be clear that the measured oscillation frequencies determine Δm_d and Δm_s and not x_d and x_s. Fundamental physics quantities like CKM elements are related to Δm_d and Δm_s, so that the errors of the lifetimes entering x_q are irrelevant.

In order to predict the mass difference Δm_q within the Standard Model or one of its extensions, one must first calculate the $|\Delta B| = 2$ transition amplitude, which triggers $B^0 - \overline{B}^0$ mixing. The lowest order contribution to this amplitude in the Standard Model is the box diagram in Fig. 1.2. Then one must match the result to an effective field theory, in which the interactions mediated by heavy particles are described by local operators represented by pointlike vertices. In the Standard Model only one operator, Q in (1.118), emerges. This procedure separates short- and long-distance physics and is described in Sect. 1.5.1. It results in the effective Hamiltonian in (1.117). The interesting short-distance physics is contained in the Wilson coefficient C in (1.119). New physics can modify C and can introduce new operators in addition to Q in (1.118). The Standard Model prediction is readily obtained from (1.117) to (1.121):

$$\Delta m_q = 2|M_{12}^q| = \frac{|\langle B_q^0 | H^{|\Delta B|=2} | \overline{B}_q^0 \rangle|}{m_{B_q}} = \frac{G_F^2}{6\pi^2} \, \eta_B \, m_{B_q} \, \widehat{B}_{B_q} f_{B_q}^2 \, M_W^2 \, S\Big(\frac{m_t^2}{M_W^2}\Big) \, \Big| V_{tb} V_{tq}^* \Big|^2 . \tag{8.60}$$

where $q = s$ or d.

Next we discuss the phenomenology of Δm_d in the Standard Model. We first insert the numerical values of those quantities which are well-known into (8.60). The QCD factor $\eta_B = 0.55$ [31] corresponds to the $\overline{\rm MS}$ scheme for m_t. The $\overline{\rm MS}$ value of $m_t = 167 \, {\rm GeV}$ is numerically smaller than the pole mass measured at the Tevatron by roughly 7 GeV. Solving (8.60) for $|V_{td}|$ one finds:

$$|V_{td}| = 0.0078 \sqrt{\frac{\Delta m_d}{0.49 \, {\rm ps}^{-1}}} \, \frac{200 \, {\rm MeV}}{f_{B_d}} \sqrt{\frac{1.3}{\widehat{B}_{B_d}}} . \tag{8.61}$$

†Author: Ulrich Nierste

observable	defined in	SM prediction for B_d in	SM prediction for B_s in
$\Delta m \simeq 2\lvert M_{12}\rvert$	(1.64a)	(8.60),(8.69)	(8.60),(8.65),(8.69)
ϕ	(1.62)	(8.83)	(8.83)
$\Delta\Gamma \simeq 2\lvert\Gamma_{12}\rvert\cos\phi$	(1.64b)	(8.87),(8.89)	(8.86),(8.87)
$\Delta\Gamma_{\rm CP} \simeq 2\lvert\Gamma_{12}\rvert$	(8.98)		
$\Delta\Gamma'_{\rm CP} \simeq 2\lvert\Gamma_{12}\rvert\cos^2\phi$	(8.113)		
$\Delta\Gamma^{cc}_{\rm CP} = 2\lvert\xi_c^{d\,2}\Gamma^{cc}_{12}\rvert$	(8.133)	(8.134)	
$a = \left\lvert\frac{\Gamma_{12}}{M_{12}}\right\rvert\sin\phi$	(1.65)	(8.138)	(8.138)

Table 8.1: Observables related to $|M_{12}|$, $|\Gamma_{12}|$ and ϕ discussed in Sect. 8.3.

The relation of $|V_{td}|$ to the improved Wolfenstein parameters is

$$|V_{td}| = A\lambda^3 R_t \left(1 + \mathcal{O}(\lambda^4)\right) = |V_{cb}|\,\lambda\,R_t \left(1 + \mathcal{O}(\lambda^4)\right) \tag{8.62}$$

and

$$R_t = \sqrt{(1-\overline{\rho})^2 + \overline{\eta}^2} \tag{8.63}$$

is the length of one side of the unitarity triangle. Hence the measurement of Δm_d defines a circle in the $(\overline{\rho},\overline{\eta})$ plane centered around $(1,0)$. Yet the hadronic uncertainties associated with $f_{B_d}\sqrt{\widehat{B}_{B_d}}$ obscure a clean extraction of $|V_{td}|$ and R_t from the well-measured Δm_d. The summer 2000 world averages from lattice calculations are $f_{B_d} = (200 \pm 30)$ MeV and $\widehat{B}_{B_d} = 1.30 \pm 0.17$ [32]. This gives $|V_{td}| = 0.0078 \pm 0.0013$ and, with $|V_{cb}| = (40.4 \pm 1.8)\times 10^{-3}$, $R_t = 0.88 \pm 0.15$.

For the discussion of Δm_s we first note that the corresponding CKM element in (8.60) is fixed from CKM unitarity:

$$|V_{ts}| = |V_{cb}|\left[1 + \lambda^2\left(\overline{\rho} - \frac{1}{2}\right) + \mathcal{O}(\lambda^4)\right]. \tag{8.64}$$

$|V_{ts}|$ is smaller than $|V_{cb}|$ by roughly 1%. Hence within the Standard Model a measurement of Δm_s directly probes the calculation of the hadronic matrix element. (8.60) specifies to

$$\Delta m_s = 17.2\,\mathrm{ps}^{-1}\left(\frac{|V_{ts}|}{0.04}\,\frac{f_{B_s}}{230\,\mathrm{MeV}}\right)^2 \frac{\widehat{B}_{B_s}}{1.3}. \tag{8.65}$$

This can be rewritten as

$$f_{B_s}\sqrt{\widehat{B}_{B_s}} = \sqrt{\frac{\Delta m_s}{14.9\,\mathrm{ps}^{-1}}}\,\frac{0.04}{|V_{cb}|}\,247\,\mathrm{MeV}. \tag{8.66}$$

The present 95% C.L. limit of $\Delta m_s \geq 14.9\,\mathrm{ps}^{-1}$ [33] implies a lower bound on $f_{B_s}\sqrt{\widehat{B}_{B_s}}$ which is only marginally consistent with some of the quenched lattice calculations. Hence global fits of the unitarity triangle (using $\Delta m_d/\Delta m_s$ to constrain R_t) which use too small

values of $f_{B_s}\sqrt{\widehat{B}_{B_s}}$ confine the apex of the triangle to a too small region of the $(\overline{\rho},\overline{\eta})$ plane or may even be in conflict with the measured lower bound on Δm_s.

The determination of R_t profits enormously from a measurement of Δm_s, because the ratio of the hadronic matrix elements entering $\Delta m_d/\Delta m_s$ can be calculated with a much higher accuracy than the individual matrix elements:

$$\xi = \frac{f_{B_s}\sqrt{\widehat{B}_{B_s}}}{f_{B_d}\sqrt{\widehat{B}_{B_d}}} \tag{8.67}$$

is equal to 1 in the limit of exact $SU(3)_F$ symmetry. Hence the theorists' task is reduced to the calculation of the deviation from 1. The current world average from lattice calculations is [32]

$$\xi = 1.16 \pm 0.05. \tag{8.68}$$

Further $|V_{cb}|$ drops out from the ratio

$$\frac{\Delta m_d}{\Delta m_s} = \lambda^2 R_t^2\left(1 + \lambda^2(1-2\overline{\rho}) + \mathcal{O}(\lambda^4)\right)\frac{m_{B_d}}{m_{B_s}}\,\frac{1}{\xi^2}. \tag{8.69}$$

With the expected experimental accuracy of $\Delta m_{d,s}$ and the anticipation of progress in the determination of ξ in (8.68) a determination of R_t at the level of 1-3% is possible. Then, eventually, even the uncertainty in λ cannot be neglected anymore. Keeping the overall factor of λ^2 while inserting $\lambda = 0.22$ in the subleading terms one finds from (8.69):

$$R_t = 0.880\sqrt{\frac{\Delta m_d}{0.49\,\mathrm{ps}^{-1}}}\sqrt{\frac{17\,\mathrm{ps}^{-1}}{\Delta m_s}}\,\frac{0.22}{\lambda}\,\frac{\xi}{1.16}\,(1 + 0.05\,\overline{\rho})\,. \tag{8.70}$$

Here the omission of $\mathcal{O}(\lambda^4)$ terms induces a negligible error of less than 0.1%. At present R_t is obtained from a global fit of the unitarity triangle and (8.69) is used to predict $\Delta m_s = 17.3^{+1.5}_{-0.7}$ [34]. One should be aware that some of the quantities entering the global fit, especially ϵ_K, are sensitive to new physics. Hence the measurement of a Δm_s well above the quoted range would be very exciting. In a large class of extensions of the Standard model Δm_d and Δm_s change, while their ratio does not. In these models Δm_s could be in conflict with (8.66) without affecting R_t in (8.70). Therefore it is desirable to gain additional experimental information on f_{B_s}, so that the dependence on non-perturbative methods is reduced. This information can be obtained from the B_s width difference discussed in Sect. 8.3.2.

8.3.2 Width difference

8.3.2.1 Calculation

The two mass eigenstates B_L and B_H in (1.54) differ not only in their masses but also in their widths. The prediction of the width difference $\Delta\Gamma = \Gamma_L - \Gamma_H \simeq 2\,|\Gamma_{12}|\cos\phi$

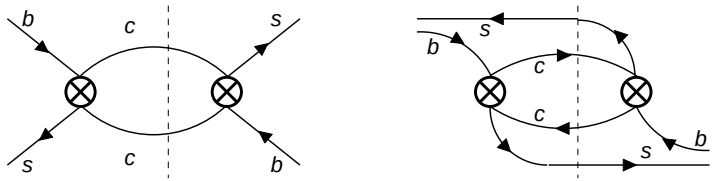

Figure 8.3: Leading order diagrams determining Γ_{12}^s. Only the CKM-favored contribution $\xi_c^{s*2}\Gamma_{12}^{cc}$ is shown. The left diagram is the *weak annihilation diagram* and the right one is the *spectator interference diagram*. The dashed line indicates the cut through the final state.

in (1.64b) requires the calculation of $|\Gamma_{12}|$ and ϕ. Γ_{12} is determined from the absorptive part of the $|\Delta B| = 2$ transition amplitude. It receives contributions from all final states which are common to B^0 and $\overline{B}^0$ as shown in the first line of (1.146). The leading order (LO) diagrams contributing to Γ_{12} in the B_s system are shown in Fig. 8.3. The dominant contribution comes from the spectator interference diagram, the weak annihilation diagram is color-suppressed. We write

$$\Gamma_{12}^q \;=\; -\left[\xi_c^{q*2}\Gamma_{12,q}^{cc} \;+\; 2\xi_u^{q*}\xi_c^{q*}\Gamma_{12,q}^{uc} \;+\; \xi_u^{q*2}\Gamma_{12,q}^{uu}\right], \qquad q = d, s, \tag{8.71}$$

where the three terms denote the contributions from the diagram with (anti-)quarks i and j in the final state. The ξ_i^q's denote the corresponding CKM factors:

$$\xi_u^q \;=\; V_{uq}V_{ub}^*, \qquad \xi_c^q \;=\; V_{cq}V_{cb}^*, \qquad \xi_t^q \;=\; V_{tq}V_{tb}^*. \tag{8.72}$$

They satisfy $\xi_u^q + \xi_c^q + \xi_t^q = 0$ from CKM unitarity and read in terms of the improved Wolfenstein parameters [35]:

$$\begin{aligned}
\xi_u^d \;&=\; A\lambda^3\,(\overline{\rho} + i\overline{\eta}) + \mathcal{O}(\lambda^5), \qquad & \xi_c^d \;&=\; -A\lambda^3 + \mathcal{O}(\lambda^5), \\
& & \xi_t^d \;&=\; A\lambda^3\,(1 - \overline{\rho} - i\overline{\eta}) + \mathcal{O}(\lambda^5), \\
\xi_u^s \;=\; A\lambda^4(1 + \frac{\lambda^2}{2})\,(\overline{\rho} + i\overline{\eta}) + \mathcal{O}(\lambda^8), \qquad & \xi_c^s \;&=\; A\lambda^2(1 - \frac{\lambda^2}{2}) + \mathcal{O}(\lambda^6), \\
& \xi_t^s \;&=\; -A\lambda^2\left[1 - \lambda^2(\frac{1}{2} - \overline{\rho} - i\overline{\eta})\right] + \mathcal{O}(\lambda^6),
\end{aligned} \tag{8.73}$$

$-\xi_u^d/\xi_c^d$ and $-\xi_t^d/\xi_c^d$ define two sides of the standard unitarity triangle depicted in Fig. 1.1. One has

$$-\frac{\xi_u^d}{\xi_c^d} \;=\; R_b e^{i\gamma}, \qquad -\frac{\xi_t^d}{\xi_c^d} \;=\; R_t e^{-i\beta}, \tag{8.74}$$

where $R_b = \sqrt{\overline{\rho}^2 + \overline{\eta}^2}$ and R_t is defined in (8.63). The ratio ξ_t^s/ξ_c^s involves the phase β_s measured from the mixing-induced CP asymmetry in $B_s \to D_s^+ D_s^-$:

$$-\frac{\xi_t^s}{\xi_c^s} \;=\; [1 + \overline{\rho}\lambda^2 + \mathcal{O}(\lambda^4)]\; e^{i\beta_s} \qquad \text{with } \beta_s = \overline{\eta}\lambda^2[1 + (1 - \overline{\rho})\lambda^2] + \mathcal{O}(\lambda^6). \tag{8.75}$$

The coefficients Γ_{12}^{ij} in (8.71) are positive. They are inclusive quantities and can be calculated using the heavy quark expansion described for the heavy hadron lifetimes in Sect. 8.2. The leading term of the power expansion in Λ_{QCD}/m_b contains two Dirac structures, each of which can be factorized into a short-distance Wilson coefficient and the matrix element of a local operator:

$$\Gamma_{12,q}^{ij} = \frac{G_F^2 m_b^2}{6\pi} f_{B_q}^2 M_{B_q} \left[F^{ij}(z)\frac{2}{3}B_{B_q} - F_S^{ij}(z)\frac{5}{12}B_{B_q}^{S\prime}\right]\left[1 + \mathcal{O}\left(\frac{\Lambda_{QCD}}{m_b}\right)\right]. \tag{8.76}$$

Here $z = m_c^2/m_b^2$. The operator Q, which we already encountered in the discussion of Δm, was defined in (1.118). When Q occurs in the context of B_s^0–$\overline{B}_s^0$ mixing, we understand that the d quarks in (1.118) are appropriately replaced by s quarks. In $\Gamma_{12,q}$ a second operator occurs:

$$Q_S = \overline{q}_L b_R\, \overline{q}_L b_R, \qquad q = d \text{ or } s. \tag{8.77}$$

B_{B_q} and $B_{B_q}^{S\prime}$ (or, equivalently, $B_{B_q}^S$) are 'bag' parameters quantifying the hadronic matrix elements of Q and Q_S:

$$\begin{aligned}
\langle B_q^0|Q(\mu)|\overline{B}_q^0\rangle &= \frac{2}{3} f_{B_q}^2 m_{B_q}^2 B_{B_q}(\mu)\,, \\
\langle B_q^0|Q_S(\mu)|\overline{B}_q^0\rangle &= -\frac{5}{12} f_{B_q}^2 m_{B_q}^2 B_{B_q}^{S\prime}(\mu) \;=\; -\frac{5}{12} f_{B_q}^2 m_{B_q}^2 \frac{m_{B_q}^2}{[m_b(\mu) + m_q(\mu)]^2} B_{B_q}^S(\mu).
\end{aligned} \tag{8.78}$$

$B_{B_q}^S$ and $B_{B_q}^{S\prime}$ simply differ by the factor $m_{B_q}^2/[m_b(\mu) + m_q(\mu)]^2$. While lattice results are usually quoted for $B_{B_q}^S$, the forthcoming formulae are shorter when expressed in terms of $B_{B_q}^{S\prime}$. These 'bag' factors depend on the renormalization scale μ and the renormalization scheme. In the literature on $\Delta\Gamma$ it is customary to use B_{B_q} and $B_{B_q}^S$ in the $\overline{\text{MS}}$ scheme as defined in [36]. Numerical values obtained in lattice calculations are usually quoted for $\mu = m_b$. The invariant bag factor $\widehat{B}_{B_q}$ defined in (1.121) is related to $B_{B_q}(\mu)$ by

$$\begin{aligned}
\widehat{B}_{B_q} &= B_{B_q}(\mu)\, b_B(\mu) \\
b_B(\mu) &= [\alpha_s(\mu)]^{-6/23}\left[1 + \frac{\alpha_s(\mu)}{4\pi}\frac{5165}{3174}\right], \qquad b_B(m_b) \;=\; 1.52 \pm 0.03.
\end{aligned} \tag{8.79}$$

A recent preliminary lattice calculation with two dynamical flavors found $B_{B_s}(m_b) = 0.83 \pm 0.08$ and $B_{B_s}^S(m_b) = 0.84 \pm 0.08$ [37]. No deviation of B_{B_s}/B_{B_d} and $B_{B_s}^S/B_{B_d}^S$ from 1 is seen. The quoted value for $B_{B_q}(m_b)$ corresponds to $\widehat{B}_{B_q} = 1.26 \pm 0.12$. The short distance physics entering Γ_{12}^q in (8.76) is contained in $F(z)$ and $F_S(z)$. To leading order in α_s they read:

$$\begin{aligned}
F^{cc}(z) &= \sqrt{1-4z}\left[(1-z)K_1 + \frac{1-4z}{2}K_2\right] \\
F_S^{cc}(z) &= \sqrt{1-4z}\,(1+2z)\,(K_1 - K_2) \\
F^{uc}(z) &= (1-z)^2\left[\frac{2+z}{2}K_1 + \frac{1-z}{2}K_2\right] \\
F_S^{uc}(z) &= (1-z)^2\,(1+2z)\,(K_1 - K_2)
\end{aligned}$$

$$F^{uu}(z) = F^{cc}(0) \;=\; F^{uc}(0) \;=\; K_1 + \frac{1}{2}K_2$$
$$F_S^{uu}(z) = F_S^{cc}(0) \;=\; F_S^{uc}(0) \;=\; K_1 - K_2. \qquad (8.80)$$

K_1 and K_2 are combinations of the Wilson coefficients C_1 and C_2, which are tabulated in Table 1.3:

$$K_1 \;=\; 3C_1^2 + 2C_1C_2, \qquad K_2 \;=\; C_2^2. \qquad (8.81)$$

The scale at which the Wilson coefficients are evaluated must equal the scale used in $B_{B_q}(\mu)$ and $B_{B_q}^S(\mu)$. In (8.76) and (8.80) we have neglected the small contributions from penguin coefficients, which can be found in [36].

It is instructive to eliminate $\xi_c^q = -\xi_t^q - \xi_u^q$ in favor of ξ_u^q and ξ_t^q in (8.71):

$$\Gamma_{12}^q \;=\; -\xi_t^{q*2}\left[\Gamma_{12,q}^{cc} \;+\; 2\,\frac{\xi_u^{q*}}{\xi_t^{q*}}\left(\Gamma_{12,q}^{cc} - \Gamma_{12,q}^{uc}\right) + \frac{\xi_u^{q*2}}{\xi_t^{q*2}}\left(\Gamma_{12,q}^{cc} - 2\Gamma_{12,q}^{uc} + \Gamma_{12,q}^{uu}\right)\right]. \qquad (8.82)$$

In the limit $z = 0$ all the Γ_{12}^{ij}'s become equal and $\arg M_{12} = \arg(-\Gamma_{12}) = \arg(\xi_t^{q*2})$, so that ϕ vanishes in this limit. With (8.73) one verifies that $\phi_d = \mathcal{O}(\overline{\eta}z)$ and $\phi_s = \mathcal{O}(\lambda^2\overline{\eta}z)$. This GIM suppression is lifted, if new physics contributes to $\arg M_{12}^q$ spoiling the cancellation between $\arg M_{12}$ and $\arg(-\Gamma_{12}^q)$. Therefore ϕ is extremely sensitive to new physics.

Combining (8.82) and (8.80) we find the Standard Model predictions for $\phi_d = \phi(B_d)$ and $\phi_s = \phi(B_s)$:

$$\phi_d = -\frac{2\overline{\eta}}{R_t^2}\,\frac{\Gamma_{12,d}^{uc} - \Gamma_{12,d}^{cc}}{\Gamma_{12,d}^{cc}}\left[1 + \mathcal{O}\left(\overline{\eta}z^2, \overline{\eta}\lambda^4\right)\right] \approx -\frac{24}{5}\,\frac{\overline{\eta}}{R_t^2}\,\frac{B_{B_d}}{B_{B_d}^{S\prime}}\,\frac{K_1+K_2}{K_2-K_1}\,z \approx -0.1 \;=\; -5^\circ,$$

$$\phi_s = 2\lambda^2\overline{\eta}\,\frac{\Gamma_{12,s}^{uc} - \Gamma_{12,s}^{cc}}{\Gamma_{12,s}^{cc}}\left[1 + \mathcal{O}\left(\overline{\eta}z^2, \overline{\eta}\lambda^4\right)\right] \approx \frac{24}{5}\,\overline{\eta}\,\lambda^2\,\frac{B_{B_s}}{B_{B_s}^{S\prime}}\,\frac{K_1+K_2}{K_2-K_1}\,z \;\approx\; 3\times10^{-3} \;=\; 0.2^\circ. \qquad (8.83)$$

That is, in the Standard Model, we can safely neglect the factor of $\cos\phi_q$ in the relation $\Delta\Gamma_q = 2|\Gamma_{12}^q|\cos\phi_q$ (see (1.64b)). For Γ_{12}^s the CKM-suppressed contributions $\Gamma_{12,s}^{uc}$ and $\Gamma_{12,s}^{uu}$ are completely irrelevant. Γ_{12}^d is also dominated by the double-charm contribution $\Gamma_{12,d}^{cc}$, with up to $\mathcal{O}(5\%)$ corrections from the second term in (8.82):

$$\Delta\Gamma_s^{\rm SM} = 2|\Gamma_{12}^s| \;=\; |\xi_t^s|^2\,2|\Gamma_{12,s}^{cc}|$$
$$\Delta\Gamma_d^{\rm SM} = 2|\Gamma_{12}^d| \;=\; |\xi_t^d|^2\,2|\Gamma_{12,d}^{cc}|\left|1 + 2\frac{R_t^2 + \overline{\rho} - 1}{R_t^2}\,\frac{\Gamma_{12,d}^{uc} - \Gamma_{12,d}^{cc}}{\Gamma_{12,d}^{cc}} + \mathcal{O}\left(\frac{R_B^4}{R_t^4}\,z^2\right)\right|. \qquad (8.84)$$

$\Gamma_{12,s}^{cc}$ has been calculated in the next-to-leading order of α_s [36] and Λ_{QCD}/m_b [38]. The result gives the following prediction for $\Delta\Gamma_s^{\rm SM}$:

$$\frac{\Delta\Gamma_s^{\rm SM}}{\Gamma} \;=\; \frac{2|\Gamma_{12}^s|}{\Gamma} \;=\; \left(\frac{f_{B_s}}{245\ \text{MeV}}\right)^2\left[(0.234 \pm 0.035)\,B_{B_s}^S - 0.080 \pm 0.020\right]. \qquad (8.85)$$

Here the coefficient of $B_{B_s}^S$ has been updated to $m_b(m_b) + m_s(m_b) = 4.3\,\text{GeV}$ (in the $\overline{\rm MS}$ scheme) compared to [36]. Since the coefficient $F^{cc}(z)$ of B_{B_s} in (8.76) is very small, B_{B_s} in (8.85) has been fixed to $B_{B_s}(m_b) = 0.85 \pm 0.05$ obtained in quenched lattice QCD [37]. Recently the KEK–Hiroshima group succeeded in calculating f_{B_s} in an unquenched lattice QCD calculation with two dynamical fermions [39]. The result is $f_{B_s} = (245 \pm 30)\,\text{MeV}$. With this number and $B_{B_s}^S(m_b) = 0.87 \pm 0.09$ from quenched lattice QCD [37,40] one finds from (8.85):

$$\frac{\Delta\Gamma_s^{\rm SM}}{\Gamma} \;=\; 0.12 \pm 0.06. \qquad (8.86)$$

Here we have conservatively added the errors from the two lattice quantities linearly. f_{B_s} drops out from the ratio

$$\frac{\Delta\Gamma_s^{\rm SM}}{\Delta m_s^{\rm SM}} \;\simeq\; \frac{5\pi}{6}\,\frac{m_b^2}{M_W^2\,\eta_B b_B S(m_t^2/M_W^2)}\,|F_S(z)|\,\frac{B_{B_s}^{S\prime}}{B_{B_s}}\left[1 + \mathcal{O}\left(\frac{\Lambda_{QCD}}{m_b}\right)\right]. \qquad (8.87)$$

The full result with next-to-leading order corrections in α_s and Λ_{QCD}/m_b can be found in [36]. Including these corrections one finds [36]:

$$\frac{\Delta\Gamma_s^{\rm SM}}{\Delta m_s^{\rm SM}} \;=\; \left(3.7^{+0.8}_{-1.5}\right) \times 10^{-3}. \qquad (8.88)$$

The uncertainty in (8.88) is dominated by the renormalization scale dependence. Its reduction requires a painful three-loop calculation. The numerical value in (8.88) is obtained with $B_{B_s}^S/B_{B_s} = 1.0 \pm 0.1$ [37], which is larger than the one used in [36].

Next we consider the width difference in the B_d meson system: since the second term in (8.84) is negligible in view of the other uncertainties, (8.87) also holds for $\Delta\Gamma_d^{\rm SM}/\Delta m_d^{\rm SM}$ with the replacement $B_{B_s}^{S\prime}/B_{B_s} \to B_{B_d}^{S\prime}/B_{B_d}$. The $SU(3)_F$ breaking in these 'bag' factors and in the Λ_{QCD}/m_b corrections can safely be neglected, so that the numerical range (8.88) also holds for $\Delta\Gamma_d^{\rm SM}/\Delta m_d^{\rm SM}$. With $\Delta m_d = 0.49\,\text{ps}^{-1}$ and $\tau_{B_d} = 1.5\,\text{ps}$ one finds $\Delta\Gamma_d^{\rm SM} \approx 3\times10^{-3}\Gamma_d$. Since $\Delta\Gamma_d$ and Δm_d are affected by new physics in different ways, it is instructive to consider the ratio of the two width differences: from (8.84) and (8.85) one finds

$$\frac{\Delta\Gamma_d^{\rm SM}}{\Delta\Gamma_s^{\rm SM}} \;=\; \frac{|\Gamma_{12}^d|}{|\Gamma_{12}^s|} \;\simeq\; \frac{f_{B_d}^2 B_{B_d}^S}{f_{B_s}^2 B_{B_s}^S}\left|\frac{\xi_t^d}{\xi_t^s}\right|^2 \;\simeq\; 0.04\,R_t^2. \qquad (8.89)$$

In the last line we have used $f_{B_s}/f_{B_d} = 1.16 \pm 0.05$ and $B_{B_s}^S = B_{B_d}^S$. The numerical predictions for $\Delta\Gamma_d$ from (8.88) and (8.89) are consistent with each other. Since $\Delta\Gamma_d$ stems from the CKM-suppressed decay modes, it can be substantially enhanced in models of new physics.

8.3.2.2 Phenomenology of $\Delta\Gamma_s$

Time Evolution: The width difference $\Delta\Gamma_s$ can be measured from the time evolution of an untagged B_s sample, as shown in sect. 1.3.3. In general the decay $\overline{(B)}_s \to f$ is governed

by the two-exponential formula in (1.85). With (1.54) and (1.72) we can calculate $\langle f|B_{L,H}\rangle$ and find from (1.85):

$$\Gamma[f,t] \;=\; \mathcal{N}_f\,\frac{|A_f|^2}{2}\left(1+|\lambda_f|^2\right)\left[\left(1-\mathcal{A}^f_{\Delta\Gamma}\right)e^{-\Gamma_L t}+\left(1+\mathcal{A}^f_{\Delta\Gamma}\right)e^{-\Gamma_H t}\right] \tag{8.90}$$

with $\mathcal{A}^f_{\Delta\Gamma}$ defined in (1.83). Throughout this Sect. 8.3.2.2 we neglect small terms of order a. The time-independent prefactor of the square bracket can be eliminated in favor of the branching ratio $Br\,(\overline{B}\to f\,)$ using (1.84). In principle one could measure $\Delta\Gamma_s=\Gamma_L-\Gamma_H$ by fitting the decay distribution of any decay with $|\mathcal{A}^f_{\Delta\Gamma}|\neq 1$ to $\Gamma[f,t]$ in (8.90). In practice, however, one will at best be able to measure the deviation from a single exponential up to terms linear in $\Delta\Gamma_s t$. In (1.82) $\Gamma[f,t]$ is expressed in terms of $\Gamma_s=(\Gamma_L+\Gamma_H)/2$ and $\Delta\Gamma_s$. With (1.84) one finds

$$\Gamma[f,t] \;=\; 2\,\mathrm{BR}\,(\overline{B}_s\to f\,)\,\Gamma_s\,e^{-\Gamma_s t}\left[1+\frac{\Delta\Gamma_s}{2}\mathcal{A}^f_{\Delta\Gamma}\,\left(t-\frac{1}{\Gamma_s}\right)\right]+\mathcal{O}\left((\Delta\Gamma_s\,t)^2\right). \tag{8.91}$$

That is, unless one is able to resolve quadratic $\mathcal{O}\left((\Delta\Gamma_s)^2\right)$ terms, one can only determine the product $\mathcal{A}^f_{\Delta\Gamma}\Delta\Gamma_s$ from the time evolution. A flavor-specific decay mode like $B_s\to D_s^-\pi^+$ is characterized by $\lambda_f=0$ and therefore has $\mathcal{A}^f_{\Delta\Gamma}=0$. In these decay modes the term involving $\Delta\Gamma_s$ in (8.91) vanishes. Flavor-specific decays therefore determine Γ_s up to corrections of order $(\Delta\Gamma_s)^2$. For those decays $\Gamma[f,t]$ is insensitive to new physics in M_{12}, because $\lambda_f=0$. In order to gain information on $\Delta\Gamma_s$ from (8.91), one must consider decays with $\lambda_f\neq 0$. But λ_f and $\mathcal{A}^f_{\Delta\Gamma}$ depend on the mixing phase ϕ_M (see (1.67)) and therefore change in the presence of new physics in M_{12}. In the Standard Model we can calculate ϕ_M and then extract $\Delta\Gamma_s$ from the measured $\mathcal{A}^f_{\Delta\Gamma}\Delta\Gamma_s$. In the presence of new physics, however, one needs additional information. We therefore discuss these two cases independently below.

Lifetimes are conventionally measured by fitting the decay distribution to a single exponential. We now write the two-exponential formula of (8.90) as

$$\begin{aligned}\Gamma[f,t] &= A\,e^{-\Gamma_L t}\;+\;B\,e^{-\Gamma_H t}\\ &= e^{-\Gamma_s t}\left[(A+B)\cosh\frac{\Delta\Gamma_s t}{2}+(B-A)\sinh\frac{\Delta\Gamma_s t}{2}\right],\end{aligned} \tag{8.92}$$

where $A=A(f)$ and $B=B(f)$ can be read off from (8.90). If one uses a maximum likelihood fit of (8.92) to a single exponential,

$$F\,[f,t] \;=\; \Gamma_f\,e^{-\Gamma_f t}, \tag{8.93}$$

it will yield the following result [41]:

$$\Gamma_f \;=\; \frac{A/\Gamma_L+B/\Gamma_H}{A/\Gamma_L^2+B/\Gamma_H^2}. \tag{8.94}$$

We expand this to second order in $\Delta\Gamma_s$:

$$\Gamma_f \;=\; \Gamma_s+\frac{A-B}{A+B}\,\frac{\Delta\Gamma_s}{2}\;-\;\frac{2\,AB}{(A+B)^2}\frac{(\Delta\Gamma_s)^2}{\Gamma_s}+\mathcal{O}\left(\frac{(\Delta\Gamma_s)^3}{\Gamma_s^2}\right). \tag{8.95}$$

In flavor-specific decays we have $A=B$ (see (1.82)). We see from (8.95) that here a single-exponential fit determines

$$\Gamma_{\rm fs} \;=\; \Gamma_s\;-\;\frac{(\Delta\Gamma_s)^2}{2\,\Gamma_s}\;+\;\mathcal{O}\left(\frac{(\Delta\Gamma_s)^3}{\Gamma_s^2}\right). \tag{8.96}$$

Heavy quark symmetry predicts that the average *widths* Γ_s and Γ_d are equal up to corrections of less than one percent [38,42]. From (8.96) we then realize that the average B_s *lifetime* (defined as $1/\Gamma_f$) can exceed the B_d lifetime by more than one percent, if $\Delta\Gamma_s$ is sizable.

***CP* Properties and Branching Ratios:** In the B_s system $\Delta\Gamma$ is dominated by $\Gamma_{12}^{s,cc}$. In the following we will neglect the Cabibbo-suppressed contributions from $\Gamma_{12}^{s,uc}$ and $\Gamma_{12}^{s,uu}$. We also specify to the PDG phase convention for the CKM matrix, in which $\arg(V_{cb}V_{cs}^*)=\mathcal{O}(\lambda^6)$, see (8.75). For the discussion in the forthcoming paragraphs it will be useful to define the CP eigenstates

$$|B_s^{\rm even}\rangle \;=\; \frac{1}{\sqrt{2}}\left(|B_s\rangle-|\overline{B}_s\rangle\right),\qquad\text{and}\qquad |B_s^{\rm odd}\rangle \;=\; \frac{1}{\sqrt{2}}\left(|B_s\rangle+|\overline{B}_s\rangle\right). \tag{8.97}$$

Here we have used the standard convention for the CP transformation: $CP|B_s\rangle=-|\overline{B}_s\rangle$.

Interestingly, one can measure $\Delta\Gamma_s$ from branching ratios, without information from lifetime fits. We define

$$\Delta\Gamma^s_{\rm CP} \;\equiv\; 2|\Gamma^s_{12}| \;=\; 2\sum_{f\in X_{c\bar{c}}}\left[\Gamma(B_s\to f_{{\rm CP}+})\;-\;\Gamma(B_s\to f_{{\rm CP}-})\right]. \tag{8.98}$$

Here $X_{c\bar{c}}$ represents the final states containing a $(c,\overline{c})$ pair, which constitute the dominant contribution to $\Delta\Gamma^s_{\rm CP}$ stemming from the decay $b\to c\bar{c}s$. In (8.98) we have decomposed any final state f into its CP-even and CP-odd component, $|f\rangle=|f_{{\rm CP}+}\rangle+|f_{{\rm CP}-}\rangle$[6] and defined

$$\Gamma(B_s\to f_{{\rm CP}\pm}) \;=\; \mathcal{N}_f\,|\langle f_{{\rm CP}\pm}|B_s\rangle|^2 \;=\; \frac{|\langle f_{{\rm CP}\pm}|B_s\rangle|^2}{|\langle f|B_s\rangle|^2}\,\Gamma(B_s\to f). \tag{8.99}$$

$\mathcal{N}_f$ is the usual normalization factor originating from the phase-space integration. $\Delta\Gamma^s_{\rm CP}$ equals $\Delta\Gamma_s$ in the Standard Model, but these quantities differ by a factor of $\cos\phi_s$ in models of new physics, see (1.64b). We will later exploit this feature to probe the Standard Model and to determine $|\cos\phi_s|$.

We now prove the second equality in (8.98) and subsequently discuss how $\Gamma(B_s\to f_{{\rm CP}\pm})$ can be measured. Start from the definition of Γ^s_{12}:

$$\Gamma^s_{12} \;=\; \sum_f \mathcal{N}_f\,\langle B_s|f\rangle\langle f|\overline{B}_s\rangle \;=\; \frac{1}{2}\sum_f \mathcal{N}_f\left[\,\langle B_s|f\rangle\langle f|\overline{B}_s\rangle+\langle B_s|\overline{f}\rangle\langle\overline{f}|\overline{B}_s\rangle\,\right]. \tag{8.100}$$

[6] The factor of 2 in (8.98) is an artifact of our normalization of $|f_{{\rm CP}\pm}\rangle$.

In the second equation we have paired the final state $|f\rangle$ with its CP conjugate $|\overline{f}\rangle = -CP|f\rangle$. In the next step we trade f for $f_{\rm CP+}$ and $f_{\rm CP-}$ and use the CP transformation

$$\langle f_{\rm CP\pm}|\overline{B}_s\rangle \;=\; \mp\,\langle f_{\rm CP\pm}|B_s\rangle \tag{8.101}$$

in our phase convention with $\arg(V_{cb}V_{cs}^*) = 0$. Then (8.100) becomes

$$\begin{aligned} -\,\Gamma_{12}^s &= \sum_{f\in X_{c\bar c}} \mathcal{N}_f \left[|\langle f_{\rm CP+}|B_s\rangle|^2 - |\langle f_{\rm CP-}|B_s\rangle|^2\right] \\ &= \sum_{f\in X_{c\bar c}} \left[\Gamma(B_s\to f_{\rm CP+}) \;-\; \Gamma(B_s\to f_{\rm CP-})\right]. \end{aligned} \tag{8.102}$$

Interference terms involving both $\langle f_{\rm CP+}|B_s\rangle$ and $\langle f_{\rm CP-}|B_s\rangle$ drop out when summing the two terms $\langle B_s|f\rangle\langle f|\overline{B}_s\rangle$ and $\langle B_s|\overline{f}\rangle\langle\overline{f}|\overline{B}_s\rangle$. An explicit calculation of Γ_{12}^s reveals that the overall sign of the LHS of (8.102) is positive, which completes the proof of (8.98).

Loosely speaking, $\Delta\Gamma^s_{\rm CP}$ is measured by counting the CP-even and CP-odd double-charm final states in B_s decays. Our formulae become more transparent if we use the CP-eigenstates defined in (8.97). With $|B_s\rangle = (|B_s^{\rm even}\rangle + |B_s^{\rm odd}\rangle)/\sqrt{2}$ one easily finds from (8.102):

$$\Delta\Gamma^s_{\rm CP} \;=\; 2|\Gamma^s_{12}| \;=\; \Gamma\,(B_s^{\rm even}) - \Gamma(B_s^{\rm odd}). \tag{8.103}$$

Here the RHS refers to the total widths of the CP-even and CP-odd B_s eigenstates. We stress that the possibility to relate $|\Gamma^s_{12}|$ to a measurable quantity in (8.98) crucially depends on the fact that Γ^s_{12} is dominated by a single weak phase. For instance, the final state K^+K^- is triggered by $b\to u\bar u s$ and involves a weak phase different from $b\to c\bar c s$. Although K^+K^- is CP-even, the decay $B_s^{\rm odd}\to K^+K^-$ is possible. An inclusion of such CKM-suppressed modes into (8.102) would add interference terms that spoil the relation to measured quantities. The omission of these contributions to Γ^s_{12} induces a theoretical uncertainty of order 3–5% on (8.103).

A measurement of $\Delta\Gamma^s_{\rm CP}$ has been performed by the ALEPH collaboration [43]. ALEPH has measured

$$2\,{\rm BR}\,(\overline{B}_s \to D_s^{(*)+}D_s^{(*)-}) \;=\; 0.26^{+0.30}_{-0.15} \tag{8.104}$$

and related it to $\Delta\Gamma^s_{\rm CP}$. For this the following theoretical input has been used [44]:

i) In the heavy quark limit $m_c\to\infty$ and neglecting certain terms of order $1/N_c$ (where $N_c = 3$ is the number of colors) the decay $B_s^{\rm odd}\to D_s^\pm D_s^{*\mp}$ is forbidden. Hence in this limit the final state in $\overline{B}_s\to D_s^\pm D_s^{*\mp}$ is CP-even. Further in $\overline{B}_s\to D_s^{*+}D_s^{*-}$ the final state is in an S-wave.

ii) In the small velocity limit when $m_c\to\infty$ with $m_b - 2m_c$ fixed [45], $\Delta\Gamma^s_{\rm CP}$ is saturated by $\Gamma(\overline{B}_s\to D_s^{(*)+}D_s^{(*)-})$. With i) this implies that in the considered limit the width of $B_s^{\rm odd}$ vanishes. For $N_c\to\infty$ and in the SV limit, $\Gamma(\overline{B}_s\to D_s^{(*)+}D_s^{(*)-})$ further equals the parton model result for $\Delta\Gamma^s_{\rm CP}$ (quark-hadron duality).

Identifying $\Gamma(B_s^{\rm even}\to D_s^{(*)+}D_s^{(*)-}) \simeq \Delta\Gamma^s_{\rm CP}$ and $\Gamma(B_s^{\rm odd}\to D_s^{(*)+}D_s^{(*)-}) \simeq 0$ we can integrate $\Gamma\left[D_s^{(*)+}D_s^{(*)},t\right] = \Gamma(B_s^{\rm even}\to D_s^{(*)+}D_s^{(*)-})\exp(-\Gamma_L t)$ over t to find:

$$2\,{\rm BR}\,(\overline{B}_s\to D_s^{(*)+}D_s^{(*)-}) \;\simeq\; \frac{\Delta\Gamma^s_{\rm CP}}{\Gamma_L}. \tag{8.105}$$

Thus the measurement in (8.104) is compatible with the theoretical prediction in (8.86).

When using (8.105) one should be aware that the corrections to the limits i) and ii) adopted in [44] can be numerically sizeable. For instance, in the SV limit there are no multibody final states like $D_s^{(*)}\overline{D}X_s$, which can modify (8.105). As serious would be the presence of a sizeable CP-odd component of the $D_s^{(*)+}D_s^{(*)-}$ final state, since it would be added with the wrong sign to $\Delta\Gamma^s_{\rm CP}$ in (8.105). A method to control the corrections to the SV limit experimentally is proposed below in the paragraph on new physics. One feature of the SV limit is the absence of CP-odd double-charm final states. (Indeed there are only very few CP-odd final states in Table 8.5.) This has the consequence that $\Delta\Gamma^s_{\rm CP}$ cannot be too small, because for $\Gamma(B_s^{\rm odd}\to X_{\bar c c})$ the spectator contributions and non-spectator diagrams like those in Fig. 8.3 must sum to zero. This favors values of $\Delta\Gamma^s_{\rm CP} = \Delta\Gamma_s^{\rm SM}$ in the upper range of (8.86).

Standard Model: In the Standard Model the $B_s^0 - \overline{B}_s^0$ mixing phase $\phi_M^s = -2\beta_s$ can be safely neglected for the discussion of $\Delta\Gamma_s$. Then the mass eigenstates coincide with the CP eigenstates defined in (8.97) with $|B_L\rangle = |B_s^{\rm even}\rangle$ and $|B_H\rangle = |B_s^{\rm odd}\rangle$. Any $b\to c\bar c s$ decay into a CP-even final state like $D_s^+D_s^-$ stems solely from the $|B_L\rangle$ component in the untagged B_s sample. A lifetime fit to this decay therefore determines Γ_L. Conversely, the $b\to c\bar c s$ decay into a CP-odd eigenstate determines Γ_H. We can easily verify this from (8.90) by calculating $\mathcal{A}^f_{\Delta\Gamma}$: q/p in (1.66) equals -1 and $\overline{A}_f/A_f = -\eta_f$, where η_f is the CP parity of the final state. Then (1.72) yields $\lambda_f = \eta_f$, so that $\mathcal{A}^f_{\Delta\Gamma} = -\eta_f$. Hence for any $b\to c\bar c s$ decay the coefficient of $\exp(-\Gamma_H t)$ in (8.90) vanishes for a CP-even final state, while the $\exp(-\Gamma_L t)$ term vanishes for a CP-odd final state. In practice one will encounter much more statistics in CP-even final states, so that the best determination of $\Delta\Gamma_s$ will combine Γ_L with $\Gamma_{\rm fs}$ measured in a flavor-specific decay. From (8.96) and $\Gamma_L = \Gamma_s + \Delta\Gamma_s/2$ one finds

$$\Delta\Gamma_s \;=\; 2\,(\Gamma_L - \Gamma_{\rm fs})\left(1 - 2\frac{\Gamma_L - \Gamma_{\rm fs}}{\Gamma_{\rm fs}}\right) \;+\; \mathcal{O}\left(\frac{(\Delta\Gamma_s)^3}{\Gamma_s^2}\right). \tag{8.106}$$

Here we have expanded to second order in $\Delta\Gamma_s$, which should be sufficient for realistic values of $\Delta\Gamma_s$.

It should be stressed that every $b\to c\bar c s$ decay encodes the same information on $\Delta\Gamma_s$, once its CP parity is known. This is also true for $b\to c\bar u d$ decays into CP eigenstates, because the decay amplitude carries the same phase as the one in $b\to c\bar c s$. Therefore the extracted values for $\Delta\Gamma_s$ in these decays can be combined to gain statistics. Interesting decay modes are summarized in Table 8.5. Many of the listed modes, like $\overline{B}_s\to\psi\phi$, require an angular analysis to separate the CP-even from the CP-odd component. This procedure is described in detail in Sect. 8.3.5.

It is tempting to use $\overline{(}B_s^{)} \to K^+K^-$ to measure $\Delta\Gamma_s$ because of its nice experimental signature. But such CKM-suppressed decay modes cannot be used, because the weak phase of the decay amplitude is not known. If $B_s \to K^+K^-$ were dominated by penguin loops and new physics were absent from these loops, $\lambda_{K^+K^-}$ would indeed be equal to $+1$ and the coefficient of $\exp(-\Gamma_H t)$ in (8.90) would vanish. In practice, however, the tree-level amplitude $b \to u\overline{u}s$ is expected to give a non-negligible contribution. Since this amplitude carries a different phase, $2\arg(V_{ub}) = -2\gamma$, $\lambda_{K^+K^-}$ deviates from ± 1 and both exponentials in (8.90) contribute.

New Physics: In the presence of new physics the CP-violating phase ϕ in (1.62) and (1.64b) can be large. Since various observables in untagged B_s decays depend on $\cos\phi_s$ in different ways, one can reveal new physics and determine $|\cos\phi_s|$ by combining different measurements. We have already seen above that $\Delta\Gamma^s_{\rm CP}$ in (8.98) does not depend on ϕ_s at all, while $\Delta\Gamma_s$ is diminished in the presence of new physics:

$$\Delta\Gamma_s \;=\; \Delta\Gamma^s_{\rm CP}\cos\phi_s. \tag{8.107}$$

On the other hand $\sin\phi_s$ can be obtained from CP asymmetries in B_s decays like $B_s \to \psi\phi$. Therefore measurements of $\Delta\Gamma$ are complementary to the study of CP asymmetries, which require tagging and the resolution of the rapid B_s–$\overline{B}_s$ oscillation and come with a loss in statistics, efficiency and purity. Both avenues should be pursued and their results combined, because they measure the same fundamental quantities. A detailed analysis of both tagged and untagged decays can be found in [46].

In our phase convention $\arg(V_{cb}V_{cs}^*) = 0$ we simply have

$$\arg(M_{12}) \;=\; \phi_s. \tag{8.108}$$

The mass eigenstates can be expressed as

$$\begin{aligned} |B_L\rangle &= \;\; \frac{1+e^{i\phi}}{2}\,|B_s^{\rm even}\rangle - \frac{1-e^{i\phi}}{2}\,|B_s^{\rm odd}\rangle, \\ |B_H\rangle &= -\frac{1-e^{i\phi}}{2}\,|B_s^{\rm even}\rangle + \frac{1+e^{i\phi}}{2}\,|B_s^{\rm odd}\rangle. \end{aligned} \tag{8.109}$$

Whenever we use $B_s^{\rm even}$ and $B_s^{\rm odd}$ we implicitly refer to our phase conventions for the CKM matrix and the CP transformation. If formulae involving $B_s^{\rm even}$ and $B_s^{\rm odd}$ are used to constrain models with an extended quark sector, the phase convention used for the enlarged CKM matrix must likewise be chosen such that $\arg(V_{cb}V_{cs}^*) \simeq 0$.

We next consider the time evolution of a $b \to c\overline{c}s$ decay into a CP eigenstate with CP parity η_f. $\mathcal{A}^f_{\Delta\Gamma}$ reads

$$\mathcal{A}^f_{\Delta\Gamma} \;=\; -\eta_f\cos\phi_s. \tag{8.110}$$

In the Standard Model, where $\phi_s \simeq 0$, $\Gamma[f,t]$ simplifies to a single-exponential law, which can be verified from (8.91) or by inserting (8.109) into (1.85).

Since $\Delta\Gamma^s_{\rm CP}$ is unaffected by new physics and $\Delta\Gamma^s_{\rm CP} > 0$, several facts hold beyond the Standard Model:

i) There are more CP-even than CP-odd final states in B_s decays.

ii) The shorter-lived mass eigenstate is always the one with the larger CP-even component in (8.109). Its branching ratio into a CP-even final state $f_{\rm CP+}$ exceeds the branching ratio of the longer-lived mass eigenstate into $f_{\rm CP+}$, if the weak phase of the decay amplitude is close to $\arg V_{cb}V_{cs}^*$.

iii) For $\cos\phi_s > 0$ B_L has a shorter lifetime than B_H, while for $\cos\phi_s < 0$ the situation is the opposite [47].

Allowing for a new physics phase ϕ_s the result in (8.105) is changed. In the SV limit one now predicts:

$$\begin{aligned} 2\,{\rm BR}\left(\overline{(}B_s^{)} \to D_s^{(*)+}D_s^{(*)-}\right) &\simeq \Delta\Gamma^s_{\rm CP}\left[\frac{1+\cos\phi_s}{2\,\Gamma_L} + \frac{1-\cos\phi_s}{2\,\Gamma_H}\right] \\ &= \frac{\Delta\Gamma^s_{\rm CP}}{\Gamma_s}\left[1+\mathcal{O}\left(\frac{\Delta\Gamma_s}{\Gamma_s}\right)\right]. \end{aligned} \tag{8.111}$$

The term in square brackets accounts for the fact that in general the CP-even eigenstate $|B_s^{\rm even}\rangle$ is a superposition of $|B_L\rangle$ and $|B_H\rangle$. It is straightforward to obtain (8.105): inserting (8.109) into (1.85) expresses $\Gamma[f,t]$ in terms of $\Gamma(B_s^{\rm even} \to f)$ and $\Gamma(B_s^{\rm odd} \to f)$. After integrating over time the coefficient of $\Gamma(B_s^{\rm even} \to f)$ is just the term in square brackets in (8.111). We verify from (8.111) that the measurement of ${\rm BR}\left(\overline{(}B_s^{)} \to D_s^{(*)+}D_s^{(*)-}\right)$ determines $\Delta\Gamma^s_{\rm CP}$. Its sensitivity to the new physics phase ϕ_s is suppressed by another factor of $\Delta\Gamma_s/\Gamma_s$ and is irrelevant in view of the theoretical uncertainties.

Next we discuss the determination of $\Delta\Gamma_s$ and $|\cos\phi_s|$. There are two generic ways to obtain information on $\Delta\Gamma_s$ and ϕ_s :

i) The measurement of the B_s lifetime in two decay modes $\overline{(}B_s^{)} \to f_1$ and $\overline{(}B_s^{)} \to f_2$ with $\mathcal{A}^{f_1}_{\Delta\Gamma} \neq \mathcal{A}^{f_2}_{\Delta\Gamma}$.

ii) The fit of the decay distribution of $\overline{(}B_s^{)} \to f$ to the two-exponential formula in (1.82).

As first observed in [47], the two methods are differently affected by a new physics phase $\phi_s \neq 0$. Thus by combining the results of methods i) and ii) one can gain information on ϕ_s. In this paragraph we consider two classes of decays:

- flavor-specific decays, which are characterized by $\overline{A}_f = 0$ implying $\mathcal{A}^f_{\Delta\Gamma} = 0$. Examples are $B_s \to D_s^-\pi^+$ and $B_s \to X\ell^+\nu_\ell$,
- the CP-specific decays of Table 8.5, with $\mathcal{A}^f_{\Delta\Gamma} = -\eta_f\cos\phi_s$.

In both cases the time evolution of the untagged sample in (1.82) is not sensitive to the sign of $\Delta\Gamma_s$ (or, equivalently, of $\cos\phi_s$). For the CP-specific decays of Table 8.5 this can be seen by noticing that

$$\mathcal{A}^f_{\Delta\Gamma}\,\sinh\frac{\Delta\Gamma_s\,t}{2} = -\,\eta_f\,|\cos\phi_s|\,\sinh\frac{|\Delta\Gamma_s|\,t}{2}. \tag{8.112}$$

Here we have used the fact that $\Delta\Gamma_s$ and $\cos\phi_s$ always have the same sign, because $\Delta\Gamma^s_{\rm CP} > 0$. Hence our untagged studies can only determine $|\cos\phi_s|$ and therefore lead to a four-fold ambiguity in ϕ_s. The sign ambiguity in $\cos\phi_s$ reflects the fact that from the untagged time evolution in (1.82) one cannot distinguish, whether the heavier or the lighter eigenstate has the shorter lifetime. (Methods to resolve the discrete ambiguity can be found in [46].)

In order to experimentally establish a non-zero $\Delta\Gamma_s$ from the time evolution in (1.82) one needs sufficient statistics to resolve the deviation from a single-exponential decay law, see (8.91). As long as we are only sensitive to terms linear in $\Delta\Gamma_s t$ and $\Delta\Gamma_s/\Gamma_s$, we can only determine $\mathcal{A}^f_{\Delta\Gamma}\,\Delta\Gamma_s$ from (8.91). $\mathcal{A}^f_{\Delta\Gamma}\,\Delta\Gamma_s$ vanishes for flavor-specific decays and equals $-\eta_f\Delta\Gamma_s\cos\phi_s$ for CP-specific final states. Hence from the time evolution alone one can only determine the product $\Delta\Gamma_s\,\cos\phi_s$ in the first experimental stage.

Determination of Γ_s and $\Delta\Gamma_s\cos\phi_s$: In Eqs. (8.92) – (8.95) we have related the width found in a single-exponential fit to the parameters $A(f)$, $B(f)$, Γ_s and $\Delta\Gamma_s$ of the two-exponential formula.

In (8.96) we found that a single-exponential fit in flavor-specific decays (which have $A = B$) determines Γ_s up to corrections of order $(\Delta\Gamma_s)^2/\Gamma_s^2$.

With (1.82) and (8.92) we can read off A and B for the CP-specific decays of Table 8.5 and find $A(f_{\rm CP+})/B(f_{\rm CP+}) = (1+\cos\phi)/(1-\cos\phi)$ and $A(f_{\rm CP-})/B(f_{\rm CP-}) = (1-\cos\phi)/(1+\cos\phi)$ for CP-even and CP-odd final states, respectively. Our key quantity for the discussion of CP-specific decays $\overline{(B_s)} \to f_{\rm CP}$ is

$$\Delta\Gamma^{s\prime}_{\rm CP} \equiv -\eta_f\mathcal{A}^f_{\Delta\Gamma}\,\Delta\Gamma_s = \Delta\Gamma_s\,\cos\phi_s = \Delta\Gamma^s_{\rm CP}\,\cos^2\phi_s. \tag{8.113}$$

With this definition (8.95) reads for the decay rate $\Gamma_{{\rm CP},\eta_f}$ measured in $\overline{(B_s)} \to f_{\rm CP}$ [46]:

$$\Gamma_{{\rm CP},\eta_f} = \Gamma_s + \eta_f\,\frac{\Delta\Gamma^{s\prime}_{\rm CP}}{2} - \sin^2\phi_s\,\frac{(\Delta\Gamma_s)^2}{2\Gamma_s} + \mathcal{O}\left(\frac{(\Delta\Gamma_s)^3}{\Gamma_s^2}\right). \tag{8.114}$$

That is, to first order in $\Delta\Gamma_s$, comparing the $\overline{(B_s)}$ lifetimes measured in a flavor-specific and a CP-specific final state determines $\Delta\Gamma^{s\prime}_{\rm CP}$. The first term in (8.114) agrees with the result in [47], which has been found by expanding the time evolution in (8.92) and (8.93) for small $\Delta\Gamma_s\,t$.

From (8.96) and (8.114) one finds

$$\Gamma_{{\rm CP},\eta_f} - \Gamma_{\rm fs} = \frac{\Delta\Gamma^{s\prime}_{\rm CP}}{2}\left(\eta_f + \frac{\Delta\Gamma^{s\prime}_{\rm CP}}{\Gamma}\right) + \mathcal{O}\left(\frac{(\Delta\Gamma)^3}{\Gamma^2}\right). \tag{8.115}$$

Hence for a CP-even (CP-odd) final state the quadratic corrections enlarge (diminish) the difference between the two measured widths. A measurement of $\Delta\Gamma^{s\prime}_{\rm CP}$ has a high priority at Run II of the Tevatron. The LHC experiments ATLAS, CMS and LHCb expect to measure $\Delta\Gamma^{s\prime}_{\rm CP}/\Gamma_s$ with absolute errors between 0.012 and 0.018 for $\Delta\Gamma^{s\prime}_{\rm CP}/\Gamma_s = 0.15$ [48]. An upper bound on $\Delta\Gamma^{s\prime}_{\rm CP}$ would be especially interesting. If the lattice calculations entering (8.86)

mature and the theoretical uncertainty decreases, an upper bound on $|\Delta\Gamma^{s\prime}_{\rm CP}|$ may show that $\phi_s \neq 0, \pi$ through

$$\frac{\Delta\Gamma^{s\prime}_{\rm CP}}{\Delta\Gamma^s_{\rm CP}} = \cos^2\phi_s. \tag{8.116}$$

Note that conversely the experimental establishment of a non-zero $\Delta\Gamma^{s\prime}_{\rm CP}$ immediately helps to constrain models of new physics, because it excludes values of ϕ_s around $\pi/2$.

The described method to obtain $\Delta\Gamma^{s\prime}_{\rm CP}$ can also be used, if the sample contains a known ratio of CP-even and CP-odd components. This situation occurs e.g. in decays to $J/\psi\phi$, if no angular analysis is performed or in final states, which are neither flavor-specific nor CP eigenstates. We discuss this case below for $\overline{(B_s)} \to D_s^{\pm}D_s^{(*)\mp}$. Further note that the comparison of the lifetimes measured in CP-even and CP-odd final states determines $\Delta\Gamma^{s\prime}_{\rm CP}$ up to corrections of order $(\Delta\Gamma_s/\Gamma_s)^3$.

The theoretical uncertainty in (8.86) dilutes the extraction of $|\cos\phi_s|$ from a measurement of $\Delta\Gamma^{s\prime}_{\rm CP}$ alone. One can bypass the theory prediction in (8.86) altogether by measuring both $\Delta\Gamma^{s\prime}_{\rm CP}$ and $|\Delta\Gamma_s|$ and determine $|\cos\phi_s|$ through

$$\frac{\Delta\Gamma^{s\prime}_{\rm CP}}{|\Delta\Gamma_s|} = |\cos\phi_s|. \tag{8.117}$$

To obtain additional information on $\Delta\Gamma_s$ and ϕ_s from the time evolution in (1.82) requires more statistics: the coefficient of t in (8.91), $\Delta\Gamma_s\,\mathcal{A}^f_{\Delta\Gamma}/2$, vanishes in flavor-specific decays and is equal to $-\eta_f\Delta\Gamma^{s\prime}_{\rm CP}/2$ in the CP-specific decays of Table 8.5. Therefore the data sample must be large enough to be sensitive to the terms of order $(\Delta\Gamma_s\,t)^2$ in order to get new information on $\Delta\Gamma_s$ and ϕ_s. We now list three methods to determine $|\Delta\Gamma_s|$ and $|\cos\phi_s|$ separately [46]. The theoretical uncertainty decreases and the required experimental statistics increases from method 1 to method 3. Hence as the collected data sample grows, one can work off our list downwards. The first method exploits information from branching ratios and needs no information from the quadratic $(\Delta\Gamma_s\,t)^2$ terms.

Method 1: We assume that $\Delta\Gamma^{s\prime}_{\rm CP}$ has been measured as described on page 365. The method presented now is a measurement of $\Delta\Gamma^s_{\rm CP}$ using the information from branching ratios. With (8.116) one can then find $|\cos\phi_s|$ and subsequently $|\Delta\Gamma_s|$ from (8.117). In the SV limit the branching ratio BR$(\overline{(B_s)} \to D_s^{(*)+}D_s^{(*)-})$ equals $\Delta\Gamma^s_{\rm CP}/(2\Gamma_s)$ up to corrections of order $\Delta\Gamma_s/\Gamma_s$, as discussed above [44]. Corrections to the SV limit, however, can be sizeable. Yet we stress that one can control the corrections to this limit experimentally, successively arriving at a result which does not rely on the validity of the SV limit. For this it is of prime importance to determine the CP-odd component of the final states $D_s^{\pm}D_s^{*\mp}$ and $D_s^{*+}D_s^{*-}$. We now explain how the CP-odd and CP-even component of any decay $\overline{(B_s)} \to f$ corresponding to the quark level transition $b \to c\bar{c}s$ can be obtained. This simply requires a fit of the time evolution of the decay to a single exponential, as in (8.93). Define the contributions of the CP-odd and CP-even eigenstate to $B_s \to f$:

$$\Gamma(B_s^{\rm odd} \to f) \equiv \mathcal{N}_f\,|\langle f|B_s^{\rm odd}\rangle|^2, \qquad \Gamma(B_s^{\rm even} \to f) \equiv \mathcal{N}_f\,|\langle f|B_s^{\rm even}\rangle|^2. \tag{8.118}$$

It is useful to define the CP-odd fraction x_f by

$$\frac{\Gamma(B_s^{\rm odd} \to f)}{\Gamma(B_s^{\rm even} \to f)} = \frac{|\langle f|B_s^{\rm odd}\rangle|^2}{|\langle f|B_s^{\rm even}\rangle|^2} = \frac{|\langle \overline{f}|B_s^{\rm odd}\rangle|^2}{|\langle \overline{f}|B_s^{\rm even}\rangle|^2} = \frac{x_f}{1-x_f}. \quad (8.119)$$

The time evolution $(\Gamma[f,t] + \Gamma[\overline{f},t])/2$ of the CP-averaged untagged decay $\stackrel{(-)}{B}_s \to f, \overline{f}$ is governed by a two-exponential formula:

$$\frac{\Gamma[f,t] + \Gamma[\overline{f},t]}{2} = A(f)\, e^{-\Gamma_L t} + B(f)\, e^{-\Gamma_H t}. \quad (8.120)$$

With (8.109) and (1.85) one finds

$$\begin{aligned} A(f) &= \frac{\mathcal{N}_f}{2}\,|\langle f|B_L\rangle|^2 + \frac{\mathcal{N}_f}{2}\,|\langle \overline{f}|B_L\rangle|^2 \\ &= \frac{1+\cos\phi}{2}\,\Gamma(B_s^{\rm even} \to f) + \frac{1-\cos\phi}{2}\,\Gamma(B_s^{\rm odd} \to f), \\ B(f) &= \frac{\mathcal{N}_f}{2}\,|\langle f|B_H\rangle|^2 + \frac{\mathcal{N}_f}{2}\,|\langle \overline{f}|B_H\rangle|^2 \\ &= \frac{1-\cos\phi}{2}\,\Gamma(B_s^{\rm even} \to f) + \frac{1+\cos\phi}{2}\,\Gamma(B_s^{\rm odd} \to f). \end{aligned} \quad (8.121)$$

With (8.119) we arrive at

$$\frac{A(f)}{B(f)} = \frac{(1+\cos\phi)\Gamma(B_s^{\rm even} \to f) + (1-\cos\phi)\Gamma(B_s^{\rm odd} \to f)}{(1-\cos\phi)\Gamma(B_s^{\rm even} \to f) + (1+\cos\phi)\Gamma(B_s^{\rm odd} \to f)} = \frac{1+(1-2x_f)\cos\phi}{1-(1-2x_f)\cos\phi}. \quad (8.122)$$

In (8.121) and (8.122) it is crucial that we average the decay rates for $\stackrel{(-)}{B}_s \to f$ and the CP-conjugate process $\stackrel{(-)}{B}_s \to \overline{f}$. This eliminates the interference term $\langle B_s^{\rm odd}|f\rangle\langle f|B_s^{\rm even}\rangle$, so that $A(f)/B(f)$ only depends on x_f. The single-exponential fit with (8.93) determines Γ_f. Equations (8.95) and (8.122) combine to give

$$2\,(\Gamma_f - \Gamma_s) = (1-2x_f)\,\Delta\Gamma_s\,\cos\phi_s = (1-2x_f)\,\Delta\Gamma_{\rm CP}^s\,\cos^2\phi_s = (1-2x_f)\,\Delta\Gamma_{\rm CP}^{s\prime}, \quad (8.123)$$

up to corrections of order $(\Delta\Gamma_s)^2/\Gamma_s$. In order to determine x_f from (8.123) we need $\Delta\Gamma_{\rm CP}^{s\prime}$ from the lifetime measurement in a CP-specific final state like $D_s^+ D_s^-$ or from the angular separation of the CP components in $\stackrel{(-)}{B}_s \to \psi\phi$. The corrections of order $(\Delta\Gamma_s)^2/\Gamma_s$ to (8.123) can be read off from (8.95) with (8.122) as well. Expressing the result in terms of Γ_f and the rate $\Gamma_{\rm fs}$ measured in flavor-specific decays, we find

$$1 - 2\,x_f = 2\,\frac{\Gamma_f - \Gamma_{\rm fs}}{\Delta\Gamma_{\rm CP}^{s\prime}}\left[1 - 2\,\frac{\Gamma_f - \Gamma_{\rm fs}}{\Gamma_s}\right] + \mathcal{O}\left(\frac{(\Delta\Gamma_s)^2}{\Gamma_s^2}\right). \quad (8.124)$$

In order to solve for $\Gamma(B_s^{\rm even} \to f)$ and $\Gamma(B_s^{\rm odd} \to f)$ we also need the branching ratio $\mathrm{BR}\,(\stackrel{(-)}{B}_s \to f\,) + \mathrm{BR}\,(\stackrel{(-)}{B}_s \to \overline{f}\,)$. Recalling (1.84) one finds from (8.120) and (8.121):

$$\begin{aligned} \mathrm{BR}\,(\stackrel{(-)}{B}_s \to f\,) + \mathrm{BR}\,(\stackrel{(-)}{B}_s \to \overline{f}\,) = \;& \Gamma(B_s^{\rm even} \to f)\left[\frac{1+\cos\phi_s}{2\Gamma_L} + \frac{1-\cos\phi_s}{2\Gamma_H}\right] \\ &+ \Gamma(B_s^{\rm odd} \to f)\left[\frac{1-\cos\phi_s}{2\Gamma_L} + \frac{1+\cos\phi_s}{2\Gamma_H}\right]. \end{aligned} \quad (8.125)$$

By combining (8.119) and (8.125) we can solve for the two CP components:

$$\begin{aligned} \Gamma(B_s^{\rm even} \to f) &= \left[\Gamma_s^2 - (\Delta\Gamma_s/2)^2\right]\left(\mathrm{BR}\,(\stackrel{(-)}{B}_s \to f\,) + \mathrm{BR}\,(\stackrel{(-)}{B}_s \to \overline{f}\,)\right)\frac{1-x_f}{2\Gamma_s - \Gamma_f} \\ &= (1-x_f)\left(\mathrm{BR}\,(\stackrel{(-)}{B}_s \to f\,) + \mathrm{BR}\,(\stackrel{(-)}{B}_s \to \overline{f}\,)\right)\Gamma_s + \mathcal{O}\,(\Delta\Gamma_s) \\ \Gamma(B_s^{\rm odd} \to f) &= \left[\Gamma_s^2 - (\Delta\Gamma_s/2)^2\right]\left(\mathrm{BR}\,(\stackrel{(-)}{B}_s \to f\,) + \mathrm{BR}\,(\stackrel{(-)}{B}_s \to \overline{f}\,)\right)\frac{x_f}{2\Gamma_s - \Gamma_f} \\ &= x_f\left(\mathrm{BR}\,(\stackrel{(-)}{B}_s \to f\,) + \mathrm{BR}\,(\stackrel{(-)}{B}_s \to \overline{f}\,)\right)\Gamma_s + \mathcal{O}\,(\Delta\Gamma_s)\,. \end{aligned} \quad (8.126)$$

From (8.103) we now find the desired quantity by summing over all final states f:

$$\begin{aligned} \Delta\Gamma_{\rm CP}^s = \Gamma\,(B_s^{\rm even}) - \Gamma\left(B_s^{\rm odd}\right) &= 2\left[\Gamma_s^2 - (\Delta\Gamma_s/2)^2\right]\sum_{f\in X_{c\bar{c}}}\mathrm{BR}\,(\stackrel{(-)}{B}_s \to f\,)\,\frac{1-2\,x_f}{2\Gamma_s - \Gamma_f} \\ &= 2\,\Gamma_s\sum_{f\in X_{c\bar{c}}}\mathrm{BR}\,(\stackrel{(-)}{B}_s \to f\,)\,(1-2\,x_f)\left[1 + \mathcal{O}\left(\frac{\Delta\Gamma_s}{\Gamma_s}\right)\right]. \end{aligned} \quad (8.127)$$

It is easy to find $\Delta\Gamma_{\rm CP}^s$: first determine $1-2x_f$ from (8.124) for each studied decay mode, then insert the result into (8.127). The small quadratic term $(\Delta\Gamma_s/2)^2 = \Delta\Gamma_{\rm CP}^s\Delta\Gamma_{\rm CP}^{s\prime}/4$ is negligible. This procedure can be performed for $\mathrm{BR}\,(\stackrel{(-)}{B}_s \to D_s^{\pm}D_s^{*\mp}\,)$ and $\mathrm{BR}\,(\stackrel{(-)}{B}_s \to D_s^{*+}D_s^{*-}\,)$ to determine the corrections to the SV limit. In principle the CP-odd P-wave component of $\mathrm{BR}\,(\stackrel{(-)}{B}_s \to D_s^{*+}D_s^{*-}\,)$ (which vanishes in the SV limit) could also be obtained by an angular analysis, but this is difficult in first-generation experiments at hadron colliders, because the photon from $D_s^* \to D_s\gamma$ cannot be detected. We emphasize that it is not necessary to separate the $D_s^{(*)+}D_s^{(*)-}$ final states; our method can also be applied to the semi-inclusive $D_s^{(*)\pm}D_s^{(*)\mp}$ sample, using $\Delta\Gamma_{\rm CP}^{s\prime}$ obtained from an angular separation of the CP components in $\stackrel{(-)}{B}_s \to \psi\phi$. Further one can successively include those double-charm final states which vanish in the SV limit into (8.127). If we were able to reconstruct all $b \to c\bar{c}s$ final states, we could determine $\Delta\Gamma_{\rm CP}^s$ without invoking the SV limit. In practice a portion of these final states will be missed, but the induced error can be estimated from the corrections to the SV limit in the measured decay modes. By comparing $\Delta\Gamma_{\rm CP}^s$ and $\Delta\Gamma_{\rm CP}^{s\prime}$ one finds $|\cos\phi_s|$ from (8.116). The irreducible theoretical error of method 1 stems from the omission of CKM-suppressed decays and is of order $2|V_{ub}V_{us}/(V_{cb}V_{cs})| \sim 3-5\%$.

Method 1 is experimentally simple: at the first stage (relying on the SV limit) it amounts to counting the $\stackrel{(-)}{B}_s$ decays into $D_s^{(*)+}D_s^{(*)-}$. The corrections to the SV limit are obtained by one-parameter fits to the time evolution of the collected double-charm data samples. This sample may include final states from decay modes which vanish in the SV limit, such as multiparticle final states. No sensitivity to $(\Delta\Gamma_s\, t)^2$ is needed. A further advantage is that $\Delta\Gamma_{\rm CP}^s$ is not diminished by the presence of new physics.

Method 2: In the Standard Model the decay into a CP eigenstate $f_{\rm CP}$ is governed by a single exponential. If a second exponential is found in the time evolution of a CKM-favored decay $\stackrel{(-)}{B}_s \to f_{\rm CP}$, this will be clear evidence of new physics [49]. To this end we

must resolve the time evolution in (1.82) up to order $(\Delta\Gamma_s\, t)^2$. At first glance this seems to require a three-parameter fit to the data, because $\Gamma[f,t]$ in (1.82) depends on Γ_s, $\Delta\Gamma_s$ and (through $\mathcal{A}^f_{\Delta\Gamma}$, see (8.110)) on ϕ_s. It is possible, however, to choose these parameters in such a way that one of them enters $\Gamma\,[f_{\rm CP},t]$ at order $(\Delta\Gamma_s)^3$, with negligible impact. The fit parameters are Γ' and Y. They are chosen such that

$$\Gamma[f_{\rm CP+},t] \;=\; 2\,{\rm BR}\,(\overline{B}_s \to f_{\rm CP+})\,\Gamma' e^{-\Gamma' t}\left[1 + Y\,\Gamma'\,t\,\left(-1+\frac{\Gamma' t}{2}\right) + \mathcal{O}\left((\Delta\Gamma_s)^3\right)\right]. \quad (8.128)$$

Here we have considered a CP-even final state, for which a lot more data are expected than for CP-odd states. With (8.128) we have generalized the lifetime fit method described in (8.91) – (8.96) to the order $(\Delta\Gamma\, t)^2$. A non-zero Y signals the presence of new physics. The fitted rate Γ' and Y are related to Γ_s, $\Delta\Gamma_s$ and ϕ_s by

$$Y \;=\; \frac{(\Delta\Gamma_s)^2}{4\Gamma'^2}\sin^2\phi_s, \qquad\qquad \Gamma' \;=\; \Gamma_s(1-Y) + \frac{\cos\phi_s}{2}\Delta\Gamma_s. \quad (8.129)$$

Note that for $|\cos\phi_s| = 1$ the rate Γ' equals the rate of the shorter-lived mass eigenstate and the expansion in (8.128) becomes the exact single-exponential formula. After determining Γ' and Y we can solve (8.129) for Γ_s, $\Delta\Gamma_s$ and ϕ_s. To this end we need the width $\Gamma_{\rm fs}$ measured in flavor-specific decays. We find

$$\begin{aligned}
|\Delta\Gamma_s| \;&=\; 2\sqrt{(\Gamma'-\Gamma_{\rm fs})^2+\Gamma_{\rm fs}^2}\left[1+\mathcal{O}\left(\frac{\Delta\Gamma_s}{\Gamma_s}\right)\right],\\
\Gamma_s \;&=\; \Gamma_{\rm fs} + \frac{(\Delta\Gamma_s)^2}{2\Gamma_s} + \mathcal{O}\left(\left(\frac{\Delta\Gamma_s}{\Gamma_s}\right)^3\right)\\
\Delta\Gamma^{s\prime}_{\rm CP} \;&=\; 2\left[\Gamma' - \Gamma_s\,(1-Y)\right]\left[1+\mathcal{O}\left(\left(\frac{\Delta\Gamma_s}{\Gamma_s}\right)^2\right)\right],\\
|\sin\phi_s| \;&=\; \frac{2\Gamma_s\sqrt{Y}}{|\Delta\Gamma_s|}\left[1+\mathcal{O}\left(\frac{\Delta\Gamma_s}{\Gamma_s}\right)\right]. \qquad (8.130)
\end{aligned}$$

The quantity $\Delta\Gamma^{s\prime}_{\rm CP}$, which we could already determine from single-exponential fits, is now found beyond the leading order in $\Delta\Gamma_s/\Gamma_s$. By contrast, $\Delta\Gamma_s$ and $|\sin\phi_s|$ in (8.130) are only determined to the first non-vanishing order in $\Delta\Gamma_s/\Gamma_s$.

In conclusion, method 2 involves a two-parameter fit and needs sensitivity to the quadratic term in the time evolution. The presence of new physics can be invoked from $Y \neq 0$ and does not require to combine lifetime measurements in different decay modes.

Method 3: Originally the following method has been proposed to determine $|\Delta\Gamma_s|$ [47,49]: The time evolution of a $\overline{B}_s$ decay into a flavor-specific final state is fitted to two exponentials. This amounts to resolving the deviation of $\cosh(\Delta\Gamma_s\, t/2)$ from 1 in (1.82) in a two-parameter fit for Γ_s and $|\Delta\Gamma_s|$. If one adopts the same parameterization as in (8.128), Γ' and Y are obtained from (8.129) by replacing ϕ_s with $\pi/2$. The best suited flavor-specific decay modes at hadron colliders are $\overline{B}_s \to D_s^{(*)\pm}\pi^\mp$, $\overline{B}_s \to D_s^{(*)\pm}\pi^\mp\pi^+\pi^-$

and $\overline{B}_s \to X\ell^\mp\nu$.Depending on the event rate in these modes, method 3 could be superior to method 2 in terms of statistics. On the other hand, to find the "smoking gun" of new physics, the $|\Delta\Gamma_s|$ obtained must be compared to $\Delta\Gamma^{s\prime}_{\rm CP}$ from CP-specific decays to prove $|\cos\phi_s| \neq 1$ through (8.117). Since the two measurements are differently affected by systematic errors, this can be a difficult task. First upper bounds on $|\Delta\Gamma_s|$ using method 3 have been obtained in [50].

The L3 collaboration has determined an upper bound $|\Delta\Gamma_s|/\Gamma_s \leq 0.67$ by fitting the time evolution of fully inclusive decays to two exponentials [51]. This method is quadratic in $\Delta\Gamma_s$ as well. The corresponding formula for the time evolution can be simply obtained from (8.92) with $A = \Gamma_L$ and $B = \Gamma_H$.

8.3.2.3 Phenomenology of $\Delta\Gamma_d$

The Standard Model value $\Delta\Gamma_d^{\rm SM}/\Gamma_d \approx 3\times 10^{-3}$ derived before (8.89) is presumably too small to be measured from lifetime fits. In extension of the Standard Model, however, $\Delta\Gamma_d/\Gamma_d$ can be large, up to a few percent. The expected high statistics for the decay $B_d \to \psi K_S$ can be used to measure the lifetime $1/\Gamma_{B_d\to\psi K_S}$ in this channel with

$$\Gamma_{B_d\to\psi K_S} = \Gamma_d - \frac{\Delta\Gamma^d}{2}\cos(2\beta_{\psi K_S}) \;=\; \Gamma_d - |\Gamma^d_{12}|\cos(2\beta_{\psi K_S})\cos\phi_d. \quad (8.131)$$

$\sin(2\beta_{\psi K_S})$ is the quantity characterizing the mixing-induced CP asymmetry measured from tagged $B_d \to \psi K_S$ decays. Γ_d is obtained from a lifetime measurements in flavor-specific decay modes. We stress that this measurement of $\Gamma_{B_d\to\psi K_S}$ can be done from the *untagged* $\overline{B}_d \to \psi K_S$ data sample. If Γ^d_{12} is dominated by new physics, its phase and therefore also ϕ_d is unknown. If one neglects the small SM contribution in (8.83) to ϕ_d, (8.131) reads

$$\Gamma_{B_d\to\psi K_S} \simeq \Gamma_d - |\Gamma^d_{12}|\,\cos(2\beta_{\psi K_S})\cos(2\beta_{\psi K_S} - 2\beta) \;=\; \Gamma_d - |\Gamma^d_{12}|\cos(\phi_d+2\beta)\cos\phi_d, \quad (8.132)$$

where β is the true angle of the unitarity triangle as defined in (1.32). Note that in the presence of new physics β is unknown. When combined with the CP asymmetry in flavor-specific decays discussed in Sect. 8.3.3 one can determine $|\Gamma^d_{12}|$ and $\sin\phi_d$. Then up to discrete ambiguities also $\beta = \beta_{\psi K_S} - \phi_d/2$ can be determined. Depending on whether the enhancement of Γ^d_{12} is due to $b \to \overline{c}cd$, $b \to \overline{u}cd$ or $b \to \overline{u}ud$, transitions, CP asymmetries in these channels can also help to disentangle $|\Gamma^d_{12}|$ and ϕ_d.

Interestingly, one can isolate the contribution to $|\Gamma^d_{12}|$ from $b \to \overline{c}cd$ decays. Define

$$\Delta\Gamma^{d,cc}_{\rm CP} \equiv 2\,|\xi^{d\,2}_c\Gamma^{d,cc}_{12}| \;=\; 2\sum_{f\in X_{c\overline{c}}}\left[\Gamma(B_d \to f_{\rm CP+}) \;-\; \Gamma(B_d \to f_{\rm CP-})\right]. \quad (8.133)$$

in analogy to (8.98). In the Standard Model $\Delta\Gamma^{d,cc}_{\rm CP}$ is slightly larger than $2|\Gamma^d_{12}|$, by a factor of $1/R_t^2$. From (8.89) one finds

$$\frac{\Delta\Gamma^{d,cc}_{\rm CP}}{\Delta\Gamma^{s}_{\rm CP}} \simeq \frac{f^2_{B_d}B^S_{B_d}}{f^2_{B_s}B^S_{B_s}}\left|\frac{\xi^d_c}{\xi^s_t}\right|^2 \;\simeq\; 0.04, \quad (8.134)$$

i.e. $\Delta\Gamma^{d,cc}_{\rm CP}/\Gamma_d \simeq 5\times 10^{-3}$. Now $\Delta\Gamma^{d,cc}_{\rm CP}$ can be measured by counting the CP-even and CP-odd final states in $b\to c\bar{c}d$ decays, just as described in Sect. 8.3.2.2 for $b\to c\bar{c}s$ decays of B_s mesons. Again, in the SV limit the inclusive decay $\overline{(B)}_d \to X_{c\bar{c}d}$ is exhausted by $\overline{(B)}_d \to D^{(*)+}D^{(*)-}$, which is purely CP-even in this limit. With (8.127) one can find $\Delta\Gamma^{d,cc}_{\rm CP}$. That is, in the SV limit one just has to measure $Br(\overline{(B)}_d \to D^{(*)+}D^{(*)-})$, which equals $\Delta\Gamma^{d,cc}_{\rm CP}/(2\Gamma_d)$. However, the lifetime method described in 'Method 1' above cannot be used to determine the corrections to the SV limit, because $\Delta\Gamma_d$ is too small. Yet in the limit of exact U-spin symmetry ($m_d = m_s$) the CP-odd components of $D^{(*)+}D^{(*)-}$ from B_d decay and $D_s^{(*)+}D_s^{(*)-}$ from B_s decay are the same. Finally in $b\to c\bar{c}d$ transitions CP violation in decay could be relevant. It results from penguin loops involving top- or up-quarks and spoils the relation (8.127) between branching ratios and $\Delta\Gamma^{d,cc}_{\rm CP}$. This effect, however, is calculable for inclusive decays like $\overline{(B)}_d \to X_{c\bar{c}d}$. In the Standard Model CP violation in this inclusive decay is of order 1% and therefore negligible [52]. CP-violation from non-standard sources can be revealed by comparing CP-asymmetries in $b\to c\bar{c}d$ decays with those in $b\to c\bar{c}s$ decays (namely $\sin 2\beta$ from $B_d\to\psi K_S$). Since (8.134) depends on no CKM elements and the hadronic factor is known exactly in the $SU(3)_F$ limit, a combined measurement of $\Delta\Gamma^{d,cc}_{\rm CP}$ and $\Delta\Gamma^{s}_{\rm CP}$ provides an excellent probe of new physics in $b\to c\bar{c}d$ transitions.

8.3.3 *CP* Asymmetry in Flavor-specific Decays

In the preceding sections we have set the small parameter $a_q \equiv a(B_q)$, $q = d, s$, defined in (1.65) to zero. In order to study CP violation in mixing we must keep terms of order a_q. The corresponding "wrong-sign" CP asymmetry is measured in flavor-specific decays $B_q\to f$ and equals

$$a^q_{\rm fs} = \frac{\Gamma(\overline{B}^0_q(t)\to f) - \Gamma(B^0_q(t)\to \overline{f})}{\Gamma(\overline{B}^0_q(t)\to f) + \Gamma(B^0_q(t)\to \overline{f})} = {\rm Im}\,\frac{\Gamma^q_{12}}{M^q_{12}} = a_q\,, \qquad \text{for } \overline{A}_f = 0 \text{ and } |A_f| = |\overline{A}_{\overline{f}}|. \tag{8.135}$$

A special case of $a^q_{\rm fs}$ is the semileptonic asymmetry, where $f = X\ell^+\nu$, introduced in Sect. 1.4.1. A determination of a_q gives additional information on the three rephasing-invariant quantities $|M^q_{12}|$, $|\Gamma^q_{12}|$ and ϕ_q characterizing $B^0-\overline{B}^0$ mixing.

Observe that $a^q_{\rm fs}$ in (8.135) is time-independent. While both numerator and denominator depend on t, this dependence drops out from the ratio. The "right-sign" asymmetry, vanishes:

$$\Gamma(B^0_q(t)\to f) - \Gamma(\overline{B}^0_q(t)\to \overline{f}) = 0\,, \qquad \text{for } \overline{A}_f = 0 \text{ and } |A_f| = |\overline{A}_{\overline{f}}|. \tag{8.136}$$

This implies that one can measure $a^q_{\rm fs}$ from *untagged* decays [46,53]. It is easily verified from the sum of (1.73) and (1.74) that to order a_q the time evolution of untagged decays exhibits oscillations governed by Δm_q. Since a is small, a small production asymmetry $\epsilon = N_{\overline{B}}/N_B - 1$, which also leads to oscillations in the untagged sample, could introduce an

experimental bias. To first order in the small parameters a_q, and ϵ one finds

$$a^{q,unt}_{\rm fs} = \frac{\Gamma[f,t]-\Gamma[\overline{f},t]}{\Gamma[f,t]+\Gamma[\overline{f},t]} = \frac{a_q}{2} - \frac{a_q+\epsilon}{2}\,\frac{\cos(\Delta m_q t)}{\cosh(\Delta\Gamma_q t/2)}\,, \qquad \text{for } \overline{A}_f = 0 \text{ and } |A_f| = |\overline{A}_{\overline{f}}|. \tag{8.137}$$

Note that the production asymmetry between B^0_q and $\overline{B}^0_q$ cannot completely fake the effect of a non-zero a_q in (8.137): while both $a_q\neq 0$ and $\epsilon\neq 0$ lead to oscillations, the offset from the constant term indicates $a_q\neq 0$.

The Standard Model predictions for a_d and a_s are

$$\begin{aligned} a_d &\approx -\frac{\overline{\eta}}{R_t^2}\frac{4\pi\,(K_1+K_2)\,m_c^2}{M_W^2\,\eta_B b_B S(m_t^2/M_W^2)} \;\approx\; -8\times 10^{-4} \\ a_s &\approx \overline{\eta}\lambda^2\,\frac{4\pi\,(K_1+K_2)\,m_c^2}{M_W^2\,\eta_B b_B S(m_t^2/M_W^2)} \;\approx\; 5\times 10^{-5}. \end{aligned} \tag{8.138}$$

The huge GIM suppression factor $m_b^2/M_W^2\sin\phi_d \propto m_c^2/M_W^2$ leads to these tiny predictions for CP violation in mixing. a_d plays a preeminent role in the search for new physics :

- its sensitivity to new physics is enormous, it can be enhanced by two orders of magnitude,
- it is affected by a wide range of possible new physics effects: new CP violating effects in ϕ_d relax the GIM-suppression $\propto m_b^2/M_W^2\sin\phi_d$, because ϕ_d is no more proportional to $z = m_c^2/m_b^2$. New physics contributions to *any* of the CKM-suppressed decay modes $b\to\overline{c}cd$, $b\to\overline{u}cd$ or $b\to\overline{u}ud$ can significantly enhance $|\Gamma^d_{12}|$ and thereby a_d.

Of course new physics contributions to $\arg M^d_{12}$ will not only affect ϕ_d, but also the CP asymmetry in $B^0_d\to\psi K_S$. But from this measurement alone one cannot extract the new physics contribution, because one will know the true value of $\beta = \arg(-\xi_t^{d*}/\xi_c^{d*})$ only poorly, once new physics affects the standard analysis of the unitarity triangle. For the discussion of new physics it helps to write

$$a_q = \frac{2|\Gamma^q_{12}|}{\Delta m_q}\sin\phi_q = \frac{|\Delta\Gamma_q|}{\Delta m_q}\,\frac{\sin\phi_q}{|\cos\phi_q|}. \tag{8.139}$$

If both $|\Delta\Gamma_d|$ and a_d are measured, one can determine both $|\Gamma^d_{12}|$ and $\sin\phi_d$.

a_s is less interesting than a_d, because Γ^s_{12} stems from CKM-favored decays and is not very sensitive to new physics. The ratio $\Delta\Gamma^s_{\rm CP}/\Gamma_s \le 0.2$ from (8.86) and the current experimental limit $\Delta m_s \ge 14.9\,{\rm ps}^{-1}$ [33] imply that $|a_s|\le 0.01$. New physics can affect ϕ_s only through $\arg M^s_{12}$, but this new physics can be detected most easily through CP asymmetries in $B_s\to\psi\phi$ or $B_s\to D_s^{(*)+}D_s^{(*)-}$ decays. Since the Standard Model predictions for these asymmetries are essentially zero, there is no problem here to disentangle standard from non-standard physics. Note that the measurement of $\mathrm{sgn}\sin\phi_s$ reduces the four-fold ambiguity in ϕ_s from the measurement of $|\cos\phi_s|$ to a two-fold one. The unambiguous determination of ϕ_s is discussed in detail in [46].

8.3.4 Angular analysis to separate the CP components †

8.3.5 CP-odd and CP-even components in $B_s \to J/\psi\phi$

The most general amplitude for $B_s \to J/\psi\phi$ can be written in terms of the polarization states of the two vector mesons as [55,56]

$$A(B_s(t) \to J/\psi\ \phi) = \frac{A_0(t)}{x}\,\epsilon^{*L}_{J/\psi}\,\epsilon^{*L}_{\phi} - A_{\|}(t)\,\epsilon^{*T}_{J/\psi}\cdot\epsilon^{*T}_{\phi}/\sqrt{2} - iA_{\perp}(t)\,\epsilon^{*}_{J/\psi}\times\epsilon^{*}_{\phi}\cdot\hat{\mathbf{p}}_{\phi}/\sqrt{2}\,, \quad (8.140)$$

where $x \equiv p_{J/\psi}\cdot p_{\phi}/(m_{J/\psi}m_{\phi})$ and $\hat{\mathbf{p}}_{\phi}$ is the unit vector along the direction of motion of ϕ in the rest frame of J/ψ.

Since the "CP violation in decay" of $B_s \to J/\psi\phi$ is vanishing,

$$\overline{A}_0(0) = A_0(0)\,, \qquad \overline{A}_{\|}(0) = A_{\|}(0)\,, \qquad \overline{A}_{\perp}(0) = -A_{\perp}(0)\,. \quad (8.141)$$

The final state is thus an admixture of different CP eigenstates: A_0 and $A_{\|}$ are CP-even amplitudes whereas $A_{\perp}$ is CP-odd. The decay rate is given by

$$\Gamma(t) \propto |A_0(t)|^2 + |A_{\|}(t)|^2 + |A_{\perp}(t)|^2\,, \quad (8.142)$$

where the time evolutions of the individual terms are [57]

$$\begin{aligned} |A_{0,\|}(t)|^2 &= |A_{0,\|}(0)|^2\left[e^{-\Gamma_L t} - e^{-\overline{\Gamma}t}\sin(\Delta m_s t)\delta\phi\right], \\ |A_{\perp}(t)|^2 &= |A_{\perp}(0)|^2\left[e^{-\Gamma_H t} + e^{-\overline{\Gamma}t}\sin(\Delta m_s t)\delta\phi\right]. \end{aligned} \quad (8.143)$$

Here, $\overline{\Gamma} \equiv \Gamma_s = (\Gamma_L + \Gamma_H)/2$. Note that this is *not* the average lifetime of B_s as measured through its semileptonic decays [58].

The value of

$$\delta\phi \equiv 2\beta_s \approx 2\lambda^2\eta \approx 0.03 \quad (8.144)$$

is small in the standard model[7], so that the terms proportional to $\delta\phi$ in (8.143) can be neglected in the first approximation. The time evolution of (8.142) is then a sum of two exponential decays with lifetimes $1/\Gamma_H$ and $1/\Gamma_L$.

In principle, a fit to the time dependence of the total decay rate (8.142) can give the values of Γ_H and Γ_L separately, but $\Delta\Gamma_s/\overline{\Gamma}$ is expected to be less than 20%, and it is not easy to separate two closely spaced lifetimes. The inclusion of angular information will increase the accuracy in the measurement of $\Delta\Gamma_s$ multi-fold, as we'll see in the section 8.3.6 below.

† Author: Amol Dighe

[7] Generalizations of the formulae to the case of new physics can be found in [46].

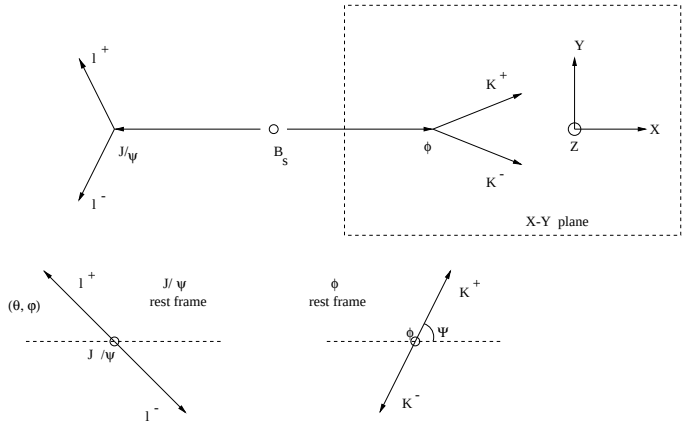

Figure 8.4: The definitions of angles θ, φ, ψ. Here θ is the "transversity" angle.

8.3.6 The transversity angle distribution

Since there are four particles in the final state, the directions of their momenta can define three independent physical angles. Our convention for the definitions of angles [56,57] is as shown in Fig. 8.4. The x-axis is the direction of ϕ in the J/ψ rest frame, the z axis is perpendicular to the decay plane of $\phi \to K^+K^-$, and $p_y(K^+) \geq 0$. The coordinates (θ, φ) describe the direction of l^+ in the J/ψ rest frame and ψ is the angle made by $\vec{p}(K^+)$ with the x axis in the ϕ rest frame. With this convention,

$$\begin{aligned} &\mathbf{x} = \mathbf{p}_{\phi}, \qquad \mathbf{y} = \frac{\mathbf{p}_{K^+} - \mathbf{p}_{\phi}(\mathbf{p}_{\phi}\cdot\mathbf{p}_{K^+})}{|\mathbf{p}_{K^+} - \mathbf{p}_{\phi}(\mathbf{p}_{\phi}\cdot\mathbf{p}_{K^+})|}, \qquad \mathbf{z} = \mathbf{x}\times\mathbf{y}, \\ &\sin\theta\cos\varphi = \mathbf{p}_{\ell^+}\cdot\mathbf{x}, \qquad \sin\theta\sin\varphi = \mathbf{p}_{\ell^+}\cdot\mathbf{y}, \qquad \cos\theta = \mathbf{p}_{\ell^+}\cdot\mathbf{z}\,. \end{aligned} \quad (8.145)$$

Here, the bold-face characters represent *unit* 3-vectors and everything is measured in the rest frame of J/ψ. Also

$$\cos\psi = -\mathbf{p}'_{K^+}\cdot\mathbf{p}'_{J/\psi}, \quad (8.146)$$

where the primed quantities are *unit vectors* measured in the rest frame of ϕ.

The θ defined here is the *transversity* angle [59], which separates out the CP-even and CP-odd components. The angular distribution in terms of θ is given by [56]:

$$\frac{d\Gamma(t)}{d\cos\theta} \propto (|A_0(t)|^2 + |A_{\|}(t)|^2)\,\frac{3}{8}\,(1+\cos^2\theta) + |A_{\perp}(t)|^2\,\frac{3}{4}\sin^2\theta\,, \quad (8.147)$$

where the time evolutions of the terms are as given in (8.143).

The CP-even and CP-odd components are now separated by not only their different lifetimes (which are very close) but also by their decay angular distributions (which are

distinctly different). The study of information content about the value of $\Delta\Gamma_s$ in the time and angular measurements [60] suggests that, in order to get the same degree of accuracy in $\Delta\Gamma_s$ with only time measurements, one would need about two orders of magnitude more number of events than if both the time and angular measurements were used (see Fig. 3 in [60]). This indicates that the strategy of selecting one decay mode (*e.g.* $J/\psi\phi$) and studying its angular distribution will turn out to be more fruitful than trying to combine all CP eigenstate decay modes and determine Γ_H and Γ_L solely from their time evolutions. Note that, in the limiting case of $\Gamma_H = \Gamma_L$, the time evolution by itself *cannot* separate the CP even and odd components, whereas the angular measurements can.

A fit to the transversity angle distribution (8.147) with its complete time evolution (8.143) also gives the value of $\delta\phi$ and Δm_s, though a better measurement of the latter may be obtained through other decay channels.

The transversity angle distribution (8.147) is valid for any $B_s \to J/\psi(\to \ell^+\ell^-)C_1C_2$ decay, where C_1 and C_2 are (a) self-conjugate particles, or (b) scalars and CP conjugates of each other [59]. The particles C_1 and C_2 need not be the products of any resonance, and their total angular momentum is irrelevant. So the time and transversity angle measurements from all the resonant and non-resonant decays of this form may be combined to gain statistics. Here the values of $(|A_0(0)|^2 + |A_\parallel(0)|^2)$ and $|A_\perp(0)|^2$ are just some *effective* average values, but the decay widths Γ_H and Γ_L are the same for all such decay modes, and hence for the whole data sample.

8.3.7 Three-angle distribution in $B_s \to J/\psi(\to l^+l^-)\,\phi(\to K^+K^-)$

While the one-angle distribution (8.147) is in principle sufficient to determine the values of Γ_H, Γ_L, $\delta\phi$ and Δm_s, using the information present in all the angles (θ, ϕ, ψ) will improve the measurements. In addition, one also gets access to the magnitudes of all the three amplitudes $A_0(0)$, $A_\parallel(0)$, $A_\perp(0)$ and the strong phases between them, which was not possible with the one-angle distribution [57]. A method to combine the three-angle distributions of $B_s \to J/\psi\phi$ and $B_d \to J/\psi K^*$ to resolve a discrete ambiguity in the CKM angle β has also been proposed [61].

The three angle distribution of an initially present (i.e. tagged) B_s meson is [56,57]

$$\begin{aligned}\frac{d^3\Gamma[B_s(t) \to J/\psi(\to l^+l^-)\phi(\to K^+K^-)]}{d\cos\theta\, d\varphi\, d\cos\psi} &\propto \frac{9}{32\pi}\Big\{2|A_0(t)|^2\cos^2\psi(1-\sin^2\theta\cos^2\varphi)\\ &+ \sin^2\psi\left[|A_\parallel(t)|^2(1-\sin^2\theta\sin^2\varphi) + |A_\perp(t)|^2\sin^2\theta - \mathrm{Im}\left(A_\parallel^*(t)A_\perp(t)\right)\sin 2\theta\sin\varphi\right]\\ &+ \frac{1}{\sqrt{2}}\sin 2\psi\left[\mathrm{Re}\left(A_0^*(t)A_\parallel(t)\right)\sin^2\theta\sin 2\varphi + \mathrm{Im}\left(A_0^*(t)A_\perp(t)\right)\sin 2\theta\cos\varphi\right]\Big\}. \qquad (8.148)\end{aligned}$$

Note that the same angular distribution (8.148) is also valid for $B_d \to J/\psi(\to \ell^+\ell^-)K^*(\to K^\pm\pi^\mp)$. The angular distribution for the CP conjugate decay is obtained simply by replacing all A's by $\bar{A}$'s [57].

The time evolution of the observables in the angular distribution (the coefficients of the angular terms in (8.148) and its CP conjugate mode) are given in Table 8.2 and 8.3

Observable	Time evolution
$\lvert A_0(t)\rvert^2$	$\lvert A_0(0)\rvert^2\left[e^{-\Gamma_L t} - e^{-\overline{\Gamma}t}\sin(\Delta m_s t)\delta\phi\right]$
$\lvert A_\parallel(t)\rvert^2$	$\lvert A_\parallel(0)\rvert^2\left[e^{-\Gamma_L t} - e^{-\overline{\Gamma}t}\sin(\Delta m_s t)\delta\phi\right]$
$\lvert A_\perp(t)\rvert^2$	$\lvert A_\perp(0)\rvert^2\left[e^{-\Gamma_H t} + e^{-\overline{\Gamma}t}\sin(\Delta m_s t)\delta\phi\right]$
$\mathrm{Re}(A_0^*(t)A_\parallel(t))$	$\lvert A_0(0)\rvert\lvert A_\parallel(0)\rvert\cos(\delta_2-\delta_1)\left[e^{-\Gamma_L t} - e^{-\overline{\Gamma}t}\sin(\Delta m_s t)\delta\phi\right]$
$\mathrm{Im}(A_\parallel^*(t)A_\perp(t))$	$\lvert A_\parallel(0)\rvert\lvert A_\perp(0)\rvert\left[e^{-\overline{\Gamma}t}\sin(\delta_1-\Delta m_s t) + \frac{1}{2}\left(e^{-\Gamma_H t} - e^{-\Gamma_L t}\right)\cos(\delta_1)\delta\phi\right]$
$\mathrm{Im}(A_0^*(t)A_\perp(t))$	$\lvert A_0(0)\rvert\lvert A_\perp(0)\rvert\left[e^{-\overline{\Gamma}t}\sin(\delta_2-\Delta m_s t) + \frac{1}{2}\left(e^{-\Gamma_H t} - e^{-\Gamma_L t}\right)\cos(\delta_2)\delta\phi\right]$

Table 8.2: Time evolution of the decay $B_s \to J/\psi(\to l^+l^-)\phi(\to K^+K^-)$ of an initially (i.e. at $t = 0$) pure B_s meson. Here $\bar{\Gamma} \equiv (\Gamma_H + \Gamma_L)/2$.

Observable	Time evolution
$\lvert\overline{A}_0(t)\rvert^2$	$\lvert A_0(0)\rvert^2\left[e^{-\Gamma_L t} + e^{-\overline{\Gamma}t}\sin(\Delta m_s t)\delta\phi\right]$
$\lvert\overline{A}_\parallel(t)\rvert^2$	$\lvert A_\parallel(0)\rvert^2\left[e^{-\Gamma_L t} + e^{-\overline{\Gamma}t}\sin(\Delta m_s t)\delta\phi\right]$
$\lvert\overline{A}_\perp(t)\rvert^2$	$\lvert A_\perp(0)\rvert^2\left[e^{-\Gamma_H t} - e^{-\overline{\Gamma}t}\sin(\Delta m_s t)\delta\phi\right]$
$\mathrm{Re}(\overline{A}_0^*(t)\overline{A}_\parallel(t))$	$\lvert A_0(0)\rvert\lvert A_\parallel(0)\rvert\cos(\delta_2-\delta_1)\left[e^{-\Gamma_L t} + e^{-\overline{\Gamma}t}\sin(\Delta m_s t)\delta\phi\right]$
$\mathrm{Im}(\overline{A}_\parallel^*(t)\overline{A}_\perp(t))$	$-\lvert A_\parallel(0)\rvert\lvert A_\perp(0)\rvert\left[e^{-\overline{\Gamma}t}\sin(\delta_1-\Delta m_s t) - \frac{1}{2}\left(e^{-\Gamma_H t} - e^{-\Gamma_L t}\right)\cos(\delta_1)\delta\phi\right]$
$\mathrm{Im}(\overline{A}_0^*(t)\overline{A}_\perp(t))$	$-\lvert A_0(0)\rvert\lvert A_\perp(0)\rvert\left[e^{-\overline{\Gamma}t}\sin(\delta_2-\Delta m_s t) - \frac{1}{2}\left(e^{-\Gamma_H t} - e^{-\Gamma_L t}\right)\cos(\delta_2)\delta\phi\right]$

Table 8.3: Time evolution of the decay $\overline{B_s} \to J/\psi(\to l^+l^-)\phi(\to K^+K^-)$ of an initially (i.e. at $t = 0$) pure $\overline{B_s}$ meson. Here $\bar{\Gamma} \equiv (\Gamma_H + \Gamma_L)/2$.

respectively. Here $\delta_1 \equiv \mathrm{Arg}(A_\perp^* A_\parallel)$ and $\delta_2 \equiv \mathrm{Arg}(A_0^* A_\parallel)$. A finite lifetime difference $\Delta\Gamma$ implies that the CP violating terms proportional to

$$\left(e^{-\Gamma_H t} - e^{-\Gamma_L t}\right)\cos(\delta_{1(2)})\,\delta\phi \qquad (8.149)$$

survive even when the B_s is untagged [57,62]. An experimental feasibility study for extracting the parameters from the time dependent three angle distribution has been performed for the LHC in [63].

8.3.8 Angular moments method

The likelihood fit to the complete angular distribution (8.148) – including the time evolution of the observables (Tables 8.2 and 8.3) – is a difficult task due to the large number of parameters involved. The method of angular moments proposed in [57] can disentangle the angular dependences and split up the likelihood fit into a number of likelihood fits with a smaller number of parameters.

The angular distributions ((8.147) or (8.148)) are of the form

$$f(\Theta, \mathcal{P}; t) = \sum b^{(k)}(\mathcal{P}; t)\, g^{(k)}(\Theta)\,, \qquad (8.150)$$

where $\mathcal{P}$ represents the parameters, and Θ denotes the angles. If we can find *weighting functions* $w^{(i)}$ such that

$$\int [\mathcal{D}\Theta]\, w^{(i)}(\Theta)\, g^{(k)}(\Theta) = \delta_{ik}\,, \tag{8.151}$$

then

$$b^{(i)} \approx \sum_{events} w^{(i)}(\Theta)\,, \tag{8.152}$$

and the observables are determined directly from the data. It can be shown [57] that such a set of weighting functions exists for any angular distribution of the form (8.150) and such a set can be determined without any *a priori* knowledge of the values of the observables $b^{(i)}$. A likelihood fit can then be performed on each observable $b^{(i)}$ independently in order to determine the parameters.

The angular moments (AM) method is more transparent and easier to implement than the complete likelihood fit method. Although the AM method in its naive form involves some loss of information, the extent of this loss of information in the case of the transversity angle distribution has been found to be less than 10% in the parameter range of interest (see Fig. 5 of [60]). In its full form, the AM method can determine the values of parameters almost as well as the likelihood fit method (see, *e.g.* [64]).

To conclude, the angular analysis of $B_s \to J/\psi\phi$ decays can separate the CP even and odd components in the final state, and it is perhaps the best way to determine the lifetime difference between B_s^H and B_s^L. As a byproduct, it also helps the measurement of CP odd and even components and their relative strong phases, and with enough statistics, the determination of Δm_s and $\delta\phi$. The angular analysis, possibly employing the angular moments method if the likelihood fit is inadequate, is highly recommended.

8.3.9 $D^0 - \overline{D}^0$ mixing †

We define the mass eigenstates in $D^0 - \overline{D}^0$ mixing as

$$\begin{aligned} |D_1\rangle &= p|D^0\rangle + q|\overline{D}^0\rangle\,, \\ |D_2\rangle &= p|D^0\rangle - q|\overline{D}^0\rangle\,, \qquad \text{with } |p|^2 + |q|^2 = 1\,. \end{aligned} \tag{8.153}$$

q and p are obtained from the solution of the eigenvalue problem for $M - i\Gamma/2$. In (1.61c) q/p is determined in terms of M_{12} and Γ_{12}. We define

$$\Delta m_D = m_2 - m_1, \qquad \Delta\Gamma_D = \Gamma_1 - \Gamma_2 \tag{8.154}$$

$$x_D = \frac{\Delta m_D}{\Gamma} \qquad y_D = -\frac{\Delta\Gamma_D}{2\Gamma} = \frac{\Gamma_2 - \Gamma_1}{2\Gamma}. \tag{8.155}$$

The definitions in (8.153) and (8.154) comply with the conventions of Sect. 1.3 for $B^0 - \overline{B}^0$ mixing. In particular the time evolution formulae of (1.58) - (1.60) are also valid for D^0–$\overline{D}^0$ mixing with the replacement $B^0 \to D^0$. Unlike in the case of $B^0 - \overline{B}^0$ mixing we cannot

† Author: Ulrich Nierste

expand in $\Delta\Gamma_D/\Delta m_D$. We also refrain from expanding in a defined in (1.65). Then (1.73) - (1.77) can be used for D^0 mesons, if $1+a$ in (1.74) is replaced by $|p/q|^2$ and $1-a$ in (1.76) is replaced by $|q/p|^2$. Note that the definition of y_D in (8.155) is opposite in sign to the one of y in the B meson system in (1.93). In (8.155) we have used the sign convention which is usually used in $D^0 - \overline{D}^0$ mixing. Since $D^0 - \overline{D}^0$ mixing is very small, one can expand in $\Delta m_D t$ and $\Delta\Gamma_D t$. Using x_D and y_D from (8.155) the small t expansion of (1.73) - (1.77) gives

$$\begin{aligned} \Gamma(D^0(t) \to f) \;=\; & \mathcal{N}_f\, |A_f|^2\, e^{-\Gamma_D t} \Big[1 + (-\mathrm{Im}\,\lambda_f\, x_D \;+\; \mathrm{Re}\,\lambda_f\, y_D)\,\Gamma_D t \\ & + \left(\frac{|\lambda_f|^2 + 1}{4}\, y_D^2 + \frac{|\lambda_f|^2 - 1}{4}\, x_D^2 \right) (\Gamma_D t)^2 \Big]\,, \end{aligned} \tag{8.156}$$

$$\begin{aligned} \Gamma(\overline{D}^0(t) \to f) \;=\; & \mathcal{N}_f\, |A_f|^2\, e^{-\Gamma_D t} \left|\frac{p}{q}\right|^2 \Big[|\lambda_f|^2 + (\mathrm{Im}\,\lambda_f\, x_D \;+ \mathrm{Re}\,\lambda_f\, y_D)\,\Gamma_D t \\ & + \left(\frac{|\lambda_f|^2 + 1}{4}\, y_D^2 - \frac{|\lambda_f|^2 - 1}{4}\, x_D^2 \right) (\Gamma_D t)^2 \Big]\,, \end{aligned} \tag{8.157}$$

$$\begin{aligned} \Gamma(D^0(t) \to \overline{f}) \;=\; & \mathcal{N}_f\, \left|\overline{A}_{\overline{f}}\right|^2\, e^{-\Gamma_D t} \left|\frac{q}{p}\right|^2 \Big[|\lambda_{\overline{f}}|^{-2} + \left(\mathrm{Im}\,\frac{1}{\lambda_{\overline{f}}}\, x_D + \mathrm{Re}\,\frac{1}{\lambda_{\overline{f}}}\, y_D \right) \Gamma_D t \\ & + \left(\frac{|\lambda_{\overline{f}}|^{-2} + 1}{4}\, y_D^2 - \frac{|\lambda_{\overline{f}}|^{-2} - 1}{4}\, x_D^2 \right) (\Gamma_D t)^2 \Big]\,, \end{aligned} \tag{8.158}$$

$$\begin{aligned} \Gamma(\overline{D}^0(t) \to \overline{f}) \;=\; & \mathcal{N}_f\, \left|\overline{A}_{\overline{f}}\right|^2\, e^{-\Gamma_D t} \Big[1 + \left(-\mathrm{Im}\,\frac{1}{\lambda_{\overline{f}}}\, x_D + \mathrm{Re}\,\frac{1}{\lambda_{\overline{f}}}\, y_D \right) \Gamma_D t \\ & + \left(\frac{|\lambda_{\overline{f}}|^{-2} + 1}{4}\, y_D^2 + \frac{|\lambda_{\overline{f}}|^{-2} - 1}{4}\, x_D^2 \right) (\Gamma_D t)^2 \Big]\,, \end{aligned} \tag{8.159}$$

with $\Gamma_D = (\Gamma_1 + \Gamma_2)/2$. Δm_D and $\Delta\Gamma_D$ are very small, because they are GIM-suppressed by a factor of m_s^2/M_W^2. For this reason they are also difficult to calculate, because at scales of order m_s non-perturbative effects become important. A recent calculation, which incorporates non-perturbative effects with the help of the quark condensate, can be found in [54].

8.3.10 New Physics Effects in Meson Mixing †

The existence of new physics may modify the low-energy effective Hamiltonian governing B and D physics in several ways: (i) via contributions to the Wilson coefficients of the Standard Model operators, (ii) by generating new operators, or (iii) through the presence of new CP violating phases. These effects may originate from new interactions in tree-level meson decays or from the virtual exchange of new physics in loop-mediated processes. The

† Author: JoAnne Hewett

scale of new physics is expected to be large compared to M_W, and hence it is generally anticipated that additional tree-level contributions to meson decays are suppressed [65]. However, large new contributions may be present in loop processes, making meson mixing a fertile ground to reveal the influence of new interactions. All three above classes of new physics contributions may play a role in meson mixing. Such effects may be discovered in observables which are suppressed in the Standard Model, such as the asymmetry $a_{\rm fs}^q$ measuring CP violation in $B_{d,s}$ mixing or in D^0 meson mixing, they may modify the mixing-induced CP asymmetries in $B \to \psi K_S$ and $B \to \pi\pi$ decays, or they may alter the precisely calculated SM value of the ratio of B_s to B_d mixing. We will discuss each of these observables in this section. The effects of new physics on meson width differences is described in Sect. 8.3.2.2.

8.3.10.1 B_d Mixing

It is well-known that new physics can play a large role in B_d mixing. One important consequence of this is that the constraints in the $\rho - \eta$ plane from Δm_d can be altered, resulting in a significant shift [66] of the allowed region in this plane from its Standard Model range. This in turn modifies the expected values for $\sin 2\beta$ and $\sin 2\alpha$, even if new sources of CP violation are not present. In fact, this comprises the most significant effect from new physics on the CP asymmetries in $B \to \psi K_S$ and $B \to \pi\pi$ decays in a large class of models.

A model independent determination of such effects has been presented in Ref. [67]. New physics contributions to B_d mixing can be parameterized in a model independent fashion by considering the ratio

$$\frac{\langle B_d^0|\mathcal{H}^{\rm full}|\bar{B}_d^0\rangle}{\langle B_d^0|\mathcal{H}^{\rm SM}|\bar{B}_d^0\rangle} = \left(r_d\, e^{i\theta_d}\right)^2 , \tag{8.160}$$

where $\mathcal{H}^{\rm full(SM)}$ represents the Hamiltonian responsible for B_d mixing in the case of the Standard Model plus new physics (just Standard Model), and $r_d(\theta_d)$ represents the new physics contribution to the magnitude (phase) of B_d mixing. In the Standard Model, the unitarity triangle is constrained by measurements of $\sin 2\beta$, $\sin 2\alpha$, the ratio of semileptonic decays $\Gamma(b \to u\ell\nu)/\Gamma(b \to c\ell\nu)$, and $x_d = C_t R_t^2$, where R_t is defined in Section 8.3.1.These quantities are then modified in the presence of new interactions via $a_{\psi K_S} = \sin(2\beta + 2\theta_d)$, $a_{\pi\pi} = \sin(2\alpha - 2\theta_d)$, and $x_d = C_t R_t^2 r_d^2$. Note that the new phase contributions in $a_{\psi K_S}$ and $a_{\pi\pi}$ conspire to cancel in the triangle constraint and the relation $\alpha + \beta + \gamma = \pi$ is retained.Measurement of these four quantities allows one to disentangle the new physics effects and fully reconstruct the true unitarity triangle (*i.e.*, find the true values of α, β, and R_t) as well as determine the values of r_d and θ_d in a geometrical fashion. This is depicted in Fig. 8.5. While this technique is effective in principle, in practice it is limited by theoretical uncertainties in $x_d\,, \alpha$, and the ratio of semileptonic decays, as well as discrete ambiguities.

Model independent bounds on new physics contributions to B_d mixing can also be directly placed from measurements of Δm_d and $\sin 2\beta$. In the class of models which respect 3×3 CKM unitarity, where tree-level B decays (in particular their phase) are dominated

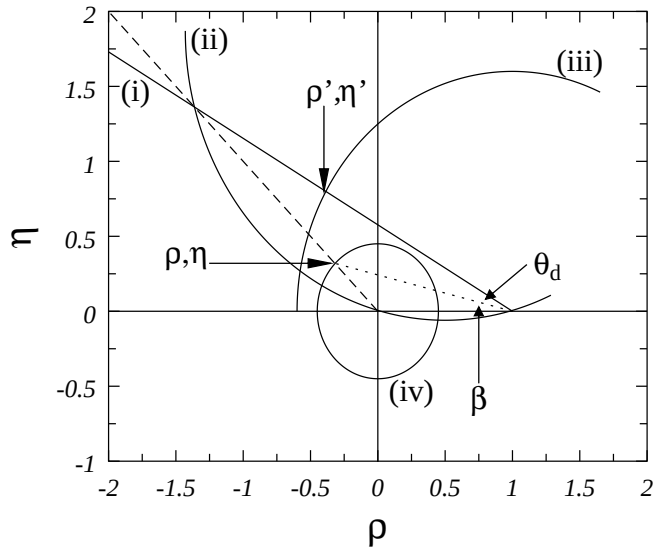

Figure 8.5: The model independent analysis in the $\rho - \eta$ plane: (i) the $a_{\psi K_S}$ ray, (ii) the $a_{\pi\pi}$ circle, (iii) the x_d circle, (iv) the semileptonic decay ratio circle. The γ ray is given by the dashed line and the true β ray corresponds to the dotted line. The true vertex of the unitarity triangle is at (ρ, η), while the point (ρ', η') serves to determine r_d and θ_d.

by the SM, and where $\Gamma_{12} \simeq \Gamma_{12}^{\rm SM}$, the new physics effects in B_d mixing can be isolated. The modification to M_{12} can then be described as above in terms of $r_d\,, \theta_d$. The direct determination of Δm_d provides a bound on the magnitude of new physics contributions, r_d, while measurement of $\sin 2\beta$ constrains the new phase θ_d. Taking into account the uncertainties on the values of the relevant CKM factors and the hadronic matrix elements, present data constrains $0.5 \leq r_d \leq 1.8$ and $\sin 2\theta_d \geq -0.53$ at 95% C.L. It is clear that large contributions to B_d mixing from new interactions are still allowed, and may hence admit for an exciting discovery as future measurements improve.

We note that another useful parameterization of new physics contributions which is common in the literature is given by

$$M_{12}^{\rm NP} = h\, e^{i\sigma} M_{12}^{\rm SM}\,, \tag{8.161}$$

where these variables are related to the previous ones via

$$r_d^2\, e^{2i\theta_d} = 1 + h\, e^{i\sigma}\,. \tag{8.162}$$

Constraints on this set of parameters from current data is presented in [68] in various classes of models.

These parameters can be related to new physics contributions in other observables. For instance, the CP asymmetry in flavor-specific B_d decays (see Sect. 8.3.3), which is given by

$$a_{\rm fs}^d = {\rm Im}\,\frac{\Gamma_{12}^d}{M_{12}^d}\,, \tag{8.163}$$

and has a value of -8×10^{-4} in the Standard Model (see (8.138)), provides a good opportunity to probe the existence of new interactions. Since Γ_{12}^d/M_{12}^d is essentially real in the Standard Model, the contributions of new interactions to the flavor-specific CP asymmetry can be written as

$$a_{\rm fs}^d = -\left(\frac{\Gamma_{12}^d}{M_{12}^d}\right)_{\rm SM}\frac{\sin2\theta_d}{r_d^2}\,. \tag{8.164}$$

The above bounds from present data on the new physics contributions to B_d mixing restrict

$$-2.1 \le \frac{a_{\rm fs}^d}{(\Gamma_{12}^d/M_{12}^d)_{\rm SM}} \le 4.0\,. \tag{8.165}$$

It is important to note that $a_{\rm fs}^d$ can lie outside this range, if new new physics enhances Γ_{12}^d, which is composed of CKM-suppressed decay modes.

There are a plethora of new physics scenarios which can yield substantial contributions to B_d mixing; some examples are briefly cataloged here. Models which respect the structure of the 3×3 CKM matrix contribute simply to the Wilson coefficient of the Standard Model operator. This is best illustrated by the virtual exchange in the box diagram of charged Higgs bosons which are present in flavor conserving two-Higgs-doublet models [69] and by the contributions of supersymmetric particles [70] when a Standard Model-like super-CKM structure is assumed.If the super-CKM angles ($\tilde{V}$) are allowed to be arbitrary, the structure of the Wilson coefficients are altered. In this case, the supersymmetric amplitude relative to that of the Standard Model is roughly given by $\sim (M_W/\tilde{m})^n(\tilde{V}_{td}\tilde{V}_{tb}/V_{td}V_{tb})$ and can constitute a flavor problem for Supersymmetry if the sparticle masses, $\tilde{m}$, are near the weak scale. The existence of a fourth generation would also modify the CKM structure of the Wilson coefficients. New $|\Delta B| = 2$ operators are generated in scenarios [71] such as Left-Right Symmetric models, theories of strong dynamics, as well as in Supersymmetry. Tree-level contributions [72] are manifest in flavor changing two-Higgs-doublet models, in scenarios with a flavor changing extra neutral gauge boson, and in Supersymmetry with R-parity violation.Most of these examples also contain new phases which may be present in B_d mixing. It is interesting to note that various forms of Supersymmetry may affect B_d mixing in all possible manners!

While it is possible to obtain large effects in B_d mixing in all of these scenarios, it is difficult to use Δm_d at present to tightly restrict these contributions and constrain the parameter space in the models, due to the current sizable errors on the Standard Model theoretical prediction arising from the imprecisely determined values of the CKM factors and the hadronic matrix elements. Frequently, other flavor changing neutral current processes, such as $b\to s\gamma$, provide more stringent constraints.

8.3.10.2 B_s Mixing

A similar analysis as employed above may be used to constrain new physics contributions to B_s mixing. In the class of models which respect the 3×3 CKM unitarity and where tree-level decays are dominated by the Standard Model contributions, we can again parameterize potential new contributions to Δm_s via $M_{12} = (r_s e^{i\theta_s})^2 M_{12}^{\rm SM}$. This gives

$$\frac{\Delta m_d}{\Delta m_s} = \frac{\lambda^2 R_t^2}{\xi^2}\,\frac{m_{B_d}}{m_{B_s}}\,\frac{r_d^2}{r_s^2}\,, \tag{8.166}$$

which reduces to the Standard Model expression when $r_d = r_s$. The parameter θ_s can be constrained once CP asymmetries in the B_s system are measured or, if θ_s is large, from measurements of $\Delta\Gamma_s$ as described in Sect. 8.3.2.2.

As discussed above, the ratio $\Delta m_d/\Delta m_s$ yields a good determination of the CKM ratio $|V_{td}/V_{ts}|$ within the Standard Model, since the ratio of hadronic matrix elements is accurately calculated in lattice gauge theory. Remarkably, this remains true in many scenarios beyond the Standard Model. In a large class of models which retain the 3×3 CKM structure, the virtual exchange of new particles in the box diagram alters the Inami-Lim function, but not the remaining factors in the expression for $\Delta m_{d,s}$. The effects of new physics thus cancel in the ratio. As an explicit example, consider charged Higgs exchange in the box diagram within the context of two-Higgs-doublet models. The expression for the mass difference in B_s mixing in this case is

$$\begin{aligned}\Delta m_s &= \frac{G_F^2 M_W^2}{6\pi^2}\,f_{B_s}^2 B_{B_s}\eta_{B_s} m_{B_s}\,|V_{tb}V_{ts}^*|^2\left[S(m_t^2/M_W^2) + F(m_t^2/m_{H^\pm}^2,\tan\beta)\right]\\ &= \Delta m_d\,\xi^2\,\frac{m_{B_s}}{m_{B_d}}\,\frac{|V_{ts}|^2}{|V_{td}|^2}\,,\end{aligned} \tag{8.167}$$

where $m_{H^\pm}$ represents the charge Higgs mass and $\tan\beta$ is the ratio of vevs. Here, we see that the charged Higgs contribution is the same for B_d and B_s mixing (neglecting d- and s-quark masses) and thus cancels exactly in the ratio. This cancellation also occurs in several other classes of models, including minimal Supersymmetry with flavor conservation. Notable exceptions to this are found in models which (i) change the structure of the CKM matrix, such as the addition of a fourth generation, or extra singlet quarks, or in Left-Right symmetric models, (ii) have sizable Yukawa couplings to the light fermions, such as leptoquarks or Higgs models with flavor changing couplings, or (iii) have generational dependent couplings, including supersymmetry with R-parity violation.

8.3.10.3 Mixing in the Charm Sector

The short distance Standard Model contribution to Δm_D proceeds through a W box diagram with internal d,s,b-quarks. In this case the external momentum, which is of order m_c, is communicated to the light quarks in the loop and can not be neglected. The effective Hamiltonian is

$$\mathcal{H}_{eff}^{\Delta c=2} = \frac{G_F\alpha}{8\sqrt{2}x_w}\left[|V_{cs}V_{us}^*|^2\,(I_1^s\,\mathcal{O} - m_c^2 I_2^s\,\mathcal{O}') + |V_{cb}^*V_{ub}|^2\,(I_3^b\,\mathcal{O} - m_c^2 I_4^b\,\mathcal{O}')\right], \tag{8.168}$$

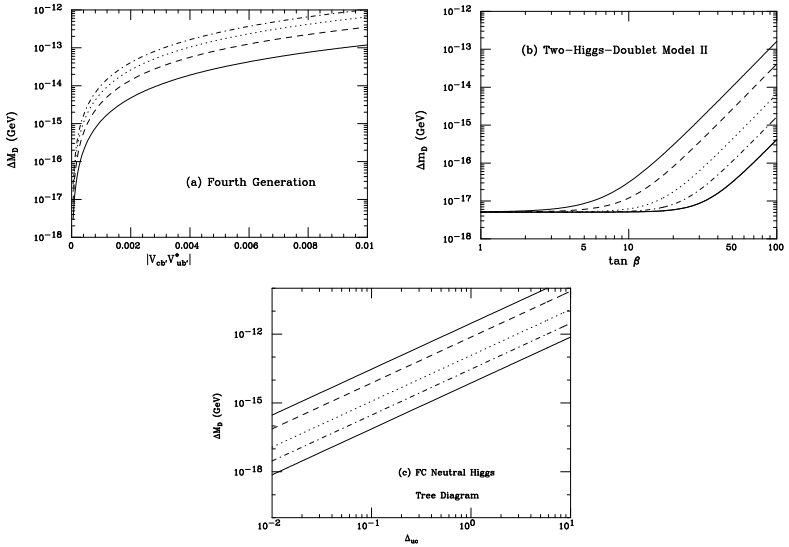

Figure 8.6: Δm_D in (a) the four generation Standard Model as a function of the appropriate 4×4 CKM elements, taking the b'-quark mass to be $100, 200, 300, 400$ GeV from top to bottom, (b) the two-Higgs-doublet model II as a function of $\tan\beta = v_2/v_1$ with $m_{H^\pm} = 50, 100, 250, 500, 1000$ GeV from top to bottom, and (c) the flavor-changing Higgs model with tree-level contributions as a function of the mixing factor, with $m_{h^0} = 50, 100, 250, 500, 1000$ GeV from top to bottom.

where the I_j^q represent integrals [73] that are functions of m_q^2/M_W^2 and m_q^2/m_c^2, and $\mathcal{O} = [\bar{u}\gamma_\mu(1-\gamma_5)c]^2$ is the usual mixing operator, while $\mathcal{O}' = [\bar{u}\gamma_\mu(1+\gamma_5)c]^2$ arises in the case of non-vanishing external momentum. The numerical value of the short distance contribution is $\Delta m_D \sim 5 \times 10^{-18}$ GeV (taking $f_D = 200$ MeV). The long distance contributions have been computed via an intermediate state dispersive approach and in heavy quark effective theory, yielding values [74] in the range $\Delta m_D \sim 10^{-17} - 10^{-16}$ GeV. The Standard Model predictions are clearly quite small and allow for a large window for the observation of new physics effects.

Since the Standard Model expectation is so small, large enhancements in Δm_D are naturally induced by new interactions. A compilation of such effects in various models and list of references can be found in [75]. This article shows that the present experimental bound on D-mixing already constrains the parameter space in many scenarios, and an order of magnitude improvement would exclude (or discover) some models. Here, for purposes of illustration, we present the potential enhancements that can occur in three scenarios [66]. We examine (i) the case of a fourth generation to demonstrate the effect of heavy fermions participating in the box diagram, (ii) the contributions from charged Higgs exchange in flavor conserving two-Higgs-doublet models, which is often used as a benchmark in studying

new physics, and (iii) the tree-level contributions in flavor-changing Higgs models, where the flavor changing couplings are taken to be $\lambda_{h^0 f_i f_j} \sim (\sqrt{2}G_F)^{1/2}\sqrt{m_i m_j}\Delta_{ij}$ with Δ_{ij} being a combination of mixing angles.The mass difference as a function of the model parameters is shown in Fig. 8.6 for each case. We see that in each case the parameter space is already restricted by the current experimental value, and that an improvement in the bound would provide a sensitive probe of these models.

8.4 Interesting decay modes [†]

In this section we list the decay modes which are useful for the determination of Δm_q, $\Delta\Gamma_q$ and B meson lifetimes. Flavor-specific decay modes are summarized in Table 8.4, CKM-favored decays into CP eigenstates are listed in Table 8.5 and decays which are neither flavor-specific nor CP-specific can be found in Table 8.6.

quark decay	hadronic decay	remarks
$\overline{b} \to \overline{c}\ell^+\nu_\ell$	$B_{d,s} \to D_{(s)}{}^-\ell^+\nu_\ell$	
	$B_{d,s} \to X\ell^+\nu_\ell$	
$\overline{b} \to \overline{c}u\overline{d}$	$B_d \to D^{(*)-}\pi^+$	
	$B_d \to D^{(*)-}\pi^+\pi^+\pi^-$	
	$B_d \to D^{*-}\pi^+\pi^+\pi^-\pi^0$	
	$B_d \to \overline{D}^{(*)0}\rho^0$ [$\to K^+\pi^-$ or $K^+\pi^+\pi^-\pi^-$ or $K^{(*)+}\ell^-\overline{\nu}_\ell$ etc.]	BR($\rho^0 \to \pi^+\pi^-$) $\approx 100\%$. The $\overline{D}^{(*)0}$ must be detected in a final state f such that $D^{(*)0} \to f$ is forbidden or suppressed.
	$B_s \to D_s^{(*)-}\pi^+$	
	$B_s \to D_s^{(*)-}\pi^+\pi^+\pi^-$	
	$B_s \to D_s^{*-}\pi^+\pi^+\pi^-\pi^0$	
	$B_s \to \overline{D}^{(*)0}K_S$ [$\to K^+\pi^-$ or $K^+\pi^+\pi^-\pi^-$ or $K^{(*)+}\ell^-\overline{\nu}_\ell$ etc.]	
$\overline{b} \to \overline{c}c\overline{s}$	$B_d \to \psi K^+\pi^-$	mainly $B_d \to \psi K^{(*)}$ [$\to K^+\pi^-$]
	$B_d \to D^{(*)+}D_s^{(*)-}$	
$\overline{b} \to \overline{c}c\overline{d}$	$B_s \to \psi K^-\pi^+$	mainly $B_s \to \psi\overline{K}^{(*)}$ [$\to K^-\pi^+$]
	$B_s \to D_s^{(*)-}D^{(*)+}$	
$\overline{b} \to \overline{c}X$	$B_d \to D^{(*)-}X$	small contamination from $\overline{b} \to \overline{c}c\overline{d}$

Table 8.4: Interesting flavor-specific decays.

[†] Author: Ulrich Nierste

quark decay	hadronic decay	remarks
$\overline{b} \to \overline{c}u\overline{d}$	$B_d \to \overline{D}^{(*)0}\rho^0$ [$\to \rho_0 K_S$ or $K\overline{K}$ or $\pi^+\pi^-$]	The $\overline{D}^{(*)0}$ must be detected in a CP-specific final state f (hence $D^{(*)0} \to f$ is equally allowed).
	$B_d \to \overline{D}^{(*)0}\pi^+\pi^-$ [$\to \rho_0 K_S$ or $K\overline{K}$ or $\pi^+\pi^-$]	This decay mode has color-unsuppressed contributions.
	$B_s \to \overline{D}^{(*)0}K_S$ [$\to \rho_0 K_S$ or $K\overline{K}$ or $\pi^+\pi^-$]	
$\overline{b} \to \overline{c}c\overline{s}$	$B_d \to \psi K_S$	
	$B_d \to \psi K_S\rho^0$	The $\overline{B}_d$ can decay into the same final state $K_S\rho^0$. Angular analysis separates CP-eigenstates.
	$B_d \to \psi\phi K_S$ or $\psi K_S\rho^0$	Angular analysis required.
	$B_d \to \psi\phi K^*$ [$\to K_S\pi^0$]	Angular analysis required, π^0 is problematic.
	$B_d \to D_s^{(*)+}D_s^{(*)-}K_S$	Angular analysis required.
	$B_s \to \psi\phi$	Angular analysis required.
	$B_s \to \psi K\overline{K}$ or $\psi K^*\overline{K}^*$	Same remark
	$B_s \to \psi\phi\phi$	Same remark.
	$B_s \to \psi\eta$	
	$B_s \to \psi\eta'$	
	$B_s \to D_s^+D_s^-$	
	$B_s \to D_s^{*+}D_s^{*-}$	Angular analysis required.
	$B_s \to D^{(*)+}D^{(*)-}$ or $D^{(*)0}\overline{D}^{(*)0}$	Non-spectator decays.
	$B_s \to \psi f_0$	CP-odd final state.
	$B_s \to \chi_{c0}\phi$	CP-odd final state.
$\overline{b} \to \overline{c}c\overline{d}$	$B_d \to D^+D^-$	CP-even final state.
	$B_d \to D^{*+}D^{*-}$	
	$B_d \to \psi\rho^0$	
	$B_s \to \psi K_S$	
	$B_s \to \psi K_S\pi^0$	Mainly $B_s \to \psi\overline{K}^{(*)}$ [$\to K_S\pi^0$].

Table 8.5: Interesting CKM-favored decays into CP-eigenstates.

quark decay	hadronic decay	remarks
$\overline{b} \to \overline{c}c\overline{s}$	$B_s \to \psi K\overline{K}^*$ combined with $\psi K^*\overline{K}$	angular analysis plus analysis analogous to $B_s \to D_s^{\pm}K^{\mp}$ required.

Table 8.6: Interesting CKM-favored decays into CP non-eigenstates accessible to B and $\overline{B}$.

8.5 Introduction and Physics Input for CDF

This section summarizes technical issues and physics inputs that are relevant to mixing and lifetime measurements at CDF. The CDF detector improvements that are critical for these measurements are the following :

1. The Level-1 and Level-2 trigger systems have been upgraded to allow triggers on high momentum tracks at Level-1, using the central drift chamber ("XFT"), and on large impact parameter tracks at Level-2, using the silicon vertex detector ("SVT"). This in turn allows CDF to trigger on all-hadronic decays of b hadrons, such as $B_s \to D_s\pi$. Extensive simulations, together with run I data, have been used to estimate trigger rates and event yields for the analyses discussed below.

2. The silicon vertex detector has been upgraded for improved silicon tracking and extended fiducial coverage. This upgrade is most relevant to analyses which depend critically on vertex position resolution, in particular the measurement of B_s mixing.

3. The CDF muon system has been upgraded to allow extended fiducial coverage and lower trigger thresholds. The increase of the fiducial volume is treated as a simple scale factor for all analyses using muons; the change in trigger threshold applies to the analysis of central di-muons only.

The basic information needed to make projections for Tevatron Run II is the event yield for the b hadron decay channels in question. Projections are relatively simple for channels obtained from lepton triggers using extrapolations from the Run I data. An example of this scaling is given in 6.2.2. The projections for channels which are triggered by the newly implemented displaced track trigger system, often referred to as the hadronic trigger, are more difficult and are based primarily on simulations.

The CDF trigger system is organized in three levels of which only the first two are simulated for the following studies, since the third level should not reject good signal events. In addition to the trigger simulation, physics inputs are needed for the total B cross sections and production and branching fractions. Both the physics inputs and the description of the trigger simulation are given below. Some of the issues are already partially covered in the CP violation chapter in Section 6.2.2. Here the emphasis is mostly on the hadronic trigger.

8.5.1 Physics Input

The Monte Carlo program Bgenerator [76] is used to generate b hadrons; it parameterizes the p_T and y distributions for b quarks according to next-to-leading-order calculations [77]. The b quarks are fragmented into b hadrons using the Peterson [78] function with a fragmentation parameter value of $\epsilon_b = 0.006$. The CLEO Monte Carlo Program QQ [79] is used to decay the b hadrons. Events generated with Bgenerator contain particles only from the decay of the b hadrons, and do not include particles produced in the b quark fragmentation or the underlying event from the $p\overline{p}$ collision.

Quantity	Value	Reference
$B(D_s^+ \to \phi\pi^+)$	$(3.6 \pm 0.9) \times 10^{-2}$	[82]
$B(D_s^+ \to K^+\overline{K^{*0}})$	$(3.3 \pm 0.9) \times 10^{-2}$	[82]
$B(D_s^+ \to \pi^+\pi^+\pi^-)$	$(1.0 \pm 0.4) \times 10^{-2}$	[82]
$B(D^0 \to K^-\pi^+)$	$(3.85 \pm 0.09) \times 10^{-2}$	[82]
$B(D^0 \to K^-\pi^+\pi^+\pi^-)$	$(7.6 \pm 0.4) \times 10^{-2}$	[82]
$B(\Lambda_c^+ \to pK^-\pi^+)$	$(5.0 \pm 1.3) \times 10^{-2}$	[82]
$B(\Lambda_c^+ \to \Lambda\pi^+\pi^-\pi^+)$	$(3.3 \pm 1.0) \times 10^{-2}$	[82]
$B(\Lambda \to p\pi^-)$	$(63.9 \pm 0.5) \times 10^{-2}$	[82]
$B(\phi(1020) \to K^+K^-)$	$(49.1 \pm 0.8) \times 10^{-2}$	[82]
$B(K^*(892) \to K\pi)$	1	[82]
f_{Λ_b}	$(0.116 \pm 0.020) \times 10^{-2}$	[82]
$f_s/(f_u + f_d)$	$(0.213 \pm 0.038) \times 10^{-2}$	[81]
$\sigma_B^0(p_T(B^0) > 6$ GeV; $\lvert y\rvert < 1)$	$(3.52 \pm 0.61)\mu b$	[80]

Table 8.7: Physics input used for event yield estimates.

Quantity	Value	Reference
$B(B_s \to D_s\pi)$	$(3.0 \pm 0.4) \times 10^{-3}$ from B^0	[82]
$B(B_s \to D_s\pi\pi\pi)$	$(8.0 \pm 2.5) \times 10^{-3}$ from B^0	[82]
$B(B_s \to D_sD_s)$	$(8.0 \pm 3.0) \times 10^{-3}$ from B^0	[82]
$B(B_s \to D_s^*D_s)$	$(2.0 \pm 0.6) \times 10^{-2}$ from B^0	[82]
$B(B_s \to D_s^*D_s^*)$	$(2.0 \pm 0.7) \times 10^{-2}$ from B^0	[82]

Table 8.8: Branching fraction estimates for B_s decays.

The overall production cross section is normalized using the CDF measurement for B^0 production with $p_T > 6$ GeV, $|y| < 1$ [80]. The B_s and Λ_b production fractions in $p\bar{p}$ collisions are based on the CDF measurement of $f_s/(f_u+f_d)$ [81] and the world average value for f_{Λ_b}, respectively. Assuming the b hadron production spectra follow the distributions from [77], and using the CDF measurement from Reference [80], a total production cross section for B^0 mesons of 50.1 μb is obtained. Table 8.7 lists the measured rates and production fractions assumed in the CDF analyses, together with the relevant hadronic decay branching fractions that are known. In addition, we have estimated the branching fractions for b-hadron decays that have not been measured directly, using various symmetry assumptions as described below.

Branching Fraction Estimates Since many of the hadronic decay channels have so far not been measured or even observed, certain branching ratios have to be estimated. This is relatively simple for B_s decays, using related B^0 decay modes. These estimates are summarized in Table 8.8. The related uncertainties should be small, on the order of roughly 10% in the form factors or 20% in the event yields.

For Λ_b baryons the situation is more complicated. Several patterns arise when comparing bottom and charm branching fractions, as well as meson and baryon branching fractions.

The most important is the fact that the branching fractions of B mesons are often quite small compared to those of the corresponding D decays. For instance

$$\begin{aligned} \mathcal{B}(B^0 \to D^-\pi^+) &= (3.0 \pm 0.4) \times 10^{-3}\,, \\ \mathcal{B}(D^0 \to K^-\pi^+) &= (3.83 \pm 0.09) \times 10^{-2}\,. \end{aligned} \tag{8.169}$$

Comparing the two gives a B to D ratio of 0.08. One might suppose, neglecting that $c \to s$ involves a light quark, that the widths of these modes would be similar, but the total widths reflected in the mean lifetimes are different. Moreover, the b sector involves considerably more decay channels. The semileptonic decays, however, remain qualitatively different, and do not scale in the same way.

A similar pattern for the hadronic decay modes may reasonably be expected for baryons. Indeed, in the one hadronic branching fraction measured for the Λ_b, we have:

$$\begin{aligned} \mathcal{B}(\Lambda_b \to J/\psi\Lambda) &= (4.7 \pm 2.8) \times 10^{-4}\,, \\ \mathcal{B}(\Lambda_c^+ \to pK^{*0}) &= (1.6 \pm 0.5) \times 10^{-2}\,, \\ \mathcal{B}(\Lambda_c^+ \to p\phi) &= (1.2 \pm 0.5) \times 10^{-3}\,. \end{aligned} \tag{8.170}$$

In comparing the Λ_c^+ branching fraction to the Λ_b branching fraction, it is assumed that virtual $W^- \to \bar{c}s$ occurs about as frequently as $W^- \to \bar{u}d$. The Λ_b to Λ_c^+ ratio is about 0.03 when comparing to $\Lambda_c^+ \to pK^{*0}$. A similar comparison can be made with the second Λ_c^+ decay mode, which, aside from the $|V_{us}/V_{ud}|^2$ factor, is most similar to $\Lambda_b \to J/\psi\Lambda$; the ratio is about 0.02. However, since applying this factor to a color-suppressed mode is problematic, the first ratio is preferred

$$g_{bc} = 0.03 \tag{8.171}$$

to multiply Λ_c^+ hadronic branching fractions to obtain estimates of corresponding Λ_b fractions.

Another difference between charm and bottom decays is that the bottom hadrons can avail themselves of the virtual $W^- \to \bar{c}s$ transition which is disallowed for charm decays. The ratio of branching fractions for an external $W^- \to \bar{c}s$ to $W^- \to \bar{u}d$ is similar to the ratio of the square of the decay constants

$$g_{D_s}^2 = \left(\frac{f_{D_s^+}}{f_{\pi^+}}\right)^2 = \left(\frac{280 \text{ MeV}}{130.7 \text{ MeV}}\right)^2 = 4.58\,, \tag{8.172}$$

the effect of which is seen in comparing branching fractions of $B^0 \to D^-D_s^+$ and $D^-\pi^+$, with the usual caveats.

Adding a $\pi^+\pi^-$ to the final state of a decay mode tends to result in a larger branching fraction. This effect is observed in the mesons, but the ratio calculated among Λ_c^+ modes is preferred because of the different baryon structure:

$$g_{\pi\pi} = \frac{\mathcal{B}(\Lambda_c^+ \to \Lambda\pi^+\pi^+\pi^-)}{\mathcal{B}(\Lambda_c^+ \to \Lambda\pi^+)} = \frac{3.3}{0.9} = 3.7\,. \tag{8.173}$$

Λ_b decay	Λ_c decay	$\mathcal{B}(\Lambda_c^+)$	estimate	$\mathcal{B}(\Lambda_b)$ estimate
$\Lambda_c^+\pi^-$	$\Lambda\pi^+$	$b_1 = (9.0 \pm 2.8) \times 10^{-3}$	$b_1 g_{bc}$	2.6×10^{-4}
$\Lambda_c^+\pi^-\pi^+\pi^-$	$\Lambda\pi^+\pi^-\pi^+$	$b_2 = (3.3 \pm 1.0) \times 10^{-2}$	$b_2 g_{bc}$	9.7×10^{-4}
$pD^0\pi^-$(nr)	$pK^-\pi^+$(nr)	$b_3 = (2.8 \pm 0.8) \times 10^{-2}$	$b_3 g_{bc}$	8.2×10^{-4}
pK^-			$b_1 g_{bc} g_{bu} g_{\pi K}$	8.1×10^{-6}
$p\pi^-$			$b_1 g_{bc} g_{bu}$	2.0×10^{-6}
$p\pi^-\pi^+\pi^-$			$b_2 g_{bc} g_{bu}$	7.4×10^{-6}

Table 8.9: Branching ratio estimates for Λ_b decays using scale factors described in the text.

Another factor is used to estimate the branching fractions where the external W yields a D_s^{*+} rather than a D_s^+. Here the B^0 branching fractions are used

$$g_* = \frac{\mathcal{B}(B^0 \to D^{(*)-} D_s^{*+})}{\mathcal{B}(B^0 \to D^{(*)-} D_s^+)} = \frac{1.0 + 2.0}{0.80 + 0.96} = 1.7. \tag{8.174}$$

A similar factor is obtained when comparing analogous decays with ρ^+ and π^+ final states of B^0 decays. Decay modes such as $\Lambda_c^+ \to \Lambda\rho^+$ have not been observed.

Once certain $b \to c$ branching fractions have been estimated, they are scaled by

$$g_{bu} = |V_{ub}/V_{cb}|^2 \sim 0.0077 \tag{8.175}$$

to obtain estimates for corresponding $b \to u$ transitions. Finally, the recently measured branching fractions

$$\begin{aligned} \mathcal{B}(B^0 \to \pi^+\pi^-) &= (4.3 \pm 1.6) \times 10^{-6}, , \\ \mathcal{B}(B^0 \to K^+\pi^-) &= (17.2 \pm 2.8) \times 10^{-6}, \end{aligned} \tag{8.176}$$

are used to estimate $\Lambda_b \to pK^-$ from $\Lambda_b \to p\pi^-$:

$$g_{\pi K} = \frac{17.2}{4.3} = 4. \tag{8.177}$$

The resulting branching ratio estimates for the different Λ_b decay modes are summarized in Table 8.9.

8.5.2 Detector Simulation

Hadronic Trigger Only The Level-1 track trigger is based on a set of kinematic cuts originally developed for two-body decays of neutral B mesons. The Level-1 triggering algorithm is therefore based on pairs of XFT trigger tracks. To reduce the background of inelastic collisions relative to B hadron production, only track pairs in which both tracks have transverse momentum p_T greater than a specified value are considered. Because of the time that would be spent on combinatorics, an event with more than six such tracks passes Level-1 automatically. For real B^0 and B_s^0 decays of interest, the two highest p_T tracks are correlated in angle and generally have opposite charge; consequently, the Level-1 requirements are chosen as follows:

B_s decay	ϵ_{L1}	ϵ_{L2Bs}	ϵ_{L2Bd}	$\epsilon_{\mathrm{L2Tot}}$	ϵ_{fid}	N_{RunII}
$B_s \to D_s\pi$	0.025	0.0045	0.0029	0.0050	0.0027	36900
$B_s \to D_s\pi\pi\pi$	0.018	0.0032	0.0018	0.0033	0.0011	38300
$B_s \to D_s D_s$	0.019	0.0035	0.0015	0.0037	0.0014	2500
$B_s \to D_s^* D_s$	0.016	0.0031	0.0011	0.0032	0.0013	5700
$B_s \to D_s^* D_s^*$	0.014	0.0030	0.0011	0.0031	0.0012	5200

Table 8.10: Event yields for hadronic B_s decays relevant for CP violation and $\Delta\Gamma_s$ measurements. Only the feasible D_s decays to $\phi\pi$, K^*K and $\pi\pi\pi$ are considered.

Λ_b (sub)decay	ϵ_{L1}	ϵ_{L2Bs}	ϵ_{L2Bd}	$\epsilon_{\mathrm{L2Tot}}$	ϵ_{fid}	N_{RunII}
$\Lambda_b \to \Lambda_c^+\pi^-(\Lambda_c^+ \to pK^-\pi^+)$	0.026	0.0040	0.0029	0.0045	0.0031	2400
$\Lambda_b \to \Lambda_c^+\pi^-\pi^+\pi^-(\Lambda_c^+ \to pK^-\pi^+)$	0.017	0.0024	0.0014	0.0026	0.0012	3400
$\Lambda_b \to pD^0\pi^-(D^0 \to K^-\pi^+)$	0.029	0.0043	0.0036	0.0048	0.0032	6100
$\Lambda_b \to pD^0\pi^-(D^0 \to K^-\pi^+\pi^-\pi^+)$	0.020	0.0028	0.0018	0.0030	0.0012	4300
$\Lambda_b \to p\pi^-$	0.056	0.0054	0.011	0.011	0.011	1300
$\Lambda_b \to p\pi^-\pi^+\pi^-$	0.030	0.0041	0.0032	0.0046	0.0030	1300
$\Lambda_b \to pK^-$	0.056	0.0053	0.011	0.011	0.011	5400

Table 8.11: Event yields for most sizeable hadronic Λ_b decays.

- two tracks having opposite charge
- individual track $p_T > 2.0$ GeV/c
- $p_T, 1 + p_T, 2 > 5.5$ GeV/c
- $\delta\phi < 135$ deg

The Level-2 trigger is based on tracking information provided by the SVT [83,84]. One application for the hadronic b trigger is the decay $B^0 \to \pi^+\pi^-$, where the two pions give oppositely-charged tracks with high transverse momenta and large impact parameters. The trigger is also used to select other multibody hadronic b decays, but due to the different kinematics of these decays, the Level-2 selection criteria are modified to optimize the efficiencies [84]. An event passes the Level-2 track trigger if it satisfies either option A) or option B)

A) Multi hadronic B trigger
- $120\mu\mathrm{m} < |d_0| < 1\mathrm{mm}$
- $2\,\mathrm{deg} < \delta\phi < 90\,\mathrm{deg}$
- $p_T \cdot X_v > 0$

B) Hadronic pair trigger
- $100\mu\mathrm{m} < |d_0| < 1\mathrm{mm}$
- $20\,\mathrm{deg} < \delta\phi < 135\,\mathrm{deg}$
- $p_T \cdot X_v > 0$
- $d_{0,B} < 140\mu\mathrm{m}$

For an event to be useful in offline analysis after it passes the trigger, all the b hadron decay products have to be reconstructible in the detector. The requirement for a b hadron to be considered reconstructible in this simulation is that all its stable, charged daughter particles are within $|\eta| < 1$ and have transverse momenta greater than 400 MeV/c. These requirements are probably conservative in two ways: first, track reconstruction in

Run II will be possible over a larger η range; stand-alone silicon tracking will probably be possible up to $|\eta| < 2$. Second, the reconstruction efficiency for the COT will be similar to that for the CTC during Run I. The efficiency for track reconstruction in the CTC extended down to $p_T \simeq 200$ MeV/c and rose over the transverse momentum range 200 MeV/$c < p_T < 400$ MeV/c, reaching about 93% for tracks with $p_T > 400$ MeV/c.

Applying the trigger to various B_s and Λ_b decays, we estimate the event yields at the two trigger levels. A summary of these estimates is given in Tables 8.10 and 8.11 for B_s and Λ_b, respectively.

Hadronic Trigger Combined with Lepton Apart from the purely hadronic trigger there is the possibility of using the hadronic trigger in conjunction with the lepton triggers. Therefore, a single lepton requirement is combined with the requirement of a displaced track in the SVT. This trigger option is studied for the semi-inclusive $B_s \to \nu\ell D_s X$ sample.

The additional requirement of a displaced track allows a lower threshold for the lepton momentum, while keeping the trigger rate at a reasonable level. The trigger cross section for an 8 GeV inclusive electron trigger would need to be prescaled in Run II. However, it is possible to lower the cross section for a 4 GeV electron trigger below 100 nb by adding the displaced track found by SVT with $p_T > 2$ GeV/c and $d_0 > 120$ μm.

Since Run I data are considered to be most reliable for predictions, the signal yield for Run II CDF is obtained by scaling the Run I analysis results with the ratio of the acceptances between Run I and Run II. The acceptance ratio between Run I and Run II is obtained using a Monte Carlo sample of semileptonic B_s decays containing a D_s. The SVT tracking efficiency is assumed to be $\sim 75\%$ per track, or 56% for 2-tracks.

The $\ell + D_s$ sample composition is assumed to be,

- $eD_s : \mu D_s = 50\% : 50\%$
- $B_s \to \ell\nu D_s : \ell\nu D_s^* : \ell\nu D_s^{**} = 2 : 5 : 0$; $\quad D_s^{**}$ usually decays to $D^{0,\pm}$

The E_T and SVT d_0 resolutions are taken to be of $14\%/\sqrt{E_T}$ and 35 μm, respectively. All tracks (ℓ, K, and π) are required to have $p_T > 400$ MeV/c, and to be in the fiducial volume of the tracking detector. The silicon vertex detector coverage is $|z| < 30$ cm in Run I and $|z| < 45$ cm in Run II. The standard analysis Run I cuts are applied to the final state particles, namely $p_T(K) > 1.2$ GeV/c, $p_T(\pi) > 0.8$ GeV/c, and 3 GeV/$c^2 < M(\ell D_s) <$ 5 GeV/c^2.

The event yields for different lepton p_T values are summarized in Table 8.12, which shows signal yields per 2 fb^{-1}. Choosing a value of 3 GeV/c lepton p_T, roughly 40k semileptonic B_s decay are obtained in 2 fb^{-1} of integrated luminosity.

Rate Estimates – Hadronic Trigger Because the trigger rates depend on the way in which the Tevatron is operated in Run II, different XFT trigger cuts were considered for three different running scenarios. Scenario A corresponds to a luminosity of less than 1×10^{32} cm^{-2}s^{-1} with collisions every 396 ns, while scenarios B and C correspond to luminosities of $1 - 2 \times 10^{32}$ cm^{-2}s^{-1} with collisions every 132 ns and 396 ns, respectively.

Trigger	Run II/Run I	$N_{\text{Run II}}$
8 GeVℓ	1.0	14000
2 GeVℓ + SVT	5.9	64000
3 GeVℓ + SVT	4.0	43000
4 GeVℓ + SVT	2.7	30000
5 GeVℓ + SVT	1.9	21000

Table 8.12: Event yields corresponding to 2 fb^{-1} for semileptonic B_s decays ($B_s \to \nu\ell D_s X$) for different lepton p_T trigger thresholds.

	Scenario A	Scenario B	Scenario C
$\mathcal{L}$	$< 1 \times 10^{32}$ cm^{-1}s^{-1}	1-2 $\times 10^{32}$ cm^{-1}s^{-1}	1-2 $\times 10^{32}$ cm^{-1}s^{-1}
BX interval	396 ns	132 ns	396 ns
$p_T^{(1)}, p_T^{(2)}$	> 2 GeV/c	> 2.25 GeV/c	> 2.5 GeV/c
$p_T^{(1)} + p_T^{(2)}$	> 5.5 GeV/c	> 6 GeV/c	> 6.5 GeV/c
$\delta\phi$	$< 135°$	$< 135°$	$< 135°$
cross section	252 ± 18 μb	152 ± 14 μb	163 ± 16 μb

Table 8.13: Level-1 XFT trigger cuts and cross sections for the three Tevatron operating scenarios considered.

The cuts considered for each scenario are listed in Table 8.13 along with the total cross section. These expectations were derived using tracks recorded in Run I with additional hit occupancy close to the beam axis generated using the MBR [85] Monte Carlo program. The trigger cuts provide trigger rates which are compatible with the total Level-1 bandwidth of approximately 50 kHz.

At Level-2, the impact parameter information associated with the tracks is available, and the cuts described above are used to select b hadron decays. The requirements are that the impact parameters of both tracks satisfy 120 μm $< |d| < 1$ mm, that their point of intersection occurs with a positive decay length, and that their opening angle is further restricted to $\delta\phi < 90°$. The trigger cross sections are reduced to approximately 489, 386 and 283 nb for scenarios A, B and C, respectively, and produce Level-2 trigger rates between 38 Hz and 67 Hz. This is well within the available Level-2 bandwidth of 300 Hz.

For efficiency estimates in the sections below, scenario A has been chosen. When implementing trigger option B the numbers of expected events do not vary significantly compared with the uncertainties quoted above. The trigger scenario C is not likely to be implemented, asssuming that the Tevatron will be upgraded to 132 ns bunch spacing.

8.6 Projections for Δm

8.6.1 B_s mixing measurement at CDF †

The probability that a B_s meson decays at proper time t in the same state, or has mixed to the $\overline{B}_s$ state is given by

$$P_{\rm unmix}(t) = \frac{1}{2}\left(1 + \cos\Delta m_s t\right) \ ,$$
$$P_{\rm mix}(t) = \frac{1}{2}\left(1 - \cos\Delta m_s t\right) \ , \qquad (8.178)$$

where the mixing frequency, Δm_s, is the mass difference between the heavy and light CP eigenstates.

The canonical B_s mixing analysis, in which oscillations are observed and the mixing frequency, Δm_s, is measured, proceeds as follows. The B_s meson flavor at the time of its decay is determined by reconstructing a flavor specific final state. The proper time, $t = m_{B_s^0} L/pc$, at which the decay occurred is determined by measuring the decay length, L, and the B_s momentum, p. Finally, the production flavor must be tagged in order to classify the event as being mixed or unmixed at the time of its decay. Oscillations manifest in a time dependence of, for example, the mixed asymmetry:

$$A_{\rm mix}(t) = \frac{N_{\rm mixed}(t) - N_{\rm unmixed}(t)}{N_{\rm mixed}(t) + N_{\rm unmixed}(t)}. \qquad (8.179)$$

In practice, the production flavor will be correctly tagged with a probability $\mathcal{P}_{\rm tag}$ which is significantly smaller than unity. The functional form of the mixed asymmetry follows

$$A_{\rm mix}(t) = -D\cos\Delta m_s t \qquad (8.180)$$

with the dilution, D, related to $P_{\rm tag}$ by $D = 2P_{\rm tag} - 1$. The mixing frequency is determined for example by fitting the measured asymmetry to a function of this form.

So far, B_s oscillations have not been observed experimentally, and the lower limit on x_s is above 15. This means that B_s mesons oscillate much more rapidly than B^0 mesons. The rapidity of the B_s oscillation implies a significant difference in the experimental requirements for the B^0 and B_s analyses. The limiting factor in B^0 mixing analyses is solely the effective tagging efficiency, which is equivalent to the effective statistics. In B_s mixing measurements the resolution of the proper time becomes another very critical issue. To determine the proper time, not only the positions of primary and secondary vertices have to be measured precisely, but also the measurement of the B_s momentum is crucial. Therefore, it is desirable to have fully exclusive final states such as $B_s \to D_s\pi(D_s \to \phi\pi, \phi \to KK)$. Semileptonic B_s decays have the intrinsic disadvantage that the neutrino momentum is undetected.

In Run I CDF reconstructed 220 and 125 B_s semileptonic decay events with fully reconstructed $D_s \to \phi\pi$ and $D_s \to K^*K$ channels, respectively, in low p_T (> 8 GeV/c) inclusive

† Authors: M. Jones, Ch. Paus, M. Tanaka.

lepton (e and μ) trigger samples [89]. An additional 600 semileptonic B_s decays were used, reconstructed in the $D_s \to \phi X$ + track channel. Those events were part of the dilepton ($\mu\mu$ and $e\mu$) trigger samples, where the second lepton was used for the B flavor tag. The best limit on x_s was given by the dilepton trigger dataset [90].

In Run II much more statistics will be available using the lepton trigger, the lepton trigger plus one secondary vertex track and the all hadronic trigger. From the event yield estimates in Tables 8.12 and 8.10, we expect 40k events in the lepton plus displaced track and 75k events in the all hadronic trigger.

In the following four sections the measurements of B_s mixing using semileptonic or hadronic decays are discussed. Since the flavor tagging and the sensitivity estimates are very similar for the semileptonic and hadronic B_s decay samples, they will be discussed first.

8.6.1.1 Projections for Sensitivity to x_s

The mixing frequency can be determined by calculating, for example, a maximum likelihood function derived from the measured and expected asymmetries and minimizing this function with respect to Δm_s. The significance of an observation of mixing is quantified in terms of the depth of this minimum compared with the second deepest minimum or some asymptotic value at large Δm_s. To a good approximation, the *average* significance is given as

$${\rm Sig}(\Delta m_s) = \sqrt{\frac{N\epsilon D^2}{2}} e^{-(\Delta m_s \sigma_t)^2/2} \sqrt{\frac{S}{S+B}} \qquad (8.181)$$

where $N = S$ is the number of reconstructed B_s signal events, S/B is the signal-to-background ratio, ϵ is the efficiency for applying the flavor tag with associated dilution D, and σ_t is the average resolution with which the proper time is measured. This definition is essentially the same as what would be used to define $n\sigma$ confidence intervals for a Gaussian probability density function.

Given estimates for these parameters, the limit of sensitivity is defined as the maximal value of Δm_s for which the significance is above a specified value. The studies described here use the canonical 5 standard deviations to define an unambiguous observation of mixing. In the following sections the estimates for N, ϵD^2, σ_t and S/B are described.

8.6.1.2 Flavor Tagging Efficiency

In Run II, a Time-of-Flight detector will provide CDF with the ability to distinguish kaons from pions at the 2σ level below a momentum of about 1.6 GeV/c. This allows two new flavor tags to be implemented which rely on the charge of kaons identified in the event to tag the production flavor of the B_s. As a summary, in Table 8.14 the tagging efficiency for $B_s \to D_s\pi$ expected for Run II is compared to equivalent numbers obtained in Run I. We compare the standard figure of merit for each tagger, namely ϵD^2. The two additional kaon taggers are briefly explained below.

Method	Run I – ϵD^2	Run II – ϵD^2
SLT	1.7%	1.7%
JQT	3.0%	3.0%
SST(kaon)	1.0%	4.2%
OSK	—	2.4%
Total	5.7%	11.3%

Table 8.14: Comparison of the various flavor taggers in terms of the ϵD^2 parameter between Run I and expectations for Run II. The most significant differences are the kaon taggers based on the new Time-of-Flight detector.

Opposite Side Kaon Tag Due to the $b \to c \to s$ weak decays, B-mesons containing a b quark will be more likely to contain a K^- in the final state than a K^+. As for all the other opposite side taggers the determination of the quark flavor on the opposite side determines the flavor on the vertexing side, since $b\bar{b}$ quarks are produced in pairs.

For the opposite side kaon tagging, kaon candidates are selected that are well separated from the reconstructed B_s decay. Kaon candidates coming from a b hadron decay are separated from prompt kaons by requiring a large impact parameter. These requirements are implemented by imposing an isolation cut of

$$\Delta R_{\eta\phi} = \sqrt{\Delta\eta^2 + \Delta\phi^2} > 1 \tag{8.182}$$

and a cut on the combined transverse and longitudinal impact parameters of

$$\chi^2_{d_0 z_0} = \frac{d_0^2}{\sigma^2_{d_0}} + \frac{z_0^2}{\sigma^2_{z_0}} > 9. \tag{8.183}$$

Tagging the production flavor of the B_s using the charge of the kaon selected in this way gives a contribution to the tagging efficiency of

$$\epsilon D^2 = (2.4 \pm 0.2)\%. \tag{8.184}$$

Same Side Kaon Tag Same side kaon tagging in B_s decays is the equivalent of same side pion tagging in B^0 decays. In the hadronization process, when a B_s meson is produced, an $s\bar{s}$ pair must be popped from the vacuum during fragmentation. The remaining s or $\bar{s}$ quark is likely to join with a $\bar{u}$ or u quark to form a charged kaon. The charge of the kaon thus depends on the flavor of the B_s meson at production.

To estimate the ϵD^2 of the same side kaon tagging algorithm the same side pion tagging algorithm is extended with particle identification using Time-of-Flight information. It should be noted that ϵD^2 for this algorithm is strongly dependent on the momentum spectrum of the B_s meson. Therefore, a rough simulation of the Level-1 and Level-2 triggers are applied to the Monte Carlo sample. The B_s p_T spectrum of this event sample peaks at around 10 GeV/c, and ϵD^2 is estimated to be

$$\epsilon D^2 = (4.2 \pm 0.3)\%. \tag{8.185}$$

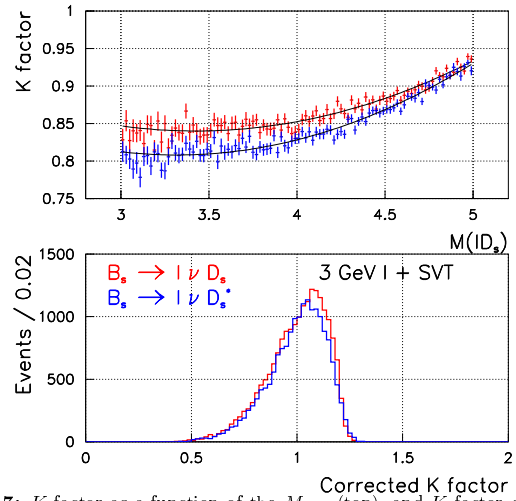

Figure 8.7: K factor as a function of the $M_{\ell D_s}$ (top), and K factor distribution after the $M_{\ell D_s}$ correction (bottom).

8.6.1.3 B_s Mixing with Semileptonic Decays

As discussed in the introduction the key issue for semileptonic B_s decays is the resolution of the proper time measurement. Including the estimates for flavor-tagged event yields, the x_s sensitivity determination is straightforward.

Proper Time Resolution The proper decay time in semileptonic decays is derived as follows

$$ct = \frac{L_T(B_s)M(B_s)}{p_T(B_s)} = \frac{L_T(B_s)M(B_s)}{p_T(\ell D_s)} \cdot K,, \qquad K = \frac{p_T(\ell D_s)}{p_T(B_s)}\,, \tag{8.186}$$

where the transverse decay length, $L_T(B_s)$, and transverse momentum, $p_T(\ell D_s)$, are measured from data. The K factor which is used as an average correction for the the incomplete B_s reconstruction is obtained from Monte Carlo samples, and $M(B_s)$ is the B_s mass [82]. The proper time resolution is given as

$$\sigma_t = \sigma_{t_0} \oplus t \cdot \frac{\sigma K}{K}, \tag{8.187}$$

where the constant term ($\sigma_{t_0} \sim 60$ fs) is due to the beam spot and the vertex detector resolution, and the K factor resolution ($\sigma K/K \sim 14\%$) is due to the momentum spectrum of the undetected particles, namely the neutrino in the B_s decay or the photon/π^0 in the subsequent D_s^* decay.

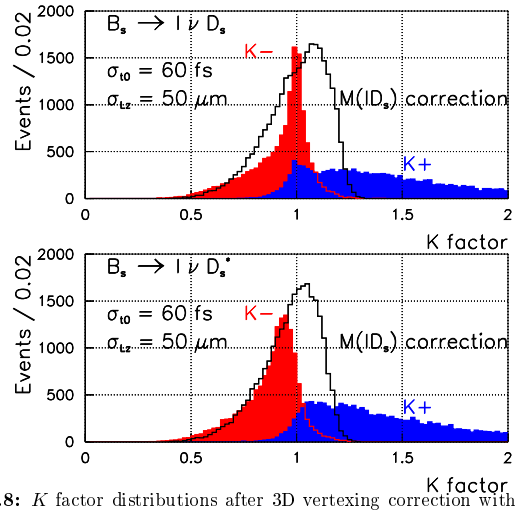

Figure 8.8: K factor distributions after 3D vertexing correction with vertex detector resolutions of $\sigma_{t_0} = 60$ fs and $\sigma_{L_z} = 50$ μm.

The K factor depends strongly on the lepton + D_s invariant mass, $M(\ell D_s)$; this dependence is shown in Figure 8.7 for the D_s and D_s^* channels. Since the invariant lepton + D_s mass is measured, this dependence is corrected for on an event-by-event basis to improve the K factor resolution.

For the $B_s \rightarrow \ell D_s X$, $X = \nu + x$ channel, the following energy and momentum conservation rules are given

$$E_{B_S} = E_{\mu D_S} + E_X\,,$$
$$p_X = |\vec{p}_X|^2 = |\vec{p}_{B_S} - \vec{p}_{\mu D_S}|^2 = p_{B_S}^2 + p_{\mu D_S}^2 - 2p_{B_S}p_{\mu D_S}\cos\Theta, \qquad (8.188)$$

where Θ is the angle in the laboratory frame between the B_s and $\ell + D_s$ directions, which are obtained using the 3D vertex information of the Run II SVX. By assuming $M_X = 0$ the quadratic equation can be solved exactly. Notice that the equation gives generally two solutions, $K^- < K^+$. The equation sometimes has nevertheless no physical solutions due to the finite detector resolution. Furthermore, the equation does not give the correct answer for the $B_s \rightarrow \ell\nu D_s^*$ channel because of the missing photon, $M_X = M_{\nu\gamma} > 0$.

The K factor distributions after all the trigger and offline selection cuts are shown in Figure 8.8. A vertex resolution of $\sigma_{t_0} = 60$ fs and $\sigma_{L_z} = 50$ μm has been assumed. The D_s and the D_s^* channels are displayed in the upper and lower plots, respectively. The probability for the quadratic equation to have a real solution is approximately 50 percent. However, the correction still improves the K factor resolution if there is a physical solution.

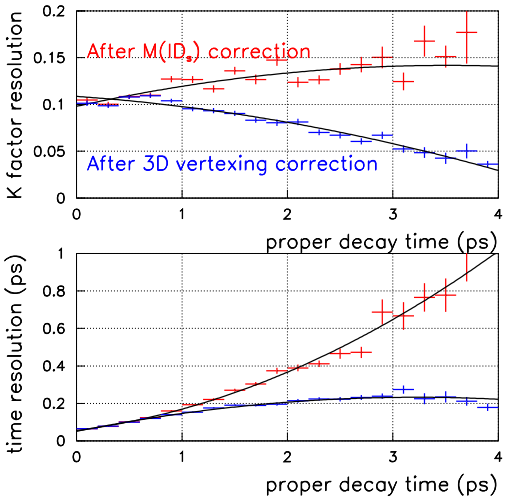

Figure 8.9: K factor and time resolution for $B_s \rightarrow \ell\nu D_s$ decays.

Since the 3D vertexing correction strongly depends on the Θ resolution, it improves for longer B_s decay lengths. In Figure 8.9 the K factor and time resolutions are shown as functions of the proper decay time for the D_s channel after the $M_{\ell D_s}$ correction and 3D vertexing correction.

To perform the 3D vertexing correction, it is assumed that the correct solution, K^- or K^+, is known, and that the $M(\ell D_s)$ corrected K factor is used if there are no physical solutions. The K factor resolution is significantly improved for the longer decay time events. Both channels D_s and D_s^* show similar results. Unfortunately, the improved K factor resolution is not sufficient to greatly improve the sensitivity to x_s; practically all of the sensitivity comes from the very short decay length events.

Backgrounds In Run I the signal to background ratio in B_s reconstruction in the semileptonic channels was typically 1:1. Since the kinematics of the Run II event sample will be somewhat different, a conservative signal to background ratio of 1:2 is assumed in the following.

Projected Sensitivity The parameters which influence the projected B_s mixing sensitivity, calculated using equation 8.181, are summarized as follows:

$$N(B_s) : 43k \text{ see Table 8.12}$$
$$\epsilon D^2 : 11.3\% \text{ see Table 8.14}$$

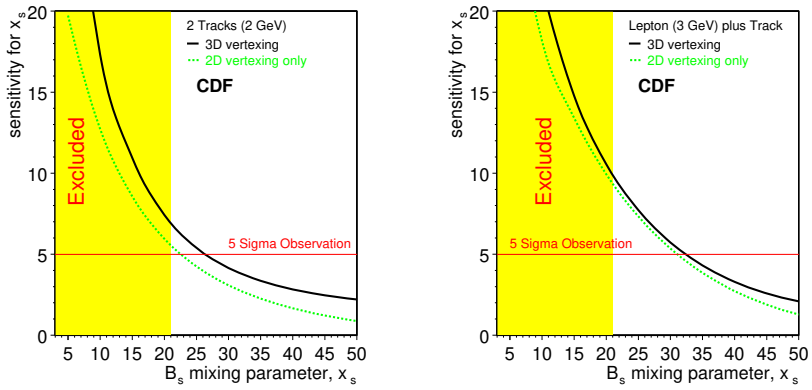

Figure 8.10: Sensitivity for measuring x_s using B_s semileptonic decays for the hadronic two track trigger (left) and the lepton plus displaced track trigger (right). The dashed lines show the significance after $M_{\ell D_s}$ correction, the solid lines after further applying the 3D vertex correction.

σ_t : see Figure 8.9
S/B : 1 : 2 as explained above

The analysis described above for the 3 GeV/c lepton plus displaced track triggers can easily be extended to the hadronic two-track triggers defined in Table 8.13, where the trigger path is satisfied by a semileptonic decay; given the large ($\sim$ 20%) semileptonic combined branching ratio, the hadronic trigger turns out to be highly efficient for semileptonic decay modes. The significances for measuring x_s for the two-track trigger (left) and the lepton plus displaced track (right) are shown in Figure 8.10. The dashed lines show the significance after the $M_{\ell D_s}$ correction, and the solid lines after the additional 3D vertexing correction. The x_s reach of the semileptonic decay sample is estimated to be about 30 for an observation with five standard deviations. This is significantly less than that for the fully reconstructed hadronic channels, which are discussed below, but it does provide an independent trigger path.

8.6.1.4 B_s Mixing with Hadronic Decays

The fully hadronic event sample is particularly important for B_s mixing analyses since the fully reconstructed decays $B_s \to D_s^- \pi^+$ and $B_s \to D_s^- \pi^+ \pi^- \pi^+$ have excellent proper time resolution, much smaller than the expected period of oscillation.

Proper Time Resolution The proper time of a B_s decay is calculated from the measured decay length, and the reconstructed B_s momentum. The uncertainty on the proper time is then given by

$$\sigma_t = t \sqrt{\left(\frac{\sigma_L}{L}\right)^2 + \left(\frac{\sigma_P}{P}\right)^2}. \tag{8.189}$$

To resolve the rapid oscillations of the B_s it is generally required that this resolution not be significantly larger than the period of oscillation. For partially reconstructed semileptonic B_s decays, the uncertainty in the momentum is the limiting factor in the mixing analyses. However, for the fully reconstructed B_s decays obtained using the XFT+SVT triggers, the momentum uncertainty will be less than 0.4%. This does not contribute significantly to the overall proper time resolution and has been ignored in the projections described below.

Backgrounds To date, no hadron collider experiment has operated with a displaced track based trigger. Hence, the level of backgrounds to be expected in the B_s sample is uncertain. Data recorded by CDF in Run I based on the single lepton triggers are used to study the purity of the B_s signal after imposing the XFT and SVT trigger cuts on the opposite side b hadron decays.

It has been observed that even a modest decay length cut suppresses the light flavor contribution significantly. Therefore, the main concern is that the signal is not overwhelmed by background from events containing real b- and c-quarks.

Because of the small branching ratios of the $B_s \to D_s^+ \pi^-, D_s^+ \pi^+ \pi^- \pi^-$ decays, few, if any, such decays are expected to be present in the Run I data after imposing the XFT and SVT trigger cuts. A similar set of cuts with higher efficiency was used to search for the hadronic B^0 and B^+ decays in the $D\pi$ final states. As a result of those studies it is concluded that a signal to background ratio of 1:1 should be achievable. To see the dependence of the significance on this parameter, this ratio is varied between 1:2 and 2:1 in the following projections.

Projected Sensitivity The parameters which influence the projected B_s mixing sensitivity, calculated using equation 8.181, are summarized as follows:

$N(B_s) = 75k$ see Table 8.12
$\epsilon D^2 = 11.3\%$ see Table 8.14
$\sigma_t = 0.045$ ps
$S/B = 1:2-2:1$ as explained above

The results are again presented in terms of the dimensionless mixing parameter $x_s = \Delta m_s \tau_{B_s}$ where the B_s lifetime of 1.54 ps [86] is used. In addition to the analytic expression for the sensitivity, Equation 8.181, an alternative analysis has been performed using a series of simulated Monte Carlo experiments. The lifetime distributions of mixed and unmixed decays are generated and the mixed asymmetry is fitted to Equation 8.180. An example

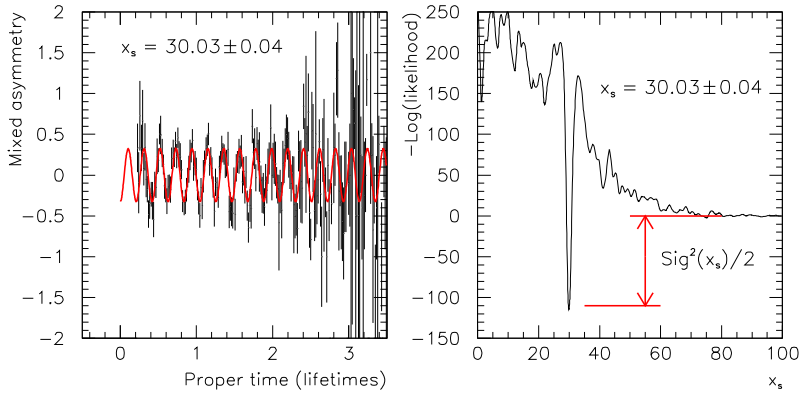

Figure 8.11: Example of a single toy Monte Carlo experiment: the mixed asymmetry distribution (left) and negative log-likelihood from the fit as a function of x_s (right)

of the mixed asymmetry distribution and the negative log-likelihood curve is shown in Figure 8.11. The negative log-likelihood curve is shown as a function of x_s, obtained from one of these Monte Carlo experiments. The comparison of the analytic expression with the averages of many Monte Carlo simulations indicates that the analytic approximation is very good.

The average significance for B_s oscillation measurements is shown in Figure 8.12. Various event yields and signal-to-background scenarios are considered. As stated above, the default event yield is 75k events and the signal-to-background fraction is 1:1.

From the analytic expression, equation 8.181, the following 5 standard deviation sensitivity limits are derived:

$$\text{Maximum: 75k events } x_s = \begin{cases} 74 & \text{for } S/B = 2:1 \\ 69 & \text{for } S/B = 1:2 \end{cases}$$

$$\text{Maximum: S:B = 1:1 } x_s = \begin{cases} 73 & \text{for 125k events} \\ 59 & \text{for 25k events} \end{cases}$$

The Monte Carlo samples give very similar results as indicated above. It is concluded that even in the worst case the reach is $x_s \sim 60$.

Fits to various experimental results which assume the Standard Model indicate that $22.0 < x_s < 30.8$ at the 95% confidence level [87]. If mixing occurs near the frequency expected in the Standard Model, it should be easily observable by CDF in Run II. Figure 8.13 (left) shows the luminosity required to achieve an observation with an average significance of 5 standard deviations as a function of x_s. The figure indicates that if mixing occurs

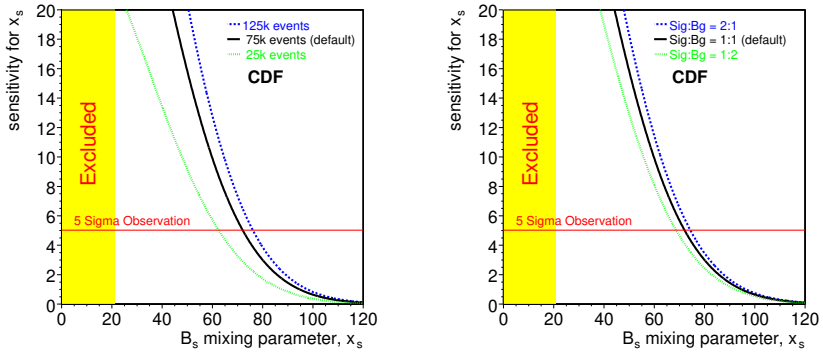

Figure 8.12: Average significance of mixing measurements expected as a function of the mixing parameter x_s for various event yields (left) and signal-to-background ratios (right). The default is 75k events at a signal-to-background ratio of 1:1. The shaded area is excluded by the combined world lower limit on x_s.

within the context of the Standard Model, then it should be observed with a small fraction of 2 fb^{-1}, with CDF in a fully operational state.

While the significance of an observation of mixing is determined from the depth of the minimum in the negative log-likelihood curve, the uncertainty on the measured value of x_s is determined by how sharp this minimum is. In the case of rapid oscillations, many periods will be reconstructed over a few B_s lifetimes and the minimum is expected to be very sharp leading to a small uncertainty.

The average uncertainty is described approximately by the analytic expression

$$\frac{1}{\sigma_{x_s}} = \sqrt{N\epsilon D^2} e^{-(x_s\sigma_t/\tau)^2/2} \sqrt{\frac{S}{S+B}}. \tag{8.190}$$

The expected uncertainty from the analytic formula versus the mixing parameter, x_s, is shown in Figure 8.13 (right(). This formula is confirmed using a series of Monte Carlo samples.

8.6.2 B_s mixing measurement at DØ †

The expected luminosity of the Tevatron, 2×10^{32} cm^{-2}s^{-1}, in Run II will lead to a huge rate for $b\bar{b}$ production, $\sim 10^{11}$ events/year. These enormous statistics combined with the upgraded detector will allow us to search for B_s mixing. The resulting measurement of Δm_s, when used to determine the ratio $\Delta m_d/\Delta m_s$ using the well-measured value for Δm_d,

†Authors: N. Cason, R. Jesik, and N. Xuan.

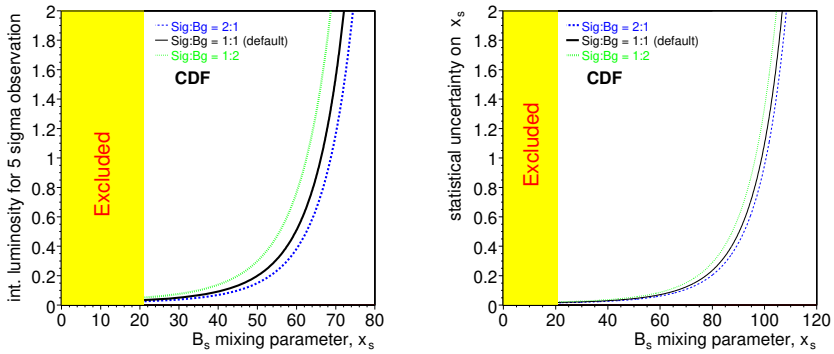

Figure 8.13: Luminosity required to achieve a 5 standard deviation observation of mixing (left) and the statistical uncertainty as a function of the mixing parameter, x_s (right). The curves on the right are calculated using Equation 8.190.

gives a theoretically clean measurement of $|V_{td}|^2/|V_{ts}|^2$. This puts a precise constraint on the CKM parameters ρ and η.

For B_s^0 mesons, existing data exclude small values of the mixing parameter $x_s = \Delta m_s/\Gamma_s$, requiring $x_s > 19.0$ at the 95% CL [82]. Consequently the mass difference Δm_s is much larger than Δm_d, and the $B_s^0 - \overline{B_s^0}$ oscillation frequency will therefore be much higher than that for the B_d^0. Excellent decay length and momentum resolutions are thus essential in order to observe the rapid oscillations as a function of proper time.

Various decay modes of B_s^0 mesons are under investigation by the DØ collaboration. Among them are:

$$\begin{aligned}
&B_s^0 \to D_s^-(K^-K^+\pi^-)\pi^+, && (\mathrm{BR} = 1.1\times 10^{-4}),\\
&B_s^0 \to D_s^-(K^-K^+\pi^-)3\pi, && (\mathrm{BR} = 2.8\times 10^{-4}),\\
&B_s^0 \to J/\psi(\mu^+\mu^-, e^+e^-)K^*(K^\pm\pi^\mp), && (\mathrm{BR} = 5.1\times 10^{-6}),\\
&B_s^0 \to D_s^-(K^-K^+\pi^-)\ell^+\nu, && (\mathrm{BR} = 1.1\times 10^{-4}).
\end{aligned} \tag{8.191}$$

Taking advantage of the good SMT resolution, we can select B_s decays by using displaced secondary vertices or using tracks with large impact parameters. The B_s final states will be flavor tagged by the charge of the lepton, the charge of the reconstructed charm meson or the charge of the kaon as appropriate.

The actual measurement strategy for x_s will depend on the frequency of the oscillation. For smaller oscillation frequencies, semileptonic B_s decays can be used. The lepton in the final state provides an easy trigger, giving a large statistics sample. If nature cooperates, a measurement in this range will come very early in Run II.

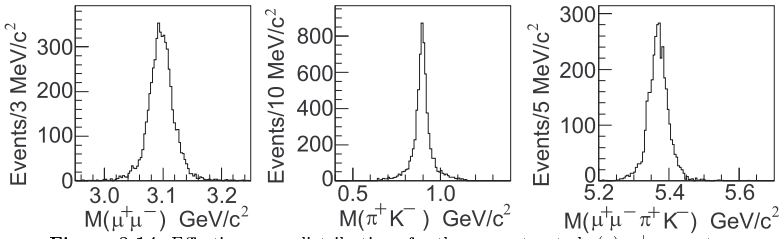

Figure 8.14: Effective mass distributions for the reconstructed: (a) $\mu^+\mu^-$ system, (b) π^+K^- system, and (c) $\mu^+\mu^-\pi^+K^-$ system. These distributions are prior to using vertex and mass constraints.

For higher oscillation frequencies, the measurement becomes more difficult. Exclusive decays must be used in order to achieve the necessary momentum (and therefore proper time) resolution. Decays which DØ has focused on include: $B_s \to D_s^-\pi^+(\pi^-\pi^+)$, where the D_s^- decays to $\phi\pi^-$ or $K^{*-}K^0/K^-K^{*0}$; and $B_s \to J/\psi\overline{K}^{*0}$ followed by $J/\psi \to e^+e^-$ or $\mu^+\mu^-$ and $\overline{K}^{*0} \to K^-\pi^+$. We can only trigger on B_s decays into fully hadronic final states when the other B in the event decays semileptonically. Using single lepton triggers, we expect to be able to collect about a thousand reconstructed exclusive B_s decays in each mode in the first two years, allowing us to measure x_s values up to $\sim 20-30$. We are presently investigating better trigger scenarios, such as lowering the p_T threshold of the lepton and requiring another moderately high p_T track (or tracks), which would increase our Δm_s reach.

A Monte Carlo study of the $B_s \to J/\psi\overline{K}^{*0}$ decay has been carried out in order to estimate the number of events which will be in a data sample based on a 2 fb^{-1} exposure. We have analyzed 20,000 events using the MCFast program. The events were generated using Pythia and a simulation of the upgraded DØ detector. Each event had a $B_s \to J/\psi\overline{K}^{*0}$ decay as well as a generic $\overline{B}$ decay. The J/ψ decayed to $\mu^+\mu^-$ (83% of the time) or $\mu^+\mu^-\gamma$ (17% of the time). (The radiative decays are not discussed further here.) The $\overline{K}^{*0}$ decayed to π^+K^-.

Event reconstruction efficiency was estimated using the geometric acceptance of the silicon vertex detector and of the fiber tracker. (Tracking inefficiencies are not yet included.) We find that 21% of the events have all four charged tracks reconstructed.

Shown in Fig. 8.14 are the reconstructed $\mu^+\mu^-$, π^+K^-, and $\mu^+\mu^-\pi^+K^-$ effective mass distributions for the reconstructed tracks. The mass resolution of the B_s improves by more than a factor of two when vertex and J/ψ mass constraints are imposed. Effective mass resolutions are given in Table 8.15.

Resolutions of vertex position, decay length, and proper time were estimated using the nominal silicon vertex detector and fiber tracker resolutions. Shown in Fig. 8.15 are distributions of the fitted minus measured decay length of the B_s, the fitted minus measured proper decay time of the B_s, and the ratio of the decay length to the error in the decay length (L/σ_L). We summarize the resolutions in vertex positions, decay length and proper

Quantity		Level σ (MeV/c^2)
$M(B_s)$	Reconstruction	37
$M(B_s)$	J/ψ mass fit	15
$M(\mu^+\mu^-)$	Reconstruction	29

Table 8.15: Mass Resolutions

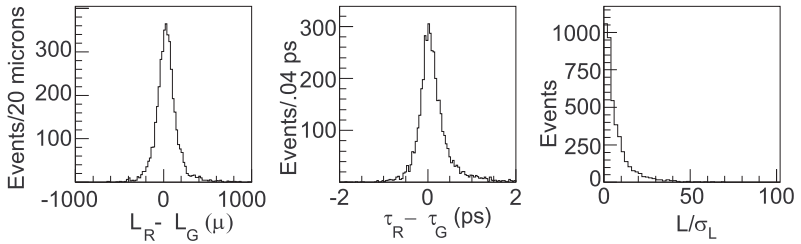

Figure 8.15: Distributions of: (a) the reconstructed B_s decay length minus the generated B_s decay length; (b) the reconstructed B_s proper time minus the generated B_s proper time; and (c) the reconstructed B_s decay length divided by its error.

time in Table 8.16.

In order to get a realistic estimate of the number of events which would be available for analysis, additional cuts were placed on the sample. The muons were required to have $p_T > 1.5\ GeV/c$ and to have $|\eta| < 2$. A total of 24% of the reconstructed events satisfied these cuts. Combined with the reconstruction efficiency of 21%, we are left with a sample of 5.0% of the generated events for further analysis.

For most purposes, additional cuts will be required to obtain a sample of events with a good signal-to-noise ratio. To estimate the sample size after such cuts, we impose a cut on the variable L/σ_L. Of the 5.0% of the events satisfying all the previous cuts, 83% have $L/\sigma_L > 2.0$, 73% have $L/\sigma_L > 3.0$, and 63% have $L/\sigma_L > 4.0$. The required cut value will not be known until the data is in hand, but we use the $L/\sigma_L > 3.0$ cut for further estimates. Hence the overall combined efficiency which we use below is (.050)*0.73=0.036.

In order to do mixing studies, it is necessary to tag the flavor of the B_s (or $\overline{B_s}$). This can be tagged if we identify the sign of the charged kaon in the K^*. Although DØ does

Quantity	σ
Production vertex (x,y, and z) (μm)	34, 34, 80
Decay vertex (x,y, and z) (μm)	50, 50, 140
B_s decay length (μm)	140
Proper time (ps)	0.40

Table 8.16: Resolutions

not have particle identification in the traditional sense, it is possible in this event sample to determine whether the positive or negative particle from the K^* decay is the charged kaon by calculating the effective mass under the two assumptions ($K^+\pi^-$ and $K^-\pi^+$) and taking as correct that combination which gives an effective mass closest to the nominal K^* mass ($0.890\ GeV/c^2$). We find that we are correct using this assignment 67% of the time. Flavor tagging of the other b quark will have the efficiency and dilution summarized previously in Table 6.3.

Using estimates of the $b\bar{b}$ production cross section (158 μb); the fraction of this cross section producing B_s (0.167); the $B_s \to J/\psi\overline{K}^{*0}$ branching ratio (5.1 x 10^{-6}); the $J/\psi \to \mu^+\mu^-$ branching ratio (0.06); the luminosity (2 fb^{-1}); and the overall combined efficiency from above (.036), we obtain a signal of 1000 events. We would expect a similar sample will be obtained using the $J/\psi \to e^+e^-$ mode.

8.6.3 Measurement of B_s Mixing in BTeV [†]

In this section, the x_s reach of BTeV will be demonstrated using $B_s \to D_s^-\pi^+$ and $B_s \to J/\psi\overline{K}^{*0}$. This study was carried out in several steps, the first step being a simulation of the BTeV detector response to signal events. The output of this step was treated as real data and passed through a physics analysis program to determine the yield, the time resolution and the signal-to-background ratio in each mode. This information was then passed to a separate program which computed the x_s reach; this program is discussed in section 8.6.3.2. A separate background study was performed.

8.6.3.1 Yields, Resolutions and Signal-to-Background Ratios

The mode for which BTeV has the most sensitivity to x_s is $B_s \to D_s^-\pi^+$, where the D_s^- decays either by $D_s^- \to \phi\pi^-$, $\phi \to K^+K^-$, or by $D_s^- \to K^{*0}K^-$, $K^{*0} \to K^+\pi^-$. Both of these D_s^- modes have narrow intermediate states and characteristic angular distributions, both of which can be used to improve the signal-to-background ratio.

For this study, Monte Carlo events were generated using Pythia and QQ and the detector response was simulated using BTeVGeant. The simulated events were analyzed as real data. For the $D_s \to \phi\pi$ decay mode the following cuts were used:

- All tracks were required to have at least 3 hits in the silicon pixel detector.
- Each of the tracks in the B_s candidate were required to have an impact parameter with respect to the primary vertex of $> 3\sigma$.
- To reduce the background due to tracks that really come from other interactions it was required that all 4 tracks have an impact parameter with respect to the primary vertex of less than 0.2 cm.

[†]Author: R. Kutschke.

- At least one of the kaons from the ϕ decay was required to be strongly identified as a kaon by the RICH detector. The second kaon was only required to be loosely identified. No particle ID requirements were placed on the pion candidates.
- The ϕ and D_s candidates were required to be within $\pm 2.5\sigma$ of their nominal masses.
- It was required that the distance between the primary vertex and D_s decay vertex be $L < 8.0$ cm and the D_s decay vertex have a decay length significance of $L/\sigma_L(D_s) > 10.0$.
- It was required that the B_s have decay length significance of $L/\sigma_L(B_s) > 4.0$.
- The B_s candidate was required to point back to the primary vertex: the transverse momentum of the B_s with respect to its line of flight from the primary vertex was required to be less than 1.0 GeV/c and the impact parameter of the B_s with respect to the primary vertex was required to be less than 3σ.

The combined geometric acceptance and reconstruction efficiency was found to be 2.7%. Of the events that passed these analysis cuts, 74% passed the level 1 trigger. For the $D_s \to K^*K$ mode we used the same cuts except that both kaons from the D_s decay were required to be identified in the RICH. There was also a broader cut on the intermediate K^* mass. The combined reconstruction efficiency and geometric acceptance for the $D_s \to K^*K$ mode was found to be 2.3%, and the level 1 trigger efficiency for the events passing the analysis cuts was 74%. For both modes the resolution on the mass of the B was found to be 18 MeV/c^2 and the mean resolution on the proper decay time was found to be 43 fs. The nominal acceptance of the BTeV level 2 trigger for the accepted events is 90% of the events which remain after the level 1 trigger. The nominal flavor tagging power of BTeV was estimated in chapter 5 to be $\epsilon D^2 = 0.1$ which arises from $\epsilon = 0.70$ and $D = 0.37$.

It is believed that the dominant source of backgrounds will be events of the form $X_b \to D_s^- X$, where X_b may be any b flavored hadron. The background combinations arise when a true D_s^- combination is combined with some other track in the event. An MC-Fast based study of 1 million $B \to D_s^- X$ events was performed using an older version of the detector geometry, the one used for the BTeV Preliminary Technical Design Report (PTDR) [91]. Comparisons between BTeVGeant and MCFast, and comparisons between the old and new detector geometries, show that these background studies remain valid. When the 1 million $B \to D_s^- X$ events were passed through MCFast and analyzed as real data, 8 entries remained in a mass window 6 times larger than the mass window used to select signal B_s candidates. From this it is estimated that the signal-to-background ratio in this channel is 8.4:1. This study was performed without the proper treatment of multiple interactions in one beam crossing. To account for this, the signal-to-background ratio used in the estimate of the x_s reach is 3:1.

The background from direct charm production has not yet been investigated. While direct charm production has a cross-section about 10 times higher than that for production of charm via B decay, it is triggered much less efficiently. Moreover the the requirement of two, distinct detached vertices greatly reduces the background from direct charm. In the end it is expected that the background from $B \to D_s^- X$ will dominate.

Quantity	Value	Yield (Events/year)
Luminosity:	2×10^{32} cm^{-2}s^{-1}	
One Year:	10^7 s	
$\sigma_{b\bar{b}}$:	100 μb	
$\mathcal{B}(B_s \to D_s^- \pi^+)$:	3.0×10^{-3}	
$\mathcal{B}(D_s^- \to \phi\pi^-)$:	0.030	
$\mathcal{B}(D_s^- \to K^{*0}K^-)$:	0.036	
$\mathcal{B}(\phi \to K^+K^-)$:	0.49	
$\mathcal{B}(K^{*0} \to K^+\pi^-)$:	0.67	
$\mathcal{B}(\bar{b} \to B_s)$	0.13	6,210,000
ϵ(Geometry + cuts : $\phi\pi^-$)	0.027	
ϵ(Geometry + cuts : $K^{*0}K^-$)	0.023	
ϵ(Trigger) Level 1	0.74	
ϵ(Trigger) Level 2	0.90	
ϵ(Tag)	0.70	72,000
Tagging Dilution	0.37	
S/B	3:1	
σ(Proper Decay time)	43 fs	

Table 8.17: Projected yield for $B_s \to D_s^- \pi^+$ in one year of BTeV running. The numbers in the third column give the expected yield when all of the factors down to and including that line have been considered. The branching fraction $\mathcal{B}(B_s \to D_s^- \pi^+)$ was estimated to be the same as $\mathcal{B}(B_d \to D^- \pi^+)$.

Table 8.17 gives a summary of the preceding results and discusses a list of all assumptions which went into the computation of the yield. The value for $\mathcal{B}(\bar{b} \to B_s)$ is obtained from Reference [92]. In one year it is expected that 72,000 events will trigger, survive all analysis cuts and have their birth flavor tagged.

Another mode with good x_s sensitivity is $B_s \to J/\psi \overline{K}^{*0}$, $J/\psi \to \mu^+\mu^-$, $\overline{K}^{*0} \to K^-\pi^+$. Although this mode is Cabibbo suppressed, other factors are in its favor: the final state consists of a single detached vertex and the state is triggerable with several independent strategies, including impact parameter triggers, secondary vertex triggers and dimuon triggers [93]. While this mode does not have the x_s reach of $D_s^- \pi^+$ it does cover much of the expected range and it provides a powerful check with partly independent systematics.

For reasons of time limitations, the simulation of the $J/\psi \overline{K}^{*0}$ mode used MCFast, not BTeVGeant. The analysis of this mode proceeded as follows. To be considered as part of a signal candidate, a track was required to have at least 20 total hits and at least 4 pixel hits. The only further requirement placed on $\pi^\pm$ candidates was that they have a momentum greater than 0.5 GeV/c. In order to be considered a muon candidate, a track was required to have a momentum $p > 5$ GeV/c, to penetrate the hadron filter and to leave hits in the most downstream muon chambers. Kaon candidates were required to satisfy a simplified model of the RICH system: the track was required to have a momentum in the range $3 < p < 70$ GeV/c and was required to have hits in the tracking station downstream

of the RICH mirror. True kaons which satisfied this criteria were identified as kaons with an efficiency of 90%; other hadrons which satisfied this criteria were (mis)identified as kaons 3% of the time.

A $\mu^+\mu^- K^-\pi^+$ combination was accepted as a B_s candidate if the confidence level of fitting all four tracks to a single vertex was greater than 0.005. It was also required that the resonant substructure requirements be satisfied. Combinations were considered for further analysis provided the decay length of the B_s candidate, L, satisfied $L/\sigma_L > 10$ and the impact parameter of the B_s candidate with the primary vertex, d, satisfied $d < 3\sigma_d$. Each of the four B_s granddaughters were required to have an impact parameter with the primary vertex, d, of $d > 2\sigma_d$. Candidates with poor time resolution were rejected by demanding $\sigma_t \leq 0.09$ ps. Also the mass of the J/ψ was constrained to its PDG value. The above procedure found that the efficiency for the 4 tracks to be within the fiducial volume of the tracking system was $14.2 \pm 0.3\,\%$ and the efficiency for the remaining candidates to pass the analysis cuts was 0.29 ± 0.01. The resolution on the mass of the B_s was found to be 8.6 ± 0.3 MeV/c^2 and the mean resolution on the proper decay time was found to to be 36 fs.

The BTeV Level 1 trigger simulation was run on the $J/\psi\overline{K}^{*0}$ sample and, of the candidates which passed all analysis cuts, $68 \pm 2\,\%$ also passed the trigger; the error is statistical only. However, this mode can also be triggered by the dimuon trigger. Section 8.3, of the BTeV proposal [94], which describes the algorithms and performance of the muon trigger, estimates a trigger efficiency of 50% for this decay mode. There is, as yet, no calculation of the total Level 1 trigger efficiency which takes into account the correlations between the two triggers. For this proposal it will be estimated that the combined Level 1 trigger efficiency is 85%. As for the $D_s\pi$ final state, the Level 2 trigger is expected to have an efficiency of about 90%.

By far the dominant background is expected to come from decays of the form $X_b \to J/\psi X$, $J/\psi \to \mu^+\mu^-$, where X_b is any b flavored hadron. An MCFast based simulation of 500,000 such decays was performed and the signal-to-background level was estimated to be about 2:1. Some sources of background that one might, at first, think to be important turn out not to be a problem. First, the more copious $B_s \to J/\psi\,\phi$ final state is not a significant source of background because of the excellent particle ID provided by the RICH system. Second, the mass resolution is sufficient to separate the decay $B_d \to J/\psi\overline{K}^{*0}$.

Finally, the expected yield can be increased by at least 50% by using the decay mode $J/\psi \to e^+e^-$. This mode will have an efficiency for secondary vertex triggers which is comparable to that for $J/\psi \to \mu^+\mu^-$ but the acceptance of the ECAL is smaller than that of the muon detectors. The smaller acceptance of the ECAL is somewhat offset by also using the RICH for electron identification.

The information reported here is summarized in Table 8.18 and is used in the mini-Monte Carlo described in the next section. The estimate for $\mathcal{B}(B_s \to J/\psi\overline{K}^{*0})$ is obtained from Reference [93] and that for $\mathcal{B}(\overline{b} \to B_s)$ is obtained from Reference [92].

Quantity	Value	Yield (Events/year)
Luminosity:	2×10^{32} cm^{-2}s^{-1}	
One Year:	10^7 s	
$\sigma_{b\overline{b}}$:	100 μb	
$\mathcal{B}(B_s \to J/\psi\overline{K}^{*0})$:	8.5×10^{-5}	
$\mathcal{B}(J/\psi \to \mu^+\mu^-)$:	0.061	
$\mathcal{B}(\overline{K}^{*0} \to K^-\pi^+)$:	0.667	
$\mathcal{B}(\overline{b} \to B_s)$	0.13	180000
ϵ(Geometric)	0.142	
ϵ(Analysis cuts)	0.26	6600
ϵ(Trigger) Level 1 Tracking only	0.60	
ϵ(Trigger) Level 1 Total	0.85	
ϵ(Trigger) Level 2	0.90	5100
ϵ(Tag)	0.70	3600
Include $J/\psi \to e^+e^-$	1.5	5300
Tagging Dilution	0.37	
S/B	2:1	
σ(Proper Decay time)	36 fs	

Table 8.18: Projected yield for $B_s \to J/\psi\overline{K}^{*0}$ in one year of BTeV running. The numbers in the third column give the expected yield when all of the factors down to and including that line have been considered. The trigger efficiency is quoted as a fraction of those events which pass the analysis cuts.

8.6.3.2 Computation of the x_s Reach

The final step in the study was to use a mini-Monte Carlo to study the x_s reach of BTeV. This mini-Monte Carlo generates two lifetime distributions, one for mixed events and one for unmixed events, smears the distributions and then extracts a measured value of x_s from a simultaneous fit of the two distributions. The time smearing is a Gaussian of fixed width, using the mean time resolutions determined above. The model includes the effects of mistagging, background under the signal, and the minimum time cut which is implied by the L/σ_L cut. It is assumed that the lifetime distribution of the background is an exponential with the same mean lifetime as that of the B_s.

Figures 8.16 a) and b) show the proper time distributions which result from one run of the mini-Monte Carlo for a generated value of $x_s = 40$. The simulation is for the decay mode $B_s \to D_s^-\pi^+$ for one month of BTeV running. Part a) shows the proper time distribution for unmixed decays while part b) shows the distribution for mixed decays. Part c) of the figure shows, as a function of x_s, the value of the unbinned negative log likelihood function computed from the simulated events. A clear minimum near the generated value of x_s is observed and the likelihood function determines the fitted value to be $x_s = 39.96 \pm 0.08$. A step of 0.5 in the negative log likelihood function determines the 1 σ error bounds and a line is drawn across the figure at the level of the 5 σ error bound.

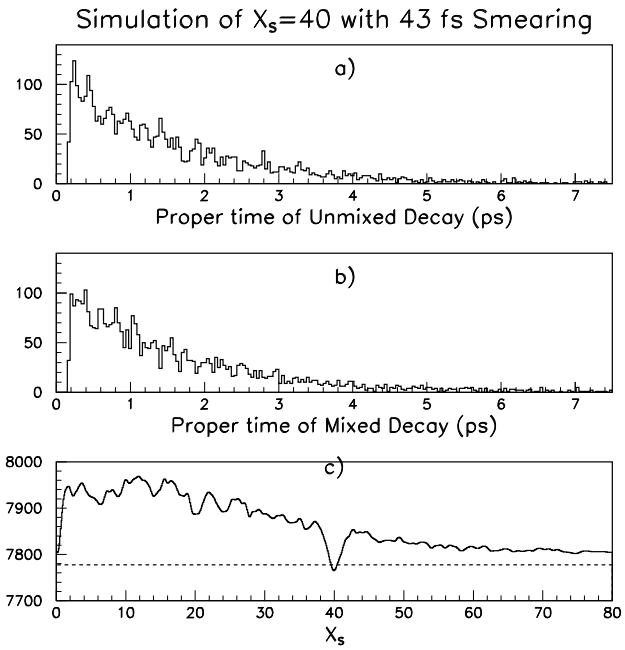

Figure 8.16: Mini Monte Carlo proper lifetime plots of a) unmixed and b) mixed decays for a generated value of $x_s = 40$. The plots simulate the results of the $B_s \to D_s^- \pi^+$ channel after one month of running. The oscillations are prominent. Part c) shows the negative log likelihood function which was obtained from the entries in parts a) and b). A prominent minimum is seen at the generated value of x_s. The dashed line marks the level above the minimum which corresponds to 5 σ significance.

This figure nicely illustrates the distinction between two quantities which are often confused, the significance of the result and the error on x_s. The significance of the signal is determined by how far the depth of the global minimum falls below that of the next most significant minimum. The error on x_s is determined by the curvature of the likelihood function at the global minimum. While these quantities are clearly related, they are distinct; in particular, the significance of the signal is not the relative error on x_s.

The error returned by the fit was checked in two ways. First, an ensemble of mini-Monte Carlo experiments was performed and the errors were found to correctly describe the dispersion of the measured values about the generated ones. Second, the errors returned by the fit were found to be approximately equal to the Cramer-Rao minimum variance bound.

The mini-Monte Carlo was also used to study the level of statistics below which the

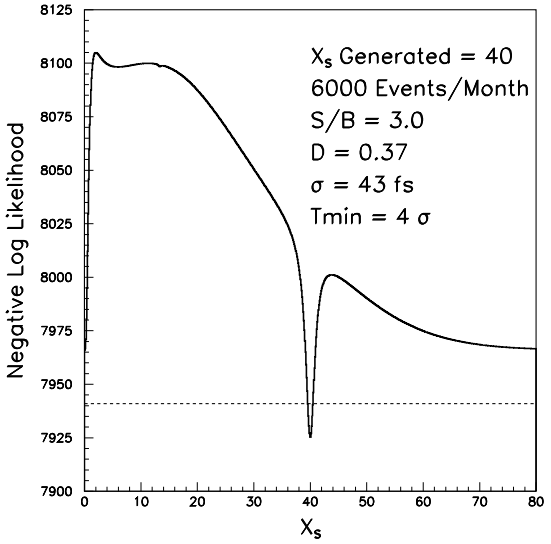

Figure 8.17: The same likelihood function as in part c) of the previous figure but obtained using the integral method described in the text. The overall shape is the same but the statistical fluctuations have been removed. There is also an overall level shift which is related to the goodness of fit in the previous figure.

experiment is unable to measure x_s. As the number of events in a trial is reduced, the negative log likelihood function becomes more and more ragged and the secondary minima become more pronounced. Eventually there are secondary minima which reach depths within 12.5 units of negative log likelihood (5 σ) of the global minimum. When this happens in a sufficiently large fraction of the trials, one must conclude that only a lower limit on x_s can be established. In the region of the parameter space which was explored, the absolute error on x_s was approximately 0.1 when this limit was reached. This was independent of the generated value of x_s; that is, the discovery measurement of x_s will have errors of something like ± 0.1, even if x_s is large, say 40.

It is awkward to map out the x_s reach of the apparatus by running a large ensemble of mini-Monte Carlo jobs; instead the following automated procedure was used. Following ideas from McDonald [95], the sum over events in the likelihood function was replaced with an integral over the parent distribution. Because the parent distribution does not have any statistical fluctuations, the fluctuations in the likelihood function are removed, leaving only the core information. An example of such a likelihood function is shown in Fig. 8.17.

A likelihood function computed in this way has the property that it scales linearly with the number of events being simulated. This can be stated formally as follows. Let x_0 denote the generated value of x_s and let $\mathcal{L}(x; x_0, N)$ denote the value of the likelihood function,

evaluated at x, for a sample which has a true value of x_0 and which contains N events. Then,

$$\mathcal{L}(x; x_0, N) = N\,\mathcal{L}(x; x_0, 1)\,. \tag{8.192}$$

Now, one can define the significance of the minimum, n, as,

$$n^2 = 2.0\,N\,[\mathcal{L}(\infty; x_0, 1) - \mathcal{L}(x_0; x_0, 1)]\,. \tag{8.193}$$

For practical purposes ∞ was chosen to be 160. If one did not have to worry about the missing statistical fluctuations it would be normal to define a significant signal as $5\,\sigma$, or $n^2 = 25$. Instead, sufficient significance was defined as $n^2 = 31.25$, by adding a somewhat arbitrary safety margin; this allows for the usual $5\,\sigma$ plus a downwards fluctuation of up to $2.5\,\sigma$ anywhere else in the plot. Equation 8.193 was solved for N, which was then converted into the running time required to collect N events. This procedure was repeated for many different values of x_0 to obtain Fig. 8.18. The solid line shows, for the $D_s^-\pi^+$ mode, the number of years needed to obtain a measurement with a significance of $5\,\sigma$ plus the safety margin. The safety margin reduces the x_s reach at 3 years by only 3 or 4 units of x_s. For small values of x_s, the effect of the safety margin is not visible. The dashed line shows the same information but for the $J/\psi\overline{K}^{*0}$ mode; for this mode the effect of the safety margin is similarly small.

Inspection of Fig. 8.18 shows that, using the $D_s^-\pi^+$ mode, BTeV is capable of observing all x_s less than 75 in one year of running, which is equivalent to an integrated luminosity of 2 fb^{-1}.

8.6.4 Summary of Projections for Mixing

The Standard Model expectation for B_s mixing is $22 < x_s < 31$ [87]. All three experiments CDF, DØ and BTeV have shown that they will be able to reconstruct a substantial amount of B_s decays which will allow for mixing studies.

With 2 fb^{-1} CDF and BTeV safely cover the range for mixing as predicted by the Standard Model. The CDF sensitivity for a 5 standard deviation observation reaches from x_s values of 59 to 74 depending on the event yields and the signal-to-background ratios. BTeV's sensitivity comfortably covers x_s values of 75 with even some conservative safety margins included. Due to the large event yields CDF will be able to observe B_s mixing within the first few month of data taking provided that the displaced track trigger and the silicon detector work as advertised.

Once the oscillations are observed the statistical uncertainty on x_s will be small and in conjunction with an accurate B^0 mixing measurement it will constitute a stringent constraint on the unitarity triangle.

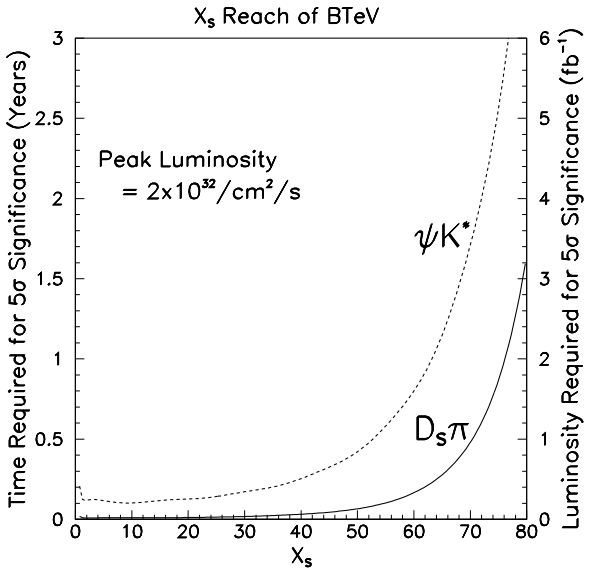

Figure 8.18: The x_s reach of the BTeV detector. The curves indicate the number of years of running which are required to make a measurement of x_s with a statistical significance of $5\,\sigma$; a safety margin, discussed in the text, has been included in the definition of $5\,\sigma$. The curves are for the two different decay modes indicated on the figure.

8.7 Projections for $\Delta\Gamma$

8.7.1 B_s Lifetime Difference in CDF †

The promise of large B_s samples in Run II puts in reach the measurement of the width difference between the two weak eigenstates of this meson. With its analysis of semileptonic decays in Run I, CDF has already published a limit of $\Delta\Gamma_s/\Gamma_s < 0.85$ at 95% confidence level [96]. This limit was established by fitting the lifetime distribution of the ℓD_s events with two exponentials.

In Run II, however, it becomes possible to measure the lifetime of samples in which the weak eigenstates are separated: for instance, 2 fb^{-1} of data yield approximately 4000 $B_s \to J/\psi\,\phi$ events, which is expected to be dominated by the shorter-lived eigenstate, B_s^H, and for which an angular analysis is used to separate the two components [98]. Further it is expected to yield roughly 75,000 of flavor-specific $B_s \to D_s\pi$ and $B_s \to D_s\pi\pi\pi$decays, which are well-defined mixtures of B_s^H and B_s^L.

†Authors: Ch. Paus, J. Tseng

It is straightforward to show that computing the difference between two lifetimes has more statistical power than fitting for two exponentials or fitting for $\Delta\Gamma_s$ in B_s mixing in flavor-specific samples. The leading term in taking the difference between two measured lifetimes is $\Delta\Gamma_s$. On the other hand, the lifetime distribution in a flavor-specific sample is

$$f(t) = \Gamma_H \left[e^{-\Gamma_H t} + e^{-\Gamma_L t}\right] = \Gamma_H\, e^{-\overline{\Gamma} t}\left[e^{-\Delta\Gamma t/2} + e^{+\Delta\Gamma t/2}\right] = \Gamma_H\, e^{-\overline{\Gamma} t}\left[1 + \left(\frac{\Delta\Gamma t}{2}\right)^2 + \ldots\right], \tag{8.194}$$

where $\Delta\Gamma$ enters as a second-order effect.

The B_s decay to $D_s^+ D_s^-$ is another valuable source of information to determine the lifetime difference of the B_s meson. First of all $D_s^+ D_s^-$ is a pure CP even eigenstate and thus its lifetime is a clean measurement of the CP even lifetime. In addition its branching fraction directly measures $\Delta\Gamma/\Gamma$ under certain theoretical assumptions [99]. The complication in this particular decay mode comes from the associated production of $D_s^{*\pm}$.

8.7.1.1 Lifetime Difference Measurements

$B_s \to J/\psi\,\phi$ The decay mode $B_s \to J/\psi\,\phi$ has been analyzed at CDF in two Run I analyses, examining its lifetime [106] and angular distributions [98] separately. The basic strategy for Run II is to combine these two analyses into a maximum likelihood fit of the proper decay time, and *transversity angle* of each candidate. In addition to account properly for the background the invariant mass distribution will be simultaneously fitted.

The transversity angle,θ_T, is defined by the angle between the μ^+ and the z axis in the rest frame of the J/ψ decay, where the z axis is orthogonal to the plane defined by the ϕ and the K^+ directions. This angle allows to distinguish CP even and CP odd components: the probability density function for the CP even component is $\frac{3}{8}(1+\cos^2\theta_T)$ and for the CP odd component is $\frac{3}{4}\sin^2\theta_T$. The amplitude of the CP even component sums the squares of the unpolarized and linearly polarized state amplitudes, $|A_0|^2 + |A_{||}|^2$, of the ϕ in the J/ψ rest frame, and the CP odd component the square of the transversely polarized state amplitude, $|A_\perp|^2$, of the same. The analysis depends upon the weak eigenstates being also CP eigenstates which is a good approximation for the $B_s \to J/\psi\,\phi$ decays.

A toy Monte Carlo study was performed to estimate the uncertainty in $\Delta\Gamma_s$ with 4000 $B_s \to J/\psi\,\phi$ decays. The background shapes in mass and proper decay time and the relative fraction of the signal to the background were assumed to be identical to that in the Run I lifetime analysis. The mass resolution was assumed to be the same as in Run I, and all the lifetime distributions were convoluted with the 18 μm resolution projected for Run II. The background was assumed to have a flat transversity angle distribution.

The error on $\Delta\Gamma_s/\Gamma_s$ depends on the CP admixture of the final state. The decay $B_s \to J/\psi\,\phi$ is dominated by CP even eigenstates. Therefore the smaller the admixture of CP odd component the larger the sensitivity. Assuming the CP composition as measured in Run I [98] corresponding to a CP even fraction of 0.77 ± 0.19 the expected uncertainty on $\Delta\Gamma_s/\Gamma_s$ is 0.05. This uncertainty varies between 0.08 and 0.035 for CP even fractions of 0.5 and 1.0, respectively.

$B_s \to D_s^{(*)+} D_s^{(*)-}$ The decay modes $B_s \to D_s^{(*)+} D_s^{(*)-}$ are also promising for lifetime difference studies, though with smaller sample sizes. These decays are expected to be present among the two-track trigger data. The decay $B_s \to D_s^+ D_s^-$, in particular, is purely CP even, and requires no angular analysis. Its companion decays, involving D_s^* decays, are expected in the heavy quark limit, and in the absence of CP violation, to be sensitive to CP-even B_s states as well [101]. While these decays are attractive in that they significantly increase the sample size over that of $B_s \to D_s^+ D_s^-$ alone, their identification is a challenge, since the missing photons from the decay $D_s^{*+} \to D_s^+\gamma$ and $D_s^{*+} \to D_s^+\pi^0$ considerably broaden the $D_s^+ D_s^-$ invariant mass distribution. On the other hand, the missing mass introduces only about 3% to the proper lifetime resolution.

In a full GEANT based simulation and reconstruction of $B_s \to D_s^{(*)+} D_s^{(*)-}$ in the CDF detector it is found that the three different cases are separated quite cleanly by using the invariant mass spectrum of the charged decay products. Shifts in the invariant B_s mass are due to the neutral particles which are not reconstructed. PYTHIA has been used to generate $b\bar{b}$ quarks and fragment them to b hadrons. The B_s mesons are decayed using the CLEOMC program according to the branching ratios given in Table 8.8.

In Figure 8.19 the invariant mass spectra of the three different cases are depicted. The spectra are essentially free of combinatoric background since the reconstructions of the resonances at each step allow stringent cuts. For this picture the D_s is always decayed into $K^{*0}K$ which has more combinatorics than the $\phi\pi$ decay mode due to the large width of the K^{*0}.

To estimate the error on the $\Delta\Gamma_s/\Gamma_s$ from this channel several assumptions have to be made since this mode has not been reconstructed in Run I.

In the most conservative estimate only $B_s \to D_s D_s$ is used which is a clean CP even state. GEANT based Monte Carlo studies indicate that a signal to background fractions of 1:1 - 1:2 are achievable. This is similar to signal to background fraction achieved for the decay mode $B_s \to \nu\ell D_s$, measured in Run I. The expected error on the lifetime is 0.044 ps is obtained using an event sample of 2.5k events and a signal to background fraction of 1:1.5. This converts into an error on $\Delta\Gamma_s/\Gamma_s$ of 0.06.

Assuming that also the other two decay modes involving D_s^* mesons are clean CP even modes a total of 13k events are available. The estimated error on $\Delta\Gamma_s/\Gamma_s$ is then reduced to 0.025.

8.7.1.2 Related Branching Fractions

The decay modes $B_s \to D_s^{(*)+} D_s^{(*)-}$ are also interesting because it is expected that they are the largest contribution to the actual difference between the heavy and light widths. Indeed, the other decay modes are estimated to contribute less than 0.01 to the projected ~ 0.15 value of $\Delta\Gamma_s/\Gamma_s$ [102]. The branching fraction to this final state is in the small velocity (SV) limit related to $\Delta\Gamma_s$ by

$$\mathcal{B}(B_s^H \to D_s^{(*)+} D_s^{(*)-}) = \frac{\Delta\Gamma_s}{\overline{\Gamma}_s(1 + \frac{\Delta\Gamma_s}{2\Gamma_s})}\,. \tag{8.195}$$

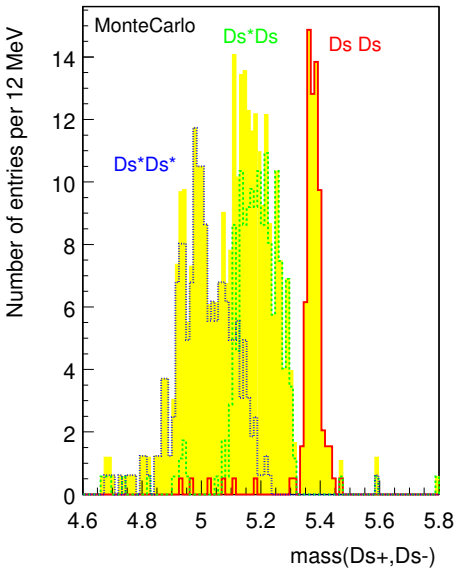

Figure 8.19: D_s^+, D_s^- invariant mass spectra for the three decay modes $B_s \to D_s D_s$ (solid), $B_s \to D_s^{(*)} D_s$ (large dashes) and $B_s \to D_s^{(*)} D_s^{(*)}$ (small dashes). The D_s is always decayed into $K^{*0}K$. The shaded background is the sum of the three decay modes.

This method has been exploited by ALEPH, using $\phi\phi$ correlations, to obtain a value of $\Delta\Gamma_s/\Gamma_s = 0.25^{+0.21}_{-0.14}$ [103]. However the small velocity assumption also referred to a Shifman-Voloshin limit may be very approximative.

The following estimates are made assuming the validity of this limit. Further when measuring branching fractions many systematic effects have to be considered. For example the tracking efficiency for the kinematics of the particular decays has to be determined carefully. Since it is difficult if not impossible to predict those effects only the statistical uncertainties are discussed below.

The statistical error on the branching fraction for 13k events (see Table 8.10) with a signal to background ratio of 1:1 is 0.012. Following Equation 8.195 the turns out to be also the statistic uncertainty on $\Delta\Gamma_s/\Gamma_s$ since the branching ratio is very small. This uncertainty deteriorates to 0.015 when making the signal to background ratio 1:2.

8.7.1.3 Combined CDF Projection

With the analysis possibilities discussed thus far, the lifetime difference method conservatively yields a statistical uncertainty of 0.04 on $\Delta\Gamma_s/\Gamma_s$, utilizing both $J/\psi\,\phi$ and $D_s^+ D_s^-$ decays and just using the lifetime measurements.

If one assumes that the decay modes involving D_s^* are also mostly CP even the sample for the lifetime measurement is extended and the branching ratios can be used in the SV limit. This decreases the statistical uncertainty on $\Delta\Gamma_s/\Gamma_s$ to 0.01.

These numbers refer to the projected Run II luminosity of 2 fb^{-1} and bear all the caveats mentioned in the text.

8.7.2 Estimate of Sensitivity on ΔΓ in BTeV †

Since $\Delta\Gamma_{B_s}$ is expected to be much larger than $\Delta\Gamma_{B^0}$, only projections for measurements of $\Delta\Gamma_{B_s}$ have been studied at BTeV for this report. The B_s^0 decay modes studied include CP-even, CP-mixed and flavor specific decay modes and are listed in Table 8.19. The total decay rate for the flavor specific decay $B_s^0 \to D_s^- \pi^+$ is given by the average of the CP-even and CP-odd rates. The decays $B_s^0 \to J/\psi\eta$, $J/\psi\eta'$ should be CP-even while the decay to $J/\psi\,\phi$ is predominantly CP-even.

B_s^0 Decay Mode	CP Mode	Branching Ratio	BR Used
$J/\psi\,\phi$	Mostly CP-even	$(9.3 \pm 3.3) \times 10^{-4}$	8.9×10^{-4}
$J/\psi\eta$	CP-even	< 0.0038	3.3×10^{-4}
$J/\psi\eta'$	CP-even	< 0.0038	6.7×10^{-4}
$D_s^-\pi^+$	Flavor specific	< 0.13	3.0×10^{-3}

Table 8.19: The B_s^0 decay modes studied for $\Delta\Gamma_{B_s}$ sensitivity studies at BTeV.

CDF has measured the CP-odd fraction of total rate for $J/\psi\,\phi$ to be $0.229 \pm 0.188(stat) \pm 0.038(syst)$ [104]. The all charged mode decay $B_s^0 \to K^+K^-$ has a large enough expected branching fraction ($\sim 1 \times 10^{-5}$) and reconstruction efficiency to get high statistics. However although the K^+K^- final state is CP-even, the decay can proceed via both a CP conserving Penguin contribution as well as a CP violating Tree level contribution. Unless the Penguin contribution is completely dominant or the Penguin and Tree level contributions can be exactly calculated it would be difficult to use this mode without significant theoretical errors.

8.7.2.1 Signal yields and backgrounds

Estimation of the signal yields and signal/background ratios were determined using a MC-FAST simulation for the B_s^0 decay mode to $J/\psi\,\phi$, while all the other modes were simulated using a Geant simulation of BTeV. Although it is easy to simulate the signal to determine

†Author: H.W.K. Cheung.

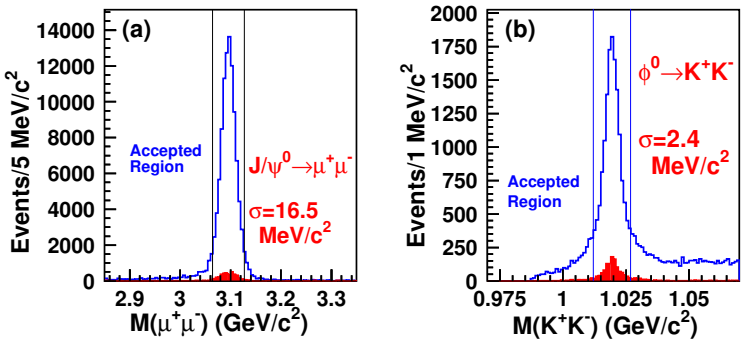

Figure 8.20: (a) The $\mu^+\mu^-$ invariant mass and (b) the K^+K^- invariant mass for a $b\bar{b} \to J/\psi\,\phi X$ background sample (open histogram) and for an appropriately normalized $B_s^0 \to J/\psi\,\phi$ signal sample (filled histogram).

the reconstruction efficiency, the background simulation can be more troublesome. The signal sample always has an average of two embedded min-bias events. Since it takes too much time to generate enough background one has to determine which backgrounds are dominant for a particular decay.

The decay $B_s^0 \to J/\psi\,\phi$ was studied through the decay channels $J/\psi \to \mu^+\mu^-$ and $\phi \to K^+K^-$. Studies show that since the $J/\psi \to \mu^+\mu^-$ is expected to be so clean, the dominant backgrounds come from $b\bar{b} \to J/\psi X$. For this study only backgrounds from $b\bar{b} \to J/\psi\,\phi X$ have been studied. Figure 8.20(a) shows the $\mu^+\mu^-$ invariant mass for a $b\bar{b} \to J/\psi\,\phi X$ background sample compared to an appropriately normalized signal sample of $B_s^0 \to J/\psi\,\phi$. The two muons were required to form a vertex with a confidence level of greater than 1%. Figure 8.20(b) shows a similar comparison for the K^+K^- invariant mass, again with a vertex requirement of $CL > 1\%$.

Figure 8.21(a) shows the $\mu^+\mu^-K^+K^-$ invariant mass for the $b\bar{b} \to J/\psi\,\phi X$ background sample without requiring that the $\mu^+\mu^-$ and K^+K^- masses are consistent with the J/ψ and ϕ masses respectively. The four tracks are required to form a single vertex with a confidence level greater than 1%. This is compared in the plot to an appropriately normalized signal sample. Figure 8.21(b) shows the $J/\psi\,\phi$ invariant mass plot with vertexing and requirements on the $\mu^+\mu^-$ and K^+K^- masses. The $\mu^+\mu^-$ and K^+K^- masses are required to be within $\pm 2\sigma$ of the true J/ψ and ϕ masses respectively. Both signal and backgrounds are included in the plot and compared to the signal only sample. The signal/background ratio is seen to increase when one applies a primary-to-secondary vertex detachment requirement of $L/\sigma_L > 15$ in Figure 8.21(c). Where L is the 3-dimensional distance between the primary vertex and the B_s^0 decay vertex and σ_L is the error on L calculated for each candidate B_s^0 decay. For $L/\sigma_L > 15$ the reconstruction efficiency is 6.0%, and the signal/background ratio is 47/1 with an error of 32% for the backgrounds considered.

Table 8.20 shows projections for the $B_s^0 \to J/\psi\,\phi$ signal yields for 2 fb^{-1}. A total $b\bar{b}$

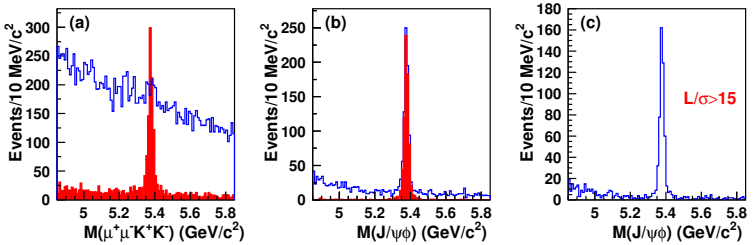

Figure 8.21: (a) The $\mu^+\mu^-K^+K^-$ invariant mass for a $b\bar{b} \to J/\psi\,\phi X$ background sample (open histogram) and for a correctly normalized $B_s^0 \to J/\psi\,\phi$ signal sample (filled histogram). (b) $J/\psi\,\phi$ invariant mass for the background plus signal sample (open histogram) compared to just the signal sample (filled histogram). (c) $J/\psi\,\phi$ mass for $L/\sigma_L > 15$.

production cross-section of 100 μb is assumed and we take the fraction of $B_s^0/\overline{B_s^0}$ per $b\bar{b}$ from Pythia as 1 in 4.3. The branching fraction of $B_s^0 \to J/\psi\,\phi$ is taken to be equal to $BR(B_d^0 \to J/\psi K^0) = 8.9 \times 10^{-4}$. A total of ~41400 signal events is expected for 2 fb^{-1}. The expected error on the lifetime for 2 fb^{-1} was determined with a toy Monte Carlo generating 1000 experiments with 41400 signal events and S/B=47. The background lifetime distribution was simulated with a short and a long lifetime component as seen in the background studies and is typical of backgrounds seen in fixed target experiments. In the toy MC the short and long components were set to be 0.33 and 1.33 ps respectively. A binned likelihood fit was used to extract the measured lifetime for each of the 1000 experiments, where the lifetime distribution from sidebands is used as a measure of the lifetime distribution in the signal B_s^0 mass region. The method is described in Reference [105]. The expected error is taken to be the *r.m.s.* of the 1000 measured lifetimes and is 0.50%.

Quantity	**Value**		
Number of $b\bar{b}$	2×10^{11}		
Number of $B_s^0/\overline{B_s^0}$	4.7×10^{10}		
	$B_s^0 \to J/\psi\,\phi$	$B_s^0 \to D_s^-\pi^+$	
	$J/\psi \to \mu^+\mu^-$	$D_s^- \to \phi\pi^-$	$D_s^- \to K^{*0}K^-$
	$\phi \to K^+K^-$	$\phi \to K^+K^-$	$K^{*0} \to K^+\pi^-$
# of Events	1.2×10^6	2.5×10^6	3.1×10^6
Reconstruction efficiency (%)	6.0	2.7	2.3
S/B	47:1	3:1	
L1 Trigger efficiency (%)	70	74	
L2 Trigger efficiency (%)	90	90	
# of reconstructed decays	41400	91700	

Table 8.20: Projections for yields of B_s^0 decays for 2 fb^{-1} assuming a total $b\bar{b}$ production cross-section of 100 μb.

Although the $J/\psi\,\phi$ signal sample can be obtained through the $J/\psi \to \mu^+\mu^-$ trigger,

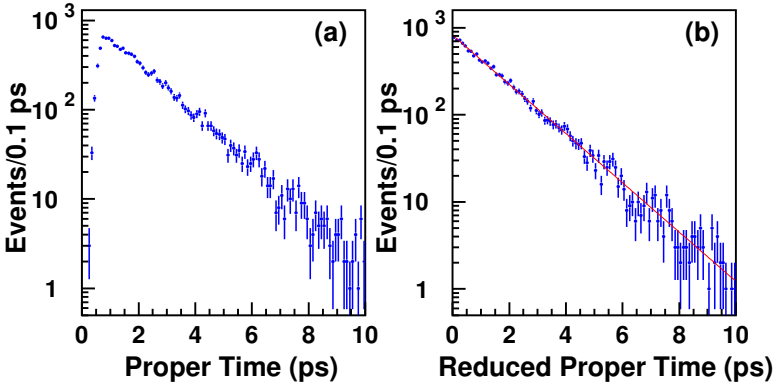

Figure 8.22: (a) Proper time distribution for reconstructed $B_s^0 \to J/\psi\,\phi$; (b) Reduced proper time distribution for the same decays, the line is an exponential fit.

the effect of the Level 1 vertex trigger on this mode was studied to determine the effect of the L1 trigger on the lifetime analysis. Figure 8.22(a) shows the proper time ($t = L/\beta\gamma c$) distribution for reconstructed $B_s^0 \to J/\psi\,\phi$ signal events for a $L/\sigma_L > 15$ requirement. The loss of short lifetime decays is due to the detachment requirement. One can obtain an exponential distribution if we use the reduced proper time, $t' = t - N\sigma_L/\beta\gamma c$, for a $L/\sigma_L > N$ requirement. This starts the clock at the minimum required decay time for each decay candidate and works because the lifetime follows an exponential distribution irrespective of the when the clock is started. Figure 8.22(b) shows the reduced proper time distribution and an exponential fit gives a lifetime of 1.536 ± 0.014 ps, compared to the generated lifetime of 1.551 ps.

Figure 8.23(a) shows the reduced proper time after applying the Level 1 vertex trigger. Short lifetime decays are again lost because the impact parameter requirements of the Level 1 trigger effectively gives a larger minimum required decay time than $N\sigma_L/\beta\gamma c$. The lifetime acceptance function is just the observed reduced proper distribution divided by a pure exponential with the generated lifetime and is given in Figure 8.23(b). In order to extract the correct lifetime from the observed reduced proper time distribution one needs the correct lifetime acceptance function. This is obtained from Monte Carlo and can be checked by using decays modes like $J/\psi\,\phi$ that can be obtained with the L1 vertex trigger and separately through the L1 $J/\psi \to \mu^+\mu^-$ dimuon trigger which has no vertexing selection criteria. The L1 trigger lifetime acceptance correction obtained from MC can also be checked by taking samples of prescaled triggers that do not have the L1 trigger requirement.

Note that since the L1 trigger can increase the effective minimum required decay time cut, if one puts on a large impact parameter selection requirement on the B decay daughters, it may be possible to redefine the reduced proper time to take this into account and thereby reduce the lifetime acceptance corrections with some lost of statistics. This still needs to be studied and the details of the L1 trigger may change since one may be able to redesign

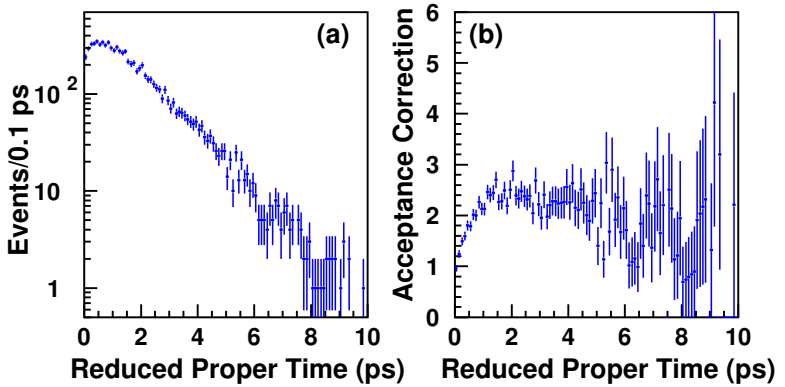

Figure 8.23: (a) Reduced proper time distribution for reconstructed $B_s^0 \to J/\psi\,\phi$ decays that pass the Level 1 vertex trigger; (b) Lifetime correction function, obtained by dividing the distribution in (a) by a pure exponential distribution with the generated B_s^0 lifetime.

it to reduced the lifetime acceptance correction.

When an acceptance correction like that given in Figure 8.23(b) is simulated in the toy Monte Carlo, the expected error on the measured lifetime increases to 0.58%, from the previous value of 0.50%. For the decay mode $B_s^0 \to D_s^-\pi^+$ where the signal to background is smaller the effect is similar, the error increases to 0.44% when adding the acceptance correction effects compared to 0.39%.

Tables 8.21 and 8.20 show the expected signal yields and signal/background ratios for the decays modes $B_s^0 \to J/\psi\eta$, $B_s^0 \to J/\psi\eta'$ and $B_s^0 \to D_s^-\pi^+$. Backgrounds from $b\,\bar{b} \to J/\psi X$ were studied for the decay modes $B_s^0 \to J/\psi\eta^{(\prime)}$, while backgrounds from $b\,\bar{b} \to D_s^+ X$ were included in the $B_s^0 \to D_s^-\pi^+$ analysis. Details of the analyses of these modes can be found in Reference [94]. Expected errors on the lifetimes were determined using toy Monte Carlo simulations as before, where acceptance corrections were also simulated for the $D_s^-\pi^+$ mode. Table 8.22 gives the expected errors on the lifetimes for all modes.

Note that although only backgrounds from $b\,\bar{b} \to J/\psi\,\phi X$ were included in the study of $B_s^0 \to J/\psi\,\phi$ to obtain the value of S/B=47/1, the effect of lower values of S/B were studied. If the S/B is decreased to 10/1 which is the expected level for $B_d^0 \to J/\psi K_s^0$ [94], the expected error on the measured lifetime only increases from 0.50% to 0.51% for 2 fb^{-1}. (For a much lower S/B=3/1 the expected error would be 0.58%.)

8.7.2.2 Results for $\Delta\Gamma/\Gamma_{B_s}$ Sensitivity

With just two lifetime measurements, like τ_{CP+} and τ_{CP-}, which are defined as $\tau_{CP+} = 1/\Gamma(B_s^{even})$ and $\tau_{CP-} = 1/\Gamma(B_s^{odd})$, one can determine the error on $\Delta\Gamma_{CP}/\Gamma$ from the errors

Quantity	Value		
Number of $b\bar{b}$	2×10^{11}		
Number of $B_s^0/\overline{B_s^0}$	4.7×10^{10}		
	$B_s^0 \to J/\psi\eta$	$B_s^0 \to J/\psi\eta'$	
	$J/\psi \to \mu^+\mu^-$		
	$\eta \to \gamma\gamma$	$\eta' \to \rho^0\gamma$	$\eta' \to \pi^+\pi^-\eta$
# of Events	3.5×10^5	5.4×10^5	3.2×10^5
Reconstruction efficiency (%)	0.71	1.2	0.60
S/B	15:1	30:1	
L1 Trigger efficiency (%)	75	85	
L2 Trigger efficiency (%)	90	90	
# of reconstructed decays	1700	6400	

Table 8.21: Projections for yields of B_s^0 decays for 2 fb^{-1} assuming a total $b\bar{b}$ production cross-section of 100 μb.

Decay Mode	Error on Lifetime (%)		
	2 fb^{-1}	10 fb^{-1}	20 fb^{-1}
$J/\psi\,\phi$	0.50	0.23	0.16
$J/\psi\eta$	2.49	1.19	0.80
$J/\psi\eta'$	1.36	0.55	0.39
$D_s^-\pi^+$	0.44	0.20	0.14

Table 8.22: Projections for statistical errors on lifetimes measured in different modes for 2, 10 and 20 fb^{-1}.

on the two lifetimes:

$$\sigma_{\frac{\Delta\Gamma_{CP}}{\Gamma}} = 4\,\frac{\tau_{CP+}\tau_{CP-}}{(\tau_{CP+}+\tau_{CP-})^2}\sqrt{\left(\frac{\sigma_{\tau_{CP+}}}{\tau_{CP+}}\right)^2+\left(\frac{\sigma_{\tau_{CP-}}}{\tau_{CP-}}\right)^2}, \tag{8.196}$$

where $\Delta\Gamma_{CP} = \Gamma(B_s^{even}) - \Gamma(B_s^{odd})$ and $\Gamma = (\Gamma(B_s^{even}) + \Gamma(B_s^{odd}))/2$. In the case that one measures τ_{CP+} and τ_{FS} where $\tau_{FS} = 2/(\Gamma(B_s^{even}) + \Gamma(B_s^{odd}))$, the error on $\Delta\Gamma_{CP}/\Gamma$ is

$$\sigma_{\frac{\Delta\Gamma_{CP}}{\Gamma}} = 2\,\frac{\tau_{FS}}{\tau_{CP+}}\sqrt{\left(\frac{\sigma_{\tau_{CP+}}}{\tau_{CP+}}\right)^2+\left(\frac{\sigma_{\tau_{FS}}}{\tau_{FS}}\right)^2}. \tag{8.197}$$

It can be seen that for small $\Delta\Gamma_{CP}/\Gamma$, the error is about 2 times larger when one measures with similar errors τ_{CP+} and τ_{FS} compared to measuring τ_{CP+} and τ_{CP-}. Using τ_{CP+} from the $J/\psi\eta^{(\prime)}$ decay modes and τ_{FS} from $D_s^-\pi^+$, we project an error on $\Delta\Gamma_{CP}/\Gamma$ of 0.027 for $\Delta\Gamma_{CP}/\Gamma = 0.15$ for 2 fb^{-1}.

Including the lifetime measurement for the decay mode to $J/\psi\pi$ is more complicated as this is not an equal mixture of CP-even and CP-odd rates. Although a combined lifetime and angular analysis should be done to determine the fraction of CP-odd decay in this mode, and the appropriate error on τ_{CP+}, it was not done for this study. A simpler determination

is made assuming that the fraction of CP-odd has already been determined within some error in a separate analysis or in some other experiment. If the lifetime for this decay mode is defined by $\tau_X = 1/\Gamma_X$ where $\Gamma_X = (1-f)\Gamma(B_s^{even}) + f\Gamma(B_s^{odd})$, then

$$\frac{\Delta\Gamma_{CP}}{\Gamma} = \frac{2(\tau_{FS}-\tau_X)}{(1-2f)\tau_X}, \tag{8.198}$$

$$\sigma_{\frac{\Delta\Gamma_{CP}}{\Gamma}} = \frac{2\tau_{FS}}{(1-2f)\tau_X}\sqrt{\left(\frac{\sigma_{\tau_X}}{\tau_X}\right)^2+\left(\frac{\sigma_{\tau_{FS}}}{\tau_{FS}}\right)^2+\left(\frac{\tau_{FS}-\tau_X}{\tau_{FS}}\right)^2\frac{4f^2}{(1-2f)^2}\left(\frac{\sigma_f}{f}\right)^2}.$$

Setting the value of f to the central valued measured by CDF and assuming the total error can be improved in Run 2 by a factor of $\sqrt{20}$, then for $f = 0.229 \pm 0.043$ and using the $J/\psi\,\phi$ and $D_s^-\pi^+$ modes only, the projected error on $\Delta\Gamma_{CP}/\Gamma$ is 0.035 for $\Delta\Gamma_{CP}/\Gamma = 0.15$ and 2 fb^{-1}. Although reducing the error on f has only a small effect on the projected error on $\Delta\Gamma_{CP}/\Gamma$, the actual value of f has a huge effect, since as f approaches 0.5 we lose all sensitivity to $\Delta\Gamma_{CP}$ when only comparing to the $D_s^-\pi^+$ mode. It can be seen that even with relatively low statistics, the $J/\psi\eta^{(\prime)}$ decay modes are just as sensitive to $\Delta\Gamma_{CP}$.

Table 8.23 shows the projected errors on $\Delta\Gamma_{CP}/\Gamma$ for different integrated luminosities for the two different combinations of modes used. The error on f is assumed to reduced by $\sqrt{R}$ where R is the ratio of integrated luminosities. The total projected error when all modes are used is also shown. To determine the expected error when all modes are used, a likelihood fit is used where f is constrained by a Gaussian probability likelihood term to be within the 0.043 error of the central value of 0.229. Note that the projected errors have a weak dependence on the value of $\Delta\Gamma_{CP}/\Gamma$ used but a strong dependence on the value of f used. It should also be noted that we are assuming that any systematic errors are insignificant compared to the statistical errors, so that these projected statistical errors are taken as the total error on $\Delta\Gamma_{CP}/\Gamma$. For the range of lifetime errors we are considering this assumption is reasonable since the charm lifetimes can be measured to this level in fixed target experiments with only small systematics. However the lifetime acceptance correction in BTeV may be somewhat larger for the hadronic modes.

Decay Modes Used	Error on $\Delta\Gamma_{CP}/\Gamma$		
	2 fb^{-1}	10 fb^{-1}	20 fb^{-1}
$J/\psi\eta^{(\prime)}$, $D_s^-\pi^+$	0.0273	0.0135	0.0081
$J/\psi\,\phi$, $D_s^-\pi^+$	0.0349	0.0158	0.0082
$J/\psi\eta^{(\prime)}$, $J/\psi\,\phi$, $D_s^-\pi^+$	0.0216	0.0095	0.0067
with $\Delta\Gamma_{CP}/\Gamma = 0.03$	0.0198	0.0088	0.0062
with $f = 0.13$	0.0171	0.0077	0.0054
with $f = 0.33$	0.0258	0.0112	0.0078

Table 8.23: Projections for statistical errors on $\Delta\Gamma_{CP}/\Gamma$ for combining lifetimes from different modes and for using all modes for 2, 10 and 20 fb^{-1}. The values $\Delta\Gamma_{CP}/\Gamma = 0.15$ and $f = 0.229$ are used for the main results and the results for other values of $\Delta\Gamma_{CP}/\Gamma$ and f are also shown for comparison.

The statistical error can be improved by including also the $J/\psi \to e^+e^-$ decay mode

for the J/ψ reconstruction. The increase in statistics is less than by a factor of 2 since the BTeV ECAL acceptance is smaller than the muon detector and there is no dedicated $J/\psi \to e^+e^-$ trigger.

It should also be noted that additional measurements of the CP-even rate and especially of the CP-odd rate, even with low statistics, can have a very significant effect on the $\Delta\Gamma_{CP}/\Gamma$ sensitivity. Unfortunately the CP-odd modes look difficult experimentally. For example, two CP-odd modes are $B_s^0 \to J/\psi f_0(980)$ and $B_s^0 \to \chi_{c0}\phi$. The $f_0(980)$ is relatively broad compared to the ϕ^0 and decays to $\pi\pi$ or KK and thus will have large backgrounds. The χ_{c0} has small branching fractions, and the dominant decays are to non-resonant states with pions and kaons and thus will also be background challenged. However it will still be worthwhile looking for these CP-odd states.

8.7.3 Summary of Projections for ΔΓ

The most sensitive direct measurement of $\Delta\Gamma_{B_s}$ will be from measuring the lifetime differences between decays to CP-specific final states, (*i.e.* to CP-even, CP-odd or CP-mixed modes) and flavor specific decays.

The decay modes to flavor specific final states like $D_s\pi$ will be the most precisely measured. Other decays with larger branching fractions that can be reconstructed with high efficiency and good signal-to-background will be to CP-mixed final states, like $J/\psi\,\phi$ and $D_s^{(*)+}D_s^{(*)-}$ involving at least one $D_s^{(*)}$. These decays proceed through an unknown admixture of CP-even and CP-odd amplitudes that must be determined experimentally via an angular analysis. The error on $\Delta\Gamma_s/\Gamma_s$ obtained using these modes will be very sensitive to the actual fractions of CP-even and CP-odd, where the sensitivity is poorest for equal mixtures of CP-even and CP-odd.

The decays to purely CP-even or purely CP-odd final states are difficult experimentally, either because the backgrounds are larger and/or the branching fractions are small (*e.g.* for $D_s^+D_s^-$, $J/\psi K_s$ and $J/\psi f_0(980)$), or they contain difficult to reconstruct neutrals in the final state (*e.g.* like in $J/\psi\eta^{(\prime)}$). However it is important to try to use these decay modes as even with small samples of events they improve the error on the $\Delta\Gamma_s/\Gamma_s$ measurement significantly.

With 2 fb^{-1} CDF should be able to determine $\Delta\Gamma_s/\Gamma_s$ with a statistical error of 0.04 through lifetime measurements, improving to as good as 0.025 if the decay to $D_s^{*+}D_s^{*-}$ proceeds through a 100% CP-even amplitude. CDF can reach a statistical error of 0.01 on a *model dependent* determination of $\Delta\Gamma_s/\Gamma_s$ using just branching ratio measurements.

With a vertex (hadronic) trigger at Level-1 and excellent particle identification and neutral reconstruction, the BTeV experiment should be able to measure the lifetimes of the purely CP-even or purely CP-odd final states well enough to give a model independent determination of $\Delta\Gamma_s/\Gamma_s$ with a statistical error of smaller than 0.02 with 2 fb^{-1} of data. This error is further decreased as low as 0.01 if the decay to $D_s^{*+}D_s^{*-}$ proceeds through a 100% CP-even amplitude. With 20 fb^{-1} of data a statistical error of 0.005 on $\Delta\Gamma_s/\Gamma_s$ should be obtainable. Systematic uncertainties are expected to be under control to a similar level.

8.8 Projections for Lifetimes

8.8.1 *b* Hadron Lifetimes at CDF †

Lifetime measurements have formed an important part of the CDF research program in b physics since the 1992 introduction of the silicon vertex detector with its precision tracking capabilities. This part of the research program has been very successful, producing some of the most precise lifetime measurements with semi-inclusive data samples, but also the most precise measurements with exclusive channels. It is expected that the combination of the Tevatron's large $\bar{b}b$ cross section and precise tracking capabilities will continue to reap benefits in Run II, pushing the comparison between experiment and theoretical calculation to more stringent levels.

A lifetime measurement consists of reconstructing the decay point of a b hadron by tracing back its long-lived charged descendants. For instance, the decay $\overline{B}^0 \to e^-\overline{\nu}_e D^+ X$ is reconstructed by intersecting the e^- track with the trajectory of the D^+ meson; this trajectory in turn is reconstructed from its own daughters, such as in the decay $D^+ \to K^-\pi^+\pi^-$. The distance between the primary interaction vertex and the b decay vertex gives the flight distance of the b hadron. In Run I, this flight distance was measured most precisely in the plane transverse to the beam and the proper time of decay, ct, calculated with the formula

$$ct = \frac{L_{xy}\, m}{p_T}\,, \tag{8.199}$$

where L_{xy} is the transverse flight distance, m is the mass of the b hadron, and p_T is the momentum of the b hadron projected in the with respect to the beam direction transverse plane. The transverse momentum is calculated by combining the measured momenta of the charged daughter particles. Unlike the flight distance, this combination requires either the identification and reconstruction of all the daughter particles, as in the analyses of an exclusive hadronic channel, or a correction factor for the particles that are not reconstructed, as in the analyses of much larger semi-inclusive samples. A third possibility, applicable in some special circumstances, allows a constraint to be applied to the momentum of a single particle of known mass; this technique was not applied in Run I but may become more important in Run II with the advent of three-dimensional silicon tracking.

As opposed to the electron–positron machines at the $\Upsilon(4S)$ where only B^+ and B_d^0 mesons are produced, Tevatron produces the full spectrum of b hadrons. Due to this uniqueness in the following particular emphasize is put on lifetime measurements of B_s^0, B_c^0 and Λ_b.

8.8.1.1 Run I Results at CDF

The Run I CDF lifetime results are summarized in Figure 8.24. They represent a combination of several analyses of different types but have one thing in common: all data samples have been obtained by using the trigger on at least one high-momentum lepton candidate.

†Authors: Ch. Paus, J. Tseng.

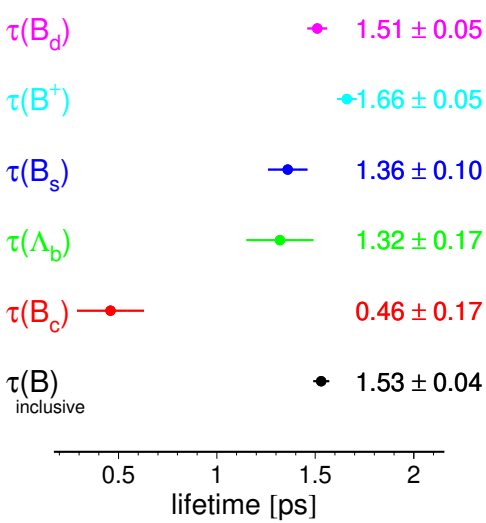

Figure 8.24: Summary of lifetime measurements from CDF during Run I.

Three different types of analyses are performed. There are the exclusive, the semi-exclusive and finally the inclusive analyses. While in the exclusive analyses one or more distinct b hadron decay channels are fully reconstructed, in the semi-inclusive analyses some neutral particle cannot be reconstructed, most typically the neutrino from the semileptonic b hadron decay. In the inclusive analyses the secondary vertex indicates the presence of a b hadron but no attempt is made to reconstruct the mass explicitly.

The features of the different analysis types are complementary. Exclusive analyses usually have small data samples and thus a large statistical uncertainty but the systematic uncertainty is small. Inclusive analyses have usually very large data samples and thus small statistical uncertainties but the systematic errors are large.

The exclusive modes measured also used the J/ψ trigger sample: in Run I, these analyses yield 436 ± 27 decays of the type $B^0 \to \psi(1S,2S)K^{(*)0}$, 824 ± 36 of the type $B^+ \to \psi(1S,2S)K^{(*)+}$, and 58 ± 12 of the mode $B_s \to J/\psi\,\phi$. As will be detailed in the following sections, the B_s lifetime thus measured is expected to mostly reflect the lifetime of the shorter-lived weak eigenstate of the B_s. A small sample of $\Lambda_b \to J/\psi\Lambda^0$ decays was also reconstructed but was too small for lifetime analysis in light of the large $B^0 \to J/\psi K^0_S$ backgrounds. The systematic errors are due to background and resolution modeling and detector alignment.

For the semi-exclusive modes the B^0, B^+, B_s, and Λ_b hadrons are measured using their semileptonic decays. The charm daughters $D^{(*)}$, D_s, and Λ_c^+ are reconstructed in data.

Since these decays contain neutrinos as well as possible unreconstructed intermediate states such as the D^{**}, they are subject to systematic uncertainties due to production and decay modeling, as well as uncertainties in background and resolution and detector alignment.

An inclusive $b \to J/\psi X$ lifetime is also measured, where the $J/\psi \to \mu^+\mu^-$ is registered on a dilepton trigger, as well as the lifetime of the B_c meson through its decays to $J/\psi\ell X$.

The lifetime measurements have also yielded measurements of the lifetime ratio between charged and neutral B mesons. The measurement of lifetime ratios is particularly interesting since experimental uncertainties and theoretical uncertainties cancel out and thus allow more sensitive tests of some aspects of the theory of heavy quarks. Combining the exclusive and the semileptonic decay modes yields a ratio of 1.09 ± 0.05 in agreement with the world average 1.07 ± 0.02 and both well within the range of the theoretical prediction $1.0 - 1.1$.

The lifetime ratio between B_s and B^0 has not yet been measured with sufficient precision to test the prediction which is within ≈ 1 percent of unity. The experimental value of the lifetime ratio of the Λ_b to the B^0 is of similar precision, but lies well below the current theoretical prediction range of $0.9 - 1.0$. More data is needed to clarify whether there is a discrepancy. From the theoretical point of view baryons are more difficult to calculate and thus the experimental data will hopefully shed some light on this area.

8.8.1.2 Run II Projections for CDF

To derive the expected lifetime uncertainties for the Run II data samples it is assumed that the Run I measurements are statistically limited. This is certainly true for the exclusive decay modes. For the other decay channels it is less clear although experience shows that most systematic errors can be improved when more statistics is available. Therefore in the following only the exclusive measurements are used to estimate the uncertainties on the b hadron lifetime measurements achievable with the Run II data samples. This is a conservative procedure and it is likely that CDF will do better. The increase in statistics for the exclusive decays involving $J/\psi \to \mu^+\mu^-$ with respect to Run I is obtained applying simple scale factors as summarized in section 6.2.2.

Leptonic Triggers Considering the lifetime measurement capabilities of CDF in Run II, it is useful as a first step to make a direct extrapolation from the Run I lifetime analyses of exclusive channels. These are shown in Table 8.24, assuming 2 fb^{-1} of J/ψ dimuon triggers with increased muon coverage, lower muon trigger thresholds, and increased silicon tracking cover. The projected uncertainties are only statistical, and, given Run I experience, are likely to be comparable to the levels of systematic uncertainty. Other improvements, not accounted for in the table, include the possibility of a di-electron trigger, which adds approximately 50% more data, and the effect of smaller-radius silicon as well as three-dimensional microstrip tracking, which improves S/N and hence the lifetime measurements.

It is evident from the table that already the projections of only the exclusive decay modes as measured by CDF in Run I improves on the current world-averaged B^-/B^0 lifetime ratio and combined with other experiments, including the B factories, this ratio will be very precisely known.

	Run 1	Run 2	projected
Species	sample size	sample size	$c\tau$ error [ps]
B^-	824	40000	0.01
B^0	436	20000	0.01
B_s	58	3000	0.03
Λ_b	38	2000	0.04

Table 8.24: Run II projections for the Run I exclusive lifetime measurements at CDF corresponding to 2 fb^{-1}.

In the case of the B_s, however, since the $J/\psi\,\phi$ final state is mostly sensitive to one weak eigenstate, it is useful primarily in measuring $\Delta\Gamma_s$ rather than the average Γ_s which is to be compared with Γ_d. The $\Lambda_b \to J/\psi\Lambda^0$ lifetime is expected to be known within 0.04 ps — significantly better than the current world average — but depends upon being able to more effectively distinguish the signal from $B^0 \to J/\psi K^0_S$ decays, which are topologically very similar.

Comparable projections for B_c and Ξ_b exclusive lifetime analyses cannot be made, since their exclusive decays were not observed in Run I data.

Hadronic Triggers Beyond the $J/\psi \to \ell^+\ell^-$ trigger samples, there are expected to be large data samples that will be made available by the hadronic displaced-track trigger. Although those samples will also improve on the B^- and B^0 lifetimes most interestingly they will improve on the B_s and Λ_b lifetime measurements. Since the hadronic trigger is a new hardware device all predictions are less certain than the predictions for decay modes originating from the leptonic triggers.

Most branching fractions for the decay modes used below are not measured and have to be estimated. This is particularly difficult for the Λ_b decay modes. Errors of 50 percent for the B_s decays and 100 percent for the Λ_b decays are assumed.

Another principle difficulty in these data samples lies in the understanding of the effect of the trigger on the lifetime distributions. The displaced vertex trigger prefers large lifetime events and introduces a bias in the proper time distribution. In the following it is assumed that it is possible to model the trigger bias and use all of the statistical power of the projected yields.

For the B_s decay modes $D_s\pi$ and $D_s\pi\pi\pi$ there are approximately 75k events projected. This includes the D_s decay modes to $\phi\pi$ and K^*K only, as indicated in Table 8.10. Further it is expected that the signal to background ratios is one, which is rather conservative. This results in an uncertainty of the B_s lifetime of approximately 0.007 ps.

For the lifetime ratio of B_s and B^0 this corresponds to an error of roughly half a percent and is thus in the same order as the theoretical prediction for the deviation from unity.

For the Λ_b decay modes $\Lambda_c\pi(\Lambda_c \to pK\pi)$, $pD^0\pi(D^0 \to K\pi$ and $D^0 \to K\pi\pi\pi)$, $p\pi$ and pK there are approximately 24.4k events projected. Again assuming a signal to background ratio of one, a statistical uncertainty of 0.01 ps is obtained. This is more precise than the

expectation from the $J/\psi\Lambda^0$ decay mode. A stringent test will be available for the theoretical predictions of the lifetime ratio of Λ_b to B^0.

More inclusive strategies, using triggerable combinations of leptons and displaced tracks, will also significantly increase the precision of the lifetime ratios of the rarer b hadrons, such as the B_c and so far by CDF not observed baryons as Ξ_b might be accessible. These strategies have yet to be investigated in detail.

8.8.2 Lifetime measurements at DØ [†]

A rich spectroscopy and lifetime measurement program is planned for both beauty mesons and baryons. We will study any species that has significant decay modes that result in at least one lepton. One of the highlights of this program is a measurement of the Λ_b lifetime in the exclusive decay mode $\Lambda_b \to J/\psi + \Lambda$. This is particularly interesting since the measured ratio $\tau(\Lambda_b)/\tau(B_d) = 0.78 \pm 0.04$ [107] is significantly different from the naive spectator model prediction of unity. Current theoretical understanding of non-spectator processes such as final-state quark interference and W boson exchange cannot account for such a large deviation. Another important measurement which we will make is a measurement of the B_s lifetime using modes such as $B_s \to J/\psi\phi$.

Measurements of the Λ^0_b baryon lifetime have long been hampered by a dearth of statistics. For this reason, the lifetime was measured in the semileptonic decay mode, where the branching fraction is orders of magnitude higher than for any fully reconstructed mode [108–111]. The disadvantage of the semileptonic mode is that the neutrino information is lost. To obtain the true decay length in the absence of neutrino information, the ratio $p_T(\Lambda_c\ell)/p_T(\Lambda^0_b)$ (called the K factor) was obtained from a Monte Carlo calculation and used in the lifetime fit. The limited knowledge of the value of the K factor represented a modest contribution to the uncertainty of this measurement.

In Run II at DØ we can expect to collect 2 fb^{-1} of $p\overline{p}$ collisions or twenty times the statistics of Run 1. This provides the opportunity to probe the Λ^0_b lifetime in a fully reconstructed mode: $\Lambda^0_b \to J/\psi\Lambda^0$, where the J/ψ meson decays into two leptons (muon or electron) and the Λ^0 baryon decays into a proton and a pion. Using a fully reconstructed channel avoids the introduction of the K factor and any uncertainty associated with it.

To study this mode, we generated 75 000 Λ^0_b baryon events using Pythia, simulated the DØ Run II detector using MCFast, and forced the decay mode $\Lambda^0_b \to J/\psi\Lambda^0$, followed by $J/\psi \to \mu^+\mu^-$ and $\Lambda^0 \to p\pi^-$ with QQ, the CLEO Monte Carlo program. We use this sample to predict the trigger and reconstruction acceptances and to estimate the lifetime resolution. For the purpose of this study, we assume that electrons from J/ψ decays will be reconstructed with a similar efficiency to that of the muons, an assumption which is expected to be approximately true.

The DØ J/ψ triggeridentifies events resembling J/ψ decays. The presence of two muon tracks, each with $|\eta| \leq 2.0$ and $p_T \geq 1.5$ GeV/c, is sufficient for passing the J/ψ trigger criteria. The trigger acceptance is found to be 16.8% for the muons in these generated

[†] Author: W. Taylor.

Multiplier	Events
$\mathcal{L} = 10^{32}$ cm^{-2}s^{-1} $= 10^{36}$ m^{-2}s^{-1}	
$t = 2 \times 10^7$ s	
$\sigma_{b\bar{b}} = 158$ μb $\times 10^{-28}$ m^2/b	
$b, \bar{b} = 2$	6.32×10^{11}
$\mathcal{B}(b \to \Lambda_b^0) = 0.090$	5.7×10^{10}
$\mathcal{B}(\Lambda_b^0 \to J/\psi \Lambda^0) = 4.7 \times 10^{-4}$	2.7×10^7
$\mathcal{B}(J/\psi \to \mu\mu, ee) = 2 \times 0.06$	3.2×10^6
$\mathcal{B}(\Lambda^0 \to p\pi) = 0.639$	2.0×10^6
Detector acceptance $= 0.55$	1.1×10^6
ϵ(trigger) $= 0.168$	1.9×10^5
ϵ(track efficiency) $= 0.95^4$	1.5×10^5
ϵ(reconstruction) $= 0.096$	14 850

Table 8.25: Event yield determination after 1 year or 2 fb^{-1}.

Monte Carlo events. We introduce by hand an additional acceptance cut of 55% for the holes in the muon detection system not modeled in MCFast.

Track quality cuts are applied to all the tracks in the events passing the trigger. The muon tracks from the J/ψ decay are required to have at least four stereo hits in the tracking system (silicon detector and central fiber tracker combined) and at least eight hits (stereo and axial combined) in the silicon detector. For tracks in the central region ($|\eta| \leq 1.7$), at least fourteen hits are required in the central fiber tracker. The transverse momentum is required to be above 400 MeV/c.

The Λ^0 baryon daughters are required to have at least three stereo hits in the tracking system (silicon detector and central fiber tracker combined) and a minimum of eight hits in the central fiber tracker. The transverse momentum is required to be above 400 MeV/c. The long lifetime of the Λ^0 baryon prevents the use of strict silicon hit requirements, as the Λ^0 baryon often decays outside of the fiducial volume of the silicon detector.

The muons are constrained to come from a common vertex in three dimensions as are the Λ^0 daughters. Finally, the location of the Λ_b^0 decay vertex is obtained by extrapolating the Λ^0 baryon momentum direction in three dimensions back to the J/ψ decay vertex. The resulting vertex defines the decay length of the Λ_b^0 baryon.

The acceptance for these selection criteria is 9.6%. We introduce by hand an additional acceptance cut of $(0.95)^4$=0.81 for the tracking efficiency not modeled in MCFast. The final acceptance times efficiency for the trigger and reconstruction criteria is 0.72%. We therefore predict about 15 000 events to be reconstructed in 2 fb^{-1}. Table 8.25 shows the values used to obtain this prediction for the yield.

The mass distributions for the J/ψ and Λ^0 particles are shown in Figures 8.25 and 8.26, respectively. With the application of constraints on both the J/ψ mass and the Λ^0 mass, we predict the Λ_b^0 mass resolution to be 16 MeV/c^2, as indicated in Figure 8.27. The lifetime resolution is found to be 0.11 ps (Figure 8.28).

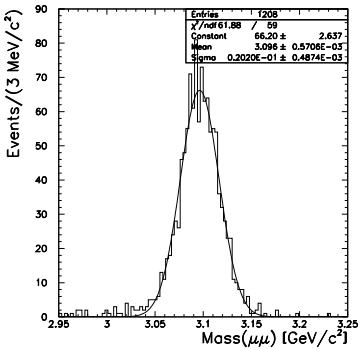

Figure 8.25: J/ψ mass distribution.

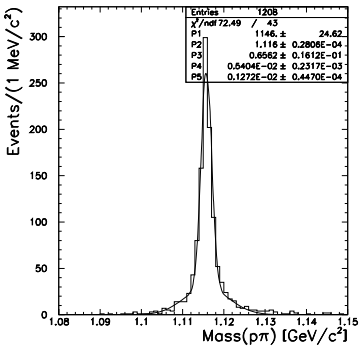

Figure 8.26: Λ^0 mass distribution.

8.8.3 Summary of Projections for Lifetimes

The exclusive b hadron event samples involving $J/\psi \to \mu^+\mu^-$ alone will enable CDF and DØ during Run II to push the precision of lifetime measurements to values close to 1 fs. Further inclusion of other hadronic decay modes will decrease the statistical error further below 1 fs.

In particular the lifetime measurements of B_s and Λ_b which cannot be measured by the B factories will achieve a statistical precision of about 0.007 ps and 0.01 ps, respectively. Those measurements determine the ratio of $\tau(B_s)/\tau(B^0)$ to roughly half a percent which allows a first test of the theoretical predictions.

Lifetimes of other interesting b hadrons like the B_c will be improved significantly, and there is a good chance to observe Ξ_b for the first time and measure its lifetime.

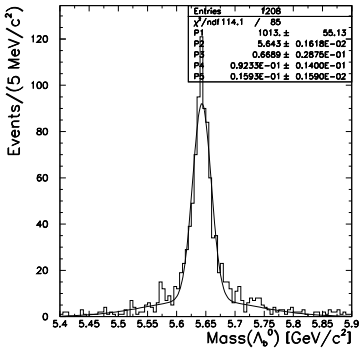

Figure 8.27: Λ_b^0 mass distribution.

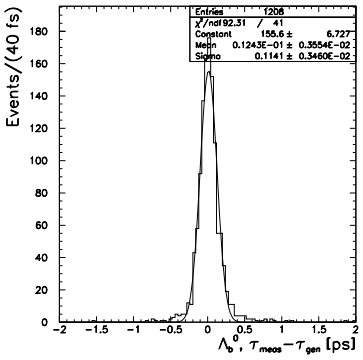

Figure 8.28: $\tau(\Lambda_b^0)_{meas} - \tau(\Lambda_b^0)_{gen}$.

8.9 Conclusions

The Tevatron provides a unique testing ground for mixing and lifetime studies. For these measurements it is superior to the B-factories, because the large boosts of the produced hadrons and the higher statistics allow to study the decay distributions more precisely. Moreover, studies of B_s mesons and b-flavored baryons are not possible at current B-factories running at the $\Upsilon(4S)$ resonance. At Run II B_s^0–$\overline{B}_s^0$ mixing will be discovered and the mass difference Δm_s will be determined very precisely. This measurement is of key importance for the phenomenology of the unitarity triangle. Our knowledge of the lifetime pattern of b-flavored hadrons will significantly improve, the yet undetected width difference $\Delta\Gamma_s$ between the B_s mass eigenstates is within reach of Run II and the Λ_b lifetime puzzle will be addressed.

References

[1] Particle Data Group, Eur. Phys. J. **C 3** (1998) 1.

[2] M.A. Shifman and M.B. Voloshin, (1981) unpublished, presented in the review V.A.Khoze and M.A. Shifman, Sov. Phys. Usp. 26 (1983) 387.

[3] M.A. Shifman and M.B. Voloshin, Sov. J. Nucl. Phys. 41 (1985) 120.

[4] M.A. Shifman and M.B. Voloshin, Sov. Phys. JETP 64 (1986) 698.

[5] B. Chibisov, R.D. Dikeman, M.A. Shifman, and N. Uraltsev, Int. J. Mod. Phys. A12 (1997) 2075.

[6] I. Bigi, M. Shifman, N. Uraltsev, and A. Vainshtein, Phys. Rev. D59 (1999) 054011.

[7] I.I. Bigi, N.G. Uraltsev, and A.I. Vainshtein, Phys. Lett. B293 (1992) 430; [E: B297 (1993) 477].

[8] B. Guberina, S. Nussinov, R. Peccei, and R. Rückl, Phys. Lett B89 (1979) 11.

[9] N. Bilić, B. Guberina, and J. Trampetić, Nucl. Phys. B248 (1984) 261.

[10] I. Bigi, B. Blok, M.A. Shifman, and A. Vainshtein, Phys. Lett. B323 (1994) 408.

[11] G. Altarelli and S. Petrarca, Phys. Lett. B261 (1991) 303.

[12] E. Bagan, P. Ball, V.M. Braun, and P. Gosdzinsky, Phys. Lett. B342 (1995) 362.

[13] Q. Hokim and X.Y. Pham, Phys. Lett. B122 (1983) 297; Ann. Phys. (NY) 155 (1984) 202.

[14] Y. Nir, Phys. Lett. B221 (1989) 184.

[15] A. Czarnecki and M. Jezabek, Phys. Lett. B427 (1994) 3.

[16] E. Bagan, P. Ball, V.M. Braun and P. Gosdzinsky, Nucl. Phys. B432 (1994) 3.

[17] M.B. Voloshin, Int. J. Mod. Phys. A11 (1996) 4931.

[18] M.B. Voloshin, Surv. High En. Phys. 8 (1995) 27.

[19] P. Ball and V. Braun, Phys. Rev. D49 (1994) 2472.

[20] M. Neubert, Trieste Summer School Lectures, Report CLNS 00/1660, Jan. 2000; [hep-ph/001334].

[21] M. Neubert and C.T. Sachrajda, Nucl. Phys. B483 (1997) 339.

[22] M.A. Shifman and M.B. Voloshin, Sov. J. Nucl. Phys. 45 (1987) 292.

[23] M.B. Voloshin, Phys. Lett. B385 (1996) 369.

[24] H.-Y. Cheng, Phys. Rev. D56 (1997) 2783.

[25] B. Guberina and B. Melić, Eur.Phys.J. C2 (1998) 697.

[26] Particle Data Group. *1999 WWW Update*, http://pdg.lbl.gov/1999/bxxx.html

[27] UKQCD Collaboration: M. Di Pierro, C.T. Sachrajda, and C. Michael, Univ. of Southampton report SHEP 99-07, June 1999; [hep-lat/9906031].

[28] M.B. Voloshin, Phys. Rep. 320 (1999) 275.

[29] M.B. Voloshin, Phys.Rev. D61 (2000) 074026.

[30] M.B. Voloshin, Phys.Lett. B476 (2000) 297.

[31] A. J. Buras, M. Jamin and P. H. Weisz, Nucl. Phys. B **347**, 491 (1990).

[32] C. Bernard, Nucl. Phys. Proc. Suppl. **94**, 159 (2001).

[33] A. Stocchi, talk at *ICHEP 2000 Conference*, 7 Jul – 2 Aug 2000, Osaka, Japan.

[34] M. Ciuchini *et al.*, hep-ph/0012308.

[35] L. Wolfenstein, preprint no. NSF-ITP-90-29 (unpublished), and Phys. Rev. D43 (1991) 151. A. J. Buras, M. E. Lautenbacher, G. Ostermaier, Phys. Rev. D50 (1994) 3433.

[36] M. Beneke, G. Buchalla, C. Greub, A. Lenz and U. Nierste, Phys. Lett. B **459**, 631 (1999).

[37] S. Hashimoto and N. Yamada, hep-ph/0104080.

[38] M. Beneke, G. Buchalla and I. Dunietz, Phys. Rev. **D54** (1996) 4419.

[39] S. Hashimoto, Nucl. Phys. Proc. Suppl. **83-84** (2000) 3.

[40] N. Yamada et al. (JLQCD coll.), contr. to the *18th Intern. Symposium on Lattice Field Theory (Lattice 2000)*, Bangalore, India, 17-22 Aug 2000, hep-lat/0010089.

[41] K. Hartkorn and H. G. Moser, Eur. Phys. J. **C8** (1999) 381.

[42] I. Bigi, B. Blok, M. Shifman, N. Uraltsev and A. Vainshtein, in *B decays*, ed. S. Stone, revised 2nd edition, p. 132–157, hep-ph/9401298. M. Neubert and C. T. Sachrajda, Nucl. Phys. **B483** (1997) 339. Y. Keum and U. Nierste, Phys. Rev. **D57** (1998) 4282.

[43] R. Barate *et al.* [ALEPH coll.], Phys. Lett. **B486** (2000) 286.

[44] R. Aleksan, A. Le Yaouanc, L. Oliver, O. Pène and J. C. Raynal, Phys. Lett. **B316** (1993) 567.

[45] M. A. Shifman and M. B. Voloshin, Sov. J. Nucl. Phys. **47** (1988) 511.

[46] I. Dunietz, R. Fleischer and U. Nierste, hep-ph/0012219.

[47] Y. Grossman, Phys. Lett. **B380** (1996) 99.

[48] Report of the *b*-decay Working Group of the Workshop *Standard Model Physics (and More) at the LHC*, P. Ball *et al.*, CERN-TH/2000-101 [hep-ph/0003238].

[49] I. Dunietz, Phys. Rev. **D52** (1995) 3048.

[50] F. Abe *et al.* [CDF Collaboration], Phys. Rev. **D59** (1999) 032004. A. Borgland *et al.* [DELPHI Collaboration], talk at *EPS-HEP 99 conference*, 15–21 Jul 1999, Tampere, Finland.

[51] M. Acciarri *et al.* [L3 Collaboration], Phys. Lett. **B438** (1998) 417.

[52] A. Lenz, U. Nierste and G. Ostermaier, Phys. Rev. D **59**, 034008 (1999).

[53] H. Yamamoto, Nucl. Phys. Proc. Suppl. **65** (1998) 236; Phys. Lett. **B401** (1997) 91.

[54] I. I. Bigi and N. G. Uraltsev, Nucl. Phys. B **592**, 92 (2001).

[55] J. L. Rosner, Phys. Rev. D**42**, 3732 (1990).

[56] A. S. Dighe, I. Dunietz, H. J. Lipkin and J. L. Rosner, Phys. Lett. B**369**, 144 (1996).

[57] A. S. Dighe, I. Dunietz and R. Fleischer, Eur. Phys. J. C **6**, 647 (1999).

[58] M. Paulini and K. Burkett, CDF/ANAL/BOTTOM/CDFR/4665 (1998).

[59] I. Dunietz, H. R. Quinn, A. Snyder, W. Toki and H. J. Lipkin, Phys. Rev. D**43**, 2193 (1991).

[60] A. S. Dighe and S. Sen, Phys. Rev. D**59**, 074002 (1999).

[61] A. S. Dighe, I. Dunietz and R. Fleischer, Phys. Lett. B**433**, 147 (1998).

[62] R. Fleischer and I. Dunietz, Phys. Rev. D**55**, 259 (1997).

[63] P. Ball *et al.*, hep-ph/0003238.

[64] G. Bonvicini *et al.*, CLEO conf 98-23, ICHEP98 852.

[65] We note that this need not be the case in some specific scenarios, *e.g.*, supersymmetry with R-parity violation.

[66] See, for example, J.L. Hewett, T. Takeuchi, S. Thomas, in *Electroweak Symmetry Breaking and Beyond the Standard Model*, ed. by T. Barklow, *et al.* (World Scientific, Singapore) 1996, hep-ph/9603391.

[67] Y. Grossman, Y. Nir, M. Worah, *Phys. Lett.* **B407**, 307 (1997).

[68] S. Bergmann and G. Perez, hep-ph/0103299; G. Eyal and Y. Nir, Jour. H. E. Phys. **9909**, 013 (1999); G. Barenboim, G. Eyal, and Y. Nir, *Phys. Rev. Lett.* **83**, 4486 (1999).

[69] S.L. Glashow and E. Jenkins, *Phys. Lett.* **B196**, 223 (1987); V. Barger, J.L. Hewett, and R.J.N. Phillips, *Phys. Rev.* **D41**, 3421 (1990); A.J. Buras *et al.*,, *Nucl. Phys.* **B337**, 284 (1990); J.F. Gunion and B. Grzadkowski, *Phys. Lett.* **B243**, 301 (1990).

[70] For a review, see, Y. Okada, lectures given at *Int. Symp. on Supersymmetry, Supergravity and Superstrings*, Seoul, Korea, 23-26 Jun 1999, hep-ph/9910457.

[71] G. Burdman, K. Lane, and T. Rador hep-ph/0012073; G. Buchalla, G. Burdman, C.T. Hill, and D. Kominis *Phys. Rev.* **D53**, 5185 (1996); G. Beall, M. Bander, and A. Soni, *Phys. Rev. Lett.* **48**, 848 (1982).

[72] D. Atwood, L. Reina, and A. Soni, *Phys. Rev.* **D55**, 3156 (1997); Y. Nir and D. Silverman, *Phys. Rev.* **D42**, 1477 (1990); H. Dreiner in *Perspectives on Supersymmetry*, ed. by G.L. Kane, World Scientific, hep-ph/9707435.

[73] A. Datta, *Z. Phys.* **C27**, 515 (1985); S. Nandi, L. Zhang, *Phys. Rev.* **D41**, 240 (1990).

[74] E. Golowich, and A. Petrov, *Phys. Lett.* **B427**, 172 (1998); G. Burdman, hep-ph/9407378, hep-ph/9508349; H. Georgi, *Phys. Lett.* **B297**, 353 (1992); T. Ohl *et al.*,, *Nucl. Phys.* **B403**, 605 (1993).

[75] H. Nelson, talk given at the 19^{th} *International Symposium on Lepton Photon Interactions at High Energies*, Stanford, CA, Aug 1999, hep-ex/9908021.

[76] P. Sphicas, *A* $b\bar{b}$ *Monte Carlo Generator*, CDF Note 2655, (1999);
K. Anikeev, P. Murat, Ch. Paus, *Description of Bgenerator II*, CDF Note 5092, (1999);

[77] P. Nason, S. Dawson and R.K. Ellis, Nucl. Phys. **B303** (1988) 607; Nucl. Phys. **B327** (1989) 49.

[78] C. Peterson *et al.*, Phys. Rev. **D27** (1983) 105.

[79] P. Avery, K. Read and G. Trahern, Cornell Internal Note CSN-22, 1985 (unpublished).

[80] T. A. Keaffaber, J. D. Lewis, M. W. Bailey, D. Bortoletto, S. Tkaczyk, A. F. Garginkel, *Measurement of the B Meson Differential Cross Section Using the Exclusive Decay* $B \to J/\psi K$, CDF Note 4911 (to be updated, 2000).

[81] F. Abe *et al.*, The CDF Collaboration, Phys. Rev. **D60** (1999) 92005.

[82] C. Caso, *et al.* [Particle Data Group], Eur. Phys. Jor. **C15** (2000) 1.

[83] CDF Run II Technical Design Report.

[84] The CDF Collaboration, Update to Proposal P-909: *Physics Performance of the CDF II Detector with An Inner Silicon Layer and A Time of Flight Detector*, Submitted to the Fermilab Director and PAC (1999)

[85] S. Belforte *et al.*, *A Complete Minimum Bias Event Generator*, CDF Note 4219.

[86] C. Caso, *et al.* [Particle Data Group], Eur. Phys. Jor. **C3** (1998) 1.

[87] F. Parodi, P. Roudeau and A. Stocchi, Nuovo Cim. **A112** (1999) 833.

[88] Particle Data Group, Eur. Phys. J. **C 15** (2000) 1.

[89] F. Abe *et al.* [CDF Collaboration], Phys. Rev. **D59** (1999) 032004.

[90] F. Abe *et al.* [CDF Collaboration], Phys. Rev. Lett. **82** (1999) 3576.

[91] BTeV Preliminary Technical Design Report.

[92] F. Abe *et. al.* [The CDF Collaboation], Phy. Rev. **D54**, 6596 (1996).

[93] P. McBride and S. Stone, Nucl. Instrum. Meth. **A368**, 38 (1995).

[94] BTeV Collaboration, *Proposal for an Experiment to Measure Mixing, CP Violation and Rare Decays in Charm and Beauty Particle Decays at the Fermilab Collider – BTeV*, May 2000.

[95] K.T. McDonald, *Maximum Likelihood Analysis of CP Violating Asymmetries*, PRINCETON-HEP-92-04, Sep 1992. 12pp, unpublished.

[96] F. Abe *et al.* [CDF Collaboration], Phys. Rev. **D59** (1999) 032004.

[97] F. Abe *et al.* [CDF Collaboration], Phys. Rev. Lett. **77** (1996) 1945.

[98] F. Abe *et al.* [CDF Collaboration], Phys. Rev. Lett. **75** (1995) 3068, Phys. Rev. Lett. **85** (2000) 4668.

[99] I. Dunietz, R. Fleischer, U. Nierste, *In Pursuit of New Physics with* B_s *Decays*, CERN-TH/2000-333 [hep-ph/0012219].

[100] F. Abe *et al.*, *Phys. Rev. Lett.* 77(1996)1945.

[101] R. Aleksan, A. Le Yaouanc, L. Oliver, O. Pène, J.-C. Raynal, *Phys. Lett.* **B317** (1993) 173.

[102] R. Aleksan, A. Le Yaouanc, L. Oliver, O. Pène, J.-C. Raynal, *Phys. Lett.* **B316** (1993) 567.

[103] The ALEPH Collaboration, CERN-EP/2000-036, to be submitted to *Phys. Lett.* **B**.

[104] T. Affolder *et al.*, CDF Collaboration, Phys. Rev. Lett. **85** (2000) 4668.

[105] P. L. Frabetti *et al.*, E687 Collaboration, Phys. Rev. Lett. **70** (1993) 1755.

[106] F. Abe *et al.*, *Phys. Rev. Lett.* 77(1996)1945.

[107] LEP B Lifetime Working Group, http://home.cern.ch/~claires/lepblife.html.

[108] ALEPH Collaboration, R. Barate *et al.*, *Measurement of the b Baryon Lifetime and Branching Fractions in Z Decays*, Eur. Phys. J. **C2**, (1998) 197.

[109] CDF Collaboration, F. Abe *et al.*, *Measurement of the* Λ_b^0 *Lifetime Using* $\Lambda_b^0 \to \Lambda_c^+ \ell^- \overline{\nu}$, Phys. Rev. Lett. **77**, (1996) 1439.

[110] DELPHI Collaboration, P. Abreu *et al.*, *Determination of the Average Lifetime of b Baryons*, Z. Phys. **C71**, (1996) 199.

[111] OPAL Collaboration, K. Ackerstaff *et al.*, *Measurements of the* B_s^0 *and* Λ_b^0 *Lifetimes*, Phys. Lett. **B426**, (1998) 161.

Chapter 9

Production, Fragmentation and Spectroscopy

G. Bodwin, E. Braaten, K. Byrum, R.K. Ellis, G. Feild, S. Fleming, W. Hao, B. Harris, V.V. Kiselev, E. Laenen, J. Lee, A. Leibovich, A. Likhoded, A. Maciel, S. Menary, P. Nason, E. Norrbin, C. Oleari, V. Papadimitriou G. Ridolfi, K. Sumorok, W. Trischuk, R. Van Kooten

The Tevatron is distinguished from the other current facilities involved in the study of particles containing heavy quarks by the size of the cross sections and the range of hadrons containing heavy quarks which are produced. The production of heavy quarks at the Tevatron and their subsequent fragmentation to a wide range of states is the subject of the present chapter. These processes offer a unique chance to study the dynamics of heavy quark systems in a region where perturbative methods can be applied.

9.1 Open beauty production

We outline the state of the art in theoretical calculations of B hadron production at a hadron collider. We refer to this as open beauty production to distinguish it from quarkonium production considered in Section 9.2. We follow up with some considerations of the experimental difficulties involved in measuring open beauty production at the Tevatron. We do not draw any firm conclusion beyond the fact that theory and experiment disagree by a factor of about 3. The discrepancy favors the experiments by providing three times as many b quarks as theory would expect.

9.1.1 The theory of b-quark production[†]

The cross section for the production of a b quark is calculable in perturbative QCD inasmuch as the heavy quark mass, m, is larger than Λ, the scale of the strong interactions. The results of the calculations are described in refs. [1–5].

[†]Author: R.K. Ellis

The cross section in the QCD improved parton model is

$$\sigma(S) = \sum_{i,j} \int \frac{dx_1}{x_1}\frac{dx_2}{x_2}\, \hat{\sigma}_{ij}(x_1x_2S, m^2, \mu^2) F_i(x_1,\mu^2) F_j(x_2,\mu^2) \ , \tag{9.1}$$

where the F_i are the momentum densities of the partons in the incoming hadrons. The quantity $\hat{\sigma}_{ij}$ is the short distance cross section

$$\hat{\sigma}_{ij}(\hat{s}, m^2, \mu^2) = \sigma_0\ c_{ij}(\hat{\rho}, \mu^2) \ , \tag{9.2}$$

where $\sigma_0 = \alpha_s^2(\mu^2)/m^2$, $\hat{\rho} = 4m^2/\hat{s}$ and $\hat{s} = x_1x_2S$ is the parton total center-of-mass energy squared. The function c_{ij} has a perturbative expansion,

$$c_{ij}(\hat{\rho}, \mu^2/m^2) = c_{ij}^{(0)}(\hat{\rho}) + 4\pi\alpha_s\Big[c_{ij}^{(1)}(\hat{\rho}) + \ln(\frac{\mu^2}{m^2})\bar{c}_{ij}^{(1)}(\hat{\rho})\Big] + O(\alpha_s^2) \ . \tag{9.3}$$

The lowest order short distance cross section is calculated from the diagrams in Fig. 9.1. The results for the lowest order total cross sections derived from these diagrams are

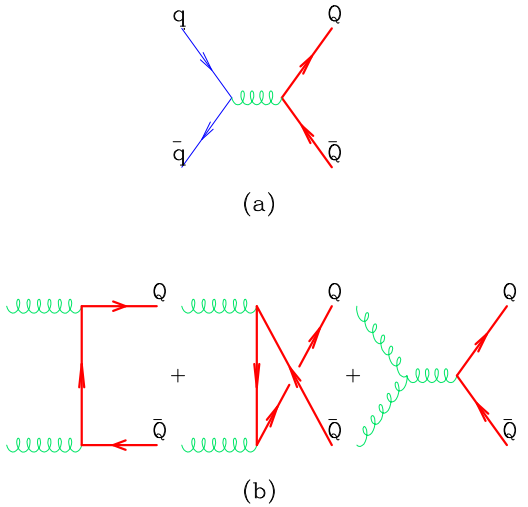

Figure 9.1: Diagrams for heavy quark production at lowest order.

$$c_{gg}^{(0)}(\rho) = \frac{\pi\beta\rho}{12}\left\{\frac{3}{N}\Big[(1+\rho-\frac{\rho^2}{2})L(\beta) - 1 - \rho\Big] + \frac{N}{2V}\Big[3\rho^2 L(\beta) - 4 - 5\rho\Big]\right\} ,$$
$$c_{q\bar{q}}^{(0)}(\rho) = \frac{V}{N^2}\frac{\pi\beta\rho}{24}[2+\rho] \ , \tag{9.4}$$

where $V = N^2 - 1 = 8, N = 3$ and $\beta = \sqrt{1-\rho}, \rho = 4m^2/\hat{s}$ and

$$L(\beta) = \frac{1}{\beta}\log\Big[\frac{1+\beta}{1-\beta}\Big] \ . \tag{9.5}$$

The quantities $\bar{c}_{ij}^{(1)}$ and $c_{ij}^{(1)}$ are also known [1], the former analytically and the latter as a numerical fit. The results for these functions as a function of the incoming $\hat{s}$ are shown in Figs. 9.2, 9.3 and 9.4. Two features of $c_{ij}^{(1)}$ as shown in Figs. 9.2, 9.3 and 9.4 are worthy

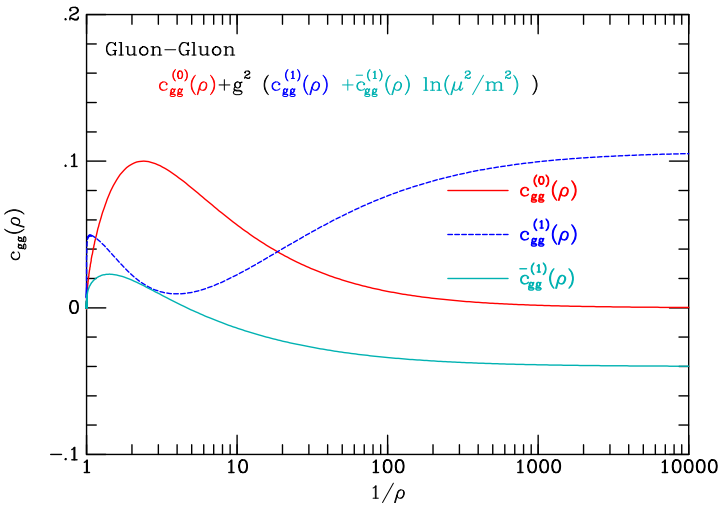

Figure 9.2: The parton level cross section for the gg process.

of note. The quark-antiquark and gluon-gluon initiated processes have a very rapid rise at threshold:

$$c_{q\bar{q}}^{(1)} \to \frac{c_{q\bar{q}}^{(0)}(\rho)}{8\pi^2}\left[-\frac{\pi^2}{6\beta}+\frac{16}{3}\ln^2(8\beta^2)-\frac{82}{3}\ln(8\beta^2)\right],$$
$$c_{gg}^{(1)} \to \frac{c_{gg}^{(0)}(\rho)}{8\pi^2}\left[\frac{11\pi^2}{42\beta}+12\ln^2(8\beta^2)-\frac{366}{7}\ln(8\beta^2)\right], \qquad (9.6)$$

due to Coulomb $1/\beta$ singularities and to Sudakov double logarithms. Near threshold, these terms give large contributions and require special treatment, such as resummation to all orders. In addition the gg and gq contributions to $c_{ij}^{(1)}$, which involve spin-one gluon exchange in the t-channel, tend to a constant value at large $\hat{s}$. In agreement with the results in Figs. 9.2 and 9.4, the intercept at large s is given by

$$c_{gg} \to 6k \sim 0.1074\ , \qquad (9.7)$$
$$c_{gq} \to \frac{4}{3}k \sim 0.02388\ , \qquad (9.8)$$

where [6]

$$k = \frac{7291}{16200}\frac{1}{8\pi} \approx 0.01791\ . \qquad (9.9)$$

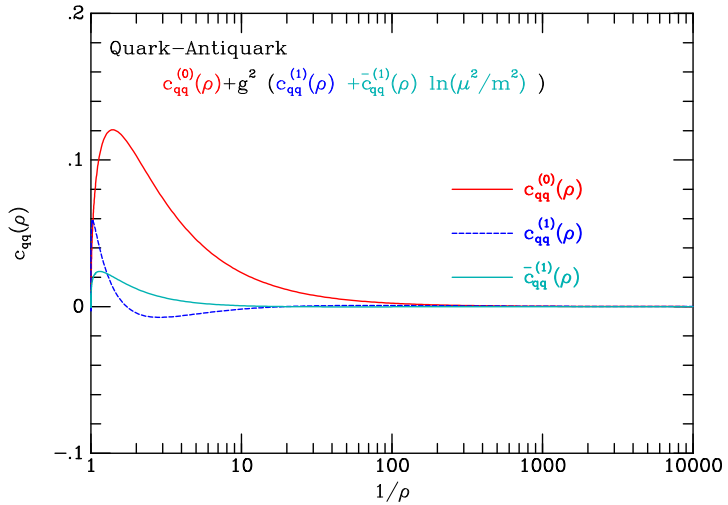

Figure 9.3: The parton level cross section for the $q\bar{q}$ process.

The significance of these results for the NLO cross section is shown in Fig. 9.5, illustrating that, at the energy of the Tevatron, both the threshold region and the large $\hat{s}$ region are important at NLO.

The resummation of the threshold soft gluon corrections is best carried out in ω-space, where ω is the moment variable after Mellin transform with respect to $\hat{s}$. In ω-space the threshold region corresponds to the limit $\omega \to \infty$ and the structure of the threshold corrections is as follows

$$\hat{\sigma} = \sigma^{LO}\Big\{1+\sum_{j=1}^{\infty}\sum_{k=1}^{2j} b_{jk}\alpha_s^j \ln^k\omega\Big\}\ . \qquad (9.10)$$

Detailed studies [7] indicate that such threshold resummation is of limited importance at the Tevatron where b-quarks are normally produced far from threshold. Resummation effects lead to minor changes in the predicted cross section and only a slight reduction in the scale dependence of the results.

At high energy, heavy quark production becomes a two scale problem, since $\hat{s} \gg m^2 \gg \Lambda^2$ and the short distance cross section contains logarithms of $\hat{s}/m^2$. As we proceed to higher energies such terms can only become more important, so an investment in understanding these terms at the Tevatron will certainly bear fruit at the LHC. At small ω the dominant terms in the heavy quark production short distance cross section are of the form

$$\hat{\sigma} \sim \frac{\alpha_s^2}{m^2}\sum_{j=0}^{\infty}\alpha_s^j\sum_{k=0}^{\infty}c_{jk}\Big(\frac{\alpha_s}{\omega}\Big)^k\ . \qquad (9.11)$$

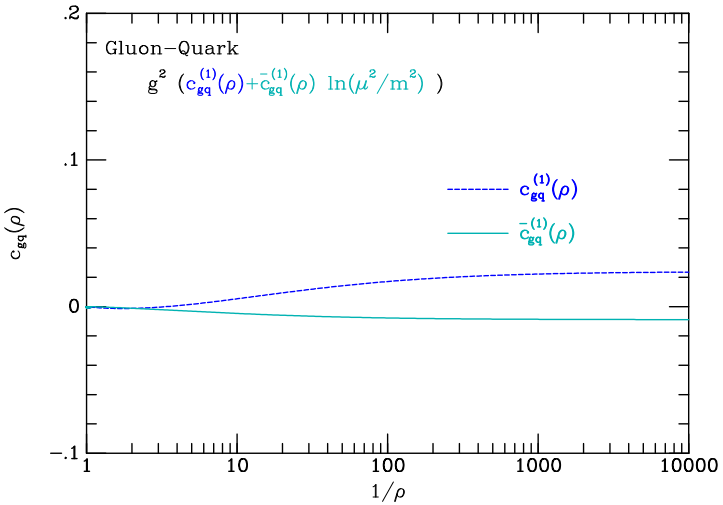

Figure 9.4: The parton level cross section for the gq process.

For $j = 0$ we obtain the leading logarithm series. Resummation of these terms has received considerable theoretical attention in the context of the k_T-factorization formalism [8–14].

In Ref. [15] an interpretation of the excess bottom-quark production rate at the Tevatron is proposed via the pair-production of light gluinos, of mass 12 to 16 GeV, with two-body decays into bottom quarks and light bottom squarks. Among the predictions of this SUSY scenario, the most clearcut is pair production of like-sign charged B mesons at the Tevatron collider.

9.1.2 Run II reach for b-quark production

We now consider some of the experimental boundary conditions on the determination of the cross-section for open beauty production at the Tevatron.

9.1.3 DØ Study of b Jet Production and Run II Projections †

The differential cross section for b-jet production as a function of jet transverse energy is obtained from a sample of muon tagged jets. We discuss b jets as an added tool for understanding b production, and use the present analysis to propose a follow up measurement in Run II. Focus on doubly tagged, two b-jet events should significantly reduce both theoretical and experimental uncertainties.

† Author: Arthur Maciel

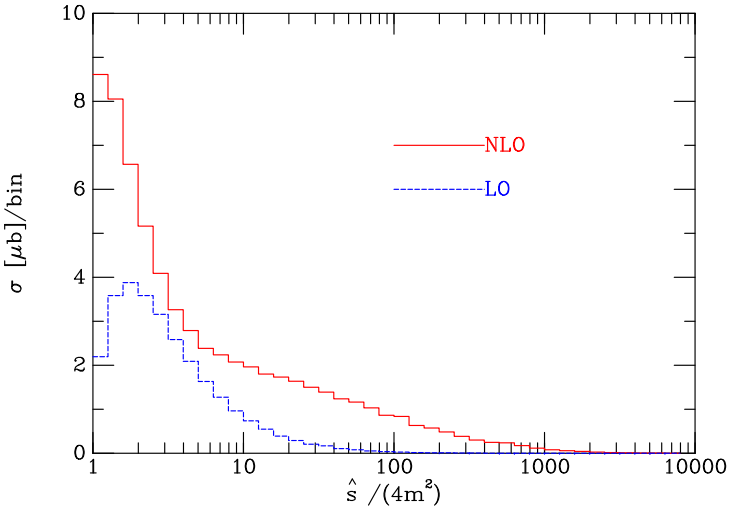

Figure 9.5: Contributions to the total cross section in LO and NLO.

9.1.3.1 Introduction

Previous studies on inclusive b production by the DØ collaboration have concentrated on the b quarks themselves, either as integrated production rates as a function of the b quark p_T^{min} [16], or the azimuthal correlations between the $b\bar{b}$ pair [17].

In contrast with such studies, we present a complementary measurement with the main focus on "b jets" rather than b quarks. "b jets" are defined as hadronic jets carrying b flavor. As such, the object of study is directly observable, and introduces less model dependence when the connection between observation and theory is made.

This measurement is in direct correspondence with a NLO-QCD calculation by S. Frixione and M. Mangano [19], who highlight the theoretical advantages of considering the cross section for producing jets rather than open quarks. For instance, large logarithms that appear at all orders in the open quark calculation (due to hard collinear gluons) are naturally avoided when all fragmentation modes are integrated and it no longer matters what portion of the jet energy is carried by heavy quarks or by radiation.

Following a brief presentation of our results, we try to assess what improvements over present measurements can be expected in Run II, taking into account the upgraded capabilities of the DØ detector. Moreover, we consider new experimental possibilities that might contribute to the ongoing process of understanding heavy quark production in the context of perturbative QCD.

9.1.3.2 The p_t Spectrum of b Jets

This measurement uses 5 pb^{-1} of Run I data from a muon plus jet trigger, from which an inclusive sample of muon tagged jets is extracted. Tagged jets have hadronic E_T above 20 GeV, pseudorapidity $\eta < 0.6$, and carry within their reconstruction cone ($\Delta R \equiv \sqrt{\Delta\eta^2 + \Delta\phi^2} = 0.7$) a muon track with p_T above 6 GeV and $\eta < 0.8$. About 36K events are thus selected, and less than 0.5% of them have either a second tagged jet or a doubly tagged one. This is because of the relatively high muon threshold, which also enriches the b flavor content of the sample.

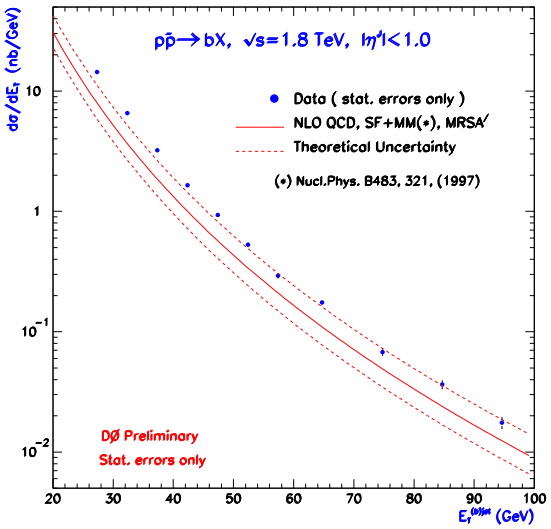

Figure 9.6: The differential b jet cross section and the next-to-leading order QCD prediction [19]. Data errors shown here are statistical only.

After detection efficiencies and resolution corrections are applied to the inclusive spectrum, the background of light flavors decaying to muons needs to be removed. This is done on a statistical basis, through fits of the distribution of muon transverse momentum with respect to the associated jet axis (P_T^{rel}). We use Monte Carlo templates representing light and heavy quark decay patterns. These templates are floated so as to fit the observed P_T^{rel} spectra in four different transverse energy ranges. Such fits determine the fraction of muons from b decay as a function of tagged jet E_T.

Tagging acceptance corrections are the last step towards a cross section. These stem from the tagging muon threshold, pseudorapidity ranges and the muon-jet association criterion.

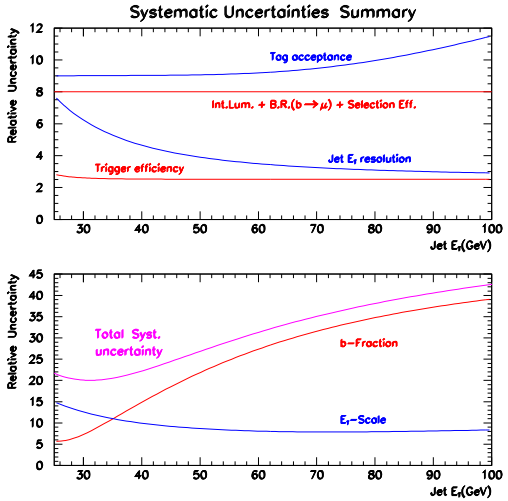

Figure 9.7: A summary of all systematic uncertainties expressed as a relative percentage.

The unseen lepton energy along the jet also needs to be added (statistically) to the hadronic portion registered in the calorimeter. After such corrections we obtain the b jet differential cross section shown in Fig. 9.6 and defined as the total number of jets carrying one or more b quarks in a given jet E_T bin, and within $|\eta| < 1$. ($\overline{b}$'s are not counted; technically we count tagging muons of either charge, and divide by twice the inclusive branching ratio of $b \to \mu + X$).

It is observed that this result repeats the general pattern of past b-production studies where data lies significantly above the central values of theory prediction, but not incompatibly so, considering both the experimental and theoretical uncertainties.

The measurement uncertainties are driven by the P_T^{rel} fits for the b-fraction, and to a lesser extent the tagging acceptance losses, and calorimeter energy scale at lower E_T. A summary of the systematic uncertainties (mostly correlated) in this measurement is shown in Fig. 9.7, and this leads us naturally to a discussion of Run II possibilities.

9.1.3.3 b Tagging for Run II

A detector with a precision vertex detector and a magnetic spectrometer should be able to study b jets. The measurement described above is limited in many directions by its tagging method. First, the b content of the sample decreases with jet E_T, and the P_T^{rel} fit

is not sensitive enough to extract a b signal reliably for jets above 100 GeV. Second, part of the advantage of studying b jets over b quarks is the removal of fragmentation model dependence. This dependence is partially reintroduced when corrections for muon tagging acceptances are performed.

The use of displaced vertex distributions for b tagging not only reduces the b fraction uncertainty to a secondary level in the analysis, but also removes the current upper limit on jet E_T imposed by the P_T^{rel} fits. Some fragmentation model dependence still remains associated with the determination of proper time distributions (decay lengths).

9.1.3.4 A Measurement Proposal

One puzzle that arises in the comparison of heavy flavor production data to theory is that despite the discrepancy in normalization, there is generally fair agreement in angular correlations [17,18,20]. This brings some conflict to the understanding of relative effects between the leading- and next-to-leading-order QCD amplitudes. The goal of resolving this puzzle, coupled with an interest in b jets, suggests a promising program for Run II.

In an attempt to minimize the current uncertainties on both theory and experiment, we consider a production measurement that is restricted to a limited kinematic regime to optimize uncertainties. We consider the cross section for pairs of b jets which are nearly back-to-back, have relatively high E_T and lie in the central rapidity region.

From the theoretical point of view, this experiment favors phase space regions that are far from production thresholds and have high x-values where PDF choices play a much reduced role. In addition, the back-to-back kinematics suppresses NLO amplitudes in the pQCD calculation [18].

From the experimental point of view there are many advantages. A muon plus jet trigger, very natural to the DØ architecture, (i) enhances the b-content of the sample, (ii) collects an ideal sample for a second tag by displaced vertex on the non-muon side and (iii) minimizes the bias towards soft b quarks inside hard jets because of the imposed muon p_T threshold.

9.1.3.5 Di-b-jets with DØ in Run II.

Inspection of Run I DØ data shows that over 70% of the muons in a muon plus jet trigger are naturally associated with a jet. Double tagging (of the b and $\overline{b}$ jets with muon and displaced vertex) improves b purity, and largely removes the limitations that are inherent to the P_T^{rel} fits method, in particular the limitation to low E_T because of increasing systematic uncertainties with b jet E_T.

For acceptance projections we take the Run I measurement as a starting point: 36K events in 5 pb^{-1} of data. The requirement of a recoil jet (central, opposite hemisphere) having $E_T \geq 20$ GeV reduces the sample to 15K muon tagged (p_T above 6 GeV) back-to-back dijet events. With a vertex tagging rate near 10% for the opposite jet, we can establish a rule of thumb of 300 events per pb^{-1}.

To access the transverse momentum of the b quark inside the muon tagged jet, we can focus on the tagging muon p_T spectrum (see next section). By applying the methods in reference [16] for determining the minimum b quark p_T compatible with our muon and jet thresholds, we find $p_T^{min}(b)$ around 20 GeV.

9.1.3.6 b Quark Production

A natural extension to the Run I b-jets study presented above is to use the same data sample and study b quarks rather than b jets. This offers a consistency check of our previous measurements [16,17], but also significantly extends the kinematic reach.

Starting from the data sample described in Section 9.1.3.2 we repeat the analysis steps of [16] to obtain the integrated b quark production cross section as a function of minimum b quark p_T. Our results are shown in Fig. 9.8 as the higher p_T^{min} points (triangles). In this figure, the present (and preliminary) measurement is confronted with previous results from DØ, CDF (resonant dimuons), and theory [5].

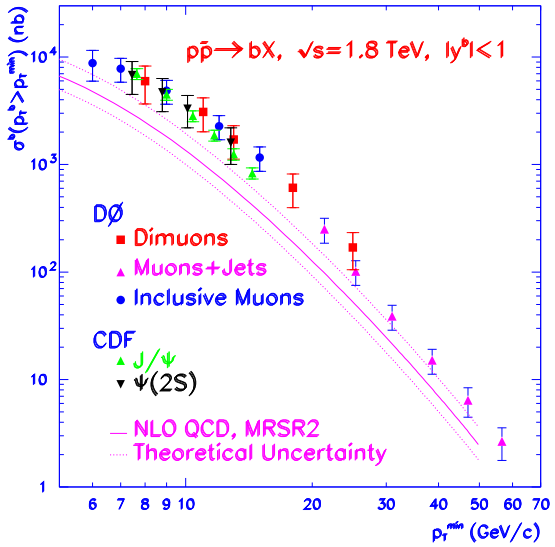

Figure 9.8: A summary of b production (integrated) cross section measurements, shown as a function of minimum b-quark p_T. The preliminary analysis described here is represented by the higher $p_T^{min}(b)$ triangles. The QCD prediction is also shown.

The consistency of the measurements is good. Our new results practically double the p_T^{min} reach to 60 GeV. A general trend that can be extracted from Fig. 9.8 is that data and theory agree better at higher p_T^{min}.

Of course this trend could be confirmed with extended and improved measurements in Run II. But the inclusive muon method described in this section has some limitations. Our uncertainties are dominated by systematics rather than statistics. Because the b-quark signal increases with muon p_T, b tagging with P_T^{rel} as a function of muon p_T is more precise than with jet E_T. It is the model dependence, introduced in relating the b-quark thresholds to the muon acceptance, that completely dominates the uncertainties in this type of measurement.

The full reconstruction of specific B-meson final states avoids some uncertainties. The CDF experiment [21] probes a lower B-meson p_T where the comparison of data to theory exhibits some of the same characteristics as the earlier measurements ($p_T^{min}(b) < 30$ GeV) in Fig. 9.8. It will be interesting to push fully reconstructed B-meson cross-sections to higher meson p_T. Various triggering and offline selection handles exist that could significantly extend meson p_T range. Such studies however lie beyond the scope of the present report.

9.1.3.7 Conclusion

We have presented a Run I cross-section measurement of jets carrying b flavor, and have illustrated the experimental advantages of studying b jets (which are complementary to b quarks). The b quark cross section extracted from the same data sample confirms previous measurements and significantly extends the b quark p_T reach, while hinting at improved agreement between data and theory at higher b p_T.

For Run II, a related measurement is envisaged that (i) focuses on dijets (doubly tagged) rather than single jets and (ii) restricts the kinematic region of the final states to reduce systematic uncertainties both in the theory and the measurements.

A muon plus jet(s) trigger is one of the strengths of the DØ experiment, and a center piece for various other physics projects. In Run II DØ will for the first time have an internal magnetic volume for precision tracking and vertexing. A muon tagged jets sample is an ideal starting point for the displaced vertex tagging of "other side" jets.

Our brief analysis demonstrates the possibility of a very useful and relatively fast measurement for early Run II.

9.1.4 CDF P_T Reach in the B Cross Section for Run II [†]

The differential cross section for $B \to D^0 + e + X$ as a function of B-hadron p_T is studied using Monte Carlo events. We predict the p_T reach for such a measurement in Run II.

The discrepancy between the next-to-leading order QCD predictions and the published Tevatron cross-sections remains unsolved. Recently, M. Cacciari, M. Greco and P. Nason [22] have presented a cross section formalism which is less sensitive to the renormalization and factorization scales at larger b-quark p_T ($p_T^b > 50$ GeV/c). We estimate the P_T reach for the B cross section using the exclusive decay $B \to D^0 + e + X$.

[†] Author: Karen Byrum

9.1.4.1 Run II P_T Reach

We use the PYTHIA Monte Carlo program to generate $b\bar{b}$ and use CLEO QQ [24] to decay the B mesons. The simulated sample is normalized to Run I data to provide a prediction of the cross section reach for Run II.

In Run II, CDF does not foresee low E_T inclusive single lepton triggers as were available in Run I. Still, we calculate Run II yields first using Run I trigger thresholds and then using the expected Run II higher thresholds. We include the following assumptions:

- an electron trigger similar to Run Ib with kinematic cuts on the electron of $E_T >$ 8 GeV and $p_T >$7.5 GeV/c or the proposed in Run II threshold of $E_T >$ 12 GeV;
- the Run Ib measured trigger efficiency;
- the electron selection efficiencies predicted by the CDF-II detector simulation;
- kinematic cuts on the D^0 decay products of $P_{Tot}^{\pi} > 0.5$ GeV/c, $P_{Tot}^{K} >$1.5 GeV/c, $\Delta(R) <$ 0.6 for both π, K; and
- a scale factor equal to the luminosity increase for Run I of 20.

Using the above assumptions, we estimate the number of $B \to D^0 eX$ events above some p_T^{min} and use this number to estimate the size for the statistical precision for a given p_T^{min}. The true statistical uncertainty will be larger than this and will depend on the signal-to-noise ratio of the D^0 mass peak. From the Run I data, we estimate that the statistical uncertainty will be a factor of two times greater than that determined from a signal-only Monte Carlo. This scale factor is conservative since we have not applied lifetime cuts to our Run I sample and these cuts are known to greatly increase the signal to noise ratio which would reduce the statistical uncertainty, approaching the predictions from a signal-only Monte Carlo.

We estimate the systematic uncertainty using the published $b \to eX$ measurement [23]. The uncertainties from that measurement are shown in Table 9.1. By measuring the B meson cross section as opposed to the b-quark cross section, we should be able to remove the systematics due to fragmentation of the b quark into a B meson from the measurement.

Source	Uncertainty
Models of B decays	10%
Underlying event contribution	8%
Hadron simulation	10%
B hadron semileptonic decay branching ratio	10%
Luminosity	7%
Total	20%

Table 9.1: Uncertainties in the published $b \to eX$ measurement [23] which are expected to contribute at the same level in Run II.

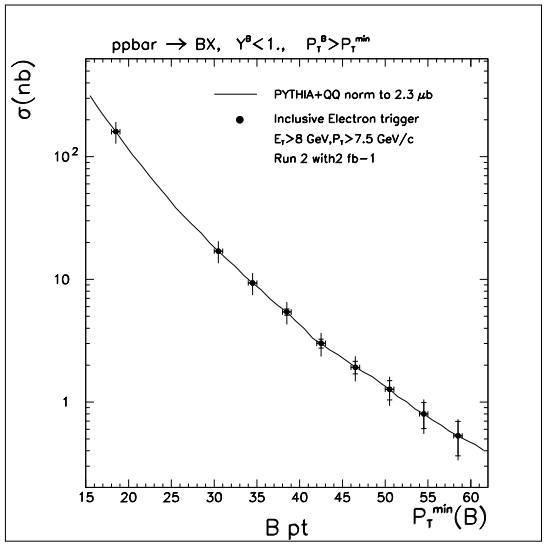

Figure 9.9: The predicted cross section reach as of function of B P_T for $B \to D^0 eX$ with the kinematic cut on the electron of $E_T > 8$ GeV and $P_T > 7.5$ GeV/c with 2 fb^{-1} of luminosity. The statistical errors are predicted from Monte Carlo and scaled by a factor of two to include the effect of background. A constant 20% systematic error is based on published results.

However there will still be an uncertainty on the theoretical prediction. The other uncertainties may be more difficult to reduce even with large statistics. For Run II we estimate a total systematic uncertainty of 20%.

9.1.4.2 Conclusions

The predicted p_T reach for $B \to D^0 eX$ with a kinematic cut on the electron of $E_T > 8$ GeV and $p_T > 7.5$ GeV/c for 2 fb^{-1} is shown in Figure 9.9. The statistical uncertainties come from our signal-only Monte Carlo simulation and scaled by a factor of two as an estimate of the influence of background. A flat 20% systematic error is based on published results [23].

We also show the predicted p_T reach for kinematic cut on the electron of $E_T > 12$ GeV for 2 fb^{-1} in Figure 9.10. The p_T requirement reduces the number of events in the largest B meson p_T bins by a modest 20%.

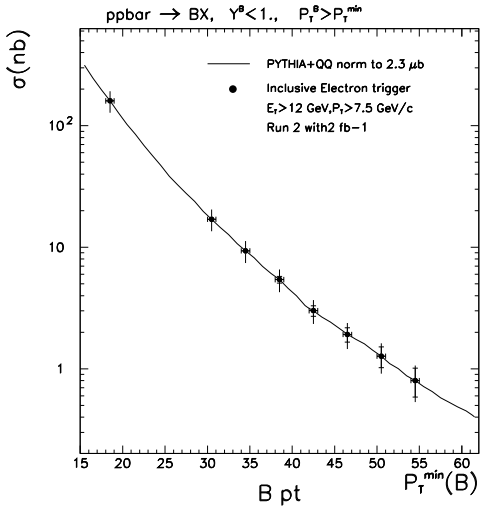

Figure 9.10: The predicted cross section reach as of function of B P_T for $B \to D^0 eX$ with the kinematic cut on the electron of $E_T > 12$ GeV/c with 2 fb^{-1} of luminosity. The statistical errors are predicted from Monte Carlo and scaled by a factor of two to include the effect of background. A constant 20% systematic error is based on published results.

9.2 Quarkonium production

The two heavy quarkonium systems provided by nature are bottomonium ($b\bar{b}$ bound states) and charmonium ($c\bar{c}$ bound states). The clean signatures provided by the $J^{PC} = 1^{--}$ quarkonium states make them a particularly clear window for studying the dynamics of heavy quarks. Although the major thrust of this report is bottom quark physics, we will discuss charmonium as well as bottomonium, since the physics of these two systems is very similar.

9.2.1 Spectroscopy [†]

The charmonium and bottomonium systems have rich spectra of orbital and angular-momentum excitations. The masses of these states can be predicted using potential models whose parameters are tuned to reproduce the spectrum of observed states. Some of the states that have not yet been discovered should be produced abundantly at the Tevatron. The obstacle to their discovery is finding a decay mode with a large enough branching fraction that can be used as a trigger.

[†] Author: Eric Braaten

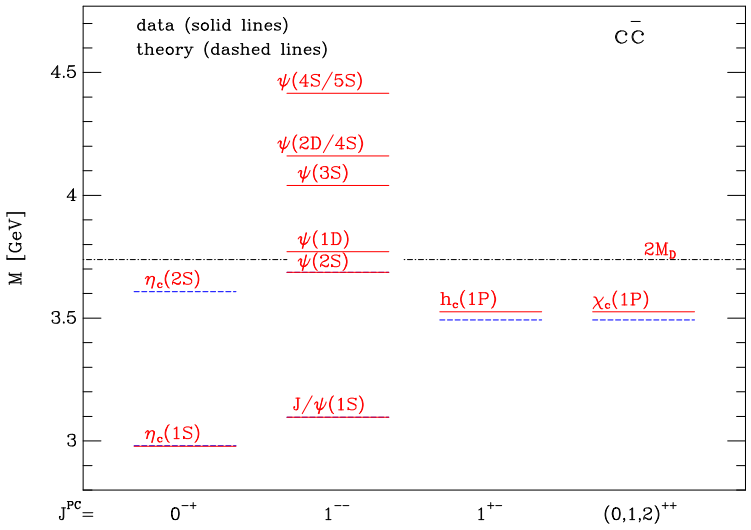

Figure 9.11: Spectrum of $c\bar{c}$ mesons: observed states (dotted red lines) and theoretical predictions (dashed blue lines). The $\chi_c(1P)$ lines are averaged over the spin states.

The charmonium spectrum is shown in Fig. 9.11. The observed states are shown as dotted (red) lines and the theory predictions are shown as dashed (blue) lines. The most prominent of the missing states are the spin-singlet states $\eta_c(2S)$ and $h_c(1P)$. A signal for $h_c \to J/\psi\pi^0$ has been observed in $p\bar{p}$ annihilation at resonance, but has not been confirmed. The states in the spectrum that were observed by the CDF collaboration in Run I of the Tevatron are the J/ψ and $\psi(2S)$, through their decays into $\mu^+\mu^-$, and the $\chi_{c1}(1P)$ and $\chi_{c2}(1P)$, through their decays into $J/\psi\gamma$. The χ_{c1} and χ_{c2}, which have a mass splitting of only 45.7 MeV, were resolved by conversions of the decay photon into e^+e^- in the material of the detector. The D0 collaboration also observed a $J/\psi/\psi(2S)$ signal, but they were unable to resolve the two states.

The charmonium state with the greatest prospects for discovery at the Tevatron is the $\eta_c(2S)$. One possibility is through the radiative decay $\eta_c(2S) \to J/\psi + \gamma$, whose branching fraction is estimated to be about 10^{-3} [25,26]. This is much smaller than the branching fraction for $\chi_{cJ}(1P) \to J/\psi+\gamma$, which is about 27% for $J = 1$ and 14% for $J = 2$. In Run Ia, CDF observed about 1200 $\chi_c(1P)$ or $\chi_c(2P)$ candidates in a data sample of about 18 pb^{-1}. The cross section for $\eta_c(1S)$ is probably a little larger than that for $\chi_c(1P)+\chi_c(2P)$. Thus the rate for $\eta_c(2S) \to J/\psi + \gamma$ should be large enough to observe in Run II.

It is also possible that the $\eta_c(2S)$ could be discovered through one of its annihilation decay modes. However a prerequisite would be the observation of the $\eta_c(1S)$, since it has a larger cross section and it probably has a larger branching fraction into any triggerable

decay mode. Of the measured decay modes of the $\eta_c(1S)$, the most promising for observation at the Tevatron is $\eta_c \to \phi\phi$, with one ϕ decaying into $\mu^+\mu^-$ to provide a trigger and the other decaying into K^+K^-. This decay path has a branching fraction of about 2×10^{-6}, which is small compared to the 6% branching fraction for $J/\psi \to \mu^+\mu^-$. The muons from the decay of the ϕ will typically be softer than those from the decay of a J/ψ with the same p_T as the $\eta_c(1S)$. The steep dependence of the acceptance of the muons on their transverse momentum could give a large reduction factor compared to the acceptance for $J/\psi \to \mu^+\mu^-$. In Run Ia, CDF observed about 2×10^5 J/ψ candidates in a data sample of about 15 pb^{-1}, and the cross section for $\eta_c(1S)$ is probably several times larger than that for J/ψ. Thus the rate for $\eta_c \to \phi\phi$ may be large enough to observe in Run II.

The bottomonium spectrum is shown in Fig. 9.12. The observed states are shown

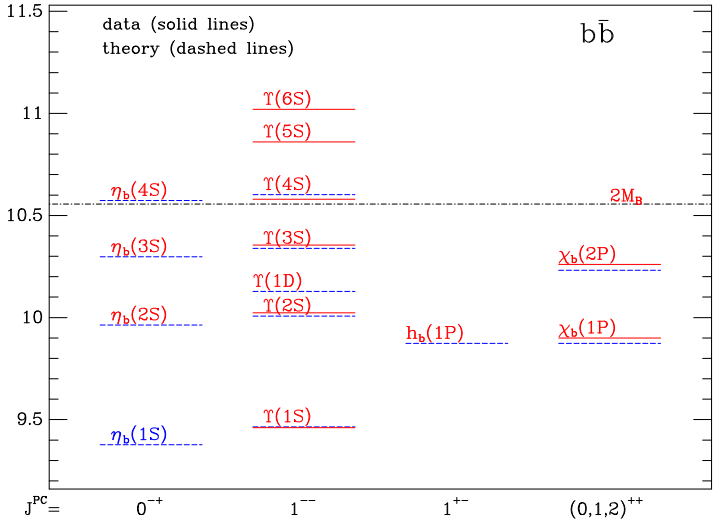

Figure 9.12: Spectrum of $b\bar{b}$ mesons: observed states (solid red lines) and theoretical predictions (dashed blue lines). The $\chi_b(1P)$ and $\chi_b(2P)$ lines are averaged over the spin states.

as dotted (red) lines and the theory predictions are shown as dashed (blue) lines. None of the spin-singlet states in the spectrum have been observed, not even the ground state $\eta_b(1S)$. The states in the spectrum that were observed by the CDF collaboration in Run I of the Tevatron are the $\Upsilon(1S)$, $\Upsilon(2S)$ and $\Upsilon(3S)$, (through their decays into $\mu^+\mu^-$), and the $\chi_{bJ}(1P)$ and $\chi_{BJ}(2P)$, (through their decays into $\Upsilon(nS)\gamma$). The $J = 0, 1, 2$ states of $\chi_{bJ}(nP)$ were not resolved. The D0 collaboration also observed a $\Upsilon(nS)$ signal, but they were unable to resolve the $n = 1, 2, 3$ states.

The bottomonium state with the greatest prospects for discovery at the Tevatron is the

ground state $\eta_b(1S)$. The discovery requires finding a triggerable decay mode with a large enough branching fraction. The branching fractions for exclusive decay modes of $\eta_b(1S)$ can not be predicted accurately. For final states containing light hadrons, a conservative estimate can be obtained by multiplying the corresponding branching fraction for $\eta_c(1S)$ by the appropriate suppression factor $(m_c/m_b)^n$ that would hold for asymptotically large quark masses. For the vector meson decay mode $\eta_b(1S) \to \rho\rho$, the appropriate factor is $(m_c/m_b)^4 \approx 10^{-2}$. A promising discovery mode at the Tevatron is $\eta_b(1S) \to J/\psi J/\psi$ [27], with one J/ψ decaying into $\mu^+\mu^-$ to provide a trigger and the other decaying into either $\mu^+\mu^-$ or e^+e^-. This decay has almost identical kinematics to $\eta_c(1S) \to \phi\phi$, whose branching fraction is 0.7%, except that all masses are scaled up by a factor of 3. The branching fraction for $\eta_b \to J/\psi J/\psi$ is probably smaller, but the suppression factor is probably not as severe as the asymptotic factor 10^{-2}. If the branching fraction for $\eta_b(1S) \to J/\psi J/\psi$ is greater than 10^{-4}, the prospects for the discovery of $\eta_b(1S)$ in Run II of the Tevatron look bright.

9.2.2 Theory of quarkonium production †

Heavy quarkonia (bottomonium and charmonium mesons) are to a good approximation nonrelativistic bound states consisting of a heavy quark and its antiquark. The bound-state dynamics involves both perturbative and nonperturbative aspects of QCD. Due to the large mass, m_Q, of the heavy quark, the bound-state dynamics can be described more simply using an effective field theory called *nonrelativistic QCD* (NRQCD) [28]. This effective field theory can be exploited to organize quarkonium production rates into systematic expansions in $\alpha_s(m_Q)$ and in v, the typical relative velocity of the heavy quark [29].

The physical picture of quarkonium production begins with a hard scattering that creates a heavy quark-antiquark pair in an angular momentum and color state that we will denote $b\bar{b}(n)$. The color state can be color-singlet ($b\bar{b}_1$) or color-octet ($b\bar{b}_8$). The angular momentum state is denoted by the standard spectroscopic notation $^{2S+1}L_J$. The $b\bar{b}$ subsequently evolves into the final state quarkonium H through nonperturbative dynamics that can be accurately described by the effective theory NRQCD.

The NRQCD factorization formula is the mathematical realization of the above picture. To be specific, we will focus on the production of spin-triplet bottomonium states. The inclusive differential cross section for producing a bottomonium state, H, in a proton-antiproton collision can be written as

$$d\sigma[p + \bar{p} \to H + X] \;=\; \sum_{ij} \int dx_1 dx_2 \; f_{i/p}(x_1) f_{j/\bar{p}}(x_2) \; d\sigma[ij \to H + X], \tag{9.12}$$

where the functions $f_{k/A}$ are parton distribution functions and the sum runs over the partons i and j in the initial state hadrons. The cross section $d\sigma[ij \to H + X]$ for the direct production of H by the collision of partons i and j can be written as the sum of products of short-distance cross sections and long-distance matrix elements:

$$d\sigma[ij \to H + X] \;=\; \sum_n d\hat{\sigma}[ij \to b\bar{b}(n) + X] \; \langle O^H(n) \rangle. \tag{9.13}$$

† Authors: Eric Braaten, Sean Fleming, Jungil Lee, Adam Leibovich

To obtain the completely inclusive cross section, one must also add the cross section for indirect production via the decay of higher bottomonium states. The short-distance cross section $d\hat{\sigma}$ can be calculated as a perturbative expansion in α_s evaluated at a scale of order m_Q or larger. The *NRQCD matrix element* $\langle O^H(n) \rangle$ encodes the probability for $b\bar{b}(n)$ to evolve into the quarkonium state H. Each of the NRQCD matrix elements scales as a definite power of v, allowing the sum over quantum numbers n in Eq. (9.13) to be truncated at some order in the v expansion. The approximate spin symmetry of NRQCD also implies relations between the matrix elements. Most of these matrix elements can be determined only by fitting them to production data. The exceptions are the color-singlet matrix elements with the same angular momentum quantum numbers as the bound state H, which can be related to the wavefunction of the meson. For the spin-triplet S-wave and P-wave bottomonium states, these color-singlet matrix elements can be expressed as

$$\langle O_1^{\Upsilon(nS)}(^3S_1) \rangle \simeq \frac{9}{2\pi} |R_{nS}(0)|^2, \tag{9.14}$$

$$\langle O_1^{\chi_{bJ}(nP)}(^3P_J) \rangle \simeq (2J+1) \frac{9}{2\pi} |R'_{nP}(0)|^2. \tag{9.15}$$

They can be extracted from data on annihilation decays, estimated from potential models, or calculated from first principles using lattice gauge theory simulations of NRQCD.

The NRQCD factorization formula provides a general framework for analyzing inclusive quarkonium production. Any model of quarkonium production that is consistent with QCD at short-distances must reduce to assumptions about the NRQCD matrix elements. For example, the *color-singlet model* assumes that only the color-singlet matrix elements with the same angular momentum quantum numbers as the bound state are important, namely $\langle O_1(^3S_1) \rangle$ for $\Upsilon(nS)$ and $\langle O_1(^3P_J) \rangle$ for $\chi_{bJ}(nP)$. To the extent that the *color-evaporation model* is consistent with QCD at short distances, it reduces to the assumption that the S-wave matrix elements $\langle O_1(^1S_0) \rangle$, $\langle O_1(^3S_1) \rangle$, $\langle O_8(^1S_0) \rangle$, and $\langle O_8(^3S_1) \rangle$ dominate and that they are equal up to color and angular momentum factors. However the color evaporation model is usually implemented by starting with the NLO cross section for producing $b\bar{b}$ pairs with invariant mass below the heavy meson threshold, imposing an ad hoc cutoff on the invariant mass of exchanged gluons, and multiplying by a phenomenological probability factor for each quarkonium state.

The effective field theory NRQCD also gives definite predictions for the relative importance of the NRQCD matrix elements, because they scale as definite powers of the typical relative velocity v. Given equal short-distance cross sections, the most important matrix element for direct $\Upsilon(nS)$ production should be the parameter $\langle O_1(^3S_1) \rangle$ of the color-singlet model. However the short-distance cross sections are not equal. From counting the color states, we expect the cross section for a color-octet $b\bar{b}$ pair to be about 8 times larger than the cross section for a color-singlet pair. There are also dynamical effects that enhance the color-octet cross section relative to that for $b\bar{b}_1(^3S_1)$ both at small p_T and at large p_T. At small p_T, the color-octet cross section is enhanced, because it can proceed through order-α_s^2 processes like $ij \to b\bar{b}$. At large p_T, the color-octet cross sections are enhanced because the leading order cross section for $b\bar{b}_1(^3S_1)$ is suppressed by m_b^4/p_T^4 relative to $b\bar{b}_8(^3S_1)$. According to NRQCD, the next most important matrix elements for direct $\Upsilon(nS)$ production

are suppressed by v^4 and can be reduced by spin-symmetry relations to three color-octet parameters $\langle O_8(^3S_1)\rangle$, $\langle O_8(^1S_0)\rangle$, and $\langle O_8(^3P_0)\rangle$ for each of the radial excitations $\Upsilon(nS)$. Including only these matrix elements, the NRQCD factorization formula (9.13) for direct $\Upsilon(nS)$ production reduces to

$$\sigma[\Upsilon(nS)] = \sigma[b\bar{b}_1(^3S_1)]\langle O_1^{\Upsilon(nS)}(^3S_1)\rangle + \sigma[b\bar{b}_8(^3S_1)]\langle O_8^{\Upsilon(nS)}(^3S_1)\rangle + \sigma[b\bar{b}_8(^1S_0)]\langle O_8^{\Upsilon(nS)}(^1S_0)\rangle + \left(\sum_J (2J+1)\sigma[b\bar{b}_8(^3P_J)]\right)\langle O_8^{\Upsilon(nS)}(^3P_0)\rangle. \quad (9.16)$$

NRQCD predicts that the most important matrix elements for the direct production of the P-wave states $\chi_{bJ}(nP)$ are suppressed by v^2 relative to $\langle O_1^{\Upsilon(nS)}(^3S_1)\rangle$. They can be reduced by spin symmetry relations to a color-singlet parameter $\langle O_1(^3P_0)\rangle$ and a single color-octet parameter $\langle O_8(^3S_1)\rangle$ for each radial excitation. Including only these matrix elements, the NRQCD factorization formula (9.13) for direct $\chi_{bJ}(nP)$ production reduces to

$$\sigma[\chi_{bJ}(nP)] = (2J+1)\left(\sigma[b\bar{b}_1(^3P_J)]\langle O_1^{\chi_{b0}(nP)}(^3P_0)\rangle + \sigma[b\bar{b}_8(^3S_1)]\langle O_8^{\chi_{b0}(nP)}(^3S_1)\rangle\right). \quad (9.17)$$

The factors of $2J+1$ comes from using spin-symmetry relations.

The NRQCD approach to quarkonium production is a phenomenologically useful framework only if the NRQCD expansion in (9.13) can be truncated after the matrix elements of relative order v^4. For S-waves, the truncation at order v^2 essentially reduces to the color-singlet model, which has been decisively ruled out by the CDF data on charmonium production in Run I [30,31]. Truncation at order v^6 introduces too many additional adjustable parameters to have any predictive power. In the NRQCD approach truncated at relative order v^4, the direct production of each S-wave radial excitation is described by four matrix elements $\langle O_1(^3S_1)\rangle$, $\langle O_8(^3S_1)\rangle$, $\langle O_8(^1S_0)\rangle$, and $\langle O_8(^3P_0)\rangle$. The production of each P-wave radial excitation is described by two matrix elements $\langle O_1(^3P_0)\rangle$ and $\langle O_8(^3S_1)\rangle$. The NRQCD framework has considerable flexibility, because the color-octet matrix elements are all adjustable parameters, but it is still restrictive enough to have predictive power. Since the color-octet matrix elements are predicted to dominate at large p_T, the NRQCD approach has sometimes been called the *color-octet model*. This terminology should be avoided, because NRQCD predicts that some production processes are dominated by color-singlet matrix elements. The phrase *NRQCD model* would more accurately reflect the theoretical assumptions that are involved.

The short-distance cross sections $d\hat{\sigma}$ in Eq. (9.13) can be calculated using perturbative QCD. Most of the parton cross sections required by the NRQCD approach have been calculated only to leading order in α_s. There are three regions of p_T that require somewhat different treatments: $p_T \ll 2m_b$, $p_T \sim 2m_b$, and $p_T \gg 2m_b$. The simplest region is $p_T \sim 2m_b$. Here the leading order cross sections are of order α_s^3 and come from the parton processes $ij \to b\bar{b} + k$. For lack of a better term, we refer to these as the *fusion cross sections*. The fusion cross sections are known only to leading order in α_s [32,33]. If they could be calculated to next-to-leading order, it would allow for more accurate predictions for quarkonium production in the region $p_T \sim 2m_b$.

That the region $p_T \gg 2m_b$ must be treated differently can be seen from the behavior of the fusion cross sections as $p_T \to \infty$. The order-α_s^3 cross sections $d\hat{\sigma}/dp_T^2$ fall like m_b^4/p_T^8 for $b\bar{b}_1(^3S_1)$, like m_b^2/p_T^6 for $b\bar{b}_1(^3P_J)$, $b\bar{b}_8(^1S_0)$, and $b\bar{b}_8(^3P_J)$, and like $1/p_T^4$ for $b\bar{b}_8(^3S_1)$. At higher orders in α_s, all the $b\bar{b}$ channels will exhibit the scaling behavior $d\hat{\sigma}/dp_T^2 \sim 1/p_T^4$. The scaling contributions can be expressed in the form

$$d\hat{\sigma}[ij \to b\bar{b}(n) + X] = \int_0^1 dz\, d\hat{\sigma}[ij \to k + X]\, D_{k\to b\bar{b}(n)}(z), \quad (9.18)$$

where $D_{k\to b\bar{b}(n)}(z)$ is the fragmentation function that specifies the probability for a parton k produced by a hard scattering to "decay" into a $b\bar{b}$ pair in the state n with a fraction z of the parton's longitudinal momentum. The fragmentation functions begin at order α_s for $b\bar{b}_8(^3S_1)$, at order α_s^2 for $b\bar{b}_1(^3P_J)$, $b\bar{b}_8(^1S_0)$, and $b\bar{b}_8(^3P_J)$, and at order α_s^3 for $b\bar{b}_1(^3S_1)$. They have all been calculated only to leading order in α_s, with the exception of the $b\bar{b}_8(^3S_1)$ fragmentation function, which has been calculated to next-to-leading order [34]. If they could all be calculated to order α_s^3, it would allow more accurate predictions for quarkonium production at large p_T.

That the region $p_T \ll 2m_b$ must be treated differently can be seen from the behavior of the fusion cross sections as $p_T \to 0$. The order-α_s^3 cross sections $d\hat{\sigma}/dp_T^2$ for $b\bar{b}_1(^3S_1)$ and for $b\bar{b}_1(^3P_1)$ are well-behaved in this limit, but those for $b\bar{b}_1(^3P_{0,2})$, $b\bar{b}_8(^3S_1)$, $b\bar{b}_8(^1S_0)$, and $b\bar{b}_8(^3P_J)$ diverge like $1/p_T^2$. These are precisely the channels in which a $b\bar{b}$ pair can be created at $p_T = 0$ by the order-α_s^2 parton process $ij \to b\bar{b}$. If the cross section is integrated over p_T, the singular term proportional to $1/p_T^2$ in the cross section for $ij \to b\bar{b} + g$ is canceled by a singular term proportional to $\delta(p_T^2)$ in the next-to-leading order correction to the cross section for $ij \to b\bar{b}$, so that the cross section integrated over p_T is finite. These next-to-leading order corrections have been calculated [35], and they allow the cross section integrated over p_T to be calculated to next-to-leading order. However what is really needed to compare with the Tevatron data is the differential cross section in p_T. To turn the naive perturbative prediction for $d\hat{\sigma}/dp_T^2$, which includes $1/p_T^2$ terms from $ij \to b\bar{b} + g$ and $\delta(p_T^2)$ terms from $ij \to b\bar{b}$, into a smooth p_T distribution requires taking into account multiple soft-gluon radiation. Reasonable prescriptions for doing this are available, but they have not yet been applied to this problem. This is the biggest obstacle to more quantitative analyses of quarkonium production at the Tevatron.

9.2.2.1 Bottomonium

A pioneering NRQCD analysis of the CDF data on bottomonium production in Run IA of the Tevatron was carried out by Cho and Leibovich [32]. An updated NRQCD analysis of the CDF data from Run Ib was recently carried out in Ref. [27]. An alternative analysis that uses PYTHIA to take into account some of the effects of soft gluon radiation has been presented in Ref. [37]. In the analysis of Ref. [27], the color-singlet matrix elements were extracted from Υ decay data or estimated using potential models. The color-octet matrix elements were extracted from the CDF cross sections for $\Upsilon(1S)$, $\Upsilon(2S)$, and $\Upsilon(3S)$ and the fractions of $\Upsilon(1S)$ coming from $\chi_b(1P)$ and $\chi_b(2P)$. To avoid the complications of soft-gluon re-summation at small p_T, the analysis used only the data for $p_T > 8$ GeV.

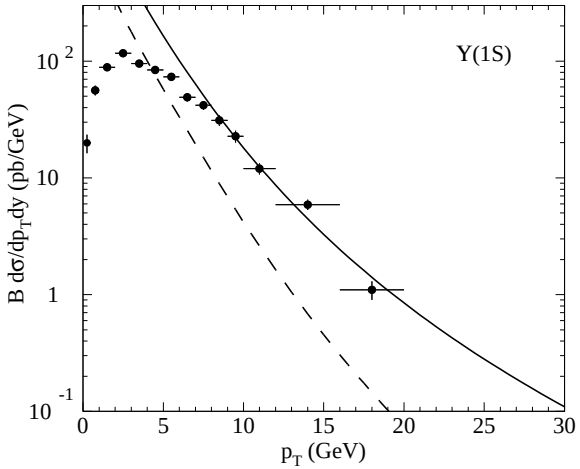

Figure 9.13: Inclusive cross section for $\Upsilon(1S)$ at Run I multiplied by its branching fraction into $\mu^+\mu^-$: CDF data, the NRQCD fit of Ref. [27] (solid line), and the color-singlet model prediction (dashed line).

Because the cross sections for $b\bar{b}_8(^1S_0)$ and $b\bar{b}_8(^3P_J)$ have similar dependences on p_T, only the linear combination $M_r = \langle O_8(^1S_0)\rangle + r\langle O_8(^3P_0)\rangle/m_b^2$ with $r \sim 5$ could be determined. Two different sets of parton distribution functions were used for the analysis: MRST98LO and CTEQ5L. The bottom quark mass was set to $m_b = 4.77 \pm 0.11$ GeV. The resulting color-octet matrix elements have large statistical error bars and many of them are consistent with zero. There are also large uncertainties due to the renormalization and factorization scales. The large errors limit the usefulness of these matrix elements for predicting bottomonium production in other high energy processes.

In Figs. 9.13, 9.14, and 9.15, we show the CDF data on the differential cross sections for $\Upsilon(1S)$, $\Upsilon(2S)$, and $\Upsilon(3S)$ at Run I of the Tevatron. The cross sections are integrated over the rapidity range $|y| \leq 0.4$ and then divided by 0.8. The solid curves are the central curves for the NRQCD fits. The dashed curves are the leading order predictions of the color-singlet model. The NRQCD curves agree with the data in the region $p_T > 8$ GeV used to fit the matrix elements, but the agreement deteriorates quickly at lower values of p_T. The data turns over and then approaches 0 at small p_T. This is to be expected, because the differential cross section $d\sigma/dp_T^2$ should be an analytic function of p_T^2, which implies that there is a kinematic zero in $d\sigma/dp_T = 2p_T d\sigma/dp_T^2$. In contrast with the data, the NRQCD curves for $\Upsilon(1S)$ and $\Upsilon(3S)$ diverge like $1/p_T$ as $p_T \to 0$. This unphysical behavior is an artifact of fixed-order perturbation theory and could be removed by carrying out the appropriate resummation of soft gluons. The NRQCD curve for $\Upsilon(2S)$ turns over and goes negative at small p_T. This unphysical behavior is an artifact of the fit, which gives a negative central value for M_5 that is consistent with zero to within the errors. The fact

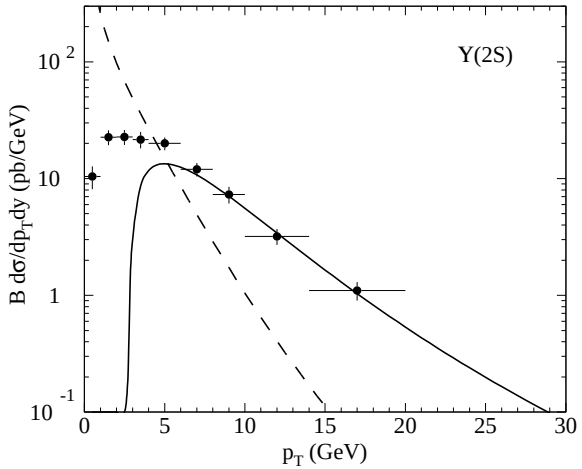

Figure 9.14: Inclusive cross section for $\Upsilon(2S)$ at Run I multiplied by its branching fraction into $\mu^+\mu^-$: CDF data, the NRQCD fit of Ref. [27] (solid line), and the color-singlet model prediction (dashed line).

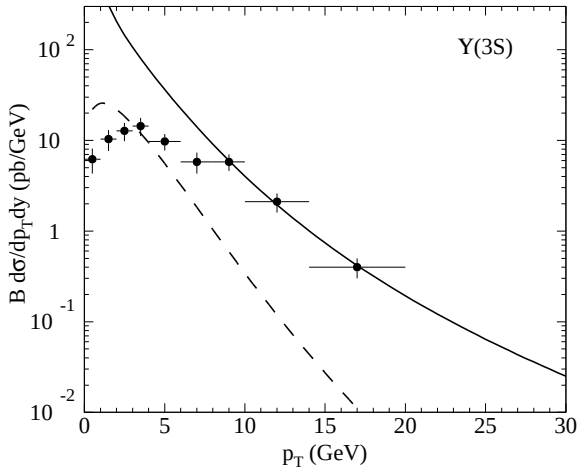

Figure 9.15: Inclusive cross section for $\Upsilon(3S)$ at Run I multiplied by its branching fraction into $\mu^+\mu^-$: CDF data, the NRQCD fit of Ref. [27] (solid line), and the color-singlet model prediction (dashed line).

H	$R^H(1.8\ \text{TeV})$	$R^H(2.0\ \text{TeV})$
$\Upsilon(3S)$	0.31 ± 0.14	0.36 ± 0.16
$\chi_{b2}(2P)$	0.44 ± 0.26	0.52 ± 0.30
$\chi_{b1}(2P)$	0.34 ± 0.16	0.39 ± 0.19
$\chi_{b0}(2P)$	0.20 ± 0.07	0.24 ± 0.08
$\Upsilon(2S)$	0.65 ± 0.35	0.76 ± 0.41
$\chi_{b2}(1P)$	0.57 ± 0.26	0.66 ± 0.31
$\chi_{b1}(1P)$	0.41 ± 0.17	0.48 ± 0.19
$\chi_{b0}(1P)$	0.23 ± 0.08	0.26 ± 0.09
$\Upsilon(1S)$	1	1.16 ± 0.02

Table 9.2: Inclusive cross sections for spin-triplet bottomonium states H at 1.8 TeV and 2.0 TeV divided by the inclusive cross section for $\Upsilon(1S)$ at 1.8 TeV. The cross sections are integrated over $p_T > 8$ GeV and $|y| < 0.4$.

that the NRQCD fit fails to describe the data below $p_T = 8$ GeV emphasizes the need for an analysis that takes into account soft gluon resummation at low p_T. Such an analysis could use the data from the entire range of p_T that has been measured, and it would therefore give matrix elements with much smaller error bars.

Because of the large uncertainties in the matrix elements, the only reliable predictions that can be made based on the NRQCD analysis of Ref. [27] are those for which the large errors cancel out. One such prediction is the increase in the cross section when the center-of-mass energy is increased from 1.8 TeV in Run I of the Tevatron to 2.0 TeV in Run II. In order to cancel out the large uncertainties in the matrix elements, it is convenient to normalize the cross section for the bottomonium state H at center-of-mass energy $\sqrt{s}$ to that for inclusive $\Upsilon(1S)$ at $\sqrt{s} = 1.8$ TeV. We therefore define the ratio

$$R^H(\sqrt{s}) = \frac{\sigma[H;\ \sqrt{s}]}{\sigma[\text{inclusive } \Upsilon(1S);\ \sqrt{s} = 1.8\ \text{TeV}]}, \tag{9.19}$$

where the cross sections are integrated over $p_T > 8$ GeV and $|y| < 0.4$. In Table 9.2, we give the ratios $R^H(\sqrt{s})$ for the inclusive production of spin-triplet bottomonium states, both at $\sqrt{s} = 1.8$ TeV and at $\sqrt{s} = 2.0$ TeV. When the center-of-mass energy is increased from 1.8 TeV to 2.0 TeV, all the cross sections increase by about the same amount. The increase depends on p_T, changing from about 15% at $p_T = 8$ GeV to about 19% at $p_T = 20$ GeV. The percentage increase for $\Upsilon(1S)$ is shown as a function of p_T in Fig. 9.16.

Another reliable application of the NRQCD analysis is to predict the cross sections for the spin-singlet bottomonium states $\eta_b(nS)$ and $h_b(nP)$. The most important matrix elements for $\eta_b(nS)$ and $h_b(nP)$ are related to those for $\Upsilon(nS)$ and $\chi_b(nP)$ by the spin symmetry of NRQCD. Thus, once the color-octet matrix elements are determined from the production of spin-triplet states, the NRQCD approach truncated at order v^4 predicts the cross sections for the spin-singlet states without any new nonperturbative parameters. The resulting expressions for the direct cross sections of $\eta_b(nS)$ and $h_b(nP)$ are

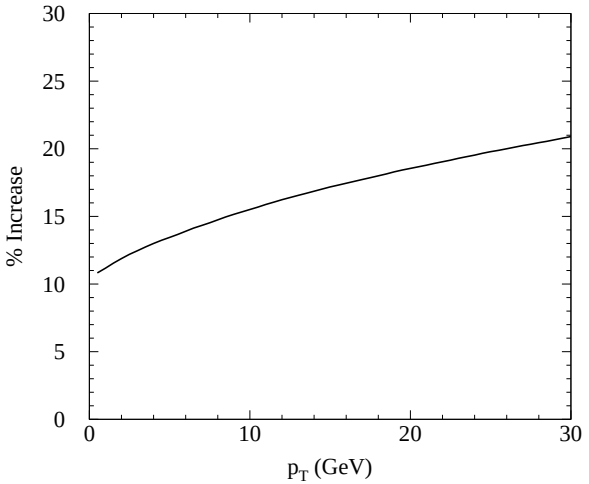

Figure 9.16: Percentage increase in the inclusive cross section for $\Upsilon(1S)$ at 2.0 TeV compared to 1.8 TeV. The cross sections are integrated over $p_T > 8$ GeV and $|y| < 0.4$.

$$\sigma[\eta_b(nS)] = \frac{1}{3}\sigma[b\bar{b}_1(^1S_0)]\langle O_1^{\Upsilon(nS)}(^3S_1)\rangle + \frac{1}{3}\sigma[b\bar{b}_8(^1S_0)]\langle O_8^{\Upsilon(nS)}(^3S_1)\rangle + \sigma[b\bar{b}_8(^3S_1)]\langle O_8^{\Upsilon(nS)}(^1S_0)\rangle + 3\sigma[b\bar{b}_8(^1P_1)]\langle O_8^{\Upsilon(nS)}(^3P_0)\rangle, \tag{9.20}$$

$$\sigma[h_b(nP)] = 3\left(\sigma[b\bar{b}_1(^1P_1)]\langle O_1^{\chi_{b0}(nP)}(^3P_0)\rangle + \sigma[b\bar{b}_8(^1S_0)]\langle O_8^{\chi_{b0}(nP)}(^3S_1)\rangle\right). \tag{9.21}$$

In Table 9.3, we give the ratios $R^H(\sqrt{s})$ defined in (9.19) for the direct production of the spin-singlet states, not including any effects from the feed down of higher bottomonium states. The cross sections for direct $h_b(nP)$ are significantly smaller than for inclusive $\Upsilon(1S)$. Since the h_b does not seem to have any distinctive decay modes that can be used as a trigger, its discovery at the Tevatron is unlikely. However the cross sections for direct

H	$R^H(1.8\ \text{TeV})$	$R^H(2.0\ \text{TeV})$
$\eta_b(3S)$	1.83 ± 0.54	2.13 ± 0.62
$h_b(2P)$	0.07 ± 0.07	0.08 ± 0.09
$\eta_b(2S)$	1.60 ± 0.59	1.87 ± 0.69
$h_b(1P)$	0.11 ± 0.08	0.13 ± 0.09
$\eta_b(1S)$	4.59 ± 0.83	5.34 ± 0.96

Table 9.3: Direct cross sections for spin-singlet bottomonium states H at 1.8 TeV and 2.0 TeV divided by the inclusive cross section for $\Upsilon(1S)$ at 1.8 TeV. The cross sections are integrated over $p_T > 8$ GeV and $|y| < 0.4$.

$\eta_b(nS)$, $n = 1, 2, 3$ are significantly larger than for inclusive $\Upsilon(1S)$. Thus it should be possible to discover the η_b if one can identify a suitable decay mode that can be used as a trigger. One promising possibility is the decay $\eta_b \to J/\psi + J/\psi$ [27].

9.2.2.2 Charmonium

The NRQCD factorization approach can be applied to charmonium production at the Tevatron as well as to bottomonium production. The differences are only quantitative. First, the coupling constant $\alpha_s(m_c) \approx 0.36$ is larger than $\alpha_s(m_b) \approx 0.22$, so the radiative corrections to the short-distance parton cross sections are larger for charmonium. Second, the typical relative velocity v of the heavy quark is significantly larger for charmonium ($v^2 \sim 1/4$) than for bottomonium ($v^2 \sim 1/10$). In the NRQCD approach truncated at relative order v^4, the terms that are neglected are suppressed only by an additional factor of v^2 and are therefore larger for charmonium than for bottomonium. A third difference is that the value of p_T above which fragmentation contributions become important is smaller by a factor of 3 for charmonium, simply because $m_c \approx m_b/3$.

An important experimental difference from bottomonium production is that charmonium is also produced by decays of B hadrons. We define the prompt cross section for a charmonium state to be the inclusive cross section excluding the contribution from B hadron decays. Thus the prompt cross section is the sum of the direct cross section and the indirect contributions from decays of higher charmonium states that were produced directly. The experimental signature of prompt production is the absence of a displaced vertex that would signal the weak decay of a B hadron.

NRQCD analyses of the CDF data on charmonium production from Run IA have been carried out by several groups [32,38–41]. We describe briefly the analysis of Ref. [41]. The color-singlet matrix elements were determined from annihilation decays of the charmonium states. The color-octet matrix elements were obtained by fitting the CDF cross sections for J/ψ, $\psi(2S)$, and χ_{cJ} and by imposing the constraint from a preliminary CDF measurement of the ratio of χ_{c1} to χ_{c2}. Because the cross sections for $c\bar{c}_8(^1S_0)$ and $c\bar{c}_8(^3P_J)$ have similar dependences on p_T, only the linear combination $M_r = \langle O_8(^1S_0)\rangle + r\langle O_8(^3P_0)\rangle/m_b^2$ with $r \sim 3.5$ could be determined. The sets of parton distribution functions that were used were MRST98LO and CTEQ5L. The charm quark mass was set to $m_c = 1.50 \pm 0.05$ GeV.

In Figs. 9.17 and 9.18, we show the CDF data on the differential cross sections for J/ψ and $\psi(2S)$ from Run IA [30,31]. The cross sections are integrated over the pseudorapidity range $|\eta| < 0.6$. The curves are the results of the NRQCD fit and the leading-order predictions of the color-singlet model. If the cross sections were measured at lower values of p_T, they would turn over and go to zero like the $\Upsilon(1S)$ cross section in Fig. 9.13. In contrast, the NRQCD curves continue rising and diverge like $1/p_T$ as $p_T \to 0$. In order to obtain the correct physical behavior at small p_T, it would be necessary to carry out an analysis that includes the effects of soft-gluon radiation. Neglecting these effects may introduce large systematic errors into the NRQCD matrix elements. In an analysis using a Monte Carlo event generator to take into account initial-state gluon radiation at the Tevatron, the values of some of the color-octet matrix were decreased by an order of magnitude [42]. One should

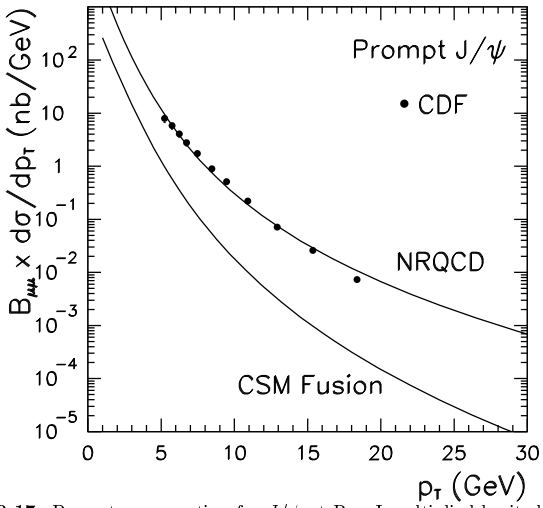

Figure 9.17: Prompt cross section for J/ψ at Run I multiplied by its branching fraction into $\mu^+\mu^-$: CDF data, the NRQCD fit of Ref. [41], and the color-singlet model prediction.

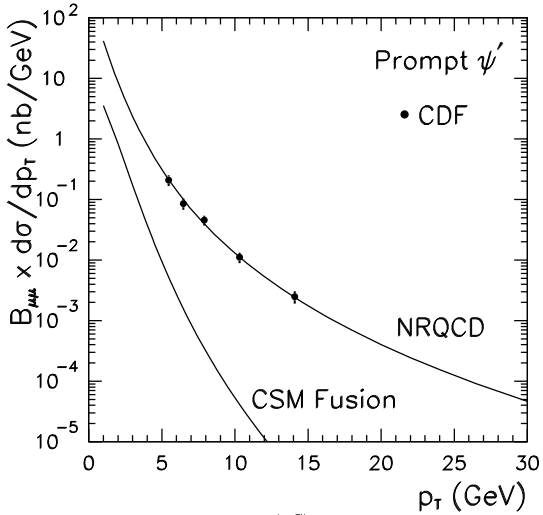

Figure 9.18: Prompt cross section for $\psi(2S)$ at Run I multiplied by its branching fraction into $\mu^+\mu^-$: CDF data, the NRQCD fit of Ref. [41], and the color-singlet model prediction.

H	R^H(1.8 TeV)	R^H(2.0 TeV)
$\psi(2S)$	0.21 ± 0.07	0.23 ± 0.08
$\chi_{c2}(1P)$	0.44 ± 0.08	0.50 ± 0.10
$\chi_{c1}(1P)$	0.40 ± 0.08	0.45 ± 0.09
$\chi_{c0}(1P)$	0.14 ± 0.03	0.16 ± 0.03
J/ψ	1	1.14 ± 0.08

Table 9.4: Prompt cross sections for spin-triplet charmonium states H at 1.8 TeV and 2.0 TeV divided by the prompt cross section for J/ψ at 1.8 TeV. The cross sections are integrated over $p_T > 5.5$ GeV and $|\eta| < 0.6$.

H	R^H(1.8 TeV)	R^H(2.0 TeV)
$\eta_c(2S)$	0.37 ± 0.11	0.42 ± 0.12
$h_c(1P)$	0.033 ± 0.006	0.037 ± 0.007
$\eta_c(1S)$	1.73 ± 0.15	1.97 ± 0.72

Table 9.5: Direct cross sections for spin-singlet charmonium states H at 1.8 TeV and 2.0 TeV divided by the prompt cross section for J/ψ at 1.8 TeV. The cross sections are integrated over p_T between 5 and 20 GeV and $|\eta| < 0.6$.

therefore be wary of using the matrix elements from existing analyses of the Tevatron data to predict production rates in other high energy processes.

The safest applications of the NRQCD analysis are to observables for which the errors associated with the extractions of the matrix elements tend to cancel out. One such observable is the increase in the cross section when the center-of-mass energy is increased from 1.8 TeV to 2.0 TeV. It is convenient to normalize the cross section for the charmonium state H at center-of-mass energy $\sqrt{s}$ to that for prompt J/ψ at $\sqrt{s} = 1.8$ TeV by defining the ratio (in analogy with Eq. (9.19))

$$R^H(\sqrt{s}) = \frac{\sigma[H;\ \sqrt{s}]}{\sigma[\text{prompt } J/\psi;\ \sqrt{s} = 1.8 \text{ TeV}]}, \tag{9.22}$$

where the cross sections are integrated over $p_T > 5.5$ GeV and over $|\eta| < 0.6$. In Table 9.4, we give the ratios $R^H(\sqrt{s})$ for the inclusive production of spin-triplet charmonium states, both at $\sqrt{s} = 1.8$ TeV and at $\sqrt{s} = 2.0$ TeV. When the center-of-mass energy is increased from 1.8 TeV to 2.0 TeV, all the cross sections increase by about the same amount. The increase depends on p_T, changing from about 13% at $p_T = 5.5$ GeV to about 18% at $p_T = 20$ GeV. The percentage increase for J/ψ is shown as a function of p_T in Fig. 9.19.

Another reliable application of the NRQCD analysis is to predict the cross sections for the spin-singlet bottomonium states $\eta_c(nS)$ and h_c. The most important matrix elements for $\eta_c(nS)$ and h_c are related to those for the spin-triplet states by the spin symmetry of NRQCD. Thus, once the color-octet matrix elements are determined from the production of spin-triplet states, the NRQCD approach predicts the cross sections for the spin-singlet states without any new nonperturbative parameters. In Table 9.5, we give the ratios $R^H(\sqrt{s})$ defined in (9.22) for the direct production of the spin-singlet states, not including

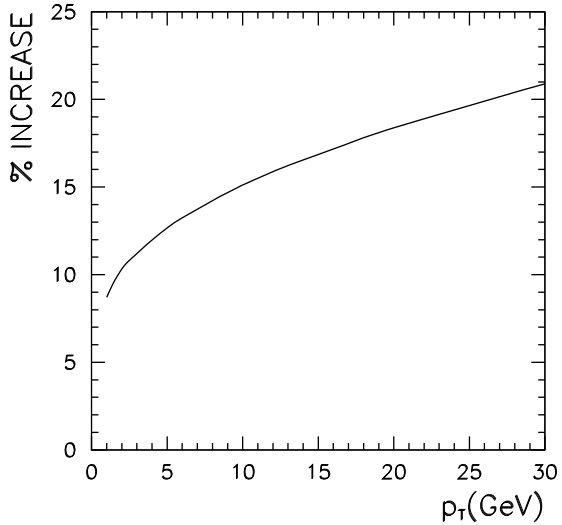

Figure 9.19: Percentage increase in prompt cross section for J/ψ at $\sqrt{s} = 2.0$ TeV compared to 1.8 TeV as a function of p_T. The cross sections are integrated over $p_T > 5.5$ GeV and $|\eta| < 0.6$.

any effects from the feed-down of higher charmonium states. The cross sections for direct h_c are significantly smaller than for prompt J/ψ, but the cross sections for direct $\eta_c(nS)$, $n = 1, 2$ are significantly larger. It may be possible to observe the $\eta_c(1S)$ and perhaps even discover the $\eta_c(2S)$ if one can identify a suitable decay mode that can be used as a trigger.

9.2.2.3 Quarkonium polarization

The most dramatic prediction of the NRQCD factorization approach for quarkonium production at the Tevatron is that the $J^{PC} = 1^{--}$ states like the J/ψ should be transversely polarized at sufficiently large p_T. This prediction follows from three simple features of the dynamics of heavy quarks and massless partons. (1) The inclusive production of quarkonium at large p_T is dominated by gluon fragmentation [43]. (2) At leading order in α_s, the $c\bar{c}$ pair produced by gluon fragmentation is in a color-octet $^3S_1$ state [44] with transverse polarization. (3) The approximate spin symmetry of NRQCD guarantees that the hadronization of a transversely polarized $c\bar{c}$ pair produces a J/ψ that is predominantly transversely polarized [45].

In the NRQCD approach truncated at relative order v^4, the cross sections for polarized quarkonium states can be calculated in terms of the matrix elements that describe unpolarized production. The only complication is that both the parton cross sections and the NRQCD matrix elements in the NRQCD factorization formula (9.13) become density

matrices in the angular momentum quantum numbers of the $c\bar{c}$ pairs. Thus the NRQCD approach gives definite predictions for polarized quarkonium cross sections, without any new nonperturbative parameters. In contrast, one of the basic assumptions of the color evaporation model is that quarkonium is always produced unpolarized. This model can therefore be ruled out by a measurement of nonzero polarization of quarkonium.

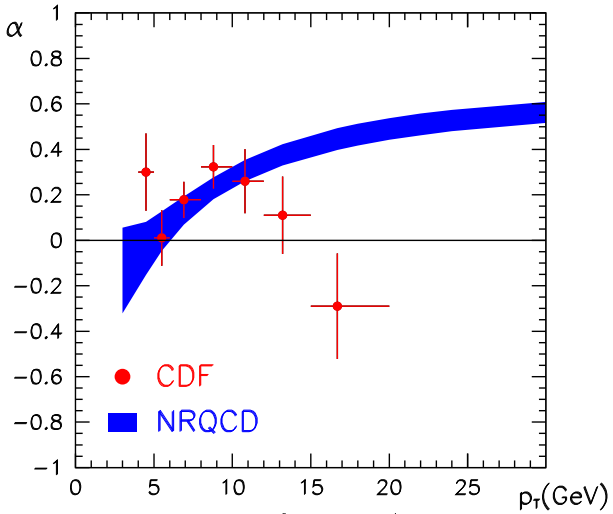

Figure 9.20: Polarization variable α for prompt J/ψ at Run I: CDF data and the NRQCD prediction of Ref. [41].

Defining the angle θ by the direction of the μ^+ with respect to the ψ direction in the ψ center of mass frame, the normalized angular distribution $I(\theta)$ is given by

$$I(\theta) = \frac{1}{\sigma_L + \sigma_T}\left[\frac{3}{8}(1+\cos^2\theta)\,\sigma_T + \frac{3}{4}\sin^2\theta\,\sigma_L\right] \equiv \frac{3}{2(\alpha+3)}(1+\alpha\cos^2\theta). \quad (9.23)$$

A convenient measure of the polarization of $J = 1$ quarkonium states is therefore the variable $\alpha = (\sigma_T - 2\sigma_L)/(\sigma_T + 2\sigma_L)$, where σ_T and σ_L are the cross sections for transversely and longitudinally polarized states, respectively. In Figs. 9.20 and 9.21, we show the CDF measurements of α for prompt J/ψ and prompt $\psi(2S)$ [46]. In Fig. 9.21 for $\psi(2S)$, the bands are the predictions from the NRQCD analyses of Leibovich [47], Beneke and Kramer [48] and Braaten, Kniehl and Lee [41]. The widths of the bands and the deviations between the predictions are indicators of the size of the theoretical errors. The calculation of α for prompt J/ψ is complicated by the need to take into account the feed-down from χ_{cJ}. The band in Fig. 9.20 is the prediction by Braaten, Kniehl and Lee [41]. For both prompt J/ψ and prompt $\psi(2S)$, the theoretical prediction for α is small around $p_T = 5$ GeV, but

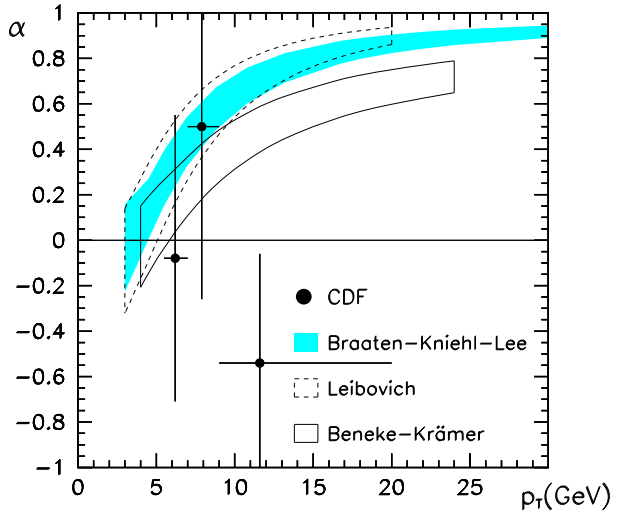

Figure 9.21: Polarization variable α for prompt $\psi(2S)$ at Run I: CDF data and the NRQCD predictions of Refs. [41] (shaded band), [47] (dashed box), and [48] (solid box).

then increases steadily with p_T. If the data is taken at its face value, it suggests exactly the opposite trend, decreasing at the largest values of p_T for which it has been measured. There are many effects, such as higher order corrections, that could dilute the polarization or delay the onset of the rise in α, but the basic conclusion that α should increase to a positive value at large p_T seems to follow inescapably from the NRQCD factorization approach. If this behavior is not observed in Run II, it will be a serious blow to this approach to quarkonium production.

In Ref. [49], the polarization variable α has also been calculated for inclusive $\Upsilon(nS)$ using the matrix elements from the NRQCD analysis of Ref. [27]. The prediction for inclusive $\Upsilon(1S)$ as a function of p_T is shown in Fig. 9.22. The variable α is predicted to be small for p_T less than 10 GeV, but it increases steadily with p_T. The prediction is compatible with the CDF measurement for p_T in the range from 8 GeV to 20 GeV, which is $\alpha = 0.03 \pm 0.28$. The data from Run II should allow the prediction to be tested.

9.2.3 Polarization in quarkonium production †

Measurements of the J/ψ and $\psi(2S)$ differential cross sections by CDF [30] separate the cross sections into those ψ mesons coming from b-flavored hadron production and those originating from prompt production mechanisms. This separation is made by reconstructing

† Authors: G. Feild, K. Sumorok, W. Trischuk

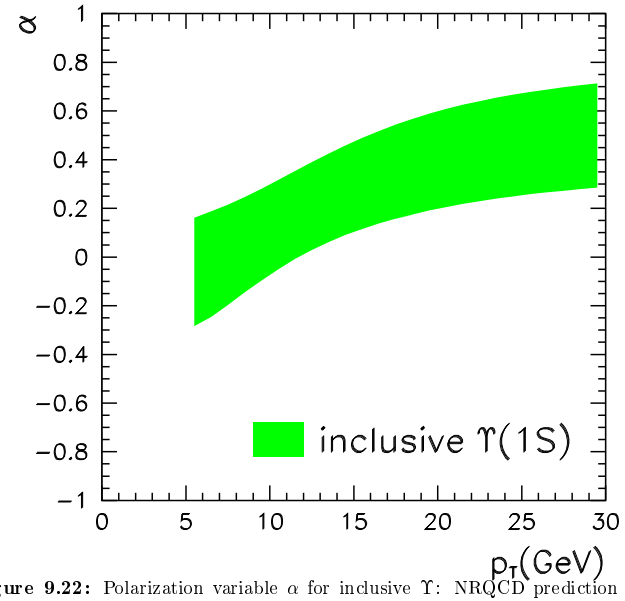

Figure 9.22: Polarization variable α for inclusive Υ: NRQCD prediction from Ref. [49].

the decay vertex of the J/ψ and $\psi(2S)$ mesons using the CDF Silicon Vertex detector (SVX). The fraction of J/ψ mesons coming from b-flavored hadron production increases from 15% at 5 GeV/c to 40% at 18 GeV/c $P_T^{J/\psi}$. For $\psi(2S)$ mesons, a similar increase is seen in the range from 5 to 14 GeV/c. The prompt production of J/ψ mesons has three components: a feed-down from χ_c production, a feed-down from $\psi(2S)$ and a direct component. Only the latter occurs in the production of $\psi(2S)$ mesons. CDF has measured the fraction of prompt J/ψ mesons coming from χ_c production to be $(29.7 \pm 1.7 \pm 5.7)\%$ of the total prompt production [31]. From the measured $\psi(2S)$ production cross section, the fraction of the prompt J/ψ's feeding down from $\psi(2S)$ meson decays is calculated to be $7 \pm 2\%$ at $P_T^{J/\psi} = 5$ GeV/c and $15 \pm 5\%$ at $P_T^{J/\psi} = 18$ GeV/c. The fraction of directly produced J/ψ mesons is $64 \pm 6\%$, independent of $P_T^{J/\psi}$ between 5 and 18 GeV/c.

Having separated out the prompt J/ψ mesons coming from χ_c, both direct/prompt J/ψ and $\psi(2S)$ production appear to be $\approx$ 50 times higher than color-singlet model (CSM) predictions [50].

9.2.3.1 NRQCD predictions for ψ meson polarization

Calculations based on the NRQCD factorization formalism are able to explain this anomalous production [32,38]. The model increases the prompt production cross section by including color-octet $c\bar{c}$ states ${}^1S_0^{(8)}$, ${}^3P_0^{(8)}$ and ${}^3S_1^{(8)}$ in the hadronization process. At leading order in α_s, the color-singlet term in the parton cross section $d\hat{\sigma}/dp_T^2$ has a $1/p_T^8$ dependence at large p_T, the ${}^1S_0^{(8)}$ and ${}^3P_0^{(8)}$ terms have a $1/p_T^6$ dependence, and the ${}^3S_1^{(8)}$ term has a $1/p_T^4$ dependence. This last term, which corresponds to the fragmentation of an almost on-shell gluon into a $c\bar{c}$ pair, dominates at high P_T. An on-shell gluon is transversely polarized and NRQCD predicts this polarization is transfered to the J/ψ or $\psi(2S)$ mesons in the final state.

A consequence of this mechanism is that the direct prompt J/ψ mesons and the $\psi(2S)$ mesons will approach 100% transverse polarization at leading order in α_s for transverse momenta $p_T \gg m_c$ where m_c is the charm quark mass [45,51]. The observation of such a polarization would be an indication of the NRQCD hadronization mechanism.

9.2.3.2 CDF polarisation measurements from Run I

CDF has made a measurement of the production polarization of J/ψ and $\psi(2S)$ (collectively ψ) mesons by analyzing decays into $\mu^+\mu^-$ [46]. Defining the angle θ by the direction of the μ^+ with respect to the ψ direction in the ψ center of mass frame, the normalized angular distribution $I(\theta)$ is given by Eq. (9.23).

Unpolarized ψ mesons would have $\alpha = 0$, whereas $\alpha = +1$ and -1 correspond to fully transverse and longitudinal polarizations respectively. The polarization parameter for prompt ψ production can be separated from the B-hadron decay component by fitting the proper decay length distribution for ψ candidates with both muons reconstructed in the SVX. Fig. 9.23 shows the fitted polarization of J/ψ mesons obtained by CDF from prompt production and B-hadron decay compared with an NRQCD prediction for the prompt production [41]. The prediction for J/ψ meson polarization includes dilutions due to the contributions from χ_c and $\psi(2S)$ decays. Fig. 9.24 shows the fitted polarization for $\psi(2S)$ mesons obtained by CDF from prompt production and B-hadron decay compared with NRQCD predictions for prompt production from Refs. [48] and [41].

9.2.3.3 Polarization predictions for Run II

The measurements in Run I were based on a luminosity of 110 pb^{-1}. Estimates for Run II are made assuming a factor of 20 increase in integrated luminosity, or 2 fb^{-1}. CDF is also planning to increase the yield of its dimuon trigger by 50% by lowering the p_T threshold. In addition, the SVX will have increased coverage along the beam line leading to better acceptance for dimuons fully reconstructed in the SVX. This is crucial for separation of prompt and B hadron decay production in this measurement. Overall a factor of 50 increase in the effective statistics for Run II is assumed in our projections. We have extrapolated to higher p_T by using the fitted shape of the cross section below 20 GeV/c^2 in order to predict the number of events in a given p_T bin. We have estimated the errors by scaling the statistics from Run I measurements. In Run I, systematic uncertainties on the polarization measurement were small compared to the statistical errors. We anticipate that the systematics can be improved with the Run II data samples, but even if this is not the case systematics

REPORT OF THE B PHYSICS AT THE TEVATRON WORKSHOP

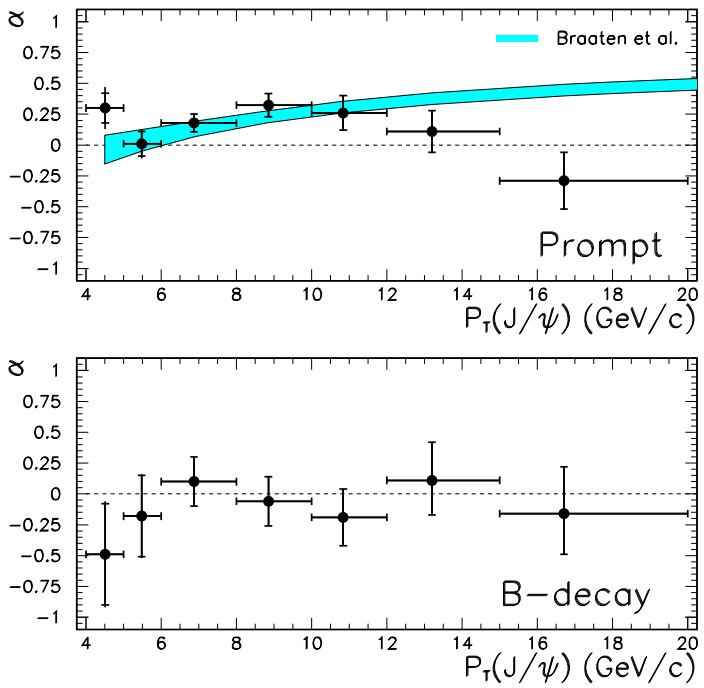

Figure 9.23: The fitted polarization of J/ψ mesons from prompt production and B-hadron decay. The shaded curve shows an NRQCD prediction from Ref. [41].

should still be negligible at the highest transverse momenta. Fig. 9.25 shows the expected precision for a polarization measurement in Run II of promptly produced J/ψ and $\psi(2S)$ mesons. Relative to Run I, the p_T range should be extended and the statistical precision on the measurement improved. The points are slightly scattered about zero to ease visibility.

9.2.3.4 Upsilon production and polarization in CDF Run II

The CDF Run IB Υ(1S) differential production cross section, measured as a function of transverse energy, is shown in Fig. 9.26. As discussed in section 9.2.2.1, this cross section can be described by including NRQCD color-octet matrix elements in the fit to the data. However, due to the free parameters in the fit, this compatibility alone is not enough to demonstrate that the NRQCD description is correct. As in the case of the J/ψ and ψ(2S) mesons, observation of transversely polarized Υ(1S) production due to gluon fragmentation at high p_T would provide further evidence in favor of the NRQCD framework over other proposed models, such as the color-singlet model and the color-evaporation model.

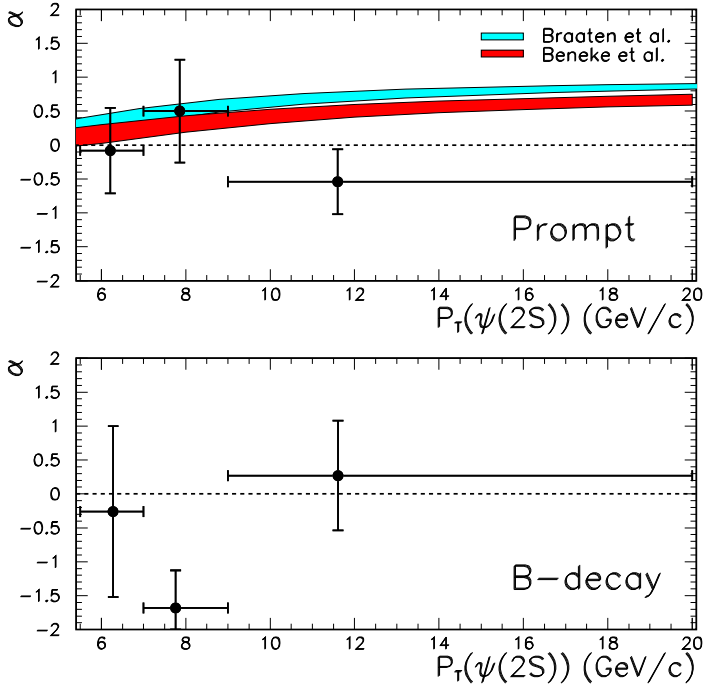

Figure 9.24: The fitted polarization of $\psi(2S)$ mesons from prompt production and B-hadron decay. The shaded curves are NRQCD predictions from Refs. [48] and [41].

The $\Upsilon(1S) \to \mu\mu$ production polarization for events in the transverse energy range 8 GeV/c $< p_T(\Upsilon) <$ 20 GeV/c has been determined in Run IB by measuring the muon decay angle in the Υ rest frame as described in section 9.2.3.2. This measurement is done by fitting longitudinally and transversely polarized Monte Carlo templates to the data shown in Fig. 9.27. In this case the longitudinal fraction Γ_L/Γ is measured to be 0.32 ± 0.11. The longitudinal fraction can be related to the usual polarisation parameter, α, by: $\Gamma_L/\Gamma = (1-\alpha)\ (3+\alpha)$. Thus our polarisation measurement in Υ decays yields a value of $\alpha = 0.03 \pm 0.25$. Our data is compatible with unpolarized production. This result does not contradict the predictions of NRQCD as the transverse polarisation is only expected to be large for transverse momenta $p_T \gg m_b$, where m_b is the b quark mass. We are probably not probing sufficiently high p_T with our current data.

An extrapolation of the Run IB cross section from Fig. 9.26 yields no appreciable cross section for $p_T(\Upsilon) > 20$ GeV. However, assuming a factor 20 increase in data for Run II, a polarization measurement statistically comparable to that from Run IB could be made in

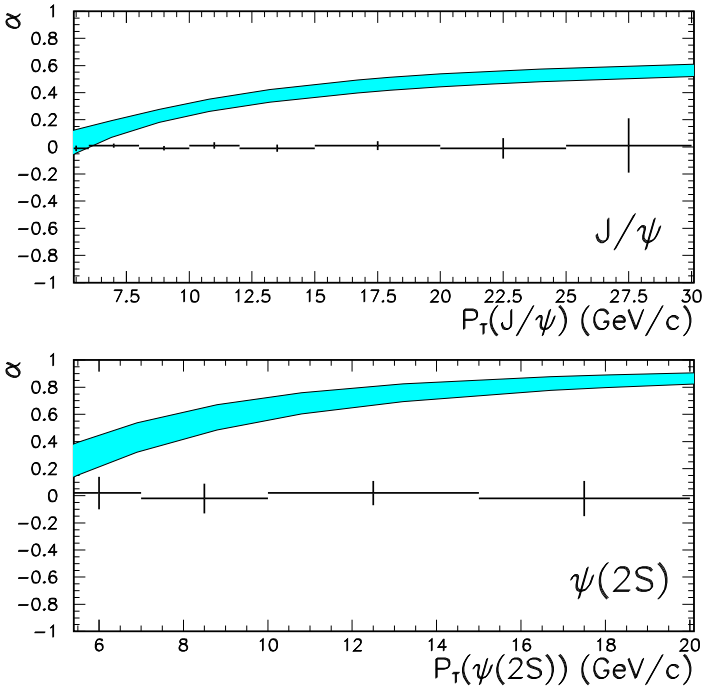

Figure 9.25: The expected precision for a polarization measurement in Run II of promptly produced J/ψ and $\psi(2S)$ mesons. The shaded curves are NRQCD predictions from [41].

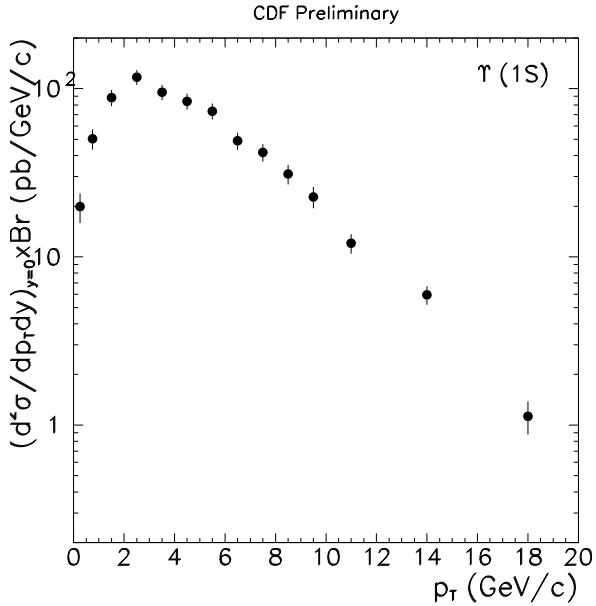

Figure 9.26: The differential cross-section for $\Upsilon(1S)$ production measured by CDF in Run I.

the transverse energy range 14 GeV $< p_T(\Upsilon) <$ 20 GeV. Conversely, the prediction from fits to the Run IB data shown in Fig. 9.13, predict a flattening of the cross section above 20 GeV. It will be quite interesting if such events are seen in Run II.

9.3 The B_c Meson

The B_c meson is the ground state of the $\bar{b}c$ system, which in many respects is intermediate between charmonium and bottomonium. However because $\bar{b}c$ mesons carry flavor, they provide a window for studying heavy-quark dynamics that is very different from the window provided by quarkonium. The observation of approximate 20 B_c events in the $B_c \to J/\psi l\nu$ decay mode by the CDF-collaboration [52] in Run I of the Tevatron demonstrates that the experimental study of the $\bar{b}c$ meson system is possible.

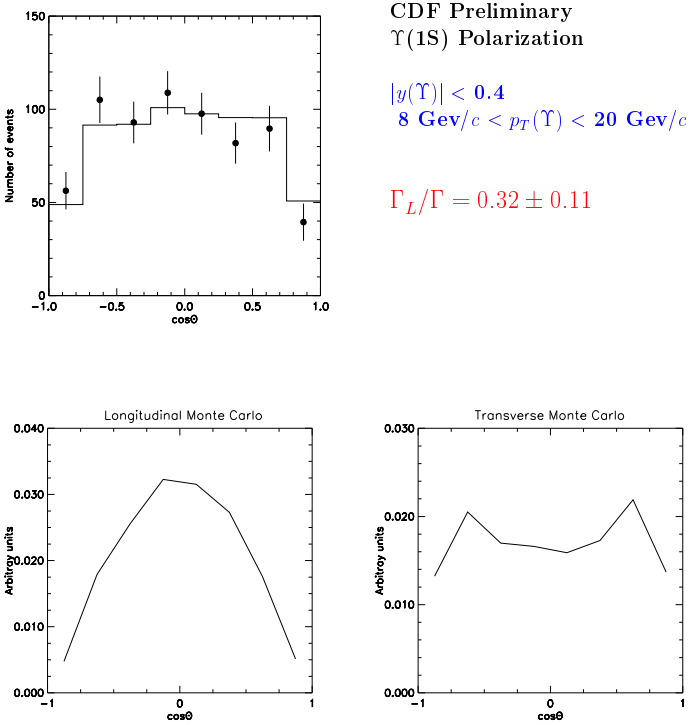

Figure 9.27: The polarisation measured in $\Upsilon(1S)$ decays by CDF in Run I.

9.3.1 Spectroscopy[†]

The $\bar{b}c$ system has a rich spectroscopy of orbital and angular-momentum excitations. The predicted spectrum is shown in Fig. 9.28. The only state that has been observed is the ground state B_c, which was discovered by the CDF collaboration in Run I of the Tevatron [52]. They measured the mass to be 6.4 ± 0.4 GeV. The masses of the B_c and the other states in the $\bar{b}c$ spectrum can be predicted using potential models whose parameters are tuned to reproduce the spectra of the observed charmonium and bottomonium states [53–58]. The range of the resulting predictions for the B_c mass is 6.24 ± 0.05 GeV. The first excited state is the spin-1 state B_c^*, which is predicted to be heavier by 78 ± 13 MeV. The mass of the B_c has also been calculated using lattice gauge theory to be 6.4 ± 0.1, where the uncertainty is dominated by the error from the omission of dynamical quarks [59].

[†]Authors: E. Braaten, R. K. Ellis

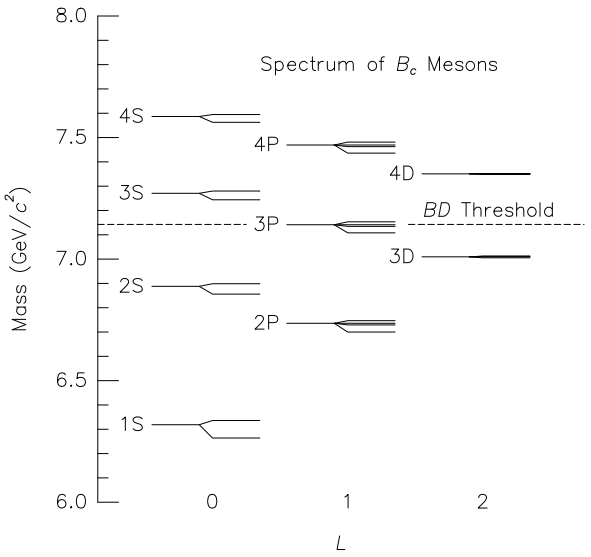

Figure 9.28: Predicted spectrum for the $\bar{b}c$ mesons [56].

The majority of the B_c mesons produced at the Tevatron are produced indirectly via the decay of excited $\bar{b}c$ mesons. The excited states cascade down through the spectrum via a sequence of hadronic and electromagnetic transitions, until they reach the ground state $B_c(1S)$, which decays via the weak interaction [56]. The $\bar{b}c$ states with the best prospects for discovery at the Tevatron are those that decay into $B_c + \gamma$. The discovery of the B_c^* is made difficult by the very low energy of the photon (~ 80 MeV). The first radial excitation $B_c^*(2S)$ decays into $B_c + \gamma$ with a much more energetic photon (~ 600 MeV), but a smaller fraction of the decay chains that end in B_c will have the $B_c^*(2S)$ as the next-to-last step. States in the $\bar{b}c$ spectrum could also be discovered via 2-pion transitions into the B_c. The most promising is the first radial excitation $B_c(2S)$, whose mass is higher than that of the B_c^* by about 600 MeV.

9.3.2 Production[1]

One can think of the production of a B_c as proceeding in three steps. First, a $\bar{b}$ and c with small relative momentum are created by a parton collision. Second, the $\bar{b}$ and c bind to form the B_c or one of its excited states below the BD threshold. Third, the excited states all cascade down to the ground state B_c via hadronic or electromagnetic transition. Thus,

[1]Authors: Eric Braaten, A. Likhoded

the total production cross section for B_c is the sum of the direct production cross sections for B_c and its excited states.

The direct production of the B_c and other $\bar{b}c$ mesons can be treated within the NRQCD factorization framework described in Section 9.2.2. The cross section for the direct production of a $\bar{b}c$ meson H can be expressed in the form of Eqs. (9.12) and (9.13), with $b\bar{b}(n)$ replaced by $\bar{b}c(n)$. The short-distance cross section $d\hat{\sigma}[ij \to \bar{b}c(n) + X]$ for creating the $\bar{b}c$ in the color and angular-momentum state n can be calculated as a perturbative expansion in α_s at scales of order m_c or larger. The nonperturbative matrix element $\langle O^H(n)\rangle$ encodes the probability for a $\bar{b}c$ in the state n to bind to form the meson H. The matrix element scales as a definite power of the relative velocity v of the charm quark. For S-wave states, the leading color-octet matrix element is suppressed by v^4 relative to the leading color-singlet matrix element. For P-wave states, the leading color-singlet matrix element and the leading color-octet matrix element are both suppressed by v^2 relative to the leading color-singlet matrix element for S-waves.

The production mechanisms for $\bar{b}c$ differ in an essential way from those for $b\bar{b}$, because two heavy quark-antiquark pairs must be created in the collision. While a $b\bar{b}$ pair can be created at order α_s^2 by the parton processes $q\bar{q}, gg \to b\bar{b}$, the lowest order mechanisms for creating $\bar{b}c$ are the order-α_s^4 processes $q\bar{q}, gg \to (\bar{b}c) + b\bar{c}$. At the Tevatron, the gg contribution dominates. The parton process $gg \to (\bar{b}c) + b\bar{c}$ can create the $\bar{b}c$ in either a color-singlet or color-octet state. We expect the cross section for color-octet $\bar{b}c$ to be about a factor of 8 larger than for color-singlet $\bar{b}c$, just from counting the color states. This factor of 8 can partially compensate any suppression factors of v from the probability for the color-octet $\bar{b}c$ to bind to form a meson. However, unlike the case of $\bar{b}b$, there is no dynamical enhancement of color-octet $\bar{b}c$ at low p_T or at high p_T. Color-octet production processes should therefore be less important for $\bar{b}c$ mesons than for quarkonium.

All existing calculations for the cross sections of $\bar{b}c$ mesons have been carried out within the color-singlet model. The $\bar{b}c$ is assumed to be created in a color-singlet state with the same angular-momentum quantum numbers as the meson. The appropriate long-distance matrix elements can be determined from the radial wavefunctions of the mesons as in Eqs. (9.14) and (9.15). For the B_c and the first excited state B_c^*, the matrix element is proportional to $|R_{1S}(0)|^2$. Since the wavefunctions are known from potential models, the cross sections for $b\bar{c}$ mesons in the color-singlet model are absolutely normalized.

The production of $\bar{b}c$ mesons in the color-singlet model at leading order in α_s was studied in detail in the series of papers [60]. The cross sections are proportional to $\alpha_s^4(\mu)$ and to a wavefunction factor, which is $|R_{nS}(0)|^2$ for S-waves and $|R'_{nP}(0)|^2$ for P-waves. The largest uncertainties in the theoretical predictions arise from the factor $\alpha_s^4(\mu)$. There is a large ambiguity in the choice of the scale μ, since the short-distance process involves several scales, including m_c, m_b, and p_T. For example, if the scale μ is varied from m_c up to $2(m_c + m_b)$, the $\bar{b}c$ cross-section changes by a factor of 7. There are additional ambiguities from the wave function factors and from the c-quark mass, but the resulting uncertainties are less than a factor of 2.

The result of the order-α_s^4 color-singlet model calculation for $d\sigma/dp_T$ of the B_c meson at the Tevatron at 1.8 TeV are presented in Fig. 9.29. The cross section integrated over p_T

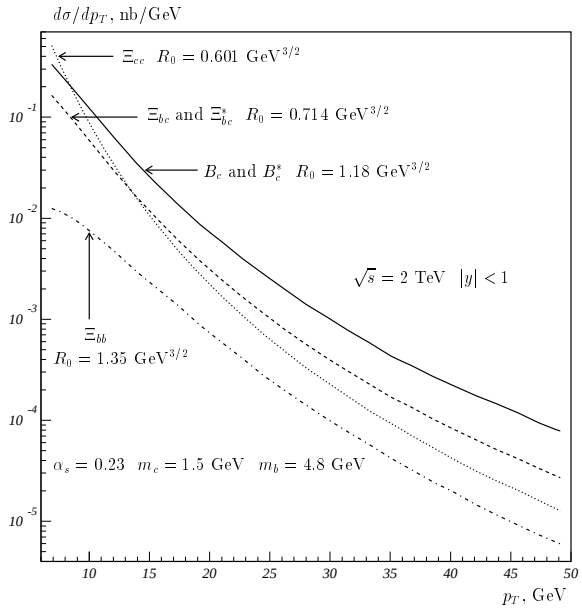

Figure 9.29: Differential cross sections for the B_c meson and doubly-heavy baryons.

greater than p_{Tmin} is shown in Fig. 9.30. The prediction includes the feeddown from B_c^*, but not from any of the higher $\bar{b}c$ states. The cross sections are integrated over $|y| < 1$. In our calculations we used the following values of parameters. The quark masses were taken to be $m_c = 1.5$ GeV and $m_b = 4.8$ GeV. The QCD coupling constant was frozen at the value $\alpha_s = 0.23$, which describes the experimental data of the OPAL Collaboration on the production of additional $c\bar{c}$-pairs in e^+e^--annihilation [60]. The radial wavefunction at the origin for the B_c and B_c^* was taken to be $R_{1S}(0) = 1.18$ GeV$^{3/2}$. The cross-section for B_c mesons is roughly three orders of magnitude smaller than that for B mesons due to the presence of two heavy quark-antiquark pairs in the final state.

To estimate the inclusive B_c cross section, we must take into account the feeddown from all the $\bar{b}c$ mesons below the BD threshold, all of which eventually cascade down into the B_c via hadronic or electromagnetic transitions. Including the feeddown from all the higher $\bar{b}c$ states and integrating over $p_T > 6$ GeV and $|y| < 1$, the inclusive cross section for B_c is predicted to be

$$\sigma_{th}(B_c^+) = 2.5 \text{ nb}, \tag{9.24}$$

with an error that is roughly a factor of 3. This should be compared with the cross section obtained from the experimental result [52], using the value $(2.5 \pm 0.5) \times 10^{-2}$ for the branching

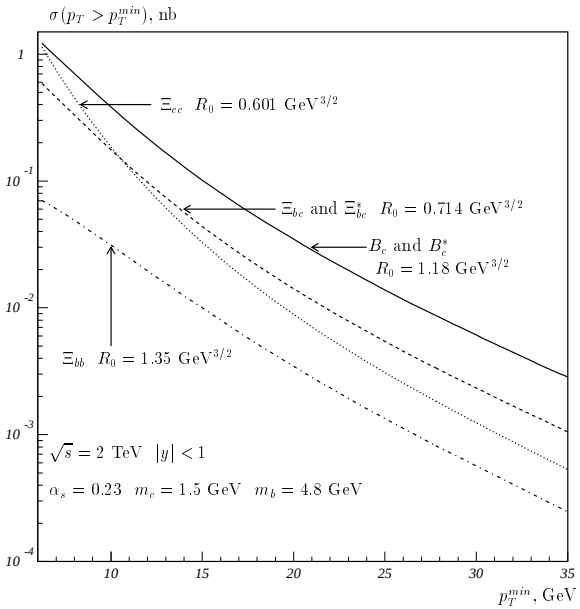

Figure 9.30: Integrated cross sections for the B_c meson and doubly-heavy baryons.

fraction for $B_c^+ \to J/\psi + l\nu$,

$$\sigma_{exp.} \sim 10 \pm 6 \text{ nb} . \tag{9.25}$$

The B_c cross section should be measured much more accurately in Run II. If the cross section proves to be significantly higher than predicted by the color-singlet model, it may indicate that color-octet production mechanisms are also important.

9.3.3 Theory of B_c Decays[2]

Decays of the long-lived heavy meson B_c, which contains two heavy quarks of different flavors, were considered in the pioneering paper written by Bjorken in 1986 [61]. Bjorken's report gave a unified view of the decays of hadrons with heavy quarks: mesons and baryons with a single heavy quark, the B_c meson, and baryons with two and three heavy quarks. A major effort was recently directed to study the long-lived doubly-heavy hadrons using modern understanding of QCD dynamics in the weak decays of heavy flavors. The modern theoretical tools are the Operator Product Expansion, sum rules of QCD and NRQCD, and potential models adjusted using data from hadrons with a single heavy quark. Surprisingly,

[2]Authors: V.V.Kiselev, A.K.Likhoded

Bjorken's estimates of total widths and various branching fractions are close to what is evaluated in a more strict manner.

Various hadronic matrix elements enter in the description of weak decays. Measuring the lifetimes and branching ratios therefore provides information about nonperturbative QCD interactions. This is important in the determination of electroweak parameters, such as the quark masses and the mixing angles in the CKM matrix, which enter into constraints on the physics beyond the Standard Model. The accumulation of more data on hadrons with heavy quarks will provide greater accuracy and confidence in our understanding of the QCD dynamics that is necessary to isolate the electroweak parameters.

A new laboratory for such investigations is the doubly-heavy long-lived quarkonium B_c recently observed for the first time by the CDF Collaboration [52]. The measured B_c lifetime is equal to

$$\tau[B_c] = 0.46^{+0.18}_{-0.16} \pm 0.03 \text{ ps} . \tag{9.26}$$

In studying the B_c meson, we can take advantage of two features that it has in common with the $\bar{b}b$ and $\bar{c}c$ quarkonia: the nonrelativistic motion of the $\bar{b}$ and c quarks and the suppression of the light quark-antiquark sea. These two physical conditions imply two small expansion parameters for B_c: the relative velocity v of quarks and the ratio Λ_{QCD}/m_Q of the confinement scale to the heavy quark mass. The double expansion in v and $1/m_Q$ generalizes the HQET approach [62,63] to what is called NRQCD [64]. The energy release in heavy quark decays determines the $1/m_Q$ parameter to be the appropriate quantity for the operator product expansion (OPE) and also justifies the use of potential models (PM) in the calculations of hadronic matrix elements. The same arguments ensure the applicability of sum rules (SR) of QCD and NRQCD.

The B_c decays were first calculated using potential models [65]. Various models gave similar estimates after adjusting parameters to reproduce the semileptonic decay rates of B mesons. The OPE evaluation of inclusive decays gave values for the lifetime and inclusive widths that agreed with the sum of the dominant exclusive modes predicted by the potential models. Quite unexpectedly, QCD sum rules gave values for the semileptonic B_c widths [66] that were an order of magnitude smaller than predicted by the potential models and by the OPE. The reason for this was that Coulomb-like α_s/v corrections had been neglected in the sum rule calculations. These corrections can be taken into account by summing up α_s/v corrections to all orders. They are significant both for heavy quarkonia and for the B_c [67,68]. At present, all three approaches give similar results for the lifetime and inclusive decay modes of the B_c for similar sets of parameters. Nevertheless, various dynamical questions remain open:

- What is the appropriate renormalization scale for the nonleptonic weak Lagrangian, which basically determines the lifetime of the B_c?
- What are the values of masses for the charmed and beauty quarks?
- What are the implications of NRQCD symmetries for the form factors of B_c decays and partial widths?

- How consistent is our understanding of the hadronic matrix elements that characterize B_c decays with the data on the other heavy hadrons?

In the present short review of B_c decays, we summarize the theoretical predictions and discuss how direct experimental measurements can answer the questions above.

9.3.3.1 Lifetime and inclusive decay rates

The B_c-meson decay processes can be subdivided into three classes:

- the $\bar{b}$-quark decay with a spectator c-quark,
- the c-quark decay with a spectator $\bar{b}$-quark and
- the annihilation decays $\bar{b}c \to l^+\nu_l, c\bar{s}, u\bar{s}$, where $l = e,\ \mu,\ \tau$.

In the $\bar{b} \to \bar{c}c\bar{s}$ decays, one separates also the *Pauli interference* with the c-quark from the initial state. In accordance with the given classification, the total width is the sum over the partial widths from $\bar{b}c$ annihilation, $\bar{b}$ decay, c decay, and Pauli interference.

The annihilation width is the sum of the widths from the annihilation of the $\bar{b}c$ into leptons and quarks. In the width from annihilation into quarks, one must take into account the hard-gluon corrections to the effective four-quark interaction of weak currents, which give an enhancement factor $a_1 = 1.22 \pm 0.04$. The nonperturbative effects of QCD can be absorbed into the leptonic decay constant $f_{B_c} \approx 400$ MeV. This estimate of the contribution from annihilation into quarks does not depend on a hadronization model, since a large energy release of the order of the meson mass takes place. Because of helicity suppression, the decay width is proportional to the square of the masses of leptons or quarks in the final state. Thus the only important annihilation channels are $\bar{b}c \to \tau^+\nu_\tau$ and $\bar{b}c \to c\bar{s}$.

B_c decay mode	OPE, %	PM, %	SR, %
$\bar{b} \to \bar{c}l^+\nu_l$	3.9 ± 1.0	3.7 ± 0.9	2.9 ± 0.3
$\bar{b} \to \bar{c}u\bar{d}$	16.2 ± 4.1	16.7 ± 4.2	13.1 ± 1.3
$\sum \bar{b} \to \bar{c}$	25.0 ± 6.2	25.0 ± 6.2	19.6 ± 1.9
$c \to sl^+\nu_l$	8.5 ± 2.1	10.1 ± 2.5	9.0 ± 0.9
$c \to su\bar{d}$	47.3 ± 11.8	45.4 ± 11.4	54.0 ± 5.4
$\sum c \to s$	64.3 ± 16.1	65.6 ± 16.4	72.0 ± 7.2
$B_c^+ \to \tau^+\nu_\tau$	2.9 ± 0.7	2.0 ± 0.5	1.8 ± 0.2
$B_c^+ \to c\bar{s}$	7.2 ± 1.8	7.2 ± 1.8	6.6 ± 0.7

Table 9.6: Branching ratios of B_c decay modes calculated using the operator product expansion (OPE) approach, by summing up the exclusive modes from potential models (PM) [65,67], and by using sum rules (SR) of QCD and NRQCD [67].

For the non-annihilation contributions to the width of the B_c, one can apply the *operator product expansion* (OPE) for the quark currents of weak decays [69]. One takes into account the α_s-corrections to the free quark decays and uses quark-hadron duality for the final states.

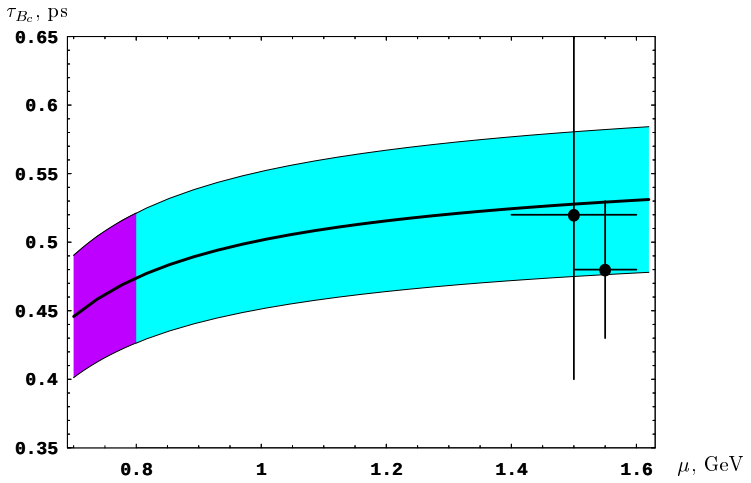

Figure 9.31: The B_c lifetime calculated in QCD sum rules versus the scale of hadronic weak Lagrangian. The shaded region shows the uncertainty of estimates, the dark shaded region is the preferable choice as given by the lifetimes of charmed mesons. The points represent the values in OPE approach taken from Ref. [69].

Then one considers the matrix element for the transition operator in the bound meson state. The latter allows one also to take into account the effects caused by the motion and virtuality of decaying quark inside the meson because of the interaction with the spectator. In this way the $\bar{b} \to \bar{c}c\bar{s}$ decay mode turns out to be suppressed almost completely due to the Pauli interference with the charm quark from the initial state. The c-quark decays with a spectator $\bar{b}$ are also suppressed compared to the decay of a free c-quark, because of the large binding energy of the initial state. Possible effects of interference between the leading-order weak amplitudes and the penguin corrections in B_c decays were considered in the framework of OPE in Ref. [70], and these corrections were estimated to be about 4%.

To calculate inclusive widths in the potential model approach, it is necessary to sum up the widths of exclusive decay modes [65]. For semileptonic decays via the transition $\bar{b} \to \bar{c}l^+\nu_l$, one finds that the hadronic final state is almost completely saturated by the most deeply bound states in the $\bar{c}c$ system, *i.e.* by the $1S$ states η_c and J/ψ. For semileptonic decays via the transition $c \to sl^+\nu_l$, one finds that the only $\bar{b}s$ states that can enter the accessible energy gap are the B_s and B_s^*. Furthermore, the $\bar{b} \to \bar{c}u\bar{d}$ channel, for example, can be calculated by multiplying the decay width for $\bar{b} \to \bar{c}l^+\nu_l$ by a color factor and by taking into account hard-gluon corrections to the four-quark interaction. It can be also obtained as a sum over the widths of decays involving specific $u\bar{d}$ bound states.

The calculations of the total B_c width in the inclusive OPE approach and the exclusive potential model approach give consistent values, if one takes into account the largest uncer-

tainty, which comes from the quark masses (especially the charm quark). The final result is

$$\tau(B_c) = 0.55 \pm 0.15 \text{ ps}, \tag{9.27}$$

which agrees with the measured value of the B_c lifetime.

The OPE estimates of inclusive decay rates agree with recent calculations in the sum rules of QCD and NRQCD [67], where one assumed the saturation of hadronic final states by the ground levels in the $c\bar{c}$ and $b\bar{s}$ systems as well as the factorization that allows one to relate the semileptonic and hadronic decay modes. The Coulomb-like corrections in the heavy quarkonia states play an essential role in the B_c decays and allow one to remove the disagreement between the estimates in sum rules and OPE. In contrast to OPE, where the basic uncertainty is given by the variation of heavy quark masses, these parameters are fixed by the two-point sum rules for bottomonia and charmonia, so that the accuracy of sum rule calculations for the total width of B_c is determined by the choice of scale μ for the hadronic weak Lagrangian in decays of charmed quark. We show this dependence in Figure 9.31, where $m_c/2 < \mu < m_c$ and the dark shaded region corresponds to the scales preferred by data on the charmed meson lifetimes. Taking the preferred scale in the $c \to s$ decays of B_c to be equal to $\mu^2_{B_c} \approx (0.85 \text{ GeV})^2$ and setting $a_1(\mu_{B_c}) = 1.20$ in the charmed quark decays, we predict the lifetime to be [67]

$$\tau(B_c) = 0.48 \pm 0.05 \text{ ps}. \tag{9.28}$$

9.3.3.2 Semileptonic and leptonic modes

The semileptonic decay rates were underestimated in the QCD sum rule approach of Ref. [66], because large Coulomb-like corrections were not taken into account. The recent sum rule analysis in [67,68] decreased the uncertainty, so that the estimates agree with the calculations in the potential models. The widths and branching fractions calculated using QCD sum rules are presented in Table 9.7. The expected accuracy is about 10%. In practice, the most important semileptonic decay mode is to the J/ψ which is easily detected in experiments via its leptonic decays [52].

The estimates for exclusive semileptonic decay rates of the B_c into $1S$ charmonium states obtained from QCD sum rules agree with the values obtained from potential models in Ref. [65], which also considered the contributions of decays to the excited $2S$ and $1P$ states. The direct decay rate into P-wave charmonium states is about 20% of the direct decay rate into the $1S$ states. The radiative decay of the χ_c states increases the total semileptonic decay rate of B_c to J/ψ by about 5%. The exclusive semileptonic decay rates of the B_c into the P-wave states χ_c and h_c have also been calculated within a framework that involves overlap integrals of the wavefunctions of the B_c and the charmonium states [71].

The dominant leptonic decay of B_c is given by the $\tau\nu_\tau$ mode (see Table 9.6). However, it has a low experimental efficiency of detection because of hadronic background in the τ decays and missing energy. Recently, in Refs. [72] the enhancement of muon and electron channels in the radiative modes was studied. The additional photon allows one to remove the helicity suppression for the leptonic decay of a pseudoscalar particle, which leads to an increase of the muonic decay rate by a factor of 2.

mode	Γ, 10^{-14} GeV	BR, %
$B_s e^+\nu_e$	5.8	4.0
$B_s^* e^+\nu_e$	7.2	5.0
$\eta_c e^+\nu_e$	1.1	0.75
$\eta_c \tau^+\nu_\tau$	0.33	0.22
$J/\psi e^+\nu_e$	2.8	2.1
$J/\psi \tau^+\nu_\tau$	0.7	0.51

Table 9.7: Widths and branching fractions for the semileptonic decay modes of the B_c meson calculated using QCD sum rules. (For the branching fractions, we set $\tau_{B_c} = 0.46$ ps.)

9.3.3.3 Nonleptonic modes

The inclusive nonleptonic width of the B_c can be estimated in the framework of quark-hadron duality (see Table 9.6). However, calculations of exclusive nonleptonic modes usually involve the approximation of factorization [73]. This approximation is expected to be quite accurate for the B_c, since the light quark-antiquark sea is suppressed in $\bar{b}c$ mesons. Thus, the important parameters are the factors a_1 and a_2 in the nonleptonic weak Lagrangian, which depend on the renormalization scale for the B_c decays. The QCD SR estimates for the widths of exclusive modes involving the nonleptonic decay of the charmed quark in B_c are presented in Table 9.8 [67]. They agree with the values predicted by the potential models.

For decays involving large recoils as in $B_c^+ \to \psi\pi^+(\rho^+)$, the spectator picture of the transition breaks down due to hard gluon exchanges. Taking these nonspectator effects into account increases the estimates of potential models by a factor of 4 [74]. The corresponding estimates in the factorization approach are determined by the leptonic decay constants and by the QCD coupling constant at the scale of the virtuality of the hard gluon. Numerically, one finds the values represented in Table 9.9. Due to the contribution of a t-channel diagram, the matrix element is *enhanced* by a factor of 2 compared to the potential model value. The spin effects in such decays were studied in [75]. The relative yield of excited charmonium states can be also evaluated. For example, the branching fraction for $B_c^+ \to \psi(2S)\pi^+$ should be smaller than that for $B_c^+ \to \psi\pi^+$ by about a factor of 0.36. The contributions to two-particle hadronic decays of B_c from P-wave states of charmonium were considered in Refs. [76] and [71] using methods that involve the hard-scattering of constituents with large recoil and the overlap of wave functions, respectively. In Ref. [76], the form factors have power-law tails that come from one-gluon exchange, and they therefore obtain larger values for the widths than Ref. [71], in which the form factors fall exponentially. The ratios of the widths for $B_c^+ \to \psi(2S)\pi^+$ in these two approaches agree with each other. The estimates of $B_c^+ \to \psi(2S)\rho^+$ modes are more model dependent. The cascade electromagnetic transitions of the χ_c states increase the inclusive $B_c \to J/\psi\pi(\rho)$ decay rates by about 8%. Finally, suppressed decays caused by flavor-changing neutral currents have been studied in Ref. [77].

CP-violation in B_c decays can be investigated in the same manner as for B decays, although it is very difficult in practice because of the low relative yield of B_c compared to

mode	Γ, 10^{-14} GeV	BR, %
$B_s\pi^+$	15.8 a_1^2	17.5
$B_s\rho^+$	6.7 a_1^2	7.4
$B_s^*\pi^+$	6.2 a_1^2	6.9
$B_s^*\rho^+$	20.0 a_1^2	22.2

Table 9.8: Widths and branching fractions of nonleptonic decay modes of the B_c meson. (For the branching fractions, we set $\tau_{B_c} = 0.46$ ps and a_1=1.26.)

mode	BR, %
$\psi\pi^+$	0.67 ± 0.07
$\eta_c\pi^+$	0.87 ± 0.09
$\psi\rho^+$	1.96 ± 0.20
$\eta_c\rho^+$	2.43 ± 0.24

Table 9.9: Widths and branching fractions of charmonium decay modes of the B_c meson. (For the branching fractions, we set $\tau_{B_c} = 0.46$ ps and a_1=1.26.)

ordinary B mesons: $\sigma(B_c)/\sigma(B) \sim 10^{-3}$. The expected CP-asymmetry of $\mathcal{A}(B_c^\pm \to J/\psi D^\pm)$ is about $4 \cdot 10^{-3}$, but this decay mode has a very small branching ratio of about 10^{-4} [78]. Another possibility is lepton tagging of the B_s in $B_c^\pm \to B_s^{(*)} l^\pm \nu$ decays for the study of mixing and CP-violation in the B_s sector [79].

9.3.3.4 Discussion and conclusions

We have reviewed the current status of theoretical predictions for the decays of B_c meson. We have found that the operator product expansion, potential models, and QCD sum rules all give consistent estimates for inclusive decay rates. The sum rule approach, which has been explored for the various heavy quark systems, leads to a smaller uncertainty due to the quite accurate knowledge of the heavy quark masses. The dominant contribution to the B_c lifetime is given by the charmed quark decays ($\sim 70\%$), while the b-quark decays and the weak annihilation add about 20% and 10%, respectively. The Coulomb-like α_s/v corrections play an essential role in the determination of exclusive form factors in the QCD sum rules. The form factors are expected to obey the relations dictated by the spin symmetry of NRQCD and HQET with quite good accuracy.

The accurate direct measurement of the B_c lifetime can provide us with the information on both the masses of charmed and beauty quarks and the normalization point of the nonleptonic weak Lagrangian that is responsible for the B_c decay (the a_1 and a_2 factors). The experimental study of semileptonic decays and the extraction of ratios for the form factors can test the spin symmetry derived in the NRQCD and HQET approaches. It can also decrease the theoretical uncertainties in the theoretical evaluation of quark parameters as well as the hadronic matrix elements that take into account nonperturbative effects caused by quark confinement. The measurement of branching fractions for the semileptonic and nonleptonic modes can give information on the values of factorization parameters, which

depend again on the normalization of the nonleptonic weak Lagrangian. The counting of charmed quarks in B_c decays is also sensitive to nonperturbative effects, because it is determined not only by the contribution from b quark decays, but also by the suppression of $\bar{b} \to c\bar{c}\bar{s}$ transitions due to destructive Pauli interference.

Thus, progress in measuring the B_c lifetime and decays should enhance the theoretical understanding of what really happens in heavy quark decays.

9.3.4 DØ Study of B_c: Triggering and Reconstruction [3]

9.3.4.1 Introduction

The B_c meson is a particularly interesting system to study since it contains two different heavy quarks that are often in competition regarding subsequent decays. As a result, measurements of its properties such as mass, lifetime, and decay branching ratios offer a unique window into heavy quark hadrons. Since it has nonzero flavor, it has no strong or electromagnetic annihilation decay channels, and it is the heaviest such meson predicted by the Standard Model. Its weak decay is expected to yield a large branching fraction to final states containing a J/ψ which is a useful experimental signature. The B_c meson (like the single-b baryons and doubly-heavy baryons) is too massive to produce at the B factories running at the $\Upsilon(4S)$. LEP has only a few B_c candidates, while CDF isolated a sample of 23 B_c decays in approximately 100 pb^{-1} of data [52] in Run I resulting in the estimate that $\sigma(B_c)/\sigma(b) \approx 2 \times 10^{-3}$.

9.3.4.2 DØ simulations

To examine DØ prospects for Run II, simulations were made of B_c production using PYTHIA and reweighting the resulting spectrum to match the differential $d\sigma/dp_T$ cross section calculated using code supplied by the authors of Ref. [80]. After reweighting, the production spectrum of produced B_c mesons is shown in Fig. 9.32. The mass of the B_c meson was set to 6.40 GeV and the lifetime to 0.50 ps, consistent with CDF and LEP measurements [52,81]. The fraction of $b \to B_c$ was increased to 0.5 while the fractions of $b \to B_d^0$, B^+, B_s^0, and Λ_b were scaled down appropriately. Any events containing two B_c mesons were discarded in order to get the hadron composition of the "away-side" B hadron correct. Events with $p_T(B_c) > 3$ GeV and $|\eta(B_c)| < 3$ were retained.

The CLEO QQ package was used to force the semileptonic decay $B_c \to J/\psi\ell\nu$ (Br $\approx$ 2.5% [82]) and $B_c \to J/\psi\pi$ (Br $\approx$ 0.2% [82]) followed by the subsequent decays of $J/\psi \to e^+e^-$ or $J/\psi \to \mu^+\mu^-$. The distinctive trilepton signature of the first decay mode was used to allow efficient triggering, from the presence of at least two electrons or muons with significant transverse momentum, with reasonable background rates.

Detector simulations were performed at a number of different levels of sophistication: MCFAST [83], PMCS (a DØ parameterized fast Monte Carlo), and full GEANT simulated

[3] Author: R. Van Kooten

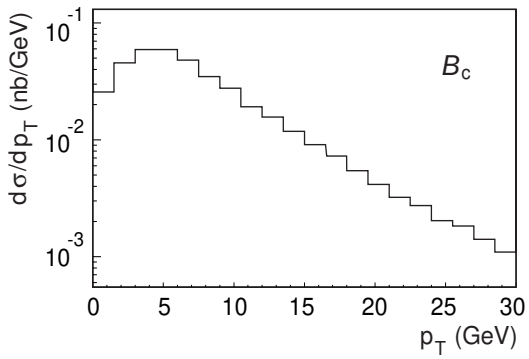

Figure 9.32: The differential cross section for the B_c meson used in the following studies.

events to allow the use of a more realistic trigger simulator and reconstruction resolution determination. Typical distributions of B_c decay products from the MCFAST simulation are shown in Fig. 9.33.

9.3.4.3 Results

MCFAST simulations could be used to determine kinematic and trigger efficiencies; however, the DØ trigger simulator was run on GEANT fully simulated events for a more sophisticated and reliable treatment. Starting with the case of a semileptonically decaying B_c where all three leptons are muons, Table 9.10 gives the DØ muon trigger efficiency for the indicated criteria. "Medium" and "Tight" muon identification refers to the correspondingly tighter requirements of coincidence of greater number of muon detector layers.

The status of the simulation of triggering on electrons is less complete, and trigger efficiencies in this case were extrapolated from prior studies [84] for the decay $B_d^0 \to J/\psi K_S^0$. At Level 1, information from the electromagnetic calorimeter, the fiber tracker, and matches between these and hits in the central preshower detector are expected to lead to a trigger efficiency of approximately 30%, but with a substantial background rate. This background rate is expected to be lowered to a reasonably low value with invariant mass cuts on the electrons from the $J/\psi \to e^+e^-$ decay applied at Level 2 of the trigger. An overall efficiency for triggering on states with di-electrons from the J/ψ decay is estimated to be 12.8%.

Although DØ will initially be running without a vertex silicon track trigger, studies were made of the potential for such a trigger to help isolate a large sample of B_c mesons. Note that the events were generated with a B_c lifetime set to 0.50 ps rather than the usual lifetimes of 1.5–1.6 ps of the other B mesons. A decay length resolution of 116 μm has been measured in MCFAST simulated events. A vertex silicon track trigger would operate by

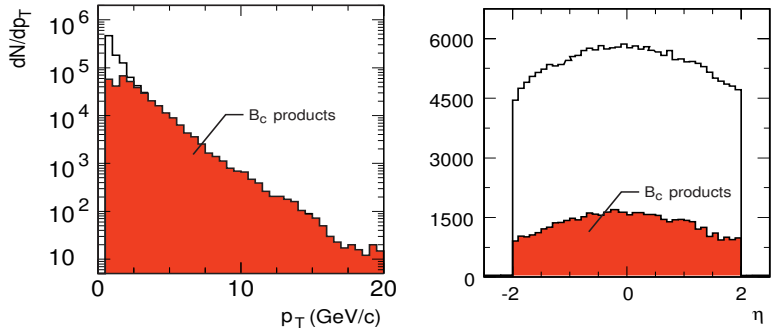

Figure 9.33: Kinematic distributions of (a) p_T and (b) η for all particles (open histograms) and for B_c semileptonic decay products (dark histograms)

examining the impact parameter significance, i.e., b/σ_b, where b is the impact parameter of a track and σ_b its error. The distribution of this quantity for tracks from B_c decay is shown in Fig. 9.34(a). This distribution is substantially narrower than for tracks from other B meson decays due to the shorter lifetime of the B_c. The trigger efficiency obtained by cutting on the presence of one or more tracks with large impact parameter significance is shown in Fig. 9.34(b). For the same background rate, the efficiency is about a factor of 2.5 times smaller than the comparable rate for $B_d^0 \to J/\psi K_S^0$ decays.

In the $B_c \to J/\psi \ell\nu$ channel, a typical mass reconstruction of the J/ψ through its decay into $\mu^+\mu^-$ is shown in Fig. 9.35(a) indicating a mass resolution σ_m of 29 MeV. Events are required to have the invariant mass of the two leptons assigned to the J/ψ within $2\sigma_m$ of the J/ψ mass. To reduce backgrounds, the p_T of the combined (J/ψ plus lepton) system was required to be greater than 8 GeV, and the decay length of the J/ψ-lepton vertex was required to be greater than 50 μm. Kinematic quantities such as the trilepton invariant mass yield information on the mass of the decaying state (Fig. 9.35).

Similar studies were extended to the $B_c \to J/\psi\pi$ decay channel that would allow an exclusive reconstruction of the B_c meson but with smaller statistics due to the small (0.2%) branching ratio for this final state. With only two leptons to trigger on, the overall trigger efficiency for the di-muon final state analogous to that shown in Table 9.10 is found to be slightly lower with a value of 0.24. The mass resolution of the reconstructed B_c without constraints on the J/ψ mass is found to be 52 MeV.

We proceed to estimate the expected number of B_c events reconstructed by DØ in Run II with an integrated luminosity of 2 fb^{-1}. One could use the estimate of $\sigma(B_c^+)/\sigma(\bar{b}) = 1.3 \times 10^{-3}$ compared to the measurement of $\sigma(B^+)/\sigma(\bar{b}) = 0.378 \pm 0.022$. It is more straightforward to use the CDF measurement [52] of

$$\frac{\sigma(B_c^+) \cdot \mathrm{Br}(B_c^+ \to J/\psi\ell\nu)}{\sigma(B^+) \cdot \mathrm{Br}(B^+ \to J/\psi K^+)} \tag{9.29}$$

and comparisons of DØ's trigger and reconstruction efficiency with the corresponding CDF

Criteria	Efficiency	DØ Designation
Single Muon		
$p_T^\mu > 4$ GeV $\|\eta^\mu\| < 1.5$ "Medium"	0.23	MTM5, MUO(1,4,A,M)
$p_T^\mu > 4$ GeV $\|\eta^\mu\| < 1.5$ "Tight"	0.08	MTM6, MUO(1,4,A,T)
Di-Muon		
Both $p_T^\mu > 2$ GeV $\|\eta^\mu\| < 1.5$ "Medium"	0.16	MTM10, MUO(2,2,A,M)
Both $p_T^\mu > 4$ GeV $\|\eta^\mu\| < 2.0$ "Medium"	0.15	MTM12, MUO(2,4,A,M)
"Or" of above	0.28	

Table 9.10: DØ Level 1 muon trigger efficiencies for trilepton final states from semileptonic decay of B_c mesons with $p_T(B_c) > 3$ GeV and $|\eta(B_c)| < 3$.

efficiencies. This leads to an estimate that approximately 600 identified $B_c^+ \to J/\psi\ell\nu$ would be produced. This sample is large enough to make improvements in the lifetime and mass measurements that would significantly increase our understanding of the B_c system. In addition, samples of 30–40 fully exclusive decays such as $B_c^+ \to J/\psi\pi$ can also be expected that would clearly supplement the semileptonic decay measurements which suffer from the escaping neutrino. Of course, proportionally much larger samples would be expected in subsequent runs of the Tevatron beyond Run IIa.

9.3.5 CDF Projections for B_c^+ yield in Run II[†]

9.3.5.1 Introduction

We present here the CDF projections for the B_c^+ yield in Run II by performing studies with Run I data and with Monte Carlo simulation and by using theoretical expectations for the branching ratios of various B_c^+ decay channels. We are making some simple projections for the decays $B_c^+ \to J/\psi\pi^+$, $B_c^+ \to B_s^0\pi^+$ and $B_c^+ \to J/\psi l^+\nu$. Please keep in mind for the rest of this section that references to a specific state imply the charge-conjugate state as well.

[†]Authors: Wei Hao, Vaia Papadimitriou

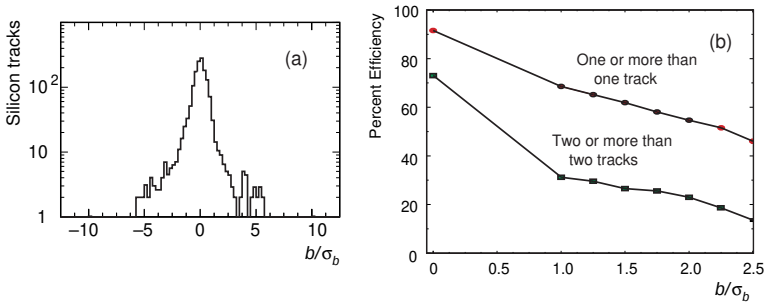

Figure 9.34: (a) Impact parameter divided by its error for track from $B_c \to J/\psi\ell\nu$; (b) efficiency of future silicon track trigger as a function of cut on b/σ_b.

9.3.5.2 Monte Carlo generation and simulation

B_c^+ Monte Carlo events were generated with a "toy" Monte Carlo using the P_t spectrum from a full α_s^4 perturbative QCD calculation of hadronic production of the B_c^+ meson [98] and assuming a flat rapidity y distribution (see Fig. 9.36). The B_c^+ mesons were generated with the mass set to 6.2 GeV/c^2, lifetime set to 0.3335 ps and in the region $P_t(B_c^+) >$ 3.0 GeV/c and $|y(B_c^+)| < 1.5$. The B_c^+ mesons were decayed to $J/\psi\pi^+$ or other decay channels using the CLEO decay table (QQ) and then they were simulated by the CDF Run I simulation package QFL′.

B^+ events, for comparison, were generated with a Monte Carlo which is generating b quarks according to the next-to-leading order QCD predictions [99], using a scale $\mu = \mu_0/2 \equiv \sqrt{(P_t)^2 + (m_b)^2}/2$ where P_t is the transverse momentum of the b quark and m_b its mass. m_b is set to 4.75 GeV/c^2. The b quark is fragmented into b hadrons using Peterson fragmentation [100] with the fragmentation parameter, ϵ_b, set to 0.006 . In Fig. 9.37 we show the P_t spectrum of the B^+, at the generation level, for $P_t(min)$ of the b-quark equal to 5.0 GeV and in the rapidity region $-1.3 < Y_{RANGE} < 1.3$. The B^+ events were decayed to $J/\psi K^+$ using QQ and then they were simulated by QFL′.

The theoretical cross sections used for the Monte Carlo generations were calculated for $\sqrt{s} = 1.8$ TeV.

9.3.5.3 Selection Criteria for the $B_c^+ \to J/\psi\pi^+$ decay channel

To select $J/\psi \to \mu^+\mu^-$ candidates, we require that the transverse momentum, P_t, of each muon is greater than 2.0 GeV/c. The CMU muon chambers, at a radius of 3.5 m from the beam axis, cover the pseudorapidity region $|\eta| < 0.6$. These chambers are complemented by the central muon upgrade system (CMP) which consists of four layers of drift tubes behind two feet of steel. In addition we have the CMX muon chambers covering the pseudorapidity

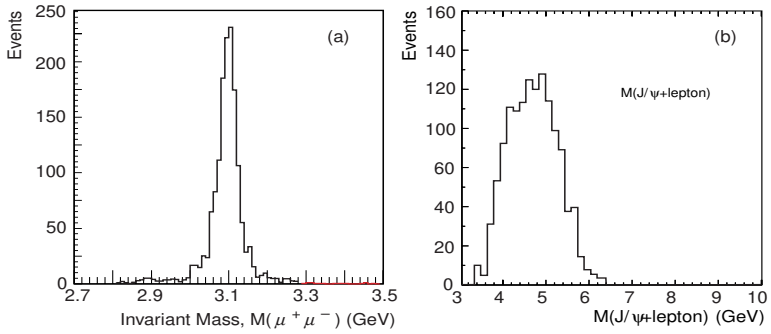

Figure 9.35: (a) $\mu^+\mu^-$ invariant mass distribution in $B_c \to J/\psi\ell\nu$ events; (b) tri-lepton invariant mass distribution that can be used to extract the B_c mass.

region $0.6 < |\eta| < 1.0$. The position matchings between muon chamber track and the track as measured in the Central Tracking Chamber (CTC) are required to have $\chi^2 < 9.0$ in r-ϕ and $\chi^2 < 12$ in r-z. There is no requirement on a specific trigger path. We require that at least one muon is reconstructed in the Silicon VerteX detector (SVX) (*i.e.* at least 3 associated SVX hits were found). We then keep the J/ψ candidates so that the muon pair passes a vertex constrained fit and the mass of the pair is within 50 MeV of the known value [101] of the J/ψ mass.

After the J/ψ candidates are found, events are scanned for other daughter particle candidates, π^+'s in this case, from B_c^+ decays. We reconstruct the B_c^+ by performing a vertex-constrained fit. The tracks with more than 3 associated SVX hits are considered to be SVX tracks, and all others are considered to be CTC tracks. We apply no further quality cuts to the SVX tracks. In the vertex constrained fit the invariant mass of the $\mu^+\mu^-$ pair is constrained to the known J/ψ mass [101]. For each B_c^+ candidate, we require that the χ^2 probability of the fit be greater than 1%.

After the B_c^+ is reconstructed, the following cuts are applied: all the B_c^+ candidates are required to have transverse momentum $P_t(B_c^+)$ greater than 6.0 GeV/c; proper lifetime $ct(B_c^+)$ greater than 80 μm; impact parameter with respect to the beam line $|I_{xy}(B_c^+)|$ less than 80 μm. We also require that the π^+ is reconstructed in the SVX and that $P_t(\pi^+) > 2.5$ GeV/c.

9.3.5.4 Acceptance Calculation using QFL′

Using the QFL′ Monte Carlo we find that the geometric/kinematic acceptance for $B_c^+ \to J/\psi\pi^+$ is equal to ∼0.018 while the same acceptance, and with the same selection criteria, for $B^+ \to J/\psi K^+$ is equal to ∼0.04 [102]. These acceptances are calculated in the region $6.0 < P_t < 30.0$ and $|y| < 0.9$ where P_t and y are the transverse momentum and rapidity, respectively, of the B_c^+ or B^+ mesons. The acceptances are calculated with the default kine-

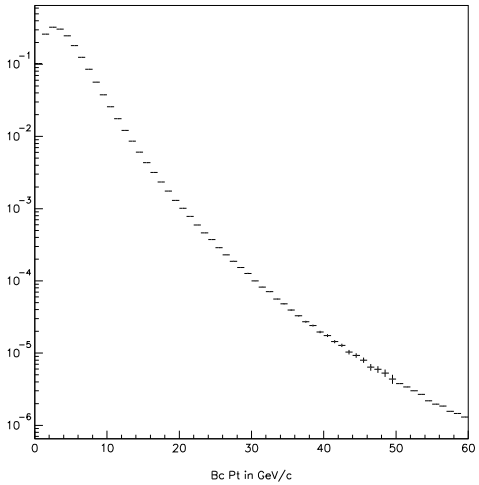

Figure 9.36: P_t distribution of B_c^+ mesons in GeV/c, at the generation level.

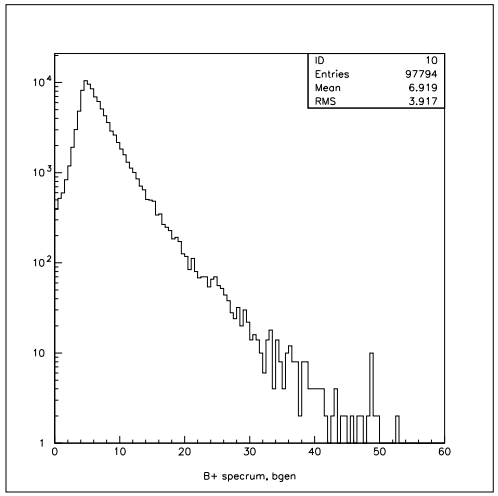

Figure 9.37: P_t distribution of B^+ mesons in GeV/c, at the generation level.

matic cuts of $P_t(B_c^+, B^+) > 6.0 GeV/c$, $P_t(\pi^+, K^+) > 2.5 GeV/c$, $|I_{xy}(B_c^+, B^+)| < 80\mu m$ and $ct(B_c^+, B^+) > 80\mu m$. At least one of the two muons forming the J/ψ has to be reconstructed in the SVX. These acceptances do not include any trigger efficiency corrections.

9.3.5.5 Yield estimate for the $B_c^+ \to J/\psi\pi^+$ decay channel

We know that $\sigma(B_c^+) \cdot BR(B_c^+ \to J/\psi\pi^+)$ is equal to:

$$R_l \cdot \sigma(B^+) \cdot BR(B^+ \to J/\psi K^+) \cdot \frac{BR(B_c^+ \to J/\psi\pi^+)}{BR(B_c^+ \to J/\psi l^+\nu)},$$

where

$$R_l = \frac{\sigma(B_c^+) \cdot BR(B_c^+ \to J/\psi l^+\nu)}{\sigma(B^+) \cdot BR(B^+ \to J/\psi K^+)} \tag{9.30}$$

and σ stands for production cross section and BR stands for branching ratio. We get the ratio R_l from [52], $\sigma(B^+)$ from [103] and $BR(B^+ \to J/\psi K^+)$ from [101]. We tabulate the theoretical expectations for the value of the ratio

$$R = \frac{BR(B_c^+ \to J/\psi\pi^+)}{BR(B_c^+ \to J/\psi l^+\nu)} \tag{9.31}$$

in Table 1. These values cover a wide spectrum from 0.06 to 0.32 according to References [104]- [61]. For this study we use as a default value the one from Reference [104]. $\sigma(B_c^+) \cdot BR(B_c^+ \to J/\psi\pi^+)$ is equal to $(0.132^{+0.061}_{-0.052}) \cdot (3.52 \pm 0.61\mu b) \cdot (9.9 \pm 1.0) \times 10^{-4} \cdot (0.091) = (4.6 \pm 2.3) \cdot 10^{-4} \cdot 0.091$ μb. Then we multiply the calculated value of $\sigma(B_c^+) \cdot BR(B_c^+ \to J/\psi\pi^+)$, which is the cross section times the branching ratio of either positively charged or negatively charged B_c's, by the branching ratio of the decay $J/\psi \to \mu^+\mu^-$ [101], by the total integrated luminosity (100 pb^{-1}) and by the kinematic/geometric acceptance of the decay $B_c^+ \to J/\psi\pi^+$ (0.018). This way we get the number, S, of $B_c^+ \to J/\psi\pi^+$ events expected in our Run I sample. Then we multiply that number by 2 to account for both positively and negatively charged particles. S is approximately equal to 9 events. If we consider the variations in R discussed above, then the expected number of $B_c^+ \to J/\psi\pi^+$ events in Run I varies between 6 and 32.

One could think that we could possibly exclude the possibility of an R in the range of 0.3 based on the number of events we currently observe or based on the limit we set on

$$R_\pi = \frac{\sigma(B_c^+) \cdot BR(B_c^+ \to J/\psi\pi^+)}{\sigma(B^+) \cdot BR(B^+ \to J/\psi K^+)} \tag{9.32}$$

in [108] using Run I data. As can be seen from Fig. 9.38, which is taken from Reference [108], $R_\pi < 0.10$ for a B_c^+ lifetime of 0.33 ps and $R_\pi < 0.07$ for a B_c^+ lifetime of 0.50 ps. We can write R_π as equal to:

$$R_l \cdot \frac{BR(B_c^+ \to J/\psi\pi^+)}{BR(B_c^+ \to J/\psi l^+\nu)}.$$

We get the ratio R_l from ref. [52] to be equal to 0.132 and the ratio $\frac{BR(B_c^+ \to J/\psi\pi^+)}{BR(B_c^+ \to J/\psi l^+\nu)}$ to be in the range 0.06-0.32. This results in R_π in the range 0.008-0.04. We see that we cannot really exclude the value 0.32 for R based on our published limit for R_π.

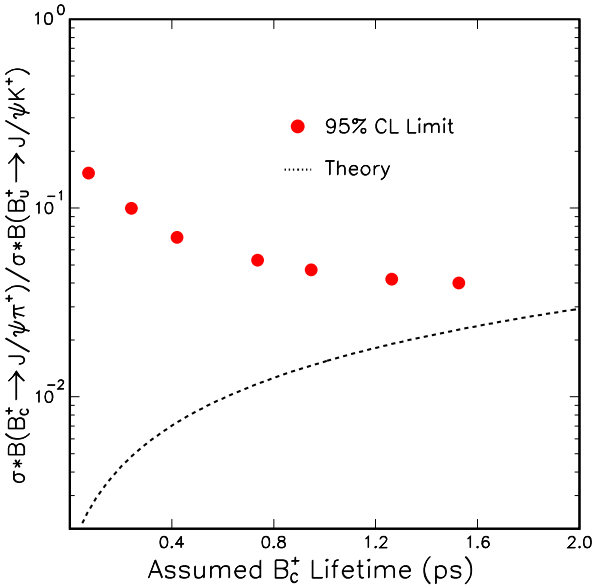

Figure 9.38: The circular points show the different 95% CL limits on the ratio of cross section times branching fraction for $B_c^+ \to J/\psi\pi^+$ relative to $B^+ \to J/\psi K^+$ as a function of the B_c^+ lifetime. The dotted curve represents a calculation of this ratio based on the assumption that the B_c^+ is produced 1.5×10^{-3} times as often as all other B mesons and that $\Gamma(B_c^+ \to J/\psi\pi^+) = 4.2 \times 10^9$ s^{-1}.

For Run IIa we expect to have an integrated luminosity of 2 fb^{-1}, that is an increase by a factor of 20 in comparison with Run I. In Run II we will take data with an upgraded silicon detector that has extended coverage in comparison to Run I by a factor of 1.4. We also plan to run with extended muon coverage for muons of type CMP (x1.2) and CMX (x1.3) and with lower muon P_t thresholds. For CMU type muons we plan to lower the thresholds from 2.0 GeV/c to 1.5 GeV/c. If we lower our P_t muon thresholds from 2.0 GeV/c to 1.5 GeV/c in our current Run I analysis we get an increase of acceptance by a factor of 1.43. According to reference [109] there will be a factor of 2 increase in the $B^0 \to J/\psi K_s^0$ yield due to the extended muon coverage and due to the lowering of the muon P_t threshold from 2.0 GeV/c to 1.5 GeV/c. Assuming conservatively an increase in yield in Run IIa by a factor of 40 in comparison to Run I we expect to have approximately 360 events in the decay channel $B_c^+ \to J/\psi\pi^+$.

In Fig. 9.39 we show the distribution of the B_c^+ mass from Monte Carlo after the selection requirements described above. Here we have lowered the muon P_t threshold to 1.5 GeV/c. The mass resolution is 17.9±0.3 MeV.

Reference	$B_c^+ \to J/\psi\pi^+$	$B_c^+ \to J/\psi l^+\nu$	R
Chang, Chen (1994) [104]	$\Gamma = 3.14 \cdot 10^{-6}$ eV	$\Gamma = 34.4 \cdot 10^{-6}$ eV	0.091
Gershtein et al (1998) [106]	BR = 0.2%	BR = 2.5%	0.08
Gershtein et al (1995) [105]	$\Gamma = 3.14 \cdot 10^{-6}$ eV	$\Gamma = 38.5 \cdot 10^{-6}$ eV (ISGW1)	0.08
	$\Gamma = 3.14 \cdot 10^{-6}$ eV	$\Gamma = 53.1 \cdot 10^{-6}$ eV (ISGW2)	0.06
Kiselev et al. (1999) [107]	BR = 0.67%	BR = 2.1%	0.32
Bjorken (1986) [61]	BR = 0.6%	BR = 2.0%	0.29

Table 9.11: Theoretical estimations of the branching ratios of two B_c^+ decay modes and of their ratio R.

9.3.5.6 Yield estimate for the $B_c^+ \to B_s^0\pi^+$ decay channel

From Reference [104] we see that $\Gamma = 73.3 \cdot 10^{-6}$ eV for the decay channel $B_c^+ \to B_s^0\pi^+$ and that $\Gamma = 34.4 \cdot 10^{-6}$ eV for the decay channel $B_c^+ \to J/\psi l^+\nu$. Using the fact that from References [61,106,107] the branching ratio of $B_c^+ \to J/\psi l^+\nu$ is expected to be ~2.2%, we derive the branching ratio for $B_c^+ \to B_s^0\pi^+$ to be equal to 4.7%.

According to Reference [110] we had 58 ± 12 $B_s^0 \to J/\psi\phi$ events in Run I and if we multiply the yield by a factor of 40 for Run IIa we will have ~ 2,400 events.

From Reference [109] we see that we expect 23,400 fully reconstructed B_s^0 events in the decay channels $B_s^0 \to D_s^-\pi^+$ and $B_s^0 \to D_s^-\pi^+\pi^-\pi^+$ for scenario A and 15,300 events for scenario C. Scenario A corresponds to a Tevatron running with bunch spacing of 396 ns and instantaneous luminosity of 0.7×10^{32} cm^{-2}s^{-1} and scenario C corresponds to a Tevatron running with bunch spacing of 396 ns and instantaneous luminosity of 1.7×10^{32} cm^{-2}s^{-1}. Based on these we conservatively assume a total of 25,000 fully reconstructed B_s^0 events in Run IIa.

From the CDF measurement of R_l [52], from the branching ratios of $B_c^+ \to J/\psi l^+\nu$ = 2.2% and $B^+ \to J/\psi K^+$ = 0.099% [101] and from the fact that 39.7% of b quarks fragment into B^+ mesons [101] we get that $\sigma(B_c^+)/\sigma(b)$ is equal to $2.3 \cdot 10^{-3}$. On the other hand we know that $\sigma(B_s^0)/\sigma(b)$ is equal to 10.5% [101], that is, $\sigma(B_s^0)/\sigma(B_c^+)$ is equal to 45.6. Therefore the observed number of $B_c^+ \to B_s^0\pi^+$ events in Run IIa will be equal to $25,000/45.6 \cdot 4.7\% \cdot A_\pi$ where A_π is the acceptance for finding the pion in $B_c^+ \to B_s^0\pi^+$ after having found the B_s^0. For $A_\pi = 100\%$, we would observe 26 such decays.

If we wanted to estimate how many of the expected 25,000 fully reconstructed B_s^0 events in Run IIa will originate from B_c^+ decays, we would have to multiply $25,000/45.6 = 548.2$ by the branching ratio $BR(B_c^+ \to B_s^0/B_s^{0*}X)$ and the acceptance of reconstructing X in the presence of the B_s^0/B_s^{0*}.

In Table 9.12 we show the widths of various B_c^+ decays involving a B_s^0 or a B_s^{0*} meson from Reference [104]. If this is a complete list of the B_c^+ decays involving a B_s^0 or a B_s^{0*} and if we use the fact (as in the beginning of this section) that $\Gamma = 34.4 \cdot 10^{-6}$ eV for the decay $B_c^+ \to J/\psi l^+\nu$ and the corresponding branching ratio is expected to be ~2.2%, then $BR(B_c^+ \to B_s^0/B_s^{0*}X)$ is expected to be equal to 29.5%. It will be very useful to measure the above branching ratios. If the expectations are correct though, the above discussion

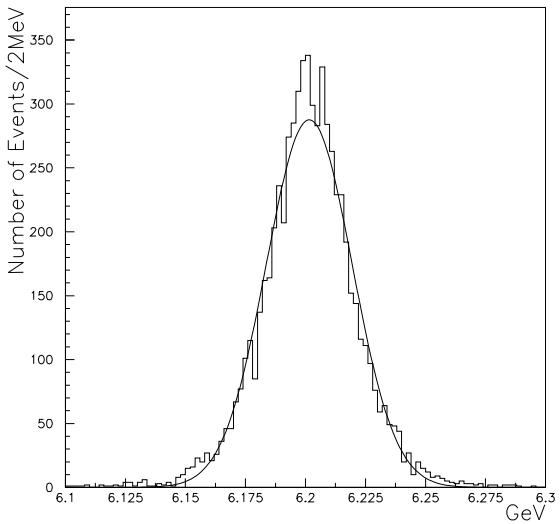

Figure 9.39: Mass distribution of B_c^+ mesons in GeV/c^2.

indicates that we will not have many B_c^+ candidates decaying to a B_s^0 or a B_s^{0*}. We have to also take into account that it will not be easy to detect the photon from the B_s^{0*} decay or to reconstruct the ρ meson in some of the above decays.

9.3.5.7 Yield estimate for the $B_c^+ \to J/\psi l^+\nu$ decay channel

For the decay channel $B_c^+ \to J/\psi l^+\nu$ we expect to observe ~ 800 events in Run IIa based on the 20.4 candidates of Run I [52] and the factor of 40 expected increase in the yield.

9.3.5.8 Conclusion

In Run IIa we expect to see ~ 800 $B_c^+ \to J/\psi l^+\nu$ events, ~ 360 $B_c^+ \to J/\psi\pi^+$ events and maybe a small number of events from other exclusive decay channels. We can use these events to measure accurately the B_c^+ mass and lifetime as well as ratios of various B_c^+ branching ratios.

Decay Mode	Width in 10^{-6} eV [104]
$B_c^+ \to B_s^0 e^+ \bar{\nu_e}$	26.6
$B_c^+ \to B_s^{0*} e^+ \bar{\nu_e}$	44.0
$B_c^+ \to B_s^0 \pi^+$	73.3
$B_c^+ \to B_s^0 \rho^+$	56.1
$B_c^+ \to B_s^{0*} \pi^+$	64.7
$B_c^+ \to B_s^{0*} \rho^+$	188.0
$B_c^+ \to B_s^0 K^+$	5.27
$B_c^+ \to B_s^{0*} K^+$	3.72
Total	461.69

Table 9.12: Theoretical estimates of the width of B_c^+ decay modes involving B_s^0 or B_s^{0*} in the final states.

9.4 Doubly-heavy Baryons

Doubly-heavy baryons are baryons that contain two heavy quarks, either cc, bc or bb. These hadrons provide yet another window onto the dynamics of heavy quarks. Doubly-heavy baryons are expected to be produced at respectable rates at the Tevatron; the basic production cross sections are in the nanobarn range. Also of interest are the states formed from three heavy quarks: bbb, bbc, bcc or ccc. We do not provide cross section estimates for these triply-heavy baryons.

9.4.1 Spectroscopy†

The spectroscopy of baryons containing two heavy quarks QQ is of interest because of similarities both to a quarkonium state, $Q\bar{Q}$ and to a heavy-light meson, $\bar{Q}q$. On the one hand, the slow relative motion of the two heavy quarks is similar to quarkonium. On the other hand, the lighter degree of freedom moves relativistically around the slowly moving QQ. Since the QQ is in a color antitriplet state, in the heavy quark limit the system is very similar to a $\bar{Q}q$ system.

A rich spectrum of excitations is expected, both excitations of the QQ system as well as the light degrees of freedom. However from the experimental point of view, a detailed discussion of the excited states is probably premature. We will limit our discussion here to the estimates of the masses of the lowest lying states, $\Xi_{QQ'} = (QQ'q)$, $\Omega_{QQ'} = (QQ's)$ containing two heavy quarks and the states $\Xi_{QQQ'} = (QQQ')$, $\Omega_{QQQ} = (QQQ)$ containing three heavy quarks. Where the corresponding $J = \frac{1}{2}$ state exists, the $J = \frac{3}{2}$ states are unstable decaying to the ground state by photon emission. The hyperfine splittings with the spin-$\frac{1}{2}$ states are calculated using the procedure of De Rujula et al. [125]. Ignoring electromagnetism we have that

$$H = H_0 + \alpha \sum_{i<j} \frac{s_i \cdot s_j}{m_i m_j} \,, \tag{9.33}$$

†Author: R.K. Ellis

where the sum runs over the three pairs of quarks and α is a constant fixed using the normal decuplet-octet splitting.

Estimates for the masses and spectra of the baryons containing two or more heavy quarks have been considered by many authors [111]- [124]. We are not aware of a reference which gives the masses of all the states we are interested in. This is of some importance since the separation between states may be more reliable than the absolute energy scale. We have therefore created a complete list, using the simple procedure suggested by Bjorken [111]. The mass of the spin-$\frac{3}{2}$, QQQ baryons are calculated by scaling from the $Q\bar{Q}$ state,

$$\frac{M_{QQQ}}{M_{Q\bar{Q}}} = \frac{3}{2} + \frac{k}{m^{\frac{4}{3}}} + \frac{k'}{\ln^2 m/m_0} \,. \tag{9.34}$$

Experience from the Δ, ρ and Ω, ϕ systems suggest the values

$$M_{ccc} = (1.59 \pm 0.03) M_{c\bar{c}}, \quad M_{bbb} = (1.56 \pm 0.02) M_{b\bar{b}} \,. \tag{9.35}$$

The other spin-$\frac{3}{2}$ baryons are estimated using an equal spacing rule to interpolate between the QQQ state and normal $J = \frac{3}{2}$ baryons. This results in the rule that replacing a b-quark by a c-quark costs 3.280 GeV, a c-quark by an s-quark costs 1.085 GeV, and an s-quark by a u-quark costs 0.145 GeV. Finally the masses of the spin-$\frac{1}{2}$ baryons are calculated using the procedure and mass values of DGG [125]. The results for the hyperfine splitting are

$$\begin{aligned}
E(abc, J = \frac{3}{2}) &= E_0 + \frac{\alpha}{4}\Big(\frac{1}{m_a m_b} + \frac{1}{m_b m_c} + \frac{1}{m_c m_a}\Big), \\
E(bbc, J = \frac{1}{2}) &= E_0 + \frac{\alpha}{4}\Big(\frac{1}{m_b^2} - \frac{3}{m_b m_c}\Big), \\
E(abc, J = \frac{1}{2}) &= E_0 + \frac{\alpha}{4 m_a m_b m_c}\Big(-\Sigma - 2\sqrt{\Delta}\Big), \\
E'(abc, J = \frac{1}{2}) &= E_0 + \frac{\alpha}{4 m_a m_b m_c}\Big(-\Sigma + 2\sqrt{\Delta}\Big) \,,
\end{aligned} \tag{9.36}$$

where $\Sigma = m_a + m_b + m_c, \Delta = \Sigma^2 - 3(m_a m_b + m_b m_c + m_c m_a)$. The values found using this procedure are compared with the results of other authors in Table 9.13. We quote only the central values and refer the reader to the original publications for the estimated errors. There is substantial agreement between all estimates if these errors are taken into account.

9.4.2 Production†

The direct production of a doubly-heavy baryon can be treated within the NRQCD factorization framework described in Section 9.2.2. The cross section for the direct production of a bc baryon H can be expressed in the form (9.1) and (9.13), except that $b\bar{b}(n)$ is replaced by $bc(n)$. The short-distance cross section $d\hat{\sigma}[ij \to bc(n) + X]$ for creating the bc in the color and angular-momentum state n can be calculated as a perturbative expansion in α_s at scales of order m_c or larger. The nonperturbative matrix element $\langle O^H(n) \rangle$ encodes the

†Authors: E. Braaten, A. Likhoded

State	Mass ref. [113]	Mass ref. [112]	Mass ref. [114]	Mass
$\Xi_{cc}^{++}(ccu, J=\frac{3}{2})$	3.735	3.81	3.746	3.711
$\Omega_{cc}^{+}(ccs, J=\frac{3}{2})$	3.84	3.89	3.851	3.848
$\Omega_{ccc}^{++}(ccc, J=\frac{3}{2})$				4.925
$\Xi_{cc}^{++}(ccu, J=\frac{1}{2})$	3.70	3.66	3.676	3.651
$\Omega_{cc}^{+}(ccs, J=\frac{1}{2})$	3.72	3.76	3.787	3.811
$\Xi_{bc}^{+}(bcu, J=\frac{3}{2})$	7.02	7.02	7.083	7.000
$\Omega_{bc}^{0}(bcs, J=\frac{3}{2})$	7.105	7.11	7.165	7.128
$\Xi_{bcc}^{+}(bcc, J=\frac{3}{2})$				8.202
$\Xi_{bc}^{+}(bcu, J=\frac{1}{2})$	6.93	6.95	7.029	6.938
$\Xi_{bc}^{\prime +}(bcu, J=\frac{1}{2})$		7.00	7.053	6.971
$\Omega_{bc}^{0}(bcs, J=\frac{1}{2})$	7.00	7.05	7.126	7.095
$\Omega_{bc}^{\prime 0}(bcs, J=\frac{1}{2})$		7.09	7.148	7.115
$\Xi_{bcc}^{+}(bcc, J=\frac{1}{2})$				8.198
$\Xi_{bb}^{0}(bbu, J=\frac{3}{2})$	10.255	10.28	10.398	10.257
$\Omega_{bb}^{-}(bbs, J=\frac{3}{2})$	10.315	10.36	10.483	10.399
$\Xi_{bbc}^{0}(bbc, J=\frac{3}{2})$				11.481
$\Omega_{bbb}^{-}(bbb, J=\frac{3}{2})$				14.760
$\Xi_{bb}^{0}(bbu, J=\frac{1}{2})$	10.21	10.23		10.235
$\Omega_{bb}^{-}(bbs, J=\frac{1}{2})$	10.27	10.32		10.385
$\Xi_{bbc}^{0}(bbc, J=\frac{1}{2})$				11.476

Table 9.13: Mass estimates in GeV for low-lying baryons with two or more heavy quarks. The last column shows our values derived using the methods of Ref [111].

probability for a bc in the state n to bind to form the baryon H. The matrix element scales as a definite power of the relative velocity v of the charm quark.

The production mechanisms for bc are similar to those for $\bar{b}c$, because two heavy quark-antiquark pairs must be created in the collision. The lowest order mechanisms for creating bc are the order-α_s^4 processes $q\bar{q}, gg \to (bc) + \bar{b}\bar{c}$. The color state of the quark-quark system can be either color-antitriplet or color-sextet. From counting the color states, we expect the color-sextet cross section to be about a factor of 2 larger than the color-antitriplet cross section. Thus the relative importance of the two color states should be determined primarily by the probability for the b and c to bind with a light quark to produce a doubly-heavy baryon.

In the ground state Ξ_{bc} of the bc baryon system, the bc is in a color-antitriplet S-wave state that is relatively compact compared to the size of the baryon. The bc diquark behaves very much like the heavy antiquark in a heavy-light meson. The probability that b and c quarks that are created with small relative momentum in a parton collision will hadronize into the Ξ_{bc} is therefore expected to be greatest if the bc is in a color-antitriplet S-wave state. All other NRQCD matrix elements are suppressed by powers of v. If we keep only the color-antitriplet S-wave contribution, the formula for the cross section of Ξ_{bc} is very similar to that for the B_c in the color-singlet model. The short-distance cross section for creating

a color-singlet $\bar{b}c$ is replaced by the cross section for creating a color-antitriplet bc. The long-distance factor for B_c, which is proportional to the square of the radial wavefunction at the origin $R_{1S}(0)$, is replaced by a color-antitriplet matrix element for the Ξ_{bc}. This matrix element can be treated as a phenomenological parameter analogous to the color-octet matrix elements for quarkonium production. It can also be estimated using a quark potential model for the doubly-heavy baryon, in which case it is proportional to the square of an effective radial wavefunction at the origin $R_{1S}^{bc}(0)$ for the bc diquark. The quark model estimate is probably much less reliable than the potential model estimate of $R_{1S}(0)$ for B_c. We will refer to the cross sections obtained by using the leading order bc cross section and a quark model estimate for the S-wave color-antitriplet matrix element as the *diquark model* for doubly-heavy baryon production.

The production of doubly-heavy baryons in the diquark model at order α_s^4 was studied in detail in the series of papers [60]. The resulting differential cross sections $d\sigma/dp_T$ for Ξ_{cc}, Ξ_{bc} and Ξ_{bb} baryons are presented in Fig. 9.29 and compared to that of the B_c meson. The cross sections integrated over p_T greater than ${p_T}^{min}$ are shown in Fig. 9.30. The cross sections are evaluated at 2.0 TeV and integrated over $|y| < 1$. The quark masses were set to $m_c = 1.5$ GeV and $m_b = 4.8$ GeV. The QCD coupling constant was fixed at $\alpha_s = 0.23$. The radial wave functions at the origin for the heavy diquarks were taken to be $R_{1S}^{cc}(0) = 0.601$ GeV$^{3/2}$, $R_{1S}^{bc}(0) = 0.714$ GeV$^{3/2}$, and $R_{1S}^{bb}(0) = 1.35$ GeV$^{3/2}$ [86]. The largest uncertainties come from the choice of scale in the overall factor $\alpha_s^4(\mu)$ and from the radial wave functions at the origin for the heavy diquarks. The production rates for Ξ_{cc} and Ξ_{bc} are predicted to be as large as 50% of the production rate for $(B_c + B_c^*)$ for ${p_T}^{min} = 10$ GeV.

The uncertainties in the prediction of the Ξ_{bc} cross section can be greatly reduced by normalizing the cross section to that of the B_c. The reason is that the short-distance cross sections come from exactly the same Feynman diagrams, except that the color-singlet $\bar{b}c$ is replaced by a color-antitriplet bc. Regions of phase space with various gluon virtualities μ are weighted in almost the same way, so the factor of $\alpha_s^4(\mu)$ that gives the largest uncertainty in the B_c cross section cancels in the ratio $\sigma(\Xi_{bc})/\sigma(B_c)$ given that $\mu_{bc} = \mu_{b\bar{c}}$. The largest remaining uncertainty comes from the radial wave function at the origin $R_{1S}^{bc}(0)$ for the heavy diquark in the Ξ_{bc}. Using the value $R_{1S}^{bc}(0) = 0.714$ GeV$^{3/2}$, one gets the estimate

$$\sigma(\Xi_{bc})/\sigma(B_c) \simeq 0.5\,. \tag{9.37}$$

Taking into account the cascade decays of excited bc baryon states, the inclusive Ξ_{bc} cross-section integrated over $p_T > 6$ GeV and $|y| < 1$ is predicted to be

$$\sigma(\Xi_{bc}) = 1.5\ nb\,. \tag{9.38}$$

Alternatively, taking the experimental value for the B_c cross section [52], we get

$$\sigma(\Xi_{bc}) = 5 \pm 3\ nb\,. \tag{9.39}$$

With an integrated luminosity of about 100 pb^{-1} in Run I, this corresponds to more than 10^5 events with Ξ_{bc} baryons in the considered kinematical region.

The predicted cross sections for bb and cc baryons have larger uncertainties than those for bc baryons. The large uncertainties from the $\alpha_s^4(\mu)$ factor can not be removed by normalizing

to $b\bar{b}$ or $c\bar{c}$ quarkonium cross sections, since they arise from very different short-distance parton processes. However, from the predictions in Fig. 9.29, one can expect roughly the same number of Ξ_{cc} and Ξ_{bc} events in the kinematical region of $p_T > 10$ GeV and $|y| < 1$. The total number of Ξ_{bb} events will be about a factor of 10 smaller.

9.4.3 Decays†

Since the major thrust of this report is B-physics, we may be tempted to limit discussion to baryons containing b quarks. However, such baryons often decay by cascades into baryons containing c quarks and identification of the latter may be an important first step in reconstructing doubly-heavy baryons containing b quarks.

The lifetimes for the ground states of the doubly-heavy baryons have been calculated in the framework of the operator product expansion, which involves an expansion in inverse powers of the heavy quark mass [87]. In leading order of $1/m_Q$, the inclusive widths are determined by the spectator approximation with QCD corrections. The next order in $1/m_Q$ takes into account corrections connected with quark motion in the doubly-heavy baryon and with the chromomagnetic quark interaction. In doubly-heavy baryons, there is Pauli interference (PI) of quark decay products with identical quarks from the initial state, as well as weak scattering (WS, or weak exchange) where exchange of a $W^{\pm}$ occurs between quarks. Both effects play important roles in the mechanism of doubly-heavy baryon decay. For example, Pauli interference leads to the increase of the b-quark decay contribution to bc-baryon by a factor of two. In this case, the sign is basically determined from the interference of the charm quark of the initial state with the charm quark from the b-quark decay. The antisymmetric color structure of the baryon wave function leads to the positive sign for the Pauli interference. The overall effect of the corrections to the spectator mechanism can reach 40–50%. In Tables 9.14 and 9.15, we show the contributions of the different modes to the total decay widths of cc and bc baryons. One can see from these tables that the weak scattering contributions are comparable with the spectator contributions. The estimates of the lifetimes of the Ξ_{cc} and Ξ_{bc} baryons from the operator product expansion are [90–92]:

$$\begin{aligned} \tau_{\Xi_{cc}^{++}} &= 0.43 \pm 0.1 \text{ ps}, \\ \tau_{\Xi_{cc}^{+}} &= 0.12 \pm 0.1 \text{ ps}, \\ \tau_{\Xi_{cc}^{0}} &= 0.28 \pm 0.07 \text{ ps}, \\ \tau_{\Xi_{bc}^{+}} &= 0.33 \pm 0.08 \text{ ps}. \end{aligned} \tag{9.40}$$

We proceed to discuss exclusive decay modes of the doubly-heavy baryons that may be observable. Let us first consider spectator decay modes, in which the doubly-heavy baryon decays into either a lighter doubly-heavy baryon or a baryon containing a single heavy quark. In Table 9.16, we give branching fractions for exclusive spectator decay modes that were calculated in the framework of QCD sum rules [88]. Some of the decay modes have surprisingly large branching fractions, particularly $\Xi_{cc}^{+} \to \Xi_{cs}^{0}\pi^{+}(\rho^{+})$, $\Xi_{cc}^{++} \to \Xi_{cs}^{+}\pi^{+}(\rho^{+})$

† Authors: A. Likhoded, R. Van Kooten

Mode	width, ps^{-1}	Fraction of Ξ_{cc}^{++} width	Fraction of Ξ_{cc}^{+} width
$c \to sdu$	2.894	1.24	0.32
$c \to s\ell^{+}\nu$	0.760	0.32	0.09
PI	-1.317	-0.56	–
WS	5.254	–	0.59
$\Gamma_{\Xi_{cc}^{++}}$	2.337	1	–
$\Gamma_{\Xi_{cc}^{+}}$	8.909	–	1

Table 9.14: Fractional contributions of different modes to the total decay width of doubly-charmed baryons, Ξ_{cc}. PI and WS are Pauli interference and weak scattering effects, respectively.

Mode	Fraction of Ξ_{bc}^{+} width	Fraction of Ξ_{bc}^{0} width
$b \to c + X$	0.120	0.17
$c \to s + X$	0.37	0.31
PI	0.23	0.20
WS	0.20	0.31

Table 9.15: Fractional contributions of different modes to the total decay width of Ξ_{bc} baryons. PI and WS are Pauli interference and weak scattering effects, respectively.

and semileptonic decays. A recent work from Onishchenko calculating these branching ratios including results from three-point NRQCD sum rules [93] give even larger values.

We also consider another class of exclusive decay modes for doubly-heavy baryons that may be observable. As pointed out above, the contribution from weak scattering to the Ξ_{bc}^{+} and Ξ_{bc}^{0} decay width is about 20%. This type of decay is characterized by specific kinematics. In the rest frame of the Ξ_{bc} baryon, the c and s quarks from the scattering process $bc \to cs$ move in the opposite directions with a high momentum of about 3.2 GeV. Both the c and s quarks then fragment, producing multiparticle final states. These states include the 3-particle states $D^{(*)}K^{(*)}N$. The $D^{(*)}$ and $K^{(*)}$ can be produced by fragmentation processes: $c \to D^{(*)} + X_q$ and $s \to K^{(*)} + X_q$. However, in order for only one additional particle N to be produced in the decay of Ξ_{bc}, the $D^{(*)}$ and $K^{(*)}$ must be in the hard part of fragmentation spectrum with $z > 0.8$. We can use a well-known parametrization of the fragmentation functions to estimate the probability for such a decay:

$$\begin{aligned} Br(\Xi_{bc} \to D^{(*)}K^{(*)}N) &\approx Br(WS) \times W(z_D > 0.8) \times W(z_K > 0.8) \\ &= 0.2 \times 0.2 \times 0.04 \ . \end{aligned} \tag{9.41}$$

The resulting rough estimate of the branching fraction for $\Xi_{bc} \to D^{(*)}K^{(*)}N$ is 0.2%. We conclude that the branching fractions for these modes may be large enough to be observed.

Baryon	Mode	Br (%)	Baryon	Mode	Br (%)
$\Xi^{\diamond}_{bb}$	$\Xi^{\diamond}_{bc}\ l^-\bar{\nu}_l$	11.2			
	$\Xi^{\diamond}_{bc}\ \pi^-$	0.3			
	$\Xi^{\diamond}_{bc}\ \rho^-$	3.4			
Ξ^0_{bc}	$\Xi^+_{cc}\ l^-\bar{\nu}_l$	3.3	Ξ^+_{bc}	$\Xi^{++}_{cc}\ l^-\bar{\nu}_l$	3.5
	$\Xi^-_{bs}\ l^+\nu_l$	2.8		$\Xi^0_{bs}\ l^+\nu_l$	3.0
	$\Xi^+_{cc}\ \pi^-$	0.55		$\Xi^{++}_{cc}\ \pi^-$	0.6
	$\Xi^+_{cc}\ \rho^-$	1.4		$\Xi^{++}_{cc}\ \rho^-$	1.5
	$\Xi^-_{bs}\ \pi^+$	12.3		$\Xi^0_{bs}\ \pi^+$	13.1
	$\Xi^-_{bs}\ \rho^+$	5.2		$\Xi^0_{bs}\ \rho^+$	5.6
Ξ^+_{cc}	$\Xi^0_{cs}\ l^+\nu_l$	6.9	Ξ^{++}_{cc}	$\Xi^+_{cs}\ l^+\nu_l$	14.9
	$\Xi^0_{cs}\ \pi^+$	4.2		$\Xi^+_{cs}\ \pi^+$	8.1
	$\Xi^0_{cs}\ \rho^+$	24.8		$\Xi^+_{cs}\ \rho^+$	45.1

Table 9.16: Exclusive (spectator) decay modes of doubly-heavy baryon calculated in the framework of QCD sum rules. The symbol $^\diamond$ represents electric charge, i.e., $^{\diamond=\pm,0}$.

9.4.4 Experimental Observability[†]

To set the scale for observability of doubly-heavy baryons, we note that CDF has observed [52] about 20 events of the type $B_c \to J/\psi\ell^\pm\nu$ in 0.11 fb^{-1} using the $\mu^+\mu^-$ decay of the J/ψ. We take this process to have a total branching ratio of 0.3%. We assume comparable trigger and reconstruction efficiencies for the B_c and typical doubly-heavy baryon decay modes. In Section 9.4.3, the cross sections for baryons containing cc or bc were predicted to be within about a factor of 2 of the cross section for B_c for $p_T > 10$ GeV. With data samples of 3, 10, and 30 fb^{-1}, we are therefore initially restricted to doubly-heavy baryon decay modes with branching ratios greater than of order 10^{-4}, 5×10^{-5}, and 1.5×10^{-5} respectively. Special purpose detectors with better triggering abilities (such as BTeV) will be able to investigate rarer modes.

Historically, larger samples of rarer b-quark states are available for measuring properties such as lifetimes and polarization through "semi-exclusive" decays where not all the decay products are reconstructed and/or there is an escaping neutrino from semileptonic decay. As an example, the Λ_b state was first observed at LEP [85] through an excess of "correct-sign" Λ-ℓ^- and Λ-ℓ^+ correlations over the "wrong-sign" correlations. A similar situation will exist for doubly-heavy baryons, but now there can be two leptons in the decay chain exhibiting charge correlations.

If a doubly-heavy baryon decays semileptonically into either a lighter doubly-heavy baryon or a baryon containing a single heavy quark, and if the second baryon also decays semileptonically, they will give rise to two leptons associated with the same jet. Due to the large masses of the heavy baryons, both of these leptons tend to be at large values of p_T relative to the jet axis. It is also interesting to note that cascading semileptonic decays in the case of Ξ_{bb} or Ξ_{cc} can result in same-sign leptons in the same jet, a process with

[†]Authors: R.K. Ellis, R. Van Kooten

very little background. The largest irreducible background comes from a gluon splitting into $b\bar{b}$ to produce a jet containing two b-hadrons, one of which decays semileptonically and the other mixes before decaying semileptonically. Another background is the decay of one b quark semileptonically along with a same-sign lepton from the cascade decay through charm of the other $\bar{b}$ quark. However, this background level can be reduced by appropriate kinematic cuts on the lepton from the cascade decay. More problematic in this case would be lepton misidentification faking the same-sign lepton signal.

Other doubly-heavy baryon decays resulting in two opposite-sign leptons may still be distinctive due to the kinematics of the decay, but can suffer from a large physics background due to generic $b \to c \to s$ decays. Typical branching ratios for both types of decays are collected in Table 9.17 using the semileptonic rates predicted in ref. [93].

Mode			Br (%)	Lepton charge correlation
Ξ^-_{bb}	$\to \Xi^0_{bc}\ell^-\nu$	$\to \Xi^+_{cc}\ell^-\nu$	0.69%	same-sign
		$\to \Xi^-_{bs}\ell^+\nu$	0.61%	opp-sign
Ξ^0_{bb}	$\to \Xi^+_{bc}\ell^-\nu$	$\to \Xi^{++}_{cc}\ell^-\nu$	0.73%	same-sign
		$\to \Xi^-_{bs}\ell^+\nu$	0.61%	opp-sign
Ξ^0_{bc}	$\to \Xi^+_{cc}\ell^-\nu$	$\to \Xi^0_{cs}\ell^+\nu$	0.35%	opp-sign
	$\to \Xi^-_{bs}\ell^+\nu$	$\to \Xi^0_{cs}\ell^-\nu$	0.37%	opp-sign
Ξ^+_{bc}	$\to \Xi^{++}_{cc}\ell^-\nu$	$\to \Xi^+_{cs}\ell^+\nu$	0.82%	opp-sign
	$\to \Xi^0_{bs}\ell^+\nu$	$\to \Xi^+_{cs}\ell^-\nu$	0.40%	opp-sign
Ξ^{++}_{cc}	$\to \Xi^+_{cs}\ell^+\nu$	$\to \Xi\ell^+X$	1.5%	same-sign
Ξ^+_{cc}	$\to \Xi^0_{cs}\ell^+\nu$	$\to \Xi\ell^+X$	0.68%	same-sign

Table 9.17: Decay rates of cascading semileptonic decays from doubly-heavy baryons.

For fully exclusive decays, decay diagrams involving either spectator decays or W-exchange (including Cabibbo-suppressed decays) were considered. For a doubly-heavy baryon of the form bbq or bcq, the decays into J/ψ's are the favored decay modes, because of the ease of triggering on subsequent decays into $\mu^+\mu^-$ and e^+e^- and also because they absorb Q-value which would otherwise produce pion multiplicity contributing to combinatorial background. It is predicted that "golden" exclusive decay modes such as $\Xi^+_{bc} \to \Lambda^+_c J/\psi$ or $\Xi^0_{bb} \to \Lambda^0_b J/\psi$ into triggerable modes have small total branching ratios between 10^{-5} and 10^{-7}, although the inclusive rate for all decays containing a J/ψ may be as high as 10^{-3} [94].

Decays without a distinctive J/ψ may still be accessible due to the abundance of cascading decays. These cascade decays can then result in triggerable decays either from jets containing multiple leptons due to sequences of semi-leptonic decays as discussed above or from many tracks with relatively large impact parameter significance.

A doubly-heavy baryon decaying into either a b-baryon or another doubly-heavy baryon will have a decay length that gives rise to a large number of high-impact parameter tracks that could allow the use of a vertex/silicon track trigger. A doubly-heavy baryon with a

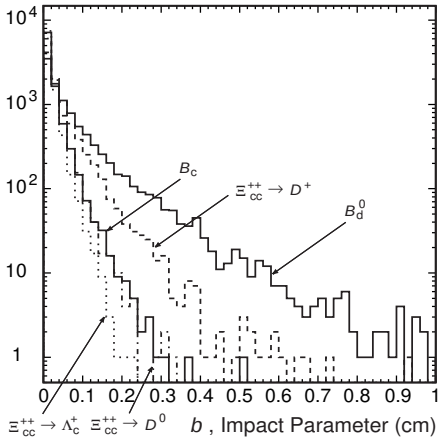

Figure 9.40: Impact distribution of all charged decay products in the cascade decays of Ξ_{cc}^{++} via Λ_c, D^0, and D^+ compared to the same distribution of the decay products from B_c and B_d^0.

short lifetime (e.g., $\tau(\Xi_{cc}^{++}) \approx 0.4$ ps, $\tau(\Xi_{bc}^0) \approx 0.3$ ps, and $\tau(\Xi_{bb}^0) \approx 0.7$ ps) can decay into a charm meson with a reasonably long lifetime (e.g., $\tau(D^+) = 1.06$ ps). The large mass of the doubly-heavy baryon parent can give substantial transverse momentum kick with respect to the original flight direction. Including a fairly long charm decay length, the final decay products can have impact parameters comparable to those of b hadrons with typical lifetimes of 1.5 ps. These decays can be found with reasonable efficiency using a vertex/silicon track trigger. To test this idea, a Monte Carlo study was made at the four-vector level. Ξ_{cc}^{++} baryons were generated with a p_T distribution according to Ref. [80] with a lifetime of 0.43 ps. This doubly-heavy baryon was allowed to decay to a singly-charmed meson or baryon in a two-body decay for simplicity. The impact parameters of the resultant decay products of the Λ_c, D^0, or $D^\pm$ were found. Distributions of these impact parameters are shown in Fig. 9.40 which, for the case of $\Xi_{cc}^{++} \to D^+$, is intermediate in extent between that of the products from B_c decay and from B_d^0 decay. Considering the earlier description of the efficiency of a typical vertex/silicon track trigger (see 9.3.4.3), there is potential promise in triggering on doubly-heavy baryons in cascade decays.

Finally, the decay mode $\Xi_{bc} \to D^{(*)}K^{(*)}N$ discussed in Section 9.4.3 shows promise due to its potentially relatively large rate and the nature of its decay products which allows a fairly clean reconstruction. If $N = p$, the proton would allow for the use of particle identification. The D^* can be identified by the standard procedure of cutting on the small value of $\Delta_m = m(D^*) - m(D)$, where $m(D^*)$ is the reconstructed mass of the D^* using the soft pion in $D^* \to D\pi$. Triggering would rely on a silicon track trigger as described above.

Decay modes containing a Λ_c in the cascade chain also have potential due to the possibility of the clean reconstruction of this charm baryon in the decay $\Lambda_c \to pK\pi$. Of note is that CDF cleanly reconstructed 197 signal events with Λ_c for a Λ_b lifetime measurement [95]. They used the lepton from the semileptonic decay $\Lambda_b \to \Lambda_c \ell\nu X$ as part of their trigger. Triggering certainly is a serious issue for any all-hadronic decay mode.

State	Lifetime [ps]	Mass [GeV]	Interesting Exclusive Decay Modes	Estimated Br
$\Xi_{cc}^{++}(ccu)$	0.43 [92]	3.651	$D^{*+}\pi^+\Lambda^0 \to p\pi^-$ $\hookrightarrow K^-\pi^+\pi^+$ $D^{*+}p\bar{K}^0 \to \pi^+\pi^-$ $\hookrightarrow K^-\pi^+\pi^+$ $\Lambda_c^+(cdu)\ \pi^+\ \bar{K}^0 \to \pi^+\pi^-$ $\hookrightarrow pK^-\pi^+$	9.4×10^{-4} 4.7×10^{-4} 4×10^{-4}
$\Xi_{cc}^{+}(ccd)$	0.11 [92]	3.651	$D^{*+}\ \Lambda^0 \to p\pi^-$ $\hookrightarrow K^-\pi^+\pi^+$ $D^0p\bar{K}^0 \to \pi^+\pi^-$ $\hookrightarrow K^-\pi^+$ $\Lambda_c^+(cdu)\ \bar{K}^0 \to \pi^+\pi^-$ $\hookrightarrow pK^-\pi^+$	4×10^{-4} 2×10^{-4} 1.6×10^{-4}
$\Omega_{cc}^{+}(ccs)$	0.5 [61]	3.811	$\Lambda^0K^0D^+$	
$\Omega_{ccc}^{++}(ccc)$	0.3 [61]	4.925	Cascades to Ξ_{cc}^+	–

Table 9.18: Properties and interesting exclusive hadronic decay modes of multiple-charm baryons.

With these considerations, a list of potentially interesting exclusive hadronic decay modes for doubly-heavy baryons are collected in Tables 9.18 and 9.19. These decay modes, in addition to the semi-exclusive decays from semileptonic decays, deserve further study as possible discovery modes for doubly-heavy baryons.

9.5 Fragmentation

The fragmentation of quarks and gluons into hadrons involves confinement dynamics, and occurs at time scales that are long compared to those of the hard scattering that produced the quarks and gluons. Accordingly, in single-particle inclusive hard-scattering processes, the fragmentation process is factorized in perturbative QCD (see [126] and references therein) from the hard interaction and summarized in a nonperturbative fragmentation function (FF) $D_i^H(z,\mu)$ [127]. $D_i^H(z,\mu)$ is the probability density of a hadron H to form from parton i with momentum fraction z at factorization scale μ. Just as initial-state parton distribution functions (PDFs), fragmentation functions are not completely calculable in perturbation theory, although their evolution with μ is. The evolution equations for FFs are identical in form to those for PDFs, although the evolution kernels differ from second order

State	Lifetime [ps]	Mass [GeV]	Interesting Exclusive Decay Modes	Estimated Br
$\Xi_{bc}^+(bcu)$	0.33 ± 0.08 [91]	6.971	$\Lambda_c^+ J/\psi \to \mu^+\mu^-$ $\hookrightarrow pK^-\pi^+$	$< 2 \times 10^{-7}$
			$D^{(*)0}\, p\bar{K}^0 \to \pi^+\pi^-$ $\hookrightarrow K^-\pi^+$	2.1×10^{-5}
			$D^{(*)+}\, pK^{(*)-}$ $\hookrightarrow K^-\pi^+\pi^+$	4×10^{-5}
$\Xi_{bc}^0(bcd)$	0.28 ± 0.07 [91]	6.971	$\Xi_c^0(csd)\ J/\psi \to \mu^+\mu^-$ $\hookrightarrow \Lambda^0\bar{K}^0$	$< 2 \times 10^{-7}$
			$D^{(*)0}\, pK^{(*)-}$ $\hookrightarrow K^-\pi^+$	6.2×10^{-5}
			$D^{(*)+}\, p\pi^- K^{(*)-}$ $\hookrightarrow K^-\pi^+\pi^+$	4×10^{-5}
$\Omega_{bc}^0(bcs)$	–	7.095	$\Omega_c^0(ssc)\ J/\psi \to \mu^+\mu^-$ $\hookrightarrow \Omega^-\pi^+$	$< 1.44 \times 10^{-6}$
$\Xi_{bcc}^+(bcc)$	–	8.198	Cascades to above states	

Table 9.19: Properties and interesting exclusive hadronic decay modes of heavy baryons containing both a b and a c quark.

State	Lifetime [ps]	Mass [GeV]	Interesting Exclusive Decay Modes	Estimated Br
$\Xi_{bb}^0(bbu)$	0.79 [90]	10.235	$\Xi_{bc}^+(bcu)\ \pi^-$ $\hookrightarrow$ as in Table 9.19	
			$\Lambda_b^0(bdu)\ J/\psi \to \mu^+\mu^-$ $\hookrightarrow \Lambda_c^+\pi^-$	3×10^{-6}
				2.4×10^{-7} if $\Lambda_b^0 \to \Lambda_c\ell\nu X$
$\Xi_{bb}^-(bbd)$	0.8 [90]	10.235	$\Xi_{bc}^0(bcd)\ \pi^-$ $\hookrightarrow$ as in Table 9.19	
			$\Xi_b^-(bsd)\ J/\psi \to \mu^+\mu^-$ $\hookrightarrow \Xi_c^0\pi^-$	6×10^{-5}
$\Omega_{bb}^-(bbs)$	0.8 [90]	10.385	Cascades to above states	
$\Xi_{bbc}^0(bbc)$	–	11.476	Cascades to above states	
$\Omega_{bbb}^-(bbb)$	–	14.76	Cascades to above states	

Table 9.20: Properties and interesting exclusive hadronic decay modes of heavy baryons containing two b quarks.

onwards [128–130]. Though nonperturbative, these FFs are universal and so, they may be determined for each hadron H in a few calibration experiments at some fixed scale μ_0, for subsequent use in other experiments and at other values of μ (see for example [131–135]).

The fragmentation of heavy quarks[4] is somewhat different. When the heavy quark is produced with an energy E not much larger than its mass m, the fragmentation process consists mainly of the nonperturbative transition of the heavy quark to the hadron H, which one assumes can be described by a nonperturbative FF. One may make a general ansatz for the functional form of this FF, the parameters of which are to be fixed by fitting to data. One may also be inspired by physical considerations in motivating a functional form. Within this philosophy, the best known form is that of Peterson et al. [136]. More recent forms are based on heavy-quark effective field theory. Both are described in section 9.5.2. When the heavy quark is produced with an energy E much larger than its mass m, large logarithms of E/m occur in the perturbative expression for the heavy-quark inclusive cross section, which must be resummed. These logarithms may be traced to the fragmentation stage of the reaction, and the resummation may be achieved using the formalism of perturbative FFs (PFFs). They describe the fragmentation process from scale E down to scale m. These PFFs are perturbative because, first, the coupling constant is small enough in the range from m to E and second, the heavy-quark mass regulates the collinear divergences, which would otherwise have to be absorbed into nonperturbative FFs. These perturbative and nonperturbative FFs must be properly matched together to avoid miscounting contributions and to enable a comparison with data.

Outside the context of factorization-based perturbative QCD, there is the successful string model of the Lund group. Yet other approaches to heavy-quark fragmentation exist [137,138], but for lack of space we shall not discuss them here.

We begin with a discussion of perturbative fragmentation and describe an attempt to learn more about the nonperturbative FF from the very precise SLD data. Next we examine what heavy-quark production data in $p\bar{p}$ collisions tell us about the nonperturbative FF. Then in section 9.5.2 we review and clarify the theory of the nonperturbative FFs. Next we discuss the phenomenon of beam drag in the context of the Lund string model, as (perhaps) observed at HERA in charm DIS and photoproduction, and present a study of the possible impact of this effect on CDF/D0 and BTeV studies. In section 9.5.4, we discuss various "systematic errors" in heavy quark FFs, and we conclude with observations on the experimental impact of the various issues in heavy-quark fragmentation.

We refer to the recent LHC Workshop report on bottom production [139] for additional studies involving heavy-quark fragmentation.[5]

[4] By heavy quarks we mean charm and bottom quarks. The top quark decays by the weak interaction before it has time to hadronize.

[5] In particular, in the context of section 9.5.4, one can find there a study by Frixione and Mangano on effective $z > 1$ support for fragmentation functions in certain event generators.

9.5.1 Perturbative fragmentation

9.5.1.1 Heavy-quark fragmentation in e^+e^- collisions [†]

A well-defined fragmentation function is a universal function, so that its study can be undertaken in the context of e^+e^- collisions without the complication due to initial state hadrons. We are interested in the situation where the scale E of the process is much larger than the heavy-quark mass m, a typical situation at the Tevatron. This requires the resummation of large logarithms $\ln(E/m)$ for a reliable computation of a differential cross section. This is achieved via the formalism of the perturbative FF (PFF), which we briefly review. The PFF satisfies the DGLAP [140–142] evolution equation:

$$\frac{dD_{i,\mathrm{pert}}(x,\mu)}{d\ln\mu} = \sum_j \int_x^1 \frac{dz}{z} P_{ij}\left(\frac{x}{z},\alpha_s(\mu)\right) D_{j,\mathrm{pert}}(z,\mu)\,, \tag{9.42}$$

where i,j label parton flavors. With initial condition at $\mu_0 \simeq m$, Eq. (9.42) determines the PFF at x,μ, and resums logarithms $\ln(\mu/\mu_0)$ to all orders. This initial condition for the PFF was first computed to NLO in [143] and is, for $i=Q$, given by the distribution

$$D_{Q,\mathrm{pert}}(z,\mu_0) = \delta(1-z) + \frac{\alpha_s(\mu_0)C_F}{2\pi}\left[\left(\frac{1+z^2}{1-z}\right)\left(\ln\left(\frac{\mu_0^2}{m^2}\right) - 1 - 2\ln(1-z)\right)\right]_+ . \tag{9.43}$$

For heavy quark production at $E \gg m$, the choice $\mu = E$ in the solution of (9.42) then resums terms containing $\ln^n(E/m)$ to all orders in α_s, to next-to-leading logarithmic (NLL) accuracy.

To study the PFF in the context of e^+e^- collisions at center-of-mass energy E

$$e^+\,e^- \to Z/\gamma(q) \to Q(p) + X, \tag{9.44}$$

one defines

$$x_E = x = \frac{2p\cdot q}{q^2}\,, \tag{9.45}$$

and factorizes the single heavy *quark* inclusive cross section as

$$\frac{d\sigma}{dx}(x,E,m) = \sum_i \int_x^1 \frac{dz}{z}\frac{d\hat{\sigma}_i}{dz}(z,E,\mu_F)\; D_{i,\mathrm{pert}}\left(\frac{x}{z},\mu_F,m\right)\,, \tag{9.46}$$

where $d\hat{\sigma}_i(x,E,\mu_F)/dx$ are the (scheme-dependent) partonic cross sections for producing the parton i, and $D_{i,\mathrm{pert}}(x,\mu_F,m)$ are the (scheme- but not process-dependent) perturbative fragmentation functions (PFFs) for parton i to evolve into the heavy quark Q. The factorization scale μ_F must be chosen of order E, to avoid the appearance of large logarithms $\ln(E/\mu_F)$ in the partonic cross sections.

The single-*hadron* inclusive cross section, including nonperturbative corrections, is then usually written as multiple convolution

[†] Author: C. Oleari

$$\frac{d\sigma^H}{dx}(x,E,m) = \sum_i \frac{d\hat{\sigma}_i}{dx}(x,E,\mu_F) \otimes D_{i,\mathrm{pert}}(x,\mu_F,m) \otimes D^H_{\mathrm{NP}}(x)\,. \tag{9.47}$$

Therefore the full fragmentation function requires the combination of the perturbative FF with a nonperturbative part which models the final hadronization. Note that for heavy-quark production in hadronic collisions at hadron transverse momentum $p_T \gg m$, one must replace the CM energy E with the boost-invariant p_T.

In Eq. (9.43) the initial condition is expressed as an expansion in terms of $\alpha_s(m)$. This is a beneficial property of heavy-quark fragmentation, but one should keep in mind that higher-order terms in this condition may be important. Moreover, irreducible, nonperturbative uncertainties of order Λ_{QCD}/m are present. We assume that all these effects are described by a nonperturbative fragmentation function D^H_{NP}, that takes into account all low-energy effects, including the final nonperturbative hadronization of the heavy quark. There are theoretical approaches to the fragmentation-function calculation that employ heavy-quark effective theory in order to study nonperturbative effects [144,145] more systematically. These will be discussed in the next subsection. Here we want to establish a connection with the most commonly used parameterizations, and thus we will use the Peterson form and the "Euler" form $x^\alpha(1-x)^\beta$.

9.5.1.2 Impact of SLD data

Let us first briefly review the present situation. Heavy-flavor production in e^+e^- collisions has been thoroughly studied both at fixed order [146–148] and in a combined fixed order plus next-to-leading logarithmic (here $\ln(E/m)$ with E the center of mass energy) resummed approach [149], using the Peterson function for the nonperturbative transition[6]. The results of this study [149], based on LEP [150,151] and ARGUS [152] data can be summarized as follows:

- Either increasing the order of the finite order perturbative expansion or including next-to-leading log (NLL) effects in a resummed approach reduces the Peterson parameter ϵ obtained from fitting to the data, corresponding to a harder nonperturbative fragmentation function.
- The differential cross section obtained by matching the α_s^2 fixed order and the NLL resummed expressions, the "NLL improved", is harder than pure NLL, so that the ϵ parameter needed in the nonperturbative part is, in general, larger, but only slightly so, than in the NLL case.
- At LEP energies, the importance of $\mathcal{O}(m/E)$ terms is found to be minor.

Let us now show some new results obtained from a fit to SLD [153] B-production data in e^+e^- collision at $E = 91.2$ GeV, in Fig. 9.41. The theoretical curves have been determined

[6] This combined approach is actually a variable flavor number scheme (VFNS) for heavy-quark fragmentation.

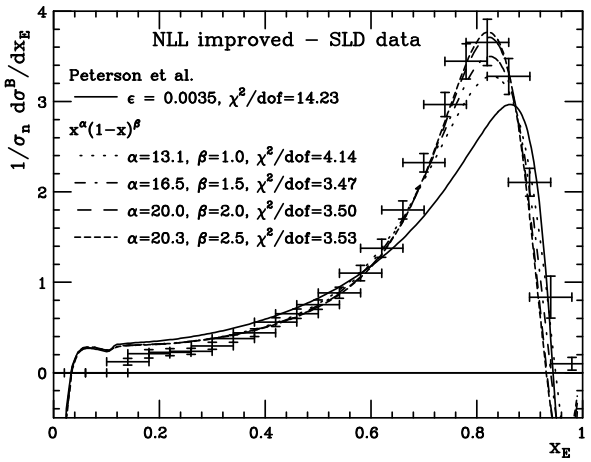

Figure 9.41: Fit to SLD data of Peterson and Euler nonperturbative fragmentation function via NLL improved calculation. The χ^2 are per degree of freedom.

from Eq. (9.47), at the same level of accuracy as used in [149]. We have used two families of nonperturbative FF: the Peterson form and the Euler form $x^\alpha(1-x)^\beta$. We have fitted the data by χ^2 minimization, keeping $\Lambda^{(5)}_{\rm QCD}$ fixed to 200 MeV. With this procedure we have fitted both the value of ϵ and the normalization (which was allowed to float) for the Peterson FF, and for the Euler form the value of α and the normalization, varying β in the range between 1.0 and 2.5, with an increment of 0.5.

We should caution at this point that the values of ϵ for the Peterson FF fitted above *cannot* be used for LEP studies, as the SLD and LEP collaborations use different values for some key input parameters such as the fraction of b quarks producing B^{**} mesons.

We find the Peterson form to have a very poor χ^2/d.o.f. The Euler form can accommodate the data better, at the values $\alpha = 16.5, \beta = 1.5$. To compare the fit results, we plot in Fig. 9.42 the nonperturbative FF at their best χ^2/d.o.f. values. We see that all curves are strongly peaked near $x = 1$, with the best fit value corresponding to a fairly hard fragmentation.

We note that in Ref. [154], and more recently in [155], the formalism used in the previous analysis of e^+e^- collisions has been applied to the Tevatron b-quark p_T cross section, for which the data exceed the central NLO-theory estimate by a factor of two[7]. At large p_T the theoretical uncertainty due to scale variations was found to be reduced with respect to the fixed-order approach, but the cross section decreased. At moderate p_T, the cross section gets somewhat enhanced, but not enough to explain the data-theory discrepancy. Another study involving FFs in heavy-quark hadroproduction, in the context of the so-called ACOT VFNS, was performed in [156]. The PFF formalism was also applied to γp [157] and $\gamma\gamma$ [158]

[7] This is somewhat less the case for the b-jet cross section, see section 1.3 in this chapter.

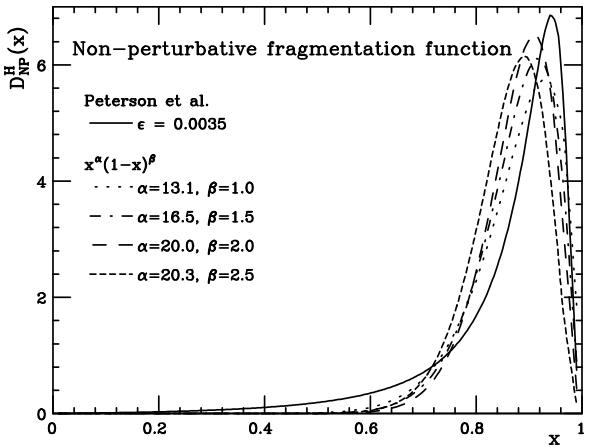

Figure 9.42: Functional forms of the nonperturbative fragmentation functions that produced the best fit to SLD data.

charm production. Similar conclusions were reached as for $p\bar{p}$ b-quark production.

9.5.1.3 Heavy-quark fragmentation in $p\bar{p}$ collisions [†]

It is well known that Tevatron data for the integrated transverse momentum spectrum in b production are systematically larger than QCD predictions. This problem has been around for a long time, although it has become less severe with time. The present status of this issue has been previously presented in Fig. 9.8. A similar discrepancy is also observed in UA1 data (see ref. [159] for details).

The theoretical prediction has a considerable uncertainty, which is mainly due to neglected higher-order terms in the perturbative expansion. In our opinion, it is not unlikely that we may have to live with this discrepancy, which is certainly disturbing, but not strong enough to question the validity of perturbative QCD calculations. In other words, the QCD $\mathcal{O}(\alpha_s^3)$ corrections for this process are above 100% of the Born term, and thus it is not impossible that higher order terms may give contributions of the same size. Nevertheless, it is conceivable that also nonperturbative effects contribute to enhance the cross section for this observable.

In this note, we present a study of the effects of b-quark fragmentation on the predicted single-inclusive p_T spectrum. In analogy with the case of charm production, the agreement between theory and data improves if one does not include any fragmentation effects. It is then natural to ask whether the fragmentation functions commonly used in these calculations are appropriate. The LEP [150,160,161] and SLD [153] measurements have shown

[†] Authors: P. Nason, G. Ridolfi

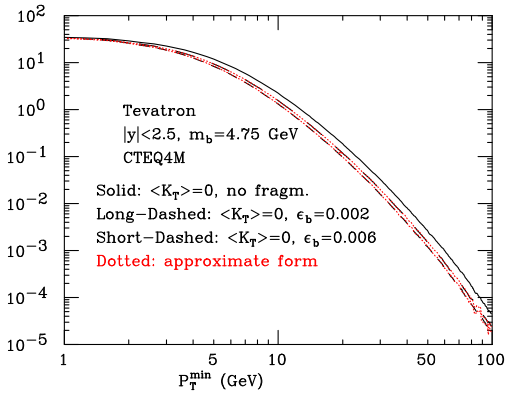

Figure 9.43: The effect of a Peterson fragmentation function [136] on the inclusive b cross section. The (red) dotted lines correspond to the approximation Eq. (9.50), and are almost indistinguishable from the exact results.

that fragmentation functions are harder than previously thought.

The effect of a nonperturbative fragmentation function on the p_T spectrum is easily quantified if one assumes a steeply-falling transverse momentum distribution for the produced b quark

$$\frac{d\sigma}{dp_T} = Ap_T^{-M} . \tag{9.48}$$

The corresponding distribution for the hadron is

$$\frac{d\sigma_{\rm had}}{dp_T} = A\int \hat{p}_T^{-M}\,\delta(p_T - z\hat{p}_T)D(z)\,dz\,d\hat{p}_T = Ap_T^{-M}\int_0^1 dz z^{M-1}D(z) . \tag{9.49}$$

We can see that the hadron spectrum is proportional to the quark spectrum times the $M^{\rm th}$ moment of the fragmentation function $D(z)$. Thus, the larger the moment, the larger the enhancement of the spectrum.

In practice, the value of M will be slightly dependent upon p_T. We thus define a p_T dependent M value

$$\frac{d\log\sigma(p_T > p_T^{\rm cut})}{d\log p_T^{\rm cut}} = -M(p_T^{\rm cut}) + 1 \tag{9.50}$$

and

$$\sigma_{\rm had}(p_T > p_T^{\rm cut}) = \sigma(p_T > p_T^{\rm cut}) \times \int_0^1 dz z^{M(p_T^{\rm cut})-1}D(z) . \tag{9.51}$$

This gives an excellent approximation to the effect of the fragmentation function, as can be seen from fig. 9.43.

Since the second moment of the fragmentation function is well constrained by e^+e^- data, it is sensible to ask for what shapes of the fragmentation function, for fixed $\langle z\rangle$, one

gets the highest value for $\langle z^{M-1}\rangle$. We convinced ourselves that the maximum is achieved by the functional form

$$D(z) = A\delta(z) + B\delta(1-z) , \tag{9.52}$$

which gives

$$\langle z\rangle = \frac{B}{A+B}; \quad \langle z^{M-1}\rangle = \frac{B}{A+B} . \tag{9.53}$$

This is however not very realistic: somehow, we expect a fragmentation function which is concentrated at high values of z, and has a tail at small z. We convinced ourselves that, if we impose the further constraint that $D(z)$ should be monotonically increasing, one gets instead the functional form

$$D(z) = A + B\delta(1-z) , \tag{9.54}$$

which gives

$$\langle z\rangle = \frac{A/2+B}{A+B}; \quad \langle z^{M-1}\rangle = \frac{A/M+B}{A+B} . \tag{9.55}$$

We computed numerically the M^{th} moments of the Peterson form:

$$D(z) \propto \frac{1}{z\left(1-\frac{1}{z}-\frac{\epsilon}{1-z}\right)^2} , \tag{9.56}$$

of the form

$$D(z) \propto z^\alpha(1-z)^\beta , \tag{9.57}$$

for $\beta = 1$ (Kartvelishvili [162]), for which

$$\langle z^{M-1}\rangle = \frac{\Gamma(\alpha+M)\Gamma(\alpha+\beta+2)}{\Gamma(\alpha+1)\Gamma(\alpha+\beta+M+1)} , \tag{9.58}$$

of the form of Collins and Spiller [163]

$$D(z) \propto \frac{\left(\frac{1-z}{z}+\frac{(2-z)\epsilon}{1-z}\right)(1+z^2)}{\left(1-\frac{1}{z}-\frac{\epsilon}{1-z}\right)^2} , \tag{9.59}$$

and of the form in Eq. (9.54), at fixed values of $\langle z\rangle$ corresponding to the choices $\epsilon_b = 0.002$ and 0.006 in the Peterson form. We found that the p_T distribution at the Tevatron, for p_T in the range 10 to 100 GeV, behaves like p_T^{-M}, with M around 5. Therefore, we present in Tables 9.21 and 9.22 values of the $4^{\rm th}$, $5^{\rm th}$ and $6^{\rm th}$ moments of the above-mentioned fragmentation functions. We thus find that keeping the second moment fixed the variation of the hadronic p_T distribution obtained by varying the shape of the fragmentation function among commonly used models is between 5% and 13% for both values of ϵ_b. Therefore, it seems difficult to enhance the transverse momentum distribution by suitable choices of the form of the fragmentation function. With the extreme choice of Eq. (9.54), one gets at most a variation of 50% for the largest values of ϵ_b and M. It would be interesting to see if such an extreme choice is compatible with e^+e^- fragmentation function measurements.

$\langle z\rangle = 0.879$	$M=4$	$M=5$	$M=6$
Peterson	0.711	0.649	0.595
Kartvelishvili	0.694	0.622	0.562
Collins-Spiller	0.729	0.677	0.633
Maximal (Eq. (9.54))	0.818	0.806	0.798

Table 9.21: Values of the $4^{\rm th}$, $5^{\rm th}$ and $6^{\rm th}$ moment, at fixed $\langle z\rangle$ (corresponding to $\epsilon_b = 0.002$ in the Peterson form), for different forms of the fragmentation function.

$\langle z\rangle = 0.828$	$M=4$	$M=5$	$M=6$
Peterson	0.611	0.535	0.474
Kartvelishvili	0.594	0.513	0.447
Collins-Spiller	0.626	0.559	0.505
Maximal (Eq. (9.54))	0.742	0.724	0.713

Table 9.22: Values of the $4^{\rm th}$, $5^{\rm th}$ and $6^{\rm th}$ moment, at fixed $\langle z\rangle$ (corresponding to $\epsilon_b = 0.006$ in the Peterson form), for different forms of the fragmentation function.

9.5.2 Fragmentation in the nonperturbative regime †

In this subsection we review the theory of the nonperturbative transition of a heavy quark into a heavy meson.

First, we examine the model of Peterson *et al.* [136] for the fragmentation of a fast-moving heavy quark Q with mass m_Q into a heavy hadron H (consisting of $Q\overline{q}$) with mass m_H and a light quark q with mass m_q. The basic assumption in this model is that the amplitude for the fragmentation is proportional to $1/(\Delta E)$, where $\Delta E = E_H + E_q - E_Q$ is the energy denominator for the process in old-fashioned perturbation theory. It follows that the probability for the transition $Q \to H + q$ is proportional to $1/(\Delta E)^2$. Taking the momentum of the heavy quark to define the longitudinal axis, one can express ΔE in terms of the magnitude of P_Q, the heavy-quark momentum, the fraction z of the heavy-quark momentum that is carried by the heavy hadron, and the transverse momentum $p_\perp$ of the heavy hadron or the light quark:

$$\begin{aligned}\Delta E &= \sqrt{m_H^2 + p_\perp^2 + z^2 P_Q^2} + \sqrt{m_q^2 + p_\perp^2 + (1-z)^2 P_Q^2} - \sqrt{m_Q^2 + P_Q^2} \\ &\approx \frac{m_H^2 + p_\perp^2}{2zP_Q} + \frac{m_q^2 + p_\perp^2}{2(1-z)P_Q} - \frac{m_Q^2}{2P_Q} + \cdots \\ &\approx -\frac{m_Q^2}{2P_Q}[1 - 1/z - \epsilon/(1-z)]. \end{aligned} \tag{9.60}$$

In the last line, we have set $m_H \approx m_Q$ and neglected $p_\perp^2$ relative to m_Q^2 and used the definition $\epsilon \equiv (m_q^2 + p_\perp^2)/m_Q^2$. Multiplying $1/(\Delta E)^2$ by a factor $1/z$ for the longitudinal

† Authors: G. Bodwin, B. Harris

phase space, one arrives at the following *ansatz* for the fragmentation function [136]:

$$D_Q^H(z) = \frac{N}{z[1 - 1/z - \epsilon/(1-z)]^2}, \tag{9.61}$$

where the normalization N is fixed by the condition

$$\sum_H \int dz D_Q^H(z) = 1, \tag{9.62}$$

and the sum extends over all hadrons that contain Q. Contrary to the claims in Ref. [136], we find that $D_Q^H(z)$ has a maximum at $z \approx 1 - \sqrt{\epsilon}$ and a width of order $\sqrt{\epsilon}$. Previously it was believed that the shape of the Peterson et al. form is incompatible with results obtained from heavy-quark effective theory (HQET). However, as we shall discuss below, our new results for the maximum point and width are compatible with the HQET analysis.

Next we discuss the work of Jaffe and Randall [145], which provides a QCD-based interpretation of heavy-quark fragmentation in terms of the heavy-quark mass expansion. One begins with the standard Collins-Soper [127] definition of the fragmentation function for a heavy quark into a heavy hadron:

$$\hat{f}(z,\mu^2) = \frac{z}{4\pi}\int d\lambda e^{i\lambda/z} \frac{1}{2N_c} \mathrm{Tr}\, \not{n} \langle 0| h(\lambda n) \left|H'(P)\right\rangle \left\langle H'(P)\right| \overline{h}(0) |0\rangle , \tag{9.63}$$

where the trace is over color and Dirac indices, N_c is the number of colors, $h(x)$ is the heavy-quark field at space-time position x, P is the four-momentum of the heavy hadron, and n is defined by $n^2 = 0$ and $n \cdot p = 1$. The state $\left|H'(P)\right\rangle$ consists of the heavy hadron plus any number of additional hadrons. The matrix element is understood to be evaluated in the light-cone gauge $n \cdot A = 0$. We note that the definition (9.63) contains a factor z relative to the definition of the fragmentation function used in Ref. [145]. This factor z will be important in comparing with the work of Braaten *et al.* below.

Following the standard method for obtaining the heavy-quark mass expansion, one decomposes the field $h(x)$ into the sum of large $h_v(x)$ and small $\underline{h}_v(x)$ components:

$$h_v(x) = e^{-im_Q v\cdot x} P_+ h(x) \tag{9.64}$$

$$\underline{h}_v(x) = e^{-im_Q v\cdot x} P_- h(x), \tag{9.65}$$

with $P_\pm = (1 \pm \not{v})/2$ and v the hadron's four velocity. The leading term in the mass expansion of $f(x,\mu^2)$ is contained in the large-large combination of fields:

$$\begin{aligned}\hat{f}(z,\mu^2) = \frac{z}{4\pi}\int d\lambda e^{i\lambda/z} \frac{1}{2N_c} \mathrm{Tr}\, \not{n} \\ \times \langle 0| P_+ h(\lambda n) \left|H'(P)\right\rangle \left\langle H'(P)\right| \overline{P_+ h(0)} |0\rangle\, e^{-im_Q \lambda n\cdot v} + \ldots . \end{aligned} \tag{9.66}$$

In Ref. [145], it is argued that the matrix element in Eq. (9.66) is a dimensionless function $\mathcal{F}(\lambda\delta)$. This function may be written in terms of its Fourier transform:

$$\mathcal{F}(\lambda\delta) = 2\int_{-\infty}^{\infty} d\alpha e^{-i\alpha\lambda\delta}\, a(\alpha) , \tag{9.67}$$

where $\delta = 1 - m_Q/m_H$ which in terms of the parameter ϵ appearing in the Peterson et al. form is $\delta \approx \sqrt{\epsilon}$. Inserting Eq. (9.67) into Eq. (9.66), one can evaluate the integral, with the result

$$\hat{f}(z,\mu^2) = \frac{z}{\delta}\hat{a}\left(\frac{1/z - m_Q/m_H}{\delta}\right) + \dots \ . \tag{9.68}$$

A more complete analysis in Ref. [145] also yields the next-to-leading term in the hadron mass expansion:

$$\hat{f}(z,\mu^2) = z\left[\frac{1}{\delta}\hat{a}(y) + \hat{b}(y) + \cdots\right] , \tag{9.69}$$

where $y = (1/z - m_Q/m_H)/\delta$. The analysis in Ref. [145] does not yield a precise prediction for the functional form of a and b, but some general properties may be deduced. The function a describes, in the limit of infinite heavy-quark mass, the effects of binding in the heavy hadron on the heavy-quark momentum distribution. For a free heavy quark, $a(y)$ would be a δ-function at $y = 1$. In a heavy hadron, the binding smears the heavy-quark momentum distribution. It can be shown [145] that the distribution has a maximum at $z \approx 1 - \delta$ and a width of order δ. Using the fact the $\delta \approx \sqrt{\epsilon}$, we find that the maximum is at $z \approx 1 - \sqrt{\epsilon}$ and the width is of order $\sqrt{\epsilon}$ in agreement with the Peterson *et al.* model, as described above.

Braaten *et al.* [144] present a QCD-inspired model for the fragmentation of a heavy quark into an $S-$wave light-heavy meson. In this model, the fragmentation function is computed in perturbative QCD (Born level) in an expansion in inverse powers of the heavy-quark mass. For the projection of the Qq state onto the meson, Braaten *et al.* take the standard nonrelativistic-bound-state expression. For example, in the case of a $^1S_0$ meson, they assume the Feynman rule for the QqH vertex to be

$$\frac{\delta_{ij}}{\sqrt{3}}\frac{R(0)\sqrt{m_H}}{\sqrt{4\pi}}\gamma_5(1+\not{v})/2, \tag{9.70}$$

where $R(0)$ is the radial wave function at the origin. Braaten *et al.* make use of a definition of the fragmentation function that is equivalent to the Collins-Soper definition (9.63). From the terms of leading order in the heavy-quark mass expansion, they obtain, in the case of a $^1S_0$ meson,

$$\hat{f} \approx N\left[\frac{1}{\delta}\frac{(1-y)^2}{y^6}(3y^2+4y+8) - \frac{(1-y)^3}{y^6}(3y^2+4y+8)\right] , \tag{9.71}$$

where $N = 2\alpha_s^2|R(0)|^2/(81\pi m_q^3)$. At first glance, this result may seem to contradict the Jaffe-Randall analysis, which shows that the terms of leading order in the heavy-quark mass expansion give a contribution that is contained entirely in the function $a(y)$ in Eq. (9.69). However, the factor z in the definition of the fragmentation function (9.63) is crucial here. From the definitions of y and δ, we have $z = 1/[1 - \delta(1-y)]$, and, so, we can re-write Eq. (9.71) as

$$\hat{f}/z \approx \frac{N}{\delta}\frac{(1-y)^2}{y^6}(3y^2+4y+8), \tag{9.72}$$

which is of the form of $a(y)$ in Eq. (9.69).

There are several additional studies of the perturbative-QCD fragmentation function in the limit of a large heavy-quark mass. See the paper of Braaten *et al.* [144] for references.

9.5.3 Beam drag †

A puzzling situation has arisen in charm electroproduction and photoproduction at HERA. The data are well-described by NLO QCD [164,165] plus Peterson fragmentation [136], except at low p_t and large rapidity. To show this effect the charm electroproduction data of the ZEUS collaboration [166] is shown in Fig. 9.44. The figure shows the D^* meson cross sections

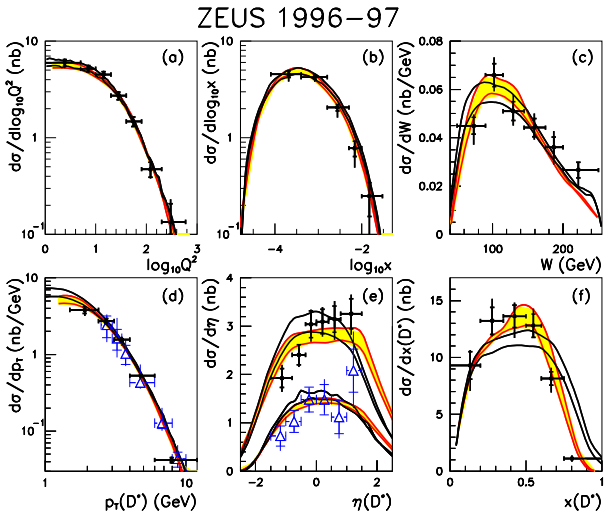

Figure 9.44: Effects of beam drag at HERA vs NLO theory and data from [166].

differential in momentum transfer Q^2, Bjorken x, hadronic energy W, transverse momentum p_t, pseudo-rapidity η, and D^* momentum fraction $x(D^*) = 2|\vec{p}_{\gamma P\mathrm{cms}}|/W$, compared with theory [164]. The boundaries of the bands correspond to varying the charm quark mass of 1.4 GeV by ± 0.1 GeV. The overall agreement is good, but the theory underestimates the data in the forward region and overestimates it in the backward region. Additionally, the D^* momentum fraction data, which is particularly sensitive to the charm hadronization process, is poorly described. Similar effects are seen in the D^* photoproduction data [167] at HERA. Variations of the parton distribution set, renormalization/factorization scale, charm mass, or fragmentation parameter ϵ are unable to account for the differences between data and theory. It also appears unlikely that an evolving fragmentation function would help since the p_t range covered is so small. A similar effect has been observed by the H1 collaboration in their charm electroproduction data [168].

One explanation [169] proposed for the photoproduction data [167] appears to work for the DIS data as well. One imagines a color string connecting the hadronizing charm quark

† Author: E. Norrbin

and the proton remnant which pulls (drags) the charmed meson to the forward region. This beam-remnant drag effect is made quantitative in the Lund String model modified for heavy-flavor production [170], as implemented in Pythia [171]. The shaded band in Fig. 9.44 shows that agreement is better when the Peterson *et al.* model is replaced by an effective fragmentation model extracted from the Pythia-based Monte Carlo RAPGAP [172].

Another way to improve the agreement between data and theory is to simply raise the minimum p_t of the events that are selected. Data from a slightly different decay chain, but higher minimum p_t cut are shown as open triangles. Here the Peterson and RAPGAP improved NLO predictions give essentially the same results, as expected from a power-suppressed effect. Note however that raising $p_t^{\rm min}$ may not be an option in some situations.

Let us adopt the view that beam remnant drag effects, which appear naturally in the string fragmentation model [173], exert influence here. This effect is closely related to the collapse of small strings, which is the most extreme case of string drag when all the energy and momentum of the remnant is taken up by the produced hadron. This latter effect has been used to describe the large charm asymmetries observed at several fixed target experiments [174,175]. It is important to understand this effect, as it affects $B-\bar{B}$ asymmetries at e.g. HERA-B [176], and thus CP violation measurements. An open problem is how to match the string model for beam drag to factorized QCD. In the rest of this section the Lund string fragmentation model is summarized and its influence on the distribution of final state hadrons in $p\bar{p}$ collisions is reviewed.

The Lund string fragmentation model provides a different approach to the problem of hadronization than the methods discussed so far. The Lund model in its basic form is simply a prescription for turning a partonic state (no matter how it was produced) into a hadronic final state. A string is the tube-like QCD force field stretched between a triplet and an anti-triplet color charge. In a high-energy process the string contains a lot of energy and decays into hadrons by the production of new $q\bar{q}$ pairs along the force field. The decay dynamics is constrained by a few physical assumptions such as Lorentz invariance, confinement and independence of the final state on the order in which string breaks are considered in the fragmentation process ('left-right symmetry'). This results in a fragmentation function with two free parameters, called the Lund symmetric FF [173]

$$f(z) \propto \frac{1}{z}(1-z)^a e^{-bm_\perp^2/z} \tag{9.73}$$

with a modification needed for heavy flavors [170]

$$f(z) \propto \frac{1}{z^{1+bm_Q^2}}(1-z)^a e^{-bm_\perp^2/z}, \tag{9.74}$$

where $m_\perp$ is the transverse mass of the produced hadron, m_Q is the heavy-quark mass and a and b are the two free parameters, which are common for all flavors and hadrons. The z variable represents the light cone fraction along the string direction and unlike 'stand alone' fragmentation functions no ambiguity is involved (cf. section 9.5.4).

To be practically useful, the Lund model must be hooked on to a perturbative description of the underlying hard process (such as $e^+e^- \to q\bar{q}$ or $gg \to q\bar{q}$). Normally a parton shower

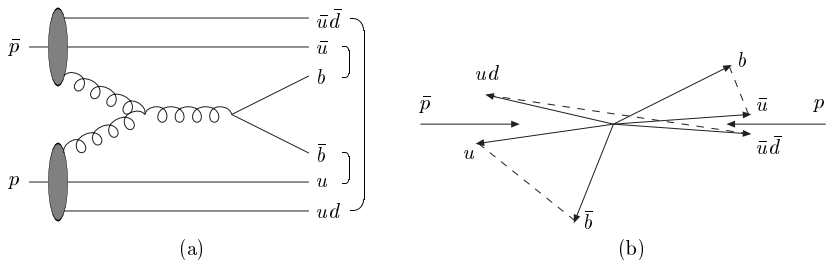

Figure 9.45: Example of a string configuration in a $p\bar{p}$ collision. (a) Graph of the process, with brackets denoting the final color singlet subsystems. (b) Corresponding momentum space picture, with dashed lines denoting the strings.

approximation is used, where the final state of a LO process is evolved down in virtuality by parton emission to some cut-off scale Q_0. Using a fixed lower scale for the perturbative treatment it has been possible in e^+e^- experiments to fit the two parameters of the Lund model to data and get excellent results. If the Q_0 scale is changed, the nonperturbative parameters of the Lund model will have to be re-tuned, so Q_0 can be seen as the scale at which perturbation theory is abandoned and replaced by the nonperturbative model. In the ideal case the value of Q_0 should not matter. In practice this is true only as long as it is at the order of 1 GeV. Any small change in Q_0 around this value is absorbed by a change of the fragmentation parameters. In a Monte Carlo program some additional parameters are needed to fully describe the process $e^+e^- \to$ hadrons, such as the transverse smearing along the string direction and the flavor composition of the new $q\bar{q}$ pairs [171].

When the model is carried over to hadron collisions several new aspects have to be considered. First of all, the particles entering the hard subprocess are not color singlets but quarks or gluons confined to hadrons. This problem is well known and solved by introducing PDFs which have been measured to good accuracy at e.g. HERA. Less well known is the consideration of color flow, beam remnants, small strings in the hadronization and beam drag. The remainder of this section will cover these aspects including a discussion of their possible implications in $p\bar{p}$ physics.

To be able to use the Lund string fragmentation model for hadronization, the strings in the event must be constructed. The string topology can be derived from the color flow of the hard process. For example, consider the LO process $u\bar{u} \to b\bar{b}$ in a $p\bar{p}$ collision. The color of the incoming u is inherited by the outgoing b, so the b will form a color-singlet together with the proton remnant, here represented by a color anti-triplet ud diquark. In total, the event will thus contain two strings, one b–ud and one $\bar{b}$–$\bar{u}\bar{d}$. In $gg \to b\bar{b}$ a similar inspection shows that two distinct color topologies are possible. Representing the proton remnant by a u quark and a ud diquark (alternatively d plus uu), one possibility is to have three strings b–$\bar{u}$, $\bar{b}$–u and ud–$\bar{u}\bar{d}$, Fig. 9.45, and the other is the three strings b–ud, $\bar{b}$–$\bar{u}\bar{d}$ and u–$\bar{u}$. When the remnant energy is to be shared between two objects, as e.g. in Fig. 9.45, further nonperturbative parameters are introduced, with a limited but not always negligible

impact on the uncertainty of the results [176].

Once the string topology has been determined, the Lund string fragmentation model [173] can be applied to describe the nonperturbative hadronization. Presupposing that the fragmentation mechanism is universal, i.e. process-independent, the good description of e^+e^- annihilation data should carry over. The main difference between e^+e^- and hadron–hadron events is that the latter contain beam remnants which are color-connected with the hard-scattering partons.

Depending on the invariant mass of a string, practical considerations lead to the need to distinguish three hadronization prescriptions:

1. *Normal string fragmentation.* In the ideal situation, each string has a large invariant mass. Then the standard iterative fragmentation scheme, for which the assumption of a continuum of phase-space states is essential, works well. The average multiplicity increases linearly with the string 'length', which means logarithmically with the string mass. In practice, this approach can be used for all strings above some cut-off mass of a few GeV.

2. *Cluster decay.* If a string is produced with a small invariant mass, maybe only two-body final states are kinematically accessible. The continuum assumption above then is not valid, and the traditional iterative Lund scheme is not applicable. We call such a low-mass string a cluster, and consider it separately from above. When kinematically possible, a Q–$\bar{q}$ cluster will decay into one heavy and one light hadron by the production of a light quark–antiquark pair in the color force field between the two cluster endpoints, with the new quark flavor selected according to the same rules as in normal string fragmentation. Close to the two-body threshold the decay is isotropic, while it should smoothly attach to the string picture of a preferential longitudinal direction for heavier clusters.

3. *Cluster collapse.* This is the extreme case of the above situation, where the string mass is so small that the cluster cannot decay into two hadrons. It is then assumed to collapse directly into a single hadron, which inherits the flavor content of the string endpoints. The original continuum of string/cluster masses is replaced by a discrete set of hadron masses, mainly D/B and D^*/B^* (or corresponding baryon states). In order to preserve overall energy and momentum, nearby string pieces have to absorb a recoil of the collapse, according to a procedure intended to minimize disturbances to the event. This mechanism plays a special rôle, in that it allows large flavor asymmetries in favor of hadron species that can inherit some of the beam-remnant flavor content.

Thus the cluster collapse mechanism tends to enhance the production of heavy hadrons which share its light flavor with the hadron beam. For charm this has been observed at several fixed-target experiments, where the effect is very large for large x_F [174]. This effect is yet to be studied for B mesons. It is expected to be fairly large at HERA-B [176] but small for the Tevatron, see [176] and below.

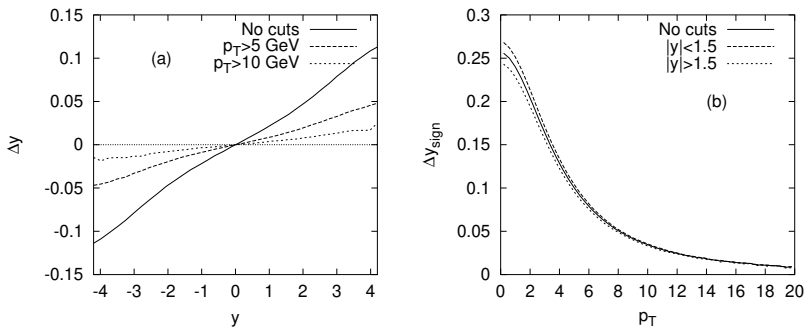

Figure 9.46: (a) Average rapidity shift Δy as a function of y for some different p_T cuts for a $p\bar{p}$ collider at 2 TeV. (b) Average rapidity shift Δy_{sign} as a function of p_T for some different rapidity cuts.

The color connection between the produced heavy quarks and the beam remnants in the string model gives rise to an effect called beam remnant drag. In an independent fragmentation scenario, a quark jet fragments symmetrically around the quark direction. The light cone (along the quark axis) energy-momentum of the quark is then simply scaled by some factor, picked from a fragmentation function, in order to give the momentum of the hadron. Thus, on the average, the rapidity would be conserved in the fragmentation process. This is not necessarily so in string fragmentation where both string ends contribute to the four-momentum of the produced heavy hadron. If the other end of the string is a beam remnant, the hadron will typically be shifted in rapidity in the direction of the beam remnant, often resulting in an increase in $|y|$. This beam-drag is shown qualitatively in Fig. 9.46, where the rapidity shift for bottom hadrons in a 2 TeV $p\bar{p}$ collision is shown as a function of rapidity and transverse momentum. We use two different measures of the rapidity shift. The first is the average rapidity shift $\Delta y = \langle y_B - y_b \rangle$. Here the heavy quark can be connected to a beam remnant on either side of the event, giving rise to shifts in both directions which tend to cancel in inclusive measures. A better definition is therefore

$$\Delta y_{sign} = \langle (y_B - y_b) \cdot sign(y_{other\ end}) \rangle, \tag{9.75}$$

which measures the rapidity shift in the direction of the other end of the string. This shift should almost always be positive. The rapidity shift is not directly accessible experimentally, only indirectly as a discrepancy between the shape of perturbatively calculated quark distributions and data. As can be seen from the figures this effect is large only at large rapidities and small p_T.

A possible observable consequence of the beam drag effect is the asymmetry between B^0 and $\bar{B}^0$ for large rapidities. Fig. 9.47 shows the distribution of bottom quarks and the hadrons produced from them, as well as the asymmetry between B^0 and $\overline{B}^0$ without any kinematic cuts, using pair production only. The asymmetry is antisymmetric because of the asymmetry of the initial state. Therefore the asymmetry is zero at $y = 0$ and increasing in different directions for increasing/decreasing rapidities. Consider the situation when the

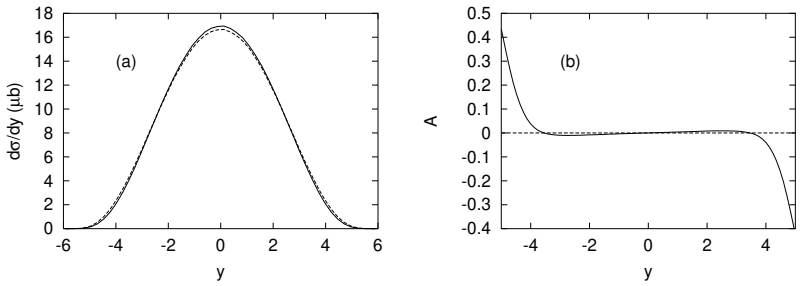

Figure 9.47: Bottom production at the Tevatron. (a) Rapidity distribution of bottom quarks (full) and the B hadrons produced from them (dashed). (b) The asymmetry $A = \frac{\sigma(B^0)-\sigma(\overline{B}^0)}{\sigma(B^0)+\sigma(\overline{B}^0)}$ as a function of rapidity. For simplicity, only pair production is included.

kinematic limit at large positive rapidities (the proton fragmentation region) is approached. Here the asymmetry changes sign for large rapidities because of the drag-effect; b quarks connected to diquarks from the proton beam remnant which carry most of the remnant energy often produce $\overline{B}^0$ hadrons which are shifted more in rapidity than the B^0's are. The $\overline{B}^0$ rapidity distribution is thus harder than for B^0. Cluster collapse, on the other hand, tends to enhance the production of 'leading' particles (in this case B^0) so the two mechanisms give rise to asymmetries with different signs. Collapse is the main effect at central rapidities while eventually at very large y, the drag effect dominates. The situation is reversed in the $\bar{p}$ fragmentation region. Despite the superficial differences between cluster collapse and beam drag it should be realized that they are simply two consequences of the same thing, namely the color connection between the products of the hard process and the beam remnants and the subsequent hadronization of the resulting string.

In Fig. 9.48 we introduce cuts in order to study the region of large (positive) rapidities and small p_T. The $\overline{B}^0$ spectrum is slightly harder than the B^0 one, but the size of the effect is quite small, approaching 4% at very large rapidities. Still, if large precision is desired in CP violation studies, this effect could be non-negligible. The effect is much larger at HERA-B because of the much smaller CM-energy, so the effect should be studied there first to assess its size. Further details and applications are given in [176].

9.5.4 Heavy-quark fragmentation ambiguities[†]

Unlike massless quarks, heavy quarks cannot have all of their four-momentum components degraded and stay on their mass shell simultaneously. Hence, only some components get scaled by z; which ones is to some degree a matter of choice, and a source of ambiguity. Moreover, the action of boosting between the parton-parton center-of-mass and the

[†]Authors: B. Harris, E. Laenen

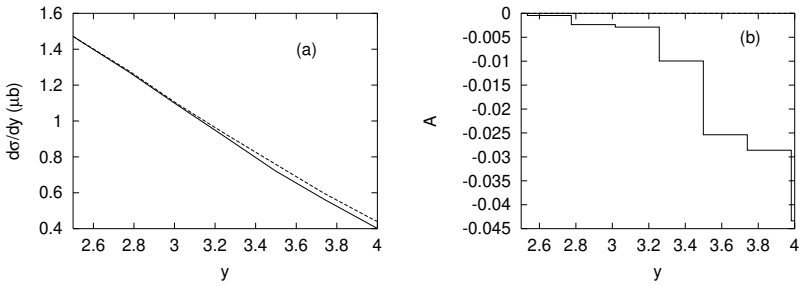

Figure 9.48: Bottom production at the Tevatron for $2.5 < |y| < 4$ and $p_T < 5$ GeV. (a) B^0 (full) and $\overline{B}^0$ (dashed) rapidity spectra. (b) The asymmetry $A = \frac{\sigma(B^0)-\sigma(\overline{B}^0)}{\sigma(B^0)+\sigma(\overline{B}^0)}$ as a function of rapidity. For simplicity, only pair production is included.

laboratory frame, and fragmenting do not commute for heavy quarks, generating another ambiguity. We have studied these ambiguities numerically at leading order, in the context of B-meson production at the Tevatron.

When fragmenting a heavy quark to a heavy hadron one must choose the momentum component to be scaled. Some common choices are

1. scaling the space component $\vec{p}_H = z\vec{p}_Q$ and adjusting the energy via the mass-shell condition $E_H = \sqrt{\vec{p}_H + m_H^2}$;

2. scaling the plus component $(E + p_{||})_H = z(E + p_{||})_Q$ and adjusting the minus component via the mass-shell condition $(E - p_{||})_H = m_H^2/(E + p_{||})_H$ (here $||$ refers to the Q direction, not the beam);

3. scaling the full four-momentum, ignoring the mass-shell requirement.

In Fig. 9.49 we show the effects of these choices on the P_T distribution of a generic B-meson in $p\bar{p}$ collisions at 1.8 TeV. We have taken $m_B = m_b = 5$ GeV, a Peterson et al. [136] fragmentation function with $\epsilon = 0.006$, and performed the fragmentation in the parton-parton center-of-mass. Choices 1 and 3 handle the p_x and p_y components in the same fashion so no effect is observed. The second method mixes the p_x and p_y components with the E and p_z components producing a pronounced difference at small p_T. All methods are identical in the limit of large p_T indicating that this is a source of power suppressed corrections.

There is also an ambiguity in the order in which the fragmentation of the heavy quark, and the boosting from the parton-parton center-of-mass to the lab frame is implemented. To see why this is so, one may compute, e.g. for the fragmentation choice $\vec{p}_H = z\vec{p}_Q$ with $m_H \simeq m_Q$, the difference in energy of a massive particle arising from the order of boosting

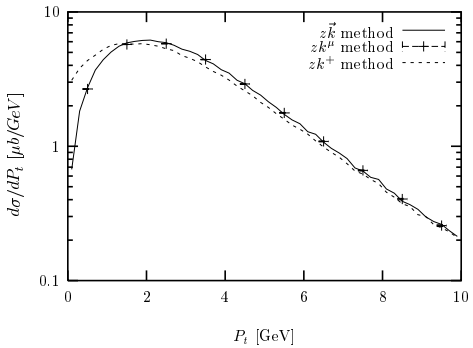

Figure 9.49: Effect of the different four-vector smearing methods on the P_T distribution of the B-meson.

(along z-axis with rapidity η) and fragmenting

$$\Delta E = \frac{m_Q^2}{2|\vec{p}_Q|}\sinh(\eta)\frac{1-z^2}{z} \tag{9.76}$$

for small $m_Q/|\vec{p}_Q|$.

The result of this non-commutativity (for the $\vec{p}_H = z\vec{p}_Q$ method) is shown in Figs. 9.50 and 9.51 for the pseudo-rapidity and transverse momentum distribution, respectively, of the $B-$meson. The interplay of such ambiguities with acceptance cuts is given in Table 9.23. For a transverse momentum above 5 GeV the effect is negligible.

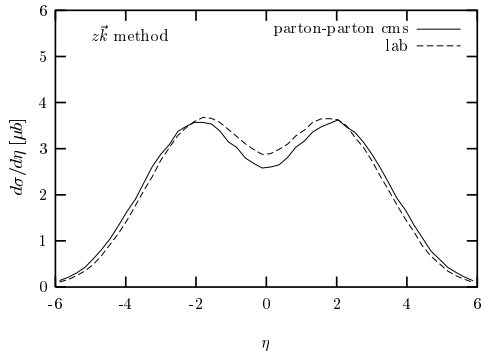

Figure 9.50: Commutativity of boosting and fragmenting for pseudo-rapidity distribution of the B-meson.

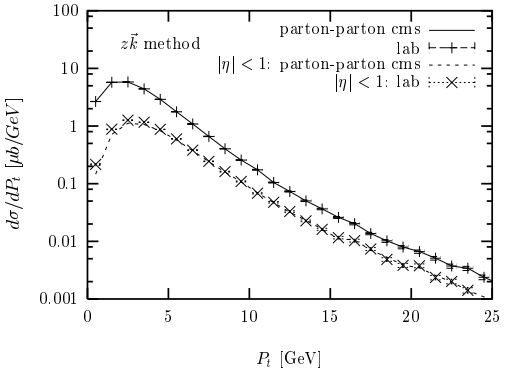

Figure 9.51: Commutativity of boosting and fragmenting for P_T distribution of the B-meson.

acceptance	$\sigma[\mu b]$ lab.	parton cms $\sigma[\mu b]$	difference
no cuts	26.24	26.24	-
$p_T > 0.5, \|\eta\| < 1.5$	9.66	8.87	8%
$p_T > 5, \|\eta\| < 1.5$	2.58	2.53	2%

Table 9.23: Interplay of boosting ambiguity with acceptance cuts.

9.5.5 Experimental impact†

In this section we shall try to address the extent to which fragmentation issues are relevant for heavy-quark studies at the Tevatron, specifically with respect to detector design and optimization.

The results from LEP and SLD on b fragmentation in e^+e^- collisions clearly indicate that the spectrum is harder than can be described by the standard Peterson *et al.* fragmentation function. This has little experimental impact other than in analyses which attempt to extract the b quark cross-section from the observed b hadron momentum spectrum. This could potentially have a small effect on the efficiency of 'same-side' tagging using the π from B^{**} decays. That is, a harder or softer fragmentation function will directly feed into the relation of this pion to the B from the decay.

There are some interesting correlations, both in b production and fragmentation, which feed, perhaps only weakly, into predictions of tagging efficiencies and strategies. The correlation of b and $\bar{b}$ directions in the forward and backward regions increases the "away-side" tagging power of a forward detector like BTeV since it implies that if one b is produced going forward (or backward) then most likely the other is also to be found in the same fiducial volume. On the other hand, 'same-side' tagging will be affected by the distribution of fragmentation particles produced along with the b hadron. This has been studied by

†Author: S. Menary

CDF who rely on data to extract efficiencies and tune the Monte Carlos.

The beam drag effect discussed in section 1.5.3 is potentially an issue for measurements in the very forward direction. The fact that BTeV is a two arm spectrometer can minimize this considerably since they can measure asymmetries in both the p and $\bar{p}$ arms and essentially subtract out the beam drag effect. In particular this can be done using very high statistics non-CP modes where an asymmetry is dominantly produced by this effect. This could be more problematic at LHCb which is a single arm spectrometer at a pp collider.

References

[1] P. Nason, S. Dawson and R. K. Ellis, Nucl. Phys. **B303**, 607 (1988).

[2] W. Beenakker, H. Kuijf, W. L. van Neerven and J. Smith, Phys. Rev. **D40**, 54 (1989).

[3] P. Nason, S. Dawson and R. K. Ellis, Nucl. Phys. **B327**, 49 (1989).

[4] W. Beenakker, W. L. van Neerven, R. Meng, G. A. Schuler and J. Smith, Nucl. Phys. **B351**, 507 (1991).

[5] M. L. Mangano, P. Nason and G. Ridolfi, Nucl. Phys. **B373**, 295 (1992).

[6] R. K. Ellis and D. A. Ross, Nucl. Phys. **B345**, 79 (1990).

[7] R. Bonciani, S. Catani, M. L. Mangano and P. Nason, Nucl. Phys. **B529**, 424 (1998) [hep-ph/9801375].

[8] S. Catani, M. Ciafaloni and F. Hautmann, Phys. Lett. **B242**, 97 (1990).

[9] J. C. Collins and R. K. Ellis, Nucl. Phys. **B360**, 3 (1991).

[10] S. Catani, M. Ciafaloni and F. Hautmann, Nucl. Phys. **B366**, 135 (1991).

[11] G. Camici and M. Ciafaloni, Phys. Lett. **B386**, 341 (1996) [hep-ph/9606427].

[12] G. Camici and M. Ciafaloni, Nucl. Phys. **B496**, 305 (1997) [hep-ph/9701303].

[13] S. P. Baranov and M. Smizanska, Phys. Rev. **D62**, 014012 (2000).

[14] R. D. Ball and R. K. Ellis, JHEP **0105**, 053 (2001) [hep-ph/0101199].

[15] E. L. Berger, B. W. Harris, D. E. Kaplan, Z. Sullivan, T. M. Tait and C. E. Wagner, hep-ph/0012001.

[16] DØ Collaboration, S. Abachi *et al.*, Phys. Rev. Lett. **74**, 3548 (1995).

[17] DØ Collaboration, Fermilab-PUB-99/144-E [hep-ex/9905024].

[18] CDF Collaboration, F. Abe *et al.* Phys. Rev. **D61**, 32001 (2000).

[19] S. Frixione, M. Mangano, Nucl. Phys. **B483**, 321 (1997).

[20] CDF Collaboration, F. Abe *et al.* Phys. Rev. **D53**, 1051 (1996).

[21] CDF Collaboration, F. Abe *et al.* Phys. Rev. Lett. **75**, 1451 (1995).

[22] M. Cacciari, M. Greco and P. Nason, JHEP **05**, 007 (1998) [hep-ph/9803400].

[23] CDF Collaboration, F. Abe *et al.*, Phys. Rev. Lett. **71** 500 (1993).

[24] P. Avery, K. Read, G. Trahern, Cornell Internal Note CSN-212 (1985) unpublished.

[25] F. Daghighian and D. Silverman, Phys. Rev. D **36**, 3401 (1987).

[26] E. Eichten, K. Gottfried, T. Kinoshita, K. D. Lane and T. M. Yan, Phys. Rev. D **21**, 203 (1980).

[27] E. Braaten, S. Fleming and A. K. Leibovich, hep-ph/0008091.

[28] G. P. Lepage *et al.*, Phys. Rev. D **46**, 4052 (1992).

[29] G. T. Bodwin, E. Braaten and G. P. Lepage, Phys. Rev. D **51**, 1125 (1995); erratum Phys. Rev. D **55**, 5853 (1997).

[30] F. Abe *et al.,* Phys. Rev. Lett. **79**, 572 (1997).

[31] F. Abe *et al.,* Phys. Rev. Lett. **79**, 578 (1997).

[32] P. Cho and A. K. Leibovich, Phys. Rev. **D53**, 6203 (1996); Phys. Rev. **D53**, 150 (1996).

[33] M. Beneke, M. Krämer, and M. Vänttinen, Phys. Rev. **D 57**, 4258 (1998).

[34] E. Braaten and J. Lee, Nucl. Phys. **B586**, 427 (2000).

[35] A. Petrelli et al., Nucl. Phys. **B514**, 245 (1998).

[36] F. Abe et al., Phys. Rev. Lett. **75**, 4358 (1995).

[37] J. L. Domenech and M. A. Sanchis-Lozano, Phys. Lett. **B476**, 65 (2000) [hep-ph/0012296].

[38] M. Cacciari, M. Greco, M.L. Mangano, and A. Petrelli, Phys. Lett. **B 356**, 553 (1995).

[39] B. A. Kniehl and G. Kramer, Eur. Phys. J. **C6**, 493 (1999); Phys. Rev. **D60**, 014006 (1999).

[40] A. Petrelli, hep-ph/9910274.

[41] E. Braaten, B. Kniehl and J. Lee, Phys. Rev. **D62**, 094005 (2000).

[42] M. A. Sanchis-Lozano and B. Cano-Coloma, Nucl. Phys. **B508**, 753 (1997).

[43] E. Braaten and T.C. Yuan, Phys. Rev. Lett. **71**, 1673 (1993).

[44] E. Braaten and S. Fleming, Phys. Rev. Lett. **74**, 3327 (1995).

[45] P. Cho and M. Wise, Phys. Lett. **B346**, 129 (1995).

[46] T. Affolder *et al.,* Phys. Rev. Lett. **85**, 2886 (2000).

[47] A. K. Leibovich, Phys. Rev. **D56**, 4412 (1997).

[48] M. Beneke and M. Kramer, Phys. Rev. **D55**, 5269 (1997).

[49] E. Braaten and J. Lee, hep-ph/0102130.

[50] E. Braaten, M.A. Doncheski, S. Fleming and M.L. Mangano, Phys. Lett. **B 333**, 548 (1994); M. Cacciari and M. Greco, Phys. Rev. Lett. **73**, 1586 (1994); D.P. Roy and K. Sridhar, Phys. Lett. **B339**, 141 (1994).

[51] M. Beneke and I. Z. Rothstein, Phys. Lett. **B372**, 157 (1996); **389**, 769(E) (1996).

[52] CDF Collaboration, F. Abe *et al.*, Phys. Rev. Lett. **81**, 2432 (1998); Phys. Rev. **D58**, 112004 (1998).

[53] S.S. Gershtein *et al.*, Sov. J. Nucl. Phys. **48**, 327 (1988).

[54] Y.-Q. Chen and Y. Kuang, Phys. Rev. **D 46**, 1165 (1992).

[55] V. V. Kiselev, A. K. Likhoded and A. V. Tkabladze, Phys. Rev. **D 51**, 3613 (1995).

[56] E. J. Eichten and C. Quigg, Phys. Rev. **D 49**, 5845 (1994).

[57] M. Baldicchi and G. M. Prosperi, Phys. Rev. **D 62**, 114024 (2000).

[58] W. Kwong and J.L. Rosner, Phys. Rev. **D 44**, 212 (1991).

[59] H. P. Shanahan, P. Boyle, C. T. Davies and H. Newton [UKQCD Collaboration], Phys. Lett. **B453**, 289 (1999).

[60] A.V. Berezhnoy, A.K. Likhoded, M.V. Shevlyagin, Yad. Fiz. **58**, 730 (1995); A.V. Berezhnoy, A.K. Likhoded, O.P. Yushenko, Yad. Fiz. **59**, 742 (1996); C.-H. Chang *et al.*, Phys. Lett. **B364**, 78 (1995); K. Kolodziej, A. Leike, R. Rückl, Phys. Lett. **B355**, 337 (1995); A.V. Berezhnoy, V.V. Kiselev, A.K. Likhoded, Z. Phys. **A356**, 79 (1996).

[61] J.D. Bjorken, 'Estimate of Decay Branching ratios for hadrons containing Charm and Bottom Quarks', draft report, 07/22/86 (1986) [unpublished]. (http://www-theory.fnal.gov/people/ellis/Bphysics/bjorken.PDF).

[62] M. Neubert, Phys. Rep. **245**, 259 (1994).

[63] I. Bigi, M. Shifman and N. Uraltsev, Ann. Rev. Nucl. Part. Sci. **47**, 591 (1997).

[64] G.T. Bodwin, E. Braaten, G.P. Lepage, Phys. Rev. **D51**, 1125 (1995); T. Mannel, G.A. Schuler, Z. Phys. **C67**, 159 (1995).

[65] M. Lusignoli, M. Masetti, Z. Phys. **C51**, 549 (1991); V.V. Kiselev, Mod. Phys. Lett. **A10**, 1049 (1995); V.V. Kiselev, Int. J. Mod. Phys. **A9**, 4987 (1994); V.V. Kiselev, A.K. Likhoded, A.V.Tkabladze, Yad. Fiz. **56**, 128 (1993); V.V. Kiselev, A.V. Tkabladze, Yad. Fiz. **48**, 536 (1988); G.R. Jibuti, Sh.M. Esakia, Yad. Fiz. **50**, 1065 (1989); Yad. Fiz. **51**, 1681 (1990); C.-H. Chang, Y.-Q. Chen, Phys. Rev. **D49**, 3399 (1994); D. Scora, N. Isgur, Phys. Rev. **D52**, 2783 (1995); A.Yu. Anisimov, I.M. Narodetskii, C. Semay, B. Silvestre–Bra, Phys. Lett. **B452**, 129

(1999);
A.Yu. Anisimov, P.Yu. Kulikov, I.M. Narodetsky, K.A. Ter-Martirosian, Phys. Atom. Nucl. **62**, 1739 (1999).

[66] P. Colangelo, G. Nardulli, N. Paver, Z. Phys. **C57**, 43 (1993);
E. Bagan *et al.*, Z. Phys. **C64**, 57 (1994).

[67] V.V. Kiselev, A.K. Likhoded, O.A. Onishchenko, Nucl. Phys. **B569**, 473 (2000);
V.V. Kiselev, A.K. Likhoded, A.E. Kovalsky, Nucl. Phys. **B585**, 353 (2000).

[68] V.V. Kiselev, A.V. Tkabladze, Phys. Rev. **D48**, 5208 (1993).

[69] I. Bigi, Phys. Lett. **B371**, 105 (1996);
M. Beneke, G. Buchalla, Phys. Rev. **D53**, 4991 (1996);
A.I. Onishchenko, hep-ph/9912424.

[70] C.-H. Chang, S.-L. Chen, T.-F. Feng and X.-Q. Li, Commun. Theor. Phys. **35**, 51 (2001) [hep-ph/0007162].

[71] C.-H. Chang, Y.-Q. Chen, G.-L. Wang and H.-Sh. Zong, hep-ph/010215, hep-ph/0103036.

[72] G. Chiladze, A.F. Falk, A.A. Petrov, Phys. Rev. **D60**, 034011 (1999);
C.H. Chang, J.P. Cheng, C.D. Lü, Phys. Lett. **B425**, 166 (1998);
T.M. Aliev, M. Savci, Phys. Lett. **B434**, 358 (1998); J. Phys. **G25**, 1205 (1999);
P. Colangelo, F. De Fazio, Mod. Phys. Lett. **A33**, 2303 (1999).

[73] M. Dugan and B. Grinstein, Phys. Lett. **B255**, 583 (1991);
M.A. Shifman, Nucl. Phys. **B388**, 346 (1992);
B. Blok, M. Shifman, Nucl. Phys. **B389**, 534 (1993).

[74] S.S. Gershtein *et al.*, hep-ph/9803433;
V.V. Kiselev, Phys. Lett. **B372**, 326 (1996) [hep-ph/9605451].

[75] O.N. Pakhomova, V.A. Saleev, Phys. Atom. Nucl. **63**, 1999 (2000).

[76] V.A. Saleev, hep-ph/0007352.

[77] D. Du, X. Li, Y. Yang, Phys. Lett. **B380**, 193 (1996);
S. Fajfer, D. Prelovsek, P. Singer, Phys. Rev. **D59**, 114003 (1999);
T.M. Aliev, M. Savci, Phys. Lett. **B480**, 97 (2000).

[78] M. Masetti, Phys. Lett. **B286**, 160 (1992);
Y.S. Dai, D.S. Du, Eur. Phys. J. **C9**, 557 (1999).

[79] C. Quigg, in Proc. of the Workshop on B Physics at Hadron Accelerators, Snowmass, Colorado, 1993, eds. P. McBride and C.S. Mishra [Fermilab, Batavia (1994)].

[80] S.S. Gershtein *et al.*, hep-ph/9803433.

[81] OPAL Collaboration, K. Ackerstaff *et al.*, Phys. Lett. **B420**, 157 (1998);
ALEPH Collaboration, R. Barate *et al.*, Phys. Lett. **B402**, 213 (1997);
DELPHI Collaboration, P. Abreu *et al.*, Phys. Lett. **B398**, 207 (1997).

[82] V.V. Kiselev, A.E. Kovalsky, A.K. Likhoded, hep-ph/0002127;
V.V. Kiselev, A.A. Likhoded, A.I. Onishchenko, Nucl. Phys. **B569**, 473 (2000);
A. Abd El-Hady, J.H. Munoz, J.P. Vary, hep-ph/9909406;
C.H. Chang, Y.Q. Chen, Phys. Rev. **D49** 3399 (1994).

[83] P. Avery *et al.*, MCFAST: A Fast Simulation Package for Detector Design Studies, FERMILAB-CONF-97-151, June 1997, to be published in the proceedings of Computing in High-energy Physics (CHEP 97), Berlin, Germany, 7-11 Apr. 1997.

[84] P. Grannis and A. Lucotte, 'Extending the sensitivity to $\sin 2\beta$ in the $B^0/\bar{B}^0$ system using a low p_t $J/\psi \to e^+e^-$ trigger at D0 for Run II', D0 Note 3596, 10 Feb. 1999.

[85] R. Akers *et al.*, Z. Phys. **C67**, 27 (1995);
R. Akers *et al.*, Phys. Lett. **B353**, 545 (1995).

[86] S.S. Gerstein *et al.*, Phys. Atom. Nucl. **63**, 274 (2000).

[87] V. V. Kiselev, A. K. Likhoded and A. I. Onishchenko, Phys. Rev. D **60**, 014007 (1999);
V.V. Kiselev, A.K. Likhoded, A.I. Onishchenko, Eur. Phys. J. **C16**, 461 (2000);
A.K. Likhoded, A.I. Onishchenko, hep-ph/9912425.

[88] A.I. Onishchenko, private communication;
X.-H. Guo, H.-Y. Jin, X.-Q. Li, Phys. Rev. **D58**, 114007 (1998).

[89] V. V. Kiselev, A. E. Kovalsky and A. K. Likhoded, Nucl. Phys. **B585**, 353 (2000).

[90] A. K. Likhoded and A. I. Onishchenko, hep-ph/9912425.

[91] V. V. Kiselev, A. K. Likhoded and A. I. Onishchenko, Eur. Phys. J. **C16**, 461 (2000) [hep-ph/9901224].

[92] V. V. Kiselev, A. K. Likhoded and A. I. Onishchenko, Phys. Rev. **D60**, 014007 (1999).

[93] A. I. Onishchenko, hep-ph/0006295.

[94] A. K. Likhoded, private communication, (25 Feb. 2000).

[95] CDF Collaboration, F. Abe *et al.*, Phys. Rev. Lett. **77**, 1439 (1996).

[96] M. J. Savage and R. P. Springer, Int. J. Mod. Phys. **A6**, 1701 (1991).

[97] B. Guberina, B. Melic and H. Stefancic, hep-ph/9911241.

[98] C. H. Chang, Y. Q. Chen and R. J. Oakes, Phys. Rev. **D54**, 4344 (1996).

[99] P. Nason, S. Dawson, R. K. Ellis, Nucl. Phys. **B327**, 49 (1988).

[100] C. Peterson *et al.*, Phys. Rev. **D27**, 105 (1983).

[101] Particle Data Group, Eur. Phys. J. **C15**, 1 (2000).

[102] W. Hao, V. Papadimitriou, internal CDF note 4884, March 1999, (unpublished).

[103] T. Keaffaber, Ph.D. Thesis, Purdue University, May 2000.

[104] C. H. Chang, Y. Q. Chen, Phys. Rev. **D49**, 3399 (1994).

[105] S. S. Gershtein *et al.*, "Physics of B_c mesons", Phys. Usp. **38**, 1 (1995).

[106] S. S. Gershtein *et al.*, "Theoretical Status of the B_c meson", hep-ph/9803433.

[107] V.V. Kiselev and A.K. Likhoded, these proceedings, section (9.3.3)

[108] F. Abe *et al.*, Phys. Rev. Lett. **77**, 5176 (1996).

[109] "Summary or B Physics Prospects with the CDF II Detector", CDF Collaboration, internal CDF note 5045, June 1999 (submitted to the Fermilab PAC).

[110] F. Abe *et al.*, Phys. Rev. Lett. **77**, 1945 (1996).

[111] J.D. Bjorken, 'Is the *ccc* a new deal for baryon spectroscopy', Fermilab-Conf-85/69.

[112] D. Ebert, R. N. Faustov, V. O. Galkin, A. P. Martynenko and V. A. Saleev, Z. Phys. **C76**, 111 (1997) [hep-ph/9607314].

[113] J. Richard, hep-ph/9407224.

[114] D. B. Lichtenberg, R. Roncaglia and E. Predazzi, Phys. Rev. D **53**, 6678 (1996) [hep-ph/9511461].

[115] S. Fleck and J. M. Richard, Prog. Theor. Phys. **82**, 760 (1989).

[116] D. U. Matrasulov, M. M. Musakhanov and T. Morii, Phys. Rev. C **61**, 045204 (2000) [hep-ph/0004147].

[117] M. A. Moinester, Z. Phys. **A355**, 349 (1996) [hep-ph/9506405].

[118] E. Bagan, M. Chabab and S. Narison, Phys. Lett. **B306**, 350 (1993).

[119] S. S. Gershtein, V. V. Kiselev, A. K. Likhoded and A. I. Onishchenko, Mod. Phys. Lett. **A14**, 135 (1999) [hep-ph/9807375].

[120] S. S. Gershtein, V. V. Kiselev, A. K. Likhoded and A. I. Onishchenko, Phys. Rev. **D62**, 054021 (2000).

[121] M. L. Stong, hep-ph/9505217.

[122] V. V. Kiselev and A. I. Onishchenko, Nucl. Phys. **B581**, 432 (2000) [hep-ph/9909337].

[123] M. A. Sanchis-Lozano, Nucl. Phys. **B440**, 251 (1995) [hep-ph/9502359].

[124] S.S. Gershtein, V.V. Kiselev, A.K. Likhoded, A.I. Onishchenko, Mod. Phys. Lett. **A14**, 135 (1999) [hep-ph/9807375];
Heavy Ion Phys. **9**, 133 (1999) [hep-ph/9811212].

[125] A. De Rujula, H. Georgi and S. L. Glashow, Phys. Rev. **D 12**, 147 (1975).

[126] J. C. Collins, D. E. Soper and G. Sterman, in: *Perturbative QCD*, ed. A. H. Mueller (World Scientific, 1989).

[127] J. C. Collins and D. E. Soper, Nucl. Phys. **B194**, 445 (1982).

[128] W. Furmanski and R. Petronzio, Phys. Lett. **97B**, 437 (1980).

[129] G. Curci, W. Furmanski, and R. Petronzio, Nucl. Phys. **B175**, 27 (1980).

[130] R. K. Ellis, W. J. Stirling and B. R. Webber, *QCD and collider physics, Cambridge, UK: Univ. Pr. (1996).*

[131] J. Binnewies, B. A. Kniehl, and G. Kramer, Z. Phys. **C65**, 471 (1995) [hep-ph/9407347].

[132] M. Greco and S. Rolli, Phys. Rev. **D52**, 3853 (1995), [hep-ph/9409356].

[133] B. A. Kniehl, G. Kramer and B. Potter, Nucl. Phys. **B582**, 514 (2000) [hep-ph/0010289].

[134] S. Kretzer, Phys. Rev. **D62**, 054001 (2000) [hep-ph/0003177].

[135] L. Bourhis, M. Fontannaz, J. P. Guillet and M. Werlen, hep-ph/0009101.

[136] C. Peterson, D. Schlatter, I. Schmitt, and P. Zerwas, Phys. Rev. **D27**, 105 (1983).

[137] A. V. Berezhnoy, V. V. Kiselev, and A. K. Likhoded, hep-ph/9901333.

[138] A. V. Berezhnoy, V. V. Kiselev, and A. K. Likhoded, hep-ph/9905555.

[139] P. Nason *et al.*, hep-ph/0003142.

[140] G. Altarelli and G. Parisi, Nucl. Phys. **B126**, 298 (1977).

[141] V. N. Gribov and L. N. Lipatov, Yad. Fiz. **15**, 781 (1972).

[142] Y. L. Dokshitzer, Sov. Phys. JETP **46**, 641 (1977).

[143] B. Mele and P. Nason, Nucl. Phys. **B361**, 626 (1991).

[144] E. Braaten, K. Cheung, S. Fleming, and T. C. Yuan, Phys. Rev. **D51**, 4819 (1995), [hep-ph/9409316].

[145] R. L. Jaffe and L. Randall, Nucl. Phys. **B412**, 79 (1994), [hep-ph/9306201].

[146] P. Nason and C. Oleari, Nucl. Phys. **B521**, 237 (1998), [hep-ph/9709360].

[147] G. Rodrigo, M. Bilenky, and A. Santamaria, Nucl. Phys. **B554**, 257 (1999), hep-ph/9905276.

[148] W. Bernreuther, A. Brandenburg, and P. Uwer, Phys. Rev. Lett. **79**, 189 (1997), [hep-ph/9703305].

[149] P. Nason and C. Oleari, Nucl. Phys. **B565**, 245 (2000), [hep-ph/9903541].

[150] ALEPH, D. Buskulic *et al.*, Phys. Lett. **B357**, 699 (1995).

[151] OPAL, R. Akers *et al.*, Z. Phys. **C67**, 27 (1995).

[152] ARGUS, H. Albrecht *et al.*, Z. Phys. **C52**, 353 (1991).

[153] SLD, K. Abe *et al.*, Phys. Rev. Lett. **84**, 4300 (2000), [hep-ex/9912058].

[154] M. Cacciari and M. Greco, Nucl. Phys. **B421**, 530 (1994), [hep-ph/9311260].

[155] M. Cacciari, M. Greco, and P. Nason, JHEP **05**, 007 (1998), [hep-ph/9803400].

[156] F. I. Olness, R. J. Scalise, and W.-K. Tung, Phys. Rev. **D59**, 014506 (1999), [hep-ph/9712494].

[157] M. Cacciari and M. Greco, Z. Phys. **C69**, 459 (1996), [hep-ph/9505419].

[158] M. Cacciari *et al.*, Nucl. Phys. **B466**, 173 (1996), [hep-ph/9512246].

[159] S. Frixione, M. L. Mangano, P. Nason, and G. Ridolfi, hep-ph/9702287, published in *Heavy Flavours II*, eds. A.J. Buras and M. Lindner, (World Scientific, Singapore).

[160] DELPHI, P. Abreu *et al.*, Z. Phys. **C57**, 181 (1993).

[161] OPAL, G. Alexander *et al.*, Phys. Lett. **B364**, 93 (1995).

[162] V. G. Kartvelishvili, A. K. Likhoded, and V. A. Petrov, Phys. Lett. **B78**, 615 (1978).

[163] P. D. B. Collins and T. P. Spiller, J. Phys. **G11**, 1289 (1985).

[164] B. W. Harris and J. Smith, Phys. Rev. **D57**, 2806 (1998), [hep-ph/9706334].

[165] S. Frixione, M. L. Mangano, P. Nason and G. Ridolfi, Nucl. Phys. **B412**, 225 (1994), [hep-ph/9306337].

[166] ZEUS, J. Breitweg *et al.*, Eur. Phys. J. **C12**, 35 (2000), [hep-ex/9908012].

[167] ZEUS, J. Breitweg *et al.*, Eur. Phys. J. **C6**, 67 (1999), [hep-ex/9807008].

[168] H1, C. Adloff *et al.*, Z. Phys. **C72**, 593 (1996), [hep-ex/9607012].

[169] E. Norrbin and T. Sjostrand, hep-ph/9905493.

[170] M. G. Bowler, Zeit. Phys. **C11**, 169 (1981).

[171] T. Sjostrand, Comput. Phys. Commun. **82**, 74 (1994).

[172] H. Jung, Comp. Phys. Commun. **86**, 147 (1995).

[173] B. Andersson, G. Gustafson, G. Ingelman, and T. Sjostrand, Phys. Rept. **97**, 31 (1983).

[174] WA82 Collaboration, M. Adamovich *et al.*, Phys. Lett. **B305** 402 (1993); WA92 Collaboration, M. Adamovich *et al.*, Nucl. Phys. **B495** 3 (1997); E769 Collaboration, G.A. Alves *et al.*, Phys. Rev. Lett. **72** 812 (1994); E791 Collaboration, E.M. Aitala *et al.*, Phys. Lett. **B371** 157 (1996).

[175] E. Norrbin and T. Sjostrand, Phys. Lett. **B442**, 407 (1998), [hep-ph/9809266].

[176] E. Norrbin and T. Sjostrand, Eur. Phys. J. C **17**, 137 (2000) [hep-ph/0005110].

Chapter 10

Summary and Highlights

During the coming decade a wide range of measurements in the production and decay of b flavored hadrons will be made at the Tevatron. In this chapter, we summarize the most important ones. Particularly in the decays, some observables are key to pinning down the flavor structure of the Standard Model and, possibly, uncovering new physics. Some are unique to the Tevatron, and some are expected to be competitive with measurements at the e^+e^- B factories. The Tevatron enjoys a few advantages that compensate for the clean environment in e^+e^- collisions. First, the $b\bar{b}$ production cross section is much higher at the Tevatron than at e^+e^- machines. Thus, despite the higher background rates at the Tevatron, it is possible to use selective triggers to obtain high statistics samples with good signal-to-noise ratio. Second, all b flavored hadrons are created (B_s, Λ_b, etc.), whereas an e^+e^- machine operating at the $\Upsilon(4S)$ resonance produces only $B^\pm$, $\overline{B}{}^0_d$ and B^0_d. Consequently, the B decay program at hadron colliders complements that at the e^+e^- B factories.

The CDF, DØ, and BTeV detectors and simulation tools used for this report are described in Chapters 2–5. Since Run I, both CDF and DØ have gone through major upgrades, and both will be much more powerful for doing B physics in Run II. Both detectors feature excellent charged particle tracking using solenoidal magnetic fields, and both have silicon (Si) vertex detectors capable of tracking in three dimensions. The magnetic field is 2 T at DØ and 1.4 T at CDF. DØ has a smaller radius tracking volume (50 cm), which allows for Si and scintillating fiber tracking out to $\eta = 1.6$, and Si disk tracking to $\eta = 3$. CDF has a larger tracking radius (140 cm), with full Si and drift chamber tracking out to $\eta = 1$, and Si-only tracking (to 30 cm radius) out to $\eta = 2$. DØ muon coverage extends to $\eta = 2$; CDF to $\eta = 1.5$. Both detectors have track based triggers at level-1 and Si vertex impact triggers at level-2. Because of the larger level-1 bandwidth (40 kHz) and the use of deadtimeless SVX3 chip readout, CDF can deploy a Si vertex hadronic decay trigger at level-2, which is directly sensitive to decays like $B \to \pi^+\pi^-$ and $B_s \to D_s^-\pi^+$. With a smaller level-1 bandwidth (10 kHz), DØ does not plan to implement such a strategy. CDF has two methods for particle ID — time-of-flight at low momentum ($p < 2\,\mathrm{GeV}/c$) and relativistic rise dE/dx for high momentum ($p > 2\,\mathrm{GeV}/c$); the latter is crucial for channels like $B \to \pi^+\pi^-$, where a statistical separation of $\pi\pi$ and $K\pi$ signals can be used. In summary, both CDF and DØ have comparable B physics reach; CDF has an advantage in particle ID and in Si vertex triggering.

BTeV is slated to run in earnest after Run II, following construction and some running during Run IIb. It will have competition from LHC-b at CERN, and from experiments at the e^+e^- B factories, which by then are expected deliver an order of magnitude higher luminosity than at present. BTeV is not a central detector (as are CDF and DØ), but a

two-arm forward spectrometer. The key features of its design are a silicon pixel detector, a flexible trigger based on detached vertices, particle ID with excellent K/π separation, and an electromagnetic calorimeter capable of identifying π^0's and photons.

In this workshop, simulations of the CDF, DØ and BTeV detectors have made common assumptions about production rates, branching ratios, and flavor tagging efficiencies. The common starting point is needed for comparing the reaches of the three detectors, but it is nevertheless difficult to make meaningful comparisons without Run II data. At hadron colliders all signal channels, as well as issues like flavor tagging, have backgrounds that will be detector dependent and that, in many cases, cannot be reliably predicted from a heavy flavor production Monte Carlo. These backgrounds affect both signal-to-background statistics and also the strategies used to reject background, which in turn affect signal yields. For example, for $B \to \pi^+\pi^-$, to reject the combinatorics from all sources of backgrounds, making harder cuts on the detachment of the secondary vertex and other quantities will affect both the statistical accuracy and the ability to separate the direct and mixing induced CP asymmetries. While CDF has Run I data on many channels and flavor tags, DØ and BTeV will need real data to understand fully the effects of backgrounds.

Most simulations carried out during this workshop considered an integrated luminosity of $2\,\mathrm{fb}^{-1}$, corresponding to Run IIa for DØ and CDF and to the first year of running for BTeV. Other workshops in this series, which focused on high p_T physics, considered also the potential for $10\,\mathrm{fb}^{-1}$ and $30\,\mathrm{fb}^{-1}$. In the case of B physics, the role of real data in optimizing event selection makes it difficult to make sensible estimates for such high luminosity until more experience is at hand.

The most important measurements at the Tevatron can be divided roughly into two categories. Some modes have a relatively simple theoretical interpretation, in the context of the Standard Model, either because hadronic uncertainties are under good control, or because loops, small CKM angles, or GIM effects suppress the Standard Model rate. These modes test the CKM mechanism and probe for non-CKM sources of CP and flavor violation. Other measurements are more sensitive to QCD in ways that are theoretically challenging. They do not (yet) probe flavor dynamics, but, clearly, better understanding of QCD in B physics can be reinvested in understanding the flavor sector. We therefore present two semi-prioritized lists labeled "tests of flavor and CP violation" and "test of QCD", but both labels should be construed loosely. Moreover, the composition of these lists is colored by our understanding during the course of the workshop. In the coming decade theoretical and experimental developments are likely to spur changes in the lists. Many other interesting observables, not discussed in this summary, are covered throughout Chapters 6–9.

Tests of flavor and CP violation

- $B^0_s - \overline{B}{}^0_s$ mixing: Both CDF and DØ can measure $x_s \lesssim 30$ from events with a semileptonic B_s decay. This covers some of the expected range $x_s \lesssim 45$. With nonleptonic modes, CDF can measure $x_s \lesssim$ 59–74, depending on assumptions, and BTeV $x_s \lesssim 75$. As soon as a 5σ observation of mixing is made, the statistical error of x_s is very small, about ± 0.14. In the Standard Model, x_s/x_d can be used to determine $|V_{ts}/V_{td}|$, relying on input from lattice QCD for the size of $SU(3)$ breaking.

- CP asymmetries in $B_s \to \psi\phi$, $\psi\eta^{(\prime)}$: These measure the relative phase between the amplitudes for $B_s^0 - \overline{B}_s^0$ mixing and $b \to c\bar{c}s$ decay, β_s. In the Standard Model $\sin 2\beta_s$ is a few percent, so observation of a large CP asymmetry would be a clear sign of new physics. The expected error at CDF is about 1.6 times that of $\sin 2\beta$, further diluted by the CP-odd contribution to the $\psi\phi$ final state. Although this CP-odd contribution is expected to be small, it can be avoided by using the decay modes $B_s \to \psi\eta^{(\prime)}$, which are pure CP-even. With its excellent photon detection, BTeV is well optimized to measure the asymmetries in these neutral modes.

- CP asymmetries in $B_s \to D_s^{\pm} K^{\mp}$: Combining the time dependent asymmetries in these four modes allows the cleanest determination of $\gamma - 2\beta_s$. These measurements must be carried out in the presence of the large Cabibbo allowed $B_s \to D_s\pi$ background. Combined with the measurement (or bound) on β_s, one obtains γ, one of the angles of the unitarity triangle. At the Tevatron, this measurement will probably be possible only at BTeV, with an expected precision of $\sigma(\gamma) \simeq 10^{\circ}$.

- CP asymmetries in $B_d \to \rho\pi$: These asymmetries seem to be the cleanest way to measure α, the angle at the apex of the unitarity triangle. Once enough events are available to isolate the $\Delta I = 3/2$ channel, it is possible to measure α without uncertainties from penguin amplitudes, which contribute only to $\Delta I = 1/2$. With its excellent electromagnetic calorimetry, BTeV should compete well with BaBar and Belle, on a similar time scale.

- CP asymmetry in $B_d \to \psi K_S$: These asymmetries measure the relative phase between the amplitudes for $B_d^0 - \overline{B}_d^0$ mixing and $b \to c\bar{c}s$ decay. In the Standard Model, this is the angle β of the unitarity triangle, and it is obtained with very small theoretical uncertainty. By the end of Run IIa, the CDF and DØ measurements may become competitive with BaBar and Belle. Based on $B \to J/\psi K_S$ only, DØ and CDF anticipate a precision on $\sin 2\beta$ in the range 0.04–0.05, with $2\,\mathrm{fb}^{-1}$.

- CP asymmetries in $B_{d,s} \to h_1^+ h_2^-$, $h_i = K$, π: The utility of these modes depends on how well the uncertainty from flavor $SU(3)$ breaking can be controlled. Data for these and other processes will tell us the range of such effects; the resulting Standard Model constraints could be quite stringent. A study by CDF shows that 20% effects from $SU(3)$ breaking lead to an uncertainty of only $\sim 3^{\circ}$ on γ, which is much smaller than CDF's expected statistical error with $2\,\mathrm{fb}^{-1}$ of $\sim 10^{\circ}$.

- Rare semileptonic and radiative decays, such as $B \to K^*\ell^+\ell^-$ or $B \to K^*\gamma$: Although the rate for $B \to K^*\gamma$ is higher, the Tevatron detectors will probably not compete with BaBar and Belle. In the case of $B \to K^*\ell^+\ell^-$, the high rate of a hadron machine is needed, and the lepton pair provides a good trigger. In $B \to K^*\ell^+\ell^-$ the forward-backward asymmetry is especially intriguing, because it is sensitive to short distance physics.

- Search for $B_{d,s} \to \ell^+\ell^-$: These flavor-changing neutral current processes are highly suppressed in the Standard Model. Limits on the rate constrain non-standard models, which often have other ways to mediate such decays. Late in Run II or at BTeV, it may be possible to observe a handful of events at the standard model rate.

- CP asymmetries in flavor specific final states: These can be used to measure the relative phase between the mass and width mixing amplitudes, analogous to $\mathrm{Re}\,(\epsilon_K)$ in the kaon sector. The most often cited example is semileptonic decays, but if this asymmetry is sufficiently large, it may be possible to detect it using fully reconstructed modes such as $B_s \to D_s^- \pi^+$. In the B system, the SM predicts the relative phase to be very small, but new physics could make these asymmetries measurable without pushing the measured value of $\sin 2\beta$ outside its expected range.

The most striking thing about this list is that the whole program, taken together, is much more interesting than any single measurement. Indeed, if one adds in measurements from the e^+e^- machines, the list becomes even more compelling. In the near future, BaBar, Belle, CDF, and DØ will measure $\sin 2\beta$ at the few percent level; the Tevatron measurement of x_s combined with the known value of x_d will determine $|V_{td}/V_{ts}|$; BaBar's and Belle's measurements of semileptonic decays will determine $|V_{ub}/V_{cb}|$. Apart from $\sin 2\beta$, some input from hadronic physics is needed, but the combination of these results will still test the unitarity of the CKM matrix below the 10% level.

Tests of QCD

- B_s width difference $\Delta\Gamma_s$: The theoretical prediction of $\Delta\Gamma_s$ requires hadronic matrix elements of two four-quark operators, so it relies on lattice QCD calculations to a greater extent than x_s. It is still an interesting measurement, especially if it is smaller than expected in the Standard Model.

- Λ_b lifetime: The measured value of the Λ_b lifetime does not agree with theoretical expectations. It is important to improve the measurements with fully reconstructed hadronic decays. If the discrepancy remains, it would presumably imply a failure of the operator product expansion employed in inclusive decays and lifetimes, and one would have to reconcile the failure here with success for other lifetimes and for inclusive semileptonic decay distributions.

- Semileptonic form factors: The q^2 dependence of the decay distribution for $\Lambda_b \to \Lambda_c \ell \overline{\nu}$, $B \to K^{(*)}\ell^+\ell^-$, etc., can be combined with theoretical information, potentially reducing the (theoretical) error on $|V_{cb}|$, $|V_{ub}|$, and $|V_{ts}|$.

- Quarkonium production and polarization: Run I data for charmonium production disagrees at large p_T with predictions from NRQCD. If the discrepancies persist, and are confirmed through bottomonium production, they would pose an important riddle. To make meaningful measurements, experiments must collect higher statistics, extend to higher p_T, cleanly separate states with different quantum numbers, and distinguish feed-down from direct production.

- $b\bar{b}$ production cross section: The cross section $\sigma(p_T > p_T^{\mathrm{min}})$ measured in Run I data is about twice the prediction from perturbative QCD. With all scales (m_b, $\sqrt{\hat{s}}$, p_T) much larger than Λ_{QCD}, perturbative QCD should be reliable. A variety of QCD effects have been studied, but do not seem to account for the excess. If the excess is confirmed (with much higher statistics) in Run II, one must ask whether something in the theory has gone awry, or whether a non-standard mechanism produces $b\bar{b}$ events.

- Spectra of B_c and other doubly heavy hadrons: CDF's B_c mass and lifetime measurements from Run I will be improved. Fully reconstructed nonleptonic decays are needed to obtain a good measurement of the mass, which can be compared to calculations based on potential models or from lattice QCD. Because there are now two heavy quarks, the lifetimes and decay widths of B_c and other doubly heavy hadrons provide novel tests of the theory.

Each of these is interesting for its interaction with QCD theory, and, at least for the next several years, each can be studied only at the Tevatron.

In conclusion, one sees that B physics at the Tevatron will produce a program of many interesting and, in some cases, essential measurements. In the case of B decay measurements, the information gained is competitive with and complementary to that gained from experiments in e^+e^- accelerators at the $\Upsilon(4S)$. Indeed, the full suite of measurements from B_u, B_d, and B_s decays is much more interesting than any one or two measurements taken in isolation.

Index

a
  definition, 20
$A_{CP}^{\rm dir}$ and $A_{CP}^{\rm mix}$ definitions, 24
$A_{\Delta\Gamma}$
  and untagged decay, 359
  definition, 23
D(tagging dilution), 83
ϵD^2 (tagging power), 83
η (psuedo-rapidity)
  β vs η, 78
  coverage of detectors, 76
  definition of, 75
λ_f
  $\mathrm{Im}\,\lambda_f \neq 0$, 27
  $|\lambda_f| \neq 1$, 26
  definition, 21
$|\Delta B| = 2$ transition, 18
e^+e^- machines
  comparison with, 94
q/p, 20
y (rapidity)
  definition of, 75

absorptive part, 27, 57
anomalous fermion couplings, 273
anomalous triple gauge boson couplings, 272
anti-unitary transformation, 16, 17

$B \to X_s\ell^+\ell^-$, 246
  $Q\bar{Q}$ background, DØ, 282
  charmonium resonances, 249
  convergence of OPE, 250
  decay amplitude, 246
  dimuon mass spectrum, DØ, 283
  event rates, DØ, 283
  forward-backward asymmetry, 248
  intended approach, BTeV, 300
  SM prediction, 246
$B \to \ell^+\ell^-$, 268
  branching ratio, 269
  event rates, CDF, 294
  event rates, DØ, 285
  SM prediction, 270
$B \to D^{(*)}\ell\bar{\nu}$, 304
  Q^2 reconstruction, BTeV, 319
  Q^2 resolution, BTeV, 319
  background rates, BTeV, 317
  event rates, BTeV, 318
$B \to K\ell^+\ell^-$, 254
  CP asymmetries, 265
  analysis cuts, BTeV, 299
  backgrounds, BTeV, 300
  event rates, BTeV, 300
  form factors, 251
  in large energy limit, 257
$B \to K^*\ell^+\ell^-$, 254
  CP asymmetries, 265
  analysis cuts, BTeV, 296
  analysis cuts, DØ, 280
  angular distribution, 262
  backgrounds, BTeV, 295, 297
  charmonium resonances, 260
  event rates, BTeV, 297
  event rates, CDF, 288
  event rates, DØ, 281
  form factors, defined, 252
  forward-backward asymmetry, 263
  forward-backward asymmetry, BTeV, 297
  forward-backward asymmetry, CDF, 289, 290
  forward-backward asymmetry, DØ, 282
  forward-backward asymmetry, zero-point extraction, CDF, 290
  in large energy limit, 257
  phase space, 278
  SM prediction, 260

  trigger strategy, CDF, 288
$B \to K^*\gamma$, 266
  event rates, CDF, 287
  form factors, defined, 252
  HQET prediction, 256
  measured branching fractions, 266
  trigger, CDF, 286
$B \to K_2^*(1430)\gamma$, 266
$B \to X_d\gamma$, 246
$B \to X_s\gamma$, 244
  decay amplitude, 244
  measured branching fraction, 245
  SM prediction, 245
$B \to \pi(\rho)\ell\bar{\nu}$, 306
$B \to \rho\gamma$, 267
  long distance contribution, 267
B decay
  nonleptonic, 44
  semileptonic, 41, 335, 379
B decays
  $B^0 \to D^-X$, 384
  $B^0 \to D^-\ell^+\nu$, 384, 426
  $B^0 \to D^-\pi^+\pi^+\pi^-$, 384
  $B^0 \to D^-\pi^+$, 26, 384
  $B^0 \to D^0K^-$, 191, 196, 210, 214, 233
  $B^0 \to D^\pm\pi^\mp$, 29
  $B^0 \to D^{(*)+}D^{(*)-}$, 384, 385
  $B^0 \to D^{(*)}\ell\nu$, 60
  $B^0 \to D^{*-}X$, 384
  $B^0 \to D^{*-}\pi^+\pi^+\pi^-\pi^0$, 384
  $B^0 \to D^{*-}\pi^+\pi^+\pi^-$, 384
  $B^0 \to D^{*-}\pi^+$, 384
  $B^0 \to D^{*\pm}\pi^\mp$, 29
  $B^0 \to D_s^{(*)+}D_s^{(*)-}K_S$, 385
  $B^0 \to K\pi$, 151, 153, 171, 182, 233
  $B^0 \to KK$, 171
  $B^0 \to X\ell^+\nu$, 22, 26, 379, 384
  $B^0 \to \overline{D}^0\rho^0$, 384, 385
  $B^0 \to \overline{D}^{*0}\pi^+\pi^-$, 385
  $B^0 \to \overline{D}^{*0}\rho^0$, 384, 385
  $B^0 \to \overline{D}^0\pi^+\pi^-$, 385
  $B^0 \to \pi\ell\nu$, 60
  $B^0 \to \pi\pi$, 29, 150, 152, 168, 170, 171, 179, 181, 187, 188, 232, 379
  $B^0 \to \psi K^+\pi^-$, 384
  $B^0 \to \psi K_S\rho^0$, 385
  $B^0 \to \psi K_S$, 28, 59, 150, 157, 158, 160, 164, 168, 232, 370, 372, 379, 489
  $B^0 \to \psi\phi K^*$, 385
  $B^0 \to \psi\phi K_S$, 385
  $B^0 \to \psi\rho^0$, 385
  $B^0 \to \rho\pi$, 29, 152, 215, 217, 233
B meson
  CP transformation, 15
  decay constant f_B, 15
  mass difference Δm, 19, 20, 331, 352
    Δm_d, 352, 379
    Δm_s, 353, 382
    new physics, 379, 382
    SM prediction for Δm_s, 354
  width difference $\Delta\Gamma$, 19, 20, 354
    $\Delta\Gamma_s$ and branching ratios, 360, 362, 368
    $\Delta\Gamma_s$ and lifetimes, 362
    measurement of $\Delta\Gamma_d$, 370
    measurement of $\Delta\Gamma_s$, 358
    new physics, 363
    sign convention, 19
    SM prediction for $\Delta\Gamma_d$, 358
    SM prediction for $\Delta\Gamma_s$, 357
B mixing, 17–22, 352
  B^0 mixing, 352, 379
  B_s^0 mixing, 331, 353, 382
  new physics, 18
B_s^0 mixing, 138
  average significance, 394
  average significance in BTeV, 410, 413
  average significance in CDF, 401
  average significance in DØ, 404
  hadronic, 399
  K factor, 397
  mixing frequency, 394
  semileptonic, 396
b-jet
  p_t spectrum, 447
  production, 445, 447
b-quark production
  impact on experiments, 69
  Coulomb singularities, 443
  high energy behavior, 443

Run II, 451
Run II reach, 445
Sudakov logarithms, 443
theory, 441
threshold resummation, 443
via gluino decay, 445
bag constants, 342
B_{B_q}, 356
$B^S_{B_q}$, 356
baryons
doubly-heavy, 499
triply-heavy, 499
B_c decays
$B_c \to B_s^0 \pi^+$, 497
$B_c \to B_s^{(*)} \ell^+ \nu$, 485
$B_c \to B_s^{(*)} \pi^+$, 486
$B_c \to B_s^{(*)} \rho^+$, 486
$B_c \to \eta_c \ell^+ \nu$, 485
$B_c \to \eta_c \pi^+$, 486
$B_c \to \eta_c \rho^+$, 486
$B_c \to \psi \ell^+ \nu$, 485, 488, 498
$B_c \to \psi \pi^+$, 486, 488, 490, 492, 495
$B_c \to \psi \rho^+$, 486
B_c meson, 476
decay, 481
leptonic, 485
nonleptonic, 486
semileptonic, 485
lifetime, 482
mass, 477
production, 478
cross section, 480
reconstruction, 488
triggering, 488
$\overline{b}c$-system
spectroscopy, 477
beam drag, 520, 524
bottomonium
decay
$\eta_b(1S) \to \psi\psi$, 457
$\eta_b(1S)$, 456
polarization
CDF, 473
production, 454
B_s^0 decays
$B_s^0 \to \psi\eta^{(\prime)}$, 221, 225, 230, 233
$B_s^0 \to D^{(*)+} D^{(*)-}$, 385
$B_s^0 \to D_s^- K^+$, 147, 190, 193, 203, 214, 233
$B_s^0 \to D_s^- \ell^+ \nu$, 384, 397, 403
$B_s^0 \to D_s^- \pi^+ \pi^+ \pi^- \pi^0$, 384
$B_s^0 \to D_s^- \pi^+ \pi^+ \pi^-$, 370, 384, 387, 403, 414, 429
$B_s^0 \to D_s^- \pi^+$, 22, 26, 194, 359, 364, 370, 384, 387, 394, 403, 406, 414, 418, 422, 429
$B_s^0 \to D_s^\pm K^\mp$, 29
$B_s^0 \to D_s^{(*)+} D_s^{(*)-}$, 24, 155, 355, 361, 364, 367, 368, 372, 384, 385, 387, 416
CP-odd fraction, 368, 372
$B_s^0 \to D_s^{*-} \pi^+ \pi^+ \pi^- \pi^0$, 384
$B_s^0 \to D_s^{*-} \pi^+ \pi^+ \pi^-$, 370, 384
$B_s^0 \to D_s^{*-} \pi^+$, 370, 384
$B_s^0 \to KK$, 182, 188, 361, 362
$B_s^0 \to K\pi$, 233
$B_s^0 \to X \ell^+ \nu$, 22, 364, 370, 384
$B_s^0 \to \chi_{c0} \phi$, 385, 425
$B_s^0 \to \overline{D}^{(*)0} K_S$, 384, 385
$B_s^0 \to \pi\pi$, 171
$B_s^0 \to \psi K^- \pi^+$, 384
$B_s^0 \to \psi K^{(*)} \overline{K}^{(*)}$, 385, 403
$B_s^0 \to \psi K_S \pi^0$, 385
$B_s^0 \to \psi K_S$, 145, 385
$B_s^0 \to \psi K^{*0}$, 408
$B_s^0 \to \psi\eta^{(\prime)}$, 385, 418, 422
$B_s^0 \to \psi\phi\phi$, 385
$B_s^0 \to \psi\phi$, 145, 155, 158, 367, 368, 372, 385, 415, 418, 427
$B_s^0 \to \psi f_0$, 385, 425
BTeV
$B^0 \to D^0 K^-$ prospects, 210
$B^0 \to \pi\pi$ prospects, 181
$B^0 \to \rho\pi$ prospects, 217, 220
$B_s^0 \to \psi\eta^{(\prime)}$ prospects, 225
$B_s^0 \to D_s^- K^+$ prospects, 203
B_s^0 mixing, 406
$\sin 2\beta$ prospects, 164, 167
$\sin 2\beta_s$ prospects, 225, 230
$\sin\gamma$ prospects, 203, 208

detector, 121
charged particle identification, 126
data acquisition system, 128
detached vertex trigger, 125
electromagnetic calorimeter, 126
forward tracking system, 127
forward vs central, 121
key features, 122
muon detection, 128
pixel vertex detector, 123
RICH, 126
sketch, 122
flavor tagging, 131
away side combined, 132
away side vertex charge, 132
same and away combined, 133
away side kaon, 132
away side lepton, 131
same side, 133
presumed $b\overline{b}$ cross-section, 121
presumed luminosity, 121
schedule, 133
software
analysis tools, 128
calorimeter clustering, 130
RICH simulation, 130
simulation tools, 128
tracking, 129
trigger simulation, 130

Cabibbo-Kobayashi-Maskawa matrix
V_{cb}, 304
V_{td}, 57, 58, 352
V_{ts}, 57, 58, 353
V_{ub}, 379
CDF
$B^0 \to D^0 K^-$ prospects, 196
$B^0 \to \pi\pi$ prospects, 170
$B_s^0 \to \psi\eta^{(\prime)}$ prospects, 221
$B_s^0 \to D_s^- K^+$ prospects, 193
B_s^0 mixing, 393
Υ polarization, 473
ψ polarization, 472
$\sin 2\beta$ prospects, 158
$\sin 2\beta_s$ prospects, 221
$\sin\gamma$ prospects, 170, 193
B_c, 491
Bgenerator, 386
calorimetry, 102
detector improvements, 99, 386
detector simulation, 109, 389
dimuon trigger, 159
flavor tagging, 159, 394
opposite side kaon, 395
same side kaon, 395
hadronic B decays, 202
hadronic trigger, 170, 202, 389
muon systems, 102
proper time resolution
hadronic, 399
semileptonic, 396
charge conjugation, 14, 16
charmonium
decay
$\chi_{cJ}(1P) \to \psi + \gamma$, 455
$\eta_c \to \phi\phi$, 456
$\eta_c(2S) \to \psi + \gamma$, 455
$h_c \to \psi\pi^0$, 455
$\eta_c(1S)$, 455
$\eta_c(2S)$, 455
$h_c(1P)$, 455
polarization
CDF, 472
production, 454
chromomagnetic energy of a heavy quark, 336
CKM angle
γ, 189, 191, 214
color evaporation model, 458
color octet model, 459
color singlet model, 458, 479
CP asymmetry
$\sin 2\beta$, 28
in B_s^0 decay, 144
in charged B decay, 23
in flavor-specific decay, 26, 371, 381
SM prediction, 372
interference type, 24
mixing-induced, 24
semileptonic, 26, 156, 371

time-dependent, 23, 28, 148, 155
time-integrated, 24, 155
CP conjugate state, 21
CP transformation
B meson, 15, 360, 361
Higgs boson, 16
quark currents, 15
vector boson, 16
CP violation
clean modes, 28, 29
complex couplings, 16
direct, 24, 26, 29
in $\Delta F = 1$ transitions, 29, 56
in decay, 24, 26, 141, 148, 174
kaon, 56
in mixing, 26, 140, 174
kaon, 55
in non-CP eigenstates, 29
indirect, 29
interference type, 24, 27, 141, 148
kaon, 55, 56, 59
kaon physics, 53
ϵ_K, 30, 55
ϵ_K constraint on $\overline{\rho}$,$\overline{\eta}$, 58, 59
ϵ'_K, 30, 55
semileptonic asymmetry, 53
Kobayashi-Maskawa mechanism, 7, 17
Standard Model, 16, 137
superweak, 30
T violation, 17
tagged decay, 141
untagged decay, 144
CPT theorem, 17
CPT transformation, 17
CPT violation
string theory, 17
CPT violation, 19
cross-sections
DØ measurement, 77
table of, 70

D meson
mass difference Δm_D, 377
new physics, 382
width difference $\Delta\Gamma_D$, 377
D mixing, 18, 377, 382
DØ
$B^0 \to \pi\pi$ prospects, 179
B_s^0 mixing, 402
ψ trigger, 430
$\sin 2\beta$ prospects, 160, 162
B_c, 488
flavor tagging, 164
DØ calorimetry, 113
DØ central fiber tracker, 111
DØ dielectron trigger, 118
DØ muon detector, 113
DØ muon trigger
Level 1
ψ event rates, 115
$Q\bar{Q}$ dimuon rates, 115
description, 114
efficiency for dimuon events, 115
notation, 114
trigger rates, 115
Level 2 and 3
description, 116
DØ Silicon Tracker Trigger, 116
efficiency, 118
impact parameter resolution, 116
prompt ψ separation, 118
DØ silicon vertex detector, 111
DØ trigger system, 113
decay amplitude, 21, 139
decay matrix Γ, 18
eigenvalues, 20
eigenvectors, 20
detector
desired properties, 87
central vs forward, 88
dilepton mass spectrum
$Q\bar{Q}$ production, 277
sequential decays, 278
trigger rates, DØ, 279
discrete ambiguity of CP phase, 372
dispersive part, 57
doubly-heavy baryon decays
$\Omega_{ccc}^{++}(ccc)$, 508
$\Omega_{cc}^{+}(ccs)$, 508
$\Omega_{bb}^{-}(bbs)$, 508

$\Omega_{bc}^{0}(bcs)$, 508
$\Xi_{cc}^{++}(ccu)$, 508
$\Xi_{bcc}^{+}(bcc)$, 508
$\Xi_{bc}^{+}(bcu)$, 508
$\Xi_{cc}^{+}(ccd)$, 508
$\Xi_{bb}^{-}(bbd)$, 508
$\Xi_{bbc}^{0}(bbc)$, 508
$\Xi_{bb}^{0}(bbu)$, 508
$\Xi_{bc}^{0}(bcd)$, 508
doubly-heavy baryons, 499
decays, 503
lifetimes, 503
observability, 505
production, 500
spectrum, 499

effective Hamiltonian, 242
Wilson coefficients defined, 242
for $B \to \ell^+\ell^-$, 268
renormalization group, 242, 244, 269
Wilson coefficients in SM, 242, 269
EM Calorimeter
BTeV, 126
overview of, 92
$\eta_b(1S)$, 456
$\eta_c(1S)$, 455
$\eta_c(2S)$, 455
event
cartoon of a typical, 72

FCNC transitions, 241
flavor tagging
BTeV, 131
CDF, 394
description of
away side, 83
overall strategy, 86
same side, 84
dilution (D), 83
motivation for, 82
power (ϵD^2), 83
flavor-specific, 22
decay modes, 352
fourth generation, 384
fragmentation, 508
color string model, 521
experimental impact, 528
heavy quark
e^+e^- collisions, 511
$p\bar{p}$ collisions, 514
ambiguities, 525
non-perturbative, 517
perturbative, 511
fragmentation function, 508
heavy quarks, 510
in HQET, 518
Peterson, 512, 517

gluino production, 445

hadronic parameter
B_{B_q}, 356
$B_{B_q}^S$, 356
$\hat{B}_B$, 37, 353
relation to B_{B_q}, 356
$\hat{B}_K$, 57
ξ, 354
f_{B^0}, 353
f_{B_s}, 353
and $SU(3)_F$ symmetry, 354
in lattice QCD, 50
Hamiltonian
$|\Delta B| = 1$, 32
$|\Delta B| = 2$, 35
$h_c(1P)$
$h_c \to \psi\pi^0$, 455
heavy baryons
$SU(3)$ antitriplet, 343
average decay rate, 347
matrix elements, 344
heavy quark expansion, 40–45
heavy quark symmetry, 37
Higgs sector, 275
strong dynamics, 275
HQET (heavy quark effective theory), 37–40
λ_1 and λ_2, 39, 43
constraints on semileptonic form factors, 303
flavor symmetry relations, 255
for lattice QCD, 51

in inclusive decays, 43
perturbative corrections, 303
spin symmetry relations, 255

inclusive weak decay rates
effective Lagrangian, 334
kinematical integrals, 337
operator product expansion, 333
Pauli interference, 335
semileptonic decay of charm, 341
spectator quark effects, 339
splitting for baryons, 346
theoretical predictions summary, 351
weak scattering, 335
interactions
mean rates of, 80
Poisson distribution of, 81

K decays
$K \to \pi\pi$, 54
$K^+ \to \pi^+\nu\bar{\nu}$, 58
$K_L \to \ell^\pm\nu\,\pi^\mp$, 53
$K_L \to \pi^0\nu\bar{\nu}$, 59
K mixing, 17, 53
kaon
q/p, 53
isospin, 54
mass difference Δm_K, 53
mass eigenstates, 53
rare decay, 58
width difference $\Delta\Gamma_K$, 53
kinetic energy of a heavy quark, 336

$\Lambda_b \to \Lambda\gamma$
event rate, CDF, 287
trigger strategy, CDF, 287
$\Lambda_b \to \Lambda_c\ell\bar{\nu}_\ell$, 304
Q^2 efficiency, CDF, 312
Q^2 reconstruction, BTeV, 319
Q^2 reconstruction, CDF, 312
Q^2 resolution, BTeV, 319
Q^2 resolution, CDF, 312
analysis cuts, CDF, 312
background from excited hadrons, 305
backgrounds, BTeV, 317, 320
backgrounds, CDF, 315
event rates, BTeV, 318
event rates, CDF, 312
trigger, CDF, 309
Λ_b decays
$\Lambda_b \to \Lambda_c^+\pi^-$, 389, 429
$\Lambda_b \to \Lambda_c^+\pi^-\pi^+\pi^-$, 389
$\Lambda_b \to \psi\Lambda$, 388, 429, 430
$\Lambda_b \to pD^0\pi^-$, 389, 429
large energy limit, 257
corrections, 258
zero in forward-backward asymmetry, 263
lattice QCD, 253
$B \to D^{(*)}\ell\bar{\nu}$, 304
$B \to \pi(\rho)\ell\bar{\nu}$, 306
lattice spacing effects
heavy quarks, 50–52
light quarks and gluons, 50
lattice spacing errors, 253
momentum dependent errors, 254
predictions for $B \to K^*\gamma$, 266
quenched approximation, 49
semileptonic decays, 304
sources of uncertainty, 253
unquenched f_B, 49
lifetime
B^+, 331
B^0, 331
B_s^0, 331
Λ_b, 331
b-flavored hadron, 331
at CDF, 426
hadronic triggers, 429
leptonic triggers, 428
at DØ, 430
experimental lifetime, 432
ratios, 428
light-cone sum rules, 259, 266
luminosity, 121
Lund string model, 521

mass difference Δm, 331, 352
Δm_d, 352, 379
new physics, 379
Δm_s, 138, 353, 382

new physics, 382
SM prediction, 354
mass eigenstates, 18, 138
mass matrix M, 18
eigenvalues, 20
eigenvectors, 20
mixing asymmetry, 22
mixing parameter
x, 24, 138
y, 24, 138
muon detection
BTeV, 128
overview of, 92

new physics
fourth generation, 384
in B_s^0 mixing, 154
left-right symmetry, 381
strong dynamics, 381
supersymmetry, 381
two-Higgs doublet model, 384
flavor-changing Higgs, 381, 384
nonleptonic weak interaction
QCD renormalization, 337
NRQCD (nonrelativistic QCD), 457, 479

OPE (operator product expansion), 31, 32, 482, 483
operator
$O_\pm$, 33
O_{1-2}, 33
O_{3-6}, 33
$O_{7-10}^{\rm ew}$, 34
O_7, 34
O_8, 33
O_{9-11}, 34
Q, 352
chromomagnetic, 33
current-current, 33
electroweak penguin, 34
magnetic, 34
QCD penguin, 33
semileptonic, 34

parity, 14, 16
particle identification
BTeV RICH, 126
overview, 90
Pauli interference, 483
penguins
in B decay, 148
in $B^0 \to \psi K_S$, 150
in $B^0 \to K\pi$, 153
in $B^0 \to \pi\pi$, 150
pollution, 148, 151, 168
phase
in decay matrix, 20
kaon, 57
in mass matrix, ϕ_M, 20, 21
kaon, 56
of CP violation in mixing, ϕ, 20, 357
kaon, 54, 55
SM prediction for ϕ_d and ϕ_s, 357
phase convention, 25
CKM matrix, 15
phase transformation
quark field, 15
pixel detector, 123
potential models, 482
production
b-quark, 441
proper decay time, 86
psuedo-rapidity (η)
β vs η, 78
coverage of detectors, 76
definition of, 75

QCD improved parton model, 442
quark models, 258
quark-hadron duality, 243
quarkonium
polarization, 468
CDF, 472, 473
production, 454, 457
spectroscopy, 454

rapidity (y)
definition of, 75
renormalization group, 33, 34
resummation, 444

Schrödinger equation, 18, 19

semileptonic decays
lepton-displaced track trigger, CDF, 310
muon identification, BTeV, 317
simulation method, CDF, 308
trigger strategy, CDF, 307
short distance cross section, 442, 479
spectator model, 483
strong phase shifts
from lattice QCD, 52
from perturbative QCD, 13
$SU(3)$, 256
breaking, 256
relations, 152, 178
summary
B_s^0 mixing projections, 413
lifetime projections, 432
width difference $\Delta\Gamma_s$ projections, 425
supersymmetry, 262, 381

Tevatron parameters, 70
time evolution
decay rate, 21
D meson, 378
untagged B, 23
time reversal, 14, 16
tracking system
BTeV, 127
required properties, 90
transversity angle, 415
triggering
B_c meson, 488
BTeV, 125
detached vertex, 125
overview of, 91
twist expansion, 243
two-Higgs doublet model, 381, 384
flavor-changing Higgs, 381, 384

unitarity triangle
and $B_d^0-\overline{B}_d^0$ mixing, 59, 331, 352
and $B_s^0-\overline{B}_s^0$ mixing, 59, 331
and V_{ub}, 59, 379
angle α, 379
angle β, 355, 379
angle β_s, 355
angle γ, 355
kaon physics, 58, 59
untagged B
branching ratio, 23
two-exponential decay, 359, 365, 368, 369
Υ
polarization
CDF, 473
production, 454

vertex detector
BTeV pixel, 123
desired properties, 89

width difference $\Delta\Gamma$, 354
B_s^0, 45, 138, 155
$\Delta\Gamma_{CP}$, 422
measurement of $\Delta\Gamma_d$, 370
measurement of $\Delta\Gamma_s$, 358
at BTeV, 418
at CDF, 414, 418
branching ratios, 360, 368
effect of vertex trigger, 421
lifetimes, 362
sensitivity, 422
summary, 425
new physics, 363
SM prediction for $\Delta\Gamma_d$, 358
SM prediction for $\Delta\Gamma_s$, 357
Wigner-Weisskopf approximation, 19
Wilson coefficient, 32, 34, 352
$|\Delta B| = 2$, 37
table, 36
Wolfenstein parameters
for $V_{cd}V_{cb}^*$, 355
for $V_{cs}V_{cb}^*$, 355
for V_{td}, 353
for $V_{td}V_{tb}^*$, 355
for V_{ts}, 353
for $V_{ts}V_{tb}^*$, 355
for $V_{ud}V_{ub}^*$, 355
for $V_{us}V_{ub}^*$, 355